

AD-A114 893

AMERICAN INST OF PHYSICS NEW YORK  
LOW ENERGY X-RAY DIAGNOSTICS - 1981.(U)  
1981 D T ATTWOOD; B L HENKE

F/G 14/2

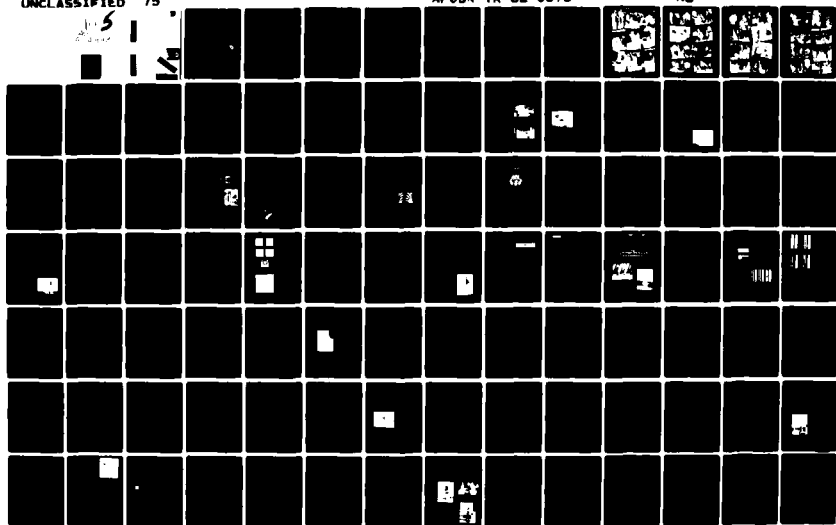
UNCLASSIFIED

75

AFOSR-TR-82-0378

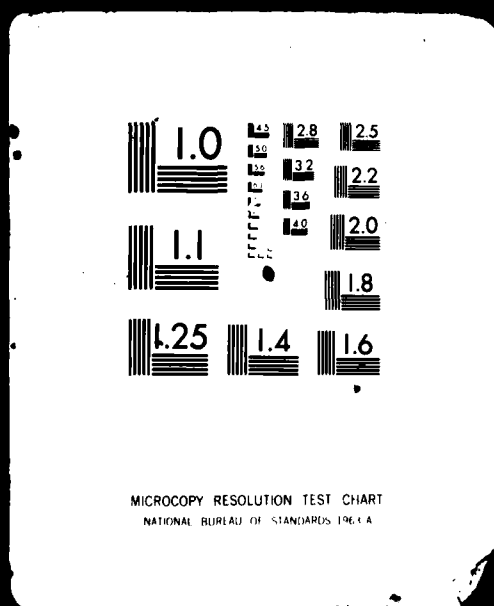
AFOSR-ISSA-81-00024

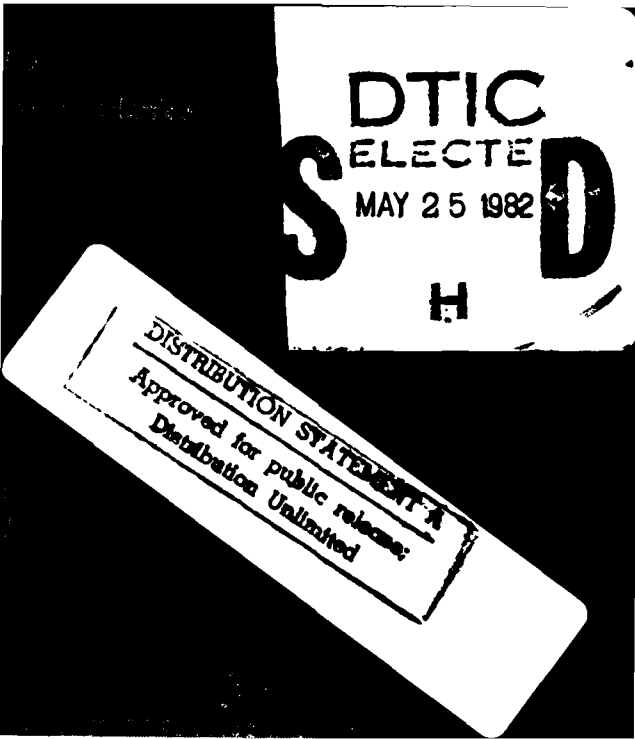
NL



# ASSIFIED

1 OF 5  
AD  
A114893





DTIC

ELECTE

MAY 25 1982

S

D

H

DISTRIBUTION STATEMENT A

Approved for public release;  
Distribution Unlimited

REPORT DOCUMENTATION PAGE		READ THIS FIRST REPORT DOCUMENTATION FORM
1. REPORT NUMBER <b>AFOSR-TR- 82-0378</b>	2. GOVT ACCESSION NO. <b>A114 893</b>	3. REPORT DOCUMENTATION NUMBER
4. TITLE (and Subtitle)  <b>LOW ENERGY X-RAY DIAGNOSTICS - 1981</b>	5. TYPE OF REPORT & PERIOD COVERED <b>FINAL</b> <b>Feb 81 - 20 Sep 81</b>	6. PERFORMING ORG. REPORT NUMBER
7. AUTHOR(s)  <b>D. T. Attwood and B. L. Henke</b>	8. CONTRACT OR GRANT NUMBER(s)  <b>AFOSR-1551-81-00024</b>	
9. PERFORMING ORGANIZATION NAME AND ADDRESS <b>Department of Energy        Lawrence Livermore National Laboratory        Livermore, CA 94550</b>	10. PROGRAM ELEMENT, PROJECT, TASK AREA & WORK UNIT NUMBERS  <b>5.102F        2801/A*</b>	
11. CONTROLLING OFFICE NAME AND ADDRESS <b>AFOSR/NP        Bolling AFB, Building 410        Washington, DC 20332</b>	12. REPORT DATE  <b>1981</b>	13. NUMBER OF PAGES <b>304</b>
14. MONITORING AGENCY NAME & ADDRESS (if different from Controlling Office)	15. SECURITY CLASS. (of this report)  <b>UNCLASSIFIED</b>	16. SECURITY CLASSIFICATION TO BE GRADING SCHEDULE
16. DISTRIBUTION STATEMENT (of this Report)  <b>Approved for public release; distribution unlimited</b>		
17. DISTRIBUTION STATEMENT (of the abstract entered in blocks 20, 21, and 22, if different from 16)		
18. SUPPLEMENTARY NOTES  <b>AIP CONFERENCE PROCEEDINGS, No. 75, 1981</b>		
19. KEY WORDS (Continue on reverse side if necessary and identify by block number)		
20. ABSTRACT (Continue on reverse side if necessary and identify by block number) At a time when technical calendars are overcrowded and the explosion of information is overwhelming, one requires a particularly strong motivation to organize a new scientific meeting. The motivation here is that the field associated with sub-kilovolt x-ray measurement is undergoing a renaissance, driven by new applications and new capabilities. The pressure for advancement comes from studies of hot, dense matter on the one hand, and from an interest in characterizing sub-micron electronic and biologic materials on the other.		

**DTIC  
 COLLECTED  
 MAY 25 1982  
 H**

The new capabilities are provided by long sought advances in the field of "x-ray optics": new sources, new detectors, and new components for the manipulation of x-rays. For instance, it is now possible to fabricate structures having characteristic dimensions on the scale of x-ray wavelengths, 10-100Å, permitting the pursuit of diffraction limited applications on a scale heretofore unattainable. The purpose of this meeting was to bring together the major participants in the field, many of whom would meet for the first time, so that new ideas, new collaborations, and the exchange of technological capabilities would enhance progress for all. The style of the meeting was planned to be informal and unhurried, so as to encourage the largest transfer of information and the germination of these new collaborations.

DTIC  
COPY  
INSPECTED  
2

Accession For	
NTIS GRA&I	<input checked="" type="checkbox"/>
DTIC TAB	<input type="checkbox"/>
Unannounced	<input type="checkbox"/>
Justification	
By _____	
Distribution/	
Availability Codes	
Dist	Avail and/or Special
A	

**AEOSR-TR- 82-0378**

**Approved for public release,  
distribution unlimited.**

**Low Energy X-ray Diagnostics—1981**  
(Monterey)

**AIP Conference Proceedings**  
Series Editor: Hugh C. Wolfe  
Number 75

**Low Energy X-ray Diagnostics—1981**  
(Monterey)

Edited by  
**David T. Attwood**  
Lawrence Livermore National Laboratory  
**Burton L. Henke**  
University of Hawaii

**American Institute of Physics**  
**New York**

**1981**



Copying fees: The code at the bottom of the first page of each article in this volume gives the fee for each copy of the article made beyond the free copying permitted under the 1978 US Copyright Law. (See also the statement following "Copyright" below). This fee can be paid to the American Institute of Physics through the Copyright Clearance Center, Inc., Box 765, Schenectady, N.Y. 12301.

Copyright © 1981 American Institute of Physics

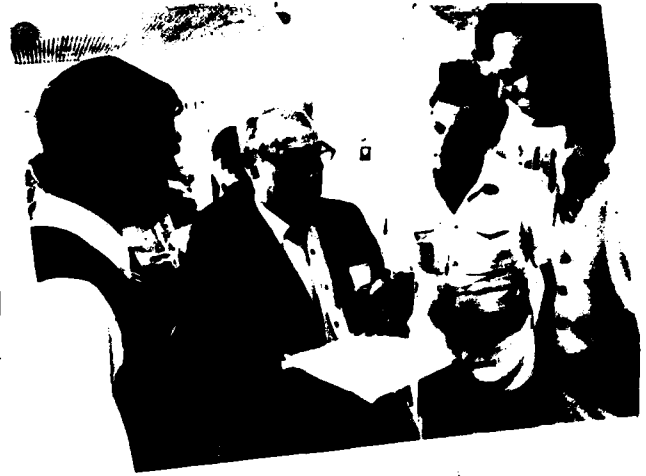
Individual readers of this volume and non-profit libraries, acting for them, are permitted to make fair use of the material in it, such as copying an article for use in teaching or research. Permission is granted to quote from this volume in scientific work with the customary acknowledgment of the source. To reprint a figure, table or other excerpt requires the consent of one of the original authors and notification to AIP. Republication or systematic or multiple reproduction of any material in this volume is permitted only under license from AIP. Address inquiries to Series Editor, AIP Conference Proceedings, AIP.

L.C. Catalog Card No. 81-69841  
ISBN 0-88318-174-6  
DOE CONF. 810651

PHOTOGRAPH IDENTIFICATIONS

1. Richard Sigel of West Germany and David Attwood.
2. Elisabeth Källne and Ingolf Lindau.
3. Emmett Leith, Natale Ceglie, and Henry Smith (l. to r.). In the rear is Erik Diets.
4. Steven Manson, center
5. Albert Franks (l.) and William Friedhorsky (center).
6. Paul Kirkpatrick during his historical review.
7. Session Chairman Ralph Wuerker.
8. David Fehl of Sandia (l.), Robert Carmen of Los Alamos (c.), and Nancy Kerr Del Grande of Livermore.
9. Session Chairman Arthur Toor.
10. Eberhard Spiller, Troy Barbee, and Victor Rehn.
11. Nat Ceglie, Emmett Leith, Barukh Yaakobi, and Andrew Hawryluk.
12. Thesis advisor Paul Kirkpatrick (c.) discussing issue of the day with former student Ralph Wuerker (l.).
13. Victor Rehn, Henry Smith, and Troy Barbee.
14. Elisabeth Källne and Robert Madden.
15. Harry Kornblum and Richard Sigel.
16. Albert Franks, Troy and Wendy Barbee.
17. Graduate students Tina Tanaka (U. Hawaii), Julie Kananui (U.C. Davis), Andy Hawryluk (MIT), Alan Rosenbluth (Rochester), Gary Stone (RIT), Gary Stradling (U.C. Davis), David Gaines (BYU), Ray Perkins (BYU), and Johnny Peterson (BYU).
18. Paul Kirkpatrick and Emmett Leith.
19. Emmett Leith (r.) with Kevin and David Attwood.
20. Albert Franks and Victor Rehn.
21. Paul Kirkpatrick and Albert Franks.
22. Hal Ahlstrom, Mark Roth, Julie Kananui, and Andy Hawryluk.
23. Nat Ceglie and Paul Kirkpatrick.
24. Roman Tatchyn and Jim Underwood.
25. The French Delegation.
26. Peter Lyons and George Charatis.
27. Bill Slivinsky, Martin Zombeck, and Paul Kirkpatrick.
28. Andy Hawryluk, Mark Roth, Nat Ceglie, Emmett Leith, Hank Smith, Grace Ceglie, and Barukh Yaakobi.
29. Left to right, Jim Wobser, Ching Wang, Bob Kuckuck, Art Toor, Hal Mallet, and Tom Harper.
30. Bob Kauffman, Dick Lee of Imperial College (London), and Steve Lane.
31. Emmett Leith, Paul Kirkpatrick, and Nat Ceglie.
32. Hector Meddecki and David Attwood.
33. The Kauffmans and the Clarks.







26



27



28



29



30



31



32



33



## TABLE OF CONTENTS

### PREFACE

I. SUB-KILOVOLT SOURCES OF X-RAY EMISSION Session Chairman: Ingolf Lindau, Stanford University		
Storage Rings as Sources of Soft X-Ray Emission	R.P. Madden and S.C. Ebner	1
X-Ray Emission from Laser Fusion Targets	V.W. Slivinsky	6
Low Energy X-Ray Emission from Magnetic Fusion Plasmas	K.W. Hill, M. Bitter, D. Eames S. von Goeler, N.R. Sautoff, and E. Silver	8
Low Energy X-Ray Emission from Light Ion Targets	L.P. Mix, E.J.T. Burns, D.L. Fehl, D.L. Hanson, and D.J. Johnson	25
A New, Efficient Pulsed Plasma Soft X-Ray Source	G. Dahlbacka, S.M. Matthews, R. Stringfield, I. Roth, R. Cooper, B. Ecker, and H.M. Sze.	32
Sub-kilovolt X-Ray Emission from Imploding Wire Plasmas	John C. Riordan, J.S. Pearlman, M. Gersten and J.E. Rauch	35
II. DETECTORS FOR SUB-KILOVOLT RADIATION Session Chairman: Jerry Gaines, Lawrence Livermore National Laboratory		
Photoemission Measurements for Low Energy X-Ray Detector Applications	Robert H. Day	44
Time-Resolved X-Ray Diagnostics	P.B. Lyons	59
Quantitative Measurements Using Soft X-Ray Streak Cameras	R.L. Kauffman, G.L. Stradling, E.L. Pierce and Hector Medeckí	66
Area X-Ray Detectors	D.J. Nagel	74
Gas Scintillation Proportional Counters and Other Low-Energy X-ray Spectrophotometers	William H.-M. Ku and Robert Novick	78
III. SUB-KILOVOLT X-RAY SPECTROSCOPY Session Chairman: Kenneth Mitchell, Los Alamos National Laboratory		
Low Energy X-Ray Spectroscopy with Crystals and Multilayers	B.L. Henke*	85
Applications of Gratings in the Low Energy X-Ray Region	E. Källne	97
Soft X-Ray Instrumentation for Fusion Plasma Studies	N.J. Peacock	101
Spectrometric Properties of Crystals for Low Energy X-Ray Diagnostics	D.M. Barrus, R.L. Blake, H. Felthouser, E.E. Fenimore, and A.J. Burek	115
Evaporated Multilayer Dispersion Elements for Soft X-Rays	E. Spiller	124
Sputtered Layered Synthetic Microstructure (LSM) Dispersion Elements	Troy W. Barbee, Jr.	131
IV. ATOMIC SCATTERING COEFFICIENTS AND CALCULATIONS Session Chairman: Arthur Toor, Lawrence Livermore National Laboratory		
Low Energy X-Ray Interactions: Photoionization, Scattering, Specular and Bragg Reflection	B.L. Henke	146
Theory of Sub-keV Photoionization Cross Sections	Steven T. Manson	156

Focusing, Filtering, and Scattering of Soft X-Rays by Mirrors	V. Rehn	162
Synthetic Multilayers as Bragg Diffractors for X-Rays and Extreme Ultraviolet: Calculations of Performance	J.H. Underwood and T.W. Barbee, Jr.	170
<b>V. REFLECTIVE AND DIFFRACTIVE X-RAY IMAGING</b>		
Session Chairman: Paul Kirkpatrick, Stanford University		
The Metrology of X-Ray Optical Components	A. Franks	179
X-Ray Microscopy Using Grazing Incidence Reflection Optics	R.H. Price	189
Astrophysical Observations with High Resolution X-Ray Telescopes	M.V. Zombeck	200
The Impact of Microfabrication Technology on X-Ray Optics	N.M. Ceglio	210
Fabrication of Diffractive Optical Elements for X-Ray Diagnostics	H.I. Smith	223
X-Ray Microscopy Using Fresnel Zone Plates	G. Schmahl, D. Rudolph, and B. Niemann	225
<b>VI. COHERENCE, INTERFERENCE AND FUTURE POSSIBILITIES</b>		
Session Chairman: Ralph Wuerker, TRW		
Overview and Advances in X-Ray Laser Research	R.C. Elton	228
Anti-Stokes Scattering as an XUV Radiation Source	S.E. Harris et al	235
Some Applications of X-Ray Interferometry	D.P. Siddons	236
Optical Holography with Partially Coherent Radiation	E. Leith	242
<b>VII. POSTER PAPERS</b>		
Low Energy X-Ray Calibration Sources at the Lawrence Livermore National Laboratory	J.L. Gaines	246
Calculation of Spectra from Electron-Impact X-Ray Sources	D.B. Brown and D.J. Nagel	253
Studies of Radiation Conversion and Transport in a 0.53 $\mu\text{m}$ Laser Produced Gold Plasma	H. Nishimura, F. Matsuoka, M. Yagi, K. Yamada, H. Niki, T. Yamanaka, C. Yamanaka, G.H. McCall	261
Soft and Ultrasoft X-Ray Measurements of Air Force Weapons Laboratory Shiva Imploding Plasma Liner	J.H. Degnan and R.J. Sand, G.F. Kiuttu and D.M. Woodall	264
Laser Heated Gas-Jet - A Soft X-Ray Source	G. Charatis, D.C. Slater, F.J. Mayer, J.A. Tarvin, G.E. Busch, D.L. Matthews and L. Koppel	270
A Sensitometric Calibration of the RAR 2497 Film for the Low Energy X-Ray Region	E.R. Dietz, T.S. Durland, B.L. Henke and M.A. Tester	275
A Study of Bare X-Ray Diode Saturation Due to a High Fluence X-Ray Pulse	R.B. Spielman and J.P. Anthes	278
The Reflecting Properties of Soft X-Ray Multilayers	Alan E. Rosenbluth and J.M. Forsyth	280
Soft X-Ray Spectroscopy Using Thick Gold Transmission Gratings of 0.2 to 0.3 $\mu\text{m}$ Spatial Periods	A.M. Hawryluk, N.M. Ceglio, R.H. Price, J. Melngailis and Henry I. Smith	286
A Streaked, X-Ray Transmission Grating Spectrometer	N.M. Ceglio and M. Roth, A.M. Hawryluk	290



Streaked Spectrometry Using Multilayer X-Ray Interference Mirrors to Investigate Energy Transport in Laser Plasma Applications	G.L. Stradling, T.W. Barbee, Jr., B.L. Henke, E.M. Campbell and W.C. Mead	292
High Quality Fraunhofer Diffraction Spectra Taken at SSRL in the Soft X-Ray Range	R. Tatchyn, I. Lindau and M. Hecht et al	297
Canonically Blazed Transmission Gratings: Analysis and Modeling Results	R. Tatchyn and I. Lindau	301
Holographic X-Ray Gratings to be Produced at Synchrotron Radiation Facilities	P.L. Csonka and R. Tatchyn	304
Evaluation of Ultrasoft X-Ray Optics and Sources, and Detectors for High Resolution Molecular X-Ray Emission Spectroscopy	G. Andermann, R. Kim and F. Burkard	309
Low Energy X-Ray Spectrometer	Wayne R. Woodruff	314
Efficiencies of Bent Mica Crystal X-Ray Spectrometers	A.F. Clark	320
A New Method for Measuring Thin-Film Optical Constants Using Transmission Gratings in the Soft X-Ray Range	R. Tatchyn and I. Lindau	321
An Extended Maximization Technique for Measuring Optical Constants Using Transmission Gratings in the Soft X-Ray Range	R. Tatchyn and I. Lindau	323
Uranium Soft X-Ray Total Attenuation Coefficients	N. Kerr Del Grande and A.J. Oliver	326
Epoxy Replication for Wolter X-Ray Microscope Fabrication	W. Priedhorsky	332
Monochromatic X-Ray Images of X-Ray Emitting Sources	R.R. Whitlock and D.J. Nagel	334
Crossed-Crystal Imaging of X-Ray Sources	Benjamin S. Fraenkel	338
Ultrahigh-Spectral-Brightness Excimer Lasers as Pump Sources for Coherent Soft X-Ray Generation	H. Egger, H. Pummer, T. Scrinivasan, and C.K. Rhodes	339
APPENDIX: The Atomic Scattering Factor, $f_1 + if_2$ , for 94 Elements and for the 100 to 2000 eV Photon Energy Region	B.L. Henke, P. Lee, T.J. Tanaka, R.L. Shimabukuro and B.K. Fujikawa	340
List of Attendees		389

## PREFACE

At a time when technical calendars are overcrowded and the explosion of information is overwhelming, one requires a particularly strong motivation to organize a new scientific meeting. The motivation here is that the field associated with sub-kilovolt x-ray measurement is undergoing a renaissance, driven by new applications and new capabilities. The pressure for advancement comes from studies of hot, dense matter on one hand, and from an interest in characterizing sub-micron electronic and biological entities on the other. The new capabilities are provided by long sought advances in the field of "x-ray optics": new sources, new detectors, and new components for the manipulation of x-rays. For instance, it is now possible to fabricate structures having characteristic dimensions on the scale of x-ray wavelengths, 10-100 Å, permitting the pursuit of diffraction limited applications on a scale heretofore unattainable. The purpose of this meeting was to bring together the major participants in the field, many of whom would meet for the first time, so that new ideas, new collaborations, and the exchange of technological capabilities would enhance progress for all. The style of the meeting was planned to be informal and unhurried, so as to encourage the largest transfer of information and the germination of these new collaborations.

Applications of interest to the participants included the study of matter at high temperature, plasmas radiating in the soft x-ray regime, as encountered in the magnetic and laser fusion programs, as well as in x-ray astronomy. Other areas of interest, attracted by the short wavelength, included x-ray lithography for replicating sub-micron electronic structures, and imaging at sub-micron resolution for biological and other applications. New capabilities described included the ability to construct multilayer coatings with spatial periods of several tens of angstroms, and an evergrowing list of materials that could be engineered for use in x-ray interference mirrors and splitters. Near normal incidence x-ray mirrors were reported for the first time. Zone plate lenses and transmission gratings were reported with smallest features approaching 1000 Å. The outlook for extending this capability to smaller features appears promising. These advances all permit the manipulation of x-rays with increasing efficiency and ease, moving towards the capabilities we now enjoy in the visible portion of the spectrum. Advancements were also reported on the availability of intense broadband sources of sub-kilovolt radiation, as well as prospects for future, high spectral purity, XUV sources, which are being actively pursued with coherent and quasi-coherent upconversion techniques. Progress was also reported on the quantitative understanding of conventional, and more sensitive, photoelectric detectors. Time resolved detection in the picosecond regime was also described.

As we began looking to the future in our last session, we were quite fortunate to benefit first from the historical perspective provided by Dr. Paul Kirkpatrick, Professor Emeritus of Physics at Stanford University, and a significant contributor in the early, formative years of x-ray optics. His lively presentation was greatly appreciated and thoroughly enjoyed by all. He reviewed the evolution of the field, citing historically important works and insights, and the potential for growth provided by recent developments. Discussions of work within his own group at Stanford, including warm recollections of collaborations with Albert Baez were particularly interesting. We had hoped that Baez would also participate, but unfortunately he had previously made a long term overseas commitment that prevented him from attending. His best wishes were appreciated.

Professor Kirkpatrick provided an historically valuable copy of an earlier conference proceedings,<sup>1</sup> the first ever on x-ray astronomy, organized in 1960 by Baez while at the Smithsonian Observatory in Cambridge. That document now resides in the American Institute of Physics' Neils Bohr Library in New York.

Looking to the future, several areas stand out where considerable progress would be beneficial. One, of course, is the further development of spatially and temporally coherent sources in the XUV and soft x-ray regimes. Another is the development of more efficient x-ray lenses. As reported at the conference, there is innovative work just getting underway with regard to the development of charge coupled devices (CCD's), which are two-dimensional arrays of computer compatible electronic wells, capable of single photon counting. On the other hand, however, there is great need for improvements in continuous, high speed, high resolution recording media. Such developments could greatly affect present requirements for both x-ray imaging and interference experiments. Such recording advancements are currently underway in the visible regime.<sup>2,3</sup> An application which would become more accessible to us as a result of such recording developments is x-ray holography, a subject only briefly discussed at the conference. For example, Kikuta and Aoki,<sup>4-6</sup> and others,<sup>7,8</sup> constrained by sources of limited spatial and temporal coherence, poor recording materials, and an absence of x-ray focusing elements, have made preliminary but important contributions using lensless Fourier transform, x-ray holographic techniques. With improved recording media, and x-ray optical techniques as described at this conference, new advancements can definitely be made.<sup>10</sup>

Many of the participants at the conference commented on the collective progress that had been made over the past several years. It will be exciting to watch these emerging technologies and the new results they bring, as they evolve over the next 5-10 years. It will be particularly satisfying if some of those future contributions are traced back to a comment, an idea, or a collaboration launched in 1981 in Monterey.

In addition to our sponsoring institutions, we are pleased to acknowledge the assistance of Irene Freiberg, Vivian Bunda, Jaci Nissen, Michael Trulson and the composition staff at LLNL who made the organization of this conference, and its published proceedings a pleasure. We also appreciate the fine photographic work of RIT/LLNL graduate student, Gary Stone.

August, 1981

David T. Attwood  
Livermore, California

Burton L. Henke  
Honolulu, Hawaii

## References:

1. Proceedings of the Conference on X-Ray Astronomy, Smithsonian Astrophysical Observatory, Cambridge, Mass., May 1960. Organized by A. Baez, edited by A. Berman.
2. N.J. Phillips and D. Porter, An Advance in the Processing of Holograms, *J. Phys. E. (London)* **9**, 631 (1976).
3. N.J. Phillips, *White Light Holography*, Wireless World (London) May, 1979.
4. S. Kikuta, S. Aoki, S. Kosaki and K. Kohra, X-Ray Holography of Lensless Fourier-Transform Type, *Optics Comm.* **5**, 86 (1972).

5. S. Aoki, Y. Ichihara and S. Kikuta, X-Ray Hologram Obtained by Using Synchrotron Radiation, J. Appl. Physics (Japan) 11, 1857 (1972).
6. S. Aoki and S. Kikuta, X-Ray Holographic Microscopy, J. Appl. Phys. (Japan) 13, 1385 (1974).
7. B. Reuter and H. Mahr, Experiments with Fourier Transform Holograms Using 4.48 nm X-Rays, J. Phys. E. (London) 9, 746 (1976).
8. V.V. Aristov and G.A. Ivanova, On the Possibility of Utilizing Holographic Schemes in X-Ray Microscopy, J. Appl. Cryst. 12, 19 (1979).
9. V.V. Aristov, G.A. Bashkina and A.I. Erko, Holography of Microobjects in Soft X-Rays, Optics Comm. 34, 332 (1980).
10. D.W. Sweeney, Purdue University, private communication.

PROCEEDINGS OF THE TOPICAL CONFERENCE ON  
LOW ENERGY X-RAY DIAGNOSTICS  
June 8-10, 1981  
Monterey, California

Sponsored by

The American Physical Society  
The United States Department of Energy  
The Lawrence Livermore National Laboratory  
The Air Force Office of Scientific Research

Conference Co-Chairmen

D.T. Attwood, Lawrence Livermore National Laboratory  
B.L. Henke, University of Hawaii

Program Committee

D.T. Attwood, Lawrence Livermore National Laboratory  
B.L. Henke, University of Hawaii  
K.W. Hill, Princeton University  
P.B. Lyons, Los Alamos National Laboratory  
D.J. Nagel, Naval Research Laboratory  
H.I. Smith, Massachusetts Institute of Technology

## Storage Rings as Sources of Soft X-Ray Emission

R. P. Madden and S. C. Ebner  
SURF Laboratory, National Bureau of Standards  
Washington, D.C. 20234

## ABSTRACT

The properties of synchrotron radiation will be discussed and the outputs and characteristics of the storage rings available in the U.S. will be intercompared. The use of these sources for the radiometric calibration of plasma diagnostic instrumentation will be discussed in some detail. The importance of the proper treatment of polarization, overlapping orders, and solid angle effects will be covered. The experience gained at NBS in the calibration of plasma diagnostics instruments will be examined.

## I. INTRODUCTION

The availability of synchrotron radiation (SR) has allowed the performance of many experiments, heretofore difficult or impossible. The impact has been rewarding on many fields, such as atomic, molecular, solid state and surface physics, structure and scattering in materials science and biology to name a few. The currently operating SR sources in this country are, in chronological order of their initiation: SURF, a 250 MeV storage ring at the National Bureau of Standards in Washington, D.C.; Tantulus, a 240 MeV storage ring at the University of Wisconsin in Stoughton, Wisconsin; SPEAR, a 3.5 GeV storage ring at Stanford University in California; and CESR, an 8 GeV storage ring at Cornell University in Ithaca, New York.

Three new storage rings will be in operation in 1982. These are: Aladdin, a 1 GeV machine being built at the University of Wisconsin in Stoughton, Wisconsin; and the NSLS facility at BNL on Long Island, New York consisting of a 700 MeV and a 2.5 GeV storage ring. This expansion of facilities, including also increased capacity at SPEAR, means that many more users and many new uses of SR will develop in the next few years.

The applications of SR of interest to the plasma diagnosticians might be in several categories. First, these new capabilities mean that new data on the interaction of high energy photons with matter will be forthcoming, such as location of high-lying states of atoms and ions and studies of their photoionization continua. Also studies of the interactions of high-energy photons with surfaces, such as the photoelectron emission and photo-atom and photon-ion desorption. Perhaps the most immediate and most important application of SR, however, is in the area of the test and calibration of diagnostic spectrometer or photometer systems. In the remainder of this paper we will focus on this application.

## II. PROPERTIES OF SYNCHROTRON RADIATION

Synchrotron radiation is a unique source with unusual properties caused by the relativistic velocity of the electrons which generate it. The most important features are listed below:

1) Continuum - SR is comprised of the harmonics of the fundamental orbital frequency of the turning electrons. These harmonics merge into a true continuum in the VUV x-ray regions which extends up to a cut-off photon energy dictated by the electron energy and the radius of curvature of the turning electron.

2) Collimation - SR is radiated in a very slender cone pointing in the direction of the velocity vector for the turning electron. The half-angle of this cone, for the total power radiated, is equal to  $\gamma (m_e c^2/E)$  for the relativistic electron. Thus, for example at 1 GeV<sup>-4</sup> electron energy, this cone angle is only  $\sim 5 \times 10^{-4}$  radians. As the electron turns horizontally through a bending magnet this narrow cone sweeps horizontally resulting in a thin "sheet" of radiation with a uniform horizontal distribution.

3) Polarization - SR is highly plane-polarized with the E vector of the radiation in the plane of orbit. The degree of polarization depends on the electron energy, wavelength, and vertical viewing angle. Figure 1 illustrates this angular dependence of the polarization for 240 MeV electrons at several wavelengths. A further important point is that the perpendicular (to the orbital plane) and parallel components are 90 degrees out of phase so that in general the radiation is elliptical.

4) Source size - Typically the electron beam cross section in a storage ring turning magnet is elliptical in shape with gaussian distributions with half-maximum widths of 1 - 3 mm horizontally and 0.1 - 1.0 mm vertically.

5) Temporal profile - The electrons in a storage ring are bunched with a number of bunches in the ring simultaneously, depending on what harmonic of the the electron circulation frequency the rf cavity is operated. Each bunch passes an observational tangent point in typically 0.2 - 1.0  $\mu$ sec. Large multi-bunch storage rings have been run, by selective filling, in a mode where only a single bunch is present - giving nearly one  $\mu$ sec between radiation pulses for some experiments.

6) Spectral distribution - The spectral distribution of SR depends on the electron energy and the radius of curvature of the turning electron. The distribution for several storage rings in use or under construction in the U.S. for typical or predicted operating conditions respectively, are shown in Figure 2. Similarly, the spectral distribution for SURF, the storage ring at NBS, is shown in Figure 3. The storage ring at Tantulus at the University of Wisconsin in Stoughton has a spectral distribution similar to that at SURF.

### III. WIGGLERS AND UNDULATORS

Wigglers are magnet systems installed in a straight section of a storage ring to present a strong periodic magnetic field to the electron beam with the result that the electrons "wobble" their way through. At the peaks of this oscillation the electrons are turning with a smaller radius than in the regular storage ring turning magnets with the result that the SR spectrum is shifted toward higher frequencies. It is also possible to view several of these maxima along a single line of sight and in this direction the intensity is increased by a factor of  $N$ , where  $N$  is the number of such maxima viewed. A wiggler has been in successful operation for several years at Stanford's SPEAR ring, where its increased performance has made it a very popular beam line. The typical flux advantage for this wiggler line is shown in Figure 4.

Undulators are undulatory magnetic field systems installed in storage ring straight sections similar to wigglers. However, in undulators there are typically many more oscillations, more closely spaced, and the amplitude of the electron beam displacement is much less.

The secret of the undulator is to meet the conditions required so that the radiation from the  $N$  oscillations can be added coherently producing an intensity advantage of  $N^2$  (in principle) over regular turning magnet radiation when the undulator is viewed in a small cone in the forward direction.

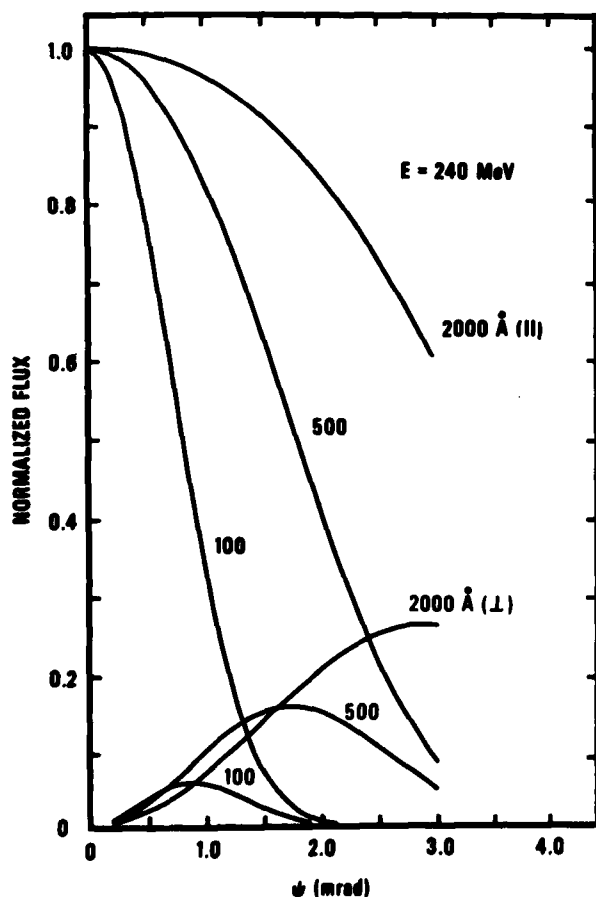


Fig. 1. Angular distributions of SR for the components of polarization with the E vector perpendicular ( $\perp$ ) and parallel ( $\parallel$ ) to the orbital plane for 240 MeV electrons.  $\psi$  is the angle the radiation makes to the orbital plane measured in a plane perpendicular to the orbit.

The spectrum of the undulator is made up of the fundamental wavelength of the periodic field and its harmonics shifted to higher frequencies by a relativistic factor. A successful undulator operated at SPEAR early in 1981 realized a fundamental somewhat tunable around 1 keV and a number of higher harmonics. For further discussion on Wigglers and Undulators, see reference 2.

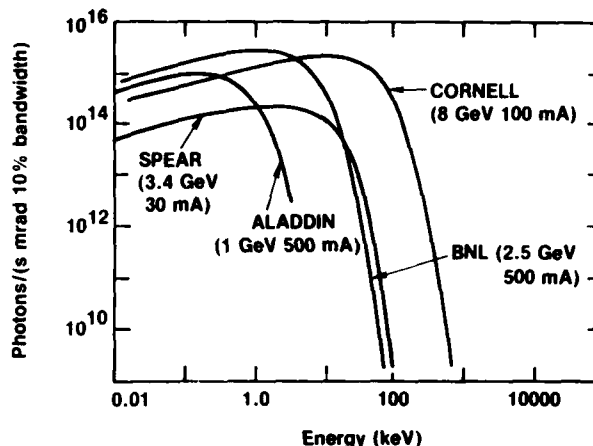


Fig. 2. Spectral distribution (photons/s-mrad of orbit subtended -10% bandpass) of SR from several machines. Conditions specified are typical for SPEAR and for Cornell and predicted for BNL and Aladdin.

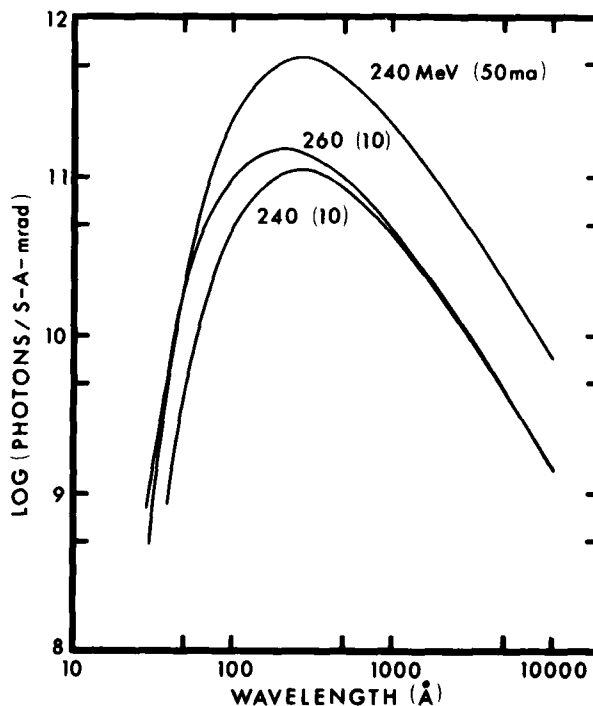


Fig. 3. Spectral distributions (photons/s-mrad of orbit subtended-one Å bandpass) of SR for several operating conditions of the NBS-SURF storage ring. 250 MeV with 10-20 mA are typical.

IV. RADIOMETRIC APPLICATIONS OF SYNCHROTRON RADIATION

SR can be used as a convenient source for the radiometric calibration of detectors or photometers, or alternatively it can be utilized as an absolute source standard for the radiometric calibration of spectrometer or photometer systems. The highest development of either of these applications of SR has been on the SURF storage ring at the National Bureau of Standards in Washington, D.C.

The irradiance delivered from a SR source depends on the electron energy, the turning radius of the electrons where viewed, the number of electrons viewed, and the geometry of collection. The electron energy can be determined to 0.1% by accurately measuring the magnetic field. At SURF, which is unique among storage rings in that its orbit is truly circular, the radius of turning is determined by the rf cavity frequency since the electrons are traveling with a speed which closely approximates the velocity of light. SURF also has a smaller electron beam cross section than other storage rings which means that smearing of the angular distribution of the radiation is minimized. These facts imply that the radiation from SURF can be accurately calculated if the number of electrons circulating (the current) can be accurately determined.

Recent developments in the precise counting of circulating electrons in the SURF storage ring now allow the counting of up to several thousand electrons in the ring. This is accomplished by actually counting the steps in the output radiation by the electrons in the ring as they are gradually scattered out of the electron beam. By this method, a highly linear silicon diode detector is calibrated in the range of  $10^4$  to  $10^7$  circulating electrons and then this detector is used to measure currents ranging from  $10^4$  -  $10^7$  circulating electrons. The overall uncertainty of predicting the irradiance delivered by the SURF facility is currently around 3% and this uncertainty may be reduced further in the near future.

Detector Calibrations

Broad-band and narrow-band detectors have been calibrated at SURF using a monochromator and an absolute detector for A-B type intercomparison. In addition, NBS has developed transfer standard diodes which are available for use in other laboratories as radiometric references. These are windowed evacuated diodes for the region above 115 nm and a windowless diode for the region 5-115 nm. Curves showing the quantum efficiency of these detectors are shown in Figure 5.

Spectrometer Calibrations

For the calibration of spectrometer systems, a well-characterized beam line has been developed at SURF which allows the calculation of the irradiance from the storage ring which falls on a 13 mm x 13 mm square aperture located either 11.5 or 17 m from the tangent point source. Here, spectrometers or photometers can be located to receive an absolute system calibration over a spectral range of 5-400 nm. In either position, instrument mounting platforms are provided which can be translated in the vertical and horizontal directions normal to the incident radiation. The platforms are also mounted in a gimbal which allows rotation of the instrument about vertical and horizontal axes normal to the incident radiation. The difference between the two platforms is that the 17 m one is located in a large vacuum chamber which was constructed with the requirements of satellite and rocket instruments particularly in mind. Either of these two calibration platforms will be made available for the radiometric calibration of diagnostic instrumentation, depending on the nature of that instrumentation.

The vertical and horizontal translations provided by this calibration facility not only facilitate the location of the instrument properly in the beam, but also allow calibration of an instrumental system which uses a large collecting optic in front of the spectrometer. In this case, the SR beam provided would illuminate only a small segment of the collecting optic, but the translations allow the mapping of the system efficiency over the full aperture of the system.

The gimbal systems provided facilitate the angular alignment of the spectrometer systems and further, allow a mapping over the operational solid angle of the instrument. Since the SR falling on the entrance slit of a spectrometer (used without a collecting optic) has a very large f/no, the system's response is measured over only a very small angular aperture relative to that for which most systems are designed to collect radiation. When the entrance slit of the spectrometer is located at the intersection of the vertical and

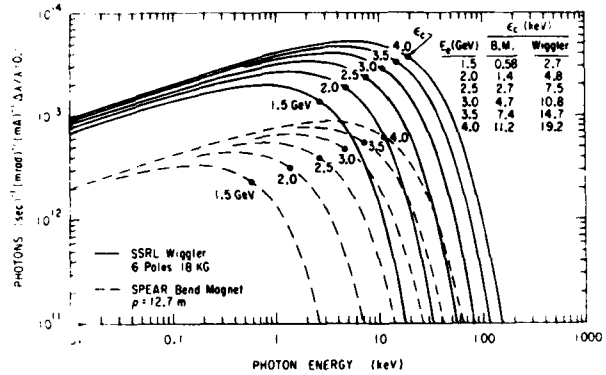


Fig. 4. Spectral distributions comparing the spectrum produced by the SSRL Wiggler with the SR spectrum produced by the normal SPEAR bending magnet for several operating conditions,  $E_c$  as a critical energy (or frequency) in the theory of SR above which the spectrum drops rapidly. A rule of thumb is that a storage ring is useful up to about a frequency of four times  $E_c$ .

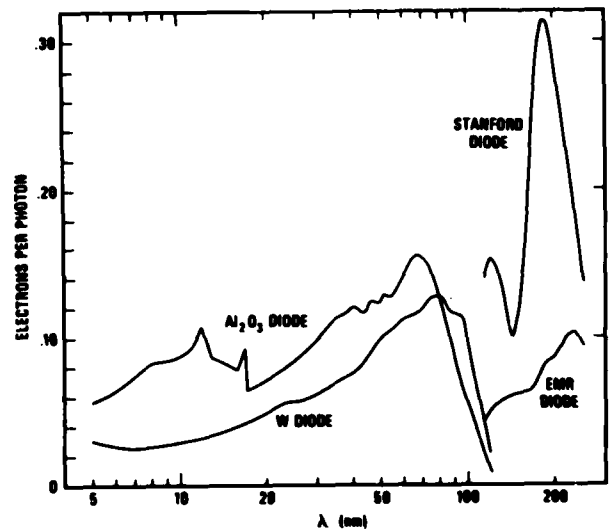


Fig. 5. Spectral distribution of the efficiency of the transfer standard photodiodes available from NBS for the far UV. Below 115 nm the diodes are windowless.

horizontal axes of rotation, the angular scans of those rotations then allow a mapping of the instrument response over the full solid angle of acceptance of the spectrometer.

Since SR is highly polarized it is also required that the instrument be calibrated in two angular orientations (i.e., slit vertical and slit horizontal). The average of the response in these two orientations should be the response to unpolarized radiation. An advantage to this additional complication is that the response of the instrument to polarized radiation is then known.

Since SR is a continuum source, overlapping orders are often a problem which must be dealt with. At SURF, we have been able to unfold the first and second order contributions by performing the calibration at two different electron energies, e.g., 250 MeV and 140 MeV. At these two energies, the spectral distributions have very different shapes, allowing two equations with two unknowns to be solved for the first and second order instrumental response.

#### Description of Large Spectrometer Calibration Chamber

Figure 6 shows a diagram of the spectrometer calibration beam line (BL 2) at the NBS-SURF facility, showing the location of the spectrometer calibration platform at 17 m. Not shown is the calibration platform at the 11.5 m distance. Also indicated is a device called the Orbital Plane Locator (OPL) which allows the beam line and final aperture to be accurately located on the orbital plane. In addition, a laser alignment system using retractable mirrors provides a laser beam simulation of the SR beam for alignment purposes.

The second platform, as mentioned above, is located inside a large vacuum tank at the end of the calibration beam line. The dimensions of this tank are 1.2 m x 1.2 m x 2.5 m long. Figure 7 is a photograph of the vacuum tank. It is all stainless steel, cryopumped ( $1 \times 10^{-7}$  Torr), and completely compatible with the SURF requirement that hydrocarbon contamination be kept to a very low level. The chamber is connected to the beam line through a 40 cm i.d. compound bellows which allows the vacuum tank to be moved vertically and horizontally through an excursion of 40 cm. The vertical motion is accomplished by operating four large screw jacks in synchronization.

Inside the vacuum tank is the gimbal system containing the spectrometer mounting platform. Figure 8 is a photograph of the gimbal. The clear dimensions for mounting a spectrograph within the gimbal are 76 cm vertical and 76 cm horizontal. With a maximum-sized

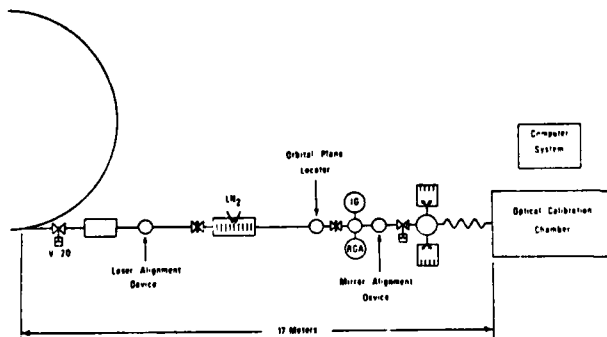


Fig. 6. A diagram of the beamline at NBS-SURF which is devoted to spectrometer calibration. The large vacuum tank at 17 m from the orbital tangent point is indicated as the optical calibration chamber. The spectrometer mounting platform at 11.5 m, not indicated, is just to the right of the Orbital Plane Locator.

instrument package the gimbal allows  $\pm 3^\circ$  of pitch and yaw motion with a resolution of 1.3 seconds. This allows a mapping of the efficiency over the solid angle of an f/10 spectrometer.

All of the motions of translation and rotation are computer controlled, and the parameters  $x, y, \theta, \phi$  and the electron beam current can be read out or fed into the customer's computer during a calibration.

Typical irradiance levels falling on an instrument located inside the calibration chamber are  $2.4 \times 10^2$  photons/s-Å-mm<sup>2</sup> at 120 nm or  $8 \times 10^3$  photons/s-Å-mm<sup>2</sup> at 10 nm. Flux levels at the 11.5 m calibration platform are higher by a factor of about 2.2.

Both the 11.5 m and the 17 m spectrometer calibration platforms have been used for instrument calibrations, including rocket and satellite packages and plasma diagnostic instruments. All of these calibrations to date have been quite successful and in cases where other calibration data was available, the intercomparisons have been excellent.

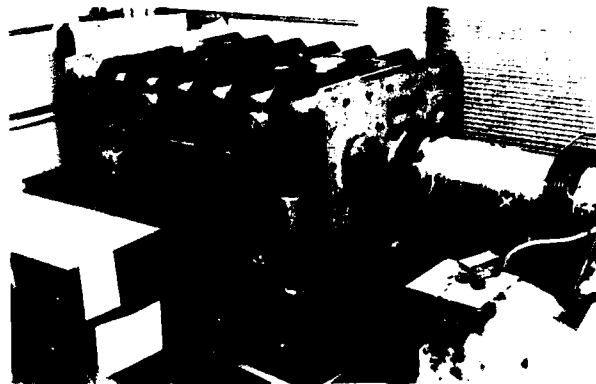


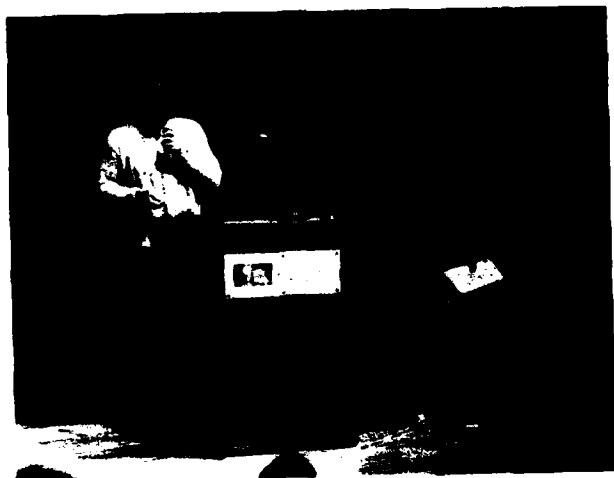
Fig. 7. Photograph of the spectrometer calibration chamber at NBS-SURF. Note compound bellows allowing vertical and horizontal motion of the chamber and the large screw jacks which provide the vertical displacement.



Fig. 8. Photograph of the two axis gimbal which holds the test spectrometer in position. The gimbal rolls into the vacuum chamber shown at right and allows a vertical and horizontal axis of rotation normal to the incident radiation.

## REFERENCES

1. E.M. Rowe, *Physics Today* 34, 28 (May 1981).
2. H. Winick, G. Brown, K. Halbach and J. Harris, *Physics Today* 34, 50 (May 1981).
3. R.P. Madden, *Nuc. Insts. & Methods* 172, 1 (1980).
4. E.B. Saloman, S.C. Ebner and L.R. Hughey, *Proceedings of SPIE Symposium* 297 (July 1981); also L.R. Hughey and R. Schaefer, private communication.
5. E.B. Saloman, *Nuc. Insts. & Methods* 172, 79 (1980).
6. L.R. Canfield, R.G. Johnston and R.P. Madden, *Applied Optics* 12, 1611 (1973).
7. E.B. Saloman and D.L. Ederer, *Applied Optics* 14, 1029 (1975).



Dr. Robert Madden responding to questions from the audience. To the right is session chairman Dr. Ingolf Lindau.



## X-RAY EMISSION FROM LASER FUSION TARGETS\*

V.W. Slivinsky

University of California, Lawrence Livermore National Laboratory  
P.O. Box 5508, Livermore, CA 94550

This paper is a brief summary of x-ray measurements from disks irradiated by high power, 1.06  $\mu\text{m}$  laser at the Lawrence Livermore National Laboratory. Most of this work was done at the Argus and Shiva laser facilities using instruments described in this text.

A typical x-ray spectrum from a laser irradiated disk is shown in figure 1. The target was high Z material on a 2  $\mu\text{m}$  thick CH substrate. We found that high Z targets maximizes the x-ray yield. Note that there is structure in the 600 eV region of the spectrum, probably due to Au N line emission. At higher photon energies the spectrum decreases rapidly with most of the x-ray energy below 1 keV.

The total x-ray energy emitted in the subkeV region is shown in figure 2. Using 10 KJ incident laser energy, about 1/3 is absorbed by the disk, and

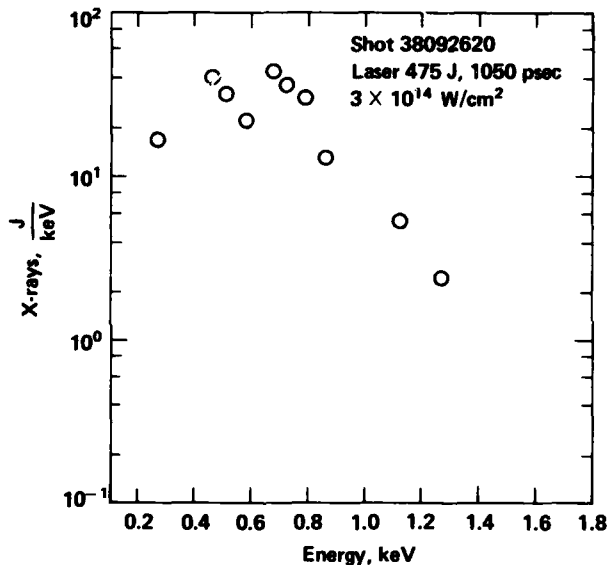
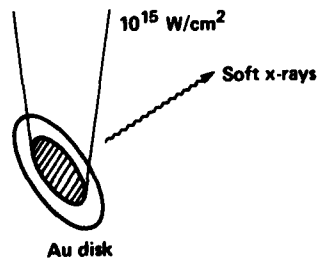


Figure 1. X-ray spectrum from a 0.2  $\mu\text{m}$  Au disk irradiated at  $3 \times 10^{14}$  W/cm<sup>2</sup>. The structure at 600 eV is probably due to Au lines. Most of the x-ray energy resides in the subkeV energy region.



$$10 \text{ kJ} \times \frac{1}{3} (\text{abs}) \times \frac{1}{3} (\text{CE}) \sim 1 \text{ kJ in } 1 \text{ ns}$$

Figure 2. Conversion efficiency from incident laser energy to soft x rays.



Figure 3. The Dante 10 channel x-ray spectrometer. The front five filter-detector channels measure the higher energy portion of the spectrum, and the back five filter-reflector-detector channels measure the lower energy portion of the spectrum.

about 1/3 of the absorbed energy is emitted by the hot plasma as x-rays. At higher laser intensities the absorption improves but the conversion to soft x-rays does change very much. Sparse measurements<sup>1</sup> of the angular distribution show that the x rays are peaked normal to the disk.

Measurements are now being made at the Argus laser facility using frequency doubled, and tripled 1.06  $\mu\text{m}$  light. Preliminary results<sup>2</sup> show that at these shorter wavelengths both absorption and conversion to x rays are increased.

The major instrument used to measure the subkeV x rays at LLNL has been the Dante spectrometer<sup>3</sup> shown in figure 3. Five channels are composed of filtered x ray diodes, and five channels incorporate small angle reflectors to define the energy limits of the bite of the spectrum. X-ray streak camera spectrometers also play a key role in our soft x-ray measurements. These instruments are described by Rober Kauffman in a following paper.

An innovative design for one filter-detector combination uses a compound filter.<sup>4</sup> The uniqueness of this channel design is that instead of taking a narrow bite out the spectrum it has a relatively flat response over a wide range of energies from .1 keV to 1.5 keV. Figure 4 shows conceptually the role of each element in this scheme. The flat response means that the signal output of the detector is proportional to the incident x-ray energy regardless of the spectral shape. An absolutely calibrated channel of this kind is particularly useful for measuring x-ray energy if spectral information is not necessary.

Proceeding now to higher x-ray energies, a composite spectrum extending from 5 keV to 350 keV for a Ta disk is shown in figure 5. It can be seen that a much smaller fraction of the absorbed laser energy ends up in high energy x-rays (approximately  $10^{-4}$ ) than in thermal x rays. The spectrum decreases four orders of magnitude over this energy range.

This Ta spectrum incorporates points from all of the channels in our filter-fluorescer spectrometer. The spectrometer is shown in figure 6. Design information is given in reference 5. The fluorescer technique was recently extended all the way out to

\* Work performed under the auspices of the U.S. Department of Energy by the Lawrence Livermore National Laboratory under Contract No. W-7405-ENG-48.

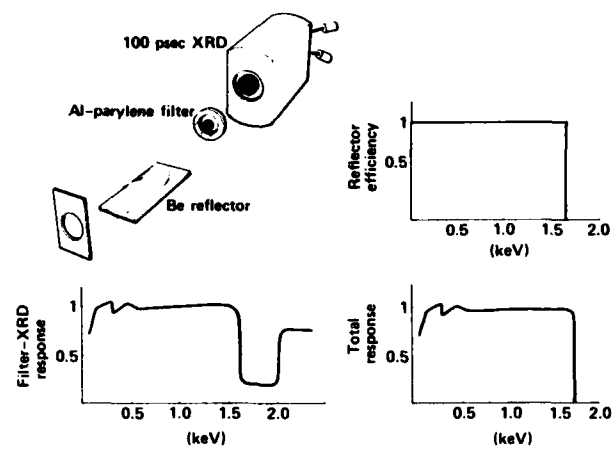


Figure 4. The flat response compound filter-detector x-ray channel. The reflector efficiency is flat with photon energy, and the compound filter-x-ray diode combination is also relatively flat. The total response implies that the signal output is proportional to incident x-ray energy.

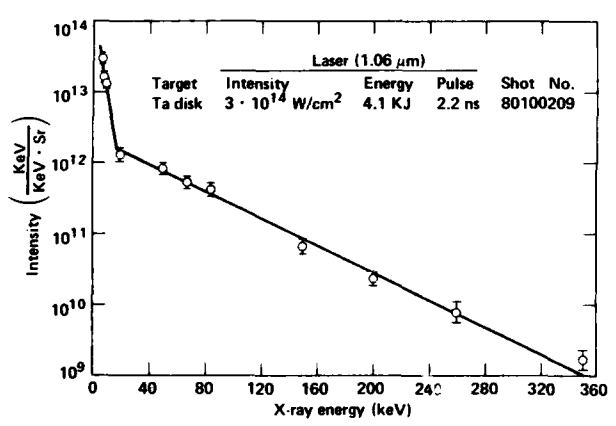


Figure 5. The suprathreshold x-ray spectrum from a Ta target. Each datum point was generated by the 20 channel filter-fluorescer spectrometer.

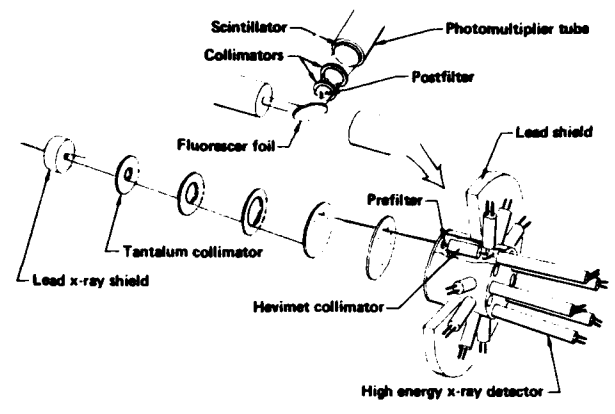


Figure 6. The 20 channel filter fluorescer spectrometer. The 10 spokes in the wheel are filter-fluorescer channels, and the 10 straight through detectors are filter-detector combinations.

250 keV<sup>0</sup>. Beyond 250 keV we use thick Pb filters to define very broad energy responses.

These x-ray instruments and measurements have been made and supported by a number of staff people at LLNL too numerous to mention here. Further information on this work can best be obtained from the references or by contacting me or the reference authors.

References

1. G. McClellan, P.H.Y. Lee, and G. Caporaso, Phys. Rev. Lett. 44, 661 (1980) and Z-Dependence of Sub-keV X-ray Emission and Laser Intensity Threshold for Inhibited Electron Thermal Conduction, UCRL-50021-9 (1980).
2. P.H.Y. Lee and K.G. Tirsell X-ray Conversion Efficiency, Laser Program Annual Report (1980) to be published.
3. K.G. Tirsell, H.N. Kornblum, V.W. Slivinsky, UCRL 81378, Time Resolved, Sub-keV Measurements Using Filtered X-ray Diodes (1979) unpublished.
4. H.N. Kornblum and V.W. Slivinsky, Rev. Sci. Inst. 49, 1205 (1978)
5. H.N. Kornblum, B.I. Pruett, K.G. Tirsell and V.W. Slivinsky UCRL-81471. Filter Fluorescer Experiment on the Argus Laser (1978).
6. C.L. Wang, UCRL 84800. Hyper-Filter-Fluorescer Spectrometer for X-rays Above 120 keV (1981) Rev. Sci. Inst. (in press).

Dr. V. W. Slivinsky during his presentation at the conference.



## Low Energy X-Ray Emission from Magnetic Fusion Plasmas\*

K.W. Hill, M. Bitter, D. Eames, S. von Goeler, N.R. Sauthoff, and E. Silver

Princeton University, Plasma Physics Laboratory, Princeton, New Jersey 08544

## ABSTRACT

Complex, transient, spatially inhomogeneous tokamak plasmas require careful diagnosis. As the reactor regime is approached, soft x rays become more important as a versatile diagnostic tool and an energy-loss mechanism. Continuum emission provides a measure of electron temperature and light impurity content. Impurity lines serve as a probe for ion and electron temperature, impurity behavior, and radiative cooling. The entire spectrum yields vital information on instabilities and disruptions. The importance of impurities is illustrated by the extensive efforts toward understanding impurity production, effects, and control. Minute heavy impurity concentrations can prevent reactor ignition. Si(Li) - detector arrays give a broad overview of continuum and line x-ray emission (.3 - 50 keV) with moderate energy (200 eV) and time (50 ms) resolution. Bragg crystal and grating spectrometers provide detailed information on impurity lines with moderate to excellent ( $E/\Delta E = 100 - 23,000$ ) resolving power and 1 - 50 ms time resolution. Imaging detector arrays measure rapid ( $\sim 10 \mu s$ ) fluctuations due to MHD instabilities and probe impurity behavior and radiative cooling. Future tokamaks require more diagnostic channels to avoid spatial scanning; higher throughput for fast, single-shot diagnosis; increased spectral information per sample period via fast scanning or use of multi-element detectors with dispersive elements; and radiation shielding and hardening of detectors.

## I. INTRODUCTION

Controlled fusion offers the hope of an essentially unlimited supply of energy with fuel available to all nations [1]. Diagnostics instrumentation plays an important role in controlled-fusion research [2-5]. It serves as the "eyes" and "ears" of the experimental physicist, enabling him to monitor his progress in the quest for attaining optimal conditions for fusion. The transient plasma of most of today's fusion-research devices and the large number and complexity of important interacting physical processes demand measurement of several physical parameters with good temporal and spatial resolution. As plasma temperatures become higher, the electromagnetic spectrum emitted by the plasma shifts toward shorter wavelengths, and x rays become more important both as a source of radiative power loss and as a means of making diagnostic measurements [6]. Several types of instruments have been developed over the years to probe fusion plasmas by measuring various properties of the x-ray emission [3-30]. A necessary part of these developments has been the contribution of expertise by scientists in many areas, such as solid state, nuclear, and atomic physics, astrophysics, crystallography, electronics, etc. These instruments permit measurement of a variety of important plasma parameters. These include electron [8,37,45] and ion [22] temperature, density [31], plasma equilibrium and stability [23,24], plasma position, and plasma rotation [6]. Other parameters inferred from x rays relate to impurities and include radiative energy loss [10,32-35], concentration [6,8,10] and motion [36], charge-state distribution [21,37], wavelengths of emission lines [38-42], and atomic physics parameters such as cross sections for excitation, ionization, and recombination [43,44,46,47]. This paper is a review of x-ray diagnostic techniques and apparatus, used in magnetic confinement fusion experiments, involving measurement of x-ray emission in both the low energy or ultrasoft x-ray (USX) region (0.1 to 1 keV) and the soft x-ray region (SX) (1 - 10 keV). This extended range is addressed because some instruments operate in both regions and others are applicable to both ranges but have historically operated in the SX region due to the greater complexity required for USX operation. The low energy or USX range, however, is particularly important because the emission in this region is often a significant fraction of the energy loss in tokamaks [10,32-35]. Although various types of magnetic confinement devices exist and some are addressed in the

paper, the bulk of the work reported involves tokamaks.

This paper focuses on describing magnetic fusion energy (MFE) x-ray diagnostics to scientists who may not be involved in or have intimate knowledge of MFE. Review information on basic principles of MFE are presented without going into detail. The tokamak is used as an example although some x-ray diagnostic work from other MFE devices is presented. An effort is made to illustrate what the diagnostic needs and problem areas are so that researchers in other fields can understand how they might contribute to the diagnostic effort. In Section II we review the basic principles of the tokamak. Section III emphasizes the importance of impurities. This importance is supported by (a) the extensive work done toward studying impurities, their effects, and their control, and (b) a summary of some specific impurity effects. In Section IV the mechanisms for x-ray production in plasmas and properties of this emission are reviewed. Section V describes the major x-ray diagnostic instruments used on tokamaks. The purpose, principle of operation, and characteristics of each instrument are summarized. Examples of data are presented and discussed briefly. Section VI describes some problems with present x-ray diagnostics, some improvements planned for the Tokamak Fusion Test Reactor (TFTR) at Princeton Plasma Physics Laboratory (PPPL), and further development that would benefit the fusion program.

## II. THE TOKAMAK

At Princeton two tokamaks, the Princeton Large Torus (PLT) and Poloidal Divertor Experiment (PDX) are operating presently. A third larger machine, the Tokamak Fusion Test Reactor (TFTR) [56], will begin operation in 1982. The major goal of TFTR is to achieve "breakeven" (fusion power out = heating power in) in deuterium-beam-heated tritium plasma (DT operation). Several other tokamaks are in operation at other laboratories in the United States and other countries. These include the Alcator tokamaks at MIT, ISX-B (Impurity Studies Experiment) at Oak Ridge, Doublet III at General Atomic, DITE at Culham, U.K., TFR at Fontenay aux Roses, France, and others in Italy, Germany, Japan, the U.S.S.R., etc.

The tokamak has been reviewed in several papers [1,48-55]. A brief description follows. The basic components are shown schematically in Fig. 1. A hydrogen-isotope plasma characterized by major radius R

(130 cm for PLT, 265 cm for TFTR) and minor radius  $r = a$  (40 cm for PLT, 85 cm for TFTR) is created and heated in a toroidal vacuum vessel. A strong, static magnetic field  $B_T$  (1 - 10 T, depending on the type of tokamak and the regime of operation being studied) is superposed throughout the vacuum vessel by external toroidal field (TF) coils. The basic purpose of  $B_T$  is to confine the plasma ions and electrons by constraining them to move in helical orbits about the field lines. A transient toroidal current  $I_p$  is then induced in the conducting plasma by transformer action.

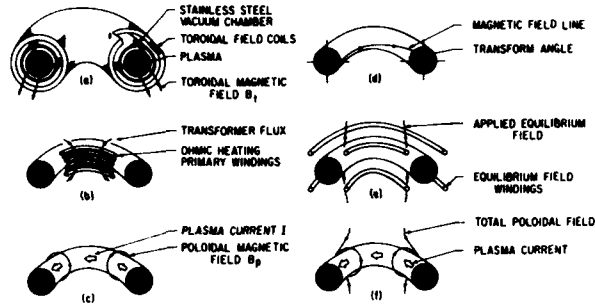


Fig. 1 Schematic illustrating principles of tokamak operation. (PPPL-753361)

This current usually has a quasi-steady "flat top" value of several hundred kiloamperes for a period of several hundred milliseconds. A time-varying vertical magnetic field induced by ohmic heating (OH) windings around the toroidal direction generates the toroidal current, which heats the plasma via resistive or "ohmic" heating to a high temperature. In addition, the current produces a poloidal magnetic field (PF) around the smaller cross section of the torus. The net effect of the TF and PF is a helical magnetic field as illustrated. This field is characterized not only by the net field strength, but also its rotational transform  $\iota$ . This transform is the poloidal angle a field line traverses during one toroidal circuit around the tokamak. It is this helical or torsional property of the field lines which gives the tokamak its equilibrium and stability characteristics. A parameter more commonly used than  $\iota$  is the "safety factor"  $q = 2\pi/\iota$ , which depends on  $r$ ,  $B_T$ ,  $I_p$ , and major radius  $R$ . The value of  $q$  varies with minor radius  $r$ , and has a strong bearing on the stability properties of the plasma.

The plasma is characterized basically by the temperature of the electrons ( $T_e$ ) and ions ( $T_i$ ), typically one to several keV, and electron density  $n_e$  (typical peak value  $1-10 \times 10^{13} \text{ cm}^{-3}$ ). These parameters typically have large values near the center of the minor cross section, and decrease to small values near the limiter (a metal aperture which defines the plasma diameter) as illustrated in Fig. 2. Also important are the particle and energy confinement times for ions,  $\tau_i$  and  $\tau_{Ei}$ , and electrons,  $\tau_e$  and  $\tau_{Ee}$ . The basic goal of the tokamak is to heat the plasma so that the colliding ions can overcome the repulsive Coulomb barrier (to permit fusion), and to provide sufficient density and confinement for a sustained burn, i.e., heat input from fusion reaction products  $>$  power losses from plasma. The temperature required for the easiest fusion reaction to attain, that of deuterium and tritium, is about 10 keV or  $10^8$  degrees K (1 eV = 11,600 K). The required density  $n$  and confinement time  $\tau$  are specified by the Lawson criterion,  $n\tau = 10^{14} \text{ cm}^{-3} \text{ sec}$  [57]. Working contrary to achievement of these

goals are several power-loss mechanisms and other processes which tend to cool and destabilize the plasma and prevent attainment of high temperature, high density, and good confinement [51,58]. Power-loss mechanisms include radiation, ionization, charge-exchange losses (a hot ion is neutralized by capturing an electron from a cold neutral atom, and is no longer confined), conduction, and convection. Because of the large thermal and density gradients possible and the profound effect gradients can have on cross field transport of energy and particles, spatially resolved measurements, of  $T_e$ ,  $n_e$ ,  $I_p$ , impurity concentration and all other quantities of interest are of great importance.

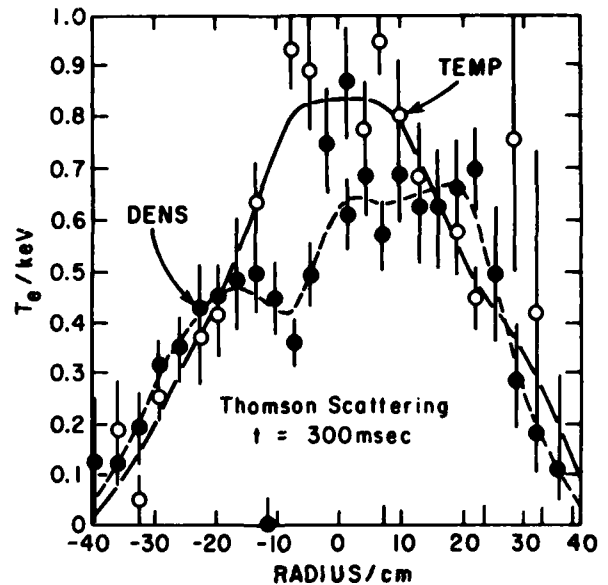


Fig. 2 Sample electron temperature and density profile from PLT measured by Thomson scattering. (PPPL-809052)

Because temperatures achievable by ohmic heating are limited to 3-4 keV, [51] several auxiliary heating schemes are in use. Injection of intense beams (up to 3 MW of power) of 40-keV neutral deuterium ( $D^0$ ) atoms into the PLT tokamak [32,59,60] has raised the ion temperature from 1 to 7 keV. Recently, the ion temperature in PDX was increased from 1 to 5.8 keV by 7 MW of neutral-beam power. Neutral-beam injection experiments have been done on other tokamaks [61-63]. Heating by absorption of radio-frequency (RF) electromagnetic radiation at several resonance frequencies characteristic of the plasma (like a microwave oven) has been successfully tested [32,64]. Adiabatic compression is another successful auxiliary heating technique.

### III. IMPURITIES

In addition to the working gas, traces of impurity ions inevitably enter the plasma. These include oxygen and carbon in the 1-10% range (relative to  $n_e$ ) and smaller quantities (<1%) of wall and limiter materials (Fe, Cr, Ni, Ti, and Mo) [65]. Tungsten (W) was also used for limiters in earlier times. These impurities can have profound effects, some deleterious and some beneficial, on the plasma. The importance of these effects is indicated by the extensive experimental [66-100] and theoretical [101-118] efforts by many groups and individuals toward understanding impurity transport and impurity effects on the plasma, impurity production mechanisms, and toward developing schemes for reducing impurity influx and removing impurities from the plasma. Recipes for removal of adsorbed oxygen and

carbon from the vacuum-vessel wall [119] are used for all tokamaks. Titanium is evaporated onto walls to cover up adsorbed oxygen [58]. Special low Z limiters have replaced high Z materials to avoid the deleterious effects of high Z impurities in the plasma [58]. Impurity studies and control has been a major emphasis in the PLT research program [58,60]. The PDX experiment was constructed to study, among other effects, removal of impurities by a magnetic divertor [50]. The ISX-A tokamak was constructed to do impurity studies and, in particular, to test a concept for preventing impurities from flowing to the center of the plasma [99,101]. Theoretical models of impurity transport are used to help interpret experimental data [62,102,105,111]. Calculations of radiative power loss have been done for many impurity ions. These results indicate that a W density of .01% of  $n_e$  can prevent ignition of DT plasma in a tokamak reactor [107]. Because of the importance of impurity effects and because a major emphasis of x-ray diagnostics is measurement of impurity radiation and behavior, we give here a brief review of this subject.

As an impurity atom enters a tokamak plasma it is ionized by electron impact to successively higher charge states until a balance is reached between ionization and recombination [6,112,113], assuming steady-state conditions. Under these equilibrium conditions a distribution of charge states exists (Fig. 3). This distribution can be altered by motion of ions from hot to cooler regions, or vice-versa, in tokamaks. The most probable charge state typically has an ionization potential approximately 1-2 times  $T_e$ . The distribution is usually narrow, with 4 or 5 ionization stages existing at any particular temperature. Thus, in a tokamak, whose temperature varies significantly with radius (Fig. 2), the distribution progresses continuously from low degrees of ionization at the periphery to higher stages at the center. A given charge state tends to cluster in a shell of several centimeters radius. Low Z impurities such as C and O tend to be fully stripped at the center, whereas high Z ions are only partially stripped.

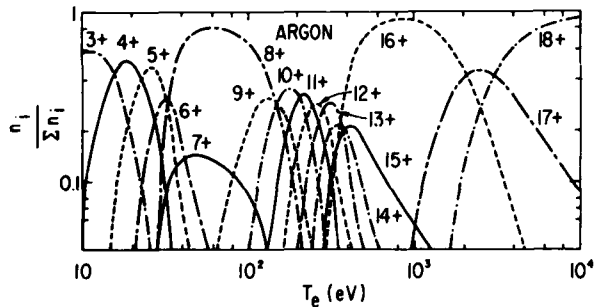


Fig. 3 Fractional abundance of several charge states of Ar vs. electron temperature for coronal equilibrium. (PPPL-783804)

These impurities affect the plasma in several ways. They cool the plasma by causing power to be radiated away via bremsstrahlung, radiative recombination, and line emission (Fig. 4) [6,52,107]. This cooling can be deleterious in the plasma center, which we are trying to heat. Or radiation cooling of

the periphery of a reactor by low Z impurities can be beneficial; low edge temperatures tend to reduce the influx of higher Z wall impurities, presumably by reducing sputtering [32]. The low Z impurities are relatively benign in the center, as far as energy loss is concerned, since fully stripped ions produce no line radiation. High Z impurities in the center can radiate profusely because they have several bound electrons which can be excited [10,33,34,62,80]. Several people have been involved in calculations of radiation power from plasmas [87,106-108,110].

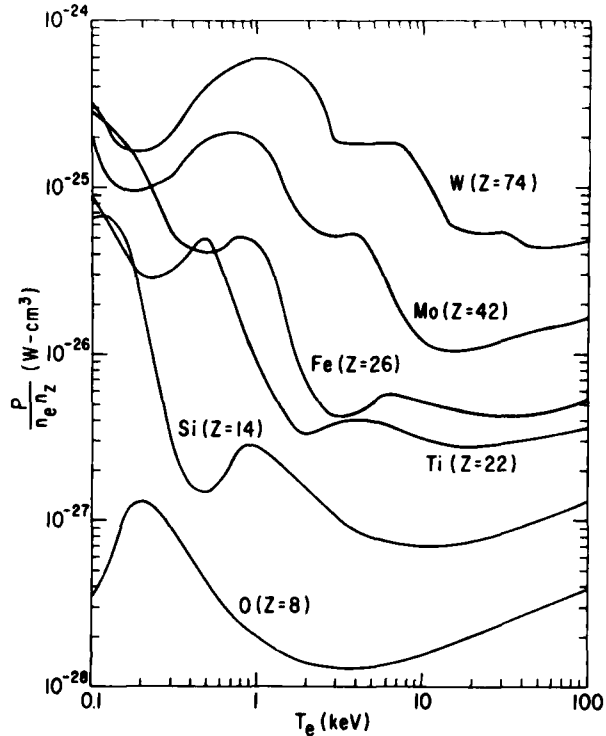


Fig. 4 Comparison of the radiative power loss for a variety of impurities. (PPPL-772499)

Also, impurities increase the plasma resistivity and can change the plasma-current radial distribution, thereby affecting stability [109,120]. Low Z impurities are usually the worst offenders here since high Z impurities are typically not present in sufficient quantities to affect the plasma resistivity significantly. As impurity content increases the range of stable operating conditions diminishes; the onset of degraded confinement and disruptive instabilities occurs at lower density and plasma current [120].

A third harmful effect of impurities is dilution of the reacting fuel ions. The overall effect of impurities is often described in terms of their contribution to the effective charge

$$Z_{\text{eff}} = \frac{\sum_i n_i Z_i^2}{n_e} \quad (1)$$

where the summation is over charge states  $Z_i$  of all ions of density  $n_i$ . For a burning plasma the reaction rate of fusion power for fixed  $n_e$  and  $T_i$  is reduced by a factor

$$f = \left( \frac{Z_I - Z_{\text{eff}}}{Z_I - 1} \right)^2 \quad (2)$$

for a single impurity of charge  $Z_i$ , relative to an impurity-free plasma. For a 3% fully stripped C contamination, we get  $Z_{eff} = 2$  and  $f = .64$  which corresponds to a 50% increase in the cost of electricity [120].

Impurities can also reduce the penetration of neutral beams used for auxiliary heating due to the large cross section for electron capture by highly stripped impurities from deuterium.

#### IV. X-RAY EMISSION CHARACTERISTICS

The x-ray emission spectrum from tokamaks consists of a continuum with characteristic peaks superimposed. The continuum has two components resulting from electron-ion collisions:

- (1) free-free (ff) bremsstrahlung on hydrogen isotopes and impurity ions, and
- (2) free-bound (fb) recombination of electrons with impurity ions.

The dependence of the continuum intensity on atomic and plasma parameters has been treated in detail [6,8]. For our purposes it is sufficient to note that the bremsstrahlung emission is

$$\left(\frac{\Delta W}{\Delta k}\right)_{ff} = n_e \sum_i n_i Z_i^2 \exp(-k/T_e), \quad (3)$$

where  $\Delta W$  is the radiated power per  $\text{cm}^3$  into the photon energy interval  $\Delta k$ ,  $n_e$  and  $n_i$  the electron and ion density,  $Z_{iff}$  the ion charge relevant for free-free transitions (= nuclear charge),  $k$  the photon energy, and  $T_e$  the electron temperature. For recombination radiation in the energy range above the ionization potential of the recombining ion, we can write

$$\left(\frac{\Delta W}{\Delta k}\right)_{fb} = \left(\frac{\Delta W}{\Delta k}\right)_{ff} (\gamma_i - 1), \quad (4)$$

because fb and ff radiation have the same spectral shape. The parameter  $\gamma_i$  is the enhancement of the continuum radiation over bremsstrahlung due to the recombination radiation. The dependence of the line radiation spectrum on impurity content, atomic physics, and plasma parameters has also been treated in detail for some impurities [118,121].

Examples of typical x-ray emission spectra from the PDX tokamak and the EBT device at Oak Ridge National Laboratory, respectively, are shown in Figs. 5 and 6. Absolute measurements of some impurity line intensities in the USX region have been given [92]. The volume emissivity of photons varies strongly with energy and impurity concentration. Typical values may range from near  $10^{15} \text{ cm}^{-3} \text{ sec}^{-1}$  for the Ni XXV 118 Å line [92] to  $10^{13} \text{ cm}^{-3} \text{ sec}^{-1} \text{ keV}^{-1}$  and  $10^9 \text{ cm}^{-3} \text{ sec}^{-1} \text{ keV}^{-1}$  for the continuum at 1 and 10 keV, respectively, for a plasma with  $T_e = 1 \text{ keV}$  and  $n_e = 5 \times 10^{13} \text{ cm}^{-3}$ . We see that line and continuum intensities can vary by many orders of magnitude over the spectral range of interest. Thus x-ray diagnostics must cover a wide dynamic range. We make three general observations:

- (1) The continuum spectrum has an exponential dependence on photon energy. The slope on a semilogarithmic plot is  $-1/T_e$ . Using this we can measure  $T_e$  from the continuum spectrum.
- (2) The intensity of the continuum depends on the relevant ion charge  $Z_i$  as  $n_i Z_i^2$ . Thus a relatively small ion fraction  $n_i$  can produce a relatively large contribution since  $Z_i^2$  is typically large.

- (3) The enhancement factor  $\gamma_i$  is typically  $< 10$  for clean discharges [8, 15] but under some circumstances can be as large as  $\sim 1000$  [15,36]. This factor depends strongly on the ionization stage of an impurity ion [6]. Thus for a quantitative evaluation of the continuum, the ion densities and charge-state distributions must be known.

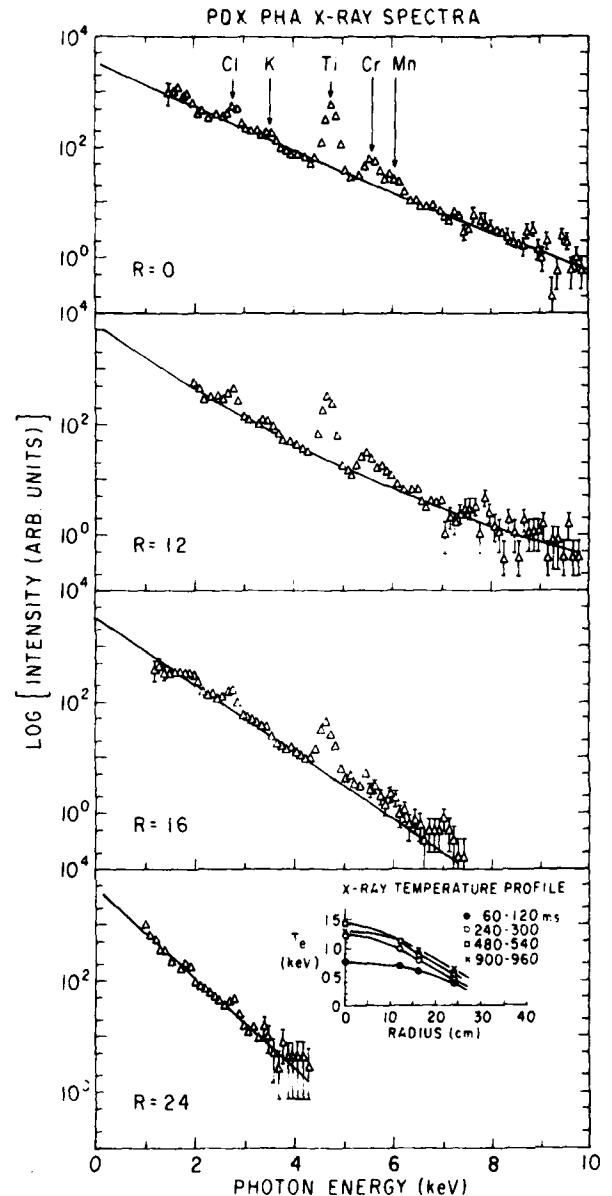


Fig. 5 PHA x-ray spectra from four chords of PDX at  $r = 0, 12, 16,$  and  $24 \text{ cm}$ . Temperature profiles at several times, deduced from x-ray continua, are shown in inset. (PPPL-793687)

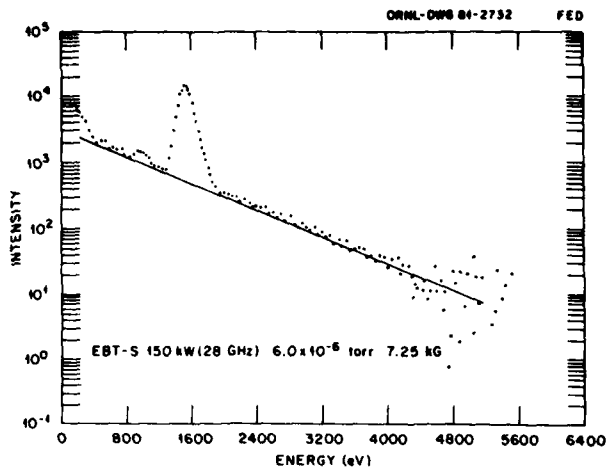


Fig. 6 X-ray spectrum from the EBT device measured by an array of Si(Li) detectors. (Ref. 122).

#### V. X-RAY DIAGNOSTIC INSTRUMENTS

There are several types of x-ray diagnostics used for tokamak research. Each has its own purpose based on its characteristics. These include: (1) energy range, (2) energy resolution, (3) time resolution, and (4) spatial resolution.

In the following sections some of these instruments will be described. Their principles, geometry, mode of operation, characteristics, and examples of data with some interpretation will be presented. The grazing incidence diffraction-grating spectrometer, traditionally considered a vacuum-ultraviolet (VUV) instrument, will be included since important work in the low energy x-ray region has been done using this instrument.

Briefly the instruments to be described and their basic characteristics are as follows:

- (1) Pulse Height Analyzer (PHA) - wide spectral range, moderate time and energy resolution, and moderate spatial resolution.
- (2) X-ray Crystal Spectrometer (XCS) - Narrow spectral range, very good energy resolution, and moderate time and spatial resolution.
- (3) X-ray Imaging System (XIS) - broad spectral range, crude energy resolution, very good time resolution, and good spatial resolution.
- (4) Rotating Crystal Spectrometer (RCS) - moderate spectral range, good energy resolution, moderate to good time resolution, and moderate spatial resolution.
- (5) Grazing Incidence Spectrometer and Monochromator (GISMO) - broad spectral range, good time resolution, good to very good energy resolution, and good spatial resolution.
- (6) Other Instruments with various characteristics.

The diagnostic names, acronyms, and instrument descriptions to follow are characteristic of instruments used at PPPL in the x-ray group and UV, visible spectroscopy group. Similar types of diagnostics, however, are used at many other laboratories.

#### A. PULSE HEIGHT ANALYZER

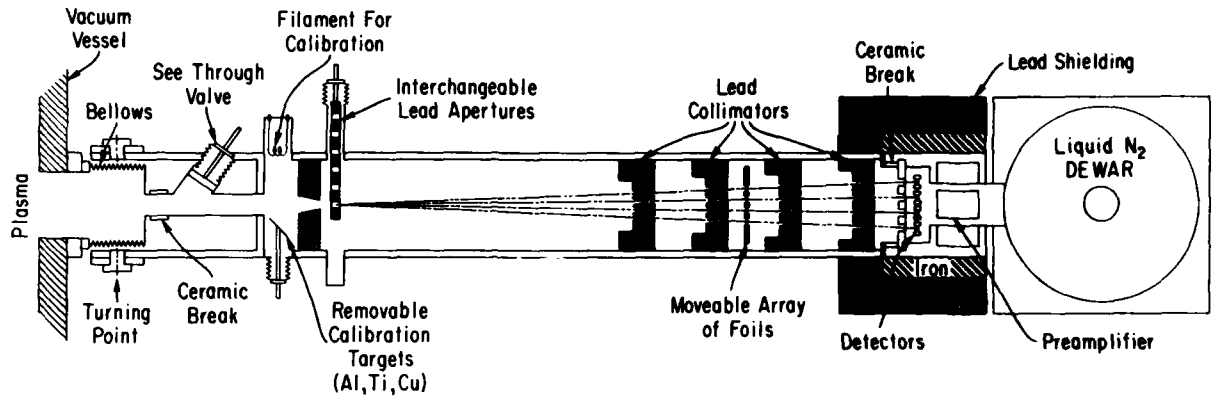
The Pulse-Height Analyzer (PHA) x-ray diagnostic is a very useful and versatile instrument. It is used

on many present day tokamaks [6,13,15,17, 18, 30, 123,] and other fusion experiments [122]. It provides a broad overview of the x-ray emission and yields temporally and spatially resolved measurements of  $T_e$  from the slope of the continuum, high and low  $Z$  impurity concentration (from respectively, impurity line intensities and enhancement of the continuum over bremsstrahlung via recombination), and information on non-Maxwellian features of the electron-velocity distribution [6]. Sample PHA spectra have been shown in Fig. 5. The x-ray energy range at PPPL has historically been limited to 1-30 keV because of beryllium vacuum windows and thin lithium-drifted silicon or Si(Li) detectors. Recently, however, the PHA on PDX has been extended to the sub-kilovolt region by implementation of a windowless Si(Li) detector. This type of detector has already been in use at other laboratories [122]. Figure 7 (located after references) illustrates the principle of the PHA [6]. The PHA may consist of one pivotable tube (for spatial scanning) or several tubes to view several regions of the plasma simultaneously. In each tube a set of collimators directs the x rays to one or more Si(Li) detectors. Multi-detectors are used to improve the time resolution and statistics by increasing the net count rate of the system. The main technical limitation here is pulse pile-up at high rates [6,14] (two pulses arriving simultaneously at the detector are additive and register as one pulse at higher energy). The effects of pulse pile-up are exacerbated by the exponentially decreasing continuum spectrum. A few piled-up low energy pulses, due to high intensity, can cause a relatively large distortion of the spectrum at higher energy where the count rate is much lower. The PHA minimizes this problem by constraining, by means of absorber foils and apertures, each of several detectors to focus on a portion of the total spectrum. The low-energy detector has a thin foil to pass low energy radiation and a small aperture to reduce the count rate to an acceptable range. Higher energy channels have successively thicker foils and larger apertures to equalize count rate. From the partial spectra from each detector the computer synthesizes a single total spectrum by:

- (a) correcting each spectrum for its absorber and aperture size,
- (b) discarding the higher energy portions which may be susceptible to pile-up distortion, and
- (c) overlaying the separate spectra (mathematically) on a common scale.

Four composite spectra measured from four different chords of the PDX tokamak are displayed in Fig 5. The energy resolution of the PHA must be  $\sim 200$  eV FWHM at 6 keV to permit separation of  $K\alpha$  impurity peaks from Fe, Cr, and Ni. These peaks are shifted toward higher energy, relative to the  $K\alpha_{1,2}$  peaks, and broadened because of the distribution of emitting charge states [21]. Good energy resolution is also important to permit separation of peaks from the continuum so that undistorted regions of the continuum are available for  $T_e$  determination. To obtain time resolution, sixteen or more spectra are taken during a single 1-second discharge. This time resolution is limited at present to about 50 ms by (a) the need for reasonable statistics in a spectrum, (b) count-rate limitations of the detectors at the required energy resolution, and (c) the maximum number of detectors which can reasonably be used in one PHA tube. The PHA on PLT has four detectors [6,9], PDX has three detectors per tube for each of five tubes [30], and the TFTR PHA will have eight tubes each with six detectors [125]. Any improvement in the time resolution such as by improvement of pulse-pileup rejection, development of higher transconductance FET's [126], etc., would be welcomed.

Figure 6 is a nice spectrum from the 5-detector Si(Li) array on EBT showing a prominent Al  $K\alpha$  peak [122]. The continuum slope indicates a  $T_e$  value of 850 eV.



**ELECTRONICS**

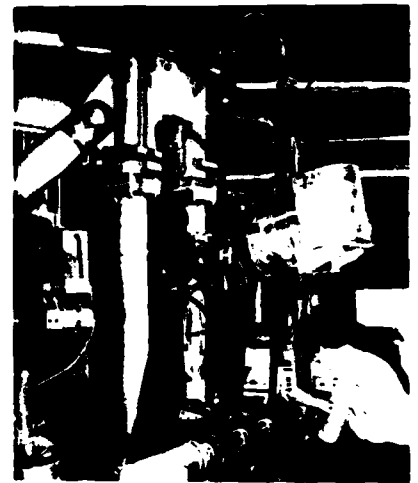
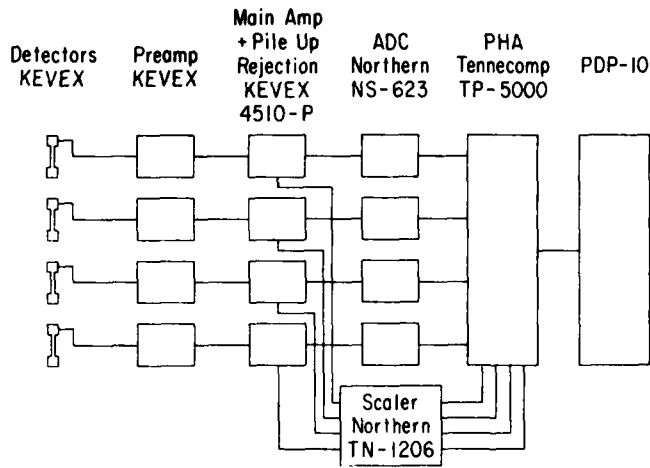


Fig. 7 Schematic of the multidetector PHA system installed on PLT. (PPPL-773872)



### B. THE X-RAY CRYSTAL SPECTROMETER

Crystal spectrometers have been used for detailed investigations of impurity line radiation in both the soft x-ray region (SX) and the ultra-soft x-ray (USX) region. Wavelength scanning (point by point) flat crystal spectrometers and curved crystal multiwavelength polychrometers will be treated in this section. A newly developed dynamically rotating flat crystal spectrometer will be described in a separate section.

Shot-to-shot scanning of x-ray spectra using flat crystal spectrometers has been used both on  $\theta$ -pinches for measurement of impurities [127] and for investigation of temperature diagnostics by measurement of dielectronic-recombination line intensities [45], and on tokamaks for separation of  $K\alpha$  radiation from different charge states of Fe [128], for investigation of oxygen K and Fe L spectra in the region .5-1 keV [6], and for measurement of Mo and Cl emission [82]. Curved crystal spectrometers which are much superior to the scanning flat crystal instruments have been recently developed. These have much higher intensity and are equipped with a position sensitive detector which allows simultaneous measurement of an entire spectrum, avoiding the problems associated with shot-to-shot reproducibility [21]. While these instruments have so far been used only in the SX region, the principle is capable of extension to the USX region, although complications exist. These include: (1) operation in vacuum, (2) use of thin window or windowless detectors, and (3) more severe limitations on resolution because of the relatively broad ( $E/\Delta E < 2000$ ) crystal rocking curves.

The multiwavelength Johann curved crystal spectrometer, recently dubbed X-Ray Crystal Spectrometer (XCS), was first used on tokamaks (PLT) with film recording [129] for investigation of Fe  $K\alpha$  spectra. Subsequently, an improved version with time-dependent readout using a position-sensitive multiwire proportional counter was developed [21]. The principle of operation of this XCS is illustrated in Fig. 8. Also shown is a crystal mounted in a jig used for bending and holding it to a cylindrical shape. X rays from the plasma pass through a vacuum tight beryllium window into tubes filled with helium to minimize x-ray attenuation. X rays of different wavelengths (e.g.,  $\lambda_1$  and  $\lambda_2$ ) from different parts of the plasma are diffracted according to the Bragg relation  $n\lambda = 2d \sin\theta$  ( $n$  = order,  $\lambda$  = wavelength,  $d$  = spacing of crystal

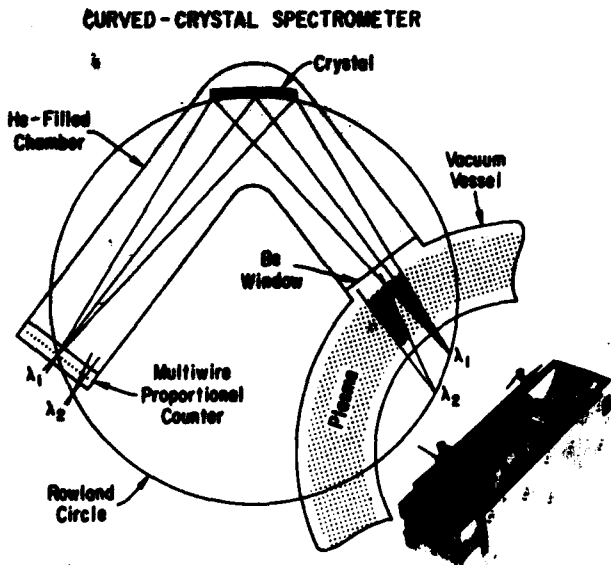


Fig. 8 Schematic of the Johann X-Ray Crystal Spectrometer used on PLT and PDX. (PPPL-773846)

lattice planes,  $\theta$  = Bragg angle) and focussed to corresponding points on the Rowland circle of radius  $R$ . The range of wavelengths or energies which can be covered during a single integration period is determined by the crystal angular dispersion, the detector length  $l$ , and the crystal-to-detector distance  $R \sin\theta$ ,

$$\frac{\Delta E}{E} = \frac{l}{R \sin\theta} \cot\theta \quad (5)$$

The energy resolution is determined by the position resolution of the detector, the distance from crystal to detector, and the crystal rocking-curve width.

The XCS was first used on PLT to study the charge-state distribution of Fe XVIII - Fe XXV ions [21]. A knowledge of this distribution is important for (a) absolute measurement of Fe concentration from the Fe peak of the PHA spectrum (since excitation rate varies with charge state), (b) realistic studies of transport of Fe ions, and (c) verification of theoretical excitation and recombination rates. As the central electron temperature  $T_e$  (0) increases the iron is ionized to a higher charge state and the spectrum shifts to higher energies (Fig. 9).

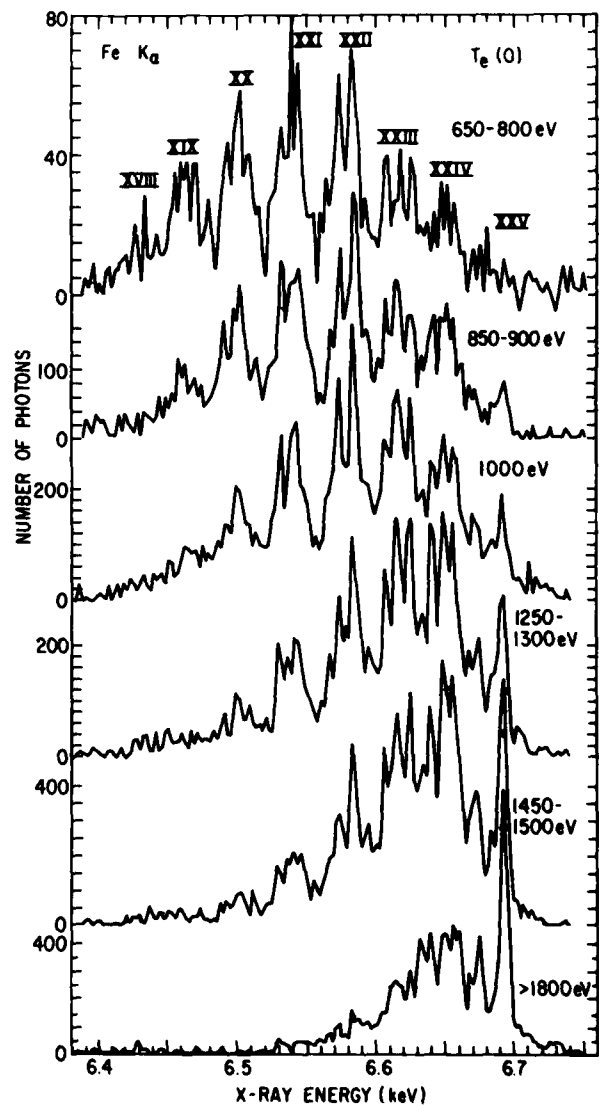


Fig. 9 Sample Fe  $K\alpha$  spectra at different electron temperatures illustrate the shift to higher ionization states as temperature increases. (PPPL-7733660)

For these measurements an XCS with  $R = 5\text{m}$ ,  $E/\Delta E = 1700$ , and using a Ge (220) crystal was used. The spatial resolution of the proportional counter was .4 mm. To obtain time resolution of  $\sim 50$  ms, 16 spectra can be recorded during a 1 second discharge, although data from several similar discharges may have to be added for reasonable statistics.

More recently the XCS on PLT was greatly improved by substitution of an  $\alpha$ -quartz (22 $\bar{4}$ 3) crystal with  $R = 3.33$  m to provide a resolving power  $E/\Delta E = 15000$ . An Fe spectrum measured with this spectrometer is shown in Fig. 10 [22,37]. The peaks shown include resonance lines of Fe XXIII - Fe XXV ( $\beta$ ,  $q$ ,  $w$ , respectively), forbidden ( $z$ ) and intercombination ( $x, y$ ) lines of Fe XXV, and lithium-like satellites excited mostly via dielectronic recombination.

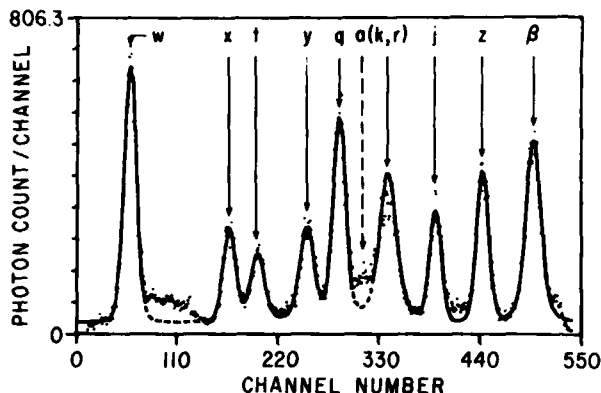


Fig. 10 Sample ultra-high resolution Fe K $\alpha$  spectrum from PLT. The resonance line  $w$  of Fe XXV at 1.85Å is used for Doppler ion-temperature measurement. (PPPL-793023)

This ultra-high resolution XCS was developed mainly to measure ion temperature  $T_i$  by Doppler broadening of the Fe XXV helium-like resonance line  $w$ . A similar high resolution ( $E/\Delta E = 23000$ ) XCS using an  $\alpha$ -quartz (20 $\bar{2}$ 3) crystal has been installed on the PDX tokamak at PPPL for  $T_i$  measurements and other investigations using x rays from highly ionized titanium ions. As shown in Fig. 11 this spectrometer has measured ion temperature increases from  $\sim 1.0$  to 5.8 keV resulting from  $\sim 7$  MW of NBI heating. This figure shows the time history of  $T_i$  as inferred from Voigt-function fits to the Doppler broadened titanium XXI 1s-2p resonance line.

Detailed studies of intensity ratios of various peaks indicated in Fig. 10, relative to line  $w$ , as a function of  $T_e$  and  $n_e$  have demonstrated several other useful aspects of the high-resolution spectra. These include measurement of  $T_e$  from the ratio  $I_x/I_w$ , the departure of Fe charge states from ionization equilibrium, dielectronic recombination rates, and impurity transport rates. Theoretical work by Gabriel and coworkers was used as a basis for some of these measurements [37]. The TFR Group has recently reported similar studies in the USX region for oxygen ions [124].

A different type of high resolution crystal spectrometer using the design of von Ramos and a resistive-anode position sensitive proportional counter has recently become operational on the Alcator C tokamak at MIT [130]. Measurements of Cl and S K spectra have been reported. A higher resolution version has just been implemented for ion-temperature determination [131].

The importance of the XCS for  $T_i$  measurement increases for larger, higher density future tokamak

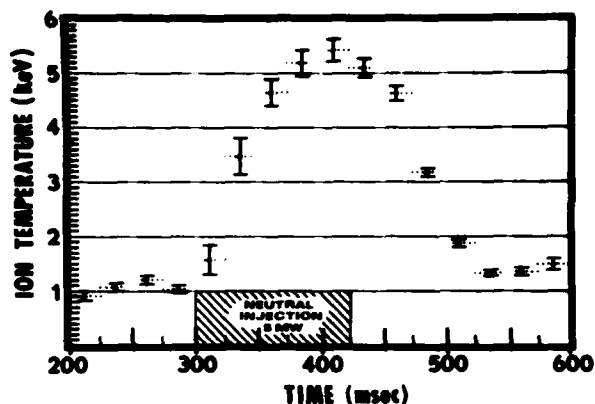


Fig. 11 The ion temperature in PDX derived from Doppler broadening of the Ti XXI 2.61Å line during a neutral-beam heated discharge. (PPPL-81X2151)

plasmas. Other  $T_i$  measurement techniques will become severely limited for reactor plasmas [5].

### C. THE X-RAY IMAGING SYSTEMS

Development of the technique used for the X-ray Imaging Systems (XIS) has revolutionized the study of magnetohydrodynamic (MHD) plasma instabilities or fluctuations in tokamaks. Use of this technique of measuring x ray fluctuations in tokamaks has been actively pursued at many laboratories since about 1972 [23-27,132-138] when "sawtooth oscillations" were discovered in the intensity of x-ray emission from the ST tokamak, as measured by a two-detector system [132]. Because of the profound effect, deleterious in some cases and beneficial in others, the various modes of oscillation can have on plasma particle and energy confinement, MFE theorists and experimentalists have devoted much effort to measurement and interpretation of these fluctuations [23-27,132-139]. In addition, the XIS has been extremely useful in characterizing the effects of impurity radiation on tokamak behavior and understanding the behavior and means of controlling impurities [10]. Various investigators have also used the XIS technique on tokamaks to measure plasma toroidal rotation [6], electron heat conductivity [140], and dielectronic recombination coefficients of impurity ions [47]. A further use is measurement of plasma position.

The principle of the XIS is illustrated in Fig. 12. It is essentially a slot-hole x-ray camera. An array of x-ray detectors views the plasma through a slot, permitting measurement of the line integrated x-ray intensity from several chords of the plasma. This x-ray intensity is modulated by rapid density and temperature variations which accompany the propagation of waves or fluctuations through the plasma. The detectors are typically silicon surface-barrier or PIN diodes, operated in current mode. The x-ray energy range of sensitivity of the diodes is usually limited to greater than .1 keV by absorption in a gold contact layer, typically  $40 \mu\text{g}/\text{cm}^2$ , and a  $\text{SiO}_2$  dead layer, typically  $7 \mu\text{g}/\text{cm}^2$ , on the surface of the detector. The transmission of these layers is given in [6]. The high energy efficiency depends on the effective thickness of the detector. Rough estimates of the spectral composition of the radiation are obtained by inserting absorber foils into the x-ray path. Reference [6] shows the transmission factor for various foils used on the PLT XIS.

The time scale for fluctuations in tokamaks ranges from the millisecond to the microsecond range. Typical

currents generated in the detectors range from a few nanoamperes to tens of microamperes. Thus the current in the detectors must be amplified by low noise, wide band amplifiers. Typical noise levels are .3 nA rms for a 500 kHz bandwidth [6]. The current is recorded by transient digitizers at rates of a few kHz to 1 MHz

### PLT/PDX X-RAY WAVE DETECTOR SYSTEM

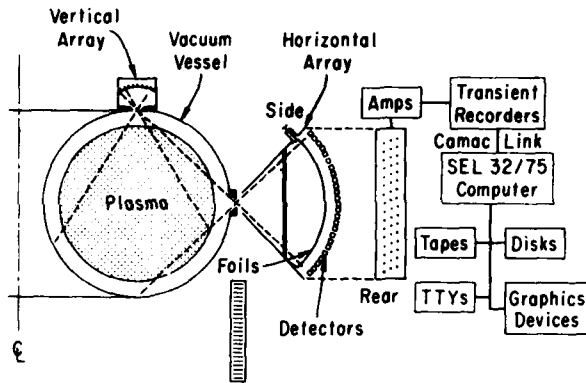


Fig. 12 Schematic of x-ray imaging system using an array of silicon surface-barrier detectors, as used on PLT. (PPPL-796219)

or stored on magnetic tape for later analysis. On PLT the digitizing rate is switchable during the plasma shot, in order to permit measurement of details of fast phenomena such as disruptions.

Figure 13 shows typical data from several detectors of the imaging array on PDX during a portion of a discharge. Graphed is detector current or line integrated x-ray emissivity as a function of time. The stars indicate both chord radius and the zero intensity level for that chord. An  $m=1$  oscillation of the plasma column about its equilibrium position occurs, where  $m$  refers to the mode number of a Fourier expansion of the displacement in the poloidal angle  $\phi$ . From these data we can also construct the time dependence of the radial emissivity profiles as shown in Fig. 14. These particular  $m=1$  oscillations were caused by neutral beam heating.

Emission in the ultra-soft x-ray (USX) range ( $0.1 < E < 1$  keV) is often a significant energy-loss mechanism and an excellent medium for monitoring particle transport and magnetic field evolution. A detailed presentation of the use of the broadband XIS arrays for studying the USX with good spatial ( $\sim 1$  cm) and temporal ( $\sim 1$  ms -  $1$   $\mu$ s) resolution has been given by Eames [10]. Several interesting and significant phenomena have been observed. For example rf heating at the ion cyclotron frequency (ICRH) resulted in a factor of 2.5 increase in the influx of both Fe and deuterium into the plasma, with little change in confinement time ( $\tau \sim 40$  ms). With neutral beam injection in the direction opposite to the plasma current, evidence was noted of an increase in both the tungsten flux and its concentration at the center of the plasma. The power emission density at the center of the discharge was a very large  $2$  W/cm<sup>3</sup> just before a disruption occurred. The tungsten concentration, relative to  $n_e$ , was four times larger at the center than at one half the minor radius.

Another unusual observation was inverted "sawtooth" oscillations in the USX emission. While the soft x-ray (SX) emission ( $E > 1$  keV) decreases at the center, the USX radiation increases. Sawtooth

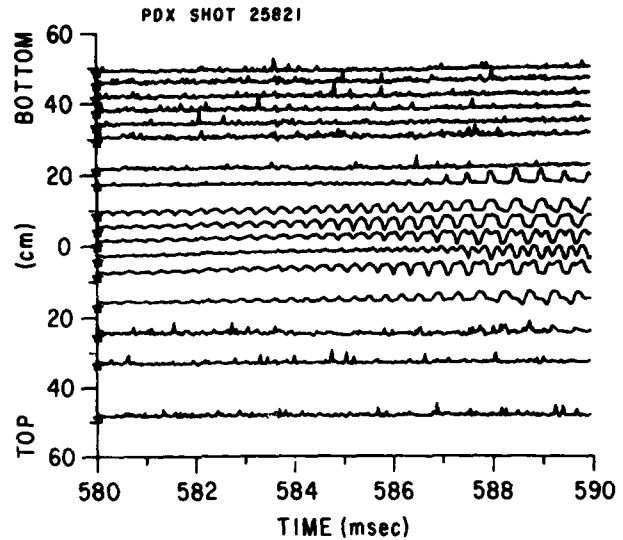


Fig. 13 X-ray emissivity vs. time for several chords from PDX, showing an  $m=1$  oscillation. Stars indicate chord radius and zero level of emissivity. (PPPL-796219)

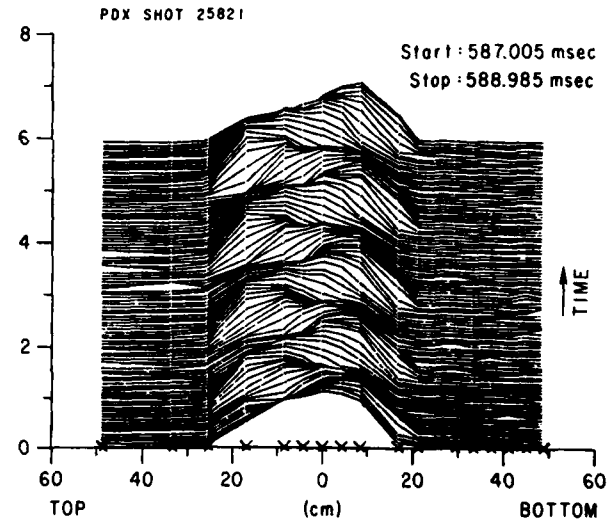


Fig. 14 Radial profiles of x-ray emissivity vs. time for the  $m=1$  oscillation of Fig. 13. (PPPL-806833)

oscillations are explained as a cyclic process in which the plasma is preferentially heated in the center causing the soft x-ray emissivity to slowly rise and the current to redistribute to a more peaked profile [23,26]. At some point MHD or microstability processes become unstable, and the peak collapses or flattens, the energy being rapidly transported outwards. This causes a sudden drop in soft x-ray emission near the center where the temperature drops and a sudden rise in emission at large radii, where the heat is deposited.

A puzzling observation was that of so-called "implosive" disruptions [10]. During the more common "explosive" disruptions both the USX and the SX (Fig. 15) emission decrease rapidly at the center and

increase at the edges. This is suggestive of a movement of the plasma outward from the center, hence, the name "explosive." During "implosive" disruptions, while the SX emission exhibits the usual behavior, the USX emission increases at all radii (Fig. 16). The increase at the center is suggestive of movement of the plasma toward the center, from which the term "implosive" derives. Also observed during the implosive disruption are an asymmetric soft x-ray flash lasting for 10-20  $\mu$ s and a simultaneous doubling of the USX emission over the plasma cross section in 10  $\mu$ s. The soft x-ray flash is believed to be due to conversion of magnetic energy into kinetic energy. The doubling of the USX emission over such a short time scale was somewhat difficult to explain. A tentative explanation is enhanced oxygen radiation [10].

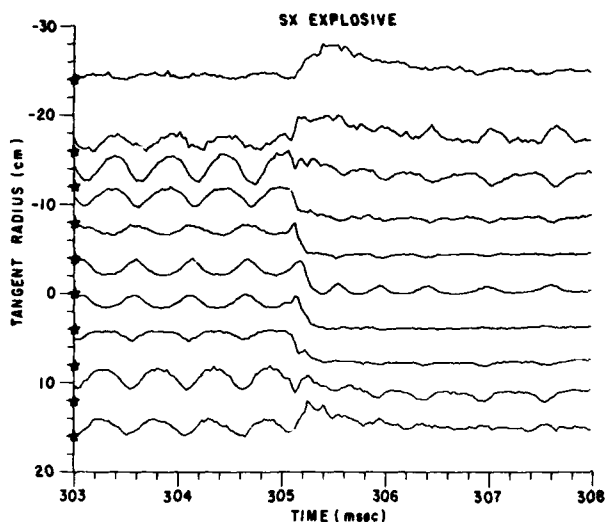


Fig. 15 Soft x-ray traces vs. time from imaging system on PLT showing an explosive disruption at 305.2 ms. (PPPL-793050)

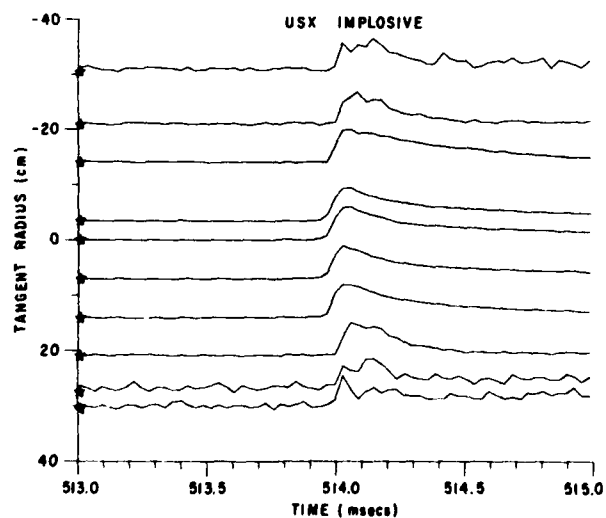


Fig. 16 Implosive type of disruption at 514 ms as measured by ultra soft x-ray imaging system on PLT. (PPPL-793049)

#### D. THE ROTATING CRYSTAL AND GRAZING INCIDENCE SPECTROMETERS

The recent development of the Rotating Crystal Spectrometer (RCS) [10,141] at PPL has caused a tremendous increase in the volume of high resolution USX data measurable from tokamaks, as compared to grazing-incidence grating spectrometers. The small size, light weight, and relative simplicity of construction of the RCS all represent significant improvements in versatility and in suitability as a multichordal instrument for tokamak measurements. Even so, the RCS is by no means a replacement for the grazing-incidence grating monochromator and spectrometer (GISMO) which has been used for decades for high resolution spectrometry of MFE plasma. The two instruments are, rather, complementary, with GISMO extending to longer wavelength and providing absolute intensity measurements. GISMO is compared with the RCS here only because the two instruments partially overlap in spectral range and are used for similar purposes.

The RCS can scan the entire spectrum from 500 eV to 2 keV with good energy resolution ( $E/\Delta E = 400$ ) twenty times during a tokamak discharge, giving a time resolution of 50 ms. Alternatively, the RCS crystal can be fixed at one setting to provide very good time resolution for one spectral point. The GISMO - type instrument using film requires instead twenty discharges to cover the range 200-1000 eV. Using photoelectric readout the GISMO can measure the intensity at only two points of the entire spectrum during one discharge, so that many discharges would be required to scan the entire spectrum. The RCS, however, may present some problems with regard to absolute calibration since its detector, a series of microchannel plates, has rapid variations in efficiency as the angle of incidence of the radiation is varied.

The RCS is shown in Fig. 17 (following references). A soller collimator limits the angular divergence of the radiation from the plasma to roughly .1 degree. A set of absorber foils of 1  $\mu$ m parylene and .6  $\mu$ m Al reduces background due to intense radiation at wavelengths longer than 26 $\text{\AA}$  [141]. The radiation is Bragg diffracted from a TAP or ADP plane crystal and detected by a set of four Chevron microchannel plates (MCP) arranged on a semicircle. The front surface of each MCP pair has a MgF<sub>2</sub> coating to enhance its sensitivity to soft x rays. The signal output consists of current to the collector plates. In order to obtain spectra the crystal is rotated, typically at 10 revolutions per second, and the collector current is measured as a function of time. The energy calibration, i.e., the Bragg angle, is determined by interrupting the light from an LED to a photodetector by a slotted disk which rotates synchronously with the crystal.

Figure 18 shows output traces during a plasma shot recorded with a transient analyzer. Traces (a) show the signal from the photodetector, which is produced by the slotted disk interrupting the light beam from the LED. One of the slots has been covered to provide a reference for angle determination. Figure 18b shows the current to the collector plates of the MCP. Spectra are produced alternately by the TAP and the ADP crystal. The spectra with higher intensity are from the TAP crystal, which spans the wavelength region 10-17  $\text{\AA}$  where the iron L radiation is located. The two lower spectra show iron L lines on an expanded time scale early and late in the discharge. During the early times Fe XVII lines are dominant ( $t = 109-110$  ms). Later all Fe charge states are present ( $t = 309-310$  ms). Figure 19 (after references) shows an Fe L spectrum late during a PLT discharge. Peak identifications were made from identifications of prominent Fe L lines in solar flare and laser plasmas [10,141]. Another spectrum from an oxygen-rich discharge is shown in Fig. 20. By tilting the RCS about a pivot point, chordal profiles of x-ray emission can be measured. Figure 21 shows such profiles of

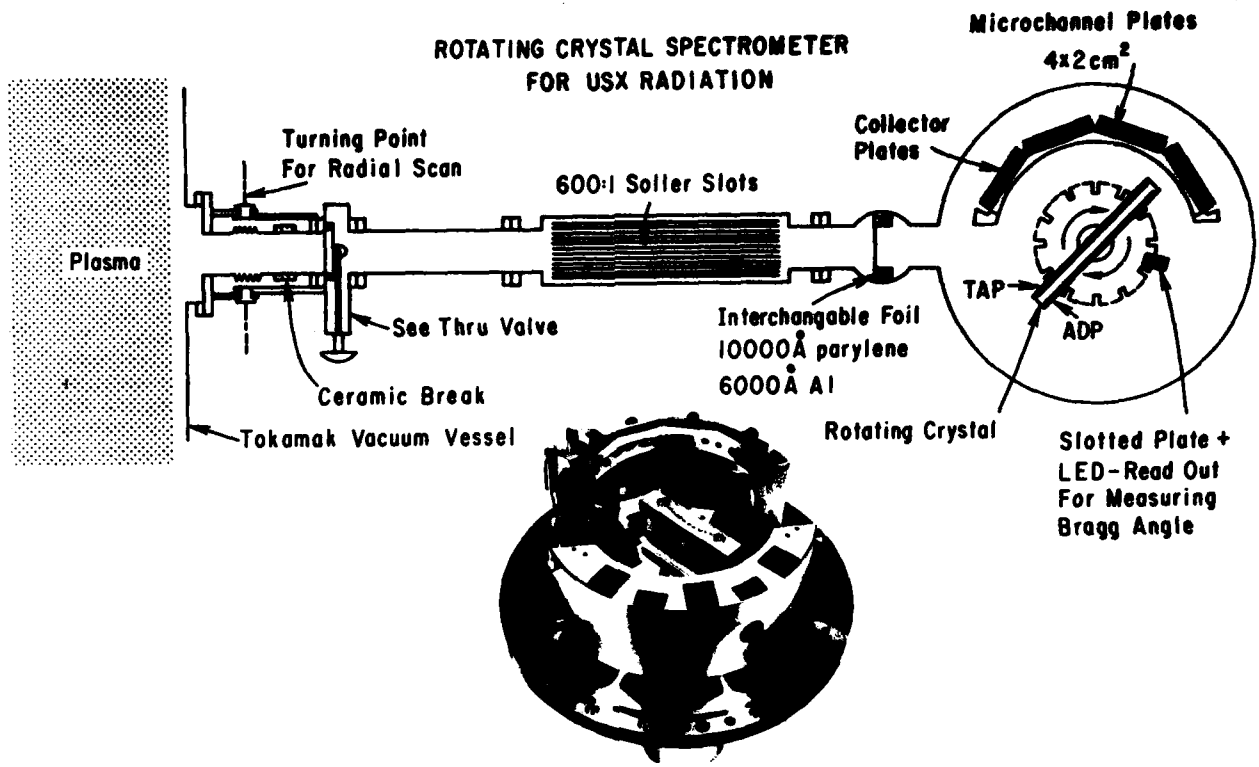


Fig. 17 Schematic of the rotating crystal spectrometer installed on PLT and photograph of the crystal and detector assembly. (PPPL-809045)

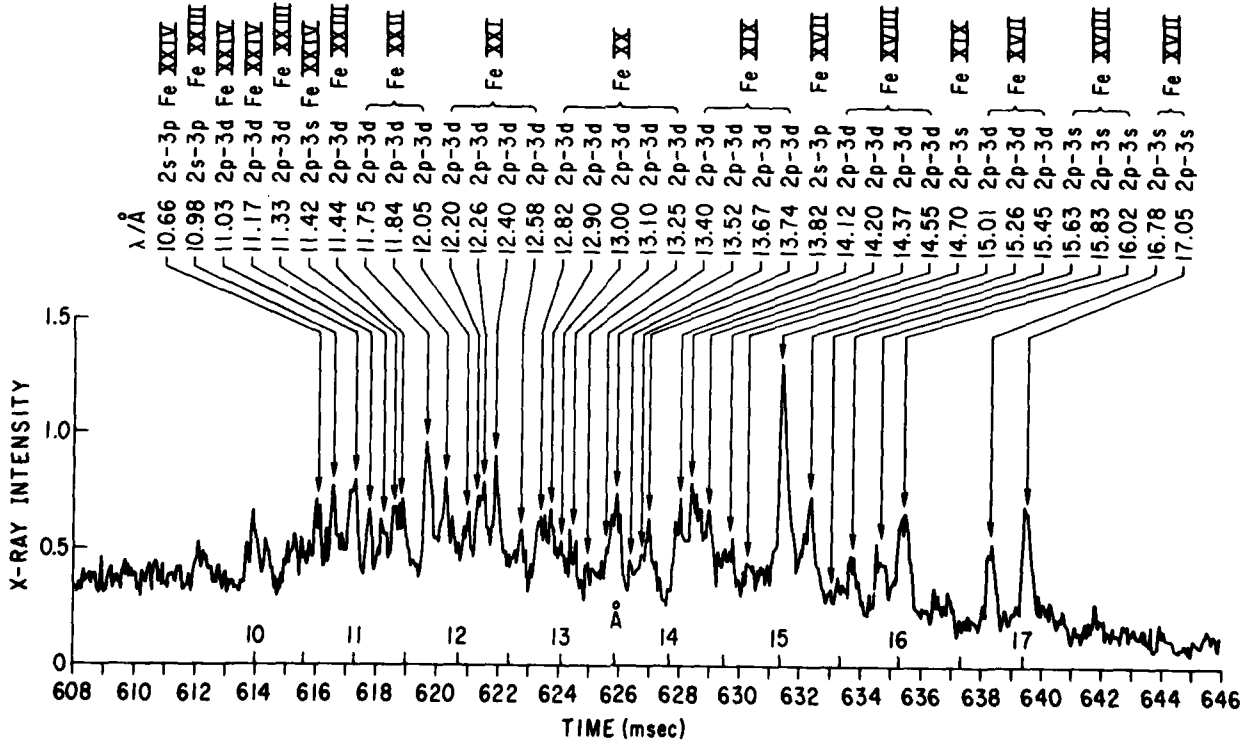


Fig. 19 Iron L spectrum measured with the rotating crystal spectrometer. (PPPL-806747)

several major iron L-transitions for different charge states.

The grazing incidence diffraction grating spectrometer and monochromator has long been used as a standard diagnostic for monitoring radiation from tokamak plasmas, both in the low energy x-ray region and at lower energies ( $E < .1$  keV). These instruments are commercially available and are described in the literature [29]. Both photographic (broadband, time-integrated) and photoelectric (one or two narrow wavelength regions, time-resolved) detection have been

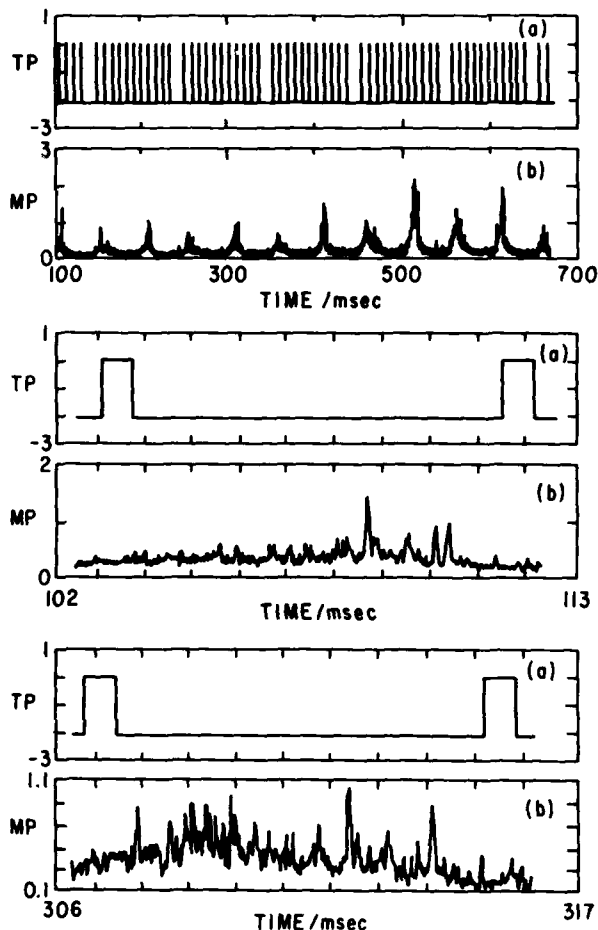


Fig. 18 Output from rotating crystal spectrometer with 3 different time scales. (a) Timing pulses generated when a slot in the rotating disk passes the LED. (b) Microchannel plate output obtained as the crystal rotates. (PPPL-809056)

used [63,79,80].

Comparison of photographic spectra from ORMAK with theoretical calculations for emission from tungsten XXXI-XXXIV identified  $\Delta n=0$  transitions as the source of intense pseudo-continua in the 40-70 Å region [80]. Similar pseudo-continua near 50 Å and other bands at longer wavelength have also been observed in the Japanese tokamak DIVA [34,35,94]. These continua are evidently largely due to thousands of unresolved  $\Delta n=0$  transitions involving the 4d electrons of several charge states of tungsten. In ORMAK [80] and PLT [33] these bands of radiation often accounted for 40-80% of the radiated power and led to or contributed toward undesirable effects such as poor confinement and hollow temperature profiles (cool central plasma). It was

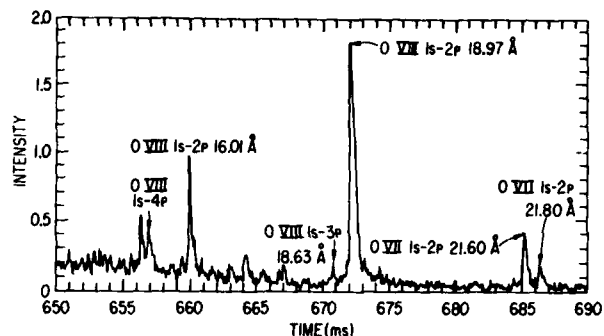


Fig. 20 Oxygen K spectrum from PLT discharge with high oxygen level. (PPPL-809110)

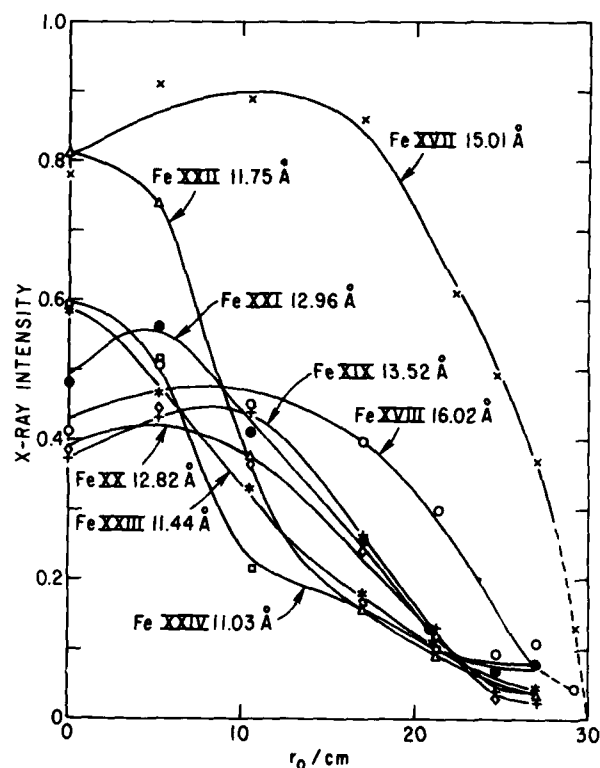


Fig. 21 Chord integrated intensity profiles of several iron-L transitions for different charge states, measured by the rotating crystal spectrometer. (PPPL-806748)

possible to reduce the tungsten content through cooling of the plasma edge by adding small amounts of neon or oxygen, or by appropriate programming of the hydrogen influx. These experiments identifying tungsten as a malefactor, and further experiments with tungsten limiters replaced by low Z limiters of stainless steel and carbon (which yielded much more favorable plasma behavior), led to the policy at PPPL [58] and ORNL of excluding high Z materials from the interior of tokamaks.

Grazing incident spectrometers are routinely used to monitor the OVII and OVIII radiation at 21.6Å and

18.96Å, respectively. An interesting rapid increase in intensity of the O VIII 102Å line from ORMAK coincident with neutral beam injection has been interpreted to be the result of charge transfer from hydrogen (whose density is increased significantly by the beams) to  $O^{7+}$  ions in excited states [63]. Anomalously high (relative to excitation by electrons) intensities of the 115.8-Å line of  $O^{5+}$  and the 81.9-Å line of  $O^{6+}$  in ISX-A have been attributed to excitation via charge transfer from hydrogen atoms into excited states of  $O^{n+}$  [79].

#### E. OTHER X-RAY DIAGNOSTICS

The filter-detector scheme has long been used for measurements of x rays from plasmas [3,7]. A major defect of this method for temperature measurement is the uncertainty of interpretation and interference from impurity radiation.

The gas proportional counter has also been used for tokamak x-ray spectroscopy [142]. The energy resolution is poor making it difficult to separate K $\alpha$  peaks from Fe, Cr, and Ni. The gas scintillation proportional counter, however, (GSPC) [143] has better resolution, although not as good as the Si(Li), and high rate capability. Because of its radiation-damage resistance, it may be good for reactor-plasma  $T_e$  measurement were good energy resolution is not so critical. Photoelectron spectroscopy has been used to deduce the carbon content in the center of the T-4 tokamak [67] following electron capture by CVII from hydrogen. This technique may have further application.

#### VI. FUTURE DEVELOPMENTS

The controlled fusion research program has always suffered from insufficient information on plasma behavior. Designing instrumentation to provide ideal unambiguous data has always been an elusive goal. Often two or more schemes are developed to measure one plasma property, and neither method is fully adequate, e.g.,  $T_e$ ,  $T_i$ ,  $n_e$ ,  $I(r)$ . In addition the research effort has often suffered from a shortage of money, manpower, time, and particularly physicists and engineers with the appropriate expertise to develop optimal diagnostics. The trend at PPPL has recently been more toward either hiring specialists in particular areas of physics relevant to the development of needed diagnostics, or tapping the pool of expertise external to the fusion program through cooperative development efforts, subcontracts, DOE sponsored contracts to outside laboratories, etc. Such collaborative efforts are certainly beneficial to the fusion effort and are probably beneficial, for various reasons, to the external parties involved. The MFE x-ray diagnostics program has several areas where improvements in instrumentation and techniques and new creative ideas for measurements would be welcomed. In the following paragraphs I will discuss some improvements in x-ray instrumentation that are desirable, some of which are currently being developed for TFTR.

In former times when tokamaks were smaller and diagnostics budgets were leaner than today, many experiments required shot-to-shot adjustment of spatial view or time windows to get adequate spatial or temporal information, or accumulation of data over several shots to get usable statistics. In view of the magnitude, cost, importance, and more urgent nature of future fusion experiments such as TFTR and MFTF-B, such arduous, time consuming approaches are no longer practical. This is especially true for operation of full tritium plasmas in TFTR (the crucial experiments), since the maximum number of such discharges is 4000, being limited by the allowable tritium inventory on site and neutron activation. Thus, the hope for TFTR x-ray diagnostics, and others, is to have several spatial channels and to improve throughput in each channel so that statistically significant data can be recorded during each shot with suitable spatial and

temporal resolution.

Much of the development required for TFTR x-ray diagnostics is associated with the increased radiation levels, as compared to present-day tokamaks, expected during neutral beam injection (NBI) heating. For 45 MW (beam power) DD plasmas a 2.5-MeV neutron flux density of  $10^{11}$  neutrons/cm<sup>2</sup>/sec is expected near the tokamak, for a 1 second pulse. For DT plasmas a flux density of  $6 \times 10^{13}$  14-MeV neutrons/cm<sup>2</sup>/sec is predicted. These neutron intensities can quickly damage solid state detectors. The neutrons and concomitant secondary gamma rays from the tokamak structure and concrete walls can generate background noise levels in detectors which completely mask the x-ray signals. Thus all x-ray diagnostics are being redesigned to include extensive neutron and gamma-ray shielding and collimation to maximize the signal to noise ratio. For the XIS, fast gridded ionization chambers are being developed, because of their resistance to radiation damage, to replace the easily damaged silicon surface barrier detectors.

The TFTR PHA will view more (8-12) radial chords than previously for PLT (1-chord) and PDX (5-chords). To accommodate the larger range of  $T_e$  and, thus, intensity and improve time resolution, a combination of more detectors per channel (6 vs 3 or 4) and faster electronics is being implemented. One germanium detector per channel will be added since higher energy x rays will be produced by the higher temperature plasmas. Since overall reliability decreases as the number of detectors increases, and a vacuum failure is potentially more serious, detector passivation techniques will be developed to improve the probability for detector survival under adverse conditions. Fourteen-MeV neutrons can generate large pulses (up to 11 MeV) in Si(Li) detectors. Special precautions must be taken in the design of electronics to prevent saturation or overloading by these pulses. The amount of remote control, monitoring, and testing is being increased due to the higher degree of complexity and sophistication and the reduced accessibility of the diagnostics. Tokamak diagnostics have always had to be more reliable and automatic than laboratory instruments because of remote operation and limited accessibility. This will be even more true for TFTR.

Some further improvements planned for the TFTR XIS are more detectors, an infrared-emitting diode for system testing and comparison of detector responses, a remotely movable standard detector for calibration of fixed detectors during operation, division of the amplifier into two modules with the first (preamplifier) directly on the detector feedthrough to reduce electrical pickup and minimize input capacitance, and a wider range of gains in the electronics. Because of the tremendous data-generating capacity of the XIS when digitization rates up to 500 kHz are used (240 detectors  $\times$   $5 \times 10^5$  words/detector/sec), mass-storage techniques have been investigated. A scheme using FM multiplexing was devised to store data from up to 320 detectors at 500 kHz bandwidth on a 42-track high speed analog tape recorder. Up to 100 shots per reel could be stored for later playback and digitization.

Developments for the TFTR XCS include improving time resolution by means of higher x-ray fluxes at the detector. This will be achieved by (1) using lower Z seed impurities, such as argon, which radiate higher photon fluxes and produce usable signals at lower  $T_e$  (This enables us also to make measurements further from the plasma center where  $T_e$  is lower.); (2) increasing the crystal and detector size; and (3) choosing crystals with higher reflectivity. To accommodate higher x-ray intensity, faster detectors and electronics are being developed. The larger dynamic range provided by these improvements will be important for TFTR since the temperature excursion during a discharge (and, thus, the range of x-ray flux) will be large due to intensive neutral beam, rf, and

compression heating.

Grating monochromators are being converted to polychromators by use of multi-element detectors such as the intensified Reticon photodiode array [145].

There is need for further improvement of x-ray diagnostics both for near future experiments such as TFR and for future reactors. The need for higher count rates has been mentioned. Shielding and collimation will just prevent damage to the PHA Si(Li) detectors over the life of TFR ( $\sim 10^{10}$  neutrons/cm<sup>2</sup>). Reactors, however, will have much higher duty cycles. Thus the detectors will have to either withstand neutron fluences two orders of magnitude higher than present Si(Li) detectors can, or be exposed to the reactor only for brief periods to make a measurement. A possible replacement detector is the gas scintillation proportional counter [143]. Improvement of reflectivity and resolution of multilayer synthetic crystals would make them attractive for extension of the rotating crystal spectrometer to longer wavelength. The present design of the TFR x-ray imaging array (XIS) makes it suitable for operation with DD plasmas only. Use of the ionization chamber only hardens the system for DT survival; in DT operation background noise levels from radiation will render the system inoperable. For a DT-operational XIS further development must be done. The detectors must be moved further from the plasma and more extensively shielded. In addition reflective x-ray optics, such as grazing incident mirrors or Bragg crystals will probably have to be used to permit removal of the detector from direct view of the neutron-emitting plasma. One candidate for an improved detector for both the XIS (radiation resistance) and the XCS (high count rate, good position resolution) is the microchannel plate preceded by a high efficiency x-ray photocathode. Solid photocathodes are not suitable. Porous photocathodes of CsI have demonstrated high efficiency [144]. Further work must be done, however, to answer questions about their reliability, construction, degradation with use, efficiency, etc.

#### VII. SUMMARY

The Tokamak is a major contender for demonstration of controlled fusion as an eventual power source. X-ray diagnostics are an important part of the experimental effort. These instruments permit measurement of plasma conditions from various aspects of the continuum and line radiation due largely to impurities in the plasma. Soft x-ray diagnostics range from (a) instruments with moderate energy and time resolution, which provide an overview of the soft x-ray emission and a measure of electron temperature and impurity concentration, to (b) those with very good energy resolution and moderate time resolution, which measure ion temperature, impurity charge-state distributions, low energy impurity radiative power and other parameters, from details of impurity spectral line profiles, to (c) instruments which view many spatial chords simultaneously with very fast time response but crude spectral resolution to monitor low energy impurity radiation and fast fluctuations in x-ray emission due to MHD instabilities.

Development required for near future tritium-burning tokamaks includes shielding and collimation of neutrons and gamma rays, development of radiation-hard detector substitutes in some cases, and improvement of instrumental throughput. Problem areas are limited count rate for detectors and electronics, high response to background radiation, low crystal reflectivity, and broad crystal rocking curves in the low energy x-ray region. For reactors, radiation damage susceptibility will preclude use of all solid state detectors for direct view of the plasma; substitute measurement schemes must be developed.

#### REFERENCES

\*Work supported by Department of Energy Contract No. DE-AC02-76-CHO-3073.

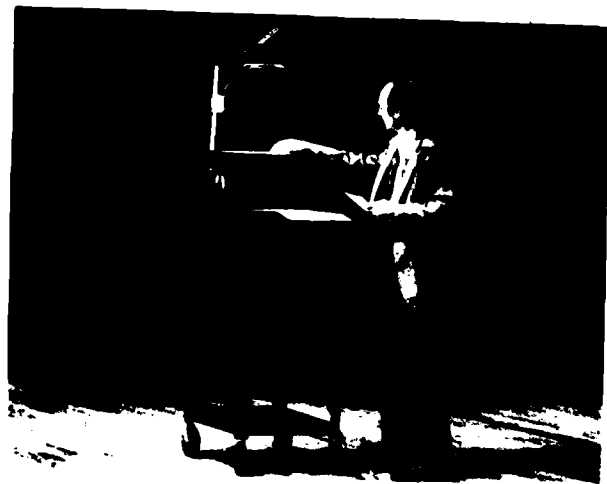
- [1] IEEE Spectrum, New York (December 1, 1980) p.1.
- [2] E. Sindoni and C. Wharton, eds., Diagnostics for Fusion Experiments, (Pergamon Press, New York, 1979).
- [3] T.F. Stratton in Plasma Diagnostics Techniques, edited by Huddleston and Leonard, (Academic Press, New York, 1965) 359-397.
- [4] C.B. Wharton, in Physics Today, 52 (May 1979).
- [5] Equipe TFR, Nucl. Fusion 18, 647 (1978).
- [6] S. von Goeler, in Diagnostics for Fusion Experiments, (Pergamon Press, New York, 1979) 79-109.
- [7] C. de Michelis and M. Mattioli, "Soft X-Ray Spectroscopic Diagnostics of Laboratory Plasmas," EUR-CEA-FC-1084 (March, 1981) 207 pp.
- [8] S. von Goeler, W. Stodiek, H. Eubank, H. Fishman, S. Grebenshikov, E. Hinnov, Nucl. Fusion 15, 301 (1975).
- [9] S. von Goeler, N. Sauthoff, M. Bitter, K. Brau, D. Eames, B. Fraenkel, A. Greenberger, K. Hill, R. Horton, G. Hovey, J. Hovey, W. Roney, W. Stodiek, "Soft X-Ray Measurements on the PLT Tokamak," PPPL-1383 (1977) 15 pp.
- [10] D.R. Eames, "Ultra-Soft X-Ray Emission from the Princeton Large Torus Tokamak," Doctoral Dissertation, Princeton University (January, 1981) 204 pp.
- [11] P. Blanc, P. Brouquet, N. Uhre, "Soft X-Ray Spectrometry at High Count Rates," EUR-CEA-FC-962, (June 1978) 17 pp.
- [12] Equipe TFR, Nucl. Fusion 17, 213 (1977).
- [13] G.R. Dyer, G.H. Neilson, G.G. Kelly, Nucl. Inst. Meth. 161, 365 (1979).
- [14] S. von Goeler, W. Stodiek, H. Eubank, Y. Sun, P. Thompson, S. Slusky, "The X-Ray Pulse Height Analysis System of the ST Tokamak," MATT-1060 (1974) 15 pp.
- [15] R.D. Gill, K. B. Axon, J.W.M. Paul, R. Prentice, Nucl. Fusion 19, 1003 (1979).
- [16] N.J. Peacock, D.D. Burgess, "New Developments in Measurement Techniques for High Temperature Plasmas," CLM-P612 (April, 1980) 32 pp.
- [17] F. Rohl, "X-Ray Pulse Height Analysis," IPP 6/193 (February, 1980) 105 pp.
- [18] R. Bartiromo, A. Tuccillo, "X-Ray Spectroscopic Measurements on FT Tokamak," Associazione EURATOM-CNEN Sulla Fusione Centro di Frascati, Report 80.24/p (June 1980) 19 pp.
- [19] P. Platz, J. Ramette, E. Belin, C. Bonnelle, A. Gabriel, "High Throughput, High Resolution Soft X-Ray Crystal Spectrometer for Tokamak-Plasma Studies," EUR-CEA-FC-1057 (1980) 20 pp.
- [20] R. Bartiromo, P. De Marco, R. Giannella, S. Mantovani, G. Pizzicaroli, "Proposal of an X-Ray Spectrometer for Ion-Temperature Measurements in JET," Associazione EURATOM-CNEN Sulla Fusione, Centro di Frascati, Report 80.31 (July 1980) 31 pp.
- [21] K.W. Hill, S. von Goeler, M. Bitter, L. Campbell, R.D. Cowan, B. Fraenkel, A. Greenberger, R. Horton, J. Hovey, W. Roney, N.R. Sauthoff, W. Stodiek, Phys. Rev. A19, 1770 (1979).
- [22] M. Bitter, S. von Goeler, R. Horton, M. Goldman, K.W. Hill, N. Sauthoff, W. Stodiek, Phys. Rev. Lett. 42, 304 (1979).
- [23] N.R. Sauthoff, "The Analysis of Magneto-hydrodynamic Modes in Tokamaks by X-Ray Techniques," SPIE Vol. 106, X-Ray Imaging, 40 (1977).
- [24] N.R. Sauthoff, S. von Goeler, W. Stodiek, Nucl. Fusion 18, 1445 (1978).
- [25] D. R. Eames, S. von Goeler, N.R. Sauthoff, W. Stodiek, "Observations of Several Disruptions in



- PLT Using Soft and Ultra-Soft X-Ray Radiation," PPPL-1530 (March 1979) 52 pp.
- [26] G. L. Jahns, M. Soler, B.V. Waddell, J.D. Callen, H.R. Hicks, Nucl. Fusion 18, 609 (1978).
- [27] G.L. Jahns, "Observation of Tokamak Plasmas With An Array of PIN Diode Detectors," SPIE Vol. 106, X-Ray Imaging, 36 (1977).
- [28] M. Bitter, S. von Goeler, N. Sauthoff, K.W. Hill, K. Brau, D. Eames, M. Goldman, E. Silver, W. Stodiek, "X-Ray Radiation from Tokamaks," in Proceedings of the International Conference on X-Ray Processes and Inner-Shell Ionization, Stirling University, Scotland, 1980 (to be published).
- [29] J.A. R. Samson, Techniques of Vacuum Ultraviolet Spectroscopy, (John Wiley and Sons, New York, 1967).
- [30] E.H. Silver, M. Bitter, K. Brau, D. Eames, A. Greenberger, K.W. Hill, D.M. Meade, W. Roney, N.R. Sauthoff, S. von Goeler, "Initial Soft X-Ray Measurements from the PDX Tokamak," PPPL Preprint, submitted to Nucl. Fusion.
- [31] G.A. Doschek, U. Feldman, R.D. Cowan, "High Resolution X-Ray Spectra of Solar Flares V. Interpretation of Innershell Transitions in FeXX-Fe XXIII," NRL Preprint (1980) 48 pp. H.J. Kunze, "On the Density Dependence of the Intensity Ratio of Resonance and Intercombination Transitions in CV," Department of Physics and Astronomy, University of Maryland, Preprint 81-146.
- [32] S. Suckewer, E. Hinnov, D. Hwang, J. Schivell, G.L. Schmidt, K. Bol, N. Bretz, P. Colestock, D. Dimock, H. Eubank, R. Goldston, R.J. Hawryluk, J. Hosea, H. Hsuan, E. Meservey, D. McNeill, "Radiation Losses in PLT During Neutral Beam and ICRF Heating Experiments," PPPL-1768 (February 1981) 34 pp.
- [33] E. Hinnov, K. Bol, D. Dimock, R.J. Hawryluk, D. Johnson, M. Mattioli, E. Meservey, S. von Goeler, Nucl. Fusion 18, 1305 (1978).
- [34] S. Kasai, A. Funahashi, M. Nagami, T. Sugie, Nucl. Fusion 19, 195 (1979).
- [35] M. Shiho, S. Konoshima, A. Funahashi, S. Kasai, T. Sugie, N. Suzuki, M. Shimada, N. Fujisawa, Nucl. Fusion 18, 1705 (1978).
- [36] K. Brau, S. von Goeler, M. Bitter, R.D. Cowan, D. Eames, K.W. Hill, N. Sauthoff, E. Silver, W. Stodiek, "Observations of Giant Recombination Edges on PLT Tokamak Induced by Particle Transport," PPPL-1644 (March 1980) 27 pp; Phys. Rev. A 22, 2769 (1980).
- [37] M. Bitter, K.W. Hill, N. Sauthoff, P. Efthimion, E. Meservey, W. Roney, S. von Goeler, R. Horton, M. Goldman, W. Stodiek, Phys. Rev. Lett. 43, 129 (1979).
- [38] See Reference 10.
- [39] TFR Group, Phys. Lett. 74A, 57 (1979).
- [40] J.L. Schwob, M. Klapisch, M. Finkenthal, N. Schweitzer, C. Breton, C. DeMichelis, M. Mattioli, Phys. Lett. 62A, 85 (1977).
- [41] R. Engleman, Jr., D.B. Thomson, D.A. Monaghan, Los Alamos Scientific Laboratory Report LA-6275-MS (1976).
- [42] M. Klapisch, J.L. Schwob, M. Finkenthal, B.S. Fraenkel, S. Egert, A. Bar-Shalom, C. Breton, C. DeMichelis, M. Mattioli, "Identification of Forbidden Lines in the Soft X-Ray Spectrum of the TFR Tokamak," EUR-CEA-FC-945 (1978) 16 pp.
- [43] L.A. Jones, E. Kallne, D.B. Thomson, J. Phys. B: Atom. Molec. Phys. 10, 187 (1977).
- [44] A. Pospieszczyk Astron. and Astrophys. 39, 357 (1975).
- [45] R.U. Datla, L.A. Jones, D.B. Thomson, "Temperature Diagnostics Using Lithium-Like Satellites," Los Alamos Scientific Laboratory Report LA-8324-MS (1980) 12 pp.
- [46] R.L. Brooks, R.U. Datla, H.R. Griem, Phys. Rev. Lett. 41, 107 (1978).
- [47] C. Breton, C. DeMichelis, M. Finkenthal, M. Mattioli, Phys. Rev. Lett. 41, 110 (1978).
- [48] E. Hinnov, J. Nucl. Materials, 53, 9 (1975).
- [49] D.L. Dimock, H.P. Eubank, E. Hinnov, L.C. Johnson, E.B. Meservey, Nucl. Fusion 13, 271 (1973).
- [50] D. Meade, et al., "PDX Experimental Results," PPPL-1740 (1981) 30 pp.
- [51] H.P. Furth, Nucl. Fusion 15, 487 (1975).
- [52] H.P. Furth, "U.S. Tokamak Research," PPPL-1598 (1979) 11 pp.
- [53] D. Steiner, "Nuclear Fusion: Focus on Tokamak," IEEE Spectrum (July 1977) 32-38.
- [54] J.T. Hogan, "General Principles of Magnetic Fusion Confinement," ORNL/TM-7107 (1980) 32 pp.
- [55] L.A. Artsimovich, Nucl. Fusion 12, 215 (1972).
- [56] K.M. Young, "Diagnostic Problems of Large Tokamaks," PPPL-1365 (1977) 25 pp, (in Proc. 5th Int. Conf. on Atomic Physics, Berkeley, 1976) 391 (Plenum Press, New York, 1977).
- [57] J.D. Lawson, Proc. Roy. Soc. (London) B70, 6 (1957).
- [58] K. Bol, et al., "Radiation, Impurity Effects, Instability Characteristics, and Transport in Ohmically Heated Plasma in the PLT Tokamak," PPPL-1492 (December 1978) 25 pp; Plasma Physics and Controlled Nuclear Fusion Research (Proc. 7th Int. Conf. Innsbruck, 1978) 1, IAEA (1979) 11.
- [59] H. Eubank, et al., "PLT Neutral Beam Heating Results," PPPL-1491 (November 1978) 47 pp; Plasma Physics and Controlled Nuclear Fusion Research (Proc. 7th Int. Conf. Innsbruck, 1978) 1, IAEA (1979) 197.
- [60] J.C. Hosea, "Regimes of Operation in the Princeton Large Torus," PPPL-1589 (1979) 11 pp.
- [61] G.H. Neilson, J.F. Lyon, M. Murakami, "Injection-Dominated Tokamak Experiments at ORNL," ORNL/TM-6506 (1978) 11 pp.
- [62] R.C. Isler, E.C. Crume, H.C. Howe, "Impurity Behavior During Neutral Beam Injection and Gas Puffing into ORMAK," ORNL/TM-6366 (1978) 47 pp; and Nucl. Fusion 19, 727 (1979).
- [63] R.C. Isler, Phys. Rev. Lett. 38, 1359 (1977).
- [64] J. Hosea, et al., "Fast Wave Heating in the Princeton Large Torus," Presented at the Course and Workshop on Physics of Plasmas Close to Thermonuclear Conditions, Varenna, Italy (August 1979) 14 pp.
- [65] E. Hinnov, "Spectroscopy of Highly Ionized Atoms in the Interior of Tokamak Plasma," in Atomic and Molecular Processes in Controlled Thermonuclear Fusion, edited by H.R.C. McDowell and A.M. Ferenczi (Plenum Publishing Corp., New York 1980) 449-470.
- [66] A major motivation of much of the previously cited development of x-ray diagnostics was impurity studies, i.e., identification, radiative power loss, concentration, charge-state distributions, and transport.
- [67] V.V. Afrosimov, Yu. S. Gordeev, A.N. Zinov'ev, A.A. Korotkov, JETP Lett. 28, 500 (1978).
- [68] F. DeMarco, "Impurity Concentration in the ATC," Princeton Report MATT-1012 (1973) 9 pp.
- [69] E. Hinnov, L.C. Johnson, E.B. Meservey, D.L. Dimock, Plasma Physics, 14, 755 (1971).
- [70] E. Hinnov, Phys. Rev. A 14, 1533 (1976).
- [71] E. Meservey, N. Bretz, D. Dimock, E. Hinnov, "Suppression of Heavy Impurities in the ST Tokamak," MATT-1175 (1975) 3 pp.
- [72] S. Suckewer, J. Cecchi, S. Cohen, R. Fonck, E. Hinnov, "Tracer Element Injection into PDX Tokamak for Spectral Line Identification and Localized Doppler Temperature Measurement," PPPL-1712 (1980) 9 pp.
- [73] E. Hinnov, M. Mattioli, "Observations of Multiply Ionized Tungsten Radiation in the PLT Discharges," PPPL-1375 (1977) 9 pp.
- [74] S. Suckewer, E. Hinnov, "Iron Forbidden Lines in

- Tokamak Discharges," PPPL-1524 (1979) 26 pp.
- [75] S. Suckewer, R. Fonck, E. Hinnov, "Observed Magnetic Dipole Transitions in the Ground Terms of Ti XIV, Ti XV, and Ti XVII," PPPL-1591 (1979) 10 pp.
- [76] S. von Goeler, D. Eames, M. Bitter, K.W. Hill, G. Lenner, N. Sauthoff, E. Silver, W. Stodiek, "Iron and Oxygen Radiation in the Ultrasoft X-Ray Region (USX) from PLT," Baton Rouge, LA (1981), see Ref. 130.
- [77] S. Suckewer, E. Hinnov, K. Bol, R. Fonck, R.J. Hawryluk, R.A. Jacobsen, D.M. Meade, M. Okabayashi, G.L. Schmidt, E.H. Silver, J.C. Sennis, "Titanium Density Measurements in the PDX Tokamak Using Ti XVII Forbidden Line," PPPL-1563 (1979) 12 pp.
- [78] W. Stodiek, et al., "Transport Studies in the Princeton Large Torus," Plasma Physics and Controlled Nuclear Fusion Research (Proc. 8th Int. Conf. Brussels, 1980) to be published.
- [79] R.C. Isler, E.C. Crume, Phys. Rev. Lett. 41, 1296 (1978).
- [80] R.C. Isler, R.V. Neidigh, R.D. Cowan, Phys. Lett. 63A, 295 (1977).
- [81] E.S. Warden, H.W. Moos, N.H. Lazar, "Observations of Low Charge State Impurities in EBT," ORNL/TM-5899 (1977) 15 pp.
- [82] J.E. Rice, E.S. Marmor, T. Coan, S.L. Allen, R.D. Cowan, Phys. Rev. A22, 310 (1980).
- [83] J.L. Terry, K.I. Chen, H.W. Moos, E.S. Marmor, Nucl. Fusion 18, 485 (1978).
- [84] K.I. Chen, J.L. Terry, H.W. Moos, E.S. Marmor, Nucl. Fusion 20, 189 (1980).
- [85] E.S. Marmor, D. Overskei, H. Helava, K.I. Chen, J.L. Terry, H.W. Moos, Nucl. Fusion 19, 485 (1979).
- [86] S.L. Allen, H.W. Moos, R.K. Richards, J.L. Terry, E.S. Marmor, Nucl. Fusion 21, 251 (1981).
- [87] C. Breton, C. DeMichelis, M. Mattioli, Nucl. Fusion 16, 891 (1976).
- [88] Equipe TFR, Nucl. Fusion 15, 1053 (1975).
- [89] R.P. Drake, H.W. Moos, Nucl. Fusion 20, 599 (1980).
- [90] TFR Group, "Are Heavy Impurities in Tokamak Plasmas at Ionization Equilibrium?," EUR-CEA-FC-1033 (1980) 23 pp.
- [91] TFR Group, Phys. Rev. Lett. 36, 1306 (1976).
- [92] C. Breton, C. DeMichelis, M. Mattioli, "Spectroscopic Study of Ohmically Heated Tokamak Discharges," EUR-CEA-FC-1060 (1980) 42 pp.
- [93] M. Nagami, Y. Shimomura, H. Maeda, S. Kasai, T. Yamauchi, S. Sengoku, T. Sugie, S. Yamamoto, K. Odajima, H. Kimura, K. Ohasa, Nucl. Fusion 18, 1347 (1978).
- [94] K. Odajima, H. Maeda, M. Shiho, H. Kimura, S. Yamamoto, M. Nagami, S. Sengoku, T. Sugie, S. Kasai, M. Azumi, Y. Shimomura, Nucl. Fusion 18, 1337 (1978).
- [95] R. Paul Drake, "Extreme Ultraviolet Diagnosis of a Neutral-Beam-Heated Mirror Machine," UCRL-52751 (1980) 169 pp.
- [96] N.H. Lazar, K.H. Carpenter, J.M. Tyson, E.S. Warden, H.W. Moos, Nucl. Fusion 19, 571 (1979).
- [97] S. Sesnic, "Evolution of Internal Modes, Disruptions, and High-Z Impurities at High Density in Pulsator," IPP III/22 (1976) 83 pp.
- [98] G.M. McCracken, P.E. Stott, Nucl. Fusion 19, 889 (1979).
- [99] K.H. Burrell, J.C. DeBoo, E.S. Ensberg, R. Prater, S.K. Wong, C.E. Bush, R.J. Colchin, P.H. Edmonds, K.W. Hill, R.C. Isler, T.C. Jernigan, M. Murakami, G.H. Neilson, Phys. Rev. Lett. 41, 1382 (1978).
- [100] R.J. Colchin, et al., "Plasma-Wall Impurity Experiments in ISX-A," ORNL/TM-6446 (1978) 13 pp.
- [101] K.H. Burrell, Phys. Fluids 19, 401 (1976).
- [102] P. Gratreau, "Numerical Simulation of the Diffusion and Ionization Processes for Highly Ionized Impurities in Tokamak Discharges, With Application to Confinement Time Determination," CNEN Edizioni Scientifiche Report 79.10/p (1979) 39 pp.
- [103] D.M. Meade, Nucl. Fusion 14, 289 (1974).
- [104] R.J. Hawryluk, J.A. Schmidt, Nucl. Fusion 16, 775 (1976).
- [105] P.H. Rutherford, S.P. Hirshman, R. Jensen, D.E. Post, F.G.P. Seidl, "Impurity Transport in Tokamaks," PPPL-1297 (1976) 19 pp.
- [106] R.V. Jensen, D.L. Jassby, D.E. Post, "Critical Impurity Concentrations for Ignition of Catalyzed-Deuterium Fusion Plasmas," PPPL-1368 (1977) 9 pp.
- [107] R.V. Jensen, D.E. Post, W.H. Grasberger, C.B. Tarter, W.A. Lokke, "Calculation of Impurity Radiation and Its Effects on Tokamak Experiments," PPPL-1334 (1977) 27 pp.
- [108] D. Post, "Impurity Radiation Losses in Fusion Plasmas," in Atomic Processes in Fusion Plasmas, Nagoya University Report IPPJ-AM-13 (1979) 38-43.
- [109] E.J. Caramana, F.W. Perkins, Nucl. Fusion 21, 93 (1981).
- [110] D.E. Roberts, Nucl. Fusion 21, 215 (1981).
- [111] T. Amano, E.C. Crume, "Simulation of Multispecies Impurity Transport in Tokamaks," ORNL/TM-6363 (1978) 29 pp.
- [112] C. Breton, C. DeMichelis, M. Mattioli, "Ionization Equilibrium and Radiation Cooling of a High Temperature Plasma," EUR-CEA-FC-853 (1976) 25 pp.
- [113] C. Breton, C. DeMichelis, M. Finkenthal, M. Mattioli, "Ionization Equilibrium of Selected Elements from Neon to Tungsten of Interest in Tokamak Plasma Research," EUR-CEA-FC-948 (1978) 18 pp.
- [114] M.E. Puiatti, C. Breton, C. DeMichelis, M. Mattioli, "Impurity Charge Exchange Processes in Tokamak Plasmas," EUR-CEA-FC-1085 (1981) 35 pp.
- [115] D.E.T.F. Ashby, M.H. Hughes, "A Study of the Effect of Impurity Radiation from the Peripheral Plasma of a Tokamak Reactor," CLM-P625 (1980) 52 pp; Nucl. Fusion 20, 451 (1980).
- [116] C.S. Chang, "Anomalous Impurity Transport in a Tokamak with Large Toroidal Plasma Rotation," GA-A16123 (1981) 10 pp.
- [117] D.M. Meade, H.P. Furth, P.H. Rutherford, F.G.P. Seidl, D.F. Duchs, "The Effects of Impurities and Magnetic Divertors on High Temperature Tokamaks," Plasma Physics and Controlled Nuclear Fusion Research (Proc. 5th Int. Conf. Tokyo, 1974) 1, IAEA (1975) 605.
- [118] A.L. Merts, R.D. Cowan, N.H. Magee, "The Calculated Power Output from a Thin Iron-Seeded Plasma," LASL Rep. LA-6220-MS (1976).
- [119] E.B. Meservey, et al., "The Effect of Plasma Surface Interactions on PLT Plasma Parameters," PPPL-1677 (1980) 14 pp.
- [120] "Status of Tokamak Research," edited by J.M. Rawls, DOE/ER-0034 (1979).
- [121] R.D. Cowan, "Spectra of Highly Ionized Atoms of Tokamak Interest," LA-6679-MS (1977) 81 pp.
- [122] D. Hillis, Oak Ridge National Laboratory, EBT group, private communication.
- [123] J.E. Rice, K. Molvig, H.I. Helava, "Continuum X-Ray Emission from the Alcator A Tokamak," PPC/JA-81-5 (1981) 75 pp.
- [124] TFR Group - J. L. Schwob, "Intercombination to Resonance Line Intensity Ratio for He-Like Oxygen Ions in TFR Tokamak Plasmas," EUR-CEA-FC-1072 (1980) 15 pp.
- [125] K.W. Hill, S. von Goeler, M. Bitter, E. Silver, N.R. Sauthoff, "The Pulse-Height Analyzer X-Ray Diagnostic for TFR," presented at the Third APS Topical Conference on High Temperature Plasma Diagnostics, Los Angeles CA, March 17-19, 1980.
- [126] F. S. Goulding, J.M. Jaklevic, A.C. Thompson, "Semiconductor Detectors for Fluorescent EXAFS,"

- Proceedings of Workshop on X-Ray Instrumentation for Synchrotron Radiation Research, SSRL Report NO. 78/04, II-22 (1978).
- [127] G.A. Sawyer, A.J. Bearden, I. Henins, F.C. Jahoda, F.L. Ribe, Phys. Rev. 131, 1891 (1963).
  - [128] N. Bretz, D. Dimock, A. Greenberger, E. Hinnov, E. Meservey, W. Stodiek, S. von Goeler, "Radiation From Plasmas in the ST Tokamak," MATT 1077 (1974) 10 pp.
  - [129] B.S. Fraenkel, X-Ray Spectroscopy 9, 189 (1980).
  - [130] E. Kallne, J. Kallne, J.E. Rice, "X-Ray Emission Spectra From Helium-Like Ions in the Alcator C Tokamak," presented at the Third Topical Conference of the APS on Atomic Processes in High Temperature Plasmas, Baton Rouge, LA, February 25-27, 1981; L.V. Hamos, Zeitschr. F. Kristallographie 101 Bd., 17 (1938).
  - [131] E. Kallne, private communication.
  - [132] S. von Goeler, W. Stodiek, N. Sauthoff, Phys. Rev. Lett. 33, 1201 (1975).
  - [133] S. Sesnic, "Evolution of Internal Modes, Disruptions, and High-Z Impurities at High Density in Pulsator," IPP III/22 (1976) 83 pp.
  - [134] N.R. Sauthoff, S. von Goeler, D.R. Eames, W. Stodiek, "Successor Oscillations of Internal Disruptive Instabilities in the PLT Tokamak," PPPL-1553 (1979) 17 pp.
  - [135] R. Petrasso, M. Gerassimenko, F.H. Seguin, J. Ting, R. Krogstad, P. Gauthier, W. Hamilton, A.T. Ramsey, P. Burstein, R. Granetz, Rev. Sci. Instrum. 51, 585 (1980).
  - [136] W VII-A Team, "Mode and Sawtooth Behavior During Neutral Beam Injection in the W VII-A Stellarator," IPP 2/250 (1980) 21 pp.
  - [137] T.F.R. Group, "Structure of Low Frequency Oscillations of the Disruptive Instability in the TFR Tokamak," EUR-CEA-FC-883 (1977) 55 pp.
  - [138] The T.F.R. Group, Plasma Phys. 19, 349 (1977).
  - [139] R.B. White, D.A. Monticello, "Causes of Major Tokamak Disruptions," PPPL-1674 (1980) 15 pp.
  - [140] M. Soler, J.D. Callen, "On Measuring the Electron Heat Diffusion Coefficient in a Tokamak from Sawtooth Oscillation Observations," ORNL/TM-6165 (1978) 37 pp.
  - [141] S. von Goeler, D. Eames, M. Bitter, K.W. Hill, N. Sauthoff, E. Silver, W. Stodiek, Bull. Am. Phys. Soc. 25, 998 (1980).
  - [142] N.D. Vinogradova, et al., "Investigation of Plasma X-Ray Emission in the T-10 Tokamak," in Plasma Physics and Controlled Nuclear Fusion Research (Proc. 7th Int. Conf. Innsbruck, 1978) 1, IAEA (1979) 257.
  - [143] T.T. Hamilton, C.J. Hailey, W.H.-M. Ku, R. Novick, IEEE Trans. Nucl. Sci. NS-27, 190 (1980).
  - [144] J.E. Bateman, R.J. Apsimon, "A New Photocathode for X-Ray Image Intensifiers Operating in the 1-50 keV Region," Rutherford Laboratory, Chilton, UK, Report RL 79-087 (1979).
  - [145] Private communication, R. Fonck and B. Hodge.



Dr. Kenneth Hill presenting his invited paper at the Monterey conference.

Low Energy X-Ray Emission from Light Ion Targets

L. P. Mix, E. J. T. Burns, D. L. Fehl, D. L. Hanson, and D. J. Johnson

Sandia National Laboratories, Albuquerque, NM 87185

ABSTRACT

The light ion fusion program is expected to achieve breakeven conditions in an inertial fusion target in experiments on the PBFA II accelerator. This goal is expected to require ion power densities of  $\leq 10^{14}$  W/cm<sup>2</sup>. The diagnostics which have been employed to diagnose this deposition are described and some soft x-ray plasma measurements which have been made on targets on the 200 times smaller Proto I accelerator are presented. Plasma brightness temperatures of 20 eV have been observed in the deposition region and 35 eV (100 eV electron temperature) in the stagnation region of imploding conical Al targets on Proto I.

INTRODUCTION

Sandia National Laboratories is developing techniques to use the energy and power from pulsed power accelerators to ignite DT filled inertial fusion capsules. This program, which had its beginning in the early 1970's, has made significant progress in developing techniques for delivering the output of these inexpensive and efficient accelerators to a target. The achievement of breakeven conditions in a target is generally thought to require power densities  $\sim 10^{14}$  W/cm<sup>2</sup>. Consequently a comprehensive array of soft x-ray diagnostics is required to diagnose the plasmas produced by the deposition in the target.

In this paper the techniques for generating and delivering this power to a target will be discussed with the specific examples of the recently completed 1 MJ, PBFA I accelerator<sup>1</sup> and the applied-B radial ion diode.<sup>2</sup> The various diagnostic constraints associated with the pulsed power environment will be presented. Finally, a review of the x-ray measurements and diagnostics which have been used to characterize target plasmas on the smaller 20 kJ, Proto I accelerator will be given with some indications of future area of interest.

PBFA I

The PBFA I accelerator<sup>1</sup> (1 MJ, 30 TW, 35 ns) was fired for the first time on June 28, 1980. Since that time it has been undergoing various tests to prepare for ion diode experiments which were initiated in May, 1981. The accelerator (Fig. 1) is cylindrical in shape with a diameter of  $\sim 30$  m and a height of  $\sim 5$  m. The accelerator is modular in design with 36 small accelerators arranged around the cylinder with their outputs directed radially inward toward the target or diode chamber. Each accelerator module consists of an outer oil section where the high voltage is generated, an intermediate water section where the pulse is compressed to  $\sim 40$  ns duration, and an inner portion containing magnetically insulated transmission lines (operating at stresses over 2 MV/cm) which transport the pulses from the individual modules to the target chamber. This modular approach requires

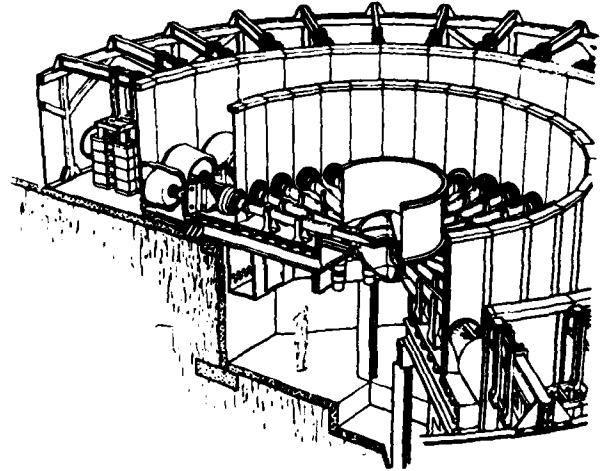


Figure 1. PBFA I Accelerator.

reliable, low-jitter switching for synchronism of the outputs at the diode; typical operation indicated an RMS variation of  $\sim 3$  ns can be obtained on PBFA I. Through a minor modification of the initial design, it is possible to operate the accelerator with either positive or negative polarity output at the full rated power. The high output power of each module is achieved through a series of power amplification stages which are shown schematically in Fig. 2. Through the various stages, the power is increased by a factor of 6 with an energy efficiency of 25%. More importantly, the energy density goes from 0.075 TW/m<sup>2</sup> at the marx generators to 500 TW/m<sup>2</sup> in the diode region. In the diode region, each of the 36 modules may be coupled to individual diodes for converting the electrical energy to ion beams which can then be focused onto a target. In addition, tests conducted on the accelerator during the early part of 1981 indicate that the outputs of the individual modules either can be connected in parallel to drive a single 2 MV, 30 TW diode or that alternate positive and negative

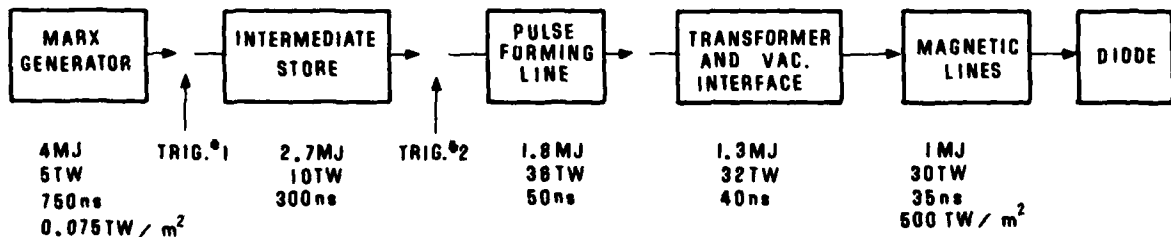


Figure 2. Schematic representation of the power amplification and intensification in pulsed accelerators.  
0094-243X/81/750025-07\$1.50 Copyright 1981 American Institute of Physics

modules could be connected in series to drive a 4 MV, 30 TW diode to take advantage of favorable voltage scaling predicted for ion focusing.

#### APPLIED-B ION Diode

Several techniques can be used to deliver the electrical energy from a pulsed accelerator to an inertial fusion target. In this section we shall consider one such device, the applied-B radial ion diode.<sup>2</sup> Although in conventional diodes, the majority of the current is carried by electrons, the applied-B diode, shown in Fig. 3, uses an externally applied magnetic field to

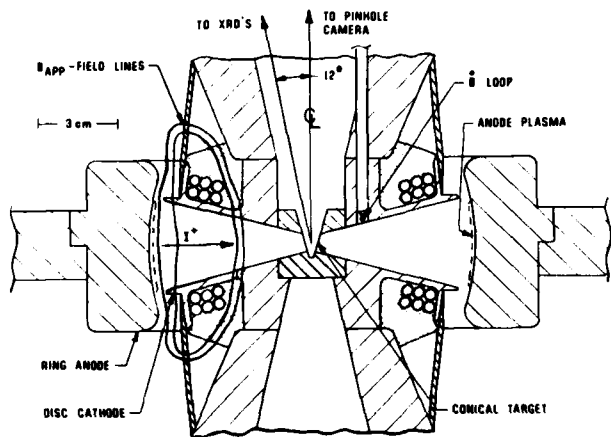


Fig. 3. Schematic of applied-B radial ion diode. The diode is cylindrically symmetric around center line on the right of the figure.

restrict the flow of electrons so that most of the diode current is available for the ion beam. Successful diode operation requires the following sequence of events. The magnetic field coils are pulsed from an external capacitor bank. A positive pulse is applied to the anode when the magnetic field reaches peak. Electrons are emitted from the cathode, but, because of the strong field, are forced to ExB drift around the circumference of the diode forming a space charge cloud and virtual cathode opposite the anode. The positive pulse on the anode also causes a plasma to form on the anode both due to induced voltages developed across dielectric material imbedded in the anode and due to some electron leakage early in the pulse. Although the electron leakage represents almost 100% of the diode current early in the pulse it quickly falls to almost zero such that overall ion extraction efficiencies of > 80% are typically observed. The ions emitted from the anode plasma are focused to the target region both by the geometrical shape chosen for the anode as well as by the self field pinch forces produced by the ion flow. Although the anode source plasma is composed of hydrocarbons, over 80% of the extracted ion current is carried in protons.

A number of ion focusing experiments have been fielded with this diode on the Proto I accelerator (2 MV, 20 ns, 1 TW). The diagnostics for these have included nuclear activation, prompt- $\gamma$ , hard and soft x-ray measurements and mass acceleration measurements using both ablative and exploding pusher-type target geometries. The experimental results indicate peak intensities of 1-3 TW/cm<sup>2</sup> on 3 mm diameter targets with the average intensities somewhat lower due to beam non-uniformities. The main limitations to the focused intensities are believed due to non-uniformi-

ties in the anode plasma and to variations in the current and voltage during the pulse which change the magnetic component of the ion focus. If the focus is indeed limited by these mechanisms, then analytic calculations indicate that the total intensity should improve as the square of the voltage ( $V^2$ ) for non-uniform anode plasma limiting the focus and as  $V^{3/2} (m/Z)^{3/2}$  if magnetic bending is the focusing limit (where  $m$  and  $Z$  are the ion mass and charge, respectively). Particle-in-cell simulations are consistent with these scalings. Thus by going to higher voltages and slightly heavier ions to maintain the optimum range, intensities adequate for inertial fusion will be obtained. Initial tests of this scaling will be conducted using the 2 MV and 4 MV options on PBFA I over the next two years. In the remainder of the paper, the soft x-ray diagnostics, which have been used to diagnose the Proto I ion focus, will be described and results presented.

#### SOFT X-RAY DIAGNOSTICS

Several soft x-ray diagnostic techniques were applied to cylindrical and conical targets located at the center of the applied-B radial ion diode. Evacuated line-of-sight pipes located on axis and at 12° to the axis permitted simultaneous time-resolved measurements of both the spatial and spectral emission from diagnostic targets. Time-integrated quantities with higher resolution were also determined. In this section each of the various measurements will be described with the implication they have on the determination of ion beam parameters. The environment for diagnostics on pulsed accelerators is particularly severe on the larger accelerators such as PBFA. Electron losses during the turn-on phases of the magnetically insulated transmission lines and ion diode are likely to represent over 200 kilojoules of electrons and will generate an intense Bremsstrahlung background with an end point energy of 2 or 4 MeV depending on the diode configuration. Electric fields near the accelerator are well in excess of 100 kV/m requiring care in the acquisition of electrical signals. The relatively low vacuum ( $10^{-4}$  torr) makes detector surface contamination a real concern. The debris which results when several hundred kilojoules of energy is deposited in a target can cause considerable damage to spectrograph slits, filters, attenuating screens, etc. Although slightly less severe, these same constraints apply to the 20 kJ Proto I accelerator.

#### INNER-SHELL EXCITATION DIAGNOSTICS

The  $K_{\alpha}$ -line emission due to beam induced atomic excitation in conical aluminum targets was used to determine the beam profile in the axial and azimuthal directions. Spatial data were obtained with x-ray pinhole cameras mounted on and at 12° to the diode axis. The emission was also observed with 20  $\mu$ m thick PIN diodes which integrated over the spatial dimensions of the target. Since the x-ray production cross section increases with proton energy below 3 MeV, it is necessary to compute the theoretical atomic excitation emission for the target geometry and detection angle used to allow for pulse to pulse comparison of the experimental data. The data acquisition computer provided on-line calculations of the expected emission using published x-ray production cross sections<sup>3</sup> and the measured proton energy and current. (Electron loss is measured with absolutely calibrated, hard x-ray ( $h\nu > 80$  keV) PIN detectors and is subtracted from the total diode current to obtain the net ion current.) Typical targets used for these measurements were hollow truncated Al

cones; with  $8\ \mu\text{m}$  wall thickness and half angles of  $30^\circ$ ,  $15^\circ$ , or  $3.5^\circ$ . The calculations indicated that the  $3.5^\circ$  configuration yielded reduced emission and significant self-absorption of the  $1.49\ \text{keV}$  characteristic photons in the target.

The symmetry and stability of the ion focus was measured with a time-resolved x-ray pinhole camera system (Fig. 4). In this camera x-ray radiation from

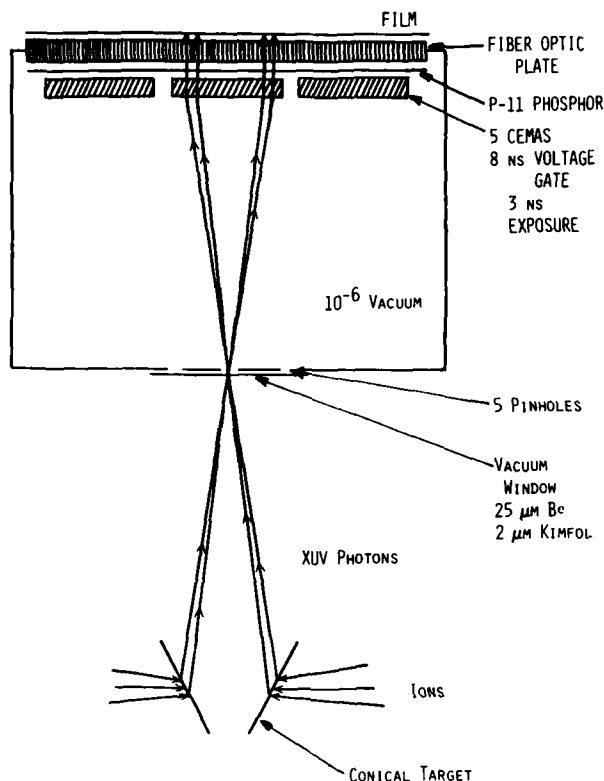


Figure 4. Five frame proximity focused soft x-ray pinhole camera.

the inside surface of the conical targets is focused on five individual microchannel plates (MCPs) via five pinholes. Each MCP is sequentially and independently gated with  $8\ \text{ns}$  voltage pulses. The output of the MCPs is proximity focused onto a P-11 phosphor and a visible image is conducted to the film (Polaroid or Royal X-Pan) by a fiber optics vacuum interface. Thus five individual frames are obtained. The actual exposure time has yet to be determined experimentally but is estimated to be  $\sim 3\ \text{ns}$  when the voltage pulse is folded with the MCP gain characteristics.

For the example shown in Fig. 5, clear images were observed on four of the five frames. This exploding pusher target had a diameter at the midplane of the diode of  $7\ 1/2\ \text{mm}$  and a half angle of  $30^\circ$ . The gains for each MCP were not well characterized and therefore only qualitative information can be derived from the exposures. For these measurements the imaging optics consisted of a  $0.75\ \text{mm}$  pinhole with 1:1 magnification. The photographs obtained indicate a focus with  $2.8\ \text{mm}$  FWHM in the axial direction. This diagnostic confirmed that the  $\pm 25\%$  azimuthal variation of the beam profile observed with the time integrated x-ray pinhole cameras was constant throughout the ion pulse.

The on axis time integrated atomic excitation pinhole camera photograph from an  $8\ \text{mm}$  diameter,  $15^\circ$  half

angle aluminum cone target with  $8\ \mu\text{m}$  thickness is shown in Fig. 6. The annular ring is the inner shell excitation image. This surrounds a bright spot at the center of the target which represents thermal emission from high temperature foil material stagnating on axis. The film exposure due to inner shell excitation can be used to estimate the magnitude of the proton current incident upon the target. This exposure was converted to the number of photons emitted from the target, via the sensitivity<sup>4</sup> of the Kodak no screen film used, and then compared with calculations. The comparison indicates a peak current of  $290\ \text{kA}$  for this pulse. This is in good agreement with the value obtained for similar size targets using the prompt-nuclear technique. The peak proton currents calculated in a similar manner for conical targets from  $3$  to  $17\ \text{mm}$  diameter ranged from  $100$  to  $400\ \text{kA}$ , respectively, with a reproducibility of  $\pm 30\%$ . The same currents were observed for targets with  $3.5$  and  $15^\circ$  half angles and with cameras mounted at  $12^\circ$  off axis. The time resolved PIN diodes gave similar results with the signals proportional to target diameter for targets smaller than  $5\ \text{mm}$ , and gradually increasing until they were a factor of  $1.7$  larger for  $15\ \text{mm}$  targets.

The axial FWHM for a given proton pulse was estimated from densitometer scans of the pinhole photographs after an approximately  $10\%$  correction was made for pinhole broadening of the image. In addition, an attempt was made to correct for second pass image effects produced by protons passing completely through the target. This effect was judged to broaden the observed FWHM by  $10\%$  also. The typical minimum FWHM of a given proton pulse, after corrections, was  $3.5\ \text{mm}$ , with  $+1.5$ ,  $-0.5\ \text{mm}$  deviations as a function of the azimuthal position on the target. The FWHM was rather constant for targets ranging from  $3$  to  $17\ \text{mm}$  diameter with a slight tendency for smaller values with larger targets. Since the target foil expands approximately  $1\ \text{mm}$  due to hydrodynamics during the pulse and the focus position may move slightly with time,  $3.5\ \text{mm}$  is an upper limit on the beam FWHM.

#### THERMAL RADIATION DIAGNOSTICS

Thermal emission from ion beam targets has provided valuable information on the ion beam source parameters. Aluminum photocathode x-ray diodes<sup>5</sup> (XRDs), PINs, and grazing incidence spectrographs have seen extensive use in determining the plasma parameters in the ion focal region. Temperature information from XRDs was obtained by comparing the observed signals with the calculated XRD response for various blackbody temperatures assuming the beam focus area obtained in the atomic excitation pinhole photographs. Techniques are also being developed to measure the total radiated energy from ion beam targets.

Typical XRD signals from  $3$ ,  $5$ , and  $9\ \text{mm}$  diameter,  $8\ \mu\text{m}$  thick aluminum cones with  $3.5^\circ$  half angle are shown in Fig. 7. The signals were obtained with aluminum cathode XRDs, operated bare and with a  $2\ \mu\text{m}$  thick polycarbonate filter, and represent thermal emission at  $10$  to  $25\ \text{eV}$  and  $150$  to  $280\ \text{eV}$ , respectively. With the two larger targets an initial radiation peak is seen at  $40\ \text{ns}$ . This first signal corresponds to thermal radiation from the inner surface of the foil which reaches its maximum temperature late in the power pulse when the Bragg peak in the proton deposition function is near the inner surface. This occurs at a proton energy of approximately  $700\ \text{keV}$  for the  $8\ \mu\text{m}$  thick aluminum used. A first order analysis of these XRD signals as well as  $0.8\ \mu\text{m}$  Al and  $0.33\ \mu\text{m}$  parylene ( $\text{C}_6\text{H}_6$ ) filtered XRDs indicates blackbody radiation spectra with temperatures of  $21$ ,  $18$  and  $15\ \text{eV}$  on the inner surface of the targets. These spectra are

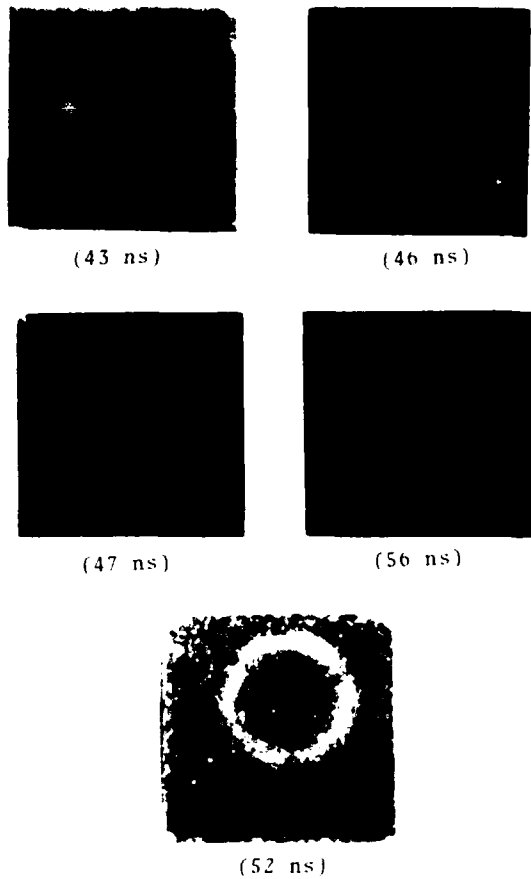


Figure 5. Five frame pinhole camera record of ion deposition in a conical target. Times indicated are relative time for each exposure.

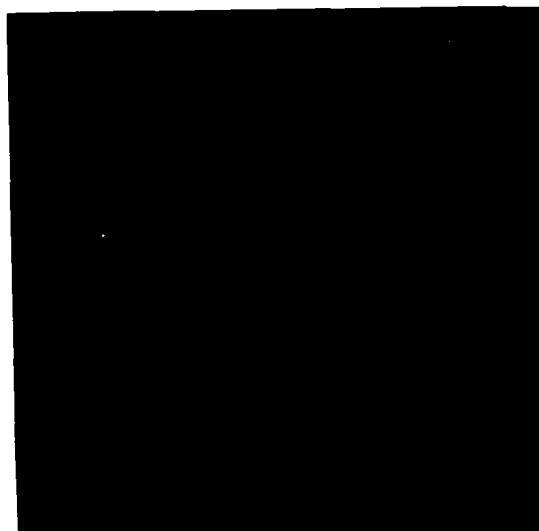


Fig. 6. Pinhole photograph taken of an 8 mm diameter conical target.

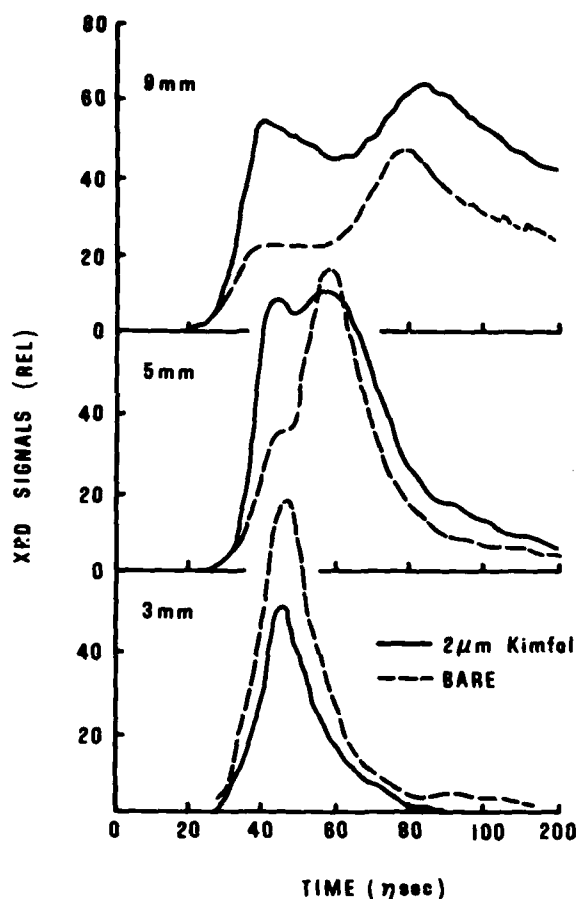


Figure 7. XRD signals.

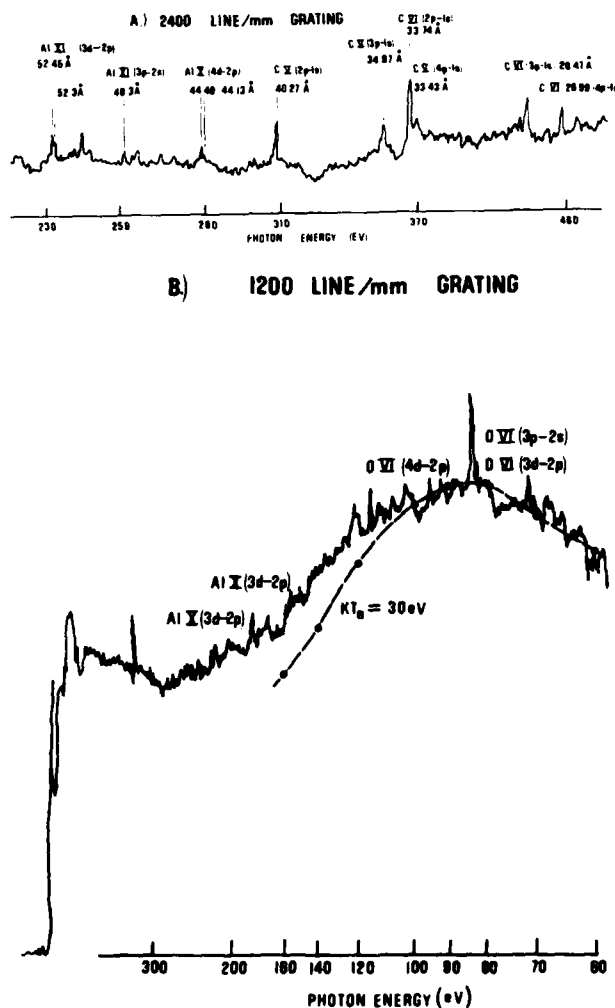
reduced a factor of two at photon energies below 20 eV apparently due to absorption of radiation by cooler plasma outside of the maximum focus.

A second radiation pulse is observed 5, 15, and 40 ns later for the 3, 5, and 9 mm targets, respectively. This emission is also of thermal origin but originates from the stagnation of high temperature foil material at the center of the target. This signal represents an optically thin plasma with peak emission occurring when the optimum high temperature and density are achieved. Since less convergence is necessary to assemble a high density plasma with a smaller target, the mass will be assembled faster than  $r^{-1}$  for a constant implosion velocity as the target diameter is decreased. This explains the apparent implosion velocities of 30, 17, and 10 cm/s for the 3, 5, and 9 mm targets, which at first estimate would imply peak proton current densities scaling as  $r^{-2}$  rather than  $r^{-1}$  as determined from other observations of beam on target.

Electron and ion densities and electron temperatures for the stagnation region of the 8  $\mu$ m thick aluminum targets have been deduced from radiation measurements above 400 eV photon energy. The detector system consisted of thin aluminum filters in front of the 20  $\mu$ m thick PIN diode detectors. The filter thicknesses were 3.2, 4, 8, and 12  $\mu$ m. By virtue of the strong K-edge of neutral aluminum, the Lyman series of line emission associated with helium-like and hydrogen like aluminum would be strongly attenuated. The radiation spectrum above 400 eV photon energy is therefore

assumed to be composed primarily of free-bound continuum associated with free electrons recombining with aluminum ions in their ground state. The ground state ion populations of a pure aluminum plasma are given by the coronal model with the ionization levels depressed to the collision limit. This is a close approximation to the correct model, the collisional-radiative-equilibrium model (CRE).<sup>6</sup> For the source volume of  $1.1 \times 10^{-3} \text{ cm}^3$  observed for 3 mm diameter targets with pinhole cameras, a peak electron temperature of 100 eV and peak ion and electron densities of  $2.3 \times 10^{19} \text{ cm}^{-3}$  and  $2.5 \times 10^{20} \text{ cm}^{-3}$ , respectively, have been achieved.

The time-integrated radiation spectrum from the stagnation region of a 3 mm diameter, 8  $\mu$ m thick aluminum cone was measured with a one meter, split grating (600 and 1200 lines/mm) grazing incidence ( $88^\circ$ ) spectrograph (resolving powers  $E/\Delta E = 1250$  and 2500 at 124 eV photon energy, respectively). Figure 8 shows the radiation spectrum taken on the same pulse

Fig. 8. Radiation spectra from 8  $\mu$ m thick conical aluminum targets.

with the 1200 and 2400 split grating. On the 2400 line/mm grating there is line emission from H-like and He-like carbon contamination, in addition to Li-like ( $\text{Al}^{10+}$ ) and Be-like ( $\text{Al}^{9+}$ ) line emission. This carbon emission is believed to emanate from the inside



surface of the target and is likely due to hydrocarbon contamination. Using a coronal model with the ionization potential depressed to the collisional limit, the intensity ratio of the 2p-1s and 1s2p-1s<sup>2</sup> transitions in H-like and He-like carbon are consistent with an electron temperature of 100 eV, assuming opacity effects are dominated by doppler broadening and the ratio of ground state populations of H-like to He-like carbon ions is 3:1. Table I lists the integrated intensities of the line emission from Li-like aluminum. The letters (c) through (f) are those used by

LINE	WAVELENGTH	INTEGRATED INTENSITY ON FILM (ERGS-A/cm <sup>2</sup> )	RELATIVE INTENSITY
2p-3d (c)	52.299 52.446	.04	100
2s-3p (d)	48.297 48.338	.007	18
2p-4d (e)	39.091 39.180	.0036	9
2p-3s (f)	54.388	< .0004	< 1

TABLE I. Li-like Al lines between 39 A and 55 A.

Davis and Whitney.<sup>7</sup> By comparing our intensities with calculations of Davis and Whitney, we see line (e) exceeds line (f) and therefore our electron density is greater than  $10^{19}$  cm<sup>-3</sup>, consistent with the PIN results. Also shown in Fig. 8 is a comparison of the spectrum taken with the 1200 line/mm grating and a 30 eV blackbody spectrum. The comparison between 60 eV and 100 eV photon energy is quite good. Above 100 eV photon energy, the spectrum has a temperature greater than a 30 eV blackbody. Above 220 eV photon energy, the spectrum is optically thin as noted by the appearance of Be-like aluminum line radiation. This 30 eV blackbody temperature compares quite well with the  $35 \pm 10$  eV (i.e., uncertainty in the emitting source area accounts for the large error bars) brightness temperature determined from the XRD signals for the stagnation region at the center of the target.

Methods to make time resolved measurements of the total radiated energy have been developed for the magnetically imploded foil program at Sandia. To cover the levels of x-ray fluence from  $10^{-3}$  to  $10^4$  J/cm<sup>2</sup>, two principle techniques are being pursued, thin film bolometers<sup>8</sup> and piezoelectric pressure gauges.<sup>9</sup> Both techniques provide ~ ns time resolution and will be fielded on future experiments to diagnose ion beam generated plasmas.

Thin film bolometers (Fig. 9) consist of a narrow strip of metal whose resistance increases almost linearly with absorbed x-ray energy. Determination of the change in the resistance of the resistive element provides a large amplitude, fast response signal which is particularly useful for determining radiated energy in the fluence range of  $10^{-3}$  J/cm<sup>2</sup> to  $10^{-1}$  J/cm<sup>2</sup>. Bolometer resistive elements consisting of ~ 1 μm thick films of Al, Ni, Ta evaporated onto a MACOR glass ceramic substrate have been tested. Film material, geometry, and thickness are chosen to optimize the detector sensitivity and spectral response for

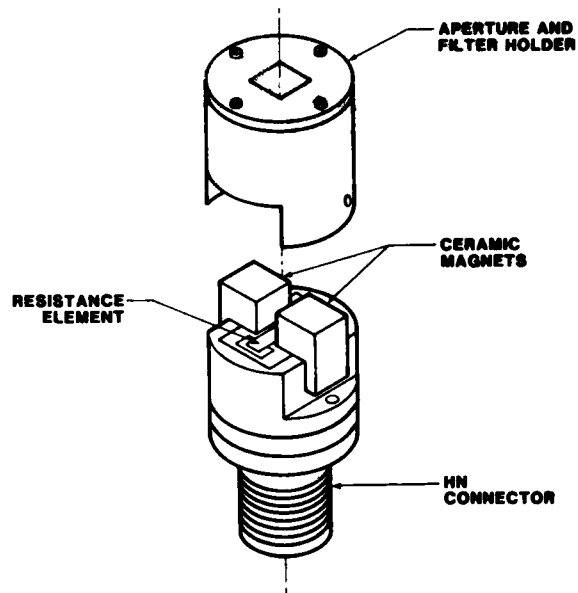


Figure 9. Bolometer module with magnets for foil photoelectron suppression.

a given experiment. The substrate mounted resistance elements have proven more rugged and reliable than free-standing foils, while no significant differences in thermal response between the two have been observed at least for the fast signals (< 100 ns) of interest. The time response of 0.75-1.0 μm thick Al film bolometers has been studied by energy deposition with a ruby laser. The bolometers were able to accurately integrate laser pulses of 30, 6, and 3.5 ns FWHM, and the original laser pulse shapes were recovered by differentiation of the bolometer signals (Fig. 10). Time-resolved measurements of ultra-soft x-ray energy pulses of < 20 ns have been performed in the harsh EMP noise environment of the Proto II accelerator (300 kJ, 30 ns, 10 TW) using a differential bolometer circuit and common mode noise reduction techniques.

Work is also underway to develop large area stand-off pressure gauges for time resolved measurement of total radiated energy at high fluence levels. These detectors consist of thin quartz or lithium niobate piezoelectric transducers which measure the thermo-elastic or ablation (depending on fluence) pressure wave generated by x-ray energy deposition in a thin metal surface absorber. These gauges should be useful at low energy x-ray fluence levels of  $10^{-1}$  -  $10^4$  J/cm<sup>2</sup>. Initial tests of a 1 cm diameter quartz gauge were performed with an intense x-ray source. For a shot where the incident power level at the gauge was below the threshold for absorber ablation, the quartz gauge pulse shape was in excellent agreement with the shape of the bare XRD signals (Fig. 11). The negative pulse is due to bremsstrahlung which penetrated the 12 μm thick Au absorber on the face of the piezo-electric gauge. Additional stand-off gauge tests are being carried out on the Proto II accelerator at SNL and work is in progress to relate the observed pressure to the incident radiation flux and spectrum through hydrodynamic calculations.

#### SUMMARY

Ion diode experiments have been initiated on the 1 MJ, PBFA I accelerator. In experiments on the

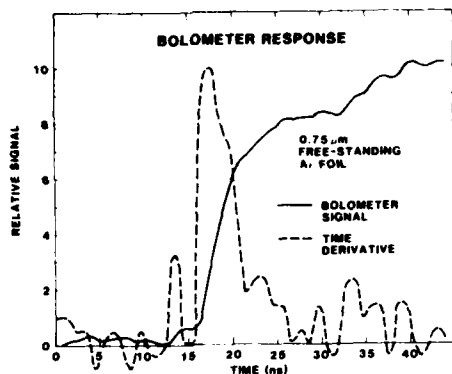
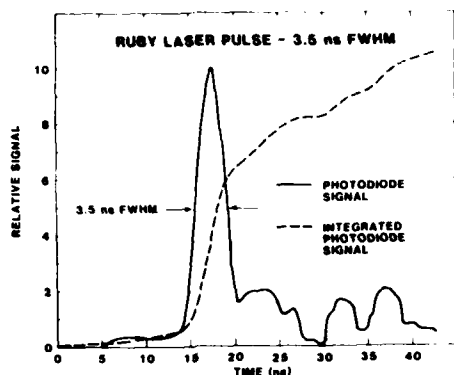


Figure 10. Bolometer time response.

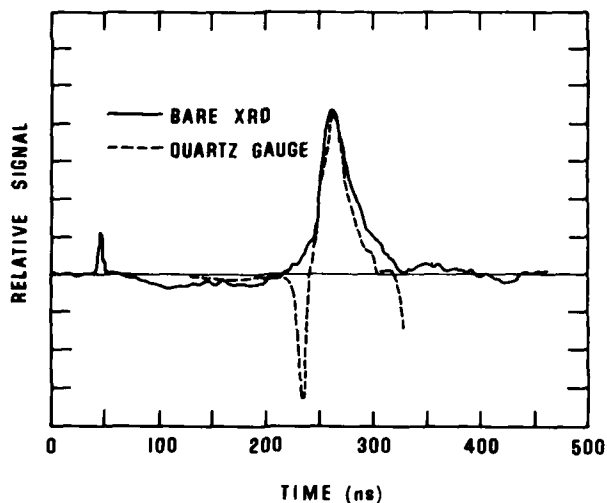


Figure 11. Comparison of bare aluminum XRD signal with a quartz gauge signal.

smaller 20 kJ, Proto I accelerator target plasma temperatures over 20 eV have been measured with a variety of soft x-ray diagnostics. At the higher fluences expected on PBFA I, saturation<sup>10</sup> of XRD diagnostics can easily occur if present techniques are employed. The use of x-ray mirrors and pinhole imaging are presently under investigation for reducing the flux at the XRDs. The next step toward fusion

will occur with the completion of PBFA II in 1985. This 4 MJ, 100 TW accelerator should produce hot plasmas with ion intensities approaching  $10^{14}$  W/cm<sup>2</sup>.

#### ACKNOWLEDGEMENT

We gratefully acknowledge the loan of the NRL 1 m grazing incidence spectrograph from George Doschek and Uri Feldman (NRL, Washington, DC) which was used for the acquisition of the grazing incidence data in this paper. This work was supported by the U. S. Dept. of Energy under contract DE-AC04-76-DP00789.

#### REFERENCES

1. T. H. Martin, J. P. VanDevender, G. W. Barr, D. L. Johnson, Proc. of the 3rd Int'l. Conf. on High Power Electron and Ion Beam Research and Technology, July 3-6, 1979, Institute of Nuclear Physics, Novosibirsk (1979) p 151, Vol. I.
2. D. J. Johnson, G. W. Kuswa, A. V. Farnsworth, J. P. Quintenz, R. J. Leeper, E. J. T. Burns, and S. Humphries, Jr., Phys. Rev. Letts. **42**, 610 (1979).
3. H. Tawara, Y. Hachiya, K. Ishii, and S. Morita, Phys. Rev. A **13**, 572 (1976).
4. C. M. Dozier, D. B. Brown, L. S. Birks, P. B. Lyons, and R. F. Benjamin, J. Appl. Phys. **47**, 3732 (1976).
5. X-Ray Diodes for Laser Fusion Plasma Diagnostics, R. H. Day, P. Lee, E. B. Saloman, D. J. Nagel, LA-7941-MS, LASL, Los Alamos, NM 87545.
6. R. W. McWhirter, Plasma Diagnostic Techniques, Ed. R. H. Huddlestone and S. L. Leonard, Academic Press (1965), pp 201-264.
7. J. Davis and K. G. Whitney, J. Appl. Phys. **47**, No. 4, April 1976, pp 1432-1433.
8. Time Response of Fast, Thin-Film Bolometers for Ultrasoft X-Ray Fluence Measurement, D. L. Hanson, R. B. Spielman, and J. P. Anthes, Bull. Am. Phys. Soc. **25**, 890 (1980).
9. D. L. Hanson, Sandia Nat'l. Labs, private communication.
10. R. B. Spielman and J. P. Anthes, this meeting.



Dr. L. Paul Mix during his presentation in Monterey.

## A NEW, EFFICIENT PULSED PLASMA SOFT X-RAY SOURCE

G. Dahlbacka, S. M. Matthews, R. Stringfield, I. Roth,  
R. Cooper, B. Ecker, and H. M. Sze

Physics International Company  
2700 Merced Street  
San Leandro, California 94577

## ABSTRACT

A compact, efficient, high-brightness pulsed plasma X-ray source has been demonstrated. The source has a conversion efficiency, from electrical input to usable X-ray energy, of greater than 1%. For example, total radiated yields of 150 joules of neon K-line radiation have been produced in a single pulse. X-rays are emitted from a cylindrical volume approximately 1 mm in diameter and 10 mm long. Various wavelengths can be obtained by the choice of appropriate plasma materials. This X-ray source compares favorably to synchrotron radiators in intensity, and most users of synchrotrons will find this source attractive.

For example,\* using X-rays in the 12 Å region, submicrometer features have been replicated by exposing a wafer, coated with FRM resist (~ 50X PMMA sensitivity), through a polyimide/gold X-ray mask. The exposure was made through a 1-mil-thick beryllium filter with the wafer 30 cm from the source. Twenty X-ray pulses were required to fully expose the resist. For this experiment, the available electrical pulse power supply was limited to one pulse every few minutes; however, the X-ray source itself is capable of much faster pulse rates and electrical driver technology to power the X-ray source at one or more pulses per second is within the present state of the art. Other applications and experiments using this source are discussed and a comparison with synchrotron sources is made.

## DISCUSSION

As a result of the experiments conducted at PI for the Defense Nuclear Agency and the Air Force Weapons Laboratory, we have developed an intense pulse plasma X-ray source that is very efficient in converting capacitively stored electrical energy into X-ray energy. The reason this source is so efficient is that it is pulsed in a very short period of time, creating high plasma temperatures. It is well known, for example, that blackbody plasmas radiate power as  $T^4$ , and the nonlinear temperature dependence of the radiation creates the efficiency. The processes that govern radiation from plasmas are bremsstrahlung, free-bound, or bound-bound radiation. The bound-bound and free-bound processes have the largest cross sections for creating X-rays. The plasmas we create predominantly radiate due to the free-bound and bound-bound processes. Plasmas are created with electron densities of  $10^{20} \pm 1$  with dimensions of 1 mm in diameter and 7 mm in length (see Figure 1). These plasmas presently convert electrical energy driven from the power grid into full spectrum X-ray yield with an efficiency of about 7%. Efficiencies in excess of 7% are certainly possible but have not been accomplished to date.

\*The X-ray lithographs were made in collaboration with Lincoln Labs (N. P. Economou and D. C. Flanders), and were sponsored by the Department of the Air Force and DARPA.

"The U.S. Government assumes no responsibility for the information presented."



Fig. 1. Pinhole photograph of 7 Å plasma x-ray source - three shot overlay

The desirability of an intense pulsed X-ray source is apparent when one examines existing laboratory X-ray source technology. Presently, rotating anode sources are the most powerful X-ray source available in the laboratory. They have conversion efficiencies to X-rays in the 1 keV regime on the order of  $10^{-4}$ . The sources we have developed at PI have conversion efficiencies of  $10^{-2}$ . Thus, because the plasma sources are very hot they are approximately 100 times more efficient than the conventional rotating anode sources in this regime. Synchronization sources are also very efficient, but experimenters must typically go to a large facility in order to conduct experiments. Synchrotrons do not qualify as laboratory sources for this reason. There are very few synchrotron facilities available, so it would be desirable to have a source that had the efficiency, short pulsed duration, and wavelength selectability of the synchrotron for use in smaller laboratories.

The Physics International X-ray Illuminator (PIXI) class pulser can be used for a variety of applications in the lab. The source can be used to facilitate development of X-ray diagnostics and to study the physics of atomic X-ray sources. In addition, the source can be used to heat high-atomic-number gases for spectroscopic studies of these materials. The source is also capable of flash radiography when the sample density distance product on the order of  $10^{-3}-10^{-2}$  g/cm<sup>2</sup> assuming typical mass absorption coefficients. The PIXI source can also be used for flash X-ray microscopy of blood cells using the technique of contact printing on a photo sensitive resist. In addition, the source could be used to perform organic and normal crystal diffraction studies, presently carried out using conventional X-ray sources. The new fields of extended X-ray absorption and fine structure (EXAFS) and surface extended of absorption fine structure (SEXAFS) will also benefit from the development of these sources where the fundamental relationships of atoms to their crystal lattice and nearest neighbors can be studied. The most significant impact of the sources may occur in the field of X-ray microlithography. Because of the high efficiencies, it is possible to envision commercial production of microlithographs with half micron line features. This accomplishment would extend the state of the art of computer memory, density, and speed by a factor of 30 to 100 from that most recently available (HP 0.5 Mbyte RAM).

The pulsed power driver PI has used to date has 7.5 kJ in the capacitor bank. This driver has created 150 joules of X-rays in neon-helium- and hydrogen-like lines (~ 12 Å). Figure 2 shows a spectrum obtained in

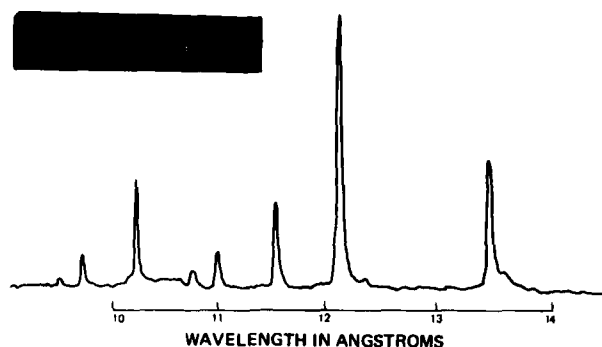


Fig. 2. Neon plasma x-ray source.

the vicinity of 12 Å in neon plasma. The source was 2% efficient in this case. Figure 3 is the spectrum of a krypton plasma X-ray source that has a radiated yield of 25 joules representing 0.33% efficiency. Figure 4 shows an argon plasma source with an X-ray output of around 4 Å. These spectra were taken using KAP crystal spectrographs. The radiated yields for the various gases were determined using X-ray diodes, calorimeters, TLD detectors, and PIN detectors.

The temporal history of the X-ray emission is very short. X-ray diode measurements of the source show that the X-ray pulse is roughly a 15 to 20 ns full width at half maximum. Figure 5 shows a neon X-ray pulse measured using an X-ray diode. This rapid pulse can be used to stop motion in many systems where other X-ray sources would smear the data. Thus, crystal diffraction studies, studies of transport across biological membranes, flash radiography of systems moving up to  $10^6$  cm/s, and other rapid phenomena can be studied by using this X-ray source.

As an example of the power of this source, microlithography exposures were made in collaboration with

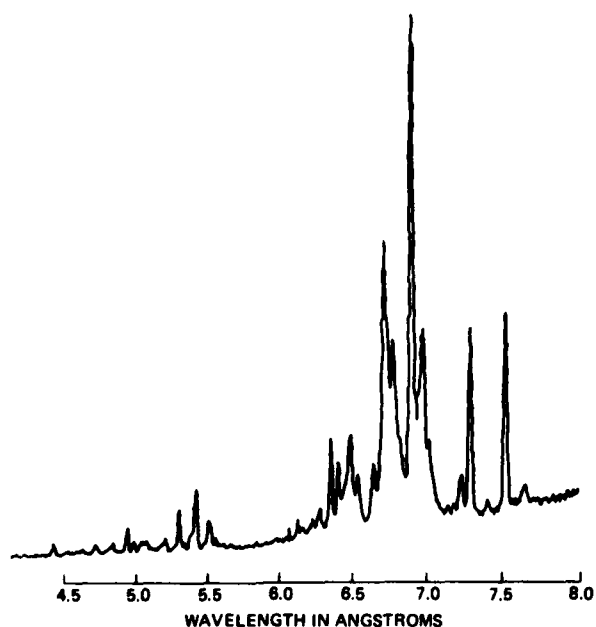


Fig. 3. Krypton plasma x-ray source.

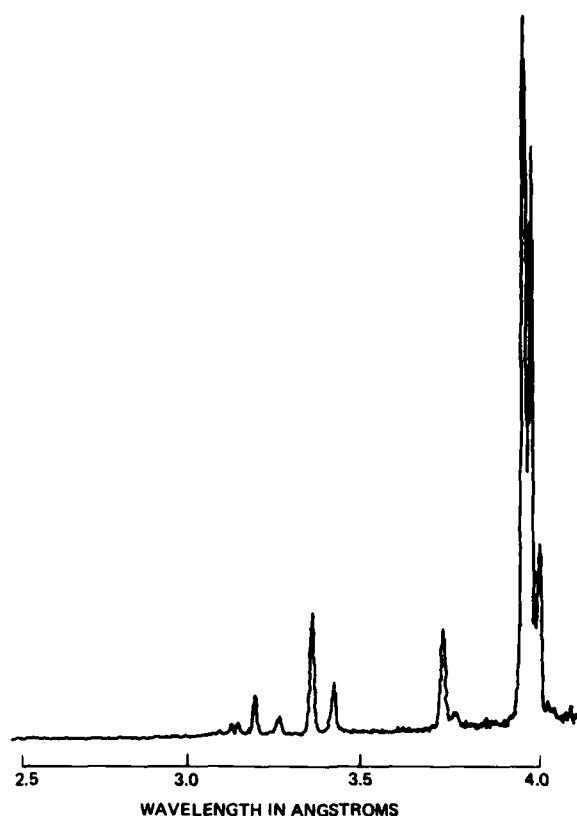


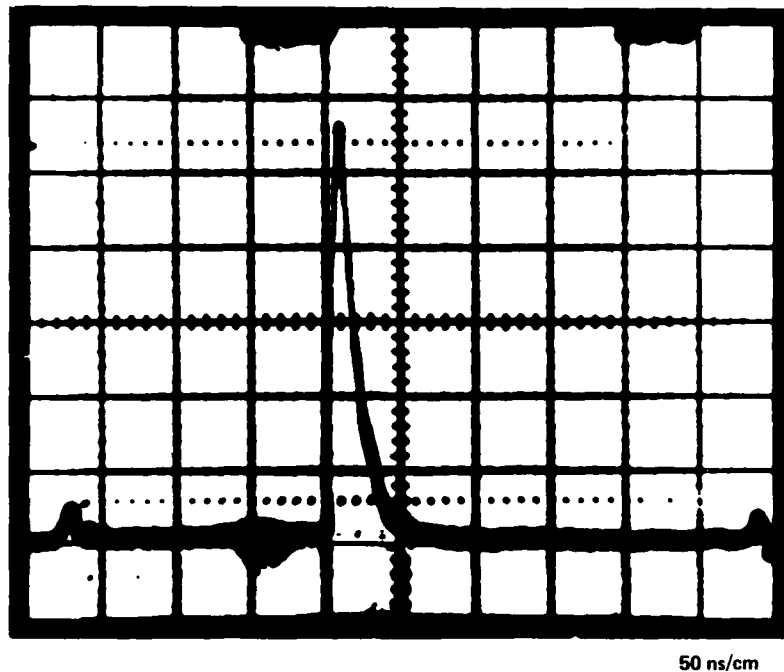
Fig. 4. Argon plasma x-ray source.

N. P. Economou and D. C. Flanders of Lincoln Laboratories at MIT. These experiments prove the principle of pulsed plasma X-ray microlithography for semiconductor applications.

An X-ray mask of 0.5 micron lines and spaces was placed in contact with a FBM-coated (fluorobutyl methacrylate) silicon wafer. The wafer was placed 25 cm from the source with a 1 mil beryllium filter between the source and the assembly. The X-ray machine was pulsed nine times using neon as the radiation source. Each neon pulse contributed 80 joules to the total exposure. In addition, 17 pulses of krypton (7 Å) radiation were used, with each pulse having 8 joules of energy. The reason for the mixture of neon and krypton radiation was strictly for source development reasons and not for wafer exposure. The total X-ray dose on the wafer was  $56 \text{ mJ/cm}^2$ . The wafer was developed for 2 minutes in 150:1 IPA MIBK developer and 10 seconds in 100:1 IPA MIBK developer.

Figure 6 shows a scanning electron microscope view of the results of this exposure. The pattern shows clear 0.5 micron lines and space with 0.10 micron edges on the photoresist. These results were conducted in  $10^{-4}$  torr of vacuum. No precautions were taken to avoid dust or other airborne surface contaminants. Thus, X-rays produced from our source have exposed photoresist in an environment that is thousands of times less clean than those experienced in typical semiconductor assembly lines. In addition, the resolution shown in this photograph demonstrates potential for X-ray microscopy of very small objects.

In summary, we have conducted the first demonstration of an efficient pulsed plasma X-ray source



50 ns/cm

Fig. 5. X-ray pulse is 15 ns FWHM as measured on an x-ray diode.



Fig. 6. Wafer exposure #2.

for the use in the laboratory for a variety of applications. We envision a future source that will use a power of 10 kW with a minimum X-ray power of 200 W at 12 Å assuming a 2 pps operation. This source would have a kilowatt overall X-ray yield at much longer wavelengths. The source size will be selectable around 5 to 10 mm in length and have a reproducible 1 mm diameter. Objects for investigation can be placed as close as 10 cm to this source.

In principle, the source can be constructed to achieve repetition rates up to 500 Hz. This repetition rate is limited by the vacuum pumps necessary to extract plasma debris and inject gas from the vacuum chamber. At these repetition rates, motion pictures

of many processes can be made. We anticipate that this machine would have a footprint upon the order of 1 m<sup>2</sup> in the laboratory. The source then would be compact and provide a new range of intensities and pulse lengths for research in the future.



Dr. Glen Dahlbacka describing new results at PI.

## Sub-kilovolt X-ray Emission from Imploding Wire Plasmas

John C. Riordan, Jay S Pearlman, Miriam Gersten and John E. Rauch

Maxwell Laboratories, Inc.  
8835 Balboa Avenue  
San Diego CA 92123

## ABSTRACT

We present measurements of the sub-kilovolt X-ray emission from imploding wire arrays on the 1 TW BLACKJACK 3 pulsed power generator. The plasma is created by driving a 1 MA, 100 ns current pulse through a cylindrical array of 12 fine wires. The wires form individual plasmas which then implode to become a single plasma on the axis of the array; this hot, dense plasma is an intense source of soft X-rays. Calorimeter measurements show that maximum soft radiation yield is produced from arrays having a linear density of 100 to 200  $\mu\text{g}/\text{cm}$ ; for such arrays the implosion occurs within 20 ns of the current peak. The dependence of the total yield on mass is largely independent of wire material. The radiation pulsewidth measured with an unfiltered X-ray diode increases monotonically with array mass from a 25 ns FWHM observed for 50  $\mu\text{g}/\text{cm}$  arrays.

The soft X-ray spectra radiated by the imploding plasmas approach a blackbody spectrum with increasing wire mass and atomic number. Tungsten and silver plasmas radiate continuum spectra in the sub-kilovolt range; no lines are discernable in either case. Stainless steel plasmas radiate a similar continuum, but L and M lines are present for lower mass arrays. The continuum radiated by aluminum plasmas is less smooth, and significant K and L lines are present for lower masses. Carbon plasmas radiate intense K and L lines and an optically thin continuum. Similar soft X-ray emissions can also be achieved with small imploding gas jet plasmas.

## I. INTRODUCTION

Soft X-ray emission from exploding wire plasmas was first observed 20 years ago by Vitkovitsky et al(1) using a 10 GW capacitive discharge system to explode fine aluminum wires and hollow cylinders. With the development of terawatt pulse power generators 10 years ago, creation of significantly more intense soft X-ray emission sources became possible. Mosher et al(2,3) produced tens of joules in the 1-10 keV range by exploding single wires on Gamble II; detailed spectral measurements on these plasmas were reported by Burkhalter et al(4). The coupling of electrical energy to the wire plasma was significantly improved by Stallings et al(5), who showed that a better match to the  $\approx 1\Omega$  impedance of the terawatt generators could be achieved with an array of parallel wires. Measurement and analysis of the  $h\nu \geq 1$  keV spectrum from these imploding wire array plasmas were reported by Burkhalter et al(6).

Imploding wire array plasmas are also intense sources of ultra-soft X-ray ( $h\nu \lesssim 1$  keV) emission. In this paper we will characterize the sub-kilovolt emission from these plasmas with experimental measurements of the relative radiation yield, pulsewidth, and spectrum. Since wire mass and material have previously been shown to strongly affect the  $h\nu > 1$  keV emission (2-7), we shall also present a detailed study of these two parameters on the  $h\nu \lesssim 1$  keV emission.

A typical experimental arrangement for imploding wire arrays is illustrated schematically in Figures 1-1 and 1-2. The plasma is created by driving a cylindrical wire array with a mega-ampere current pulse from a terawatt pulse power generator(8). A typical 1 MA, 100 ns current pulse from the BLACKJACK 3 pulse power generator(9) is shown in Figure 1-3a. The current initially vaporizes and ionizes the wires to form individual wire plasmas. These wire plasmas are then accelerated by the  $\vec{j} \times \vec{B}$  force toward the axis(10), where they collide to form a hot, dense plasma. The dense plasma emits a strong radiation pulse (Figure 1-3b), which is monitored

with an unfiltered X-ray diode (XRD) and an unfiltered calorimeter. The spectrum of the radiation is measured with grating and curved crystal spectrographs. The spatial character of the plasma is recorded with a soft X-ray pinhole camera and a high speed visible framing camera. The framing camera photographs show not only the array implosion (Figure 1-4a), but also the growth of instabilities in the pinched plasmas (Figure 1-4b).

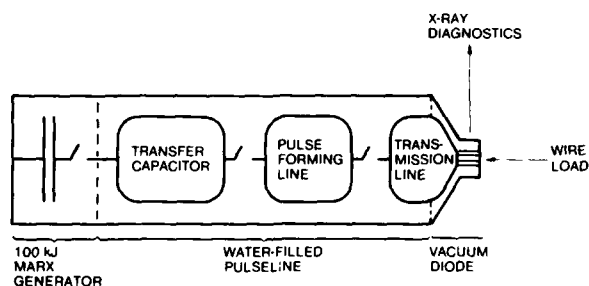


Figure 1-1. Wire load on BLACKJACK 3 pulseline.

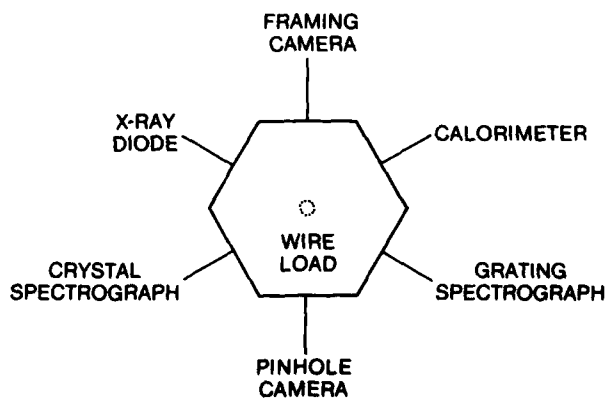


Figure 1-2. Soft X-ray diagnostics.

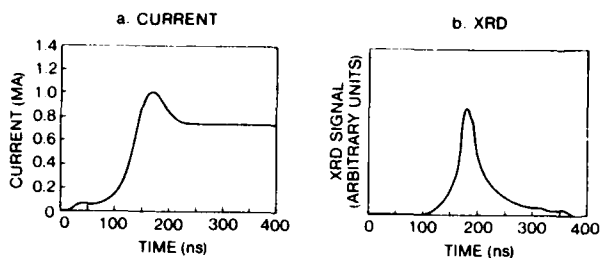


Figure 1-3. Typical experimental waveforms (shot 3682).

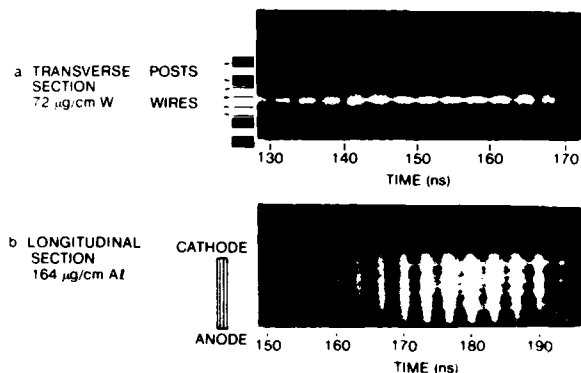


Figure 1-4. Typical framing camera photographs.

To provide a wide range of conditions for examining the effects of wire mass and material on soft X-ray emission, one element was selected from each row of the periodic table, viz., carbon ( $Z = 6$ ), aluminum ( $Z = 13$ ), iron ( $Z = 26$ ), silver ( $Z = 47$ ) and tungsten ( $Z = 74$ ). In each case, the load consisted of 12 identical fine wires strung in an array 3 cm long by 4 mm in diameter (Figure 1-5). The wire diameters were varied from 7.5-40  $\mu\text{m}$  to obtain arrays with linear densities from 50-500  $\mu\text{g}/\text{cm}$ . The 1 mm dia current return posts were located on a 9 mm dia circle to provide a 3.5 mm wide view of the plasma between the posts; the outermost wires are obscured by the posts. The 2 mm gap between the wires and current return posts is magnetically insulated (8).

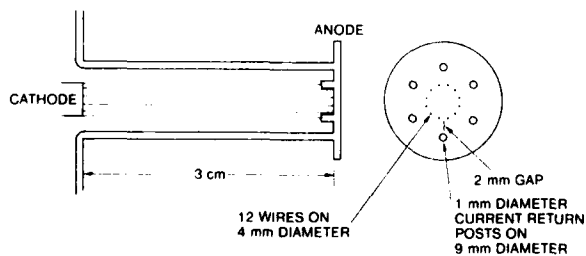


Figure 1-5. Wire array configuration.

The soft X-ray emission from imploding plasmas is the subject of this report. The spatial distribution of the radiation is discussed in Section II. In Section III, the relative radiation yield and pulse-width measurements are presented, while in Section IV the spectra obtained with the various wire materials are given. In Section V, emission from an imploding gas jet is described. Finally, the important findings are summarized in Section VI.

## II. SOFT X-RAY PHOTOGRAPHS

The spatial distribution of soft X-ray emission from the plasma was recorded using a pinhole camera and Kodak Fine Grain Positive film. One of the two pinholes was filtered with 100  $\mu\text{g}/\text{cm}^2$  of carbon to produce a strongly peaked spectral response in the 100-300 eV range and a weaker response in the range above 500 eV. The other pinhole was filtered with

200  $\mu\text{g}/\text{cm}^2$  of aluminum to match the transmission of the carbon filter above 500 eV, but with no significant lower energy window. Figure 2-1a shows two images of the same aluminum plasma, one produced primarily by L-shell radiation near 200 eV and the other by K-shell radiation near 1500 eV. The left image made with softer X-rays shows a plasma column with many lateral flares; the right image of the harder X-ray emission shows a string of intense sources (hot spots) along the column. Both the flares and hot spots appear to be caused by the "sausage" instability, an axially symmetric ( $m = 0$ ) current-driven MHD instability. The dark strips bounding the plasma are the nearest two current return posts (Figure 1-5), which obscure the edges of the plasma.

As the mass of the wire array is increased, a smaller number of less intense hot spots are observed. This trend is illustrated in Figure 2-1 for aluminum plasmas, but is equally valid for stainless steel, silver and tungsten plasmas. With the most massive arrays, the plasma column exhibits lateral plasma displacements produced by the "kink" ( $m = 1$ ) instability, another current-driven MHD instability. The  $m = 1$  instability is also present to a lesser degree for the lower mass array, but it is somewhat masked by the  $m = 0$  instabilities. Photographs of the massive arrays also show shadows of the wires in their initial positions backlighted by the pinched plasma. This indicates that the implosion of massive arrays leaves behind a substantial amount of cooler wire mass.

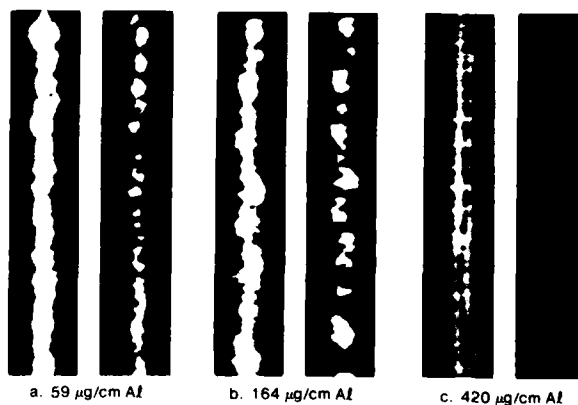


Figure 2-1. Soft X-ray photographs -- effects of array mass.

For a given array mass, as the atomic number of the wire material is increased the hot spots become tighter and more nearly colinear (Figure 2-2). This effect has been noticed previously in single exploded wire plasmas(4). The photograph of a tungsten plasma (Figure 2-2b) shows many  $m = 0$  hot spots, but no evidence of any  $m = 1$  instability. Carbon plasmas, on the other hand, show a striking  $m = 1$  instability and no  $m = 0$  instability (Figure 2-3). Carbon wire implosions clearly leave substantial wire mass at the original array position, whereas equally massive arrays of other materials show no mass left behind. The backlighted fibers of organic polyolefin (Figure 2-3b) even show the wrinkles that existed when the fibers were mounted.

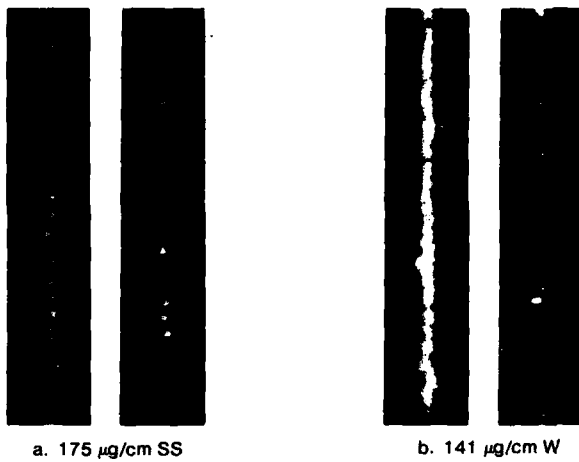


Figure 2-2. Soft X-ray photographs -- effects of wire material.

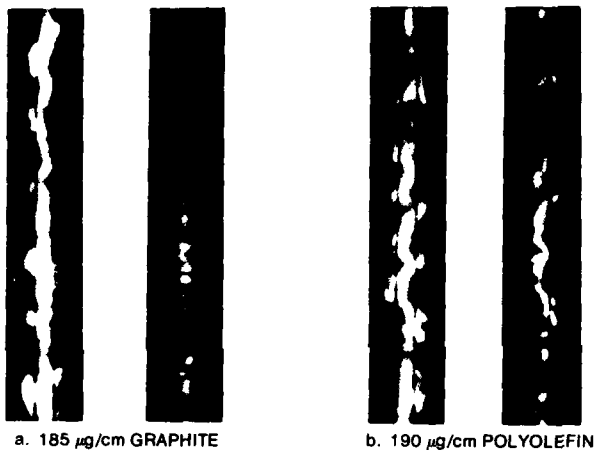


Figure 2-3. Soft X-ray photographs -- carbon plasmas.

A rough estimate of the average ion density for the imploded plasmas can be obtained using the soft X-ray and framing camera photographs. Assuming that most of the wire array mass is compressed into the 1 mm dia region from which the strongest emission occurs, one obtains a mass density of  $0.013 \text{ g/cm}^3$  for a  $100 \text{ μg/cm}$  array. The corresponding ion density ranges from  $4.3 \times 10^{19} \text{ cm}^{-3}$  for tungsten arrays to  $2.9 \times 10^{20} \text{ cm}^{-3}$  for aluminum arrays. For the complete range of array masses used in these experiments, the ion average density lies in the  $10^{19}$ - $10^{21} \text{ cm}^{-3}$  range.

### III. RADIATION MEASUREMENTS

The total energy radiated by the plasma was measured with two unfiltered tantalum foil calorimeters which agreed to within five percent. Both calorimeters were placed approximately 2 m from the source and were protected by fast ( $<1 \text{ ms}$ ) shutters to prevent erroneous readings due to hot gasses. Relative total radiation yield measurements are shown in Figure 3-1 for stainless steel wire plasmas; each point represents a single experimental shot. The lines drawn through the data points illustrate the extremes of the data.

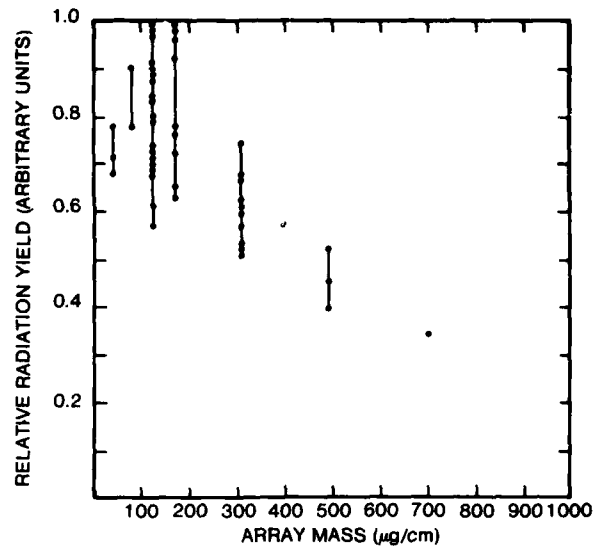


Figure 3-1. Radiation yield vs. array mass -- stainless steel.

The relative radiation yield for all the wire materials is presented in Figure 3-2. Each plotted point represents the energy averaged over all shots for that particular array; arrays with nine or more shots also have the standard deviation marked by error bars. With the exception of carbon, all the data points of Figure 3-2 appear to be within a standard deviation of a single curve. This yield curve shows that the peak yield occurs for array masses of  $100$ - $200 \text{ μg/cm}$ . The radiated energy from the lower mass arrays is only one standard deviation below the peak and, thus, may represent a plateau rather than a fall-off.

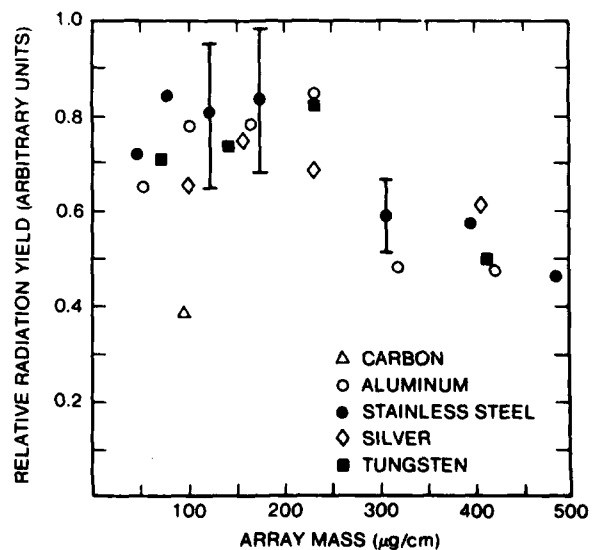


Figure 3-2. Radiation yield vs. array mass and wire material.



The pulsewidth of the radiation emission was measured with aluminum X-ray diodes (XRD). Most of the data was taken with an unfiltered XRD, which is most sensitive to the softest radiation, i.e., ultraviolet. The bare XRD FWHM pulsewidth was found to increase monotonically with array mass (Figure 3-3). Again, the data all lie within a standard deviation of a single curve with the exception of carbon. A minimum pulsewidth of  $\approx 25$  ns was measured for 44  $\mu\text{g}/\text{cm}$  arrays. Several measurements were taken with an XRD filtered with 100  $\mu\text{g}/\text{cm}^2$  of carbon. The XRD then responds primarily to 100-283 eV photons; these data suggest that much of the radiation is emitted in a pulse whose width is half that measured by the bare XRD.

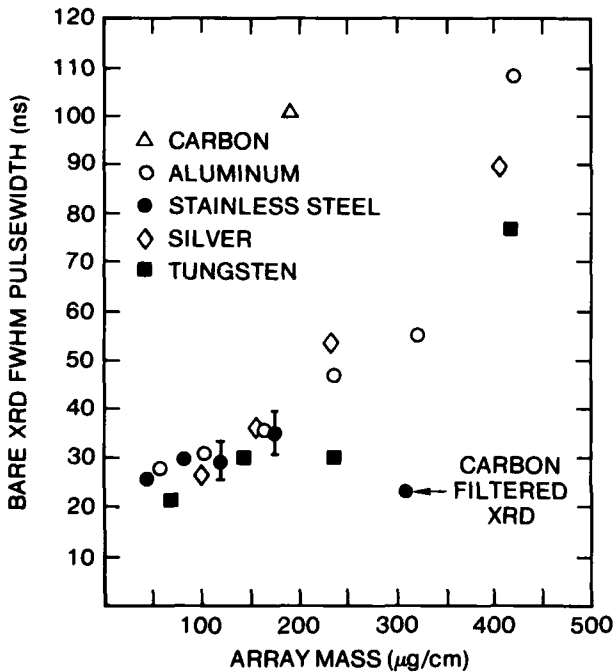


Figure 3-3. XRD pulsewidth vs. array mass and wire material.

The bare XRD was also used to monitor the timing of the radiation pulse relative to the current waveform. The data of Figure 3-4 show that, for all material studied, the radiation pulse occurs later in time as the array mass increases. The highest yields occur on shots whose XRD signal peaks 10-20 ns after the current peak. We also observe that the radiation pulse is simultaneous with a current dip due to an increase in the impedance of the plasma load. When the dip occurs near peak current, a shift occurs in the timing of the current peak. This is particularly obvious with the low mass arrays where the dip is most pronounced.

One of the major unanswered questions in the physics of imploding wire arrays is the nature of the plasma heating. According to the early theories, the plasma is heated by a rapid thermalization of the kinetic energy of the individual imploding wires as they collide on axis(11,12). Improved experimental measurements such as those presented here show that this process can account for only a fraction of the radiated energy.

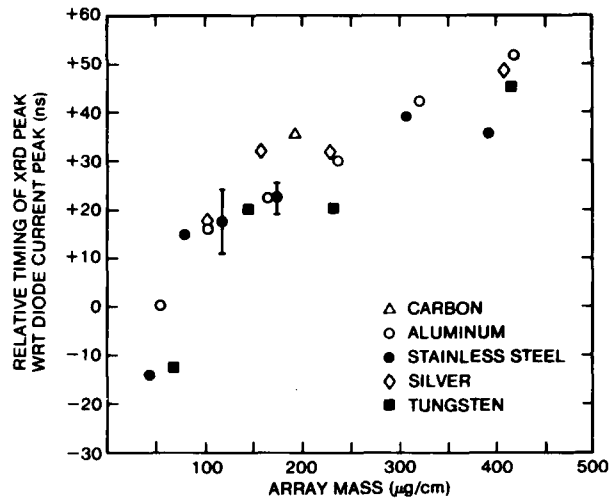


Figure 3-4. XRD peak timing vs. array mass and wire material.

One can calculate the kinetic energy transferred to the imploding wire plasmas by considering the equation of motion for a thin annular cylinder driven only by the  $\vec{j} \times \vec{B}$  force

$$m\ddot{r} = -\frac{\mu_0 \ell I^2}{4\pi r} \quad (1)$$

Here  $I$  is the current flowing along the cylinder, and  $m$ ,  $r$  and  $\ell$  are its mass, radius and length, respectively. Multiplying by  $\dot{r}$  and integrating with respect to time we obtain

$$\int_{t_0}^{t_1} m\ddot{r}\dot{r} dt = -\int_{t_0}^{t_1} \frac{\mu_0 \ell I^2 \dot{r}}{4\pi r} dt \quad (2)$$

If  $I$  is constant, this equation can easily be integrated to obtain a simple relation between the increase in kinetic energy and the compression ratio:

$$\frac{m(\dot{r}_1^2 - \dot{r}_0^2)}{2} = \frac{\mu_0 \ell}{4\pi} I^2 \ln \frac{r_0}{r_1} \quad (3)$$

When the appropriate experimental values are used the observed radiation yield is found to be significantly higher than the kinetic energy input.

Calculations with a one-dimensional fluid code have obtained reasonable agreement with experimental yields and pulsewidths when the classical resistivity is multiplied by an ad hoc factor of fifty(13). Additional evidence for the anomalous resistivity hypothesis is provided by two dimensional fluid calculations with a non-classical resistivity, which predict saturated sausage instability wavelength and amplitude in good agreement with experimental observations(14). While anomalous joule heating may well be the major plasma heating process, this hypothesis has never been directly verified because of the extreme difficulty of measuring electric fields and current densities in the plasma. Furthermore, the cause and scaling of the anomalous resistivity are open to speculation.

The experimental data do show that the plasma radiation and, thus, the plasma heating, are strongly correlated with the  $m = 0$  instability which is so prominent in the pinhole camera photographs. The framing camera photograph (Figure 1-4b) shows that the peak of the radiation pulse (Figure 1-3b) coincides with the presence of  $m = 0$  sausages in the plasma ( $t = 170$ - $180$  ns). Furthermore, the larger radiation yields are strongly correlated with the presence of the  $m = 0$  instability. Carbon plasmas, whose yields are half those of the other wire materials, show virtually no  $m = 0$  sausages (Figure 2-2). For the other wire materials, higher yields were obtained for the lower mass arrays, which showed prominent  $m = 0$  sausages (Figures 2-1 and 2-2). The fact that the yield was independent of wire material (except for carbon) suggests that the current is still being carried primarily by electrons rather than by ions. Additional experiments are planned to investigate the plasma power balance and the evolution of the  $m = 0$  instability. Hopefully, this will lead to an understanding of the nature and scaling of the plasma heating.

#### IV. SPECTRAL MEASUREMENTS

Several spectrographs were used to obtain temporally and spatially integrated spectra of the plasma radiation in the 40-4000 eV range. An extreme ultraviolet (XUV) spectrograph with a 1 m radius, 1200 lines/mm grating covered the 40-500 eV region; Kodak 101-01 film was used to record the spectrum. Lead myristate and potassium acid phthalate (KAP) curved crystal spectrographs with Kodak 2490 film were used to measure the spectrum in the 700-4000 keV region. These instruments were uncalibrated for spectral intensity, and so only qualitative observations on the radiation spectra will be presented. In general, the spectra show lines superimposed on an intense XUV continuum; isolated lines are also present at higher energy in some cases. The lines merge into a smooth continuum as the mass and atomic number of the wires is increased.

The XUV spectra of carbon plasmas show intense K and L lines superimposed on the continuum (Figure 4-1). The continuum appears optically thin when compared to the line intensities. This is not surprising considering not only the relative lack of carbon transitions in the XUV range, but also the mass left behind in the implosion. The ionization state is primarily C VI (hydrogen-like) with lesser amounts of C V (helium-like) and presumably C VII (fully-stripped). Although the plasma is time-varying and inhomogeneous, one can estimate a temperature of  $\geq 50$  eV from the line intensities.

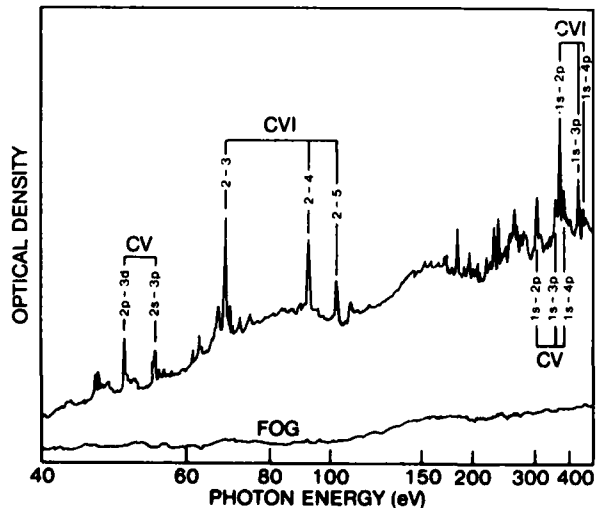


Figure 4-1. Carbon XUV spectrum -- 185  $\mu\text{g}/\text{cm}$  (shot 3723).

Aluminum plasmas created from the lighter arrays ( $\leq 150$   $\mu\text{g}/\text{cm}$ ) radiated intense K lines. In the K spectrum measured with the KAP spectrograph (Figure 4-2), the strongest lines are from Al XII (helium-like) but significant Al XIII is also present. The XUV spectrum taken with the grating spectrograph (Figure 4-3) shows L lines primarily from Al XI (lithium-like) but also from Al X. Simultaneous observation of emission from all these ionization states is indicative of temperature gradients in the plasma. The Al XII and Al XIII radiation emanates from the hot spots, whose temperature is estimated to be  $\approx 300$  eV, while the Al X and Al XI radiation comes primarily from cooler regions with  $\geq 50$  eV temperatures.

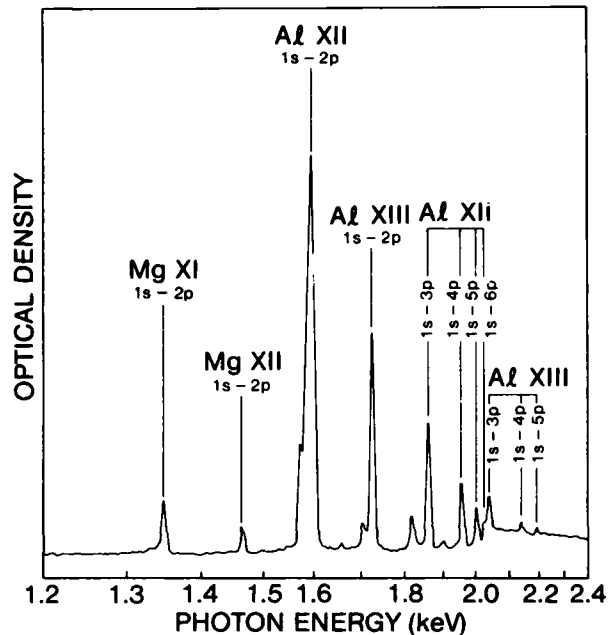


Figure 4-2. Aluminum K spectrum -- 164  $\mu\text{g}/\text{cm}$  (shot 3661).

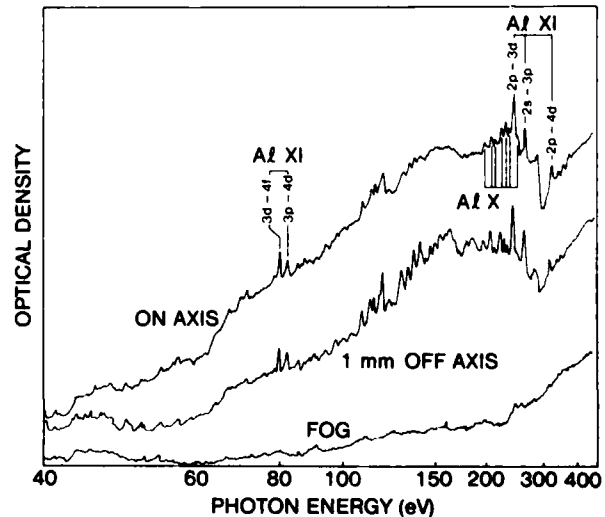


Figure 4-3. Aluminum XUV spectrum -- 59  $\mu\text{g}/\text{cm}$  (shot 3746).

As the mass of the aluminum array was increased, the intensity of the K line radiation was observed to decrease monotonically, while the continuum became relatively more intense. For the 164  $\mu\text{g}/\text{cm}$  array, several L lines are barely perceptible above the continuum (Figure 4-4), while for the lighter 59  $\mu\text{g}/\text{cm}$  array the continuum is weaker and the L lines are more prominent (Figure 4-3).

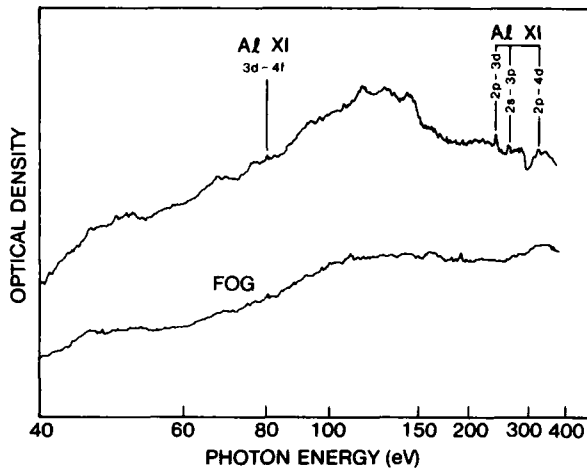


Figure 4-4. Aluminum XUV spectrum -- 164  $\mu\text{g}/\text{cm}$  (shot 3733).

The radially resolved spectra of Figure 4-3 show that when the line of sight is moved off axis, the continuum intensity falls faster than the line intensity, revealing additional lines. This is consistent with the theoretical expectation that the continuum results from a complicated merging of opacity-broadened lines and radiative recombination continua from the L-shell of many aluminum species. This hypothesis is further confirmed by the observation that the lines merge more completely into a continuum for heavier arrays (more matter in the line of sight) and for higher Z arrays (more transitions available in the XUV range).

With stainless steel plasmas, L lines are observed only for the lighter arrays. The L lines measured with the KAP spectrograph (Figure 4-5) are from highly ionized species: neon-like (Fe XVII, Ni XIX), fluorine-like (Fe XVIII, Cr XVI) and oxygen-like (Fe XIX, Cr XVII). The XUV spectra also show intra-shell ( $\Delta n = 0$ ) L lines from the same highly ionized species (Figure 4-6). These species are presently only in localized hot spots, where the temperature is estimated at  $\approx 200$  eV. For the heavier arrays, the L lines disappear.

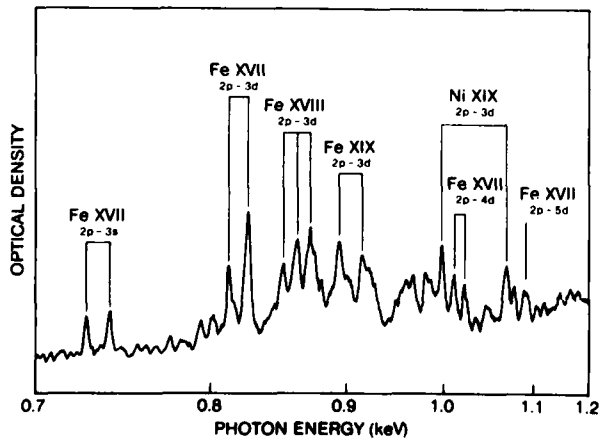


Figure 4-5. Stainless steel L spectrum -- 44  $\mu\text{g}/\text{cm}$  (shot 3121).

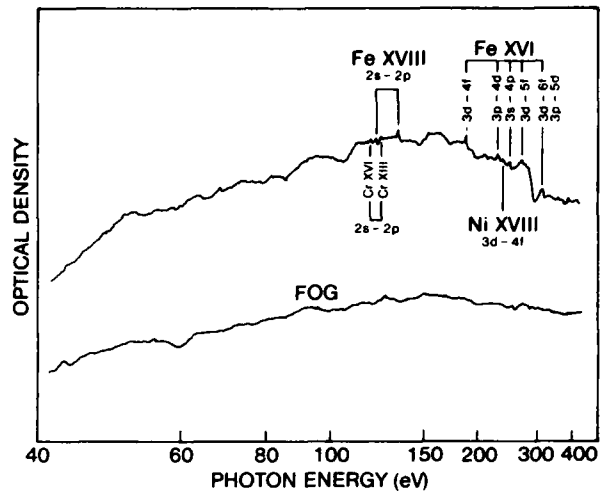


Figure 4-6. Stainless steel XUV spectrum -- 44  $\mu\text{g}/\text{cm}$  (shot 3736).

Stainless steel plasmas also radiate distinct M lines and a continuum for lighter arrays (Figure 4-6), but for heavier arrays, the M lines merge into the continuum (Figure 4-7). The prominent M lines are from the sodium-like species Fe XVI and Ni XVIII; from these we estimate a plasma temperature of  $\approx 250$  eV. The lower ionization states of the stainless steel species are undoubtedly also present. Note that the continuum is smoother and more intense than that of the aluminum plasmas.

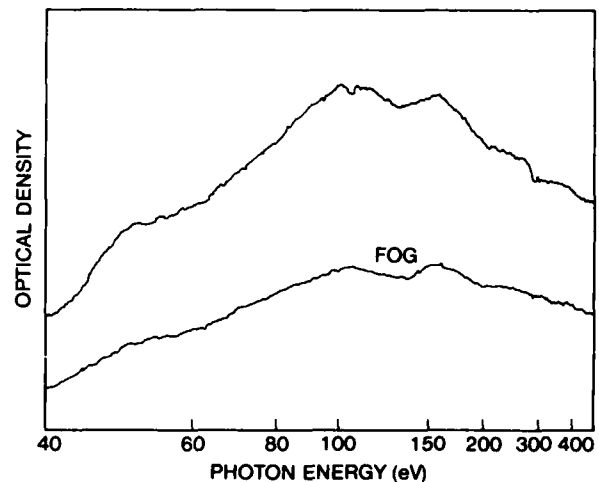


Figure 4-7. Stainless steel XUV spectrum -- 176  $\mu\text{g}/\text{cm}$  (shot 3731).

The XUV spectra of silver (Figure 4-8) and tungsten (Figure 4-9) plasmas show smooth, single-peaked continua with no discernable lines. The similarity of the two spectra suggests that high Z plasmas are sufficiently opaque throughout the XUV range that the emission spectrum no longer depends upon the electronic details of the constituent ions. Even the light arrays of high Z wires show the same spectrum indicating that the plasma is still optically thick.

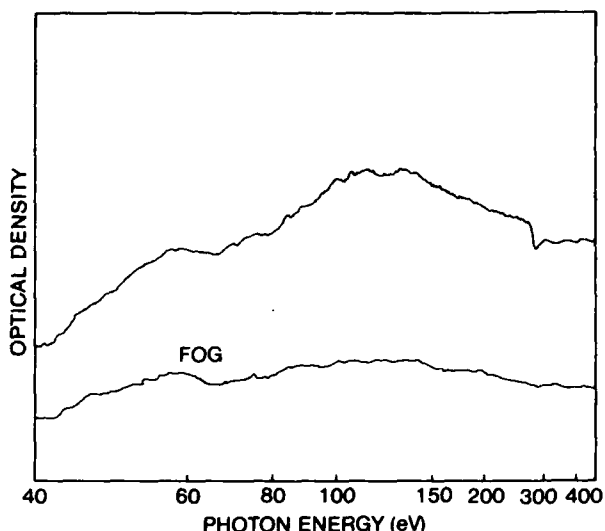


Figure 4-8. Silver XUV spectrum -- 102  $\mu\text{g}/\text{cm}$  (shot 3722).

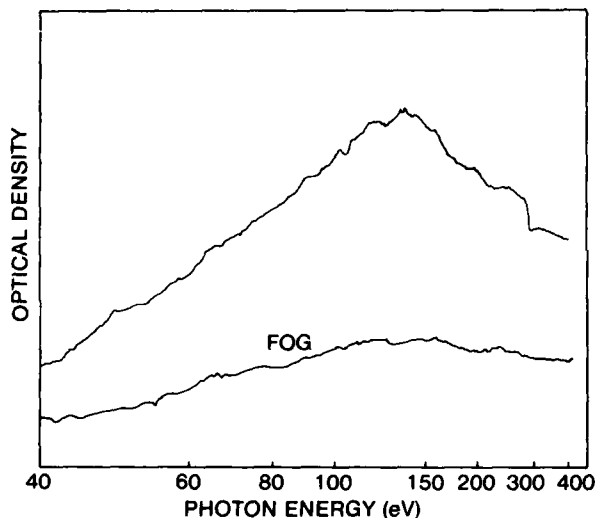


Figure 4-9. Tungsten XUV spectrum -- 141  $\mu\text{g}/\text{cm}$  (shot 3715).

X-ray measurements of tungsten and silver plasmas with the crystal spectrographs show no significant emission above 700 eV, indicating that essentially all the energy is radiated in the continuum. In contrast, the same spectrographs recorded significant aluminum K radiation ( $\approx 1.6$  keV) and iron L radiation ( $\approx 0.8$  keV). In a previous investigation(4) single exploded wires of 50-100  $\mu\text{g}/\text{cm}$  did produce silver L radiation ( $\approx 3$  keV) and tungsten M radiation ( $\approx 2$  keV) when driven with twice the electrical energy available in the present experiments.

The spectral data show a number of significant trends running through the complete range of array mass and wire material. The most important of the trends is an apparent, consistent increase in emissivity below 1 keV with both increasing mass and increasing atomic number. Furthermore, the shape of the  $<1$  keV continuum appears to be converging with increasing  $Z$ ; for sufficiently high  $Z$  the spectral shape is independent of the electronic details of the plasma species. Both high and low  $Z$  plasmas heat

up to  $>50$  eV, whereupon they convert their input energy to radiation. High  $Z$  plasmas radiate all their energy in the  $<1$  keV range, whereas low  $Z$  plasmas radiate significant energy in  $\geq 1$  keV lines because of their lesser emissivity in the  $<1$  keV range.

The spectra also show a consistent trend with array mass. Low mass plasmas have lower emissivity below 1 keV and, thus, their  $<1$  keV continua are less intense while their  $\geq 1$  keV lines are more intense. Increasing the mass, transfers more radiation into the  $<1$  keV range, but only up to a point. For masses above 200  $\mu\text{g}/\text{cm}$ , the decrease in plasma input energy is more important and the continuum intensity diminishes.

## V. IMPLoding GAS JET PLASMAS

Imploding plasmas, such as those discussed above, are intense X-ray sources which can be important for a variety of applications. For example, X-ray diagnostic development, micro-lithography, biological microscopy, absorption spectroscopy(15), and extended X-ray absorption fine structure (EXAFS) studies have already been performed using imploding wire plasmas on BLACKJACK 3. These and other areas of study can be actively pursued with the BLACKJACK 3 user facility by interested scientist.

A more compact laboratory source of soft X-ray emission than BLACKJACK 3 is provided by imploding a hollow, cylindrical gas jet with a direct capacitive drive. The gas jet implosion dynamics are quite similar to those observed with wire arrays. The advantages of the gas jet are: first, the ability to use gases and thus complement the line spectra available with wire arrays, and second, the ease with which the gas load can be repetitively pulsed. The gas jet, shown schematically in Figure 5-1, is produced by opening a fast valve and allowing gas to pass through an annular nozzle. A capacitor bank is then discharged through the jet causing the gas (plasma) to implode onto its axis. The pinched 1 mm dia plasma emits a burst of soft X-rays which typically lasts several tens of nanoseconds.

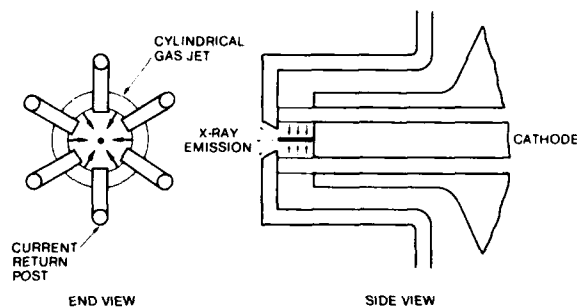


Figure 5-1. Imploding gas jet plasma.

The small pulsed gas jet plasma source, LEXIS 1, has been operated with a number of gases. Preliminary measurements show that the line and continuum spectra can be adjusted by varying the mass and atomic number of the gas; the relationships between X-ray emission and gas jet parameters appear to be similar to those observed with imploding wire array plasmas. With krypton, for example, 20 J pulses of 1.65-1.95 keV radiation from the L lines of neon-like Kr XXVII (Figure 5-2) have been observed. This radiation has been used successfully to expose resists for X-ray micro-lithography(16). The source also produces several hundred joules per shot of softer ( $h\nu < 1$  keV) radiation, with a continuum-like spectrum (Figure 5-3). This softer radiation has proven to be very useful in applications such as the microscopy of biological materials and surface EXAFS. A detailed description of the source and some of its applications has been presented elsewhere(17).

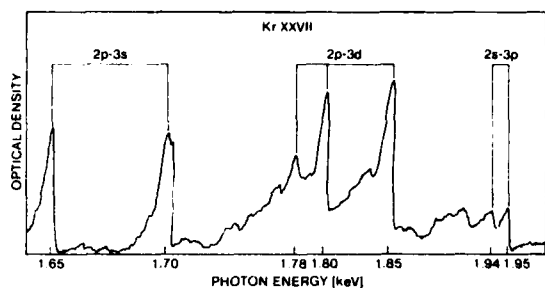


Figure 5-2. Krypton L-shell spectrum.

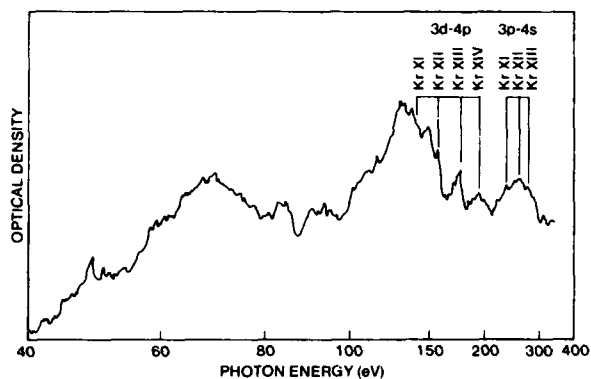


Figure 5-3. Krypton XUV spectrum.

## VI. CONCLUSION

We have shown that plasmas created from imploding wire arrays provide intense sources of subkilovolt radiation. Both the radiation yield and pulsewidth depend strongly upon the mass of the wire array and weakly upon the wire material. All materials give nearly the same yield and pulsewidth except for carbon, which gives half the yield and three times the pulsewidth. The yield is a maximum for array masses of 100-200  $\mu\text{g}/\text{cm}$  which implode near peak current; the yield falls off sharply for heavier arrays. The bare XRD pulsewidth increases monotonically with array mass from a minimum of 25 ns for the lightest arrays.

Pinhole camera photographs of the plasma show that the radiation is emitted primarily from an imploded or pinched plasma  $\approx 1$  mm in diameter by 3 cm long. The average temperature of the bulk plasma is estimated to reach  $>50$  eV, and average ion densities are estimated to range from  $10^{19}$ - $10^{21}$   $\text{cm}^{-3}$  for the various masses and materials used. The photographs also show that the linear plasma is constricted by the sausage instability into flares and hot spots (with temperatures of several hundred electron volts). Because these hot spots are correlated with the radiation yields and timing, we believe that sausage instability may play an important role in the plasma heating.

All the imploding wire plasmas radiate a soft X-ray continuum which results from a complicated merging of opacity-broadened lines and radiative recombination continua. As the atomic number ( $Z$ ) of the plasma is increased, the increased opacity produces a continuum which is smoother and more intense. For high  $Z$  plasmas such as silver and tungsten, the mass of the array has little effect on the continuum until it exceeds 200  $\mu\text{g}/\text{cm}$ ; above this point, the increased mass and decreased energy coupling produce cooler plasmas and, consequently, diminished continuum intensity. For lower  $Z$  materials such as aluminum

and iron, an increase in mass also increases the opacity, which produces a smoother, more intense continuum; however, above 200  $\mu\text{g}/\text{cm}$ , an increase in mass diminishes the continuum intensity for the same reasons as in high  $Z$  plasmas.

In addition to the soft X-ray continuum, the plasmas also emit line radiation (primarily from the hot spots). The intensity of these lines increases with decreasing atomic number and decreasing array mass. With lower mass arrays ( $\leq 150$   $\mu\text{g}/\text{cm}$ ) aluminum plasmas radiate intense K lines, while stainless steel plasmas radiate less intense L lines; aluminum L lines and stainless steel M lines are observed above the continuum for low mass arrays. No distinct line radiation is observed for either silver or tungsten plasmas.

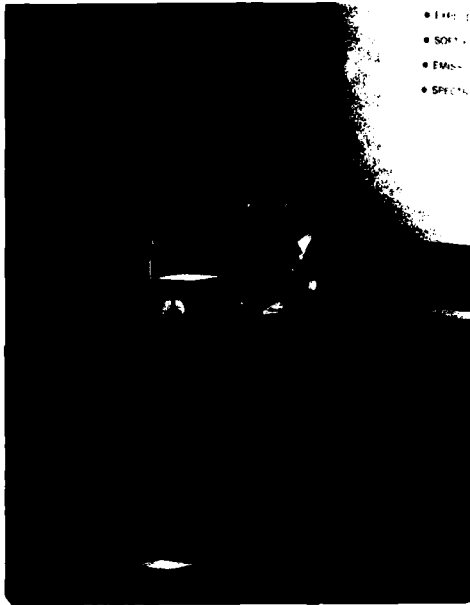
Imploding gas jet plasmas provide compact, convenient laboratory sources of intense soft X-ray emission for diagnostic development and other applications. The line radiation of the lower  $Z$  plasmas has already been successfully applied in X-ray micro-lithography and in biological microscopy. The smooth continuum of the high  $Z$  plasmas has been shown to be an ideal backlighting source for absorption spectroscopy and extended X-ray absorption fine structure studies.

We are grateful for the technical assistance of J. Devlin, G. Hulse, W. Kaiser, J. Mangelsdorf, D. Powell, and A. Vasquez. Without their skill and dedication it would not have been possible to obtain such a comprehensive set of data in the limited time available. We are also grateful to Dr. B. Henke for providing the lead myristate crystal, and to J. Owren and Marco Scientific for support in making the framing camera photographs.

## REFERENCES

- \*Work supported by the Defense Nuclear Agency.
1. I. M. Vitkovitsky, P. P. Bey, W. R. Faust, R. Fulper, Jr., G. E. Veavitt, and J. D. Shipman, Jr., in "Exploding Wires", W. G. Chase and H. K. Moore (editors), V.2, Plenum, New York (1962).
  2. D. Mosher, S. J. Stephanakis, I. M. Vitkovitsky, C. M. Dozier, L. S. Levine and D. J. Nagel, *Appl. Phys. Lett.* **23**, 429 (1973).
  3. D. Mosher, S. J. Stephanakis, K. Hain, C. M. Dozier and F. C. Young, *Ann. NY Acad. Sci.* **251**, 632 (1975).
  4. P. Burkhalter, C. Dozier, D. Nagel, *Phys. Rev. A* **15**, 700, (1976).
  5. C. Stallings, K. Neilsen and R. Schneider, *Appl. Phys. Lett.* **29**, 404 (1976).
  6. P. Burkhalter, J. Davis, J. Rauch, W. Clark, G. Dahlbacka and R. Schneider, *J. Appl. Phys.* **50**, 705, (1979).
  7. W. Clark, *Bull. Am. Phys. Soc.* **24**, 1053 (1979).
  8. J. C. Martin in "Energy Storage, Compression, and Switching", W. H. Bostick, V. Nardi and O. S. F. Zucker (editors) Plenum, NY (1974).
  9. R. Miller, "Sub-ohm Coaxial Pulse Generators, BLACKJACK 3, 4 and 5", Third IEEE International Pulsed Power Conference, Albuquerque 1981 (to be published in IEEE Transactions).
  10. R. F. Benjamin, J. S. Pearlman, E. Y. Chu and J. C. Riordan, Maxwell Laboratories Report 1059 "Dynamics of an Imploding Wire Plasma", 1981 (to be published).
  11. H. A. B. Bodin, A. A. Newton and N. J. Peacock, *Nuclear Fusion* **1**, 54, (1960).
  12. J. Katzenstein, *J. Appl. Phys.* **52**, 676 (1981).
  13. D. Colombant, M. Lampe, J. Davis and H. Bloomberg, "Dynamics and Radiative Yields from Aluminum Multiple Wire Arrays", NRL Memorandum Report 3840, 1978 (unpublished).

14. T. W. Hussey, N. F. Roderick and R. J. Faehl, Appl. Phys. Lett. **33**, 230 (1978).
15. J. C. Riordan and J. S. Pearlman, "XUV Absorption Spectroscopy of a Backlighting Aluminum Plasma", Maxwell Laboratories Report 1005, 1980 (to be published Appl. Phys. Lett.).
16. J. S. Pearlman and J. C. Riordan, "X-ray Lithography Using a Pulsed Plasma Source", presented at 16th Symposium on Electron, Ion, and Photon Beam Technology, Dallas, 1981 (to be published in J. Vac. Sci. Tech.).
17. J. S. Pearlman, J. C. Riordan, J. DeVoss, M. Gersten and G. Hughes, Maxwell Laboratories Report 1062 "X-ray Lithography Using a Pulsed Plasma Source", 1981 (to be published).



Dr. John Riordan describing work at Maxwell with imploding wire arrays.

## Photoemission Measurements for Low Energy X-Ray Detector Applications

Robert H. Day

Los Alamos National Laboratory, P. O. Box 1663, MS-410, Los Alamos, NM 87545

## ABSTRACT

Photoemission has been studied for nearly 100 years as both a means of investigating quantum physics, and as a practical technique for transducing optical/x-ray photons into electrical currents. Numerous x-ray detection schemes, such as streak cameras and x-ray sensitive diodes, exploit this process because of its simplicity, adaptability, and speed. Recent emphasis on diagnostics for low temperature, high density, and short-lived, plasmas for inertial confinement fusion has stimulated interest in x-ray photoemission in the sub-kilovolt regime. In this paper, a review of x-ray photoemission measurements in the 50 eV to 10 keV x-ray region is given and the experimental techniques are reviewed. A semiempirical model of x-ray photoemission is discussed and compared to experimental measurements. Finally, examples of absolutely calibrated instruments are shown.

## INTRODUCTION

The subject of this afternoon's session will focus our attention on detectors for sub-keV x-ray plasma diagnostics. It is frequently desirable to transform x-ray emission into an electrical current for subsequent recording and the photoelectric effect is a useful mechanism for transducing electromagnetic radiation into free electrons. This paper is a brief review of this process as it applies to pulsed plasma x-ray detectors.

The photoelectric process is conceptually simple as outlined schematically in Fig. 1. Radiation incident on a photosensitive surface interacts with the cathode via photoelectric absorption or Compton scattering, creating energetic primary and Auger electrons. These electrons traverse the material creating low energy secondary electrons. Some fraction of the primary and secondary electrons are emitted from the surface of the photocathode.

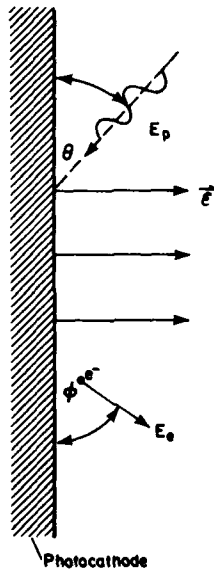


Fig. 1. Schematic of the photoelectron emission process.

This emission is a complicated function of space, energy, and time characterized by the distribution  $N(E_e, E_p, \theta, \phi, t)$ , where  $E_e$  is the emitted electron energy,  $E_p$  is the incident photon energy,  $\theta$  is the photon angle of incidence from the photocathode surface,  $\phi$  is the electron emission angle relative to

the photocathode surface, and  $t$  is time. Photoelectrons are extracted by an applied electric field, and can be used directly as the detector signal or the photocathode return current can be measured.

The photoelectric process has three important properties which make it useful in low energy x-ray pulsed plasma detectors.

1. Speed: The intrinsic speed of the photoelectric emission is  $<10^{-17}$  s. Transport of electrons to the surface takes  $<10^{-14}$  s and collection of the emitted current can take  $<10^{-12}$  s.
2. Linearity: For many metallic photocathodes and modest extraction field, the process is linear to better than 1% over 15 orders of magnitude in photon intensity.
3. Simplicity: The technique is adaptable to many experimental geometries, is sensitive over a broad range of x-ray energies, and can be tailored to specific needs by choice of materials.

Because of these features, photoelectric emission has found widespread use in many detector systems. This paper reviews the status of our knowledge of this process as it applies to the design, calibration, and use of low energy x-ray diagnostics. It starts with an historical perspective on research into this process and then summarizes a model of photoemission. The measuring techniques of each major differential electron distribution are described and typical experimental data is presented. The long term stability of the photoelectric emission process is discussed and it is shown how these elements are applied in a practical, absolutely calibrated, sub-keV x-ray spectrometer system.

## HISTORICAL PERSPECTIVE

Photoelectric emission is one thread in the fabric of modern physics which is deeply woven into the tapestry of quantum electrodynamics. The photoelectric effect has been observed, studied, and utilized for nearly 100 years with the first descriptions reported in 1887 by Hertz, (1) Schuster, (2) and Arrhenius. (3)

During the next 18 years, the basic properties of photoemission were discovered:

1. The total emitted current is linear with electromagnetic intensity.
2. The highest electron energy increases linearly with the exciting photon's energy irrespective of the incident intensity.
3. The emission is essentially instantaneous.

It was recognized that properties 2 and 3 in the list above are incompatible with Maxwell's classical electromagnetic theory and this contradiction motivated the second of Albert Einstein's three seminal papers published in *Annalen der Physik* in 1905. (4) It was entitled "On a Heuristic Viewpoint Concerning the Production and Transformation of Light" and laid the groundwork for representing photons as localized

particles with energy and momentum. During the next 20 years, detailed experimental investigations by Millikan(5), Compton(6), and others established the photon as the particle component of the electromagnetic wave-particle duality.

As interest in the photoelectric effect fell behind the frontiers of quantum physics, interest increased in applying this unique process to a broad range of applications. Many modern detector systems such as ionization chambers, proportional counters, photomultiplier tubes, photodiodes, x-ray streak and framing cameras make use of this effect.

#### PHOTOEMISSION MODELS

Despite nearly 100 years of research, we still do not have a complete theory of photoelectric emission as it applies to practical detector systems. The mechanisms that must be accurately modeled include: 1) the generation of the primary electron either through photoelectric absorption or incoherent scattering, 2) the transport of primary and Auger electrons to the photocathode surface and their energy loss to secondaries, and 3) the generation of a detectable signal from these electrons. Of these three steps, the secondary generation and transport process is by far the least well-understood.

The photon interaction is dominated by photoelectric absorption and recent theoretical studies by Pratt, et al.(7) demonstrate that good models of photoelectric cross sections exist above ten kilovolts. More important, for a predictive model of detector behavior, excellent compilations of x-ray cross sections are available for all elements at photon energies above 100 eV,(8-11) and for selected elements at lower energies.(12-13) Thus, it is possible to model the primary electron production mechanism quite accurately.

The primary electron transport and secondary generation and transport provides a much greater challenge. A typical electron distribution,  $dN/dE_e$ , for photoemitted electrons is shown in Fig. 2 as reprinted from Henke, et al.(14) The important features of this spectrum are "no loss" peaks for the photo and Auger electrons, their associated loss tails, and a large secondary electron emission in a distribution a few eV wide below 10 eV.

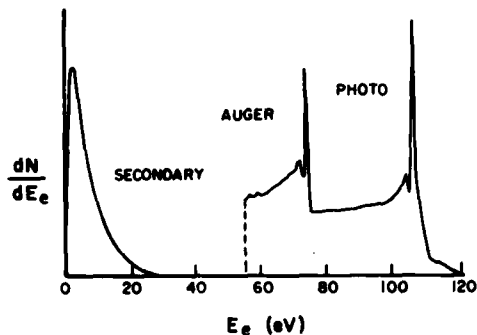


Fig. 2. A typical photoemission spectrum.

Henke, et al.(14) have proposed a semiempirical model that accounts for the "no loss" peak and provides shapes of the secondary electron distribution. The model has also been modified to account for the internal electron scattering processes in semiconductors and insulators.(15) Though absolute predictions of electron yield or spectra, are not yet possible, this model quite accurately predicts the shape of the secondary electron distribution and the photon energy dependence of the total emitted electron yield.

Once an accurate model or measurement of the electron distribution at the surface of the photocathode has been obtained, the transport of this distribution through the electron-optical detector is usually well understood. This step establishes the time response of the detector system. For example, the energy width of the secondary electron distribution establishes the maximum time resolution in a streak camera system.

Similarly, the rise time,  $t_r$ , of a photodiode detector is given by the flight-time of the electrons across an anode-cathode gap spacing,  $d$ ,(16). For an anode-cathode gap voltage,  $V$ ;  $t_r \propto d/\sqrt{V}$ . This functional dependence has been verified(17) and the data is shown in Fig. 3. With modest accelerating voltages,  $\sim 3$  kV, and anode-cathode gap spacings of the order of 1-mm, it is possible to build photodiode detector systems with sub-100 ps response times.

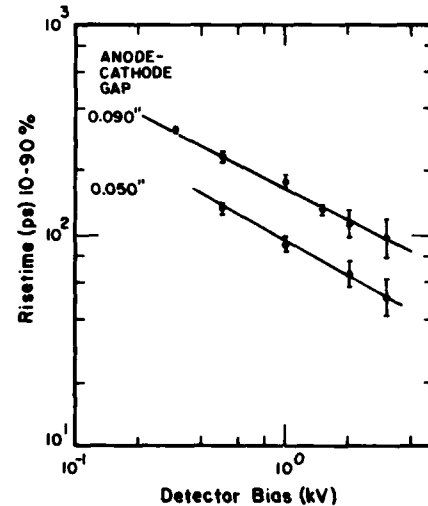


Fig. 3. Detector risetime versus anode-cathode gap voltage and anode-cathode separation.

#### PHOTOEMISSION DATA

Because there is no complete theory of photoemission, and photoemission is a surface phenomena which depends critically on surface condition and contaminants, it is necessary to perform extensive measurements on individual materials and geometries of practical interest. Each parameter in the electron distribution,  $E_p$ ,  $E_e$ ,  $\theta$ , and  $\phi$ , critically affects different types of detector systems.

In the following subsections, a brief description will be given of how a particular parameter affects different types of diagnostic devices, the techniques utilized to measure the parameter. Samples of the available data will be presented with comparison to models when possible.

No attempt is made to compile a complete bibliography of the available data in the text of this paper. Rather, it is presented in the Appendix as a thorough but not exhaustive list of references on photoemission data above 10 eV. Tables are also included which organize the different types of data by element and energy.

#### A. Quantum Efficiency $dN/dE_p$

The quantum efficiency, number of electrons emitted per incident photon, is the most common photoemission data and is required for most absolutely calibrated systems.



A quantum efficiency experiment is performed as shown schematically in Fig. 4. A monochromatic photon beam is incident on the photocathode, and the incident flux and emitted current are monitored to derive the quantum efficiency. The primary beam energy is changed and the photon energy dependence is determined.

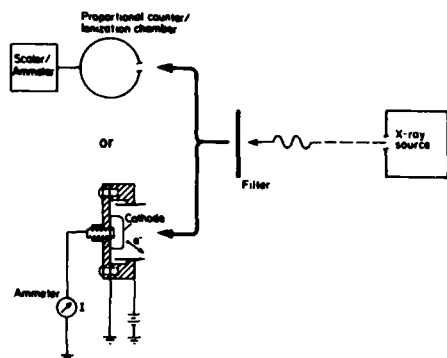


Fig. 4. Quantum efficiency measurements are performed by comparing the emitted photoelectron current to the x-ray flux.

Many such measurements have been made on a wide variety of metallic, semiconductor, and insulating surfaces as part of detector development programs over the past 50 years. Our interest in characterizing x-ray detectors for subkilovolt x-ray measurements has required extending this data into the 50 eV to 1 keV photon energy regime where few measurements have been made. Typical results for photon energies of 20 eV to 10 keV are shown in Fig. 5 for photocathodes of gold, aluminum, copper, and nickel. Many references for this type of data are listed in Table I of the Appendix.

The best available photoemission models such as Henke's model mentioned above, predict quantum efficiencies, QE, with an energy dependence:

$$QE \propto E_p^{\mu} \mu(E_p) f(E_p)$$

where  $\mu(E_p)$  is the incident radiation photoelectric cross section and  $f(E_p)$  is a slowly varying function of photon energy related to the efficiency of converting photo and Auger electrons into secondaries.

To test this result,  $QE/(\mu(E)E)$  vs  $E$  is plotted in Fig. 6 for carbon, aluminum, and gold samples. The resultant curve is the energy dependence of  $f(E)$ . The lines drawn through the data points of Fig. 6 are provided to guide the eye and do not represent a model of  $f(E)$ .

In general,  $f(E)$  is a slowly varying function of energy and the  $\mu(E)E$  term accounts for most of the two or three orders of magnitude variation in quantum efficiency. For gold,  $f(E)$  does not vary by more than 20-30% from 20 eV to 10 keV. A small anomaly is seen near 150 eV at the N absorption feature and again at 1.8 keV at the M absorption edge. Aluminum shows the largest absorption edge and large changes in  $f(E)$  over the entire range of energies. The aluminum surface was modeled as  $Al_2O_3$ , and if we use a pure aluminum surface, the effect is even more pronounced. For the carbon surface,  $f(E)$  is again slowly varying except at very low energies and with a 30% decrease from 100 eV to 1.5 keV.

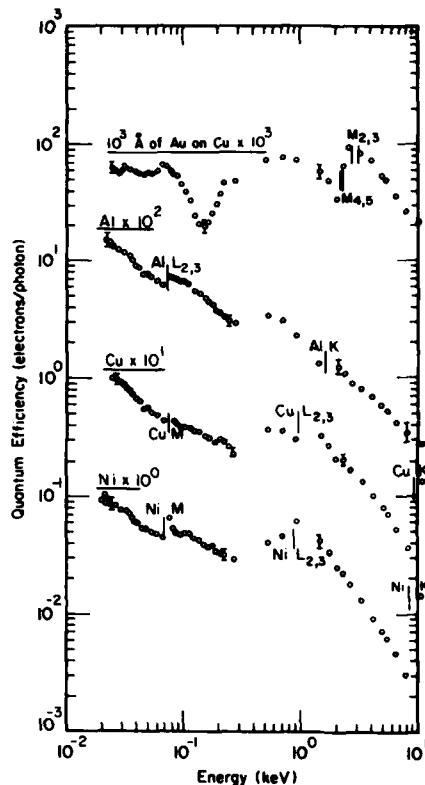


Fig. 5. Quantum efficiencies for gold, aluminum, copper, and nickel. Quantum efficiency is defined as the number of electrons emitted per incident photon.

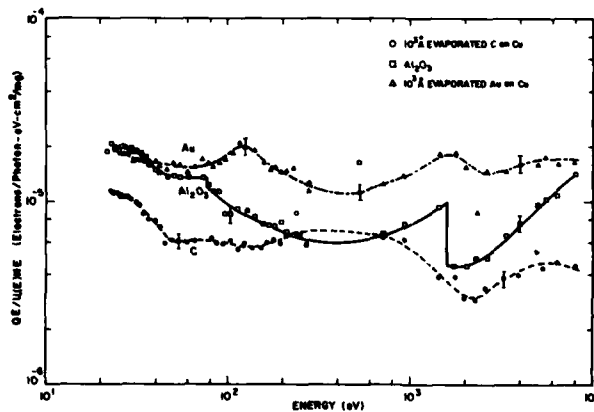


Fig. 6. Energy dependence of  $f(E)$  for carbon,  $Al_2O_3$ , and gold.

#### B. Electron Spectra, $dN/dE_e$

As indicated above, the electron spectrum is a complicated function of electron energy, reflecting the

energy loss and scattering of the initial electrons during transport through the bulk material. Such spectra are the subject of photoelectron spectroscopy and are a powerful tool in surface analysis. However, the electron energy distribution is also an important element in modeling detector time response.

As shown in Fig. 2, the spectrum is primarily a two component system consisting of the photo and Auger electrons and a secondary electron spectrum peaked at a few eV with a few eV half-width. With this type of spectrum, a simple retarding-potential spectrometer(18) can be used to measure the relative primary and secondary contributions.

In this measurement, a reverse bias is applied to the photocathode and only electrons above a critical voltage can escape and contribute to the "high energy yield,"  $Y_{H.E.}$ . Subtracting the photocathode quantum efficiencies measured under forward and reverse bias conditions produces the "low energy yield,"  $Y_{L.E.}$ . The ratio of the low to high energy electron yield for gold in the 1 to 10 keV photon energy range is shown in Fig. 7 as reprinted from Gaines, et al.(19) This level of information is sufficient for modeling photodiode time response.

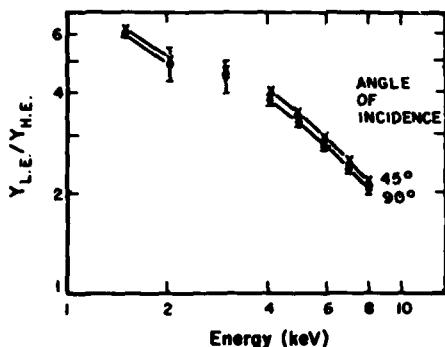


Fig. 7. The ratio of low energy (<50 eV) electron yield,  $Y_{L.E.}$ , to high energy (>50 eV) electron yield,  $Y_{H.E.}$ , for a .194 mg/cm<sup>2</sup> gold foil.(19)

For other applications, such as predicting streak camera time response at the few picosecond level, more detailed secondary electron energy distribution information is required. Such studies have been undertaken by Henke, et al.(14) using an electrostatic focusing electron spectrometer. A sample of the data for Au excited by Al K x-rays is reprinted in Fig. 8. The solid lines shown in this figure are fits to Henke's semiempirical model of photocurrent and demonstrate that the shape predictions are acceptable.

However, this model predicts an absolute yield which is a factor of three too small for the case shown here. This occurs because the model only handles secondary electron scattering empirically. The assumption is made that the secondary electron distribution shape is only slightly modified by secondary electron scattering while the absolute numbers of secondaries is increased.

This model has been extended to insulators and semiconductors(15) where the presence of a band gap restricts the phase-space for electron scattering. The case of insulators is particularly interesting because small energy loss electron-phonon scattering and/or density of states distributions generate structures in the secondary electron energy distribution. A guide to these and additional electron distribution measurements is contained in Table II of the Appendix.

### C. Angular Distributions, $d^2N/d\Omega d\phi$

The electron emission process is dependent upon both the photon angle of incidence relative to the cathode surface,  $\theta$ , and on the angle,  $\phi$ , at which the electrons are emitted relative to the cathode surface. These distributions are important since angle of incidence is frequently used to reduce the incident x-ray flux by going to grazing angle or to enhance electron emission(20).

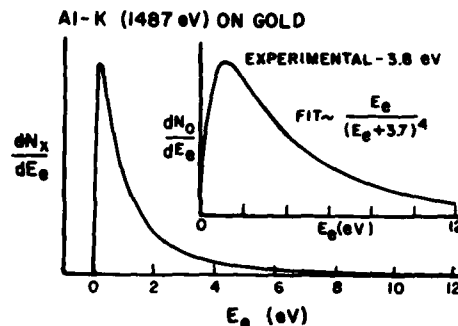


Fig. 8. Secondary electron distribution from gold at 105°C in a  $3 \times 10^{-8}$  Torr vacuum. The lower curve is the distribution as measured by the spectrograph of Henke(14) and the upper curve has been corrected for the instrument response and is the electron distribution at the photocathode surface. The solid line is a fit to Henke's semiempirical model.

The standard technique for measuring quantum efficiency vs photon incidence angle is reported by Gaines and Hansen(19). In this experiment, a simple parameter such as total yield or primary to secondary electron ratio is monitored as a function of photon angle of incidence. For angles greater than a few degrees, quantum efficiency decreases as  $1/\sin\theta$  due to decreased photon deposition within a secondary electron escape depth as reported by both Gaines and Hansen(20) and by Ganeev and Izrailev(21).

An enhanced "no loss" primary photoelectron yield is seen for photon incidence angles just above the critical angle for total x-ray reflection(20). This effect is due to increased photon deposition within a primary photoelectron escape depth of the cathode surface when the photons are refracted nearly parallel to the photocathode surface. This effect will decrease the time response of a photodiode detector due to a decrease in the electron flight time across the anode-cathode spacing.

The more complicated measurement of electron emission versus  $\phi$  is much less commonly reported. Henke's model of secondary yield predicts a Lambertian,  $\sin\theta$ , dependence to the secondary emission resulting from isotropy of the secondary distribution below the photocathode surface. This assumption, however, is not valid for all primary electrons and data from Fernstein and Smith(18) and Paired and Fadley(22) contain such results.

Angular distribution photoemission data is summarized in Table III of the Appendix. It is compiled by element and angle of incidence or emission.

### D. Enhanced Photoemission

Studies of total yield(23-26) and secondary electron distribution(14) have indicated that certain alkali halides, iodides, and semiconductors exhibit enhanced secondary electron emission under x-ray excitation. A comparison of CsI data with Au is shown in Fig. 9. Over most of the energy range from 1 to 10 keV, CsI shows an enhanced photoemission by a factor of

30. This allows significant latitude in designing systems with greater low flux sensitivity.

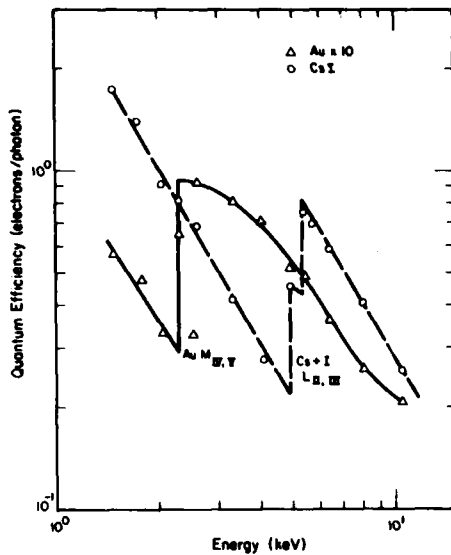


Fig. 9. A comparison of quantum efficiency for gold and cesium iodide photocathodes.

This effect for dielectrics can be understood qualitatively by noting the increased scattering length for low energy electrons below the fermi level. This allows electrons to be collected from deeper within the cathode resulting in higher electron yield.

This enhancement does not come without penalty, however. First, the alkali iodides are deliquescent and care must be taken to maintain them in a water-vapor free environment. We know that heat sealing CsI photocathodes in plastic bags filled with dry nitrogen and storing them in a dessicator will induce no apparent degradation in cathode appearance for as long as six months. However, exposure of these cathodes to air at 20 to 25% relative humidity for more than a few hours impairs performance.

Second, the time response of these cathodes may be less rapid. The emission process seems to have a slower component at the level of a few percent of the main emission which persists for approximately 100 picoseconds(27). Furthermore, effects caused by large photoemissive currents and the finite cathode material resistivity may cause time dependent sensitivity. At present, these materials show promise as useful photoemissive cathodes but care should be taken to carefully characterize their energy and time response until further study answers some of these outstanding concerns.

Another class of enhanced photoemissive materials based upon gallium-arsenide and gallium-arsenic-phosphide has been reported by Bardas et al.(28). These materials show quantum efficiencies of 100 at 2 keV x-ray energy. Of even greater interest, is the linear increase of quantum efficiency with x-ray energy. However, these materials are very sensitive to vacuum contaminants and are generally used at less than  $10^{-10}$  torr. This greatly limits their practical application.

#### PHOTOCATHODE AGING EFFECTS

Aging effects similar to those seen on alkali iodide cathodes are also present on any metallic

surface. Photoelectric emission is a surface physics effect and any change in the surface composition or structure will appear as a change in the secondary electron yield. Some discussion of long term aging is available in the literature(25,29), but historically, most photocathodes have been utilized in sealed vacuum environments where aging effects are minimal.

Experience at the Los Alamos National Laboratory, LANL, indicates that with care, photocathodes can be used for extended periods of time in the laser fusion experimental environment as subkilovolt, x-ray transducers without large, >15%, changes in system calibration. Photocathode surface preparation is important to achieve this level of stability. Figure 10 is a long term aging study of micromachined aluminum cathodes. It shows that for this type of surface quantum efficiency changes of less than 10% are possible over six months exposure to air. These cathodes are used in the LANL low energy x-ray spectrometer at the HELIOS laser facility. They are used behind replaceable filter windows and are exposed to the laser chamber vacuum on each shot. Between shots, the diodes are housed in a self-contained ion pumped vacuum system. Several aging and use studies at LANL indicate that an absolute calibration of better than  $\pm 15\%$  can be maintained over four months in the operational environment.

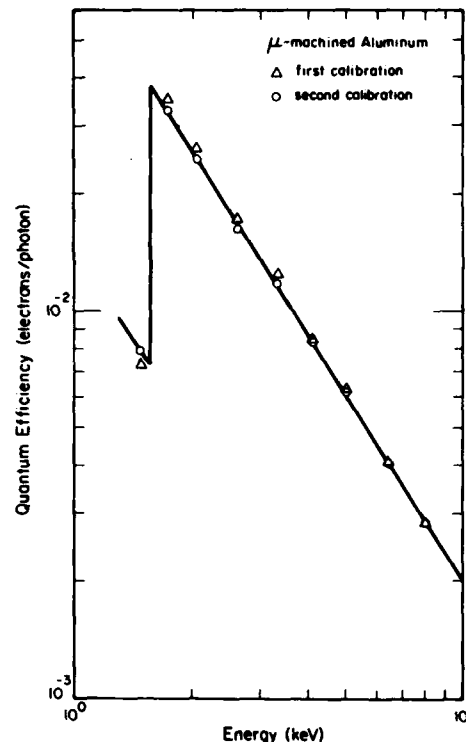


Fig. 10. A before and after comparison of cathode quantum efficiency for micromachined aluminum. The two calibrations are separated by six months storage in air.

Less stringent manufacturing and handling precautions can have a very damaging effect on absolute photocathode sensitivity as shown in Fig. 11. This before and after comparison is described in detail by Day, et al.(25) and includes a one month use on the LANL GEMINI laser facility during which time the

cathodes were continually exposed to the target chamber vacuum.

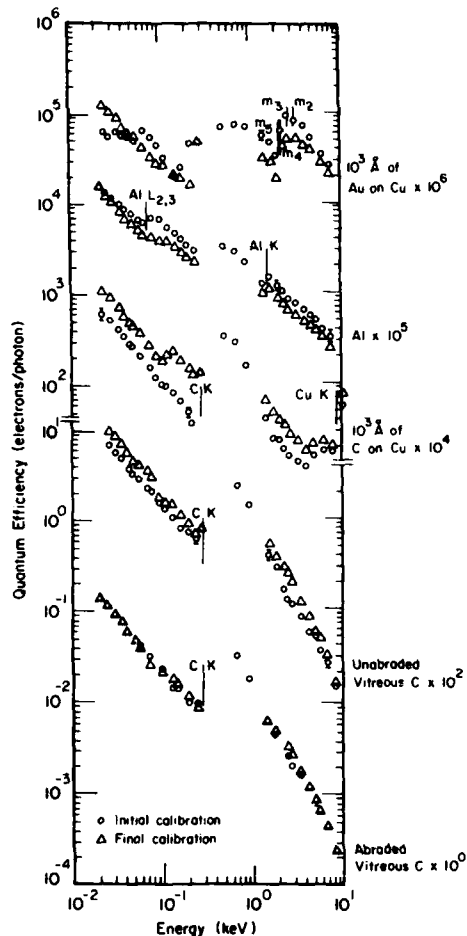


Fig. 11. The quantum efficiency of gold, aluminum, carbon, and abraded and unabraded vitreous carbon. The cathodes were stored in air for six months and used in the LANL GEMINI laser facility between calibrations.

The aging effects for these samples can exceed plus or minus a factor of two. Obviously, significant care must be taken in handling photocathodes for windowless detector applications. The procedure we have adopted to use windowless detectors(25) is to establish a reproducible photocathode manufacturing process and to replace and recalibrate photocathodes frequently, every few weeks.

#### APPLICATIONS

The primary purpose of this paper has been to discuss the status of photoelectric emission measurements as they apply to subkilovolt x-ray diagnostics. The topic of this section will be the practical application of photoemission measurements in an absolutely calibrated time resolved x-ray spectrometer for laser fusion plasma diagnostics.

The detectors are simple biplanar x-ray sensitivity photodiodes, XRD's, in a seven element array covering the spectral range from 20 eV to 2 keV with low resolving power,  $E/\Delta E = 1-9$ . The detector system's acronym is MULTIFLEX for multiple fast low energy x-ray detector. XRD's are simple detectors consisting of an x-ray cathode and anode mesh. The photoelectric current resulting from x-rays impinging on the photocathode is the detector signal.

The energy dependent response of the system is determined by the energy dependent sensitivity of the photocathode convolved with the filter window transmission. The sensitivity of four typical channels is shown in Fig. 12.

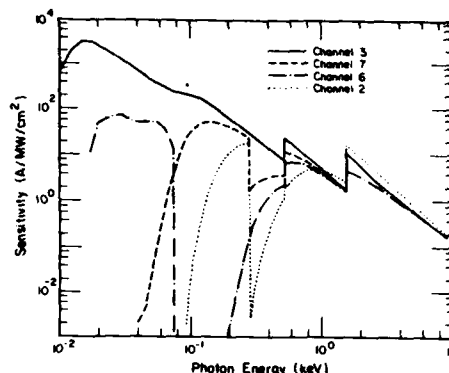


Fig. 12. Typical MULTIFLEX response functions.

- Channel 3 - bare photocathode plus three layers of Ni mesh.
- Channel 7 - 70  $\mu\text{g}/\text{cm}^2$  of polypropylene plus three layers of Ni mesh.
- Channel 6 - 7600 Å of Aluminum plus three layers of Ni mesh.
- Channel 2 - 272  $\mu\text{g}/\text{cm}^2$  Kimfoil plus 400 Å of aluminum.

The risetime of the detector is determined by the photoelectron flight time across the anode-cathode gap; while the decay-time is given by the decay-time of the anode-cathode gap capacitance into the characteristic impedance of the signal line. The detectors we have built for MULTIFLEX have a full-width-at-half-maximum, FWHM, time response of 75 ps; which is more than adequate to measure the 1 ns x-ray pulses from CO<sub>2</sub> laser plasmas.

The data consists of seven oscilloscope traces showing detector currents versus time, all common timed to  $\pm 50$  ps. These currents are sampled at 100 ps time intervals and used as inputs to a deconvolution code. This code accepts the absolutely calibrated detector response curves, the set of seven detector currents, and iteratively minimizes the difference between the most recent spectrum and the observed currents. A typical time resolved spectra for a glass microballoon irradiated by 8.2 TW of CO<sub>2</sub> laser light is shown in Fig. 13.

#### SUMMARY

The MULTIFLEX system is one of several detectors we will hear about in this conference, which utilizes photoelectric emission in the detection of soft x-radiation. Photoelectric emission is a complicated spatial, energy, angular, and temporally dependent process and our empirical and theoretical understanding is not sufficient to model all potential device performance criteria.

In this paper, the most important parameters which are used to describe photoemission have been discussed and it was indicated how they affect detector system performance. An outline of the measurement techniques has been provided and typical data was shown in comparison with available models. The Appendix provides a guide to the literature where the interested reader can go for data and details of the measurements. Photoemission studies have played a vital role in the development of modern physics and the detailed study of this process will continue to be important in our pulsed plasma diagnostic instrumentation.

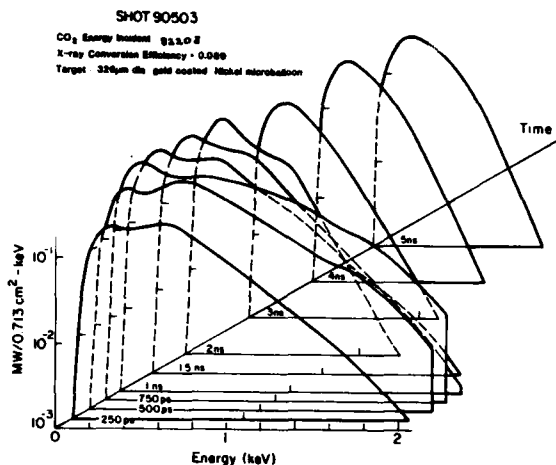


Fig. 13. Time resolved x-ray spectra from a gold coated nickel microballoon irradiated with 8.2 TW of 10.6  $\mu\text{m}$  CO<sub>2</sub> laser light.

#### ACKNOWLEDGEMENTS

I would like to thank Dr. Burton Henke for many useful discussions on this subject and J. Gaines for permission to use his experimental results. I would especially like to thank Robert Hockaday for much hard work in assembling, checking, and collating the data in the Appendix.

#### REFERENCES

1. H. Hertz, "Über Einen Einflug des Ultravioletten Lichtes auf die Electriche Entladung," *Wiedemannsche Annalen der Physik*, **31**, pp. 982-1000 (1887).
2. A. Schuster, "Experiments on the Discharge of Electricity Through Gases," *Proceedings of the Royal Society of London (A)*, **42**, pp. 371-379 (1887).
3. S. Arrhenius, "Über das Leitungsvermögen der Phosphorescirenden Luft," *Wiedemannsche Annalen der Physik*, **32**, pp. 545-572 (1887).
4. A. Einstein, "Über Einen die Erzeugung und Verwandlung des Lichtes Betreffenden Heuristischen Gesichtspunkt," *Annalen der Physik*, **17**, pp. 132-148 (1905).
5. R. A. Millikan, "A Direct Photoelectric Determination of Plank's 'h'," *Physical Review*, **7**, pp. 355-388 (1916).
6. A. H. Compton, "The Spectrum of Secondary Rays," *Physical Review*, **19**, pp. 267-268 (1922).
7. R. H. Pratt, A. Ron, and H. K. Tseng, "Atomic Photoelectric Effect Above 10 keV," *Rev. Mod. Phys.*, **45**, p. 273 (1973).
8. B. L. Henke and E. S. Ehsu, "Low Energy X-Ray and Electron Absorption Within Solids," *Adv. in X-ray Anal.*, **17**, pp. 150-213 (1973).
9. W. J. Viegele, E. Briggs, L. Rates, E. M. Henry, and B. Bracewell, "X-Ray Cross Section Compilation from 0.1 keV to 1 MeV," *Kaman Sciences Corporation Report KN-71-431(R)* (1971).
10. E. Storm and H. I. Israel, "Photon Cross Sections from 1 keV to 100 MeV for Elements Z = 1 to Z = 100," *Nuc. Data Tables*, **7**, p. 565 (1970).
11. W. H. McMaster, N. K. Del Grande, J. H. Mallett, and J. H. Hubbell, "Compilation of X-Ray Cross

- Sections," Lawrence Livermore Report UCRL 50174 (1969).
12. H. J. Hagemann, W. Gudat, and C. Kunz, "Optical Constants from the Far Infrared to the X-Ray Region: Mg, Al, Cu, Au, Bi, C, and Al<sub>2</sub>O<sub>3</sub>," *Deutsches Elektronen-Synchrotron Report, DFSY SR-74/7* (1974).
13. J. H. Weaver, C. Krafka, D. W. Lynch, and F. F. Koch, "Optical Properties of Metals I: The Transition Metals, 0.1 < hν < 500 eV Ti, V, Cr, Mn, Fe, Co, Ni, Zr, Nb, Mo, Ru, Rh, Pd, Hf, Ta, W, Re, Os, Ir, Pt," *Deutsches Elektronen-Synchrotron Report, DFSY F41* (1981).
14. B. L. Henke, J. A. Smith, and David T. Attwood, "0.1-10-keV X-Ray-Induced Electron Emissions from Solids - Models and Secondary Electron Measurements," *J. App. Phys.*, **48**, pp. 1852-1866 (1977).
15. B. L. Henke, J. Liesegang, and S. D. Smith, "Soft X-Ray-Induced Secondary-Electron Emission from Semiconductors and Insulators: Models and Measurements," *Phys. Rev. E.*, **19**, p. 3004 (1979).
16. G. Beck, "Photodiode and Holder with 60-psec Response Time," *Rev. Sci. Instrum.*, **47**, p. 849 (1976).
17. R. H. Day, P. Lee, E. P. Saloman, and D. J. Nagel, "X-Ray Diodes for Laser Fusion Plasma Diagnostics," *Los Alamos Report, LA-7941-MS* (1981).
18. M. J. Bernstein and J. A. Smith, "Primary and Secondary Photoelectron Yields Induced by Soft X-Rays," *IEEE Trans. on Nuc. Sci.*, **26**, pp. 4978-4983 (1979).
19. J. L. Gaines and R. A. Hansen, "Ultrasoft-X-Ray Reflection, Refraction and Production of Photoelectrons (100-1000-eV Region)," *J. Appl. Phys.*, **47**, pp. 3923-3928 (1976).
20. B. L. Henke, "X-Ray-Induced Electron Emission from Thin Gold Foils," *Phys. Rev. A*, **6**, p. 94 (1972).
21. A. S. Ganeev and I. M. Izrailev, "Photoelectric Yield for Soft X-Rays," *Sov. Phys. - Tech. Phys.*, **31**, p. 270 (1961).
22. R. J. Baird and C. S. Fadley, "X-Ray Photoelectron Angular Distributions with Dispersion-Compensating X-Ray and Electron Optics," *J. of Elec. Spec. and Rel. Phenom.*, **11**, pp. 39-65 (1977).
23. L. G. Eliseenko, V. N. Shchemelov, and M. A. Rumsh, "Quantum Yields of the Surface X-Ray Photoeffect at 1-10Å," *Sov. Phys. - Tech. Phys.*, (English Translation) **13**, pp. 122-129 (1968).
24. E. P. Saloman, J. S. Pearlman, and P. L. Henke, "Evaluation of High Efficiency CsI and CuI Photocathodes for Soft X-Ray Diagnostics," *Appl. Opt.*, **19**, pp. 749-753 (1980).
25. R. H. Day, P. Lee, E. P. Saloman, and D. J. Nagel, "Photoelectric Quantum Efficiencies and Filter Window Absorption Coefficients from 20 eV to 10 keV," to be published in *J. of Appl. Phys.*
26. B. L. Henke, J. P. Knauer, and K. Premaratne, "The Characterization of X-Ray Photocathodes in the 0.1-10 keV Photon Energy Region," *J. of Appl. Phys.*, **52**, pp. 1509-1520 (1981).
27. G. L. Stradling, H. Medeck, R. L. Kauffman, D. T. Attwood, and B. L. Henke, "Relative Responses of CsI and Au Photocathodes to 70-psec, 500-eV X-Ray Pulses," *Appl. Phys. Lett.*, **37**, pp. 782-784.
28. D. Bardas, E. Kellogg, and S. Murray, "Detection of Soft X-Rays with NEA III-V Photocathodes," *Rev. Sci. Instrum.*, **49**, pp. 1273-1278 (1978).
29. R. P. Cairns and J. A. R. Samson, "Metal Photocathodes as Secondary Standards for Absolute Intensity Measurements in the Vacuum Ultraviolet," *J. Opt. Soc. Am.*, **56**, pp. 1568-1573 (1966).

## APPENDIX

The Appendix consists of four major components: 1) a master list of most references on photoemission data above 10 eV in alphabetical order by author; 2) a table of available quantum efficiency data listed by element or compound and incident photon energy; 3) a table of electron energy distribution data by element and 4) a table of electron and photon angular distribution data by element and angle of incidence or emission.

In the tables the reference numbers refer to the master reference list. In Tables I and II, the numbers in parenthesis following the reference number refer to the exciting photon energy in eV unless the photon energy is marked in other units. In Table I, a "p" following the reference number indicates a measurement of primary photoelectron quantum efficiency, and in Table II, an asterisk, "\*" preceding a reference number indicates an unusual broad-band x-ray source. In Table III, the numbers in parenthesis are angles in degrees.

## Reference List

1. L. Apker, E. Taft, and J. Dickey, "Electron Scattering and the Photoemission from Cesium Antimonide," *J. Opt. Soc. Am.* **43**, p. 78, (1952).
2. R. F. Baker, "A Grating Monochromator for the Schumann Region," *J. Opt. Soc. Am.* **28**, p. 55 (1938).
3. R. J. Baird and C. S. Fadley, "X-Ray Photoelectron Angular Distributions With Dispersion-Compensating X-Ray and Electron Optics," *J. Elec. Spect. Rel. Phen.* **11**, p. 39, (1977).
4. D. Baradas, E. Kellogg, S. Murray, and R. Enck, Jr., "Detection of Soft X Rays with NEA III-V Photocathodes," *Rev. Sci. Instr.* **49**, p. 1273, (1978).
5. J. E. Bateman and R. J. Apsimon, "A New Photocathode for X-Ray Image Intensifiers Operating in the 1-50 keV Region," *Adv. Elec. Phys.* **52**, p. 189 (1979).
6. M. J. Bernstein, "Photoelectron Energy Spectra Generated by Low-Energy X-Rays From Intense Plasmas," *IEEE Trans. Nuc. Sci.* **24**, p. 2512, (1977).
7. M. J. Bernstein and J. A. Smith, "Primary and Secondary Photoelectron Yields Induced by Soft X-Rays," *IEEE Trans. Nuc. Sci.* **26**, p. 4978, (1979).
8. M. J. Bernstein and K. W. Paschen, "Forward and Backward Photoemission Yields From Metals at Various X-Ray Angles of Incidence," *IEEE Trans. Nuc. Sci.* **20**, p. 6, 111, (1973).
9. M. A. Blokhin, E. G. Orlova, I. G. Shveitzer, and G. Kokh, "Ultrasoft X-Ray Spectra of Inorganic Compounds of Beryllium," *Seriya Fizicheskaya*, **40**, p. 91, (1976).
10. J. N. Bradford, "X-Ray Induced Electron Emission II," *IEEE Trans. Nuc. Sci.* **20**, 5, p. 105, (1973).
11. E. J. T. Burns and J. F. Thurston, "The Use of Some Metal Photocathodes for Absolute Intensity Measurements in the Soft X-Ray-Vacuum Ultraviolet," *Appl. Spec.* **31**, p. 317, (1977).
12. R. B. Cairns and J. A. R. Samsom, "Metal Photocathodes as Secondary Standards for Absolute Intensity Measurements in the Vacuum Ultraviolet," *J. Opt. Soc. Am.* **56**, p. 1568, (1966).
13. L. R. Canfield, R. G. Johnston, and R. P. Madden, "NBS Detector Standards for the Far Ultraviolet," *Applied Optics* **12**, p. 1611, (1973).
14. R. H. Day and E. J. T. Purns, "Absolute Calibration of Photoelectric Diodes," *Advances in X-Ray Analysis*, **19**, p. 597, (1976).
15. R. H. Day, P. Lee, E. B. Salomon, and D. J. Nagel, "X-Ray Diodes for Laser Fusion Plasma Diagnostics," *IEEE International Conf. on Plasma Sci. (Invited Paper)*, LA-UR-79-1360 or LA-7941-MS, June 1979.
16. J. Dickey, "New Aspects of the Photoelectric Emission from Na and K," *Phys. Rev.* **81**, p. 612, (1951).
17. T. H. DiStefano and W. E. Spicer, "Photoemission from CsI: Experiment," *Phys. Rev. P.* **7**, p. 1554, (1973).
18. S. W. Duckett and P. H. Metzger, "Intrinsic Photoemission of Alkali Halides," *Phys. Rev.* **137**, A953, (1965).
19. L. Dunkelmann, "Ultraviolet Photodetectors," *J. Quant. Spectrosc. Radiat. Transfer*, **2**, p. 533, (1962).
20. P. J. Ebert, J. L. Gaines, and G. R. Leipelt, "Measurement of X-Ray-Induced Electron Currents from Metal Targets," Lawrence Livermore Laboratory Report No. UCRL-50691, (1969).
21. L. G. Eliseenko, V. N. Shchemelev, and M. A. Rumsh, "Quantum Yields of the Surface X-Ray Photoeffect at 1-10 Å," *Sov. Phys.-Tech. Phys.* **13**, p. 122, (1968).
22. J. G. Endriz and W. E. Spicer, "Experimental Evidence for the Surface Photoelectric Effect in Aluminum," *Phys. Rev. Lett.* **27**, p. 570, (1971).
23. D. A. Fromme, V. A. J. Van Lint, R. Strettner, and C. Mallon, "Electron Emission Spectra Produced by Exploding-Wire Photon Sources," *IEEE Trans. Nuc. Sci.* **24**, p. 2527 (1977).
24. J. L. Gaines and R. A. Hansen, "X-Ray-Induced Electron Emission from Thin Gold Foils," *J. Applied Phys.* **47**, p. 3923, (1976).
25. A. S. Ganeev and I. M. Izrailev, "Photoelectric Yield for Soft X-Rays," *Sov. Phys. - Tech. Phys.* **31**, p. 270, (1961).
26. G. W. Goetze, A. H. Poerio, and M. Green, "Field-Enhanced Secondary Electron Emission From Films of Low Density," *J. Appl. Phys.* **35**, p. 482 (1963).
27. P. Göblich, "Über zusammengesetzte, durchsichtige Photokathoden," *Z. Phys.* **101**, p. 335 (1936).
28. M. Ya Grudskii, A. V. Mlyshenkov, and V. V. Smirnov, "Electron Yield From Metals Under the Action of 30 to 90 keV Photon Radiation," *Sov. Phys.-Tech. Phys.* **21**, p. 172, (1976).
29. H. J. Hagemann, W. Gudat, and C. Kunz, "Optical Constants From the Far Infrared to the X-Ray Region: Mg, Al, Cu, Ag, Pt, C, and Al<sub>2</sub>O<sub>3</sub>," DESY-report SR-74/7, May 1974.
30. W. J. Harper and W. J. Choyke, "Semitransparent Photocathodes at Low Temperatures," *Rev. Sci. Instr.* **27**, p. 966, (1956).
31. P. L. Hartman, "Investigations on Some Alkali Halides in the Vacuum Ultraviolet," *J. Quant. Spectrosc. Radiat. Transfer*, **2**, p. 579, (1962).
32. B. L. Henke, "The Characterization of Photocathodes for Application to Time-Resolved X-Ray Spectroscopy," Technical Progress Report (April, 1979), DOE Cont. No. DE-AS03-76SF00235.
33. B. L. Henke, "Some Recent Studies in Low Energy X-Ray Physics," in lab review.
34. B. L. Henke, "Ultrasoft-X-Ray Reflection Refraction and Production of Photoelectrons (100-1000 eV Region)," *Phys. Rev. A* **6**, p. 94, (1972).
35. B. L. Henke, J. A. Smith, and D. T. Attwood, "0.1-10 keV X-Ray-Induced Electron Emission From Solids - Models and Secondary Electron Measurements," *J. Appl. Phys.* **48**, p. 1852, (1977).
36. B. L. Henke, J. A. Smith, and D. T. Attwood, "Secondary Electron Energy Distribution for Gold as Excited by C K (277 eV) and Al K (1487 eV) X Rays," *Appl. Phys. Lett.* **29**, p. 539, 1976.
37. B. L. Henke, "On the Theory and Development of X-Ray Photocathode Systems for Applications in High Temperature Plasma Diagnostics," *Progress Report*, April, 15, 1977.
38. B. L. Henke, "Models and Measurement for the Response of Dielectric X-Ray Photocathodes," *Tech. Report*, March 1978 (in lab).

39. B. L. Henke, X-Ray Spectroscopy in the 100-1000 eV Region," *Nuc. Instr. Meth.* 177, p. 161 (1980).
40. B. L. Henke, J. Liesegang, and S. D. Smith, "Soft X-Ray-Induced Secondary-Electron Emission From Semiconductors and Insulators: Models and Measurements," *Phys. Rev. B*, 19, p. 3004 (1979).
41. B. L. Henke, J. P. Knauer, and K. Premaratne, "The Characterization of X-Ray Photocathodes in the .1-10 keV Photon Energy Region," *Bull. Am. Phys. Soc.* 24, p. 1098 (1979).
42. H. E. Hinteregger, "Photoelectric Emission in the Extreme Ultraviolet," *Phys. Rev.* 96, p. 538 (1954).
43. H. E. Hinteregger and K. Watanabe, "Photoelectric Cells for the Vacuum Ultraviolet," *J. Opt. Soc. Am.* 43, p. 604, (1953).
44. C. S. Inouye and W. Pong, "Ultraviolet Photoelectron Spectra for Rubidium Halides," *Phys. Rev. B*, 15, p. 2265, (1977).
45. I. M. Izrailev, "Photoelectric Yield for Soft X-Rays," *Sov. Phys.-Technical Phys.* 7, p. 1020, (1963).
46. C. Kenty, "Photoelectric Yields in the Extreme Ultraviolet," *Phys. Rev.* 44, p. 891, (1933).
47. Zh. Kh. Khachatryan, A. E. Melamid, and A. A. Guzhov, "Study of Photoelectric Emission in the Vacuum Ultraviolet," *Bulletin of the Academy of Sciences, USSR Physical Series* 35, p. 574, (1971).
48. G. S. Kvater and E. D. Mischenko, "Multielectron Nature of Cesium-Antimony Photocathode Photoemission in the Ultraviolet," *Optics & Spectrosc. (Eng. Trans.)* 33, p. 57, (1971).
49. A. P. Lukirskii, E. P. Savinov, I. A. Brytov, and Yu. F. Shepelev, "Efficiency of Secondary-Electron Multipliers with Au, LiF, Mg F<sub>2</sub>, SrF<sub>2</sub>, BeO, KCl, and CsI, Photocathodes in the 23.6 to 113 Å Wavelength Region," *Bull. Acad. Sci., USSR Phys. Ser.* 28, p. 774, (1964).
50. A. P. Lukirskii, M. A. Rumsh, and I. A. Karpovich, "Measurement of the Photoelectric Yield of the External Photoeffect Under the Action of X-Rays in the Wavelength Range 1.54-13.3Å," *Optics and Spectroscopy* 9, p. 343, (1960).
51. A. P. Lukirskii, M. A. Rumsh, and L. A. Smirnov, "Measurement of the Photoelectric Yield for Ultra-soft X-Radiation," *Optics and Spectroscopy* 9, p. 265, (1960). (*Optika i spektro*)
52. P. H. Metzger, "On the Quantum Efficiencies of Twenty Alkali Halides in the 12-21 eV Region," *J. Phys. Chem. Solids*, 26, p. 1879, (1965).
53. C. Mori and T. Watanabe, "Photoelectric Emission of Metals by X-Rays in the keV Region," *Japanese J. Appl. Phys.* 9, p. 666, (1970)
54. N. G. Nakhodkin and P. V. Mel'nik, "A Comparative Study of the Energy Distribution of Secondary Electrons and Photoelectrons Excited by Soft X-Rays," *Soviet Phys.-Solid State* 10, p. 1462, (1968).
55. Yu. A. Nemilov and V. E. Privalova, "On the Influence of Alkali Metals Upon the Properties of Antimony Photocathodes," *Sov. Phys-Solid State*, 2, p. 1189, (1960).
56. H. Petersen and S. B. M. Hagström, "Optical Excitation of the Surface Photoelectric Effect of Metals Using Synchrotron Radiation," *Phys. Rev. Lett.* 41, p. 1314, (1978).
57. W. Pong, "Photoemission from Al-Al<sub>2</sub>O<sub>3</sub> Films in the Vacuum Ultraviolet Region," *J. Appl. Phys.*, 40, p. 1733, (1969).
58. W. Pong and C. S. Inouye, "Ultraviolet Photoemission Study of LiF," *J. Elec. Spec. Rel. Phenomena* 11, p. 165, (1977).
59. W. Pong and J. A. Smith, "Photoemission Studies of LiCl, NaCl, and KCl," *Phys. Rev. B*, 9, p. 2674 (1974).
60. W. Pong, R. Sumida, G. Moore, "Attenuation Length for Photoelectrons in Metal Films," *J. Appl. Phys.* 41, p. 1869 (1969).
61. H. C. Rentschler, D. E. Henry, and K. O. Smith, "Photoelectric Emission From Different Metals," *Rev. Sci. Instr.* 3, p. 794 (1932).
62. M. A. Rumsh and V. N. Shchemelev, "Role of Secondary Emission Phenomena in the X-Ray Photoeffect in Metallic Cathodes," *Soviet Physics - Solid State* 5, p. 46, (1963).
63. E. B. Saloman, "Typical Photoefficiency Between 20-250 eV of Windowless XUV Photodiodes With Tungsten and Anodized Aluminum Oxide Photocathodes," *Applied Physics*, 17, p. 1489, (1978).
64. E. B. Saloman and D. L. Ederer, "Absolute Radiometric Calibration of Detectors Between 200-600 Å," *Applied Optics*, 14, p. 1029, (1975).
65. E. B. Saloman, J. S. Pearlman, and B. L. Henke, "Evaluation of High Efficiency CsI and CuI Photocathodes for Soft X-Ray Diagnostics," *Applied Optics*, 19, p. 749, (1980).
66. J. A. R. Samson, "Absolute Intensity Measurements in the Vacuum Ultraviolet," *J. Opt. Soc. Am.* 54, p. 6, (1964).
67. J. A. R. Samson and R. B. Cairns, "Photoelectric Yield of Aluminum From 300 to 1300 Å," *Rev. Sci. Instr.* 36, p. 19, (1965).
68. E. P. Savinov and A. P. Lukirskii, "The Efficiency of Secondary Electron Multipliers With Au, Al, Ni, LiF, MgF<sub>2</sub>, SrF<sub>2</sub>, CsI, KCl, and BeO Photocathodes at Wavelengths of 75-300 Å," *Optika i Spektrosk. (USSR) (English trans. - Optics and Spectrosc.)* 23, p. 163, (1967).
69. E. P. Savinov, A. P. Lukirskii, and Yu. F. Shepelev, "The Problem of External Photoeffect of Metal Photocathodes for Radiation of Wavelength 23.6-113 Å," *Sov. Phys. - Solid State* 6, p. 2624 (1965).
70. V. N. Shchemelev, L. B. Eliseenko, E. P. Denisov, and M. A. Rumsh, "Current and Pulse Measurements of the X-Ray Photoemission of a Massive Cathode," *Soviet Physics - Solid State* 6, p. 2051, (1965).
71. V. N. Schemelev and M. A. Rumsh, "X-Ray Photoeffect in Dielectric Cathodes," *Sov. Phys. - Solid State* 5, p. 43, (1963).
72. Yu. A. Shuba and I. V. Smirnova, "Photoemission of Electrons by Copper and Silver Iodides," *Soviet Phys. - Solid State* 6, p. 1201, (1960). (*Fizika Tverdogo Tela*)
73. W. E. Spicer, "Photoemissive, Photoconductive, and Optical Absorption Studies of Alkali-Antimony Compounds," *Phys. Rev.* 112, p. 114, (1958).
74. W. E. Spicer and R. L. Bell, "The III-V Photocathode: A Major Detector Development," *Pub. Astron. Soc. Pacific* 84, p. 110, (1972).
75. D. J. Strickland, "Soft X-Ray Photoemission," *IEEE Trans. Nuc. Sci.* 24, 2499, (1977).
76. J. L. Stanford, R. N. Hamm, and E. T. Arakawa, "Effect of Photon Refraction on Angular Dependence of Photoelectric Yields in the Wavelength Region 300-1200 Å," *J. Opt. Soc. Am.* 56, p. 124, (1966).
77. A. Suna and R. H. Tait, "Ultraviolet Photon Induced Secondary Electron Emission from TiO<sub>2</sub>: Theory and Experiment," *Solid State Comm.* 29, p. 215, (1979).
78. E. A. Taft and H. R. Philipp, "Photoelectric Emission From the Valence Band of Some Alkali Halides," *J. Phys. Chem. Solids* 3, p. 1, (1957).
79. E. Taft and L. Apher, "Photoemission From Cesium and Rubidium Tellurides," *J. Opt. Soc. Am.* 43, p. 81, (1953).
80. L. Van Speybroeck, E. Kellogg, S. Murray, and S. Duckett, "Negative Affinity X-Ray Photocathodes," *IEEE Trans. Nuc. Sci.* 21, p. 408, (1974).
81. N. Wainfan, W. C. Walker, and G. L. Weissler, "Preliminary Results on Photoelectric Yields of Pt and Ta and on Photoionization in O<sub>2</sub> and N<sub>2</sub> in the Vacuum Ultraviolet," *J. Appl. Phys.* 24, p. 1318, (1953).

82. W. C. Walker and G. L. Weissler, "Excitation of the Sodium D Lines in the Nightglow," *Phys. Rev.* **97**, p. 1178, (1954).
83. W. C. Walker and G. L. Weissler, "Vacuum Ultraviolet Optical and Photoelectric Effects in Solids," *J. Quant. Spectrosc. Radiat. Transfer* **2**, 613, (1962).
84. W. C. Walker, N. Wainfan, and G. L. Weissler, "Photoelectric Yields in the Vacuum Ultraviolet," *J. Appl. Phys.* **26**, p. 1366, (1955).
85. W. C. Walker, O. P. Rustgi, and G. L. Weissler, "Optical and Photoelectric Properties of Thin Metallic Films in the Vacuum Ultraviolet," *J. Opt. Soc. Am.* **49**, p. 471, (1959).
86. J. H. Weaver, C. Krafka, D. W. Lynch, and E. F. Koch, "Optical Properties of Metals I: The Transition Metals,  $0.1 < h\nu < 500$  eV," DESY F 41, HASYLAB 81/01, Jan. 1981.

Table I

Quantum Efficiencies

This table of elements and compounds lists measurements of photoelectric quantum efficiency for each element. The entries refer to reference numbers in the master reference list at the beginning of the Appendix and the numbers in parenthesis give the energy range of the measurement in eV. A "P" following a reference number indicates that only primary photoelectron emission was measured.

Acetone	19(8-12)
Arrodag	7(1-6 keV), 7P(1-6 keV)
Ag	85(6-30), 12(10-62), 84(12-25), 61(4-5), 28(30-90 keV), 45(.5-30 keV), 23P(1.2-3.3 keV), 25(4-8 keV), 7(1-6 keV), 7P(1-6 keV), 28P(30-90 keV), 20(6-100 keV)
AgCl	31(6-10)
AgI	72(5-11), 31(6-10)
Al	83(7-27), 85(7-27), 14(0.01-10 keV), 32(100-1000), 21(1200-8000), 53P(1.7-8 keV), 65(21-248), 75(0.1-10 keV), 15(0.01-10 keV), 11(0.01-1.5 keV), 61(4-5), 28(30-80 keV), 70(8000), 22(6-12), 45(4-30 keV), 62(8000), 12(10-62), 68(41-124), 60(7-12), 23P(1.2-3.3 keV), 25(4-8 keV), 7(1-6 keV), 7P(1-6 keV), 28P(3080), 70P(8000), 62P(8000), 67(10-41), 20(10-60 keV), 69(109, 185, 284, 394, 525), 21P(1200-8000), 41P(150-01500)
Al-Mg	12(12-31)
Al <sub>2</sub> O <sub>3</sub>	57(8-21), 64(10-65), 63(20-250), 28P(30-75 keV), 7(1-6 keV), 7P(1-6 keV), 32(100-1000)
Ar	66(14-31)
Au	85(8-27), 12(10-62), 24(1.5-8 keV), 21(1200-8000), 49(109-525), 53P(1.7-8 keV), 65(21-248), 66(10-31), 84(12-25), 15(0.01-10 keV), 76(10-41), 28(30-90 keV), 70(8000), 62(8000), 68(41-124), 60(7-12), 23P(1.2-3.3), 39(.5-8 keV), 39P(.5-8 keV), 7(1-7 keV), 7P(1-7 keV), 32(100-1000), 28P(30-90 keV), 70P(8000), 62P(8000), 13(21), 20(10-100 keV), 41(0.1-10 keV), 41P(150-1500), 21P(1200-8000)
Ba	61(2-4)
BaO	61(2-4)
Be	42(8-17), 12(10-62), 51(100-500)
BeO	49(109-525), 9(110-140), 68(41-124)
BeSiO <sub>3</sub>	9(110-140)
Be(OH) <sub>2</sub>	9(110-140)
BeSO <sub>4</sub> ·4H <sub>2</sub> O	9(110-140)
Be <sub>3</sub> (PO <sub>4</sub> ) <sub>2</sub>	9(110-140)
Bi	85(8-27), 70(8000), 62(8000), 70P(8000), 62P(8000)
C	15(0.01-10 keV), 23P(1.2-3.3 keV)
CS <sub>2</sub>	19(8-12)
Ca	61(3-5)



CaF <sub>2</sub>	21(1200-9000), 51(100-500), 71(8000), 71P(8000), 21P(1200-9000)
Ce	61(3-5)
Cd	85(8-27), 2(4-12), 61(4-5)
CdS	74(7-25)
CONSTANTAN	46(10-20)
CORTEX-D GLASS	61(3-5)
Cr	15(0.01-10 keV), 70(8000), 45(5-30 keV), 62(8000), 62P(8000), 70P(8000)
CsBi	30(2-3.5), 27(1.5-3)
CsBr	19(5-12), 78(7-11), 52(12-22)
CsCl	21(1200-9000), 78(7-11), 52(12-22), 70(8000), 70P(8000), 21P(1200-9000)
CsF	52(12-22)
CsI	19(5-12), 17(5-12), 32(100-1000), 21(1200-9000), 49(109-750), 50(1-8 keV), 78(6-11), 52(12-22), 65(21-248), 5(6-60 keV), 15(1-10 keV), 39(100-1000), 39(25-310), 31(6-11), 70(8000), 68(41-124), 70P(8000), 41(0.1-10 keV), 41P(150-1500), 21P(1200-9000)
[Cs](NaK) <sub>3</sub> Sb	73(1.3-4.3)
Cs <sub>3</sub> Sb	1(1-6), 74(2-12), 73(1.6-4)
Cs-Bi	30(1.8-3)
Cs-C <sub>2</sub> O-Ag	27(1.4-3)
Cs-Sb	19(4-12), 30(2-3.5), 27(1.5-3.0)
CsTe	19(3.5-6), 30(2-3.5)
Cs <sub>2</sub> Te	79(1.5-6)
Cu	21(1200-8000), 84(9-31), 11(0.1-1.5 keV), 61(4-5), 28(30-90 keV), 45(.5-30 keV), 62(8000), 62P(8000), 28P(30-90 keV), 12(12-31), 17(4-11), 12(12-21), 17(4-11), 15(0.1-10 keV), 21P(1200-9000)
Cu-CsI	17(4-11)
CuI	19(5-12), 47(7-25), 65(21-248), 72(5-11), 41(0.1-10 keV), 41P(150-1500)
ETHELENE OXIDE	19(8-12)
ETHYL SULFIDE	19(8-12)
Fe	12(10-62), 11(0.1-10 keV), 70(8000), 70P(8000),
GaAs+Cs	74(2-12)
GaAs-Cs+O <sub>2</sub>	80(0.5-4 keV)
GaAs	47(7-25), 74(1-12)
GLASS	7(1-6 keV), 7P(1-6 keV)
In	85(8-27), 12(10-62)
InAsP	74(1-12)
K	16(2-6), 27(1.5-3.0)
K <sub>2</sub> BeF <sub>4</sub>	9(110-140)
KBr	19(5-12), 18(8-22), 78(8-11), 52(12-22), 70(8000), 21(1200-9000), 70P(8000), 21P(1200-9000)
KCl	18(8-22), 21(1200-9000), 49(109-750), 78(8-11), 31(8-12), 52(12-22), 70(8000), 71(8000), 68(41-124), 70P(8000), 71P(8000), 26(5-9 keV), 21P(1200-9000)
KF	18(8-22), 78(10.5-11), 52(12-22)

KI	18(8-22), 21(1200-9000), 78(2-12), 31(7-11), 52(12-22), 21P(1200-9000)
KSb	55(2-6)
K <sub>3</sub> Sb	73(1.8-4.6)
Kr	66(14-31)
LiBr	18(8-22), 52(12-22)
LiCl	18(8-22), 52(12-22), 21P(1200-9000)
LiF	18(8-22), 21(1200-9000), 51(100-500), 49(109-750), 58(10-24), 31(7-17), 52(12-22), 68(41-124)
LiI	18(8-22), 78(6-10), 52(12-22)
LiSb	55(2-6)
Mg	46(10-20), 61(3-5)
MgF <sub>2</sub>	13(10-25), 49(109-750), 71(8000), 68(41-124), 71P(8000)
Mo	12(10-62), 45(.5-30 keV), 84(9-25)
MYLAR	7(1-6 keV), 7P(1-6 keV)
N <sub>2</sub>	81(15-25)
Na	16(2-6)
NaBr	18(8-22), 50(1-8 keV), 52(12-22)
NaCl	18(8-22), 21(1200-9000), 51(100-500), 31(8-12) 70(8000), 71(8000), 70P(8000), 71P(8000), 52(12-22), 21P(1200-9000)
Na <sub>2</sub> BeF <sub>4</sub>	9(110-140)
NaF	18(8-22), 21(1200-9000), 51(100-500), 52(12-22)
NaI	18(8-22), 78(7-11), 52(12-22)
NaSALICYLATE	66(10-31)
NaSb	55(2-6)
Na <sub>3</sub> Sb	73(2.4-4.8)
NaKSb	55(2-6)
(NaK) <sub>3</sub> Sb	73(1.4-4.6)
NO	19(8-12)
Ne	66(14-31)
Ni	46(10-20), 43(5-25), 12(10-40), 51(100-500), 84(9-31), 15(0.01-10 keV), 68(41-124), 20(10-100 keV)
O <sub>2</sub>	81(12-25)
Pb	12(10-62), 21(1200-8000), 70(8000), 70P(8000), 62(8000), 62P(8000), 21P(1200-9000)
Pd	84(12-25)
Pt	43(5-25), 12(10-62), 18(10-22), 50(1-8 keV), 81(12-25), 84(9-31), 76(10-41), 52(12-20), 45(5-30 keV)
RbBi	30(2-3.5)
RbBr	52(12-22)
RbCl	21(1200-9000), 52(12-22), 21P(1200-9000)
RbF	52(12-22)
RbI	19(5-12), 78(7-11), 52(12-22)
RbSb	30(2-3.5)
RbTe	19(4-8), 30(2-3.5)

Rb <sub>3</sub> Sb	73(1.6-4)
[Rb](NaK <sub>3</sub> )Sb	73(1.4-3.5)
Sc	15(0.01-10 keV)
SARAN	7(1-6 keV), 7P(1-6 keV)
Si	47(7-25), 7(1-6 keV), 7P(1-6 keV)
Sn	83(7.5-27), 85(8-27), 12(10-62), 21(1200-8000), 70(8000), 70P(8000), 62(8000), 62P(8000), 20(10-100 keV), 21P(1200-9000)
SrF <sub>2</sub>	19(4-12), 21(1200-9000), 51(100-500), 49(109-750), 50(1-8 keV), 68(41-124), 21P(1200-9000)
Ta	19(4-6), 12(10-62), 81(12-25), 61(4-5), 45(.5-30 keV), 12(10-62), 25(4-8 keV), 20(10-100 keV)
Te	21(1200-8000), 79(1.5-6), 62(8000), 62P(8000)
Ti	12(10-62), 21(1200-8000), 50(1-8 keV), 11(0.1-1.5 keV), 61(4-5), 70(8000), 7(1-6 keV), 7P(1-6 keV), 70P(8000), 45(.5-30 keV), 21P(1200-9000)
Th	61(3-5)
W	46(10-20), 19(4-12), 12(10-41), 43(5-25), 51(100-500), 50(1-8 keV), 63(20-250), 84(12-25), 61(4-5), 45(5-30 keV), 47(7-25), 25(4-8 keV)
W-O	46(10-20)
U	61(4-5)
Xe	66(14-31)
Zn	61(4-5), 12(10-41)
Zr	61(4-5)

Table II

Electron Energy Distribution

This table of elements and compounds lists measurements of electron energy distributions. The entries refer to reference numbers in the master list at the beginning of the Appendix and the numbers in parenthesis give the energies of the measurement. Reference 6 is indicated by a "\*" to indicate the measurements were made with an unusual broadband x-ray source.

Ag	*6(.5-3 keV), 8(30-100 keV)
Al	56(1-24), 65(277), *6(.5-3 keV), 65(277), 35(277, 1487, 8048), 10(8-50 keV), 8(15-100 keV), 22(9.7, 10.2, 11.2, 11.5), 41(277, 8048)
Al <sub>2</sub> O <sub>3</sub>	*6(.5-3 keV)
AgCl	40(1487), 38(1487)
Au	65(277), 39(277, 8048), 83(10.2, 14.9, 17.6), 82(10, 15, 18), 54(1.5, 4.5, 8 keV), 38(1487), *6(.5-3 keV), 37(1487), 36(277, 1487), 35(277, 1487, 8048), 24(8 keV), 40(1487), 41(277, 8000), 32(1487)
C	*6(.5-3 keV), 8(15-100 keV)
C <sub>22</sub> H <sub>10</sub> N <sub>2</sub> O <sub>5</sub>	*6(.5-2.2 keV)
CdS	40(1487), 38(1487)
CsI	17(4.5-10.2), 40(1486), 65(277), 39(277, 8048), 38(1487), 37(1487), 65(277), 32(1487), 47(7.1, 7.88, 10.2, 11.6, 13.3, 18.6), 41(277, 800)
Cs <sub>2</sub> Te	79(6.7, 6.19, 5.38, 4.89)
Cs-Sb	48(2.1, 8.5)

Cs <sub>3</sub> Sb	1(6.7, 5.8, 4.7, 4.3, 4.0)
Cu	10(14-50 keV)
CuI	40(1487), 65(277), 39(277, 8048), 38(1487), 37(1487), 65(277), 32(1487), 41(277, 8000)
GaAsP	4(.85, 1.25, 1.49, 2.17, 2.98 keV)
Ge	40(1487), 82(10, 18), 54(1.5, 4.5, 8 keV), 38(1487)
K	16(3.39, 3.96, 4.89, 6.71)
KBr	40(1487), 38(1487)
KCl	40(1487), 59(12-19), 38(1487), 37(1487)
KI	40(1487), 38(1487), 37(1487)
Kr	66(13)
LiBr	87(5-30)
LiCl	59(17-23)
LiF	58(13-27), 38(1487), 40(1487)
MgO	71(8000)
Mo	10(14-50 keV)
Na	16(4-.6.7)
NaCl	40(1487), 59(14-21), 38(1487), 71(8000)
NaI	40(1487), 38(1487)
Ne	66(5.3)
PbI <sub>2</sub>	40(1487), 38(1487)
PbS	40(1487), 38(1487)
RbBr	40(1487), 44(12-16), 38(12-21)
RbCl	44(13-23)
RbF	44(16-27)
RbI	40(1487), 38(1487), 44(12-21)
Se	40(1487), 38(1487)
SrF <sub>2</sub>	71(8000)
Ta	10(14-50 keV), 8(15-100 keV)
TiO <sub>2</sub>	77(21.2)
W	43(7.71)
Xe	66(15)

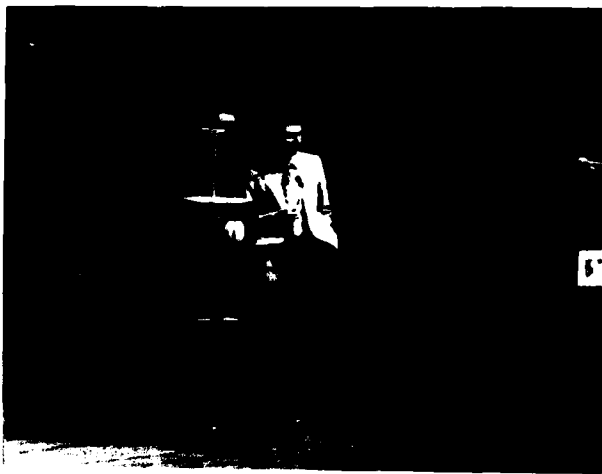
Table III

Angular Distribution

This table of elements and compounds lists measurements of photoemission angular dependence. The entries refer to reference numbers in the master reference list at the beginning of the Appendix. The numbers in parenthesis refer to the angles at which measurements were made.

Ag	25(15°, 35°, 45°, 60°)
Al	67(0°-90°), 68(0°-40°), 69(0°-40°), 25(15°, 35°, 45°, 60°), 8(0°-80°)
Au	24(30°, 45°, 60°, 75°, 90°), 68(0°-40°), 34(0°-60°), 6(0°, 60°, 90°, 180°), 76(0°, 45°, 70°), 20(30°, 60°, 90°)

BeO	49(0°-40°)
C	3(1°, 10°, 20°, 30°, 40°, 50°, 60°, 70°, 80°, 90°, 95°)
CsI	49(0°-40°), 68(0°-40°)
Cu	8(0°-80°)
KCl	49(0°-40°), 68(0°-40°)
LiF	49(0°-40°), 68(0°-40°)
MgF <sub>2</sub>	13(0°-75°), 49(0°-40°), 68(0°-40°)
Pt	76(0°, 45°, 70°)
SrF <sub>2</sub>	49(0°-40°), 68(0°-40°)
Ta	25(15°-60°), 10(0°-70°), 8(0°-80°)
Ti	8(0°-80°)
W	25(15°-60°)



Dr. Robert Day of Los Alamos describing his work on low energy x-ray detectors.

## TIME-RESOLVED X-RAY DIAGNOSTICS

P. B. Lyons

Los Alamos National Laboratory, P. O. Box 1663, MS 410, Los Alamos, NM 87545

## ABSTRACT

Techniques for time-resolved x-ray diagnostics will be reviewed with emphasis on systems utilizing x-ray diodes or scintillators. System design concerns for high-bandwidth (>1 GHz) diagnostics will be emphasized. The limitations of a coaxial cable system and a technique for equalizing to improve bandwidth of such a system will be reviewed. Characteristics of new multi-GHz amplifiers will be presented. An example of a complete operational system on the Los Alamos Helios laser will be presented which has a bandwidth near 3 GHz over 38 m of coax. The system includes the cable, an amplifier, an oscilloscope, and a digital camera readout.

Nanosecond and sub-ns time resolution of low energy x rays may be achieved with at least three types of diagnostic systems. Photoelectric x-ray diodes or scintillators and optical detectors provide electrical signals for electronic recording and processing. The photoelectric process may also be used to provide a source of electrons for deflection in a streak tube.(1)

The first two types of diagnostic systems will be discussed in this paper. The paper is organized in sections that highlight specific sub-systems: the detector, the cable transmission system, the data recorder, supporting instrumentation, and system considerations. Examples will be drawn from experiences at the Los Alamos National Laboratory with the large CO<sub>2</sub> laser systems (primarily the Helios system). The final section reviews the parameters of an operational system at the Helios facility which is providing a 3 GHz bandwidth over 38 m of coax.

## X-RAY DETECTOR

X-ray photoelectric diodes provide a very simple and, potentially, very high speed, detector for low energy x rays. The detector relies on x-ray interaction in an x-ray photocathode with subsequent release of photoelectrons, Auger electrons, and secondary electrons from the material surface.

The sensitivity of the detector is approximately proportional to the x-ray attenuation coefficient and demonstrates increased sensitivity in spectral regions (above x ray edges) with increased attenuation. The detector current is dominated by secondary electrons and is thus very sensitive to surface conditions. Surface conditions are, in turn, strongly influenced by the techniques used to prepare and store the photocathode. These concerns, as well as detailed sensitivity data, are available in published literature.(2-3)

The time response of an x-ray diode is governed by simple considerations. The detector geometry resembles a parallel electrode configuration. The response in such a geometry is simply calculated.(4) The rise time is given by the time for electrons to traverse the anode-cathode gap. The fall time is given by the RC time constant. The transition between the diode and the transmission line must be carefully engineered to minimize reflections. A poor transition can completely dominate the excellent time response possible with an optimized diode geometry. Rise and fall times below 50 ps have been demonstrated in an x-ray diode.(5) A FWHM for such a diode below 50 ps should be achievable.

Scintillators are also useful for low energy x-ray detection.(6) In a scintillator, the energy of incident x rays is transferred to excitation of the solvent (base plastic) molecules with subsequent transfer to other scintillating molecular species. The time response is dominated by the inter-molecular transfer times and the decay time of the final scintillator molecule. Standard commercial scintillators provide time response as short as 1.3 ns(7) and special scintillators provide time response below 200 ps with reduced light output.(8)

The choice between x-ray diodes and scintillators depends on several factors. The diodes will provide a faster system but require considerable care in surface

preparation and protection for accurate measurements. A good vacuum, below at least  $10^{-5}$  Torr, is essential for operation. Gain is achieved only with electronic amplification. The scintillators are less sensitive to vacuum requirements and care in storage but require that the photodetector be shielded from all extraneous sources of visible light. Gain is easily achieved if needed with photomultipliers (PMT), but the PMT may be susceptible to high energy background photons in the same environment.

In Fig. 1 a sensitivity comparison between NE111 plastic and a windowless Al x-ray diode is given. The plastic is assumed to be coupled to a photodiode with a typical S-20 surface. At lower energies, the x-ray diode sensitivity is superior. Some x-ray diode surfaces show sensitivity well above the Al diode.(2)

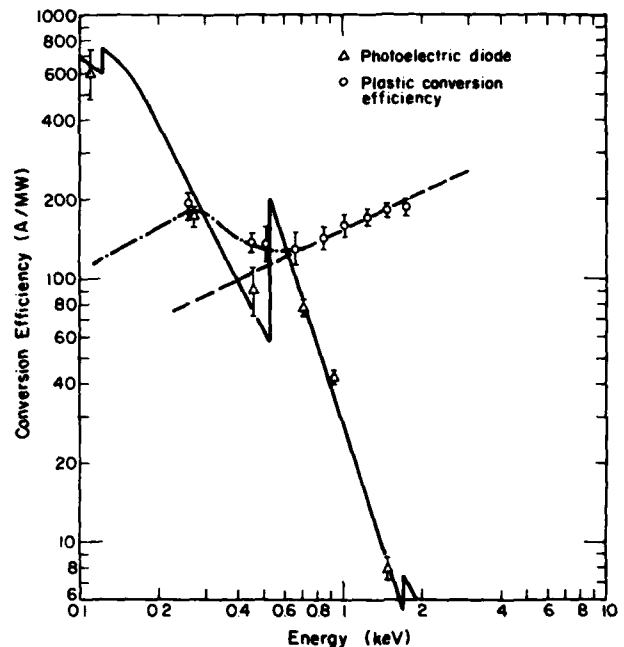


Fig. 1. Comparison of representative Al x-ray diode<sup>2</sup> and scintillator<sup>6</sup> sensitivity for low x-ray energies.

The scintillation must be measured with some type of photosensitive detector. This detector can be a simple biplanar photodiode or a photomultiplier (PMT) with significant gain. Several types of PMTs with sub-ns response are available.(9) The fastest suitable PMTs commercially available utilize a microchannel plate (MCP) as the gain stage and provide a FWHM of 200 ps. Biplanar diodes are available with FWHM of 100 ps, but do not provide gain. Faster solid state devices do exist, but their very limited detection areas are not usually compatible with scintillators. When a PMT is used, attention must be given to limitations on peak

linear charge and/or current output capability of the unit. Most PMTs have definite limits on these output values which are largely independent of PMT gain. Operation of a PMT at high gain can restrict the dynamic range of the instrument to a very small value. For most applications, gains of  $10^4$ - $10^5$  are optimum.

Either scintillator or x-ray diode systems can provide sensitivity in selected x-ray spectral regions. The x-ray diodes show a rapid variation of sensitivity with x-ray energy and demonstrate significant changes in sensitivity near x-ray edges of the cathode material (cf Fig 1). Scintillator sensitivity can be varied by changing the thickness of the scintillator, thereby altering the sensitivity at high energies. The system sensitivity can be further defined through the use of:

- x-ray reflectors - providing reflection only below a critical energy.
- x-ray filters - providing transmission as a function of the material attenuation properties. The use of x-ray edges can provide considerable spectral resolution.
- x-ray fluorescers - providing (ideally) sensitivity only for x-ray energies exceeding the x-ray edge of the fluorescer.
- Bragg reflectors - providing reflection only when the Bragg conditions are satisfied.
- grazing incidence gratings - providing reflection when the grating equations are satisfied.

Low energy x-ray systems frequently require the use of very thin foils. Such foils can be rolled, stretched, or vacuum deposited depending on the particular material.

Many low-resolution systems use either a filtered diode or a filter-fluorescer geometry. Figure 2 provides an example of filter-fluorescer system sensitivity for a detection channel intended for temperatures near 1 keV. The system consists of a Ni pre-filter and a Ti fluorescer in the x-ray beam with a Ti post-filter and Al diode at  $90^\circ$ . This figure shows the variation in channel response vs x-ray energy as additional elements of the channel are included. Filter-fluorescer systems are much less sensitive than filtered diode systems. For many applications in ICF diagnostics, the filter-detector system is used(10) and typical responses are given in ref. 2.

#### DATA TRANSMISSION SYSTEMS

Coaxial cables are far from perfect transmission media. High bandwidth signals suffer serious distortion as they propagate along coax cables. The simplest solution would involve location of the recording instrumentation very close, within a few meters, of the detector. In practice, however, this is not a feasible alternative. Significant radiation and electrical background can be anticipated near the target area of any laser system and an e-beam pumped laser (like the Los Alamos Helios laser) would be an even more difficult environment. In addition, personnel are excluded from the target area during tests and the recording equipment would have to be remotely controlled.

Radiation background provides a particularly severe problem with modern high speed oscilloscopes(11) which utilize a micro-channel plate (MCP) gain element preceding the phosphor. The MCP exhibits significant radiation sensitivity.

These considerations require that the recorder be located some distance from the detector. Thus coax lines, typically 20-40 m in length, are required. The severe limitations of the cable then become a serious concern.

In Fig. 3 the attenuation in db is shown as a function of frequency for 37 m of several types of high frequency cable. Larger cable shows significantly lower loss at all frequencies, but other considerations argue against the large cable. As a practical matter, the largest cables are extremely difficult to handle. A more serious concern is shown in Fig. 4 where the

non-linear phase characteristics of several cables are shown. Thus while the largest cable has the least attenuation, it shows the greatest phase distortion. A coax system will "ring" or oscillate at the approximate frequency,  $f_R$ , where the dispersive, or nonlinear,

phase shift exceeds  $180^\circ$ . In practice a system will be stable if the ringing frequency is attenuated by 7-10 db below the attenuation at the half power frequency,  $f_{3db}$ .

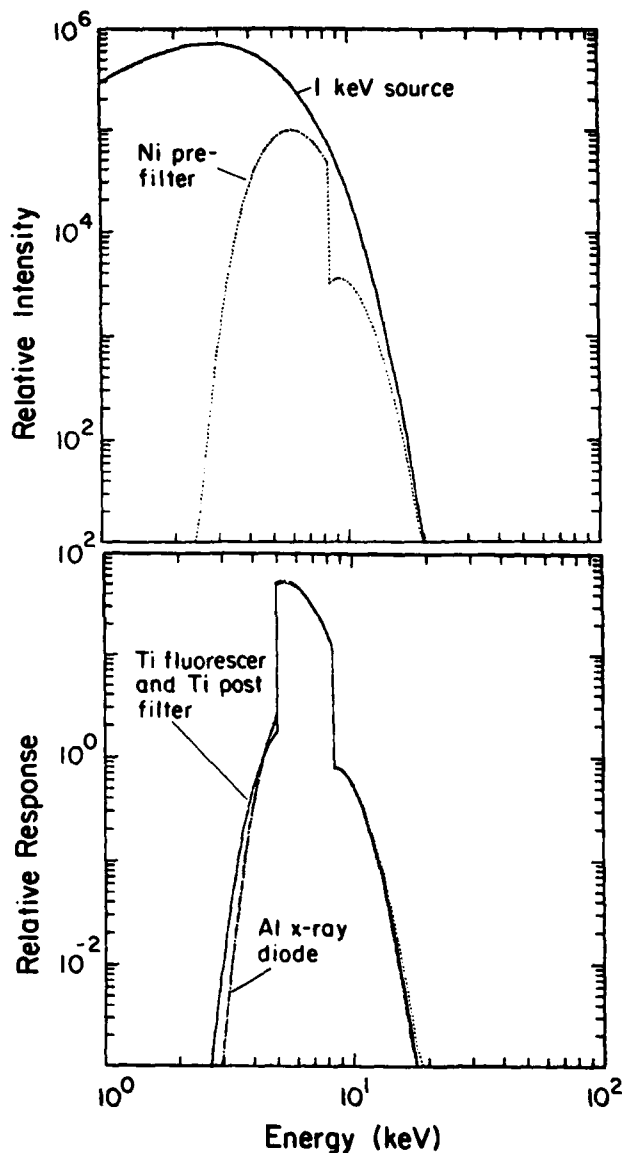


Fig. 2. System sensitivity for a Ni pre-filter-Ti fluorescer-Ti post-filter-Al diode configuration. In Fig. 2a the 1 keV Planck source is attenuated by transmission through the Ni pre-filter. When the Ti fluorescer is added in Fig. 2b, only energies above the Ti-K edge contribute fluorescence at  $90^\circ$ . All energies also scatter off the Ti fluorescer foil. A Ti post-filter provides slight additional shaping and prevents any UV light from reaching the Al diode. The Al diode (with a Be entrance window) then detects the predominantly Ti fluorescence in the  $90^\circ$  beam. The resulting channel has almost all of its sensitivity between the Ti-K and Ni-K edges.

In Fig. 3, the ringing frequency,  $f_R$ , is shown for each cable. Note that the largest cable rings at about 2.5 GHz. The ringing frequency can also be thought of as the approximate frequency above which modes other than TEM can propagate. Cable ringing is shown experimentally in Fig. 5 where a short pulse was used to excite a 15-m length of large diameter cable. The output was measured with a sampling system.

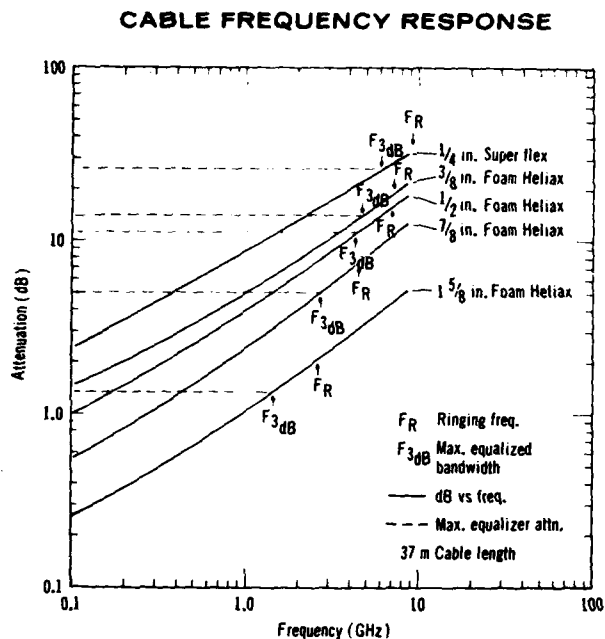


Fig. 3. Attenuation vs. frequency for selected high-frequency coaxial cables. See text for discussion of figure abbreviations.

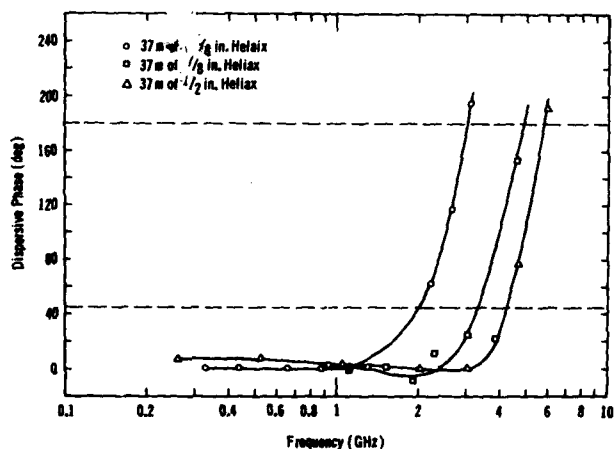


Fig. 4. Non-linear phase characteristics for 37 m lengths of several coaxial cables.

The bandwidth of any system can be improved through equalization. This technique involves the introduction into the line of a high pass filter whose frequency characteristics compensate for the frequency roll-off of the original system. The system

sensitivity is reduced but an improved system bandwidth results. This is illustrated in Fig. 6a. It is important to note that equalization may be applied to any electrical system whose frequency characteristics are known. The "system" may be only a cable, only an oscilloscope, or a complete detector/cable/amplifier/oscilloscope combination.

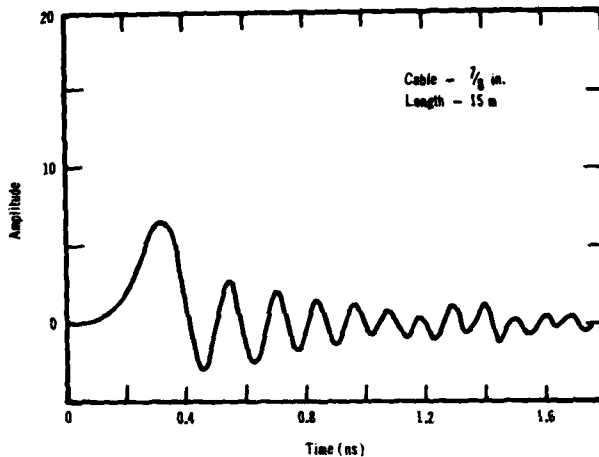


Fig. 5. Cable ringing in a 15 m sample of 7/8 inch coaxial cable.

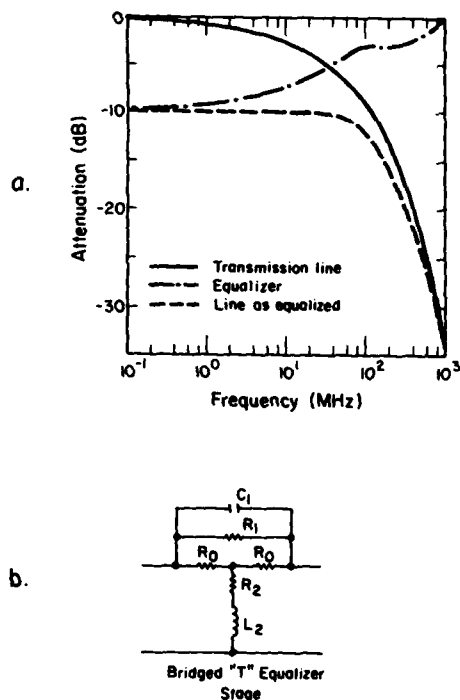


Fig. 6. a) An example of the concept of equalization and b) one possible equalizer configuration.

Many texts deal with equalizer technology(12) and describe a variety of equalizer constructions involving resistive, inductive, and capacitive elements. Equalizers may be matched to the line characteristics to provide a "matched" or "non-reflective" equalizer or may be reflective. While reflective equalizers are



simpler to design and fabricate, care must be exercised to assure that either 1) the coaxial cables are of sufficient length that the reflections do not impair the data, or 2) that the system is suitably back-terminated to prevent multiple reflections. A standard type of matched equalizer, the "bridge-tee" construction, is shown in Fig. 6b.

The various coaxial cable systems discussed earlier can be equalized. However as previously described we must assure that  $f_R$  is attenuated well below the final cable  $f_{3db}$ . With this concern as a guide, the maximum equalized bandwidth for each cable is presented in Fig. 3 and labeled as  $f_{3db}$ .

Standard components may be used to construct equalizers with frequency characteristics providing  $f_{3db}$  into the 500-1000 MHz range. However, as frequencies exceed 1 GHz, the standard discrete components have too much stray and/or distributed reactance to allow construction of computer-generated designs. A new type of equalizer has been originated to address this high frequency area.(13) This equalizer consists of a microstrip transmission line to which one or two microstrip stub lines are added. Each stub line is terminated in a resistor and the stubs may be different impedances and lengths. The reflections from the various line/stub and stub/resistor interfaces can be tailored to give suitable high pass filter characteristics.

Hybrid thick film circuit technology has also been explored for construction of multi-GHz equalizers (using conventional designs like the bridge-tee of Fig. 6b), but to date has not approached the stub equalizer success. The stub equalizers can be built with conventional printed circuit techniques and closely approach computer calculations of expected performance.

To conclude this section, Fig. 7 is constructed from the data of Fig. 3. The attenuation of four possible cable types is shown. From Fig. 7 the optimum cable choice for a 37 m cable length and a specific bandwidth can be quickly determined.

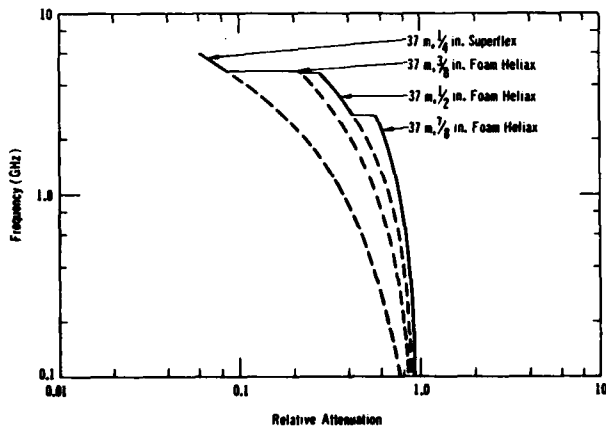


Fig. 7. Frequency and attenuation for 37 m high frequency cables within the operating range of each cable.

#### DATA RECORDERS

Few options exist for data recording above 500 MHz bandwidth. No commercial A/D converter or transient digitizer (except the 7912/direct access) can presently approach this bandwidth with acceptable resolution (8 bits). Sampling techniques do achieve this bandwidth but customarily are used only with repetitive signals.

Many parameters (cost, mode of operation, detailed frequency response, over-voltage protection, etc.) must be addressed in selecting equipment for each application. However, as a major over-simplification, several presently available recorders are compared in a two-dimensional space ( $f_{3db}$  bandwidth vs. sensibility) in Fig. 8.

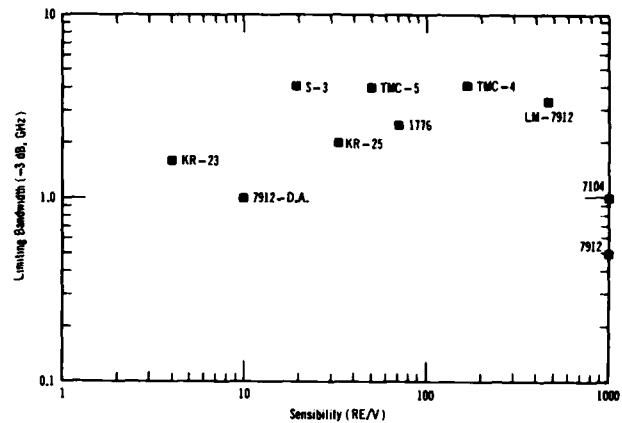


Fig. 8. Bandwidth and sensibility for several commercial recorders. See text for details.

Sensibility is defined as the number of resolution elements per input volt. A resolution element is defined either as a trace width for an oscilloscope or a least-significant-bit for a digitizer. The actual value of sensibility quoted for each recorder is open to considerable interpretation and is not an exact quantity. (Various trace widths or sensitivities may be seen in different samples of a given recorder.) The sensibility values in Fig. 8 should be treated as rough guides only. The equipment described in Fig. 8 is made by Tektronix, Inc. (7912-direct access, 7912, 7104), by EG&G, Inc. (KR-23 and KR-25), by Lockheed(14) (LM-7912), by Lockheed and EG&G(15) (S-3), by a Los Alamos/Tektronix collaboration(11) (1776) and by Thomson-CSF (TMC-4 and TMC-5). The Thomson-CSF, the 1776, and the KR-25 scopes use MCP current amplification.

All of these recorders are electron beam devices (conventional oscilloscopes or scan converters) except the single-shot-sampler (S-3) system. This system utilizes sixteen 4 GHz Tektronix, Inc. sampling heads stobed and timed by a single trigger pulse. The input signal is distributed to the 16 sampling heads. Sixteen high bandwidth samples are thus recorded. Additional units can be used to expand beyond 16 samples.

The 1776 oscilloscope is used in moderate quantities in several Los Alamos programs. It serves as another example of equalization technology. The response of the basic scope, without equalization, is shown in Fig. 9. The unequized sensitivity is about 450 mV/cm with a 700-800 MHz bandwidth. Since the attenuation curve is fairly smooth, the unit can be equalized to much higher bandwidths. (Not shown in Fig. 9, but of equal importance is that the phase characteristics are well behaved past 6 GHz.) Shown in Fig. 9 is one configuration of the 1776 used in several applications. A 4 db stub equalizer is used to provide a 1.6 GHz bandwidth at a sensitivity reduced to 700 mV/cm. The example in Figure 8 was equalized to about 2.5 GHz and provided 1.1 V/cm sensitivity. The trade-off between bandwidth and sensitivity must be guided by the specific experiment.

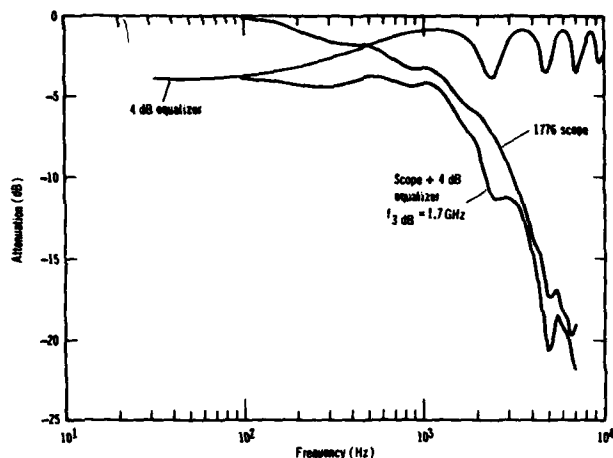


Fig. 9. Frequency response of the 1776 scope in an unequaled mode and in one equalized (4 db) mode. The equalizer response is also shown.

#### SUPPORTING INSTRUMENTATION

This section briefly addresses three classes of instrumentation which are critical in high bandwidth systems: amplifiers, test instruments, and scope digitizers.

An amplifier of suitable bandwidth can increase the sensibility values shown in Fig. 8. However, the amplifier must be carefully tested to insure that it is not introducing significant distortion into the recorded system. Some amplifiers can introduce severe ringing or other artifacts into signals. The amplifier must also have enough linear output to deflect the chosen oscilloscope.

Test instruments are required to verify the pulse response of each component of a system. Both impulse and step generators provide suitable data for subsequent Fourier analysis.(16) Both amplitude and phase must be inspected in the Fourier analysis to insure adequate pulse fidelity. Pulse generators may use either step-recovery diodes(17) or mercury pulsers.(18) These diodes can deliver up to 30 V at high repetition rates in a 60 ps impulse while the mercury pulsers can provide much larger voltages in a single shot mode. Tunnel diode pulsers(19) can provide 20 ps risetimes with 250 mV output. Mercury pulsers fabricated at Los Alamos, similar to those described in ref. 18, have demonstrated a 37 ps risetime.(20) For many applications a set of calibrated step generators(21) which provide well behaved and characterized step shapes from 50 to 200 ps is very useful and can be ordered from NBS. Delay lines are required to provide trigger advance times to the recorder system and ideally would provide ~50 ns delay without pulse distortion. Cryogenic lines at liquid He temperatures with superconducting coaxial cables have been documented with 70 ns delay and >20 GHz bandwidth.(22) Similar lines constructed with 2.1 mm diameter semi-rigid coax in liquid N<sub>2</sub> constructed at Los Alamos provide 60 ns delay with a bandwidth of 5 GHz. The Los Alamos delay line requires 7 db equalization to achieve the bandwidth.

Sampling techniques are needed to document the performance of several of the components discussed in this paper. Sampling measurements can provide bandwidth data up to 18 GHz.(23)

The importance of test instrumentation cannot be overemphasized. Attempts to rely exclusively on manufacturer's specifications or literature descriptions of specifications for similar systems will usually be met with serious failure. High bandwidth systems require careful attention to all details of system construction

and test facilities are essential. Any equalization also demands detailed knowledge of system response.

The final area of useful instrumentation concerns oscilloscope digitizers. For systems using scopes, film recording may be used. An alternative would use a vidicon tube to scan the scope face. Such systems, based on SIT vidicon tubes, are in use at Los Alamos.(24) In a rapid test schedule, the desirability of such devices is apparent.

#### SYSTEM CONSIDERATIONS

The choice of a complete system must be guided by the experimental requirements. The concept of sensibility, introduced earlier, has proven to be very useful in characterizing experimental requirements. Each experiment can be characterized by a bandwidth and sensibility needed to adequately record the anticipated data. The sensibility is deduced from a review of the required resolution and the anticipated output signal levels.

As an example of such system considerations, graphs like Fig. 10 may be constructed to show the achievable bandwidth and sensibility for several recorder systems operating through 18 and 37 m cables. If an experiment required 3 GHz bandwidth, if 100 resolution elements (R.E.) are required, and if 10 volts peak signal are expected (requiring 10 RE/V), then the 1776 and TMC-4 systems can be used with 0.5 inch cable.

The beam diagnostic system for the Helios and Antares laser was constructed from similar considerations.(25) Thirty-eight meters of 0.5 inch cable, amplification(26), a 1776 oscilloscope, and a digital camera were used. System modeling guided the choice of a 3 GHz system bandwidth. Without equalization the system was cable limited to ~250 MHz. The system frequency response (Curve A) is shown in Figure 11 along with the calculated performance (Curve P) of a stub equalizer with 18 db equalization and the calculated final system response (Curve C). A 2-3 GHz system resulted and provided the measured response of Fig. 12.

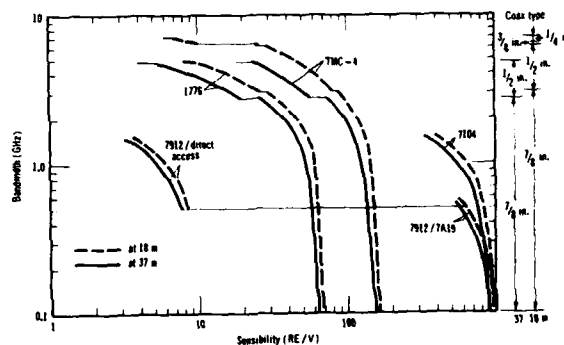


Fig. 10. System sensibility for systems based on five recorder choices at two distances. The 7A19 refers to a Tektronix, Inc. preamplifier.

## ACKNOWLEDGEMENTS

The author gratefully acknowledges extensive contributions from F. K. Hodson, R. C. Smith, D. S. Metzger, F. Pennett, and D. R. Thayer of the Los Alamos National Laboratory. The concepts discussed herein were developed during review of recording system options for the Los Alamos Antares laser facility.

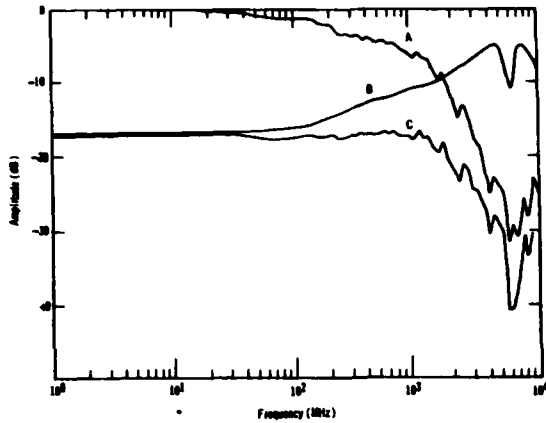


Fig. 11. Measured system frequency response for the Helios beam diagnostic channel consisting of 38 m of 0.5 inch coax, an amplifier, a 1776 oscilloscope, and a scope trace digitizer. Calculated equalizer response and anticipated system response are also shown.

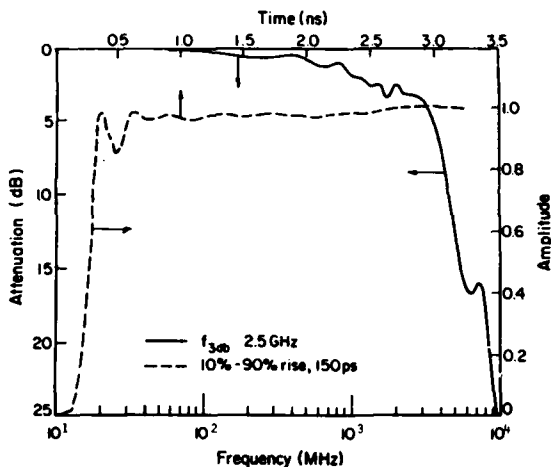


Fig. 12. System response of the Helios beam diagnostic channel.

## CONCLUSION

In this paper the elements of an x-ray detector system have been presented. System responses over 3GHz may be constructed from the technology presented herein.

As a final topic, the subject of data unfolding should be mentioned. Unfolding, or deconvolution, may be used to recover additional system bandwidth.<sup>(27)</sup> The bandwidth that can be recovered by deconvolution is highly dependent on noise either in data or in system response. In several situations at Los Alamos, bandwidth has been increased by recovering frequency attenuation of about 15 db, but this value depends critically on the individual system. Attempts at excessive deconvolution introduce serious noise into the data and can actually degrade, rather than improve, system performance.

Proper system design is providing multi-GHz recording capabilities at the Los Alamos National Laboratory.

## REFERENCES

1. D. T. Attwood, R. L. Kaufman, G. L. Stradling, K. L. Medeck, R. A. Lerche, L. W. Coleman, E. L. Pierce, S. W. Thomas, D. E. Campbell, J. Noonan, G. R. Tripp, R. J. Schnetz, and G. E. Phillips, "Picosecond X-Ray Measurements From 100 eV to 30 keV," XIV International Congress on High Speed Photography and Photonics (Moscow, USSR, Oct., 1980), and Lawrence Livermore Laboratory Report UCRL-85043.
2. R. H. Day, P. Lee, E. B. Saloman, D. J. Nagel, "Photoelectric Quantum Efficiencies and Filter Window Absorption Coefficients from 20 eV to 1 keV," to be published in *Journal of Applied Physics*, June, 1981.
3. R. H. Day, "Photoionization Measurements for Low Energy X-Ray Detector Applications," APS Conference on Low Energy X-Ray Diagnostics (Monterey, CA), June, 1981.
4. G. Beck, *Rev. Sci. Instr.* 47 (1976), p. 849.
5. R. H. Day, P. Lee, E. B. Saloman, D. J. Nagel, "X-Ray Diodes for Laser Fusion Plasma Diagnostics," Los Alamos National Laboratory Report LA-7944-MS (February, 1981).
6. P. B. Lyons, R. H. Day, D. W. Lier, T. L. Elsberry, "Sub-KeV X-Ray Calibration of Plastic Scintillators," *Proceedings of ERDA Symposium on X- and Gamma-Ray Sources and Applications* (Ann Arbor, MI, 1976), CONF-760539, p. 79.
7. P. B. Lyons and J. Stevens, *Nucl. Instr. and Meth.* 114 (1974) 313.
8. P. B. Lyons, L. P. Hocker, D. G. Crandall, J. Cheng, G. Tirsell, C. R. Hurlbut, *IEEE Trans. Nuc. Sci.* NS-24 (1977) p. 177.
9. P. B. Lyons, L. D. Looney, J. Ogle, R. D. Simmons, R. Selk, B. Hopkins, L. Hocker, M. Nelson, and P. Zagarino, "High-Speed Photodetectors for Plasma Diagnostics," presented at Los Alamos Conference on Optics (April 1981), to be published by the Society of Photo-Optical Instrumentation Engineers and Los Alamos National Laboratory Report LA-UR-81-1028.
10. P. D. Rockett, W. Priedhorsky, D. Giovenelli, "Radiation Losses from High-Z, 10  $\mu$ m Laser-Irradiated Microballoons," Los Alamos National Laboratory Report LA-UR-80-2442 (1980), submitted to *Physics of Fluids*.
11. V. T. Trexler, R. C. Smith, and D. S. Metzger, "A New High Speed Microchannel Plate Oscilloscope for Fast Plasma Diagnostics," IEEF International Plasma Physics Conference (Montreal, 1979), IEEF Catalog 79 CH 1410-0 NPS, p. 57.
12. T. Hendricks, "Equalizer Handbook," Report No. L-775/1183-1226, EG&G, Inc. (1966).
13. R. C. Smith and E. K. Hodson, "Equalization Concepts in the 1-10 GHz Range," Los Alamos National Laboratory, to be published.
14. R. V. Smith and P. R. Kaiser, "LM7912A - A Prototype Transient Digitizer," Lockheed Report LMSC/D686783, (August 1980) (Palo Alto, CA).
15. Private communication, R. K. Pardin and L. F. Chase (Lockheed Palo Alto Research Lab, CA) and M. Carlisle (EG&G, Inc., Las Vegas, NV).
16. A. Papoulis, *The Fourier Integral and Its Applications*, McGraw-Hill, (New York, 1962).
17. J. R. Andrews and F. F. Paldwin, "SHF Impulse Generators," NRSIR 7P-RRR, National Bureau of Standards (Foulder, CO), (June, 197R).

18. J. R. Andrews, "Picosecond Pulse Generators Using Microminiature Mercury Switches," NBS IR 74-377, National Bureau of Standards (Boulder, CO), March, 1974).
19. For example, Hewlett-Packard Model 1106B Tunnel Diode Pulser
20. NBS Calibration Test No. 810268 (June, 1980) Boulder, CO.
21. J. R. Andrews, N. S. Nahman, "The Measurement of Pulse Transition Duration," Colloque Int. Sur la Mesure en Telecommunications, URSI, (Lannion, France), Oct. 1977, p. 159.
22. J. R. Andrews, IEEE Trans. Instr. Meas. IM-23 (1974) p. 468.
23. W. Gans, J. R. Andrews, S. Riad, A. Cozannet, J. Debeau, "Application of an Automated Pulse Measurement System to Telecommunication Measurements," Colloque Int. Sur la Mesure en Telecommunications, URSI, (Lannion, France), Oct. 1977, p. 165.
24. S. F. Caldwell and R. C. Smith, IFFE International Plasma Physics Conference (Santa Fe, NM, 1981) IEEE Catalog No. 81 CH 1640-2NPS, p. 105.
25. R. C. Smith, F. K. Hodson, R. L. Carlson, "Multi-gigahertz Beam Diagnostics for Laser Fusion," Presented at Los Alamos Conference on Optics (April, 1981), to be published by the Society of Photo-Optical Instrumentation Engineers and Los Alamos National Laboratory Report LA-UR-81-1282.
26. F&H Electronics, Inc., Chester, N.Y.
27. E. K. Hodson, "Predictable Unfolding in the Time Domain," Los Alamos National Laboratory Report LA-3830 (1967).



Dr. Peter Lyons responding to questions after his presentation in Monterey.

Quantitative Measurements Using Soft X-Ray Streak Cameras\*

Robert L. Kauffman, Gary L. Stradling, Edward L. Pierce and  
Hector Meddecki

University of California, Lawrence Livermore National Laboratory,  
P.O. Box 5508, Livermore, California 94550

ABSTRACT

A Soft X-Ray Streak Camera (SXRS) is a fast timing instrument sensitive to x rays from 100 eV to 30 keV. The instrument has excellent time resolution ( $\sim 15$  ps) and large dynamic range ( $\sim 10^3$ ) which are well suited for measuring x-ray pulses produced by laser-fusion targets. The SXRS uses a thin transmission photocathode to convert x-rays to a secondary electron signal which is accelerated, focused, and deflected onto a phosphor producing an image of the x-ray pulse time history. In the past, such instruments have been used only to make relative measurements of the time history. At LLNL we have calibrated the SXRS in order to make absolute intensity measurements of the soft x-ray flux from laser fusion targets. Such measurements will assist in understanding the laser plasma processes and conditions needed to attain laser-produced fusion. Because of the nature of the instrument, we have calibrated it in the dynamic mode using a small laser-produced pulsed x-ray source. Details of the calibrations will be given. We have measured the SXRS response to be linear over more than two orders of magnitude with the range limited by the x-ray source strength. The dynamic range of similar instruments sensitive to optical light has been demonstrated to be greater than  $10^3$ . Based on first generation calibrations, flux measurements are accurate to  $\pm 30\%$  with the largest uncertainty in the calibrations being in determining the source spectrum and intensity. The uncertainties can possibly be reduced by a factor of two by better source characterization. In that case errors in SXRS measurements would approach those of other x-ray pulse detectors, such as x-ray diodes.

I. INTRODUCTION

X-ray streak camera technology has been developed at LLNL (1) and elsewhere (2) to time resolve x-ray pulses, primarily for application to laser-fusion plasmas. Such plasmas are intense x-ray sources lasting for nanoseconds or less. At LLNL a soft x-ray streak camera (3) (SXRS) has been developed which is sensitive to x rays from 100 eV to greater than 30 keV. Its temporal resolution of 15 psec and dynamic range of greater than  $10^3$  allows for detailed study of the target emission. Until recently, its primary application has been relative time history measurements of the x-ray emission. Efforts have begun to absolutely calibrate the SXRS for quantitative measurements. In this article some of the SXRS properties are summarized emphasizing the quantitative calibrations. The calibration method is discussed and some initial results are presented.

II. PRINCIPLE OF OPERATION

The SXRS operates similarly to optical streak cameras (4) developed at LLNL which is an application of electron imaging technology. Signal processing is illustrated schematically in Fig. 1. First, x rays are converted to an electron signal at the front of the image converter tube. A thin transmission photocathode produces a signal of low-energy secondary electrons at the rear surface whose intensity is proportional to the x-ray intensity striking the front surface. A thin narrow slit ( $\sim 100 \mu\text{m}$  wide) collimates the x rays in front of photocathode resulting in secondary electrons being emitted over the slit area. Electrostatic fields accelerate and focus the secondary electrons imaging the slit onto a phosphor at the rear of the image converter tube. The image position at the rear of

the tube is controlled by a set of deflection plates in the image converter tube. By rapidly varying the voltage on the deflection plates, the slit image position varies as a function of time resulting in a two-dimensional image on the phosphor. The temporal history of the x rays is recorded in one dimension orthogonal to the slit while the other dimension is the spatial variation of the x-ray signal along the slit. The light intensity of the phosphor image is amplified with a microchannel plate intensifier (MCP) and recorded either with film or with an active readout CCD array. (5)

An example of x-ray data from a laser fusion target is shown in Fig. 2. The data is recorded with a CCD array using an 8 bit digitizer. In this example several x-ray channels are placed across the slit and their time histories are recorded simultaneously. By combining such data with calibrations discussed below, x-ray flux versus time can be measured.

The SXRS signal,  $s$ , is related quantitatively to the incident x-ray flux,  $F_x$ , by the expression

$$s = \left( \frac{d\epsilon\gamma}{m v_s} \right) \eta F_x \quad (1)$$

where  $d$  is the entrance slit width and  $v_s$  is the sweep speed of the deflection plates. The electron transmission efficiency,  $\epsilon$ , image magnification,  $m$ , and electron to light conversion efficiency,  $\xi$ , are properties of the image converter tube and image intensifier. The detection efficiency,  $\gamma$ , for either film or CCD array averages over the spectral output of the phosphor. The SXRS response depends on x-ray energy primarily through the photocathode conversion efficiency,  $\eta$ . Photocathodes normally consist of thin Au films evaporated on carbon substrates although other substrate and cathode materials are being investigated. If the secondary electron

\* Work performed under the auspices of the U.S. Department of Energy by the Lawrence Livermore National Laboratory under Contract No. W-7405-Eng-48.

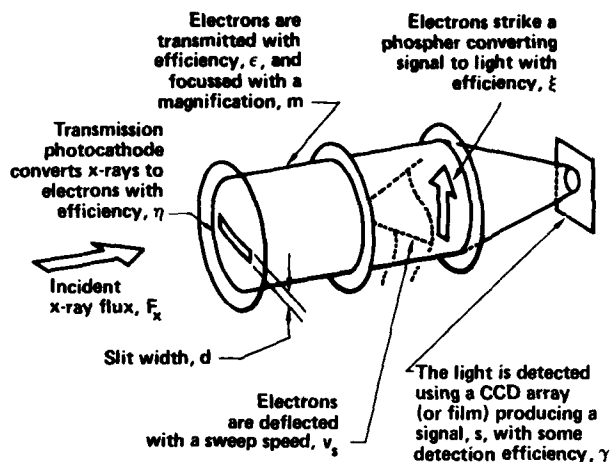


Fig. 1 Schematic showing signal processing for an x-ray streak camera.

spectrum and angular distribution from the photocathode are independent of x-ray energy, the camera parameters, in parenthesis in Eq. (1), are also energy independent. They can be replaced by a single constant,  $\alpha$ , characteristic of the instrument and independent of x-ray energy. Eq. (1) then becomes

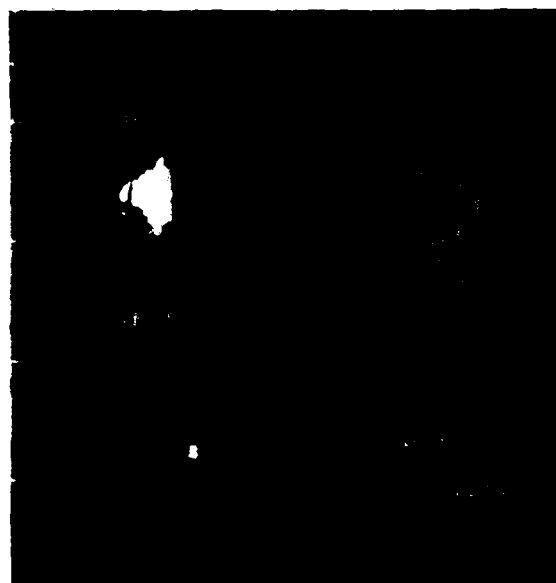
$$S_x = \alpha \eta F_x \quad (2)$$

where subscripts denote x-ray energy dependence. Henke *et al.* (6) have measured of the secondary electron spectrum for various photocathode materials and found them independent of x-ray energy. The energy dependence can also be tested by the energy dependence of the calibrations.

Another application of SXRS technology is time dependent measurements of x-ray source sizes. By using an x-ray imaging element such as an x-ray microscope (7) or pinhole (8) to image the x-ray source onto the SXRS slit, the time history of a spatial dimension is recorded. Streaked spectroscopy can also be done by placing the SXRS slit along the plane of dispersion of a diffraction device such as a crystal (9) or grating. (10)

### III. SXRS PROPERTIES

The unique feature of the SXRS is its excellent temporal response although its dynamic range, sensitivity, and one dimension of information also make the instrument attractive for pulsed x-ray measurements. Temporal response of the SXRS is estimated to be 15 psec which is an order of magnitude better than existing x-ray diode-oscilloscope systems. Fig. 3 illustrates the SXRS temporal response to a series of short x-ray pulses separated by 500 ps. (11) The short x-ray pulses (~70 psec) are created by irradiating a Ta foil with a series of 50 psec laser pulses. The pulse shapes are very uniform with little instrumental structure. Temporal data at the 50 psec resolution level can easily be interpreted without complicated instrument response unfolding techniques. The resolution limit of the SXRS has not been directly measured because a fast, intense x-ray source is not available. Resolution of optical streak cameras having similar design has been demonstrated to be in the sub-10 psec range. (12) Resolution of x-ray streak cameras is expected to be similar. Measured secondary electron distributions from x-ray photocathodes indicate that additional temporal broadening due to the greater energy spread of the secondary electrons will not decrease temporal resolution significantly. (13) Direct measurements of the temporal response are needed to better understand the instrument response in the 10 psec range.



Iron Vanadium Carbon  
Shot #80121508  
 $E_L = 3.90 \text{ kJ}, \tau_L = 900 \text{ ps}$   
 $I_{\text{max}} \sim 3 \times 10^{15} \text{ W/cm}^2$

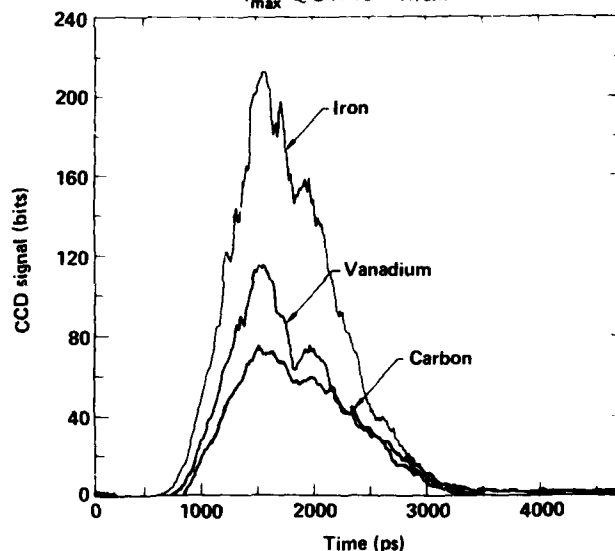


Fig. 2 Example of SXRS data. Top is the two-dimensional image of the intensity vs time recorded by a CCD array. Bottom is the time history of three subkilovolt x-ray energies defined by filter material labeled on each curve.

Spatial resolution is important especially for imaging and spectroscopy applications. Spatial resolution is influenced by broadening in the photocathode and light detection systems as well as by the quality of electron focusing optics. Fig. 4 shows portions of a streaked image from SXRS in which a 75- $\mu\text{m}$  wire grid is placed in front of the photocathode slit. On the left side of the raw data, the grid is removed displaying the unmodulated pulse. A digital scan along the cathode slit, shown on the right of Fig. 4, displays the 150- $\mu\text{m}$  period indicating that features as small as 7 l.p./mm are clearly resolvable. The noise in the data results from small scale fluctuations in the MCP gain. Signal statistics also contribute to the noise, especially in the wings of the pulse.

Although specific tests have not been made, the dynamic range and sensitivity of the SXRS are also excellent. From data such as that shown in Fig. 3,

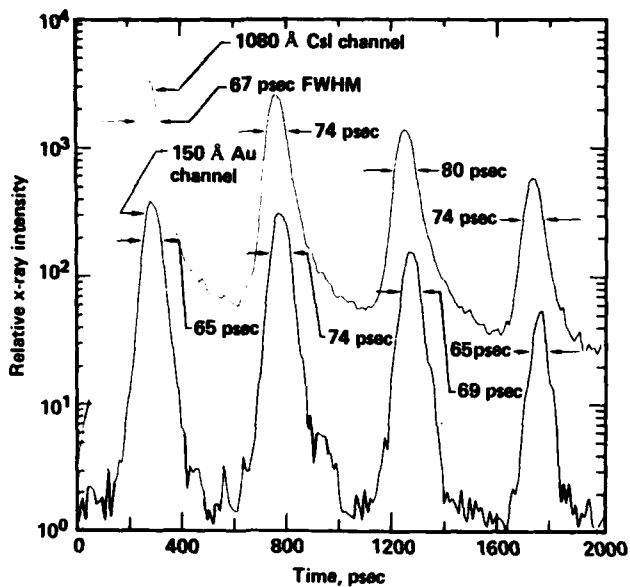


Fig. 3 Example of the temporal response of the SXRS to 70 psec x-ray pulses separated by 500 psec for Au and CsI photocathodes.

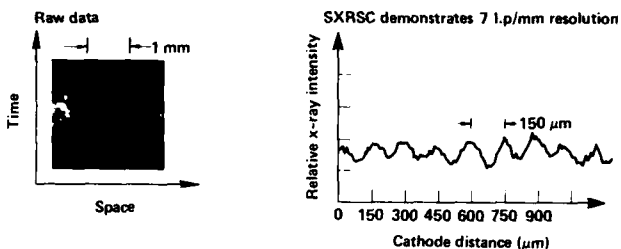


Fig. 4 SXRS response to 150  $\mu\text{m}$  period modulations across the entrance slit. On the left is the raw data while on the right is a digital scan of the data across the slit.

no significant broadening is observed at the 50 psec level over three orders of magnitude. A dynamic range of  $3 \times 10^3$  has been measured with an optical streak camera for 50 psec pulses. (12) The SXRS also has high sensitivity being determined by the photocathode efficiency. From calibration data minimum detection levels appear to be set by counting statistics due to single photon or electron events in the photocathode. Increased sensitivity can be achieved by widening the slit which enlarges the detection area. Work on optical streak cameras indicate that slits as wide as 1 mm can be used by changing the focus without significantly degrading the temporal resolution. (14) Further studies are needed to assess if the technique is applicable to x-ray streak cameras.

#### IV. X-RAY PHOTOCATHODE RESPONSE

The useful spectral range of the SXRS is limited by the x-ray photocathode response. The low energy limit is set by the minimum x-ray energy transmitted by the photocathode substrate. At high energies, both photocathode quantum efficiencies and x-ray intensity usually decrease with increasing energy, limiting the useful range to less than about 35 keV. In early development of x-ray streak camera technology, the image converter tubes were sealed requiring a cathode window which could withstand atmospheric pressure. Be windows 8  $\mu\text{m}$  thick limited the useful range of operation to greater than 1 keV. Presently, the SXRS uses auxiliary pumping equipment allowing for thinner windows which do not

have to withstand atmospheric pressure. Present windows of commercially produced vapor-deposited carbon film (15) 50  $\mu\text{g}/\text{cm}^2$  thick extend the range of sensitivity down to 100 eV. These substrates have proven to be stable under normal operation although they can be destroyed if handled improperly. Thin polymer films are being tested to reduce the lower x-ray limit and to improve detection capability around the carbon K edge which is presently attenuated by the carbon windows. The polymer films should also have improved mechanical strength. Effects of these non-conducting cathode substrate on temporal resolution and dynamic range are presently not known.

Photocathode material, usually Au, is deposited on the substrate window. Its large absorption cross section makes Au an attractive material especially at higher energies. Measurements by Day *et al.* (16) have shown that its quantum efficiency in the sub-kilovolt region is also high for a metal and relatively stable under normal applications. The photocathode layer must be thick compared to the range of secondary electron contributing to the signal, but relatively thin to minimize absorption in the front region, or dead layer from where secondary electrons cannot escape. Thin film layers also must be thick enough to insure uniform deposition. Henke *et al.* (17) have found Au thicknesses around 200  $\text{\AA}$  to be optimum. Quantum efficiencies for these transmission photocathodes vary from 0.01  $e^-/\text{photon}$  to 0.1  $e^-/\text{photon}$  over the range from 100 eV to 10 keV. The Au surfaces are easily prepared by vapor deposition and seem relatively stable when exposed to air. CsI cathodes are also being investigated for increased sensitivity (11). CsI quantum efficiencies are a factor five to thirty greater than Au quantum efficiencies in the soft x-ray region. (17) Fig. 3 compares the response of CsI and Au photocathodes to the same x-ray pulse train illustrating the increased efficiency. CsI may have a late time temporal component evidenced by the residual signal between pulses in Fig. 3 which may restrict its usefulness. Bateman and Apsimon (18) have also developed a low density CsI cathode which is being employed for x-ray streak camera applications. (19)

#### V. ABSOLUTE FLUX MEASUREMENT

Absolute flux measurements have begun at LLNL using the SXRS taking advantage of its excellent timing and large dynamic range. Such measurements require an energy discrimination technique as well as calibration of the instrument. Initial measurements, shown schematically in Fig. 5, use three broad-band channels defined using x-ray mirror-filter pairs. The channels are placed across the SXRS slit, so that their time histories are recorded simultaneously with a single instrument. For future measurements the number of channels can be expanded by adding more mirror-filter pairs. More precise spectral definition can be obtained using narrow-band interference mirrors, (20) or continuous spectral measurements can be made using a dispersive device such as a transmission grating. (10)

The composition and spectral response of the three initial channels are shown in Fig. 6. These broad-band systems provide energy resolution

$$\frac{E}{\Delta E} = 3 - 5, \text{ with good channel definition. The}$$

transmission filters define a spectral window just below the K or L edge of the filter material. The x-ray mirrors act as low-pass filters having high reflectivity in the spectral window of the filter. At higher energies where the filters become transparent, the mirrors have poor reflectivity suppressing this contribution to the signal.

The transmission filters and mirrors are calibrated individually using auxiliary x-ray sources determining the spectral flux incident on the SXRS. Below 1 keV the calibrations use a proton-induced line source (21). Results from a Ni mirror

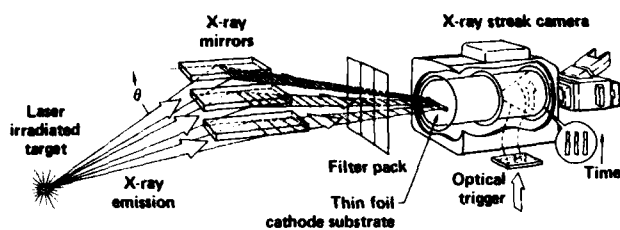


Fig. 5 Schematic of spectral flux measurements using SXRSC. X-ray mirror-filter pairs define three subkilovolt x-ray channels along the slit of the SXRSC.

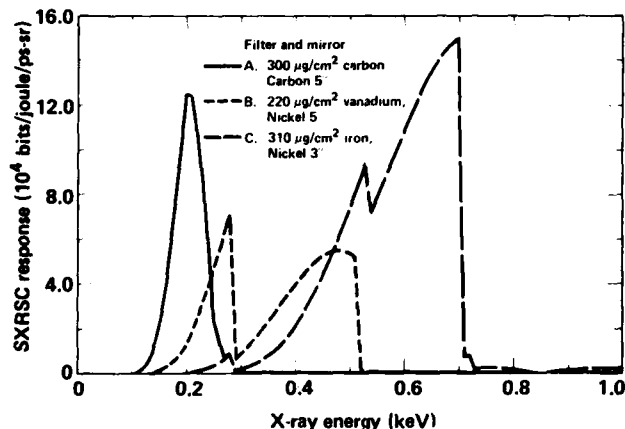


Fig. 6 Spectral response of the three SXRSC channels used for the flux measurements.

calibration is shown in Fig. 7. This mirror is made by vapor depositing 1000 Å of Ni onto a flat amorphous carbon substrate. Reflectivity measurements have been extended above 1 keV using an electron bremsstrahlung source from a Ti target. The reflectivity is predicted through the cutoff energy by a semiclassical calculation, (22) while at higher energy the measured reflectivity is less than predicted. At the higher energies x rays are not totally externally reflected at the surface but penetrate through the Ni layer to the carbon substrate. Lower reflectivity from the low Z carbon substrate produces an observed reflectivity less than predicted for bulk Ni. Use of higher Z films on a low Z substrate appears viable for improving the low pass filter qualities of x-ray mirrors. Improved computational capabilities now being developed for x-ray interference mirrors should be useful in predicting their reflectivities.

## VI. SXRSC CALIBRATIONS

SXRSC calibrations are done in the pulsed, or dynamic, mode using the broad-band channels defined above. Such calibrations are necessary because late time background signals can interfere with a steady-state, or d.c., calibrations. The background is easily suppressed electronically in pulsed operation. Other transient field effects may also affect d.c. calibration. For pulsed calibration, x-ray sources on the order of  $10^{18}$  photons/cm<sup>2</sup>-sec are required. These photon fluxes are at least three orders of magnitude greater than obtainable from a d.c. source but can be readily obtained from a pulsed x-ray source.

Present calibrations use laser-produced x-ray pulses. A schematic of the calibrations is shown in Fig. 8. Laser pulses of around one joule and 50 psec are focused at normal incidence onto targets of various material. Three calibrated x-ray diodes

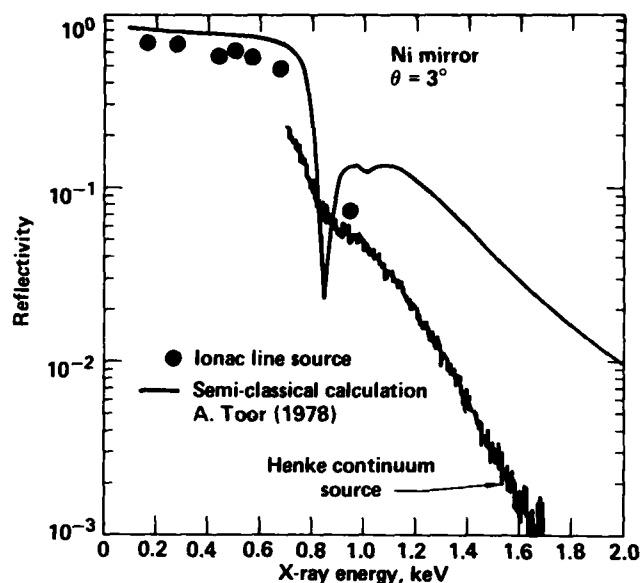


Fig. 7 Example of the x-ray mirror calibrations. The sub-kilovolt data is taken using a proton-induced line source. Above 1 keV, an electron bremsstrahlung source is used.

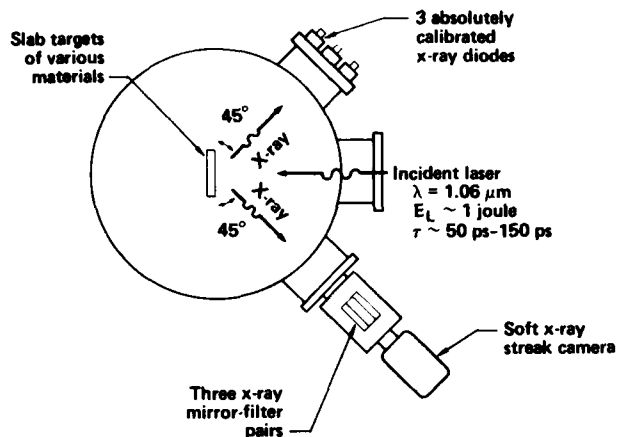
(XRD) monitor the source at 45° to the target plane. The SXRSC views the target at 45° on the opposite to the XRD's as shown in Fig. 8. The SXRSC is calibrated for the three x-ray channels described in the flux measurements. The channel response of the three XRD's have been matched as nearly as possible to the SXRSC channel responses. The SXRSC response,  $R_{\text{SXRSC}}$ , is related to the signal ratio from the two instruments as shown in Fig. 8. The signal ratio is corrected for the difference in effective width of the two corresponding energy channels and for the difference in solid angle of the two instruments. The XRD response,  $R_{\text{XRD}}$ , is the channel response averaged over the input spectrum. The  $R_{\text{SXRSC}}$  is similarly averaged by the input spectrum.

The laser source spectrum is structured depending on target material with most of its energy contained below 1 keV for these irradiation conditions. Spectral intensities for several targets measured by the XRD's is shown in the top curve of Fig. 9, and total conversion efficiency from incident laser energy to x-ray output in this spectral region is plotted in the bottom curve. While precise values depend on irradiation conditions, the high Z elements of Ta and Au produce a more intense x-ray source over this energy region. For lower Z elements, line emission effects are more evident. For example, the intensities from Fe and V targets are similar at 200 eV and 400 eV, but at 600 eV the V intensity is an order of magnitude larger, approaching that of Ta and Au. In this region V L-shell emission dominates the spectrum. Preliminary high resolution measurements in this region, shown in Fig. 10, display the complicated spectrum produced by these targets. The spectra in Fig. 10 are taken using an Fe filter which cut off the spectrum at 710 eV, although the line structure extends to higher energies. By suitably mating the filter and target material, high intensity emission in a relative narrow band region may be possible.

SXRSC calibration data is similar to that shown in Fig. 2. Intensity vs. time curves for the three x-ray channels are integrated in time and compared with the integral signal from the XRD's. An example of the comparison for the 600 eV channel is shown in Fig. 11. Similar data is obtained for the two lower energy channels. The XRD output has been converted to absolute fluences at the SXRSC, correcting for its



## A schematic of the calibrations



$$R_{\text{SXRS}} = R_{\text{XRD}} \frac{\Omega_{\text{XRD}}}{\Omega_{\text{SXRS}}} \frac{\Delta E_{\text{XRD}}}{\Delta E_{\text{SXRS}}} \frac{S_{\text{SXRS}}}{S_{\text{XRD}}}$$

## The SXRS calibrations

- Are done in the dynamic mode using 70-170 ps x-ray pulses
- Use a broad band x-ray source with  $h\nu < 1$  keV
- Use transmission filters to define three coarse x-ray channels
- Are done by comparing x-ray fluences measured by calibrated x-ray diodes (XRD's) to the integral signal from the SXRS

Fig. 8 Schematic of the absolute calibrations. The SXRS signals are compared with signals from calibrated XRD's.

solid angle and channel width. The SXRS signal unit, bit, is an arbitrary value set by the CCD digitizer which is constant for the particular instrument.

The calibration value determined by the slope of the data in Fig. 11 varies with target  $Z$ . The high  $Z$ , high intensity data are systematically above the lower  $Z$  data. These systematics are due to broad-band responses used for energy discrimination and to structure in the source spectrum. Even by including these systematics, the data group about a mean value shown as the solid line in Fig. 11 with an error of  $\pm 20\%$ . The total errors in the flux measurements are estimated to be  $\pm 30\%$  when errors in the auxiliary calibrations are included.

Similar calibrations have been done on another SXRS using Kodak Royal X-Pan film as a detector. The calibration data are from Argus, a larger, experimental laser. The data are from several experiments accumulated over a number of months. The integrated SXRS signal from each of the three x-ray channels is plotted in Fig. 12 versus the x-ray fluence from the same spectral region measured by a ten channel XRD system. (23) Each film record uses a step wedge registered on the film with a constant, chromatically matched, light source, to relate a given optical density to a light exposure. This procedure approximately corrects for shot to shot variations in film developing and film response. The mean calibration value, shown as solid lines in Fig. 12, relate the incident x-ray flux to the light intensity, or exposure. The dashed lines in Fig. 12 represent the statistical errors of the data which in this case are about  $\pm 18\%$ . The calibrations are linear over a dynamic range of two orders of magnitude. The lower limit of the dynamic range is limited by the sensitivity of the instrument. The upper limit is set by target output from this shot

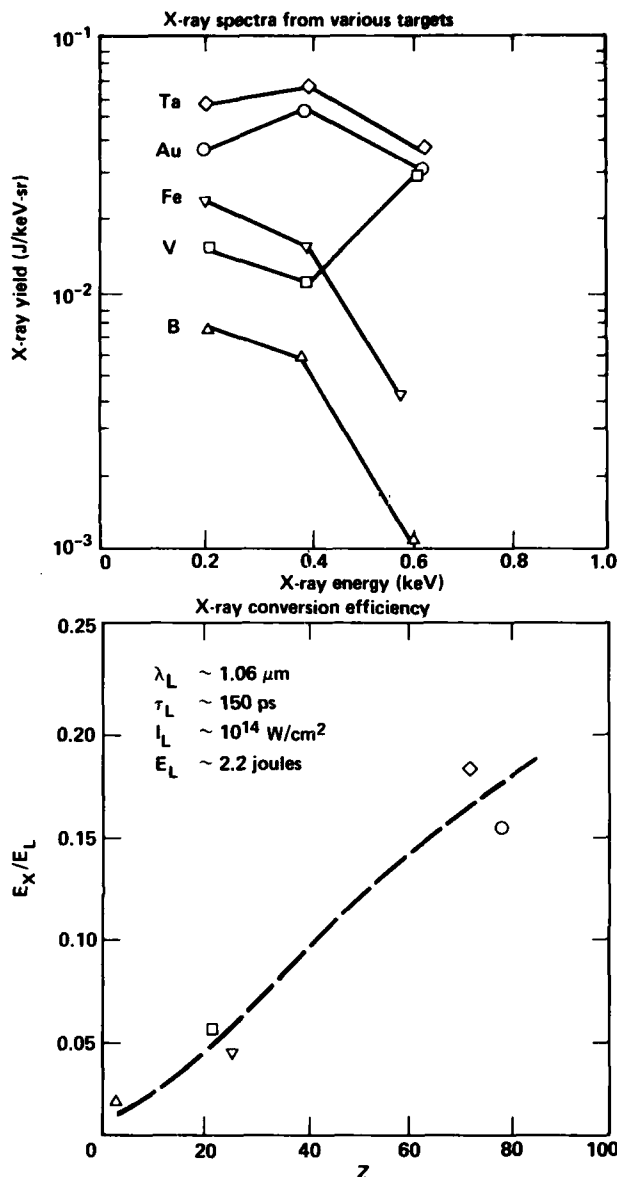


Fig. 9 X-ray yields from the laser-produced source measured using XRD's. The top curves show the spectral dependence of various targets while the lower curve shows the  $Z$  dependence of the total x-ray yield in the energy region.

series. Data from other experiments have shown linearity over at least another order of magnitude.

During the experiments several different photocathodes have been used. All are 300 Å of Au vapor deposited on 50- $\mu\text{g}/\text{cm}^2$  thick carbon foils. No systematic variations between different cathodes are observed. Sensitivity appears stable over several months and is reproducible within the errors of the measurements.

The calibrations can be used to infer the SXRS instrument response. The mean energy and width of the three channels are listed in Table I along with average photocathode response,  $R_n$ . The average photocathode response is calculated by averaging quantum efficiencies measured by Henke *et al.* (17) over the x-ray channel assuming a flat spectrum. Using these values the instrument response,  $\alpha$ , is obtained from the total channel response in Fig. 12 and is listed in Table I. The results relate film intensity to electron current density from the photocathode and are given in the final column in

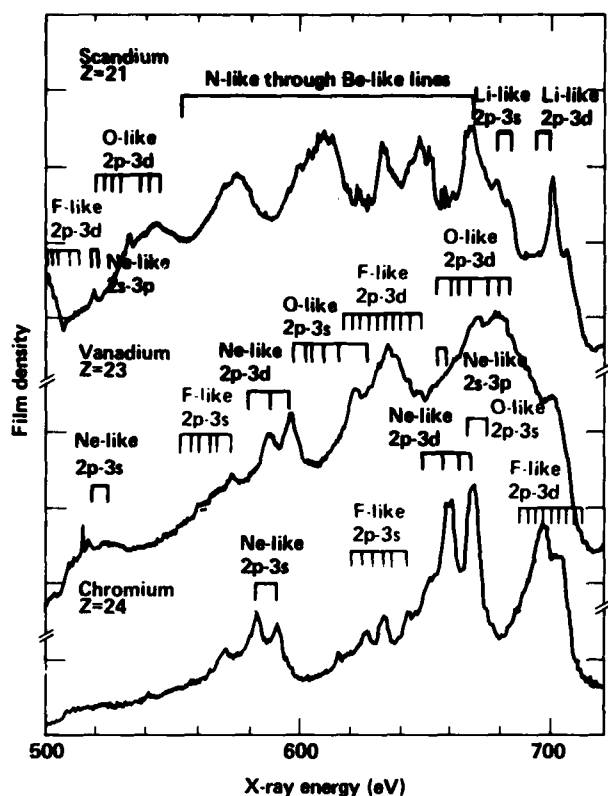


Fig. 10 High resolution measurements illustrating the complicated structure from some targets in this energy region.

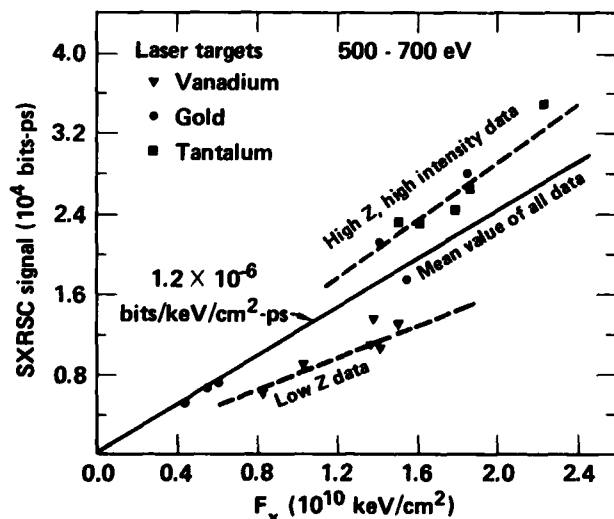


Fig. 11 Calibration data for SX-RSC. Systematics in the data indicate dependence on input spectra although all data cluster around a mean value shown as a solid line.

Table I. The values are constant for the three channels within  $\pm 25\%$  as would be expected if the photocathode secondary electron spectrum and angular dependence are independent of energy as discussed in Section IV. The calibrations can be extrapolated to other x-ray channels using these values without requiring each channel to be calibrated independently. The instrument's sensitivity can be deduced from the instrument response. For a channel 1 mm wide and

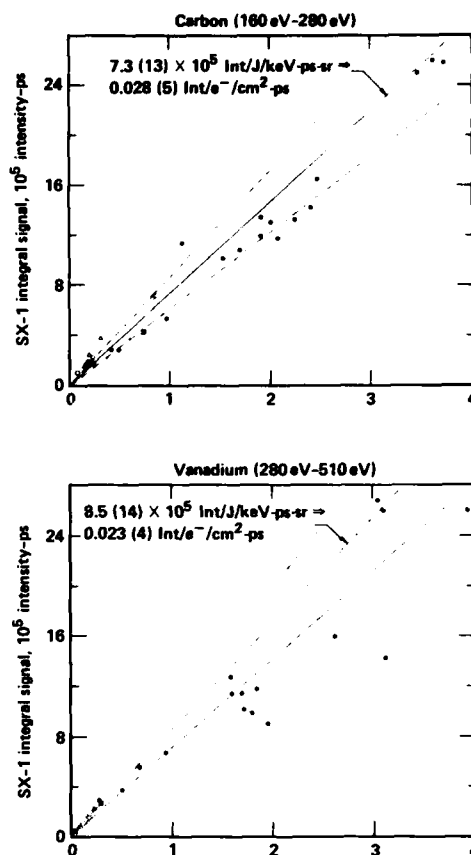


Fig. 12 Calibration curves for the three x-ray channels. The solid circles ( $\bullet$ ) are from Au targets irradiated using  $2 \omega_0$  ( $\lambda = 0.53 \mu\text{m}$ ) light and open circles ( $\circ$ ) using  $3 \omega_0$  ( $\lambda = 0.26 \mu\text{m}$ ) light. Some Ti ( $\Delta$ ,  $\triangle$ ) and Be ( $\square$ ,  $\square$ ) data are also plotted.

with 15-psec time resolution the minimum measurable intensity is about 20 for a 100  $\mu\text{m}$  wide slit. For  $\alpha = 0.022$  this corresponds to a current density of  $900 \text{ e}^-/\text{cm}^2\text{-ps}$  from that area which translates into about 13  $\text{e}^-$  from the photocathode. This lower limit approaches the limit set by electron statistics from these Au cathodes. Sensitivities can be increased by using CsI cathodes which have quantum efficiencies around one. Cathode sensitivities greater than one would not increase the instrument sensitivity because photon statistics would then limit the minimum detection level.

TABLE I  
ANALYSIS OF THE THREE CHANNEL RESPONSES

$\bar{E}$	$\Delta E$	$\overline{R\eta}$	$\overline{R\eta} \Delta E\alpha$	$\alpha$
(eV)	(eV)	(e <sup>-</sup> /keV) $\times 10^{-3}$	$\left(\frac{\text{Int.} - \text{psec}}{\text{J/keV} - \text{cm}^2}\right) \left(\frac{\text{Int}}{\text{e}^-/\text{cm}^2 - \text{psec}}\right)$ $\times 10^{10}$	
210	79	6.48	8.8 +2.2	0.028 +0.002
395	254	2.82	10.1 + 2.5	0.022 + .002
600	234	7.20	19.1 + 3.7	0.018 + .002

### VII. QUANTITATIVE ANALYSIS

The calibration values in the previous section can be used to reduce relative time history data to average flux. As an example the raw data from a representative Argus shot are analyzed, and resulting absolute flux values for the three energies are shown in Fig. 13. The data is from an Au disk irradiated with 35 joules of 0.53  $\mu\text{m}$  light with a 680 ps pulse. These can be summed appropriately to obtain total x-ray flux from the target. Such data can help understand the complicated process of laser absorption and energy transport in laser-fusion targets. By coupling the instrument with better resolution devices quantitative detailed spectral studies can be made.

### VIII. CONCLUSIONS

The SXRSC is an instrument which has demonstrated fast-timing characteristics, good dynamic range and high sensitivity making it useful for measuring fast x-ray pulses such as those from laser-fusion targets. Efforts have begun to absolutely calibrate the instrument to make a quantitative measurement. Measurements accurate to  $\pm 30\%$  are possible using the initial calibration scheme. The accuracy is limited by the use of broad band channels and x-ray diodes to monitor the source

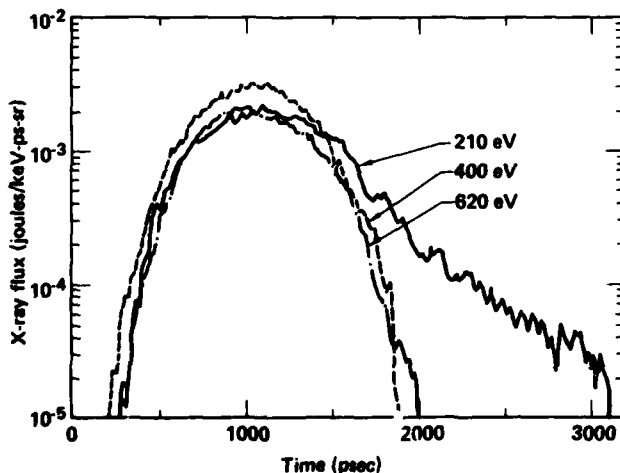


Fig. 13 Spectral fluxes from a typical shot derived using calibration values in Fig. 12. The x-ray pulse is from an Au disk irradiated with 35J, 680 ps pulse at 2  $\omega_0$  laser light.

spectra. Higher resolution measurements of the target spectrum may allow the spectral dependence to be unfolded from the data. Narrower channel definition would also improve calibrations. By using x-ray interference mirrors to define a narrow band of x rays, the dependence on the x-ray spectrum would decrease. A more powerful calibration source is needed to implement such a scheme. These improvements could improve calibrations so that SXRSC accuracies could approach XRD measurements. More accurate flux monitoring detectors are needed for further improvement of the calibrations. For a more accurate measurement, d.c. calibrations should be explored. Present state-of-the-art in quantitative SXRSC measurements can still prove valuable for pulsed x-ray flux measurements and energy balance experiments.

### IX. ACKNOWLEDGMENTS

We would like to thank Burt Henke for his support in photocathode development and for supplying us with CsI photocathodes. We would like to acknowledge Stan Thomas for electronics support of the SXRSC effort and Jack Cheng, Jack Noonan and Gary Tripp for the active readout CCD arrays. We thank Jerry Gaines, Dick Ernst, and Earl Augusta for support of the auxiliary calibrations. We acknowledge Claude Dittmore for help in film detection techniques. We also acknowledge David Gaines and Ray Perkins for their spectroscopy effort at the monojoule and Julia Kakanui for the SXRSC resolution analysis.

### REFERENCES

1. C.F. McConaghy and L.W. Coleman, *Appl. Phys. Lett.* **25**, 268 (1974); L. Coleman and D. Attwood, *Laser Program Annual Report - 1974*, edited by J.I. Davids (Lawrence Livermore Laboratory, Livermore, CA, UCRL-50021-74, 1974) pp. 315-319.
2. For a recent review of streak camera technology see *Proceedings of the 13th International Conference on High Speed Photography and Photonics*, edited by Shin-ichi Hyodo (Japanese Society of Precision Engineering, Tokyo, Japan, 1979).
3. G.L. Stradling, M. S. Thesis, Brigham Young University, 1981; Lawrence Livermore National Laboratory, UCRL-52568.
4. S.W. Thomas, G.R. Tripp and L.W. Coleman, *Proceedings of the 10th International Congress on High Speed Photography*, edited by E. Laviron (Association Nationale de la Recherche Technique, Paris, France, 1972) pp. 127-133; S. Thomas, J. Houghton, T. Owen and L. Coleman, *Laser Program Annual Report - 1974* edited by J.I. Davis (Lawrence Livermore Laboratory, Livermore, CA, UCRL-50021-74, 1974) pp. 292-296.
5. J. Cheng, G. Tripp, and L. Coleman, *International Conference on the Application of CCD devices* (San Diego, CA, 1978).
6. B.L. Henke, J.A. Smith, and D.T. Attwood, *J. Appl. Phys.* **48**, 1842 (1977).
7. R.H. Price, *Laser Program Annual Report Vol. 2*, edited by L. Coleman (Lawrence Livermore National Laboratory, Livermore, CA UCRL-50021-79, 1979) pp. 5-54 to 5-57; and "X-Ray Microscopy Using Reflection Optics" presented at this conference.
8. D.T. Attwood, L.W. Coleman, M.J. Boyle, J.T. Larsen, D.W. Phillipon, and K.R. Nanes, *Phys. Rev. Lett.* **38**, 282 (1977).
9. M.H. Key, C.L.S. Lewis, J.C. Lunney, A. Moore, J.M. Ward, and R.K. Thareja, *Phys. Rev. Lett.* **44**, 1669 (1980).
10. N.M. Ceglio, M. Roth, and A.M. Hawryluk, this conference.
11. G.L. Stradling, H. Meddecki, R.L. Kauffman, D.T. Attwood, and B.L. Henke, *Appl. Phys. Lett.* **37**, 782 (1980).

12. S.W. Thomas and G.E. Phillips, Proceedings of the 13th International Conference on High Speed Photography and Photonics, edited by Shin-ichi Byok (Japanese Society of Precision Engineering, Tokyo, Japan, 1979) 471.
13. B.L. Henke and K. Premaratne, Proceedings of the International Conference on X-Ray and XUV Spectroscopy, Jpn. J. Appl. Phys. 17 suppl. 17-2 pp. 477-482 (1978).
14. R.A. Lerche, H. Medeck, G.E. Phillips, and S.W. Thomas, IEEE Conference on Plasma Science, 1981, 1113; Lawrence Livermore National Laboratory UCRL-86019, 1981.
15. Arizona Carbon Foil Co., Tuscon, AZ
16. R.H. Day, P. Lee, E.B. Salomon and D.J. Nagel, LA-UR-79-1360, IEEE International Conference on Plasma Science, Montreal, Quebec, Canada, June 1979.
17. B.L. Henke, J.P. Knauer, and K. Premaratne, J. Appl. Phys. 52, 1509 (1981).
18. J.E. Bateman and R.J. Apsimon, unpublished.
19. M.H. Key and J.E. Bateman, Rutherford Laboratory Report, RL-79-036 (1979).
20. G.L. Stradling, T.W. Barbee, Jr., B.L. Henke, E.M. Campbell, and W.C. Mead, presented at this conference.
21. R.W. Kuckuck, J.L. Gaines and R.D. Ernst, Proceedings of the 4th Conference of Scientific and Industrial Applications of Small Accelerators, edited by J. Duggan and I.L. Morgan, (IEEE, Piscataway, NJ, 1976) 229.
22. A. Toor, private communications.
23. K.G. Tirsell, H.N. Kornblum, and V.W. Slivinsky, Bull. Amer. Phys. Soc. 23, 807 (1978); Lawrence Livermore National Laboratory UCRL-81478 (1979).



Dr. Robert Kauffman describing the absolute intensity calibration of picosecond recording instruments.



My dad is a physicist!



Dr. David Nagel reviewing progress on two-dimensional x-ray detectors, and asking attendants if the airlines had as yet delivered his lost baggage.

X-ray detectors which register the position of photon arrival are widely used. Parameters for the characterization and comparison of detectors are reviewed prior to a survey of the types of available area x-ray detectors. Research opportunities for improvement of existing systems and development of new detectors are numerous. Potential x-ray projects involving adaptation of detectors employed at infrared and visible wavelengths are suggested. The development and characterization of x-ray detectors is a field full of both intellectual challenges and practical applications.

### I. INTRODUCTION

Virtually all x-ray work involves the series of components shown in figure 1. The primary devices are (a) the source (photon emission or "birth"), (b) the optics (photon scattering or "life") and (c) the detector (photon absorption or "death"). Energy must be supplied to the source, occasionally from within, as in the case of stars. The detector sometimes serves as the recording medium as well; consider photographic film. The point is that detectors are central to all x-ray research and applications.



Figure 1. Components of systems for x-ray measurements.

It is often necessary to measure the spatial distribution of an x-ray flux in order to (a) determine the anisotropy of a source, (b) record the image of a source or (c) record a spectrum dispersed in space (angle) by a grating or crystal. Multiple-discrete or array or continuous detectors can be used for such measurements. The relationship between such detectors is shown schematically in figure 2. Conceptually, discrete and area (array or continuous) detectors form the "continuum" of possibilities shown in that figure. Hence, it is somewhat artificial to distinguish between discrete and area detectors. However, there is a long history of doing so because of the applications of area detectors in imaging and spectroscopy.

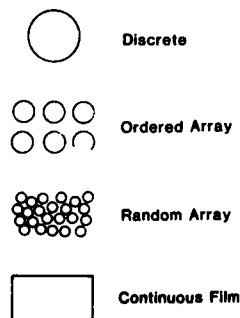


Figure 2. X-ray detectors vary geometrically from discrete devices (e.g., x-ray diodes) through ordered arrays (e.g., charge-coupled devices) and random arrays (e.g., AgBr grains in film) to continuous films (e.g., photoresists).

This paper has three purposes: (a) to examine parameters useful for characterization and comparison of any x-ray detectors, (b) to give recent or general references to work on area x-ray detectors and (c) to point out opportunities for research on area x-ray detectors. The next three sections address these topics. The emphasis here is skewed toward x-ray energies below a few keV although systems which detect x-rays above 100 keV are also mentioned. Areas of application include plasma diagnostics (1,2), structure analysis, including crystallography (3), medical radiography (4), x-ray lithography (5) and astronomy (6). Intensities in these areas range from bright plasma and synchrotron-radiation sources to "photon-starved" stellar measurements.

### II. DETECTOR CHARACTERIZATION

Regardless of photon energy, detectors can be viewed as transducers which change x-ray energy into a measurable signal, including other photons (fluorescence), electrons (photoemission), ions (photodesorption), heat, phase changes, defects or chemical changes. Whatever the response of a detector, it is desirable to know how the ratios of response-to-input vary as a function of photon energy ( $E$ ) and intensity ( $I$ ). These give the range of  $E$  and  $I$  over which a detector is useable. Sensitivities of the detector response to spatial variables of position ( $x, y$ ) and arrival angles ( $\theta, \phi$ ), and time ( $t$ ) variation are also of interest. That is, variations of the response with  $E, x, y, \theta, \phi$  and  $t$  for the full range of intensities are wanted. The threshold for operation (7), linearity, and saturation are intensity-dependent factors.

The actual performance of a detector is determined by noise factors as well as parameters associated with the radiation field. Noise sources include variations in the spatial and temporal arrival of x-ray photons ("shot" noise) as well as noise introduced in the detector and recording system (e.g., Johnson noise due to effects of thermal fluctuations on electron motion and flicker or  $1/f$  noise related to spatially-localized potential barriers (8,9)). The basic detector response parameter, including consideration of noise, is the detective quantum efficiency (DQE) defined as  $(S/N)^2$  over  $(S/N)^2$  in where  $S$  is signal and  $N$  is noise (9,10). Very little work has been done on determining the DQE of x-ray detectors (11).

Resolutions with respect to photon energy, position, arrival angle and time are needed to fully characterize a detector. Energy resolution is generally given as  $\Delta E/E$ . Spatial resolution can be characterized by the point spread function (PSF) or modulation transfer function (MTF) (12). Only occasionally are these quantities determined for x-ray systems (13). Detector resolution with respect to arrival angle is usually of little interest and rarely determined. Temporal resolution, of great interest in plasma diagnostics, is measured with short pulses and expressed in fractions of a sec (14).

Synoptic treatments of the characteristics of long wavelength (9,15-7) and x-ray (18,19) detectors are available. The point to be made here is that there is little discussion, determination, use or comparison of general characteristics, such as DQE, PSF and MTF, for x-ray detectors. Related and important quantities, such as quantum efficiency (%) and spatial resolution (in line pairs per mm), are more commonly measured. Useful lists of detector and related characteristics have been compiled (19,20). They include, in addition to the characteristics already discussed, factors such as detector size, uniformity of response, dead time, digitization and storage times, type of storage media, costs of the detector and recording systems, and special operating characteristics.

### III. AREA X-RAY DETECTORS

Many types of area x-ray detectors have already been developed. The aim of this section is discuss ways to classify such detectors and to provide references where detailed information can be found.

Classification of area detectors is problematic because they operate on a variety of physical principles, generally contain many components, and have a

wide range of spectral, spatial and temporal response characteristics. The various steps in energy conversion (e.g., x-rays  $\rightarrow$  electrons) have been used to classify longer-wavelength detectors (17). Here, area detectors are discussed first in terms of their component functions and then in terms of their temporal and spatial characteristics.

Conversion of x-rays to light or electrons is a common function in x-ray area detectors. Converters, such as fluorescers and photocathodes, are primary components in detectors. In fact, devices which transform an x-ray (or ultraviolet) image to a visible image are called image converters. The resulting image is viewed, or else detected and recorded by conventional optical means. Multiplication of signal levels is often accomplished within image converters and in other area-sensitive systems. Such gain can be achieved by electron acceleration or by electron multiplication. Image intensifier systems are commonly used for work at low light levels in the visible region (21-3). Discussions of both visible and x-ray intensifiers are available (24-6). X-ray intensifiers are also discussed separately (27-8). Accumulation of signal is another common function in area detectors. This is the case for electrons systems, such as some TV-based devices and solid-state arrays, as well as familiar detectors such as photographic film.

The classification of x-ray detectors as active (electronic) or passive (non-electronic) gives artificial emphasis to their time resolution. Electronic detectors can integrate signals; consider a Si p-i-n detector with a 5 nsec response time viewing 0.1 nsec FWHM plasma emission. Conversely, chemical systems can yield time resolution; x-ray film which takes minutes to develop and read will give the time variation (drift) in the output of an ordinary x-ray machine. Clearly, comparison of the response time of detector system and the scale of time variations in a source is relevant. Similarly, classification of detectors as discrete or continuous is flawed since (a) there is a smooth variation in type (see figure 1) and (b) the spatial resolution of the detector must be compared to the scale of variations in the incident x-ray field. Despite these factors, area detectors based on electronics (which tend to be fast) and on chemical and other effects (which are slower), both continuous and discrete, will be discussed according to these groupings.

Three major classes of electronic area x-ray detectors can be identified: (a) continuous, such as TV and electrophotographic systems, (b) devices with discrete anodes, e.g., multiwire proportional counters and (c) solid-state arrays, such as charge-coupled devices, with discrete picture elements (pixels).

Several types of detectors provide continuous spatial response. Discussions of TV-based system can be found in the references on image intensifiers (24-8). An integrating TV system sensitive to x-rays above 80 keV has been described (29). Electrophotography, prominently including xerography, involves charging of surface (30). So also does ionography, except that ions instead of electrons are accumulated on a continuous insulator to form a charge image (31). Closely related is electrophoresis, for which x-ray absorption causes particle motion within a cell, changing its reflectivity (32-33). Electronographic systems, in which electrons are recorded on film or changed to light for recording, have been used in the ultraviolet (34). They should be adaptable to the x-ray region by proper choice of entrance windows. X-ray framing cameras provide two dimensions of spatial resolution with time responses ranging down to 0.1 nsec (35).

Area detectors frequently employ anodes. In most of them, the anodes are at high potential to provide electron gain in a gas. Multiwire proportional counters are now in common use in x-ray scattering (36) and diffraction (37-8) experiments. Gas scintillation proportional counters (39) can be employed as area x-ray detectors (40). Anodes may also be placed after micro-channel plate electron multipliers (41) merely to

collect charge or to give two dimensions of spatial information (42,43). Spatial resolution finer than anode spacings can be obtained in multiwire proportional counters and collector-anode devices by electronic determination of the centroid of collected charges. Such detectors are intermediate between systems with continuous spatial response and separate pixels.

Solid-state arrays are mostly based on silicon technology, for example, p-i-n diode arrays or charge coupled devices (CCD) (44). X-rays may be recorded by such devices either by direct absorption or after conversion to light. Diode arrays, which tend to be noisy, respond to direct x-ray absorption (45,46). They have also been employed to sense light from phosphors struck by X-UV radiation, both without (47) and with (48) intensification. CCDs are quieter than p-i-n arrays due to the absence of connect/disconnect noise. They respond to direct x-ray incidence for energies above about 1 keV which penetrate the dead layer (49,50). For softer radiation, back-surface illumination of a thinned device has been employed, as in figure 3 (51-52). Recently a deep-depleted, unthinned CCD back-illuminated with 8 keV x-rays demonstrated unity quantum efficiency (53). CCDs have also been used in the UV region with phosphor wavelength shifters (54-5). The employment of solid-state arrays for x-ray detection has been reviewed recently (56). A silicon charge-injection array has been used in a solid-state TV system to record X-UV radiation (57). Pyroelectric detector arrays are now commercially available, both alone and in vidicons. Since single pyroelectric detectors were found to respond to direct x-ray incidence (58), it is expected that arrays will behave similarly. As with Si-based arrays, pyroelectric devices will also respond to fluorescence due to X-UV absorption.

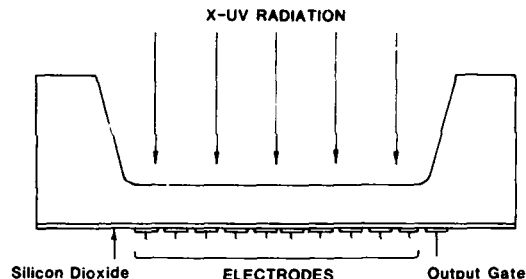


Figure 3. Cross-sectional schematic of a back-thinned device useful for detection of X-UV radiation (51).

Discussions of electronic x-ray area detectors, especially multiwire systems, relevant to synchrotron radiation work are available (59-61). Other useful reviews of electronic area detectors for long wavelengths (62-3) and x-rays (64) have been published.

Area x-ray detectors based on chemical and other non-electronic systems can be classified, similar to electronic systems, according to the continuity of the recording surface. Some passive detectors are grainy (e.g., photographic films) while others are essentially continuous (e.g., photoresists). Brief reference is made to such area x-ray detectors in the remainder of this section.

Photographic films have a long history of use for x-ray recording (65). Much experimental data is available, although there is need for characterization of new films, as well as old films over wider energy ranges. X-ray response of films containing grains has been modeled in order to interpolate, extrapolate and estimate quantitative film response (66). AgBr can be made in continuous, x-ray-sensitive layers also (67).

Photoresists consisting of organic and inorganic materials have been studied primarily for x-ray lithography. Organic systems having wide ranges of sensitivities and resolutions are available (68-70). Roughly, organic resists require at least  $10^4$  times the

exposure of Ag Br films but they offer up to 100 times better spatial resolution. Inorganic resists have received little attention. Continuous thin films can respond to the heat resulting from absorption of an intense x-ray pulse. X-rays from laser-heated plasmas were observed to melt a thin layer of lead (71). Pinhole-camera images of x-rays from exploded wires ablated Al from the surface of mylar (72). Systematic study of phase-change x-ray area detectors is needed. Multiple as well as single layer, films might be used. Layers of different absorptions and colors could be prepared, similar to "burn paper" employed to determine isointensity contours in pulsed laser beams. In the absence of color differences, chemically-sensitive readout could be used, for example, x-ray fluorescence or Auger-electron spectroscopies, or some simple, color-inducing technique such as anodization.

#### IV. RESEARCH OPPORTUNITIES

All the area x-ray detectors mentioned in the last section are open for further study since their characteristics are usually poorly known and because their responses can be improved (e.g., the sensitivity of photoresists). Some specific opportunities were also mentioned, namely development of x-ray electronography, testing of the x-ray response of pyroelectric detector arrays and study of phase-change systems. Many other openings exist for development of area x-ray detectors, notably for quiet, sensitive and fast systems and, increasing, for detectors to use with bright plasma and synchrotron-radiation sources. Ideas for detector research arise from the needs of specific situations and from knowledge of detectors used in neighboring spectral regions. Many area x-ray systems employ devices developed for imaging in and near the visible region. Consider TV-based detectors and those employing solid-state arrays (p-i-n and CCD systems). Several effects and detectors observed and used at long wavelengths, which should be adaptable to the X-UV region, are enumerated in the remainder of this section.

A rich source of ideas for x-ray detector work comes from research on optical storage materials (73-4). Another relevant area is non-silver photographic processes (75-6). Organic photochemical effects are also potentially useful in the x-ray region (77). Many effects, with widely different characteristics, have been tested and compared. They fall into categories such as electronic, mechanical, thermal and optical. Photoferroelectric materials, have been demonstrated in the optical region (78). Mechanical effects include photoelasticity (79) and light-induced expansion (80). These effects should carry over into the x-ray region.

Many thermal effects due to photon absorption observed and used in the optical region may be applicable to x-rays. Effects and techniques can be classified according to the temperature rise and physical changes induced by absorption. Optical detection of infrared radiation with commercial thermal scanners is one possibility. Another is the use of a probe beams (81). Thermoplasticity is another effect of interest (82). Melting of organic and inorganic films has been employed for image recording at long wavelengths. Initial tests in which x-ray absorption caused phase changes (71-2) should be followed by systematic calculational and experimental studies aimed at evaluating the practicality of thermal recording of intense x-rays.

Many optical effects have been employed for image recording at long wavelengths. Photopolymers (77,83) and inorganic photochromics (84) should be tested in the x-ray region. Creation of color centers in crystalline and glassy materials due to x-ray absorption is well known. However, such effects have not been studied for the purpose of developing area x-ray detectors. Many particular optical systems should also respond to x-rays, for examples, sensitized gelatins (85). Phosphorescence in minerals, sometimes excited by ultraviolet radiation, might be a useful area x-ray detector

for synchrotron-radiation beams. It would fade, allowing reuse of the materials. An optical device based on liquid-crystal behavior might provide a fast-response, erasable system for x-ray imaging. An adaptation of the visible system (87) is shown in figure 4. The original glass entrance window might be replaced with x-ray transmissive Be or mylar. The layers within the device total only about 12  $\mu$ m in thickness, excluding the window and glass. Another possible optical system could involve recording the light from electron avalanches in proportional counters. For example, the near-anode region could be imaged onto a CCD to provide both spatial and temporal, and possibly spectral, sensitivity.

Undoubtedly, many other possibilities for adaptation and modification of detectors useful at long wavelengths exist. Books on detectors of infrared and optical radiation are useful sources, both directly because x-ray detection often involves optical techniques and indirectly because detectors made for lower-energy photons commonly respond to x-rays (87-90).

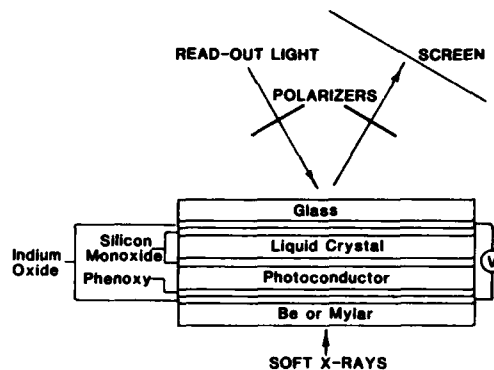


Figure 4. Potential area x-ray detector based on use of a liquid crystal light valve. The design follows from a device employed at visible wavelength (86).

#### V. CONCLUSION

X-ray detectors in general and area detectors in particular relate to many areas of research and application. They are especially relevant to the identifiable fields of dosimetry, photometry and radiometry. Area detectors involve concerns with the recording, analysis and display of images, an active area of research in optics generally.

While work with x-ray detectors can be viewed as only a means to an end, it has its own challenges and pleasures. Extensive knowledge of optics, solid-state physics and gaseous electronics is needed to understand and advance x-ray detection. For electronic detectors, intimacy with problems such as noise, as well as with circuits, is needed. Because x-ray detection can be viewed as transduction of information from x-rays to some other form, aspects of communications theory are relevant to full understanding of x-ray detectors. The development and characterization of x-ray detectors can be an exciting intellectual activity as well as being demonstrably important.

#### REFERENCES

1. C.E. Violet, *Adv. in X-ray Analysis*, 18, 26 (1975).
2. R.P. Godwin, *Adv. in X-rays Analysis*, 19, 533 (1976).
3. U.W. Arndt in U.W. Arndt and A.J. Wonacatt (Editors), *The Rotation Methods in Crystallography*, North-Holland, Amsterdam (1977).
4. A.G. Haus (Editor) *The Physics of Medical Imaging: Recording System Measurements and Techniques*, Am. Inst. of Physics, New York (1979).
5. D.J. Nagel, *Proc. N.Y. Ac. of Sci.*, 342, 235 (1980).
6. D.L. Crawford (Editor) *Instrumentation in Astronomy III*, SPIE Vol. 172 (1979).

7. J.F. Walkup and R.B. Asher, Optic News, Opt. Soc. of Am., Fall 1979, p. 8.
8. A. Van der Zeil and E.R. Chenette, Adv. in Electronic and Electron Physics, 46, 313, (1978).
9. "Infrared Detector Survey", Electro-Optical Systems Design, August 1975, p. 38.
10. P. Kowaliski and A.E. Sanders, Theory of the Photographic Process, Macmillan, New York (1978) p. 636.
11. S.M. Gruner et al., IEEE Trans. on Nucl. Sci. NS-25, 562 (1978).
12. M.A. Kraus in J.F. Hamilton (Editor) Theory of the Photographic Process, Macmillan, New York (1978) p. 592.
13. R.L. Kauffman, This Conference.
14. R.H. Day, This Conference.
15. R.F. Wagner, IEEE Trans. on Nucl. Sci. NS-27, 1028 (1980).
16. C.L. Wyatt, Radiation Calibration: Theory and Methods, Academic Press, New York (1978) ch. 6.
17. J. Meaburn, Detection and Spectrometry of Faint Light, Reidel, Dordrecht (1976) ch. 2.
18. G.F. Knoll, Radiation Detection and Measurement, Wiley, New York (1979).
19. S.M. Gruner et al., Princeton University, Second Nat. Conf. on Sych. Rad. Instr., Cornell., 15-17 July 1981.
20. P. Phizacherly, Stanford Synch. Rad. Lab. Report 78/02, Apr. 1978.
21. H.V. Soule, Electro-Optical Photography at Low Illumination Levels, Wiley, New York (1968).
22. C. Feeman (Editor) Low Light Level Devices for Science and Technology, SPIE. Vol. 78 (1976).
23. P. Gardner, Phys. Technol. 9, 47 (1978).
24. J.D. McGee et al., (Editors) Photo-Electronic Image Devices, Academic Press, New York (1972).
25. B.L. Morgan and D. McMullan, Adv. in Electronic and Electron Physics, 52 (1979).
26. T.P. McLean and P. Schagen (Editors) Electronic Imaging, Academic Press, New York, (1979).
27. R.E. Green, Adv. in X-Ray Analysis, 14, 311 (1971).
28. W. Kuhl, ch. 11 in reference 26.
29. P. Hague and J.E. Jacobs, J. Appl. Phys., 48, 2665 (1977).
30. R.M. Schaffert, Electrophotography, Focal Press, London (1975).
31. P.W. Walton, Optical Engr. 16, 408 (1977).
32. R.K. Swank et al., J. Appl. Phys. 50, 6534 (1979).
33. P.C. Murau, IEEE Trans. on El. Devices, ED-26, 1153 (1979).
34. G.C. Carruthers, Instrumentation in Astronomy III, SPIE Vol. 172, 304 (1979).
35. R. Kalibjian, Rev. Sci. Instr. 49, 891 (1978).
36. J. Schelten and R.W. Hendricks, J. Appl. Cryst. 11, 297 (1978).
37. A.L. Robinson, Science 199, 39 (1978).
38. J.R. Helliwell, Daresbury Lab Preprint 271E (1981), To be publ. in Nucl. Instr. and Methods.
39. A.J.P.L. Policarpo, Sp. Sci. Instr., Reidel, Dordrecht (1976).
40. W.H.-M. Ku, This Conference.
41. J.L. Wiza, Opt. Spectra (Apr. 1981) p. 58.
42. E. Kellog et al., Rev. Sci. Instr., 47, 282 (1976).
43. J.G. Timothy et al., Space Optics, SPIE Vol. 183, 169 (1979).
44. P.G. Jespers et al. (Editors) Solid -State Imaging, Noordhoff, Leyden (1970).
45. L.N. Koppel, Adv. in X-ray Analysis, 19, 587 (1976).
46. R.D. Bleach and D.J. Nagel, Appl. Optics 16, 572 (1977).
47. R.C. Gamble et al., Rev. Sci. Instr. 50, 1416 (1979).
48. H.W. Moos et al., Johns Hopkins University, Baltimore MD, Unpublished.
49. M.C. Peckerar, W.D. Baker and D.J. Nagel, J. Appl. Phys. 48, 2565 (1977).
50. L.H. Koppel, Rev. Sci. Instr. 48, 699 (1977).
51. P. Hurstein and D.J. Michels, Appl. Optics 19, 1563 (1980).
52. N.G. Loter et al., Unpublished.
53. M.P. Peckerar et al. Appl. Phys. Lett. 39, 55 (1981).
54. H.O. Pritchard et al., Appl. Optics, 18, 2085 (1979).
55. M.M. Blouke et al., Appl. Optics, 19, 3318 (1980).
56. N.M. Allinson, Daresbury Lab Preprint 270E (1981), To be publ. in Nucl. Instr. and Methods.
57. J.R. Roberts and T.L. Pittman, Nat. Bur. of Standards, Washington DC, Unpublished.
58. D.J. Nagel et al., Naval Research Lab. Memo. Rpt. 7838 (1974) p.65.
59. Stanford Synchrotron Radiation Lab. Rpt 78/02, Apr. 1978.
60. F. Wuilleumier and Y. Farge (Editors) Synchrotron Radiation Instrumentation and New Developments, North-Holland, Amsterdam (1978).
61. D.L. Ederer and J.B. West, Synchrotron Radiation Instrumentation, North-Holland, Amsterdam (1980).
62. Y. Talmi (Editor) Multichannel Image Detectors, Am. Chem. Soc., Washington (1979).
63. C.I. Coleman, Photog. Sci. and Engr. 21, 49 (1977).
64. J.B.A. England, Sci. Instr. 9, 233 (1976).
65. L.S. Birks, X-Ray Imaging, SPIE Vol. 106 (1977) p. 19.
66. D.B. Brown et al., J. Appl. Phys., 47, 3722 (1976).
67. J.M. Lavine et al., Int. El. Dev. Mtg. (1980) p. 420.
68. L.F. Thompson and R.E. Kerwin, Ann. Rev. of Matls, Sci., 6, 267 (1976).
69. E. Spiller and R. Feder, Topics in Appl. Phys: X-Ray Optics, Springer-Verlag, Berlin (1977) p. 35.
70. G.N. Taylor, Stanford Synchrotron Radiation Lab Report 79/02, p. 93.
71. P.J. Mallozzi et al., Fundamental and Applied Laser Physics, Wiley Interscience, New York (1971) p. 165.
72. D. Mosher and U.J. Nagel, Unpublished.
73. R.A. Bartolini, Optical Storage Materials and Methods, SPIE Vol. 123 (1977) p.2.
74. T.H. DiStefano (Editor), J.Vac. Sci. Tech., 18, 64 (1981).
75. J. Kosar, Light-Sensitive Systems, Wiley, New York (1965).
76. R.J. Cox (Editor) Non-Silver Photographic Process, Academic Press, New York (1975).
77. G.A. Delzenne, Adv. in Photochem., 11, 1 (1979).
78. V.M. Fridkin, Photoferroelectrics, Springer-Verlag, Berlin (1979).
79. T.S. Narasimhamurty, Photoelastic and Electrooptic Properties of Crystals, Plenum Press, New York (1979).
80. A. Aviram, New Scientist (20 Sept. 1979) p. 881.
81. J.C. Murphy and L.C. Aamodt, Appl. Phys. Lett. 38, 196 (1981).
82. D.S. Lo et al., Optical Storage Materials and Methods, SPIE Vol. 123 (1977) p. 32.
83. B.L. Booth, Optical Storage Materials and Methods, SPIE. Vol. 123 (1977) p. 38.
84. Z.J. Kiss, Physics Today (Jan. 1970) p. 42.
85. T. Kubota and T. Ose, Appl. Optics 18, 2528 (1979).
86. W.E.L. Haas et al., Appl. Phys. Lett., 29, 631 (1976).
87. G. Bauer Measurement of Optical Radiations, Focal Press, London (1965).
88. R.J. Keyes (Editor) Optical and Infrared Detectors, Springer-Verlag, Berlin (1977).
89. R.H. Kingston, Detection of Optical and Infrared Radiation, Springer-Verlag, Berlin (1978).
90. E. Krikorian (Editor) Infrared Image Sensor Technology, SPIE Vol. 225 (1980).



Gas Scintillation Proportional Counters  
and Other Low-Energy X-Ray Spectrophotometers

William H.-M. Ku and Robert Novick

Columbia Astrophysics Laboratory, 538 West 120th Street, New York, New York 10027

ABSTRACT

For many years, thin-window, single-wire gas proportional counters were the only general-purpose detectors available for nondispersive spectroscopy of low energy X-rays. Their large area, low background, and coarse energy resolving capabilities, combined with their low cost, long lifetime, and ease of operation, made them the workhorse instrument. During the last decade, solid state detectors and, more recently, gas scintillation proportional counters, have slowly replaced the standard gas proportional counter in many applications. Small area ( $0.2 \text{ cm}^2$ ) Si(Li) detectors with 150 eV of FWHM noise have been used for fluorescence spectroscopy above 1 keV. However, their small area and cryogenic operation make these detectors less than ideal. Moreover, the noise in the associated electronics make these detectors useless below 0.4 keV. Gas scintillation proportional counters have now been developed to the point where they are the instrument of choice below 1 keV. Large area ( $>100 \text{ cm}^2$ ) counters with high sensitivity and low noise may be made relatively easily and inexpensively. Resolution sufficient to separate the nitrogen and oxygen K-fluorescence lines have been achieved. Used with micron thin polypropylene windows, these counters have achieved 57% (FWHM) resolution at 149 eV sulfur L line. In addition, we have demonstrated that submillimeter imaging is possible with the gas scintillation proportional counter attached to a multiwire proportional counter. This paper will concentrate on a discussion of the principle of operation and design, and achieved levels of performance for the gas scintillation proportional counter. Where appropriate, their operation and performance will be compared to standard gas proportional counters and solid state detectors.

### I. INTRODUCTION

The detection of low energy X-rays depends on the absorption of the incident photon by an atom, releasing an electron carrying some fraction of the X-ray energy. This electron may generate secondary electrons which can be detected as an electrical signal, or visible or UV light which can be detected in a photomultiplier tube or photoionization detector. The detection of X-ray photons at an energy below  $\sim 2 \text{ keV}$  poses several unique challenges. One problem is absorption of the X-ray photon by the detector window. The probability of a flux  $I$  surviving from an initial value of  $I_0$  after traversing a distance  $x$  (cm) in a material of density  $\rho$  ( $\text{gm/cm}^3$ ) is

$$I = I_0 \exp[-\mu\rho x] \quad (1)$$

where  $\mu$  is the mass absorption coefficient in  $\text{cm}^2/\text{gm}$ . The photoelectric absorption cross section decreases with approximately the  $-8/3$  power of the photon energy and with the fourth power of the atomic number. Therefore, low energy X-ray windows must be made from very thin, low  $Z$  material. An additional problem is that the charge or light signal generated in the capture of low energy X-rays is generally quite small so that some amplification is required before the signal may be recorded or used. The small number of primary interactions also result in large fluctuations in the mean energy recorded for the X-ray photon. At energies below 50 eV, the noise relative to the signal becomes so large, and the attenuation of the window so high, that for all practical purposes detection becomes impossible. We therefore restrict ourselves to a discussion of the detection of X-ray photons between 0.05 and 2 keV.

Three types of instruments are currently available for nondispersive spectroscopy of low energy X-rays: (1) conventional gas proportional counters (PC); (2) gas scintillation proportional counters (GSPC); and (3) solid state detectors (SSD). We shall briefly outline the principle of operation of each type of detector and the advantages and disadvantages of their use in various applications. We shall concentrate our discussion on the operation and design of the GSPC since we believe that it has the greatest promise for low energy X-ray detection.

### II. CONVENTIONAL GAS PROPORTIONAL COUNTERS

The gas proportional counter (PC) is the most commonly-used instrument for low energy X-ray detection. Its design and operation have been widely discussed by many authors.<sup>1,2</sup> In its simplest form, the PC consists of a thin wire, commonly 5-25  $\mu$  tungsten, mounted along the axis of a metal cylinder filled with an inert gas maintained at a pressure of 1 atm. (Fig. 1). An X-ray window made from micron thin polypropylene or some other type of organic film is used to cover an entrance in the side of the grounded cylindrical body. A positive potential of 1-3 kV is applied to the central wire via a resistance of 10-100 M $\Omega$ . A low noise, charge sensitive preamplifier is used to record the charges collected on the anode wire.

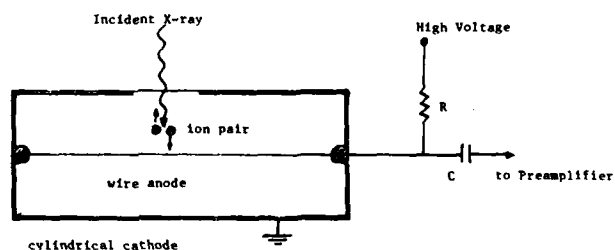


FIG. 1 - Schematic diagram of a conventional gas proportional counter.

#### A. Principle of Operation

Low energy X-ray photons passing through the window interact with atoms in the gas via the photoelectric process. An incident photon  $E_x$ , interacts with an inner shell electron causing it to be ejected, leaving the atom in an excited state. If we denote the energy of the  $j$ th shell by  $E_j$ , photoelectric absorption by the  $j$ th shell results in the emission of a photoelectron of energy  $E_e = E_x - E_j$ . The excited atom can return to its ground state via either the emission of a fluorescence photon, or the ejection of an Auger electron. The electrons released in this process are slowed down by further ionizing collisions with other gas molecules until all the energy of the incident

photon is deposited in the counter. In the case of fluorescence, the secondary photon emitted at an energy just below the absorption edge has a very long mean free path and may escape from the detector volume. The energy deposited in the counter in such a case is  $E_x - E_k$ , where  $E_k$  is the energy of the edge. The probability of such a process occurring and producing an "escape peak" is a function of the fluorescence yield and counter geometry. The fluorescence yield increases with atomic number and is highest for the K-shell electrons.

The number of primary electron-ion pairs created in this process,  $n$ , is proportional to the energy of the incident X-ray. The mean energy to create an ion pair  $W = E_x/n$  is on the order of 25 eV. Thus, a 1 keV photon will generate about 40 electrons. The fluctuation in the number of pairs created in each event is, in general, smaller than that expected from Poisson statistics. Fano<sup>3</sup> showed that the variance, instead of being  $n$ , is given by  $Fn$ , where  $F$  is on the order of 0.2.<sup>4</sup> Mixtures of gases where the excited atoms of the main gas are able to ionize the atoms of the minor gas (Penning mixtures) can yield quite low Fano factors. A value of  $F=0.05$ ,<sup>4</sup> calculated for a mixture of neon plus 0.5% argon, along with a value of  $W = 25.3$ , suggest that a resolution of 8.4% (FWHM) is possible at 1 keV. The only problem is that available charge sensitive preamplifiers cannot detect 40 electrons above the noise; generally, several hundred electrons are required for detection.

To deal with this limitation, conventional proportional counters accelerate the electrons in a high field region after photoelectric capture. These energetic electrons excite other atoms to emit secondary electrons. In this manner, a single electron can give rise to  $10^6$  electrons. The charge multiplication factor

$$M = \exp \left[ \int_{r_a}^{r_c} \alpha(r) dr \right] \quad (2)$$

is a function of  $\alpha$ , the first Townsend coefficient,  $r_a$ , the anode radius, and  $r_c$ , the cathode radius. The first Townsend coefficient is, in general, a complicated function of the electric field but can be approximated by

$$\alpha = pA \exp(-Bp/E) \quad (3)$$

where  $A$  and  $B$  are two characteristic constants of the gas and  $p$  is the pressure of the gas.<sup>5</sup> Charge multiplication introduces additional fluctuations into the total number of electrons collected. Alkhozov<sup>6</sup> has shown that the additional variance factor  $f$ , in the case of low electric fields, is well approximated by

$$f = [1 - 1/M] f_0 \quad (4)$$

Here  $f_0$  depends on  $E/p$  and the type of gas used - it approaches 1 for large values of  $E/p$ . The total relative fluctuation in the measured energy  $\sigma_{E_x}$ , for an incident X-ray of energy  $E_x$ , is then given by

$$\sigma_{E_x} / E_x = [(F + f)W/E_x]^{1/2} \quad (5)$$

The energy resolution is thus dominated by  $f$  at high charge gains but approaches the limit set by  $F$  at low charge gains. Several workers have tried to exploit the good energy resolution at low charge gains. An energy resolution of 10.7% (FWHM) at 6 keV has been obtained with a metastable Penning mixture of Ne-Ar operating at charge gains less than 100.<sup>7</sup> In general, without special low noise charge sensitive preamplifiers, the best energy resolution achievable is 16% (FWHM) at 6 keV.

#### B. Design Considerations

The cylindrical coaxial geometry shown in Figure 1 can be applied to most PC's. The electric field in

this configuration is a maximum at the surface of the central anode wire and decreases as  $1/r$  toward the cathode. Using thin, 5 $\mu$  diameter wires, very high fields can be obtained close to the anode. Multiplication occurs in a narrow region of a few wire diameters around the anode. All the electrons are collected in a few nanoseconds while it takes several hundred nanoseconds for the ions to drift to the cathode and full charge collection to occur. At low high voltages, the total charge collected is roughly constant - this is the ionization chamber regime. Above a certain threshold voltage, the electric field close to the surface is sufficiently large to cause charge multiplication - this is the proportional chamber mode. For the cylindrical geometry, the charge gain for voltages much above the threshold voltage is roughly an exponential function of the reduced electric field ( $E/p$ ). For charge gains less than  $10^4$ , the total charge collected is proportional to the energy deposited. At still higher voltages, the chamber can only maintain limited proportionality before breaking down completely at charge gains of  $10^6$ . In practice, imperfections in the anode wire and consequent distortions in the electric field may limit the ultimate charge gain and result in nonuniform gain response along the wire.

For low energy X-ray detection, the entrance window must be made as thin as possible. Submicron stretched polypropylene film, as well as cast lexan film, have been used with some success. Twenty to fifty percent transmission has been achieved at 0.1 keV with these films.<sup>8,9</sup> The inner surface of the film may be made conductive by coating it either with aluminum or carbon. The best of such thin films leak at rates on the order of  $10^{-4}$  cm<sup>3</sup> atm sec<sup>-1</sup> cm<sup>2</sup>.<sup>9</sup> Given the exponential dependence of charge gain on the pressure, an active flow and regulation system must be used to maintain pressure and gas composition for extended stable operation. The counter need not be exceptionally clean in this mode, although the presence of electro-negative gases such as oxygen and water vapor should be avoided. Otherwise, electron attachment will take place, greatly reducing the mobility of the negative charges. In this event, the charge gain and the energy resolution may be severely degraded. Other than this general proviso, almost any gas may be used in the PC. The properties of a variety of PC gases are summarized in Table 1. Noble gases are usually chosen because

TABLE 1  
Properties of Common Detector Material

Gas	$E_{ex}$ eV	$E_i$ eV	W	$F_{calc}$
He	19.8	24.6	42.8	0.17
N <sub>2</sub>	8.1	15.5	36.0	
Ne	16.6	21.6	36.2	0.17
Ar	11.5	15.8	26.2	0.17
Kr	9.9	13.9	24.3	
Xe	8.3	12.1	21.9	
CO <sub>2</sub>	5.2	13.7	34.2	
CH <sub>4</sub>		13.1	29.8	
TEA		7.5		
TMAE		5.4		
Ne-Ar	16.6	15.8	25.3	0.05
Ar-TMAE			21.9	
Si		1.1	3.6	0.07-0.11
Ge		0.5	2.9	0.09-0.21

AD-A114 893

AMERICAN INST OF PHYSICS NEW YORK  
LOW ENERGY X-RAY DIAGNOSTICS - 1981.(U)  
1981 D Y ATTWOOD, B L MENKE

F/G 14/2

AFOSR-TSSA-81-00024

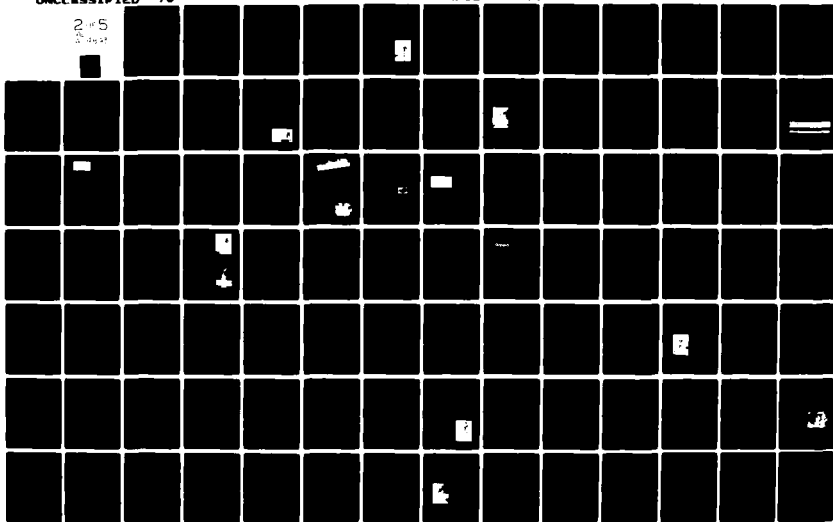
UNCLASSIFIED

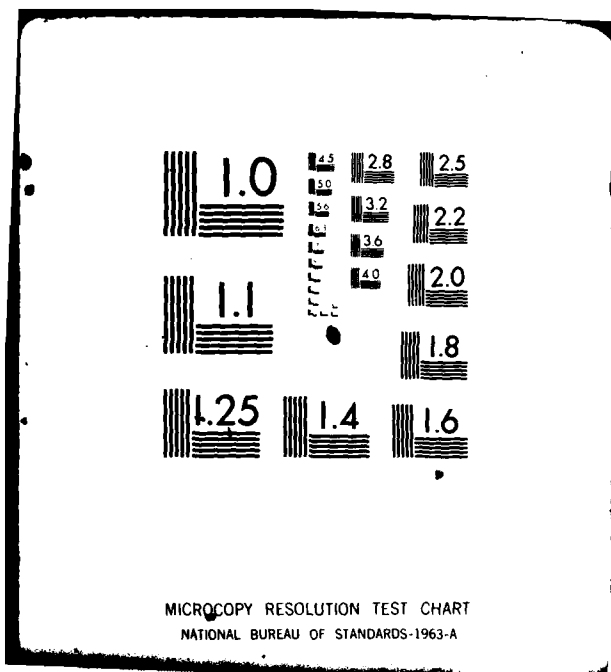
75

AFOSR-TR-82-0378

ML

2 of 5  
12/24/81





MICROCOPY RESOLUTION TEST CHART  
NATIONAL BUREAU OF STANDARDS-1963-A

avalanche multiplication takes place at much lower voltages in these gases than in gases with complex molecular structure. PCs filled with noble gases may become unstable at charge gains exceeding  $10^3$  due to the ejection of late electrons from the wire by UV photons from the avalanche or by excited ions interacting with the chamber walls. The addition of 5-10% of a quench gas such as methane or carbon dioxide will absorb most of the unwanted UV photons, deexcite the ions, and stabilize the avalanche. Charge gains in excess of  $10^6$  may then be obtained before discharge. One drawback to the use of quench gases is that some of the molecules may polymerize after extended exposure to ionizing radiation and coat the cathode, preventing the immediate collection of ions. Under high radiation flux operation, the density of charges enveloping the insulated cathode is so high that continuous discharging may occur. When this happens, the counter must be disassembled and the cathode thoroughly cleaned.

While single anode, cylindrical proportional counters still find use, much of the work in recent years has dealt with multiwire proportional counters (MWPC). These devices have found wide application since the original work of Charpak and his group at CERN.<sup>10,11</sup> Detailed discussions of these position-sensitive counters may be found elsewhere in these Proceedings. We shall only briefly discuss the MWPC as we have applied it to the GSPC in the following section.

### III. GAS SCINTILLATION PROPORTIONAL COUNTERS

Gas scintillation proportional counters (GSPC) were originally developed by Grün and Schopper<sup>12</sup> more than 30 years ago but did not come into wide use until Policarpo and his colleagues stimulated their revival in the early seventies. The results from this and other early work are summarized in a 1977 review paper by Policarpo.<sup>13</sup> Several different variants of the instrument were developed. Three basic geometries were attempted: (1) spherically symmetrical fields supplied by a ball anode in a spherical chamber; (2) radial fields supplied by a coaxial anode in a cylindrical chamber; and (3) uniform fields supplied by a set of parallel grids. A schematic of a parallel grid GSPC is shown in Figure 2. A small thin foil window permits the X-rays to enter a cylindrical glass chamber filled with 1 atm of high-purity xenon. Two transparent mesh electrodes divide the gas volume into three regions. The X-rays are absorbed in a deep drift region (A). Under the influence of a very weak field, the photoelectrons ejected in the process of absorption are pulled into a high field region (B) where they can gain enough energy to excite other atoms to radiate. A third section (C) is provided to isolate the quartz UV exit window from the high field region. The UV light that is produced is then viewed by a photomultiplier tube (PMT).

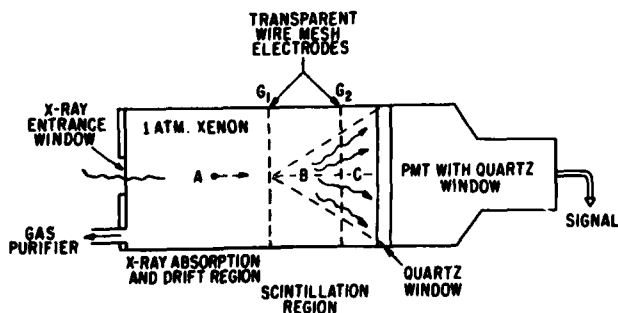


FIG. 2 - Schematic diagram of a parallel plate gas scintillation proportional counter.

### A. Principle of Operation

The GSPC operates on the principle of detecting the light associated with the capture of X-ray photons. As the atoms in the noble gas deexcite, they radiate photons in the ultraviolet region of the spectrum. The spectral distribution of the UV light emitted is shown in Figure 3 for scintillation in argon, krypton, and xenon gas.<sup>14</sup> The number of UV photons associated with the primary absorption process is usually too small to

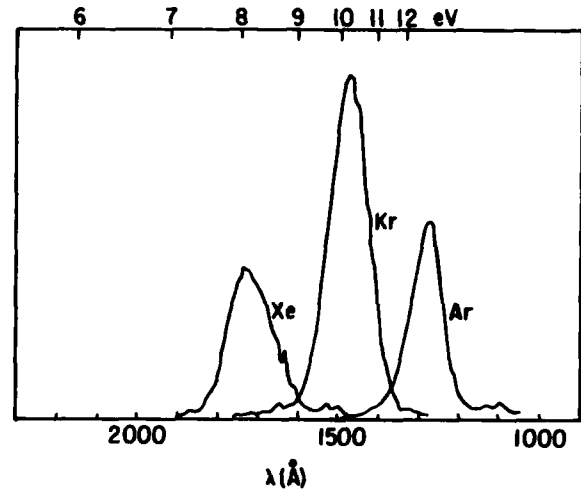


FIG. 3 - Spectrum of light emitted from pure noble gases.

be detected for low energy X-rays. Under the influence of a weak electric field, the primary electrons may gain enough energy between collisions to produce further excitations of the medium. Below a certain threshold, electric field  $E_0$ , light amplification is not possible; above a certain electric field  $E_1$ , charge multiplication begins to play a role. Between  $E_0$  and  $E_1$  the light amplification is essentially a linear function of the field and, at  $E_1$ , is close to 100% efficient.<sup>15,16,17</sup> The critical values of  $E_0$  and  $E_1$  are 900 and 3300 V/cm for krypton, and 700 and 6300 V/cm for xenon.<sup>16</sup>

A counter operated in the electric field regime below  $E_1$  does not suffer from the energy fluctuations associated with charge multiplication. Thus, in theory, the energy resolution predicted by the Fano factor should be achievable. In practice, the energy resolution is also limited by the statistics of the light detection process. If a PMT is used to detect  $N$  photons associated with each X-ray event, the energy resolution is

$$\sigma_{E_x}/E_x = [(F + f)W/E_x + K/(K - 1)N]^{1/2} \quad (6)$$

where  $K = 7 - 10$  is the gain of the first dynode of the PMT.  $N$  is a function of  $N_0$ , the number of UV photons generated and the geometry of the counter.  $N$  can be calculated from

$$N = \left[ \left( \frac{E_x}{W_1} \right) (\Delta V) \left( \frac{e}{U} \right) \left( \frac{A}{4\pi} \right) (t_w) (t_m) (e_g) \right] \quad (7)$$

where  $A$  is the solid angle intercepted in steradian measure,  $\Delta V$  is the potential drop across the grids in the GSPC,  $U$  is the mean energy required to generate a UV photon with efficiency  $e$ ,  $t_w$  and  $t_m$  are the transmission efficiencies of the UV window and the meshes, and  $e_g$  is the quantum efficiency of the UV detector. The expression within the brackets is  $N_0$  which depends

on the nature of the gas. In general, the presence of even a minute, ppm amount of water vapor, methane, or any organic molecule, strongly quenches the noble gas scintillation, mainly due to their strong absorption of UV photons and their subsequent deexcitation by non-radiative collisions. It is thus imperative that the purity of the gas be maintained at all times with some form of gettering device.

Equations 6 and 7 suggest that to obtain good energy resolution, one needs to maximize the solid angle intercepted and the quantum efficiency of the UV detector. PMTs cannot be obtained in very large sizes. Their small size (~125 mm dia.) limit the useful X-ray detection area of the GSPC since the solid angle intercepted is not only small but changes as the position of the incident X-ray is moved across a wide X-ray window. Attempts to focus the electrons into a small, well-defined light producing region have helped to reduce the amount of light fall-off near the edge of the counter.<sup>18,19</sup> An additional problem with PMTs is that their quantum efficiency at UV wavelengths is rather poor, and much work was done originally with wavelength shifters inside the counter which often created more problems in terms of purity and stability than they solved.

More recently, Policarpo has suggested substituting a photoionization detector (PID) for the PMT.<sup>20</sup> In order for such detectors to work, a gas with a suitably low ionization potential is required. Triethylamine (TEA) with an ionization potential of 7.5 eV was originally suggested by Charpak, Policarpo, and Sauli.<sup>21</sup> Subsequently, Anderson<sup>22</sup> discovered Tetrakis (Dimethyl-amino) ethylene (TMAE) with an ionization potential of 5.4 eV is best matched for xenon emission. If  $L$  denotes the ratio of the number of primary ion pairs created in the PID in the capture of UV photons generated by an X-ray of energy  $E_x$  interacting in the GSPC to the number of primary ion pairs created in the direct capture of the X-ray in the PID, the combined energy resolution of the two-stage device is then given by

$$\sigma_{E_x}/E_x = [(F + f_1)W_1/E_x + (1 + f_2)W_2/LE_x]^2 \quad (8)$$

Here  $W_1$  and  $W_2$  are the mean energies required to create an electron-ion pair in the GSPC and the PID, respectively, and  $f_1$  and  $f_2$  are the charge multiplication factors for the two stages. Compared to the PMT, the solid angle of UV photons intercepted by a large area PID is considerably larger - approaching  $2\pi$ . The only question is whether the quantum efficiency is improved.

Some work on the ionization properties of TMAE, TEA, and other low ionization potential gases have now been done. Early results suggest that the quantum efficiency of TMAE absorption of UV photons generated by xenon and krypton is very efficient - on the order of 60% or higher<sup>16,23,24</sup> - considerably higher than the 20% or so found for alkali photocathodes to xenon light (see Figure 4). The only drawback to TMAE is that TMAE vapor pressure at room temperature is only 0.35 torr and the  $1/e$  absorption depth in TMAE for xenon light is 23 mm at 20°C.<sup>24</sup> A deep absorption region is, therefore, required in a TMAE PID. TEA is found to have much higher vapor pressure at room temperature and the effective absorption length is approximately 30 times shorter. TEA, however, cannot be used to detect xenon light and its integrated quantum efficiency for krypton light is about a factor of two lower than that of TMAE. The quantum efficiency of TMAE for argon scintillation has not yet been determined, but it is estimated to be greater than 10%. The addition of a small amount of xenon can shift argon light to lower frequencies, permitting more efficient detection with TEA or TMAE.<sup>25</sup> The use of an argon-xenon mixture may also improve the energy resolution due to the existence of a nonmetastable Penning effect,<sup>26</sup> reducing the Fano factor.

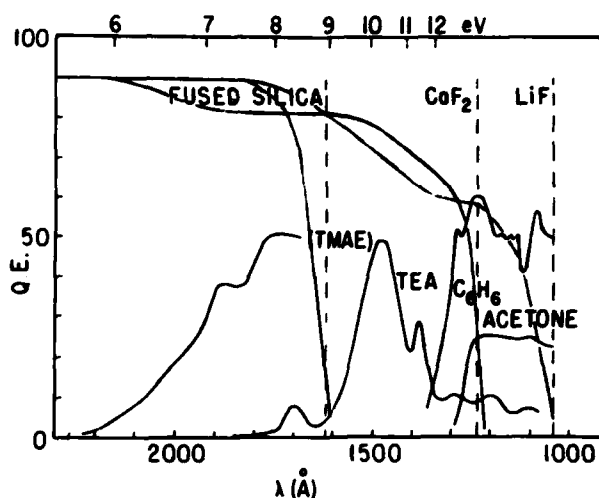


FIG. 4 - Quantum efficiency of UV sensitive gases and transparency of UV windows.

The use of the PID has also permitted a more accurate determination of the quantum efficiency of the light-production process in pure noble gases since the major uncertainty - glass windowed PMTs and wavelength shifters - has been eliminated. Recent results suggest that the quantum efficiency of the photon generation process in pure noble gases is quite high. A scintillation efficiency of  $(97 \pm 20)\%$  has been measured for krypton.<sup>27</sup> We suspect that the scintillation efficiency for xenon, contrary to several earlier measurements, is greater than 50% - also approaching 100%. These results suggest that the number of photons generated is close to the energy acquired in the electric field of the light-producing region by the electron, divided by an energy close to the average energy of the photon emitted ( $U = 10.2$  eV for krypton and  $U = 8.7$  eV for xenon).<sup>16</sup> Given such high quantum efficiencies for both UV photon generation and capture, equations 7 and 8 with  $L = NW_2/E_x$  predict that an energy resolution of better than 7% (FWHM) should be achievable at 6 keV.

#### B. Further Design Considerations

Many improvements have been made in the design of GSPCs in the last 5 years, which have extended the usefulness of the instrument to several different branches of science. Construction and purification techniques have been improved to such a stage that 7.5% (FWHM) spectral resolution has been achieved at 6 keV.<sup>28</sup> Much effort has been expended by several groups,<sup>29,30,31</sup> including ours<sup>32,33</sup> to extend the useful spectral range of the GSPC. These efforts have demonstrated that the GSPC is linear and maintains its good energy resolution from 0.1 to 120 keV. Figure 5 shows the kind of spectral resolution achievable at low X-ray energies.<sup>33</sup>

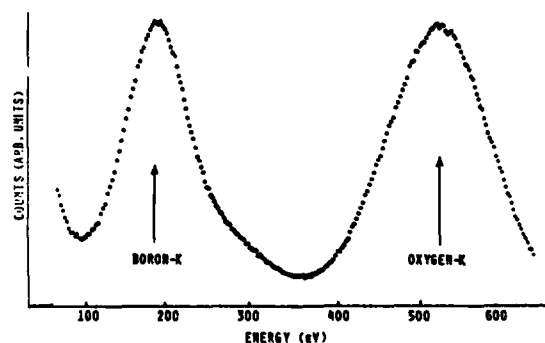


FIG. 5 - Measured energy resolution of GSPC at boron-K (60% FWHM) and oxygen-K (27% FWHM).

Various efforts to focus the primary electrons generated by X-rays captured over a wide window<sup>18,19</sup> have culminated in the construction of conical GSPCs with uniform gain and energy resolution over several hundred square centimeters of area. Work done with pulse shape analysis<sup>32,34</sup> has shown that charged particles may be distinguished from X-ray events by differences in the times required for total light collection. X-rays have a well-defined, narrow, rise-time spectrum (widths narrower than 10% have been achieved) compared to a generally broad distribution for charged particles. Background rejection efficiencies of 97% have been reported.<sup>35</sup> Large area GSPCs have also been used successfully in fast timing applications where time resolutions of 0.1  $\mu$ s have been achieved,<sup>36</sup> as well as in high flux situations where rates of 90 KHz have been obtained without significant peak shifts.<sup>37</sup> More recently, several groups have demonstrated that millimeter spatial resolution is now possible with the GSPC.<sup>29,33,38,39</sup>

Most of these performance improvements have been achieved with the GSPC and PMTs. We believe that the combination of the GSPC and the PID should do as well, and perhaps better, in all respects. We shall, therefore, concentrate on a detailed description of the design of a GSPC plus PID. Large area GSPCs have now been made with the uniform field geometry shown in Figure 6.

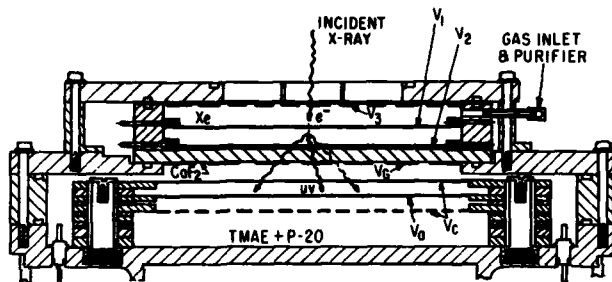


FIG. 6 - Schematic diagram of a GSPC plus a PID.

The basic elements are very similar to the counter pictured in Figure 2. The instrument consists of a pill-box shaped, parallel grid GSPC mounted on top of a PC - actually a MWPC. X-rays enter the 150 mm dia. ceramic bodied GSPC through a 75 mm dia. micron-thin polypropylene window. These photons are absorbed by noble gas atoms in a 12 mm deep drift region. Photoelectrons ejected from the noble gas are accelerated in a moderate electric field defined by two stainless steel, etched meshes held at high voltages  $V_1$  and  $V_2$ . These electrons excite other molecules to emit more UV photons. These secondary photons may be observed through a calcium fluoride, lithium fluoride, or spectroil window (see Fig. 4).

The UV transparent disk also forms the window for the MWPC below. The MWPC is a 30 cm  $\times$  30 cm  $\times$  5 cm aluminum box filled with a UV sensitive gas (Benzene, TEA, or TMAE), plus argon and a quench gas. The choice of the gas fill and the window material is a function of the spectrum of the noble gas in the GSPC (see Figs. 3 and 4). The UV photon ejects a photoelectron from the low ionization potential gas. These electrons then drift in a low field region defined by a grounded stainless steel mesh located on the lower surface of the UV window and a cathode wire plane located 11 cm below, held at a potential of  $V_c$ . The cathode plane is made from 63  $\mu$  dia. silver-plated beryllium copper wire set at 0.55 mm pitch on a 133 mm span. These wires are grouped together into 20 sets of 11 wires each. The photoelectrons are accelerated through the cathode plane toward a high voltage anode plane located 6 mm away and held at a potential of  $V_a$ . The anode wire plane is made from 20  $\mu$  dia. gold-plated tungsten wire

set at 2 mm pitch. A lower cathode plane, with wires set orthogonal to the wires on the upper cathode plane, defines a total active region of 23 mm deep. The avalanche electrons are collected on the anode wires while the ions are collected on the cathode wires. Large charge pulses are induced on the crossed cathode planes. Spatial information is obtained by calculating the two dimensional centroid of the charge distribution sensed by the grouped cathode wires.<sup>40</sup> Energy information may be obtained by collecting the electrons in a charge sensitive preamplifier attached to the anode plane or by summing the cathode signals.<sup>41</sup>

For optimal performance, the GSPC is evacuated to  $10^{-7}$  torr of vacuum before filling with 99.995% pure argon, krypton, or xenon. A built-in getter is usually required to maintain gas purity and high resolution performance in the GSPC. This may be calcium turnings or the SAES model ST171/HI/16-10/300 room temperature getter. The ceramic body may be assembled with viton O-rings, but to ease the burden on the getter, epoxying the ceramic body to the aluminum X-ray window frame and the UV window with Epibond 8510 (Furane Plastics) or substituting metal gaskets for the viton, yields better energy resolution. Micron thin polypropylene windows have been used successfully with the GSPC. As long as the counter is clean, the outside of the film window is vacuum, and the leak rate is kept sufficiently low (few torr/hour), the counter may be operated in a sealed mode for several days since the light gain is only a linear function of the gas pressure and there is only a single gas. The MWPC is also operated in the sealed mode after careful evacuation of the chamber to  $<10^{-5}$  torr and purification of the TMAE.<sup>22</sup>

#### C. Performance of the GSPC/PIC

The energy resolution of the GSPC/PID has been measured at several energies now. The best energy resolution achieved at 6 keV equals the 7.5% (FWHM) energy obtained with a GSPC and a PMT for a collimated X-ray source.<sup>42</sup> The energy resolution response to a broad diffuse X-ray source is about 1-2% worse due to small variations in gain over the 75 mm dia. window. The energy resolutions measured for low energy X-rays are consistent with an  $E^{-2}$  scaling (see Fig. 7 and eq. 8). The imaging capabilities of the instrument

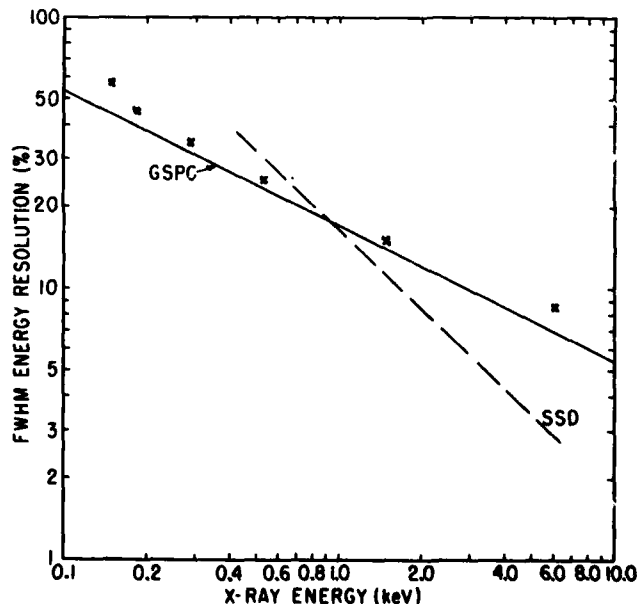


FIG. 7 - Energy resolution versus X-ray energy for a GSPC and a SSD.

should allow us to map the gain variations and correct them so that the large area energy resolution approaches the response to a collimated source. Given the submillimeter resolution measured at 6 keV,<sup>23</sup> such a correction should be possible. The imaging capability, along with the good pulse shape behavior of the signal (2  $\mu$ s with a spread of 8% (FWHM)), should permit excellent rejection of background events. Furthermore, the parallel-grid geometry permits straightforward upscaling of the detector size for increased sensitivity. This geometry should also permit easy extension of the instrument bandwidth to higher energies by simply increasing the depth and pressure of the xenon gas. Finally, the use of a pure gas in the GSPC should avoid lifetime problems due to aging effects mentioned earlier for conventional PCs. We have not yet measured the ultimate lifetime of the low ionization potential gases in PID, but we can say that such counters have operated stably on the timescale of months.

#### IV. SOLID STATE DETECTORS

##### A. Principle of Operation

A solid state detector (SSD) is essentially a junction between n-type and p-type silicon or germanium wafers operating under reverse-bias conditions (Fig. 8).

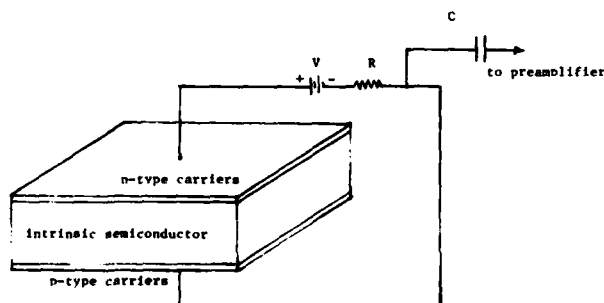


FIG. 8 - Schematic diagram of a simple semiconductor detector.

A strong electric field applied through metallic contacts sweep out the charge carriers in the semiconductor forming a depletion layer. The absorption of an incident X-ray causes electron-hole pairs to form, which then move toward their respective electrodes. The energy needed to create an ion-pair is 2.9 eV for Ge and 3.5 eV for Si, yielding a larger primary charge signal than the capture of X-rays by a gas. This, along with the calculated values of 0.1 or less for the Fano factor of silicon and germanium, leads to the higher energy resolution promised by solid state detectors.<sup>4</sup> However, no multiplication is available so that cooled, low noise preamplifiers are required to maintain good energy resolution.

A commonly used detector for low energy X-rays is the lithium-drifted silicon detector. In this device, the acceptors in a p-type silicon wafer are compensated by donor impurity atoms which are drifted into the material at a raised temperature and under an applied electric field. The material thus produced has high resistivity and low noise. Excess lithium forms the n-layer. These detectors have to be maintained at liquid nitrogen temperatures at all times to ensure that the lithium atoms occupy correct positions in the silicon lattice. Operation at very low temperatures is also required to reduce thermal electron-hole pair creation. Energy resolutions of 2.3% (FWHM) at 6 keV have been obtained with commercially available 12 mm<sup>2</sup> silicon detectors. The energy resolution behavior of a

9-mm dia. Si(Li) flown on the *Einstein* Observatory is shown in Figure 7.

##### B. Comparative Advantages and Disadvantages

SSDs offer the best energy resolution available on paper. However, achieving such resolutions with high efficiencies is extremely difficult in practice. Firstly, the requirement of a conducting electrode over the entrance window limits the transmission efficiency to less than 10% below 0.4 keV. For high purity germanium detectors, the existence of a 0.4 micron dead layer near the entrance renders them effectively useless below 2.3 keV.<sup>43</sup> Secondly, the requirement of low capacitive noise limits the useful effective areas of the silicon detectors. In fact, to compete against the GSPC in resolution below 1 keV, Si(Li) detectors larger than 1 cm<sup>2</sup> cannot be used. Thirdly, the semiconductor material offers no simple discrimination against background events. To separate charged particle events from X-ray events, bulky solid scintillator shields have to be constructed. Finally, the requirement of cryogenic operations makes silicon detectors inconvenient to use. While room temperature mercuric iodide detectors have now been used successfully to detect X-rays down to F-K<sup>44</sup>, their spectral resolution below 2 keV is worse than that of the GSPC.

#### V. CONCLUSIONS

Depending on the users' needs, conventional gas proportional counters, gas scintillation proportional counters, and solid state detectors may all be used for low energy X-ray detection. For situations where the X-ray flux is high and very much above the background, the high energy resolution of a small area (0.2 mm<sup>2</sup>) Si(Li) detector offers the best results above 1 keV. For work which does not require good spectral resolution, conventional gas proportional counters should continue to find use. In general, however, X-ray detection below 2 keV can be most versatily handled by GSPCs. These devices offer all the advantages of conventional PCs - large area, low background, low cost, long lifetime, and ease of operation - with the added feature of improved spectral resolution. As Figure 7 shows, resolution sufficient to resolve the nitrogen and oxygen K-fluorescence lines has been achieved. Combined with its millimeter imaging capabilities, the GSPC promises to be the instrument of choice for low energy X-ray detection.

We gratefully acknowledge useful discussions with Dr. David Anderson at Los Alamos Scientific Laboratories. This work was supported by the National Aeronautics and Space Administration under grant NGR 33-008-102. This is Columbia Astrophysics Laboratory Contribution No. 209.

#### REFERENCES

- Rossi, B. B., and Staub, H. H. *Ionization Chambers and Counters*, (McGraw-Hill, New York, 1949).
- Sharpe, J. *Nuclear Radiation Detectors*, 2nd ed., (Methuen, London, 1954).
- Fano, U., *Phys. Rev.*, **72**, 26 (1947).
- Alkhazov, G. D., Komar, A. P., and Vorobev, A. A., *Nucl. Instrum. Methods*, **48**, 1 (1967).
- Korff, S. A., *Electrons and Nuclear Counters*, (Van Nostrand, New York, 1955).
- Alkhazov, G. D., *Nucl. Instrum. Methods*, **89**, 155 (1970).
- Sipila, Heikki, *IEEE Trans. Nucl. Sci.*, **NS-26**, 181 (1979).



8. Barrus, D. M., and Blake, R. L. *Rev. Sci. Instrum.*, 48, 116 (1977).
9. Bleeker, J. A. M., Huizenga, H., Boggende, D., and Brinkman, A. C., *IEEE Trans. Nucl. Sci.*, NS-27, 176 (1980).
10. Charpak, G., Bouclier, R., Bressani, T., Favier, J., and Zupancic, C., *Nucl. Instrum. Methods*, 62, 235 (1968).
11. Charpak, G., *Ann. Rev. of Nucl. Sci.*, 20, 195 (1970).
12. Grun, A. E., and Schopper, E., *Z. Naturforsch.*, 6A, 698 (1951).
13. Policarpo, A. J. P. L., *Space Sci. Instrumentation*, 3, 77 (1977).
14. Suzuki, M., and Kubota, S. *Nucl. Instrum. Methods*, 164, 197 (1979).
15. Alegria Feio, M. *et al.*, *Nucl. Instrum. Methods*, submitted (1981).
16. Breskin, A. *et al.*, *IEEE Trans. Nucl. Sci.*, NS-28, 429 (1981).
17. Feio, M. A., Policarpo, A., Charpak G., and Saudi F., *Nucl. Instrum. Methods*, 176, 473 (1980).
18. Anderson, D. F., Ku, W. H.-M., Mitchell, D. D., Novick, R., and Wolff, R. S., *IEEE Trans. Nucl. Sci.*, NS-24, 283 (1977).
19. Andresen, R. D., Leimann, E.-A., Peacock, A., and Taylor, B. G., *IEEE Trans. Nucl. Sci.*, NS-25, 800 (1978).
20. Policarpo, A. J. P. L. 1978, *Nucl. Instrum. Methods*, 153, 389 (1978).
21. Charpak, G., Policarpo, A., and Sauli, F., *IEEE Trans. Nucl. Sci.*, NS-27, 212 (1980).
22. Anderson, D. F. *Nucl. Instrum. Methods*, submitted (1981).
23. Ku, W. H.-M., and Hailey, C. J. *IEEE Trans. Nucl. Sci.*, NS-28, 830 (1981).
24. Anderson, D. F., *IEEE Trans. Nucl. Sci.*, NS-28, 842 (1981).
25. Salette, M., Leite, S. C. P., Policarpo, A. J. P. L., Alegria Feio, M., and Alves, M. A., *Nucl. Instrum. Methods*, 177, 609 (1980).
26. Kubota, S. *J. Phys. Soc. Japan*, 29, 1017 (1970).
27. Alegria Feio, M., Policarpo, A. J. P. L., Charpak, G., and Sauli, F. *Nucl. Instrum. Methods*, 176, 473 (1980).
28. Peacock, A., Andresen, R. D., Leimann, E.-A., Long, A., Manzo, G., and Taylor, B. G., *Nucl. Instrum. Methods*, 169, 613 (1980).
29. Nguyen Ngoc, H. Jeanjean, J., Itoh, H., and Charpak, G. *Nucl. Instrum. Methods*, 172, 603 (1980).
30. Koyama, K., Inoue, H., and Matsuoka, M., *Nucl. Instrum. Methods*, 148, 257 (1978).
31. Taylor, B. G., Andresen, R. D., Devalaar, J., Manzo, G., Peacock, A., *IEEE Trans. Nucl. Sci.*, NS-28, 861 (1981).
32. Ku, W. H.-M., Anderson, D. F., Hamilton, T. T., and Novick, R., *IEEE Trans. Nucl. Sci.*, NS-26, 490 (1979).
33. Hamilton, T. T., Hailey, C. J., Ku, W. H.-M., and Novick, R., *IEEE Trans. Nucl. Sci.*, NS-27, 190 (1980).
34. Andresen, R. D., Leimann, E.-A., Peacock, A., and Taylor, B. G., *Nucl. Instrum. Methods*, 146, 391 (1977).
35. Manzo, G., Peacock, A., Andresen, R. D., and Taylor, B. G., *Nucl. Instrum. Methods*, 174, 301 (1980).
36. Bocklin, S. *et al.*, *Nucl. Instrum. Methods*, 176, 105 (1980).
37. Alves, M. A. F., Policarpo, A. J. P. L., Dos Santos, M. C. M., *Nucl. Instrum. Methods*, 111, 413 (1973).
38. Taylor, B. G., Devalaar, J., Manzo, G., and Peacock, A., *IEEE Trans. Nucl. Sci.*, NS-28, 857 (1981).
39. Siegmund, O., Sanford, P., Mason, I., Culhane, L., Kellock, S., Cockshott, P., *IEEE Trans. Nucl. Sci.*, NS-28, 478, (1981).
40. Charpak, G., *Nature*, 270, 479 (1977).
41. Reid, P. B., Ku, W. H.-M., Long, K. S., Novick, R., and Pisarski, R. L., *IEEE Trans. Nucl. Sci.*, NS-26, 46 (1979).
42. Anderson, D. F., private communication (1981).
43. Llacer, J. *et al.*, *IEEE Trans. Nucl. Sci.*, NS-24, 53 (1977).
44. Dabrowski, A. J. *et al.*, *IEEE Trans. Nucl. Sci.*, NS-28, 536 (1981).



Dr. William Ku of Columbia describing the advantages of gas scintillation proportional counters.

Low Energy X-Ray Spectroscopy with Crystals and Multilayers

B. L. Henke

University of Hawaii, Department of Physics and Astronomy, Honolulu, Hawaii 96822

## ABSTRACT

The molecular and sputtered/evaporated multilayers and the acid phthalate crystals can be applied for relatively fast, high efficiency spectral analysis of constant and pulsed low energy x-ray sources in the 100 to 2000 eV region. Limits of resolution are about 1 eV. Reviewed here are the basic methods for the theoretical and the experimental characterization of these analyzers as required for absolute x-ray spectrometry. The design and absolute calibration of spectrographs for pulsed low energy x-ray source diagnostics are described.

## I. INTRODUCTION--GRATING VS BRAGG SPECTROMETRY

Generally, the grazing incidence, diffraction grating spectrometry and the large angle Bragg diffraction spectrometry are complementary. Grating spectrographs can yield lower limits of resolution (<0.1 eV) but with relatively small aperture and low dispersion. The crystal/multilayer spectrographs are of higher limits of resolution (>0.5 eV) but with simpler and more flexible large angle geometry and with high dispersion. The crystal/multilayer spectrographs are of large aperture with an overall spectrographic speed that is considerably higher for constant source and somewhat higher for pulsed source spectroscopy. A precise intensity and window profile calibration of the crystal/multilayer instrument is more easily attainable. Having accurately characterized instrument window functions permits an effective resolution enhancement in the crystal/multilayer spectrometry by simple deconvolution procedures. The two spectrographic approaches are clearly complementary, and, ideally, both the grating and the crystal/multilayer spectrographs should be applied for an optimized analysis of many spectroscopic problems. (For a comprehensive review of grating spectrometry, see that by E. Källne in these Proceedings.)

Even with very intense excitation sources such as some synchrotron/storage ring and high temperature plasma sources, it may be that the crystal/multilayer spectrographs must still be used because the number of photons actually available for proper spectroscopic analysis is limited by other factors. The higher spectrographic speed may be required to achieve satisfactory statistics along with high temporal resolution in time-resolved spectroscopy. Primary monochromators may be required for needed selective excitation of spectroscopic samples which in turn may seriously limit the intensity available for high resolution spectroscopy. Finally, the spectroscopic sample may suffer appreciable radiation damage under the excitation dose that may be required for a given spectrographic measurement. An example of this type of problem is shown in Fig. 1. A low energy x-ray spectral analysis for the molecular orbital configuration of the crystalline solid sample of sodium perchlorate by a relatively fast, flat crystal spectrograph requires approximately three hours for one percent statistics. As shown here, with nine-minute scans through this period, the sample is steadily reduced through successive oxidation states with the last scan revealing the molecular orbital spectrum that is characteristic of NaCl. A successful analysis of this sample was possible [1,2] only by distributing the dosage over eight samples using selective excitation by photons of energy for which the photoionization process that is required has the highest cross section and using time

resolved data collection which permitted an extrapolation to a "zero-dose" spectrum. Resolution enhancement was used to bring the energy resolution of this measurement to about 0.5 eV, using a lead myristate, molecular multilayer analyzer.

## CHEMICAL CHANGES

INDUCED BY

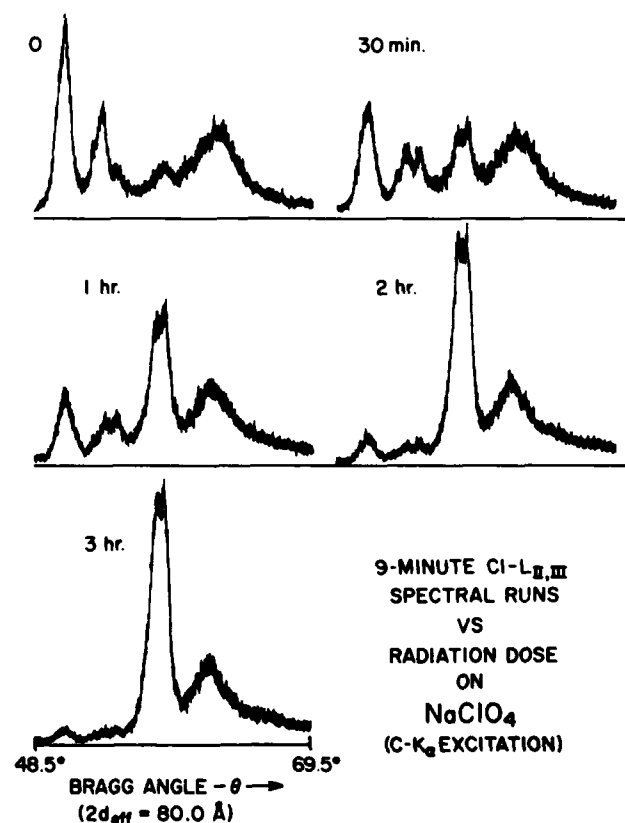
 $1.75 \times 10^{13}$  C-K $\alpha$  (277 eV) PHOTONS/SEC-CM $^2$ 

Figure 1

For high efficiency, low energy x-ray spectroscopy in the 100-2000 eV region, the sputtered/evaporated multilayers, the molecular multilayers (such as the Langmuir-Blodgett type) and the acid phthalate crystals can be used. The total intensity that may be measured within a diffracted spectral line is proportional to the integrated reflectivity,  $R$ , for the given analyzer. In Fig. 2 are plotted the integrated reflectivities for the molecular multilayer, lead myristate, and for the crystal, potassium acid phthalate (KAP), of  $2d$ -values equal to 80 and 26.6 Å, respectively. Suggested here is the fact that this type of molecular multilayer is an excellent analyzer for photon energies below 280 eV (the carbon-K edge) as is the potassium acid phthalate crystal above 530 eV (the oxygen-K edge). For the 300-500 eV region, an appropriately designed sputtered/evaporated multilayer which diffracts this spectral band around 90 degrees from the incident beam direction would be ideal. This requires a  $2d$ -value of about 44 Å for which there are no practical analyzers of the molecular or crystal types at this time.

As discussed elsewhere in these Proceedings by T. Barbee and by E. Spiller, multilayers may be constructed by either sputtering or evaporating in vacuum successive double layers of a variety of low and high atomic number materials. The thickness of the double layer (the  $d$ -spacing) may be as small as about 15 Å. It should be feasible to construct spectrographic analyzers of this type that are very effective in the 300-500 eV region.

The molecular multilayers are obtained by successive dipping of a substrate in and out of a trough of water on which is formed an insoluble monomolecular film. [3] Typically, the lead salts of straight-chain fatty acids are used following procedures that were first described by Langmuir and Blodgett. [4,5,6] A schematic which suggests how these layers (Y-type) deposit upon the substrate is presented in Fig. 3. We have made low energy x-ray analyzers of this molecular type from a series of fatty acids that have  $2d$ -values

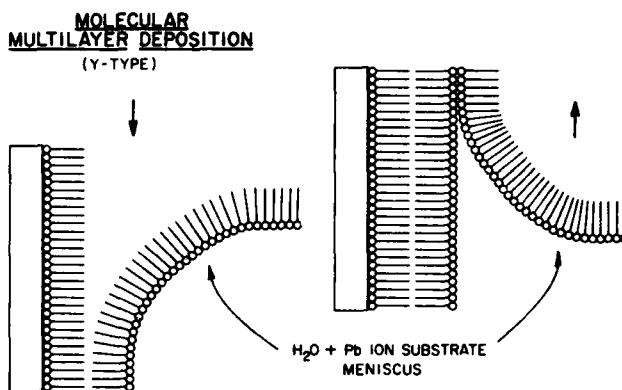


Figure 3

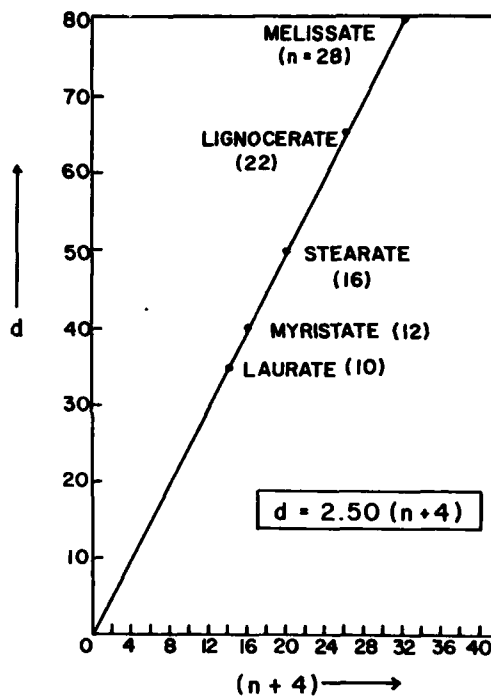
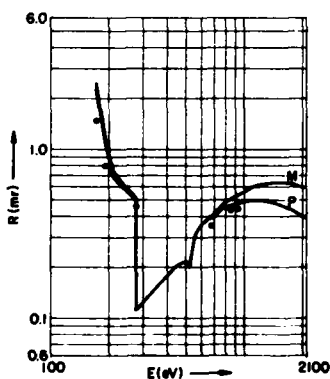


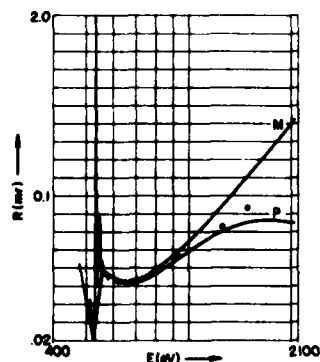
Figure 4



INTEGRATED REFLECTIVITY,  $R$   
LEAD MYRISTATE  
(200  $d$ -SPACINGS)

THEORETICAL  
M-- MOSAIC P-- DARWIN-PRINS

EXPERIMENTAL  
• HENKE, et al (1980)



INTEGRATED REFLECTIVITY,  $R$   
POTASSIUM ACID PHTHALATE (KAP)

THEORETICAL  
M-- MOSAIC P-- DARWIN-PRINS

EXPERIMENTAL  
— BLAKE, et al (1979)  
• HENKE, et al (1980)

Figure 2

LEAD MYRISTATE MOLECULE

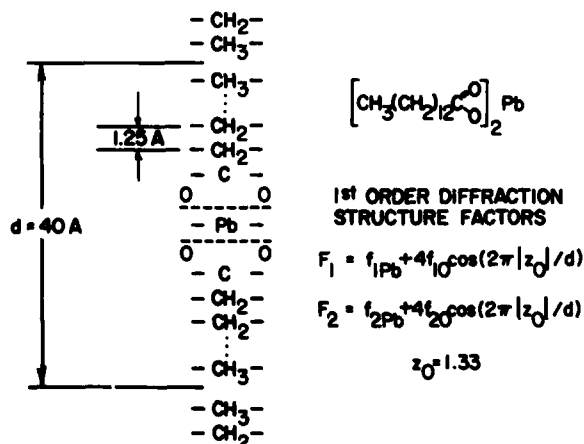


Figure 5

in the range of 70 to 160 Å. In Fig. 4 we present the measured  $2d$ -values as a function of the number,  $n$ , of  $\text{CH}_2$  groups of a lead salt of the straight-chain fatty acids. From this and other crystallographic data, we have constructed a model for the unit cell structure of these systems which is described in Fig. 5 and applied here in a theoretical description of their x-ray reflection characteristics.

The acid phthalate crystals have unit cell structures which have been determined by Okaya [7] and by Smith [8] which we have described and applied in our characterizations of these analyzers as recently reported elsewhere [9]. The practical characteristics of these analyzers are described in detail, experimentally and theoretically, in these Proceedings by R. Blake.

In this review we summarize some of the basic theoretical and experimental methods that may be applied to effectively characterize the crystals and multilayers for well calibrated, low energy x-ray spectrometry. And in the last section we describe spectrographs that have been specially designed for pulsed source diagnostics which utilizes crystal and multilayer analyzers for the low energy x-ray region. Procedures for the application of these spectrographs for absolute, resolution-enhanced spectrometry are outlined.

## II. THE THEORETICAL CHARACTERIZATION OF MULTILAYERS AND CRYSTALS FOR THE LOW ENERGY X-RAY REGION

In a companion paper in these Proceedings [10], the author has derived an expression for the analyzer reflectivity for a finite number of diffracting planes using the Darwin-Prins model. The results may be expressed in terms of complex variables in a form that is easily programmed on a small computer for effective crystal/multilayer characterization. We define:

- $I_N(\theta)$ : the reflectivity curve (rocking curve)--the ratio of the diffracted intensity to the incident intensity for a plane wave at a grazing angle of incidence and reflection,  $\theta$ , and for an analyzer of  $N$  diffracting layers.
- $I_\infty(\theta)$ : the reflectivity curve for an analyzer of an effectively infinite number of diffracting layers (a thick analyzer).
- $s$ : the fractional amplitude, for a plane wave, that is reflected at each diffracting plane.
- $\sigma$ : the fractional decrease in amplitude of the transmitted beam as it passes through each diffracting plane.
- $\xi$ : a small quantity which measures the phase change of the wave incident at angle  $\theta$  as it proceeds from one plane to the next ( $2\pi d \sin \theta / \lambda$ ) through the relation

$$\frac{2\pi d \sin \theta}{\lambda} = \frac{2\pi d \sin \theta_0}{\lambda} + \xi = m\pi + \xi, \quad (1)$$

where  $\theta_0$  is the angle defined by the Bragg relation,  $m\lambda = 2d \sin \theta_0$ .

- $n$ : a small quantity that is used to describe the effective attenuation of a wave as it transmits through  $N$  layers which dynamically includes all contributions from multiple reflections. The amplitude attenuation factor is  $x^N$ , where  $x = (-1)^m e^{-n}$  and

$$n = \pm \sqrt{s^2 - (\xi + \sigma)^2} \quad (2)$$

with + or - sign chosen so that the real part of  $n$  is greater than zero.

We may then write [9]

$$I_N = I_\infty |1 - e^{-2Nn}|^2, \quad (3)$$

where

$$I_\infty = \left| \frac{-s}{(\xi + \sigma) \mp \sqrt{(\xi + \sigma)^2 - s^2}} \right|^2, \quad (4)$$

where the + or - sign is chosen so that  $I_\infty < 1$ .

As described in the companion paper,  $\sigma$  and  $s$  can be calculated in terms of the average atomic scattering factor per unit volume,  $n_f$ , and the structure factor per unit volume,  $\phi F$ , through the relations

$$\sigma = -r_0 \lambda d \frac{n_f}{\sin \theta} \quad (5)$$

and

$$s = -r_0 \lambda d \frac{\phi F}{\sin \theta} P(2\theta) \quad (6)$$

where  $r_0$  is the classical electron radius and for the low energy x-ray region,  $n_f$  and  $\phi F$  can be readily calculated given the structure of the multilayer or crystal system and using the tabulated atomic scattering factors as presented in the Appendix of these Proceedings. In the companion paper [10],  $n_f$  is given by Eq. (5) and (6), and  $\phi F$  is given by Eqs. (32) and (33) for crystals and molecular multilayers and by Eqs. (34) and (35) for the sputtered/evaporated multilayers.

It should be noted that the diffraction order number,  $m$ , and the polarization factor  $P(2\theta)$  are introduced through the reflection parameters,  $F$  and  $s$ . For an incident wave of electric vector in the plane of diffraction,  $P(2\theta)$  is equal to  $\cos 2\theta$  and for the electric vector perpendicular to the plane of diffraction,  $P(2\theta)$  is equal to unity. For incident, unpolarized light, therefore, the corresponding intensity components,  $I_\sigma$  and  $I_\pi$ , are combined as

$$I_N(\theta) = \frac{1}{2}(I_\pi(\theta) + I_\sigma(\theta)).$$

It may be shown that the dynamical model relation for  $I_N(\theta)$  given here in Eqs. (3) and (4) will reduce to the usual kinematical approximation for the analyzer of such low scattering and absorption within the layers that the incident intensity may be assumed to be the same at each plane for the given number of planes,  $N$ . Thus by assuming  $\sigma$  and  $s$  to be very small,  $I_N(\theta)$  becomes

$$I_N = \left| \frac{-s(1 - e^{-2N\xi})}{2\xi} \right|^2.$$

Multiplying by the complex conjugate to obtain this modulus squared, and letting  $\xi$  be replaced by  $\sin \xi$  in the denominator since  $\xi$  is necessarily a small quantity for  $\theta$  near the diffraction peak, we obtain for unpolarized incident radiation

$$I_N = (r_0^2 \lambda^2 d^2) \frac{(\phi F_1)^2 + (\phi F_2)^2}{\sin^2 \theta_0} (1 + \cos^2 2\theta) \frac{\sin^2 N\xi}{\sin^2 \xi}. \quad (7)$$

Because this diffraction peak will be relatively sharp, the parameter,  $\xi$ , may be written from Eq. (1) as

$$\xi = \frac{2\pi d}{\lambda} (\sin(\theta_0 + \Delta\theta) - \sin \theta_0) \approx \frac{2\pi d}{\lambda} \cos \theta_0 \Delta\theta \quad (8)$$

and this kinematical description will assume the familiar form [12]

$$I_N(\Delta\theta) \sim \frac{\sin^2 \left( \frac{2\pi Nd}{\lambda} \cos \theta_0 \Delta\theta \right)}{\sin^2 \left( \frac{2\pi d}{\lambda} \cos \theta_0 \Delta\theta \right)}. \quad (9)$$

Applying the Rayleigh criterion, we define a limit of angular resolution as that  $\Delta\theta_1$  which corresponds to the first minimum of this diffraction pattern. Therefore

$$\frac{2\pi Nd}{\lambda} \cos \theta_0 \Delta\theta_1 = \pi \text{ and } \Delta\theta_1 = \frac{\lambda}{2Nd \cos \theta_0}.$$

Using the Bragg relation  $m\lambda = 2d \sin \theta_0$  and its derivative, we may then find the corresponding wavelength resolution as

$$\Delta\lambda = \lambda/mN \quad (10)$$

and finally, by definition, the resolving power of this analyzer of low attenuation becomes

$$\frac{\lambda}{\Delta\lambda} = mN = \frac{E}{\Delta E} \quad (11)$$

This resolving power is then an upper limit that may be expected of a multilayer of a relatively small number of layers,  $N$ , and at diffraction order,  $m$ .

For some analyzers, particularly for very low energy x-rays and with sputtered/evaporated multilayers, the effective number of diffracting planes may be limited by absorption within the multilayer and the dependence upon  $N$  drops out for  $N$  sufficiently large but finite. If then we consider the absorptive parameter,  $\sigma$ , to be large as compared with the reflective parameter,  $s$ , the reflectivity curve,  $I_N(\theta)$ , from Eq. (3), becomes the Lorentzian function

$$I(\Delta\theta) = \frac{\left(\frac{\omega}{2\pi}\right)R_m}{\left(\Delta\theta - \frac{\delta}{\sin\theta_0 \cos\theta_0}\right)^2 + \left(\frac{\omega}{2}\right)^2} = \frac{\left(\frac{\omega}{2\pi}\right)R_m}{\epsilon^2 + \left(\frac{\omega}{2}\right)^2} \quad (12)$$

This function will have its peak value displaced from the Bragg angle,  $\theta_0$ , by an amount equal to  $\delta/\sin\theta_0 \cos\theta_0$ , which is a refraction shift of the diffraction pattern that may also be predicted by combining the Bragg relation with Snell's law [11,12]. It is interesting to note that this result follows here for the case of relatively high absorption within the analyzer. For this Lorentzian rocking curve approximation, its parameters may be written as follows:

The angle,  $\epsilon$ , as measured from the diffraction peak

$$\epsilon = \Delta\theta - \delta/\sin\theta_0 \cos\theta_0 \quad (13)$$

The full-width-at-half-maximum (FWHM)

$$\omega = 2\beta/\sin\theta_0 \cos\theta_0 \quad (14)$$

The corresponding integrated reflectivity (area under the Lorentzian) for unpolarized incident radiation

$$R_m = \frac{r_0^2 \lambda^4}{16\pi\beta} [(\phi F_1)^2 + (\phi F_2)^2] \frac{1 + \cos^2 2\theta}{\sin 2\theta} \quad (15)$$

Here the optical constants,  $\delta$  and  $\beta$ , are as have been defined in Ref. 10 of these Proceedings to be given by

$$\delta = \frac{r_0 \lambda^2}{2\pi} n\bar{f}_1 \quad (16)$$

$$\beta = \frac{r_0 \lambda^2}{2\pi} n\bar{f}_2$$

The integrated reflectivity,  $R_m$ , that results from this Lorentzian, absorption-limited approximation, is identical to that which may be obtained from the mosaic crystal model [11,12] and as given in Ref. 10.

According to the mosaic crystal model, we may include the effect of a finite crystal thickness by multiplying the expression for  $R_m$  in Eq. (15) by the factor

$$(1 - \exp(-2\mu t/\sin\theta_0))$$

in which  $\mu$  is the mass photoionization cross section for the crystal material,  $\rho$  is the average mass density and  $t$  is the crystal thickness which is approximately equal to  $Nd$ . If the crystal or multilayer has a significant mosaic quality, the FWHM of its rocking curve will be greater than that expected from the perfect crystal model and will normally be determined by measurement. As is illustrated in Fig. 2, this integrated reflectivity,  $R_m$ , generally tends to be higher than  $R_p$ , that as derived by numerically integrating for the area under  $I_N(\theta)$  from Eq. (3). Well defined crystals such

as the acid phthalates, for example, will typically have experimentally measured values for the integrated reflectivity that fall between these values for the mosaic and the perfect crystal models.

As has been discussed in the companion paper of these Proceedings [10], this relatively simple Darwin-Prins model approach for the characterization of low energy x-ray analyzers is generally in good agreement with the rigorous E & M boundary values approach (the characteristic matrix approach) for the perfect multilayer systems. [13,14] Generally, the approximations that are inherent in the Darwin-Prins approach for the finite crystal/multilayer system as has been described here are appropriate inasmuch as the typical real crystal/multilayer system cannot be defined any more precisely than is this approximate model. In the design of low energy x-ray analyzers, particularly of the sputtered/evaporated type, this simple theoretical model can provide helpful, immediate insights as to the interplay of the electron scattering contrast yielded by the structure factors and the multilayer absorption, and their effect upon the analyzer performance. In Fig. 6 the integrated reflectivity,  $R_m$ , from the thick mosaic model, has been plotted for photon energies above the C-K edge and for a variety of practical sputtered/evaporated, equal-thickness double layers of  $d$  equal to 30 Å. For these calculations, structure factors were used as for sharply defined interfaces between the 15 Å layers. As has been discussed in the companion paper [10], the integrated reflectivities would be significantly reduced if a graded-density or rough interface were to be involved.

#### INTEGRATED REFLECTIVITY, $R$ ,

FOR  
SPUTTERED OR EVAPORATED MULTILAYERS  
WITH  
15 Å EQUAL THICKNESS LAYERS --  $2d = 60$  Å

- (A) TUNGSTEN/BORON
- (B) TUNGSTEN/CARBON
- (C) MOLYBDENUM/CARBON
- (D) MOLYBDENUM/TITANIUM
- (E) TITANIUM/CARBON

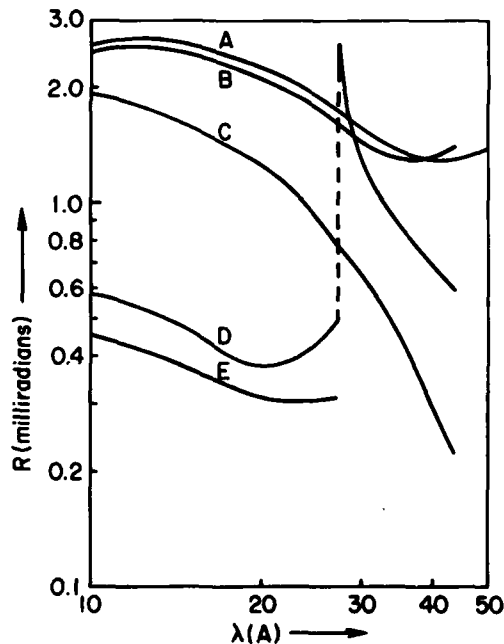


Figure 6

In Fig. 7 we compare the diffraction peak profiles for the lead myristate molecular multilayer and the tungsten-carbon sputtered/evaporated multilayer with the same  $2d$ -value of 80 Å. Here the fractional thickness of the  $d$ -spacing for the heavy layer (tungsten), defined as  $\Gamma$ , is varied. Again a sharply defined interface was assumed for the W/C multilayer which yields appreciably higher predicted peak intensities than are observed relative to those for the lead myristate. The measured angular widths of the rocking curves are in good agreement with these as predicted, however.

### III. THE EXPERIMENTAL CHARACTERIZATION OF MULTILAYERS AND CRYSTALS FOR THE LOW ENERGY X-RAY REGION

The optimized low energy x-ray analyzer will have the maximum, effective number of layers as determined essentially by the crystal/multilayer attenuation. ( $N$  for the multilayers chosen sufficiently large.) For such analyzers the perfect crystal model relation,  $I_{\infty}(\theta)$ , presented here in Eq. (4), predicts a diffraction curve with Lorentzian wings. That is, for angles not close to the peak,  $\xi$  becomes relatively large as compared with  $\sigma$  and  $s$  and the intensity distribution falls off as  $(\Delta\theta)^{-2}$  as for a Lorentzian. As already noted above, for many practical crystals and multilayers applied in the high attenuation, low energy x-ray region, the total profile tends to become Lorentzian.

In Ref. 9 we have calculated in detail the reflectivity characteristics vs photon energy for five acid phthalate analyzers and five each of 100-layer molecular and sputtered/evaporated (tungsten-carbon) multilayers. For such characterizations, we define the integrated reflectivity as the area under the reflectivity curve within the limits of plus/minus  $5\omega$ , (at which limits  $I_N(\theta) \approx .01$ ). We have compared the integrated reflectivity as obtained by precise numerical integration under the theoretical reflectivity curve to that for a Lorentzian curve having the same FWHM,  $\omega$ , and the same peak height as that given by  $I_N(\theta)$ . The two integrated reflectivities generally agree within ten percent. Finally, our measured molecular and sputtered/evaporated multilayer rocking curves, after correcting for instrumental broadening, are well described by Lorentzian fits. Similarly it has been found that the reflectivity curves for the acid phthalate crystals may be described as Lorentzian. [15]

In our experimental characterization of low energy x-ray analyzers, therefore, we assume that the reflectivity curve is essentially Lorentzian which may be then described by the relation

$$I(\epsilon) = \frac{(\omega/2\pi)R}{\epsilon^2 + (\omega/2)^2} \quad (17)$$

#### A. THE MEASUREMENT OF THE FWHM- $\omega$

Our measurements of  $\omega$  for a given analyzer are of a series of monochromatic line sources which are Lorentzian in their wavelength and photon energy distribution and produce an equivalent angular broadening of the spectral line equal to  $\epsilon_0$ . A conventional, flat crystal spectrograph is used with soller slit collimation that presents a further angular broadening of a Gaussian shape and of FWHM equal to  $g$ . Pulse height discrimination is utilized with a flow proportional counter to minimize background under the isolated spectral line.

The convolution of Lorentzians yields another Lorentzian with the widths adding linearly. The convolution of Gaussians yields another Gaussian, but with the widths adding quadratically. Because in many spectroscopic measurements the collimation is Gaussian, the measured spectral line is the result of a convolution of a Gaussian collimation function with a Lorentzian analyzer plus emission line profile. The Gaussian-Lorentzian convolution yields a Voigt curve for which there is no exact analytical function

### COMPARISON OF MOLECULAR AND SPUTTERED/EVAPORATED MULTILAYERS AT Mo-M $\alpha_1$ (64.4 Å/192.3 eV)

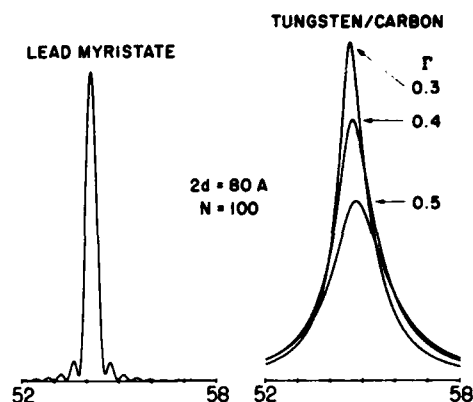


Figure 7

description.

We have shown [1] that within a sufficiently good approximation, the Voigt function can be described simply as a linear mixing of the two basic broadening functions, the Gaussian,  $G(x)$ , and the Lorentzian,  $L(x)$  through the relation

$$V(x) = \delta G(x) + (1 - \delta)L(x). \quad (18)$$

If we define the FWHM widths for the Gaussian, the Lorentzian and their fold, the Voigt function by  $g$ ,  $l$  and  $v$ , respectively, and the variable  $x$  by  $\epsilon/v$  ( $\epsilon$  is the angle from the peak), we may then write

$$G(x) = e^{-(\ln 2)x^2} \quad \text{and} \quad L(x) = \frac{1}{1+x^2} \quad (19)$$

and the mixing parameter,  $\delta$ , becomes

$$\delta = 1 - l/v \approx (g/v)^2. \quad (20)$$

In our crystal characterizations,  $l$  represents the sum of the Lorentzian crystal multilayer and emission line widths,  $\omega + \epsilon_0$ , and we may write for the analyzer width,  $\omega$ , from Eq. (20)

$$\omega = v(1 - (g/v)^2) - \epsilon_0. \quad (21)$$

These numerically derived relationships have been tested on a series of low energy x-ray emission lines for which the natural widths have been precisely measured using photoelectron spectroscopy. [1] We illustrate in Fig. 8 how the Mo-M $\alpha_1$  (64.4 Å/193 eV) line is used to determine the lead myristate molecular analyzer diffraction width,  $\omega$ , to be  $0.33^\circ$  and, equivalently, in energy width, 0.82 eV. These values may be compared with those as determined from the theoretical reflectivity curve,  $I_N(\theta)$ , given in Eq. (3) to be  $0.36^\circ$  and 0.89 eV, respectively.

#### B. THE MEASUREMENT OF THE INTEGRATED REFLECTIVITY, R

Practical flat crystal calibration for the integrated reflectivity,  $R$ , usually involves incident beams which are neither precisely monochromatic nor parallel. Let the incident beam be of cross section that is smaller than the window area of the detector and be of total direct beam intensity  $P_0$  counts per second. Consider the beam to be made up of a collection of rays with a narrow distribution of angular divergence about a central ray and each with intensity,  $\Delta P_{0n}$ . The intensity that is reflected for the  $n$ th ray near a  $\theta$  incidence angle is  $\Delta P_n$ . Then if  $I_N(\theta)$  is the reflectivity, we may write

MOLYBDENUM-M<sub>α</sub> (64.5 A/192.3 eV)  
AS MEASURED BY A  
LEAD MYRISTATE ANALYZER (2d--79.9 A)

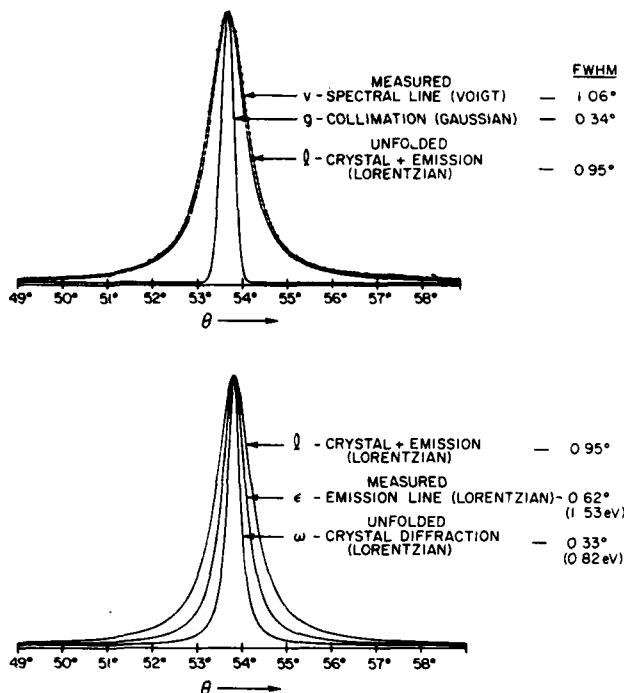


Figure 8

$$\Delta P_n = \Delta P_{0n} I_N(\theta)$$

Let the crystal be rotated through a range in  $\theta$  that completely embraces a diffraction peak for all incident rays and at an angular rate of  $\omega_0$ . If  $dE_n$  is the total counts measured by the detector for the  $n$ th ray during interval  $dt$ , we may write

$$dE_n = \Delta P_{0n} I_N(\theta) dt = \Delta P_{0n} I_N(\theta) (d\theta/\omega_0)$$

and

$$\Delta E_n = (\Delta P_{0n} \omega_0 \int I_N(\theta) d\theta) = (\Delta P_{0n} / \omega_0) R$$

Now summing over all  $n$  rays in the divergent incident beam, we obtain the total counts collected,  $E$ , as a diffraction peak is scanned as

$$E = \sum_n \Delta E_n = \frac{1}{\omega_0} R \sum \Delta P_{0n} = \frac{P_0 R}{\omega_0}$$

And thus  $R$  may be expressed in terms of measurable quantities as

$$R = \frac{E \omega_0}{P_0} \quad (22)$$

If the incident beam is not precisely monochromatic, but consists of a narrow band of wavelengths about a mean value, a similar argument as presented above may be applied to yield the same result as Eq. (22), where  $R$  would then represent an integrated reflectivity characteristic of an average wavelength. This follows from the fact that the intensity distribution for a variable wavelength component is simply shifted a small amount in angle according to the Bragg relation--but still embraced in the complete scan taken over the diffraction peak. The value of  $R$  thus determined is independent of a small departure from monochromaticity of the beam--providing that the reflectivity is slowly varying over the spread in wavelengths involved.

In Figs. 9 and 10 we have applied this flat crystal calibration procedure in order to compare the performance of a molecular and a sputtered multilayer in the 500-1000 eV photon energy region. The sputtered multilayer, constructed by T. Barbee, has a  $2d$ -value of 44.2 Å,  $N = 62$ , and  $\Gamma = 0.3$ . The molecular multilayer is lead myristate of  $2d$  equal to 80 Å and  $N = 200$ . These comparative spectral scans of characteristic line radiations were taken with soller slit collimation of Gaussian, FWHM value,  $g$ , equal to 0.34 in  $\theta$ -coordinates. The multilayer angular width, FWHM- $\omega$ , was determined using Eq. (21), its integrated reflectivity determined by Eq. (22) and the percent peak reflectivity,  $P$ , assuming a Lorentzian reflectivity curve as in Eq. (17), and equal to  $[2R/\pi\omega] \times 100$ .

With calibrated crystal/multilayer analyzers, and instrument collimation window functions, and with the measured spectral line widths, Eq. (21) may then be used to determine the emission line width with enhanced resolution. We have developed a simple method for treating overlapping spectral lines [1] by fitting a sum of Voigt functions as given in Eq. (18) by a Simplex method which fitting determines the angular position, weight and width of each component lines in the overlapping spectrum. Eq. (21) is then used to determine the individual emission line widths. Again, enhanced resolution is obtained.

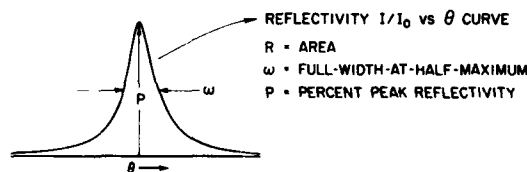
Often, rather than flat crystal optics with essentially parallel incident radiation, divergent beam optics (as with Johann circle geometry) or with non-focussing optics for an instantaneous presentation of an emitted spectrum (for pulsed source spectroscopy) may be used. For spectrographs using these divergent beam geometries, the measured intensity profiles for a monochromatic source may usually be predicted in terms of the flat-crystal reflectivity characteristic parameters and appropriate geometric factors. This is illustrated in the next section for the pulsed source spectrographs which utilize the cylindrical-convex crystal/multilayer and the elliptical crystal/multilayer.

#### IV. PULSED SOURCE SPECTROSCOPY

##### A. THE CONVEX CYLINDRICAL CRYSTAL ANALYZER

The convex cylindrical crystal [3,16-20] presents to an x-ray source a continuum of reflecting regions with Bragg angles beginning from zero value. For a particular wavelength, the effective aperture is proportional to  $\sin\theta$  and hence to  $m\lambda$  for the usual application geometry in which the cylinder radius,  $r$ , is small as compared with the distance to the source,  $s$ . We have constructed cylindrical analyzers of good quality by bending .005" cleaved sections of KAP to radii as small as one inch, and by dipping polished cylinder substrates of radii as small as a few millimeters to generate the Langmuir-Blodgett type of molecular multilayers. The

##### CHARACTERIZATION OF BRAGG ANALYZERS



COEFFICIENT OF REFLECTION,  $R$ , MEASURED DIRECTLY FROM EXPERIMENTAL DIFFRACTION LINE

$$\omega = v(1 - (g/v)^2) - \epsilon_0 \quad \left\{ \begin{array}{l} v = \text{EXPERIMENTAL LINE WIDTH (VOIGT FWHM)} \\ g = \text{COLLIMATION WIDTH (GAUSSIAN FWHM)} \\ \epsilon_0 = \text{EMISSION LINE WIDTH (LORENTZIAN FWHM)} \end{array} \right.$$

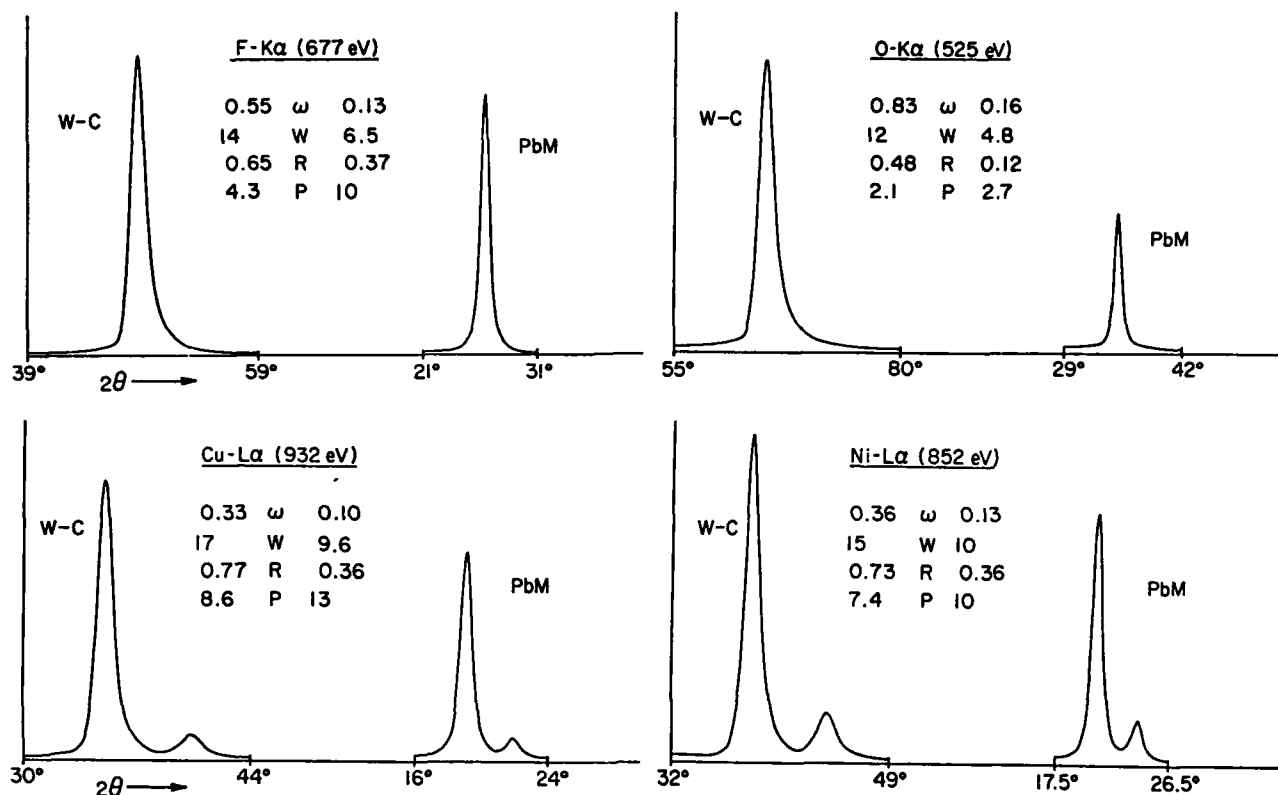
$$P = 100 \frac{2R}{\pi\omega} \quad \text{ASSUMING LORENTZIAN REFLECTIVITY CURVE}$$

$R, \omega, v, g$  and  $\epsilon_0$  ARE IN  $\theta$ -ANGLE UNITS

Figure 9

### COMPARISON OF MULTILAYER ANALYZERS--500-1000 eV REGION

TUNGSTEN-CARBON--62 11-PLUS-11 d-SPACINGS--2d = 44.2 Å  
 LEAD MYRISTATE--200 d-SPACINGS--2d = 80 Å  
 ROCKING CURVE FWHM-- $\omega$ ( $^\circ\theta$ ) AND W(eV)  
 REFLECTIVITY--INTEGRATED, R(mr) PEAK, P(%)



COLLIMATION FWHM (GAUSSIAN)--0.77 $^\circ$  ( $2\theta$ )

Figure 10

sputtered/evaporated multilayers may be deposited upon a flat, flexible substrate which may then be bent to a desired radius.

Some useful geometrical relations which characterize this analyzer are as follows (see Fig. 11):

$$\cos\theta = \cos\chi - (1/\delta)\sin\chi \quad (23)$$

and

$$(d\chi/d\theta) = \delta\sin\theta/(\delta\sin\chi + \cos\chi) \quad (24)$$

in which  $\delta = r/s$ . Now for  $\delta \ll 1$ , it follows that

$$\cos\theta = 1 - \chi/\delta \quad (25)$$

and

$$(d\chi/d\theta) = \delta\sin\theta. \quad (26)$$

To relate the reflecting region position,  $\alpha$ , with the corresponding Bragg angle,  $\theta$

$$\alpha = \theta - \chi = \theta - \delta(1 - \cos\theta). \quad (27)$$

And to relate the position of the detector,  $\beta$ , to the corresponding Bragg angle,  $\theta$ --for  $r \ll R$  (crystal-detector distance)

$$\beta = 2\theta - \chi = 2\theta - \delta(1 - \cos\theta). \quad (28)$$

And, finally, for instruments with  $\delta \ll 1$ , a relation between the divergent beam diffraction line profile,  $dN/d\theta$ , defined as  $P(\theta)$ , produced by the cylindrical crystal and the parallel beam, flat crystal reflectivity ratio,  $I_N(\theta)$ , can be obtained as

$$\frac{dN}{d\theta} = P(\theta) = I(\theta)(i_0 a \psi)(d\chi/d\theta) = \delta i_0 a \psi \sin\theta I(\theta), \quad (29)$$

where  $i_0$  is the number of photons per sec-unit source area-sterradian,  $a$  is the source slit area, and  $\psi$  is the angle at the source slit as subtended by the crystal width, and assuming the slit thickness to be negligible.

The total number of photons,  $N$ , within the diffraction line profile is proportional to the crystal's integrated reflectivity,  $R$ , and given by

$$N = \int P(\theta)d\theta = \delta i_0 a \psi \sin\theta \int I(\theta)d\theta = \delta(i_0 a \psi \sin\theta)R. \quad (30)$$

Finally, to determine the effect of slit or line source width upon the profile, we integrate the differential intensity from a section of the slit of width,  $b$ , and differential thickness,  $s d\phi$ , (as reflected into the diffraction line profile) within the limits  $-\phi_0$  to  $+\phi_0$ , where  $2\phi_0$  is the angular thickness of the slit as measured at the crystal. We obtain, assuming  $I_N(\theta)$  to be Lorentzian, as given in Eq. (17):

$$P'(\theta) = (\delta i_0 b s \sin\theta) \left( \frac{\omega}{2\pi} R \right) \int_{-\phi_0}^{\phi_0} \frac{d\phi}{(\epsilon - \phi)^2 + (\omega/2)^2}.$$



## CYLINDRICAL CRYSTAL GEOMETRY

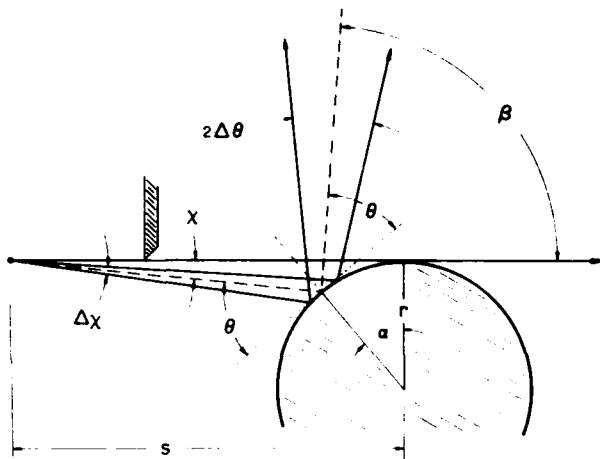


Figure 11

Thus

$$P'(\theta) = (\delta i_0 b \psi \sin \theta) (R/\pi) \left( \tan^{-1} \frac{\epsilon + \phi_0}{\omega/2} - \tan^{-1} \frac{\epsilon - \phi_0}{\omega/2} \right) \quad (31)$$

$P'(\theta)$  has been plotted for several relative values of  $\phi_0/\omega$  in Fig. 12. If the source brightness,  $i_0$ , is not uniform but rather is a function of  $\phi$ , then  $i_0(\theta)$  must be folded within the integral.

## B. THE ELLIPTICAL CRYSTAL/MULTILAYER SPECTROGRAPH

Shown in Fig. 13 are the basic features of the proposed spectrograph for the spectral analysis of a pulsed low energy x-ray source. An elliptically curved crystal or multilayer analyzer is utilized with an effective point or line source at or through one of the foci and a small exit aperture (scatter aperture) at the second focal point. The elliptical analyzer curvature may be a cylindrical section, or it may be of double curvature and as a surface of revolution about the major arcs (an ellipsoidal section).

Considerable importance in the design of this spectrograph [21] has been placed upon achieving a minimum of background radiation and presenting a spectrum that can be simply and accurately interpreted to yield the source spectral characteristics in the low energy x-ray region. The small scatter aperture into the detector module effectively eliminates the stray radiation that may diffusely scatter or fluoresce from the analyzer. An optically flat or cylindrically curved total-reflection mirror with an adjustable entrance slit along with an appropriate filter is used for an effective attenuation of high-order diffracted and the lower-energy radiation background. If the slit at the mirror is adjusted for a sufficiently small entrance aperture, a one-dimensional spatial distribution of the source intensity for the particular wavelength can be presented along the length of a corresponding spectral line for an extended source (spatial resolution in the tenth milliradian range). The spectrum is formed by a relatively small analyzer dimension normal to this drawing section so that the analyzers can thus be "stacked" for multiple band spectral coverage. This is described in Fig. 14.

The elliptically curved crystal/multilayer substrates have been made by computer controlled milling and by computer controlled diamond turning of aluminum blanks. [22] The acid phthalate cleaved sections of about .005" thickness and coverslip glass of about .010" thickness are epoxied to the curved surfaces under

light pressure. The molecular multilayers are deposited directly upon the coverslip glass curved surfaces. The coverslip glass pieces are preformed in an oven to fit a graphite substrate of identical shape as the aluminum substrates.

The diffraction geometry is shown in Fig. 15. In order to establish a focal point for radiation from a small source and thereby an effective scatter aperture, the analyzer curvature is that for the ellipse

$$\rho = \frac{h}{1 - e \cos \beta} \quad (32)$$

where  $e$  is its eccentricity and  $h$  is the characteristic radial distance,  $\rho$ , from the exit focal point for  $\beta = +90^\circ$ .

An important design feature is that the measured radiation can be normal to a circular arc detection surface (a film surface for photographic detection, a CCD array for electronic detection and for time-resolved spectroscopy, and for a proportional counter goniometer circle in a calibration chamber.) The angular position on this detection circle,  $\beta$ , is related to the Bragg reflection angle off the analyzer,  $\theta$ , by the equation

$$\theta = \tan^{-1} \left( \frac{1 - e \cos \beta}{e \sin \beta} \right) \quad (33)$$

which reduces to simply

$$\theta = \beta/2 \quad (34)$$

for applications with a large source distance (i.e., with an eccentricity,  $e$ , equal to unity for an approximately parabolic analyzer).

## EFFECT OF SOURCE SIZE ON CYLINDRICAL CRYSTAL LINE PROFILE

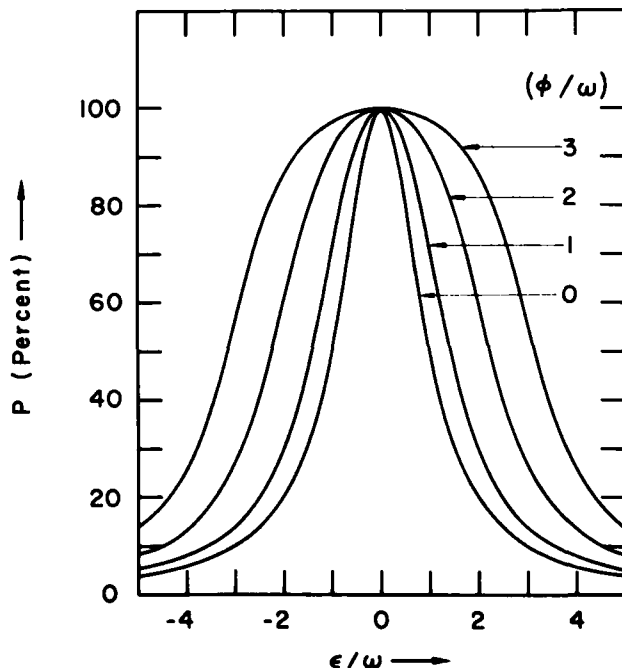


Figure 12

### PULSED X-RAY SOURCE SPECTROSCOPY

ELLIPTICALLY CURVED ANALYZING CRYSTAL

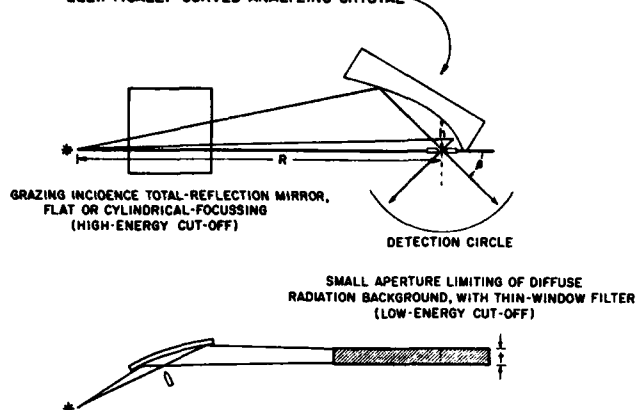


Figure 13

In Fig. 15 we define the angular position of a ray from the source,  $\chi$ , which is related to  $\theta$  and  $\beta$  by

$$\chi = 2\theta - \beta \quad (35)$$

and thus differentially

$$\frac{d\chi}{d\theta} = 2 - \frac{d\beta}{d\theta} \quad (36)$$

And from Eq. (33) we may obtain  $d\beta/d\theta$  as

$$\frac{d\beta}{d\theta} = \frac{e^2 + 1 - 2e \cos \beta}{e(1 - \cos \beta)} \quad (37)$$

We would like next to write an expression for the spectral line profile as diffracted by the elliptically curved analyzer of cylindrical section in terms of the flat crystal characteristic parameters,  $R$  and  $\omega$ . As we have described above for the convex, cylindrical analyzer, we shall define by  $dN$  the number of photons per sec diffracted by the elliptical analyzer within a differential angular region,  $d\theta$ , about a Bragg angle,  $\theta$ , and equal to  $P(\theta)d\theta$ . Thus the divergent beam angular distribution of intensity as diffracted by the elliptically curved analyzer becomes

$$\frac{dN}{d\theta} = P(\theta) = i_0 a \psi \frac{d\chi}{d\theta} I_N(\theta) \quad (38)$$

where  $a$  is the projected source area;  $\psi$  is the angular width of the beam that is accepted by the analyzer and measured in the plane normal to the Bragg reflection plane; and  $I_N(\theta)$  is the flat-crystal rocking curve, the fraction of the intensity for a parallel incident beam that is reflected at an angle,  $\theta$ . Integrating Eq. (38) through the reflecting region in  $\theta$  for a given wavelength, we obtain the total number of photons per second within the diffracted line as

$$N = i_0 a \psi \left( \frac{d\chi}{d\theta} \right) \int I_N(\theta) d\theta = i_0 a \psi \left( \frac{d\chi}{d\theta} \right) R \quad (39)$$

Finally, if we assume that the flat crystal, parallel beam rocking curve,  $I_N(\theta)$ , to be Lorentzian as in Eq. (17), we may write for  $P(\theta)$

$$P(\theta) = i_0 a \psi \left( \frac{d\chi}{d\theta} \right) \frac{(\omega/2\pi)R}{\epsilon^2 + (\omega/2)^2} \quad (40)$$

where  $\epsilon$  is measured from the position of the diffracted peak in  $\theta$ -coordinates. Eq. (40) may be expressed in  $\beta$ -coordinates, as measured along the detection circle, by multiplying the numerator and denominator of the Lorentzian by  $(d\beta/d\theta)^2$ . Here,  $d\beta/d\theta$  and  $d\chi/d\theta$  may be

### THREE-BAND SPECTROGRAPH USING "STACKED" ANALYZERS

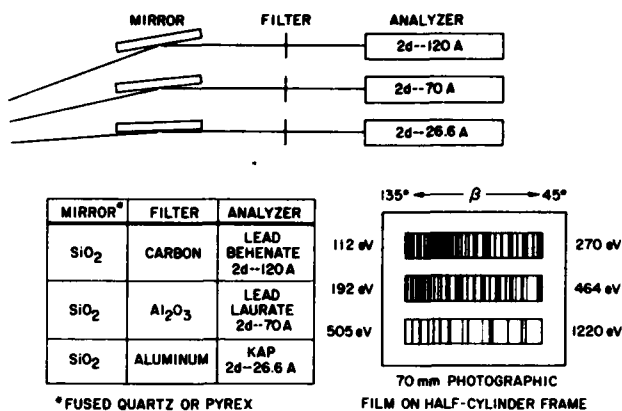


Figure 14

expressed in variable  $\beta$  through Eqs. (36) and (37). We have defined by  $\Delta\beta$  the angular position as measured from the peak position along the detection circle for the Lorentzian defined as follows:

$$\Delta\beta = \left( \frac{d\beta}{d\theta} \right) \epsilon \quad (41)$$

and its measured FWHM,  $\phi$ ,

$$\phi = \left( \frac{d\beta}{d\theta} \right) \omega \quad (42)$$

The  $\beta$ -position for a peak of wavelength  $\lambda$  is obtained by inverting Eq. (33) for the refraction-shifted peak position in  $\theta$ -coordinates, viz., (from Eq. (12))

$$\theta_0 + \frac{\delta}{\sin \theta_0 \cos \theta_0}$$

In Figs. 16, 17 and 18 are presented plots of our calculated reflectivity characteristics [9] for the three analyzers, lead behenate, lead laurate and potassium acid phthalate of  $2d$ -values of 120, 70 and 26.6 Å, respectively. We have proposed these analyzers for a three-band spectrograph for the 100-1000 eV region which has been described in Fig. 13.

In order to verify the response functions for the elliptical spectrograph as predicted here and to account for possible individual differences between the curved crystal/multilayer and the corresponding flat analyzers (on which the flat crystal characteristics have been directly measured), we measured the elliptical

### ELLIPTICAL ANALYZER GEOMETRY

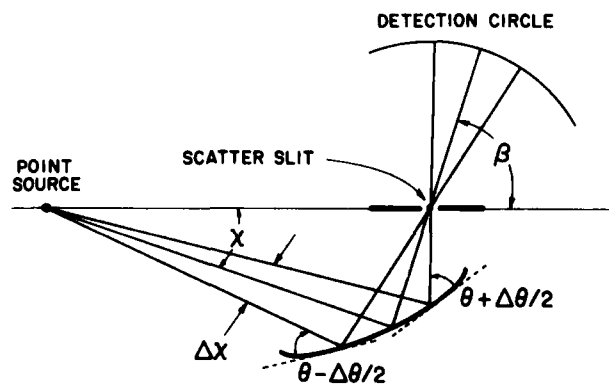


Figure 15

**LEAD BEHENATE**

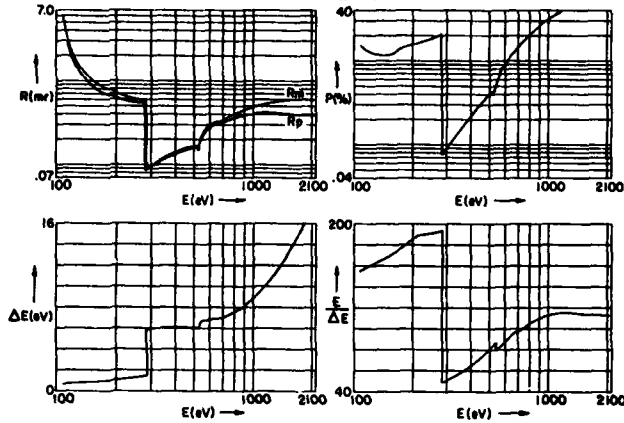


Figure 16

**LEAD LAURATE**

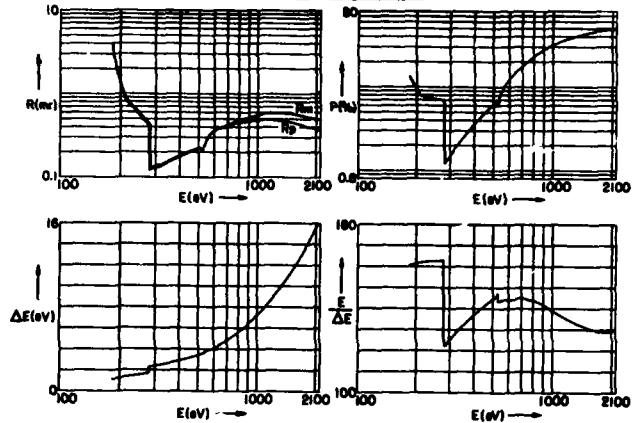


Figure 17

analyzer response function directly at a few standard wavelengths by introducing a calibrated flow proportional counter, with a precision goniometer, on the detection circle. In this way the diffraction peak is measured in  $\beta$ -coordinates and compared with the directly measured  $i_0$  for a characteristic line source that is filtered and isolated with pulse-height discrimination. Such a spectrum including several orders of the  $\text{Cu-L}\alpha$  (13.3 A/930 eV) is illustrated in Fig. 19.

To complete an absolute calibration of this spectrograph, it is necessary to include the response of the detector that is utilized. For many applications, an appropriate photographic film is used to time integrate the pulsed spectrum. We calibrate the film material by taking a series of known exposures with the film along the detection circle under the identical conditions with which a corresponding calibrated proportional counter scan has been made (as shown in Fig. 19). The exposed films are microdensitometered with a slit width that is comparable to that on the proportional counter and small as compared to that of the width of the diffraction lines. The measured densities are correlated with the measured photons/microns<sup>2</sup> exposures for the precisely known wavelength for the spectral line. The calibration of the RAR 2497 film by this procedure is described elsewhere in these Proceedings.

For many pulsed x-ray sources there may be high energy components that diffract effectively in the higher orders and make more difficult a quantitative spectral analysis. In the design of the elliptical analyzer spectrograph as described here, we have used total reflection mirror monochromators to effect the needed high-energy cut-off. We present here in Figs. 20-24 the reflectivity curves for five practical x-ray mirror monochromators which we have calculated using the methods that have been presented in the companion paper.[10] The data presented here, along with some examples of corresponding experimental data, are for mirror surfaces of beryllium, carbon, fused quartz, nickel and gold.

In the low energy diagnostics of essentially point sources (as laser-produced from microballoon sources), it is suggested here that each wavelength component will be presented in either  $\theta$  or  $\beta$  coordinates as essentially a Lorentzian spectral component of FWHM equal to  $\omega$  or  $\phi$ , respectively. If the emission line has a distribution of wavelengths because of Doppler and/or Stark broadening, the measured spectral line profile is then a convolution of these and the analyzer broadening functions. Because Doppler broadening is essentially Gaussian and Stark broadening is essentially Lorentzian, a simple resolution enhancement procedure may be possible using that described above and in Ref. 1. The Voigt function fitting may need to be limited to the wings of the spectral lines if, for example, self-absorption effects have reduced the central part of the

**POTASSIUM ACID PHTHALATE**

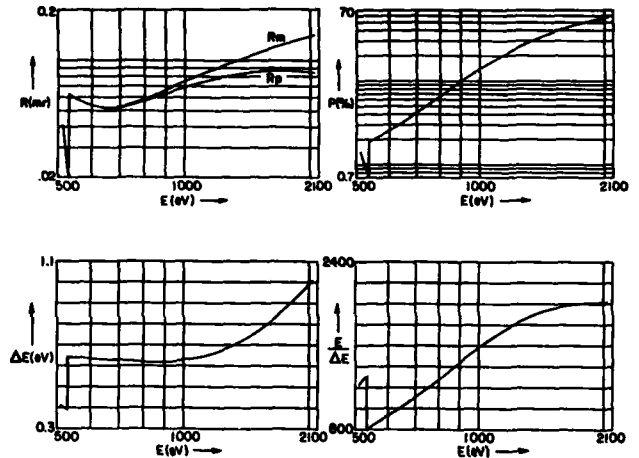


Figure 18

**Cu-L SERIES SPECTRA**  
( $L\alpha_1 = 13.336 \text{ A}$   $L\beta_1 = 13.053 \text{ A}$   $L\gamma = 15.286 \text{ A}$ )

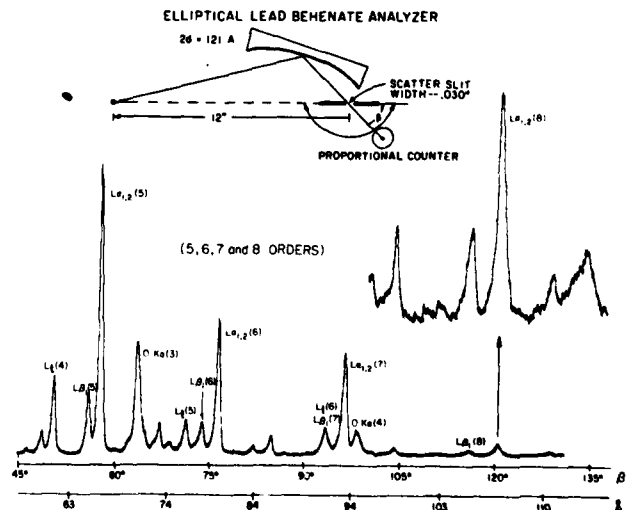


Figure 19

**REFLECTIVITY OF BERYLLIUM MIRROR**  
( $\rho = 1.85 \text{ gm/cm}^3$ )

- |            |            |                        |
|------------|------------|------------------------|
| 1 - 8.34 A | 5 - 44.7 A | — HENKE, et al. (1981) |
| 2 - 13.3 A | 6 - 64.4 A | ● -- 44.7 A            |
| 3 - 23.6 A | 7 - 114 A  | ○ -- 23.6 A            |
| 4 - 31.6 A |            | △ -- 13.3 A            |
- (WATSON, 1978)

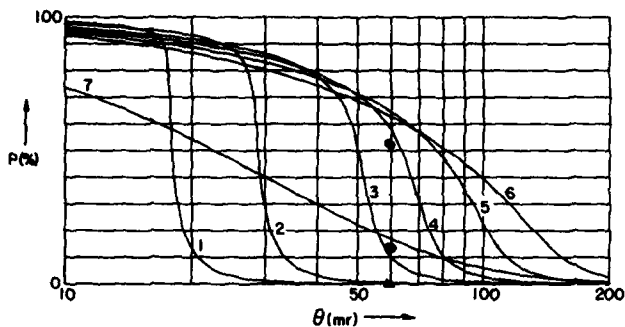


Figure 20

**REFLECTIVITY OF NICKEL MIRROR**  
( $\rho = 8.90 \text{ gm/cm}^3$ )

- |            |            |                            |
|------------|------------|----------------------------|
| 1 - 8.34 A | 5 - 44.7 A | — HENKE, et al. (1981)     |
| 2 - 13.3 A | 6 - 64.4 A | ● -- 23.6 A (ERSHOV, 1967) |
| 3 - 23.6 A | 7 - 114 A  | △ -- 13.3 A (ERSHOV, 1967) |
| 4 - 31.6 A |            | ○ -- 13.3 A (TOOR, 1978)   |
|            |            | ■ -- 8.34 A (ERSHOV, 1967) |

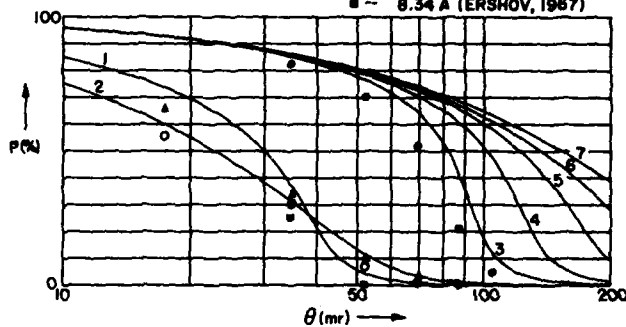


Figure 23

**REFLECTIVITY OF CARBON MIRROR**  
( $\rho = 1.54 \text{ gm/cm}^3$ )

- |            |            |                        |
|------------|------------|------------------------|
| 1 - 8.34 A | 5 - 44.7 A | — HENKE, et al. (1981) |
| 2 - 13.3 A | 6 - 64.4 A | ● -- 114 A             |
| 3 - 23.6 A | 7 - 114 A  | ○ -- 23.6 A            |
| 4 - 31.6 A |            | △ -- 23.6 A            |
|            |            | □ -- 8.34 A            |
|            |            | ■ -- 13.3 A            |
- (LUKIRSKII, 1964)  
(WATSON, 1978)

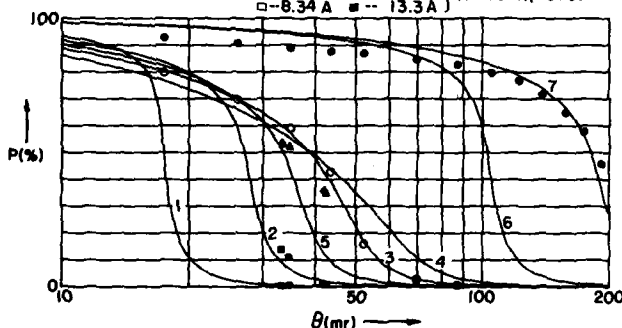


Figure 21

**REFLECTIVITY OF GOLD MIRROR**  
( $\rho = 19.32 \text{ gm/cm}^3$ )

- |            |            |                                      |
|------------|------------|--------------------------------------|
| 1 - 8.34 A | 5 - 44.7 A | — HENKE, et al. (1981)               |
| 2 - 13.3 A | 6 - 64.4 A | ● -- 114 A (LUKIRSKII, 1964)         |
| 3 - 23.6 A | 7 - 114 A  | ○ -- 114 A (JOHNSON & WUERKER, 1963) |
| 4 - 31.6 A |            | △ -- 23.6 A                          |
|            |            | ■ -- 8.34 A                          |
|            |            | ▲ -- 13.3 A                          |
- (ERSHOV, 1967)

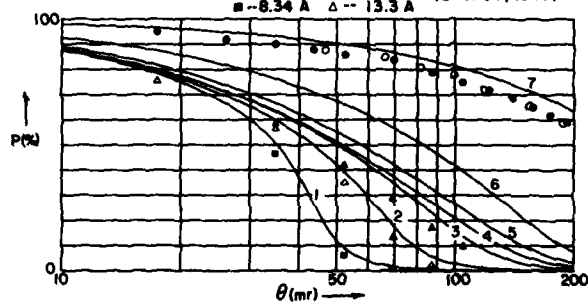


Figure 24

**REFLECTIVITY OF FUSED QUARTZ MIRROR**  
( $\rho = 2.20 \text{ gm/cm}^3$ )

- |            |            |                                       |
|------------|------------|---------------------------------------|
| 1 - 8.34 A | 5 - 44.7 A | — HENKE, et al. (1981)                |
| 2 - 13.3 A | 6 - 64.4 A | ● -- 44.7 A (JOHNSON & WUERKER, 1963) |
| 3 - 23.6 A | 7 - 114 A  |                                       |
| 4 - 31.6 A |            |                                       |

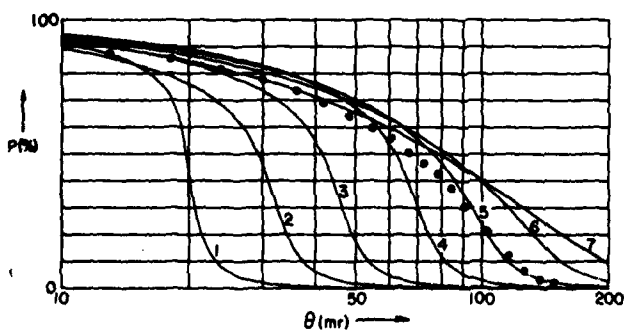


Figure 22

**ONE-DIMENSIONAL IMAGING**

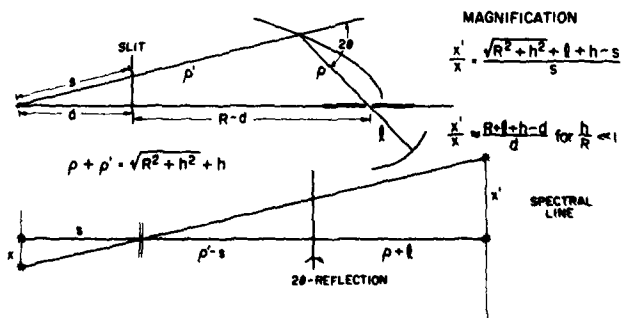


Figure 25

spectral line.

This elliptical analyzer spectrograph may be effectively applied to extended sources in order to obtain spatially resolved spectral information. In this application, the exit slit of the spectrograph becomes a limiting aperture which accepts radiation only from a linear region of the source perpendicular to the Bragg reflection plane and through the source focal point. If a vertical slit of sufficiently small width is positioned between the source focal point and the analyzer (for example at the total reflection monochromator) imaging along this linear source region occurs at nearly constant magnification along the length of the spectral line (see Fig. 25). Alternatively, this one-dimensional imaging can be obtained with larger instrument aperture by replacing the flat monochromator mirror and limiting slit by a cylindrical mirror of such curvature as to focus the radiation from a point along the accepted line source region to a corresponding point along the spectral line.

In summary, the elliptical spectrograph has three distinct advantages over the convex or flat crystal instruments for presenting an instantaneous spectrum of pulsed x-ray source. These result from the collecting and focussing into a line image within an exit aperture of radiation from a point or line source, and are: (1) the effective aperture for a given wavelength can be appreciably larger; (2) the detector circle is shielded from the total analyzer area by the exit slit acting as a scatter aperture, thus allowing a considerable reduction in background resulting from diffuse and fluorescent scatter; and (3) the sharp line image within the exit aperture allows a precise definition of the detection geometry (for example, for a film circle for a slit window of a streak camera), making possible a straightforward and accurate absolute calibration.

Finally, it should be emphasized here that for optimized low energy x-ray spectroscopy it is important to choose the  $2d$ -values of the analyzers that are comparable to the wavelengths to be measured in order to place the desired spectral bands at the largest possible Bragg angles. At these large angles, the relative effects upon spectral resolution resulting from crystal and source size broadening are minimized because of the higher dispersion. Equally important for the low energy spectroscopy is that only at the larger angles will the Bragg reflection reflectivity of the analyzer be large as compared to its specular reflectivity. At the smaller angles, below about  $20^\circ$  in Bragg angle, the specular reflection tail for the longer wavelengths can represent an appreciable background at the diffraction line. It is for this reason that in the elliptical spectrograph design described here, the spectral bands to be measured are placed at  $\beta$ -angles from  $45^\circ$  to  $135^\circ$ .

#### ACKNOWLEDGEMENTS

The author gratefully acknowledges the invaluable assistance in the preparation of this work of Priscilla Piano, Tina Tanaka and Hubert Yamada. This program is supported by a grant from the Air Force Office of Scientific Research, Grant No. 79-0027, and by a supplemental DOE/Lawrence Livermore Laboratory subcontract, No. 9072209.

#### REFERENCES

- [1] B. L. Henke, R. C. C. Perera, E. M. Gullikson and M. L. Schattenburg, *J. Appl. Phys.* **49**, 480 (1978).
- [2] B. L. Henke, R. C. C. Perera and D. S. Urch, *J. Chem. Phys.* **68**, 3692 (1978).
- [3] B. L. Henke and M. A. Tester, *Advances in X-Ray Analysis* (Plenum Press, New York, 1975), Vol. 18, p. 76.
- [4] K. B. Blodgett, *Am. Chem. Soc. J.* **57**, 1007 (1935).
- [5] K. B. Blodgett, *Phys. Rev.* **51**, 964 (1937).

- [6] K. B. Blodgett, *J. Phys. Chem.* **41**, 975 (1937).
- [7] Y. Okaya, *Acta Crystallogr.* **19**, 879 (1965).
- [8] R. A. Smith, *Acta Crystallogr. B* **31**, 2345 and 2347 (1975).
- [9] B. L. Henke, P. Lee, T. J. Tanaka, R. L. Shimabukuro and B. K. Fujikawa, *Atomic Data and Nuclear Data Tables* **27**, No. 1 (1982).
- [10] B. L. Henke, "Low Energy X-Ray Interactions: Photoemission, Scattering, Specular and Bragg Reflection," Proceedings of the 1981 Topical Conference on Low Energy X-Ray Diagnostics, Monterey, California, June 8-10, 1981.
- [11] A. H. Compton and S. K. Allison, *X-Rays in Theory and Experiment*, 2nd ed. (Van Nostrand, New York, 1935).
- [12] R. W. James, *The Optical Principles of Diffraction of X-Rays* (Cornell University Press, Ithaca, New York, 1965).
- [13] M. Born and E. Wolf, *Principles of Optics*, 5th ed. (Pergamon Press, Oxford, 1975).
- [14] P. Lee, *Opt. Commun.* **37**, 159 (1981).
- [15] R. L. Blake, private communication.
- [16] M. deBroglie and F. A. Lindemann, *C. R. Acad. Sci. Paris* **158**, 944 (1914).
- [17] L. S. Birks, *Rev. Sci. Instrum.* **8**, 1129 (1970).
- [18] M. Swartz, S. Kastner, E. Rothe and W. Neupert, *J. Phys. B* **4**, 1747 (1971).
- [19] N. J. Peacock, R. J. Speer and M. G. Hobby, *J. Phys. B* **2**, 798 (1969).
- [20] S. O. Kastner, *Appl. Opt.* **18**, 3 (1979).
- [21] B. L. Henke, *Nucl. Instrum. Methods* **177**, 161 (1980).
- [22] The fabrication of the elliptically curved aluminum blanks has been by the Sandia Corp., Albuquerque, and by the Los Alamos National Laboratory.
- [23] B. Watson, private communication, "Summary Calibration of Lawrence Livermore Laboratory Flat Mirrors," Lockheed Palo Alto Research Laboratory (January 1979).
- [24] A. P. Lukirskii, E. P. Savinov, O. A. Ershov, I. I. Zhukova and V. A. Fomichev, *Opt. Spectrosc.* **19**, 237 (1965).
- [25] G. L. Johnson and R. F. Wuerker, *X-Ray Optics and X-Ray Microanalysis* (Academic Press, New York, 1963), p. 226.
- [26] O. A. Ershov, I. A. Brytov and A. P. Lukirskii, *Opt. Spectrosc.* **22**, 127 (1965).
- [27] A. Toor, private communication (October 1978).



Co-chairman Burton Henke and session chairman Dr. Kenneth Mitchell.

## Applications of Gratings in the Low Energy X-ray Region

E. Källne

Harvard-Smithsonian Astrophysical Observatory  
Cambridge, Massachusetts 02138

## ABSTRACT

The utilization of reflection and transmission gratings as active elements for analyzing X-rays in the wavelength region of 10-250Å is discussed. Three approaches in a focussing reflection geometry are considered which all offer possibilities to enhance the experimental sensitivity or the resolution in a region of special interest. An experimental analysis of a standard grazing incidence instrument is presented. Transmission grating geometries are examined using results from planar transmission gratings with prefocussing mirrors.

## I. INTRODUCTION

The spectral analysis of X-rays in the soft wavelength region is a challenge since one has to meet the requirements of high efficiency, high resolution and spectral purity. These requirements usually have to be satisfied simultaneously and over an extended wavelength range, for instance,  $\lambda \approx 12-250\text{Å}$ . A few different approaches exist to diffract and focus the X-rays: one can use the reflection and interference properties of gratings, the Bragg diffraction of crystals (1,2) and the methods based on selective absorption in multilayer filters or films (3,4). This paper discusses some novel and exciting as well as more traditional possibilities to analyze soft X-rays with gratings and also indicates some future possibilities.

The first point of consideration is to make the right choice of dispersive system that meets the particular requirements for the experiment at hand; and, of course, these requirements must be known and suitably parametrized. This point is of special importance now that choices do exist between different, partly overlapping, dispersive techniques. By optimizing the choice one can obtain superior performance for a specific application; for example, for measurements of the carbon photon absorption edge at 280 eV. This paper discusses different approaches using gratings in reflection and transmission geometries and briefly points out special advantageous features for a few concrete cases.

The direction of X-rays is changed by diffraction or reflection. The reflectivity of materials decreases rapidly with wavelength ( $R \propto \lambda^4$ ) so there is usually no choice but using small grazing angles for the wavelengths of interest here. Furthermore, for the shorter wavelengths one also has to consider the cutoff at the angle of critical reflectivity (which is a material property) which will set a limit to the angle of incidence.

## II. FOCUSING REFLECTION GRATINGS

In view of these initial remarks, we can now examine the available techniques to diffract and focus X-rays in a reflection geometry. In the Rowland circle configuration (See Fig. 1), X-rays from a source point (the entrance slit) on the Rowland circle (diameter  $R$ ), are diffracted by the grating, (bent with radius of curvature of  $R$ ) and focussed to another point (the exit slit) on the Rowland circle. This classical approach will give the highest possible resolution at the expense of lost intensity due to severe spherical aberrations. Theoretical analysis of the X-ray optics of the grazing incidence Rowland circle geometry can be found in Ref. 5. The efficiency of the system is very sensitive to the surface properties of the diffraction grating. To overcome this problem several new developments have appeared that improve the quality and efficiency of reflection gratings (6). It can be noted that by improving the grating quality the diffraction efficiency has been increased an order of

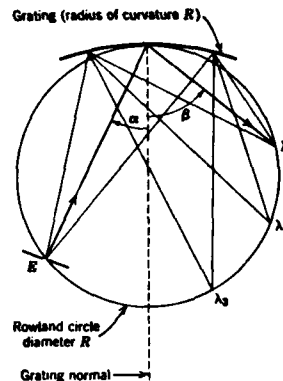


Fig. 1 The Rowland circle. Radiation from the point  $E$  is dispersed and focused by the grating at  $\lambda_1, \lambda_2$ , etc.  $\alpha$  and  $\beta$  are the angles of incidence and diffraction, respectively.

magnitude to about 10% in the most favorable case. It is worthwhile to stress the importance of having the grating as an exchangeable part of the optical system. This usually implies a nontrivial design problem as in many instruments the grating is a permanent part of the system and mechanically interfaced with other components for complicated alignment procedures.

The Rowland circle geometry has been used for many applications and I will here give a few examples of some newly implemented instrumentations.

The astigmatic image from the spherical grating in the Rowland circle geometry can be used to give a spatial imaging in the non-dispersive plane. This has recently been utilized in plasma diagnostic applications of imploding foils and laser produced plasmas (7). The spatial imaging is then achieved either by using a pinhole as the entrance slit or by imaging the source onto the entrance slit with a cylindrical mirror. A 1 m Rowland circle with a spherical grating has been found suitable to meet the resolution and sensitivity requirements of these applications.

The throughput of a grazing incidence monochromator/spectrometer as a function of wavelength can be analysed by using a second dispersive element after the monochromator. If the characteristics of this second analyser, a transmission grating for instance, have been measured earlier (8), the intensity distribution measured after the transmission grating can be related directly to the output of the grazing incidence monochromator. Such an experiment was recently performed at the 4° beamline at Stanford Synchrotron Radiation Laboratory (9) using the grazing incidence monochromator, "the Grasshopper". From Fig. 3 it can be seen that the output beam is heavily contaminated by higher order harmonics at the lower energies to an extent that would be detrimental for experiments requiring well calibrated and monochromatic light as, for instance, is needed for absolute cross section measurements. A standard technique to determine the flux  $I(\lambda)$  is by measuring the electron emission yield from a gold foil that is radiated by the

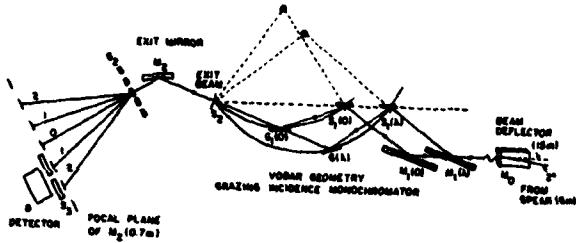


Figure 2 - Experimental setup to analyse the output beam of the grazing incidence monochromator at the 4<sup>th</sup> beam line at SSRL using transmission grating G<sub>2</sub>.

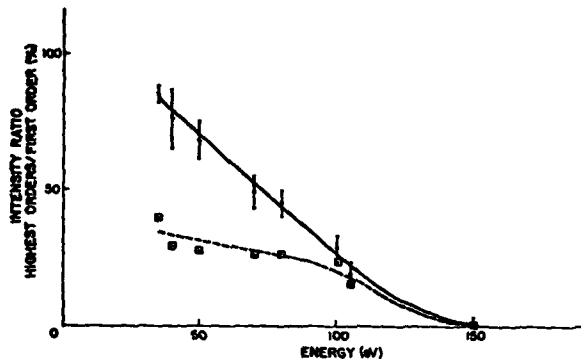


Figure 3 - Analysis of higher order admixture in the output beam of the 4<sup>th</sup> beam line at SSRL using the Gosskopf monochromator. The dashed line is the admixture corrected for the synchrotron radiation distribution.

light from the output beam. A comparison between the wavelength intensity distribution recorded in this way with the results from the spectral analysis of the beam using transmission gratings is shown in Fig. 4.

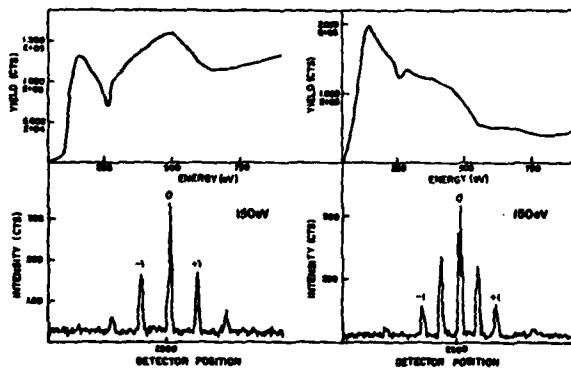


Figure 4 - Comparison of total yield and diffracted intensity distribution for two settings of the performing mirror  $\theta_0$ .

It is worth noting that the standard gold yield measurement is not only incapable of detecting higher order harmonics but their presence will also distort the  $I(\lambda)$  distributions extracted from the measured yield.

There are different ways to remedy problems with higher order harmonics, at least in part. By using appropriate filters, it is possible to absorb the second order harmonics but it is hard to find a filter combination that will pass only the first order and extinguish all other higher harmonics. A superior solution to this problem was introduced by Jaeglé (10) in a double grating monochromator with an intermediate mirror (Fig. 5 taken from ref. 11). This system gives an excellent flexibility for adjusting the number of optical components to give a sufficiently pure and intense beam for the specific requirements of each experiment; i.e. the instrument also becomes very versatile. Moreover, the possibility to change the grazing incidence angle gives a possibility to tune for

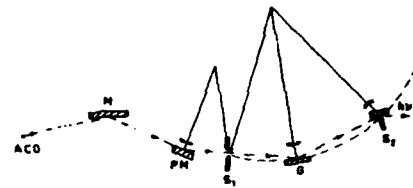


Fig. 5A Optical layout of the synchrotron radiation beam line and monochromator. M = cylindrical mirror; PM = spherical prefocusing mirror; S<sub>1</sub> and S<sub>2</sub> = entrance and exit slits; G = grating.

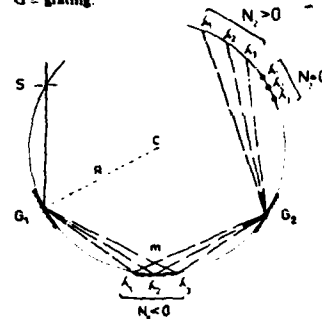


Fig. 5B Basic principle of the two-grating system.

maximum intensity in the wavelength region of interest (11).

Another approach, which uses a toroidal geometry, has recently been implemented for a number of diverse applications (See Fig. 6). In this geometry the X-rays



Figure 6 - Toroidal grazing geometry for a plane focus spectrometer that covers 20-42Å with four gratings:  
G<sub>1</sub> = 133.64/μm Δλ<sub>1</sub> = (230-425)Å, G<sub>2</sub> = 306.4/μm Δλ<sub>2</sub> = (100-220)Å  
G<sub>3</sub> = 609.4/μm Δλ<sub>3</sub> = (40-100)Å, G<sub>4</sub> = 1200.4/μm Δλ<sub>4</sub> = (10-40)Å  
Chd. 22

are focussed both in the dispersive and the non-dispersive planes which is a way to reduce the intensity losses due to aberrations (12,13). A comparison between the toroidal geometry and the spherical Rowland circle geometry was recently performed which demonstrated the superior throughput of the toroidal geometry (14). A drawback is, of course, the complex toroidal surface of the grating which introduces manufacturing difficulties and costs. In an alternative approach one circumvents these problems but retains the superior light collection of the toroidal surface by separation of focussing and dispersive elements, i.e., through the combined use of a toroidal mirror and a spherical grating (15).

As a final example of configurations with reflection gratings, I shall mention the recently proposed off axis geometry as shown in Fig. 7 from

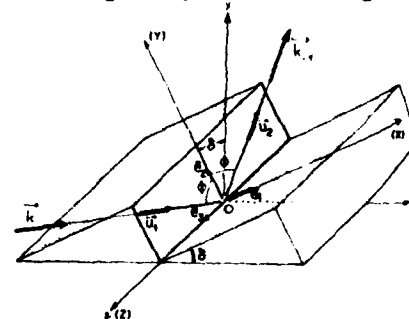


FIG. 7 Grating configuration with  $k$  parallel to the plane of the small ball (GMS mounting).

ref. 16. The advantage of this method is the increased reflectivity compared to other approaches, which could be extremely useful for experiments requiring medium wavelength resolution while the classical Rowland circle geometry still offers the superior resolution with a concave grating.

### III. TRANSMISSION GRATINGS

The difficulties with reflection geometry optics (low reflectivity, higher order overlap, surface sensitivity to impurities, etc), can all be avoided by using transmission gratings (17).

These new gratings of high transmission efficiency (typically >10%) have recently been the objective of experiments to test the full potential of these devices for X-ray optics applications as well as for basic materials measurements (18). These experiments have demonstrated the possibility to utilize the phase shift of the partially transmitted beam to enhance the diffracted intensity distribution in a limited wavelength range (Fig. 8). The implementation of transmission gratings into a spectrometer was first

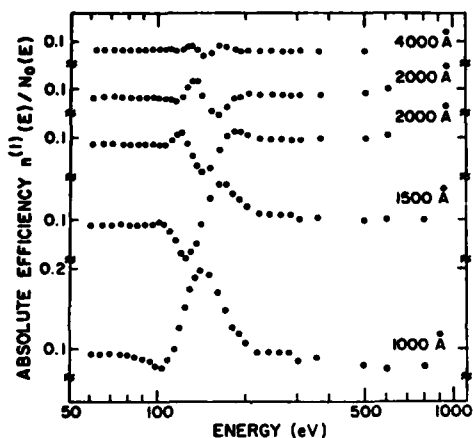


Figure 8 - First order diffraction efficiencies for gold transmission gratings as a function of energy for different grating thicknesses.

done on the Einstein Observatory (19) in a telescope geometry with a circular array of 160 transmission gratings mounted after the Wolter type mirrors. The initial tests of the performance of the system showed a resolution of  $E/\Delta E \sim 30$  limited by the telescope and the natural line width in the energy range 100-1000 eV. With a convergent beam through the planar transmission grating the resolution will be limited by the aberration introduced by the focussing mirror. Furthermore, the first approach to a transmission grating monochromator is to introduce a single rotation of the grating to scan an extended wavelength region. With a prefocussing mirror mount as in the Wolter type telescope the focal plane will not be fixed in space upon rotation of the grating and only a limited wavelength range can be covered with a fix detection (20). This problem is similar to the one encountered for a zone plate monochromator (23).

### IV. CONCLUSION

Several different reflection and transmission geometries have been discussed to analyse soft X-rays with gratings. It is clearly within reach to obtain efficiencies of 15-25% over a limited wavelength range and this opens up exciting possibilities in a variety of fields such as X-ray astronomy, plasma diagnostics and synchrotron radiation applications. It seems realistic to envision the realization of future monochromators built in modules with several gratings

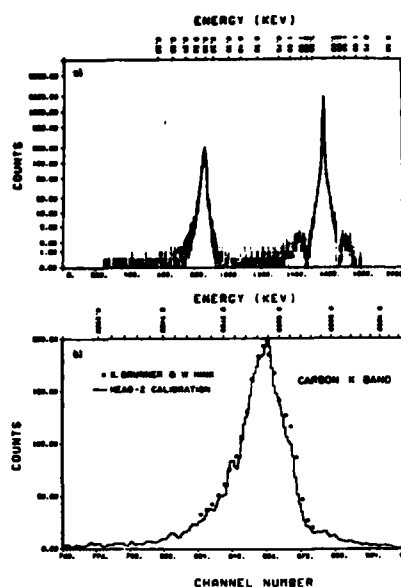


Figure 9 - Calibration data from the HEAO-2 X-ray telescope using an array of 160 aligned gratings. (a) The carbon K in zero and first order. (b) Carbon K in detail (—) HEAO-2 data, (· · · · ·) Ref. 21.

of different parameters in the same instrument to cover an extended wavelength range. With this approach it is possible to take advantage of the high reflectivity an off-axis geometry can give and also the high diffraction efficiency of a transmission grating. The narrow band application does not necessarily generate a multitude of nonversatile instruments but rather emphasizes the aspect to consider the optical components in a spectrometer to be interchangeable to suit the specific applications.

### ACKNOWLEDGEMENTS

This work has been carried out with an inspiring collaboration of several colleagues from Smithsonian Astrophysical Observatory, University of Virginia, IBM, Space Research Laboratory (Utrecht), Stanford Synchrotron Radiation Laboratory, and the Los Alamos National Laboratory. I also thank Karen Gilleece for typing this manuscript in a hurry. This work was supported by the National Science Foundation.

### REFERENCES

1. B. L. Henke, et al., J.Appl.Phys., 42, 480 (1978).
2. R. D. Deslattes, Nucl.Instr.Meth. 172, 201 (1980).
3. E. Spiller, this volume.
4. T. Barbee, this volume.
5. T. Namioka, J.Opt.Soc.Am. 49, 446 (1959).
6. R. J. Speer, in Workshop on X-ray Instrumentation for Synchrotron Radiation, Stanford, May 1978, VI-8.
7. L. A. Jones, private communication, K. Mitchell, Bull.Am.Phys. 24, 1031 (1979).
8. H. W. Schnopper, et al., Appl.Opt. 16, 1088 (1977).
9. E. Kallne, et al., to be published.
10. P. Jaeglé Thesis, Université de Paris (1965).
11. P. Dhez, et al., Nucl.Instr.Methods 152, 85 (1978).
12. R. P. Madden and D. Ederer, J.Opt.Soc.Am. 62, 722A (1972).
13. W. R. McKinney and M.R. Howells, Nucl.Instr.Methods 172, 149 (1980).
14. S. Krummacher, et al., VUV VI, Virginia, June 1980 III, 27.
15. G. Tondello, Optica Acta 26, 357 (1979).
16. W. Weiner and H. Visser, Applied Optics 2, 487 (1981).



17. E. Källne, et al., Nucl.Instr.and Methods 152, 103 (1978).
18. R. Tatchyn, I. Lindau, and E. Källne, Nucl.Instr. and Methods 172, 315 (1980).
19. The HEAO-B X-ray Observatory (CFA/HEA 78-124, p.21, and F. D. Seward, HEAO-B Objective Grating Spectrometer Calibration, Feb. 1978.
20. P. Caldwell, et al., to appear 1981.
21. K. Brunner and W. Hink, J.Appl.Phys. 17, Suppl. 17-2, 380 (1978).
22. T. Aton, et al., Nucl.Instr.Meth. 172, 173 (1980).
23. E. Spiller, in Workshop on X-ray Instrumentation for Synchrotron Radiation, Stanford, May 1978, VI-4.



Dr. Elisabeth Källne, just back from Sweden, reporting on x-ray grating spectroscopy.

N J Peacock

Culham Laboratory, Abingdon, Oxon, OX14 3DB, UK  
(Euratom/UKAEA Fusion Association)

## ABSTRACT

Both crystal dispersion and diffraction grating instruments are routinely used for soft X-ray dispersion in the fusion programme at the Culham Laboratory where the keV plasmas studied range from highly transient, high density  $n_e \sim 10^{21} \text{ cm}^{-3}$ , laser-produced plasmas to relatively low density,  $n_e \sim 10^{13} \text{ cm}^{-3}$  tokamak plasmas. In this paper the soft X-ray spectral features from these plasmas are discussed and the design parameters of appropriate instruments for X-ray studies are considered.

Useful spectral surveys of laser-processed plasmas have been obtained using crystals bent convex in the de Broglie mode; higher aperture concave Johann configurations have been designed and constructed with multichannel read out for tokamak studies. Grazing incidence diffraction grating instruments have been operated in the photographic survey mode and as double channel monochromators. Operating experience with existing instruments is assessed. Examples of spectral information in the wavelength region  $\sim 4 \text{ \AA}$  to  $\sim 400 \text{ \AA}$  are presented and their use in plasma diagnostic studies is discussed.

## I. INTRODUCTION

Within the wide range of possible measurement techniques available to physicists in their studies of high temperature plasmas of thermonuclear fusion interest [1] - [6] perhaps the most informative are those diagnostics which operate in the soft X-ray region of the spectrum,  $h\nu \sim 1 \text{ keV}$  [7].

In 'state of the art' fusion experiments, electron temperatures  $kT_e \sim 1 \text{ keV}$  are commonly achieved both in low density,  $n_e \sim 10^{13} \text{ cm}^{-3}$ , magnetic confinement devices such as tokamaks and in inertially-confined plasmas where liquid densities or above have been reached. The spectral intensity of the continuum emission, neglecting for the moment any recombination steps, will peak at  $h\nu_{\text{max}} = 2 kT_e$ . Line emission from all ions which might be present in the plasma, excepting the lightest gases, will extend throughout the VUV and soft X-ray regions; even as far as  $h\nu \sim 10 \text{ keV}$  for some, hydrogen-like and helium-like ion configurations. Figure 1, for example, illustrates the energy spread of the more intense emission lines from iron. Most of the line features have quantum energies between 31 eV and 1.24 keV, ie,  $400 \text{ \AA}$  and  $10 \text{ \AA}$ . The approximate temperature at which the ions will appear in ionisation equilibrium is the appropriate excitation energy for the  $\Delta n = 1$  transitions

divided by a factor between 1 and 4. At temperatures  $\sim 1 \text{ keV}$  the most intense resonance  $\Delta n = 1$  lines of the common metals lie in the X-ray region proper, see Figure 1; but, even in multi-keV plasmas, interest in the soft X-ray region and in the VUV region is sustained since the thermal energy X-ray lines and continua can readily be confused with emission from a high energy tail of a distorted Maxwellian electron energy distribution. This is very nicely illustrated by the coded aperture images of laser irradiated microballoon targets [8], where the higher energy X-ray emission from supra thermal electrons at the surface of the irradiated shell can in this case be clearly distinguished from the softer, thermal emission from the compressed core plasma. The soft X-ray emission,  $\sim 0.1 \text{ keV}$  to  $\sim 1 \text{ keV}$ , remains, therefore, a more characteristic monitor of the bulk thermal content of the plasma.

The present paper sets out first of all to describe the plasma and atomic rate processes which give rise to these spectral features which are of prime diagnostic interest. Although tokamaks and laser-irradiated targets frequently generate the same ion species, these sources are discussed separately since their diagnostic requirements are usually very different. In tokamaks, for example, impurity ion diffusion might be the most important parameter to derive from soft X-ray spectroscopy, while in laser compression experiments line broadening leading to values of the compressed density,  $\rho \text{ gm cm}^{-3}$  and of the inertial confinement factor,  $f\rho \text{ dr gm cm}^{-2}$ , are often the most sought after parameters.

The design criteria for X-ray instrumentation is discussed bearing in mind the possibility of investigating specific aspects of plasma behaviour. Stated in a different way, the instruments are designed with a particular diagnostic measurement in mind rather than as 'botanical' survey instruments for cataloguing spectral features. In section IV, we cite examples of the types of grazing-incidence grating spectrometers and crystal spectrometers that are in operation at the Culham Laboratory and we speculate on more ideal systems which require yet further development.

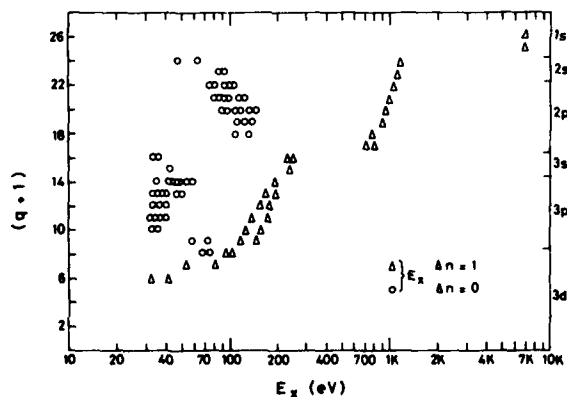


Fig 1. Excitation energies  $E_x$ , of  $\Delta n = 1$ ,  $\Delta n = 0$  transitions in Iron ions of charge state  $q$ .

II SOFT X-RAY SPECTRAL FEATURES OF keV PLASMAS  
IN LABORATORY FUSION STUDIES

## A. Tokamaks.

Tokamaks operating with plasmas whose electron temperature is typically  $kTe \sim 1$  keV and with a central electron density in the range  $5 \times 10^{18} \text{ cm}^{-3} \sim 5 \times 10^{19} \text{ cm}^{-3}$  have emission features in the soft X-ray region which are closely similar to those from solar active regions.

An electron temperature of  $\sim 1$  keV can be achieved almost routinely by simple ohmic heating. This value can, in principle, be increased by heating the electrons directly at the electron cyclotron resonance frequency, so-called ECRH heating. So far, with modest input powers of 0.1 MW, factors of two increase at sub keV temperatures have been achieved [9]. More indirectly, the electron heat content can also be increased, via the ions, by wave heating at the ion resonance frequencies [10]. Auxiliary heating with particle (eg  $H^+$ ) beams is also topical [11] [12] and indirectly heats the electrons. At the multi-MW level in the PDX and PLT tokamaks [11] [12], particle beam heating has produced something of a record with ion temperatures as high as 7 keV and electron temperatures  $kTe \sim 3$  keV; these two temperatures are decoupled partly due to electron heat loss but mainly due to the low frequency of electron-ion collisions at  $n \sim 1 \times 10^{19} \text{ cm}^{-3}$ .

The main spectral features from these plasmas in the soft X-ray region are line emission from highly ionised impurities. Light elements eg O, N, C etc are present typically to the extent of 0.01  $n_e$ , while heavier, usually metal impurities eg Ni Fe Ti Mo etc. from the walls and from current aperture limiters, have typical concentrations  $\sim 0.001 n_e$ . In particularly clean tokamaks with gettering and divertors [13], these impurity concentrations can be reduced by an order of magnitude or more. We shall see section III, that this has an important bearing on instrument aperture for soft X-ray studies.

The metallic impurity ions in the core of a tokamak plasma have ionisation potentials,  $\psi(q)$  where  $q$  is the ion charge state, which characteristically are three or four times the electron temperature and with the relative populations of the different charge states in approximately coronal equilibrium [14]. In the PLT tokamak at Princeton (PPL), however, the impurity ion species are located typically at somewhat higher values of  $Te$  on the  $Te(r)$  profile than would be predicted by coronal ionisation-recombination balance. Uncertainty in the atomic rate coefficients could account in some

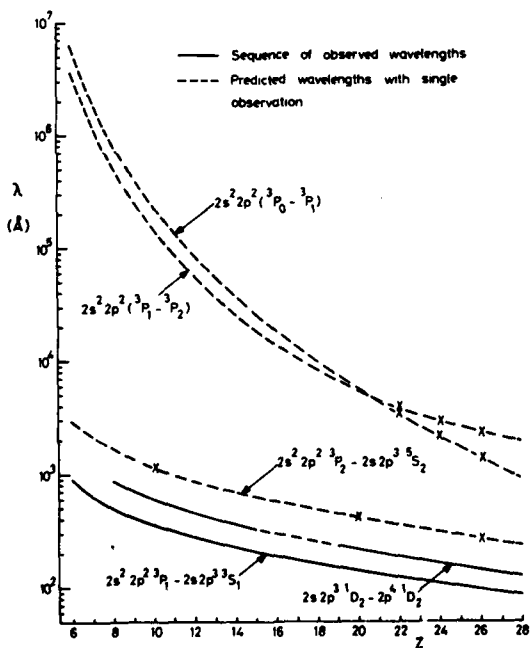


Fig 2. Wavelengths of some important transitions in carbon-like ions as a function of atomic number Z.

measure for the somewhat different conclusions of the TFR tokamak group [14] and of the Princeton Group. It appears that the spatial location of the ion populations is more sensitive to uncertainties in atomic rates than to possible variations in particle diffusion rates [15]. In the outer, lower temperature regions of the plasma, departures from coronal equilibrium are commonly observed due to the relatively rapid recycling of the impurities between the plasma boundary and the limiter and vessel walls.

The low collision rates in tokamaks,  $10^3 - 10^5 s^{-1}$  ensures that forbidden lines which also appear in the solar spectrum and extend from the X-ray region to the visible are noteworthy features of the tokamak spectrum. Figure 2 illustrates the wavelength dependence of the forbidden and allowed lines from ions belonging to the carbon iso-electronic sequence. The allowed  $\Delta n = 0$  transitions of the common metals lie in the extreme vacuum UV (XUV) region,  $100 \text{ \AA} \lesssim \lambda \lesssim 200 \text{ \AA}$ ; the inter-system lines are at somewhat longer wavelengths while the important forbidden lines due to M1 transitions

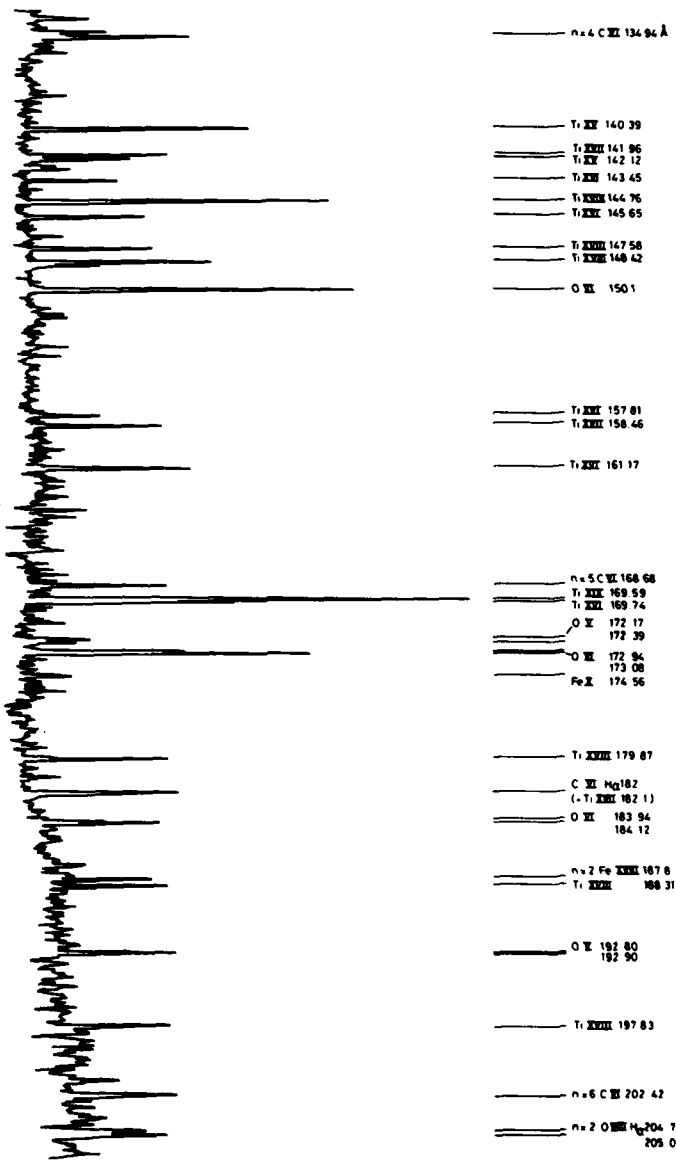


Fig 3. Section of soft X-ray spectrum ( $75 \text{ \AA} - 135 \text{ \AA}$ ) from DITE tokamak. The resonance lines of the light gas ions of O and C in high order number 'n' are interspersed through the Ti and Fe ion emission.

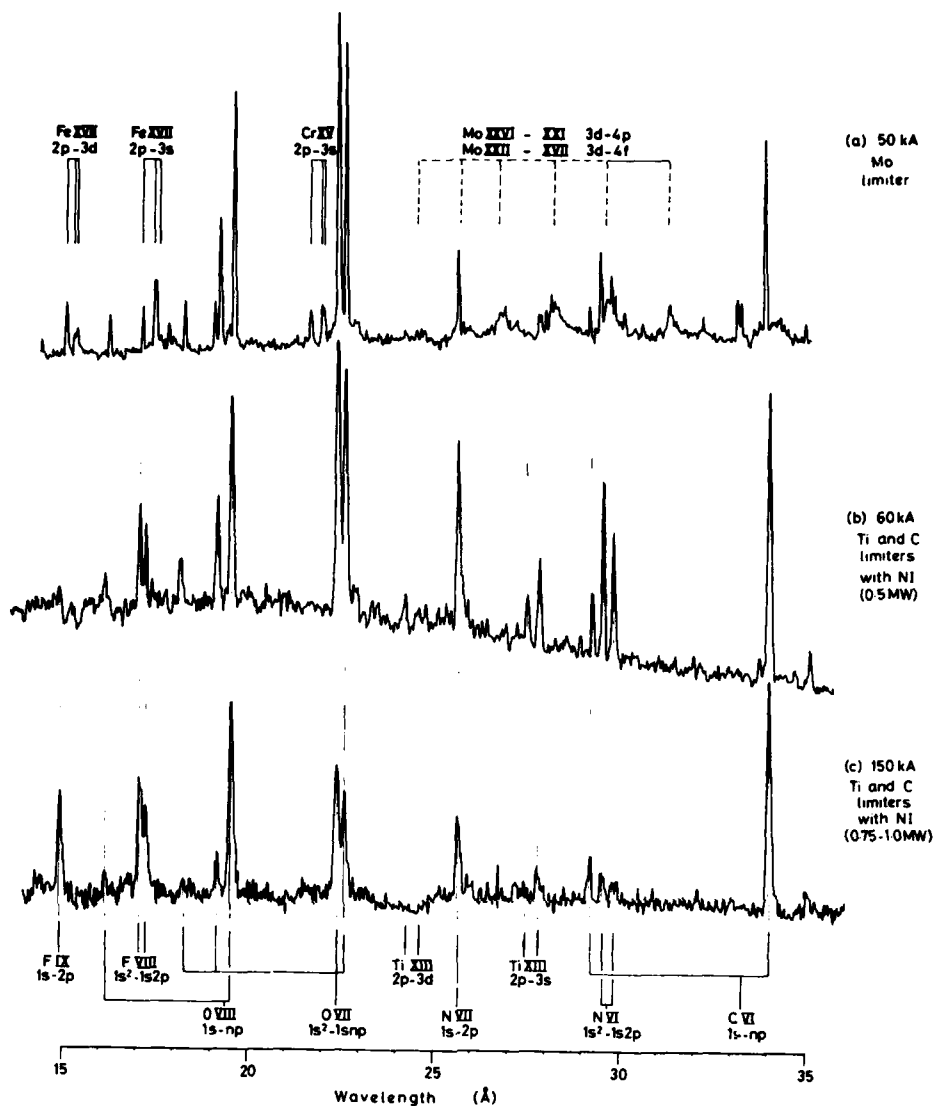


Fig 4. Section of soft X-ray spectrum ( $15 \text{ \AA} - 35 \text{ \AA}$ ) from DITE tokamak. Three different operating conditions are shown. In (a) the discharge is ohmically heated (50 kA current) and the current aperture limiters are Mo. In (b) and (c) the limiters are Ti and C while the plasma ohmic heating current and neutral injection (NI) power are as indicated.

between levels within the ground configurations lie typically in the VUV region of the spectrum.

$\Delta n > 0$  transitions of the common metals whose ions are isoelectronic with carbon or with any other ion in the neon-shell, (ie the so-called M-shell transitions), lie in the soft X-ray region. In this region of the spectrum,  $\sim 10 \text{ \AA} \rightarrow \sim 100 \text{ \AA}$ , the  $\Delta n > 0$ , M-shell metal lines form a well separated group from the  $\Delta n = 0$  lines as indicated in figure 1, and interspersed through these two groups are the K-shell  $\Delta n > 0$  resonance lines of ionised light impurities. Figure 3 illustrates a section of the spectrum near  $100 \text{ \AA}$  from the DITE tokamak: the main line features are from ionised Ti and Fe. The most highly charged states of the metals observed in these discharges with  $\text{Te}(e) \approx 800 \text{ eV}$  were  $\text{TiXX}$  and  $\text{FeXXI}$ . Emission at the shorter wavelengths, around  $25 \text{ \AA}$  in the soft X-ray region, is illustrated for a number of different DITE plasma conditions in figure 4. It is worth noting that with more limited resolution the  $\text{FeXVII}$   $2p-3d$ ,  $3s$  multiplets (upper trace) between  $15 \text{ \AA}$  and  $17 \text{ \AA}$  could easily be confused with the  $\text{FeIX}$  and  $\text{FeVIII}$  lines

which appear at or near the same wavelengths during neutral beam injection (lower trace). A resolution interval of  $0.1 \text{ \AA}$  or better is desirable therefore in this wavelength region.

Very high resolving power, sufficient to undertake line profile studies, is difficult to achieve with grating dispersion at grazing incidence. Instrumentation for line profile analyses is more easily achieved using crystal dispersion at shorter wavelengths or with normal-incidence gratings at much longer wavelengths. Of more interest in tokamak physics is the absolute soft X-ray photon fluxes from which are derived the spatial concentration of the impurity ions since these influence the overall energy balance and even plasma stability [16]. Impurity ion transport in tokamaks is a complex problem and depends on particle diffusion coupled with the atomic rate coefficients, viz,

$$\frac{\partial N_z(q)}{\partial t} + \nabla \cdot D_z(q) \nabla N_z(q) = S_z(q-1) N_z(q-1) - S_z(q) N_z(q) + R_z(q+1) N_z(q+1) - R_z(q) N_z(q) \quad \dots (1)$$

where  $S_z(q)$ ,  $R_z(q)$  are the total ionisation and recombination rates and  $D_z(q)$  is the diffusion rate [17] which depends in a complex way on the ion collisionality, and on the temperature and particle density scale lengths.  $R_z(q)$  includes collisional-radiative and dielectronic recombination as well as charge-exchange recombination from both injected high energy neutrals and from background thermal neutrals [18]. For diffusion rates much lower than the atomic rates, coronal equilibrium of the ion populations is assured. The opposite is the case for relatively fast ion diffusion. Typical ion diffusion times in tokamaks are  $10^3$  to  $10^4$  s and with  $N \sim 10^{20} \text{ cm}^{-3}$ ,  $n \tau = 10^{11}$  to  $10^{12} > \text{cm}^{-2} \text{ s}$ , where  $\tau$  is the effective ion confinement time. This value of  $n \tau$  is of the same order as that required to achieve ionisation balance between the ion species so the full rate equations (1), generally need to be solved.

Space resolution of the emission lines from tokamaks shows that each ion species occupies a limited volume of the plasma where its concentration reaches a maximum. H-like and He-like ions are somewhat anomalous relative to other ion species in that their dielectronic recombination rates are relatively low, see figure 5. These ion species can therefore 'visit' more extensive temperature regions of the plasma than the other ions, without recombining. They are therefore useful monitors of ionic diffusion and their characteristic lines and continua in the soft X-ray region, the  $1s^2 S_0 - 1s2p^3 P_1 / 1s^2 S_0 - 1s2p^3 P_1$  intercombination/allowed line ratio for example [19], and the free-bound recombination edge [20], have been used for this purpose. A corollary to the relatively low dielectronic recombination of the H- and He-like ions is their relatively high sensitivity to the presence of neutrals through charge-exchange recombination, figure 5.

Since charge exchange recombination directly populates the higher quantum levels,  $n = q$ , where  $q$  is the ion charge, the appearance, synchronous with the beam current rise-time, of high quantum transitions in impurity ions, is indicative of  $H^0$  beam injection. The concentrations of impurity nuclei, eg  $O^{8+}$ , which ordinarily are difficult to detect, can be measured in this way [21]. The emission rate, neglecting cascades from the upper levels, is simply,

$$I_{jk} = N(H^0) V_{b, \text{chx}} N(O^{8+}) \frac{A_{jk}}{\sum_{k=j-1}^j A_{jk}} \quad \dots (2)$$

where  $V_b$  is the beam velocity.

While, per charge exchange collision time (which equals the ionisation time in a steady-state beam-injected plasma), the population of the  $n = 2$  level of OVIII might increase by a factor of about two or less due to charge transfer from  $O^{8+}$ , (electron impact excitation always being a heavily competing process for low quantum states) the population of the upper levels, in contrast, can have their relative population increased by well over an order of magnitude due to charge exchange. Typically, OVIII  $H_\alpha$  will be enhanced during the beam injection pulse by a factor of 20 or more relative to its intensity prior to beam-injection. The Ly- $\alpha$  line of OVIII at 198 Å remains, therefore a good monitor of changes in the ground state population and thus of the ionisation balance, while the H doublet at 102.37, .51 Å is more useful for monitoring and mapping out the  $H^0$  particle beam penetration into the plasma. Isler [22] was the first to recognise the implications of the steep increase in OVIII  $H_\alpha$  during  $H^0$  beam injection into tokamaks. More recently he has used the prompt radiation from the 5-4 transition in OVIII at 632 Å to measure the  $O$  concentration [23]. Similar measurements have been made for  $N(C^{8+})$  using CVI Ly- $\alpha$  at 33 Å by Afrosimov et al [24].

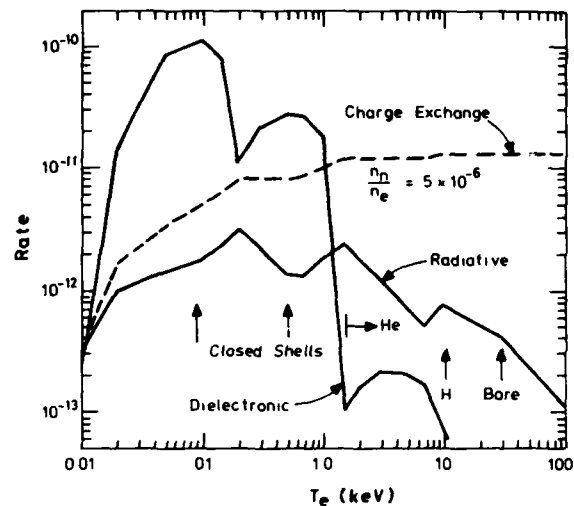


Fig 5. Recombination rates ( $\text{cm}^3 \text{s}^{-1}$ ) of the most abundant ion species of Iron in coronal equilibrium. For the H- and He-like species the dielectronic rates are relatively low while charge transfer recombination from neutral hydrogen whose concentration relative to the electron density is taken as  $n/n_e = 5 \times 10^{-6}$ , is relatively large. (D E Post and R Å Hulse, PPL).

In summary, the design guide-lines for soft X-ray instrumentation of tokamaks place a high priority on a spatial scan of the plasma. Since line profile analyses is more appropriate to the X-ray and VUV wavelength regions, soft X-ray instruments are required to have only sufficient resolving power.

$\frac{\Delta \lambda}{\lambda} \sim 10^3$  at 10 Å and  $\sim 3 \times 10^3$  at 100 Å, in order to separate out and unambiguously identify the line features. The instruments however need to be calibrated against absolute photon flux intensity falling on the diffraction element. A sufficiently high aperture to give time resolution of  $\sim 1$  ms is desirable, while continuous spectral scans with multi-channel electronic read-out would be an appealing feature.

Because of the large plasma dimensions, typically 0.1m to 1m, X-ray imaging systems such as coded apertures or grazing incidence focusing optics are less useful than tomographic analyses of the line-of-sight, chordal, soft X-ray fluxes. The derivation of spatial plasma profiles at PPL, Princeton University [25], using surface barrier detector arrays which simultaneously and continuously view as many as 20 chords through a tokamak has very adequately demonstrated the power of this technique. Nevertheless, a simple pin-hole imaging system with image intensifier cameras and I-D electronic read-out with framing rates of 50 KHz has been proposed for tokamak diagnostics [26].

## B. Laser-Produced Plasmas

Irradiation of solid targets by intense laser beams has produced approximately the same range of ion species as has magnetically confined plasmas. By 'tailoring' the light irradiation intensity at the target surface it is possible to replicate the ionic emission from tokamaks, figure 6.

Using 1  $\mu\text{m}$  laser light with a critical density for total light reflection of  $10^{21} \text{ cm}^{-3}$ , a flux intensity of  $\sim 10^{15} \text{ wcm}^{-2}$  at the target surface will produce an electron temperature,  $kT_e \sim 1 \text{ keV}$ , and light atoms, eg O, C, N etc in the critical density layer, will be stripped typically of all their electrons. The common metals appear as He- and Li-like ions while heavier elements, such as Au, can lose some 50 or more of their outer electrons.

In contrast to magnetically confined plasmas however, the interesting physics of the laser interaction, such as the light absorption, energy balance, and heat and particle transport into the solid, takes place in a highly constricted space and time scale. Measurements with 10 ps (temporal) and 1 μm (spatial) resolutions are desirable. Collision processes are extremely rapid  $\sim 10^{11} \text{ s}^{-1}$  so that radiative decays from metastable levels are not observed. For example, the  $3d^n-3d^{n-1}4s(E2)$  forbidden lines of MoXVI and MoXV, which have A values of  $\sim 10^8 \text{ s}^{-1}$  and are strong features of the Mo spectrum in a tokamak, are absent in laser irradiated Mo-targets, figure 6.

Despite the high collision frequency, ionisation-recombination equilibrium is not a general rule in laser-matter interaction experiments. This is due to the steep density gradients ( $\lambda \sim 1 \mu\text{m}$ ) where  $\lambda$  is the density scale length, the (less severe) temperature gradients, and the high streaming velocity,  $V_{iz} > 10^8 \text{ cm s}^{-1}$ , of the plasma as it expands away from the laser energy deposition layer. The effective ion confinement time  $(\lambda_s/V_{iz}) \sim (nR/q)^{-1}$  and the value of the confinement parameter  $n_e^2 Z^2 (n \lambda_s/V_{iz}) = 10^3 \text{ cm}^{-3} \text{ s}$  are less than those necessary to achieve ionisation balance [27].

The main diagnostic parameters of interest in laser-plasma interactions or laser-driven compression experiments are the spatial density structure in the inter-action region and the compressed core density  $\rho$  and the confinement factor  $\int \rho \cdot dr$ . These parameters  $\rho$  and  $\int \rho \cdot dr$  can be derived conveniently from line broadening. Linear Stark broadening of H-like transitions in these high density plasmas is often of the order  $\Delta\lambda/\lambda \sim 10^{-2}$  so that ions, eg Ar XVIII, seeded into the compressed plasma, emit lines which can act as density indicators. The use of linear Stark broadening is restricted not only to hydrogenic (degenerate) levels but in practice is often restricted, also, to intermediate quantum levels. High quantum transitions merge with the continuum while transitions from the lowest quantum levels are often optically thick to line radiation.

An optical depth  $\tau_0$  for Ly- $\alpha$  can often be between  $10 \rightarrow 100$  while for Ly- $\beta$  a value of  $\tau_0 \sim 1$  is more usual. It is important to note that a single observable such as the half intensity width of an optically thick line is not of itself a unique function of the plasma microfield broadening and therefore of  $n$  but depends also on the number density of the emitter ions [28]. More appropriately, the series members such as Ly- $\alpha$ , - $\beta$  are used to derive the product of the emitter concentration and scale length, ie  $\int \rho \cdot dr$ , from their opacity-distorted profiles, while the optically thin, higher series members eg Ly- $\gamma$  and Ly- $\delta$  and H $\epsilon$  which all suffer mainly Stark broadening, are used to derive  $n$ .

Crystal instruments are most often used for line profile analyses at  $\lambda < 25 \text{ \AA}$  [28] [29], although the plasma microfield broadening of the optically thin line wings can be sufficient at longer wavelengths to contemplate the use also of grazing-incidence grating dispersion [30]. Space resolution is simply but inefficiently effected by positioning an aperture between the plasma and dispersion element or between the input slit and the dispersion element in the case respectively of a crystal or a grating spectrometer. Relay focusing optics using grazing-incidence mirrors allows the spectrometers to be remotely positioned from the plasma. When considering X-ray imaging systems [8] [31], coded-aperture and reflection-optics microscopy allow a large increase in the soft X-ray throughput (for a given spatial resolution) over that available with a pin-hole aperture. Time-resolution of the soft X-rays is now routinely achieved by projecting an X-ray image or spectrum onto the photocathode of a gated, image-intensifier. These cameras have inherent resolutions of 1 ps and 20 μm. Remarkable advances have been made, during recent years in the diagnostics of these highly transient micron-size plasmas [31]. However, a combination of high light throughput, time resolution  $\sim 10 \text{ ps}$  space resolution  $\sim 1 \mu\text{m}$  and spectral resolution  $\Delta\lambda/\lambda \gg 10^{-3}$ , is still something of a tour de force.

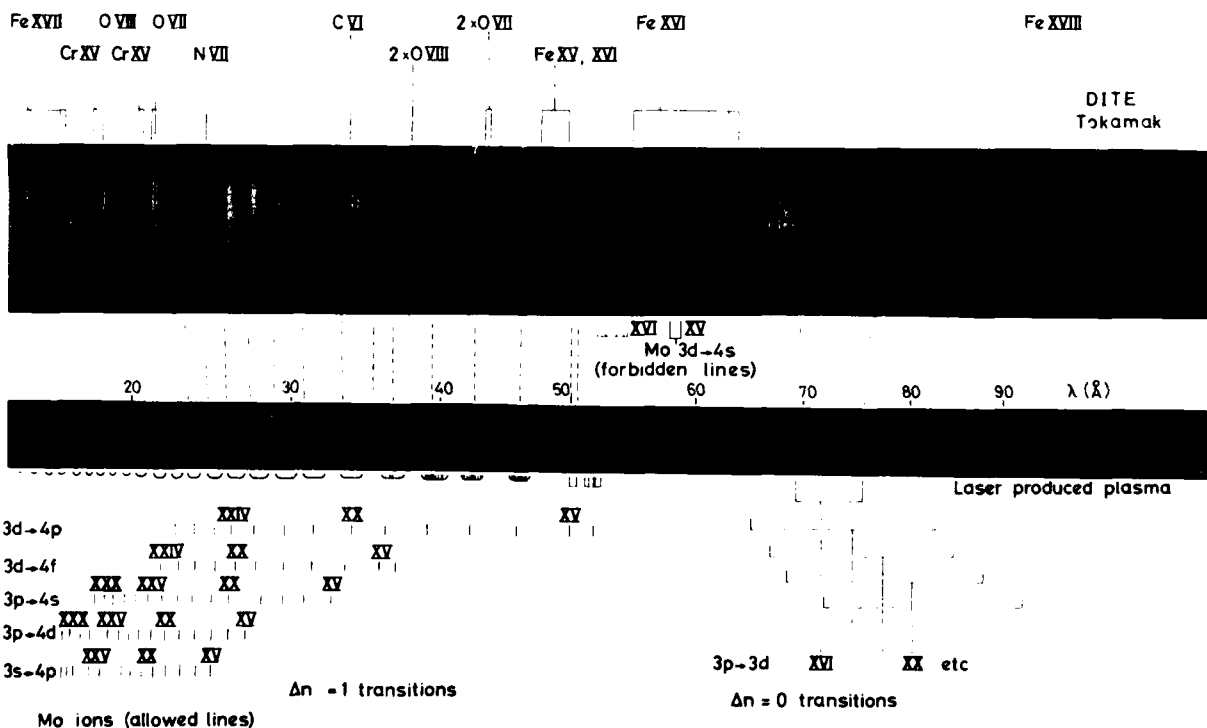


Fig 6. Soft X-ray spectrum from DITE tokamak operated with a Mo limiter (upper) compared with spectrum from laser-irradiated solid Mo target (lower). Note the appearance of the Mo forbidden lines in the tokamak spectrum.

### III DESIGN CRITERIA FOR SOFT X-RAY INSTRUMENTATION

#### A. Tokamaks

In the design of dispersion instruments for fusion studies it is pertinent to consider firstly the intensity of the emission lines from the plasma and secondly the throughput efficiency required of the spectrometer to achieve a desired time or spectral resolution. The volume emissivity of a line is simply

$$f_{\epsilon}(\lambda) d\lambda = \frac{N_z(q_j) A_{ij} h\nu_{ij}}{4\pi} \quad \dots (3)$$

The local concentrations of the ions of atomic number  $Z$  and charge state  $q$  is often the parameter of interest. The population of level  $j$  can be calculated in terms of the ground state population using appropriate numerical codes [32] which include the collisional and radiative coupling processes between a significant fraction of all the levels, including levels  $i$  and  $j$ . More simply, the coronal relation can sometimes be used.

$$f_{\epsilon}(\lambda) d\lambda = \frac{n_e N_z(q_{ij}) C_{ij} A_{ij} h\nu_{ij}}{\sum_j A_{ij}} \quad \dots (4)$$

where the excitation rate is given in terms of the collision strength  $\Omega_{ij}$ ,

$$C_{ij} (\text{cm}^{-3} \text{s}^{-1}) = \frac{8.63 \times 10^{-6}}{\omega_1(kTe)^{3/2}} \int_{\Delta E_{ij}}^{\infty} \Omega_{ij}(E) \exp(-E/kT_e) dE \quad \dots (5)$$

This relation is appropriate to allowed transitions whose upper levels are populated entirely by collisions from the ground level and where branching decays are known. The presence of metastable levels coupled to the upper level can disqualify this simple coronal excitation model, in which case one has to fall back on a numerical solution of the full set of time dependent coupled equations describing the level populations.

Volume emissivities of strong impurity lines from tokamaks range typically from  $\sim 10^{10}$  photons  $\text{cm}^{-3} \text{s}^{-1}$  in the X-ray region to  $\sim 10^{15}$  photons  $\text{cm}^{-3} \text{s}^{-1}$  in the XUV region.

#### A.(i) Grating Dispersion

Using a grazing-incidence grating spectrometer layout as illustrated in figure 7 the photon intensity in the diffracted lines can be calculated

$$F(\text{ergs cm}^{-2} \text{s}^{-1}) = \frac{T(\lambda) S W \ell L G(\lambda) f_{\epsilon}(\lambda) d\lambda}{4 R r dx_{1/2} \sin \beta} \quad \dots (6)$$

With an acceptance slit width  $s' = dx_{1/2} \sin \beta$  and length  $\ell'$  at the detector, then

$$F'(\text{quanta s}^{-1}) = \frac{T(\lambda) S W \ell \ell' L G(\lambda) f_{\epsilon}(\lambda) d\lambda}{4\pi R r h\nu} \quad \dots (7)$$

where  $T(\lambda)$  is the transmission of the  $\lambda$  ray path;  
 $s$ (cm) is the entrance slit width;  
 $\ell$ (cm) is the entrance slit length;  
 $W$ (cm) is the ruled length of the grating illuminated by  $\lambda$ ;  
 $L$ (cm) is the viewed depth of the plasma volume;  
 $G(\lambda)$  is the grating reflectivity at  $\lambda$   
 $R$ (cm) is the radius of curvature of the grating-  
 $r$ (cm) is the slit to detector distance for  $\lambda$ ;  
 $h\nu$  is  $\frac{hc}{\lambda}$

Consider two fairly strong lines which often appear in tokamak spectra viz, OVII  $1s^2-1s2p^1P_1$ , at 21.602 Å and Fe XVII  $2p^6-2p^53d$  at 15.013 Å. At a temperature of 300 eV the fractional abundance of  $O^{6+}$  is  $\sim 0.1$ . Thus for  $n = 3 \times 10^{13} \text{cm}^{-3}$  and a typical oxygen impurity level of  $1\%$ ,  $\frac{\Sigma N(O^{+q})}{n_e} = 0.01$ , then  $N(O^{6+}) = 3 \times 10^9 \text{cm}^{-3}$  and  $f_{\epsilon}(21.6 \text{ Å}) d\lambda = 1.6 \times 10^{13} \text{ph cm}^{-3} \text{s}^{-1}$ . At

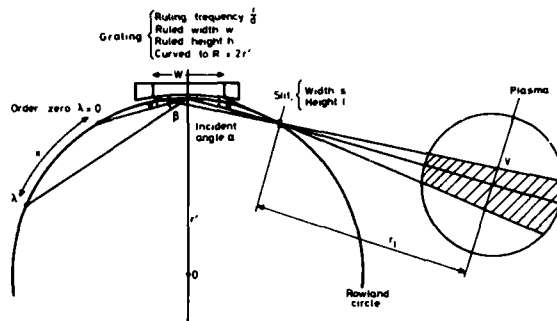


Fig 7. Schematic diagram of the optical layout of a Rowland circle grazing-incidence grating spectrograph viewing the cross section of a toroidal plasma.

a temperature of  $\sim 400$  eV when Fe XVII has a relatively high fractional abundance,  $N(\text{Fe}^{+16})/\Sigma N(\text{Fe}^{+q}) \approx 0.5 + 0.6$ , and at the same electron density,  $3 \times 10^{13} \text{cm}^{-3}$ , and an iron impurity level of 0.001  $n_e$ , then

$$f_{\epsilon}(15 \text{ Å}) d\lambda = 3 \times 10^{13} \text{ph cm}^{-3} \text{s}^{-1}$$

Setting, appropriate values for the symbols in equation (7) we derive for the flux in the diffracted line

$$F'(21.6 \text{ Å}) = \frac{1.0 \times 0.001 \times 2.0 \times 0.75 \times 1.0 \times 50 \times 0.05}{4\pi \times 200 \times 25} \frac{1.47 \times 10^4}{0.919 \times 10^{-9}} \approx 1 \times 10^6 \text{quanta s}^{-1}$$

Taking a quantum efficiency of 5%, typical of a channeltron response at  $\sim 21 \text{ Å}$ , the above flux gives a count rate of  $5 \times 10^4 \text{Hz}$ . The count rate for the Fe XVII (15 Å) line is nearly the same. Assuming an electron multiplication of  $10^7$ , the charge collection rate is  $\sim 0.08 \mu\text{A}$  for these soft X-ray lines. High count rate channeltrons such as the "Galileo 4818" can operate in excess of  $10^6 \text{Hz}$  before the detection efficiency starts to fall, and at rates up to  $10^5 \text{Hz}$  without appreciable loss in gain. A time resolution of 5ms should therefore be attainable.

Using the optical layout as in figure 7 one might then expect count rates of up to  $10^6 \text{Hz}$  for most of the intense lines in the grazing incidence region. The depth of the plasma which contribute to the line intensity is taken to be 0.5m, a reasonable value for the dimensions of the sub-keV temperature region in a JET-sized tokamak. In a smaller device such as the DITE tokamak the line count rate is less but is still a very useful value, as illustrated in figure 8 by the time variation of the CV  $1s^2-1s2p^1P_1$  transition at 40.27 Å.

A problem with photoelectric readout of the spectra, which is particularly severe for shallow grazing angles of the incident light and short wavelengths,  $\lambda < 100 \text{ Å}$ , is the competition from background light. Even for relatively intense lines, as illustrated in figure 9 by the spectral scan through the Ly- $\alpha$  OVIII line at 19 Å, the peak intensity to background can be as low as 3/1. Ideally each line should have two measuring channels, one which monitors the peak line intensity and the other the adjacent background light. On the other hand, use of a multi-channel detection system such as a micro-channel plate (MCP) or better still, a photographic emulsion, see eg figure 6, ensures a contrast of at least 20/1. The source of this background light has not been properly researched but is probably due to scattered soft X-rays or longer wavelengths scattered from the

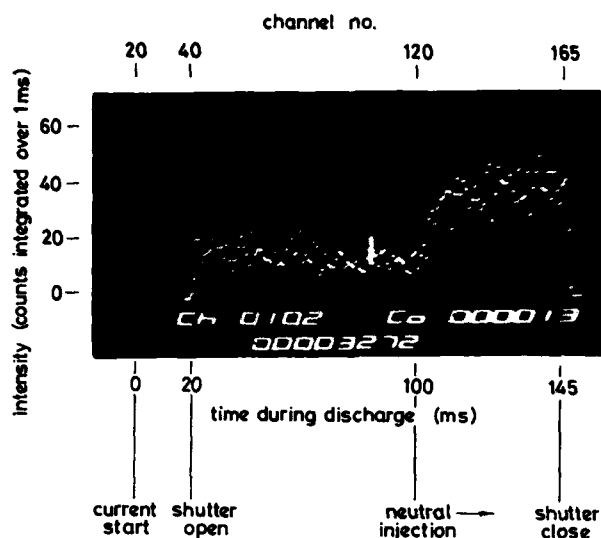


Fig 8. Time variation of CV  $1s^2-1s2p.1 P_1, 40.27 \text{ \AA}$  emission from the DITE tokamak, measured with a grazing-incidence spectrometer. Note the increased level during the neutral injection pulse and negligible background detector signal with the mechanical shutter closed.

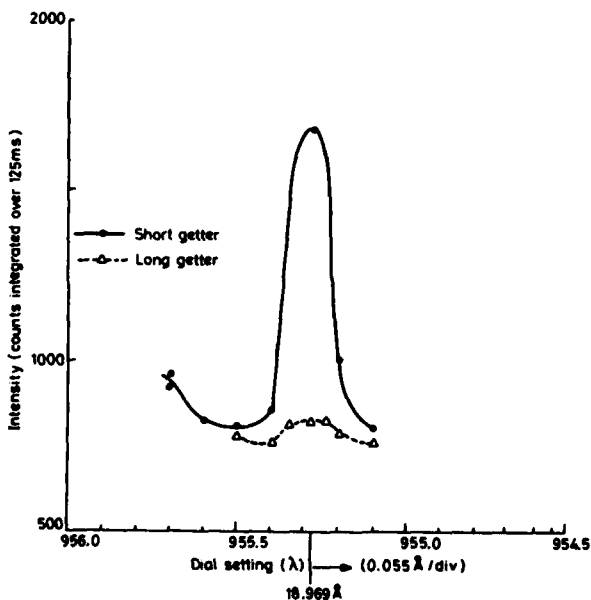


Fig 9. Wavelength scans, on successive discharges of the DITE tokamak, through the Ly- $\alpha$  OVIII emission. The 'long getter' pulsed conditions reduce the oxygen concentration and the emission from this ion falls to almost the background light level.

grating, perhaps also fluorescence of the grating to harder X-rays. Channeltrons are a poor choice of detector in the respect that they are sensitive to a wide range of wavelengths with a peak sensitivity in the XUV spectral region. The use of filters [33] and low scatter, holographically ruled gratings help to increase the line intensity/background ratio but it is very difficult to realise the same contrast over a broad spectral band as is routinely achieved with photographic emulsion. Our calculations indicate, moreover, that to achieve a density of 0.5 above fog on, say, Kodak Pathe SC-5 film with the photon flux estimated (above) for OVII at  $21.6 \text{ \AA}$  (using a 2 metre radius grating ruled with  $1200 \text{ 1/mm}$  at a  $2^\circ$  grazing angle) an exposure time of  $\sim 250 \text{ ms}$  is required. For very long-lasting plasmas such as anticipated in the JET tokamak ( $\sim 10 \text{ s}$ ) the use of a grazing-incidence spectrometer with photographic emulsion recording and with a camera shutter to control the exposure time is not an unappealing proposition.

#### A(ii) Crystal Dispersion

At wavelengths shorter than about  $25 \text{ \AA}$ , crystal dispersion becomes an alternative to the use of grazing incidence diffraction gratings. Crystals are highly effective monochromators rather than true broad band spectrometers, so that surveying a region of the spectrum conventionally involves scanning the crystal through a range of Bragg angles, either stepping the angle in a series of discrete motions or by continuous crystal rotation. If a flat crystal is used, reasonable spectral resolution can be maintained by restricting the angular divergence of the incident light at the crystal with a Soller slit. Indeed, the first crystal survey of a plasma in the soft X-ray region ( $\lambda < 22 \text{ \AA}$ ) was achieved with just such a flat crystal and Soller slit arrangement [34]. An alternative arrangement is to accept a range of Bragg angles simultaneously by the crystal convex in the "de Broglie" configuration, figure 12.

A large increase in light throughput with higher resolution can be achieved if the crystal is bent, in the "Johann" mode, concave to the diameter of a Rowland circle onto which is positioned the effective entrance aperture, the dispersion element and the detector. Better efficiency still can be achieved if the Rowland circle arrangement is retained but with the front face of the crystal ground to the Rowland circle radius as in the fully-focusing "Johansson" mode. The relative merits of these convex and concave configurations for tokamak (JET) studies are discussed by Hobby et al [35].

The schematic optical layout of a focusing crystal spectrometer attached to a toroidal plasma device is shown in figure 10 with the Rowland circle parallel to the toroidal axis. The wavelength coverage is the range of Bragg angles is clearly dependent on the entrance aperture to the torus and on the diameter of the Rowland circle. Our proposal [35] for the JET tokamak studies favours a relatively small Rowland circle diameter  $R = 75 \text{ cm}$  and a compact vacuum system. The crystal width  $W$  can then be kept reasonably small  $< 5 \text{ cm}$ , while the sensitivity is not affected since this depends on  $W/R$ . Defocusing aberrations on the other hand scale as  $(W/R)^2$  and  $(h/R)^2$  where  $h$  is the crystal dimension orthogonal to the plane of the dispersion but these will lead to only a marginal loss in resolution [35].

One consequence of the relatively tight focusing circle is the requirement for a high spatial resolution detection system. Microchannel plates provide adequate resolution ( $\sim 0.035 \text{ mm}$ ) for this purpose and we tolerate their rather poor efficiency  $\sim 5\% \rightarrow 20\%$  over the range  $10 \text{ \AA} \rightarrow 100 \text{ \AA}$  in the soft X-ray region. In order to cover the important line groups from the ion species likely to be present in a tokamak, a stack of six different crystals is proposed [35] viewing the plasma over a range of Bragg angles from  $48^\circ$  to  $58^\circ$ . A high mean viewing angle  $\sim 53^\circ$  is preferred for low optical aberration, high resolution and near normal-incidence on the detectors. The microchannel plates have a  $30^\circ$  bias of the channels to the normal as indicated in figure 11 in order that the diffracted light strikes the channels at an optimum angle  $\sim 7^\circ$ .



for maximum sensitivity.

The resolving power of the crystal instrument is

$$\frac{\lambda}{\delta\lambda} = \frac{\tan\theta}{\delta\theta} \quad \dots (8)$$

where  $\delta\theta$  is a convolution of  $\delta\theta_c + \delta\theta_B + \delta\theta_D$ .  $\delta\theta_c$  is the FWHM of the crystal diffraction pattern,  $\delta\theta_B$  is the focusing aberration,  $\delta\theta_D$  is the loss in resolution due to the finite elements of the detector.

For the spectrometer characteristics outlined above we might expect a resolving power of between  $10^4$  and  $2 \times 10^4$  for dispersion of  $2 \text{ \AA}$  light from a good quality quartz crystal [35]. Since in the soft X-ray region we are interested in rather longer wavelengths, then mica could be used to diffract  $15 \text{ \AA}$  radiation at a Bragg angle of  $48.9^\circ$  (ie within the angular viewing range of the instrument). The crystal diffraction width for  $15 \text{ \AA}$  light in first order from a mica crystal is likely to be  $\sim 100$  arc sec and this is at least an order of magnitude wider than diffraction widths for good quality crystals in the X-ray region proper. The resolution therefore at these longer wavelengths is proportionately reduced.

As for the Rowland circle grating instrument, we can calculate the sensitivity relation for the Johansson configuration, viz.

$$P = T(\lambda) \frac{W h L R(\theta_c)}{4 \pi R dx_{1/2}} \frac{f_{\epsilon}(\lambda) d\lambda}{h\nu} \quad \dots (9)$$

where the symbols are as equation (6), except that  $R(\theta_c)$  is now the integrated reflectivity of the crystal.

For a detector length  $l'$  and width  $(dx)_{1/2}$  the flux in the diffracted line is

$$P' = T(\lambda) \frac{W h L R(\theta_c) l' f_{\epsilon}(\lambda) d\lambda}{4 \pi R h\nu} \text{ (quanta } s^{-1}) \quad \dots (10)$$

Again, considering as before the Fe XVII line at  $15.013 \text{ \AA}$  from a plasma with the same parameters and the same volume emissivity  $f_{\epsilon}(\lambda) dx = 3 \times 10^{13} \text{ ph cm}^{-3} s^{-1}$ ; but now assuming mica crystal dispersion with  $R(\theta_c) = 10^{-5}$ , and a detector length of 1cm, we have,

$$P' (15 \text{ \AA}) = \frac{1.0 \times 4.0 \times 1.0 \times 50 \times 1 \times 10^{-5} \times 1.0 \times 3 \times 10^{13}}{4 \pi \times 75} \\ = 6.4 \times 10^7 \text{ quanta } s^{-1}$$

For a detector efficiency of 4% this represents for the  $15 \text{ \AA}$  line a count rate of  $2.6 \times 10^6 \text{ Hz}$  ( $\sim 1 \times 10^8$  electrons  $\text{cm}^{-2} s^{-1}$  at the detector surface). Such an instrument should provide time-resolved impurity spectra from a Jet-size plasma on the time scale of a few msec.

A cascaded channel-plate assembly with delay-line read-out satisfies most of the detector requirements giving adequate spatial resolution and quantum efficiency, though probably the dynamic range is insufficient to record the strong lines synchronously with the very weak lines.

The use of much larger radius focusing crystal instruments, for example the 3.3m Johan configuration with multi-wire proportional counter read-out used at Princeton University, has already proved very effective for line profile studies of tokamak plasmas [36]. Other intermediate-size configurations, such as the 1.5m Johann spectrometer at Fontenay aux Roses [37], with the quartz crystal held against the cylindrical former by atmospheric pressure and with linear, position-sensitive proportional counter read-out, have also been developed. The tighter Rowland circle proposed here [35] suffers in no important respect such as light throughput, resolution etc, while its compact size allows it to be tilted so as to spatially scan the plasma volume.

For soft X-ray spectral survey purposes a very simple crystal spectrometer can be based on the de Broglie convexly curved configuration, figure 12. This spectrometer can be used with photographic or photoelectric

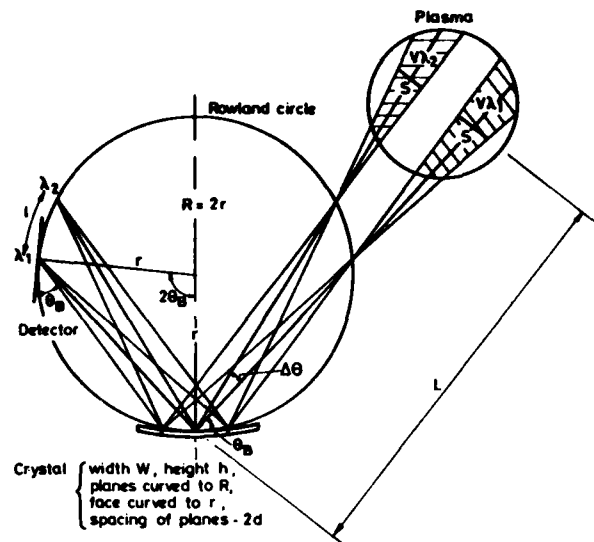


Fig 10. Schematic diagram of the optical principle of the Johansson focusing crystal spectrometer.

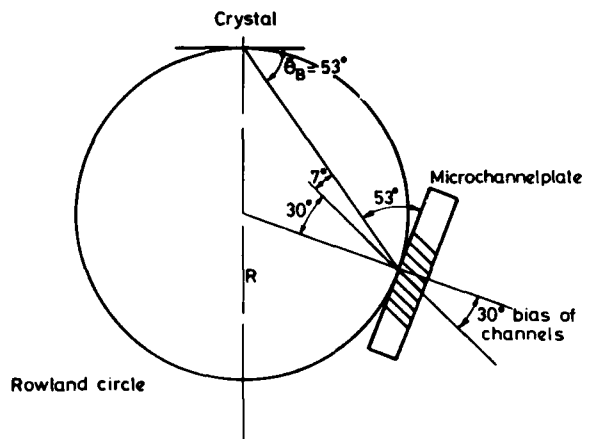


Fig 11. Tangential setting of special  $30^\circ$  bias microchannel plate for optimum efficiency (glancing angle  $7^\circ$ ).

read-out, and with a curved KAP crystal wavelength coverage from  $1 \rightarrow \sim 23 \text{ \AA}$  can be expected. The relatively low efficiency of this configuration means that only modest time-resolution is achieved. The dispersion relation for the de Broglie configuration is

$$\frac{d\lambda}{d\ell} = \frac{2d \cos\theta}{R \left[ 2 - \frac{r \sin\theta}{R} \left( 1 - \left( \frac{r \cos\theta}{R} \right)^2 \right)^{-1/2} \right]} \quad \dots (11)$$

where  $r$  is the crystal curvature and  $R$  is the radius of the detector circle around which the wavelength variation is almost linear with distance.

The count rate per emission line dispersed by the de Broglie crystal viewing an extended source through a narrow slit is given by

$$F = \frac{T(\lambda) r \sin \theta R(\theta) s b L \int \epsilon(\lambda) d\lambda (\text{quanta s}^{-1})}{4 \pi l (l + t) h \nu} \dots (12)$$

where the symbols have the same meaning as before except,

$\theta$  is the Bragg angle for wavelength  $\lambda$ ;  
 $r$  (cm) is the curvature of the crystal;  
 $l$  (cm) is the distance of the slit to the crystal;  
 $t$  (cm) is the distance from the slit to the detector;  
 $s$  (cm) is the slit width and  $b$  (cm) is the slit length;

Again, assuming a de Broglie spectrometer with a mica crystal, 5 cm high, viewing a 50 cm depth of a tokamak plasma which emits  $3 \times 10^{13}$  photon  $\text{cm}^{-3}$  of  $15 \text{ \AA}$  Fe XVII light then inserting appropriate numerical values for the symbols respectively in equation (11),

$$F = \frac{1.0 \times 5.0 \sin 49^\circ \times 10^{-5} \times 0.05 \times 5 \times 50 \times 1.0 \times 3 \times 10^{13}}{4 \pi \times 50 \times 60} = 3.8 \times 10^5 \text{ quanta/s}$$

which, with a 4% photo-detection efficiency, gives a count rate of  $1.5 \times 10^4$  Hz. With a global count rate [35] for the channeltron read out system of  $\sim 10^6$  Hz, several tens of lines can be recorded with about 1% statistical variation and a fraction of a second exposure. Even with photographic film a density of 0.5 above fog would be achieved with an exposure time  $\sim 10$  sec (ie the full pulse length of the JET tokamak).

An alternative broad-band crystal configuration makes use of a plane flat crystal which is rotated through the required range of Bragg angles. Collimation of the input light with grided apertures is necessary. In this case the detector can be a simple light 'bucket' and the spectrum is dispersed as a function of time. A 5 x 5 cm crystal with a rotational speed of 100 Hz and an acceptance angle of 100 arc sec set by the crystal rocking curve and the entrance collimator would give a total count rate per line of the same order as the static, de Broglie instrument. Comparing the merits of these two modes, the rotating and static crystals, there is a direct trade off between band-width and time resolution, the spectral resolution remaining almost constant. More sensibly therefore the light throughput should be increased at the expense of band-width by slowing the rotation to  $\sim 1$  Hz. These flat crystal configurations are used with considerable success in stellar X-ray studies eg [38].

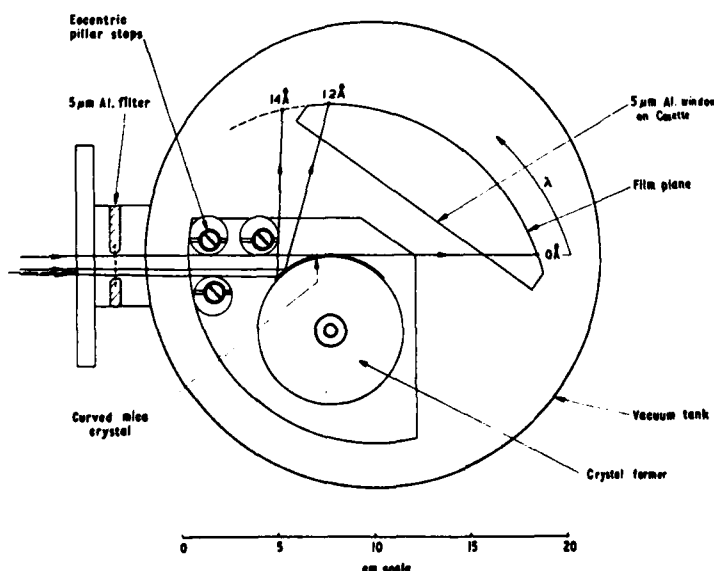


Fig 12. Optical layout of de Broglie crystal spectrometer.

### A(111) Crystal Versus Grating Dispersion At Soft X-Ray Wavelengths

For wavelengths in excess of  $25 \text{ \AA}$ , grating dispersion instruments have exclusively been used for broad band spectroscopy of fusion plasmas. At the short wavelength end of the soft X-ray region crystal instruments on the other hand have clear advantages in terms of light throughput and wavelength resolution. It is of interest to consider these parameters in the limited wavelength region  $\sim 10 \text{ \AA} \rightarrow \sim 25 \text{ \AA}$  where the advantage of one dispersion system over another is somewhat contentious. An appreciation of the problem can be gained by considering the resolving power and light throughput of the focusing crystal and grating instruments cited for  $15 \text{ \AA}$  light in sections III.A.(1) and (11).

We note in A.(1) that a  $10 \mu\text{m}$  slit width and a grating aperture of 2cm has been assumed in order to achieve a line flux  $\sim 1 \times 10^6$  quanta  $\text{s}^{-1}$  at  $15 \text{ \AA}$ . The resolution of the spectrometer is in this case determined largely by the slit width but also by the grating aperture and ruling frequency. At  $15 \text{ \AA}$  a  $10 \mu\text{m}$  slit presents no diffraction problems. The resolving power due to the finite slit width is,

$$R_{sl} = \left( \frac{\lambda}{\Delta\lambda} \right)_{sl} = \frac{\lambda 0.09 R(n) n d (\text{mm})}{s (\mu\text{m})} \dots (13)$$

where the symbols are as before, but with units in parentheses,  $n$  is the order number and  $d^{-1}$  is the grating ruling frequency. With a 2-metre radius of curvature and  $d^{-1} = (2,400/\text{mm})^{-1}$  then the slit width limited resolving power is given by

$$R_{sl} = \left( \frac{\lambda}{\Delta\lambda} \right)_{sl} = 654$$

The resolving power set by the grating aperture at grazing incidence is given by  $R(\text{opt}) = \frac{0.92 n x W(\text{opt})}{d}$

where the optimum aperture [39] is  $\sim 1.2$  cm for the above grating used at a  $2^\circ$  grazing angle.

The finite thickness of the emulsion also causes some loss in resolution. The overall resolving power however is largely determined by equation (13) and can be taken as  $< 1000$ . On the other hand we have seen, equation (8), that the resolving power of a Johann crystal spectrometer is largely dependent on the angular divergence  $\delta\theta_R$  at the crystal which will support monochromatic Bragg reflection. For diffraction of  $15 \text{ \AA}$  light from a mica crystal at a mean Bragg angle of  $49^\circ$ ,  $\delta\theta_R \sim 100$  arc sec, giving a resolving power

$$R(\theta_R) = \left( \frac{\lambda}{\delta\lambda} \right) = 2.3 \times 10^3.$$

Defocusing aberrations are given by

$$\frac{\lambda}{\delta\lambda_W} = 8R^2 \tan^2 \theta / W^2 \dots (14)$$

and

$$\frac{\lambda}{\delta\lambda_h} = 8R^2 \frac{\sin^2 \theta}{h} \dots (15)$$

and account for resolutions,  $\delta\lambda_W$  and  $\delta\lambda_h$  due to the finite aperture length  $W$  and finite height  $h$  of the crystal. The overall resolving power  $\approx R(\theta_R)$  of the Johann instrument is about a factor of  $3.5^R$  better than the grating instrument at  $15 \text{ \AA}$  and has, moreover, a light throughput (see III.A(1), (11), which is greater by a factor of  $\sim 60$ . These advantages of focusing crystals became more pronounced at shorter wavelengths provided that one chooses an appropriate crystal to preserve an almost constant Bragg angle. The indications are that the 'cross-over' wavelength at which focusing crystals and gratings have comparable performance is between  $20 \text{ \AA} \rightarrow 25 \text{ \AA}$ . In respect of total band-width, of course, a grating spectrometer used at shallow angle of incidence,  $< 1^\circ$ , will easily outperform a focusing crystal spectrometer.

## B. Laser-produced plasmas.

Despite the minute plasma dimensions,  $< 100 \mu\text{m}$ , and the short duration,  $< 1 \text{ ns}$ , of the  $1 \text{ keV}$  plasmas produced by intense laser irradiation of solid targets, the X-ray emission is sufficiently copious, typically a few percent or more of the incident laser beam power, that even the relatively inefficient grating and crystal dispersion instruments can be used [40]. A consequence of the need for micron-size space resolution, is that X-ray microscopy in one form or another is essential. A time resolution of  $\sim 10 \text{ ps}$  implies that fast electronic gating, or high-frequency response detectors capable of handling 'pileup' pulses, is necessary.

### B.(i) Grating Spectroscopy

Grating spectrometers with a slit aperture orthogonal to the entrance slit and placed between it and the grating can provide sufficient spatial and spectral resolution to diagnose the critical surface and ablated plasma regions of the irradiation target [30]. In order to collect adequate light flux however, the plasma source is placed typically a few mm from the entrance slit of the spectrometer. However, the use of aspheric reflection optics to relay the X-rays to the grating allows the spectrometer to be placed remote from the plasma. In the Rutherford laboratory laser programme, for example, toric surfaces with principle radii of  $5 \text{ m}$  and  $26 \text{ mm}$  are used both for the relay optics and for the grating substrate [41]. Spatial resolution of the object of  $10 \mu\text{m}$  and a spectral resolution of  $30 \text{ m}\text{\AA}$  at  $\lambda = 40 \text{ \AA}$  have been achieved with a toric substrate carrying holographically formed 'rulings' at a frequency of  $1200 \text{ 1/mm}$ . The formation of a stigmatic image, of course, occurs only over a limited spectral bandwidth. Photographic recording is commonly used with these grating spectrometers because there is little loss in resolution due to the emulsion thickness. Also it is often possible to map out a crude time history of the plasma expansion using the close correlation between the location of emitting ions and time.

### B.(ii) Crystal Spectroscopy.

Focusing crystals, as in the Johann configuration, give little advantage over a flat crystal when viewing laser-produced plasma since the tight radius of curvature,  $\sim 1 \text{ cm}$ , required for light collection would induce unacceptable diffracted image aberrations. Miniature flat crystal spectrometers are most frequently used the spectral resolution being set by the crystal rocking curve and/or the finite size of the source. Fortunately, some diagnostic observables, such as Stark line widths of hydrogenic transitions, can be so large that the ultimate in spectral resolution is not required. In these crystal spectrometers a slit aperture, placed between the source and the film, figure 13, allows the plasma to be space-resolved with a resolution, typically  $3 \rightarrow 20 \mu\text{m}$ . The image of the outer shell wall in micro-balloon irradiation experiments is clearly separated from the X-rays emission from the compressed core plasma.

Temporal resolution of the X-rays is effected by projecting the spectrum onto the photocathode of gated image-intensifier as illustrated in figure 14. A time resolution  $\sim 70 \text{ ps}$  and a spectral resolution  $(\lambda/\Delta\lambda) \sim 500$  are typical of this type of apparatus [42]. For X-rays in the energy range  $h\nu \sim 1 \rightarrow 10 \text{ keV}$ , the photocathodes are typically at  $200 \text{ \AA}$  thick coating of Au on a Be substrate. A spongy coating of CsI of thickness  $20 \rightarrow 200 \mu\text{m}$ , depending on the X-ray energy, can increase the overall sensitivity of the camera by a factor of  $\sim 20$ , the image being recorded either on film or digitally via a charge coupled device (CCD). Since one dimension of the image plane is reserved for the time sweep only a thin slice of the geometrical image of the plasma is displayed.

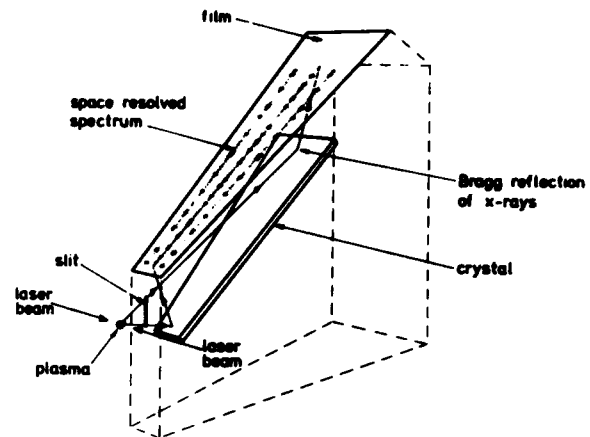


Fig 13. Flat crystal dispersion arrangement for space-resolution of the X-ray spectrum from laser-irradiated solid target.

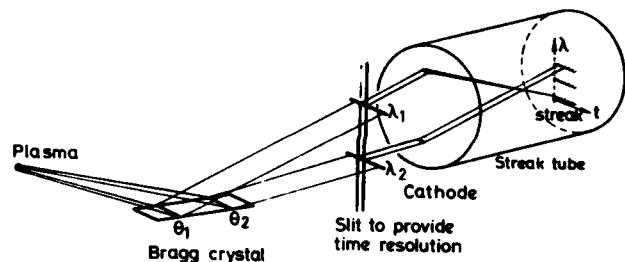


Fig 14. Schematic diagram of apparatus for X-ray streak spectroscopy of laser-produced plasma.

### B.(iii) Soft X-ray Imaging Systems

In order to appreciate the extent to which X-ray microscopy of the minute plasma volumes produced in laser compression experiments has developed over the last few years one has only to refer to the Lawrence Livermore annual reports [43]. Reflection microscopy has the advantage of good spatial resolution  $\sim 1 \mu\text{m}$  and relatively long objective distances which allows the image-forming components to remain undamaged during the micro-explosion of the target. A complementary technique developed by Ceglio and Co-workers [8][44][45] is that of coded-aperture imaging which gives the capability for 3-D analysis on reconstruction of the image. The coded apertures are typically free-standing micro Fresnel zone plates  $5 \mu\text{m} \rightarrow 25 \mu\text{m}$  thick with zone

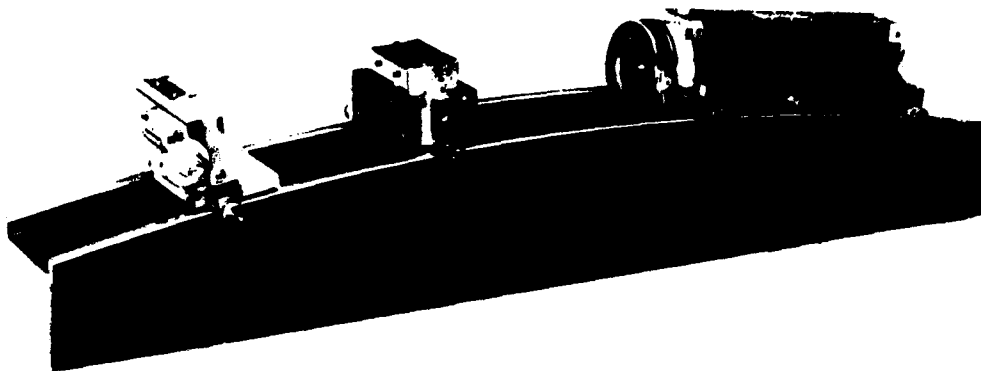


Fig 15. GML-5M grazing incidence spectrograph [51] showing entrance slit, grating and photographic cassette modules located on reference beam.

numbers  $100 \lambda N \approx 250$ , the width of the outermost zone being  $\Delta r \approx$  a few microns; this being the same order as the planar resolution. Tomographic (in depth) resolution of a few 10's of microns can be achieved. Thin transmission filters are employed, as in tokamak X-ray tomography [25], to differentiate between different regions of the spectrum - otherwise the apparatus developed for X-ray imaging of these two laboratory sources, tokamaks and laser-irradiated microballoons, could hardly be in more dramatic contrast.

#### IV. SOFT X-RAY SPECTROSCOPY AT THE CULHAM LABORATORY

Among the grazing incidence diffraction grating spectrometers at the Culham laboratory are a few which have seen continuous use since their design and construction some two decades ago. These include the E580, 2-metre instrument [46] which can be supplied, by Rank Hilger Ltd (UK), with photographic recording as in figure 4, or with a single-channel scan unit for photo-electric read out, figure 8. An earlier version of the present Mark III 1-metre spectrometer, with each of two scanning slits and associated photo-electric deflectors capable of being driven round the Rowland circle, was first used on the Zeta fusion device [47]. This illustrates the durability of the basic Rowland circle geometry for grazing-incidence grating spectroscopy.

A 'state of the art' development of these astigmatic instruments is the GLM-5 spectrograph (manufactured by Grating Instruments Ltd - UK) in which the slit, grating and detector modules are, within machining tolerance, located on the Rowland circle by virtue of their location on a one metre long segment of a reference circle [48]. This arrangement, gives flexibility in the disposition of the modules, as might be required, for example, in altering the angle of incidence, without degrading the preset focus. The basic instrument with photographic detector module is shown in figure 15 while a schematic diagram of the spectrograph in its vacuum tank, as it would be used to spatially scan a tokamak plasma, is shown in figure 16. Test spectra with a grazing angle of  $1.65^\circ$ , a holographically formed 600 1/mm grating, and a 1  $\mu$ m entrance slit indicate a resolution of  $< 0.05$  eV at  $h\nu = 150$  eV and  $< 1$  eV at  $h\nu = 1.2$  keV. A 2-channel scanning slit unit, figure 17, has been designed and fabricated [49] as an alternative photo-detection module to the photographic cassette. The slit assemblies are symmetrical about a meridian dividing plane through the mid-point of the entrance slit and the pole of the grating, and they measure equal halves of the astigmatically lengthened spectral lines. Each slit is independently driven around the Rowland circle. This arrangement is ideal for line/background intensity measurements and for the measurement of line intensity ratios eg to  $\text{Ly-}\alpha(0^+)$ / $\text{H}_\alpha(0^+)$  which are separated by  $\approx 80$   $\text{\AA}$  or for the intercombination/allowed lines of  $0^+_{2+}$  where the separation at 21.6  $\text{\AA}$  is only 0.2  $\text{\AA}$ .

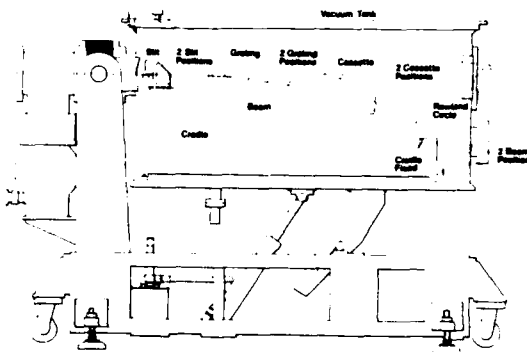


Fig 16. Optical layout of GML-5M grating spectrograph within vacuum housing. The whole assembly tilts to spatially scan the cross-section of a tokamak plasma.

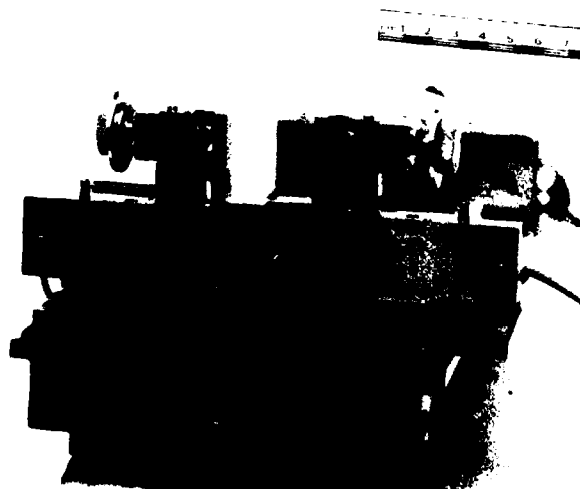


Fig 17. Two channel photo-electric detector module for GML-5M spectrometer (fig 15). Both slit units are driven independently and can be positioned to record equal lengths of the same dispersed line or of different lines within the wavelength range of the instrument.

Position read out of the slit modules via a shaft encoder (coarse control) and three Moire graticule tracks (for fine control) gives an ultimate positional accuracy of better than  $15 \mu\text{m}$ . At the time of writing the photoelectric scan unit, which will use channeltron detectors, has not been actively tested on a plasma. A comparably high resolution instrument with photographic emulsion and 2-channel photoelectric read out has been developed and used by Schwob [50].

We should not end our discussion on soft X-ray grating spectrometers without acknowledging the important developments in the technology of high efficiency lamina gratings and low light scatter holographically formed gratings [51]. For fusion studies we should like, ideally, to have true multi-channel spectral read-out. The use of toric substrates and holographically formed rulings can produce a nearly flat focal plane (at a preferred wavelength) and such an instrument, which might use a multi-element micro channel plate read-out system, has indeed been manufactured by Jobin-Yvon. A suite of gratings would be necessary for extended wavelength coverage; but it is not certain what the shortest wavelength limit of such an instrument might be. Such an instrument however, might well set the pattern for future grazing-incidence spectrometers.

We have mentioned the need in the spectroscopy of fusion plasmas for the calibration of the absolute incident photon flux against detector response. The absolute response of an instrument at characteristic  $K_{\alpha}$  wavelengths can be measured with a gas flow proportional counter and an X-ray diode source with interchangeable anodes [52]; or from separate measurements of the diffraction grating efficiency and the detector response [53]. More conveniently in fusion experiments, the plasma itself often provides pairs of emission lines originating from a common upper level.

If the emissivity of the plasma can be absolutely calibrated for one of the pair of lines, (this is generally feasible for the longer wavelength if it lies in the visible or VUV region, using a separate spectrometer of known light throughput) then the emissivity of the other line of the pair can be calculated. This branching ratio technique is commonly used [54] [55]. The use of MgF - windowed deuterium lamps as re-radiation transfer standards between  $1150 \text{ \AA}$  [56] have proved particularly useful in the calibration of VUV spectrometers at the Culham laboratory. Branching ratio line pairs, belonging to He- and Li-like ions of light elements, which commonly appear in fusion devices and which the author has found particularly useful, are OVI,  $150 \text{ \AA}/3811 \text{ \AA}$ ; OVII  $21.8 \text{ \AA}/1638.4 \text{ \AA}$  and CV  $40.73 \text{ \AA}/2277.3 \text{ \AA}$ . Extension of the branching ratio pairs to shorter wavelength  $< 20 \text{ \AA}$  is possible using the iso-electronic transitions in fluorine and neon.

### C. Crystal Spectrometers

Following our argument (section III A.(ii)) for a compact, spatially scanning crystal spectrometer the focusing Johann instrument illustrated in figure 18 has been designed and constructed. The four-pillar bending jig, see insert figure 18, holds an  $8\text{cm} \times 2\text{cm}$  crystal bent to a radius of curvature of  $50\text{cm}$ . The spectrometer is designed to observe X-radiation in the range  $0.5$  to  $25 \text{ \AA}$  from highly-ionised metals such as Ti Fe Mo and also from OVIII and OVII, these latter ions often being the most abundant ion species in tokamaks. The mean Bragg angle is altered by pivoting the Rowland circle about an axis through the crystal and orthogonal to the plane of dispersion. In order to view different chords through the plasma the whole vacuum assembly can be tilted.

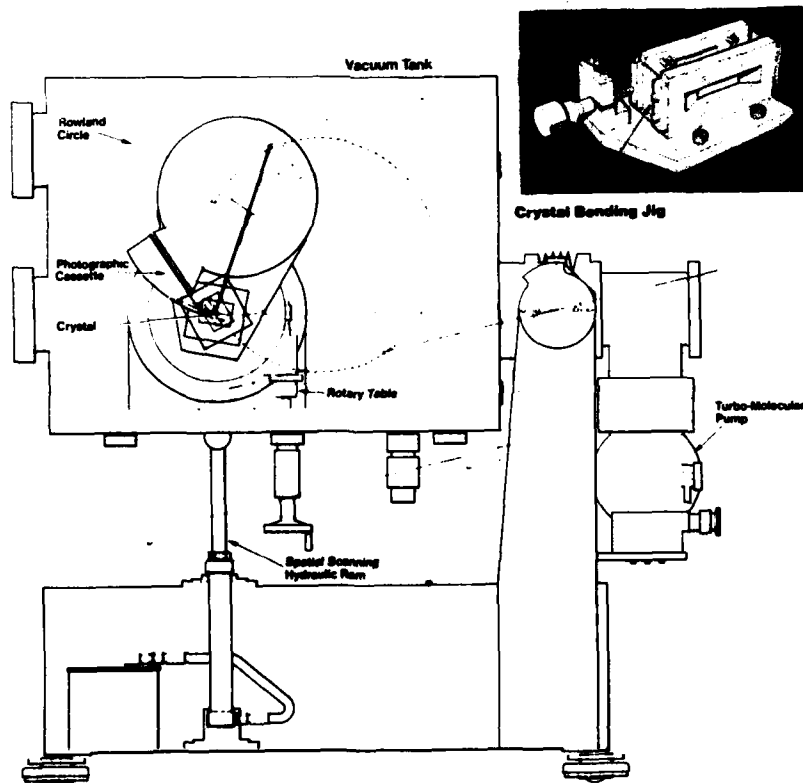


Fig 18. Optical layout of  $0.5 \text{ m}$  curved crystal spectrometer, using Johann mounting. The system is designed to observe dispersed radiation in the range  $1 \text{ \AA} - 25 \text{ \AA}$  and can be plasma tilted to spatially scan a tokamak

## ACKNOWLEDGEMENTS

The author would like to express his debt to the late M G Hobby, a resourceful collaborator in much of the X-ray instrument developments at the Culham laboratory. The paper has also benefited from discussions with J E Bateman, (the Rutherford laboratory), M F Stamp, (Oxford University), R K D Evans, (Leicester University) and R A Hulse (Princeton University).

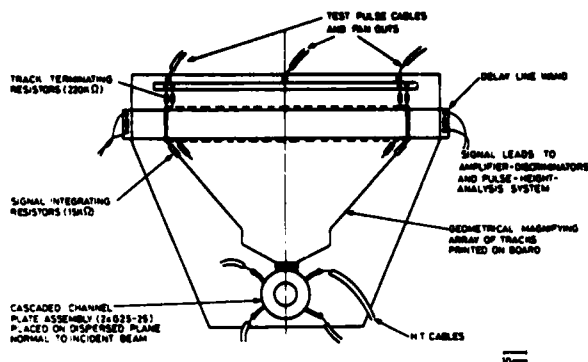


Fig 19. Schematic diagram of microchannel plate delay line readout assembly.

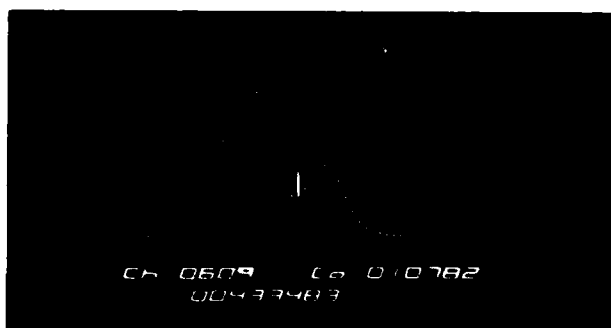


Fig 20. Resolution test of microchannel plate-delay line read out system shown in figure 19. The  $K_{\alpha_1, \alpha_2}$  lines from a Cu-anode X-ray tube is dispersed in 5th order by mica  $\Delta\lambda(\alpha_1 - \alpha_2) = 0.004 \text{ \AA}$ .

Alternative spectral read out systems are provided. In place of the photographic cassette, a multichannel electron multiplier plate (MCP) with a delay line read-out can be substituted, figure 19. Two cascaded microchannel plates provide a gain of up to  $10^8$  and operate the delay line from a single photo-electron generated at the iron face of the MCP. A cloud of at least  $10^6$  electrons from the MCP is necessary to activate a signal from the delay line, the MCP and the delay line being connected electrically by a wand of conducting tracks. The wand, which is a printed circuit board, linearly expands the detector element frequency from 4/mm at the MCP to 4/cm at the delay line, the total number of resolving element in the latter being 1024. Tests indicate that the limitations to the MCP current density  $\sim 10^5$  Hz per X-ray line and that the overall spatial resolution in the focal plane is  $\sim 35 \mu\text{m}$  [35]. In plasma experiments the plasma bandwidth recorded and the exposure time will be adjusted to the maximum count rate set by the electronics and to the access to a storage memory. Figure 20 shows a test spectrum of the  $K_{\alpha_1, \alpha_2}$

lines from Cu, dispersed in 5th order by a mica crystal. The separation between the  $\alpha_1$  and  $\alpha_2$  lines is  $0.004 \text{ \AA}$ .

For the micron-size, transient high density plasmas, the above spectrometer is not at all appropriate. A de Broglie instrument eg figure 12 has been extensively used for spectral surveys of laser-irradiated targets, see eg [57]. Without doubt however a space-resolving flat crystal instrument as in figure 13 is more appropriate when studying soft X-ray spectral features of laser-matter interactions.

## REFERENCES

1. "Plasma Diagnostics and Data Acquisition Systems", Proc. of Course held by Int. School of Plasma Physics, Varenna, Italy (1975), A Eubank and E Sindoni editors, Milan: CNR-Euratom Plasma Physics Laboratory.
2. "Diagnostics for Fusion Experiments", Proc. of Course held by Int. School of Plasma Physics, Varenna, Italy (1978), E Sindoni and C Wharton editors. Published by Pergamon Press, Oxford (1979).
3. TFR Equipe, Nuclear Fusion, 18, 647-731 (1978).
4. D T Attwood, IEEE J, Quantum Electron 14, 909-923, (1978).
5. H G Ahlstrom, L W Coleman, F Rienecker and V W Slivinsky, J.Opt.Soc.Am, 68, 1731-1741, (1978).
6. N J Peacock and D D Burgess, Phil.Trans.Roy.Soc. London, A300, 665-682, (1981).
7. C DeMichelis and M Mattioli, Euratom-CEA Report (Fontenay-aux-Roses, France). EUR-CEA-FC-1084 (1981), to be published Nuc.Fus. (1981).
8. N M Ceglio and J T Larson, Phys.Rev.Letts 44, 579-582, (1980).
9. R M Gilgenbach et al, Phys.Rev.Letts, 44 No.10, 647-650, (1980).
10. TFR Group, "Heating in Toroidal Plasmas". Vol.2, 207-216. Joint Varenna-Grenoble Int. Symp. 1978. Published by Pergamon Press, (1979).
11. H Eubank, R J Goldston et al, Nucl.Fusion Suppl. 1, 167-197. Publ. IAEA Vienna (1979).
12. R E Chrien et al, Phys.Rev.Letts, 46, No.8, 535-538 (1981).
13. M Keilhacker, (IPP Garching, FDR), private communication on performance of ASDEX tokamak, (1981).
14. TFR Group, Plasma Physics 22, 851-860 (1980).
15. D E T F Ashby and M H Hughes - private communication, the Culham Laboratory (1981). Also R A Hulse, private communication, Princeton Plasma Physics Laboratory (1981).
16. N J Peacock, Culham Laboratory Report CLM-P619 (1980).
17. D E T F Ashby and M H Hughes, Culham Laboratory Report CLM-P625 (1980). See also contribution to 10th Euro. Conf on Controlled Fusion and Plasma Physics. Moscow, Sept. (1981).
18. M E Puiatti, R Breton, C De Michelis, and M Mattioli, Euratom-CEA Report, (Fontenay-aux-Roses). EUR-CEA-FC-1085 (1981).
19. N J Peacock and H P Summers, J.Phys.B. Atom. Molec.Phys., 11, No.21, 3757-3774, (1978).
20. K Brau, S Von Goeler, M Bitter, R D Cowan, D Eames, K Hill, N Sauthoff, E Silver, N Stodiek, Princeton Plasma Physics Laboratory Report, PPPL-1644 (1980).
21. A Salop, J.Phys.B:Atom.Molec.Phys., 12 No.6, 919-928 (1979).
22. R C Isler, Phys.Rev.Letts., 38, 1359-62, (1977).
23. R C Isler and L E Murray - see article by S Suckewer in Physica Scripta 23, No.2 72-86 (1981).
24. V V Afrosimov, S Yu Gordeev, A N Zinoviev and A A Korotkov. JETP Letts, 28, No.8 500-502 (1979).

25. N R Sauthoff, S Von Goeler and W Stodiek, Nucl. Fusion 18, 1445-1453 (1978).
26. J E Bateman and M G Hobby, Culham Laboratory Report, CLM-R204 (1980).
27. N J Peacock, Culham Laboratory Report, CLM-P626, (1980).
28. J D Kilkenny, R W Lee, M H Key and J G Lunney submitted to Phys.Rev. (1980).
29. B Yaakobi, D Steel et al, Phys.Rev. A19 1247-1262 (1977).
30. C C Smith and N J Peacock, J.Phys.B:Atom. Molec.Phys., 11, No. 15, 2749-2763, (1978).
31. D T Attwood, IEEE Jnl. of Quantum Electronics 14, No.12, 909-923, (1978).
32. A K Bhatia, U Feldman and G A Doschek, J.App. Phys., 51, 1464-80, (1980).
33. R J Groebner, N H Brooks and M Shimada, General Atomic Co. Report, GA-A16248 (1981).
34. G A Sawyer, A J Dearden, I Henins, F C Jahoda and F L Ribe, Phys.Rev. 131 1891-1897 (1963).
35. M G Hobby, N J Peacock and J E Bateman, Culham Laboratory Report, CLM-R203 (1980).
36. M Bitter, S Von Goeler, R Horton, M Goldman, K W Hill, N R Sauthoff and W Stodiek, Phys.Rev.Letts. 42 304-307 (1979).
37. P Platz, J Ramette, E Belin, C Bonnelle, A Gabriel, CEA-Euratom Report, (Fontenay-aux-Roses) EUR-CEA-FC-1057 (1980).
38. J P Pye, K D Evans et al, Astron. and Astrophys. 65, 123-138 (1978).
39. J E Mack, J R Stehn, B Edlen, J.Opt.Soc. Am. 22 245 (1932).
40. N J Peacock, "Laser Plasma Interactions" (Cairns and Sanderson, editors). Proc. of 20th Scottish Universities Summer School in Physics, pp 711-806 (1979).
41. Rutherford Laboratory - Annual Report to Laser Facility Committee. Report No. RL-79-036 (1979).
42. M H Key, C L S Lewis, J G Lunney, A Moore, J M Ward, R J Thareja, Phys.Rev.Lett. 44, No.25 1669-1672 (1980).
43. Lawrence Livermore Laboratory Annual Report of the Laser Programme. UCRL-50021-77 (1977), UCRL-50021-78 (1978), UCRL-50021-79 (1979).
44. N M Ceglio and H I Smith, Rev.Sc.Instr. 49 15-20 (1978).
45. N M Ceglio, D T Attwood and E V George, Jnl. Appl. Phys. 48, No.4, 1566-1569 (1977).
46. A H Gabriel, J R Swain and W A Waller, Jnl. Sc.Instrum. 42, 94-97 (1965).
47. W M Burton and R Wilson, Proc. Phys. Soc. 78, 1416 (1961).
48. G Andermann, L Bergknut, M Karras, G Grieshaber and J Smith, Rev.Sci.Instru, 51 (6), 814-820 (1980).
49. S Mrowka, private communication, Imperial College University of London, (1981).
50. TFR Group - J L Schwob. Euratom - CEA Report (Fontenay-aux-Roses). EUR-CEA-FC-1072 (1980).
51. R J Speer, Space. Sci. Instrum 2 463-487 (1976).
52. F J Morgan, A H Gabriel, M J Barton, J.Phys.E: Sci.Instrum. 1, 998-1002 (1966).
53. M G Hobby and N J Peacock, Jnl.Phys.E: Sci. Instrum. 6 854-857 (1973).
54. E Hinnov, "Diagnostics for Fusion Experiments" 139-148. Proc. Int. School of Plasma Physics, Association CNR-Euratom, Varenna, (Sindoni and Wharton, editors) publ. Pergamon Press, Oxford (1978).
55. F E Irons and N J Peacock, J.Phys.K:Sc. Instrum. 6, 857-862 (1973).
56. P J Key and R C Preston, J.Phys.E:Sci.Instrum. 13, 866-870 (1980).
57. H Gordon, M G Hobby and N J Peacock, J.Phys.B: Atom.Molec.Phys. 13, 1985-1999 (1980).

## Spectrometric Properties of Crystals for Low Energy X-Ray Diagnostics

D. M. Barrus, R. L. Blake, H. Felthausen, and E. E. Fenimore

University of California, Los Alamos National Laboratory, Los Alamos, New Mexico 87545

A. J. Burek

National Bureau of Standards, Washington, DC 20234

## ABSTRACT

Quantitative diagnostics of fusion and astrophysical plasmas require knowledge of crystal spectrometric properties. To provide more reliable and versatile diagnostics of plasma conditions, increasingly accurate knowledge of crystal spectrometric properties is becoming necessary. We provide here a summary of the following accurately measured parameters for the crystals KAP, RbAP, T<sub>2</sub>AP, NH<sub>4</sub>AP, NaAP, ADP, and EDDT:

- 1)  $2d_m$  - the interplanar spacing of atoms
  - 2)  $\Delta$  - the angle correction for normal and anomalous dispersion that is required for application of the Bragg formula
  - 3)  $\alpha$  - the thermal expansion coefficient near room temperature for commonly used planes
  - 4)  $R_c$  - the integrated coefficient of reflection
- Measured data on  $R_c$  are compared to theory with good agreement.

## I. INTRODUCTION

Soft X-ray spectroscopy with crystals has been applied extensively to several new fields over the past two decades with considerable interaction among workers in different disciplines. From the early days of extension of quantitative x-ray analysis to the soft x-ray range (1) we have seen crystal spectroscopy extended to controlled thermonuclear confinement fusion (2), solar physics (3), laser fusion (4), and x-ray astronomy (5). A common link between these new fields is the predominance of radiation from hot plasmas in the soft x-ray range.

As diagnostics have become more sophisticated, there has been a need for quantitative knowledge of the spectrometric properties of crystals used for diffraction in the energy range below 5 keV, especially in the range 0.1 to 2 keV. Neither the crystals (beryl, gypsum, mica, and multi-layer films) nor the technology available through 1960 were adequate for the needs. Results of steady progress in the technologies of x-ray sources, detectors, gratings, collimators, and other areas are presented in other papers in this volume. We shall report on some progress in crystal diffraction.

Some applications have demanded crystals with the highest possible integrated reflection coefficient  $R_c$ . This is particularly true in x-ray astronomy. Other applications, including solar physics and fusion plasma spectroscopy, have increasingly shown the need for better resolving power, which requires narrow crystal reflection profiles for monochromatic radiation. Because signal strengths go down as resolving powers go up we have attempted to find crystals that provide an optimization of the two parameters. As a result of much work among several groups (6-18) there is now a body of evidence showing that good reproducibility of spectrometric properties can be obtained with reasonable care in selection of crystal specimens from certain vendors. It is, therefore, appropriate to summarize some often-used crystal parameters. We report here our results on integrated reflection coefficients ( $R_c$ ), interplanar spacings ( $2d_m$ ), thermal expansion coefficients ( $\alpha$ ), and dispersion corrections to measured Bragg angles ( $\Delta$ ). Crystals on which we report are ammonium acid phthalate (NH<sub>4</sub>AP), sodium acid phthalate (NaAP), potassium acid phthalate (KAP), rubidium acid phthalate (RbAP), thallium acid phthalate (T<sub>2</sub>AP), ammonium dihydrogen phosphate (ADP), and ethylene diamine dihydrogen tartrate (EDDT).

For background on definitions and techniques related to crystal reflection parameters the reader should consult references 7 and 8 and standard textbooks like Compton and Allison (19).

II.  $R_c$  MEASURED WITH LINE SOURCES AND COMPARED TO THEORY

Data reported in this section are a composite of many measurements spread intermittently over nearly two decades. Some measurements were made with line emissions from electron beam excited sources, some from fluorescence line sources, and some from both. Techniques to minimize systematic errors are extremely important. These are described in references 6 and 7 in particular. A source of systematic error not emphasized in recent literature is the spectrometer beam limiting aperture, which must be the same aperture for the direct and reflected beams. In the ultrasoft region when large beam sizes are employed it usually becomes necessary to support the thin proportional counter window with a honeycomb structure in addition to a wire mesh. Then it is necessary to assure the combination of source and detector geometries does not cause any rapid variation of direct beam intensity with angle. This is controllable in systems where the  $\theta$  and  $2\theta$  drives can be decoupled.

Figures 1 through 7 show results of measurements from line sources compared to theoretical calculations. Results for the acid phthalates are for our best crystals with cleaved and undegraded surfaces. RbAP and especially NH<sub>4</sub>AP are known to deteriorate with time but all the acid phthalates can be stabilized to better than 10 percent per year by overcoating their surfaces with ~500Å aluminum or other protective layer and storage in a desiccator jar (18). ADP and EDDT require solution polishing by the technique of Deslattes et al. (20) and the protective coating just mentioned to assume nearly perfect crystal behavior and long term stability. Without the solution polishing these two crystals can be very different from the theoretical curves because the crystals must be cut to the desired reflecting planes. The cutting process can introduce mosaic structure that causes larger  $R_c$  than for perfect crystals, or contamination of the surface that can cause lower  $R_c$ .

In Figure 6 the ADP (101) measurements at Al K $\alpha$  (51.5 deg) were done on a large crystal that had been carefully solution polished and coated two years prior to the measurement. It had also experienced three rocket flights. The three orders of reflection of CuK $\alpha$  were made on a different crystal that was a fairly good one, but was not protected by an overcoating during three months between polishing and measuring. In Figure 7 the triangles are for two orders of CuK $\alpha$  reflection from our most perfect EDDT. A three months delay between polishing and measuring without a protective coating may be responsible for the measured values falling above the theoretical Darwin-Prins curves.



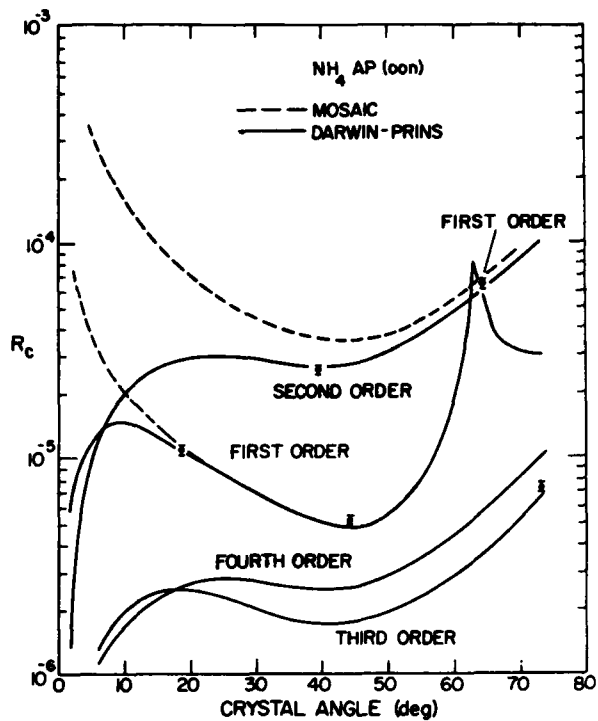


Fig. 1.  $R_c$  measured for  $\text{NH}_4\text{AP}$  and compared to  $R_c$  calculated from Darwin-Prins theory for perfect crystals. Points are measured with line x-ray sources.

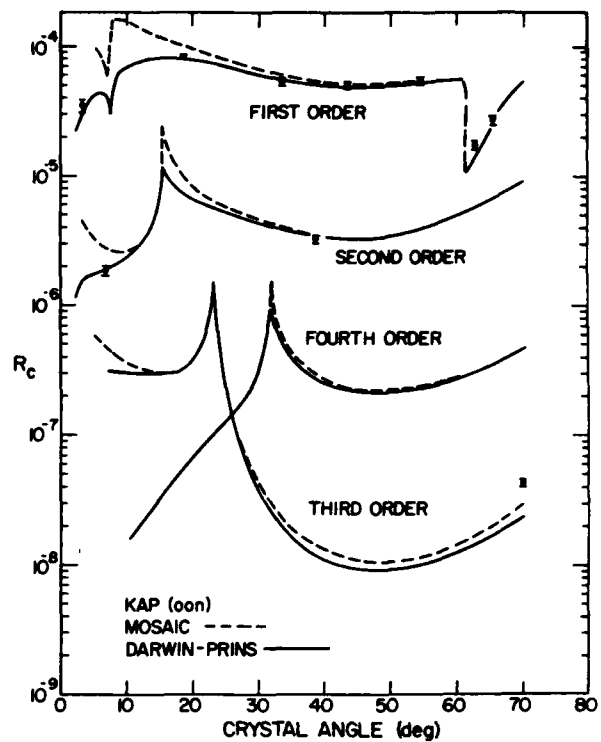


Fig. 3.  $R_c$  measured for KAP and compared to Darwin-Prins theory.

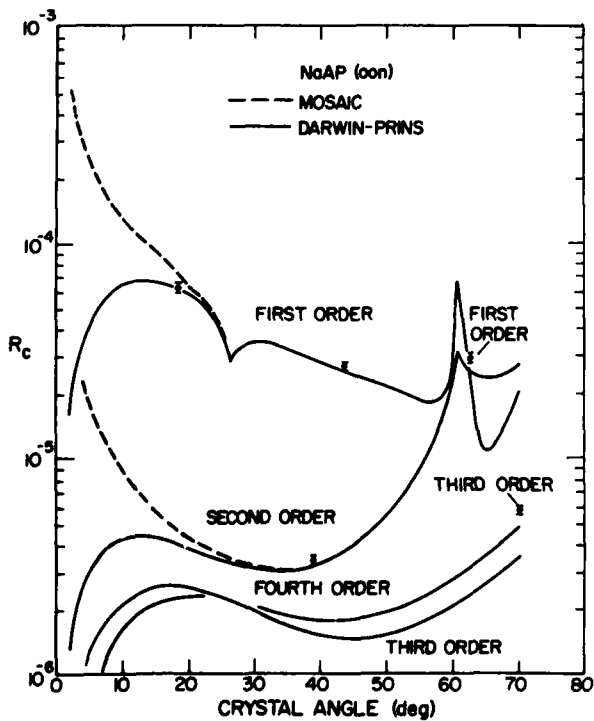


Fig. 2.  $R_c$  measured for NaAP and compared to Darwin-Prins theory.

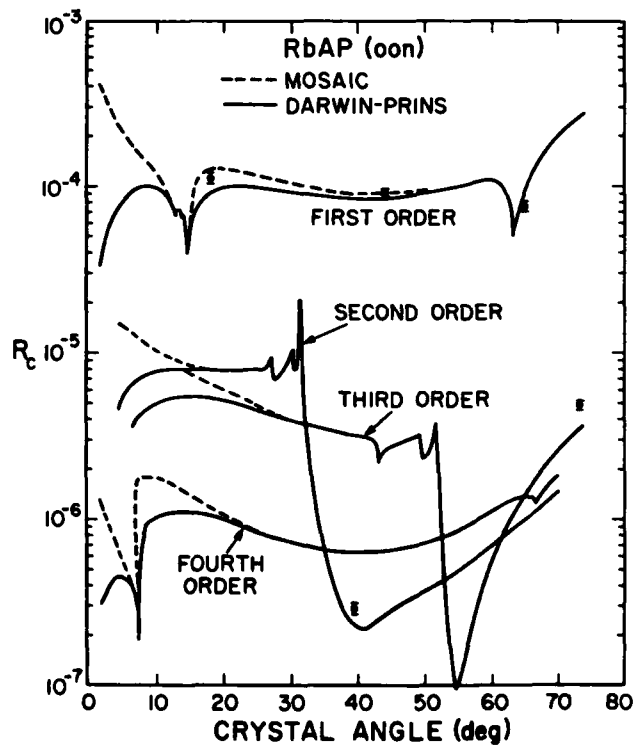


Fig. 4.  $R_c$  measured for RbAP and compared to Darwin-Prins theory.

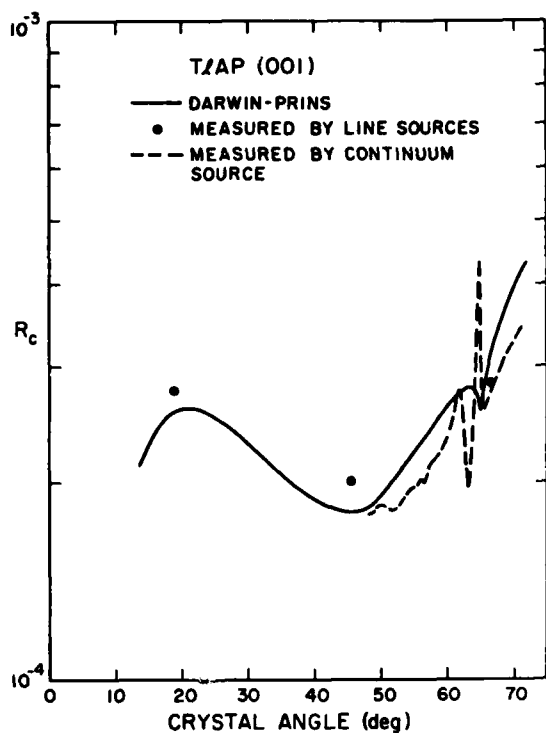


Fig. 5.  $R_c$  measured for TAP and compared to Darwin-Prins theory. It was assumed that TAP is isostructural to RbAP for the calculations, which were kindly provided ahead of publication by Ping Lee and Burton Henke.

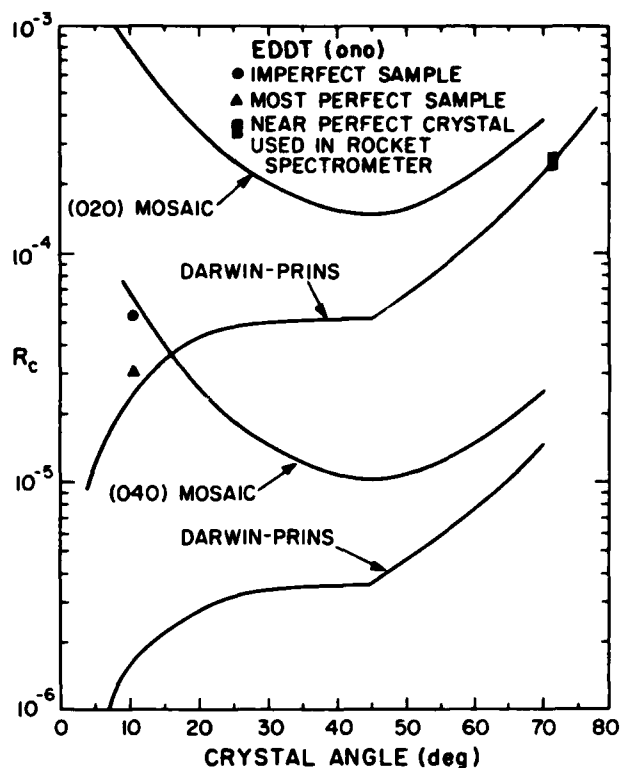


Fig. 7.  $R_c$  measured for EDT and compared to Darwin-Prins theory.

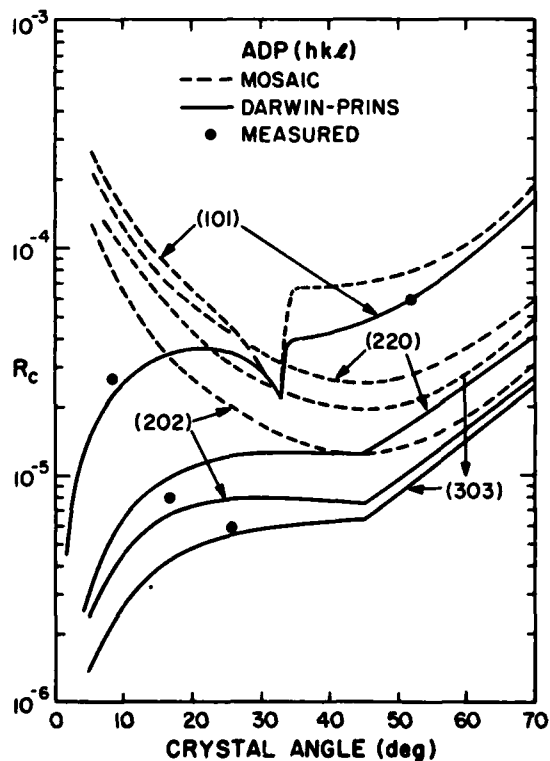


Fig. 6.  $R_c$  measured for ADP and compared to Darwin-Prins theory.

Indirect measurements of EDT resolving powers from polished and coated crystals have convinced us that nearly perfect crystal behavior (Darwin Prins) can be consistently achieved with selected specimens.

This raises the essential question of how one selects good specimens and from whom. We can give the following guidelines, which are necessary and in our experience sufficient. The acid phthalates must be transparent, colorless, flat, and free of any visible defects such as cracking, twinning, pits, scratches, or abrasion. Flatness can be easily checked by simply observing the sharpness of an autocollimator reflected reticle image. Cleavage steps on the reflecting surface are generally not a problem because the stepped layers are parallel to one another. The autocollimator test reveals whether this is true or not in each case. Because these cleavage steps can influence the tilt angle a crystal holder with tilt angle (21) adjustability is desirable for high precision measurements. All the acid phthalates except F need to be freshly cleaved just prior to use or else cleaved and coated prior to storage. Any thin coating impervious to water vapor and air should be adequate. ADP and EDT must have the same characteristics after solution polishing, and both should be coated within a day after polishing. For precision measurements above 5 keV the coating should be done immediately after polishing (22).

Our most perfect samples have come from Warren Ruderman (formerly with Isomet Corp. and now with INRAD). High quality specimens in large sizes are available from stocked crystals from Quartz Products Corp. We suspect the above criteria will be adequate

for selection of good crystals from other vendors as well.

A few points about Figures 1 to 7 are noteworthy.

The calculated curves depend on the accuracy of atomic positions taken from crystal structure determinations and on absorption coefficients (among other parameters). Small errors in structure determinations can easily account for deviations in weak higher order reflections, such as the third order  $A\lambda K\alpha$  from the acid phthalates. In the case of TAP no measured structure is available and it has been assumed isostructural to RbAP.

It has been the practice, especially in x-ray analysis literature, to quote ratios of reflectivities for a particular crystal in different orders at a given wavelength, with the implication that these ratios could be applied to other wavelengths. In the soft x-ray range this is a practice to be avoided because of the strong effects of anomalous dispersion on structure factors and reflectivities. For example the first three orders of  $R_c$  for  $CuK\alpha$  reflected off KAP are in the ratio 10000:630:100 while for  $A\lambda K\alpha$  they are in the ratio 10000:440:3. Just a glance at the figures in fact shows the problem, while pointing up the need for such a summary as we are attempting in this paper.

Among other crystals for soft x-ray diffraction we note that PET should be good in theory (8). Our one crystal was very poor but we note that Alexandropoulos (10) reported results close to theoretical. Hall et al. (12) in a detailed study of PET found a nearly perfect sample compared to theory, but also noted major degradation at short wavelengths after two years. A stabilizing coating should be tried on a good PET sample. Measurements with GYPSUM in our labs confirm the report of Stephenson and Martin (23). We found  $R_c = 3 \times 10^{-4}$  at  $NiL\alpha$  for about three hours and then a decay by a factor two in the next six hours. Based on the success at stabilizing  $NH_4AP$  by an aluminum coating the technique should be tried on GYPSUM.

Determinations of  $R_c$  at  $OK\alpha$  with line sources are susceptible of large systematic errors because of the complex nature of both the source emission line spectra and the crystal reflection coefficient structure (24). Because of the latter factor theory is also very weak around absorption edges and especially around the  $OK$ -edge. Our data, presented in the next section, will clarify  $R_c$  in this range.

### III. $R_c$ OF ACID PHTHALATES AROUND THE OXYGEN K-EDGE FROM CONTINUUM SOURCE MEASUREMENTS

A systematic experimental study of  $R_c$  measured continuously over the range 500-650 eV around the  $OK$ -edge has been completed for five commonly used acid phthalate crystals. An example of the remarkable variations of  $R_c$  over this range is shown in Figure 8. The reader should consult reference 24 for a full discussion of the background concerning these  $R_c$  variations, the measurement technique, and interpretation of the data.

Very briefly one obtains a calibrated continuum source by the following procedure. As seen in Figure 3 the measurements from line sources confirm the validity of the Darwin Prins calculations. Accordingly these calculated  $R_c$  values are used to calibrate a continuum source (gold anode) over the range  $\sim 20$ -40 deg. This monotonically declining intensity source spectrum is then extrapolated to larger angles where the procedure is inverted to yield the values of  $R_c$  with an estimated accuracy of  $\pm 15$  percent. Because  $R_c$  is continuously determined and shows large variations we refer to this approach as crystal reflection integral spectroscopy or CRIS.

In this energy range no crystals are known that simultaneously have the required long  $2d$  spacing, the absence of oxygen in the crystal composition, and useful diffraction properties. Thus the acid phthalates are presently used by nearly everyone and a summary tabulation of reference values of  $R_c$  seems appropriate.

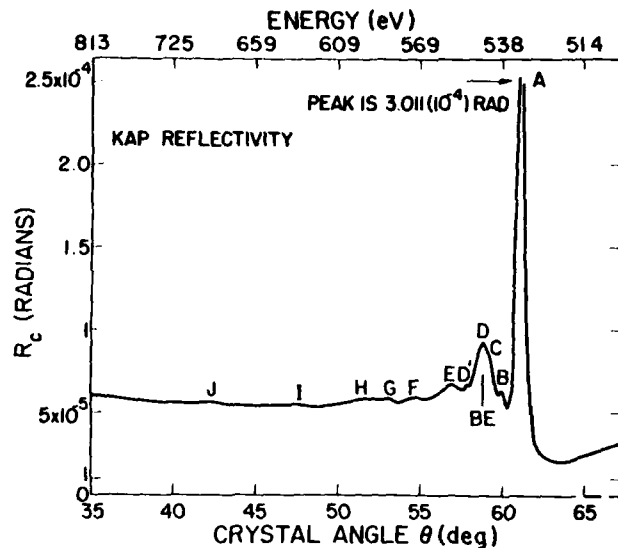


Fig. 8.  $R_c$  measured for KAP by means of a calibrated continuum x-ray source. The magnitude of  $R_c$  is determined largely by the imaginary part of the scattering factor, which is related to absorption coefficients, and these in turn vary near ionization edges because of the size and shape of the molecule and because of extended x-ray absorption fine structure (EXAFS).

Accordingly we present  $R_c$  data on five acid phthalates in Tables I through V. These are weighted averages for several scans for each crystal. Angle intervals have been selected so that each curve can be reconstructed to the accuracy of the data. Angle uncertainties are  $\pm 0.05$  deg (20). Anyone wishing to use these data to correct their measured spectra in this range will find it sufficient to simply shift the tabulated data to correct for zero error in their spectrometer. If the zero error is not known or not easily measured, a separate scan of most any oxygen emission spectrum or any continuum emission spectrum from a laboratory x-ray tube will reveal the dominant reflectivity spike A, which occurs in all five crystals and can be identified in plots from Tables I-V.

### IV. OTHER PARAMETERS REQUIRED FOR PRECISION X-RAY SPECTROSCOPY

X-ray diagnostics of fusion plasmas and the solar corona have now progressed to the point where line profile measurements and precision wavelength determinations are required. Then one must use the correct form of the Bragg equation; that is, either the angle of diffraction or the interplanar spacing must be corrected for dispersion inside the crystal. The basic crystal spectrometer equation is

$$n\lambda = 2d_{\infty} \sin\theta_B \quad (1)$$

where  $2d_{\infty}$  is the true interplanar spacing of atoms and  $\theta_B$  is related to the measured peak diffraction angle  $\theta$  by

$$\theta = \theta_B + \Delta \quad (2)$$

and  $\Delta$  is the correction for refraction of x-rays inside the crystal. For a review of how  $\Delta$  is calculated from atomic constants see references 19, 8, and 25. It is related to atomic constants through  $\delta$ , the unit decrement of the index of refraction, by

$$\Delta = \delta(\sin\theta_B \cos\theta_B)^{-1} \text{ radians.} \quad (3)$$

TABLE I  
R<sub>c</sub> MEASURED FOR T&AP

$\theta$ (deg)	$R_c \times 10^5$ (rad)	$\theta$ (deg)	$R_c \times 10^5$ (rad)	$\theta$ (deg)	$R_c \times 10^5$ (rad)	$\theta$ (deg)	$R_c \times 10^5$ (rad)
48.0	17.8	56.0	20.1	62.75	21.5	65.3	25.8
48.5	17.8	56.4	19.7	63.00	19.5	65.4	25.4
49.0	18.2	56.7	20.1	63.10	19.4	65.5	25.5
49.5	18.4	57.0	20.9	63.25	19.9	65.75	26.3
50.0	18.4	57.5	21.3	63.5	21.5	66.0	26.6
50.5	18.4	58.0	21.5	63.75	23.5	66.5	27.3
51.0	18.2	58.5	21.7	64.00	27.0	67.0	28.0
51.5	18.0	59.0	22.2	64.25	31.2	68.0	29.5
52.0	18.0	59.5	22.8	64.35	32.2	69.0	31.0
52.5	18.3	60.0	23.4	64.5	34.6	70.0	32.4
53.0	18.7	60.5	24.2	64.6	37.2	71.0	33.6
53.5	19.0	61.0	25.4	64.7	39.6	72.0	34.6
54.0	19.3	61.5	26.1	64.8	43.0	73.0	36.0
54.5	19.5	61.75	26.4	64.9	41.0	74.0	37.1
55.0	19.5	62.0	26.2	65.0	34.5	75.0	38.1
55.1	19.5	62.25	25.4	65.1	29.8	76.0	39.0
55.5	19.8	62.50	23.7	65.2	26.9	77.0	39.9
55.8	20.1					78.0	40.7

TABLE II  
R<sub>c</sub> MEASURED FOR RbAP

$\theta$ (deg)	$R_c \times 10^5$ (rad)	$\theta$ (deg)	$R_c \times 10^5$ (rad)	$\theta$ (deg)	$R_c \times 10^5$ (rad)	$\theta$ (deg)	$R_c \times 10^5$ (rad)
48.0	8.6	59.5	11.2	62.1	8.2	64.0	6.8
49.0	8.8	59.75	11.35	62.2	8.1	64.25	7.15
50.0	8.9	60.0	11.6	62.35	8.0	64.5	7.5
51.0	9.1	60.25	12.2	62.5	8.6	64.75	7.9
52.0	9.4	60.5	12.9	62.6	9.4	65.0	8.3
53.0	9.7	60.6	12.9	62.7	11.2	66.0	9.7
53.5	9.8	60.7	12.7	62.8	13.4	67.0	10.7
54.0	9.7	60.8	12.3	62.9	16.2	68.0	11.8
54.1	9.6	60.9	11.6	63.0	20.3	69.0	13.0
54.5	9.8	61.0	10.8	63.1	24.6	70.0	14.2
54.75	9.95	61.1	10.2	63.22	28.8	71.0	15.0
55.0	9.8	61.2	9.8	63.3	26.0	72.0	15.9
55.3	9.6	61.3	9.4	63.4	20.6	73.0	16.7
55.5	9.8	61.4	9.0	63.5	13.0	74.0	17.4
56.0	10.1	61.5	8.5	63.6	9.1	75.0	18.1
57.0	10.2	61.6	8.0	63.7	7.8	76.0	18.7
58.0	10.5	61.75	7.65	63.8	7.0	77.0	19.3
59.0	11.2	61.85	7.7	63.9	6.8	78.0	19.8
59.2	11.25	62.0	8.1				

TABLE III  
 $R_c$  MEASURED FOR KAP

$\theta$ (deg)	$R_c \times 10^5$ (rad)	$\theta$ (deg)	$R_c \times 10^5$ (rad)	$\theta$ (deg)	$R_c \times 10^5$ (rad)	$\theta$ (deg)	$R_c \times 10^5$ (rad)
35.0	5.78	51.0	5.42	57.85	6.32	60.9	18.0
36.0	5.65	51.5	5.51	58.0	6.35	61.0	25.5
37.0	5.54	52.0	5.56	58.1	6.42	61.10	30.0
38.0	5.42	52.5	5.49	58.25	6.89	61.25	25.5
39.0	5.32	53.0	5.56	58.4	7.44	61.35	18.3
40.0	5.29	53.15	5.58	58.5	7.98	61.45	11.0
41.0	5.32	53.5	5.42	58.6	8.26	61.55	7.70
41.5	5.33	53.75	5.32	58.7	8.55	61.65	5.80
42.0	5.35	54.0	5.42	58.85	8.84	61.75	4.60
42.5	5.37	54.5	5.57	59.0	8.53	62.0	3.15
43.0	5.30	54.75	5.60	59.25	7.77	62.25	2.48
43.5	5.22	55.0	5.59	59.5	6.60	62.5	2.02
44.0	5.18	55.25	5.55	59.65	5.94	62.75	1.90
45.0	5.11	55.5	5.59	59.75	5.80	63.0	1.94
46.0	5.13	55.75	5.70	59.85	5.93	63.25	2.01
46.5	5.13	56.0	5.80	59.95	6.03	63.5	2.10
47.0	5.18	56.25	5.98	60.0	5.90	64.0	2.18
47.35	5.24	56.5	6.11	60.1	5.64	65.0	2.50
47.75	5.16	56.75	6.35	60.35	5.09	66.0	2.80
48.0	5.18	56.9	6.38	60.45	5.32	68.0	3.48
49.0	5.16	57.1	6.36	60.5	5.60	71.0	4.42
49.5	5.16	57.4	6.16	60.6	7.32	74.0	5.28
50.0	5.22	57.65	6.03	60.7	9.50	78.0	6.21
50.5	5.30	57.75	6.13	60.8	13.3		

TABLE IV  
 $R_c$  MEASURED FOR NaP

$\theta$ (deg)	$R_c \times 10^5$ (rad)	$\theta$ (deg)	$R_c \times 10^5$ (rad)	$\theta$ (deg)	$R_c \times 10^5$ (rad)	$\theta$ (deg)	$R_c \times 10^5$ (rad)
48.0	2.40	59.25	4.00	61.6	3.90	63.5	3.3
49.0	2.35	59.50	5.00	61.7	6.90	64.0	2.4
50.0	2.40	59.75	5.50	61.8	11.8	64.5	1.8
51.0	2.45	60.00	4.90	61.9	19.6	65.0	2.05
52.0	2.55	60.25	4.15	62.0	27.0	66.0	1.45
52.5	2.60	60.30	4.10	62.06	31.1	67.0	1.5
53.0	2.55	60.5	4.60	62.1	28.0	68.0	1.65
54.0	2.40	60.6	5.40	62.2	24.4	69.0	1.9
54.4	2.30	60.7	6.00	62.3	18.5	70.0	2.15
55.0	2.40	60.8	6.20	62.4	14.0	71.0	2.5
56.0	2.25	60.9	6.15	62.5	11.4	72.0	2.8
57.0	2.15	61.0	5.60	62.6	9.4	73.0	3.05
57.5	2.35	61.1	4.70	62.7	8.1	74.0	3.4
58.0	2.95	61.2	4.40	62.8	7.0	75.0	3.7
58.35	3.20	61.3	4.10	62.9	6.1	76.0	4.0
58.5	2.15	61.4	3.50	63.0	5.5	77.0	4.25
58.75	2.05	61.5	3.20	63.25	4.3	78.0	4.55
59.0	2.25						

TABLE V

 $R_c$  MEASURED FOR  $NH_4AP$ 

$\theta$ (deg)	$R_c \times 10^5$ (rad)	$\theta$ (deg)	$R_c \times 10^5$ (rad)	$\theta$ (deg)	$R_c \times 10^5$ (rad)	$\theta$ (deg)	$R_c \times 10^5$ (rad)
48.0	0.50	61.0	3.20	62.6	6.6	64.25	8.4
49.0	0.50	61.1	3.25	62.7	11.8	64.5	7.5
50.0	0.55	61.25	3.20	62.8	18.7	64.75	6.75
51.0	0.60	61.35	3.10	62.9	26.0	65.0	6.1
52.0	0.65	61.5	3.20	63.0	30.0	65.5	5.0
53.0	0.75	61.6	3.35	63.05	32.3	66.0	4.35
54.0	0.80	61.7	3.70	63.1	35.0	67.0	3.5
55.0	0.90	61.8	4.00	63.2	26.0	68.0	3.1
56.0	0.95	61.85	4.05	63.3	22.4	69.0	2.85
57.0	1.00	61.9	3.95	63.4	18.5	70.0	2.7
58.0	1.10	62.0	3.80	63.5	16.1	71.0	2.6
59.0	1.20	62.1	3.60	63.6	14.1	72.0	2.45
59.5	1.25	62.15	3.60	63.7	12.6	73.0	2.4
60.0	1.80	62.25	3.40	63.8	11.5	74.0	2.35
60.25	2.35	62.35	3.20	63.9	10.9	75.0	2.35
60.5	3.05	62.4	3.20	64.0	10.2	76.0	2.35
60.65	3.10	62.5	4.00			77.0	2.35
60.8	3.05					78.0	2.35

One can calculate  $\delta$  from atomic scattering factors (25) which are presently being summarized by Henke (26).

Instead of Eq. (1) one can alternatively write

$$n\lambda = 2d_{\text{eff}} \sin\theta \quad (4)$$

where the effects of refraction are incorporated into an effective interplanar spacing

$$2d_{\text{eff}} = 2d_n [1 - \Delta \cot\theta_B] \quad (5)$$

In either case the required parameter is  $\Delta$ . Table VI provides  $\Delta$  in arc seconds versus wavelength for the first order (001) reflections of the acid phthalates plus the most important planes of ADP and EDDT. The Miller indices (00n) for NaAP and  $NH_4AP$  are extinctions for odd n, so the first order designations in Table VI are (002). Second order is (004), and so forth.

To obtain  $\Delta$  for any order n of these planes use the following relation

$$\Delta^n \cot\theta_B^n = \Delta^1 \cot\theta_B^1 n^{-2} \quad (6)$$

For precision spectroscopy one should pick a crystal for which the desired wavelength is not near a crystal absorption edge.

Values of  $2d_n$  for the same crystals and planes have been measured in our laboratory with the  $A\lambda K\alpha$  doublet reference spectrum. A full discussion of spectrometer alignment, sources of error, and correction procedures will be published elsewhere. Results are tabulated in Table VII based on an assumed absolute wavelength of 8.33955 Å for  $A\lambda K\alpha_1$  from a vacuum evaporated aluminum anode. A small correction was required to relate the measured peak positions to the  $A\lambda K\alpha_1$  wavelength. This correction was calculated from convolutions of a Lorentzian approximation to the Darwin-Prins crystal profile, the measured collimator profile, and the line profile. For the latter we assumed the  $A\lambda K\alpha_{1,2}$  doublet had a 2:1 intensity ratio between  $K\alpha_1$  and  $K\alpha_2$ , that each component had a Lorentzian shape, and that the  $K\alpha_1$ - $K\alpha_2$  separation was that published by Kaline and Aberg (27). We find, however, that the widths of each component line after correction for the instrument broadening should be 0.38 eV instead of 0.58 eV.

The spacings are all referenced to a crystal temperature of 26°C. For this purpose the thermal expansion coefficient of the measured planes was

separately determined by means of the expression derived from Eq. (1)

$$\alpha = -\cot\theta \Delta\theta/\Delta T \quad (7)$$

where  $\alpha$  is the expansion coefficient,  $\theta$  is the mean angle for the reference line ( $A\lambda K\alpha$ ), and  $\Delta\theta$  is the difference in peak positions for two fixed temperatures,  $T_H$  and  $T_L$ . Most of the measurements were done at  $T_H \approx 30^\circ\text{C}$  and  $T_L \approx 20^\circ\text{C}$ , so that  $\Delta T \approx 10^\circ\text{C}$ . If  $\alpha$  varies over this range, our results in Table VII are an average over the range of variation. Because the  $\alpha$  values are large (especially for  $NH_4AP$ ) it is important to have good temperature control in precision measurements with these crystals.

In Table VII the listed values of  $2d_n$  are preliminary. Some changes in the last decimal may occur when our latest temperature recalibrations have been included. If improved  $A\lambda K\alpha$  wavelengths become available, the absolute values of  $2d$  will change by  $\Delta 2d/2d = \Delta\lambda/\lambda$ . A preliminary error analysis shows a 20 uncertainty not exceeding 20 ppm for  $2d_n$  on any of the seven crystals. However, one should keep in mind possible variations from one crystal to another and the shift required if  $A\lambda K\alpha_1$  is not 8.33955 Å. A good cross check is possible on KAP by using the result of Bearden and Huffman (28),  $2d_n = 13289.51 \text{ xu}$  at  $26^\circ\text{C}$ , and the  $\text{CuK}\alpha$  conversion factor,  $\lambda = 1.0020802 \text{ Å/xu}$ , from Deslattes and Henins (29) to obtain  $2d_n = 26.63431 \text{ Å}$ . This differs from our value by 15 ppm.

## V. DISCUSSION

Several sets of calculations (8,26,30) and measurements (6,7,15,30) now exist for  $R_c$  of KAP, which is the most stable and reproducible of the acid phthalates so far as we know. In the range 10-20 Å there is agreement within plus or minus three percent from the mean for  $R_c$ . If one avoids the humps shown in figure 8 the agreement between our continuum source results and reference 30 is within one percent from 16 to 20 Å. When one considers the difficulties of handling all the observed  $R_c$  peaks theoretically it seems advisable to extrapolate from the good KAP agreement outside the peaks and take the continuum source  $R_c$  values as the standards for all the acid phthalates from ~19 to 26 Å. In the range 23 to 26 Å the absolute accuracy could be as bad as  $\pm 15\%$  (30) because of our extrapolation uncertainty and variations

TABLE VI  
INDEX OF REFRACTION CORRECTIONS<sup>a</sup>, Δ, FOR ACID PHTHALATES, ADP, AND EDDT

Wavelength Å	Δ (arc minutes)							
	(002)	(002)	(001)	(001)	(001)	(101)	(200)	(020)
	NaAP	NH <sub>4</sub> AP	KAP	RbAP	TlAP	ADP	ADP	EDDT
1.0	.20	.18	.21	.22	.30	0.094	0.066	0.068
2.0	.40	.36	.42	.45	.60	0.192	0.137	0.138
3.0	.61	.55	.62	.68	.88	0.295	0.218	0.216
4.0	.82	.74	.82	.90	1.08	0.407	0.314	0.305
5.0	1.03	.93	1.05	1.12	1.07	0.525	0.438	0.415
6.0	1.25	1.14	1.28	1.23	1.52	0.648	0.630	0.562
7.0	1.48	1.34	1.51	1.41	1.84	0.853	1.28	0.793
8.0	1.71	1.56	1.75	1.73	2.15	1.12		1.320
9.0	1.94	1.78	2.01	2.01	2.45	1.57		
10.0	2.18	2.02	2.27	2.28	2.77	2.72		
11.0	2.40	2.26	2.54	2.57	3.09			
12.0	2.65	2.52	2.83	2.87	3.43			
13.0	2.96	2.79	3.14	3.18	3.78			
14.0	3.28	3.07	3.46	3.52	4.14			
15.0	3.61	3.38	3.80	3.87	4.53			
16.0	3.95	3.71	4.16	4.26	4.99			
17.0	4.33	4.06	4.55	4.68	5.46			
18.0	4.73	4.45	4.98	5.14	6.02			
19.0	5.16	4.88	5.44	5.65	6.64			
20.0	5.64	5.35	5.95	6.22	7.33			
21.0	6.14	5.88	6.51	6.88	8.19			
22.0	6.64	6.43	7.08	7.61	9.21			
23.0	6.70	6.66	7.29	8.07	10.11			
24.0	8.55	8.68	9.20	10.48	13.47			
25.0	11.93	12.90	12.67	15.56	21.97			

<sup>a</sup> ± 5%

TABLE VII  
BEST MEASURED VALUES<sup>a</sup> OF CRYSTAL EXPANSION  
COEFFICIENTS AND INTERPLANAR SPACINGS AT 26°C

CRYSTAL	2 d <sub>n</sub> (Å)	α (10 <sup>-6</sup> C <sup>-1</sup> )
EDDT (020)	8.80479 ±.00008	18.8 +1.0
ADP (101)	10.6425 ±.0005	18.1 +0.6
NH <sub>4</sub> AP (00n)	26.1905 ±.0007	133. +9.0
NaAP (00n)	26.4185 ±.0005	41.6 +5.0
KAP (00n)	26.6347 ±.0005	39.7 +2.0
RbAP (00n)	26.1160 ±.0007	37.0 +3.0
TlAP (00n)	25.7625 ±.0010	32.7 +1.0

<sup>a</sup> In most cases there were not enough independent measurements for a reliable statistical analysis of dispersion in the data. Also, variations were found among samples. The errors quoted include upper limits to known systematic errors plus an estimate of random error taken to be three times the range of partially subjective, selected measurements. Selection factors included internal data consistency and sample purity. The final 2d values are also systematically uncertain by the amount of uncertainty in the AlK<sub>α</sub> wavelength, ±30 ppm. This error is eventually correctable.

among crystals. Below 10 Å the agreement is not as good. Future work should be concentrated on the range below 10 Å for KAP, and on better controls on sample histories for the other acid phthalates.

There are some general comments about crystals for low energy x-ray diagnostics we can make from these results.

NH<sub>4</sub>AP has particular merit in second order for combined high resolving power and reflectivity in the narrow range 11.3 to 12.3 Å for applications where the first order is negligible, such as NeX Ly $\alpha$  from solar active regions.

RbAP has good general utility because it has high R<sub>c</sub>, medium resolving power, and good separation between first order and higher orders.

TlAP is the crystal of choice when reflectivity is most in demand or when observing near the oxygen K-edge, but it has poor resolving power.

EDDT is especially good below 8.5 Å because it has high reflectivity, high resolving power, good separation of orders, absence of absorption edges, and ready availability in large sizes. In the long wavelength range where this crystal is well suited the stabilization by means of a thin overcoating works well for at least two years.

## REFERENCES

This work was supported by the US Department of Energy and by NASA grant S-40292B.

1. B. L. Henke in *Advances in X-Ray Analysis* (Plenum Press, New York 1964), p. 460.
2. G. A. Sawyer, A. J. Bearden, I. Henins, F. C. Jahoda, and F. L. Ribe, *Phys. Rev.* 131, 1891 (1963).
3. R. L. Blake, T. A. Chubb, H. Friedman, and A. E. Unzicker, *Ap. J.* 142, 1 (1965).
4. U. Feldman, *Astrophysics and Space Sci.* 41, 155 (1976).
5. H. W. Schnopper, J. P. Delville, A. Epstein, K. Kalata, and R. Sohval, *Space Science Instrumentation* 2, 243 (1976).
6. A. J. Burek, D. M. Barrus, and R. L. Blake, *Ap. J.* 191, 533 (1974).
7. K. D. Evans and B. Leigh, *Space Science Instrumentation* 2, 105 (1976).
8. A. J. Burek, *Space Science Instrumentation* 2, 53 (1976).
9. J. V. Gilfrich, D. B. Brown, and P. G. Burkhalter, *Applied Spectroscopy* 29, 322 (1975).
10. N. G. Alexandropoulos, *Applied Spectroscopy* 28, 155 (1974).
11. D. L. McKenzie, P. B. Landecker, and J. H. Underwood, *Space Science Instrumentation* 2, 125 (1976).
12. R. Hall, M. Lewis, B. Leigh, and K. Evans, *X-Ray Spectrometry* 8, 19 (1979).
13. P. Seidl, G. Schmidtke, and L. W. Acton, *Applied Optics* 16, 578 (1977).
14. A. J. Burek, D. M. Barrus, R. L. Blake, and E. E. Fenimore, *Ap. J.* 243, 660 (1981).
15. K. D. Evans, B. Leigh, and M. Lewis, *X-Ray Spectrometry* 6, 132 (1977).
16. J. F. Meekins and A. E. Unzicker, private communications 1963 to 1980.
17. R. Jenkins, *X-Ray Spectrometry* 1, 23 (1972).
18. D. M. Barrus and R. L. Blake, *X-Ray Spectrometry* 8, 199 (1979).
19. A. H. Compton and S. K. Allison, *X-Rays in Theory and Experiment* (D. Van Nostrand Company, New York 1935), p. 263-311.
20. R. D. Deslattes, B. G. Simoson, and A. T. Horton, *Rev. Sci. Instrum.* 36, 943 (1965).
21. J. S. Thomsen, *X-Ray Spectroscopy* (McGraw-Hill, New York 1974), p. 27.
22. R. D. Deslattes, J. L. Torgesen, B. Paretzkin, and A. T. Horton, *J. Appl. Phys.* 37, 541 (1966).
23. S. T. Stephenson and D. L. Martin, *Rev. Sci. Instrum.* 21, 1023 (1950).
24. D. M. Barrus, R. L. Blake, A. J. Burek, K. C. Chambers, and L. E. Cox, *Phys. Rev.* 22B, 4022 (1980).
25. L. G. Parratt and C. F. Hempstead, *Phys. Rev.* 94, 1593 (1954).
26. B. L. Henke, private communication of work on atomic scattering factors and reflection coefficients.
27. E. Källne and T. Aberg, *X-Ray Spectrometry* 4, 27 (1975).
28. A. J. Bearden and F. N. Huffman, *Rev. Sci. Instrum.* 34, 1233 (1963).
29. R. D. Deslattes and A. Henins, *Phys. Rev. Letters* 31, 972 (1973).
30. M. Lewis, P. A. Maksym, and K. D. Evans, *Astronomy and Astrophysics* 87, 213 (1980).



Dr. Richard Blake of Los Alamos during his invited paper on low energy spectrometric properties of crystals.



Dr. Eberhard Spiller of IBM explaining new developments in x-ray optics. Dr. Spiller's paper begins on the following page.



## Evaporated Multilayer Dispersion Elements for Soft X-Rays

E. Spiller

IBM T.J. Watson Research Center, Box 218, Yorktown Heights, NY 10598

## ABSTRACT

The design possibilities and limitations of multilayer structures for soft x-ray spectroscopy are summarized. Near grazing incidence structures can have a large integrated reflectivity and a large relative bandwidth close to one. The smallest possible bandwidth or highest possible resolution is obtained near normal incidence, and is determined by the absorption index  $k$  of the most transparent material available; the maximum resolution is  $N_{\max} \approx 1/2\pi k$ . Depending on the wavelength, values for  $N_{\max}$  can be between 10 and  $10^4$  in the soft x-ray region. The practical realization of a design requires good thickness control and sharp, smooth boundaries between the layers. Sufficient thickness control has been obtained by *in situ* monitoring of the x-ray reflectivities. Within the uncertainties of the optical constants the measured performance of the best multilayer systems is in agreement with theory for multilayer periods larger than  $30\text{\AA}$ . For smaller period lengths, the peak reflectivity is smaller than the theoretical values. The lower reflectivity can be explained by an effective roughness of the multilayer system in the order of  $3\text{\AA}$ .

## I. INTRODUCTION

There are two well known geometries which utilize interference effects to produce high reflectivity mirrors: the quarter wave stack, and the ideal Bragg crystal (Fig.1). The quarter wave stack consists of alternating layers of high (H) and low (L) refractive index, each of the same optical thickness  $nd = \lambda/4$  (for normal incidence), such that all boundaries add with equal phase to the reflected wave. For the case that both film materials are completely absorption free, the quarter wave stack gives the highest reflectivity with the fewest number of layers and approaches a reflectivity  $R = 100\%$ . In an ideal Bragg crystal the atomic planes are usually much thinner than a quarter wave, different planes are spaced  $\lambda/2$  apart (for normal incidence) and contribute in phase to the reflected wave. For the case that the space between the atomic plane is absorption free, the reflectivity approaches  $R = 100\%$  for a large number of layers even if the thin atomic planes are absorbing. The elimination of the absorption losses is due to the fact that the atomic planes are located at the nodes of the standing wave field generated by the superposition of the incidence and reflected wave (see Fig.1). In the quarter wave stack, on the other hand, each layer extends from a node to an antinode; if one or both layers are only slightly absorbing the performance of the quarter wave stack deteriorates fast due to the large absorption losses at the antinodes of the standing wave field.

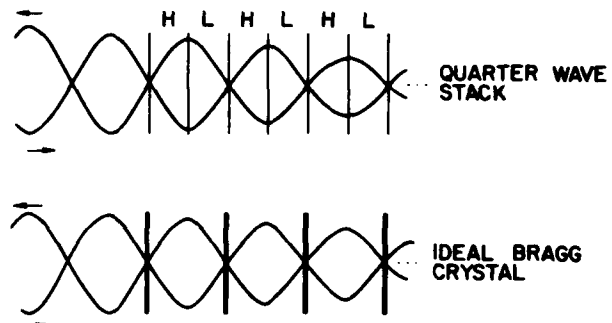


Fig.1 The quarter-wave stack (top) gives the fastest increase in reflectivity with increasing number of layers, but deteriorates fast in performance if one of the layers is absorbing. The ideal Bragg crystal (bottom) minimizes absorption by positioning the layers (atomic planes) into the standing wave produced by the superposition of the incident and reflected wave.

Optimum multilayer designs for soft x-rays are between the two limits of Fig.1. Designs for the highest possible resolution are similar to a Bragg crystal while designs

for largest integrated reflectivity are more similar to the quarter wave stack. However, due to the fact that all materials are absorbing in the soft x-ray region, the two design limits never represent an optimum design in the soft x-ray region. Optimum designs are in many cases aperiodic, being close to a quarter wave stack at the bottom of the coating and close to the crystal at the top of the coating (1).

Film deposition by evaporation offers most easily the widest choice in the selection of the thickness of each film in a multilayer; provided that sufficiently smooth films can be deposited with sufficient thickness control, evaporation methods promise the realization of customized coatings optimized for specific applications.

We will summarize in this paper the design possibilities of multilayers for spectroscopic applications and review the state of the art of fabricating these coatings by vacuum deposition.

## II. MULTILAYER CALCULATION AND DESIGN

The calculation of the performance (reflectivity, transmission, phase shift) of a multilayer structure is straightforward and treated in any textbook on optical thin films (2). Except for the periodic structures of the two limiting cases of Fig.1, analytical formulas are not very handy and the computations are best performed with a digital computer. The two most popular methods are the recurrent use of the single film formula or the Matrix method.

In the recurrent method, one starts with the equation

$$r_f = \frac{r_t + r_b e^{-2i\Delta}}{1 + r_t r_b e^{-2i\Delta}}, \quad (1a)$$

$$\Delta = \frac{2\pi d \tilde{n} \cos \alpha}{\lambda}, \quad (2a)$$

which gives the reflected amplitude of a single film as a function of the reflected amplitudes of the top ( $r_t$ ) and bottom ( $r_b$ ) of the film and of the phase retardation  $\Delta$  of a wave propagating with a propagation angle through the thickness  $d$  of the film. The refractive indices  $n$  and in general  $r_t$ ,  $r_b$  and  $\cos \alpha$  are complex quantities.

The influence of an additional layer can now be calculated by replacing  $r_b$  in Eq.1 by the value obtained previously for  $r_t$  and again using Eq.1 now for the calculation of the two layer system. Repeated application of Eq.1 gives finally the reflected amplitude (and also the transmission) for an arbitrary structure of thin films.

The reflection coefficients  $r_s$ ,  $r_p$  (for s- and p-polarization) at the boundaries of two materials (refractive indices  $\tilde{n}_1, \tilde{n}_2$ ) which have to be inserted into Eq.1 are obtained from Fresnel's equations

$$r_s = \frac{\tilde{n}_1 \cos \alpha_1 - \tilde{n}_2 \cos \alpha_2}{\tilde{n}_1 \cos \alpha_1 + \tilde{n}_2 \cos \alpha_2}, \quad (2a)$$

$$r_p = \frac{\tilde{n}_1 \cos \alpha_2 - \tilde{n}_2 \cos \alpha_1}{\tilde{n}_1 \cos \alpha_2 + \tilde{n}_2 \cos \alpha_1}, \quad (2b)$$

where the propagation angles in the materials are obtained by Snell's law from the angle of incidence  $\alpha_0$  in vacuum

$$\tilde{n}_1 \sin \alpha_1 = \tilde{n}_2 \sin \alpha_2 = \sin \alpha_0 \quad (3)$$

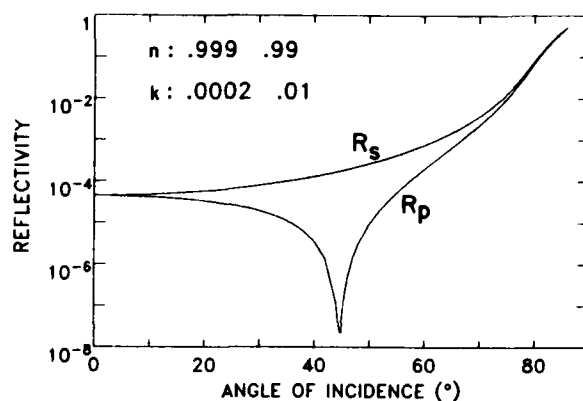


Fig.2 Reflectivities  $R_s$  and  $R_p$  for s- and p-polarization at the boundary of 2 materials versus the angle of incidence in vacuum calculated from Eqs.1 and 2. The optical constants are those for C and Au from Ref.3.

Fig.2 gives typical reflectivity curves  $R_s = |r_s|^2$ ,  $R_p = |r_p|^2$  at the boundary of two materials in the soft x-ray region; the optical constants used are those given in Ref.3 and 4 for carbon and gold. Except for very grazing incidence angles the reflectivity of all material is very low in the soft x-ray region, and the purpose of a multilayer coating is to enhance the reflectivity to a value close to 1 by utilizing constructive interference between many boundaries.

The matrix method is due to Abeles (5) and utilizes the fact that for any linear system the output field vector ( $E_{out}, H_{out}$ ) can be obtained from the input ( $E_{in}, H_{in}$ ) by multiplication with a characteristic matrix. The matrix  $M_i$  for a single film can be easily derived and the matrix for a multilayer coating is simply the product of all its single film matrices. (See Born and Wolf for details and note that for soft x-rays all matrix elements are complex). All properties of an arbitrary multilayer are then obtained from the matrix elements of the product matrix. The matrix method can be very elegantly programmed on a digital computer, especially in a computer language like APL, where matrix operations are directly incorporated.

The inversion of a multilayer calculation, i.e., the task to find a multilayer coating which approaches a given reflectivity (or transmission or phase shift) curve is much more complicated and may also lead to solutions that cannot be realized in practice. The problem and some approaches are reviewed in two books (6,7). Due to the limited range of available optical constants in the soft x-ray region design possibilities are much more limited here than at visible wavelengths.

We will in the following restrict ourselves to the most simple designs with the goal to explain the available design choices and will only give the directions towards more sophisticated designs. Trial-and-error methods are in many cases sufficient in the soft x-ray range.

## III. ROUGH BOUNDARIES AND GRADUAL TRANSITION BETWEEN LAYERS

A rough boundary or a gradual transition between two materials reduces the reflectivity at this boundary. The simplest theory gives for the reduction of the reflected amplitude  $r/r_0$

$$r/r_0 = \exp - 2 \left( \frac{2\pi\sigma \cos \alpha}{\lambda} \right)^2, \quad (4)$$

when  $r_0$  is the amplitude reflectivity of a smooth and sharp boundary, and  $\sigma$  is the rms roughness. (8-10) Equation 4 is valid under the assumption that the surface heights variations are described by a Gaussian of variance  $\sigma$  and that the slopes are sufficiently small such that polarization effects, shadowing and multiple scattering can be neglected. Equation 4 also describes the reflectivity reduction by a smooth Gaussian transition layer between two materials if the reflectivity is small ( $r_0 \ll 1$ ). While the loss in reflectivity will appear as scattered light for the rough surface it will show as increased transmission for the smooth transition layer. The theory of multilayer structures with rough boundaries has been developed by several authors. (11-13) Experimental data which can be compared to the detailed theory have not been obtained up to now; for soft x-rays authors have used the single boundary Eq. 4 to describe the measured performance of a multilayer coating. The "effective" roughness obtained this way may deviate from the real topographical roughness of the interfaces.

One important result of the multilayer theory is, that scattering is greatly reduced for a boundary at the node of a standing wave. (11) Therefore for the same topographical roughness, we can expect less scattering for the design of Fig. 1b than that of Fig. 1a; furthermore, scattering decreases as the standing wave ratio or the reflectivity increases.

#### IV. DESIGN LIMITS

The design possibilities and limits can be estimated by considering two parameters  $N_{\min}$  and  $N_{\max}$ .  $N_{\min}$  is the minimum number of periods required to give a reflectivity close to 1, considering only the Fresnel reflection coefficients  $r$  at each boundary and neglecting absorption losses due to propagation through the films, while  $N_{\max}$  is the maximum number of periods which can be penetrated due to the absorption. For the case  $N_{\max} \gg N_{\min}$  a reflectivity close to 100% can be achieved and the freedom to select substantially different designs is proportional to the ratio  $N_{\max}/N_{\min}$ , while for the case that  $N_{\max} \ll N_{\min}$  the maximum possible reflectivity is small ( $R_{\max} \ll 1$ ) and essentially no freedom is available to choose designs with different characteristics.

We can estimate  $N_{\min}$  by assuming a periodic multilayer which is close to the quarter wave stack. All boundaries add in phase to the reflected wave and neglecting multiple reflections and considering that we have 2 boundaries per period we estimate the total reflected amplitude of the multilayer to be  $N_{\min} \cdot 2|r|$ . The condition that this value is close to one gives

$$N_{\min} = 1/2 \cdot |r|, \quad (5)$$

where  $r$  is the amplitude reflection coefficient at the boundary of the two coating materials, which can be calculated from Fresnel's equations (2). For normal incidence and under the assumption that  $n_1$  and  $n_2$  are close to 1 we can approximate

$$N_{\min} = 1/\sqrt{\Delta n^2 + \Delta k^2}, \quad (6)$$

where  $\Delta n$  and  $\Delta k$  are the differences in the optical constants of the coating materials. The full curve in Fig. 3 gives  $N_{\min}$  as a function of wavelength calculated for the optical constants of carbon and Au from Ref. 3. Also plotted in Fig. 3 is the value of

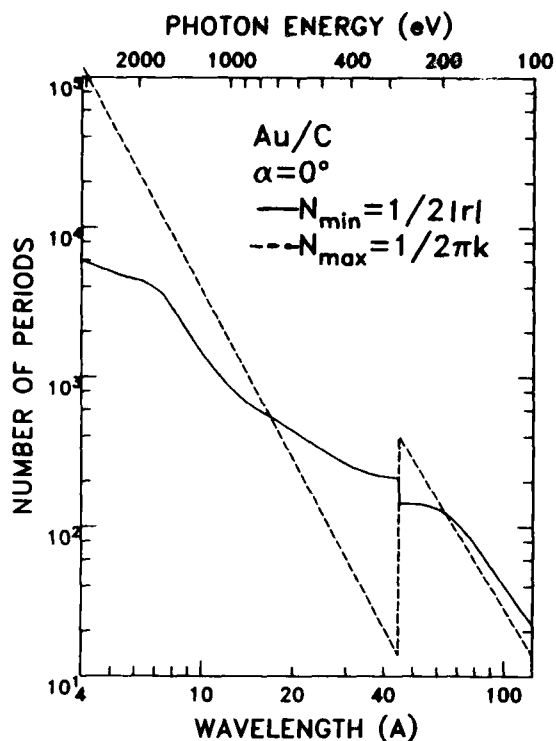


Fig. 3 The minimum number of periods  $N_{\min}$  required to obtain a reflectivity close to 1, if propagation losses due to absorption are neglected and the maximum number of periods  $N_{\max}$  permitted due to absorption in the carbon spacer layer for a Au/C multilayer system as a function of wavelength. In those regions where  $N_{\max} \geq N_{\min}$  reflectivities can approach 1 and coating designs can be optimized for different applications.

$$N_{\max} = \frac{\cos^2 \alpha}{2\pi k} = \frac{\sin^2 \theta}{2\pi k} \quad (7)$$

using normal incidence and the absorption index  $k$  of carbon.  $N_{\max}$  is obtained for the design limit in Fig. 1b, where the multilayer consists mostly of the spacer material and the absorption in the heavier material is reduced by the standing wave field.

The spectral bandwidth or resolution of a multilayer coating is determined by the total number of periods  $N$  contributing in phase to the reflectivity:

$$\frac{\lambda}{\Delta\lambda} \approx N. \quad (8)$$

The maximum possible resolution is  $N_{\max}$  and Fig. 3 shows that its value increases towards shorter wavelengths from 20 to over 200 for wavelengths decreasing from 130 Å to 45 Å. In the wavelength region  $\lambda = 30 - 44$  Å (for energies above the absorption edge of carbon)  $N_{\max}$  is much smaller than  $N_{\min}$  and coatings with carbon spacer layers have only poor reflectivities. For wavelengths below 30 Å the possible best resolution increases fast with decreasing wavelength reaching values over 1000 for  $\lambda < 10$  Å, while the maximum possible reflectivity approaches 100%. Coatings with the largest bandwidth and integrated reflectivity are obtained for designs that require close to  $N_{\min}$  layers.  $N_{\min}$  and  $N_{\max}$  decrease at oblique angles of incidence, and near grazing incidence  $N_{\min}$  can reach values close to 1 (see Fig. 2). The entire theoretically possible range in resolution of a multi-

layer is therefore between a value close to 1 and the value  $N_{\max}$ , where the largest bandwidth is possible near grazing, the highest resolution near normal incidence.

## V. MULTILAYER DESIGNS

The simplest multilayer designs are periodic structures, for given optical constants they contain only two parameters: the thickness ratio of the two materials within one period and the total number of periods. Figure 4 gives the peak reflectivity of a 256 period coating designed for an incidence angle  $\alpha = 45^\circ$  and a wavelength  $\lambda = 50.8\text{\AA}$  as a function of the normalized thickness of the heavy material. (The optical constants are those of C and Au from Ref.3) The peak reflectivity has a maximum for a normalized thickness of the Au of 0.22 of the period length, which corresponds to  $7.3\text{\AA}$  of gold and  $28.65\text{\AA}$  of carbon. The Curve a in Fig.5 gives the reflectivity versus wavelength curve for this design and also the values for the spectral resolution and integrated reflectivity. Larger integrated reflectivity and less penetration into the multilayer can be obtained with thicker gold films (Curve b in Fig.5) while a higher resolution is obtained with thinner gold films allowing deeper penetration (Curve c). The low resolution of 62 for Curve b indicates that only the top 62 periods of the multilayer contribute to the reflectivity. Therefore, essentially the same reflectivity curve can be obtained with much fewer periods (for example, 64) using the corresponding optimum thickness ratio.

The reflectivity versus wavelength curve of periodic structures approaches a Lorentzian for large numbers of layers. Other lineshapes can be obtained if the thickness ratio between the two materials changes throughout the depth of the film. Because the reflectivity of each film in the multilayer is a function of its thickness (approaching zero for zero thickness) one can adjust the relative weight of the contribution of each period to the total reflectivity; for example, a Gaussian reflectivity curve can be generated by creating a Gaussian as the weight with which the different periods (starting from the top) contribute to the reflectivity.

A non-periodic structure with constant period length is also obtained if one asks for the structure which gives the highest peak reflectivity with the fewest number of layers. The result is a structure which is close to the quarter wave stack (equal thickness of both materials) at the bottom and closer to the Bragg crystal at the top. For wavelengths  $\lambda < 100\text{\AA}$  and large numbers of layers, the reflectivity curve does not differ significantly from that of the optimized periodic design; aperiodic designs are more important for longer wavelengths and fewer periods (14,15).

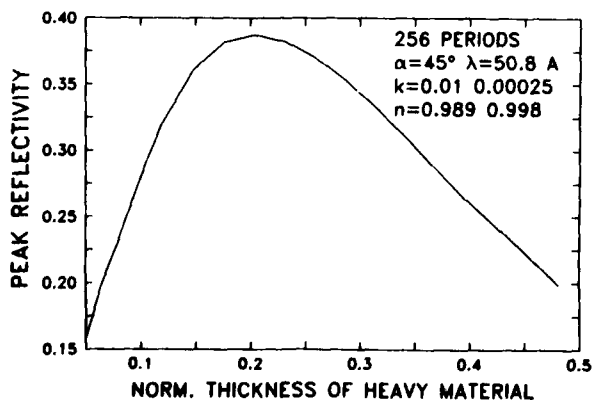


Fig.4 Peak reflectivity  $R_p$  of a multilayer with 256 periods versus the thickness of the heavy element. The coating is optimized for an angle of incidence  $\alpha = 45^\circ$  and wavelength  $\lambda = 50.8\text{\AA}$ , the thickness is normalized to the period length of  $35.95\text{\AA}$ .

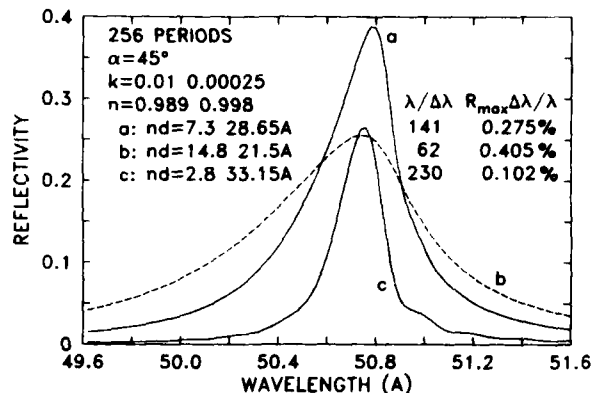


Fig.5 Reflectivity versus wavelength for multilayer coatings with 256 periods optimized for highest peak reflectivity (a) and for a larger (b) and smaller (c) bandwidth.

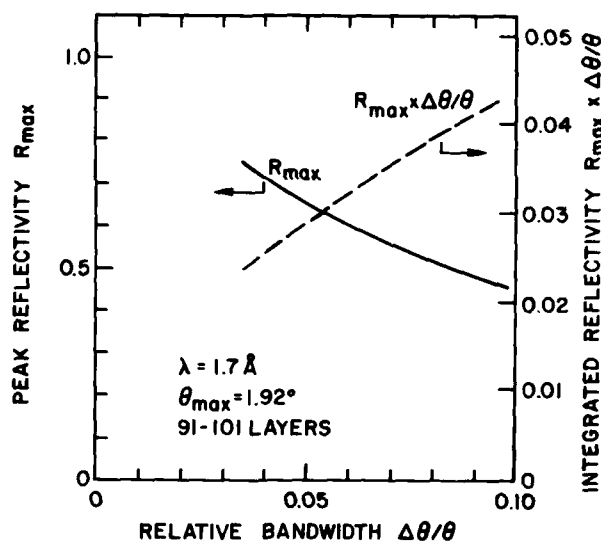


Fig.6 Peak reflectivity  $R_{\max}$  and integrated reflectivity  $R_{\max} \cdot \Delta\theta/\theta$  for multilayer system, where the period lengths varies throughout the thickness versus the relative bandwidth. The smallest bandwidth in the plot corresponds to the periodic system. Designs are found by trial and error.

In those wavelength regions where  $N_{\max} \gg N_{\min}$  it is possible to design coatings with a relative bandwidth  $\Delta\lambda/\lambda > 1/N_{\min}$  by changing the base period of the multilayer throughout the thickness of the coating (16). Figure 6 shows as an example, how the relative bandwidth and the integrated reflectivity can be increased by this method. The goal was to increase the integrated reflectivity for a grazing incidence x-ray telescope (17); the period length decreases from the bottom to the top of the multilayer and the details of the design have been obtained by trial and error.

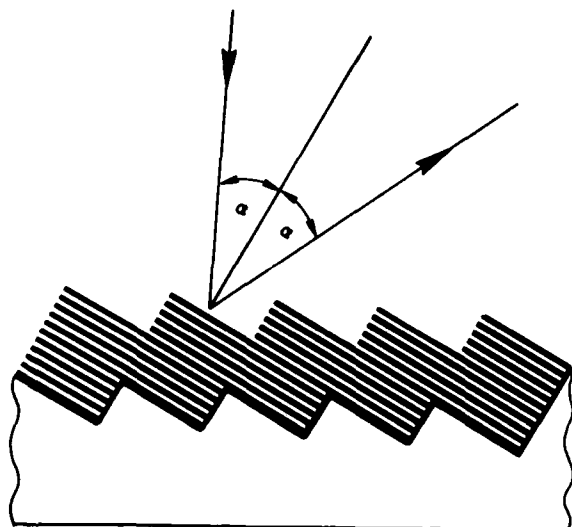


Fig.7 A blazed reflection grating overcoated with a multilayer extends the range grating monochromators towards shorter wavelengths but requires high tolerances for the grating profile.

The spectral resolution of a multilayer can be extended beyond the limit posed by  $N_{\max}$  (Eq.7) if steps are cut into the multilayer which permit the radiation to reach deeper periods (Fig.7). The structure can be realized by overcoating a blazed diffraction grating with a multilayer such that the blaze condition and the Bragg condition are fulfilled simultaneously. The process requires tighter tolerances on the smoothness and step uniformity of the grating than are standard and has not been tested up to now.

## VI. MULTILAYER DEPOSITION SYSTEM

Fig.8 is a sketch of our vacuum deposition system used for the multilayer deposition. An important feature of the system is the soft x-ray reflectometer which allows one to monitor the reflectivity of a multilayer during deposition. The interference maxima and minima observed during the deposition give an accurate measure of the thickness and can be used to eliminate the influence of any drifts in the calibration of the quartz microbalance. A main feature of this monitoring system is that thickness errors are not accumulating, the maximum accumulated thickness error is always a small fraction of one period in the multilayer. We use targets of carbon or BN in the x-ray source, giving characteristic x-ray wavelengths of 31.6, 44.7 or 67.6Å. The largest reflected signal is obtained with  $\lambda = 44.7\text{Å}$ , however, this wavelength is not very suitable for the monitoring of a multilayer that contains a carbon spacer layer, because the reflectivity changes only very little during the carbon deposition for this wavelength. The smallest signal is obtained for  $\lambda = 31.6\text{Å}$ ; however, for this wavelength a usable fringe contrast is obtained and Fig.9 shows the actual monitor signal obtained during the deposition of the first 27 layers of a 120 layer coating designed for maximum normal incidence reflectivity at  $\lambda = 67.6\text{Å}$ .

## VII. COATING MATERIALS

For the widest possible design choices  $N_{\min}$  should be as small and  $N_{\max}$  as large as possible. Therefore, two materials should be selected with the largest possible differ-

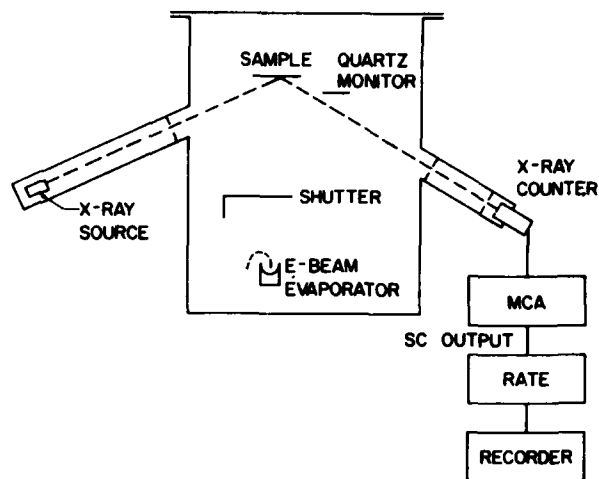


Fig.8 Vacuum evaporator with *in situ* monitoring of the soft x-ray reflectivity. Targets of B, BN or C are used in the source giving x-ray wavelengths of 31.6, 44.7, or 67.6Å.

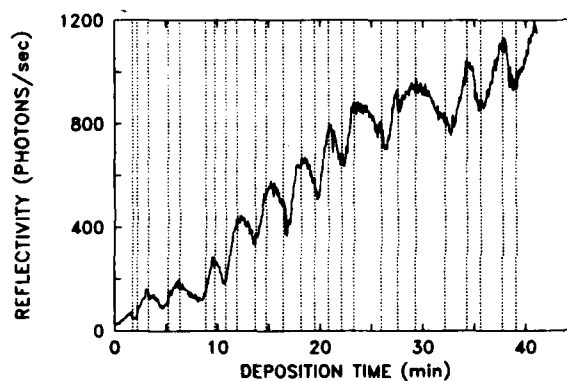


Fig.9 Monitor signal ( $\lambda = 31.6\text{Å}$ ,  $\alpha = 62^\circ$ ) obtained during the deposition of the first 27 layers of the 120-layer coating designed for maximum reflectivity at  $\lambda = 67.6\text{Å}$  and normal incidence versus accumulated deposition time. Filters and windows of  $\text{Si}_3\text{N}_4$  (1500Å thick) are used to suppress the  $\lambda = 67.6\text{Å}$  line from the BN target in the x-ray source.

ence in  $\tilde{n}$  (see Eq.6) and the spacer material should have the smallest possible absorption (Eq.7). In general, this requires one to combine a light material (Be, B, C) with a heavy material (Ta to Au). The boundaries between the layer should be abrupt, smooth, and stable. Carbon has been shown to form stable boundaries with practically all heavy metals (18) and is, therefore, the first choice for a spacer material. The change in the roughness of a film surface can be estimated from its reflectivity obtained during film deposition. Figure 10 shows the measured reflected amplitude  $\sqrt{R}$  (circles) for a film of AuPd. The theoretical curve obtained from Eq.1 is a damped oscillation around  $|r_t|$ , the reflected amplitude of the top surface. In order to explain that the average between the envelopes through the maxima and minima decreases with increasing thickness, we assume that  $|r_t|$  decreases and that the decrease is due to an increase in roughness. By multiplying  $r_t$  in Eq.1 with

Eq.4, we can fit the measured curve to the theory with  $\sigma$  as a fitting parameter. Figure 10 (full curve) shows the theoretical curve together with the values for  $\sigma$  obtained. Table I gives a listing of the roughness values obtained by this method for a variety of promising coating materials. The results are in qualitative agreement with electron micrographs (19) and with *in situ* measurements of the film conductivity. The table shows that boron and carbon are suitable low absorption spacer materials, while LiF which has low absorption in the  $\lambda = 18 - 45\text{\AA}$  range is useless due to its roughness. Of the heavy elements, W and Pt produce the smoothest surfaces; however, Pt requires high deposition rates above  $2\text{\AA}/\text{sec}$  for the smoothest surfaces (20). Gold films can be made much smoother by adding Pd. The smoothest films are obtained with amorphous ReW films; while all other heavy metals show always an increase of roughness with increasing thickness, the ReW films show sometimes no roughness increase (on smooth Si wafers) or even a smoothing effect (on rotating float glass substrates).

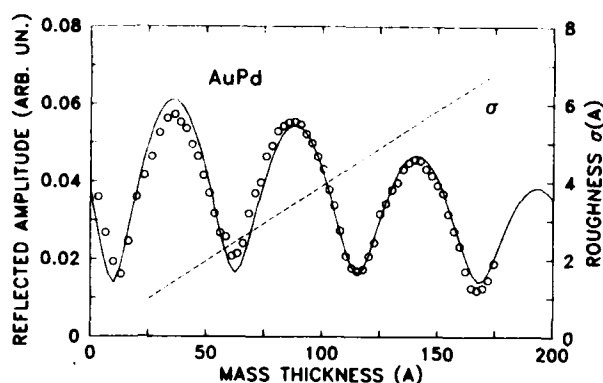


Fig.10 Measured reflected amplitude ( $\sqrt{R}$ ) obtained during the deposition of a AuPd film on a silicon substrate for  $\lambda = 44.7\text{\AA}$  and  $\alpha = 64^\circ$  (circles) and theoretical curve (full curve) obtained under the assumption that the surface roughness of the top surface is represented by the dashed curve.

TABLE I

Increase in the surface roughness  $\sigma$  of the top surface of various  $100\text{\AA}$  thick evaporated films measured during the deposition by the method of Fig.10. Negative values indicate smoothing.

material	substrate	roughness $\sigma(\text{\AA})$
B	ReW	~1
C	ReW	0
LiF	ReW	17
Ta	Si	5.2
W	Si	3
Re	Si	5.2
Os	Si	5.3
Ir	Si	4.2
Pt	Si, float glass	2.8 to 6
Au	Si	8
AuPd	Si	3.3
PtIr	Si	7
ReW	Si	0 to 2.5
ReW	float glass	-3 to +2

## VIII. MULTILAYER PERFORMANCE

We have fabricated and tested multilayers made of the following material combinations: AuPd-B, ReW-B, AuPd-C, Pt-C and ReW-C. The interfaces of the AuPd-B system become rough or gradual already during the deposition; all other material combinations form stable usable multilayer systems. The performance of the multilayers is summarized in Table II. The AuPd-C system gives the highest reflectivity for  $\lambda > 80\text{\AA}$ , while the ReW-C has the best performance at shorter wavelengths (21). The peak reflectivities of the ReW-B multilayers are smaller than those of comparable ReW-C systems. At  $\lambda = 44.7\text{\AA}$  and  $\lambda = 1.54\text{\AA}$  and multilayer periods around  $50\text{\AA}$  the performances of the Pt-C and the ReW-C system are comparable.

A quantitative comparison of the measured performance with theory is difficult for soft x-rays due to the uncertainties of the published optical constants. The optical constants of Ref.3 give a much higher reflectivity for a single boundary than has ever been measured (22) and optical constants obtained from reflectivity data are not available for soft x-rays. Theory and experiment are in agreement in the increase of the reflectivity of a multilayer over that of a single film. The peak normal incidence reflectivity obtained is around  $R = 10\%$  in the  $\lambda = 45-200\text{\AA}$  wavelength range.

Quantitative agreement between experimental and theoretical performance is obtained for  $\lambda = 1.54\text{\AA}$  and grazing incidence. Measured peak reflectivities are above 60% for periods larger than  $30\text{\AA}$ . For shorter periods the peak reflectivity drops and one can describe this drop with Eq.4 using values for  $\sigma$  between 2.5 and  $4\text{\AA}$  as fitting parameter.

The halfwidth or spectral resolution is in agreement with theory at all wavelengths; however, no attempts have been made up to now to fabricate multilayers with resolutions above 100.

## IV. CONCLUSIONS

Multilayer structures made by evaporation can contain in principle any thickness thus allowing the fabrication of a large variety of structures which might be periodic or non-periodic. Therefore, coatings can be designed and fabricated which are optimized for different purposes, for example, to give the highest integrated reflectivity, the highest spectral resolution, or which approach a specific reflectivity versus wavelength curve. The highest possible resolution is limited by the absorption in the spacer layer and has the value  $N_{\text{max}} = 1/2\pi k$  for normal incidence, where  $k$  is the absorption index of the spacer layer. For spacer layers of carbon  $N_{\text{max}}$  increases from  $N_{\text{max}} = 20$  to  $N_{\text{max}} \approx 300$  for wavelengths decreasing from  $\lambda = 100$  to  $\lambda = 45\text{\AA}$ . For a wavelength below  $\lambda = 20\text{\AA}$ ,  $N_{\text{max}}$  increases rapidly (about as  $1/\lambda^3$ ) with decreasing wavelength. The highest possible bandwidth or integrated reflectivity is obtained for the smallest number of periods  $N_{\text{min}}$  in a multilayer which still produces substantial peak reflectivity.  $N_{\text{min}}$  is determined by the Fresnel coefficient at each boundary and approaches a value close to 1 for very shallow grazing angles. Therefore, if the angle of incidence is used as a free design parameter, multilayers can be designed for any relative bandwidth from values close to 1 to values as small as  $1/N_{\text{max}}$ .

In wavelength regions where  $N_{\text{max}} \gg N_{\text{min}}$ , peak reflectivities  $R_{\text{max}}$  close to 1 can be obtained; for values of the optical constants which yield  $N_{\text{min}} \gg N_{\text{max}}$ , we can only obtain peak reflectivities  $R_{\text{max}} \ll 1$ . For multilayer systems of carbon and a heavy element peak reflectivities are above 10% for wavelengths between  $45\text{\AA}$  and  $200\text{\AA}$ , have very small values (about 1%) in the  $\lambda = 30-44\text{\AA}$

TABLE II

Measured properties of various multilayer mirror coatings.  $N$  is the number of layers,  $R_{\max}$  the maximum reflectivity measured at wavelength  $\lambda_{\max}$ ,  $\Delta\lambda$  the halfwidth of the reflectivity versus wavelength curve, and  $\alpha$  the angle of incidence ("unp" stands for unpolarized).

System	Substrate	N	$\lambda_{\max}$ (Å)	$R_{\max}$ (%)	$\lambda_{\max}/\Delta\lambda$	$\alpha$ (°)
1) AuPd-C, 49% Au	glass	6.5	132.5	14.3	14	10°
2) AuPd-C, 49% Au	glass	13.5	130	15.8	15	10°
		13.5	103	22	14	50° <sub>s</sub>
3) AuPd-C, 54% Au	Si	27.5	132	16	24	10°
		27.5	102	10.5	...	40° <sub>s</sub>
		27.5	104	1.1	...	40° <sub>p</sub>
4) ReW-C/B, 68% Re	glass	29.5	133	4.9	...	10°
5) ReW-B	Si	56.5	67.6	2.1	23	52° unp
		56.5	23.6	1.1	28	68.5° unp
		56.5	14.6	2.3	28	76.9° unp
		56.5	1.54	75	21	90°-0.9° unp
6) ReW-C	Si	62.5	1.54	65	43	90°-1.25° unp
		62.5	44.8	6.3	72	44° unp
7) ReW-C	Si	97.5	1.54	52	57	90°-1.6° unp
		97.5	44.8	2.8	73	37° unp
8) ReW-C	glass	39	1.54	57.5	35	90°-1.26° unp
9) ReW-C	glass	39	1.54	21.5	4.3	90°-1.05° unp
		39	44.8	1.25	11	59°

region, and increase to values close to 100% with decreasing wavelength for  $\lambda < 20\text{Å}$ .

For highest peak reflectivity, abrupt, smooth interfaces between layers are required. Of all material combinations explored, the ReW-C system produces the sharpest boundaries. Multilayers of ReW-C show theoretical performance for multilayer periods larger than 30Å; for smaller periods, the peak reflectivity is reduced and the observations can be described by Eq.8, with a roughness value  $\sigma \cong 3\text{Å}$ .

We control the thickness of the multilayer films by monitoring the reflectivity of a characteristic x-ray line ( $\lambda = 31.6, 44.7, \text{ or } 67.6\text{Å}$ ) *in situ* during the deposition and observing the interference effects between the top surface and the underlying multilayer. We have fabricated multilayers with up to 200 layers (100 periods) by this method; the observed resolution was in all cases in agreement with theory.

## REFERENCES

- (1) E. Spiller, *Appl. Phys. Lett* **20**, (1972); *Appl. Opt* **16**, 89 (1976); *Proc. 1CO-1X, Space Optics*, Natl. Acad. Science, Washington (1974) p.525.
- (2) O.S. Heavens, *Optical Properties of Thin Films*, (Dover, New York 1965); A. Vasicek, *Optics of Thin Films* (North Holland, Amsterdam, 1960); H.A. Macleod, *Thin-Film Optical Filters*, (Elsevier, New York, 1969); M. Born and E. Wolf, *Principles of Optics*, 5th ed. (Pergamon Press, 1975); P.H. Berning, *Theory and Calculations of Optical Thin Films*, in *Physics of Thin Films*, ed. by G. Hass, **1**, 69 (Academic Press, New York, 1963).
- (3) H.J. Hagemann, W. Gudat and C. Kunz, 1975, *J. Opt. Soc. Am.* **65**, 742 and DESY Report SR-74/17.
- (4) B.L. Henke, and E.S. Ebsu, 1973, *Advances in X-Ray Analysis* **17**, Plerm Press, New York, p.150.
- (5) F. Abeles, *Ann. Physique* 12<sup>th</sup> series, **5**, 596-640 and 706-784 (1950).
- (6) Z. Knittl, *Optics of Thin Films*, (Wiley, London 1976).
- (7) H.M. Liddell, *Computer-aided Techniques for the Design of Multilayer Filters*, (Hilger, Bristol, 1981).
- (8) P. Beckmann, and A. Spizzichino, *The Scattering of Electromagnetic Waves from Rough Surfaces*, Pergamon Press, Oxford (1963).
- (9) H.E. Bennett and J.O. Porteus, *J. Opt. Soc. Am* **51**, 123 (1961).
- (10) H.E. Bennett and J.M. Bennett, in *Physics of Thin Films*, eds. G. Hass and R.E. Thun, Academic Press, **4**, 1 (1967).
- (11) J.M. Eastman, in *Physics of Thin Films*, eds. G. Hass and M.H. Francombe, **10** (1978).
- (12) C.K. Carniglia, *Opt Engin.* **18**, 104 (1979).
- (13) J.M. Elson, *J. Opt. Soc. Am* **69**, 48 (1979).
- (14) E. Spiller, *Optik* **39**, 118 (1973).
- (15) R.-P. Haelbich, A. Segmüller and E. Spiller, *Appl. Phys. Lett* **34**, 184 (1979).
- (16) P.W. Baumeister and J.M. Stone, *J. Opt. Soc. Am* **46**, 228 (1956).
- (17) P. Gorenstein, *SPIE, Space Optics--Imaging X-ray Optics Workshop*, **184**, 63 (1979).
- (18) R.-P. Haelbich and C. Kunz, *Opt. Commun* **17**, 287 (1976).
- (19) A.N. Broers and E. Spiller, in *Scanning Electron Microscopy* (SEM Inc., AMF O'Hara) p.201 (1980).
- (20) G. Fischer and H. Hoffmann, *Z. Physik B - Condensed Matter* **39**, 287 (1980).
- (21) E. Spiller, A. Segmüller, J. Rife, and R.-P. Haelbich, *Appl. Phys. Lett.* **37**, 1048 (1980).
- (22) R.-P. Haelbich, Thesis 1980, DESY Report F41, HASYLAB 8013 (1980).

## Sputtered Layered Synthetic Microstructure (LSM) Dispersion Elements

by

Troy W. Barbee, Jr.  
 Department of Materials Science and Engineering  
 Stanford University  
 Stanford, California 94305

## ABSTRACT

The opportunities offered by engineered synthetic multilayer dispersion elements for x-rays have been recognized since the earliest days of x-ray diffraction analysis. In this paper, application of sputter deposition technology to the synthesis of Layered Synthetic Microstructure (LSM's) of sufficient quality for use as x-ray dispersion elements is discussed. It will be shown that high efficiency, controllable bandwidth dispersion elements, with  $d$  spacings varying from 15 Å to 180 Å, may be synthesized onto both mechanically stiff and flexible substrates. Multilayer component materials include tungsten, niobium, molybdenum, titanium, vanadium, and silicon layers separated by carbon layers.

Experimental observations of peak reflectivity in first order, integrated reflectivity in first order, and diffraction performance at selected photon energies in the range, 100 to 15000 eV, will be reported and compared to theory. Emphasis is placed on results giving information concerning limiting structural characteristics of these LSM's. It will be shown that the observed behavior is in accord with theory, both kinematic and dynamic regimes being clearly observed. In addition, the mosaic spread of these LSM's is not detectable, indicating that they are perfect structures. A consistent explanation of these experimental results indicates that roughness at the interfaces between constituent layers is the structural characteristic currently limiting diffracting behavior.

## 1. INTRODUCTION

Early in the development of the field of x-ray diffraction, it was proposed that synthetic man-made materials consisting of alternating layers of high atomic number and low atomic number elements would be useful as dispersion elements for x-rays. Such structures, termed layered synthetic microstructures (LSM) in this paper, were the subject of several investigations. The primary difficulties encountered in this early work were technological, being associated with the synthesis process and materials selection. In this section, a short summary of these efforts will be presented with emphasis on delineation of generic limitations and the structure of this paper outlined.

Earliest efforts (1,2) to form synthetic structures were unsuccessful, the first successful work being that of Dumond and Youtz (3) who vacuum deposited copper/gold LSM's with a characteristic period of approximately 100 Å. Strong dispersing power for Mo K $\alpha$  radiation was observed but decayed, due to the interdiffusion of the components, in approximately one week. More recently, Dinklage and Frericks (4) and Dinklage (5) prepared layers structures of lead/magnesium, gold/magnesium, and iron/magnesium. The lead, gold/magnesium systems exhibited instability due to reaction or diffusion in a manner similar to copper/gold. Iron/magnesium, on the other hand, exhibited stability projected to be longer than one year. In addition, the Fe/Mg-LSM showed many orders of reflection in diffraction scans and exhibited diffracting behavior comparable to ADP and lead stearate.

Since then, a substantial effort to synthesize normal incidence mirrors for soft x-rays has been undertaken by Spiller (6-12) and his associates. Their work has been primarily with radiation having wavelengths longer than 100 Å, though characterization has been made using Cu K $\alpha$  (1.5418 Å) radiation. Analytical procedures have also been developed that are based on optical dispersion theory that allow description of the expected behavior of LSMs. Semiquantitative comparison has been made with results obtained using Cu K $\alpha$  radiation and reasonable agreement attained. Particular emphasis in this work has revolved about improving the interface roughness between constituent layers of the LSMs. It has been demonstrated that inclusion of a correction factor for such roughness significantly improves the agreement between calculations and experiment.

The synthesis procedure initially used by Spiller was thermal evaporation controlled by quartz crystal oscillators. Difficulties with layer thickness control were encountered due to thermal drift of the oscil-

lators caused by radiation heating from the electron-beam thermal sources. This has been corrected by using an x-ray interference monitoring technique, allowing continuous determination of the individual layer thicknesses during deposition and considerable improvement has been achieved with this process control modification. In addition, the effect of substrate character has been explored with inherently smooth substrates being demonstrated as clearly optimum.

Work at Stanford by the author (13-15) initiated in early 1976 (under NSF/MRL sponsorship through its Center for Materials Research) was on the development of a technique for the synthesis of LSM materials using sputtering technology. In the fall of 1978, it was clear that high efficiency x-ray dispersion elements for Cu K $\alpha$  radiation has been synthesized with a period of ~20 Å. These samples were characterized by Mr. L. Koppel of Lawrence Livermore National Laboratory (LLNL) over the energy range 4.5 to 11.5 keV using standard powder diffractometry and a high-resolution of Si (Li) energy dispersive detector. This result represented an existence experiment and indicated that substantial research into the reproducibility and general breadth of periods and constituent materials should be undertaken.

In addition to work specifically oriented toward LSM dispersion elements for x-rays, other investigators have been pursuing the application of such materials as neutron dispersion elements. Saxena and Schoenborn (16), have investigated manganese/germanium structures. Synthesis process control difficulties resulted in substantial imperfection in their materials, though high reflectivities were achieved. These investigators also developed an analytical approach based on scattering theory allowing closed-form description of the intensities diffracted in both the kinematic and dynamic regimes, ignoring absorption effects. In summary, the work on neutron dispersion elements has been consistent with the experience of others and yielded devices of interest to this community.

It is also important to mention the ongoing research on semiconducting materials and on metal/metal LSMs. Molecular beam epitaxy (MBE) (17-21) is the term usually used to describe these processes which are being utilized in many laboratories in the world. Highly perfect LSMs have unique properties and possible significant applications. In metal/metal systems, the results are somewhat less well defined (21-25) as the field is significantly less mature and the variation in material properties definitely much broader than exhibited by semiconductor materials. Again, many of the problems already described in the discussion of dispersion element work have been encountered in this work



and engineering solutions achieved. At this time, significant advances in this field will be forthcoming as a better understanding of material effects is gained.

In summary, significant effort in a limited number of laboratories has been placed on the synthesis of LSMs with characterization by a variety of means implemented. Primary difficulties have been encountered with respect to process control, substrate character, and choice of constituent materials. These problems are now under serious investigation and will be considered more fully in the following presentation.

In the following, a short review of the theory of the diffracting behavior of LSM dispersion elements pertinent to this paper will be presented first. The sputter deposition synthesis process will then be reviewed. Experimental results obtained using tungsten/carbon (W/C), vanadium/carbon (V/C) and titanium/carbon (Ti/C) LSM's are then considered. Two applications of these LSM dispersion elements as spectroscopic devices are then presented. The paper is then summarized and recommendations as to further research discussed.

## II. MODELING AND THEORY

Modeling of the diffracting behavior of LSMs takes many approaches all of which are discussed in other papers in this Conference Proceedings. The discussion included here is specific to the data presented in the following sections and is not intended to be more than a summary.

The x-rays dispersion behavior of LSMs can be modeled from two viewpoints. One corresponds to the approach taken in the analysis of x-rays diffraction from crystal-scattering theory. The other follows directly from optical dispersion theory as applied to various types of interference structures. In this section, these two treatments are separately considered with reference to the work of Saxena and Schoenborn (15) and of Spiller (12) (optical dispersion theory), and of Underwood and Barbee (26, 27).

A LSM is made up of two materials, A and B, arranged alternately in layers of thickness  $d_A$  and  $d_B$ , respectively. The structure is thus periodic in the direction perpendicular to the planes, with a period  $d = d_A + d_B$ . x-rays of wavelength  $\lambda$ , incident at a glancing angle  $\theta$  on the planes, will be scattered by each layer of atoms. At the Bragg angles  $\theta_n$ , given by the relation

$$n\lambda = 2d \sin \theta_n \quad (1)$$

the scattered waves will add in phase and the total scattered amplitude will reach a maximum. The positive integer  $n$  represents the order of the Bragg "reflection."

Computation of the intensities of the Bragg reflections for an LSM requires the solution of Maxwell's equations in a material having a periodically varying dielectric constant. The problem is exactly analogous to the computation of Bragg reflection intensities from natural crystals, and either of two theoretical approaches may be adopted. In the kinematical theory, the scattering from each volume element is treated as being independent of that from the other volume elements. This theory neglects the details of the wave interactions within the structure, in particular the progressive reduction in amplitude of the forward wave as it travels into the structure and is partially reflected by successive planes (extinction). In the dynamical theory, all wave interactions are taken into account. The dynamical theory is customarily used in the study of the x-rays diffraction from large perfect crystals, while the kinematical theory is more appropriate to the study of thin crystals or "mosaic" crystals which can be thought of as being composed of large numbers of small crystallites whose orientations differ slightly, in a random fashion, from the mean of the crystalline planes examined.

The LSMs are essentially "perfect" from a crystallographic point of view. Although the fabrication pro-

cess may introduce variation in layer thickness, these errors are not equivalent to the mosaicity of a natural crystal. It is, therefore, more appropriate to use a dynamical theory to compute their properties, although a kinematical approximation suffices if an LSM is of low diffracting power.

### A. Scattering Theory

It has been shown by Saxena and Schoenborn (16) that the diffracting power of an LSM, from scattering theory, with  $d_A = d_B$  and sharp interfaces between layers is given by:

$$\frac{I}{I_0} = \frac{4}{\pi^2} \frac{N^2 d^4}{n} (f_A - f_B)^2 \quad (2)$$

in the kinematic approximation where  $N$  is the number of planes,  $d$  the period,  $n$  the order of the Bragg reflection, and  $f_A$  and  $f_B$  the atomic form factors for the layers A and B. In the dynamic range this becomes:

$$\frac{I}{I_0} = \tanh^2 A \quad (3)$$

where  $A = \frac{2}{\pi} \frac{Nd^2}{n} (f_A - f_B)$ . Note that the diffracted intensity is proportional to  $N^2 d^4$  in the kinematic range.

Also, in the kinematic regime the peak width of the Bragg peaks is defined by the number of reflecting planes in a manner directly analogous to the line width dependence on the number of grooves in an optical grating. Analyses of this diffraction effect for structures such as represented by LSMs (28) yields the relationship (Scherrer equation) between full width at half maximum for a Bragg peak,  $\Delta\theta_{1/2}$ , and the crystal thickness  $D = Nd$  given as

$$\Delta\theta_{1/2} = \frac{0.888\lambda}{Nd \cos \theta_n} \quad (4)$$

where  $\theta_n$  is the Bragg angle of the  $n^{\text{th}}$  order reflection. Note that dynamic calculations yield  $\Delta\theta_{1/2}$  value in agreement with this relationship in the kinematic regime.

### B. Dynamical Optical Dispersion Theory Including Absorption (DOTD)

When the incoherent absorption in the layer material is taken into account, the dynamic theory becomes difficult to treat analytically. It is therefore better to adopt a computational approach. The approach adopted is analogous to those used in the computation of properties of multilayer dielectric filters for the optical region of the spectrum. The layer material is characterized by a complex index of refraction

$$\mu = 1 - \delta - i\beta \quad (5)$$

$\delta$ , the real part of the refractive index,  $\mu$ , is related to  $f$

$$\delta = \frac{\lambda^2}{2\pi} N [(f_0 + \Delta f')^2 + \Delta f''^2]^{1/2} r_e \quad (6)$$

where  $N$  is the atomic concentration,  $r_e$  the classical radius of electron,  $f_0$  the atomic form factor and  $\Delta f'$ ,  $\Delta f''$  the anomalous dispersion coefficients while  $\beta$  is related to the linear absorption coefficient  $\mu_a$  of the material by

$$\beta = \frac{\lambda}{4\pi} \mu_a \quad (7)$$

The method used is based on a treatment of x-ray interference by a few contaminant layers on the surface of a glancing incidence x-ray mirror. However, approximations made by considering  $\theta$ ,  $\delta$ , and  $\beta$  to be small and, furthermore, considering only the  $\sigma$  component of polarization limit this theory and modifications are required to treat more general cases. The theory, together with the required modifications, is given in the article in this volume by Underwood and Barbee (27, 28).

### C. Interfacial Roughness

In the calculations described thus far it has been assumed that the interfaces between layers are ideal, smooth and fully specularly reflecting. If the surface is not smooth a fraction of the radiation is not specularly reflected and the diffraction efficiency of the LSMs is reduced. Simple theory (29, 30, 31) gives the reduction in reflectivity for a single film as a function  $\theta$ , the angle of incidence, of the x-rays as:

$$I/I_0 = I/I_0|_{\text{Ideal}} \exp[-4\pi \frac{\sin\theta}{\lambda} \Delta Z]^2 \quad (8)$$

where  $I/I_0|_{\text{Ideal}}$  is the reflectivity calculated for ideal interfaces,  $\lambda$  the wavelength and  $\Delta Z$  a surface roughness parameter. Rearrangement of eq. (1) and substitution in eq. (8) yields:

$$\frac{I}{I_0} = \frac{I}{I_0}|_{\text{Ideal}} \exp[-(2\pi n \frac{\Delta Z}{d})^2] \quad (9)$$

where  $n$  is the order of Bragg reflection and  $d$  the period of the LSM. This approach allows analysis of the surface roughness parameter,  $\Delta Z$ , if the diffraction efficiency of many orders of Bragg reflections are known and can be compared to model calculations. All calculations against which direct comparisons are made in this paper used the Dynamic Optical Dispersion Theory (DODT) approach, except where noted. Also, except where noted, all calculations are for unpolarized incident radiation. A computational program developed by J. Underwood (27, 28) was used with values of  $\delta$  and  $\beta$  taken from the literature or provided by Ping Lee and B. Henke (32). The value of  $\delta$  and  $\beta$  from the literature have given the largest uncertainty in the modeling efforts, particularly for photon energies lower than approximately 1.5 keV.

### D. Refractive Index Correction

The Bragg relationship presented in equation (1) ignored the effects of refraction on the position of the Bragg reflections. This refraction shift can be sizable and represents a method for determining the optical constants as a function of photon energy. These data can then both be compared with literature values for  $\delta$  and  $\beta$  and used in modeling calculations.

A straight forward analysis (33) yields a relationship between observed Bragg angle  $\theta$ , refractive index  $\mu$ , and the  $d$  spacing and is given as:

$$n\lambda = 2d \sin\theta \left[ 1 + \frac{(\mu+1)(\mu-1)}{\sin^2\theta} \right]^{1/2} \quad (10)$$

$\delta$  for photon energies greater than 1000 eV is typically less than  $10^{-4}$ . For small  $\delta$ , equation (8) can be approximated as:

$$n\lambda = 2d \sin\theta \left[ 1 - \frac{\delta}{\sin^2\theta} \right] \quad (11)$$

which can be used at the higher photon energies. The value of  $\delta$  for a given material is determined from the measured Bragg angle and the true period of the material,  $d$ .

It is important to note that the Bragg angle used in these calculations of  $\delta$  is not that corresponding to the peak diffracted intensity. This results from the effect of absorption on the diffracted intensity on the high angle side of the Bragg peak. The intensity in this region is markedly attenuated with the result that the Bragg peak is asymmetric. The position of the maximum in diffracted intensity falls at a slightly smaller value of  $\theta$  than the maximum intensity when absorption is ignored. An excellent approximation to the position of the Bragg peak is given by the center angle at half height diffracted intensity. This value of  $\theta$  is the one used in calculating the values of  $\delta$  from the position of the Bragg peaks in this work.

It will be seen later that the composite refractive indices for the V/C-LSM determined by this method are in good accord with the predictions of Ping Lee and

Henke (32). It is also demonstrated that these samples allow the refractive indices to be determined over a wide range of wave lengths using the same samples.

### III. LSM SYNTHESIS

The LSM preparation technique used in this work was previously developed under the sponsorship of the NSF-MRL program as part of the activities of the Center for Materials Research at Stanford University by Dr. T. W. Barbee, Jr. This process, as will be seen, represents a step on the developing path whose end can be termed molecular or atomic engineering. It has been applied to a wide variety of combinations of elements, many of which are specific to x-ray dispersion element devices.

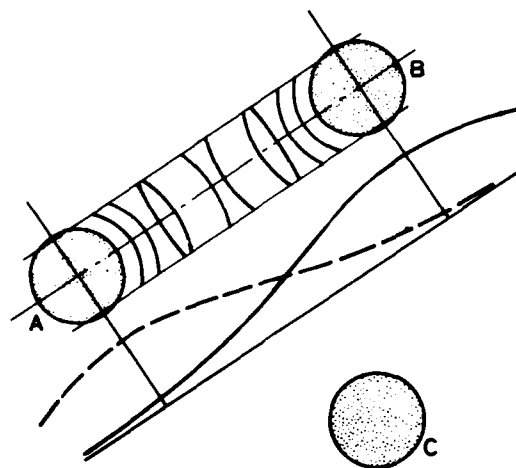


Fig. 1. Schematic diagram of a triangular array of magnetron sputter deposition sources. When the deposition profiles overlap alloy films may be formed. When the sources are sufficiently separated, the deposition profiles not overlapping, layered structures can be formed on moving substrates.

In contrast to the majority of work reported, this process uses fixed magnetron sputtering sources and moving substrates; other processes have used fixed thermal sources and fixed substrates with moving shutters. The system is shown schematically in Fig. 1. Note that all sources (A,B,C) are mounted on the same radius and that the substrate table (below the sources) rotates about the center of this mounting circle. Sources are excited using either dc or rf power and substrates are allowed to thermally float, reaching temperatures of approximately 50°C during a long (>2 hr) deposition run. In the following a more detailed description of this process is given.

Sputter deposition is a complex process into which many parameters intrinsic to vapor deposition enter. In addition, there are many extrinsic parameters associated with the particular apparatus and system geometry which must be considered. These are listed in Table 1. The effects of these parameters are considered in a general manner elsewhere (34-38) and the reader is referred there for a more complete discussion. Items 3, 4, (5, & 7), 8, and 9 are briefly considered in the following.

Also, of importance is the type of sputter source used in the deposition apparatus. Several types are currently available that can be broadly classified as standard and enhanced and are listed in Table 1 along with a simple set of comments on their specific characteristics. The most important information in the table is that it is possible, using magnetron sources, to decouple the sputter plasma from the sample minimizing the effects of high energy ion bombardment and secondary electron effects. Also, the large deposition rates

Table 1. Important Parameters in Sputter Source Vapor Deposition

1. The large atomic quench rate characteristic of vapor deposition.
2. Both surface and bulk atomic motion kinetics - primarily controlled by substrate temperature.
3. The energy distribution of the incident adatoms.
4. The substrate surface morphology.
5. The effects of deposition surface (substrate or deposited film)-adatom atomic interactions.
6. The ambient atmosphere in the experimental apparatus.
7. The effects of the adatom condensation energy.
8. Vapor source-deposition surface interactions.
9. The geometry of the vapor source-substrate configuration.

Table 2. Sputter Sources Characteristics

- I. Standard diodes (R. F., D.C.)
  - A. Rate Low
  - B. Large fraction of power deposited into substrates
  - C. Radiation damage high
- II. Enhanced sources
  - A. Magnetron (R.F., D.C.)
    1. Rate large
    2. Source isolated from substrate. Minimum plasma energy deposited in sample.
    3. Radiation damage minimized
    4. Can be scaled up
  - B. Triode supported (R.F., D.C.)
    1. Rate large
    2. Plasma interaction with substrate large
    3. Radiation damage large
    4. Can be scaled up?

available using magnetron sources, generally an order of magnitude higher than those characteristic of standard diodes, facilitate the synthesis of high quality LSMs.

In the apparatus used in this work magnetron sources (A, B, C of Fig.1) are arranged so that their deposition profiles do not overlap. Deposition onto uniformly moving substrates mounted on a table beneath the substrates at a working distance of 7.5 cm results in the synthesis of layered structures in which both composition and structure can be systematically varied normal to the deposition surface.

The magnetron sources used are 3"-diameter planar circular configurations. The characteristics of magnetron sources are well documented in the literature, and only those factors important to this application are considered here. Magnetron sources have a magnet structure behind the sputter source plate supporting a fringing field that produces a trap for the secondary electrons important in the argon sputter gas ionization. These electrons are trapped at the target surface, thereby trapping the plasma and increasing the plasma density at the target surface. This trapping mechanism is important as it minimizes the interaction of the deposition surface with the sputtering plasma as well as increasing the deposition rates by approximately an order of magnitude.

The increased sputtering rate results in synthesis of multilayer structures in short times of an engineering scale. A typical run will take no longer than

2 hr. Therefore, control requirements are for stability for a limited time, making synthesis an easier proposition. More importantly, the decoupling of the sputtering plasma from the deposition surface increases the ability to form continuous well-defined layers on the Angstrom scale. In standard sputtering diodes, strong coupling of the plasma to the deposition surface results in an ion bombardment mixing of the constituents that can extend several nanometers into the sample. This degrades the sharpness of the interfaces between layers and, if the layers are thin enough, decreases the composition fluctuation. Such characteristics may be advantageous at large layer thicknesses where interface width will strongly damp the intensities of higher-order Bragg reflections, though for thin layers, this phenomena destroys the layers and results in a homogeneous sample when the layers are sufficiently thin. The nature of the deposits is additionally affected by the sputtered adatom energy, though this is not well documented. The adatoms or depositing atoms have a mean kinetic energy of approximately 8 eV and a tail extending to 80 eV. This can cause interfacial broadening as well as reactions at interfaces where it would not normally be expected.

In addition, substrate rotation results in moving the substrates beneath the sources so that adatom deposition occurs at many angles of incidence. This minimizes the effects of substrate roughness as shadowing is minimized. The basic gain is that substrate quality does not deteriorate and that layering quality is maintained or improved through hundreds of layers.

Many different types of substrates have been investigated, with the most consistent results achieved on single crystal silicon (100) and (111) orientation wafers. Preparation of these materials is done using the technology typical of integrated circuit laboratories. I note here that cleaved mica is also an excellent substrate material yielding results as good as the best silicon substrates. In addition, float glass can be used with success if the quality is high. In some cases very high quality results are obtained with plastic film substrates. In addition, preliminary observations from LSMs deposited in mechanically prepared glass surfaces indicate very high reflectivities. In all cases the area of the sample which is usable is a 2 cm x 7.5 cm rectangular area.

#### IV. X-RAY DISPERSION BEHAVIOR OF LSM'S

Three specific material combinations will be considered in this section, tungsten/carbon, vanadium/carbon and titanium/carbon. The data discussed in the following was gathered in many laboratories by several investigators. These include L. Koppel (L.L.N.L.), G. Stradling (L.L.N.L.), B. Henke and his collaborators (U. of Hawaii), J. Gilfrich and D. Nagel (NRL), T. Barbee (Stanford University), and W. Warburton and T. Barbee, et al. (SSRL).

The techniques used were those typical of x-ray diffraction analysis using standard diffractometry. In some cases white radiation was incident on the sample which was used as a spectroscopic element, the diffracted radiation being analyzed using energy dispersive techniques. In other cases characteristic x-ray emission lines were used with standard detectors, including flow proportional and scintillation counters. At SSRL an apparatus designed to do glancing angle diffractometry by W. Warburton was used and allowed data to be collected from Bragg angles of approximately  $5 \times 10^{-3}$  radians.

##### A. Tungsten/Carbon (W/C)-LSM

The tungsten/carbon system has been extensively studied due to the high electron density fluctuation inherent to this material combination and, hence, the high scattering power per tungsten/carbon layer pair. In addition, this system is stable due to the refractory character of the components and the equilibrium

phase diagram which shows that the stable equilibrium is between tungsten carbide (WC) and carbon at temperatures up to  $\sim 2800^\circ\text{C}$ . In this section the results of a series of experiments designed to provide information concerning parameters important to the performance of LSM as dispersion elements are presented.

Diffraction spectra from a W/C-LSM (78-204;  $t_w = 11.3 \text{ \AA}$ ;  $N_w = 62$ ) deposited on (100) orientation single crystal silicon are shown in Figure 2. These spectra were taken using the Bremsstrahlung radiation from Al or Ti anodes using the LSM as a spectrographic element. The energy of the diffracted radiation varied as the Bragg angle was varied. Peak reflectivity and energy resolution for 9690 eV photons observed are 46% and 295 volts respectively. The drop in reflectivity above 10000 eV is the result of the absorption jump at the tungsten  $L_{III}$  edge ( $\sim 10300 \text{ eV}$ ). The fractional change in reflectivity at this edge is in agreement with calculation. These reflectivities are approximately 65% of those predicted by model calculations. This is believed to be the result of interfacial roughness between the constituent layers as will be demonstrated later.

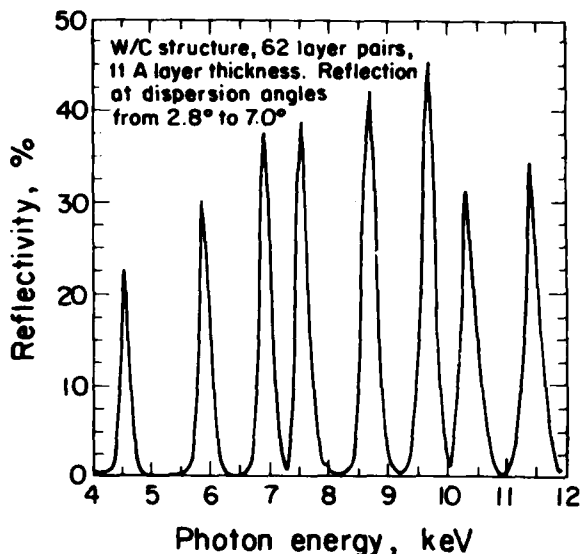


Fig. 2. X-ray dispersion response of a tungsten/carbon LSM ( $d = 22.6 \text{ \AA}$ ,  $t_w = 11.34 \text{ \AA}$ ,  $N_w = 62$ , C-Top) deposited on (100) orientation single crystal silicon is shown as a function of the energy of the diffracted radiation.

The energy resolutions ( $E/\delta E$ ) shown in Figure 2 are all of the order of 35. These are somewhat less than expected from theory and from examination of the diffracting behavior using  $\text{Cu K}\alpha$  ( $\lambda = 1.5418 \text{ \AA}$ ) radiation. This discrepancy is believed to be the result of the convolution of incident spectrum with the diffracting characteristics of the LSM.

This sample (78-204) is part of a set of samples in which the period of the LSMs was held constant at approximately  $21 \text{ \AA}$  and the number of diffracting planes varied so as to explore the transition from the kinematic to dynamic regimes of diffraction response. These samples are described in Table 3 (78-206, 78-204, 78-207, 78-208, 78-209). Peak intensities in first order for  $\text{Cu K}\alpha$  radiation were measured using a standard powder diffractometer equipped with a diffracted beam monochromator. These observed peak reflectivities are plotted along with calculated values in Figure 3 as a function of  $N^2 d^4$  where  $N$  is the number of diffracting planes and  $d$  the period of the LSM. It is clear that at small values of  $N^2 d^4$  the reflectivities are directly proportional to  $N^2 d^4$  in agreement with kinematic theory (Eq. 2). For  $N^2 d^4 > 10^{-24}$  the reflectivities saturate

projecting asymptotically to a value less than 1. This is in accord with theory as shown by the two curves with the experimental values being 50 to 60% of that calculated using the DODT.

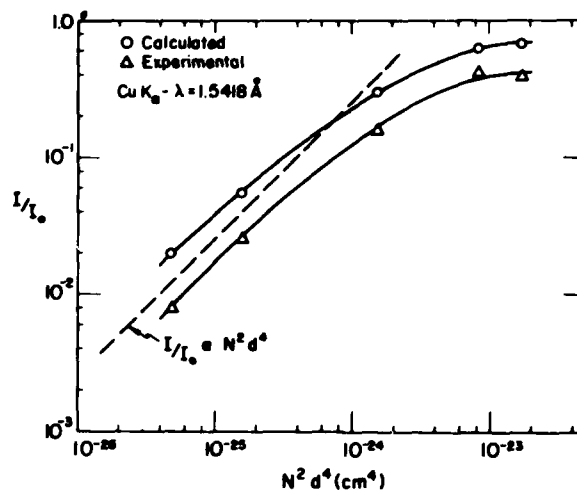


Fig. 3. Calculated and experimentally observed reflectivity in first order for  $\text{Cu K}\alpha$  radiation for W/C-LSM having  $20.3 \text{ \AA} < d < 21.0 \text{ \AA}$  and  $N_w = 6, 11, 31, 62, 106$  are plotted as a function of  $N^2 d^4$ , a parameter for which a linear relationship is expected in the kinematic diffraction regime (see eq. 2).

It is clear from these results that the experimental diffracted intensity is in general accord with theory though systematically lower. Comparison of full width at half maximum ( $\Delta 2\theta_{1/2}$ ) with calculation also yields information on the structure of these LSMs. Experimentally observed values are listed in Table 3 with values calculated using the DODT and the Scherrer equation (Eq. 4) and the tabulated values of  $d$  and  $N_w$ , the number of tungsten layers. Note that the number of diffracting planes of eq. (4),  $N$ , is given by:

$$N = N_w - 1$$

It is clear from Table 3 that the agreement between the DODT calculations and experiment is excellent. In addition, in the kinematic domain, agreement between experiment and the values of  $\Delta 2\theta_{1/2}$  calculated using the Scherrer equation is also good. These results indicate that the LSM structures are highly perfect with angular resolutions  $\Delta 2\theta_{1/2}$  in agreement with theory.

The conclusions to be drawn from this data are that the resolutions are in accord with theory demonstrating that the theoretically predicted number of planes are active in the diffraction process. Also, the peak reflectivity in first order is substantially less ( $\sim 0.6$ ) than that predicted by theory. These are exactly the characteristics attributable to interfacial roughness which is considered in more detail later in this paper.

The data presented thus far are limited in that only one photon energy has been used. In Figure 4 peak reflectivity in first order is plotted as a function of photon energy over the energy range (277 eV to 15000 eV) for W/C-LSMs (78-204,  $d=22.6 \text{ \AA}$ ; 79-086,  $d=52 \text{ \AA}$ ; 79-091,  $d=58 \text{ \AA}$ ). The reflectivities observed for the larger  $d$  spacing LSMs (79-086, 79-091) are close to values calculated using the DODT both in peak reflectivity and in angular resolution. I note that Ping Lee has calculated the reflectivity in first order ( $\sim 13\%$ ) for W/C-LSMs,  $2d=100 \text{ \AA}$  for C-K ( $E=277 \text{ eV}$ ). His results are in good accord with the reflectivity ( $\sim 12\%$ ) shown in this figure for similar samples. Also calculations indicate that the reflectivities over the full spectral range for samples 79-086 and 79-091 are very close to theoretical values. The smaller period sample (78-204)

Table 3. Full width at half maximum ( $\Delta 2\theta_{1/2}$ ) of first order reflections of Cu  $K\alpha$  ( $\lambda = 1.5418 \text{ \AA}$ ) radiation from W/C-LSMs calculated using DODT- $\Delta 2\theta_{1/2}(T)$ , the Scherrer equation- $\Delta 2\theta_{1/2}(S)$ , and experimentally observed  $\Delta 2\theta_{1/2}(E)$  are compared.

Sample	$N_w$	$d(\text{\AA})$	$t_w(\text{\AA})$	Experiment			DODT		Scherrer	
				$\Delta 2\theta_{1/2}(E)$	$\Delta 2\theta_{1/2}(T)$	$\Delta 2\theta_{1/2}(E)/\Delta 2\theta_{1/2}(T)$	$\Delta 2\theta_{1/2}(S)$	$\Delta 2\theta_{1/2}(E)/\Delta 2\theta_{1/2}(S)$		
78-206	102	20.3	10.15	0.075	0.76	0.99	0.038	1.96		
78-204	62	22.6	11.3	0.085	0.086	0.99	0.057	1.49		
78-207	31	20.3	10.15	0.133	0.137	0.97	0.129	1.03		
78-208	11	20.3	10.14	0.355	0.356	0.997	0.380	0.95		
78-209	6	21.0	10.15	0.69	0.630	1.095	0.74	0.96		
78-211	11	24.7	10.0	0.305	--	--	0.318	0.99		
78-212	11	33.8	10.0	0.23	--	--	0.232	0.99		
78-213	11	59.9	10.0	0.135	--	--	0.131	1.03		

is, as already discussed, somewhat less than theory in reflectivity. It is also important to note that the jumps in reflectivity at the  $W_M$  and  $W_{LIII}$  edges are in agreement with theory. These values of reflectivity can be easily converted to integrated reflectivity as the observed angular widths of the Bragg diffraction peaks are in excellent agreement with theory though the peak reflectivities are somewhat less than expected.

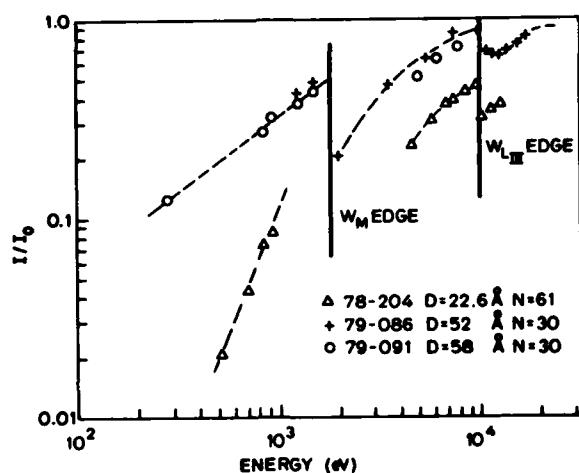


Fig. 4. Peak reflectivity in first order for W/C-LSM 78-20.  $D = 22.6 \text{ \AA}$ ,  $N_w = 62$ ; 79-086,  $D = 52 \text{ \AA}$ ,  $N_w = 31$ , and 79-091,  $D = 58 \text{ \AA}$ ,  $N_w = 31$  are presented for photon energies of 277 eV to 15000 eV. These data were collected by B. L. Henke and his students at the University of Hawaii, L. Koppel at L.L.N.L., Jim Underwood at Stanford University, and Troy W. Barbee Jr. at Stanford University and are considered minimum values.

Integrated reflectivities (39) for a series of W/C-LSMs having periods of 21  $\text{\AA}$  ( $2d=42 \text{ \AA}$ ), 30.5  $\text{\AA}$  ( $2d=61 \text{ \AA}$ ) and 60  $\text{\AA}$ , ( $2d=120 \text{ \AA}$ ) are shown in Figure 5 for radiation in the wavelength range 7 to 13  $\text{\AA}$ . These samples were synthesized so that the maximum diffracting power was expected. It is important to note that these results semiquantitatively agree with theory.

The comparison of experiment to theory shown thus far has only been parametric consisting of peak reflectivities and peak widths ( $\Delta 2\theta_{1/2}$ ). A comparison between the observed diffraction spectrum using Cu  $K\alpha$  radiation over the angular range  $0 < 2\theta < 3.0$  degrees and calculations using DODT is shown in Figure 6 for sample 80-037, a W/C-LSM. The calculation was based on design values for the sample period and the relative thicknesses of the carbon and tungsten component layers. The difference in peak positions is due to the fact that the sample period was 53  $\text{\AA}$  while the design period was 52  $\text{\AA}$ . Excellent agreement with the theory is shown, for the critical angle and the secondary Fresnel maxima. Note the experimentally observed peak reflectivity is 55 to 60% while the calculated value is 66%.

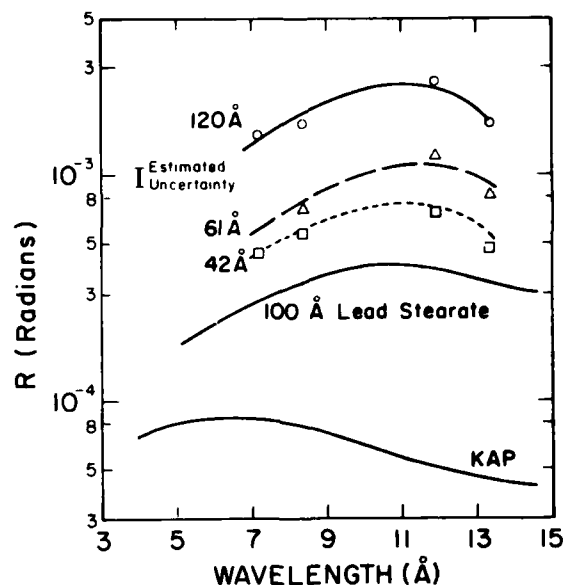


Fig. 5. Observed (39) integrated reflectivity,  $R$ , for W/C-LSMs having periods,  $d$ , of 21  $\text{\AA}$  ( $2d = 42 \text{ \AA}$ ), 30.5  $\text{\AA}$  ( $2d = 61 \text{ \AA}$ ) and 60  $\text{\AA}$  ( $2d = 120 \text{ \AA}$ ) is shown as a function of the wavelength of the incident radiation. The reflectivities are approximately half that predicted using DODT.

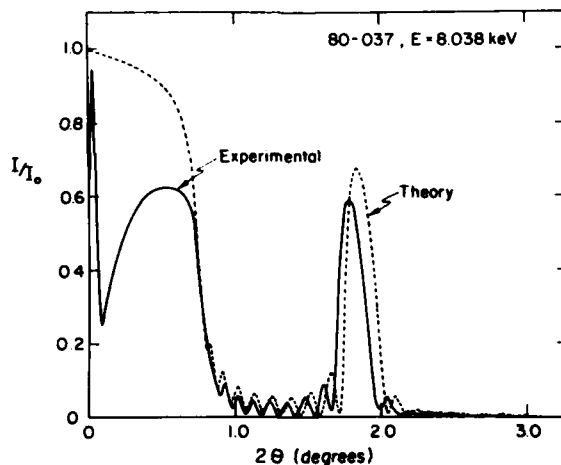


Fig. 6. Experimental and theoretical diffraction curves of Cu  $K\alpha$  from sample 80-037 ( $d = 52.0 \text{ \AA}$ ,  $t_w = 17.34 \text{ \AA}$ ,  $N_w = 11$ , w-Top) are shown and compared. The data were taken using a standard powder diffractometer equipped with a diffracted beam monochromator.

TABLE 4. Peak reflectivity in first order, experimental  $\Delta 2\theta_{1/2}$  and theoretical  $\Delta 2\theta_{1/2}$ , for W/C-LSM of varying  $d$  designed to have constant reflectivity for Cu  $K_{\alpha}$ .

$d(\text{\AA})$	$N_w$	$I/I_0(\%)$	$\Delta 2\theta_{1/2}(E)$ (degrees)	$\Delta 2\theta_{1/2}(T)$ (degrees)
80-037	53.0	11 55 to 60	0.20	0.19
80-038	30.9	30 44 to 48	0.125	0.126
80-034	20.3	69 35 to 45	0.079	0.078
80-040	15.4	123 9 to 11	0.0625	0.06
80-041	10.0	274 0.1	0.05	0.04
80-042	(5)	1094 0	--	--

The W/C-LSM 80-037 is one of a series of six samples designed to investigate the effects of interfacial roughness, the characteristics of which are given in Table 4. The samples were all designed to have reflectivities in first order of 65 to 68% for periods of 53 Å, 30.9 Å, 20.3 Å, 15.4 Å, 10 Å and 5 Å by increasing the number of diffracting planes as the period decreased, as shown in Table 4. Again note that the  $\Delta 2\theta_{1/2}$  experimentally observed is in excellent agreement with values calculated using DODT.

The observed values of peak reflectivity are plotted as a function sample period in Figure 7 with the solid line approximating the observed behavior. The circles in Figure 3 are points calculated using eq. (9) with the experimentally determined values of  $d$ , and the peak reflectivities predicted using DODT assuming an interfacial roughness  $\Delta Z$ , of 3.15 Å. The agreement is semiquantitative, with the dependence of peak reflection on the period  $d$  being clearly reproduced. This is taken as clear evidence that the interfacial roughness between constituent layers is the characteristic of these LSMs which is limiting the diffracting behavior. Values of approximately 3 Å have been reported by Spiller (12) for tungsten-rhenium/carbon LSM structures.

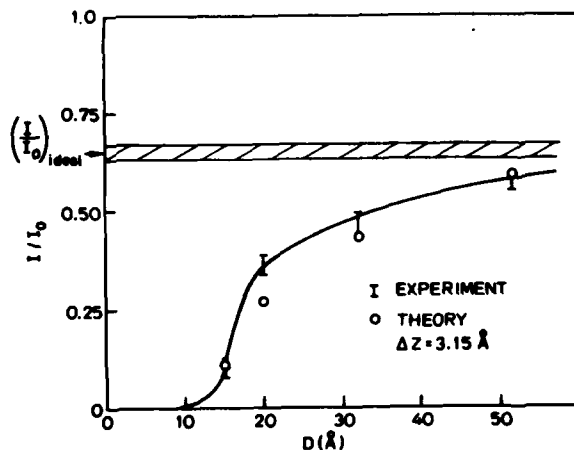


Fig. 7. Observed peak reflectivity in first order is plotted as a function of  $d(\text{\AA})$  for W/C-LSM designed to have constant reflectivity in first order and compared to the predictions of theory in which the effect of a surface roughness ( $\Delta Z = 3.15 \text{\AA}$ ) is included.

In closing this section on W/C-LSMs I will present two recent experimental results obtained at the Stanford Synchrotron Radiation Laboratory. The importance of these results is that they were obtained with tunable, low intrinsic beam divergence radiation using an apparatus that allowed excellent alignment. This apparatus allows data to be taken at angles greater than  $0.1^\circ$  in  $\theta$  and scans which span the angular range from the region of total specular reflection to higher angles where Bragg reflections are observed. In the following only data from regions about the first order Bragg reflections will be presented and compared to theory.

Results obtained using sample 80-038 (W/C-LSM, see Table 4) and photons of energy  $E=5478 \text{ eV}$  are shown in Figure 8 and compared to DODT calculations.  $\Delta 2\theta_{1/2}$  is observed to be in excellent agreement when experiment and calculation are compared. The offset between experiment and DODT calculations is believed to be due to a small error in the period  $d$  or uncertainties in the values of  $\delta$  and  $\beta$ . Also, the predicted peak reflectivity is 62% while the observed value is 54%. This value yields an effective interface roughness  $\Delta Z$  of approximately 1.8 Å compared to the 3.15 Å value seen in Figure 7. The implication of this comparison is that the laboratory data (Cu  $K_{\alpha}$ ) yields an upper limit to the interface roughness parameter as the reflectivity appears lower;  $I/I_0|_E = 44$  to 48%, vs DODT = 67%; for laboratory experiments;  $I/I_0|_E = 54\%$  vs DODT = 62% for SSRL experiments. This is supported by results on other samples of Ti/C, Nb/C, V/C-LSMs and indicate that the alignment and low beam divergence possible with synchrotron sources are advantageous in the characterization of LSMs.

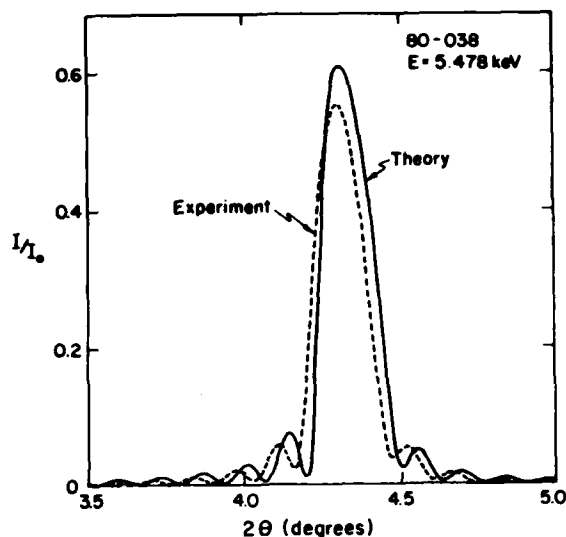


Fig. 8. The observed first order Bragg reflection for a W/C-LSM (80-038,  $d = 30.9 \text{\AA}$ ,  $t_w = 10.3 \text{\AA}$ ,  $N_w = 30$ ) for 5478 eV radiation is compared to theory. The experimental data were taken at the Stanford Synchrotron Radiation Laboratory.

The diffraction behavior of sample 81-117, a W/C-LSM, having a period of 38.5 Å ( $N_w=50$ ,  $t_w=12.8 \text{\AA}$ ,  $t_c=25.7 \text{\AA}$ ) using 10000 eV radiation is compared to DODT calculations in Figure 9. The offset in the peak reflectivity positions is approximately  $0.005^\circ$  and is due to an uncertainty with the values of  $\delta$  and  $\beta$  as well as a possible error in the period. Note that the secondary Fresnel maxima are not clearly defined in the experimental curve due to the inherent beam divergence of  $\sim 1 \times 10^{-4}$  radians in this experiment. The experimentally observed peak reflectivity is 78% while DODT predicts 82%. Note that the W-LIII edge lies at approximately 10300 eV so that absorption effects are minimized at 10000 eV. Interfacial roughness is calculated to be approximately 1.4 Å for this sample. This indicates that very high quality LSM structures are synthesizable with essentially atomically smooth interfaces between the constituent layers.

In this section it has been demonstrated that high diffraction efficiency W/C-LSMs having periods above 15 Å can be synthesized and have x-ray dispersion characteristics in accord with theory. Interfacial roughness of the order of 1.4 to 3.15 Å is inferred from experiment demonstrating that near atomic level smoothness at these interfaces can be achieved.

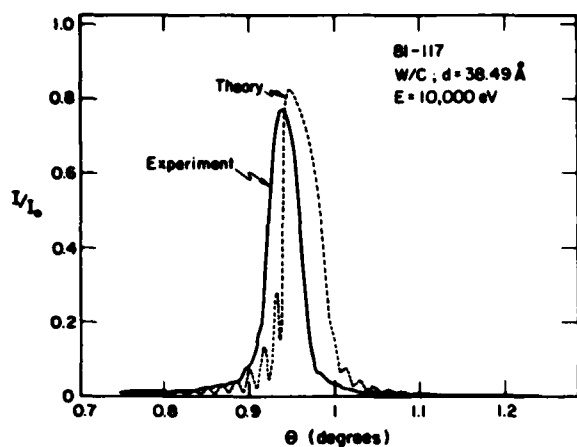


Fig. 9. The observed first order Bragg reflection for a W/C-LSM (81-117,  $d = 38.5 \text{ \AA}$ ,  $t_w = 12.8 \text{ \AA}$ ,  $N_w = 50$ ) for 10000 eV radiation is compared to theory. The experimental results were taken at the Stanford Synchrotron Radiation Laboratory.

Two important comments are made in closing this section. First, these LSM films can be formed on flexible substrates such as mica and polyimide films. Silicon substrates can also be flexed so that an 0.5 meter radii of curvature is achieved over a 7.5 cm distance. Second, these structures are quite stable and samples synthesized in early 1976, though somewhat discolored, still exhibit the x-ray diffraction behavior originally observed. When such samples are heated in inert atmospheres to temperatures of approximately 500°C for 5 to 10 hrs the tungsten layers react with the carbon to form WC which has a density of 15 to 16 gms/cc. The decrease in the carbon layer thickness due to the reaction is not as large as the increase in the thickness of the W(WC) layers during the annealing so that the period of the sample increases. There is no apparent degradation in the diffracting efficiency of the samples, an increase in resolution, and possibly an increase in the perfection of the structures as a result of such annealing.

#### B. Vanadium-Carbon (V/C)-LSM

The x-ray dispersion behavior of a specific vanadium/carbon LSM is considered in this section. This sample (80-177) consists of twenty-one-45 Å thick vanadium layers separated by 100 Å carbon layers deposited onto (100) orientation Si single crystal substrates. Vanadium was the top layer. This period, ( $d = 145 \text{ \AA}$ ), and the vanadium were chosen so that an efficient diffracting element for very soft x-rays could be constructed with absorption effects minimized.

Diffracting behavior over the photon energy range 108 to 13000 eV is discussed. Direct comparison between experiment and DODT calculations are made for data taken above and below the  $V_v$  edge [ $E=5300, 6000 \text{ eV}$ ], for C-K ( $E=277 \text{ eV}$ ) and Be-K ( $E=108 \text{ eV}$ ). Estimates of the interfacial roughness are inferred from the higher order Bragg reflections ( $E=5300, 6000 \text{ eV}$ ). Also, it is shown that the positions of the Bragg reflections in first order allow the value of  $\delta$ , the real part of the refractive index, to be estimated. The measured values are for the composite material and values for the component elements must be unfolded. These composite material values are compared to those derived from classical theory and recent results of Ping Lee and B. Henke (32). DODT calculations exploring the effects of the nature of the top layer and the polarization of the incident light are also presented.

Diffraction scans and DODT calculations for a V/C-LSM (80-177) for radiation of energy 5300 eV and 6000 eV are shown in Figure 10a,b, and 11a,b respectively.

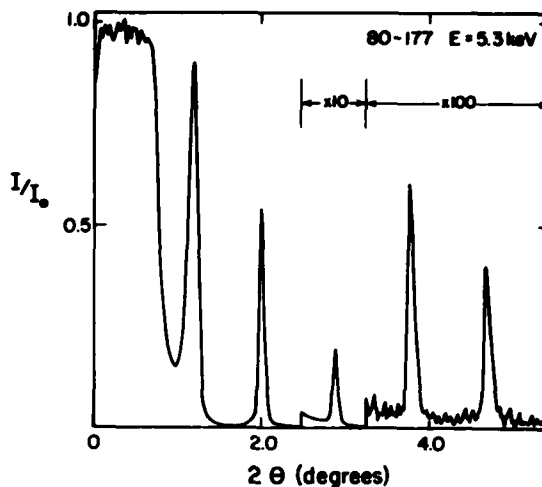


Fig. 10a. Observed diffracting behavior over the angular range 0 to 6 degrees in  $2\theta$  for a V/C-LSM (80-177),  $d = 143.5 \text{ \AA}$ ,  $t_v = 43.5 \text{ \AA}$ ,  $N_v = 21$ ) for 5300 eV radiation is shown.

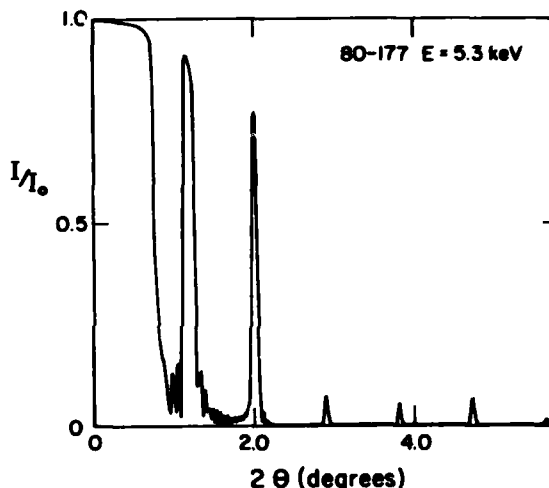


Fig. 10b. Predicted (DODT) diffracting behavior over the angular range 0 to 6° in  $2\theta$  for a V/C-LSM (80-177,  $d = 143.5 \text{ \AA}$ ,  $t_v = 34.5 \text{ \AA}$ ,  $N_v = 21$ ) for 5300 eV radiation is shown.

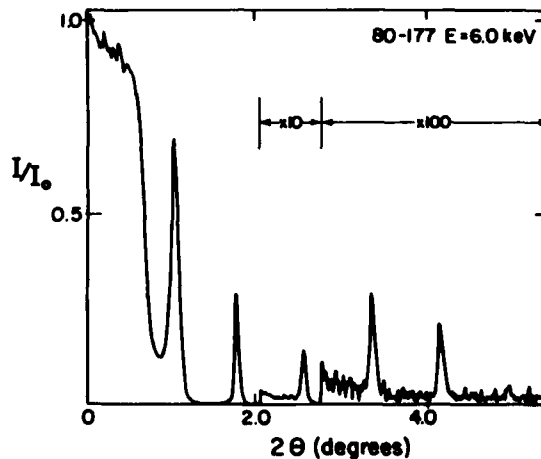


Fig. 11a. Observed diffracting behavior over the angular range 0 to 6° in  $2\theta$  for a V/C-LSM (80-177;  $d = 143.5 \text{ \AA}$ ,  $t_v = 43.5 \text{ \AA}$ ,  $N_v = 21$ ) for 6000 eV radiation is shown.

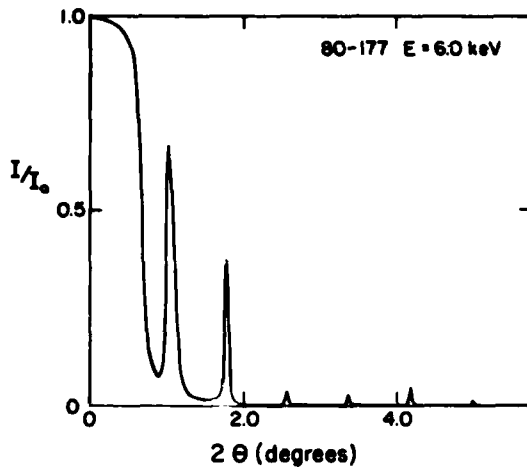


Fig. 11b. Predicted (DODT) diffracting behavior over the angular range 0 to 6° in  $2\theta$  for V/C-LSM (80-177,  $d = 143.5 \text{ \AA}$ ,  $t_v = 43.5 \text{ \AA}$ ,  $N_v = 21$ ) for 6000 eV radiation is shown.

The basic agreement is excellent with respect to the predicted critical angles,  $\theta_c$ , and the peak reflectivities in first order. The predicted values are 93% (5300 eV) and 67% (6000 eV) while experiment yields 88% (5300 eV) and 65% (6000 eV). Observed intensities for 2nd, 3rd, 4th, and 5th order Bragg reflections are all substantially less than predicted.

This disagreement between theory and experiment at the higher orders can be rationalized in terms of an interfacial roughness. In Eq. (3) a relationship between the order of reflection of a sample and the interfacial roughness parameter  $\Delta Z$  was given. Values of  $\Delta Z$  calculated using this equation are listed for photon energies of 5300 eV and 6000 eV as a function of the order of reflection in Table 5. The apparent interfacial roughness is 7.7 Å which is several vanadium interatomic distances. The values of  $\Delta Z$  are in general agreement for all orders of reflection, supporting the analysis, indicating that this simple approach provides a reasonable framework for understanding these results.

Table 5. The interfacial roughness parameter  $\Delta Z$  as a function of the order of reflection for  $E=5300 \text{ eV}$ , 6000 eV (Sample 80-177)

E(eV)	Order of Bragg Reflection				
	n=1	n=2	n=3	n=4	n=5
5300	—	6.8 Å	8.8 Å	8.4 Å	7.8 Å
6000	—	6.0 Å	7.2 Å	8.7 Å	8.0 Å

The behavior at high photon energies is not as strongly affected by absorption as at low energies, the reflectivity under the least favorable conditions at energies just above the vanadium K edge still being of the order of 65%. At low photon energies absorption dominates and it is necessary to consider the effects of the top layer composition. In addition, due to the long wavelengths, Bragg reflection occurs at high enough angles that the polarization of the incident radiation maybe important. These effects are discussed in the following for C-K ( $E=277 \text{ eV}$ ) and  $B_e$ -K ( $E=108 \text{ eV}$ ) radiation diffracted from this V/C-LSM.

DODT calculations using values of  $\beta$  and  $\delta$  provided by Ping Lee and B. Henke for C-K ( $E=277 \text{ eV}$ ) are shown in Figure 12. One curve is for carbon as the top layer and the other for vanadium as the top layer. The effect of the top carbon layer is important as it provides guidance as to the possible effects of contamination layers which will always be present in such deposited films. Such contamination layers are expected to be both oxides of the vanadium as well as carbon containing organic films.

A comparison between experimental results taken by Tester and Henke and these DODT calculations are shown in Figure 13. The predicted reflectivity is approximately 1.5 times the observed value of 30% (above background). In addition the experimental value of  $\Delta\theta_{1/2}$ (FWHM) is approximately 1.5 times the predicted value. It is likely that the disagreement between the experimental value of peak reflectivity and the predicted value is the result of an underestimate of the  $\beta$  values for the component layers, as well as of the scattering power per layer. This is supported by the fact that the integrated reflectivities compare very well.

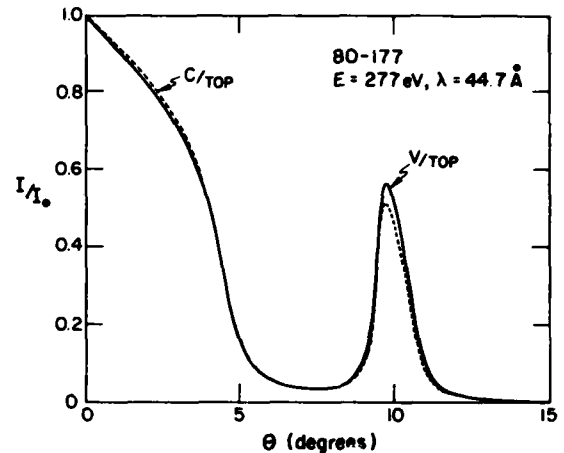


Fig. 12. The predicted diffracting behavior for a V/C-LSM (80-177,  $d = 143.5 \text{ \AA}$ ,  $t_v = 43.5 \text{ \AA}$ ,  $N_v = 21$ ) for C-K ( $\lambda = 44.7 \text{ \AA}$ ) radiation is shown for  $0 < \theta < 15$  degrees. Two cases are compared; (1) a case for which the top layer is vanadium, and (2) a case for which the top layer is carbon.

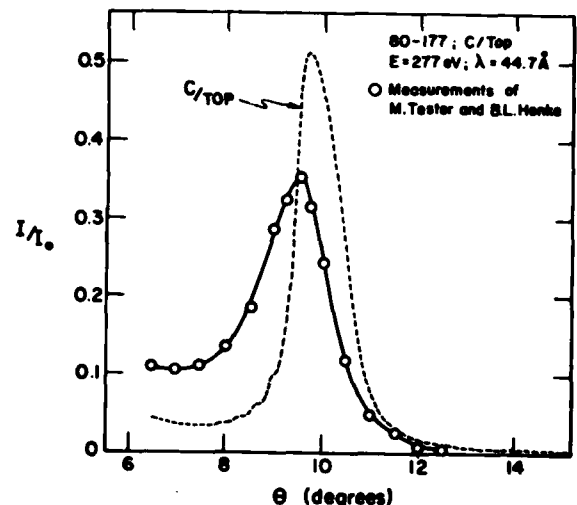


Fig. 13. Experimentally observed diffracting behavior of C-K ( $E = 277 \text{ eV}$ ,  $\lambda = 44.7 \text{ \AA}$ ) radiation from a V/C-LSM (80-177) is compared to theoretical predictions made using values of  $\delta$  and  $\beta$  for the vanadium and carbon developed by Ping Lee and Henke (32).

\* Measurements were also made of the diffracting behavior of  $B_e$ -K ( $E=108 \text{ eV}$ ). The diffracting behavior for  $\sigma$  and  $\pi$  polarized 108 eV radiation calculated using DODT are presented in Figure 14. As the Brewster angle is approached the  $\sigma$  polarization is more strongly diffracted as shown in this figure. There is essentially



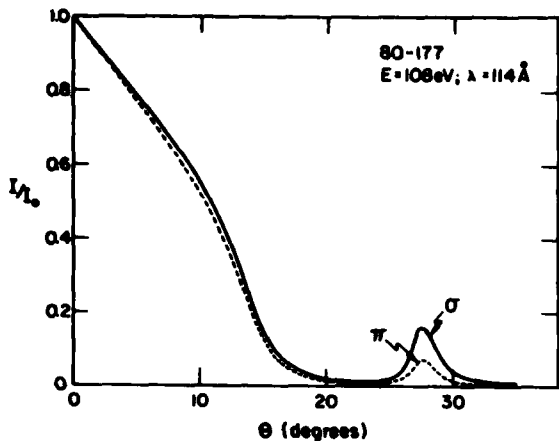


Fig. 14. Predicted diffracting behavior for a V/C-LSM (80-177) for 108 eV ( $\lambda = 114 \text{ \AA}$ ) for  $\pi$  and  $\sigma$  polarized radiation are compared. Note the Bragg reflectivity of the  $\sigma$  polarized radiation is significantly larger than the  $\pi$  polarized as the Bragg angle is a large fraction of the Brewster angle.

no difference between the  $\sigma$  and  $\pi$  polarizations in the specular region of the curve. This is included so that the possible effects of incident light polarization are delineated.

More importantly, the effect of the composition of the top most layer is seen both in the specular reflection regime and at the Bragg peak as shown in Figure 15. The calculations demonstrate that the specular reflection from a LSM having carbon as the top layer is at all angles larger than from a vanadium top layer sample. This is due to the high absorption coefficient for 108 eV radiation of the vanadium which markedly decreases the reflected intensity in the specular regime. Conversely, the vanadium top layer sample exhibits a markedly higher value of peak reflectivity in the first order Bragg peak than the carbon top layer calculation. This is more clearly shown in Figure 16 where experimental data is compared to these calculations. Note that the observed reflectivity lies at an intermediate value between the two calculated curves and that the observed  $\Delta 2\theta_{1/2}$  is again approximately 1.5 times that calculated. The observed peak reflectivity above background is approximately 6.5% and the value calculated for a vanadium top layer structure is approximately 10.5% again a factor of 1.5 larger.

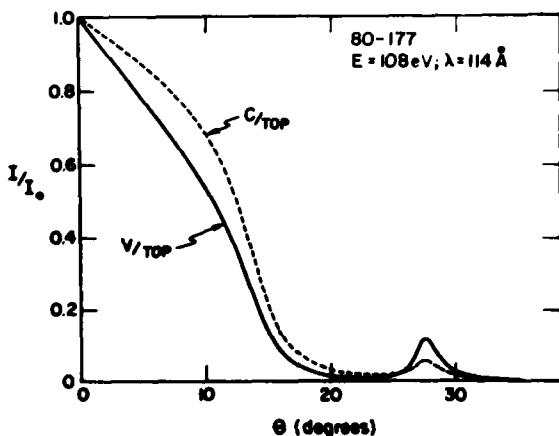


Fig. 15. The predicted behavior (DDDT) for diffraction of unpolarized 108 eV radiation ( $\lambda = 114 \text{ \AA}$ ) from a V/C-LSM (80-177,  $d = 143.5 \text{ \AA}$ ,  $t_v = 43.5 \text{ \AA}$ ,  $N_v = 21$ ) for  $0 < \theta < 3.5$  degrees is shown. Two cases are compared; (1) a case in which the top layer is vanadium, and (2) a case in which the top layer is carbon.

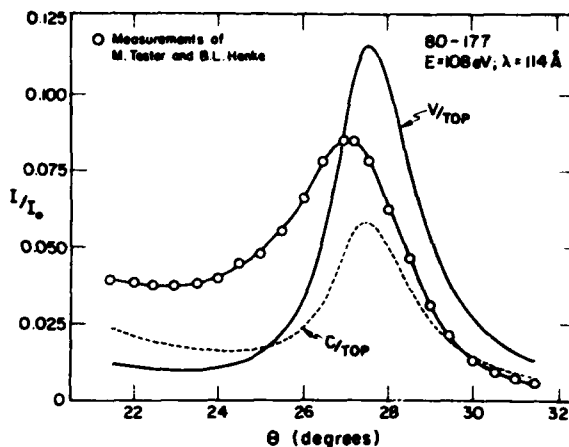


Fig. 16. Observed peak reflectivity in first order is compared with theory for 108 eV radiation ( $\lambda = 114 \text{ \AA}$ ) from a V/C-LSM (80-177,  $d = 143.5 \text{ \AA}$ ,  $t_v = 43.5 \text{ \AA}$ ,  $N_v = 21$ ). Two theoretical cases are presented (1) a sample with a vanadium top layer and (2) a sample with a carbon top layer.

As discussed in the theory section the value of the sample period,  $d$ , calculated using the observed Bragg peaks differs from the actual value of  $d$  as a result of refractive index effects (eqs. 10 and 11). This can lead to substantial error in the determination of the actual period unless higher order reflections are used as the refractive index effect decreases at higher angles. Values of  $d$  calculated from actual peak positions in  $\theta[d(\theta)]$  for five orders of Bragg reflection are shown in Figure 17 for photons of energy 13000, 10000, 6000 and 5300 eV. Also shown are values calculated from the first order position of the Bragg peaks observed for 277, 192, 151 and 108 eV radiation. These values all lie below the horizontal dotted line in the figure. Apparent values for  $d$  [ $d(\Delta 2\theta)$ ] can also be calculated from the value of  $\Delta 2\theta$ , the difference in angular position between adjacent orders of Bragg reflection are also shown and are always larger than the real sample period. They lie above the horizontal dotted

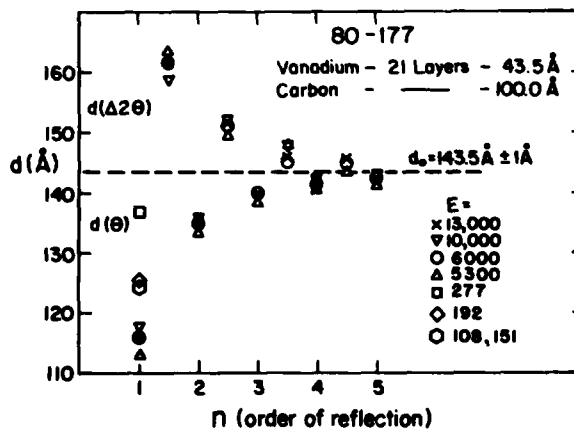


Fig. 17. Values of apparent  $d$  spacing calculated from experimentally observed positions of the Bragg reflections for radiation having energies of 108, 151, 192, 277, 5300, 6000, 10000, and 13000 eV are plotted as a function of the order of reflection. Apparent  $d$  spacings calculated from the differences in the angular positions of adjacent orders of Bragg reflections are also plotted, these points lying midway between the respective orders used in the analysis (the  $d$  values are all larger than the correct value of  $d$  for this sample).

line in this figure. These two types of analysis yield curves asymptotic to the actual period of the sample at high angles or at high orders of Bragg reflection. The horizontal line in this figure represents the actual  $d$  spacing of this V/C-LSM which, from this analysis is  $143.5 \pm 1.0 \text{ \AA}$ .

It is also possible once the value of the sample period is well established, to calculate a value of  $\bar{\delta}$ , the composite value of the real part of the refractive index for a given LSM structure. Values of  $\bar{\delta}$  derived from the positions of first order Bragg reflections observed for photon energies of 108 to 13000 eV for V/C-LSM 80-177 are presented in Table 6. These are compared to predicted values calculated assuming

$$\bar{\delta} = 2.72 \times 10^{-6} \frac{\rho \sum Z}{\sum M} \lambda^2 \quad (12)$$

and

$$\bar{\rho} = \left[ \frac{t_v}{d} \rho_v + \frac{t_c}{d} \rho_c \right] \quad (13)$$

where  $\lambda$  is the wavelength,  $z$  the atomic number,  $M$  the atomic weight,  $\rho_v$  the density of vanadium,  $\rho_c$  the density of carbon,  $t_v$  the thickness of the vanadium layers,  $t_c$  the thickness of the carbon layers and  $d$  the sample period. The values calculated assuming  $Z_v = 23$ ,  $Z_c = 6$ ,  $\rho_v = 5.96 \text{ gms/cc}$ ,  $\rho_c = 2.0 \text{ gms/cc}$ ,  $d = 143.5 \text{ \AA}$  and literature values for the atomic weights for all photon energies are shown in Table 6 as  $\delta_1$  and are all larger than experiment with major disagreement shown for the very low energy radiation, as is expected.

Table 6. The real part of the composite refractive index,  $\bar{\delta}$ , calculated from the experimental positions of the first order reflections of photons  $108 \text{ eV} < E < 13000 \text{ eV}$  from a V/C-LSM ( $d = 143.5 \text{ \AA}$ ,  $t_v = 43.5 \text{ \AA}$ ,  $N_v = 21$ ) are compared to predictions based on simple theory  $\delta_1$  and values calculated using the results of Ping Lee and B. Henke for the values of  $\delta$  and  $\beta$  of carbon and vanadium ( $928 \text{ eV} > E > 108 \text{ eV}$ ).

E(eV)	$\lambda(\text{\AA})$	$\bar{\delta}$ (Theory)			$\bar{\delta}_{\text{exp}}$
		$\delta_{\text{ideal}}$	$\delta_{\text{sum}}$	$\delta_{\text{mix}}$	
13000	0.953	$3.64 \times 10^{-6}$	$3.73 \times 10^{-6}$	$3.64 \times 10^{-6}$	$3.29 \times 10^{-6}$
10000	1.239	$6.15 \times 10^{-6}$	$6.31 \times 10^{-6}$	$6.15 \times 10^{-6}$	$5.08 \times 10^{-6}$
6000	2.066	$1.71 \times 10^{-5}$	$1.76 \times 10^{-5}$	$1.71 \times 10^{-5}$	$1.53 \times 10^{-5}$
5300	2.338	$2.19 \times 10^{-5}$	$2.23 \times 10^{-5}$	$2.19 \times 10^{-5}$	$2.27 \times 10^{-5}$
928	13.33	$7.13 \times 10^{-4}$	$7.21 \times 10^{-4}$	$6.83 \times 10^{-4}$	$7.8 \times 10^{-4}$
277	44.7	$8.01 \times 10^{-3}$	$3.18 \times 10^{-3}$	$3.74 \times 10^{-3}$	$1.21 \times 10^{-3}$
192	64.4	$1.66 \times 10^{-2}$	$9.71 \times 10^{-3}$	$8.99 \times 10^{-3}$	$7.83 \times 10^{-3}$
151	82.1	$2.7 \times 10^{-2}$	$1.58 \times 10^{-2}$	$1.42 \times 10^{-2}$	$1.29 \times 10^{-2}$
108	114.0	$5.21 \times 10^{-2}$	$2.94 \times 10^{-2}$	$2.52 \times 10^{-2}$	$2.45 \times 10^{-2}$

Comparisons of the experimental values and values calculated using the results of Ping Lee and B. Henke (32) for vanadium and carbon for energies of 928 eV or less are also shown.  $\delta_{\text{sum}}$  was calculated on the basis of volume fraction:

$$\bar{\delta}_{\text{sum}}(\lambda) = \frac{t_v}{d} \delta_v(\lambda) + \frac{t_c}{d} \delta_c(\lambda) \quad (14)$$

where  $\delta_v(\lambda)$  and  $\delta_c(\lambda)$  are the values for the elements at a wavelength  $\lambda$ .  $\delta_{\text{mix}}$  is calculated using eq. (12) and eq. (13) assuming effective values of  $Z$  for vanadium and carbon in accord with the calculation of Ping Lee and Henke (32). In general, the values of  $\bar{\delta}_{\text{sum}}$ ,  $\bar{\delta}_{\text{mix}}$  and  $\bar{\delta}_{\text{exp}}$  are in reasonable agreement at all energies with surprisingly good agreement found in the low energy region.

These data are plotted in Figure 18 where  $\bar{\delta}$  is shown as a function of  $\lambda$ , the radiation wavelength. The solid line represents values calculated using eq. (12) and eq. (13) with  $Z_v = 23$  and  $Z_c = 6$  at all wavelengths, the open circles the experimental data, and

the triangles values calculated on the basis of a mixture using values of  $Z$  predicted by Ping Lee and Henke (32). At high energies agreement of experiment with the simple model is acceptable. The largest disagreement is observed for C-K ( $\lambda = 44.7 \text{ \AA}$ ) radiation and remains currently unexplained. Again, acceptable agreement between calculated and experimental values of  $\bar{\delta}$  is shown at low photon energies.

The diffracting behavior of V/C-LSM 80-177 has been discussed and compared to calculation over the photon energy range 108 to 13000 eV. Agreement between experiment and theory has been shown to be good for high photon energies (5300 eV, 6000 eV) and less satisfactory at low energies. The disparity at low photon energies is believed to result from surface contamination and from uncertainties in the values of  $\delta$  and  $\beta$  used in the calculations. In addition it has been shown that these LSM structures allow determination of  $\bar{\delta}$  over a broad energy range using a single sample thereby maintaining the material and sample structure effects constant.

### C. Titanium-Carbon (Ti/C)-LSM

The diffracting behavior of a titanium-carbon (Ti/C)-LSM having a period of  $56.4 \text{ \AA}$  consisting of 70 titanium layers  $26.0 \text{ \AA}$  thick separated by carbon layers  $30.4 \text{ \AA}$  thick is summarized in this section. The data discussed were taken (39) at the Naval Research Laboratory and as part of a program at the Stanford Synchrotron Radiation Laboratory. Experimental values of  $R$ , the integrated reflectivity,  $P$  the peak reflectivity in first order, and angular resolution  $2\theta/\Delta 2\theta$  are summarized in Table 7.

Table 7. Experimental (39) integrated reflectivities ( $R$ ), peak reflectivities in first order ( $P$ ), and angular resolution ( $2\theta/\Delta 2\theta$ ) for a Ti/C-LSM 80-073 ( $d = 56.4 \text{ \AA}$ ) are tabulated and compared to theoretical predictions (DODT).

E(eV)	$\lambda(\text{\AA})$	Experiment			Theory		
		R(Radians)	P(%)	$\theta/\Delta\theta$	R(Radians)	P(%)	$\theta/\Delta\theta$
277	44.7	$1.9 \times 10^{-3}$	10.6	37.0	$3.1 \times 10^{-3}$	35.4	45
930	13.33	$2 \times 10^{-4}$	—	—	$6.7 \times 10^{-4}$	14.5	43.0
1040	11.91	$3.3 \times 10^{-4}$	—	—	$6.5 \times 10^{-4}$	18.6	44.0
1490	8.34	$3.6 \times 10^{-4}$	—	—	$5.9 \times 10^{-4}$	35.2	47.0
1740	7.13	$3.7 \times 10^{-4}$	—	—	$6.5 \times 10^{-4}$	43.1	45.0
2620	4.729	$3.1 \times 10^{-4}$	—	—	$6.7 \times 10^{-4}$	65.5	45.0
4795	2.585	$3.57 \times 10^{-4}$	67	45.4	$5.1 \times 10^{-4}$	82.1	42.5
4980	2.489	$6.14 \times 10^{-5}$	16	59.3	—	—	—
6000	2.066	$2.17 \times 10^{-4}$	47	41.8	$2.5 \times 10^{-4}$	52.0	45.0
13000	0.953	$1.50 \times 10^{-4}$	60.0	34.6	—	—	—
17000	0.729	$1.23 \times 10^{-4}$	60.0	31.7	—	—	—

Comparison of calculated (DODT) values of  $R$  and experimental values show that in nearly all cases the experimental values are greater than half that predicted. Calculated and observed angular resolution ( $\theta/\Delta\theta$ ) are also in reasonable agreement with the largest discrepancy observed for the lowest energy radiation C-K (277 eV). In addition the angular resolution,  $\theta/\Delta\theta$ , increases significantly at 4980 eV while both the peak reflectivity  $P$  and integrated reflectivity are markedly reduced. This photon energy lies at the titanium K edge, the decrease in reflectivity resulting from the absorption edge jump and the effect of the anomalous dispersion of the titanium on the scattering power per vanadium/carbon layer pair. This decrease in scattering power is reflected in the significant increase in the angular resolution at this energy.

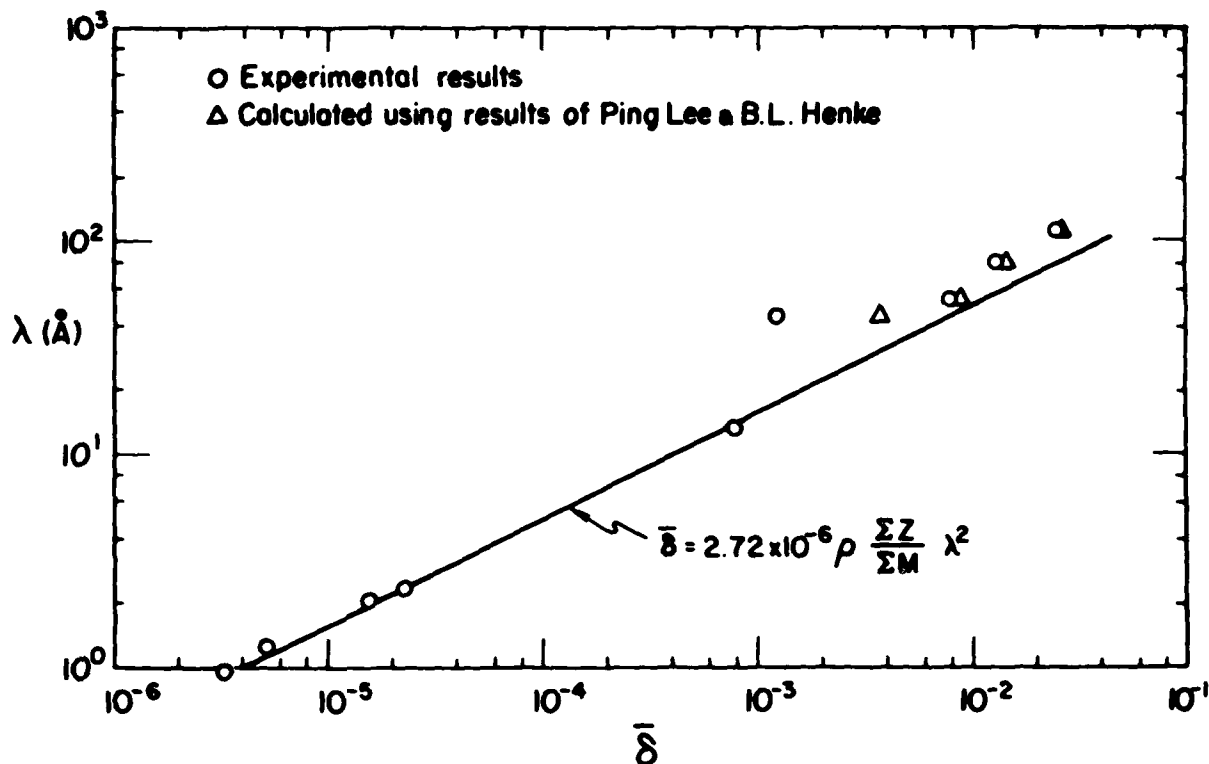


Fig. 18.  $\bar{\delta}$ , the composite refractive index of the W/C-LSM 80-177 calculated from the angular position of the first order Bragg reflection of radiation  $0.953 \text{ \AA} < \lambda < 114 \text{ \AA}$  is plotted as a function of the wavelength of the radiation. These data are compared to a simple theory in which the effective number of electrons for vanadium and carbon are assumed to be 23 and 6 respectively and to predictions made using the values of  $\delta$  and developed by Ping Lee and Henke (32).

The integrated reflectivity experimentally observed is compared to calculated values over the wavelength range of 2 to 13.1 Å in Fig. 19. R values for RAP are also shown for comparison. The general behavior is clearly in agreement while the actual experimental values are, at all wavelengths, less than the predicted values. Again, it is likely that an uncertainty in the correct values of  $\delta$  and  $\beta$  contribute to this disparity.

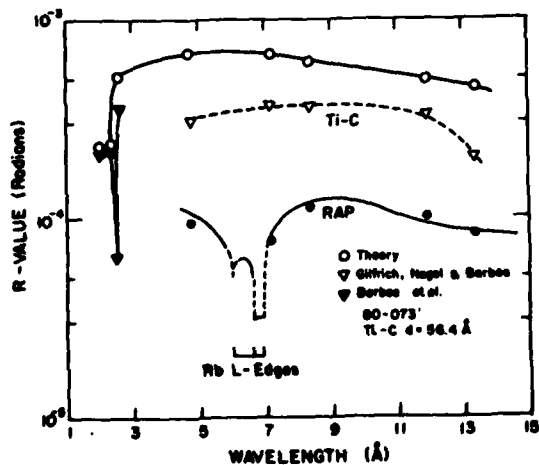


Fig. 19. Integrated reflectivities for a Ti/C-LSM (80-073);  $d = 56.4 \text{ \AA}$ ,  $t_{Ti} = 26.0 \text{ \AA}$ ,  $N_{Ti} = 70$ ) for radiation in the wavelength range  $2.066 \text{ \AA} < \lambda < 13.33 \text{ \AA}$  are shown as a function of radiation wavelength and compared to theory. Data and calculations for RAP are included for comparison. Also, data at the Ti-K edge were taken at SSRL and are in better agreement with theory, as shown in Table 7.

#### V. APPLICATION OF LSMs AS DISPERSION ELEMENTS

In this paper the primary purpose has been to present information providing a picture of the current status of the development of LSM x-ray dispersion elements synthesized using sputter deposition technology. The results discussed have demonstrated that the application of such LSM structures as dispersion elements is now possible. Two such applications are briefly discussed in the following.

A series of observations have been made by Loder, Nagel, and Barbee (40) at the Naval Research Laboratory in which a W/C-LSM was used as a spectroscopic element dispersing the emitted radiation from a laser induced plasma generated by irradiation of a Teflon Target using a ruby laser as shown in Figure 20. The arrangement of the W/C-LSM and a rubidium acid phthalate (RAP) analyzing crystal in a dual element spectrograph is also shown in Figure 20. This arrangement allowed direct comparisons of the dispersion characteristics of the two spectroscopic elements. This is shown in Figure 21 which presents microdensitometer traces of the films exposed during the same laser shot. Note the integrated and peak reflectivities of the W/C-LSM are substantially larger than those of the RAP, and the resolution is apparently a factor of 6 smaller. DODT calculations for  $\lambda = 16.807 \text{ \AA}$  have been made and are shown in Figure 22. The calculations indicate a resolution of approximately  $0.21 \text{ \AA}$  is expected compared to an observed value of approximately  $0.25 \text{ \AA}$ . Also, the ratio of the predicted value of integrated reflectivity for  $\lambda = 16.807 \text{ \AA}$  to that of RAP is  $\sim 14.3$  ignoring the effects of interfacial roughness on peak reflectivity. The experimentally observed value is 11.3. If the effects of interfacial roughness on the diffracting behavior of this LSM are included the agreement is considerably improved. Exact agreement is found for  $\Delta Z = 1.6 \text{ \AA}$ , a value similar to that observed for other W/C-LSMs discussed earlier in this paper.

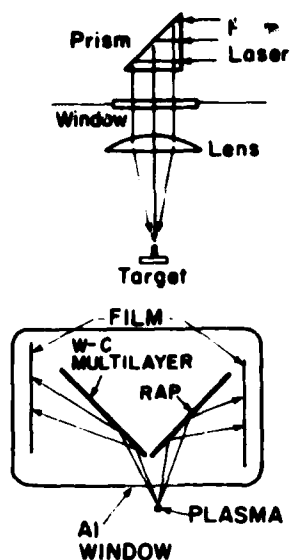


Fig. 20. Elevation and plan views of a dual element spectrograph used to compare the performance of a W/C-LSM and a RAP crystal irradiated by a laser generated plasma from a teflon ( $CF_2$ ) target are schematically shown

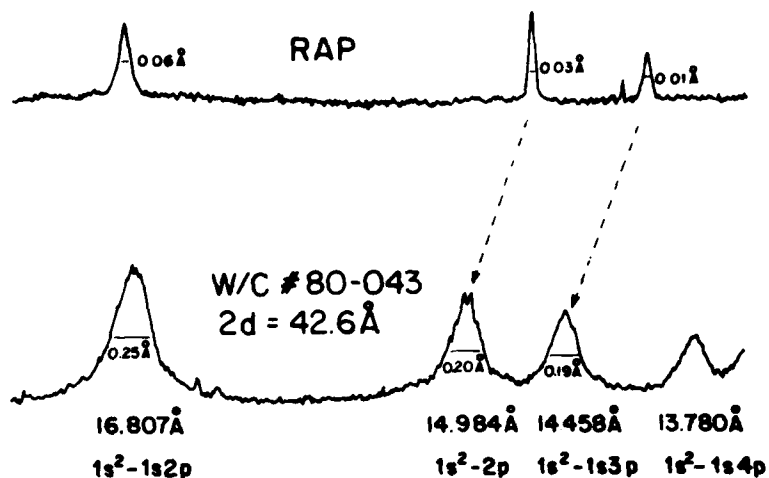


Fig. 21. Optical densitometer traces of film records of laser excited plasma spectra from  $CF_2$ , simultaneously obtained using a W/C-LSM and an RAP crystal as dispersion elements mounted in the apparatus shown in Fig. 20 are shown.

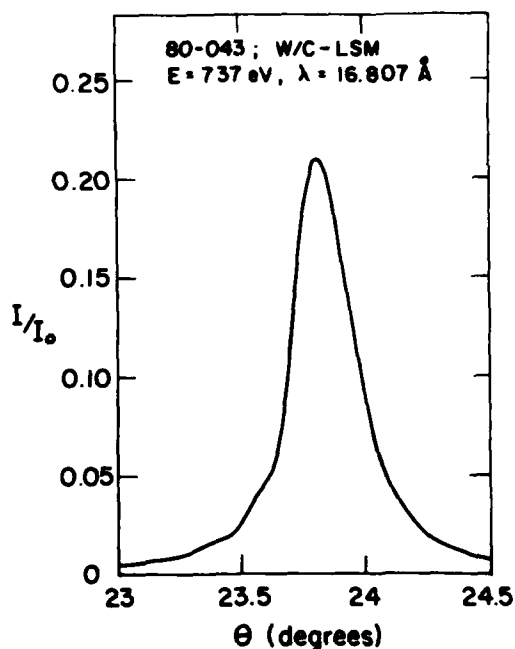


Fig. 22. A calculated (DODT) diffraction peak profile for a W/C-LSM having 125 tungsten layers 8 Å thick separated by 13 Å of carbon is shown for incident radiation having a wavelength of 16.807 Å.

These results demonstrate that W/C-LSMs provide a spectroscopic element having higher energy throughput than standard acid phthalate crystals in the X-UV range and resolution sufficient for analysis of prominent emission lines.

Another possible spectroscopic application (41) is use of these LSMs as dispersing elements in a standard powder diffraction apparatus. An example of this is shown in Figure 23 where scans of the (101) peak from polycrystalline quartz with  $Cu K_{\alpha}$  ( $\lambda = 1.5418$  Å) using a curved focusing graphite crystal and a flat W/C-LSM ( $d = 39.2$  Å and  $N_w = 50$ ) as dispersion elements in a

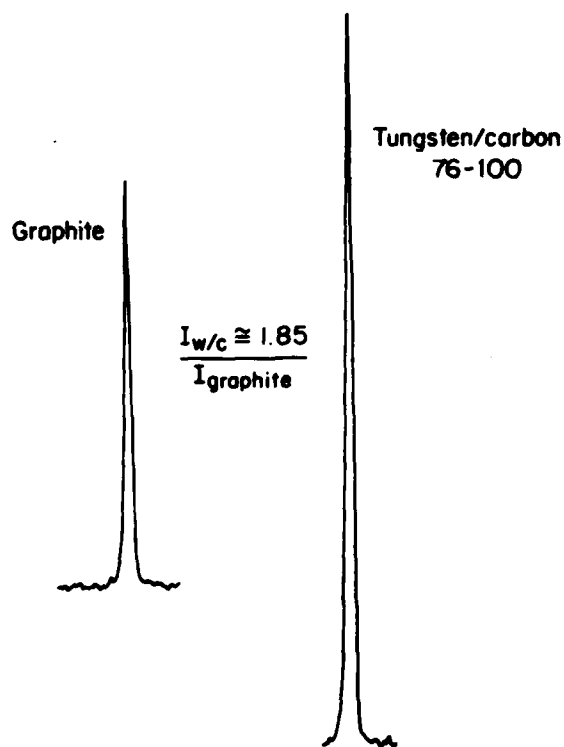


Fig. 23. A comparison of the diffracted intensity of the (101) quartz peak observed using  $Cu K_{\alpha}$  and a curved focusing graphite crystal and a flat W/C-LSM ( $d = 39.2$  Å,  $N_w = 50$ ) as dispersion elements in a diffracted beam monochromator is shown. The signal to noise ratio was observed to be 1.65 times larger with the W/C-LSM dispersion element relative to the graphite crystal.

diffracted beam monochromator are compared. Excitation of the source was the same for both scans. The peak intensity observed with the W/C-LSM was 1.85 times larger than with the graphite crystal and the signal to noise ratio 1.6 times larger. This comparison, though simple gives an indication of the utility of these LSM structures even though near grazing incidence geometries are needed.

## VI. SUMMARY

It has been demonstrated in this paper that synthetic crystals, termed layered synthetic microstructures (LSM) here, can be synthesized using sputter deposition processes with x-ray dispersion characteristics that are in accord with theory. Such structures can be synthesized with useful properties from a wide variety of materials allowing control of band width and, in special instances, the dispersion response as a function of wavelength. The periods accessible at this time have a lower limit of 15 Å though layering is evidenced for periods greater than 8 Å.

These LSM have been deposited onto a variety of substrates, the results reported here being only for materials deposited onto single crystal silicon substrates. Results on these other substrates are also in accord with theory and comparable to those obtained from LSMs deposited on single crystal silicon substrates. Many of these materials are very flexible (mica, plastic films) and allow curved surfaces to be developed. Preliminary observations of LSM behavior when deposited onto mechanically prepared figured surfaces indicate that high performance elements with periods of approximately 40 Å can be synthesized.

It has also been shown that a systematic explanation for the disagreement between experiment and model calculations can be based on the effects of the interfacial roughness between constituent layers on the angular distribution of scattered x-rays. Surface roughness,  $\Delta Z$ , for the W/C-LSMs was inferred to be in the range 1.4 to 3.15 Å with the most likely value in the range 1.4 to 1.8 Å. A somewhat larger value,  $\Delta Z = 7.7$  Å, was inferred from experimental results obtained from a V/C-LSM in which the vanadium layer was 43.5 Å thick. These results demonstrate that the character of the interface is an important parameter, and at this time, apparently the controlling factor determining the behavior of LSM dispersion elements.

Extension of this work will include investigation of new materials as components for the individual layers of an LSM. This will result in the development of understanding necessary for engineering of such LSMs for particular applications. Each new material will have characteristic interfacial effects and will require significant experimentation for development. Investigation of such interfacial effects will constitute a major part of the materials research in this field. It is likely that significant understanding of the surfaces between materials will be generated by such efforts.

In addition, actual development of optical devices for x-ray manipulation will be pursued. This will entail both model calculations and specific, designed LSM configurations which will undoubtedly extend the current synthesis process technology. A simple extension of current technology will allow synthesis of samples having multiple periods or graded periods through thickness. In addition, samples having periods varying along the substrate can also be synthesized. These now become elements for specific spectroscopic applications. The conclusion is that the variety of structures which can be envisioned is only limited by experience and imagination at this time.

A final statement concerning the sputter deposition synthesis process used here must be made. At this time usable sample areas are rectangular (2 cm x 7.5 cm). This is determined by the source geometry and by the particular system design used in this process. It is clearly possible to scale up the system so that large area substrates may be coated with high quality LSM films. In addition it is likely that highly figured surfaces may be uniformly coated with appropriate source design and substrate motion.

## ACKNOWLEDGEMENTS

The author acknowledges the continued support and contributions of his coworkers at Stanford University,

particularly those of Mr. D. L. Keith. This work has been supported both by the Department of Energy through Lawrence Livermore National Laboratory and by the NSF-MRL Program through the Center for Materials Research at Stanford University.

## REFERENCES

1. H. Koeppel, Dissertation Giessen (1929). Quoted by Deubner.
2. W. Deubner, *Ann. der Phys.* **5**, 261 (1930).
3. J. DuMond, and J. P. Youtz, *J. Appl. Phys.*, **11**, 357 (1940).
4. J. Dinklage, and R. Frerichs, *J. Appl. Phys.* **34**, 2633 (1963).
5. J. Dinklage, *J. Appl. Phys.* **38**, 3781 (1967).
6. E. Spiller, *Appl. Opt.* **15**, 2333 (1976).
7. E. Spiller, *Appl. Phys. Lett.* **20**, 365, (1972)
8. E. Spiller, "Handbook on Synchrotron Radiation," Vol. 1. (Ed. by E. E. Koch, D. E. Eastman and Y. Farge), North Holland, Amsterdam (1980).
9. R.-P. Haelbich, A. Segmüller and E. Spiller, *Appl. Phys. Lett.* **34**, 184 (1979).
10. E. Spiller in Proc. of ICO-IX, Santa Monica, Calif. (NAS-NRC, Wash. D.C., 1974), p. 525.
11. R.-P. Haelbich and C. Kunz, *Opt. Commun.* **17**, 287 (1976).
12. E. Spiller, "Evaporated Multilayer Dispersion Elements," this conference.
13. T. W. Barbee Jr. and D. L. Keith, "Workshop on Instrumentation for Synchrotron Radiation Research," Ed. by H. Winick and G. Brown, Stanford SSRL Report No. 780- (1978), III-26.
14. T. W. Barbee, Jr. and D. L. Keith, "Lithography/Microscopy Beam Line Design Workshop," Ed. by C. R. Dannemiller, Stanford SSRL Report No. 79/02 (1979), 185.
15. T. W. Barbee Jr., in "National Science Foundation - Twenty Sixth Annual Report for Fiscal Year 1976," U.S. Gov. Printing Office - Stock No. 038-000-00313-5, pg. 19.
16. A. M. Saxena, and B. P. Schoenborn, *Acta Cryst.* **A33**, 805 (1977).
17. L. L. Chang, L. Esaki, W. Howard, and R. Ludeke, Proc. 11th International Conf. on the Physics of Semiconductors, Polish Academy of Science, PWN-Polish Scientific Publishers (1972), 431.
18. L. L. Chang, L. Esaki, W. Howard, R. Ludeke and G. Schul, *J. Vac. Sci. Technol.* **10**, 655 (1973).
19. L. Esaki, *Jap. J. Appl. Phys. Suppl.* **2**, Part 1, 821 (1974).
20. A. C. Gossard, P. M. Petroff, W. Weigmann, R. Dingle and A. Savage, *Appl. Phys. Lett.* **29**, 323 (1976).
21. R. M. Fleming, D. B. McWhan, A. C. Gossard, W. Weigmann, and R. A. Logan, *J. Appl. Phys.*, **51**, 357 (1980).
22. E. M. Philofsky and J. E. Hilliard, *J. Appl. Phys.*, **40**, 2198 (1969).
23. J. E. Hilliard in "Modulated Structures -1979" (Ed. by J. M. Cowley, J.B. Cohen, M. B. Salamon, and B. J. Wuensch) A.I.P. Conf. Proc. No. 153 (1979).
24. I. K. Schuller, *Phys. Rev. Lett.* **44**, 1597 (1980).
25. W. P. Lowe, T. W. Barbee Jr., T. H. Geballe, and D. B. McWhan "X-ray Scattering from Multilayers of Nb Cu" (submitted for publication).
26. J. H. Underwood and T. W. Barbee Jr., "Layered Synthetic Microstructures as Bragg Diffractors for X-rays Extreme Ultraviolet: Theory and Performance," Accepted for publication in *Appl. Opt.*
27. J. H. Underwood and T. W. Barbee, Jr., "Synthetic Multilayers as Bragg Diffractors for X-rays and Extreme Ultraviolet: Calculations of Performance," this conference.
28. A. Guinier, "X-ray Diffraction," W. H. Freeman, London, England, 1963, pg. 121.

29. H. E. Bennett and J. M. Bennett in "Physics of Thin films," Vol. 4, Ed. by G. Hass and R. E. Thun, Academic Press, 1969, pg. 1.
30. P. Beckmann, "The Scattering of Electromagnetic Waves by Rough Surfaces," Pergamon Press, New York, 1963, Part 1.
31. J. M. Elson and J. M. Bennett, Opt. Engineering, 18, 116 (1979).
32. Ping Lee and B. Henke, Private communication.
33. L. V. Azároff, "Elements of X-ray Crystallography," McGraw-Hill, New York (1968), 130.
34. T. W. Barbee Jr. and D. L. Keith, "Synthesis of Metastable Materials by Sputter Deposition Techniques, to be published, TMS-AIME Conf. on Metastable Materials, Nov. 1979.
35. L. J. Maissel and R. Glang, Eds., "Handbook of Thin Film Technology," McGraw-Hill, New York (1970).
36. K. L. Chopra, "Thin Film Phenomena," McGraw-Hill, New York (1969).
37. J. L. Vossen and W. Kern, Eds., "Thin Film Processes," Academic Press, New York (1978).
38. S. Schiller, U. Heisig and K. Goedicke, Thin Solid Films, 40, 1977.
39. J. V. Gilfrich, D. J. Nagel and T. W. Barbee Jr., Unpublished work.
40. N. G. Loter, D. J. Nagel and T. W. Barbee Jr., unpublished work.
41. T. W. Barbee Jr., unpublished work.



Dr. Troy Barbee of Stanford describing synthetic multilayer structures with d-spacings as small as 10 Å.

Low Energy X-Ray Interactions: Photoionization, Scattering, Specular and Bragg Reflection

B. L. Henke

University of Hawaii, Department of Physics and Astronomy, Honolulu, Hawaii 96822

## ABSTRACT

For the low energy x-ray region of 100-2000 eV, the complete atomic interaction, coherent scattering and photoelectric absorption can be described by a complex scattering amplitude which may be given through the atomic scattering factor,  $f_1 + if_2$ . For this low photon energy region, it is shown by the relativistic quantum dispersion theory that the atomic scattering factors can be uniquely determined from simple relations involving only the atomic photoionization cross section dependence upon photon energy. We have compiled "state of the art" tables for the photoionization cross sections for 94 elements and for the photon energy region of 30-100,000 eV. With this compilation, we have established atomic scattering factor tables for the 100-2000 eV region. By a summing of the complex, atomic scattering amplitudes, a low energy x-ray interaction can be determined. Even for atoms in the molecular or solid state the scattering cross sections remain atomic-like except for photon energies very near the thresholds. Using practical examples, the methods of calculation, with the atomic scattering factors, are reviewed here for the following: 1) x-ray energy deposition within materials (energy response of x-ray photo-cathodes); 2) transmission through a homogeneous medium: refraction; 3) transmission through a random collection of uniform spheres: low angle scattering in an inhomogeneous medium; 4) specular, Fresnel reflection (total and large angle reflection) at smooth boundary; and 5) Bragg reflection from a periodic, layered system--(reflection by crystals and multilayers).

## I. INTRODUCTION--THE ATOMIC SCATTERING FACTORS

In this review, we would like to discuss, for the low energy x-ray region (100-2000 eV region), how the interactions of absorption, scattering and reflection can be well described by using the atomic scattering factors as the primary parameters for the material system. In the Appendix of these proceedings we present tables for the atomic scattering factors as directly derived from a recent work [1] on a "state of the art" compilation of the photoionization cross sections for 94 elements for the 30-10,000 eV region, along with the calculated atomic scattering factors for the 100-2000 eV photon energy region. We present here, as applied to selected examples of relevance in low energy x-ray diagnostics, some basic procedures for predicting low energy x-ray interactions.

The interaction physics for the conventional x-ray region (for photon energies above 1000 eV) has been presented by many excellent texts including that of Compton and Allison [2] and R. W. James [3]. What is summarized here is an extension and specialization of this physics that is useful for the long wavelength x-ray region of 10-100 Å.

For the low energy x-rays, the interaction can be defined as simply coherent scattering and photoelectric absorption. Incoherent scattering is negligible. The complete interaction with an atom may thus be described by a complex scattered amplitude defined by an atomic scattering factor,  $f_1 + if_2$ , as depicted in Figs. 1 & 2. The scattered amplitude is given by this factor multiplied by that amplitude which would be scattered if the atom were replaced by a free, Thomsonian electron. Here,  $r_0$  is the classical electron radius,  $m$  the electron mass,  $c$  the velocity of light and  $R$  the distance from the atom to the point of measurement. Because the wavelengths of interest are large as compared with the dimensions of the electron distributions within the atom, we make the important assumption here that essentially all electrons will scatter effectively in phase for all but the largest angles of scattering so that the atomic scattering factor components,  $f_1$  and  $f_2$ , may be considered angle independent. The complex amplitude of atomic scattering therefore will be dependent only upon the angle of scattering,  $2\theta$ , through the polarization

factor,  $P(2\theta)$ , of the Thomsonian term.  $P(2\theta)$  is equal to unity or  $\cos 2\theta$  depending upon whether the incident electric vector is perpendicular to or parallel to the plane of scattering. As will be discussed below, the relative roles of the coherent scattering and the photoelectric absorption will be expressed through  $f_1$  and  $f_2$ , respectively.

The relativistic quantum dispersion theory for atomic scattering and the calculation of the atomic scattering factors has been presented by Cromer and Lieberman [4] and by Jensen [5] (along with their references). In Fig. 2 are shown their results including the relativistic corrections,  $\Delta f_r$ , to the semiclassical, usual relations for  $f_1$  and  $f_2$ . Here  $Z$  is the atomic number,  $h$  Planck's constant,  $mc^2$  rest mass energy of the electron,  $E_{tot}$  the total energy of the atom and  $E$  the photon energy. Cromer and Lieberman have estimated  $E_{tot}$  (a negative quantity) for all the elements and from their table we have fit the following polynomial for the larger term in  $\Delta f_r$ .

$$\frac{5}{3} \frac{E_{tot}}{mc^2} = 2.19 \times 10^{-6} Z^3 - 1.03 \times 10^{-4} Z^2.$$

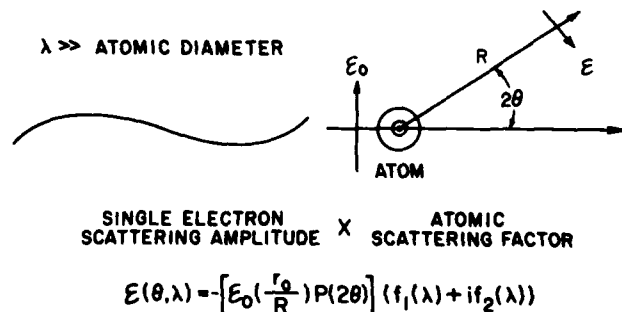
LOW ENERGY X-RAY SCATTERING

Figure 1

## THE ATOMIC SCATTERING FACTOR, $f_1 + if_2$

RELATIVISTIC QUANTUM DISPERSION RELATIONS:

$$f_2(E) = \frac{E\mu_a(E)}{2\pi r_0 hc} \quad \mu_a(E) \text{-- ATOMIC PHOTOIONIZATION CROSS SECTION}$$

AND

$$f_1(E) = Z + \frac{1}{(\pi r_0 hc)} \int_0^\infty \frac{\epsilon^2 \mu_a(\epsilon) d\epsilon}{E^2 - \epsilon^2} + \Delta f_r,$$

$$\text{WHERE } \Delta f_r = \frac{5}{3} \frac{E_{tot}}{mc^2} - \frac{Z}{2} \left( \frac{E}{mc^2} \right)^2$$

WHICH IS NEGLIGIBLE FOR THE LOW ENERGY X-RAY REGION.

Figure 2

For the low energy x-ray region it is immediately evident that this and the second relativistic term in  $\Delta f_r$  are completely negligible except near thresholds where  $f_1$  becomes small as compared with  $Z$ . An important argument here, therefore, is that for the low energy x-ray region, the atomic scattering factor,  $f_1 + if_2$ , can be uniquely determined through these relations in terms of the total atomic photoionization cross section and its dependence upon photon energy. It may be noted that  $f_2$  is directly proportional to the atomic photoionization cross section for a given photon energy,  $E$ . It will exhibit the same structures near thresholds as does the photoionization cross section,  $\mu(E)$ . The relation for  $f_1$  suggests that the important anomalous scattering contribution (through the integral term) depends upon a knowledge of the photoionization cross section dependence upon photon energy from a very small to very large value of photon energy. The nature of this integral, however, is that its value is sensitive to an integration range of energies relatively close to  $E$ . In our calculations [1] for  $f_1$ , we have found it convenient to use a range from 30 eV to 85 keV with our greatest concern for knowing precisely the cross sections in the intermediate region of 100-2000 eV.

In Figs. 3, 4 and 5 we present examples of plots of the calculated scattering factor components,  $f_1$  and  $f_2$ , for aluminum, copper and xenon. In the  $f_2$  plots for the photon energy region below about 300 eV we have indicated values corresponding to representative, available experimental data including that which we have adopted for this fitting. [6-10] It is important to note that throughout the low energy x-ray region, the  $f_1$  values are appreciably different from the classical Thomsonian value of  $Z$  (as a result of electronic binding and consequent anomalous scattering).

It is proposed here that with sufficient accuracy we may assume that the low energy x-ray photoionization cross sections and, correspondingly, the atomic scattering factors are atomic-like even in the chemical and solid states. This effect is illustrated in Fig. 6 where shown is a comparison of the photoionization cross sections as measured in the vapor and in the solid state for the elements sodium, iron and barium. [11-13] Near thresholds there are characteristically large departures from the atomic-like character when the atoms are in the molecular and solid state. At the absorption edge may be sharp excitonic structures [14] and nearby may be the extended absorption fine structure (exafs) [15]. Nevertheless, as has been discussed by many authors, [16-18] above about 50 eV and away from thresholds, the photoionization cross sections are relatively independent of the state of the atomic system. In our integrations for  $f_1$  we have used values for  $\mu(E)$  that have been averaged through such structures near the thresholds.

Thus for the low energy x-ray region of interest here (100-2000 eV) we define and have tabulated the

## ATOMIC SCATTERING FACTOR, $f_1 + if_2$ -- ALUMINUM

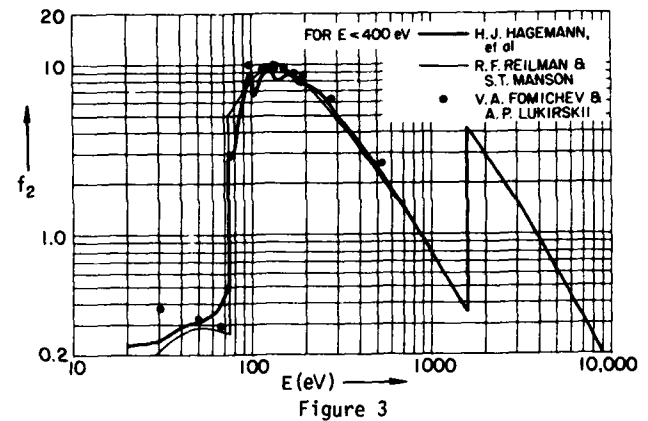
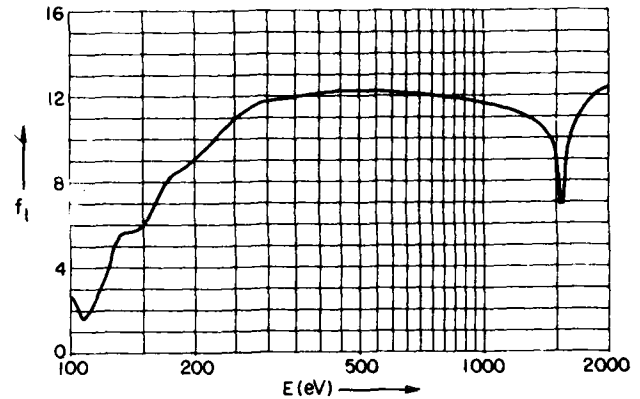


Figure 3

## ATOMIC SCATTERING FACTOR, $f_1 + if_2$ -- COPPER

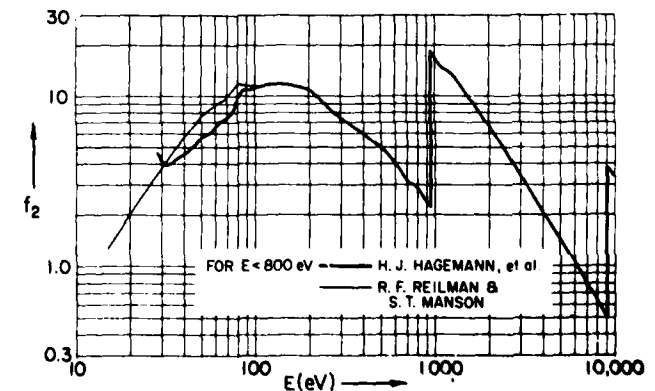
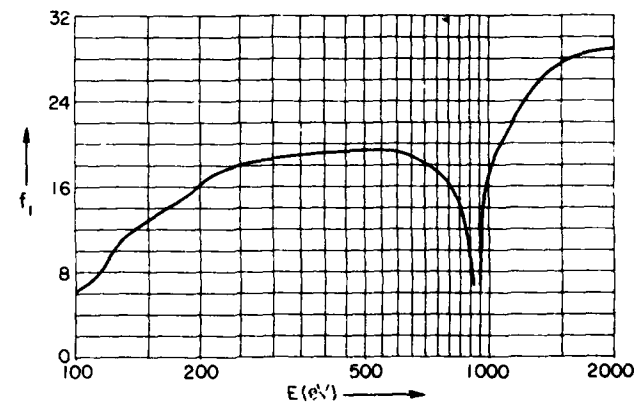


Figure 4



## ATOMIC SCATTERING FACTOR, $f_1 + if_2$ -- XENON

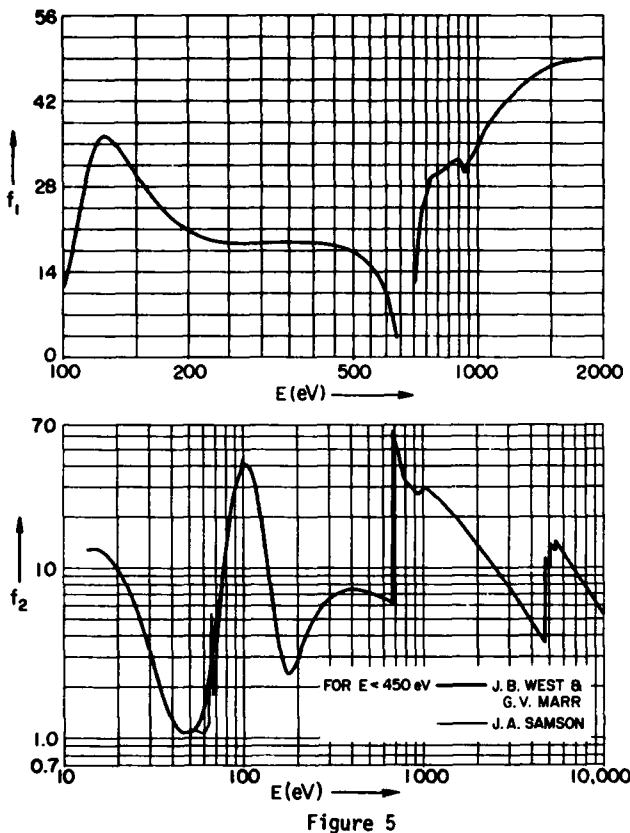


Figure 5

atomic scattering factors (a) as uniquely defined by the best available photoionization cross section data; (b) as being essentially independent of scattering angle; and (c) as being effectively independent of the state of the atomic system--except for photon energies near thresholds.

### II. LOW ENERGY X-RAY INTERACTION DESCRIPTION

Generally one may treat such problems as the transmission of radiation, particle scattering, specular and Bragg reflection with a macroscopic description as an electromagnetic wave boundary value problem using material constants such as the dielectric constant,  $K$ , and the refractive index,  $n_r$ , or equivalently, by an atomic approach by summing the atomic scattered amplitudes from the irradiated atomic system and using the atomic scattering factors. By comparing the solutions of such interaction problems by these approaches, the following relationships between the complex dielectric constant,  $K$ , the refractive index,  $n_r$ , and the atomic scattering factors for the x-ray region are directly established.

For the low energy x-ray region, we define the complex dielectric constant,  $K$ , as

$$K = 1 - \alpha - i\gamma \quad (1)$$

and the complex refractive index,  $n_r$ , by

$$n_r = 1 - \delta - i\beta, \quad (2)$$

where characteristically these unit decrements,  $\alpha$ ,  $\gamma$ ,  $\delta$  and  $\beta$ , are small as compared with unity. We then find that the following relationships between the atomic and the macroscopic parameters obtain:

$$\delta = \frac{r_0 \lambda^2}{2\pi} n \bar{f}_1 = \frac{\alpha}{2} \quad (3)$$

$$\beta = \frac{r_0 \lambda^2}{2\pi} n \bar{f}_2 = \frac{\gamma}{2}, \quad (4)$$

where the average atomic scattering factor per unit volume,  $n\bar{f}$ , is given by

$$n\bar{f}_1 = \sum_q n_q f_{1q} \quad (5)$$

$$n\bar{f}_2 = \sum_q n_q f_{2q}. \quad (6)$$

Here  $n_q$  is the number of atoms per unit volume of type- $q$ .

Usually the E & M boundary value solutions can be more formal, rigorous and, however, more tedious and less intuitive. Often a description by summing over atomic scattered amplitudes, which is phenomenological, is also more flexible and amenable to practical approximation.

In transmission, scattering, specular and Bragg reflection description, a first step in summing the atomic scattered amplitudes over a given irradiated system of atoms is illustrated in Fig. 7. Here the amplitude that is transmitted and specularly reflected by an elementary atomic plane is described. The absorptive factor,  $\sigma$ , in the transmitted direction, and the reflective factor,  $s$ , for the coherent constant phase scattering geometry as allowed only in the specular direction,  $2\theta$ , may be related to the atomic scattering factor,  $f_1 + if_2$ , by simply integrating over equiphase Fresnel zones throughout the plane [3].

If, as in many practical systems, the atomic layers are within periodic systems of layers as in planar crystals or in multilayers, with a periodicity length normal to the surface equal to  $d$ ,  $\sigma$  and  $s$  may be simply generalized for this layer system of thickness,  $d$ , in terms of the average scattering factor per unit volume,  $n\bar{f}$ , defined in Eq. (5), and a structure factor per unit volume,  $\phi F_1 + i\phi F_2$ .

Upon summing over the scattered amplitudes within this layer system a composite scattering factor per unit volume for scattering in a direction  $2\theta$  is defined as

### PHOTOIONIZATION CROSS SECTIONS ATOMIC VS SOLID STATE

VAPOR ———  
METAL ······

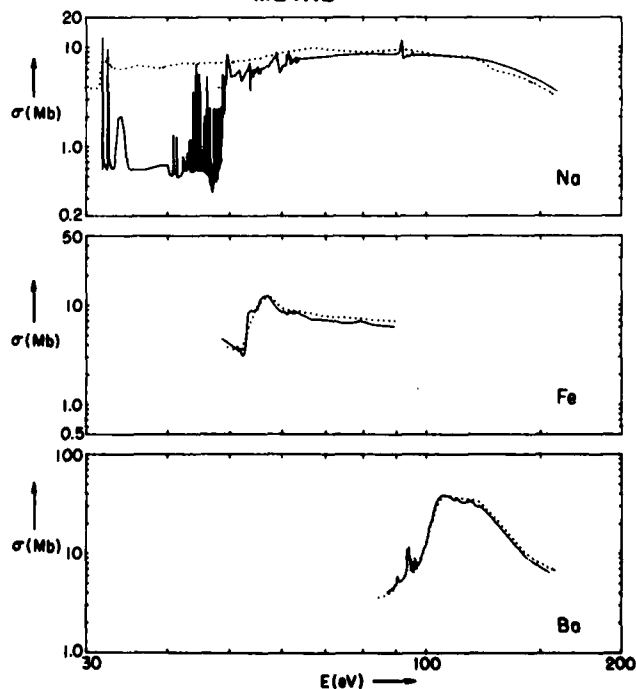
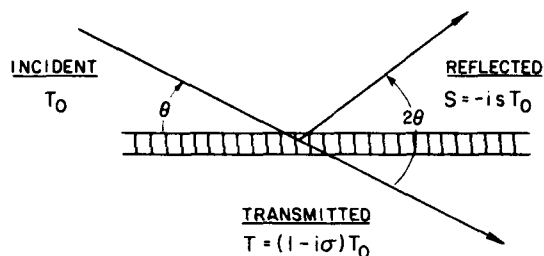


Figure 6

### AMPLITUDES REFLECTED AND TRANSMITTED



FOR  $M$  ATOMS/UNIT AREA OF ATOMIC SCATTERING FACTOR,  $f_1 + if_2$

$$\sigma = -Mr_0\lambda d \frac{f_1 + if_2}{\sin\theta} \quad \text{AND} \quad s = -Mr_0\lambda d \frac{f_1 + if_2}{\sin\theta} P(2\theta)$$

FOR  $M$  UNIT CELLS/UNIT AREA OF STRUCTURE FACTOR,  $F_1 + iF_2$ ,  
AND OF AVERAGE ATOMIC SCATTERING FACTOR,  $\bar{f}_1 + i\bar{f}_2$

$$\sigma = -Mr_0\lambda d \frac{\bar{f}_1 + i\bar{f}_2}{\sin\theta} \quad \text{AND} \quad s = -Mr_0\lambda d \frac{F_1 + iF_2}{\sin\theta} P(2\theta)$$

Figure 7

the unit cell structure factor per unit volume as follows:

$$\phi F = \frac{1}{Ad} \sum_p x_p (f_{1p} + if_{2p}) e^{-\left(\frac{4\pi\sin\theta}{\lambda}\right)z_p} \quad (7)$$

where the volume of the unit cell is  $Ad$  and within the unit cell at a position  $z_p$  from a reference plane there are  $x_p$  atoms of type- $p$ .

As is often possible, if  $z_p$  may be measured from a central symmetry plane, the  $\phi F_1$  and  $\phi F_2$  components may then be written simply as

$$\phi F_1 = \frac{1}{Ad} \sum_p x_p f_{1p} \cos\left(\frac{4\pi\sin\theta}{\lambda} z_p\right) \quad (8)$$

$$\phi F_2 = \frac{1}{Ad} \sum_p x_p f_{2p} \cos\left(\frac{4\pi\sin\theta}{\lambda} z_p\right) \quad (9)$$

The next step in an interaction description is to sum the wave amplitudes from a given system of planes of atoms (or of unit cells) and for a given angle of scattering,  $2\theta$ . As the initial wave, as depicted in Fig. 7, proceeds to the next layer it will be partially reflected again to contribute to the total reflected wave system and this partially reflected wave will also partially reflect back as a component to be added to the initial transmitted wave system, etc. In this way the total transmitted and reflected wave systems may contain the contributions of many such multiply reflected components. The works of Darwin and Prins were perhaps the first that present a relatively simple solution for the total reflected and transmitted wave systems. [2,3,19,20] Their approach was to write the self-consistent, difference equations for the transmitted amplitude,  $T_N$ , and total reflected amplitude,  $S_N$ , for successive layers (indexed by  $N$ ) taking into account the phase shift,  $kd\sin\theta$ , of the waves between layers. We refer the interested reader to the relatively simple and straightforward solution of these difference equations for the reflected wave as a function only of  $d$ ,  $\theta$ ,  $\sigma$  and  $s$ . Recently Smirnov [21] has written the difference equations as differential equations for a continuous set of close-spaced planes in order to treat, in particular, the reflection of x-rays from an amorphous medium interface. Smirnov's solution for a perfectly smooth interface immediately reduces to the familiar Fresnel equations as written for x-ray reflection by simply replacing the  $f_1$  and  $f_2$  parameters by their optical constant

equivalents through relations (3) and (4).

This inclusion of the effects of multiple reflection and absorption is called a dynamical approach. In certain problems a simple and useful approximation for the summing for the total reflected wave system from a system of planes can be obtained by neglecting the effect of the multiple reflection and the absorption reduction of the incident wave. For example, this can be appropriate for scattering by small crystals or particle systems for which relatively few planes are involved. This simplification in the summing of the reflected waves is called a kinematical approach.

In the sections that follow, we would like to summarize the results of such calculations for some examples of practical interest.

#### A. NORMAL INCIDENCE TRANSMISSION OF LOW ENERGY X-RAYS

Using the Darwin-Prins-Smirnov (DPS) approach, we have calculated the total transmitted and reflected amplitude for a normally incident, unpolarized plane wave of x-rays from uniform, amorphous solid. Taking the square of the moduli of these amplitudes, we find that the reflected intensity is negligibly small, as expected, and that the transmitted intensity is reduced exponentially with distance  $z$  from the surface as  $\exp(-2r_0\lambda n\bar{f}_2)$ , where  $n\bar{f}_2$  is the average scattering factor component,  $f_2$ , per unit volume as given by Eq. (5). From an E & M, boundary value solution for the Poynting vector describing this transmitted energy flow, we find [17] that it is reduced with  $z$  by the factor  $\exp(-4\pi\beta/\lambda z)$ . Comparing these exponential factors with that defined in terms of the linear absorption coefficient,  $\mu_L$ , we obtain the relations

$$\mu_L = \frac{4\pi\beta}{\lambda} = 2r_0\lambda n\bar{f}_2 \quad (10)$$

which is consistent with relation (4). This result may also be written as

$$\bar{f}_2 = \frac{E\mu_a(E)}{2\pi r_0 hc} \quad (11)$$

where  $\mu_a$  is an atomic (or molecular) photoionization cross section equal to  $\mu_L/n$ . This result also follows from the quantum theory of dispersion as noted in Fig. 2.

#### B. THE QUANTUM YIELD FOR LOW ENERGY X-RAY PHOTOCATHODES

In a recent work [23] we have shown experimentally and by a simple phenomenological model that the number of electrons that are photoemitted per normally incident photon, the quantum yield,  $Y$ , is dependent upon photon energy through the factor,  $\rho\epsilon\mu(E)$  or  $E\mu_L(E)$ .  $E$  is the photon energy,  $\rho$ , the mass density of the photocathode,  $\mu$  and  $\mu_L$  are the mass and linear photoionization cross sections, respectively. We may thus write for the photocathode efficiency

$$Y \sim n\bar{f}_2 \quad (12)$$

by applying Eq. (11) where  $n\bar{f}_2$  is the average scattering factor,  $f_2$ , per unit volume for the photocathode and given in Eq. (5). Thus the  $f_2$  parameters which have tabulated here and in Ref. 1 can be used directly to estimate the photon energy dependence of x-ray photocathodes.

#### C. SMALL ANGLE SCATTERING OF LOW ENERGY X-RAYS

As has been noted in Sec. II-A, a measurement of the attenuation of the transmitted intensity through a uniform, homogeneous material can be used to determine the photoionization cross section,  $\mu$ , and the atomic scattering factor component,  $f_2$ . If the sample material consists of small particles or voids of dimensions large compared with the wavelength of the incident radiation, the direct beam will be reduced further by the resulting coherent scattering. In order to estimate this effect

and/or to evaluate material scattering generally, a description of the scattering by spherical particles or voids is presented here as a relevant example.

This problem has been discussed in some detail in a previous work by the author [24]. By neglecting absorption within the sphere (each differential plane receiving essentially the same incident intensity) and neglecting multiple interference, we may calculate, relatively easily, the scattered intensity distribution by a kinematical approach. Integrating the differential amplitudes which are proportional to the circular section area of  $\pi(R^2 - z^2)$  (see Fig. 8) and with phase angle relative to that for the central plane,  $4\pi z \sin\theta/\lambda$ , (with  $2\theta$  the angle of scattering) we obtain the total amplitude of the scattered wave [24]. Taking the modulus squared, we then obtain the intensity distribution at a distance,  $r$ , from a spherical particle.

$$I = I_0 \left( \frac{4\pi^3 r_0^2 R^6}{r^2} \right) ((n\bar{f}_1)^2 + (n\bar{f}_2)^2) (1 + \cos^2 2\theta) \left( \frac{J_{3/2}(u)}{u^3} \right). \quad (13)$$

Here again  $n\bar{f}_1$  and  $n\bar{f}_2$  are the averaged scattering factor components per unit volume, from Eq. (5);  $u = \frac{4R \sin\theta}{\lambda}$ , and  $J_{3/2}(u)$  is the Bessel function of order 3/2. For small angle scattering, i.e., for  $\lambda \ll R$ , the central maximum is well approximated by a Gaussian distribution

$$I = \frac{8\pi^2}{9} \frac{R^6 r_0^2}{r^2} ((n\bar{f}_1)^2 + (n\bar{f}_2)^2) (1 + \cos^2 2\theta) I_0 e^{-\frac{u^2}{5}} \quad (14)$$

of angular width,  $\Delta\theta = \sqrt{5/8\pi^2} (\lambda/R)$ .

The E & M boundary value solution was rigorously obtained in series form using Legendre polynomials by Mie [25]. This solution was expressed in closed form by Hart and Montroll [26] and by van de Hulst [27] for "soft" spheres for which absorption was not completely neglected. We have taken this dynamical model result which may be appropriate for the lower energy x-ray region and have shown that it reduces to Eq. (13) in the low absorption limit by again replacing the optical constants,  $\delta$  and  $\beta$ , by the equivalent functions in  $f_1$  and  $f_2$  given in Eqs. (3) and (4). [24] By integrating over a sphere to obtain the total scattering through all angles we have obtained expressions for the total cross sections. The total cross section per particle,  $s_p$ , and the total cross section per gram,  $s_m$ , as derived from Eq. (13), become

$$s_p = r_0^2 \lambda^2 R^4 ((n\bar{f}_1)^2 + (n\bar{f}_2)^2) \\ s_m = \frac{3}{4\pi} \frac{R r_0^2 \lambda^2}{\rho_0} ((n\bar{f}_1)^2 + (n\bar{f}_2)^2) \quad (15)$$

( $\rho_0$  is the mass density of the particle.)

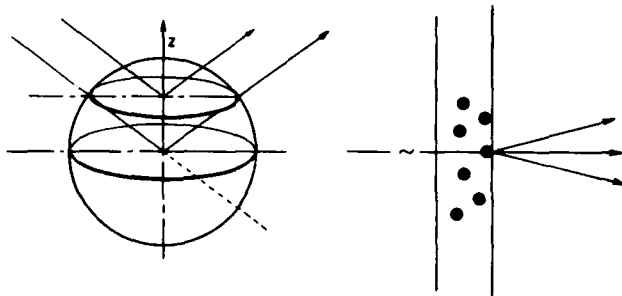
If the scattering medium consists of spherical particles of an average atomic scattering factor per unit volume,  $n'(\bar{f}_1' + i\bar{f}_2')$  imbedded in a material of that equal to  $n(\bar{f}_1 + i\bar{f}_2)$ , it can be shown that the kinematical result, Eq. (13), will obtain if we simply replace  $n\bar{f}_1$  and  $n\bar{f}_2$  by the difference parameters,  $(n\bar{f}_1 - n'\bar{f}_1')$  and  $(n\bar{f}_2 - n'\bar{f}_2')$ . For voids,  $f_1' = f_2' = 0$ .

If the transmission sample is sufficiently thick so that multiple scattering is significant, the angular distribution of the intensity is broadened over that predicted by Eq. (13). This effect is discussed in Ref. [24].

#### D. SPECULAR REFLECTION BY X-RAY MIRRORS

As noted above, Smirnov [21] has expressed the Darwin-Prins difference equations as differential equations descriptive of the reflection and transmission for a continuous set of planes with spacing between the atomic reflecting planes that is small as compared with the wavelength. (He describes this case as the zero-order Bragg reflection.) After deriving the expression for total reflection from a perfectly smooth interface that reduced immediately to that predicted through the

#### LOW ENERGY X-RAY PARTICLE SCATTERING



LOW ANGLE SCATTERING CROSS SECTION/PARTICLE

$$s_p = \phi^2 R^4 r_0^2 \lambda^2 (f_1^2 + f_2^2)$$

( $\phi$  = ATOMS/UNIT VOLUME)

Figure 8

Fresnel equations (E & M boundary value solution), Smirnov et al. [28] then extended these calculations to predict the effect of surface roughness upon x-ray mirror reflection and thus explain the often observed departures of some experimental curves from the Fresnel curves.

For the low energy x-ray region, it is important not to assume that the specular reflection occurs only for the small glancing angles as is usually assumed. [2, 3, 21, 28] In order to obtain a precise large angle solution for the reflection of low energy x-rays, the author [22] has specialized the rigorous and general solutions of Mahan [29] for the reflection of a plane electromagnetic wave from a semi-infinite homogeneous, absorbing medium. We have shown in that solution that for the x-ray region, the reflection equation can be expressed completely in terms of a complex dielectric constant given by

$$K = 1 - (1 - \epsilon) - \frac{i2\sigma}{\nu} = 1 - \alpha - i\gamma \quad (16)$$

(using here only, Mahan's notation).  $\epsilon$  is the dielectric constant,  $\sigma$  the conductivity constant and  $\nu$  the radiation frequency.

This dielectric constant may be derived from the dipole moment per unit volume within the medium through the usual relation

$$K = 1 + \frac{4\pi M}{E},$$

where  $E$  is the electric incident field. And this dipole moment per unit volume,  $M$ , can be expressed as a sum of the atomic dipole moments which are proportional to the atomic scattering factors. We can thus derive

$$\alpha = \frac{r_0 \lambda^2}{\pi} n\bar{f}_1 \\ \gamma = \frac{r_0 \lambda^2}{\pi} n\bar{f}_2 \quad (17)$$

which relations also follow from Eqs. (1) through (4) (deduced by comparing the E & M and atomic scattering solutions).

We may now write Mahan's reflection intensity as specialized for large angle, low energy x-ray reflection as a function of a convenient parameter,  $\rho$ , defined by

$$\rho^2 = \frac{1}{2} (\sin^2 \theta - \alpha + \sqrt{(\sin^2 \theta - \alpha)^2 + \gamma^2}). \quad (18)$$

Here  $\theta$  is the grazing incidence angle and  $\alpha$  and  $\gamma$  are given by  $f_1$  and  $f_2$  through Eq. (17). (For small  $\theta$ ,  $\alpha$  and  $\gamma$ , the parameter,  $\rho$ , becomes equal to the internal angle that the refracted beam makes with the reflecting surface.)

We define  $I_{\pi}$  and  $I_0$  as the ratios of the reflected intensity to the incident intensity for the polarized components with the E-vector perpendicular to and

## BERYLLIUM MIRROR REFLECTIVITY

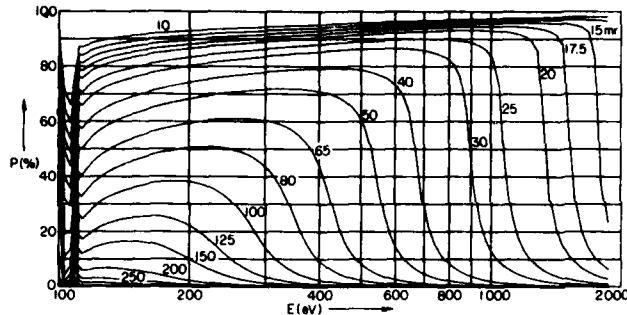


Figure 9

parallel to the plane of reflection respectively. We may then write

$$I_{\sigma}(\theta) = \frac{4\rho^2(\sin\theta - \rho)^2 + \gamma^2}{4\rho^2(\sin\theta + \rho)^2 + \gamma^2} \quad (19)$$

and for the polarization ratio

$$\frac{I_{\pi}(\theta)}{I_{\sigma}(\theta)} = \frac{4\rho^2(\rho - \cos\theta\cot\theta)^2 + \gamma^2}{4\rho^2(\rho + \cos\theta\cot\theta)^2 + \gamma^2} \quad (20)$$

and finally for the total reflected intensity for an unpolarized incident beam

$$I(\theta) = \frac{1}{2}I_{\sigma}(1 + I_{\pi}/I_{\sigma}). \quad (21)$$

We have shown from Mahan's exact solution that the absorption factor in the Poynting vector that describes the energy flow of low energy x-rays into the medium is equal to  $\exp(-2\pi\gamma z/\lambda\rho)$  where  $z$  is the penetration depth as measured normally to the reflecting surface. We may therefore define a  $1/e$  depth involved in x-ray reflection by the relation

$$d_{1/e} = \frac{\lambda\rho}{4\pi\gamma} \quad (22)$$

In Ref. [1] we have applied this description of the reflection of low energy x-rays from perfectly smooth interfaces to establish detailed tables in photon energy and reflection angle for the mirrors beryllium, carbon, aluminum oxide, aluminum, fused quartz, nickel, copper and gold. As examples of such calculations we present here in Figs. 9 and 10 the reflectivity curves for beryllium and for nickel. In a companion paper of these proceedings, we also present the reflectivity-vs- $\theta$  curves for those characteristic long wavelengths for which we could also include reported experimental points for comparison.

## D. BRAGG REFLECTION FROM MULTILAYERS AND CRYSTALS

Using the elementary interaction as described in Fig. 7 for a plane wave reflecting and transmitting at a single layer of unit cell structures, Compton and Allison have followed a Darwin-Prins approach to proceed to write equations for the total transmitted and reflected waves that obtain for any arbitrary, successive set of planes within a crystal of an infinite number of planes and of spacing equal to  $d$ . These difference equations were then solved with the following important results.

We define the incident amplitude of the plane wave as  $T_0$  and the total reflected wave amplitude leaving the surface as  $S_0$ . It is shown that the total transmitted wave proceeding into the crystal that reaches the  $N$ th layer (including the contributions of all possible multiple reflections) may be given simply by

$$T_N = T_0 x^N, \quad (23)$$

where the attenuation factor per layer,  $x$ , is assumed to

## NICKEL MIRROR REFLECTIVITY

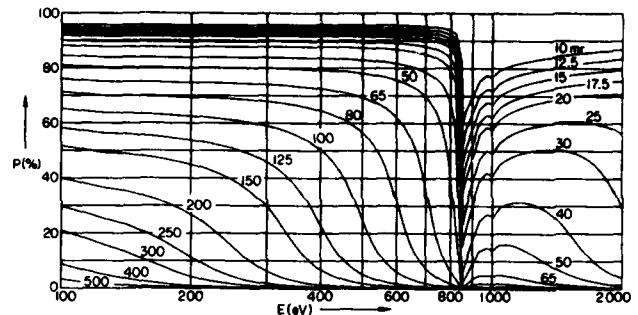


Figure 10

be only slightly less than unity and thus we may define  $x$  here by

$$x = (-1)^m e^{-\eta}, \quad (24)$$

where  $m$  is the order of diffraction and

$$\eta = \sqrt{s^2 - (\sigma + \xi)^2} \quad (25)$$

and

$$\xi = \frac{2\pi}{\lambda} d(\sin\theta - \sin\theta_0) \quad (26)$$

( $\theta_0$  is defined by the Bragg relation,  $m\lambda = 2d\sin\theta_0$ .) In Eq. (25) we choose the plus or minus sign so that the real part of  $\eta$  will have the (physically significant) positive value. It also follows as suggested in Fig. 11 that the total wave amplitude at the  $N$ th layer that is proceeding upward in the Bragg reflected direction (including all multiple interference contributions) may be written as

$$S_N = S_0 x^N. \quad (27)$$

The solution of the self-consistent difference equations for the ratios of the total reflected to incident amplitudes at the crystal surface and at the  $N$ th layer are given by

$$\frac{S_0}{T_0} = \frac{-s}{(\sigma + \xi) + \sqrt{(\sigma + \xi)^2 - s^2}} = \frac{S_N}{T_N}. \quad (28)$$

Finally, by taking the modulus squared of the amplitude ratio as a function of the angle,  $\theta$ , here in terms of the atomic scattering factors,

$$I_{\infty}(\theta) = \left| \frac{-s}{(\sigma + \xi) + \sqrt{(\sigma + \xi)^2 - s^2}} \right|^2 \quad (29)$$

We would like now to apply this Darwin-Prins approach (difference equation solution for small values of  $\sigma$  and  $s$ ) as outlined above in order to estimate the effect of limiting the crystal or multilayer to a finite number of layers,  $N$ . We suggest that the total amplitude of reflection for this finite system should be

## N-DEPENDENT DARWIN-PRINS MODEL

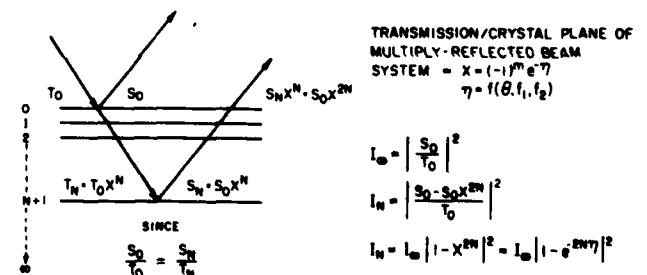


Figure 11

that reflected for the infinite-layer system minus that total wave amplitude reflected from the multilayer system from  $N+1$  to  $\infty$ . Because  $S_0/T_0$  and  $S_N/T_N$  both describe the amplitude ratios from a surface above an infinite number of layers, these must be equal. And because  $S_N$  must also be attenuated by the same factor,  $X^N$  for its value at the surface, we then obtain (as presented in Fig. 11) the amplitude ratio for the first  $N$  layers as follows:

$$\left( \frac{S_0 - S_0 x^{2N}}{T_0} \right) = \frac{S_0}{T_0} (1 - x^{2N}). \quad (30)$$

Finally we may write for a modified Darwin-Prins expression for a finite number of layers,  $N^*$

$$I_N(\theta) = I_\infty |(1 - e^{-2Nh})|^2. \quad (31)$$

Because, for practical crystal systems, the intensities are significantly large only at angle,  $\theta$ , near the diffraction peak, we may, with good approximation, rewrite the expressions for the structure factor per unit volume to be used in calculating these reflection intensities and as given in Eqs. (8) and (9) with  $\theta$  set equal to the Bragg angle,  $\theta_0$  defined by  $m\lambda = 2d \sin\theta_0$ . These become

$$\phi_{F1} = \frac{1}{Ad} \sum_p x_p f_{1p} \cos \frac{2\pi m z_p}{d} \quad (32)$$

and

$$\phi_{F2} = \frac{1}{Ad} \sum_p x_p f_{2p} \cos \frac{2\pi m z_p}{d}. \quad (33)$$

For the sputtered/evaporated multilayer systems consisting of successive double layers of thickness,  $d$ , with a "heavy" layer of thickness  $\Gamma d$  and scattering factor per unit volume,  $n(f_1 + if_2)$  and a "light" layer of thickness  $1 - \Gamma d$  and of scattering factor per unit volume  $n'(f_1' + if_2')$  we obtain from an integral equivalent of Eqs. (32) and (33) for such a system of continuous layers the following for the structure factor per unit volume.

$$\phi_{F1} = \frac{1}{m\pi} (nf_1 - n'f_1') \sin \Gamma m \pi. \quad (34)$$

and

**COMPARISON OF MULTILAYER MODEL CALCULATIONS**

CHARACTERISTIC MATRIX APPROACH (E & M BOUNDARY VALUE) -- LEE (1981)

MODIFIED DARWIN-PRINS -- LEE (1981)

MODIFIED DARWIN-PRINS -- HENKE (1981)

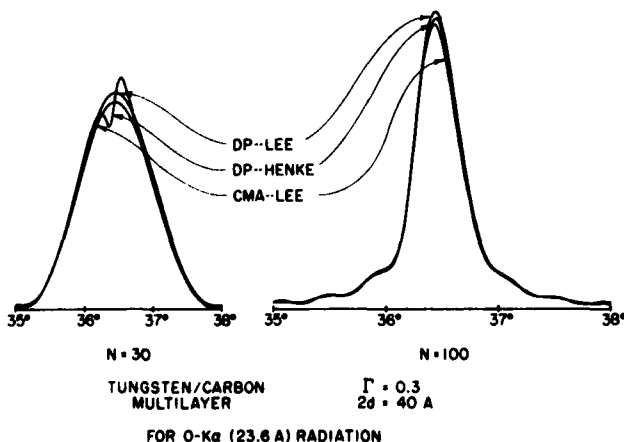


Figure 12

**EFFECTS OF INTERFACE DIFFUSION**

UPON THE STRUCTURE FACTOR/UNIT VOLUME --  $\phi_{F1} + i\phi_{F2}$   
AND THE ATOMIC SCATTERING FACTOR/UNIT VOLUME,  $nf_1 + inf_2$

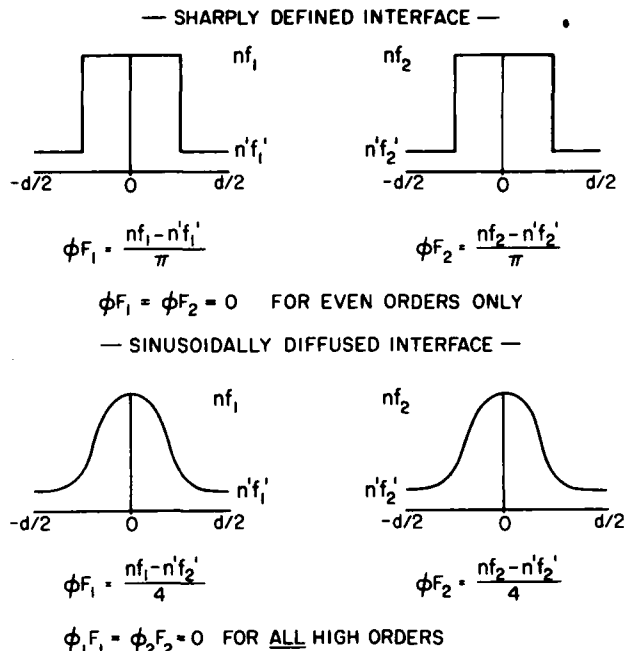


Figure 13

$$\phi_{F2} = \frac{1}{m\pi} (nf_2 - n'f_2') \sin \Gamma m \pi. \quad (35)$$

Lee [30] has recently reported an E & M boundary value solution for the periodic multilayer system as defined above using a characteristic matrix approach (CMA-Lee). He has shown that this rigorous solution for the intensity distribution at a diffraction peak will reduce to the Darwin-Prins expression for  $N_\infty$ , and that another relatively simple modified form of the Darwin-Prins equation can be written with a correction term that introduces a dependence upon a finite number of layers,  $N$ . These results have also been discussed in Ref. [1].

It is of interest to compare reflectivity curves for multilayer systems as predicted by the modified Darwin-Prins expression given in Eq. (31) (DP-Henke) with the rigorous result (CMA-Lee) and its reduced version (DP-Lee). These comparisons are presented in Fig. 12. These were calculated for the reflection of  $O-K\alpha$  (23.6 A/525 eV) radiation from a tungsten/carbon multilayer of  $2d = 40$  A,  $\Gamma = 0.3$  and for  $N$  equal to 30 and 100. It is interesting to note that the three descriptions yield essentially the same diffraction line widths and the modified Darwin-Prins expressions give somewhat higher peak values and consequently slightly higher integrated reflectivities.

As noted earlier, Smirnov et al. [28] have found the Darwin-Prins approach to be very effective in an analysis for the effects of surface roughness in x-ray reflection. They have shown that the same effects can be produced by a suitably chosen graded density interface as by a given surface roughness structure. It is suggested here that the sputtered/evaporated multilayer systems such as tungsten/carbon may exhibit changes in their reflectivity characteristics which can be explained either by interface roughness or equivalently by a graded tungsten carbide interface. For example, some of the tungsten/carbon multilayer systems which we have characterized spectroscopically have yielded essentially no high-order reflections for what were

**COMPARISON OF CALCULATED & EXPERIMENTAL FOR INTEGRATED REFLECTIVITY, R, AND ENERGY RESOLUTION,  $\Delta E$**

TUNGSTEN/CARBON MULTILAYER, 2d=44.2 Å, N=62,  $\Gamma=0.5$

CALCULATED-- (1) SHARPLY DEFINED AND  
(2) DIFFUSED INTERFACES

EXPERIMENTAL • HENKE, et al. (1980)

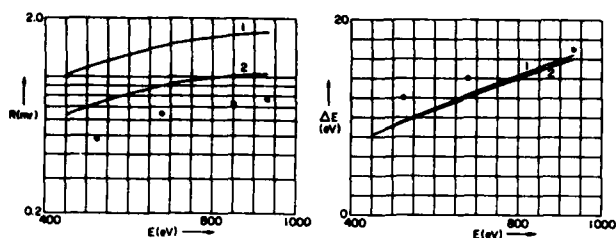


Figure 14

fabricated as  $\Gamma = 0.5$  multilayers. As may be noted from Eqs. (34) and (35), such multilayers should have zero intensity even-order reflections only if the interfaces are sharply defined. However, if we assume that the scattering factor per unit volume with the double layer varies sinusoidally, we calculate by integration a structure factor per unit volume that is of zero value for all high order reflections. In Fig. 13 these structure factors per unit volume for the sharply defined multilayer and for the corresponding diffused multilayer are presented. In Fig. 14 we show the calculated integrated reflectivities (R) and the diffraction line widths ( $\Delta E$ ) using the modified Darwin-Prins expression with  $\Delta F$  values for the two types of interface and compare these with our experimental data for the same multilayer system.

Many practical crystal and multilayer systems may also have a mosaic structure (illustrated schematically in Fig. 15) consisting of small crystal segments which, however, are usually large as compared with the wavelengths involved, and the normals to each crystal segment face have a random, small angle distribution about an average normal to the macroscopic total crystal surface. The width of the associated rocking curve,  $I(\theta)$ , from such a mosaic crystal is thereby increased by this angular distribution width which is usually not predictable. Nevertheless, the total area under the rocking curve, i.e., the integrated reflectivity, is not dependent upon the degree of mosaic alignment and can be simply calculated using a kinematical model. This is because one may usually assume that the crystal segment thickness is such that each atomic plane receives essentially the same incident intensity (negligible absorption within the crystallite). Summing over the differential amplitudes for the small crystal to obtain the amplitude of reflection and then squaring to obtain the intensity of reflection per crystal segment, adding

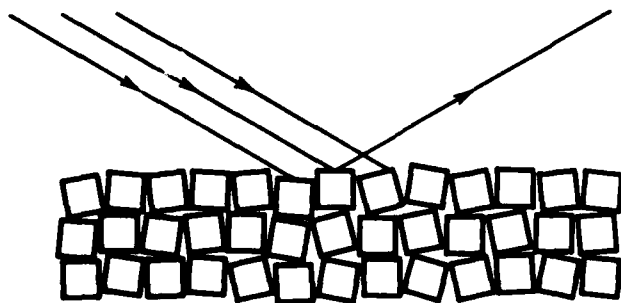


Figure 15

these intensities over the mosaic collection (assuming their amplitudes are in random phase) and finally integrating over angles the integrated reflectivity for a mosaic crystal,  $R_m$ , is obtained [2,3] which may be written as

$$R_m = \frac{v_0^2 \lambda^4 [(\phi F_1)^2 + (\phi F_2)^2]}{16\pi B} [1 - \exp(-\frac{2\mu t}{\sin \theta_0})] \times \frac{1 + \cos^2 2\theta_0}{\sin 2\theta_0}, \quad (36)$$

where, for a finite mosaic crystal,  $\nu$ ,  $\rho$  and  $t$  are the mass photoionization cross section, the average density and the thickness, respectively.

In Ref. [1] we have presented detailed tables and plots characterizing five examples each of the three important, practical analyzer systems that are effective in low energy x-ray spectroscopy, viz., the sputtered/evaporated multilayers, the molecular multilayers (Langmuir-Blodgett type) and the acid phthalate crystals. Presented here in Figs. 16, 17 and 18 are examples of such calculations using the methods and the atomic scattering factors as described here. The calculated characteristics for the tungsten/carbon multilayer, the lead myristate molecular multilayer and the thallium acid phthalate crystal plotted here are the integrated reflectivities,  $R_m$ , in milliradians (mosaic) and  $R_p$  (by integrating under the modified Darwin-Prins rocking curve), the percent reflectivity,  $P(\%)$ , at the diffraction peak, the full-width-at-half-maximum of the rocking curve in eV, and the resolving power  $E/\Delta E$ .

Finally it is of considerable current interest in x-ray optics development to determine the characteristics of Bragg reflection from multilayers and crystals at near normal incidence (for example, for possible applications in x-ray interferometers, for end "mirrors" in x-ray laser cavities, or for reflective coatings for normal incidence mirror optics for x-ray telescopes and microscopes). At near-normal incidence, the width of the diffraction pattern for a given wavelength becomes appreciably broadened and it is important not to approximate  $\xi$  as given exact in Eq. (26) in terms of the difference angle,  $\theta - \theta_0$ , as is usually done in x-ray Bragg reflection descriptions. [2,3] If the diffraction width is appreciably broadened, it may be important not to use the approximate expressions (32) and (33) for the structure factor components but rather the exact expressions (8) and (9). It may not be sufficiently accurate to discard terms of higher order than  $\xi^2$  in either the characteristic matrix approach [30] or in the Darwin-Prins approach.

As an example of a normal incidence calculation, we have calculated the rocking curve at about  $\theta = 90^\circ$  for a multilayer of tungsten/carbon of  $\Gamma = 0.4$ . The 2d values were obtained for each of five wavelengths in the low energy x-ray region by maximizing the respective intensities for  $90^\circ$  incidence. We have used the CMA model relation of Lee [30] for these calculations and have plotted the diffraction curve for  $0-K\alpha$  (23.6 Å/525 eV) and have compared the wavelengths with the optimized 2d-values in Fig. 19.

### III. CONCLUSIONS--SOME COMPARISONS WITH EXPERIMENT

The predictions of the characteristics of Bragg reflection from multilayers and crystals are usually very sensitive to the appropriateness of the models that are adopted and to the atomic scattering factor data that is used. The experimental characterization of these systems can thus be an important test of the methods and of the atomic scattering factor data that have been presented here.

At this time, it is not possible to define accurately the detailed structure of the "synthetic crystals" such as the sputtered/evaporated and the molecular multilayers as we might crystallographically

**TUNGSTEN-CARBON MULTILAYER**  
 $2d = 40 \text{ \AA}$      $\Gamma = 0.4$      $N = 100$

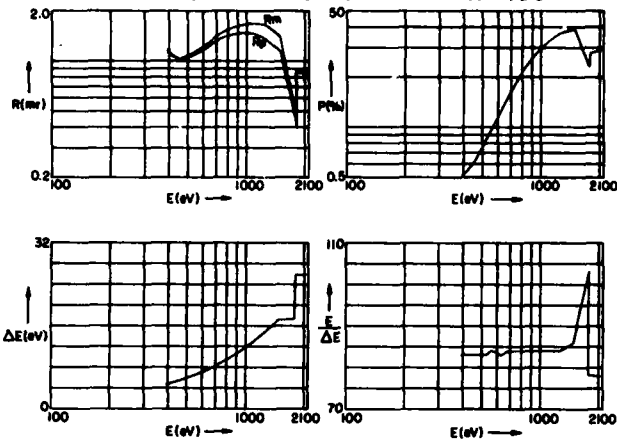


Figure 16

**LEAD MYRISTATE**     $N = 100$      $2d = 80 \text{ \AA}$

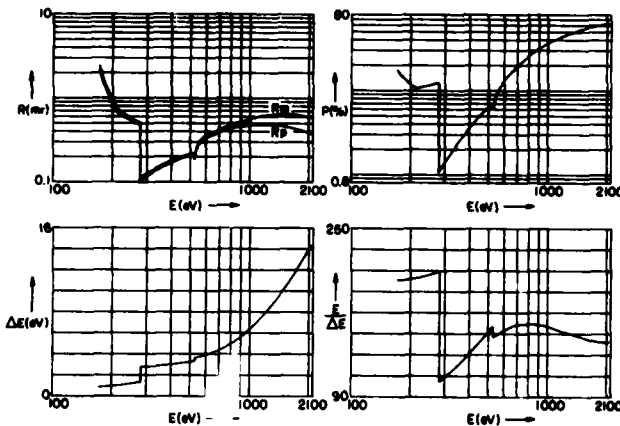


Figure 17

**THALLIUM ACID PHTHALATE**     $2d = 25.90 \text{ \AA}$

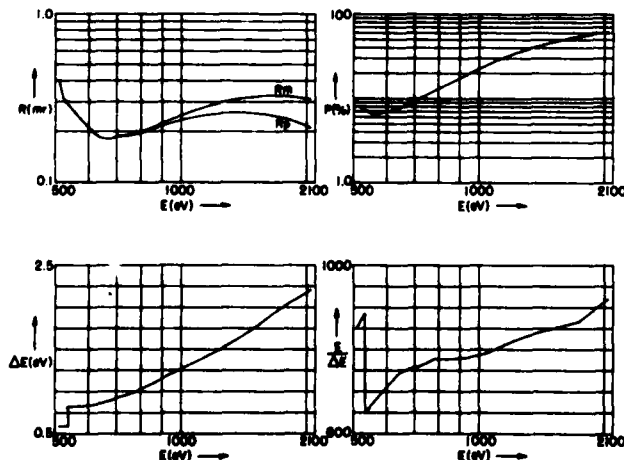


Figure 18

**NORMAL INCIDENCE REFLECTIVITY -- 23.6 \AA**

TUNGSTEN/CARBON MULTILAYER     $\Gamma = 0.4$      $N = 100$

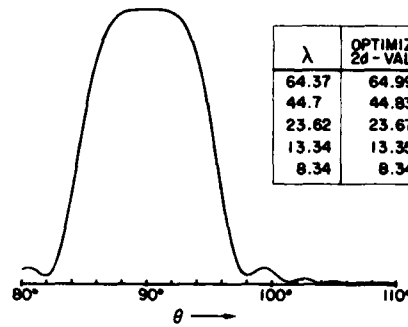


Figure 19

$\lambda$	OPTIMIZED $2d$ -VALUE	% REFLECTION AT $90^\circ$	
		CMA-LEE	DP-LEE
64.37	64.99	17.2	18.6
44.7	44.83	21.9	23.0
23.62	23.67	7.96	8.11
13.34	13.35	2.59	2.63
8.34	8.34	0.385	0.396

for the acid phthalate crystals, for example. Nevertheless, within the limits of experimental uncertainty, we feel that the agreement of the present experimental data with the calculations that have been described here has been generally very good.

In Fig. 14 we have presented a comparison of the measured values for the integrated reflection from a tungsten/carbon multilayer system. Here we have addressed the question as to the effect of a possible interface roughness or, equivalently, a graded tungsten carbide diffused interface upon the integrated reflectivity (for which the experimental values invariably fall somewhat below predicted values for the sputtered/evaporated systems). In Figs. 20 and 21 we present the integrated reflectivities vs photon energy for the molecular multilayer, lead myristate, and for the potassium acid phthalate crystal as calculated by the mosaic model and by the modified Darwin-Prins model. We compare these theoretical curves with our experimental values.

It is very important to note here, in Fig. 21, that the measured integrated reflectivity curve near the oxygen-K absorption edge (Blake et al. [31]) reveals a very sharp "spike" in the reflection at about 532 eV. This is a rather dramatic example of threshold structure that cannot be predicted with the calculated scattering factor data as has been discussed in Sec. I. Such effects may need to be explained on the basis of a detailed consideration of the electronic states of the crystal including excitonic. Presented elsewhere in these proceedings by R. L. Blake will be a complete description of the excellent measurements of this threshold resonance reflection effect.

**ACKNOWLEDGEMENTS**

The author gratefully acknowledges the invaluable assistance in the preparation of this work of Priscilla Piano, Tina Tanaka, Brian Fujikawa and Hubert Yamada. This program is supported by a grant from the Air Force Office of Scientific Research, Grant No. 79-0027, and by a supplemental DOE/Lawrence Livermore Laboratory subcontract, No. 9072209.

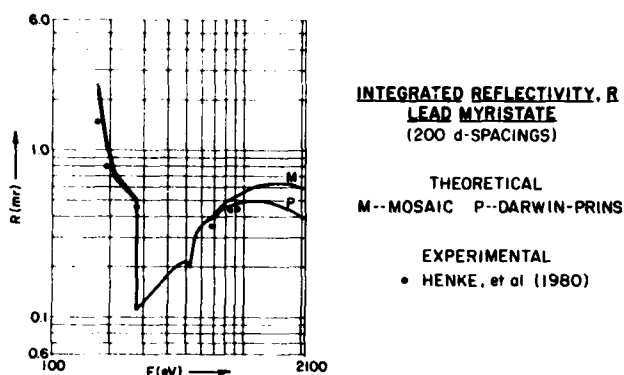


Figure 20

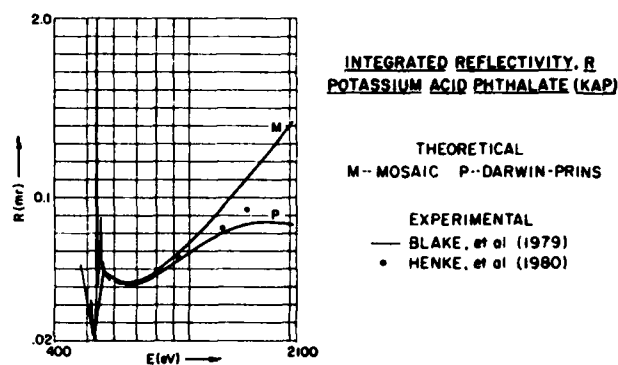


Figure 21

## REFERENCES

- [1] B. L. Henke, P. Lee, T. J. Tanaka, R. Shimabukuro and B. K. Fujikawa, *Atomic Data and Nuclear Data Tables* **27**, No. 1. (1982).
- [2] A. H. Compton and S. K. Allison, *X-Rays in Theory and Experiment*, 2nd ed. (Van Nostrand, New York, 1935).
- [3] R. W. James, *The Optical Principles of Diffraction of X-Rays* (Cornell University Press, Ithaca, New York, 1965).
- [4] D. T. Cromer and D. Lieberman, *J. Chem. Phys.* **53**, 1891 (1970).
- [5] M. S. Jensen, *Phys. Lett.* **74A**, 41 (1979).
- [6] H. J. Hagemann, W. Gudat and C. Kunz, "Optical Constants from the Far Infrared to the X-Ray Region: Mg, Al, Cu, Ag, Au, Bi, C and Al<sub>2</sub>O<sub>3</sub>," *Deutsches Elektronen-Synchrotron (DESY) SR-74/7* (1974).
- [7] R. F. Reilman and S. T. Manson, *Astrophys. J. Supp. Ser.* **40**, 815 (1979).
- [8] V. A. Fomichev and A. P. Lukirskii, *Opt. Spectrosc.* **22**, 432 (1967).
- [9] J. B. West and G. V. Marr, *Proc. R. Soc. Lond. A* **349**, 397 (1976).
- [10] J. A. Samson, *Handbuch der Physik* **31** (1980).
- [11] H. W. Wolff, K. Radler, B. Sonntag and R. Haensel, *Z. Phys.* **257**, 353 (1972).
- [12] R. Bruhn, B. Sonntag and H. W. Wolff, *J. Phys. B* **12**, 203 (1979).
- [13] P. Rabe, K. Radler, H. W. Wolff, *Vacuum Ultraviolet Radiation Physics* (Pergamon Vieweg, Berlin, 1974), p. 247.
- [14] C. Kunz, *Comments Solid State Physics* **2A**, 31 (1973).
- [15] P. J. Mallozzi, R. E. Schwerzel, H. M. Epstein and B. E. Campbell, *Phys. Rev. A* **23**, 824 (1981).
- [16] C. Kunz, *J. Phys. (Paris) Coll. C4* **32**, Supp. 10, 180 (1971).
- [17] F. Combet-Farnoux, *J. Phys. (Paris) Coll. C4* **39**, Supp. 7, 1 (1978).
- [18] B. Sonntag, *J. Phys. (Paris) Coll. C4* **39**, Supp. 7, 9 (1978).
- [19] C. G. Darwin, *Philos. Mag.* **27**, 315, 675 (1914).
- [20] J. A. Prins, *Z. Phys.* **63**, 477 (1930).
- [21] L. A. Smirnov, *Opt. Spectrosc. (USSR)* **43**, 333 (1977).
- [22] B. L. Henke, *Phys. Rev. A* **6**, 94 (1972).
- [23] B. L. Henke, J. P. Knauer and K. Premaratne, *J. Appl. Phys.* (March 1981).
- [24] B. L. Henke and J. W. M. DuMond, *J. Appl. Phys.* **26**, 903 (1955).
- [25] G. Mie, *Ann. Physik* **25**, 377 (1908).
- [26] R. W. Hart and E. W. Montroll, *J. Appl. Phys.* **22**, 376 (1951).
- [27] H. C. van de Hulst, *Optics of Spherical Particles* (N. V. Drukkerij, D. F. Duwaer en Zoon, Amsterdam, 1946).
- [28] L. A. Smirnov, T. D. Sotnikova, B. S. Anokhin and B. Z. Taibin, *Opt. Spectrosc. (USSR)* **46**, 329 (1979).
- [29] A. I. Mahan, *J. Opt. Soc. Am.* **46**, 913 (1956).
- [30] P. Lee, *Opt. Commun.* **37**, 159 (1981).
- [31] R. L. Blake, private communication.



Dr. Burton Henke during his presentation on low energy x-ray scattering factors.



Theory of Sub-keV Photoionization Cross Sections  
 Steven T. Manson  
 Department of Physics and Astronomy, Georgia State University  
 Atlanta, Georgia 30303

ABSTRACT

An overview of the calculation of photoionization cross sections for  $h\nu < 1$  keV is presented with particular emphasis on providing a guide for evaluating the accuracy of theoretical work. An attempt is made to focus upon the various approximations made in each level of calculation and point out in which ranges they should be good. Central-field, Hartree-Fock, and more sophisticated methods are reviewed, particularly as they apply to free atoms and ions. In addition, the striking similarity of such calculated cross sections to core level photoemission in solids is pointed out.

I. INTRODUCTION

The photoelectric effect, which is the overwhelmingly predominant mechanism of absorption of  $h\nu \leq 1$  keV electromagnetic radiation by matter, was one of the earliest harbingers of the breakdown of classical physics. Its discovery, well back in the nineteenth century, was followed by the explanation of the phenomenon in 1905 by Einstein.<sup>1</sup> By the end of the 1920's, with the Schrödinger and Dirac equations on firm ground, the basic theory of photoionization was worked out. An excellent review which includes this theory was written in 1933 by Bethe<sup>2</sup>; a slightly later one on photoionization exclusively was written in 1936 by Hall.<sup>3</sup>

Once the theory was set down, the problem of calculating photoionization cross sections became one of obtaining wave functions for the initial discrete and final continuum states of the system. For the hydrogen atom this can be done exactly, but for many electron systems, it cannot. The thrust of this paper, then, is to go through various of the methodologies employed for obtaining photoionization cross sections theoretically with particular emphasis on the physical approximations made at each level of calculation as well as an estimate of the accuracy of each level along with the energy range in which is expected to be useful. This is done in an effort to give experimentalists and "consumers" of such calculations the tools to assess the accuracy of published results since theoretical papers rarely, if ever, include error bars.

The literature in this field is considerable and it would be a tremendous task to attempt to give references to all of the relevant papers. Thus indicative examples, rather than complete coverages, are aimed at. In addition, references are made to other reviews, where possible, in an attempt to give access to as much of the extant literature as possible.

In this paper we shall restrict our attention to the calculation of total and subsell cross sections for free atoms and ions. Some comments shall be made about the applicability of such results to solids, however. Photoelectron angular distributions shall be omitted entirely; for reviews on that subject, see Refs. 4-8.

II. GENERAL THEORY OF PHOTOIONIZATION CROSS SECTIONS

In the photoionization process, a photon of energy  $h\nu$  collides with a target in state  $i$  and gets absorbed, its energy going to an electron which is ejected leaving the residual ion in state  $j$ , i.e.,

$$h\nu + A(i) \rightarrow A(j)^+ + e^- \quad (1)$$

Usually  $i$  and  $j$  refer to the ground states of  $A$  and  $A^+$  respectively, but they may, in principle, be excited states as well. The fundamental relationship for the energetics is a photoionization process as given by<sup>9</sup>

$$\epsilon = h\nu - I_{ij} \quad (2)$$

where  $\epsilon$  is the kinetic energy of the photoelectron and  $I_{ij}$  is the ionization energy.

The photoionization cross section for a system in

state  $i$  by an unpolarized photon beam of energy  $h\nu$  leaving the system in a final state  $f$  consisting of a photoelectron of energy  $\epsilon$  plus ions in state  $j$  is given by<sup>9</sup>

$$\sigma_{ij}(\epsilon) = (4\pi^2\alpha a_0^2/3g_i)(\epsilon + I_{ij})|M_{if}|^2 \quad (3)$$

where  $\alpha$  is the fine structure constant ( $1/137$ ),  $a_0$  is the Bohr radius ( $5.29 \times 10^{-9}$  cm),  $g_i$  is the statistical weight of the initial discrete state, and the ionization energy  $I_{ij}$  and the photoelectron energy  $\epsilon$  are expressed in Rydbergs (13.6 eV). The matrix element, expressed in Rydberg atomic units, is given by<sup>10</sup>

$$|M_{if}|^2 = \frac{4}{(I_{ij} + \epsilon)^2} \sum_{i,f} \left| \langle f | \sum_{\mu} \exp(i\vec{k}_\nu \cdot \vec{r}_\mu) \vec{\nabla}_\mu | i \rangle \right|^2 \quad (4)$$

with the summation over  $i, f$  being the sum over the degenerate initial and final states respectively,  $\vec{r}_\mu$  is the position coordinate of the  $\mu$ th electron,  $\vec{k}_\nu$  is the propagation vector of the photon ( $|\vec{k}_\nu| = 2\pi\nu/c$ ), and the wave functions are normalized such that for the initial discrete state  $|i\rangle$

$$\langle i | i \rangle = 1, \quad (5)$$

and for the final continuum state  $|f\rangle (= |j, \epsilon\rangle)$

$$\langle j, \epsilon | j', \epsilon' \rangle = \delta_{jj'} \delta(\epsilon - \epsilon'). \quad (6)$$

Up to this point the theory is essentially exact. By "essentially" is meant that Eq. (3) is really a first-order perturbation theory.<sup>11</sup> It is to be noted, however, that the second-order perturbation result is a factor of  $\alpha$  ( $1/137$ ) smaller than the first-order. Thus, it is an excellent approximation to neglect it and all higher order contributions.

In addition, for incident photon energies below several keV, the  $\exp(i\vec{k}_\nu \cdot \vec{r}_\mu)$  term in the matrix element Eq. (4) can be approximated. This is done by noting that the major concentration of wave function amplitude is around a distance from the nucleus,  $\vec{r}_\mu$ , of the order of the Bohr radius. Thus, for photon energies below several keV,  $\vec{k}_\nu \cdot \vec{r}_\mu$  is small enough so that  $\exp(i\vec{k}_\nu \cdot \vec{r}_\mu)$  can be approximated very well by unity.

Actually, the approximation for cross sections is much better than is implied by the discussion. This is because expanding the exponential out gives  $1 + i\vec{k}_\nu \cdot \vec{r}_\mu$  and taking the absolute square yields  $1 + (\vec{k}_\nu \cdot \vec{r}_\mu)^2$  so we really need have only  $(\vec{k}_\nu \cdot \vec{r}_\mu)^2$  very small compared to unity for the approximation to be valid. This approximation simplifies the matrix element considerably and is known as the "dipole approximation" or "neglect of retardation." The matrix element  $M_{if}$  can then be written<sup>10</sup>

$$M_{if} = \frac{4}{(I_{ij} + \epsilon)^2} \sum_{i,f} \left| \langle f | \sum_{\mu} \vec{\nabla}_\mu | i \rangle \right|^2 = \sum_{i,f} \left| \langle f | \sum_{\mu} \vec{r}_\mu | i \rangle \right|^2 \quad (7)$$

and it is seen that the problem of calculation of photo-

ionization cross sections reduces to one of finding wave functions for initial and final states. The details of the transformation of the matrix element in Eq. (7) are given elsewhere.<sup>4,6,10</sup>

The first expression in Eq. (7) is known as the dipole-velocity (or just "velocity") form of the matrix element while the last is the dipole-length (often referred to as "length"). These two alternate forms of the matrix element (actually there are others which are used infrequently in practice<sup>4,6,10</sup>) are shown to be equal when exact wave functions are used.

Of course, for atomic systems other than hydrogen, exact wave functions are not available. In the case of approximate wave functions, the results of using the various expressions for the dipole matrix element can differ considerably from each other and from the correct answer. On the other hand, it is possible that both expressions might give the same result with approximate wave functions, and that this result might still be incorrect. This point will be discussed further in connection with central field wave functions below. We thus see that equality among the results of the alternative forms of the dipole matrix element is a necessary but not sufficient condition for the correctness of that result. The question as to which form of the matrix element should be more accurate has been discussed,<sup>12-15</sup> but no definitive conclusion has been reached.

### III. CENTRAL FIELD CALCULATIONS

The simplest type of wave functions which are useful in calculating photoionization cross sections are those based on a central-field approximation to the exact Hamiltonian, i.e., one considers the solution to the approximate Hamiltonian

$$H_0 = \sum_{\mu} [(P_{\mu}^2/2m) + U(r_{\mu})] \quad (8)$$

for the initial and final states of the atom or ion. Note that  $U(r_{\mu})$ , the central potential seen by each electron, is a function of scalar  $r_{\mu}$  only. The solutions to  $H_0$  are antisymmetric products of one-electron wave functions,  $r^{-1}P_{n_1}(r)Y_{l_1}^m(\theta, \phi)$  [ $r^{-1}P_{\epsilon_1}(r)Y_{l_1}^m(\theta, \phi)$  for continuum electrons]. The radial parts of the one-electron functions are solutions to the one-body Schrödinger equation

$$\left[ \frac{d^2}{dr^2} - \frac{l(l+1)}{r^2} - U(r) + E \right] P(r) = 0 \quad (9)$$

for both discrete and continuum functions. Eq. (9) has  $r$  in atomic units and energies in Rydbergs. In using central-field wave functions, then, only the one electron is permitted to change quantum numbers in the photoionization process or the matrix element vanishes. Thus, multiple transitions are specifically excluded. Further, since the initial and final states are solutions to the Schrödinger equation in the same central  $U(r)$ , the orbitals not directly involved in the photoionizing transition remain unchanged. The rearrangement of the remaining electrons after a transition is known as core relaxation, i.e., core relaxation effects are excluded in the central-field model. Therefore, the nonparticipating orbitals integrate out to unity in the dipole matrix element and the photoionization cross section for an  $n_1$  electron can be written in dipole-length form as<sup>16</sup>

$$\sigma_{n_1}(\epsilon) = \frac{4}{3} \pi^2 a_0^2 \frac{N_{n_1}(\epsilon - \epsilon_{n_1})}{2l+1} [R_{l-1}(\epsilon)^2 + (l+1)R_{l+1}(\epsilon)^2], \quad (10)$$

with  $\epsilon_{n_1}$  the binding energy of an  $n_1$  electron (explicitly negative),  $N_{n_1}$  the occupation number of the  $n_1$

subshell, and the matrix element

$$R_{l\pm 1}(\epsilon) = \int_0^{\infty} P_{n_1}(r) r P_{\epsilon, l\pm 1}(r) dr, \quad (11)$$

where the continuum normalization, from Eq. (6) takes the form

$$P_{\epsilon l}(r) \xrightarrow{r \rightarrow \infty} \pi^{-1/2} \epsilon^{-1/2} \sin[\epsilon^{1/2} r - l\pi/2 - \epsilon^{-1/2} \ln 2\epsilon^{1/2} r + \sigma_l(\epsilon) + \delta_l(\epsilon)], \quad (12)$$

where  $\sigma_l(\epsilon) = \text{Arg } \Gamma(1 + l - i\epsilon^{-1/2})$  and  $\delta_l(\epsilon)$  is the phase shift. It is thus seen that the central-field calculation reduces the problem to a one-electron model of the photoionization process involving only the wave function of the photoelectron before and after the photoionization, and a single-electron Hamiltonian

$$h_0 = (P^2/2m) + U(r) \quad (13)$$

to which each is a solution.

An interesting property of the one-electron model is that the various alternative forms of the dipole matrix element, discussed above, must be equal<sup>14</sup> which shows that equality of "length" and "velocity" is no guarantee of agreement with experiment. In the central field case the alternative forms of the dipole matrix element, then, give no information as to how close to experiment the results of a central-field calculation are. They do, however, provide a powerful check on the numerical methods used in the computation. It is almost impossible, for example, to have an error in the calculation of the dipole matrix element and still retain the equality of length and velocity.

Up to this point, the detailed form of the central potential has not been dealt with. A number of choices exist and discussion of them is treated elsewhere.<sup>4</sup> It must be pointed out, however, that a reasonable potential must have the correct boundary conditions

$$U(r) \xrightarrow{r \rightarrow 0} -Z/r, \quad U(r) \xrightarrow{r \rightarrow \infty} -2/r, \quad (14)$$

in Rydbergs. A number of such potentials have been used but the most common is the Hartree-Slater (HS) potential<sup>17,18</sup> with which numerous calculations have been performed for both atoms<sup>4-7,19,20</sup> and ions.<sup>21</sup>

The strengths and weaknesses of such an approach can best be spotlighted by examples. In Fig. 1, the calculated total photoionization cross section for xenon<sup>19</sup> from threshold to above 1 keV is shown, along with experimental results.<sup>22-24</sup> From this figure, very good overall agreement in general shape is found. In addition away from the 5p and 4d ( $N_{4,5}$ ) thresholds, quantitative agreement is pretty good as well. Near those thresholds, however, there are discrepancies between the central field calculation and experiment which are as large as a factor of two.

Fig. 1 also exhibits some of the important features of photoionization cross sections.<sup>25</sup> One is the fact that each subshell cross section does not necessarily decrease monotonically from threshold. These maxima above threshold are called delayed maxima<sup>19</sup> and are caused by the angular momentum barriers in the  $n_1 + \epsilon_1 + 1$  photoionization channels. The effective potential, as seen by the continuum electron, has a repulsive centrifugal term which keeps the  $l+1$  continuum wave function very small in the core region near threshold. Thus the overlap with the bound state wave function is small, making the matrix element small and, thereby, the cross section small. With increasing energy, however, the continuum wave function begins to penetrate the barrier, increasing the overlap and increasing the cross section above the threshold value. As an example, the wave

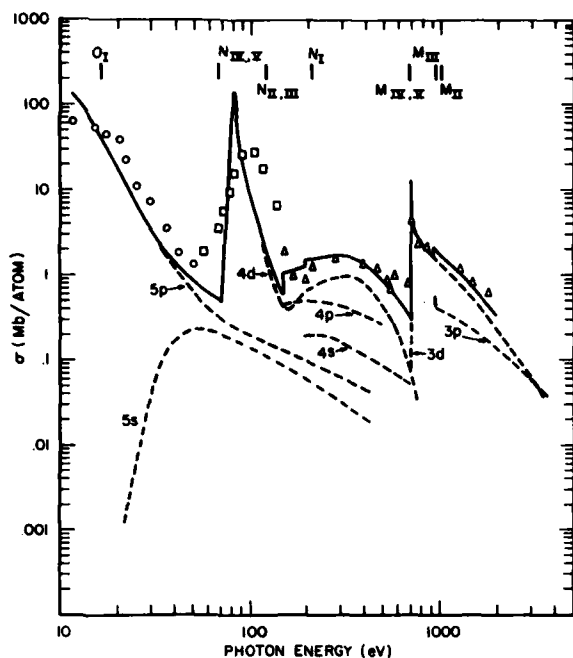


Fig. 1. Photoionization cross section of xenon. The total and subshell central field HS results<sup>19</sup> are shown in solid and dashed curves respectively, and the experimental results are shown as circles,<sup>22</sup> squares,<sup>24</sup> and triangles.<sup>23</sup>

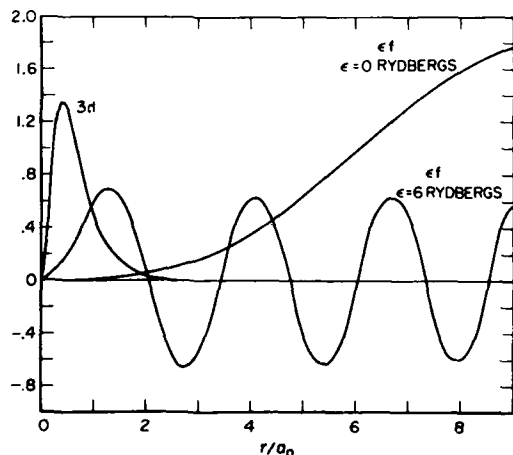


Fig. 2. The normalized 3d and  $\epsilon f$  HS central field wave functions for krypton.<sup>19</sup>

functions for the  $3d \rightarrow \epsilon f$  transition in krypton<sup>19</sup> are shown in Fig. 2 for two different continuum energies where the "penetration" of the continuum wave function with increasing energy is clearly seen.

Another feature shown in Fig. 1 is a minimum in a subshell cross section (and indeed in the total cross section) for the 4d subshell at  $h\nu \approx 140$  eV. This minimum, known as a Cooper minimum,<sup>25,26</sup> is caused by the complicated overlap between discrete and continuum wave functions in the  $l \rightarrow l+1$  transitions of outer and near outer subshells whose wave functions are not nodeless, i.e., not 1s, 2p, 3d, or 4f. When the overlap is such that the positive contributions to the matrix element

just cancel the negative contributions, a zero occurs in the  $l \rightarrow l+1$  dipole matrix element. In general it is not a zero minimum, even in the subshell cross section, because the degenerate  $l \rightarrow l-1$  transition matrix element does not vanish.

In any case, it is seen from Fig. 1 that the HS calculation does a reasonable job of reproducing both the delayed maxima and the Cooper minimum. In fact, it is quite good in the region between about 150 eV and 700 eV where the dominant contribution to the total cross section comes from the second maximum in the 4d cross section.

The discrepancies between theory and experiment near the thresholds are due to the fact that correlation is not included and that exchange is included only approximately via a central field. Before proceeding to a discussion of more exact treatments of photoionization, it is worthwhile to point out how the central field model applies to photoionization of ions.

For ions, there are only a very few photoionization measurements for singly charged ions<sup>21</sup> ( $\text{Li}^+$ ,  $\text{Na}^+$ , and  $\text{Ar}^+$ ) and none at all for multicharged ions. Despite this lack of experimental information, some general idea of the accuracy of central field calculation can be obtained by extrapolation from the neutrals. Looking at the Hamiltonian for an atom or ion with nuclear charge  $Z$ ,

$$H = \sum_i \left( \frac{p_i^2}{2m} - \frac{Ze^2}{r_i} \right) + \sum_{i \neq j} \frac{e^2}{r_{ij}}, \quad (15)$$

we note that it is the last term, the interelectron repulsion, that is a non-central force so it is just this term that is being approximated in a central field model. Noting further that  $1/r_i$  and  $1/r_{ij}$  vary as  $Z$ ,

roughly speaking, then the central nuclear attraction goes as  $-Z^2$  while the non-central term goes as  $-Z$ . Thus the ratio of the non-central to the central potential is  $-1/Z$  so that going along an isoelectronic sequence, i.e., increasing  $Z$  with a constant number of electrons, the non-central term becomes a smaller part of the total Hamiltonian. Since this is the very term being approximated, the approximation gets better for

ions as opposed to atoms.<sup>17</sup> Thus we conclude that central field calculations will give about  $\pm 20\%$  accuracy for atoms away from threshold features such as delayed maxima and Cooper minima; in the vicinity of the features the accuracy will be only a factor of two. For ions, the situation improves slowly as we go to higher and higher charge states for reasons described above as well as the fact that the various features move below threshold with increasing stage of ionization. A tabulation of total cross sections for all atoms and ions with  $Z \leq 30$  predicted by the HS central field calculation has been published.<sup>21</sup>

#### IV. HARTREE-FOCK CALCULATIONS

The simplicity of wave functions consisting of single Slater determinants<sup>28</sup>, i.e., antisymmetric products of one-electron functions, can be maintained while still treating exchange correctly. This is the Hartree-Fock (HF) method.<sup>29</sup> For calculations of discrete state wave functions, the method has been reviewed by Hartree<sup>29,30</sup> and Slater<sup>28</sup> among others. In addition, recent tabulations of extensive sets of HF discrete state wave functions have been reported.<sup>31</sup> Basically the method involves setting up a wave function  $\psi$  for the system in question, which is an antisymmetric product of one-electron functions,  $r^{-1}P_{n_l}(r)V_l^m(\theta, \phi)$ , or, more generally, a linear combination of such products so as to correctly represent the angular momentum couplings of many-electron system. The  $P_{n_l}(r)$  are treated as unknowns and the so-called energy functional

$\langle \psi | H | \psi \rangle$  is constructed;  $H$  is the exact nonrelativistic Hamiltonian. The variation principle is then applied to this functional subject to the constraints of the orthonormality of the one-electron functions. This results in a set of self-consistent coupled integro-differential equations for the  $P_{n1}(r)$  which can then be solved, yielding the HF wave functions for the given state. Note that the HF wave function is the most accurate independent-particle wave possible since it is obtained via the variation principle.

Dealing with the final continuum state resulting from the photoionization process is more difficult since the HF problem is not defined for wave functions containing continuum orbitals. This is because the HF method solves for each orbital in the field generated by the charge distribution of the other orbitals. The charge distribution for a continuum orbital is not defined since continuum orbitals are non-normalizable. Thus, one proceeds as follows: first a HF calculation for the residual ion core minus photoelectron is performed. This can be done by ordinary discrete state HF procedures as described above, although some extra care must be taken when the photoelectron comes from an inner shell and the ion core is in an excited state

well above the ionization threshold.<sup>32</sup> This done, the core orbitals are frozen and the above HF procedure can be carried out for the total ion core plus photoelectron final state with only the radial part of the continuum orbital,  $P_{e1}(r)$ , unknown. This procedure yields a single integrodifferential equation for  $P_{e1}(r)$  which is known as the continuum HF equation. The details of this method for various cases are given elsewhere.<sup>33-36</sup>

As an example of the accuracy of the HF method, Fig. 3 shows the situation for the total cross section in xenon,<sup>36</sup> just as was shown in Fig. 1 for the central field calculation. Here we see that the agreement with experiment is considerably better than before, although there still are discrepancies in the regions close to the various thresholds, but not longer a factor of two but only as bad as 40-50%. Further the difference between "length" and "velocity" results really do give an indication of the accuracy of the calculated cross sections. Thus HF represents a considerable improvement over a central field calculation, showing the importance of the exchange interaction. The remaining discrepancies are due to the neglect of correlation, which must be included either explicitly or via multiconfiguration wave functions for quantitative accuracy near the outer shell thresholds where delayed maxima and Cooper minima are exhibited. Where these features are not manifested, as in the case of neon<sup>36</sup> shown in Fig. 4, we find excellent

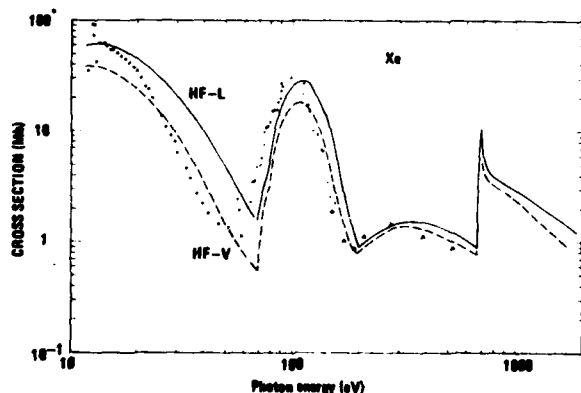


Fig. 3. Total photoionization cross section for Xe. The theoretical HF results in "length" and "velocity" approximations are shown<sup>36</sup> along with experimental results as in Fig. 1.

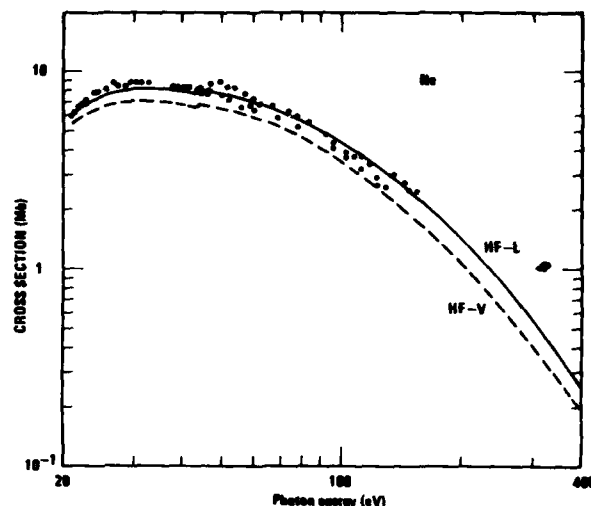


Fig. 4. Total photoionization energy cross section for Ne. The theoretical HF results in "length" and "velocity" approximations are shown<sup>36</sup> along with experimental results as in Fig. 1.

agreement with experiment as well as excellent agreement between "length" and "velocity".

#### V. SOPHISTICATED CALCULATIONS

To go beyond the HF approximation, correlation must be included. The way this is generally done is by employing multiconfiguration wave functions for initial and final states of the system. There are a number of methodologies employed for these calculations which strive for quantitative accuracy, notably many-body-perturbation-theory (MBPT), the random phase approximation (RPA), and R-matrix theory. MBPT is, as the name implies, a form of perturbation theory, developed some years ago.<sup>37,38</sup> It can in principle, be carried out to arbitrarily high order for as much accuracy as one might wish. It does however, have infinite sums as do all perturbation theories and so, in practice, approximations must be made, but it is still a very useful technique.<sup>39,40</sup> The RPA calculation is, in some ways, closely related to MBPT, although it can be derived in other ways also.<sup>41,42</sup> In essence RPA represents the sum to infinite order of certain classes of perturbation terms in MBPT, generally via the solution of coupled integro-differential equations.<sup>43,44</sup> Other classes of perturbation terms are omitted entirely, however. Thus, in a given situation, RPA may or may not be a useful technique, depending upon which perturbation terms are of importance. A further advantage of RPA is that the equality of "length" and "velocity" is preserved but, at present, its applicability is limited to closed shell systems.

The R-matrix method, as used,<sup>45</sup> is essentially a scheme in which the exact wave function is expanded in the large  $r$  region in a complete set (which is, of course, infinite) and truncated. Certain of the terms in the wave function, those referring to the continuum photoelectron, are left undetermined and they are obtained using a variational principle.<sup>45,46</sup> This might be considered multiconfiguration Hartree-Fock. In addition, in the inner region, the photoelectron is treated on the same footing as the bound electrons, and a different expansion is used. The inner and outer wave functions are joined at some intermediate value of  $r$  using the R-matrix.<sup>45,47</sup> The treatment of the wave function in the outer region is known as the close coupling approximation.<sup>48</sup> In this method the crucial point is which terms are to be included in the truncat-

ed summation.

As an example of the utility of these methods, the threshold region for the photoionization of argon is

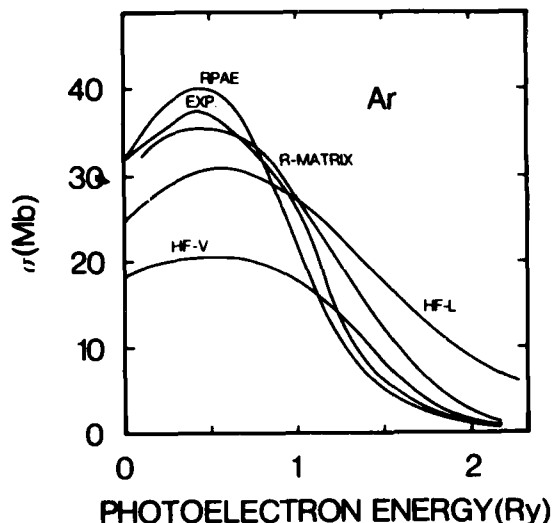


Fig. 5. Total photoionization cross section of argon. The theoretical RPA,<sup>43</sup> R-matrix,<sup>45</sup> and HF<sup>36</sup> results are shown along with the experimental<sup>49,50</sup> results.

ed summation.

As an example of the utility of these methods, the threshold region for the photoionization of argon is shown in Fig. 5 (note the linear scale) where it is seen that the HF results<sup>36</sup> are fair but both RPA<sup>43</sup> and R-matrix<sup>48</sup> give excellent agreement with experiment.<sup>49,50</sup>

In other instances, however, correlation can play a much larger role. This occurs particularly when the photoionization of a subshell with a small cross section is degenerate with one having a large cross section, i.e., when a given photon can ionize from both subshells, one with a much greater cross section. Such a case occurs for Ar 3s since it is so close to Ar 3p so that multiconfiguration effects are crucial. The situation is shown in Fig. 6 where it is seen that the

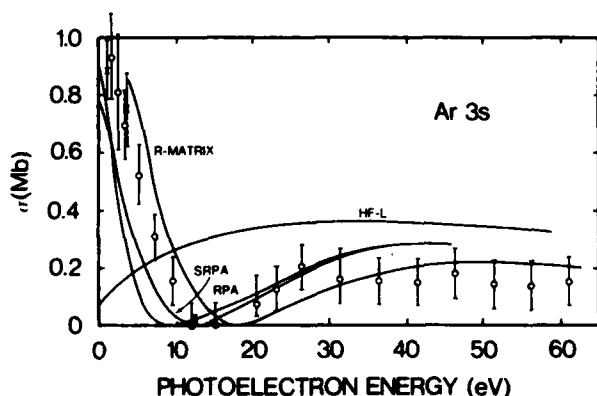


Fig. 6. Argon 3s subshell photoionization cross section. The theoretical RPA,<sup>53</sup> simplified SRPA,<sup>54</sup> R-matrix,<sup>45</sup> and HF<sup>36</sup> results are shown along with the experimental<sup>51,52</sup> results.

experimental cross section<sup>51,52</sup> has a Cooper minimum about 10 eV above threshold and these results are quite well represented by both R-matrix<sup>48</sup> and RPA<sup>53,54</sup> but not by the HF calculation<sup>36</sup> which shows no minimum. In a case like this, then, correlation must be included to get even qualitative agreement with experiment.

## VI. APPLICATION TO SOLID PHOTOABSORPTION

Photoabsorption of core levels, i.e., inner shells in solids occurs on a distance scale small compared to atomic dimensions and, therefore, to first approximation, the solid state environment should not affect the photoionization very much. This idea has been scrutinized in considerable detail<sup>55</sup> and found to be generally true. As an example, consider the case of solid Au shown in Fig. 7. The atomic HS central field cross section<sup>19,56</sup> is compared with the measured results<sup>57-59</sup> in the solid. It is seen, from this comparison, that agreement is quantitatively excellent for  $h\nu \geq 200$  eV and qualitatively quite good for 100 eV below that. This shows that simple atomic calculations can serve as useful first approximation to the photoionization of inner shells of solids. Since, however, the outer shell structure of an atom changes from its free state to the solid, thus changing the exchange and correlation interactions, the more sophisticated methods discussed above should not be applied unmodified to solids.

## VII. ACKNOWLEDGEMENT

This work was supported by the U.S. Army Research Office.

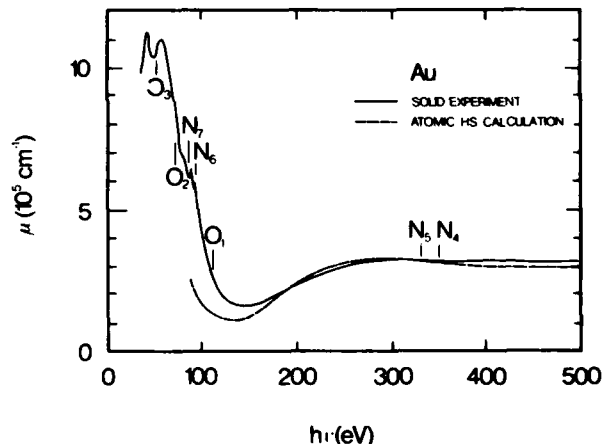


Fig. 7. Photoionization coefficient (proportional to the photoionization cross section) for gold. The dashed curve is the free atom HS central field result<sup>19,56</sup> and the solid curve is the experimental result<sup>57-59</sup> for solid gold.

## REFERENCES

1. A. Einstein, *Ann. Phys. (Leipzig) Ser. IV* **17**, 132 (1905).
2. H. A. Bethe in *Handbuch der Physik*, edited by H. Geiger and K. Scheel (Springer-Verlag, Berlin, 1933), Vol. 24/1, p. 482.
3. H. Hall, *Rev. Mod. Phys.* **8**, 358 (1936).
4. S. T. Manson, *Adv. Electronics Electron Phys.* **41**, 73 (1976).
5. S. T. Manson, *Adv. Electronics Electron Phys.* **44**, 1 (1977).
6. S. T. Manson and D. Dill in *Electron Spectroscopy, Theory, Techniques and Perspectives*, edited by C. R. Brundle and A. D. Baker, (Academic Press, N.Y., 1978).

- Vol. 2, p. 157.
7. A. F. Starace in Handbuch der Physik (in press).
  8. J. A. R. Samson in Handbuch der Physik (in press).
  9. D. R. Bates, Mon. Not. Roy. Astron. Soc. **106**, 432 (1946).
  10. H. A. Bethe and E. E. Salpeter, Quantum Mechanics of One and Two-Electron Atoms (Springer-Verlag, Berlin, 1957), pp. 247-323.
  11. W. Heitler, Quantum Theory of Radiation (Oxford Univ. Press, London, 1954).
  12. A. F. Starace, Phys. Rev. A **3**, 1242 (1971).
  13. A. F. Starace, Phys. Rev. A **8**, 1141 (1973).
  14. I. P. Grant, J. Phys. B **7**, 1458 (1974).
  15. I. P. Grant and A. F. Starace, J. Phys. B **8**, 1999 (1975).
  16. J. W. Cooper, Phys. Rev. **128**, 681 (1962).
  17. J. C. Slater, Phys. Rev. **81**, 385 (1951).
  18. F. Herman and S. Skillman, Atomic Structure Calculations (Prentice-Hall, Englewood Cliffs, N.J., 1963).
  19. S. T. Manson and J. W. Cooper, Phys. Rev. **165**, 126 (1968).
  20. E. J. McGuire, Phys. Rev. **175**, 20 (1968).
  21. R. F. Reilman and S. T. Manson, Ap. J. Supp. **40**, 815 (1979).
  22. J. A. R. Samson, J. Opt. Soc. Am. **54**, 842 (1964).
  23. A. P. Lukirskii, I. A. Brytunov, and T. M. Zimkina, Opt. Spectry. **17**, 234 (1964).
  24. D. L. Ederer, Phys. Rev. Lett. **13**, 760 (1964).
  25. U. Fano and J. W. Cooper, Rev. Mod. Phys. **40**, 441 (1968).
  26. J. W. Cooper, Phys. Rev. Lett. **13**, 762 (1964).
  27. A. Msezane, R. F. Reilman, S. T. Manson, J. R. Swanson, and L. Armstrong, Jr., Phys. Rev. A **15**, 668 (1977).
  28. J. C. Slater, Quantum Theory of Atomic Structure (McGraw-Hill, New York, 1960).
  29. D. R. Hartree, The Calculation of Atomic Structures (Wiley, New York, 1957).
  30. D. R. Hartree, Rep. Prog. Phys. **11**, 113 (1946).
  31. E. Clementi and C. Roetti, At. Data Nuc. Data Tables **14**, 177 (1974).
  32. P. S. Bagus, Phys. Rev. **139**, A 619 (1965).
  33. M. J. Seaton, Proc. Roy. Soc. Ser. A **208**, 418 (1951).
  34. A. Dalgarno, A. L. Stewart, and R. J. W. Henry, Planet. Space Sci. **12**, 235 (1964).
  35. M. Ya. Amusia, N. A. Cherepkov, L. V. Chernysheva, and S. I. Sheftel, Sov. Phys.-JETP **29**, 1018 (1969).
  36. D. J. Kennedy and S. T. Manson, Phys. Rev. A **5**, 227 (1972).
  37. J. Goldstone, Proc. Roy. Soc. Ser. A **239**, 267 (1957).
  38. K. A. Brueckner, The Many-Body Problem (Wiley, New York, 1959).
  39. H. P. Kelly in Atomic Physics 2, edited by G. K. Woodgate and P.C.H. Sanders (Plenum, New York, 1971), p. 227.
  40. H.P. Kelly in Atomic Inner Shell Processes edited by B. Crasemann (Academic, New York, 1975), Vol. I, p. 331.
  41. G. Wendorf in Photoionization and Other Probes of Many-Electron Interactions, edited by F. Wuilleumier (Plenum, New York, 1976), p. 61.
  42. T. N. Chang and U. Fano, Phys. Rev. A **13**, 263 (1976).
  43. M. Ya. Amusia, N. A. Cherepkov, and L. V. Chernysheva, Sov. Phys.-JETP **33**, 90 (1971).
  44. M. Ya. Amusia and N. A. Cherepkov, Case Studies in Atomic Physics **5**, 47 (1976).
  45. P. G. Burke and W. D. Robb, Adv. Atomic Molec. Phys. **11**, 144 (1975).
  46. W. Kohn, Phys. Rev. **74**, 1963 (1948).
  47. E. P. Wigner and L. Eisenbud, Phys. Rev. **72**, 29 (1947).
  48. P. G. Burke and K. T. Taylor, J. Phys. B **8**, 2620 (1975).
  49. J. A. R. Samson, Adv. Atomic Molec. Phys. **7**, 179 (1966).
  50. R. P. Madden, D. L. Ederer, and K. Codling, Phys. Rev. **177**, 136 (1969).
  51. J. A. R. Samson and J. L. Gardner, Phys. Rev. Lett. **33**, 671 (1974).
  52. R. G. Houlgate, J. B. West, K. Cooling, and G. V. Marr, J. Electron Spectrosc. **9**, 205 (1976).
  53. M. Ya. Amusia, N. A. Cherepkov, and L. V. Chernysheva, Phys. Lett. **40A**, 15 (1972).
  54. C. D. Lin, Phys. Rev. A **9**, 171 (1974).
  55. S.T. Manson, Topics in Applied Physics **26**, 134 (1978).
  56. F. Combet Farnoux and Y. Heno, Comptes Rend. **264B**, 138 (1967).
  57. P. Jaegle and G. Missoni, Comptes Rend. **262B**, 71 (1966).
  58. R. Haensel, C. Kunz, T. Sasaki, and B. Sonntag, Appl. Opt. **7**, 301 (1968).
  59. R. Haensel, K. Radler, B. Sonntag, and C. Kunz, Solid State Commun. **7**, 1495 (1969).



Dr. Steven Manson of Georgia State University, the conference's Theoretician in Residence, who coined the very valuable idea of theoretical "error bars".

## Focusing, Filtering, and Scattering of Soft X-Rays by Mirrors

Victor Rehn

Michelson Laboratory, Physics Division  
 Naval Weapons Center, China Lake, California 93555

## ABSTRACT

A review of grazing-incidence optical design fundamentals is presented with special emphasis on mirror material and surface roughness considerations. Angle-resolved scattering results on polished and diamond-turned soft x-ray mirrors are reviewed, along with the elements of optical scattering theory applied to soft x-rays. Reflective filtering of higher-order radiation in monochromator output beams is presented, comparing the transmission and rejection characteristics of one-, two-, and three-reflection filters.

## 1. INTRODUCTION

The need for higher-order rejection or low-pass filters in monochromatized soft x-ray (SXR) synchrotron radiation beam lines has long been recognized. As much as 90% of the radiation emerging from the monochromator may be second- or third-order diffraction by the grating. This poor higher-order rejection by grazing-incidence grating monochromators is due to the difficulties in utilizing grating blaze for higher-order rejection as is done so effectively in visible and infrared monochromators. The SXR gratings diffract radiation only a few degrees (1 to 5 degrees in the "grasshopper," for example) and are usually scanned over large spectral ranges. The small diffraction angles between orders leave little margin for the groove shape or reflectance to effect significant shifts of energy among diffraction orders. External filters are needed to purify the monochromatized radiation.

After tutorially reviewing the principles of glancing-incidence optics and the concepts of scattering by surface microirregularities, both applied to SXR mirrors, we present an analysis of reflective filtering for harmonic rejection in SXR beam lines. Single-, double-, and triple-reflection filters are considered specifically, and expected rejection ratios, spectral ranges, and filter transmission values are tabulated. Effective filtering can be accomplished without unreasonable transmission losses, but there appears to be no magic reflection filter with high performance over wide spectral ranges.

Section 2 reviews the principles of glancing-incidence reflection optics, and Section 3 reviews the concepts and data of SXR scattering by mirror surfaces, including diamond-turned mirrors. Section 4 presents the filter analysis.

## 2. FRESNEL EQUATIONS AND "TOTAL EXTERNAL REFLECTANCE"

The phenomenological laws for reflection, transmission, and absorption of light are the Fresnel equations (1). For application to x-ray wavelengths, these may be written in terms of the glancing-incidence angle,  $\theta$ , and the complex dielectric constant,  $\tilde{\epsilon}$ , or the complex refractive index,  $\tilde{n}$ :

$$\tilde{\epsilon} = (\tilde{n})^2 = n^2 - k^2 + 2ink \quad (1)$$

The complex reflection coefficients for p- or s-polarized radiation are, according to the Fresnel equations,

$$r_p = \frac{\tilde{\epsilon} \sin\theta - \sqrt{\tilde{\epsilon} - \cos^2\theta}}{\tilde{\epsilon} \sin\theta + \sqrt{\tilde{\epsilon} - \cos^2\theta}} \quad (2a)$$

$$r_s = \frac{\sin\theta - \sqrt{\tilde{\epsilon} - \cos^2\theta}}{\sin\theta + \sqrt{\tilde{\epsilon} - \cos^2\theta}} \quad (2b)$$

These coefficients multiply the incident-wave amplitude to produce the reflected-wave amplitude, which is generally shifted in phase in the reflection process.

The (real) energy-reflection coefficients are simply the absolute squares:

$$R_p = r_p^* r_p \quad (3a)$$

$$R_s = r_s^* r_s \quad (3b)$$

If  $\tilde{\epsilon}$  or  $\tilde{n}$  is known, the reflectance of a surface may be calculated for any frequency, polarization, or incidence angle, provided certain conditions are met.

The first of these conditions concerns the surface curvature. Because the Fresnel equations are derived from a consideration of plane waves incident on a planar boundary, the results are only accurate when the radius of curvature of the surface  $R_C \gg \lambda = c/\nu$ . This condition is not a problem due to the smallness of  $\lambda$ .

The second condition is of considerably greater importance in the SXR spectrum. The dielectric function assumed in Maxwell's equations, and therefore also in Fresnel's equations, is based on a continuum model for the reflecting medium. Anisotropy is accommodated by using a second-rank tensor for  $\tilde{\epsilon}$ . This approach accounts for the anisotropic reflection of light from single crystals of low symmetry. However, the atomic nature of the reflecting medium clearly becomes of greater importance as the wavelength of interest becomes shorter. We may ask at what x-ray wavelength does the dielectric model break down? This question was treated both theoretically and experimentally by A. H. Compton in 1922 (2) and by others more recently (3,4). Briefly, an extension of the dielectric model to the x-ray spectrum can be made by considering  $\tilde{\epsilon}$  to be a function of the photon momentum,  $\hbar\vec{k}$ , and the reciprocal lattice vectors,  $\vec{g}(h,k,l)$ , of the (atomic) reflecting crystal. The set of Miller indices for a crystalline plane is designated  $(h,k,l)$ . The Bragg diffraction directions,

$$\vec{k}' = \vec{k} + \vec{g} \quad (4)$$

where  $\vec{k}$  and  $\vec{k}'$  are any reciprocal-lattice points on the Ewald sphere (5) and  $\vec{g}$  is the reciprocal-lattice vector connecting them, are represented in the dielectric function,  $\tilde{\epsilon}$ .

Fresnel reflection, on the other hand, is represented by  $\vec{g} = 0$ , implying no diffraction by the crystal lattice. Fresnel reflection is represented instead by the momentum change

$$\vec{k}' = \vec{k} + \hat{n}(\vec{k} \cdot \hat{n}) \quad (5)$$

where  $\hat{n}$  is the unit surface normal. The strength of the Fresnel reflection is determined in the normal way by the polarizability of the electrons (or atoms) for given values of the incident photon momentum,  $\hbar\vec{k}$ , the frequency,  $\nu$ , and the surface normal direction,  $\hat{n}$ , relative to the crystalline lattice. It is now clear that coherent polarization which is responsible for Bragg scattering is included in  $\tilde{\epsilon}$  and may influence the

strength of the Fresnel reflection when  $\hat{n}$  and  $\hat{k}$  are appropriately chosen. The general question of the relative strengths of Fresnel and Bragg reflections is both complicated and important. Neither experimental nor theoretical treatments currently available are adequate to describe the reflectance of x-ray mirrors in detail, however.

The dielectric function phenomenologically contains the ability of the electrons to respond to an electromagnetic field of frequency  $\nu$ . At optical frequencies, the valence electrons respond most effectively and their oscillation at frequency  $\nu$  radiates the reflected wave, which by interference modifies the transmitted wave and accounts for surface absorption. As the frequency is increased, the valence electrons eventually cease to follow the field, and their "oscillator strength" is said to become exhausted. This may be calculated using a "sum rule" (6). The value of the dielectric function diminishes as  $h\nu$  increases beyond the valence-band energy, producing a characteristic decrease in the normal-incidence reflectance approximately proportional to  $\lambda^4$ , as long as core-electron responses remain negligible (7). When the photon energy is comparable to or greater than the binding energy of a core shell, additional oscillator strength becomes available for the dielectric function. This results in shoulders or peaks in the reflectance spectrum near the core-electron energies. The additional oscillator strength is not large, generally, and also becomes exhausted as the photon energy is increased still more. However, the core-electron response plays an important role in the behavior of x-ray mirrors and reflective filters, as we describe below.

A third condition for the validity of the Fresnel equations is the assumption of a planar (e.g., smooth) reflecting surface. Real surfaces are rough microscopically. We discuss some of the consequences of surface microroughness in Section 3.

In the application of the Fresnel equations to x-ray mirrors, it is the glancing-incidence behavior which is of importance. Figure 1 illustrates the

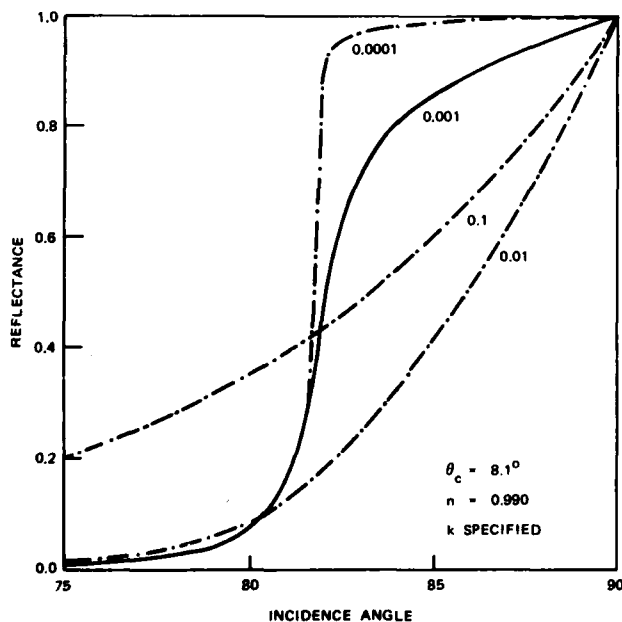


Fig. 1. Total external reflectance behavior. The reflectance vs incidence angle,  $\alpha$ , is shown for several values of the extinction coefficient,  $k$ , as calculated from Eqs. 2(a) and 3(a). The refractive index  $n = 0.99$ , yielding a critical angle,  $\theta_c = 8.1$  degrees.

phenomenon known as "total external reflectance." Although never quite "total," very high reflectance values are observed for small glancing-incidence angles for some materials in certain spectral regions of the x-ray spectrum. Figure 1 shows a series of curves of reflectance vs incidence angle, as calculated from Eqs. (2b) and (3b), in which the extinction coefficient,  $k$  (the imaginary part of the refractive index), is allowed to vary. For very small  $k$ , the reflectance is high from grazing incidence to a certain critical angle  $\theta_c$ , beyond which it drops off sharply. On the other hand, for large  $k$  the reflectance decreases monotonically and with positive curvature over the entire range of angles. If the "total reflectance" phenomenon is defined to occur only when there exists an inflection point in the  $R(\theta)$  curve, then the necessary conditions for "total reflectance" are:

$$\delta \equiv 1 - n > 0 \quad (6)$$

$$k < 0.636 \quad (7)$$

When these conditions are met, the critical angle is

$$\theta_c = \cos^{-1} n \approx \sqrt{2\delta} \quad (8)$$

Equation (8) is most easily derived by setting  $k = 0$  (or  $\epsilon_2 = 0$ ) in Eq. (2) and observing that  $R = r^*r = 1$  providing  $\epsilon = (1 - \delta)^2 < \cos^2 \theta$ . Then  $\cos \theta_c = n$  and  $\theta_c \approx \sqrt{2\delta}$  for small values of  $\theta_c$ . Figure 2 shows spectral regions where Eqs. (6) and (7) are met for several materials, and Table I shows the critical angles derived from published optical constants for some of these regions.

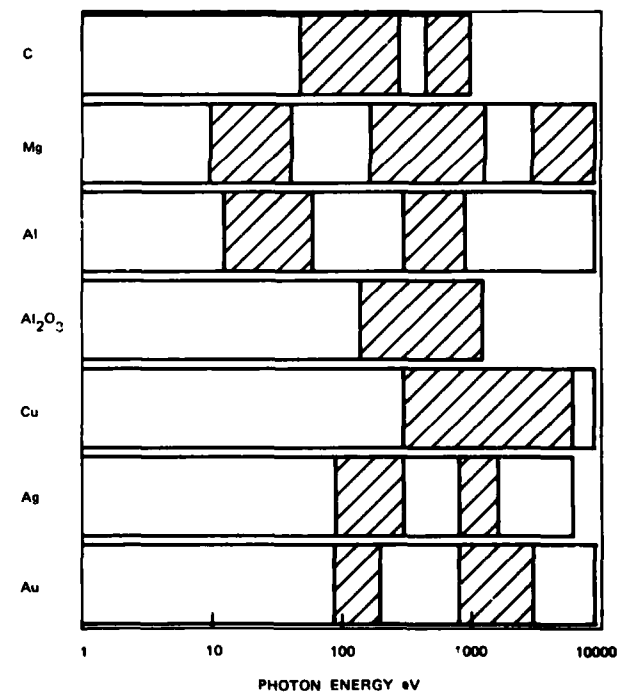


Fig. 2. Spectral regions displaying total reflectance for several materials. Using the optical constants of Ref. 27, the conditions of Eqs. 6 and 7 are satisfied only within the shaded areas.

Although clearly useful, the total reflectance phenomenon is usually not so dramatic as might be hoped due to the dirth of small  $k/\delta$  ratios. From Fig. 1, it can be noted that unless  $k/\delta \lesssim 0.1$ , the reflectance for  $0 < \theta < \theta_c$  drops considerably below unity. Nevertheless, reflectance values above 0.5 for grazing-incidence SXR mirrors can be obtained. It becomes more difficult when broad-spectrum, high-reflectance mirrors are required, as Fig. 2 and Table I illustrate.



TABLE I. Approximate Critical Angles for Several Materials.

The upper range is the photon-energy range, and the lower range is the corresponding critical-angle range. Data of Ref. 27 was used.

C	48 - 280 23° - 2.6°	450 - >1000 3.6° - <1.8°	
Mg	9.8 - 41 86° - 11°	170 - 1280 7.7° - 0.5°	3000 → ?
Al	12.5 - 60 86° - 7.3°	300 - 900 ?	
Al <sub>2</sub> O <sub>3</sub>	138 - >1000 12° - <1.8°		
Cu	300 - ~6000 8.9° - <2.6°		
Ag	90 - 300 32° - 5.1°	800 - 1600 4.1° - 2.6°	
Au	87 - 195 30° - 11°	800 - 3000 4.4° - 2.6°	

### 3. SCATTERING THEORY AND EXPERIMENT

Radiation incident on an interface between media with dissimilar dielectric constants may be reflected, absorbed, transmitted, or scattered. The fraction scattered,  $S$ , is often a great problem because it limits the dynamic range of the detector and produces systematic errors in experiments. Neither the theory nor the measurement of  $S$  has been adequately studied in the x-ray spectrum, making compensation for the scattered background difficult. We summarize here the current understanding of scattering by mirrors prepared either by diamond turning or conventional polishing.

Early work on optical scattering highlighted the dominance of surface microirregularities over scratches and digs as the source of scattering (8). Scratches and digs represent a small surface area, while the microroughness left on the surface by the polishing operation covers the entire surface. These irregularities have been modeled mathematically as a random diffraction grating, producing scattering via diffraction by surface microirregularities (9). A surface with Gaussian distributions of surface heights and of lateral spacings of topographic features is called a "normal" surface. For normal surfaces, a scalar diffraction theory of scattering predicts the total scattering integrated over all scattering angles to be independent of the lateral "peak" spacing (or autocovariance length) of the surface (8). Although the normal surface is not often achieved in polishing, this approximation has proven very useful in evaluating mirror surfaces for visible (10), vacuum ultraviolet (7), and x-ray application (11).

More recent theoretical research has produced a first-order vector theory of scattering (12-14) as well as a facet model of scattering (15). Very recently, an all-order vector theory of scattering has been developed and is currently being adapted to facet-model scattering as well (16). The first-order vector theory was the first to include the optical constants of the surface, the actual surface topography (expressed as either a Fourier transform or an autocovariance function), and the polarization and incidence angle of the incident light. Although still limited in applicability by the perturbation approximation,  $\Delta \ll \lambda$ , where  $\Delta$  is the rms surface-height deviation, this theory facilitated the first comparison of calculated and measured angle-resolved scattering (ARS) in the SXR spectrum (17). The early comparisons could not be made quantitative tests of theory because of inadequacies in both

the theory ( $\Delta \ll \lambda$ ) and the range of the measured autocovariance functions used in the calculation of scattering. The all-order theory currently evolving (16) overcomes the limitation on wavelength, and new measurements of autocovariance functions using stereographic electron microscopy show promise of extending these data into the range 10 to 1000 Å, beyond the resolution limit for stylus measurements of the autocovariance function.

For several high-quality polished and diamond-turned mirrors, ARS measurements have been reported from 15 to 750 eV (17,18) in both s- and p-polarization. Incidence angles between 70 and 85 degrees from the mirror normal were used, and the ARS was measured both within the plane of incidence and in the perpendicular plane which passes through the specularly reflected beam. These two scattering angles are called  $\theta$  and  $\phi$ , respectively, as shown in Fig. 3. Quantitative comparison with theory has not been successful with the first-order theory using autocovariance function data with

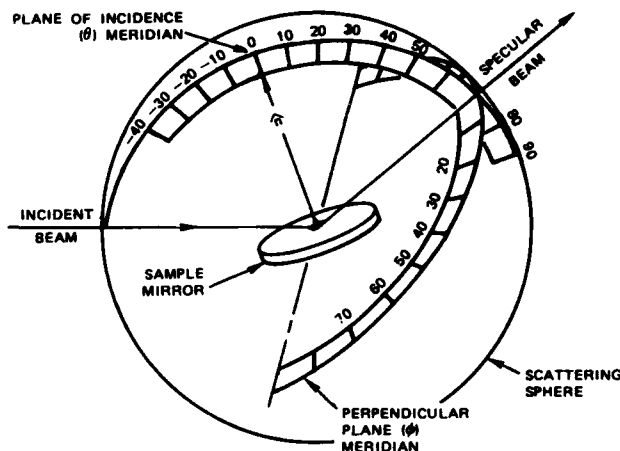


Fig. 3. The geometry of ARS.  $\theta$  is the scattering angle along the plane of incidence meridian, measured from the mirror normal. Perpendicular-plane scattering was measured from the specular-beam direction by the angle  $\phi$ .

0.1- $\mu$ m resolution. It can be concluded experimentally that high-quality polished mirrors can be made with the ARS magnitude at 25 eV photon energy of less than  $10^{-4}$  outside the  $\pm 5$ -degree cone around the specular beam. As the photon energy rises, this value increases to about  $5 \times 10^{-3}$  at 400 eV (17). For state-of-the-art diamond-turned electroless Ni surfaces, the ARS is 10 to 100 times higher in this spectral range, with a strong near-beam scattering (e.g., within  $\pm 5$  degrees) evident at 500 and 750 eV (18). Examples of these results are shown in Figs. 4 and 5.

The larger scattering of these diamond-turned surfaces clearly has nothing to do with the undulations of the surface left by the diamond tool. These mirrors were "fly cut" so that the tool grooves were nearly straight. Orienting the grooves parallel and perpendicular to the plane of incidence made no measurable change in the ARS. The rms surface-roughness height measured by a 1- $\mu$ m-radius diamond stylus was 59 Å across the grooves and 35 Å along them. The feed rate of the diamond tool was 2.5  $\mu$ m per turn, which suggests diffraction by the tool grooves to be most easily observed in the visible spectrum. This has been confirmed (14). In the SXR spectrum,  $\lambda$  is some hundred times smaller than the groove spacing; this fact limits diffraction effects to within a couple degrees of the specular beam. We did not have the angular resolution necessary to look for these effects, but it seems clear that the larger ARS of the diamond-turned mirrors shown in Figs. 4 and 5 could not be attributed to the grooves.

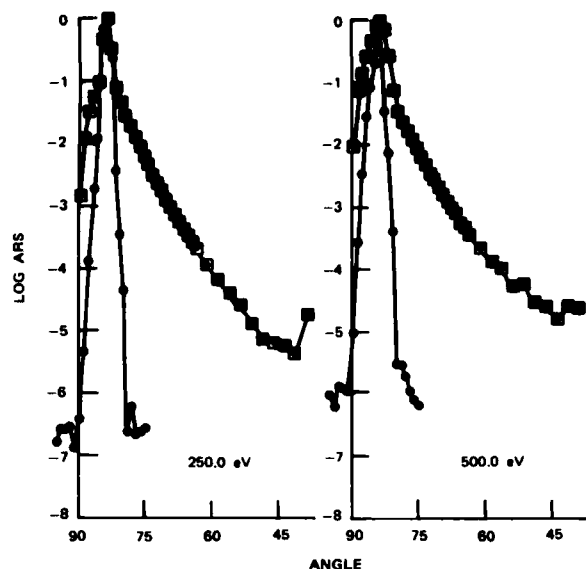


Fig. 4. ARS from a diamond-turned electroless Ni mirror with a thin Au coat. The turning grooves in this fly-cut mirror are oriented perpendicular to the incidence plane. p-Polarized light was incident at 84 degrees. Note the logarithmic scale for the ARS. The narrow peak marked with round dots represents a scan through the incident beam.

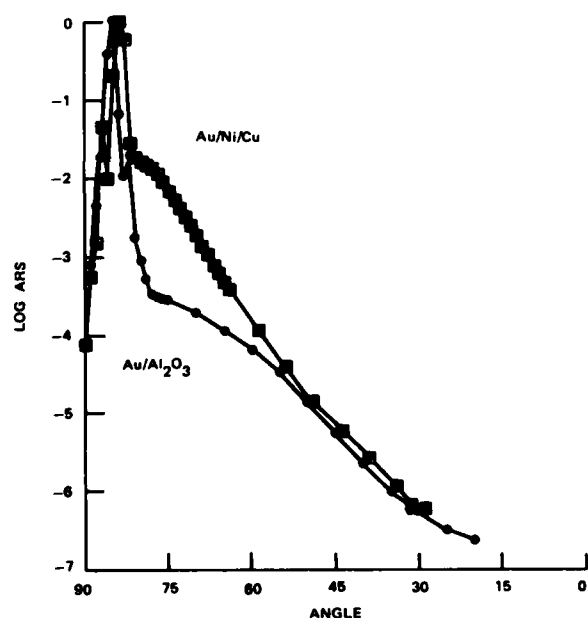


Fig. 5. ARS from a diamond-turned Ni mirror compared to that from a polished  $\text{Al}_2\text{O}_3$  mirror. Both mirrors were coated with Au and measured in p-polarized light. The conditions were not identical: For the diamond-turned Ni mirror,  $\alpha = 84$  degrees,  $h\nu = 125$  eV; for the  $\text{Al}_2\text{O}_3$  mirror,  $\alpha = 85$  degrees,  $h\nu = 120$  eV. These differences should not invalidate the comparison.

A more likely source for the increased scattering of diamond-turned mirrors lies in the mirror material itself. Neither Cu nor Ni mirrors have been polished smoother than about  $15 \text{ \AA}$  rms roughness, measured either by total scattering or stylus profiling. These diamond-turned mirrors scattered visible light ( $6471 \text{ \AA}$ ) as though they were random rough (or normal) surfaces of  $15 \text{ \AA}$  rms roughness height, while the Au-coated  $\text{Al}_2\text{O}_3$  mirror measured  $8 \text{ \AA}$  rms by the same technique. This

implies a ratio of visible scattering of only 3.5. Yet at  $h\nu = 125$  eV, the ratio is larger by more than an order of magnitude, as shown in Fig. 5. In the diffractive model of scattering, the ARS strength at a fixed scattering angle depends on the surface Fourier-transform amplitude for surface spatial frequencies proportional to the photon energy. Thus, the fixed-angle scattering at  $h\nu = 125$  eV depends on the Fourier-transform amplitude for a 60 times larger spatial frequency (e.g., 60 times finer roughness spacing) than for the visible ( $6471 \text{ \AA}$ ) radiation. We must conclude, therefore, that the Fourier-transform amplitude for very large spatial frequencies rises much faster for the diamond-turned metal mirrors than for the polished  $\text{Al}_2\text{O}_3$  mirror. This conclusion cannot be experimentally verified at present because the lateral spacings involved are smaller than the resolution of our best diamond-stylus profilometer. Beyond this conclusion, we may only speculate that the behavior of the metal under the action of the diamond tool produces this very high frequency roughness and that it may be more dependent on the material than on whether the mirror is polished or diamond turned.

The polarization dependence of ARS is shown in Fig. 6 for a diamond-turned Cu mirror (18). For large

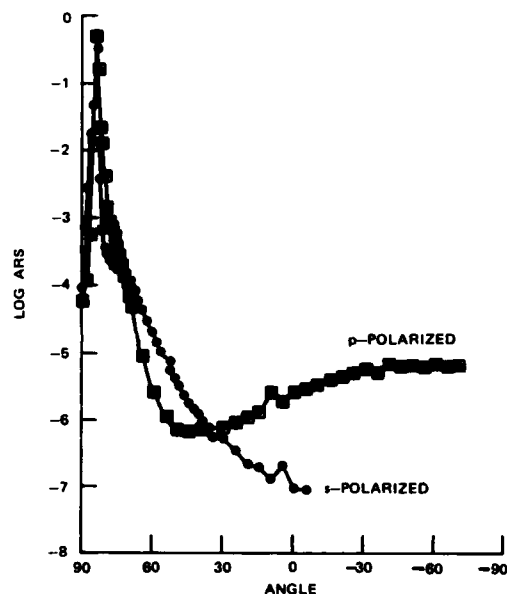


Fig. 6. Polarization dependence of ARS. The mirror is diamond-turned Cu (uncoated), measured with  $\alpha = 84$  degrees and  $h\nu = 125$  eV.

scattering angles, the scattering of p-polarized radiation rises from a minimum, while that from s-polarized radiation monotonically diminishes, as expected from the first-order vector theory (18,19). Scattered waves generated by normal and tangential components of the surface current interfere destructively for forward scattering and constructively for backward scattering. Because the normal component of the surface current is zero for s-polarized incident radiation, the minimum in the ARS caused by this interference occurs only for p-polarized incident radiation.

The pronounced shoulder on the ARS curve of Fig. 5 results from the total reflectance behavior of Au at  $h\nu = 125$  eV. ARS curves at 250, 500, and 750 eV, where  $k/\delta$  values range from 0.6 to 0.94 (see Eq. (7)), show no such shoulder. At a photon energy of 125 eV, the critical angle for Au is  $\theta_c \approx 20$  degrees and  $k/\delta = 0.24$ , which is a value small enough to provide significant total-reflectance behavior, as shown in Fig. 1. This is a clear example of how the angle-dependent reflectance influences the ARS (20).

The facet model of scattering relies on a surface topography consisting of nearly planar facets of linear dimension greater than the wavelength (15). If the normals to these facets are distributed statistically about the mirror normal, it is evident that "specular" reflection from individual facets will cause the incident radiation to be scattered out of the specular beam determined by the mirror normal. Beyond this simple picture, considerably more may be added, such as diffraction due to the small size of the facets and diffractive scattering from rough facets (15). The primary effect of facets seems best suited to very short wavelength radiation where the condition that facet size should be larger than the wavelength is better met.

Near-beam x-ray ARS has been measured at  $\lambda = 1.54 \text{ \AA}$  by T. Matsushita (21) and at  $8.3 \text{ \AA}$  by de Korte and Lainé (22). Both of these measurements were made on high-quality polished mirrors rather than on diamond-turned mirrors. Matsushita successfully fitted his ARS results to a facet model of scattering within a range of a few degrees from the specular. The de Korte and Lainé measurements were fit to a first-order vector diffractive scattering theory by Church (23) over the range  $\pm 0.2$  degree from the specular. It is not clear at this point which scattering model is better for these x-ray wavelengths. It is important to note that both models assume the same sharp-boundary, continuum dielectric model of the surface as is assumed in the Fresnel equations. In other words, no failure of the continuum dielectric constant description of the electromagnetic interaction with the surface has yet been detected in scattering even at  $\lambda = 1.54 \text{ \AA}$ .

#### 4. REFLECTIVE FILTER DESIGN

From the reflectance behavior predicted by the Fresnel equations, Eqs. (2a) and (2b), it is evident that the reflectance of x-ray radiation may be a strong function of the incidence angle and that the critical angle for total reflectance may be a strong function of photon energy. These well-recognized facts have led to the use of mirrors with variable or adjustable incidence angle as low-pass filters for x-ray photon beams (24,25). Such filters are especially well adapted to synchrotron radiation use, where excellent collimation of the beam ensures good filter performance provided materials with prescribed optical constants are used and scattering is sufficiently low. In this section, we discuss the relative merits of one-, two-, or three-mirror designs with the specific goal of reducing higher harmonic radiation in a monochromatized synchrotron radiation beam.

We discussed in Section 2 both the opportunities and the problems offered by the total reflectance phenomenon. The opportunities are evident in Fig. 1, and the problems are most clearly evident in Fig. 2, which illustrates the "disappearing critical angle" syndrome. It is apparent that there is no substitute for reliable optical constant data (26). We have explored the glancing-incidence reflectance behavior of several materials for which such data have been published (27). Figures 7 and 8 show the results for Au and  $\text{Al}_2\text{O}_3$ , respectively. In all cases, we have plotted the reflectance of only s-polarized radiation since there is little or no polarization dependence above  $\sim 50 \text{ eV}$ .

Considering the reflectance of Au, Fig. 7 shows considerable structure in the 50 to 90 eV range, which results from excitations of 4f and 5p core electrons or the  $\text{N}_6$ ,  $\text{N}_7$ ,  $\text{O}_2$ , and  $\text{O}_3$  shells. The next deeper shells are the  $\text{N}_4$  and  $\text{N}_5$  shells (4d electrons) at 334 and 352 eV. For photon energies between 90 and 300 eV, the situation appears favorable for total-reflectance behavior. A tenfold second-order rejection is available from 95 to 140 eV at an incidence angle of 75 degrees. As Fig. 7 clearly shows, however, the  $k/\delta$

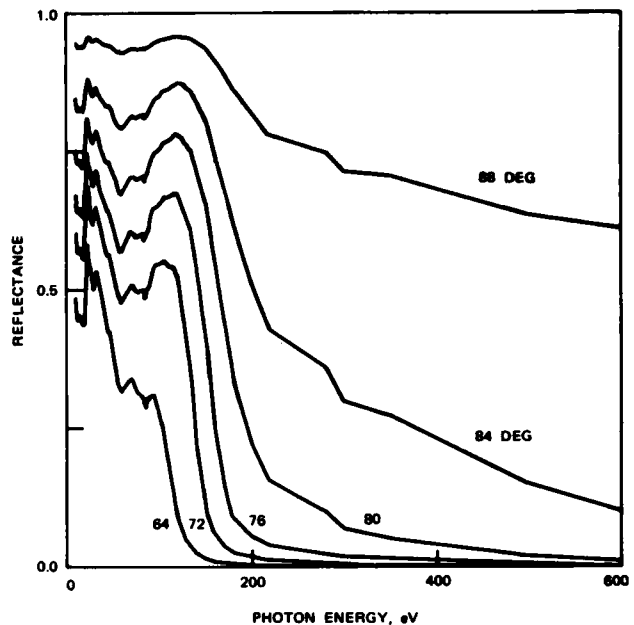


Fig. 7. Glancing-incidence reflectance vs photon energy for a Au mirror, as calculated from Eqs. 2(a) and 3(a). The optical constants are taken from Ref. 27, and the angles specified are the incidence angles,  $\alpha$ , measured from the normal.

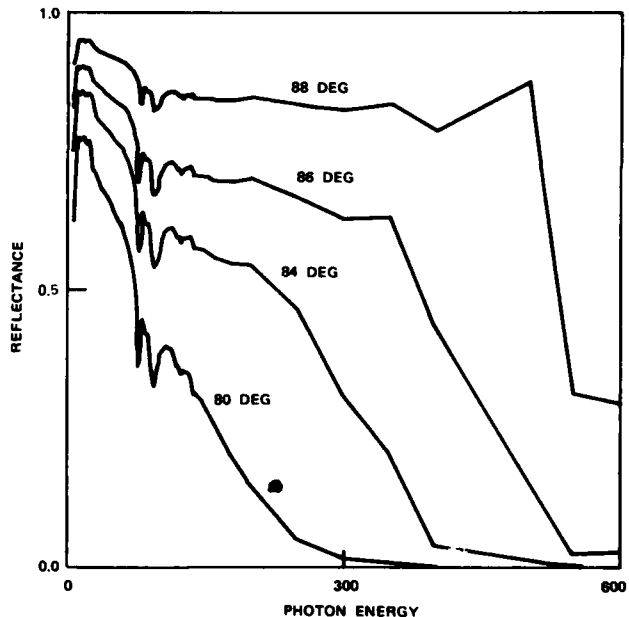


Fig. 8. Like Fig. 7, except for an  $\text{Al}_2\text{O}_3$  Mirror.

ratio is not low enough for good filtering action above 140 eV, where  $k/\delta > 0.1$ . Similarly, the optical constant data (27) shows that the next favorable spectral region for a Au reflectance filter is above 1500 eV. The conclusion is that deeper-lying core levels interfere significantly with the reflectance-filter application, and we should look for materials in which no such core levels exist.

Such a material is  $\text{Al}_2\text{O}_3$ , as shown in Fig. 8. Here we plot the reflectance vs the photon energy in electron volts. The Al(L) core shell excitations cause sharp structure between 75 and 100 eV, but the O(K)

core shell at 532 eV and the Al(K) core at 1560 eV contribute only weakly to the oscillator strength. Hence, above 100 eV  $\text{Al}_2\text{O}_3$  shows behavior quite close to the classical  $R = (h\nu)^{-4}$  pattern so desirable for reflective filtering. The drawback lies in the small values of the critical angle, which makes it necessary to use large, expensive mirrors in the filter. Heavy metal mirrors such as Au or the Pt metals offer larger critical angles, but very spotty performance due to the many core shells destroying the total-reflectance behavior over much of the spectral range. Low Z materials such as  $\text{Al}_2\text{O}_3$  or  $\text{SiO}_2$  offer excellent total-reflectance behavior but very small critical angles.

Using a single mirror, one may realistically expect to design a filter which passes at least 50% of the incident light and rejects higher harmonics by at least 10:1. A Au mirror will accomplish this between 95 and 140 eV at 75-degree incidence. For  $\text{Al}_2\text{O}_3$  at 84-degree incidence, these specifications are met between 200 and 230 eV, while at 86-degree incidence the range is 270 to 385 eV. These are high-throughput filter designs with modest rejection and still rather small ranges.

Another approach is to utilize the strong dip of the reflectance below a core-shell excitation produced by the classical oscillator dispersion. Figures 9 and 10 show the behavior of Mg-mirror filters utilizing two or three reflections, respectively. The two-reflection filter can be designed to provide a constant beam offset without direction change and with variable incidence angles (25).

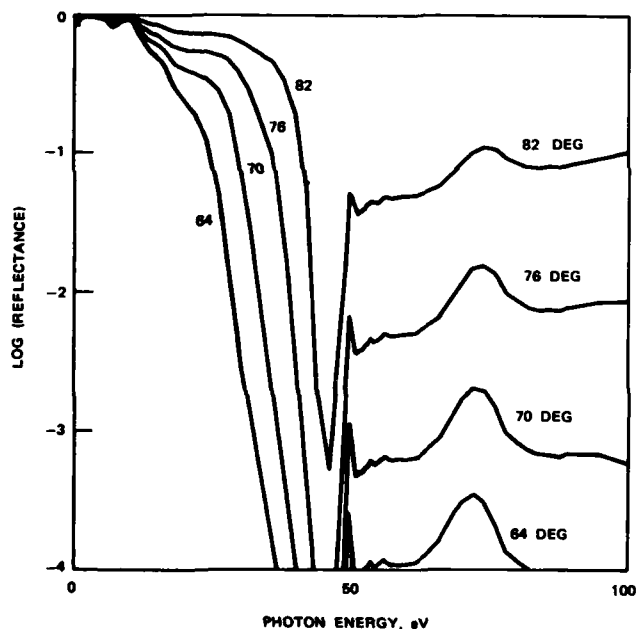


Fig. 9. Log (reflectance squared) vs photon energy for Mg for several incidence angles.

The Mg-reflection data are plotted on a semilog plot in order to facilitate analysis for high-rejection operation. If we require at least 100:1 harmonic rejection and at least 20% filter transmission, respectively, we find the overall range to be 15.5 to 28 eV, with incidence angles from 64 to 70 degrees. Table II shows more detail. Using the same requirements with a symmetric three-reflection design gives an overall range of 14 to 31 eV, with incidence angles from 64 to 76 degrees. In both cases, the maximum filter transmission compatible with the 100:1 minimum harmonic rejection is in the neighborhood of 44%.

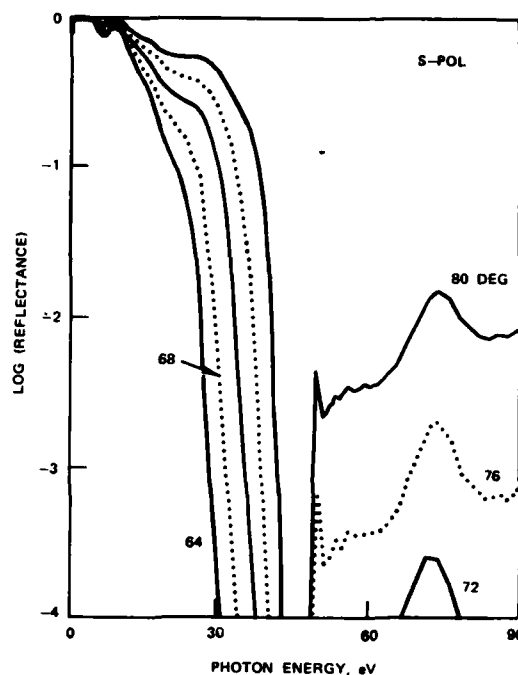


Fig. 10. Log (reflectance cubed) vs photon energy for Mg for several incidence angles.

TABLE II. Expected operating ranges for two- and three-mirror filters of Mg or C.

A requirement for harmonic rejection  $> 100:1$  and a filter transmission of  $> 20\%$  were assumed.

Mirrors Kind #	$\alpha$ , deg	$h\nu_{\min}$ , eV	T	$h\nu_{\max}$ , eV	T
Mg 2	64	15.5	.47	21.5	.20
	70	18.0	.45	27.8	.20
Mg 3	64	13.9	.40	17.4	.20
	70	16.3	.40	24.0	.20
	76	19.2	.44	30.6	.20
C 2	80	78	.37	110	.20
	82	94	.45	140	.20
	84	115	.58	182	.20
C 3	80	68	.27	86	.20
	82	82	.34	125	.20
	84	106	.45	167	.20
	86	128	.60	209	.20

Figures 11 and 12 facilitate a similar analysis for two- and three-reflection carbon-mirror filters, respectively. Using the same requirements, the two-reflection design covers the range 78 to 182 eV, with incidence angles from 80 to 84 degrees. Filter transmission varies from the chosen 20% minimum to 58% maximum. The three-reflection design, Fig. 12, covers the range 68 to 208 eV, with incidence angles from 80 to 85.8 degrees and filter transmission values from 20 to 60%. Additional details are shown in Table II.

## 5. SUMMARY

Reflective filtering of SXR radiation may be accomplished utilizing either the total-reflectance behavior or the dispersion of reflectance below a core-shell excitation. Neither offer broad-range, high-rejection filtering without changing mirrors. Proper choice of mirror material for a desired spectral range is necessary for either type of filter. For the total-reflectance filter, a large energy gap between core excitations is desired in the energy range of the filter, making low Z materials desirable. For the

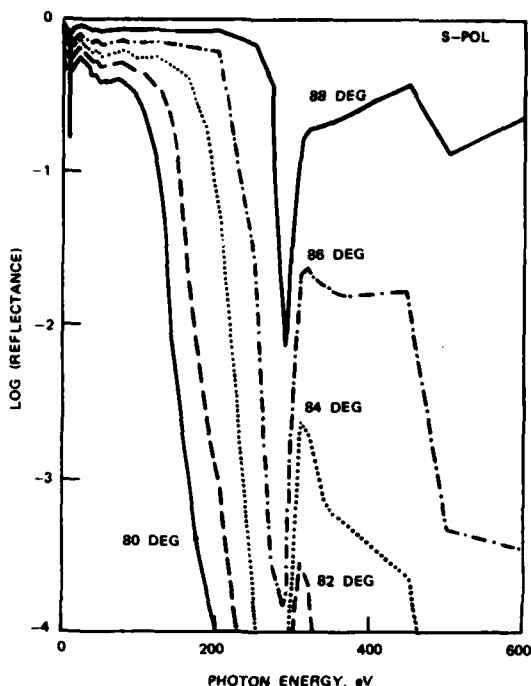


Fig. 11. Similar to Fig. 9, but for carbon.

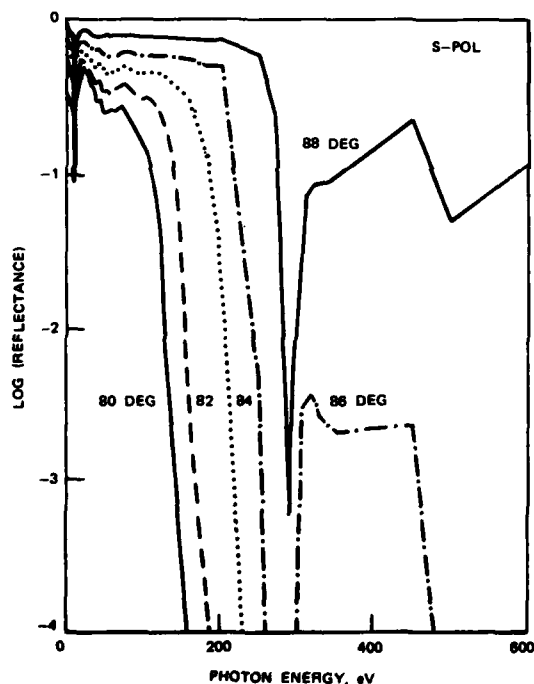


Fig. 12. Similar to Fig. 10, but for carbon.

second type, the strongest reflectance dispersions in the SXR range occur below L-shell or K-shell excitations. Hence, Mg(L), Al(L), Si(L), Be(K), B(K), C(K), Ti(L), V(L), Cr(L), etc. are promising core shells for low-pass reflective filters in the SXR spectrum. All would be expected to provide good filtering over a fairly narrow spectral region in either the two- or three-reflection design.

The choice of designs is also not so obvious. As shown in Table II, the three-reflection filter offers an undeviated exiting beam and a slightly larger total range but at the expense of greater mirror length

(because of smaller incidence angle) and the additional mirror. The two-reflection filter provides nearly equal performance at lower cost but does not facilitate easy removal of the filter for use of the unfiltered beam.

Finally, many practical considerations of filter design and manufacture have been ignored. Two major ones are the difficulty of producing high-quality, low-scatter surfaces and difficulties with chemical reactivity or long-term surface stability. In sum, no simple solution has been found, and the filtering of higher harmonic radiation in monochromatized SXR beams remains a difficult and expensive requirement to meet.

#### REFERENCES

1. See any standard text on electromagnetic theory. A particularly complete treatment is given by J. A. Stratton, *Electromagnetic Theory* (McGraw-Hill Book Co., New York, 1941), pp. 490-511.
2. A. H. Compton, *Bull. Nat. Res. Council* **20**, 48 (1922).
3. V. L. Ginzburg and V. M. Agronovich, *Optical Physics* (1966).
4. L. K. Izraileva, and I. B. Borovskii, *Bull. Acad. Sci. USSR* **36**, 401 (1973). See also B. Henke, in this proceedings.
5. See, for example, C. Kittel, *Introduction to Solid State Physics*, 3rd edition (John Wiley & Sons, New York, 1966), p. 57.
6. See, for example, H. R. Phillip and H. Ehrenreich, "Ultraviolet Optical Properties," in *Semiconductors and Semimetals, Vol. 3, Optical Properties of III-V Compounds*, edited by R. K. Willardson and A. C. Beer (Academic Press, New York, 1967), p. 93f; J. C. Phillips, "The Fundamental Optical Spectra of Solids," in *Solid State Physics, Research and Applications, Vol. 18*, edited by F. Seitz and D. Turnbull (Academic Press, Inc., New York, 1966); or H. Ehrenreich, "Electromagnetic Transport in Solids," in *The Optical Properties of Solids, Proc. of the International School of Physics Enrico Fermi, Course XXXIV*, edited by J. Tauc (Academic Press, New York, 1966), p. 106f.
7. Victor Rehn and V. O. Jones, *Opt. Eng.* **17**, 504 (1978).
8. H. E. Bennett and J. O. Porteus, *J. Opt. Soc. Am.* **51**, 123 (1961); H. E. Bennett, *J. Opt. Soc. Am.* **53**, 1389 (1963); J. O. Porteus, *J. Opt. Soc. Am.* **53**, 1395 (1963); H. E. Bennett, *Opt. Eng.* **17**, 480 (1978).
9. P. Beckmann, *The Scattering of Electromagnetic Waves From Rough Surfaces* (Pergamon Press, New York, 1963), Part I.
10. H. E. Bennett and J. L. Stanford, *J. Res. NBS* **80A**, 643 (1976).
11. Victor Rehn, "X-Ray Mirrors" in *Workshop on X-Ray Instrumentation for Synchrotron Radiation Research*, edited by H. Winick and G. Brown (Stanford Synchrotron Radiation Lab Report #78/04, 1978), p. VII-13.
12. J. M. Elson, *Phys. Rev.* **B12**, 2541 (1975).
13. J. M. Elson and J. M. Bennett, *J. Opt. Soc. Am.* **69**, 31 (1979) and references therein.
14. E. L. Church, H. A. Jenkinson, and J. M. Zavada, *Opt. Eng.* **16**, 360 (1977).
15. C. C. Sung and J. A. Holzer, *Appl. Phys. Lett.* **28**, 429 (1976); *J. Appl. Phys.* **49**, 1002 (1978); C. C. Sung and W. D. Eberhardt, *J. Appl. Phys.* **49**, 944 (1978).
16. J. M. Elson (private communication).
17. Victor Rehn, V. O. Jones, J. M. Elson, and J. M. Bennett, *Nucl. Instrum. Methods* **172**, 307 (1980).
18. J. M. Elson, V. Rehn, J. M. Bennett, V. O. Jones, and D. L. Decker, VI International Conference on Vacuum Ultraviolet Radiation Physics, Charlottesville, VA, 2-6 June 1980, Paper III-43.

19. J. M. Elson, Proceedings SPIE Conference on Periodic Structures, Gratings, Moiré Patterns and Diffraction Phenomena, edited by C. H. Chi, E. G. Loewen, and C. L. O'Bryan III, Vol. 240 (July 29-August 1, 1980, San Diego, CA), p. 128.
20. J. M. Elson, Victor Rehn, J. M. Bennett, and V. O. Jones (to be published).
21. T. Matsushita (private communication).
22. P.A.J. deKorte and R. Lainé, Appl. Opt. **18**, 236 (1979).
23. E. L. Church, Proc. SPIE, Vol. 184 (1979).
24. J.A.R. Samson, Techniques of Vacuum Ultraviolet Spectroscopy (John Wiley & Sons, New York, 1967), p. 34f. Note that Meff should be used for N in Eq. (2.47).
25. E. S. Gluskin, E. M. Trakhtenberg, and A. S. Venogradov, Nucl. Instrum. Methods **152**, 133 (1978).
26. C. Krafka, D. W. Lynch, and E. E. Koch, Physics Data, Parts 18-1 and 18-2 (Fach-Informations-Zentrum, Karlsruhe, Federal Republic of Germany, 1981).
27. H. -J. Hagemann, W. Gudat, and C. Kunz, DESY Report, DESY SR74/7 (Deutsche Elektronen-Synchrotron DESY, 2 Hamburg 52, Nolkesteig 1, May 1974).



Dr. Victor Rehn during presentation of his invited paper on grazing incidence x-ray mirrors.

Synthetic Multilayers as Bragg Diffractors for X-Rays  
and Extreme Ultraviolet: Calculations of Performance

J. H. Underwood

Jet Propulsion Laboratory, California Institute of Technology

T. W. Barbee, Jr.

Department of Materials Science, Stanford University

ABSTRACT

Recent developments in thin film technology have made it possible to construct multilayered thin film structures that act as efficient Bragg diffractors for x-rays and extreme ultraviolet (EUV) radiation (see papers by Barbee and by Spiller, these proceedings). These structures, analogous to multilayered interference filters for the visible region of the spectrum, have important potential applications in many areas of x-ray/EUV instrumentation. In this paper the theory of x-ray diffraction by multilayer structures is briefly outlined, and approximate formulae for estimating their performance presented. A more complete computation scheme based on an "optical" model of multilayers is described, and it is shown how this approach can be modified to take account of imperfections in the structure and to compute the properties of nonperiodic structures. Finally, a comparison with some experimental results is presented.

I. INTRODUCTION

A layered structure in which the refractive index varies periodically with depth selectively reflects electromagnetic waves having particular wavelengths. The Bragg diffraction of x-rays by natural crystals is an example of this principle. Shortly after the wave nature of x-rays was established and x-ray diffraction theory developed, it was realized that if such structures could be made artificially, with layer thicknesses of the order of  $\text{\AA}$  or tens of  $\text{\AA}$ , they would function as Bragg diffractors and serve as valuable experimental tools.

The earliest attempts to make them, by the evaporation or electrodeposition of metals, were reported by Koeppel (1) and Deubner (2). However, these workers were unable to observe diffraction of x-rays from the artificial layer structure (or superlattice) but only from the crystal structure of the component materials.

Du Mond and Youtz (3) reported the first positive results. By evaporation, they made periodic structures composed of alternate layers of copper and gold, with an average interplanar distance of 100  $\text{\AA}$ , and observed diffraction of Mo K x-rays ( $\lambda = 0.7 \text{\AA}$ ) from the superlattice. Stability was a problem, however; the diffracting power decayed to zero in about a month as the two metals interdiffused and the refractive index contrast between the layers was reduced.

Further work was carried out by Dinklage and Frerichs (4) and Dinklage (5), who found that the diffracting power of lead-magnesium and gold-magnesium layered structures decayed with a time scale similar to that found by Du Mond and Youtz. On the other hand, Dinklage (5) found that iron-magnesium structures, with layer repetition periods of 30-50  $\text{\AA}$ , lasted for more than a year. During this time the peak diffracted intensity for 0 K $\alpha$  radiation ( $\lambda = 23.6 \text{\AA}$ ) remained comparable with that from a lead stearate soap film multilayer structure made by the Langmuir-Blodgett technique.

More recently Spiller (6,7,8) has made multilayer interference coatings for the vacuum ultraviolet region, again by an evaporation technique. These coatings are not periodic structures in the usual sense; although the combined thickness of the two component materials remains constant, their relative thickness is graded to obtain maximum reflectivity with a given number of layers. Tests with synchrotron radiation (9) have shown that such coatings, made up of layers of carbon and copper or carbon and gold, reflect radiation of wavelength  $\lambda = 190 \text{\AA}$  approximately seven times more efficiently than a single thick gold layer, when used at normal or near-normal incidence.

Barbee and Keith (10) have developed a sputtering technique for making multilayered structures with layer thicknesses anywhere from about 5  $\text{\AA}$  to several thousand  $\text{\AA}$ . Studies of these synthetic layered microstructures (or LSMs) using x-rays of wavelength between 1.5  $\text{\AA}$  and 44  $\text{\AA}$  have shown them to be strong Bragg diffractors (11). Since the properties of LSMs (interplanar spacing, integrated reflectivity, diffraction width, etc.) can, to a large extent, be "tailored" to a specific application, they have potential for utilization in many areas of x-ray research and technology (see, e.g., Barbee and Keith (10), Underwood, Barbee and Keith (12)). In this paper the theory of LSMs is outlined and used to compute the characteristics of a variety of LSM configurations. The experimental work, and comparison with theory, is discussed in the papers by Spiller and by Barbee (these proceedings).

II. REFLECTION OF X-RAYS BY SYNTHETIC MULTILAYERS

For the interface between a dense material and vacuum, or between two materials of different density, the Fresnel equations can be used to calculate  $R(\theta) = I(\theta)/I_0$ , the fraction of the incident x-ray intensity reflected at glancing angle  $\theta$ . In the x-ray region, for glancing angles much greater than the critical angle  $\theta_c$  (i.e. outside the "total" reflection region)  $R$  is typically of the order  $10^{-4}$  to  $10^{-6}$ . Under these conditions a single surface is useless as an x-ray mirror. However, the corresponding coefficient of *amplitude* reflection  $E(\theta)/E_0$  is  $10^{-2}$  to  $10^{-3}$ ; this implies that a reflectivity  $R(\theta) \sim 1$  may be achieved if the reflections from  $10^2$  to  $10^3$  interfaces can be made to add in phase. Synthetic multilayer reflectors for x-rays operate on this principle.

A multilayer reflector consists of two evaporated or sputtered materials A and B, arranged alternately in layers of thickness  $d_A$  and  $d_B$  respectively (Fig. 1).

The structure is periodic in the direction  $z$ , perpendicular to the planes, with a period  $d = d_A + d_B$ .

Multilayers having more than two layers per period can be made, but since the theory is easily modified to cover such cases, we treat only the simplest two-layer case here. We assume that the structure consists of  $N$  such layer pairs, so that the total number of media involved, including vacuum and the substrate, is  $2N + 2 = n$ .

## III. THEORY OF SYNTHETIC

## MULTILAYERS - ABSORPTION-FREE CASE

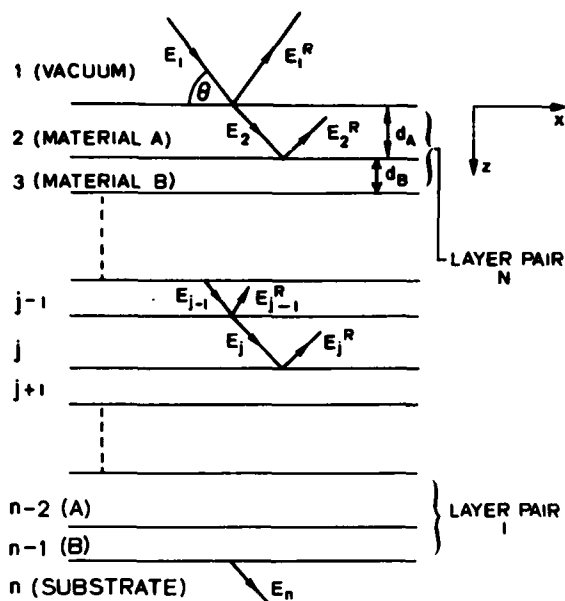


Fig. 1. Reflection of x-rays by a synthetic multilayer. The coordinate system used in the theory is shown to the right. The y-coordinate extends out of the plane of the figure.

X-rays of wavelength  $\lambda$ , incident at a glancing angle  $\theta$  on the planes, will be scattered by each layer of atoms. At the Bragg angles  $\theta_m$  given by the relation

$$m\lambda = 2d \sin \theta_m \quad (1)$$

the scattered waves will add in phase and the total scattered amplitude will reach a maximum. The positive integer  $m$  represents the order of the Bragg "reflection". Thus a structure made up of layers of the order of  $10 \text{ \AA}$  thick will reflect  $\sim 40 \text{ \AA}$  x-rays at  $\sin \theta = 1$  (near normal incidence) or shorter wavelength x-rays at smaller values of  $\sin \theta$ .

Computation of the intensity of x-ray reflection from an LSM at or near the Bragg angles, or for any other angle of incidence requires the solution of Maxwell's equations in a material having a periodically varying dielectric constant. Either of two theoretical approaches to this problem can be adopted. Since synthetic multilayers designed to reflect x-rays must be layered on an atomic scale (for example, a  $10 \text{ \AA}$  layer of tungsten is only 4 atomic layers thick), it is possible to treat their x-ray properties in a manner analogous to that used to compute Bragg reflection intensities from a natural or artificially grown crystal. Alternatively, one may adapt the multilayer theory used to design interference coatings for the visible spectral region, assuming each layer to be plane parallel and assigning it a uniform (complex) refractive index. It can be shown that these two approaches are equivalent. For illustrative purposes, a simplified crystal diffraction theory that neglects absorption is described in section 3, and then used to obtain approximate formulae for estimating the x-ray reflecting properties of synthetic multilayers. In section 4 it is shown how the "optical" multilayer theory can be used to make exact calculations.

In treating the reflection of x-rays from a natural crystal or a pseudo-crystalline structure such as a multilayer reflector either of two theoretical approaches can be adopted. In the kinematical theory, the scattering from each volume element is treated as being independent of that from the other volume elements. This theory neglects the details of the wave interactions within the structure, in particular the progressive reduction in amplitude of the forward wave as it travels into the structure and is partially reflected by successive planes (primary extinction). In the dynamical theory all wave interactions are taken into account. The dynamical theory is customarily used in the study of the x-ray diffraction from large perfect crystals, while the kinematical theory is more appropriate to the study of thin crystals, or "mosaic" crystals which can be thought of as being composed of large numbers of small thin crystallites whose orientations vary slightly, in a random fashion, from the mean orientation.

Multilayers made by, for example, sputtering, are essentially "perfect" from a crystallographic point of view. Although the fabrication process may introduce variation in layer thickness, these errors are not equivalent to the mosaicity of a natural crystal. It is, therefore, more appropriate to use a dynamical theory to compute their properties, although a kinematical approximation will suffice if a multilayer can be considered sufficiently "thin." A quantitative definition of "thin" and "thick" for multilayers is given below.

Although incoherent absorption in the layer materials may have a profound effect on the intensity and shape of the Bragg reflections, the neglect of absorption leads to a simpler theory, from which a number of expressions may be derived in closed form. Since these expressions may be used to estimate properties such as peak and integrated reflectivities, and Bragg peak width, they are useful in choosing multilayer parameters when designing for a particular application. The absorption-free case is therefore treated first. The basic derivations are not repeated here; for these the reader is referred to the book by Zachariassen (13). Saxena and Schoenborn (14) have also treated this problem in connection with the diffraction of neutrons by multilayer structures.

For x-rays of a particular wavelength  $\lambda$ , an elemental material is characterized by its complex atomic scattering factor

$$\hat{f} = f_0 + \Delta f' + i\Delta f'' \quad (2)$$

$\Delta f'$  and  $\Delta f''$  are the resonance and absorption corrections to the atomic scattering factor arising from anomalous dispersion (the Hönig corrections). Since  $2d > 10 \text{ \AA}$ , for the multilayers we shall consider,  $(\sin \theta)/\lambda < 0.1 \text{ \AA}^{-1}$ , and thus  $f_0 = Z$  (i.e. all the electrons in an atom can be considered to scatter in phase). We define  $\phi$ , the scattering amplitude density for x-rays of a particular wavelength by:

$$\phi = \mathcal{N} [(Z + \Delta f')^2 + \Delta f''^2]^{1/2} r_e \quad (3)$$

where  $r_e$  is the classical electron radius  $e^2/mc^2 = 2.818 \times 10^{-13} \text{ cm}$  and  $\mathcal{N}$  the number density of atoms. In the absorption-free case  $\Delta f'' = 0$ , and the term in square brackets reduces to  $Z + \Delta f'$ .

If the crystalline structure of the individual layers is neglected, i.e., if only the superlattice diffraction is considered, then the unit cell of a multilayer can be taken to be unit area of a single layer pair. The angle-dependent structure factor  $F(\theta)$  of a unit cell can then be defined as

$$F(\theta) = \int_0^d \phi(z) e^{iQz} dz \quad (4)$$



where  $Q = (4\pi \sin \theta)/\lambda$ . For the case of diffraction of x-rays by crystals, two solutions to the dynamical problem have been found. The first is known as the Darwin Solution and the second as the Ewald Solution (13). In the limiting case of an infinite number of layers and zero absorption these two solutions give essentially the same results. For illustrative purposes, we use the Ewald formulation.

Let a plane parallel wave of wavelength  $\lambda$  be incident on a multilayer reflector at glancing angle  $\theta$ . The intensity of the intensity of the incident wave is  $I_0$  and that of the reflected wave is  $I(\theta)$ . Then from the Ewald theory

$$\frac{I(\theta)}{I_0} = \left| y + (y^2 - 1) \cot^2 [A(y^2 - 1)^{1/2}] \right|^{-1} \quad (5)$$

where

$$A = \frac{2NdK}{m} |F(\theta_m)| \quad (6)$$

and

$$y = \frac{\pi m N}{2A \sin^2 \theta_m} [(\theta - \theta_m) \sin 2\theta_m - 2\delta_0] \quad (7)$$

The factor  $K$  is 1 for the  $\sigma$  component of the wave polarization,  $|\cos 2\theta_m|$  for the  $\pi$  component, and  $(1 + |\cos 2\theta_m|)/2$  for unpolarized radiation.  $\delta_0$  is the average refractive index decrement for the structure, i.e.

$$\delta_0 = \frac{r_e \lambda^2}{2\pi} \sum_j \bar{N}_j (Z + \Delta f'_j) \quad (8)$$

where  $\bar{N}_j$  is the number density of atoms of type  $j$ , averaged over the structure.

It should be noted that (5) is valid for both  $y^2 < 1$  and  $y^2 > 1$ , since  $\coth^2 x = -\cot^2(ix)$ . Peak reflectivity  $R_m^P$  for the  $m$ th Bragg reflection is defined as the maximum value of  $I(\theta)/I_0$ . It is evident that this maximum occurs when  $y = 0$ , and has the value

$$R_m^P = \tanh^2 A \quad (9)$$

The integrated reflectivity  $R_m^I$  is defined by

$$R_m^I = \int \frac{I(\theta)}{I_0} d(\theta - \theta_m) \quad (10)$$

and it can be shown (13) that

$$R_m^I = \frac{\tan \theta_m}{mN} (A \tanh A) \quad (11)$$

**3.1. Correction of the Bragg equation for Refraction.** From (5) and (7) we see that in the absorption-free case diffraction pattern is symmetrical, not about  $\theta = \theta_m$ , but about a slightly larger glancing angle  $\theta_m^P$ , where

$$\theta_m^P - \theta_m = 2\delta_0 / \sin 2\theta_m = \delta_0 \sec \theta_m \operatorname{cosec} \theta_m \quad (12)$$

Thus the Bragg equation must be corrected for refraction. From the definition of refractive index

$$n_0 = 1 - \delta_0 = c/v = \lambda/\lambda'$$

where  $v$  is the velocity of light,  $\lambda'$  the wavelength, and  $\theta_m'$  the glancing angle in the medium. Also, by Snell's law:

$$1 - \delta_0 = \cos \theta_m^P / \cos \theta_m'$$

Finally,

$$m\lambda' = 2d \sin \theta_m'$$

By elimination, we obtain (15):

$$m\lambda = 2d \left( 1 - \frac{2\delta_0 - \delta_0^2}{\sin^2 \theta_m^P} \right)^{1/2} \sin \theta_m^P \quad (13)$$

which, for small  $\delta_0$ , becomes

$$m\lambda = 2d \left( 1 - \frac{\delta_0}{\sin^2 \theta_m^P} \right) \sin \theta_m^P \quad (14)$$

**3.2. "Thick" case ( $A > 1.8$ ).** It is useful to consider two limiting cases of the dynamical theory, defined by  $A > 1$  and  $A < 1$ . The former is known as the "thick" crystal case since it applies when, for example,  $N$  is large. In this case  $\tanh A \approx 1$  and we may write:

$$R_m^P = 1 \quad (15)$$

$$R_m^I = \frac{A \tan \theta_m}{mN} \quad (16)$$

The reflection is thus total for  $|y| < 1$ , and the primary beam suffers complete extinction in passing through the structure. One may also derive an expression for  $\Delta\theta_m^{1/2}$ , the full width at half maximum of the reflection profile (15), viz:

$$\Delta\theta_m^{1/2} = \frac{2.3}{\pi} \frac{A \tan \theta_m}{mN}, \quad \frac{\lambda}{\Delta\lambda} = \frac{\pi m N}{2.3 A} \quad (17)$$

**3.3. "Thin" case ( $A < 0.4$ ).**  $A < 1$  defines the "thin" approximation. In this case (5) can be written

$$\frac{I(\theta)}{I_0} = \left( \frac{\sin Ay}{y} \right)^2 \quad (18)$$

and:

$$R_m^P = A^2 \quad (19)$$

$$R_m^I = \frac{A^2 \tan \theta_m}{mN} \quad (20)$$

and

$$\Delta\theta_m^{1/2} = \frac{\tan \theta_m}{mN}, \quad \frac{\lambda}{\Delta\lambda} = mN \quad (21)$$

This approximation corresponds to the kinematical theory, which is thus the "thin" limit of the dynamical theory.

**3.4. Evaluation of  $|F(\theta)|$  and  $A$ .**  $|F(\theta)|$  may be evaluated analytically for simple cases. For example, if layers A and B are homogeneous with constant scattering amplitude densities  $\phi_A$  and  $\phi_B$ , and if the transition from the value  $\phi_A$  to the value  $\phi_B$  takes place over a vanishingly small interval, i.e., the interfaces are perfectly sharp, then

$$|F(\theta)| = \frac{\sqrt{2}}{Q} [\phi_A^2 (1 - \cos Qd_A) + \phi_B^2 (1 - \cos Qd_B) + \phi_A \phi_B (\cos Qd_A + \cos Qd_B - \cos Qd - 1)]^{1/2} \quad (22)$$

which for the special case of equal layer thicknesses  $d_A = d_B = \frac{d}{2}$ , reduces to:

$$|F(\theta)| = \frac{2}{Q} \sin\left(\frac{Qd}{4}\right) [\phi_A^2 + \phi_B^2 + 2\phi_A\phi_B \cos\frac{Qd}{2}]^{\frac{1}{2}} \quad (23)$$

At the Bragg angle  $\theta_m$ ,  $Q = \frac{2\pi m}{d}$  and (22) becomes:

$$|F(\theta_m)| = \frac{d}{\pi m} \sin\left(\frac{m\pi d}{d}\right) (\phi_A - \phi_B) \quad (24)$$

We see that for equal layer thicknesses only the odd orders  $m = 1, 3, 5, \dots$  are permitted reflections.

If the layer thicknesses are equal, but the scattering amplitude density makes a smooth, sinusoidal transition from the value  $\phi_A$  to the value  $\phi_B$ , then it may be shown (14) that

$$|F(\theta_m)| = \frac{d}{4} (\phi_A - \phi_B) \quad \text{for } m = 1 \quad (25)$$

$$= 0 \quad \text{for } m \neq 1$$

By way of illustration, let us compute  $N_{\text{eff}}$ , the effective number of layer pairs contributing to the peak reflectivity of a particular Bragg reflection, and hence the maximum number needed in a multilayer reflector designed to operate at a particular wavelength. Since  $\tanh 2 = 0.96$ , most of the maximum possible peak reflectivity will be obtained if  $A = 2$ . For the case in which the interfaces are sharp, eqs. (6) and (24) together yield

$$N_{\text{eff}} = \pi m^2 / [Kd^2 \sin(m\pi d/d) (\phi_A - \phi_B)] \quad (26)$$

To consider some specific examples, at the wavelength of Al K $\alpha$  ( $\lambda = 8.34 \text{ \AA}$ ),  $\phi_W = 9.76 \times 10^{11} \text{ cm}^{-2}$  and  $\phi_C = 1.69 \times 10^{11} \text{ cm}^{-2}$ . Hence, for the first order reflection from an LSM built up of layers of tungsten and carbon, each 10  $\text{\AA}$  thick,  $N_{\text{eff}} = 100$ . A similar stack made from layers of aluminum and beryllium ( $\phi_{\text{Al}} = 2.22 \times 10^{11} \text{ cm}^{-2}$ ,  $\phi_{\text{Be}} = 1.36 \times 10^{11} \text{ cm}^{-2}$  at 8.34  $\text{\AA}$ ) would have  $N_{\text{eff}} \approx 900$ . A sinusoidal variation of  $\phi$  would increase these numbers by  $4/\pi$ , or about 30%. Absorption in the material will, of course, reduce  $N_{\text{eff}}$ , so that the figures should be treated as upper limits. In general, the results of the absorption-free theories should be used only as a guide, and the more rigorous theory, outlined below, should be used for detailed computations.

#### IV. DYNAMICAL THEORY INCLUDING ABSORPTION

If incoherent absorption in the layer materials cannot be neglected (i.e., if  $\Delta f'' \neq 0$ ) then both  $\hat{f}$  and the structure factor  $F(\theta)$  become complex. For the case of x-ray diffraction by crystals, this situation is treated using Prins' modification of the Darwin theory (17). However, the Darwin-Prins theory is analytically cumbersome, and is best suited for treating an infinite number of strictly periodic scattering layers. In addition, the theory does not take into account reflections at the multilayer-vacuum and multilayer-substrate interfaces. For computations involving a finite number of layers, or for situations in which the layer structures are not strictly periodic (for example, Spiller's (6,7,8) multilayer structures optimized for EUV reflection) it is more convenient to adopt a computational approach. Our computational approach is analogous to that used in the design of multilayer interference filters for the visible region of the spectrum, and is based on the Fresnel equations.

We characterize the material by its complex refractive index

$$\hat{n} = 1 - \delta - i\beta \quad (27)$$

where

$$\delta = \frac{\sqrt{r_e} \lambda^2}{2\pi} (Z + \Delta f') \quad (28)$$

$$\beta = \frac{\sqrt{r_e} \lambda^2}{2\pi} (\Delta f'') = \frac{\mu \lambda}{4\pi} \quad (29)$$

$\mu$  is the linear absorption coefficient. Referring again to Fig. 1, let  $E_j$  be the amplitude of the electric vector of the wave incident on the interface between the  $j$ th and the  $(j+1)$ th layers, and  $E_j^R$  the amplitude reflected from this interface. The Fresnel coefficients  $\mathcal{F}_{j,j+1}^\sigma$ ,  $\mathcal{F}_{j,j+1}^\pi$  for reflection of the  $\sigma$  and  $\pi$  components of polarization from this interface can be written

$$\mathcal{F}_{j,j+1}^\sigma = \frac{\left(\frac{E_j^R}{E_j}\right)^\sigma}{\left(\frac{E_j^R}{E_j}\right)^\sigma} = \frac{g_j - g_{j+1}}{g_j + g_{j+1}} \quad (30)$$

$$\mathcal{F}_{j,j+1}^\pi = \frac{\left(\frac{E_j^R}{E_j}\right)^\pi}{\left(\frac{E_j^R}{E_j}\right)^\pi} = \frac{g_j/\hat{n}_j^2 - g_{j+1}/\hat{n}_{j+1}^2}{g_j/\hat{n}_j^2 + g_{j+1}/\hat{n}_{j+1}^2} \quad (31)$$

where

$$g_j = (\hat{n}_j^2 - \cos^2 \theta)^{-1} \quad (32)$$

For small  $\theta$ ,  $\beta$ ,  $\delta$ , (32) becomes

$$g_j = (\theta^2 - 2\delta_j - 2i\beta_j)^{-1} \quad (33)$$

We define

$$\mathcal{R}_{j,j+1} = a_j (E_j^R/E_j)$$

where

$$a_j = \exp(-i\frac{\pi}{\lambda} g_j d_j)$$

is the amplitude factor for half the perpendicular distance  $d_j$ . Using the boundary condition that the tangential components of  $\underline{E}$  and  $\underline{H}$  be continuous at the interface, a recursion relation for  $\mathcal{R}_{j,j+1}$  may be developed, viz:

$$\mathcal{R}_{j,j+1} = a_j \frac{\mathcal{R}_{j+1,j+2} + \mathcal{F}_{j,j+1}}{\mathcal{R}_{j+1,j+2} \mathcal{F}_{j,j+1} + 1} \quad (34)$$

The computational scheme starts at the substrate, medium  $n$ , with  $\mathcal{R}_{n,n+1} = 0$  (since the substrate is considered infinitely thick). By using (34) and working backward to the first surface, where  $a_1 = 1$  and  $\mathcal{F}_1 = \sin \theta$  the value of  $\mathcal{R}_{12} = E_1^R/E_1$  may be found. This is related to the intensity  $I(\theta)$  reflected from the structure by

$$\frac{I(\theta)}{I_0} = (\mathcal{R}_{12})^2 \quad (35)$$

This computation scheme is quite general and can be used to compute the x-ray reflectance of any multilayer structure at any angle of glancing incidence. As an example, we have computed the reflectance as a function of angle for four LSMs, otherwise identical,

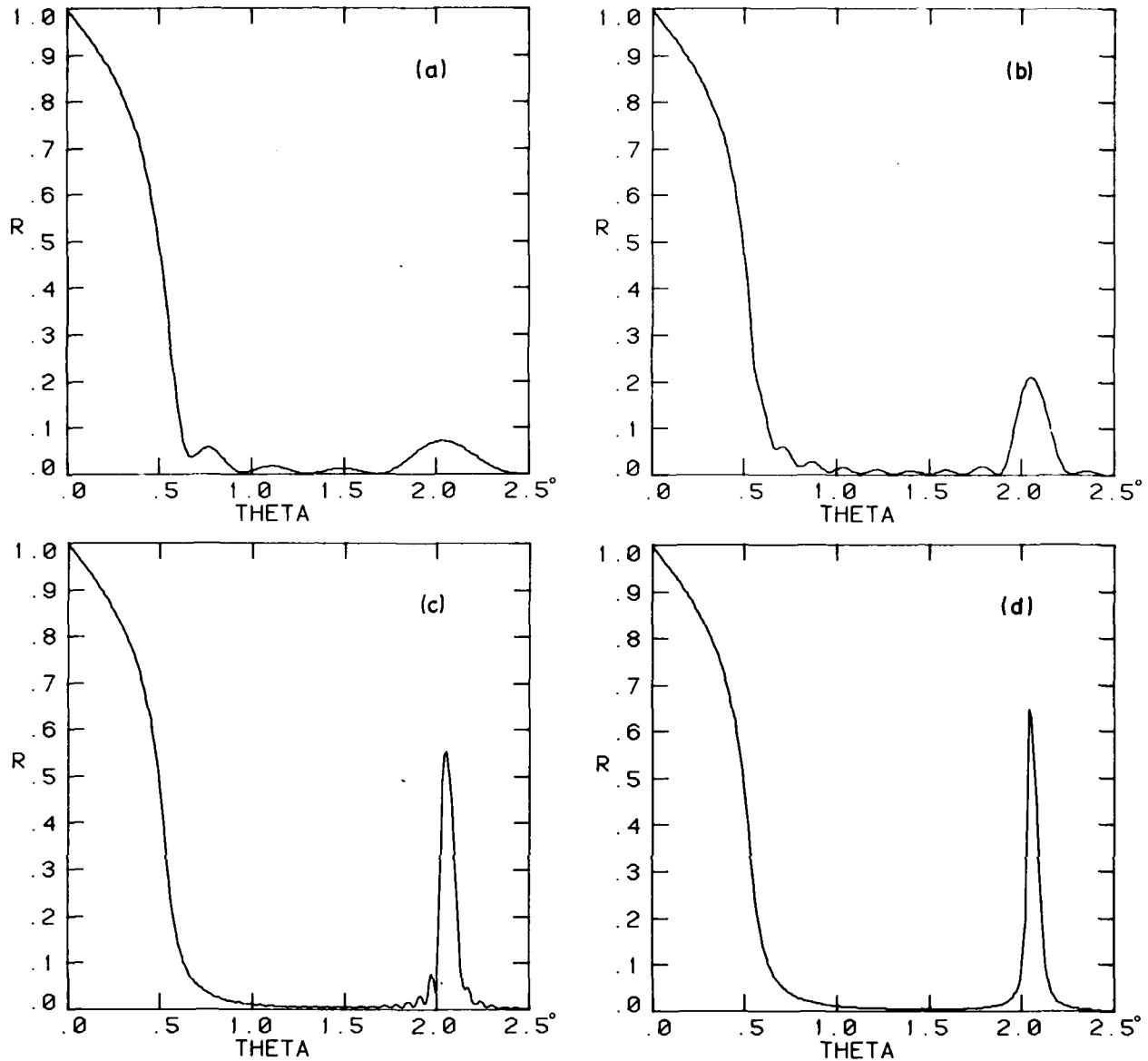


Fig. 2. Reflectivity versus glancing angle computed for a series of tungsten-carbon layered synthetic microstructures at a wavelength  $\lambda = 2.2631 \text{ \AA}$ . (a) 5 layer pairs (b) 10 layer pairs (c) 30 layer pairs (d) 100 layer pairs. Layer thicknesses and optical constants used are given in the text.

having 5, 10, 30 and 100 layer pairs (Fig. 2). These computations are for a tungsten-carbon LSM with  $d_w = 12.4 \text{ \AA}$ ,  $d_c = 20.0 \text{ \AA}$ , at a wavelength  $\lambda = 2.2631 \text{ \AA}$ . The optical constants used were: tungsten;  $\delta = 9.09 \times 10^{-5}$ ,  $\beta = 2.08 \times 10^{-5}$ , carbon;  $\delta = 1.38 \times 10^{-5}$ ,  $\beta = 1.64 \times 10^{-6}$ . In addition to the total reflection region and the first order Bragg reflection, these curves show well the subsidiary interference maxima that occur for a "thin" structure (eq. 18) and their disappearance for a "thick" structure. These calculations are for unpolarized radiation; however, at these small values of  $\theta$  the reflectivity for the  $\sigma$  and  $\pi$  states of polarization are virtually identical.

#### V. CHOICE OF MATERIALS AND LAYER THICKNESS FOR LSMs

Since, in a particular application, the principal design concerns will be the wavelength range in which the device must operate, and the range of glancing angles over which it must function, the specification

of  $d$  is relatively simple. This leaves  $\phi_A$ ,  $\phi_B$ ,  $N$  and  $d_A/d$  as adjustable parameters by which the properties of the LSM may be "tailored."

Combining (6), (11), and (24) we find that:

$$R_m^I = \frac{2d^2K}{\pi m^3} \sin\left(\frac{m\pi d}{d}\right) (\phi_A - \phi_B) \tan \theta \tanh A \quad (36)$$

If the crystal is "thick" ( $N \geq N_{\text{eff}}$ ,  $\tanh A \approx 1$ ) it is evident that the highest integrated reflectivity is achieved by making the contrast  $(\phi_A - \phi_B)$  as large as possible, and  $d_A/d = 0.5$ . When absorption is important, the optimum value of the division parameter  $d_A/d$  may be different. Vinogradov and Zeldovich (18) have examined this problem and have derived the following transcendental equation for the optimum value of  $d_A/d$ ;

$$\tan \pi \left( \frac{d_A}{d} \right)_{\text{opt}} = \pi \left[ \left( \frac{d_A}{d} \right)_{\text{opt}} + \frac{\beta_B}{\beta_A - \beta_B} \right] \quad (37)$$

This equation was originally derived for normal incidence and for a sinusoidal variation of  $n$ . However, it evidently holds for any angle of incidence and, to a good approximation, for the case where the interfaces are sharp.

We may also obtain a rough estimate of the optimum parameters for highest resolution  $\lambda/\Delta\lambda$ , using the absorption-free theory. From (16) and (17) we obtain:

$$\Delta\theta_m^2 = \frac{2.3}{\pi} R_m^I \quad (38)$$

and again assuming that the structure is "thick," we see from (36) that for highest resolution, both  $(\phi_A - \phi_B)$  and  $d_A/d$  should be made as small as possible.

#### VI. PREDICTIONS OF THE THEORY FOR REALISTIC LSM CONFIGURATIONS

One of the important factors in choosing two or more materials for an LSM is their compatibility: they must not react chemically or interdiffuse, or at least such reaction/diffusion must be limited. This places a considerable restriction on the choice of materials, and thus on attainable values of  $\phi_A - \phi_B$ .

Tungsten and carbon represent a pair of materials that meets these requirements. In reality, there is some reaction between these elements, and the resulting LSMs are composed of a mixed tungsten-tungsten carbides ( $W_2C$  and  $WC$ ) layer and a carbon layer, rather than pure tungsten and carbon. However, the structures are stable (10), and since the density of tungsten carbide ( $16.3 \text{ g.cm}^{-3}$ ) is only slightly less than that of tungsten ( $19.3 \text{ g.cm}^{-3}$ ) a strong density contrast between the carbide and carbon layers ( $\rho \sim 2.0 \text{ g.cm}^{-3}$ ) is maintained. It is useful, therefore, to present some sample calculations concerning the "tungsten-carbon" system.

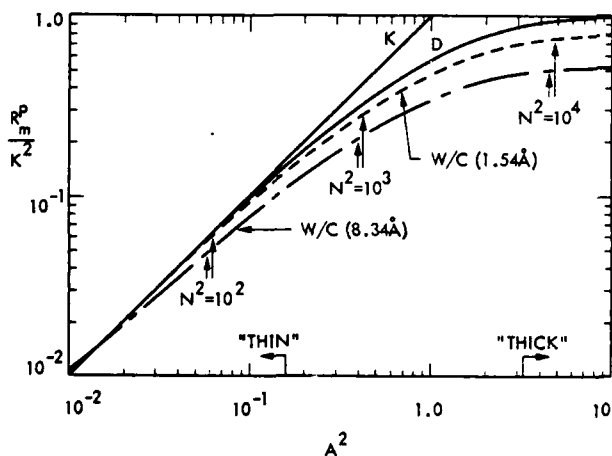


Fig. 3. Peak reflectivity of an LSM as a function of  $A^2$ . Curve K: kinematical approximation. Curve D: dynamical approximation (no absorption). These solid curves apply to any LSM structure. The lower curves are computed, using the full theory of section 3, for a particular LSM; a tungsten-carbon structure with  $d_w = d_c = 10 \text{ \AA}$ .  $A$  was varied by changing  $N$ .

In Fig. 3 the peak reflectivity  $R_m^P/K^2$ , as calculated from the kinematical and the dynamical (no absorption) approximations are plotted as a function of  $A^2$ . It is seen that in the "thin" region the reflectivity

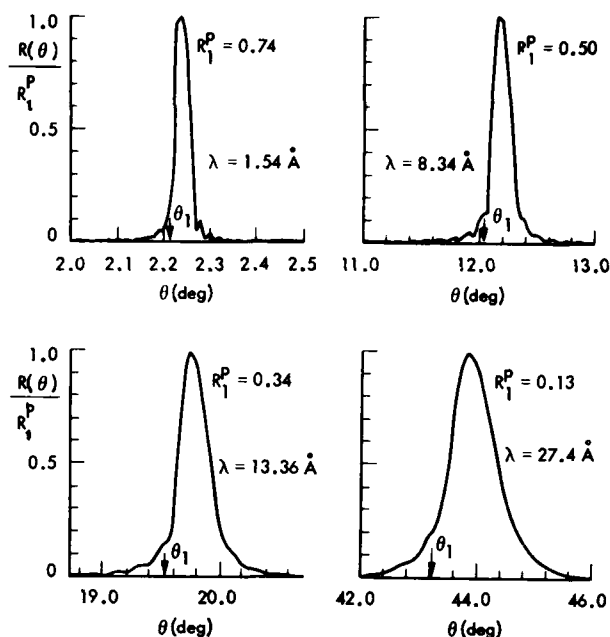


Fig. 4. Reflectivity curves computed for a LSM consisting of 101 layer pairs of tungsten and carbon, at four wavelengths and for unpolarized radiation.  $\theta_1$  indicates the position of the first-order peak predicted from the Bragg equation using  $2d = 40.0 \text{ \AA}$ . The angular difference between  $\theta_1$  and the peak in  $R$  is the refraction correction.

tivity is approximately linear in  $A^2$ , the two approximations giving the same value within 7%. Also plotted in this figure is the first order peak reflectivity computed, using the full theory of section 3, for a W/C LSM with  $2d = 40 \text{ \AA}$  ( $d_w = d_c = 10 \text{ \AA}$ ) at the wavelengths of Cu K $\alpha$  ( $1.54 \text{ \AA}$ ) and Al K $\alpha$  ( $8.34 \text{ \AA}$ ). The value of  $A$  was varied by changing  $N$ , the total number of layer pairs in the LSM stack. It can be seen that while when the absorption is small, the simpler, absorption-free dynamical theory gives values within 20% of those predicted by the full theory, it begins to deviate markedly for values of absorption which are only moderately high.

Figure 4 is a series of reflectivity versus  $\theta$  curves for the same W/C structure, computed at a variety of x-ray wavelengths; 100 layer pairs were assumed. The curves shown are for unpolarized radiation; curves for the  $\sigma$  and  $\pi$  states can be obtained by applying the appropriate value of  $K$ . The value of  $\theta_1$  calculated from the Bragg equation (1) is indicated on these curves, so that the relatively large correction for refraction can be seen. Note that, because of absorption, the diffraction curves are not symmetrical about the angle  $\theta_m^P$  defined in Eq. (12).

The integrated reflectivity is plotted as a function of  $\lambda$  in Fig. 5. For comparison, the predicted and measured integrated reflectivities of some other Bragg crystal analysers and artificial multilayers (Langmuir-Blodgett pseudo-crystals) have also been plotted. In Fig. 6 a similar comparison is made for the wavelength resolution  $\lambda/\Delta\lambda$ .

It is evident that a W/C LSM is a powerful diffractor over the whole wavelength range considered, with an integrated reflectivity  $>10^{-3}$  radians, an order of magnitude greater than that of presently available analysers (acid phthalate crystals or soap film multilayers). Its wavelength resolution is, as expected, low, but still comparable with, or slightly better than, that measured for soap film multilayers.

AD-A114 893

AMERICAN INST OF PHYSICS NEW YORK  
LOW ENERGY X-RAY DIAGNOSTICS - 1981.(U)  
1981 D T ATTWOOD, B L HENKE

F/G 14/2

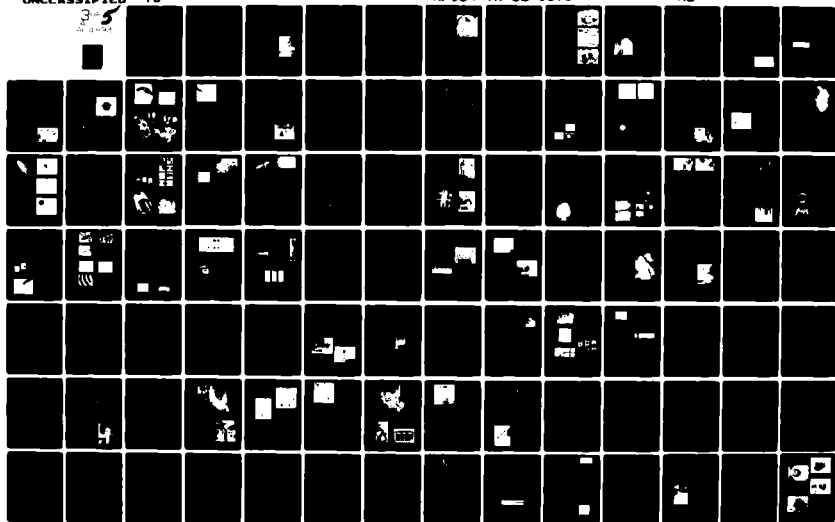
UNCLASSIFIED

75

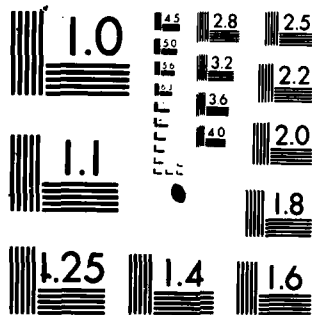
AFOSR-TR-82-0378

AFOSR-ISSA-81-00024

NL



1489



MICROCOPY RESOLUTION TEST CHART  
NATIONAL BUREAU OF STANDARDS 1963 A

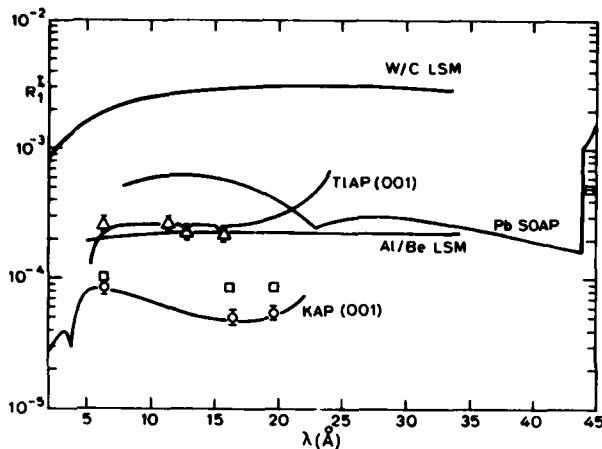


Fig. 5. First order integrated reflectivities of typical multilayer structures and crystals in the soft x-ray region. The solid curves are calculations based on dynamical theory. The LSMs are those referred to in the text and in Figures 3 and 7. "Pb Soap" is a "thick" lead stearate multilayer (Henke and Tester (19)). The curves for thallium acid phthalate (TIAP) and potassium acid phthalate (KAP) are Darwin-Prins calculations of Burek (20). The experimental points for KAP (circles) were taken from Burek (20), for TIAP (triangles) from McKenzie et al. (21), and for the optimized lead stearate multilayer (squares) from Charles (22).

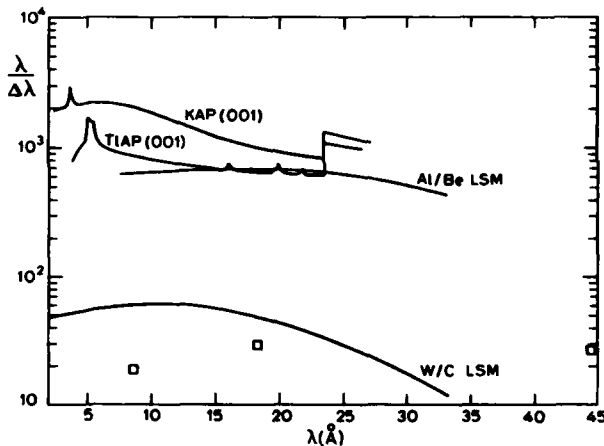


Fig. 6. First order resolving power of crystals and multilayers. The experimental points for lead stearate (squares) were taken from Charles (22). The curves for KAP and TIAP were computed by Burek (20) using the Darwin-Prins theory.

In order to build LSMs with better wavelength resolution, pairs of materials having low absorption and a low value of  $\phi_A - \phi_B$  must be chosen. A possible candidate pair for the soft x-ray region is represented by aluminum and beryllium. Although the materials science aspects involved in constructing LSMs from these two materials remain to be fully investigated, the combination appears promising, and we have computed the x-ray diffracting properties of a 100 layer pair Al/Be structure ( $d_{Al} = d_{Be} = 10 \text{ \AA}$ ) at a number of soft x-ray wavelengths (Fig. 7). The integrated reflectivity and wavelength resolution of this LSM are also plotted in Figs. 5 and 6; these properties are both close to those of thallium acid phthalate (TIAP), and its potential value perhaps lies in the extension of these properties to longer wavelengths.

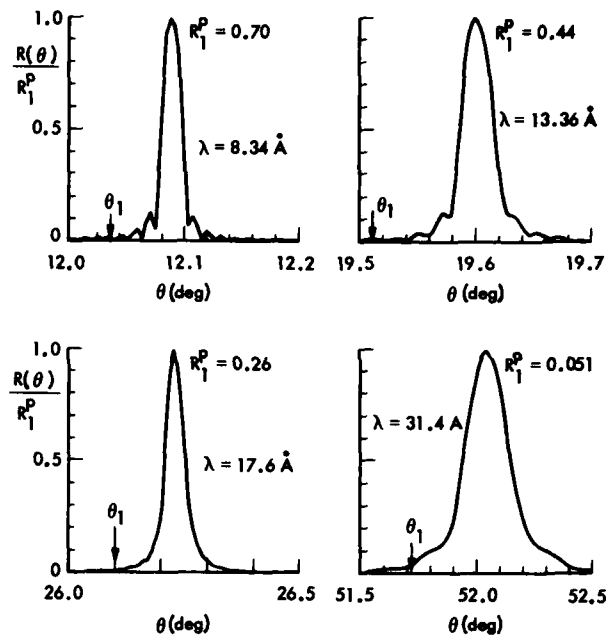


Fig. 7. Reflectivity curves computed at four wavelengths for an aluminum-beryllium LSM of 1000 layer pairs; these curves are for unpolarized radiation.  $\theta_1$  is the first order Bragg angle computed using  $2d = 40.00 \text{ \AA}$

At any particular wavelength, the performance (in terms of  $R_m^I$ ,  $R_m^P$  or  $\lambda/\Delta\lambda$ ) could be improved by optimizing  $d_A/d_B$  according to (37). However, the attainment of wavelength resolutions equal to or better than that of, say, potassium acid phthalate (KAP) requires values of contrast  $\phi_A - \phi_B$  lower than those given by the Al/Be combination. While possible material pairs exist (B/Be, Be/Mg, B/LiH) their stability as thin layer stacks needs to be established. In general, it will be more difficult to fabricate LSMs of high resolution than those of high integrated reflectivity, simply because of the much larger number of layers required over which it is necessary to maintain uniformity.

## VII. EFFECT OF LAYER IMPERFECTIONS

There are a number of ways in which the structure of an LSM can differ from the "ideal" structure upon which the theory is based. Such deviations or imperfections will affect the Bragg diffraction intensities, and so it is important to be able to model them computationally. The principal imperfections are described below.

**7.1 Imperfectly sharp interfaces.** In reality, the transition from index  $\bar{n}_A$  to index  $\bar{n}_B$  takes place over a finite distance, so that the interfaces are not infinitely sharp, as has been assumed so far. The distance over which this transition takes place, and its profile, will have a strong effect on the reflected intensities, and in particular on the relative intensities of the various orders.

The problem of computing reflection coefficients for electromagnetic waves for an interface at which there is a refractive index gradient has been treated in other contexts. In studying the reflection of radar signals from the lunar surface, for example, Simpson (23) concluded that the least cumbersome computational approach was to treat the transition zone as a large number of thin, homogeneous laminae whose index and thickness could be adjusted so as to approximate the

smooth transition by a number of finite steps. It may be shown that this approach is accurate, provided that the lamina thickness is much less than a wavelength of the radiation being reflected.

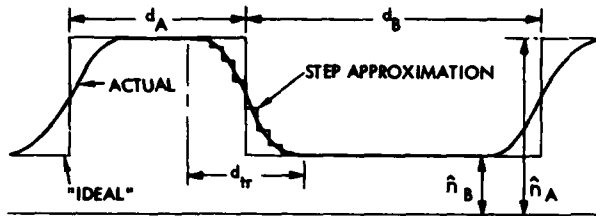


Fig. 8. Variation of refractive index through several LSM layers. The bold line indicates the "ideal" variation, with infinitely sharp gradients at the interfaces. The dashed line shows the model in which the index varies according to a cosine function over a transition distance  $d_{tr}$ . In the center of the figure, this smooth function has been approximated by ten thin sublayers of constant refractive index.

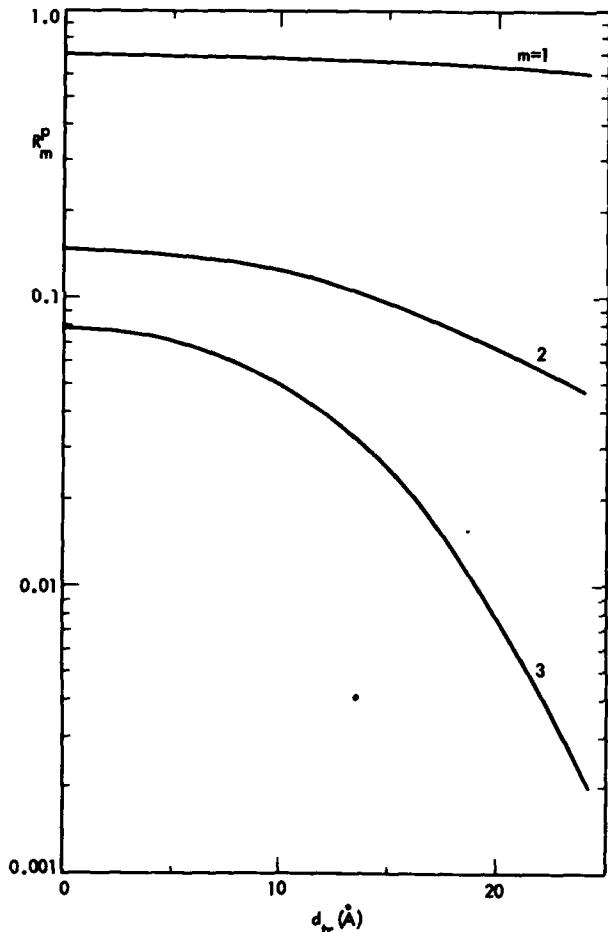


Fig. 9. Peak reflectivity  $R_m^P$  plotted as a function of  $d_{tr}$  for the first 3 orders of reflection of Al K $\alpha$  radiation ( $\lambda = 8.34 \text{ \AA}$ ) from a W/C LSM ( $d_w = 24.3 \text{ \AA}$ ,  $d_c = 33.4 \text{ \AA}$ ).

We used this method to examine the effect of a finite density gradient at the interfaces. It was assumed that the transition between the indices took place over a distance  $d_{tr}$ , and that the variation followed a cosine function, as shown in Fig. 8. This transition distance was then divided into a number of sublayers of equal thickness. The value for the index of a sublayer was then set equal to its value at the center of the layer.

In Fig. 9, the peak intensities of the first through third order reflections from a W/C LSM with  $d_w = 24.3 \text{ \AA}$ ,  $d_c = 33.4 \text{ \AA}$  are plotted as a function of  $d_{tr}$ .

**7.2. Variations in layer thickness.** Another kind of LSM imperfection arises if the layers vary in thickness through the structure, i.e. if a particular layer A has thickness  $d_A + \delta_A$  instead of the intended thickness  $d_A$ , with  $\delta_A$  varying randomly or continuously through the stack. This kind of imperfection is easy to model computationally.

In some cases, it may be advantageous to introduce a specific variation of layer thickness through the stack, in order to increase the reflectivity for a fixed number of layers (see e.g. Spiller (6,7,8)) to increase the reflected bandwidth, or for some other reason. At present the design of multilayer reflectors for x-rays and EUV is in a relatively simple stage, and there would appear to be some potential for the development of more sophisticated designs, analogous to those used for multilayer interference filters designed for use at longer wavelengths.

**7.3. Layer roughness.** Real layers will have a relatively rough, rather than a perfectly plane, surface and this will lead to scattering of the x-rays. This roughness will result from a) the intrinsic roughness of the substrate and b) roughness introduced during the layer-building process. It is conventional to quote roughness of surfaces as an rms figure in  $\text{\AA}$ , for example a "smooth" surface may have  $3 \text{ \AA}$  rms roughness. However, in order to predict how a surface will scatter electromagnetic radiation this figure is insufficient; it is necessary to know the power spectrum of the surface height variations.

It can be shown that scattering of x-rays by rough LSMs is analogous to the thermal diffuse scattering of x-rays by crystals and can be described by an analog of the Debye-Waller formula. This will be discussed in more detail elsewhere.

## VIII. COMPARISON OF EXPERIMENTAL

### RESULTS WITH THEORY

Techniques for making multilayer reflectors, both by evaporation and by sputtering are at present being perfected and much experimental data has been amassed. The experimental work is treated in the papers by Spiller and by Barbee (these proceedings), and need not be discussed in detail here. Suffice it to say that for periods above about  $30 \text{ \AA}$  (for evaporated structures) or  $15 \text{ \AA}$  (for sputtered structures) the performance of well made synthetic multilayers is close to that predicted theoretically. As an example, we show in Fig. 10 the reflectivity versus angle curve for a W/C LSM obtained at a wavelength of  $2.2631 \text{ \AA}$  using synchrotron radiation at the Stanford Synchrotron Radiation Laboratory. The structure consisted of 30 layer pairs with  $d_w = 12.4 \text{ \AA}$ ,  $d_c = 20 \text{ \AA}$ , so this curve can be compared directly with Fig. 2(c). (The deviation at angles close to zero is, of course, due to radiation spilling past the LSM at small glancing angles). The agreement is remarkably good, indicating an almost perfect layer structure in this particular LSM.



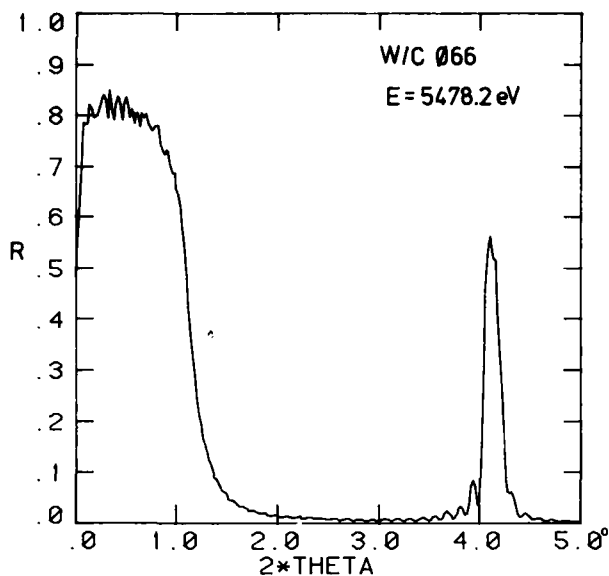


Fig. 10. Experimentally determined reflectivity versus glancing angle for a 30 layer pair W/C LSM. For layer parameters see text. These results were obtained using a Huber diffractometer at the Stanford Synchrotron Radiation Laboratory. The synchrotron radiation was rendered monochromatic with a channel-cut silicon crystal.

#### IX. CONCLUSIONS

In this paper the formalism for computing the intensity of Bragg reflection from structures layered on an atomic scale (LSMs) has been developed. It has been shown that, providing the material constraints can be overcome, it is possible to build structures whose properties complement those of presently existing x-ray analysers and reflectors. By varying such parameters as the refractive indices, layer thicknesses and total number of layers, these properties can be "tailored" for specific x-ray applications. In particular, structures with high integrated reflectivity and/or large  $2d$  spacing can be constructed. Such structures offer great potential in many areas of soft x-ray and extreme ultraviolet research and instrumentation.

The work at Stanford University was supported by the National Science Foundation through the Center for Materials Research and by the Department of Energy through the Lawrence Livermore Laboratories. The work at the Jet Propulsion Laboratory represents one aspect of research carried out under NAS7-100, supported by the National Aeronautics and Space Administration.

#### REFERENCES

1. H. Koeppel, Dissertation Giessen (1929).
2. W. Deubner, *Ann. Der Phys.* **5**, 261 (1930).
3. J. DuMond and J. P. Youtz, *J. Appl. Phys.*, **11**, 357 (1940).
4. J. Dinklage and R. Frerichs, *J. Appl. Phys.*, **34**, 2633 (1963).
5. J. Dinklage, *J. Appl. Phys.*, **38**, 3781 (1967).
6. E. Spiller, *Appl. Phys. Lett.*, **20**, 365 (1972).
7. E. Spiller, in *Space Optics*, Proceedings of ICO-IX, Santa Monica 1972, National Academy of Sciences, Washington, D. C. (1974) p. 525.
8. E. Spiller, *Appl. Opt.* **15**, 2333 (1976). (See also these proceedings).
9. R. -P. Haelbich and C. Kunz, *Opt. Comm.*, **17**, 287 (1976).

10. T. W. Barbee and D. C. Keith, in *Workshop on Instrumentation for Synchrotron Radiation Research*, (Eds: H. Winick and G. Brown) Stanford Synchrotron Radiation Laboratory Report No. 78/04, p. III-36 (May 1978).
11. T. W. Barbee, These proceedings.
12. J. H. Underwood, T. W. Barbee and D. C. Keith, in *Imaging X-ray Optics Workshop*, Proc. Soc. Photo. Opt. Inst. Eng. **184**, 123 (1979).
13. W. H. Zachariasen, *Theory of X-ray Diffraction in Crystals*, John Wiley and Sons, New York (1945) Chapter III.
14. A. M. Saxena and B. P. Schoenborn, *Acta. Cryst.* **A33**, 805 (1977).
15. A. H. Compton and S. K. Allison, *X-ray in Theory and Experiment*, 1st ed. Van Nostrand, New York (1935) p. 375 ff.
16. Based on a "mean" diffraction pattern (Reference 13, p. 126 ff.).
17. J. A. Prins, *Zeitschr. f. Phys.* **63**, 477 (1930)
18. A. V. Vinogradov and B. Ya. Zeldovich, *Appl Opt.* **16**, 89 (1977).
19. B. L. Henke and M. A. Tester, in *Advances in X-ray Analysis* (Eds.: W. L. Pickles, C. S. Barrett, J. B. Newkirk, and C. O. Ruud), Plenum Press, New York and London, Vol. **18**, p. 76 (1975).
20. A. J. Burek, *Space Sci. Inst.* **3**, 53 (1976).
21. D. L. McKenzie, P. B. Landecker and J. H. Underwood, *Space Sci. Inst.* **2**, 125 (1976).
22. M. W. Charles, *J. Appl. Phys.* **42**, 3329 (1971).
23. R. A. Simpson, *IEEE Transactions on Antennas and Propagation*, **AP-24**, 17 (1976).



Dr. Jim Underwood describing preliminary observations with the first normal incidence x-ray mirror.

## The Metrology of X-ray Optical Components

A. Franks

Division of Mechanical and Optical Metrology,

National Physical Laboratory, Teddington, Middlesex TW11 0LW, UK

## ABSTRACT

The differences in form and specifications of optical components used in the visible and X-ray spectral regions have stimulated the development of different approaches to the measurement of the latter. In general, the grazing incidence configuration is less conducive to the employment of the traditional interferometric methods of measurement than the automated probe methods which are now being developed. Optical methods become increasingly more valuable and more easily interpretable, the closer the optic approaches perfection.

## INTRODUCTION

Measurement and evaluation go hand in hand with the production of optical components, and over the years a range of measurement techniques has been devised which are in common use in the optical industry. Some X-ray optical components, such as plane or concave mirrors or diffraction grating blanks, are geometrically similar to their visible optical equivalents so that similar measurement techniques can be employed for them. However, many X-ray mirrors are very different in form and this does call for the consideration of different measuring approaches. With very few exceptions, X-ray mirrors are used in the grazing incidence configuration and typical characteristic features are that they have the form of elongated conicoids, and, often, the datum or reference surfaces are not the mirror surfaces themselves but the mounting flanges which are nearly normal to these surfaces. In the case of Wolter microscopes, problems of accessibility arise because of the small bore of the mirrors. The complex aspheric forms of the mirrors require that precise measurements be made even in the early stages of manufacture, when the mirror may still be in a non-reflecting or poorly reflecting state after grinding or diamond turning. The surface finish requirements of X-ray optics are also very demanding and have stimulated the development of specialized measuring techniques.

The measurement or evaluation of complete systems is normally undertaken with X-rays or with light, but this is a topic which is not dealt with in this paper.

## PURPOSE OF THE MEASUREMENTS

An important function of the measurement instrumentation is to establish whether the dimensions and form of the optical component lie within the manufacturing tolerances which were specified at the design stage. A whole series of measurements may be required, of increasing accuracy, as the component proceeds through its successive manufacturing stages, to enable the mirror to be corrected where necessary.

In practice, the situation is often complex in that parts of the mirror may be outside the specified tolerance, while other parts may be well within the tolerance. The important question then arises whether or not the overall performance of the mirror will meet the required specification. This information must be known in order to reduce to a minimum the costly and time-consuming work expended on figuring and finishing. A second important function of the measurement instrumentation is thus to yield data, rapidly and in computer compatible form, which will enable the X-ray performance of the mirror to be predicted. The measurement strategy must therefore be able to cater for the demands of the computer programs used for interpreting the measurement data.

## TYPES OF MEASUREMENT REQUIRED

## I. THE MIRROR SURFACE

In order to predict the performance of a mirror, the coordinates of all points on the surface are required to be known and they should be referred to fiducial datum surfaces on the mirror. For measurement, predictive and fabrication purposes, it is convenient to consider that the surface perturbations (the departures from the theoretically specified form) give rise to two broad categories of surface topography:

## (i) Macrotopography

The perturbations associated with the macrotopography of the surface have wavelengths ranging from the size of the mirror down to a few millimetres, with amplitudes down to about  $0.1 \mu\text{m}$ ; some perturbations may be non-periodic. In order to obtain a useful semi-quantitative appreciation of the quality of the mirror, it often suffices to make independent measurements of, say, diameter, circularity and axial profile.

## (ii) Microtopography

This refers to surface perturbations of wavelengths of a few millimetres down to the finest that can be measured. This would normally be down to  $0.25 \mu\text{m}$  in wavelength, but could with substantially greater difficulty, be as small as  $1 \text{ nm}$ , and with amplitudes down to less than  $0.5 \text{ nm}$ .

## II. REFERENCE SURFACES

In the case of Wolter telescopes, the relationship between the mirror axis and mounting flange requires to be known laterally and angularly. In sector telescopes, a reference surface normal to the mirror axis may be required, in addition to the mounting flange, to assist in optical alignment. Measurement of the departure of flatness of the mounting flange is also required. It is sometimes possible to orient mating flanges with respect to each other to minimize the distortions produced on clamping as a result of their lack of flatness.

## SPECIFICATIONS FOR X-RAY OPTICAL COMPONENTS

X-ray optical components form part of a system, the performance of which is usually specified in terms of factors such as linear or angular resolution, optical aperture or throughput, field of view and depth of focus. The combined effects of manufacturing and assembly errors, materials instabilities and conditions under service (such as thermal or mechanical

fluctuations) must be such that the performance of the instrument stays within the given specification. It is normal practice to produce an error budget in which the theoretically determined effects of the various errors may be traded-off against each other, within the limits imposed by the specification.

The optics of X-ray telescopes have probably received most attention in the literature. A good example of a study of the effects of misalignment and surface deformations is given by Korsch et al. (1). In their approach, which is the one most commonly employed, the surface deformations are simulated by ellipsoidal (radial) and sinusoidal (axial) deviations from the ideal surface. The image quality is defined by the axial rms spot size. The NPL approach (2) is more generalized in that the surface figure errors are described as the superposition of two uncorrelated perturbations: one being the normal displacement, and the other, the misorientation of small segments of the tangent plane relative to the ideal surface. Alternatively, if the perturbations are known to be slowly varying, they may be described by using Fourier or polynomial expansions. Non-periodic perturbations are described by a spline series. The images are evaluated by calculating the first and second moments of the intensity distribution on an appropriate image plane, which can be referred back to the object plane. The first moment is a simple measure of position, namely the centre of gravity, and the second moment (the radius of gyration,  $R$ , often called the blur circle radius) is a simple measure of image size and, hence, of resolution. The degradation of the image as a result of other perturbations, such as the misalignment of the component mirrors and surface roughness, where diffraction becomes dominant, may also be found in terms of  $R$  and may readily be combined, when expressed in this form. This general approach shares some common features with the converse calculation of the prediction of X-ray performance from the measured perturbations.

It is not possible to make generalized statements about the specifications for optical components, except to state that the trend is towards arc second or better resolution in telescopes and to sub-micrometre resolution in microscopes, which translates to sub-arc second resolution in angular terms. Some of the manufacturing tolerances for the AXAF (Advanced X-ray Astrophysics Facility) telescope have been documented (3). This is the most prestigious telescope now in the early stages of development and can serve as an example on which to base the accuracy requirements of the measurement instrumentation. The nominal resolution of the AXAF is 0.5 arc second, so that some, but not all, of the manufacturing tolerances for the somewhat less demanding telescopes currently under development may be relaxed by, say, a factor of 5 to 10.

The most demanding tolerances are those associated with the axial slope and parameters associated with deviations from roundness, and surface roughness. The axial slope tolerance for the AXAF mirrors is 0.05 arc sec, and for fabrication purposes, it is more convenient to state this in terms of the permitted amplitude variations of the surface for the spatial frequencies which may arise as a result of the manufacturing process. The tolerance is derived from geometric optical considerations, and the relevant spatial frequencies may cover a range of values starting at the length of the mirror down to the micrometre region. The scatter effects produced by the higher spatial frequencies, and usually referred to as roughness, will be discussed below. The tolerances on surface amplitude deviations corresponding to a 0.05 arc sec slope tolerance are 0.12  $\mu\text{m}$ , 0.025  $\mu\text{m}$ , 0.012  $\mu\text{m}$ , 6 nm, 2.5 nm for spatial frequencies of 500 mm, 100 mm, 50 mm, 25 mm and 10 mm respectively.

Different manufacturing procedures require to be employed to correct the longer and shorter wavelength errors. The parameters associated with roundness errors translate to sub-micrometre deviations for the possible spatial frequencies which may be present. This is by no means a comprehensive description of the fabrication tolerances but suffices to give an insight into some of the macrotopographic manufacturing tolerances. It is instructive to note that the diameter of the telescope is 1.2 m, so that in general, errors of 1 in  $10^7$  may be quite significant, and to compare this with the thermal expansion coefficient of silica which is  $5 \times 10^{-7} \text{ K}^{-1}$  and the long term stability of high quality optical materials which amounts to 1 in  $10^7$ - $10^8$  linear change per annum (4).

The effects of the micropographic structure is to degrade resolution by scattering the X-ray beam over an angular range around the central beam. The proportion of energy which falls within a one arc second diameter aperture for an on-axis point source has been calculated for the AXAF telescope (3), for different surface roughnesses and a 0.05 mm correlation length over a wavelength range of 0.15 nm to 1.25 nm, and is shown in fig. 1. This demonstrates clearly the high level of surface finish which is required in order to achieve an adequate resolution.

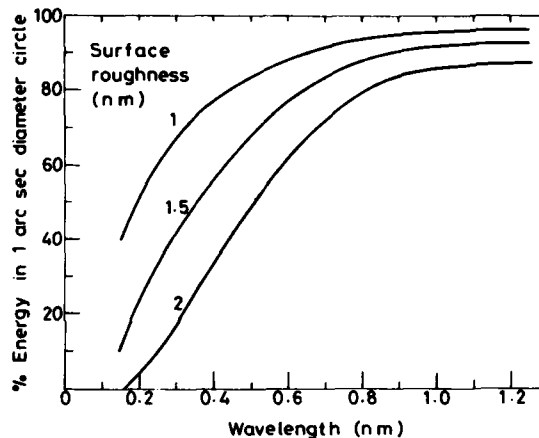


Fig. 1 Calculated proportion of energy falling within a 1 arc sec diameter aperture for an on-axis point source as a function of wavelength and surface roughness for the AXAF mirror assembly. (After (3)).

The manufacturing tolerances of high resolution, grazing incidence X-ray microscopes (5) are not dissimilar to those of telescopes. For a microscope of 40 mm diameter, a tolerance on surface form of 1 in  $10^7$  corresponds to a deviation of 4 nm. This is a demanding fabrication requirement and also presents a considerable challenge to the metrologist, but even so provides no more than an intermediate staging post to the challenges of the future. The successes achieved so far in enhancing reflectivities at large grazing angles by the use of multilayer interference coatings (6,7) raises the prospect of fully exploiting these components to achieve their potential resolution. Considerations similar to those in the visible optics region should apply, so that the surface figure should, at worst, not exceed a quarter of the wavelength employed. Both figure and surface finish requirements are thus approaching levels comparable to atomic dimensions.

A similar requirement for surface perfection has been discussed by Franks et al. (8), who showed that roughness, even at atomic levels, limited the diffraction efficiencies of X-ray gratings to less than 1% at wavelengths below 1 nm.

## MEASUREMENT TECHNIQUES

Measuring methods fall into two distinct classes: probe methods where the surface is measured sequentially, point by point, and surface measurements by interferometry where substantial areas, or the complete mirror, are measured simultaneously; although some interferograms may require to be evaluated sequentially.

## I. PROBE METHODS

Mechanical probes may be employed which are maintained in contact with the surface to be measured. The displacement of the probe, or stylus, is measured by optical or electromechanical methods. The probe may also be in the form of a beam of light in which case there is no physical contact with the surface being measured. An important advantage of the mechanical probe methods is that their use need not be restricted to reflecting surfaces and can thus be employed, for example, to measure the figure of a ground glass surface prior to polishing. Probe methods are also conveniently and conventionally employed to measure mirror datum faces or flanges and the correlation of the datum face with the mirror surface is facilitated if one instrument can be used for both these measurements.

## 1. MACROTOPOGRAPHY

## 1.1 Independent measurements of axial profile circularity and diameter

In this section, methods of measurement are described using different machines for the measurement of each of these three important parameters. It is by no means a trivial problem to correlate these independent measurements to obtain a comprehensive knowledge of the form of the component. Correlation is facilitated if well-characterized datum faces are built into the component.

Measuring machines for circularity and diameter are widely available commercially, because these are common place measurements in engineering and optics. The measurement of axial profile is a much more specialized requirement and has stimulated the development of a small number of machines, mainly for the measurement of X-ray telescope mirrors, but more recently also for X-ray microscopes.

## 1.2 Axial profile

## (1) Mechanical probe

At least three machines for the measurement of X-ray telescopes have been described in the literature. The first NPL profile measuring machine (9) has been extensively used since it became operational in 1976, not only for X-ray telescopes but also for concave and toroidal grating blanks and synchrotron mirrors (10), and has also been specially adapted to measure the small diameter (40 mm) bores of X-ray microscopes (5). Its original configuration permitted the internal measurement of cylinders down to diameters of 200 mm. It has axial and transverse travels of 250 mm and 15 mm respectively and positions on the curve are measured with resolutions of 1  $\mu$ m and 40 nm in the respective directions. The axial position is measured by a Moire fringe grating system and the sagittal position by an He-Ne laser interferometer. The interferometer monitors the separation of the stylus head from a non-load bearing reference straight edge, which is referred directly to the work being measured, and a tight metrological loop confers high immunity from the effects of environmental vibration. Measurements from the two axes are transferred into buffer stores and are

then processed to provide an output both in analogue and digital form, the latter permitting rapid data processing. Readings can be taken at up to 100 data points per minute and thus a very detailed scan can be made in a few minutes, virtually eliminating drift problems due to temperature and other environmental changes.

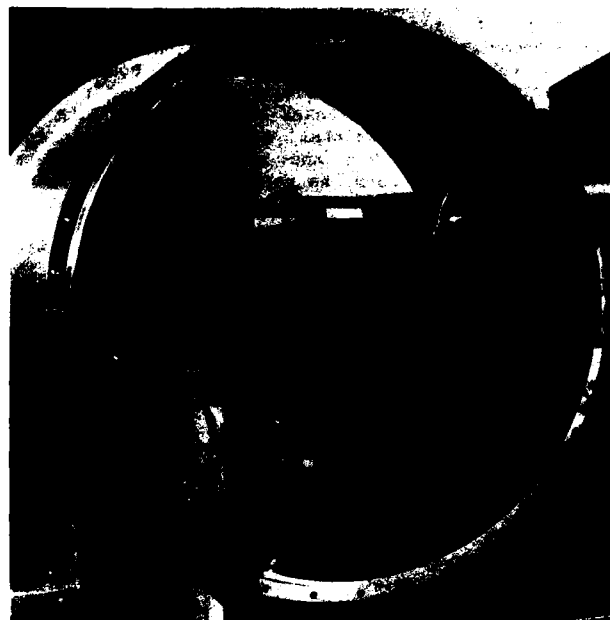


Fig. 2 Measurement of the profile of a paraboloidal telescope mirror.

The machine is shown in fig. 2 in the process of measuring a paraboloidal telescope mirror having a maximum internal diameter of 0.7 m. The main design concepts are shown in fig. 3. The reference straight edge (S) consists of a fused silica bar which has been polished optically flat and calibrated at the Laboratory to 5 nm. The bar mountings allow movement in the Y direction and permit the bar to be referenced directly to the work (W) being measured, through the stand-off posts (P). The separation of the work and the straight edge is measured by the interferometer mounted on the carriage C. The main interferometer block (I) is suspended on the carriage so as to refer directly to the straight edge, independently of the carriage motion. The moving arm carries a cube-corner reflector mounted behind the stylus which follows the work surface. The detectors (D) feed quadrature signals to an up-down counter registering the sagittal position.

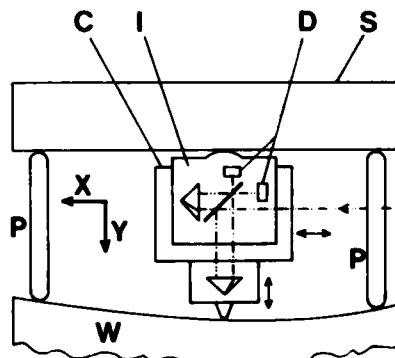


Fig. 3 Principle of the profile measuring machine.

The digital record can be processed by a computer and the output usually consists of an error curve showing the deviation of the measured profile from that of a specified curve.

The second NPL profile measuring machine (11), which is still under development, was designed specifically for the measurement of X-ray microscopes where sagittal measurements have to be made to an accuracy of a few nanometres, instead of the sub-micrometre accuracies required for the most of the current telescopes. This machine is more compact than the earlier one and this assists in further reducing the effects of environmental disturbances. Both the longitudinal and sagittal measurements are made interferometrically and the sagittal interferometer will, in its final form, be referred optically, rather than mechanically, to the reference surface, so that it is not subjected to any varying stresses. A Hewlett-Packard interferometer system is employed with a specially developed 10X resolution extender. The system has a theoretical maximum sagittal resolution of 0.8 nm. The optical reference surface can be calibrated against the standard NPL liquid surface flatness measuring interferometer (12) which has a measurement sensitivity of 1/1000 fringe or 0.27 nm. The measurement uncertainty expressed as the arithmetic sum of the individual uncertainties is  $\pm 1.2$  nm or  $\pm 0.97$  nm, if they are summed in quadrature.

An advantage of using interferometric, as opposed to analogue, measurement of the displacement of the probe is that the accuracy of the measurement (i.e. a fixed fraction of a fringe) is independent of the range of motion. For shallow curves, simple electromechanical transducers can also be employed, provided the resolution, which is a fixed fraction of the total displacement of the transducer, is adequate for the purposes. Lainé et al. (13) employ a linear air bearing (straight to  $0.1 \mu\text{m}$  and which can be calibrated to  $0.01 \mu\text{m}$ ) as their straight line reference and use an electrical gauge micrometer (having a resolution of  $0.01 \mu\text{m}$ ) to measure the deviations from straightness of an X-ray telescope. The X and Y outputs are digitized to give an error curve. Some commercially produced instruments, such as the Rank Taylor Hobson Ltd "Talytron S200" employ similar principles to measure departure from straightness, the magnification of the system being set by the maximum displacement to be measured. The sensitivity of an induction probe displacement measuring transducer has been used to maximum advantage in a telescope profile measuring machine (14) by employing a spherical instead of a linear reference surface. The circular section was a reasonably close fit to the conicoidal section so that the maximum departure did not exceed  $20 \mu\text{m}$ . The resolution of the probe was 0.05% of the full scale deviation, so that a measured accuracy to  $\pm 0.01 \mu\text{m}$  was achieved.

#### (ii) Optical probe

In the optical probe methods, the angular or linear displacements of a light beam reflected from the mirror surface provide a direct measure of changes in surface slope as the probe tracks along. The slope changes are easily converted into profile changes on the assumption that there are no discontinuities, such as steps, in the surface, to which the technique is insensitive. (Steps are not uncommon in surfaces machined by digital numerical control.) The techniques employed are closely related to the classical, and very sensitive, method of profile measurement in which changes in slope may be measured to sub-arc second accuracy by means of an autocollimator trained on a mirror, mounted perpendicular to the surface to be measured, and along which it is translated in known increments.

The requirements of X-ray microscopy stimulated the development of the NPL method (15) in which a laser beam parallel to a generator of the microscope surface is directed onto the surface after reflection by a pentaprism. Light which traverses a pentaprism is rotated through a right angle, so that the beam reflected from the surface will, after transmission through the pentaprism, return at an angle between it and the incident beam equal to twice the slope. This angle is measured by focusing the beam onto a position sensitive detector, and nulling it with an optical micrometer. In its present state of development, the machine is capable of measuring slope changes to 0.2 arc sec; the overall uncertainty in profile measurement does not exceed 5 nm. The spatial resolution is slightly less than 0.9 nm, so that the measurements are averaged over this distance.

A proprietary laser scanning technique has also been developed by Random Devices (16) for the measurement of X-ray microscopes. The beam is scanned over the surface to be measured and the local slopes are determined from the displacements of the reflected beam using a position-sensitive detector. The system also has a sensitivity of 0.2 arc sec.

#### (iii) Relative merits of mechanical and optical probes

Ultimately both systems may well be capable of measuring profiles to about 1 nm. This is of such unprecedented accuracy that it is desirable to have two entirely independent methods of measurement available, and this is the motivation to pursue the development of both techniques at NPL.

The optical probe has the two advantages of mechanical simplicity and that it is non-contacting. At worst, however, the mechanical stylus could produce damage along the line of contact, but the area damaged would be relatively small, so that its effect can be discounted. In practice, no damage has been detected with styli of radii 0.5 mm and 1 mm and loadings of a few grams. The spatial resolution of the stylus method is superior to that of the optical probe: with a 1 mm diameter stylus and a peak to valley surface roughness of  $0.1 \mu\text{m}$  and  $0.01 \mu\text{m}$ , the spatial resolutions are  $20 \mu\text{m}$  and  $6 \mu\text{m}$  respectively.

The mechanical stylus method is not dependent on the surface finish of the component under test while with the optical method the surface must be reflecting. The results must also be treated with some caution if the surface exhibits a marked topographic structure. In the case of the diamond turned surface shown in fig. 4 at least two of several periodicities are clearly visible: one of about  $18 \mu\text{m}$  equal to the turning pitch and one about 10 times greater which arises from periodicities within the machine. The diffraction spectra produced by these spacings fall within a few minutes to a few degrees from the reflected beam and may affect the output of the position-sensitive detector to give an erroneous result. As the quality of the surface improves these effects should become negligibly small.

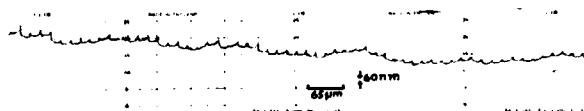


Fig. 4 Nanosurf trace of a diamond-turned bore. The  $18 \mu\text{m}$  and  $180 \mu\text{m}$  periodicities are clearly visible.

### 1.3 Circularity

The basis of circularity measurements is a precise axis of revolution. The departure from circularity is measured with a linear transducer in contact with the work. There are two options: either the work is placed on a precision rotary table and the transducer is kept stationary, or the transducer is attached to a rotating spindle, the work piece being stationary. The latter is convenient for in situ measurements. Many commercial systems are available with computer outputs to provide, for example, the best fit (least squares) circle, the maximum inscribed, the minimum circumscribed circles and an harmonic analysis of the amplitudes and phase relationships of the measured form. Spindles with radial accuracies of between  $0.01\ \mu\text{m}$  and  $0.1\ \mu\text{m}$  are readily available. Fig. 5 shows a circularity measurement being made with a stationary telescope mirror and using the Rank Taylor Hobson Talytron R300 portable spindle which incorporates centering and tilt adjustments. The instrument can conveniently be used to measure the flatness of the reference flanges and also squareness of the mirror axis by determining the centre of rotation at different levels.

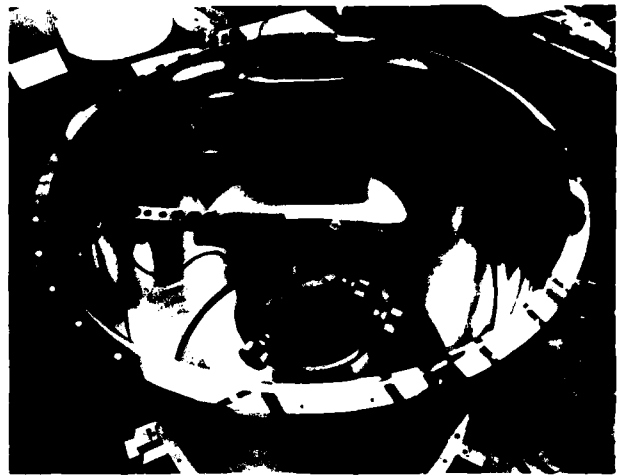


Fig. 5 Measurement of circularity with a portable spindle.

### 1.4 Diameter

The standard procedure in measuring diameters is to adjust the position of a probe until the maximum reading is obtained when the probe contacts opposite faces. This slightly arbitrary and statistically questionable procedure may be dispensed with by using a two-axis measuring machine. The microscope profile measuring machine, previously referred to, has been adapted to measure diameters and fig. 6 shows it being used to measure a silica ellipsoidal microscope mirror, made by Astron Developments Ltd (Unit 1, Aerodrome Way, Heston, UK). A number of measurements, made close to a diameter, say four on each side, are enough to establish the diameter of a circle using a least squares fitting procedure, to derive the best circle to fit the eight measurements. The measurement sensitivity is  $5\ \text{nm}$ . Absolute measurements are derived from secondary standards which are normally calibrated to  $0.1\ \mu\text{m}$ .

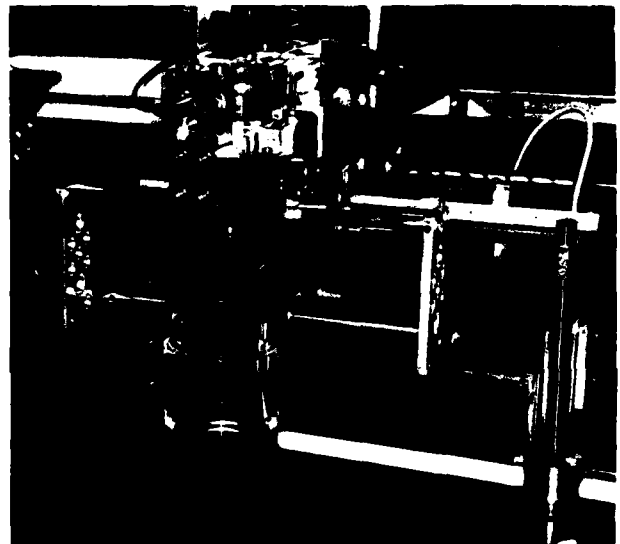


Fig. 6 Diameter measurement with a 2-axis measuring machine.

A portable gauge has been devised by Mr S.P. Poole at NPL for the measurement of large diameters and is shown in fig. 7. It consists of a length bar (a secondary standard of length), one end of which is fitted with a sensitive electronic displacement gauge. The length bar and gauge are selected to suit a particular mirror diameter and can be mounted at different heights to enable measurements of diameter and taper to be made in different diametral planes. The length bar/gauge assembly is calibrated interferometrically on the NPL length bar measuring machine (17) and can give measurements to an uncertainty of 1 part in  $10^6$ .

### 1.5 Dimensional measurements using a 3-axis measuring machine

The use of a 3-axis measuring machine would enable a self-consistent set of mirror surface coordinates to be obtained and relate these to the mirror datum focus, as well as yielding profile, circularity and diametral data. No suitable commercially made machine appears to be available so that NPL is now engaged in studying various design options prior to developing a suitable machine. The cylindrical symmetry of X-ray optical mirrors suggests that the machine should measure in cylindrical coordinates.



Fig. 7 Diameter measurement with a portable gauge.

## 2. MICROTOPOGRAPHY

### 1. Mechanical probe

Under suitable environmental conditions, measurements of microtopographic structure with amplitudes of 0.5 nm or less can be made with the Talystep (Rank Taylor Hobson Ltd). The NPL machine is housed underground in a temperature controlled environment. With a suitable stylus, a lateral resolution of 0.2  $\mu\text{m}$  is achievable. An NPL study (18) has shown that Talystep measurements agree with optical methods to within 1 nm and that the lightly loaded stylus (maximum load 2 mg) produces undetectable or negligibly little damage in a range of commonly used optical materials.

The form of the commercial version of the machine is not suitable for measurement inside bores and an instrument has been developed at the Laboratory specifically for the measurement of the surface roughness of X-ray microscopes. The instrument, now called the Nanosurf (19), is shown in fig 8.; its construction is based on the transducer system of the Talystep, and its sensitivity is the same as that of the standard instrument. The outputs from both instruments have been digitized to enable the measurements to be processed by computer. It is now possible to obtain, quite rapidly, amplitude distributions and other statistical functions of the surface topography.



Fig. 8 Measurement of the surface roughness of the bore of an X-ray microscope with the Nanosurf instrument.

### 2. Optical probe

#### (i) Optical heterodyne profilometry

In an NPL version of this technique (20), the key component is a double focus microscope objective containing a birefringent element. The objective produces two orthogonally polarized beams; one focused as a fine spot on the surface being measured and the other covering a much larger area, and acting as a reference beam. After reflection from the surface, the two beams are recombined and converted to a linear

polarization, the azimuth of which depends on the optical path difference between the constituent beams and hence on the surface profile. The length sensitivity is 0.1 nm and the lateral resolution is 0.8  $\mu\text{m}$ .

An alternative approach (21) is somewhat more complex mechanically. Two orthogonally polarized beams of slightly different frequencies are focused with a microscope objective onto the surface to be measured. Both focused beams have a diameter of 2  $\mu\text{m}$  and are separated by 100  $\mu\text{m}$ . After reflection from the surface and recombination in the optical system, the phase of the beat frequency of the interfering return beams is directly proportional to their optical path difference and this is related to the surface topography. The specimen to be measured is mounted on a precision rotary air bearing table, and one beam, centred on the axis of rotation acts as the reference for the other beam which scans over the surface. The height sensitivity is also 0.1 nm, but the spatial resolution is thus somewhat worse at 2  $\mu\text{m}$ .

Some caution must be observed in applying these techniques generally. Firstly, the optical path differences cannot be equated unequivocally with topographic differences, because phase changes may occur on reflection which are dependent on the local microstructure of the surface or on the structure of any thin films deposited on the surface. Secondly, it is well-known (22) that, as a result of obliquity effects, a microscope objective will introduce a phase shift which may average about 10% over a numerical aperture of 0.6 and which increases with increasing aperture. Hence if the light scattered from a feature on the surface does not fill the aperture uniformly, then a variable phase shift will be introduced which will produce erroneous topographic information.

#### (ii) Nomarski microscopy

The Nomarski polarization interference microscope (23) is not strictly a metrological tool because the results obtained are semi-quantitative only. It is sensitive to topographic changes in the sub-nanometre region and has a lateral resolution of 0.2  $\mu\text{m}$ . It is an extremely useful instrument for undertaking inspections during and subsequent to polishing. A special bore inspecting Nomarski microscope has been constructed and found invaluable for examining X-ray telescopes.

#### (iii) Other optical methods

Some other optical methods have been discussed by Lindsey and Penfold (24) and Bennett (25). The greatest attention has been paid to FECO interferometry and optical scatter methods. In the FECO method, the specimen and reference surface must be thickly metallized to achieve the required reflectivity, so that the measurements are made of the roughness of the coated surface. Ample electron microscope evidence exists (26) to demonstrate that, even when great care is taken, coated surfaces may be rough and that the roughness depends on factors which are not necessarily related to the roughness of the substrate. The FECO technique is most useful when the specimen and metallized coating structures are dissimilar. The technique is sensitive to height changes of 0.2 nm, but the lateral resolution is about 2  $\mu\text{m}$ ; this relatively poor resolution tends to give low values for the slopes of defects (27). It should also be noted that unless great care is taken, the accuracy of measurements with FECO fringes may be considerably poorer than that obtained more simply and quickly using the less expensive equipment for Fizeau multiple beam interferometry (18). In the scatter methods, the surface topography is deduced from the scatter

measurements and requires that a hypothetical model of the surface be postulated. The technique becomes suspect if regular periodicities exist, resulting, for example, from diamond turning (28), or where scratches or other macroscopic defects are present which are not amenable to statistical manipulation or in the case of certain coated surfaces (29).

#### (iv) Relative merits of mechanical and optical probes

The mechanical probe method has a vertical and lateral resolution equal to the best of the optical methods. In general, the optical methods are less direct and the results require interpretation: they become less suspect, the more perfect the surface.

### 3. Electron microscopy

The methods of surface roughness measurement discussed so far have at best a lateral resolution of about  $0.2 \mu\text{m}$  and a vertical resolution of  $0.1\text{--}0.5 \text{ nm}$ . A very much enhanced lateral resolution of  $1 \text{ nm}$  has been achieved by Butler (26) using transmission stereo-electron microscopy. The vertical resolution is also about  $1 \text{ nm}$ . The technique is tedious and requires that a replica be made of the surface to be examined.

## II. SURFACE EVALUATION BY INTERFEROMETRY

The advantages of interferometric examination of the optical surface is that in some types of interferometer the whole or a large part of the surface may be inspected at a time. The disadvantages are that, in most instances, the light path must follow the X-ray path in order to take advantage of the focusing properties of the component, and at a grazing angle of  $\theta$ , the interferometric measurements are desensitized by a factor of  $\sin\theta$  which is about a factor of 60 at  $1^\circ$  and 15 at  $4^\circ$ . One fringe would therefore correspond to a change in contour of  $36 \mu\text{m}$  or  $9 \mu\text{m}$  respectively, using an He-Ne  $633 \text{ nm}$  laser. The sensitivity can be enhanced by employing shorter wavelengths or by using a multi-pass interferometer, where the light emerging from the system is reflected back in, one or more times. However, with an imperfect mirror the resultant interferogram becomes so complex that detailed interpretation becomes difficult. In comparison with the probe methods, most interferometric methods are less sensitive, less amenable to in situ measurements, cannot be used when the surface is non-reflecting and the measurements are also less amenable to rapid computer processing.

### 1. Normal incidence interferometry

This is a direct method of measurement and is akin to the probe methods previously discussed. The gap between the optic and a reference optical surface is determined by measurement of the "Newton" fringe pattern. If the reference surface is flat then the fringes may be too finely spaced to yield useful information. For the Einstein mirrors, the reference surface was a toroidal test plate (30). The positions of the fringes were observed with the aid of a travelling microscope and were noted manually by pushing a control button; the information being recorded on paper tape for subsequent processing.

### 2. The Linnik interferometer

Speer et al. (31) have exploited the principle of the common-path Linnik interferometer (32, 33) to the testing of grazing incidence optics. In the system described by Linnik, a pinhole, in a partially

transmitting film, is placed at the image plane of the optic within the central maximum of the point spread function of the focused beam. The spherical wave propagated from this pinhole will interfere with the diverging wave from the optic transmitted through the semi-transparent film. The fringes produced can be related to the form of the optic.

In a grazing incidence system, the sensitivity of the interferometer is reduced a factor  $\sin\theta$ , but the sensitivity can be enhanced by reducing the wavelength. The authors describe a novel variation of the technique which should allow the interferometer to be used at least down to the hydrogen Lyman- $\alpha$  line of wavelength  $121.6 \text{ nm}$  and, in principle, at X-ray wavelengths. A grazing incidence mirror and a point scatterer (a diamond or an aluminized spot) may be substituted for the pinhole and its surrounding metallized film.

### 3. Twyman-Green and related interferometers

A simple interferometer employed by Dr K G Birch at NPL for testing optical systems having one conjugate at infinity is shown in fig. 9, with a parabolic sector X-ray mirror under test. The alignment facet facilitates the resetting of the optic, when it is used in service.

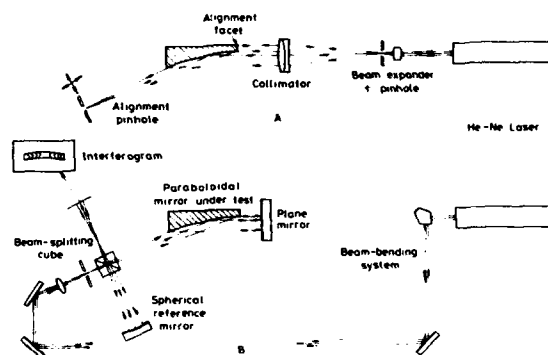


Fig. 9 Interferometric measurement of a parabolic sector mirror.

System A is used to align the laser to the mirror and to set the alignment pinhole. The mirror is adjusted so that the light reflected by the alignment facet returns to the entrance pinhole. The alignment pinhole is set to coincide with the point image formed by the X-ray mirror, and a microscope may be employed to examine the quality of the image and to optimize the setting. In order to examine the mirror interferometrically, the relative positions of the mirror and the alignment pinhole are kept fixed and a beam bending system is interposed to direct the light to a second beam expander and to illuminate the alignment pinhole as shown in System B. The interferometric components consist of a beam splitting cube, a concave spherical reference mirror and a plane mirror positioned as shown. For a perfect mirror, the interferogram will consist of straight fringes, and since this is a double-pass interferometer, the fringe spacing corresponds to a difference in contour of  $\lambda/4 \sin\theta$ .

### SOME EXAMPLES

Three examples are given to illustrate the range and relative merits of the measuring techniques which are employed.



### 1. An X-ray telescope mirror

The parabolic mirror of the LCXT (Large Cosmic X-ray Telescope) (34), is shown in Fig. 2. Its maximum diameter is just under 0.7 m and it is nearly 0.6 m long. Fig. 10 is a representation of the mirror as it might be seen by a metrologist, with an emphasis on the defects, and which presents him with the challenge of devising methods of measurement which will enable the mirror to be adequately characterized.

The mirror was diamond-turned at Oak Ridge National Laboratory and was given a detailed metrological examination on receipt. Circularity measurements were made with the Talytron (fig. 5), the output of which is a chart showing departures from circularity. Because of the complex form of the mirror section revealed by the circularity measurements, forty such measurements were made at 25 mm intervals along the axis. Such a detailed exploration also revealed the existence and location of discrete features (B) such as bulges or depressions in the surface. Some of these features extended 200 mm axially and  $20^\circ$  azimuthally and the maximum radial deviation was  $40 \mu\text{m}$ . One set of 4 depressions was disposed symmetrically about the axis. Apart from these special features, the local departures from circularity were about  $3 \mu\text{m}$  in the central region.

Another feature of the Talytron, and many other circularity measuring instruments, is that it yields the position of the mean centre (C) of the circular section relative to the axis of the spindle. Hence the direction of the axis of the mirror relative to a datum flange can be found by making a series of circularity measurements at different heights, while keeping the mirror and spindle axis fixed in position. These measurements showed that the mirror axis was straight to better than  $1 \mu\text{m}$  and made an angle of 2 arc sec with the mounting flange.

The departure from flatness of the mounting flange was measured by adjusting the indicator to measure vertical translations. This showed that the flange was saddle shaped, as indicated in fig. 10, with a maximum departure from flatness of  $4 \mu\text{m}$ . A similar measurement made on the flange of the mating mirror would indicate the optimum relative orientation of the mirrors to minimize distortion when they are clamped together.

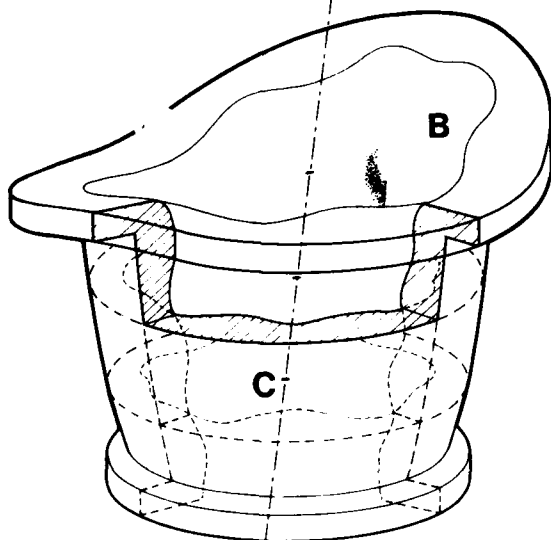


Fig. 10 An X-ray mirror showing axial and azimuthal perturbations, axial misalignment and flange distortion.

Diametral measurements (fig. 7) were made in orthogonal directions at 5 axial positions and showed that the diameters departed by about  $3 \mu\text{m}$  from their specified values, over the central region. These measurements also yielded the cone angle error (the error in the mean slope of the mirror) and this amounted to less than 1 arc sec.

A series of profile measurements were made which indicated that in general, the profile departed by no more than  $2 \mu\text{m}$  from the theoretical form over the central region, although the departures near the flanges amounted to  $20 \mu\text{m}$ .

These measurements taken together afforded an adequate basis for characterizing the form of the mirror and for planning the lapping and polishing strategy. It should be noted that some of the features described (as well as some other distortions) cannot be attributed to the characteristics of the high quality diamond turning machine which was used to fabricate the mirror. Service conditions require the mirror to be thin-walled (7.6 mm thick), so that it had to be supported in a stiff retaining shell during machining. A rubber interlayer was also extruded between the mirror and stiffening shell to assist in damping vibrations induced by the machining process. The four depressions previously referred to, correspond in position to the four injection sites for the rubber potting material, and most of the other distortions can also be directly attributed to the stiffening system. The problem of mounting thin-walled components without distortion is by no means trivial.

As well as figure measurements, surface finish measurements were also made and a Talysurf trace of part of the mirror is shown in fig. 11. The surface finish varied considerably over the length of the mirror and differed also from that of the mating hyperboloid, so that quite different finishing procedures had to be adopted for the two mirrors.

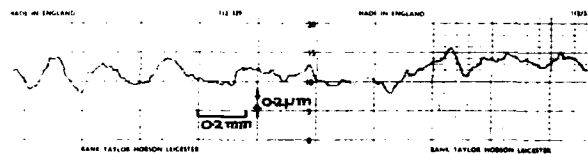


Fig. 11 Talysurf trace of the LCXT paraboloid.

Measurements of the type described were taken at successive manufacturing stages and the data were used to predict X-ray performance. The telescope was predicted to have a resolution of 40 arc sec and subsequent measurements made at the X-ray test facility at the Marshall Space Flight Center indicate that the FWHM of the mirror point spread function was less than 30 arc sec. Fig. 12 is a Nomarski photograph of the paraboloidal surface and is typical of the whole mirror. The image is virtually structureless, which indicates that any residual roughness was beyond the 1 nm resolution limit of the microscope.

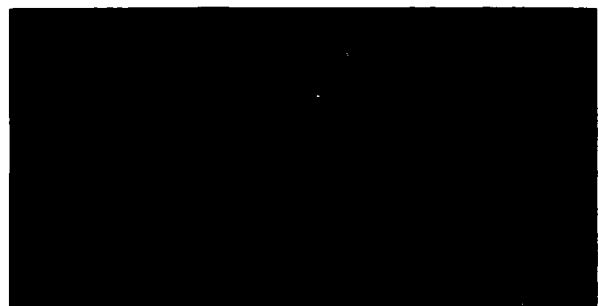


Fig. 12 Nomarski micrograph of the LCXT paraboloid.

## 2. A parabolic sector

This was the focusing optic used in the X-ray spectrograph spectrometer telescope (XSST) system (35). It is a  $60^\circ$  sector of an extreme off-axis paraboloid and the reflecting surface is approximately rectangular with dimensions of  $210 \times 104$  mm and is made of 'Spectrosil', a vitreous synthetic silica.

After initial grinding of the blank at Astron Developments Ltd, the deviations of the profile from the theoretical form were about  $1 \mu\text{m}$ , as measured on the profile measuring machine. The deviations were of such a nature that differential lapping techniques had to be employed to correct the figure and this was done by iterative lapping and measurement cycles. To maintain a high production efficiency, the measurement cycle is kept as short as possible: the blank can be cleaned adequately enough for measurements in the intermediate stages in 15 minutes, and the profile measurements of three generators and interpretation of results occupy less than an hour. The final measurement is shown in the form of an error curve in fig. 13 which indicates that the surface deviations did not exceed  $0.1 \mu\text{m}$  over the active length of the mirror.

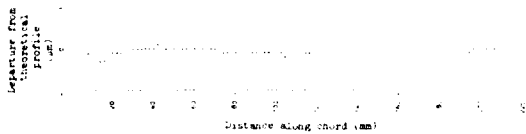


Fig. 13 Departure of the axial profile of the XSST mirror from its specified form.

An interferometric examination was also made using the interferometer shown in fig. 9, and an interferogram obtained at an intermediate stage of the figuring process is shown in fig. 14. The deviations from a straight line fringe pattern are a measure of the surface fringe errors and each fringe corresponds to a contour differential of  $\lambda/4\sin\theta = 3.5 \mu\text{m}$ .

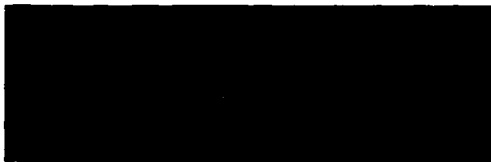


Fig. 14 Interferogram of the XSST mirror.

## 3. An X-ray microscope

The Wolter I microscope consists of complete hyperboloidal and ellipsoidal cylinders of revolution and was machined in one piece. The maximum diameter is about 40 mm and the total length is 36 mm. The substrate is steel and it is coated with approximately  $100 \mu\text{m}$  of electroless nickel. The microscope was diamond-turned at the Lawrence Livermore National Laboratory and is described in greater detail by Price (36). The metrology of the microscope was undertaken as part of a development program to improve its figure and surface finish.

The surface finish of the mirrors were measured with the Nanosurf machine (fig. 8) and the profile of part of the ellipsoidal mirror is shown in fig. 15. A variety of closely spaced larger scale undulations are clearly visible. The peak to valley amplitude of the surface irregularities does not exceed  $60 \text{ nm}$  and is generally in the range of  $10\text{--}40 \text{ nm}$ . The dramatic improvement obtained after 10 hours of lapping and polishing is shown in the figure, the residual roughness being about  $1 \text{ nm}$  peak to valley. The improvement in surface form after 10 hours of lapping

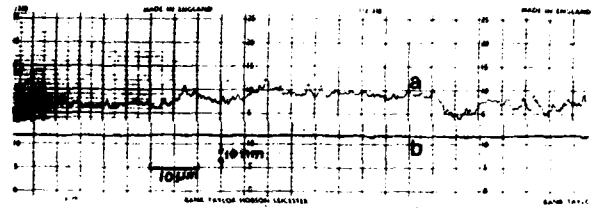


Fig. 15 Nanosurf traces of surface roughness of microscope ellipsoid (a) after diamond turning, (b) after 10 hours of lapping and polishing.

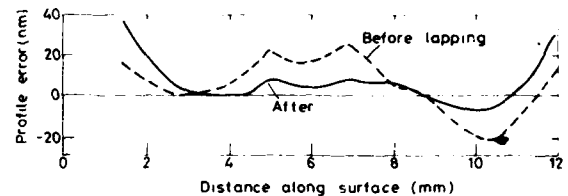


Fig. 16 Departure of the ellipsoidal mirror from its specified form before and after 10 hours of lapping.

is shown in fig. 16, which was obtained with the NPL optical probe profile measuring machine. It is interesting to note how remarkably accurate the LLNL diamond turning machine is, in that the deviations from the specified surface figure do not exceed  $50 \text{ nm}$  peak to valley and that they are comparable to the roughness amplitudes produced by turning.

## DISCUSSION

The development of mechanical and optical techniques for measuring X-ray components is now reaching the stage where some confidence can be expressed in their reliability and accuracy. In the next development phase, effort should be devoted to undertaking detailed theoretical and experimental studies to correlate these measurements with the measured X-ray performance in order to be able to predict the latter more precisely. It is not usually possible to use X-ray tests diagnostically to localize any particular source of error because X-ray evaluation is more frequently carried out on a complete assembly rather than a discrete component. Two X-ray techniques (37) have been developed to examine surface quality. In one, short wavelength X-rays (say  $0.15 \text{ nm}$ ) are incident at the nominal critical angle. Deviations in surface slope of less than  $1$  arc sec will be revealed as intensity variations in the reflected beam and this diagnostic technique has been employed to upgrade the quality of surface finishing of X-ray mirrors. In the other technique, used with focusing optics, the X-ray image is explored in the region of the focus where subsidiary foci may often be observed. The focal lengths of these subsidiary foci can be related to the magnitude of the surface ripples which act as miniature focusing elements.

The selection of the material of the X-ray optic has a bearing on the metrology. Some measurements must be made, for example, with uncertainties of 1 part in  $10^6$  or less. Fewer precautions need be taken with materials of low thermal expansion such as the optical glass ceramics (e.g. Zerodur, CerVit), ULE silica and silica having expansion coefficients of  $5 \times 10^{-8} \text{ K}^{-1}$ ,  $3 \times 10^{-8} \text{ K}^{-1}$  and  $5 \times 10^{-7} \text{ K}^{-1}$  respectively). Materials with higher expansion coefficients such as optical glass, steel and aluminium alloy ( $8 \times 10^{-6} \text{ K}^{-1}$ ,  $11 \times 10^{-6} \text{ K}^{-1}$  and  $23 \times 10^{-6} \text{ K}^{-1}$  respectively) may need to be kept at constant temperature for many hours prior to

measurement, before they reach thermal equilibrium at a known or desired temperature; the higher the thermal conductivity the more rapid is the attainment of equilibrium. Specific heat and density are also important factors which determine thermal behaviour under conditions of slow temperature changes or thermal spikes, and for a metal, beryllium has quite favourable characteristics (38), although ULE silica and the glass ceramics are better still.

The measurement of thin-walled aluminium alloy shells such as the LCXT mirror also requires that other special precautions be taken. The mirrors could be distorted by many micrometres as a result of frictional forces when placing the mirror on surface table, and special techniques had to be devised to lower the mirror without inducing any sideways forces. Similar problems were encountered with the silica mirrors of the Einstein telescope (30). The use of materials with high stiffness to weight ratios, such as beryllium, is desirable to minimize this problem and to minimize distortions which may arise in assembling the components and in service.

The macro- and micro-stabilities of the materials are also important. A year or more may elapse between the manufacture of a telescope and its launch and the telescope may be in service for many years thereafter. Whether the metrology is meaningful in terms of performance is thus very dependent on the stability of the material. The relative merits of glasses and metals for X-ray optics have been discussed by Lindsey and Franks (39), and although the siliceous materials are generally preferable, good optical components can be made of hot isostatically pressed beryllium or the non-age hardening aluminium alloy such as 5083, which was used for the LCXT mirrors.

#### CONCLUSIONS

No single method of measurement has adequate sensitivity to characterize all the defects met with in the manufacture of X-ray optical components. In general, mechanical probe methods have the advantage over interferogram methods in that the surface does not have to be reflective, the sensitivity and spatial resolution are higher, measurements may be made rapidly and in a computer compatible form. Probe methods are also more convenient for making absolute dimensional measurements and for relating the mirror surface to fiducial datum faces. On the other hand, interferograms provide an overall view of the surface. The optical methods become increasingly reliable and more easily interpretable, the closer the optic approaches perfection.

#### ACKNOWLEDGEMENTS

The extensive contributions made by Dr M. Stedman and Mr K. Lindsey are acknowledged.

Substantial financial support has been received from the UK Science and Engineering Research Council in support of the NPL program on X-ray optics. The work on the LCXT mirrors was undertaken in a joint development program with the Lockheed Palo Alto Research Laboratory and the Mullard Space Science Laboratory, that on the XSST mirrors with the Lockheed Palo Alto Research Laboratory and Imperial College, London, and that on the X-ray microscope with the Lawrence Livermore National Laboratory and the UK Atomic Weapons Research Establishment.

#### REFERENCES

1. D.Korsch, C.L.Wyman and L.M.Perry, Proc. SPIE., 184, 211 (1979).
2. B.Gale and M.Stedman, Proc. SPIE., 235, (in the press).
3. M.V.Zombeck, Opt. Eng., 20, 297 (1981).
4. G.D.Dew, Opt. Acta, 21, 609 (1974).
5. A.Franks, B.Gale, K.Lindsey, D.J.Pugh, C.J.Robbie and M.Stedman, Ann. N.Y. Acad. Sci., 342, 167 (1980).
6. E.Spiller, Proc. this conference.
7. T.W.Barbee, Proc. this conference.
8. A.Franks, K.Lindsey, J.M.Bennett, R.J.Speer, D.Turner and D.J.Hunt, Phil. Trans. Roy. Soc., 277, 503 (1975).
9. M.Stedman and V.W.Stanley, Proc. SPIE., 163, 99 (1979).
10. A.Franks, Proc. Workshop on X-ray Instrumentation for Synchrotron Research, Ed. H.Winnick and G.Brown, SSRL Rep. No. 78/04, 1978, p.VII 101-116.
11. M.Stedman, (to be published).
12. M.Debenham and G.D.Dew, Proc. Eng., 2, 93 (1980).
13. R.Laine, R.Givalt, R.Zobl, P.A.J.de Korte and J.A.M.Bleeker, Proc. SPIE., 184, 181 (1979).
14. E.Heynacher and D.Reinhardt, Proc. SPIE., 184, 167 (1979).
15. A.E.Ennos and M.S.Virdee (to be published).
16. J.K.Silk, Ann. N.Y. Acad. Sci., 342, 116 (1980).
17. S.J.Bennett, Phys. Bull., 22, 397 (1971).
18. R.J.King, M.J.Downs, P.B.Clapham, K.W.Raine and S.P.Talim, Jnl. Phys. E., 5, 445 (1972).
19. K.Lindsey (to be published).
20. M.J.Downs, British Patent No. 8037689 (1980).
21. G.E.Sommargren, App. Opt., 20, 61 (1981).
22. C.F.Bruce and B.S.Thornton, Jnl. Sci. Inst., 34, 203 (1957).
23. G.Nomarski and A.R.Weill, Rev. de Metall., 52, 121 (1955).
24. K.Lindsey and A.B.Penfold, Opt. Eng., 15, 220 (1976).
25. H.E.Bennett, Opt. Eng., 19, 610 (1980).
26. D.W.Butler, Micron, 4, 410 (1973).
27. I.J.Hodgkinson, Jnl. Phys. E, 3, 300 (1970).
28. D.L.Decker, J.M.Bennett, M.J.Soileau, J.O.Porteus and H.E.Bennett, Opt. Eng., 17, 160 (1978).
29. H.E.Bennett, Opt. Eng., 17, 480 (1978).
30. P.S.Young, Proc. SPIE., 184, 131 (1979).
31. R.J.Speer, M.Chrisp, D.Turner, S.Mrowka and K.Tregidgo, 18, 2003 (1979).
32. W.P.Linnik, C. R. Acad. Sci. URSS., 5, 210 (1933).
33. R.N.Smartt and W.H.Steel, Jpn. Jnl. App. Phys., 14, Suppl. 14-1, 351 (1975).
34. R.C.Catura, L.W.Acton, R.Berthelsdorf, J.L.Culhane, P.W.Sanford and A.Franks, Proc. SPIE., 184, 23 (1979).
35. W.A.Brown, E.C.Bruner, L.W.Acton, A.Franks, M.Stedman and R.J.Speer, Proc. SPIE., 184, 278 (1979).
36. R.H.Price, Proc. this conference.
37. K.Lindsey, Proc. X-ray Optics Symp at Mullard Space Science Lab., Science Research Council, London, 1974, 101-121.
38. A.Franks, Proc. SPIE., 184, 110 (1979).
39. K.Lindsey and A.Franks, Proc. SPIE., 163, 46 (1979).



Dr. Albert Franks (left) discussing grazing incidence x-ray microscopy with Dr. Paul Kirkpatrick (center) and Dr. Robert Price (right).

## X-Ray Microscopy Using Grazing Incidence Reflection Optics\*

Robert H. Price  
Lawrence Livermore National Laboratory  
University of California, Livermore, California

The history of x-ray optics using grazing incidence reflection now dates back more than 50 years. One of the earliest works in the field was that of Ehrenberg and Jentsch in 1929.<sup>1</sup> Jentsch was probably the first to suggest focusing x-rays with a curved mirror by means of total external reflection. He discussed many of the problems of grazing incidence reflection, including surface roughness requirements and the acute astigmatism of spherical surfaces at grazing incidence. Jentsch also carried out experiments with grazing incidence x-ray optics. To avoid the astigmatism problem he used an axisymmetric optic, consisting of a glass tube with an internal diameter of 2.7 mm. There is, however, no record of the successful formation of images with this device. In later years, Ehrenberg went on to study grazing incidence reflection from flat and from bent glass surfaces.<sup>2,3</sup> He also noted the effects of surface imperfections<sup>4</sup> which resulted in broad wings on the line focus produced by the bent glass mirrors.

It was not until 1948 that the first two dimensional focused x-ray images were produced by Kirkpatrick and Baez<sup>5</sup> using grazing incidence reflection. They avoided the problem of astigmatism at grazing incidence by crossing two cylindrical mirrors, each of which is focused in one of two orthogonal planes containing the optical axis. The effect is much the same as producing a 2-D image by crossing two cylindrical lenses.

The Kirkpatrick-Baez x-ray microscope has been an extremely successful imaging device, and is still used in many laboratories around the world. This success is largely due to the relative ease with which the required x-ray reflecting surfaces can be fabricated and to the high quality of the images produced.

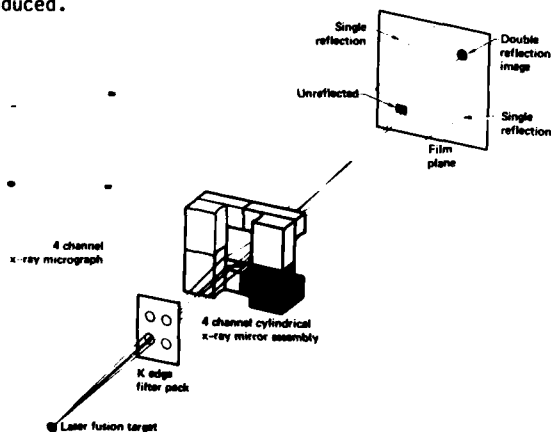


Figure 1 Each channel of a four channel Kirkpatrick-Baez x-ray microscope produces a focused double reflection image, two single reflection line foci and an unfocused spot from unreflected x rays. All four channels together, produce a pattern with four fold symmetry.

The cylindrical mirrors are nearly flat ( $\approx 1 \mu\text{m}$  saggital depth) and can be easily fabricated using conventional optical techniques. Shallow spherical

mirrors can also be used without serious degradation of performance. Optical fabrication technology has advanced to the point that a nearly perfect surface can be produced over the tiny portion of the mirror actually used in image formation. Surface finishes better than  $10 \text{ \AA}$  RMS are routinely produced on selected materials (fused silica, vitreous carbon, electrodeless nickel, silicon crystal, etc.). Absolute saggital profiles with accuracies on the order of  $100 \text{ \AA}/\text{cm}$  are frequently produced.

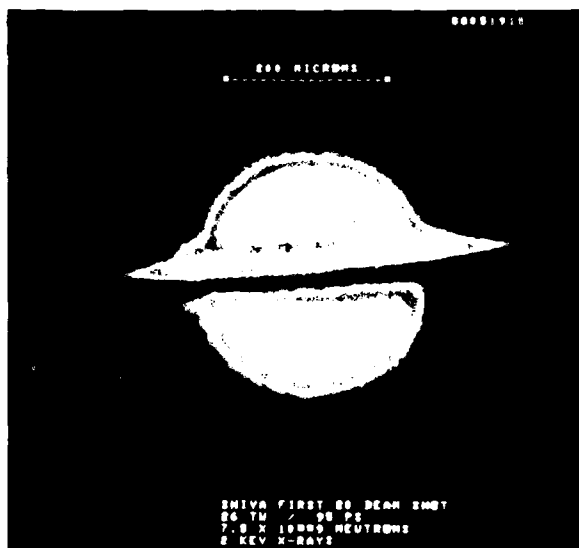


Figure 2 Kirkpatrick-Baez x-ray micrograph of a ball-in-plate target taken during the first full power (26 TW) target shot at the Shiva laser facility.

Many of the Kirkpatrick-Baez x-ray microscopes now in use are diffraction limited in the x ray portion of the spectrum. In fact, as Prince<sup>6</sup> noted, a Kirkpatrick-Baez microscope with cylindrical mirrors can be optimized by adjusting the mirror length such that the geometrical aberrations of the mirror system are balanced by diffraction. This type of optimization typically produces resolutions on the order of one micron. In certain instances, resolutions of one half micron have been achieved.<sup>7</sup>

McGee has shown<sup>8</sup> that by using surfaces with a cubic term, rather than purely cylindrical surfaces, geometrical aberrations can be reduced, mirrors lengthened, and resolution improved. Though useful for specialized applications, notably biological,

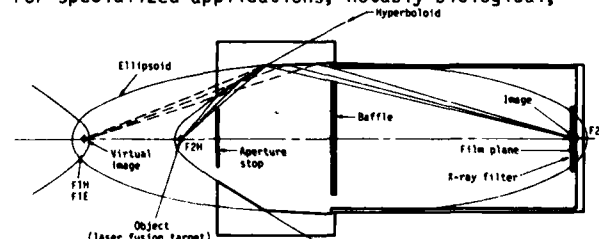


Figure 3 Ray diagram of a Wölter Hyperboloidal-Ellipsoidal Axisymmetric x-ray microscope.

\* Work performed under the auspices of the U. S. Department of Energy by the Lawrence Livermore National Laboratory under contract number W-7405-ENG-48.

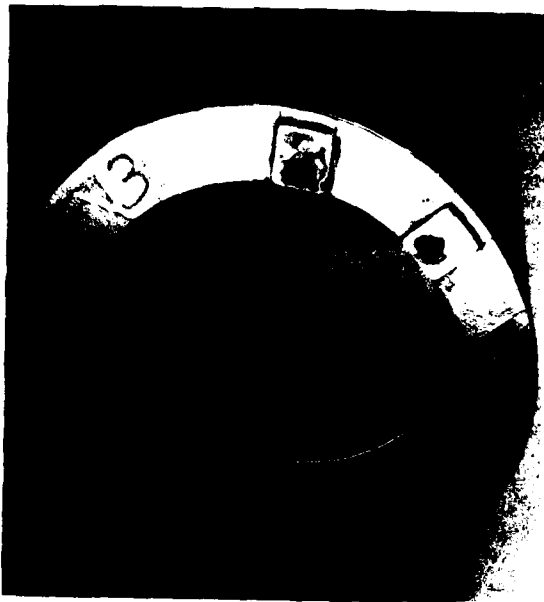


Figure 4 Wölter Axisymmetric x-ray microscope fabricated from Diamond turned electroless Nickel on a steel substrate.

this increased resolution results in decreased field of view. For this reason, as well as increased cost and difficulty of fabrication, "cubic" surfaces have not been useful for laser fusion applications.

The Kirkpatrick-Baez x-ray microscope has become one of the work horse diagnostics of the Laser Fusion program at the Lawrence Livermore National Laboratory.<sup>9,10</sup> K-B x-ray microscopes have been fielded and have provided useful information on the majority of shots since 1975. They have been used on four major laser systems: Cyclops, Janus, Argus, and Shiva, are also planned for use on the Nova laser system, where they will be coupled with CCD arrays to

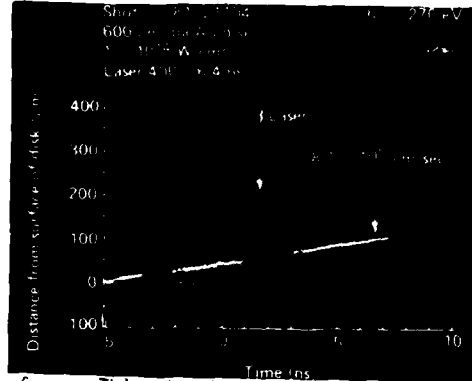


Figure 6 This streaked x-ray image of a laser irradiated gold disk (self emission at 270 eV) shows a constant velocity for the x-ray emission region while the laser intensity increases and decreases during the pulse. The FWHM of the x-ray emission region is only 15  $\mu\text{m}$  during most of the pulse.

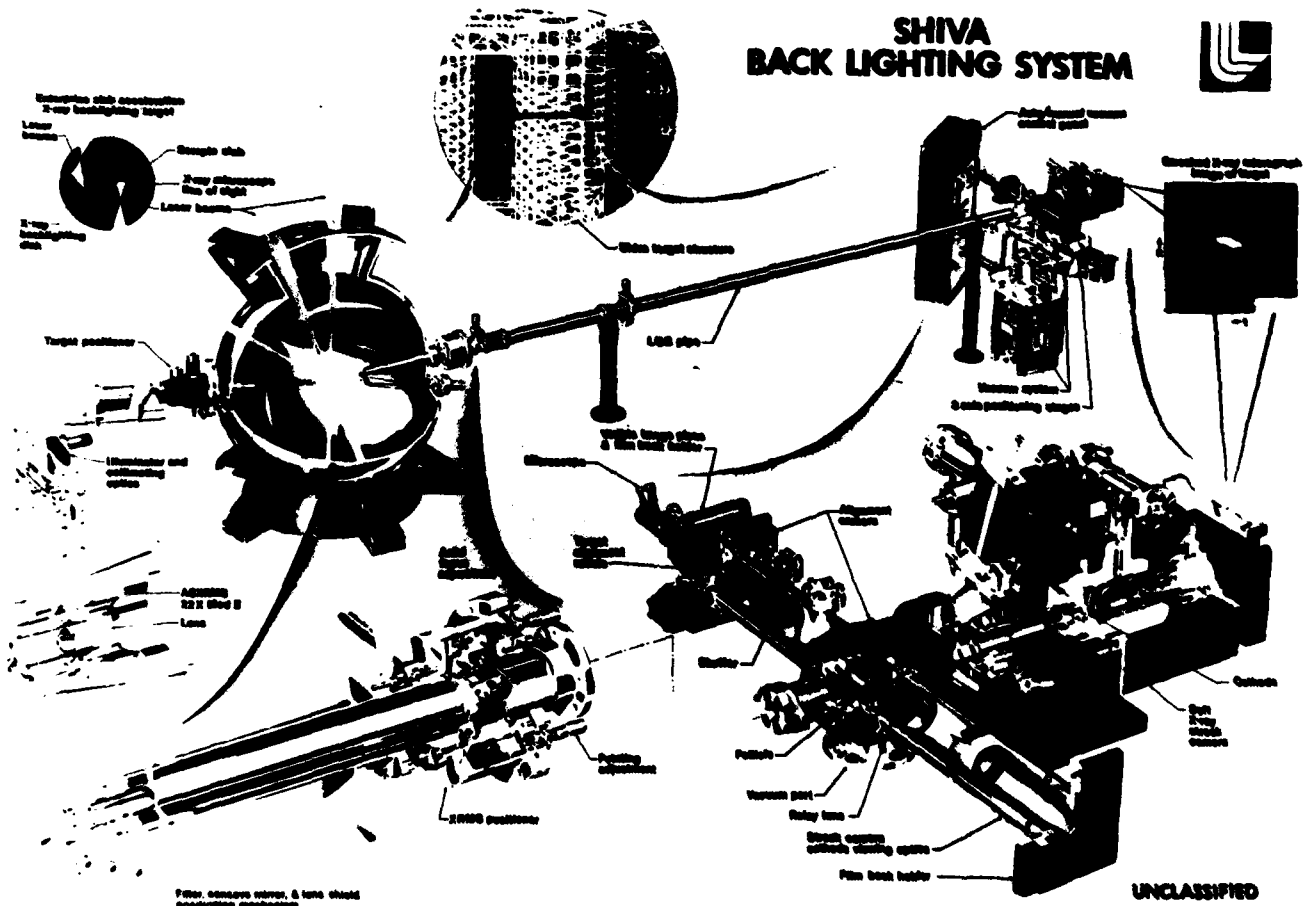


Figure 5 The Shiva x-ray backlighting system uses a Wölter Axisymmetric x-ray microscope coupled to a soft x-ray streak camera and an optical alignment system.

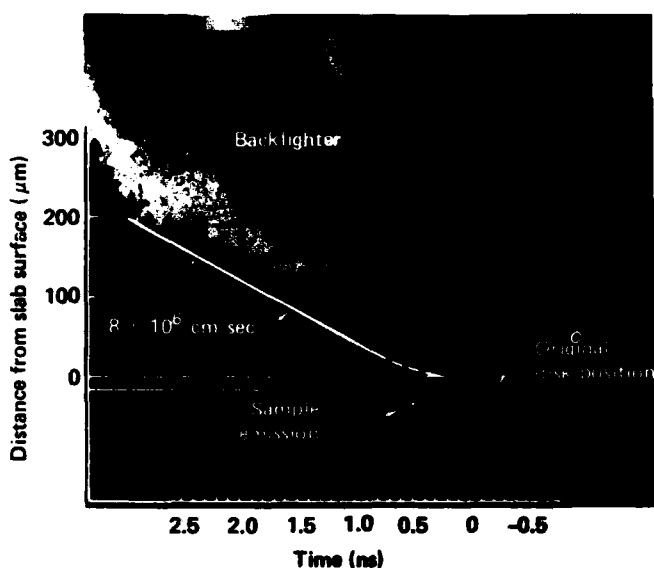


Figure 7 A 17  $\mu\text{m}$  thick Aluminum slab was accelerated to  $8 \times 10^6$  cm/sec by a 647 ps,  $5.8 \times 10^{14}$  W/cm<sup>2</sup> laser pulse and was observed using a Tantalum backlighter irradiated for 2.8 ns at  $3.9 \times 10^{14}$  W/cm<sup>2</sup>. Self emission from the Aluminum sample slab is visible below the original disk location.

provide data immediately following each shot. Figure 1 shows the x-ray optical configuration of one channel of the four channel Kirkpatrick-Baez x-ray microscope configuration commonly used at LLNL.

As shown in figure 1, the 90° intersection produced by the crossed cylindrical mirrors lends itself to a square configuration. This forms an image from the x rays reflected at each corner. By choosing the grazing angles, reflecting materials, and filters carefully, an x-ray microscope can be made which produces images at four different x-ray energies along nearly the same line of sight. A factor of four or more can be spanned in x-ray energies passed by the various channels. This feature, together with the good definition of the energy channels ( $E/\Delta E \approx 4$  to 5), makes these instruments extremely useful for laser fusion diagnostics. Kirkpatrick-Baez x-ray microscopes used to date in laser fusion applications have object distances of 25 to 40 cm and resolution in the 1 to 3  $\mu\text{m}$  range. Magnifications have ranged from 3 to 8.

One of the major advantages of the Kirkpatrick-Baez x-ray microscope is that it produces a true focused image on film which can be developed and qualitatively evaluated in less than half an hour after a target shot. This capability often provides crucial information on target performance needed to properly set up the next target experiment. The relatively long object distances are dictated by the problem of blast damage during target irradiation: filters can be ruptured and mirrors damaged. However, as presently used, the Kirkpatrick-Baez x-ray microscopes can take pictures for months at a time without attention, except for changing film.

The Kirkpatrick-Baez x-ray microscopes have been fielded with channels ranging from 200 eV to 4.5 keV. Figure 2 is an x-ray photo of a ball-in-plate target irradiated at 26 TW during the first full power target shot on the Shiva laser facility.

While Kirkpatrick-Baez x-ray microscopes combine many of the features desired of a diagnostic, for some applications more solid angle is required than can be provided by an ordinary Kirkpatrick-Baez x-ray microscope. (Kirkpatrick-Baez x-ray microscopes typically have  $10^{-6}$  to  $10^{-7}$  steradian acceptance angles for laser fusion applications.) This need is now being filled by the Wolter axisymmetric x-ray microscope.

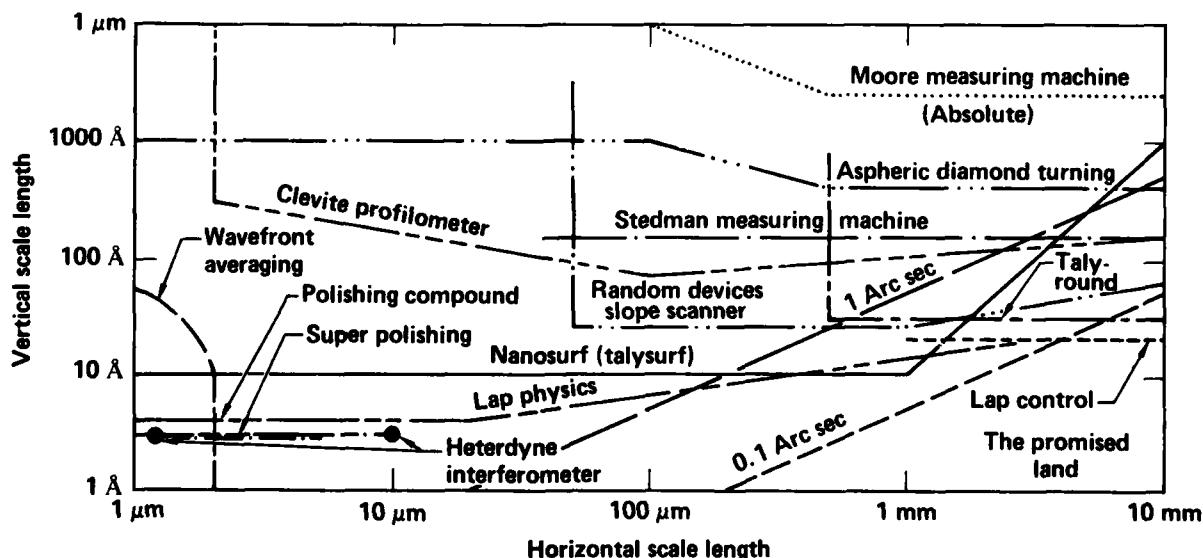


Figure 8 Vertical and horizontal scale lengths associated with various metrology devices and fabrication technologies are shown together with 1 arc second and 0.1 arc second tolerances required for advanced x-ray optics. The region with horizontal scale lengths between 100  $\mu\text{m}$  and 10 mm, with vertical scale lengths of 5 - 50 Å, is particularly difficult for optical fabrication work.

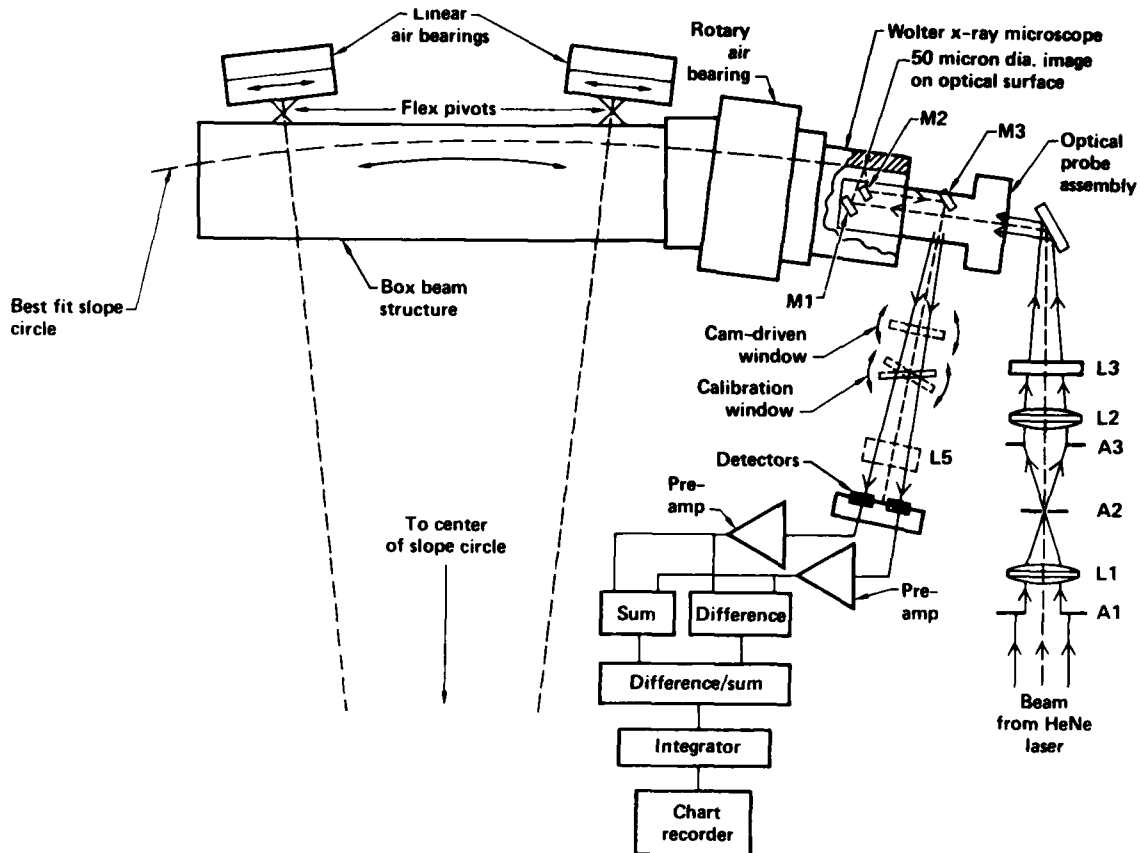


Figure 9 Random Device's sloop scanner operates on the principle of the optical lever. It is capable of measuring slope errors of a few tenths of an arc second and displacements of 10 - 20 Å. It shows potential for improvement in sensitivity by an additional order of magnitude.

Wölter developed the idea of using axisymmetric mirrors made up of conic sections of revolution in 1952.<sup>11,12</sup> His work was stimulated not only by Kirkpatrick and Baez, but also by Trurnit,<sup>13</sup> who in 1946 had successfully formed images using a paraboloid coated with a Barium Stearate crystal. Wölter also refers to Nahring's 1930 work<sup>14</sup> on grazing incidence reflectivity and Schwarzschild's 1905 work on the conditions for aplanatic imaging systems. Interestingly, though Wölter apparently did not know about the work of Jentsch, he came to the same conclusion, that is, to use an axisymmetric grazing incidence reflector to avoid astigmatism in the imaging system. He also came to similar conclusions regarding surface roughness.

Figure 3 shows the geometry of a Wölter type I x-ray microscope. In this microscope a hyperboloid and an ellipsoid of revolution are combined such that they have a common focus (F1H and F1E). An object placed at the second focus of the hyperboloid (F2H) will then form a magnified virtual image of the object at the common focus of the hyperboloid and ellipsoid (F1H and F1E). The virtual image will then be refocused at the secondary focus of the ellipsoid (F2E), forming a magnified image of the object. In a practical Wölter microscope mirror, the ellipsoid may have a minor radius of 1 or 2 cm, while the major radius may be several meters or more. Only very small segments of the hyperboloid and ellipsoid are used, not more than a few centimeters in length along the optical axis.

Figure 4 is a photo of a recently fabricated Wölter x-ray microscope. The sagitta of these conic segments differ from straight cones by less than a micron. The requirements on the surface tolerances

are similar to the tolerances of a Kirkpatrick-Baez x-ray microscope; however, the area over which these tolerances must be met is 10's of square centimeters, rather than a few square millimeters. Furthermore, these tolerances must be met on a complex internal aspheric surface. Deviations in sagittal profile must be under 100 Å and the RMS surface roughness must be under 10 Å. Axisymmetric roundness of the mirror must be maintained to better than 0.5 μm.

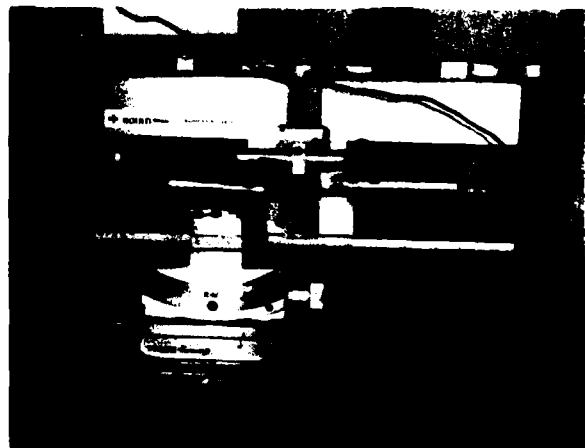


Figure 10 The Cleveite Profilometer is an inductive pickup diamond stylus device which is linear and reproducible to 70 Å.

Azimuthal slope errors must be held to a few arcseconds while longitudinal slope errors must be well under 1 arcsecond.

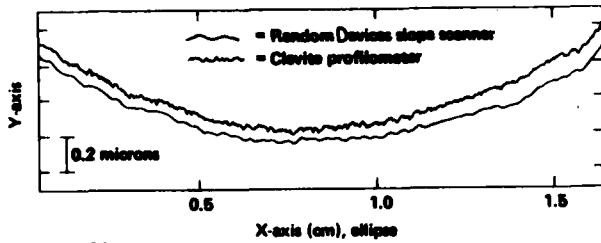


Figure 11 Comparison of Clevite profilometer and Random Device's slope scanner measurements of a Wölter axisymmetric x-ray microscope mirror surface shows agreement at the + 30 Å level for surface scale lengths greater than the 50 μm spot size of the slope scanner.

Wölter realized that such tolerances might be difficult or impossible to meet on such a complex surface, and for many years no attempts to fabricate such mirrors were reported. Subsequently, interest in x-ray astronomy stimulated the modification and development of Wölter's design for astronomical purposes. In 1975, Palmeri and Seward<sup>16</sup> suggested that a Wölter type I x-ray microscope might be applicable to the observation of high density laser fusion target implosions. Work was begun on a 9X and a 22X Wölter type I x-ray microscope design with fabrication being undertaken at LLNL and Random Devices, Inc.<sup>17</sup> Later, a contract was let to the National Physical Laboratory in England through the Atomic Weapons Research Establishment, beginning a third parallel development effort. Los Alamos also began development work on a small Wölter x-ray microscope at Random Devices, Inc.<sup>18</sup> At the time these contracts were let, the technology did not exist to fabricate the desired surface. Initially, two approaches were attempted:

1. Traditional grinding and polishing of electroless nickel on separate hyperboloidal and ellipsoidal aluminum substrates, and
2. diamond turning of the entire mirror in electroless nickel on steel substrates.

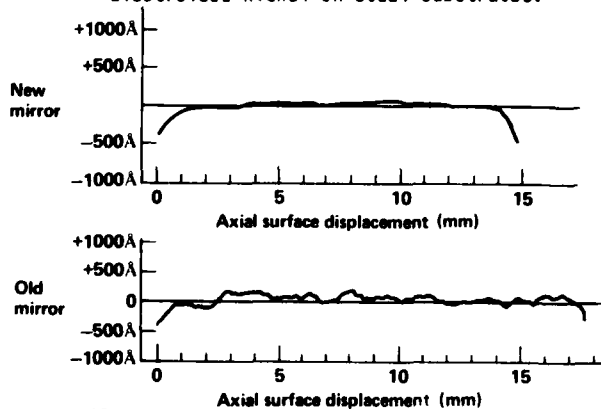


Figure 12 The deviation from desired surface profile of the Wölter mirror recently finished by Random Devices compares favorably with the surface profile deviation of an early mirror finished at the Lawrence Livermore National Laboratory.

Later, the traditional grinding and polishing approach was dropped. Passive feedback was developed for the numerically controlled diamond turning machine to allow it to attain accuracies of 1 to 2

microinches (250 to 500 Å). This is carried out by machining the mirror, then measuring the deviation of the mirror from the ideal contour and feeding the correction back into the diamond turning machine for the next cut. It was found necessary to polish the steel substrate to a 1000 Å finish in the region of the x-ray reflecting surface before electroless nickel plating and diamond turning. This avoids print through of the machining marks on the steel, onto the optical surface of the x-ray mirror during polishing. The diamond turned substrates were then turned over to the three different groups (LLNL, NPL, and Random Devices) for polishing.

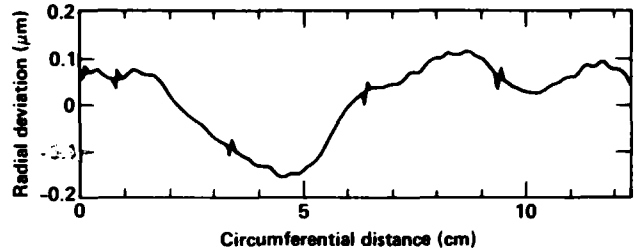


Figure 13 The deviation of the new Random Devices fabricated Wölter mirror from circularity, shows some periodic structure remaining from diamond turning.

Two 22X magnification Wölter mirrors of an early design were finished at LLNL several years ago and have been fielded at the Shiva laser facility during the past year in the streaked microscope system shown in figure 5. This system provides a spatial resolution of 4 to 5 μm over a field of view of up to 800 μm and a temporal resolution of 15 ps. The

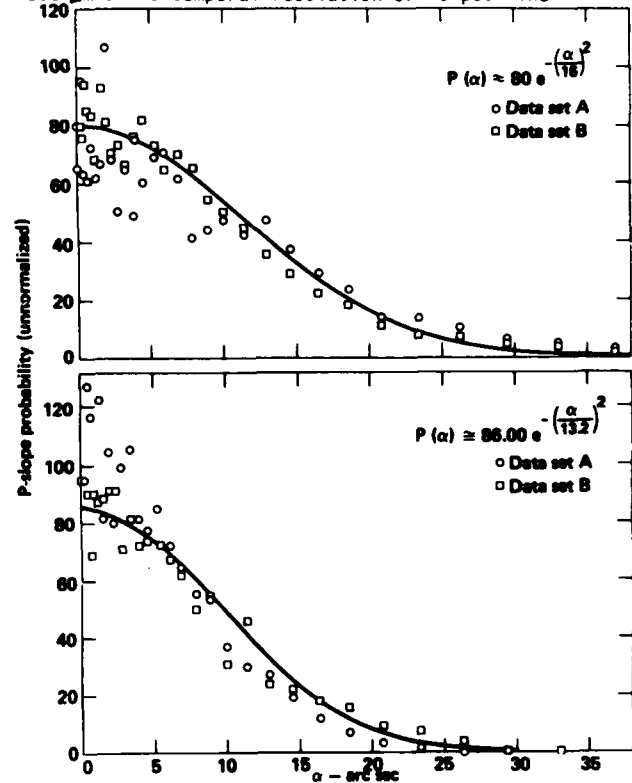


Figure 14 The longitudinal slope errors on the ellipsoid and hyperboloid of the older Wölter mirror are random in nature with standard deviations of 16 and 13.2 arc seconds respectively.



spatial resolution is limited by the 100  $\mu\text{m}$  resolution of the streak camera and the 22X magnification of the x-ray mirror. The 2  $\mu\text{m}$  resolution of the Wölter x-ray mirror does not contribute significantly to the overall spatial resolution of the system. The streaked x-ray microscope is also equipped with a collinear optical alignment system which allows alignment of the x-ray imaging device onto the target with an absolute accuracy of 5 to 10  $\mu\text{m}$ . This is accomplished through the use of an optical lens with the same optical conjugates as the Wölter x-ray mirror. The lens and mirror are coaligned so the focal points overlap. A visible image of the target can then be viewed through a visible light alignment camera coupled to the x-ray streak camera.

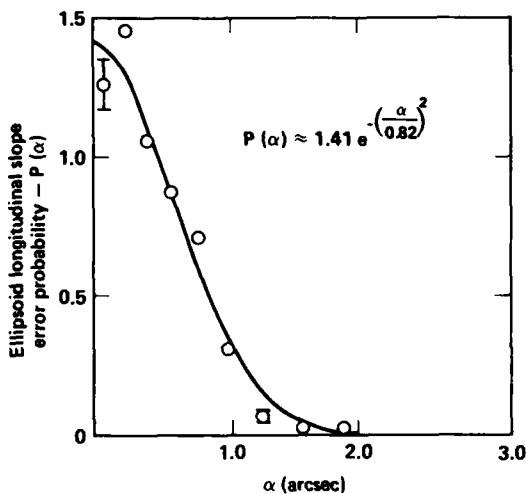


Figure 15 The longitudinal slope errors of the ellipsoid of the Random Devices mirror are primarily random in nature with a standard deviation of 0.82 arc seconds.

The streaked Wölter x-ray microscope has been used to observe targets both in self emission and in transmission together with a laser driven x-ray backlighting source. This allows time resolved radiography of the dynamical behavior of the targets.

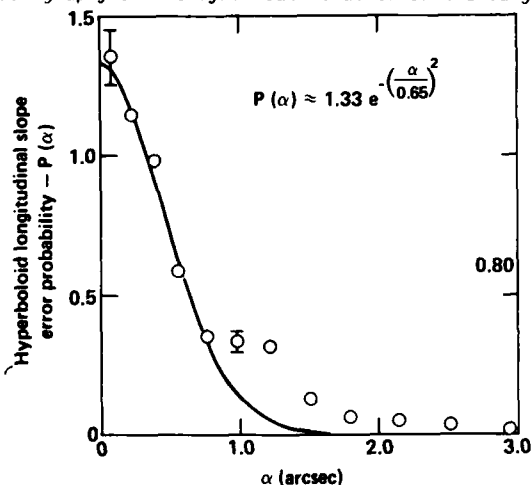


Figure 16 The longitudinal slope errors of the hyperboloid of the Random Devices mirror are also primarily random in nature with a standard deviation of 0.65 arc seconds. However, some periodic structure is evident from the peak at 1.2 arc seconds.

Figure 6 shows the time resolved x-ray self emission from a gold disk irradiated at  $1 \times 10^{14}$   $\text{W}/\text{cm}^2$  with a 6.4 ns laser pulse. This image is striking because the emitting plasma moves back toward the laser from the disk surface at nearly constant velocity, while the laser intensity increases and decreases during the pulse. It is also striking because the emitting region has a FWHM of only 15  $\mu\text{m}$ . By the peak of the laser pulse, a cold region has developed between the emission region and the disk which is quite dark when viewed in the 270 eV photons with which this image was recorded.

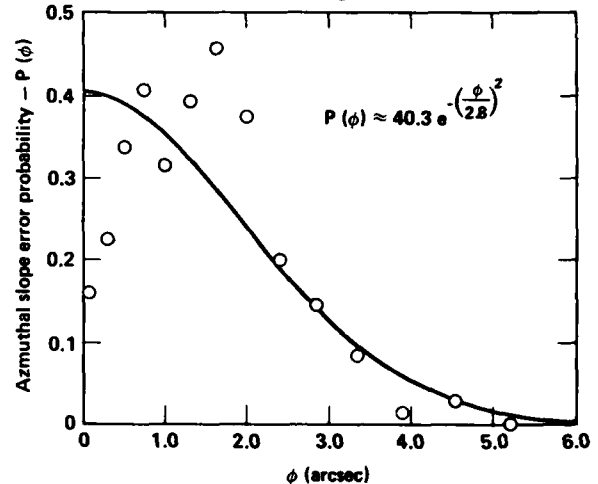


Figure 17 The azimuthal slope error distribution of the Random Devices mirror shows considerable contribution from periodic surface structures with peaks in the distribution at 0.75 and 1.7 arc seconds. To analytically model the distribution a gaussian with a standard deviation of 2.8 arc seconds was used.

Figure 7 shows a backlit image of an aluminum slab which was accelerated by ablation resulting from direct laser irradiation. It attained a velocity of  $8 \times 10^6$   $\text{cm}/\text{sec}$ . The backlighter in this case was a Tantalum slab mounted at  $45^\circ$ , 1 mm away from the aluminum slab on the x-ray microscope line of sight. The Tantalum slab was irradiated with 10 of Shiva's beams temporally stacked to produce a 3 ns pulse. Both the self emission from the 600 ps laser drive pulse striking the aluminum sample and the 3 ns emission from the Tantalum backlighter are visible in the streaked image. The shadow of the moving slab is also visible sloping up to the left in the image.

The Wölter x-ray microscope now in use has adequate resolution but has substantial large angle scattering. Only about five percent of the energy incident on the x-ray microscope is contained in the central 50  $\mu\text{m}$  (diameter) of the point spread function. To improve the throughput of the new Wölter mirror, the surface had to be substantially improved over the 250 Å peak to valley surface of the old mirror. This in turn required an improved understanding of the relation between fabrication techniques, metrology, surface profile, and the point spread function of the Wölter mirror.

Figure 8 shows the various vertical and horizontal scale sizes associated with the various fabrication, metrology, and physics processes related to x-ray mirror production and function. To produce a mirror one must first measure the deviation from the desired contour. Then, one must be able to control the machining and lapping processes to the accuracy required to produce the desired surface. This requires at least the accuracy in each of these steps which one wishes to ultimately obtain. A perfect x-ray surface would be one which had an

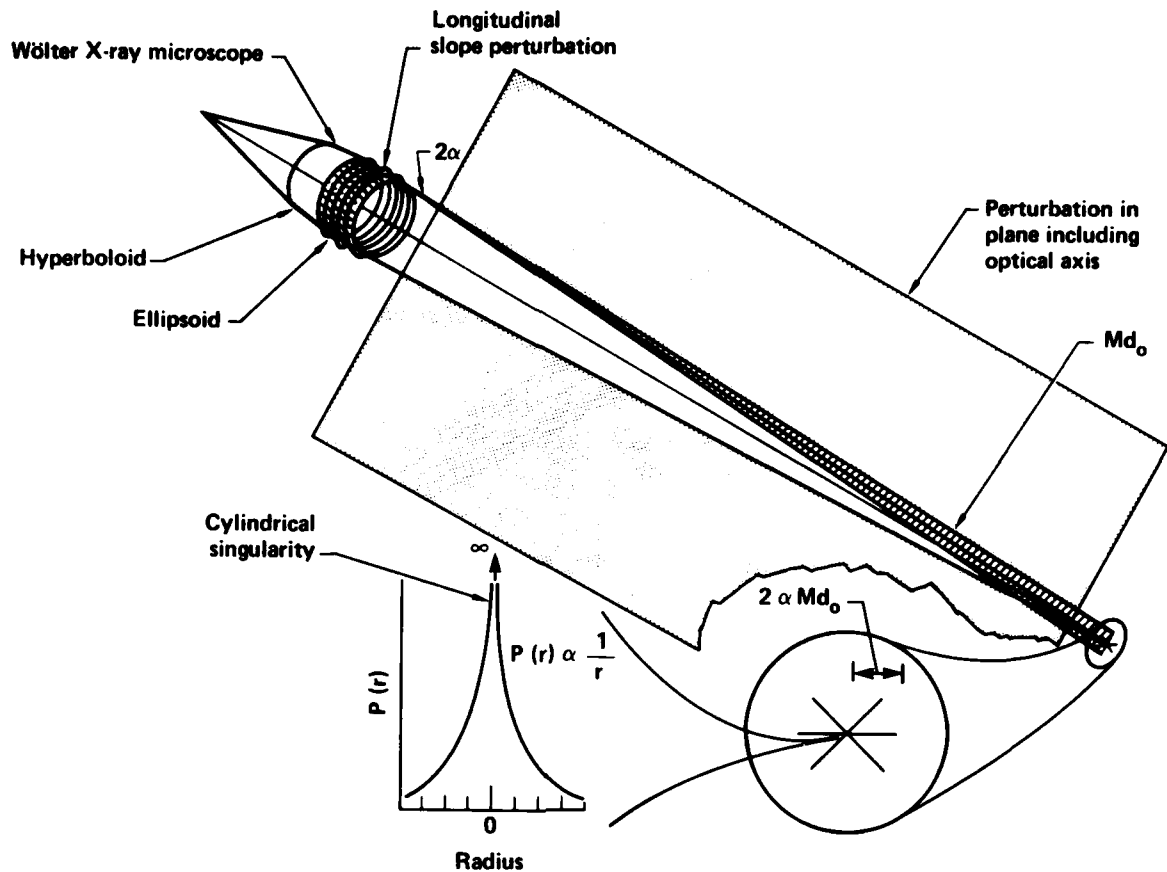


Figure 18 A Wölter mirror, perfect except for longitudinal ripples on one surface, will produce fans of radiation in planes including the optical axis. The fans of radiation cross on the optical axis producing a cylindrical ( $1/r$ ) singularity.

accuracy of 3 - 10 Å over the entire surface. This is clearly unattainable at present. A more realistic goal is a surface with 3 - 10 Å accuracy at horizontal scale lengths less than 0.5 mm, and a maximum slope error of 0.5 arcseconds for horizontal scale lengths of 0.5 mm or longer.

As one can see from figure 8, a number of problems must be faced in obtaining a surface with these specifications. Aspheric Diamond Turning, which is usually thought of as being a very accurate process, does not even come close to obtaining these tolerances. Thus, lapping must be used to improve the diamond turned surface. At short horizontal scale lengths, lapping and super-polishing appear to be able to meet these surface tolerances. At horizontal scale lengths longer than 1 mm, operator manipulation of the lap with rapid feedback from metrology, should be able to meet the surface specifications providing the required surface metrology is available. However, in the region between 0.1 and 3 mm, the physics of the lapping process still seems to present some uncertainties. This appears to be one of the more crucial horizontal scale length regions in the fabrication of grazing incidence x-ray reflecting surfaces.

As may be seen from figure 8, it is also quite difficult to obtain the required metrological accuracy to fabricate these surfaces. A few instruments, such as the Hetrodyne Interferometer, the Talysurf, and the Nanosurf are capable of measuring to accuracies of 10 Å or better over scale lengths less than 1 mm. The Random Devices Slope Scanner can measure to an accuracy of 20 to 30 Å over scale lengths less than 1 mm and 60 Å over scale lengths less than 1 cm. The Random Devices slope scanner presently suffers from a number of technical difficulties, which appear to be correctable, and may

improve its resolution by as much as an order of magnitude, as well as greatly improving its stability. The Taly-Round appears to be able to make reproducible roundness measurements down to 25 Å for scale lengths longer than 0.5 mm. The Cleveite Profjlometer can make measurements between 70 Å and 250 Å accuracy over a range of horizontal scale lengths of 2.5 μm up to several inches. Another machine which shows a great deal of promise is the Stedman measuring machine at the National Physical Laboratory in England, which presently can measure to an accuracy of 160 Å down to horizontal scale lengths less than 50 μm. In the future, this machine may be improved to yield accuracies as good as 16 Å.

Although a number of machines can make measurements of the vertical scale lengths required, only a few, and at the limits of their resolution, can reach the 0.5 arcsecond or better requirement in the range from 0.5 to 10 mm horizontal scale length. One of these devices is the Random Devices Slope Scanner, shown in figure 9. This machine operates on the principle of the optical lever. A carefully prepared beam of light is focused to a 50 μm diameter spot on the optical surface to be measured. The deflection of the reflected beam is then twice the angular deviation of the surface. The mirror to be measured is mounted on a structure supported by air bearings. This allows the mirror to be moved in an arc very nearly matching the required curvature of the optical surface. The optical surface to be measured can also be rotated on an air bearing to make azimuthal scans of the surface. The deviation of the beam reflected from the surface is measured differentially by a set of PIN Diode Detectors. The difference of the two signals is divided by the sum to null out any fluctuations in the laser intensity, then integrated and recorded.

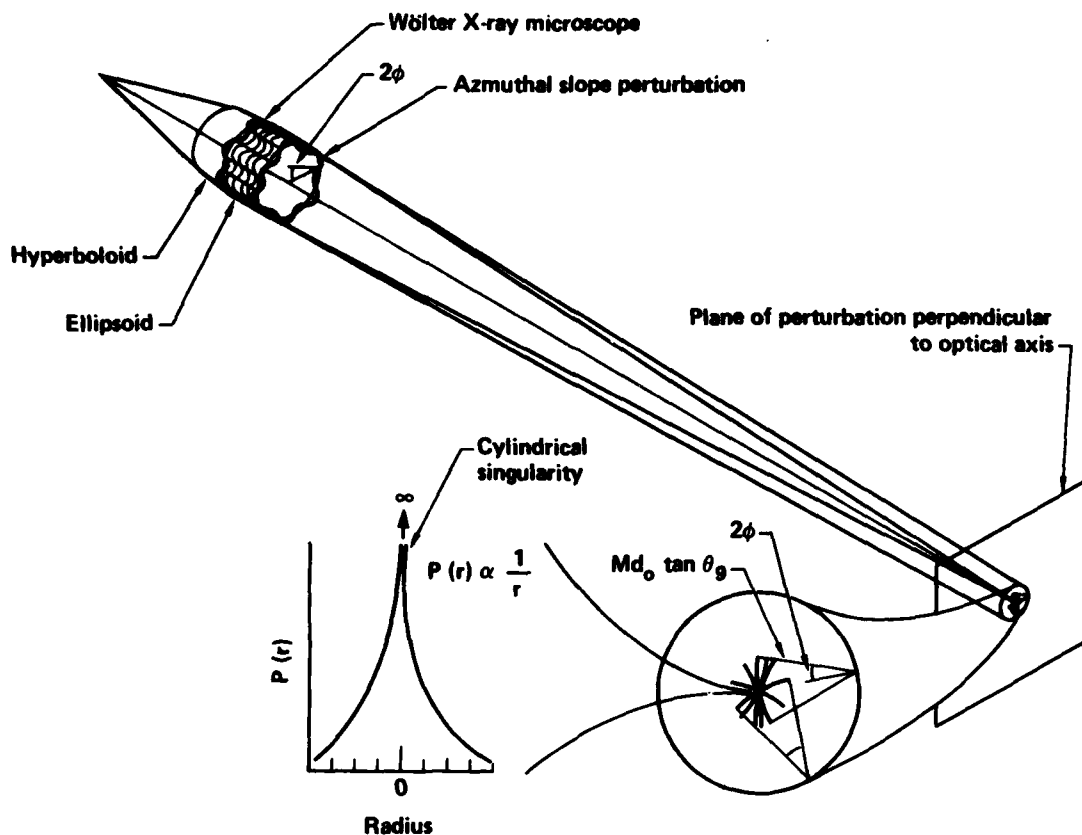


Figure 19 A Wölter mirror, perfect except for azimuthal ripples on one surface, will produce conical fans of radiation intersecting on the optical axis. This also results in a cylindrical  $(1/r)$  singularity.

A typical scan of the surface of one of the Wölter mirrors takes about 20 seconds. It may be repeated quickly and easily to determine the stability and reproducibility of the system. One benefit of measuring the slope of the surface and integrating to obtain the profile, is that the system is insensitive to mechanical vibration. The optical scanner head itself is easily removable and polishing is carried out on the mechanical portion of the scanner by simply installing a small lapping mechanism. This is done without ever removing the mirror from the mechanical portion of the scanner. This whole process can be repeated as often as every half hour, if need be.

Figure 10 shows the Clevite Profilometer, which measures the surface with a diamond stylus, using an inductive pick up. The Clevite Profilometer has been calibrated in the Metrology Lab at LLNL, and appears to be accurate and reproducible to 70 Å.

Figure 11 shows a comparison of traces made on the same Wölter mirror surface with the Clevite Profilometer and the Random Devices Slope Scanner. They appear to agree to 70 Å, when averaged over a 50  $\mu\text{m}$  horizontal scale length.

Figure 12 compares the longitudinal surface profile of the older Wölter mirror, with the surface profile of the new Wölter mirror, fabricated at Random Devices. The new mirror has a 30 Å RMS deviation from the ideal surface profile. The deviation from circularity of the hyperboloid of the new Wölter mirror is illustrated in figure 13.

Traces from the Random Devices Slope Scanner were digitized and reduced to slope error distributions. The older mirror had longitudinal slope distributions with standard deviations of 16 arc seconds for the ellipsoid and 13 arc seconds for the hyperboloid, as may be seen from figure 14.

Figures 15 and 16 show the longitudinal slope error distributions from the new Random Devices Wölter mirror. These have standard deviations of 0.82 and 0.65 arc seconds respectively.

Figure 17 is the azimuthal slope error distribution for the new mirror and has a standard deviation of 2.8 arc seconds. The measured distribution is, however, not completely random, and has correlation peaks at 0.75 and 1.7 arc seconds. The peak at 1.7 arc seconds corresponds to the ripples in figure 13, which have an approximate period of 4-5 mm.

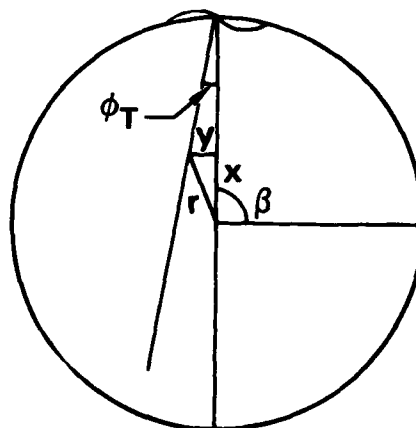


Figure 20 The combined displacement,  $r$ , of a ray due to a displacement,  $x$ , caused by a longitudinal slope error, and a displacement,  $y$ , caused by an azimuthal slope error can be determined using the above geometry.

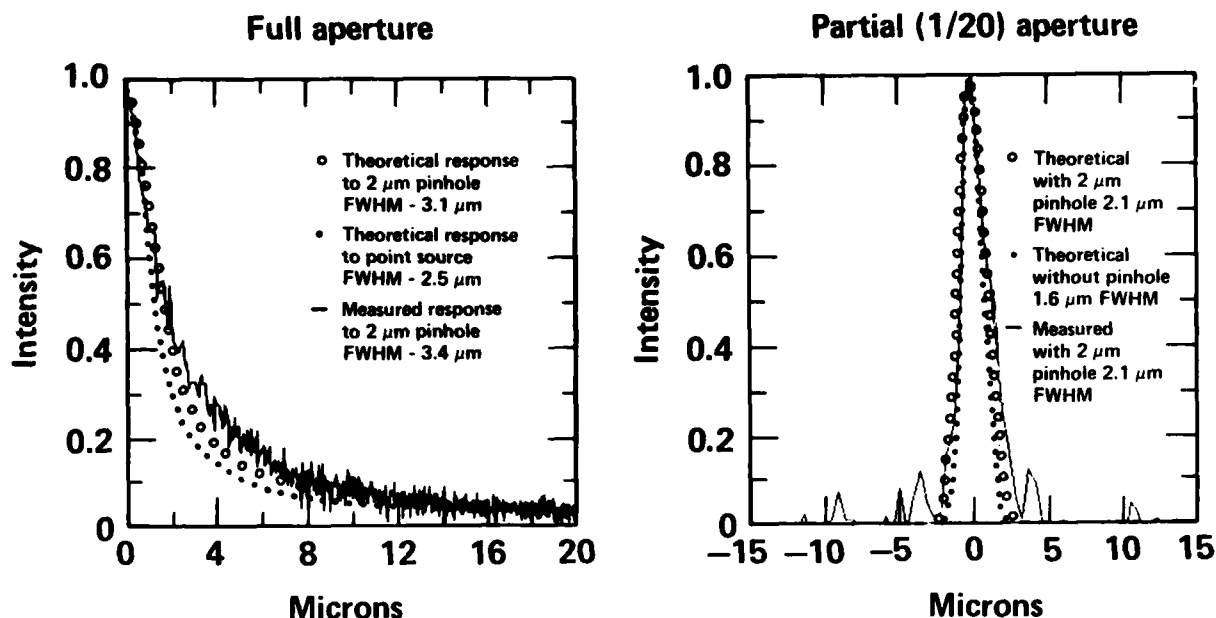


Figure 21 Comparisons of measured and theoretical point spread functions of the older Wolter Axisymmetric x-ray microscope show good agreement for both full and partial aperture operation.

One would like to be able to assemble this information into a theory which would predict the point spread function of the x-ray microscope. Such a theory can be developed from simple geometrical and statistical calculations. Figure 18 shows that a Wolter microscope which is perfect, except for longitudinal slope perturbations, will produce fans of radiation contained in planes, including the optical axis. These planes intersect on the optical axis and produce a cylindrical singularity, which is infinite on the axis.

On the other hand, if, as shown in figure 19, the mirror was perfect except for azimuthal slope perturbations, conical fans of radiation, which intersect on the optical axis, would be produced. This would again result in a cylindrical singularity, which would be infinite on the axis. However, when these types of perturbations are combined, the degenerate symmetry which allows the cylindrical singularities to be produced, is broken. This broken symmetry results in a finite value for the distribution on the optical axis.

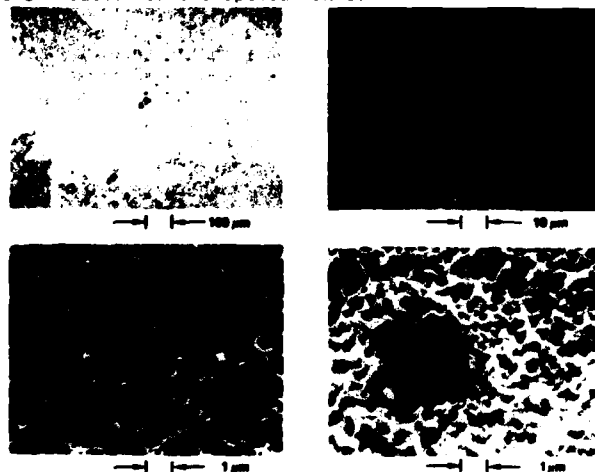


Figure 22 The resolution of the Wolter x-ray mirror is measured with a 20 by 20 array of 2 μm diameter pinholes, spaced 50 μm apart.

Using the geometry shown in figure 20, a simple statistical calculation can be used to determine the probability,  $P(r)$ , of a given ray falling a distance  $r$  from the optical axis.

$$\int P(r) r dr = \int P(x) P(y|x) dx dy \quad (1)$$

$P(x)$  is related to the longitudinal slope error distribution.  $P(y|x)$  is the probability of finding a ray at  $y$ , conditional on it having the coordinate  $x$ . We now define a few auxiliary formulae:

$$y = (d_0 (\tan \theta_g) - x) \tan \phi_T \quad (2)$$

$$x = d_0 \tan \alpha_T \quad (3)$$

$$\sigma_T = 2 \sqrt{\sigma_1^2 + \sigma_2^2} \quad (\text{Longitudinal}) \quad (4)$$

$$\alpha_T = 2 \sqrt{\alpha_1^2 + \alpha_2^2} \quad (\text{Azimuthal}) \quad (5)$$

$$a = \frac{r}{\alpha_T d_0 \tan \theta_g} \quad (6)$$

Where  $d_0$  is the object distance,  $\theta_g$  is the grazing angle,  $\phi_T$  is the total azimuthal deflection of the ray, and  $\alpha_T$  is the total longitudinal deflection of the ray.  $\sigma_T$  is the standard deviation of the longitudinal total deflection distribution.  $\alpha_T$  is the standard deviation of the azimuthal total deflection distribution.  $\sigma_1$  and  $\sigma_2$  are the standard deviations of the hyperboloid and ellipsoid longitudinal slope error distributions, respectively.  $\alpha_1$  and  $\alpha_2$  are the standard deviations of the hyperboloid and ellipsoid azimuthal slope error distributions, respectively.  $a$  is a dimensionless variable. Using these formulae, it can be shown that:

$$P(r) r dr \approx \frac{4 r dr}{\alpha_T \alpha_T d_0^2 \tan^2 \theta_g} \frac{e^{-\left(\frac{r}{d_0 \sigma_T}\right)^2}}{\sqrt{1 + a^2}} f(a) \quad (7)$$

where

$$f(a) \approx 1 + \frac{a^2}{1 + 0.58 a^2 + 1.63 a^4} \quad (8)$$

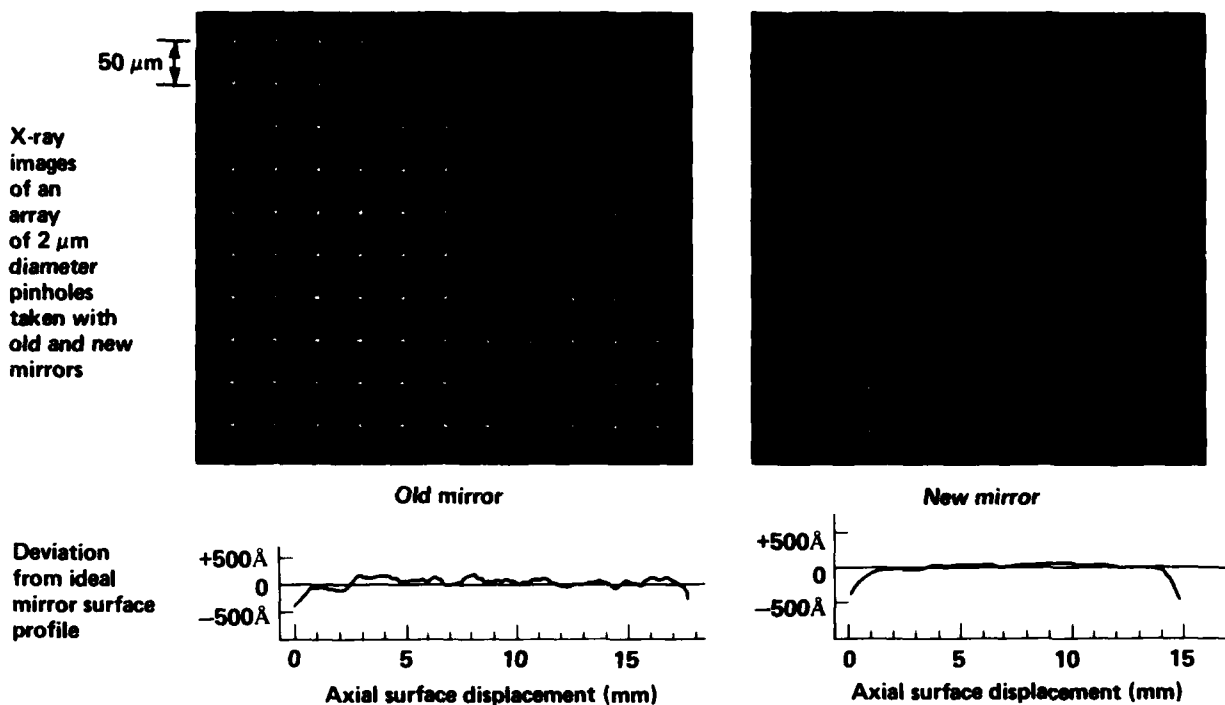


Figure 23 A comparison of images of the pinhole array taken with the old and new Wölter mirrors shows the new mirror produces smaller images with less scattering than the older mirror, but that the wings of the point spread function are less symmetrical for the new mirror.

Using formulae 7 and 8, the FWHM can be shown to be:  $\text{FWHM} \approx 7.5 \sigma_1 d_0 \tan \theta_0$ , where we have assumed that  $\sigma_1$  and  $\sigma_2$  are approximately equal. The Half Power Circle Diameter can be shown to be:  $d_{1/2} \approx 2.7 \sigma_1 d_0$ , where again we have assumed that  $\sigma_1$  is approximately equal to  $\sigma_2$ . Thus we find that the FWHM is related only to the azimuthal slope distribution, while the Half Power Circle Diameter is related only to the longitudinal slope error distribution.

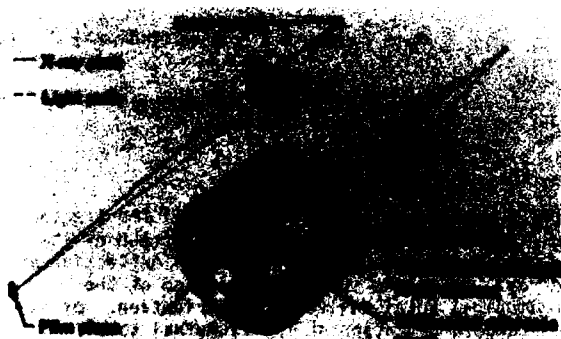


Figure 24 We are currently building a Kirkpatrick-Baez x-ray microscope with multilayer (Barbee) x-ray mirrors.

At present, this theory is limited in that it relies only on geometrical optics. However, it can be shown that for the azimuthal perturbations, the conditions for geometrical optics are well satisfied. For the longitudinal perturbations, on the other hand, geometrical optics is only valid for long scale length perturbations and diffraction optics, such as described by Bennett<sup>19,20</sup> and by Church,<sup>21,22,23</sup> must be used for shorter scale

length perturbations. Both regimes occur in x-ray optics, and both effects must be included for a completely correct calculation. In the range where both effects are comparable, the results can be approximated by either. This change in the distribution of x-rays, caused by the longitudinal perturbations, will change the details of the wings of the point spread function. However, the central portion will be largely unaffected.

Figure 21 shows the measured and theoretical point spread functions for both full and partial aperture for the older Wölter microscope, whose distribution functions were given in figure 14. The agreement in these cases appears to be excellent. The point spread function was measured with an array of 2 μm diameter pinholes.

An electron micrograph of the array of two micron diameter pinholes is shown in figure 22. This pinhole array was backlit by a tungsten anode x-ray source for the point spread function measurements.

Figure 23 shows images of the pinhole array taken with both the old and the new mirror. Two interesting points will be noted here. The much greater scattering of the older mirror is obvious as a fuzzy background in the photograph taken with it. The new mirror shows much less scattering, but the image points are much less symmetrical. The greater symmetry of the image points of the old mirror are the result of statistical averaging. On the other hand, in the new mirror, the coherent defects, in particular, the azimuthal defects, have become comparable to the random defects, leading to the unsymmetrical image points.

I believe that this type of theory is particularly successful in calculating the central shape of the point spread function. With the inclusion of diffraction effects, it may be able to provide a good fit to the entire point spread function.

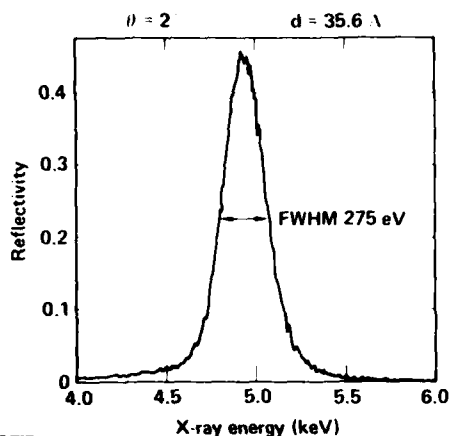


Figure 25 The use of multilayer x-ray mirrors produces good x-ray reflectivity with narrow bandpass at high energies and moderate grazing angles.

In summary, I see the Kirkpatrick-Baez microscopes maintaining their role as the workhorse of the x-ray imaging devices. This role is being extended with the development of a 22X magnification Kirkpatrick-Baez x-ray microscope with multilayer x-ray mirrors<sup>24</sup> as shown in figure 24, which can be installed in the x-ray backlighting system. As indicated in figure 25,<sup>25</sup> these mirrors can operate at large angles, high x-ray energies, and have a narrow, well defined x-ray energy bandpass. This will make them useful for numerous experiments. However, where a large solid angle is needed, the Wölter microscope will still be necessary and the technology needed to build them will be useful for many other types of x-ray optics.

#### Acknowledgements

The author would like to gratefully acknowledge the contributions of Harlow G. Ahlstrom and Vincent W. Slivinsky in inspiring and supporting this work; the contributions of Ted Zehnphennig of Visidyne and George Ransom of Random Devices, Inc. in producing the ASXRMS mirror, making surface measurements and developing some of the metrology equipment; and the help of Lianne E. Kent and Bonnie D. Quick for their assistance with the manuscript.

#### References

1. Jentsch, F. (1929). *Phys. Z.* **30**, 268.
2. Ehrenberg, W. (1947). *Nature, Lond.* **160**, 330.
3. Ehrenberg, W. (1949a). *J. Opt. Soc. Amer.* **39**, 741.
4. Ehrenberg, W. (1949b). *J. Opt. Soc. Amer.* **39**, 746.
5. Kirkpatrick, P. and Baez, A. V. (1948). *J. Opt. Soc. Amer.* **38**, 766.
6. Prince, E. (1950). *J. Appl. Phys.* **21**, 698.
7. McGee, J. F. (1957). *X-Ray Microscopy and Microradiography* (New York: Academic Press), 164.
8. McGee, J. F., Hesser, D. R., and Milton, J. W., *X-Ray Reflection Optics (Recent Developments)*, (Springer-Verlag, Berlin-Heidelberg-New York 1969).
9. Seward, F. D. and Palmieri, T. M. *Rev. Sci. Instrum.* **46**, 204 (1975).

10. Seward, F., Dent, J., Boyle, M., Koppel, L., Harper, T., Stoering, P., and Toor, A., *Rev. Sci. Instrum.*, **47**, 464, (1976).
11. Wölter, Hans (1952). *Mirror Systems with Grazing Incidence as Image-Forming Optics for X-Rays Ann. Physik, 6th Series, Vol. 10, 1952, pp. 94-114* (Translated into English November 1975, LLL Ref. 01867).
12. Wölter, Hans (1952). *Generalized Schwarzschild Systems of Mirrors with Glancing Reflection as Optical Systems for X-Rays Annalen der Physik, Vol. 10, pp. 286-295, 1952.*
13. Trurnit, *Göttinger Nachr. Math. - Phys., Kl.*, 1946, p. 29.
14. E. Nahring., *Physik. Z.* **31**, 749 (1930).
15. K. Schwarzschild, *Abh. Ges. Wiss. Göttingen*, vol. IV, No. 2 1905.
16. Palmieri, T. M., Boyle, M. J., Ahlstrom, H. G., and Monjes, J. A. *High Resolution, Large Through-Put X-Ray Microscopes for Target Diagnostics* (1975) UCRL 77081.
17. *Communication with Random Devices, Inc.*, 7 Park Street, Georgetown, Massachusetts 01833.
18. *Laboratory Evaluation of a High Resolution X-Ray Microscope*, Kevin Silk, p. 40, *Space Optics Imaging X-Ray Optics Workshop, SPIE Proceedings, 184*, May 22-24, 1979, Huntsville, Alabama.
19. Bennett, H. E. and J. O. Porteus, *J. Opt. Soc. Am.*, **51**, 123 (1961).
20. Bennett, H. E., *Opt. Engr.*, **17**, 480 (1978).
21. Church, E. L. and Zavada, J. M., *Appl. Optics* **14**, 1788 (1975).
22. Church, E. L., Jenkinson, H. A., and Zavada, J. M., *Optical Engineering* **16**, 360 (1977).
23. Church, E. L., Jenkinson, H. A., and Zavada, J. M., *Optical Engineering* **18**, 125 (1979).
24. Louis N. Koppel (LLNL) and Troy W. Barbee, Jr. (Stanford), *X-Ray Testing of Sputtered Synthetic Multilayer Structures in the 1 to 10 Å Region*. Submitted to *Appl. Phys. Letters* (1981) UCRL 85817.
25. Louis N. Koppel, personal communication.



Dr. Paul Kirkpatrick (left), session chairman, and Dr. Robert Price.

## Astrophysical Observations with High Resolution X-ray Telescopes

M. V. Zombeck

Harvard/Saithsonian Center for Astrophysics

60 Garden Street

Cambridge, Massachusetts 02138

## ABSTRACT

In slightly less than twenty years, from its birth in 1962, X-ray astronomy has developed into a major branch of astronomy, equalling in importance the more established disciplines for the study of astrophysical problems. This has resulted from two major technological advances: 1) the capability of placing into space, above the Earth's attenuating atmosphere, large and sophisticated scientific payloads, and 2) the development of high resolution X-ray imaging optics and associated detectors. This paper illustrates the rapid development of X-ray imaging optics and discusses their application to astrophysical observations, both solar and non-solar. In conjunction with various spectroscopic techniques, X-ray telescopes are being used for astrophysical plasma diagnostics, obtaining elemental abundances, temperatures, and densities. Several examples are given. Further advances in X-ray imaging optics will require the development of new metrology techniques in order to determine and control mirror figure and scattering. Future programs are discussed.

## I. INTRODUCTION

In slightly less than twenty years, from its birth in 1962, non-solar X-ray astronomy has developed into a major branch of astronomy, equalling in importance the more established disciplines for the study of astrophysical phenomena. This rapid development has resulted from two major technological advances: 1) the capability of placing into space, above the Earth's attenuating atmosphere, large and sophisticated scientific payloads, and 2) the development of high resolution X-ray imaging optics and associated imaging detectors (Figures 1 and 2).



Figure 1 - Artist's conception of the HEAO-2 (Einstein Observatory), the first high resolution telescope for non-solar X-ray astronomy.

<u>X-ray Luminosities</u>	
$5 \times 10^{27}$ erg $s^{-1}$	- Sun-like stars
$5 \times 10^{39}$ erg $s^{-1}$	- normal spiral galaxies (Milky Way)
$10^{42}$ - $10^{47}$ erg $s^{-1}$	- quasars
<u>X-ray Flux Densities</u>	
(excluding Sun) $4 \times 10^{-7}$ erg $cm^{-2} s^{-1}$	- $2 \times 10^{-14}$ erg $cm^{-2} s^{-1}$
Solar X-ray flux densities:	
- erg $cm^{-2} s^{-1}$ (large flare)	- $10^{-4}$ erg $cm^{-2} s^{-1}$ (solar min)

Distances

4.3 light years (Proxima Centauri) - 12 billion light years ( $z = 2.6$  quasar)

Figure 2 - Present range of X-ray observations.

0094-243X/81/750200-10\$1.50

1981 American Institute of Physics

For the purposes of this paper, X-ray astronomy will refer to observations of cosmic (galactic and extragalactic) sources apart from the Sun. This is not an attempt to diminish the importance of solar X-ray astronomy. On the contrary, as will be shown below, this field has played a key role, both technologically and in some cases theoretically, in the rapid rise to maturity of X-ray astronomy.

Also, in this paper high resolution imaging will refer to the imaging of X-ray sources with an angular resolution of a few arcseconds or less. The photon energy range considered is that of present and planned high resolution X-ray telescopes and is between 0.1 and 10 keV; the lower limit often being set arbitrarily or by the low transmission of detector windows and the upper limit set by the physics of grazing incidence reflection.

## II. THE IMPORTANCE OF IMAGING

Optical astronomy, from its very beginning, was an imaging science due to the capabilities of the human eye, viz., 3 arcminute spatial resolution and sensitivity to 6th magnitude stars (visual flux densities of  $1 \times 10^{-7}$  erg  $cm^{-2} s^{-1}$ ). Thus, naked eye observations alone yielded thousands of celestial objects and led to a fairly sophisticated view of the nature of the universe. From the introduction of the optical telescope by Galileo in 1610 to the future launch of the Space Telescope (ST) in 1985 there has been a steady progression in the improvement of optical observations. The ST will have an angular resolution of 0.1 arcsecond and a limiting sensitivity to point objects of 27th magnitude. (This is the magnitude that the Sun would have at a distance of  $10^6$  light years.)

X-ray astronomy developed in a different way (1-3). The first observation of a celestial X-ray source occurred in 1962 (4). The detector was an uncollimated Geiger counter on-board a sounding rocket; the angular resolution of the detector was about  $100^\circ$ ! For the next 16 years, until the launch of the Einstein Observatory, X-ray astronomy made considerable progress without the use of imaging optics. A progression of rocket and satellite experiments employing large mechanically collimated X-ray detectors led to the discovery of over a thousand X-ray sources and to the determination of the nature of many of them. This is in contrast to the rapid introduction of imaging optics in solar X-ray astronomy.

The scientific usefulness of imaging optics for X-ray astronomy was recognized in the 1960's (5,6); proposals for large satellite-borne telescopes were submitted to NASA as early as 1963, but without acceptance. It was not until 1978 that the first and only telescope for X-ray astronomy was placed in orbit.

This circumstance was probably due to the early successes in the field with collimation techniques and a desire by many members of the scientific community to continue in this way in order to perform all-sky surveys. Also, some technical problems had to be solved; the polishing of mirror surfaces had to be substantially improved in order to reduce scatter and high resolution two-dimensional imaging X-ray detectors had to be developed. However, these problems could have been solved early-on given adequate support for laboratory development programs.

The advantages of imaging in X-ray astronomy are clear, especially when one considers the limitations of mechanically collimated detectors. The resolution of these devices are seldom better than several arcminutes, which makes source identification difficult or at times impossible, and as fainter sources are detected by using larger detectors source confusion arises. The necessarily large detector areas employed also lead to high internal noise and high diffuse X-ray background rates. The detection of faint sources thus requires long observation times. In contrast, imaging leads to:

- 1) a high signal-to-noise ratio because of the reduction in the linear and angular dimensions of a detection cell;
- 2) ease of source identification by reducing the number of possible optical counterparts;
- 3) the elimination or reduction of source confusion;
- 4) the determination of the structure of extended objects;
- 5) the simultaneous observation of many sources in the field of view.

Imaging optics can also be used to feed spectrometers and polarimeters, thereby increasing the signal-to-noise ratio for these instruments. Experience with two recent X-ray observatories illustrates these points. The Large Area Sky Survey instrument on the first High Energy Astronomy Observatory (HEAO-1) (7) consisted of several thousand square centimeters of collimated gas proportional counters. This is the largest array of proportional counters launched so far (1977-1979). This instrument's ability to locate the position of faint sources was no better than about one-half degree, making source identification, in most cases, impossible. The second High Energy Astronomy Observatory (HEAO-2), called the Einstein Observatory (8), employs the first high resolution telescope for X-ray astronomy. Although the collecting area was only a few hundred square centimeters, the telescope's limiting sensitivity was a few hundred times greater than that of HEAO-1, and it was capable of determining source locations to a couple of arcseconds.

Figure 3 illustrates the difficulties of source identification when source positions are inaccurately known. The identification of optical and/or radio counterparts of X-ray sources is extremely important to further our understanding of these objects. This figure is a visible light photograph of the star field surrounding Scorpius X-1, the brightest and first cosmic X-ray source discovered. Sco X-1 was first located to be somewhere in a region about 4 times larger than the upper photograph. Then, two years later, in 1964, it was placed in the yellow circle; the next year it was thought to be in one of the two blue rectangles; then in the orange box. Finally, in 1966, by employing a modulation collimator with a resolution of about one arcminute, the source was placed in one of the two pink rectangles, one-half degree away from the previous location. Then, within a matter of weeks, it was identified as the 13th magnitude object in the right hand corner of the upper pink rectangle. In contrast, telescopic observations of the faintest X-ray sources will immediately yield the position to an accuracy of a few arcseconds leading to the unambiguous identification of an optical or radio counterpart, or the absence of one.

M31, or Andromeda, is a nearby spiral galaxy (two million light years away) and prior to the Einstein

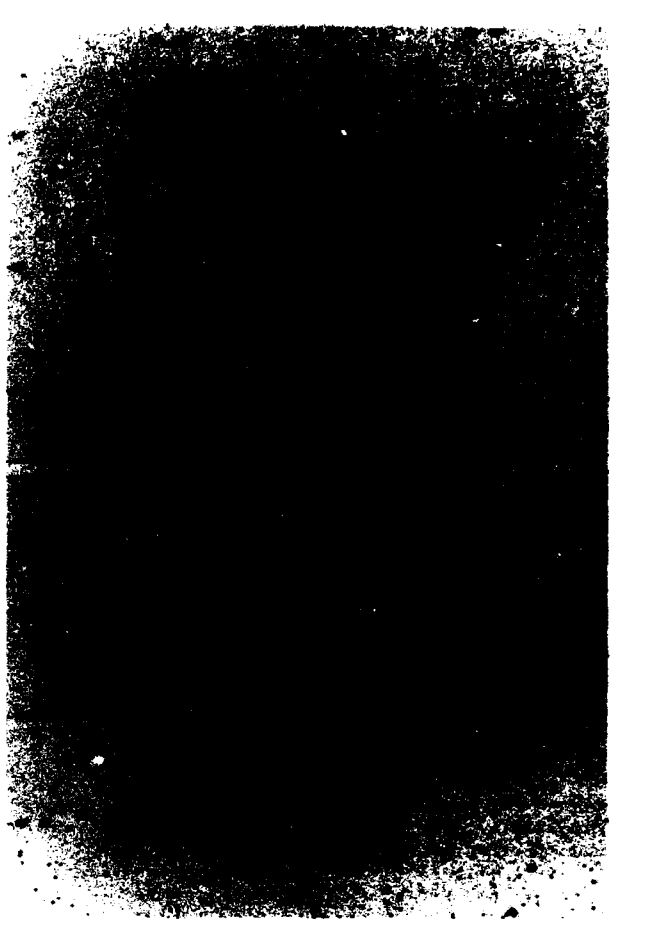


Figure 3 - the optical identification of Scorpius X-1, the first celestial X-ray source detected. The upper photograph is the visible star field containing Sco X-1. The first detection in 1962 placed Sco X-1 somewhere in a field 4X larger. Two years later the source was restricted to the circle; a year later it was thought to be in one of the two large rectangles; in 1966 it was placed in the square. Later in 1966, using a new detection technique, it was placed in either of two tiny rectangles  $\sim 1/2^\circ$  from the square. Finally, a few weeks later, it was identified as the 13th magnitude star in the upper right hand corner of the upper rectangle (the lower photograph is an 8.5X enlargement). (Courtesy of J. McClintock, MIT).

Observatory had been observed as a single source of X-rays (Figure 4). Figure 5 shows the galaxy as observed with the Einstein Observatory's imaging proportional counter at the focal plane of the telescope. This detector has a resolution of about 1 arcminute. Approximately 30 sources in addition to a large confused region near the center can be identified. This latter region is resolved into about 45 individual sources (Figure 6) when observed with the Observatory's high resolution imager. These three figures alone dramatically illustrate the qualitative leap that has been made by introducing imaging to the field of X-ray astronomy.

A further example of the importance of imaging is illustrated in Figure 7. The Alpha Centauri visual binary system is near enough (4.4 light years) to permit detection of solar-level X-ray emission by the Einstein Observatory in just a few seconds and the resolution of the telescope is sufficient to provide distinct images of the two stars, Alpha Centauri A (G2V star) and Alpha Centauri B (K1V star). The upper



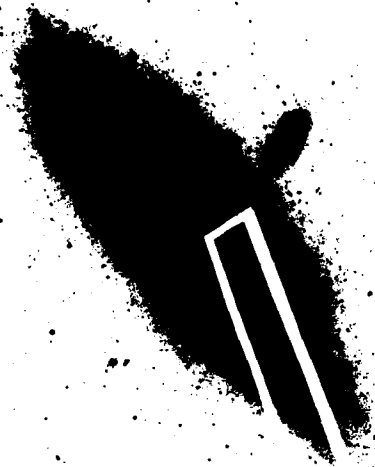


Figure 4 - A visible light photograph of the Andromeda galaxy (M31). The Uhuru satellite X-ray source location error box is shown.

image was made with the Observatory's imaging proportional counter. Alpha Centauri had been previously detected (9) with the HEAO-1, but was unresolved. It was assumed at the time that the solar-like Cen A was responsible for the X-ray emission, since current theory predicted very low emission for Cen B. The lower image taken with the high resolution imager shows the two stars clearly resolved. Contrary to expectations, the K-star Cen B is brighter than the G-star Cen A. This observation, along with similar observations of stars of all spectral types, are causing a revision of our understanding of stellar coronae. When one realizes that a large fraction of the stars in our Galaxy are in binary systems (about 30% with separations less than 10 arcseconds), one again can appreciate the value of imaging.

### III. A SUMMARY OF THE PRINCIPLES OF HIGH RESOLUTION IMAGING OF X-RAYS

The highest resolution imaging instruments used in X-ray astronomy consist of grazing incidence reflection optics. Pinhole cameras and Fresnel zone plates have been proposed for X-ray astronomy and have been used to image the Sun. At the present time, however, these techniques are of limited use because of small collecting areas and moderate resolution capabilities.

In 1922 Compton (10) demonstrated and investigated the "total" reflection of X-rays incident on polished surfaces at grazing angles, i.e., high angles of incidence (Figure 8). At X-ray energies the real part of a material's complex index of refraction is less than unity. X-rays impinging upon the surface from a media of higher index of refraction, air or vacuum, for example, are reflected provided the grazing angle is below a "critical angle" given by Snell's law. Since there is some absorption in the material the reflection is not actually "total", the reflectivity is less than unity, and some reflection occurs beyond the critical angle (Figure 9).

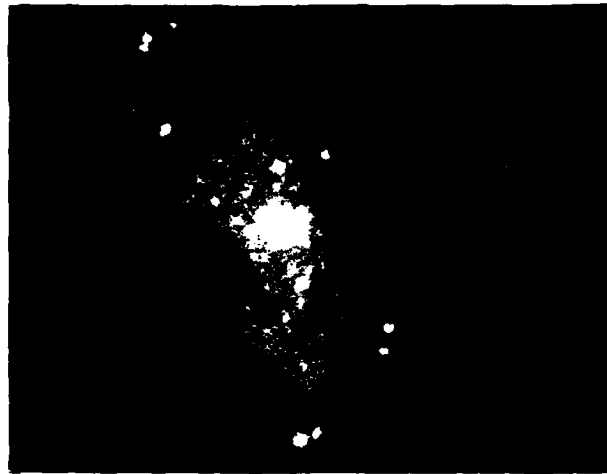


Figure 5 - Einstein Observatory imaging proportional counter exposure of Andromeda (M31). About 30 sources in addition to a large unresolved central region can be identified. (Courtesy of L. Van Speybroeck, CFA).

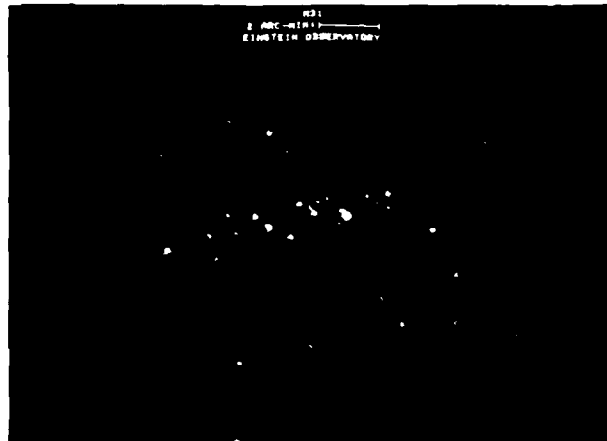


Figure 6 - Einstein Observatory high resolution imager exposure of the central region of M31. This region is resolved into 45 individual sources. (Courtesy of L. Van Speybroeck, CFA).

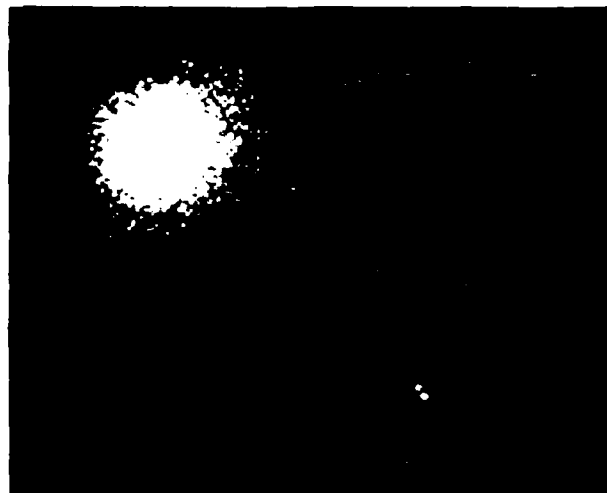
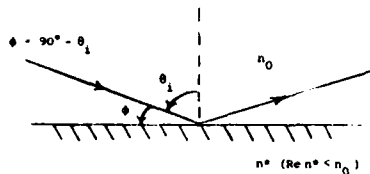


Figure 7 - Combined Einstein Observatory imaging proportional counter (IPC) and high resolution imager (HRI) exposures of  $\alpha$  Cen A and  $\beta$  Cen B. Both exposures are to the same scale. Contrary to theoretical expectations, the FIV star is brighter in X-rays than the G2V star. (Courtesy of L. Golub, CFA).

REFLECTION OF X-RAYS



Complex refractive index:

$$n^* = (1 - \delta) - i\beta$$

$$\delta, \beta \ll 1$$

By Snell's law:

$$\beta = \frac{\lambda \rho}{4\pi} \quad \text{where}$$

$$\cos \theta_c = 1 - \delta$$

( $\mu/\rho$ ) is the mass attenuation coefficient of the reflecting material at wavelength  $\lambda$  and  $\rho$  is the density.

$$\phi_c = \sqrt{2\delta}$$

$$\delta = N_e^2 \lambda^2 / 2\pi m_e c^2 \quad \text{(away from absorption edge)}$$

$$= N_0 \frac{Z}{A} \rho_e \lambda^2 / 2\pi m_e c^2 \quad \text{where}$$

$N$  is the electron density,  $N_0$  is Avogadro's constant,  $Z$  and  $A$  are the atomic number and weight of the material, respectively.

Fresnel's equations for the reflectivity:

perpendicular polarization

$$R_{\perp} = \frac{a^2 + b^2 - 2a \cos \theta_i - \cos^2 \theta_i}{a^2 + b^2 - 2a \cos \theta_i + \cos^2 \theta_i}$$

parallel polarization

$$R_{\parallel} = R_{\perp} \frac{a^2 + b^2 - 2a \sin \theta_i \tan \theta_i + \sin^2 \theta_i \tan^2 \theta_i}{a^2 + b^2 + 2a \sin \theta_i \tan \theta_i + \sin^2 \theta_i \tan^2 \theta_i}$$

where,

$$2a^2 = [(n^2 - k^2 - \sin^2 \theta_i)^2 + 4n^2 k^2]^{1/2} + (n^2 - k^2 - \sin^2 \theta_i)$$

and

$$2b^2 = [(n^2 - k^2 - \sin^2 \theta_i)^2 + 4n^2 k^2]^{1/2} - (n^2 - k^2 - \sin^2 \theta_i)$$

$\theta_i$  = angle of incidence (angle from normal to surface);  $n = 1 - \delta$ ;  $k = \beta$   
At X-ray wavelengths,  $R_{\perp}$  and  $R_{\parallel}$  differ negligibly.

Figure 8 - Principles of the reflection of X-rays

In 1952 Wolter (11) studied the imaging properties of grazing incidence optical systems employing figures of revolution generated by conic sections. He was interested in systems for X-ray microscopy but also ray-traced systems for which the object was at infinity, the situation in astronomy. One system, referred to as Wolter type I, consists of two concentric surfaces generated by a parabola and hyperbola having a common focus (Figure 10). The highest resolution mirrors currently used and being developed (12-18) for future X-ray astronomy programs are of this type. Mirrors have been fabricated with arcsecond spatial resolution over a several arcminute field of view. Because of geometric aberrations, the resolution degrades with field angle, but useful fields of view of a degree or more have been obtained. In order to increase the collecting area of a telescope, several mirrors are often nested together.

THEORETICAL REFLECTION EFFICIENCY

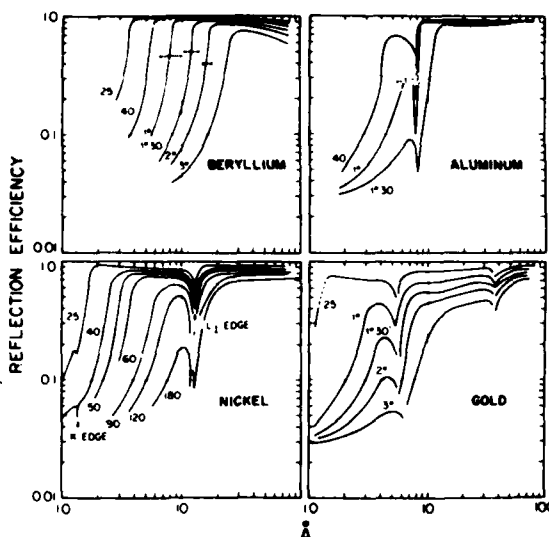
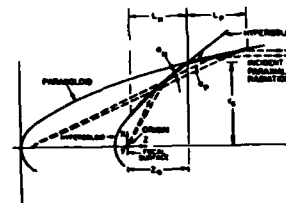


Figure 9 - Calculated reflection efficiencies as a function of wavelength for various grazing angles and materials.

WOLTER TYPE I MIRROR SYSTEM



The equations for a paraboloid and hyperboloid which are concentric and confocal can be written as:

$$r_p^2 = P^2 + 2PZ + [4Z^2 P d / (e^2 - 1)] \quad \text{(paraboloid)}$$

$$r_h^2 = e^2 (d + Z)^2 - Z^2 \quad \text{(hyperboloid)}$$

The origin is at the focus for axial rays,  $Z$  is the coordinate along the axis of symmetry, and  $r$  is the radius of the surface at  $Z$ .

RMS blur circle radius:

$$\sigma = \frac{(e+1)}{10} \frac{\tan^2 \theta}{\tan \alpha} \left( \frac{L_p}{Z_0} \right) + 4 \tan \theta \tan^2 \alpha \quad \text{radians}$$

$\xi = \alpha_p^* / \alpha_h^*$  ( $\alpha_p^*$  and  $\alpha_h^*$  are the grazing angles between the two surfaces and the path of an axial ray that strikes at an infinitesimal distance from the intersection). For most telescope designs:  $\xi = 1$ .

$$\alpha = \frac{1}{4} \tan^{-1} (r_0 / Z_0) = \frac{1}{2} (\alpha_p^* + \alpha_h^*)$$

$\theta$  = angle between incident rays and optical axis.

Geometrical collecting area:

$$A = 2\pi r_0 L_p \tan \alpha$$

Effective collecting area:

$$A_e(\alpha, E) = AR^2(\alpha, E) = 8\pi Z_0 L_p R^2(\alpha, E) \alpha^2$$

where  $R$  is the Fresnel reflectivity at energy  $E$  and mean grazing angle  $\alpha$ .

Figure 10 - Wolter type I mirror system.

## IV. THE DEVELOPMENT OF X-RAY TELESCOPES

In the early 1960's Wolter type I mirror systems for solar observations were developed at American Science and Engineering under the leadership of Riccardo Giacconi. A representative sample of early mirrors are shown in Figure 11. These were made of conventionally machined aluminum or were epoxy castings. The angular resolution was limited to several arcminutes and the effective collecting area was very low. The next generation mirrors were made of nickel electroformed on an optically polished stainless steel mandrel (Figure 12). These mirrors had a collecting area of about  $1/2 \text{ cm}^2$  at 1.5 keV and a resolution of about 30 arcseconds. By the late 1960's considerable progress had been made in fabricating X-ray mirrors using conventional optical figuring and polishing techniques that would produce astronomical quality images (Figure 13). These technical developments culminated in the design and development of an X-ray telescope for the Solar Observatory on the Skylab, launched in 1973 (Figure 14).



Figure 11 - Three X-ray mirrors produced by epoxy casting and conventional machining methods. The angular resolution was several arcminutes and the efficiency less than 1%.



Figure 12 - Electroformed nickel X-ray mirror. The geometric collecting area was  $2 \text{ cm}^2$ ; the diameter 7.5 cm; the focal length 84 cm. The resolution was  $\sim 30$  arcseconds. The efficiency at 1.5 keV was  $\sim 20\%$  when all of the photons within several arcminutes of the image were included.

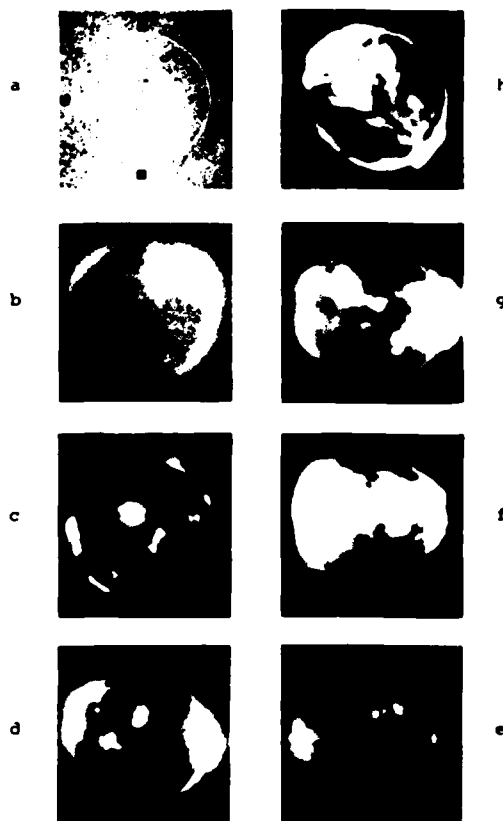


Figure 13 - a The first image of the Sun made with a grazing incidence telescope (10/15/63). The limb cannot be discerned. The telescope was similar to those in Fig. 11. b An image obtained on 3/17/65 with an electroformed nickel telescope similar to that of Fig. 12. c An image obtained on 6/8/68 with a telescope produced by conventional optical polishing and figuring techniques. The telescope has a collecting area of  $34 \text{ cm}^2$ . The resolution is 2-3 arcseconds. The reflecting surfaces of this telescope are thin layers of Kanigen, a nickel alloy, deposited on a Be support structure. d - g A series of images obtained with this telescope on 4/8/69, 11/4/69, 3/7/70 and 11/24/70. h An image obtained on 3/8/73 with a fused silica mirror.



Figure 14 - The X-ray mirror assembly of the S-054 X-ray telescope for Skylab. The reflecting surfaces are Kanigen which is coated on a beryllium support structure. In order to increase the total collecting area, the separate X-ray mirrors were nested together. The collecting area is  $42 \text{ cm}^2$ ; focal length 2.1 m; resolution 2-3 arcseconds. Over 35,000 images of the Sun were obtained on photographic film during the 9 month operational period of Skylab.

This telescope produced arcsecond images of the solar corona and was able to observe temporal variations of coronal features with time scales ranging from seconds to months. A photographic film camera was used as the imaging detector. Figure 15 shows a full disk X-ray photograph of the Sun taken during the occurrence of a flare. This photograph illustrates both the high resolution achieved and the scattering resulting from the microroughness of the mirror surfaces. The radially symmetric pattern that extends almost to the solar limb is a result of shadowing of the scattered X-rays by the support structures of the mirror assembly and both delineates the extent of the scattering and demonstrates that scattering on the mirror surface occurs preferentially in the plane of incidence.

SOLAR FLARE  
seen from SATLAS



Inset: Flare core from  
about 1000x magnif.

The point spread function (PSF) of this telescope was determined in the laboratory. The PSF was found to have a FWHM of 3 arcseconds which meant that local slope errors of the mirror surfaces were well controlled. However, at 1.7 keV for example, 50% of the imaged photons were outside a circle of radius 48 arcseconds. For a high flux situation, this loss of photons can be tolerated and high resolution can still be achieved, although faint features adjacent to bright ones are obscured. For extrasolar observations of weak sources, this loss of photons from a resolution element will result in a significant loss of sensitivity.

In order to fabricate mirrors useful for X-ray astronomy, surface roughness had to be reduced from the 50-100 Å rms surface heights achieved previously to below 30 Å. This reduction in surface roughness was the single most important improvement to be made in the development of X-ray optics and was achieved for the Einstein Observatory mirror assembly (Figure 16) (19). The PSF of the mirror assembly was determined at the Marshall Space Flight Center X-ray Calibration Facility and was found to have a FWHM of 3.5 arcseconds and at 1.5 keV, for example, 50% of the imaged photons were within a circle of radius 5.5 arcseconds. In-flight observations confirmed these measurements (Figure 17).

In order to make use of the imaging performance of the Einstein mirror assembly, focal plane detectors had to be developed. Both a moderate resolution, high quantum efficiency imaging proportional counter (20) and a high resolution microchannel plate X-ray imaging detector (21) were developed for the Observatory. Also, a focal plane solid state spectrometer and a Bragg crystal spectrometer were developed so as to provide high efficiency, moderate resolution spectroscopy and high resolution spectroscopy. Figure 18 shows a schematic diagram of the Einstein Observatory. The X-ray image of the supernova remnant Cas A (Figure 19) demonstrates the capability of the Observatory for imaging extended objects. During the slightly more than two years of operation (the Observatory ceased operations in April 1981 after its supply of gas for maneuvering was used up), 4000 target fields were observed and 8000 individual sources were detected. Supernova remnants, globular clusters, galaxies, clusters of galaxies, almost every class of star in our Galaxy, and very distant quasars have been observed.



† Figure 16 - Einstein Observatory high resolution mirror assembly. The assembly consists of 4 nested X-ray mirrors, giving a total geometric collecting area of 500 cm<sup>2</sup>.

← Figure 15 - An X-ray image of the Sun obtained during the occurrence of a flare. The insert shows the actual size of the flare as obtained with an exposure 1000 X less than that of the full disk exposure. The scattering of X-rays by the mirror surfaces is evident.

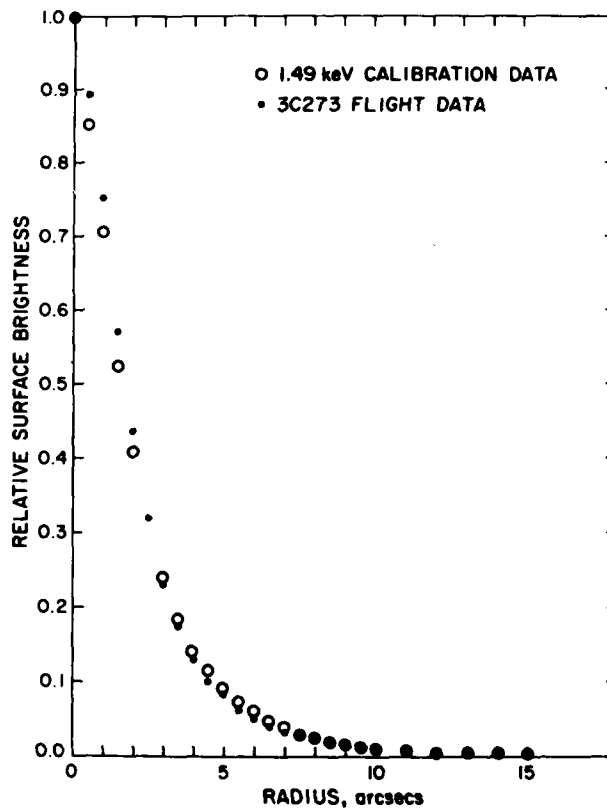


Figure 17 - Point spread function of the Einstein Observatory telescope as measured on the ground and in orbit.



Figure 18 - Schematic diagram of the Einstein Observatory.

#### V. THE DIAGNOSIS OF ASTROPHYSICAL PLASMAS

X-ray astronomy is just beginning to bring to bear on astrophysical problems the powerful observational and theoretical diagnostic techniques developed for investigating the solar corona. The use of imaging optics has made moderate and high resolution X-ray spectroscopy of celestial sources possible.

Figure 20 shows the X-ray spectrum of the Cas A supernova remnant obtained by the Goddard Space Flight Center solid state spectrometer (22) on the Einstein Observatory. The spectrometer had a FWHM energy resolution of 160 eV and an entrance aperture equivalent to 6 arcminutes. Thus, it obtained the spectrum of the remnant as a whole. Superimposed on the data is the expected response of the spectrometer to a two-component isothermal model plasma. The dashed curve is the contribution to the spectrum from the light elements H, He, C, N, O, and Ne. The dominant features at 1.86 and 2.46 keV are consistent with the line emission from helium-like Si and S, respectively.

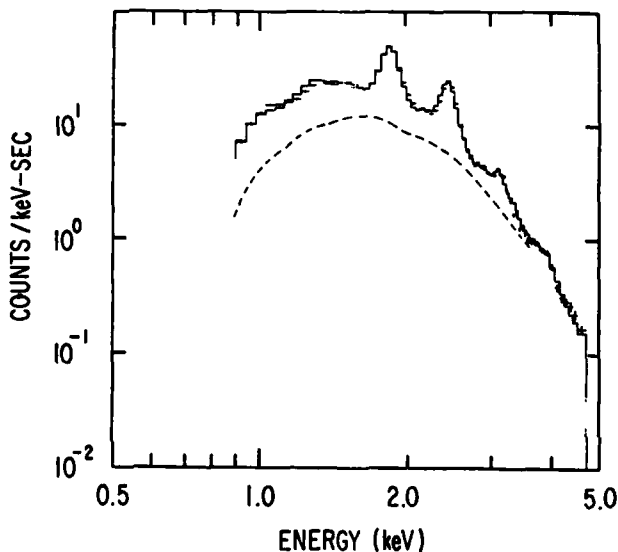


Figure 20 - X-ray spectrum of the Cassiopeia A supernova remnant obtained by the GSFC solid state spectrometer of the Einstein Observatory. The lower dashed curve represents the continuum contribution from H, He, C, N, O, and Ne components of the hot gas. The solid curve is the expected response of the spectrometer to a two-component isothermal model. The total emission from Mg, Al, Si, S, A, Ca, and Fe. The two largest peaks at 1.86 and 2.46 keV are associated with emission from Si and S, respectively. (R.H. Becker et al., *Ap. J. Lett.*, 234, L73 (1979)).

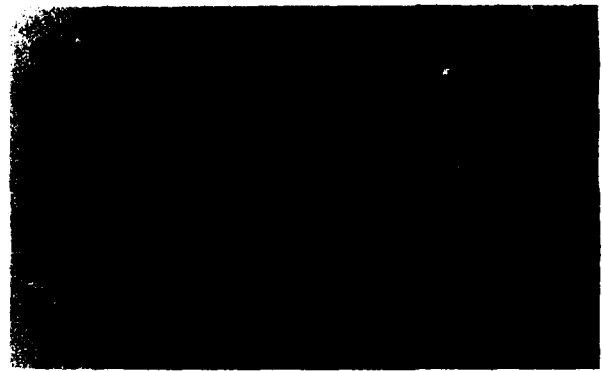


Figure 19 - High resolution X-ray image of the supernova remnant Cassiopeia A. Interesting is the absence of a central object which places an upper limit of  $\sim 1.5 \times 10^6$  °K on the temperature for a collapsed stellar remnant, below that for normal neutron stars created in supernova explosions. (Einstein Observatory photograph).

The curved crystal Bragg spectrometer (23), developed by M.I.T. for the Einstein Observatory is shown schematically in Figure 21. X-rays from a celestial source are focused on one of four selectable apertures, and then impinge on one of six curved crystals. The various crystals were used to cover the energy range of 0.2 to 3 keV with a resolving power of 50 to 500. Because of the complexity of X-ray spectra, especially below 1.5 keV, this high resolution was necessary in order to use several plasma diagnostics, e.g., Doppler broadening, line profile measurements, relative strengths of closely spaced multiple lines, etc. to determine temperatures, abundances, ionization equilibria, etc. Figure 22 is a spectrum of the supernova remnant Pup A observed by this instrument.

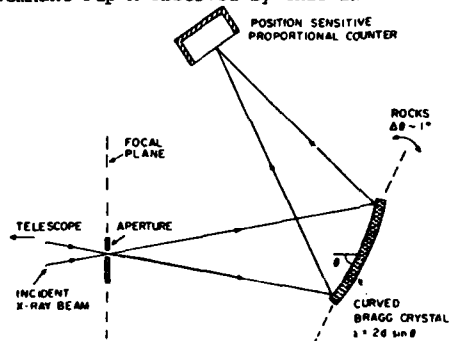


Figure 21 - A schematic diagram of the MIT focal plane crystal spectrometer on the Einstein Observatory.

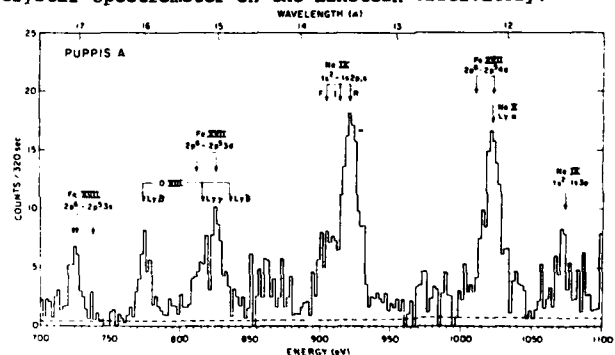


Figure 22 - X-ray spectrum of the Puppis A supernova remnant obtained by the MIT focal plane crystal spectrometer on the Einstein Observatory. The most prominent lines are those of hydrogen and helium-like ions of oxygen (OVIII) and neon (NeIX, NeX), and neon-like iron (FeXVII). This is similar to the spectra of solar active regions and suggests a temperature of  $2-5 \times 10^6$  K. (P.F. Winkler et al., *Ap. J. Lett.*, 246, L27 (1981). Photograph courtesy of C. Canizares, MIT).

An objective grating spectrometer was also developed for the Einstein Observatory. 500 lp/mm or 1000 lp/mm gratings, prepared by the University of Utrecht, could be placed in the optical path of the telescope. The high resolution imager was used to detect the dispersed images of point sources. The resolution at short wavelengths ( $\lambda < 20 \text{ \AA}$ ) was limited by the telescope resolution, whereas at longer wavelengths it was limited by aberrations. For the 1000 lp/mm grating,  $\lambda/\Delta\lambda \approx \lambda/0.4 \text{ \AA}$  and  $\lambda/\Delta\lambda \approx 60$  for the short and long wavelengths, respectively. The 1000 lp/mm grating had to be strengthened with a plastic film backing and this reduced its efficiency considerably. Over two dozen sources were observed with the grating spectrometer.

## VI. FUTURE PROGRAMS

Table I is a summary of past and future orbiting high resolution X-ray telescopes. As in optical astronomy, progress in X-ray astronomy will require the establishment of a permanent observing capability. The Advanced X-ray Astrophysics Facility (AXAF) is being designed to meet this goal.

TABLE I

HIGH RESOLUTION X-RAY TELESCOPES (satellite-borne)						
Observatory	Date	Geom. Coll. Area	Focal Length	Energy Range	Resolution FWHM	Half-power Diameter @1.5 keV
S-054 <sup>24</sup> Skylab*	1973-1974	42 cm <sup>2</sup>	2.1m	0.2-6 keV	3 arcsec	96 arcsec
S-056 <sup>25</sup> Skylab*	1973-1974	15	1.9	0.2-2	1	-
Einstein (HEAO-2) <sup>8</sup>	1978	500	3.4	0.2-4.5	4	11
EXOSAT <sup>26</sup>	1981	200	1.1	0.05-2	5	10-15
ROSAT <sup>27</sup>	1986	1250	2.4	0.1-2	5	6
AXAF <sup>28-30</sup>	1989	1700	10.0	0.1-10	0.5	0.6

\* Solar Telescopes

AXAF is to be a free-flying long-lived (10-15 years) X-ray observatory that is launched by the Shuttle, maintained on-orbit, and retrievable (Figure 23). It is conceived as an X-ray telescope consisting of six nested X-ray mirrors (Figure 24) with a maximum aperture of 1.2 m, a focal length of 10 m, and interchangeable and replaceable focal plane instruments. The telescope will provide half-arcsecond imagery over the central field for X-rays between 0.1 and 10 keV. Besides the broader spectral range, the sensitivity of AXAF is projected to be a factor of 100 or more greater than that of the Einstein Observatory.

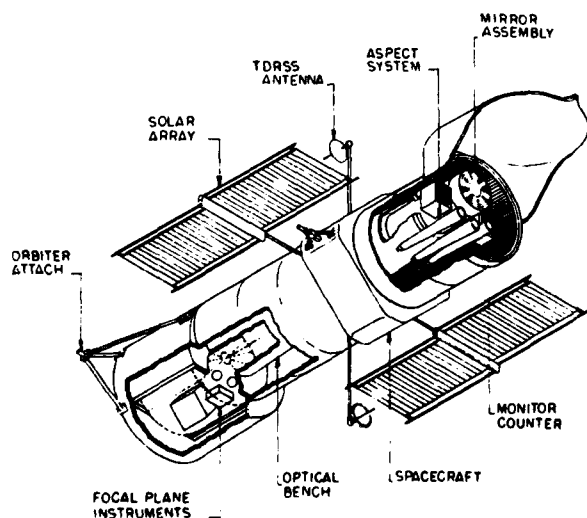


Figure 23 - The Advanced X-ray Astrophysics Facility (AXAF), a high resolution "permanent" X-ray observatory to be placed in space in the later 1980's.

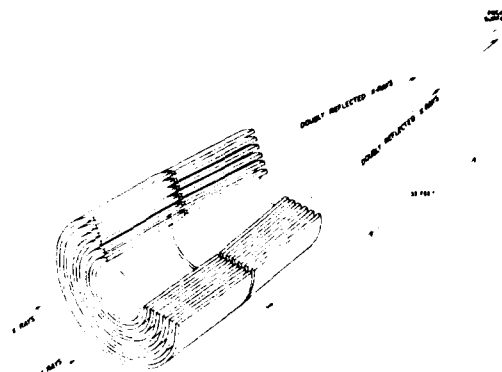


Figure 24 - Schematic of the AXAF mirror assembly.

The AXAF will provide a "permanent" observatory capability in the X-ray region of the electromagnetic spectrum that is well matched to the direction of astrophysics research and complementary to the capabilities of the Space Telescope (ST) in the optical region and the Very Large Array (VLA) in the radio region of the spectrum (Figure 25).

The mirror assembly for AXAF will represent a significant advance in the fabrication of X-ray optics for X-ray astronomy. It will have a factor of four larger geometric collecting area and a factor of seven better spatial resolution than the Einstein Observatory. Figure 26 is a comparison of the integrated point spread functions of these two observatories. The AXAF mirror performance will be achieved by maintaining local surface slopes to within tolerances of 0.05 arcsecond and surface roughness to the 10-15  $\text{\AA}$  level. Fabrication and metrology techniques are being developed to meet these requirements (31).

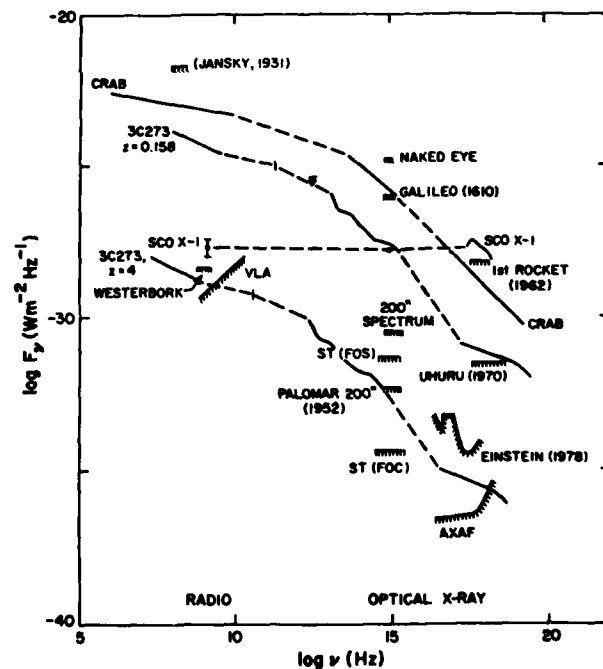


Figure 25 - The spectra of several characteristic objects (energy flux density per unit frequency interval vs frequency) are shown. Plotted on the figure are the sensitivities of a number of different instruments to emphasize the progress that has occurred in different branches of astronomy. The illustration is intended to emphasize the commonality of scientific objectives among radio, optical and X-ray observations and the complementary nature of the AXAF mission to the Space Telescope and the Very Large Array.

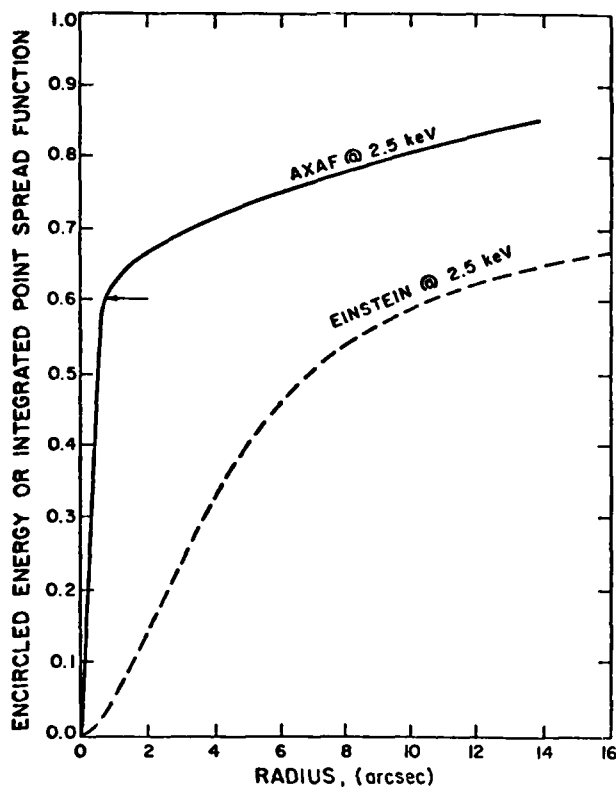


Figure 26 - A comparison of the AXAF and Einstein Observatory telescope integrated point spread functions at 2.5 keV. The AXAF curve is the design goal.

#### VII. FUTURE DEVELOPMENTS

In solar X-ray astronomy there is great interest in imaging coronal structures at the sub-arcsecond level. A grazing incidence solar telescope of a few tenths of an arcsecond has been proposed (32). As we increase the angular resolution of mirror systems, however, we start to run into difficulties with imaging detectors. Present charge transfer devices (33) and microchannel plates (21) have imaging elements of the order 15-25  $\mu\text{m}$ . For a 10 m telescope, the plate scale is 50  $\mu\text{m}$  (arcsecond) $^{-1}$ , so that these detectors would be adequate for half-arcsecond resolution. If we were to reduce the focal length and/or increase the angular resolution of a mirror system beyond this resolution, then these detectors would be inadequate. Analogous to visible light optics, it is possible to design systems (32) which employ relay optics at the prime focus to increase the overall focal length (Figure 27). A suitably modified grazing incidence microscope (34)

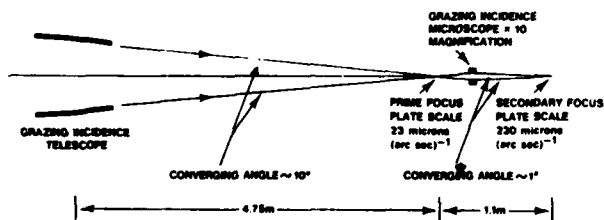


Figure 27 - Schematic diagram of the design of a grazing incidence telescope employing a grazing incidence microscope as a magnifying relay lens (J. Davis et al., op. cit.).

could be used to magnify the prime focus of a relatively short focal length primary mirror. However, such systems suffer from additional scattering and reflectivity losses and have a very narrow field of view ( $\sim$  arcminute). The feasibility of such an approach has not yet been demonstrated.

Another approach to high resolution X-ray optics should be mentioned here, although it has been discussed in greater detail at this conference. It is possible to achieve significant reflection efficiencies at normal incidence for soft X-ray wavelengths ( $\sim$  1/4 keV) by using multilayer coatings (35,36). Compared to grazing incidence mirrors, normal incidence X-ray mirrors would have larger useful fields of view, lower aberrations, and larger collecting areas for a given aperture. It appears theoretically possible to construct normal incidence mirrors with resolutions of between 0.01 and 0.1 arcsecond. A 3-inch diameter spherical test mirror optimized for 0.2 keV has recently been fabricated (37) and will be tested soon at the MSFC X-ray Test Facility (Figure 28). This mirror has been coated with 124 layers at IBM and is expected to have a peak reflectivity of several percent, a bandpass of a few Angstroms, and a resolution of 1 arcsecond (limited by the detector).

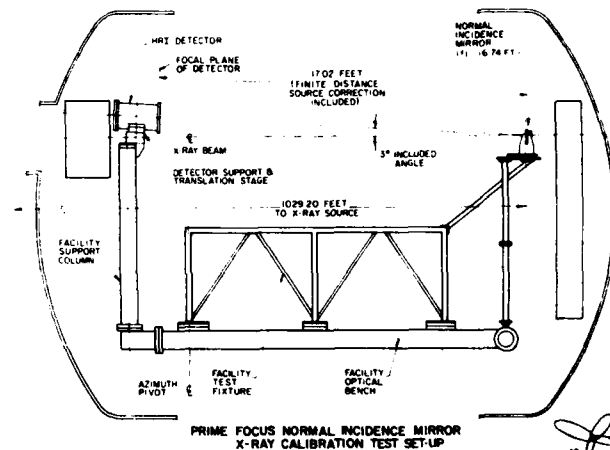


Figure 28 - Prime focus normal incidence mirror X-ray calibration test configuration at the Marshall Space Flight Center. (Courtesy of P. Henry, CFA).

#### REFERENCES

1. R. Giacconi in *X-ray Astronomy*, edited by R. Giacconi and H. Gursky (D. Reidel Publishing Co. 1974).
2. R. Giacconi et al., *Ann. Rev. Astron. Astrophys.* (1981).
3. R.F. Hirsh, Ph.D. Thesis, University of Wisconsin-Madison (1979).
4. R. Giacconi et al., *Phys. Rev. Lett.*, **9**, 439 (1962).
5. R. Giacconi and B. Rossi, *J. Geophys. Res.*, **65**, 773 (1960).
6. R. Giacconi et al., *J.O.S.A.*, **55** (1965).
7. HEAO Science Symposium, May 8-9, 1979, MSFC, NASA CP-2113 (1979).
8. R. Giacconi et al., *Ap. J.*, **230**, 540 (1979).
9. J. Nugent and G. Garmire, *Ap. J. Lett.*, **226**, L83 (1978).
10. A.H. Compton, *Phil. Mag.*, **45**, 1121 (1923).
11. H. Wolter, *Ann. Phys.*, **10**, 94 (1952).
12. L.P. Van Speybroeck and R.C. Chase, *App. Opt.*, **11**, 440 (1972).
13. J.H. Underwood, *Space Sci. Instr.*, **1**, 289 (1975).
14. J.H. Underwood, *Amer. Sci.*, **66**, 476 (1978).
15. A. Franks, *Sci. Prog. Oxf.*, **54**, 371 (1977).
16. "Imaging X-ray Optics Workshop", *SPIE Proc.*, **184**, (1979).

17. R. Giacconi et al., *Space Sci. Rev.*, 9, 3 (1969).
18. J.K. Silk, *SPIE Proc.*, 106 113 (1977).
19. L.P. Van Speybroeck, *SPIE Proc.*, 106, 136 (1977).
20. P. Gorenstein et al., *I.E.E.E. Trans.*, NS-58, 869 (1981).
21. P. Henry et al., *SPIE Proc.*, 106, 196 (1977).
22. S.S. Holt, *Space Sci. Instr.*, 2, 205 (1976).
23. C.R. Canizares et al., *SPIE Proc.*, 106, 154 (1977).
24. G.S. Vaiana et al., *Space Sci. Instr.*, 3, 19 (1977).
25. J.H. Underwood et al., *App. Opt.*, 16, 859 (1977).
26. P.A.J. de Korte et al., *App. Opt.*, 20, 1080 (1981).
27. J. Truemper et al., *SPIE Proc.*, 184, 12 (1979).
28. Advanced X-ray Astrophysics Facility (AXAF) - Science Working Group Report, NASA TM X-78285 (May 1980).
29. M.V. Zombeck, *Opt. Eng.*, 20, 297 (1981).
30. M.C. Weisskopf, *SPIE Proc.*, 228, 106 (1980).
31. M.V. Zombeck et al., *SPIE Proc.*, 257, 230 (1980).
32. J.M. Davis et al., *SPIE Proc.*, 184, 96 (1979).
33. D.A. Schwartz et al., *SPIE Proc.*, 184, 247 (1979).
34. J.K. Silk, *SPIE Proc.*, 184, 40 (1979).
35. E. Spiller, *App. Opt.*, 15, 2333 (1979).
36. J. Underwood et al., *SPIE Proc.*, 184, 123 (1979).
37. P. Henry, private communication (1981).

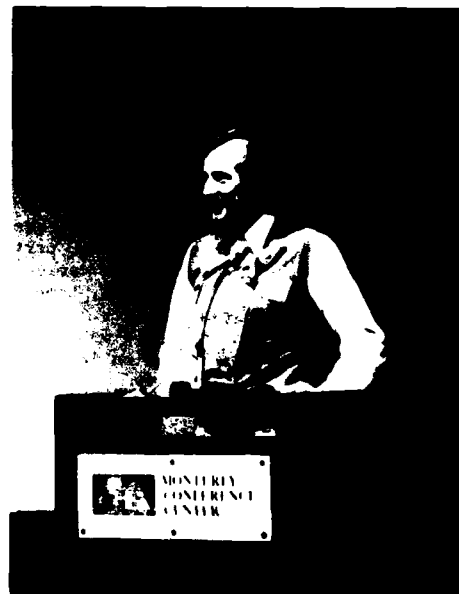
Note: The mirror was successfully tested and demonstrated a reflectivity of a few percent at  $67 \text{ \AA}$  (BK $\alpha$ ) and a resolution of a few arc-seconds,  $1/2$  degree off-axis.



Drs. Paul Kirkpatrick (left) and Martin Zombeck during the question and answer period.



Dr. Martin Zombeck of the Harvard/Smithsonian Center for Astrophysics, reviewing developments in x-ray astronomy and astrophysics.



Dr. Natale Ceglie in a post presentation discussion of advances in x-ray optics. Dr. Ceglie's paper begins on the following page.



N.M. Ceglio

Lawrence Livermore Laboratory  
 University of California  
 P.O. Box 5508  
 Livermore, California 94550

## ABSTRACT

X-ray optics stands on the threshold of realizing its early promise: precision analysis of microstructure on the scale of the x-ray wavelength. The achievement of this exciting goal will depend in large part on advances in microfabrication technology making possible the precision fabrication of periodic microstructures. A review of recent advances in, as well as future prospects for: x-ray microscopy, coded imaging, and space-time resolved spectroscopy, resulting from improved microstructure fabrication capabilities is presented.

## INTRODUCTION

- In x-ray optics there are no new ideas only new technologies to exploit. -

The past decade has brought a wide array of advances in x-ray optics placing it on the threshold of achievements which could significantly transform the fields of microbiology and materials microanalysis. Important contributions to other research disciplines such as plasma physics and surface physics may also be expected. This exciting condition results not from any conceptual breakthrough or new understanding of x-ray optical principles. It results, instead, from advances in technology which for the first time make possible the precision implementation of concepts which are many decades old. The early promise of x-ray optics: precision analysis of microstructure on the scale-length of the x-ray wavelength appears within our near term grasp.

A number of technologies have contributed to the rapid advance in x-ray optical capabilities. Improvements in the ability to accurately figure, polish and measure reflective surfaces have led to x-ray microscopes and telescopes of unprecedented resolution and reflection efficiency.<sup>1</sup> The availability of dedicated synchrotron and storage ring facilities as well as high power laser, particle beam, and discharge devices now provide a variety of bright x-ray sources with varied spectral, temporal, collimation and coherence characteristics.<sup>2</sup> Advances in solid state technology<sup>3</sup> and photoresist chemistry<sup>4</sup> have provided high resolution detectors of significantly improved sensitivity.

In addition to the above, and of particular interest to this discussion, are the significant advances in microfabrication technology which make possible the fabrication of organized structures on a sub-micron scale. This technology may very likely have the greatest near term impact on x-ray optics. This is so for at least two reasons: (1) Advances in microstructure fabrication are driven by a robust, highly competitive, billion dollar semiconductor and integrated-circuit industry. This driving force will, for at least the near term, keep the field active and creative, advancing at an ever accelerating pace. (2) Diffractive optical components - periodic microstructures - will play the key role in high resolution x-ray microscopy, and in the achievement of a diffraction limited x-ray focusing and manipulation capability in the laboratory.

The central role of diffractive optics in x-ray microscopy, and its close coupling to microstructure fabrication comprise the central theme of this article. High resolution (< 1000 Å) microscopy and microanalysis will most easily be achieved using diffraction optics. Reflection optics are more appropriate for high resolution, high speed telescopes. Telescopes generally require optical elements having large collection area and broadband spectral capability, characteristics most easily met by reflective components. Diffractive components provide a different set of characteristics, which are more appropriate to microscopy. A diffractive optical element is in essence simply a periodic structure. The resolution and speed of such an element are proportional to its minimum scale size. Its f/number may be represented,

$$f \# = \frac{\text{minimum scale size}}{\lambda_x} \quad (1)$$

where  $\lambda_x$  is the x-ray wavelength. Particularly noteworthy is the fact that the f/number does not depend on the overall surface area of the diffractive component. Such an x-ray optical component may indeed be microscopic in overall size. (A design of an x-ray lens with overall diameter of 20  $\mu\text{m}$  is presented in a subsequent section). Another significant practical feature of a diffractive lensing pattern is that its performance (i.e. resolution) is quite forgiving of random errors or defect sites in the periodic pattern.

As described above a diffractive optic for high resolution microscopy or microanalysis will require the fabrication of a microscopic periodic structure with a periodic scale size less than 1000 Å. Precision control over the periodicity of the structure will be required, but random pattern defects can be tolerated. This challenge is well matched to the capabilities of microfabrication technology.

Microfabrication technology can contribute to the development of high resolution diffractive components in at least two specific areas: (1) Advances are needed in the fabrication of small scale, planar, periodic structures such as zone plates, transmission gratings and coded apertures. These structures operate as amplitude modulation devices for x-ray focusing, imaging and spectral dispersion. (2) Advances are also needed in the precision control of material thickness and vertical profile of "planar" periodic structures, as well as in the diversity of materials from which such microstructures can be

made. These developments will make possible the fabrication of high efficiency phase modulation devices such as multilayer interference films<sup>5</sup>, Fresnel phase plates and phase gratings, matched filter pair coded apertures and perhaps even transmission blazed Fresnel phase plates and phase gratings.

The following sections are discussions of x-ray optical elements: Fresnel zone plates, coded apertures, and linear transmission gratings. Recent accomplishments in the development and application of such elements are reviewed, and areas in which future work would be most fruitful are delineated. The discussions have a specific emphasis. They stress the key role of microstructure fabrication in the recent progress in x-ray diffractive optics, and the critical dependence of future progress on continued advances in microfabrication technology. Specific attention is drawn to the current condition in which many of the more promising goals of x-ray optics can be quite simply reduced to particular challenges in microstructure fabrication.

#### FRESNEL ZONE PLATE LENSING ELEMENTS

A Fresnel zone plate pattern is shown in Fig. 1. It is a circularly symmetric array of annular zones which are alternately transparent and opaque. The concentric circles defining the successive annuli have radii,  $r_n$ , given by<sup>6</sup>

$$r_n^2 = n\lambda_x f + \frac{n^2 \lambda_x^2}{4} \quad n = 1, 2, 3, \dots \quad (2)$$

where  $f$  is the focal length,  $\lambda_x$  is the x-ray wavelength, and  $n$  is the zone number. When used in x-ray transmission, the FZP acts as a focusing (or imaging) element diffracting 10% of the incident radiation into a first order real focus. The remainder of the incident radiation is either absorbed (50%) by the opaque zones or directed into other diffractive orders (25% zeroth, 15% other). For cases in which

$$n^2 < \frac{2f}{\lambda_x} \quad (3)$$

the second term of Eq. (2) may be neglected without incurring significant spherical aberration in imaging applications.<sup>7</sup> The resulting geometric zone plate pattern is periodic in  $r^2$ , and has equi-area annular zones. It may be used as a narrowband lensing element for any x-ray wavelength satisfying

Eq. (3), with a corresponding focal length given simply by

$$f = \frac{r_1^2}{\lambda_x} \quad (4)$$

The resolution of the FZP according to the Rayleigh criterion is

$$\delta = 1.22(1 + \frac{1}{M})\Delta r \quad (5)$$

where  $M$  is the image magnification and  $\Delta r$  is the width of the outermost zone. For a geometrical zone plate the outermost (i.e. minimum) zone width may be simply expressed,

$$\Delta r = \frac{r_N}{2N} \quad (6)$$

where  $N$  is the total number of zones and  $r_N$  is the overall ZP radius. Combining eqns. (4) and (6) we see that the  $f$ /number ( $\equiv$  focal length/diameter) of the zone plate lens depends only on its minimum zone width and the x-ray wavelength used:

$$f^\# = \frac{\Delta r}{\lambda_x} \quad (7)$$

A characteristic feature of a diffractive optical element is the wavelength dependence of its focal properties, as expressed in eqn. (4). In imaging applications this leads to chromatic aberration unless the x-ray illumination is relatively narrowband. It is generally required that

$$\frac{\lambda}{\Delta\lambda} > N \quad (8)$$

for the chromatic aberration to have negligible effect on zone plate resolution. In some applications, however, the wavelength dependence of zone plate focusing properties may be used to advantage, as illustrated in Fig. 2. Shown is an off-axis segment of a Fresnel zone plate used as an imaging spectrometer to provide spatially separated, chromatically distinct images of a polychromatic x-ray source. The off-axis zone plate is a circular, off-axis segment of a circularly symmetric (on-axis) Fresnel zone plate. It has the same focal length and chromatic properties as its "parent" zone plate, but somewhat poorer resolution because of its reduced diameter.<sup>8</sup>

The interesting potential of Fresnel zone plates for high resolution microscopy, and the close coupling of this goal to microfabrication technology are expressed in Eqns. (5) and (7), wherein the resolution and speed of such elements depend linearly on the minimum zone width of the structure to be fabricated. Shaver, et al.<sup>9</sup> took a significant early step toward the fabrication of FZP lensing

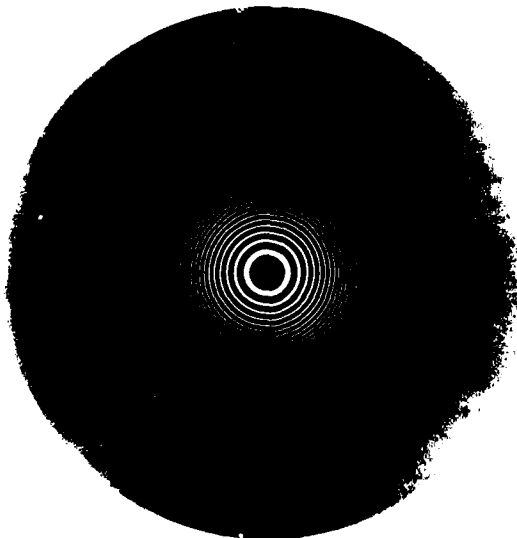


Fig. 1: Fresnel Zone Plate Pattern

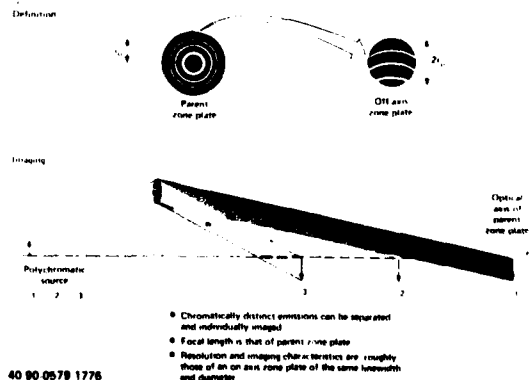


Fig. 2: An off-axis segment of a Fresnel zone plate used as an imaging spectrometer.

elements for high resolution microscopy. The result of this work is presented in Fig. 3. Shown is a free standing, thick, gold FZP with a minimum zone width  $\sim 3200$  Å, diameter  $\sim 630$   $\mu\text{m}$  (500 zones), and a thickness greater than 1  $\mu\text{m}$ . Perhaps most significant about this work is the method used for zone plate fabrication. The FZP pattern was generated directly using scanning electron beam lithography (SEBL). The thin, gold pattern so generated was subsequently used as an x-ray mask for  $C_k$  x-ray lithographic replication in "thick" x-ray resist (PMMA). The resist pattern then served as an electroplating mold for the production of the free-standing gold zone plate structure shown in Fig. 3. While other methods have been used for generating FZP lensing elements,<sup>10</sup> the power of the above described approach lies in its versatility and potential for scaling to narrower linewidths. SEBL techniques have been used for pattern generation down to sub-1000 Å linewidths,<sup>11</sup> and its capabilities continue to rapidly improve with the fast paced advance of the field. In addition, SEBL pattern generation allows changes in zone plate design or spherical aberration correction to be accomplished simply, through minor changes in the pattern generation program. The same is true for changes in support structure design for free-standing structures. Use of x-ray lithography for pattern replication provides a capability for "thick", high aspect-ratio structures, which extend the x-ray lens capability to higher energy and make possible the fabrication of thick, phase modulation x-ray elements.

FZP lensing elements have been resolution tested as imaging components in "crude", first generation x-ray microscopes, and have demonstrated image resolution approaching the diffraction limit. Such a demonstration experiment is illustrated in Fig. 4. Fig 4(a) illustrates the test set up in which the FZP of Fig. 3 was used as the objective lens in a 14x microscope to image a resolution test pattern backlit with Al K $\alpha$  radiation ( $\lambda_x = 8.34$  Å).<sup>12</sup> The resolution test pattern was in this case a "crude" zone plate having 1.0  $\mu\text{m}$  minimum zone width. The results, Fig. 4(b), show the 1.0  $\mu\text{m}$  lines and spaces clearly resolved. (The data does suffer from shot noise due to source intensity limitations). This test demonstrated a FZP lens resolution within almost a factor of two of the diffraction limit, eqn. (5). Additional tests are being conducted using test patterns with sub-micron feature size to extend the resolution test to the diffraction limit. The most

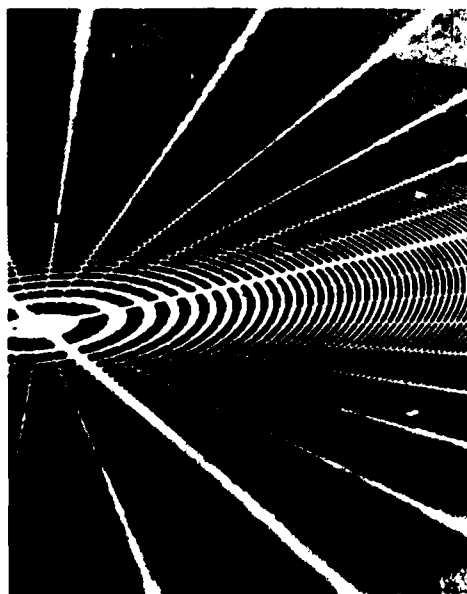


Fig. 3: Free standing Fresnel Zone Plate lensing element  $\Delta r = 3200$  Å.

impressive demonstration of diffraction limited resolution by a FZP lensing element has been performed by Schmahl, et al.<sup>13</sup>, and is displayed in Fig. 5. In this case, using a holographically generated zone plate pattern with minimum linewidth = 1200 Å, biological specimens were imaged demonstrating a resolution approaching 1500 Å in the first order.

The demonstration of diffraction limited resolution by FZP lensing elements encourages the design of next generation FZP's, which will bring us into the regime of x-ray microscopy and microanalysis on a sub-1000 Å scale. A number of criteria stand out in the design of such an optical component. The pattern should be small in order to minimize problems of SEB distortion in pattern generation, as well as problems of mechanical stability of the free standing structure. This small-size criterion establishes the zone number at  $N=100$ , the minimum number of zones for which a FZP can be expected to exhibit thin lens performance.<sup>14</sup> Image resolution requirements determine the minimum zone width,  $\Delta r$ . In this case  $\Delta r = 500$  Å is chosen. Such a lensing element would produce the sub-1000 Å probe spot size of interest in x-ray microanalysis, while taking a significant step toward the goal of  $\sim 200$  Å resolution, at which the microscopy of live microbiological samples becomes most interesting.<sup>15</sup> The parameters,  $\Delta r = 500$  Å,  $N = 100$ , set the FZP diameter at 20  $\mu\text{m}$ . The required zone plate thickness,  $t$ , as well as its focal length and  $f/\text{number}$  are established by the choice of x-ray wavelength. At  $\lambda_x = 50$  Å the focal length is 200  $\mu\text{m}$ ,  $f/\text{number}$  is 10, and a material thickness,  $t = 1000$  Å gold, is sufficient to absorb more than 90% of the radiation incident on the solid zones. This geometrical zone plate design satisfies eqn. (3), eliminating spherical aberration as a limit to resolution.

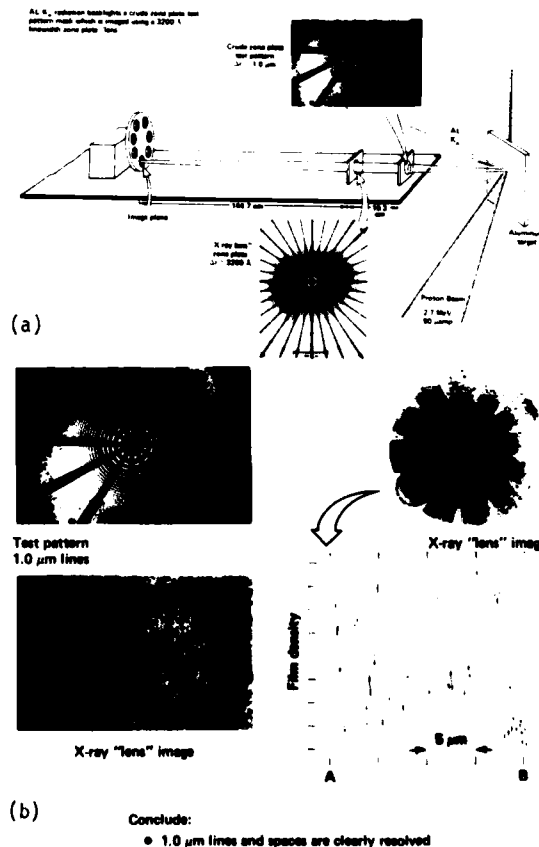


Fig. 4. (a) FZP Test Microscope: 14x. (b) Preliminary resolution test results for FZP lensing element.

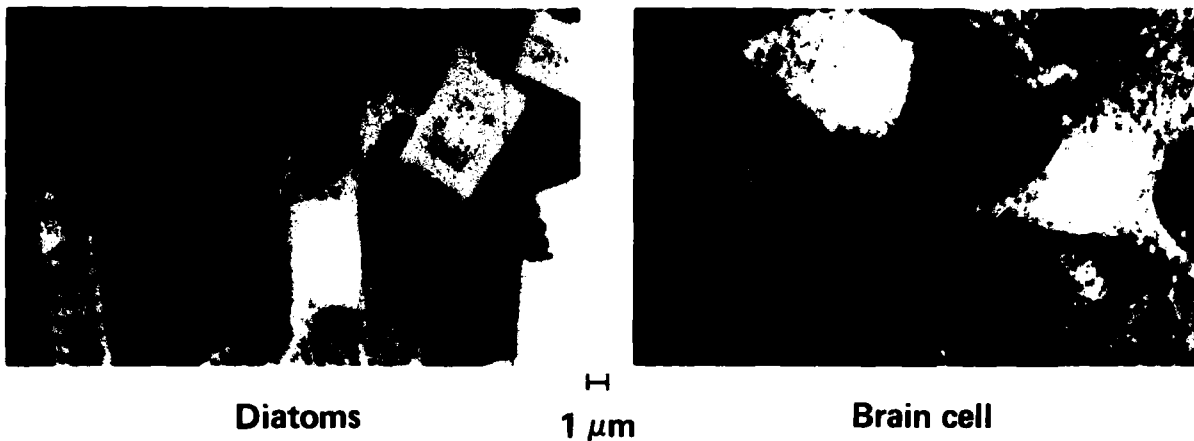


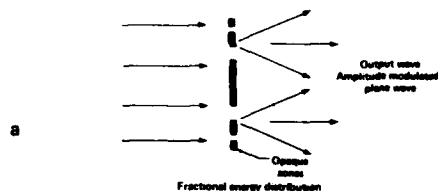
Fig. 5: Diffraction limited FZP x-ray images of biological specimens,  $\delta = 1500 \text{ \AA}$ . (Schmahl, et al, ref.13)

The FZP structure described above could be fabricated using the techniques employed by Shaver, et. al. The primary challenge would be that of the initial pattern generation using SEBL. However, in some ways generation of the proposed pattern would be simpler than that shown in Fig. 3. Although the minimum zone width is smaller by roughly a factor of seven for the proposed design, thereby requiring an electron beam exposure spot size  $\approx 200 \text{ \AA}$ , the total field area is roughly three orders of magnitude smaller, significantly reducing problems of pattern distortion and structural stability. The total number of electron beam exposures required to generate the pattern is  $\approx 10^6$ , a factor of 30 less than required for the pattern in Fig. 3. Beam placement accuracy is more stringent than in Fig. 3, requiring better than one part in  $10^3$  over the  $20 \mu\text{m} \times 20 \mu\text{m}$  field. Table I provides a brief summary of the FZP design characteristics, and SEBL pattern generation requirements.

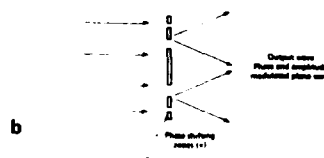
A significant feature of the above discussion of x-ray lens design and fabrication is that in the end the matter of feasibility reduces to a question of SEBL capabilities. Perhaps the most interesting challenge ever confronted in x-ray microscopy reduces quite simply to a problem in microstructure fabrication: can a microscopic pattern of concentric circles be written with 200-500  $\text{\AA}$  precision?

Significant increases in x-ray lens efficiency and background reduction (due to other orders) can be achieved by employing phase modulation effects in diffractive optical components. Employing such concepts one can design a "true x-ray lens", that is an optical component which focuses nearly all of its transmitted radiation into a single order focus.<sup>16</sup> The evolution of such a design concept is illustrated in Fig. 6. Figure 6a shows a Fresnel zone plate (FZP). The FZP performs an amplitude modulation (periodic in  $r^2$ ) of the incident plane wave,

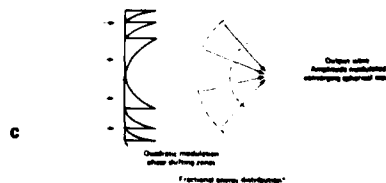
focusing roughly 10% of the incident energy into a first order focal spot. Fig. 6b shows a Fresnel phase plate, a somewhat more efficient focusing element. The FPP performs a phase and amplitude (because of finite x-ray absorption) modulation of the incident plane wave. The modulation function has the form of a square wave periodic in  $r^2$ . In the limit of small absorption, the FPP can focus roughly 40% of the incident energy into a first order focal spot. Figure 6c shows a blazed Fresnel phase plate. The BFPF transforms the incident plane wave into a converging spherical wave having an amplitude



Device	1st order real focus	Absorbed	Undiffracted	All other foci
FZP	0.1	0.5	0.25	0.15



Device	1st order real focus	Absorbed	Undiffracted	All other foci
FPP	$(\frac{1}{2})^2$	$(\frac{1}{2})^2$	$(\frac{1}{2})^2$	$\frac{1}{2} \cdot \frac{1}{2} \cdot \frac{1}{2} \cdot \frac{1}{2}$



Device	1st order real focus	Absorbed	Undiffracted	All other foci
BFPF	$(\frac{1}{2})^2$	$(\frac{1}{2})^2$	$(\frac{1}{2})^2$	$\frac{1}{2} \cdot \frac{1}{2} \cdot \frac{1}{2} \cdot \frac{1}{2}$

Fig. 6: The energy distribution is shown for a parallel, monochromatic x-ray beam incident on (a) a Fresnel zone plate, (b) a Fresnel phase plate, and (c) a blazed Fresnel phase plate.

**Design parameters:**

- Geometrical zone plate
- $N = 100$  zones ;  $\Delta r = 500 \text{ \AA}$  ;  $d_n = 20 \mu\text{m}$
- $f = 200 \mu\text{m}$  ;  $f^* = \frac{\Delta r}{\lambda} = 10$  •  $\lambda = 50 \text{ \AA}$

**Pattern generation challenges:**

- Field  $20 \times 20 \mu\text{m}$
- Spot size  $\leq 200 \text{ \AA}$
- Number of points  $\approx 10^6$
- Placement accuracy required: better than 1/1000

Table I: FZP design parameters and SEBL pattern generation requirements.

modulation (because of finite x-ray absorption) periodic in  $r^2$ . As a result of the periodic amplitude modulation, the BFPF will diffract energy into foci other than the first order real focus. However, in cases of small absorption, such effects are negligible and practically all the unabsorbed energy is directed into the first order real focus. An illustrative example comparing the performance of a FZP, FPP, and BFPF illuminated with a plane parallel x-ray beam at  $\lambda_x = 10 \text{ \AA}$  is shown in Table II. The phase modulation elements would in this case be made of aluminum. An aluminum thickness of  $1.6 \text{ \mu m}$  produces a  $\pi$  phase shift at  $\lambda_x = 10 \text{ \AA}$ .

The key to the achievement of the above x-ray optical capabilities lies in the advancement of the technology for the fabrication of precision thickness and profile controlled (for the BFPF) periodic microstructures from materials chosen for their x-ray refractive properties. The current state of the art in microfabrication technology places the BFPF beyond realistic near term capabilities. However, x-ray FPP's could indeed be fabricated from a variety of interesting materials (Al, Si, Cu, polymers, etc.) with a near term technological effort directed toward such a goal.

#### CODED APERTURES

A clever approach to x-ray imaging involving neither reflective nor diffractive optics, but nonetheless offering large radiation collection efficiency along with good resolution was first proposed by Mertz in 1960 for use in x-ray astronomy.<sup>17</sup> In this two-step, coded-imaging technique an appropriately designed periodic array of openings in an opaque mask is utilized as a coded aperture in a simple x-ray shadow camera. The x-ray source distribution casts simple geometric shadows (i.e. diffraction effects are negligible) through the coded aperture producing a coded image, which is subsequently decoded by a numerical or optical method matched to the coded aperture design. Mertz proposed a particular coded imaging technique, zone plate coded imaging (ZPCI), involving the use of a Fresnel zone plate as coded aperture, thereby allowing for the simple optical reconstruction of coded images. Fig. 7 illustrates the principles of the two-step, zone plate coded imaging technique for an incoherent laboratory source distribution. The source is represented as a distribution of points of short wavelength radiation (i.e. diffraction by the zone plate coded aperture is negligible). Each source point casts its distinct shadow through the zone plate aperture onto a shadowgraph or coded image recording medium. Note that each shadow uniquely characterizes, by its size and position, the spatial location of its associated source point: an off-axis point casts an off-axis shadow, a distant point casts a small shadow, a close point casts a large shadow. Thus, the spatial distribution of the source is recorded in the distribution (position and size) of the zone plate shadows in the coded image. The next step of this imaging process is shadowgraph decoding, which, because of the Fresnel zone plate geometry of the coded aperture, may be achieved by simple optical methods reminiscent of holographic image reconstruction. The processed coded image is

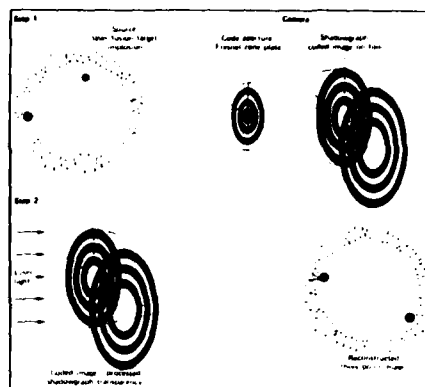


Fig. 7: Basic principles of the two step zone plate coded imaging technique.

coherently illuminated using an optical laser. Each zone plate shadow focuses the incident laser light to a diffraction limited spot, the image of its associated source point, thereby reconstructing the original source distribution point by point.

Coded imaging methods have unique capabilities which set them apart from conventional imaging techniques. Coded methods are broadly achromatic. The only requirement on the source radiation is that its wavelength be sufficiently "short" that geometrical optics prevail during image encoding, and sufficiently "long" that appreciable attenuation occur in the opaque zones of the coded aperture. Another important advantage of a coded imaging method is its large radiation collection solid angle, typically four to six orders of magnitude greater than a pinhole camera of equivalent resolution. This can provide a significant S/N advantage for coded imaging of radiation sources of limited extent.<sup>18</sup> In addition, coded techniques have a tomographic capability. Three dimensional source detail is recorded and reconstructed as illustrated in Figure 7.

For the past five years coded imaging techniques have been successfully employed for moderate resolution (microns) microscopy of high temperature laboratory plasmas.<sup>19</sup> This has been possible due to the emerging capability for precision fabrication of coded apertures on a microscopic scale.<sup>20</sup> In particular the successful implementation of ZPCI for the microscopy of laser fusion targets has required the fabrication of freestanding, gold micro-Fresnel zone plates with minimum linewidths (1-15  $\mu\text{m}$ ), thicknesses (2-38  $\mu\text{m}$ ), and diameters (0.4-15 mm). A SEM micrograph of a typical zone plate coded aperture is shown in Fig. 8. Such apertures have been used to produce moderate resolution, broadband



Fig. 8: Zone Plate Coded Aperture,  $\Delta r = 5 \text{ \mu m}$ ,  $N = 240$ ,  $t = 12 \text{ \mu m}$  thick gold.

Device	Fractional Energy Distribution			
	1st Order	Absorbed	Undiffracted	Other Orders
FZP	10%	50%	25%	15%
FPP	35%	13%	0.5%	51%
BFPF	73%	26%	0.2%	1%

Conditions: Aluminum phase structure @  $\lambda_x = 10 \text{ \AA}$

Table II: Comparative performance of x-ray lensing elements at  $\lambda_x = 10 \text{ \AA}$ .

images of x-ray (and particle) emissions from laser-induced micro-implosions of deuterium-tritium filled glass microspheres of interest in laser fusion studies. Figs. 9-11 show such ZPCI results. Fig. 9 displays the suprathreshold x-ray emission in a band 17-30 keV from a microsphere target illuminated from top and bottom with a 90 psec, 20 TW pulse of 1.06  $\mu\text{m}$  laser light. Image resolution is 15  $\mu\text{m}$ . (Other experimental details may be found in ref. (21)). Fig. 10 displays the x-ray emission from a laser imploded microsphere in four distinct energy channels. The images show the spectral evolution of emission detail at the directly illuminated spherical target surface as well as in the compressed target core (produced by the ultimate implosion of the microsphere). These multispectral x-ray images were recorded on a single target shot with a single zone plate shadow camera, utilizing a multi-layer filter-film pack for coded image recording. Image resolution is 8  $\mu\text{m}$ . (Further details may be found in ref. (22)). Fig. 11 illustrates the particle imaging capability of ZPCI. As mentioned above, coded imaging techniques are broadly achromatic working well for particle as well as photon emissions. In the experiment illustrated, the 3.5 Mev alpha particle emission from the thermonuclear burn region of a laser imploded, D-T filled microsphere was imaged with 3  $\mu\text{m}$  resolution. The coded alpha image was recorded in a thin cellulose nitrate film, a threshold-type ion track detector, which served to record the alpha particle data while discriminating against background radiations of x-rays, electrons, and protons. (Additional discussion may be found in ref. (23)).

As emphasized earlier, the important contributions of coded imaging techniques to the microscopy of laboratory plasmas have been made possible by recent advances in microfabrication technology, which have allowed the production of coded apertures with characteristics appropriate to

emerging coded imaging challenges. Strong motivations exist within a number of disciplines for extending ZPCI capabilities to higher energy x-rays ( $\sim 100$  keV) and more penetrating charged particles<sup>24</sup> (e.g.  $\sim 15$  Mev protons) with little or no loss in resolution capability. The prospect for such an extension depends almost exclusively on the development of techniques for the fabrication of high aspect-ratio (height/line width), gold, coded apertures 50-200  $\mu\text{m}$  thick. Significant progress in this area has recently been made using a combination of UV lithography and reactive ion etch techniques to produce thick zone plate patterns in polymer films<sup>25</sup>. The polymer patterns are subsequently used as electroplating molds to produce free-standing, thick, gold zone plate apertures. Fig. 12 shows a SEM micrograph of a thick zone plate pattern which has been reactive ion etched in a high purity polymer. The zone plate pattern shown has  $\Delta r = 15$   $\mu\text{m}$ , diameter  $\sim 15$  mm, and exceeds 100  $\mu\text{m}$  in thickness. Fig. 13 shows a higher magnification micrograph of a thick polymer zone plate mold. In this case  $\Delta r = 5$   $\mu\text{m}$ , pattern diameter is 5 mm and polymer thickness is 50  $\mu\text{m}$ . Figure 14 shows a high magnification micrograph of a 65  $\mu\text{m}$  thick, gold zone plate coded aperture formed by electroplating within an etched polymer mold such as shown in Fig. 12. The gold zone plate diameter is 15 mm with  $\Delta r = 15$   $\mu\text{m}$ .

Another area of strong interest for further development of coded imaging capabilities is in narrowband imaging of specific line emissions from broadband laboratory x-ray sources. Such a capability could be achieved using a coded aperture comprised of matched filter pair materials<sup>26</sup> as illustrated in Fig. 15. In such a coded aperture, alternate zones are made of materials having absorption edges of similar energies (e.g. Al  $K_{\text{ab}} = 1.56$  keV and Si  $K_{\text{ab}} = 1.84$  keV).<sup>27</sup> Material thicknesses are chosen such that adjacent zones have equal x-ray transmission except in the narrowband between the absorption edges. Under such conditions a broadband x-ray source will cast a high contrast shadow only at x-ray energies within the narrowband between the absorption edges of the matched filter pair materials. The achievement of a versatile, narrowband, coded imaging capability will depend on advances in microfabrication technology, which will make possible the production of microstructures with accurately controlled thickness made of materials chosen for their x-ray absorption properties.

#### X-RAY TRANSMISSION GRATINGS

An x-ray transmission grating is a linear periodic array of alternately transparent and opaque lines with sub-micron spatial period. In practice it is typically a linear grid of wires or bars of high Z material. As a result of its simple geometry, the transmission grating is an attractive dispersive element for x-ray spectroscopy. Fig. 16 compares the dispersive properties of the transmission grating with that of more commonly used reflective dispersive elements. All the structures satisfy a similar Bragg condition relating wavelength and period to the angle of diffraction. Their dispersive behavior differs, however, in that reflective components require the incident x-rays to also satisfy a reflection condition equating the angles of incidence and reflection. This difference is made clear by a simple thought experiment in which a plane, parallel beam of polychromatic x-rays is incident on a transmission grating and on a crystal at a specific angle. Behind the transmission grating would be displayed the entire incident spectrum dispersed in angle according to the Bragg relation,

$$\sin \theta = \frac{m\lambda}{d} \quad (9)$$

On the other hand the "spectrum" of the crystal would consist of the single wavelength satisfying the

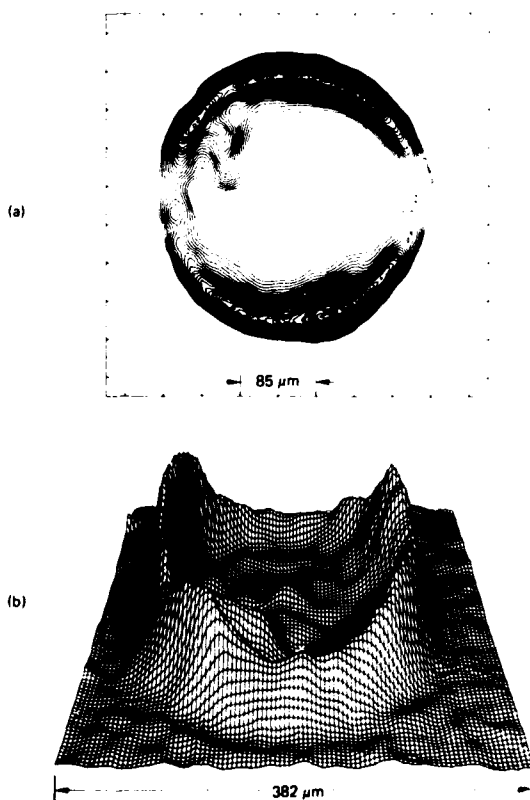


Fig. 9: Suprathreshold x-ray emission (17-30 keV) from a laser fusion target imaged using the two-step ZPCI technique.

Teflon coated microsphere target ( $145 \times 5 + 17$ ); 200 psec pulse; shot (89072010)

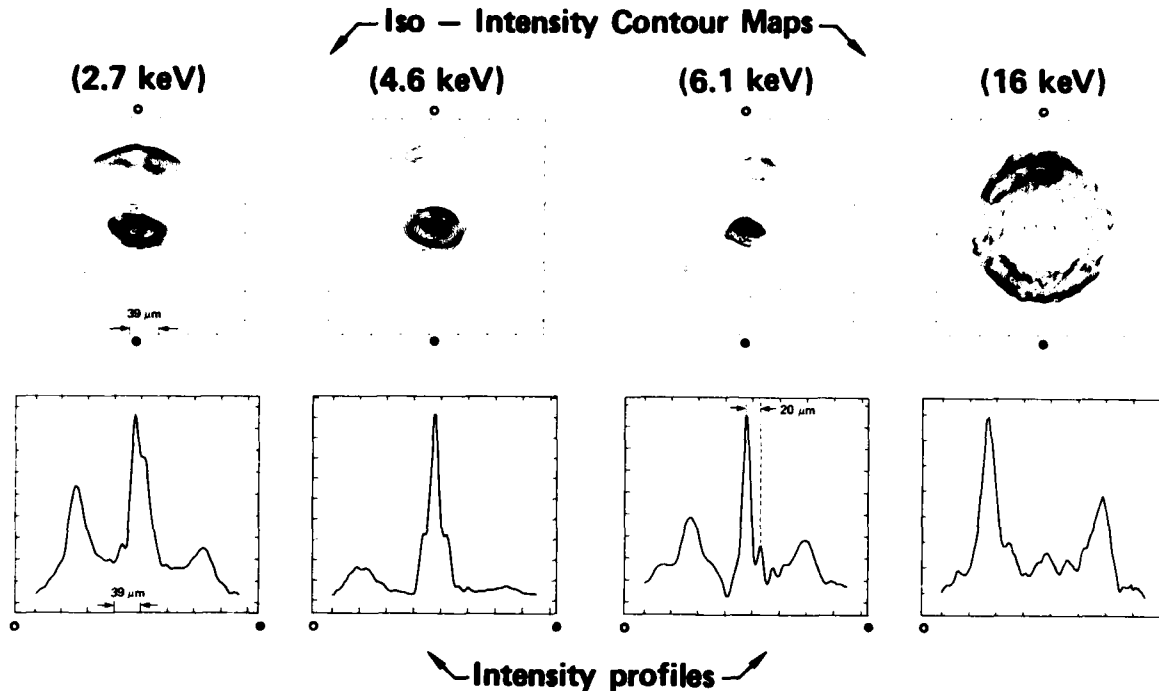


Fig. 10: Multispectral x-ray images of a laser imploded microsphere target using ZPCI.

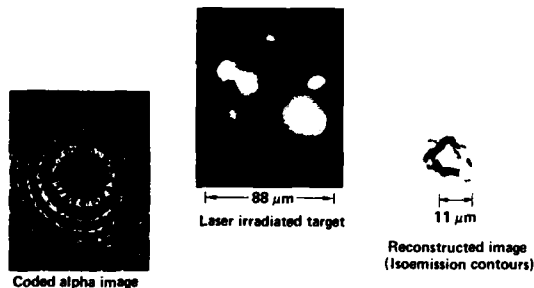


Fig. 11: An image of the thermonuclear burn region of a laser fusion implosion. ZPCI was used to image the 3.5 Mev alpha emission from the D-T reactions. Image resolution is  $\approx 3 \mu\text{m}$ .

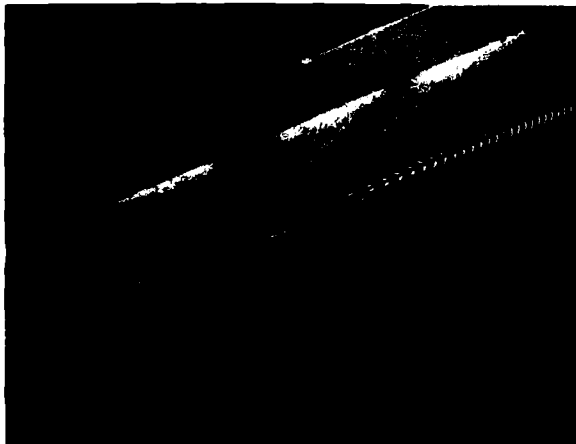


Fig. 12: Thick zone plate pattern ( $> 100 \mu\text{m}$ ) etched in a polymer material for use as an electroplating mold

crystal Bragg condition for the angle of incidence.<sup>28</sup>

The dispersive simplicity of transmission gratings account for their great strengths and limitations in spectroscopic applications. The fact that the TG accepts radiation at all angles of incidence makes it a powerfully versatile dispersive element. It requires no detailed angular alignment in its operation, and can, therefore, be easily coupled to instruments of high temporal or spatial resolution. In addition, its spectral range is large, limited only by the transmission properties of the grating itself. Its long wavelength limit is set by the grating cut-off period ( $\lambda = d$ ), and its short wavelength limit is set by the transparency of the grating wires at high x-ray energy. The trade-off for the advantage of versatility and large spectral range comes in the moderate spectral resolution of the TG. Its spectral resolution is limited in most applications by the degree of collimation of the incident radiation. However, this limitation can in many applications be used to advantage. It allows a direct trade-off between spectral resolution and collection solid angle (i.e. degree of collimation). In applications requiring moderate spectral resolution the transmission grating spectrometer provides the capability for efficient radiation collection and therefore high sensitivity.

Fig. 17 illustrates a simple, generalized design of an x-ray transmission grating spectrometer viewing a laboratory source of limited spatial extent.<sup>29</sup> The simple TG geometry allows for a great deal of diversity in the implementation of this simple spectrometer concept. The input aperture could be as simple as the one dimensional slit shown, or it could be generalized to a large solid angle collimation or imaging optic without significantly adding to the difficulty of implementation. The detector could as easily be x-ray film as the window of an x-ray framing tube or the slit of an x-ray streak camera for time resolved x-ray spectra.

The spectroscopic properties and potential of transmission gratings have been known for well over a century. Yet they had not been applied to the x-ray diagnosis of high temperature laboratory plasmas,



**Zone plate pattern parameters:**

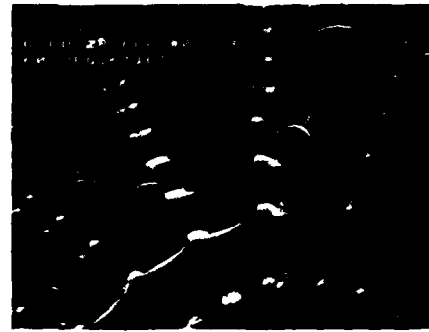
**Material: Polyimide**

**Aspect ratio: 10:1**

**Height: 50  $\mu\text{m}$**

**Minimum line width: 5  $\mu\text{m}$**

Fig. 13: High aspect ratio zone plate pattern etched in polyimide.



**Zone plate parameters:**

**Thickness: 65  $\mu\text{m}$**

**Number of zones: 250**

**Min. zone width: 15  $\mu\text{m}$**

**Material: Electroplated gold**

Fig. 14: Thick gold zone plate coded aperture for high energy x-ray imaging applications.

because of the difficulties incurred in fabricating grating structures appropriate to such applications. Such gratings require linewidths approaching 1000 Å for sufficient dispersion,<sup>30</sup> material thickness  $> 0.5 \mu\text{m}$  gold for use at energies above the soft x-ray regime<sup>31</sup>, and pattern, as well as period, fidelity to better than 0.1%. Recently, Hawryluk, et al.<sup>32</sup> fabricated x-ray transmission gratings meeting

these demanding specifications. The grating pattern was generated using "holographic lithography" at the 3250 Å wavelength of a He-Cd laser. The resulting pattern was used as a mask for  $C_k$  x-ray lithographic replication in "thick" x-ray resist (PMMA). The resist pattern then served as an electroplating mold for the production of the final gold grating. SEM micrographs of such a grating, supported on a thin (0.5  $\mu\text{m}$ )



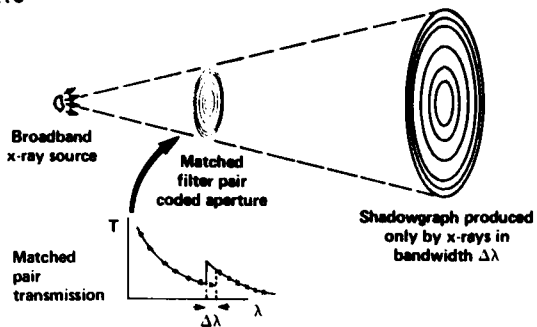


Fig. 15: Matched filter pair coded aperture proposed for narrowband imaging of a broadband x-ray source.

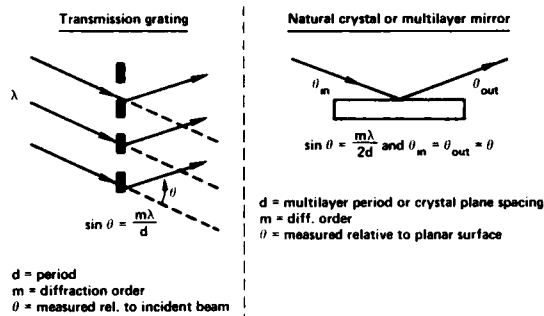


Fig. 16: Comparison of dispersive properties of a TG with reflective diffraction elements.

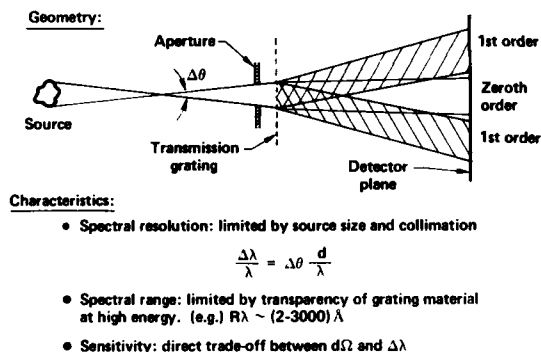


Fig. 17: A simple transmission grating spectrometer.

polyimide membrane, are shown in Fig. 18. Particularly noteworthy is the high aspect-ratio of the grating lines. They are 1500 Å wide and 6500 Å high. In addition to polyimide membrane supported gratings, free standing grating structures supported by a coarse grid (6 μm period) orthogonal to the grating lines have also been fabricated.

The x-ray transmission gratings fabricated by Hawryluk, et al. are being used for the spectroscopy of high temperature, laser produced plasmas.<sup>33</sup> They provide that research discipline with a new and powerful spectroscopic capability, offering insight to key issues of radiation production and transport, as well as energy transfer and drive in laser fusion experiments. Fig. 19 shows continuous x-ray spectra recorded over a broad spectral range (~0.1 - 5 keV) from two different laser-illuminated disk targets, one of gold and another of titanium. The spectra shown are time integrated, and were recorded using the simple spectrometer arrangement of Fig. 17. The detector was x-ray film, and the aperture was a 100 μm wide slit providing a spectral resolution of Δλ = 1 Å. The grating was freestanding without a polyimide support membrane. The  $C_{K\alpha}$  features in the spectra are due to the polymer overcoat on the x-ray film used. Note also the He-like  $Ti_{K\alpha}$  line features around 4.7 keV.

A freestanding x-ray transmission grating has been coupled to a soft x-ray streak camera, successfully recording the first time resolved (~20 psec resolution), continuous x-ray spectrum (from 0.1 - 1.5 keV) from a laser produced plasma<sup>33</sup>. A schematic representation of the experimental arrangement along with the data-record from a gold disk target are shown in Fig. 20. In these time resolved experiments spectral resolution was again collimation limited to Δλ = 1-2 Å allowing the observation of spectral detail hitherto unavailable in a time resolved mode.

The ease with which x-ray transmission gratings can be coupled to high resolution streaking (or spatially imaging) cameras is a great strength of these devices. It leads to instruments of powerful spectroscopic capabilities. This point can be illustrated using the streak camera data of Fig. 20. The total information recording capability (i.e. number of distinct resolution elements) of that two-dimensional data record may be estimated by dividing the duration of the x-ray emission (~2.5 nsec) by the temporal resolution (~20 psec), and multiplying that quantity by the quotient of the full spectral range (~124 Å) with the spectral resolution (Δλ = 2 Å). The number of resolution elements in the data record (~7.75 x 10<sup>3</sup>) represents an information capacity one to two orders of magnitude greater than any competing time-resolved spectrometer.

In addition to the above applications, an x-ray transmission grating has been coupled to a 22x, Wolter-design, grazing incidence reflection x-ray

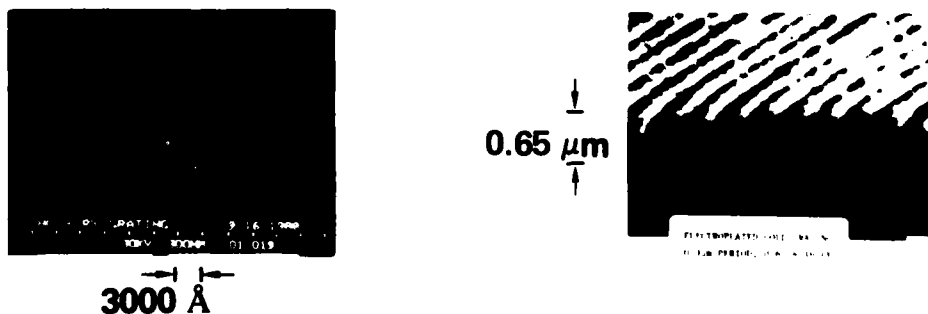


Fig. 18: X-ray transmission gratings.

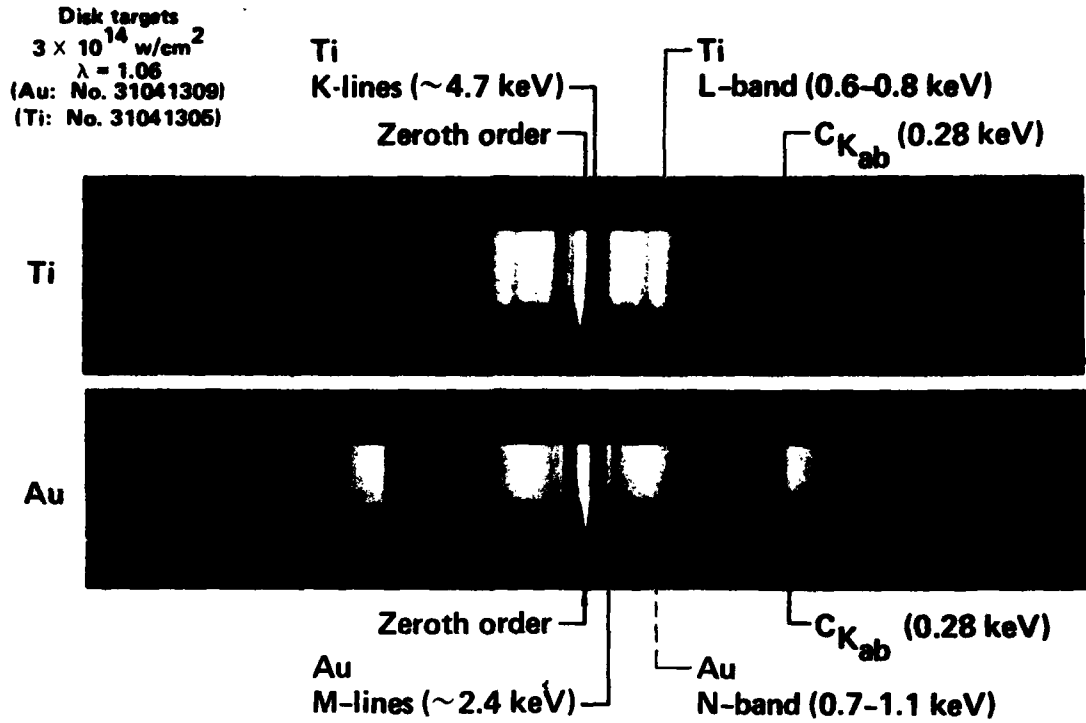


Fig. 19: Time integrated x-ray spectra from laser produced plasmas recorded by a transmission grating spectrometer.

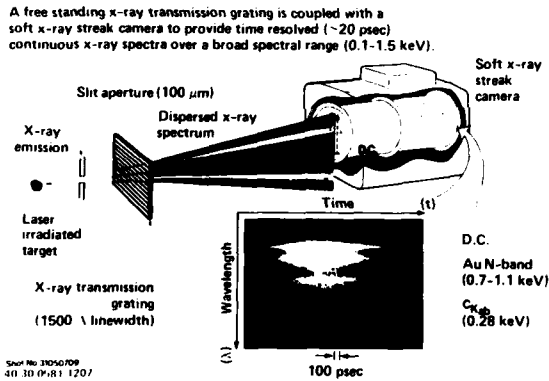


Fig. 20: A time resolved transmission grating spectrometer.

microscope to produce a high resolution imaging spectrometer for laboratory x-ray sources<sup>32</sup>. This instrument is similar in concept to imaging spectrometers used in x-ray astronomy<sup>34</sup>, but has superior spatial and spectral resolution (due to higher quality mirror surfaces), and greater spectral range (due to thicker gold gratings). Fig. 21 illustrates the experimental set-up for testing the spatial and spectral resolution of the imaging spectrometer. A test pattern mask was backlit with the M<sub>α</sub> (1.75 keV), M<sub>β</sub> (1.835 keV), and M<sub>γ</sub> (2.035 keV) line emission from a tungsten anode. The transmitted x-ray pattern was imaged by the microscope and dispersed by the grating. The resulting spatially resolved x-ray spectra are shown in Figs. 21, 22. In the test set-up used the x-ray grating intercepted only a 20° segment of the total annular ring of reflected x-rays emerging from the rear of the microscope. The remaining 340° segment of the annular ring was blocked. As is well known, surface scattering effects from a microscope mirror segment are anisotropic.<sup>35</sup> Significantly greater

image blurring occurs in the plane of incidence than normal to it. As a result the spectral and spatial resolution characteristics of the spectrometer vary depending on the relative orientation of the grating lines, and the plane of incidence at the mirror surfaces. This is illustrated in Fig. 22 using spatially resolved spectra from three different grating orientations. The best spatial resolution (nominally 1  $\mu$ m) was achieved with the grating lines normal to the plane of incidence. Under that condition a "point" x-ray source ( $\sim 0.5$   $\mu$ m diameter) was imaged as a line roughly 1  $\mu$ m x 10  $\mu$ m FWHM. The best spectral resolution was achieved with the grating lines parallel to the plane of incidence. Under that condition a spectral resolution,  $\Delta\lambda = .03 \text{\AA}$ , was measured, limited strictly by source size.<sup>36</sup> The resulting spectral resolving power,  $\lambda/\Delta\lambda = 200$ , is the highest ever achieved with this type instrument.

The preceding paragraphs serve as a dramatic example of how advances in microfabrication technology can provide new x-ray optical capabilities which make significant contributions to seemingly unrelated areas of research. Yet the applications of x-ray transmission gratings have hardly been exhausted, nor has the need for technological advances in grating fabrication been diminished. Initial testing has begun on a coded imaging spectrometer<sup>37</sup>, which couples an x-ray transmission grating with a coded aperture to produce spectrally dispersed coded images. These can subsequently be optically reconstructed into a spatially resolved x-ray spectrum as shown in Fig. 23. The spectral resolving power of this instrument (as well as the others described) improves linearly with grating dispersion,

$$\frac{\lambda}{\Delta\lambda} = \frac{\lambda L}{S} \cdot \frac{d\theta}{d\lambda} \quad (10)$$

In this expression S is the source size, L the source to grating distance, and  $d\theta/d\lambda$  the angular dispersion of the grating. There are, therefore, important gains to be had with x-ray transmission

The microscope, transmission grating combination provides spectrally separated, two-dimensional images of a micron-scale test pattern source emitting at the Tungsten  $M_\alpha$  (1.775 keV),  $M_\beta$  (1.835 keV), and  $M_\gamma$  (2.035 keV) lines.

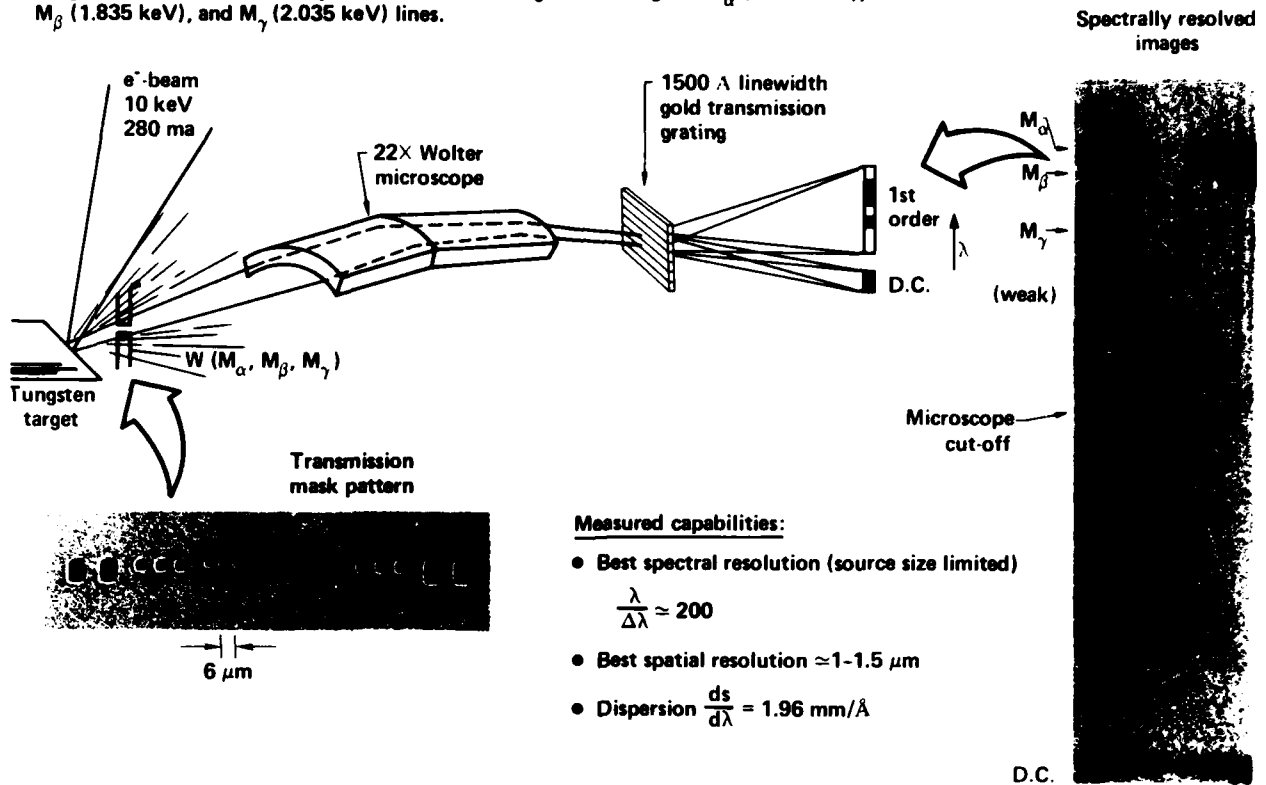


Fig. 21: A high resolution imaging spectrometer using an x-ray transmission grating.

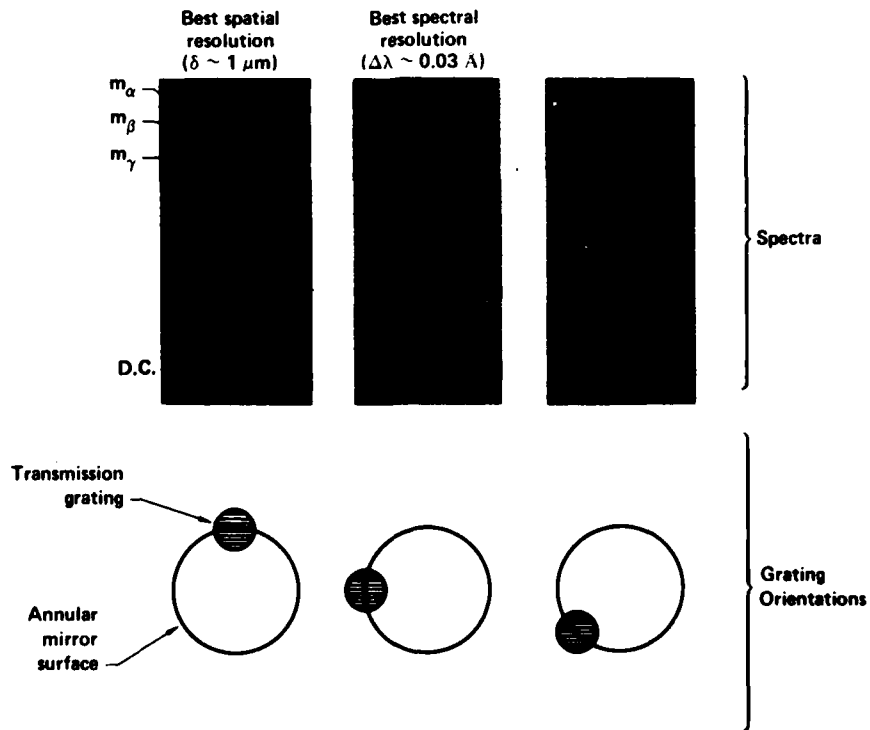


Fig. 22: Spatially resolved x-ray spectra recorded at three different relative orientations between the grating lines and x-ray plane of incidence.

A coded aperture serving as the entrance slit of a transmission grating spectrometer yields spectrally dispersed coded images, which may be reconstructed into a spatially resolved x-ray spectrum.

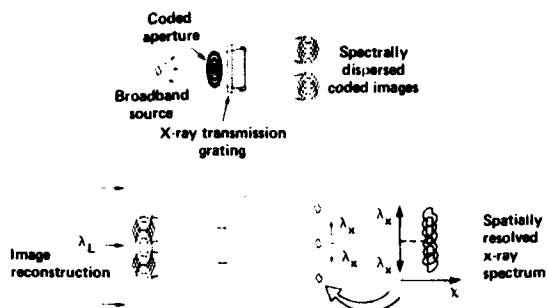


Fig. 23: Coded imaging spectrometer concept.

gratings of even smaller period (therefore larger  $d\theta/d\lambda$ ). Hawryluk, et al.<sup>32</sup> have already made significant progress in grating period reduction. X-ray grating patterns with 1000 Å period have been produced using spatial period division techniques.

As with Fresnel structures, the efficiency of linear gratings may be significantly improved by employing phase modulation effects. The fabrication of phase gratings and transmission blazed phase gratings for use as easily aligned, high efficiency, coherent x-ray beam splitters and beam steering devices could revitalize the fields of x-ray interferometry and x-ray holography. Such an advance would virtually rewrite the book on high resolution analysis of structures.

#### CONCLUSION

The preceding sections reviewed selected x-ray optical components which, with the application of appropriate microfabrication technology, could

provide significant advances in x-ray optical capabilities. These capabilities would have a broad range of applications in many diverse research disciplines. A compact restatement of this concept is provided in Table III. Listed are a number of goals in x-ray optics, along with associated challenges in microfabrication, and areas of research likely to benefit from the achievement of these goals. It would be difficult to overestimate the impact of the attainment of the x-ray goals listed. The ability to observe with 200 Å resolution, in real-time, the behavior of live biological specimens could dramatically transform the field of microbiology. Similarly, the production of a bright, 1000 Å diameter x-ray probe for microanalysis could provide unprecedented insight to the microstructure of surfaces. So too, an ability to manipulate x-rays with an ease and efficiency approaching that of optical light will provide a new beginning for x-ray interferometry and holography, expanding significantly the capability for high resolution analysis of x-ray transparent materials.

In addition to their potential for significant impact in important areas of research, the x-ray optical goals listed above have another important feature in common. For all these goals, the key to their practical realization lies in the achievement of appropriate advances in microfabrication technology. This close coupling between advances in x-ray optics and microstructure fabrication demands a heightened interest in this rapidly developing field by x-ray scientists. For us the time has come when advances in microfabrication technology are simply too important to be left solely to the semiconductor and integrated circuit industries.

<u>X-Ray Optics Goals</u>	<u>Microfabrication Challenges</u>	<u>Disciplines Which Benefit</u>
High resolution ( $\delta \approx 200$ Å) x-ray microscope	FZP (gold, $\Delta r \leq 200$ Å, $N = 100$ ) FPP (mat'l variety, precision thickness control)	Microbiological research (real-time imaging, live specimens)
X-ray focus ( $\sim 1000$ Å spot)	FZP, FPP ( $\Delta r \leq 1000$ Å, $N = 100$ )	Scanning microscopy surface microanalysis
High energy x-ray imaging ( $\rightarrow 100$ keV)	Thick, gold coded apertures ( $t \approx 50-200$ μm)	Plasma physics
Narrowband coded imaging	Coded apertures (matched filter materials, precision thickness control)	Plasma physics
Coherent beam steering & splitting	TG ( $d \approx 1000$ Å); phase gratings (mat'l variety, precision thickness control)	X-ray interferometry & holography
Space-time resolved x-ray spectroscopy		Plasma physics

Table III: X-ray optics goals and associated microfabrication challenges.

## Acknowledgements

The author wishes to acknowledge his colleagues and coworkers whose skilled efforts contributed to the data reported: G.F. Stone, A.M. Hawryluk, G. Howe, M. Roth, H., Medeck, R. Price, D. Ciarlo, C. Dittmore, W. Hermann, H.I. Smith, and J. Melngailis.

This work was performed under the auspices of the U.S. Department of Energy by Lawrence Livermore National Laboratory under Contract W-7405-Eng-48.

## References

1. M.J. Boyle, et al., LLNL report, UCRL-78594 (August 1976); J.K. Silk, Ann. N.Y. Acad. Sci. 342, 116 (1980); R. Gioconni, et al., Space Sci. Rev 9, 3 (1969); M.V. Zombeck, Opt. Eng. 20, 297 (1981).
2. R.E. Watson and M.L. Perlman, Science 199, 1295 (1978); D.J. Nagel et al., SPIE 135, Devel. Semicond. Microlith, 46, (1978), G. Dahlbacka, Proc. Topical Conf. Low Energy X-Ray Diag. (Monterey, June, '81); J. Riordon, Proc. Topical Conf. Low Energy X-Ray Diag. (Monterey, June '81).
3. L.N. Koppel and J.D. Eckels, LLNL report UCRL-78414 (October, 1976); P. Burstein, et al., Ann. N.Y. Acad. Sci 342, 252 (1980).
4. E. Spiller and R. Feder in X-Ray Optics p. 48 (Springer-Verlag, New York, 1977); G.N. Taylor, Solid State Tech 23, 73 (May, 1980)
5. Multilayer interference structures will play an important role in x-ray optics as beam splitting and steering devices, and as band-pass x-ray filters. These structures are not included in this discussion because they are adequately reviewed elsewhere: E. Spiller, Proc. Topical Conf. Low Energy X-Ray Diag. (Monterey, June '81); T.W. Barbee, Proc. Topical Conf. Low Energy X-Ray Diag. (Monterey, June '81).
6. When used as a thin lens for imaging at finite object distance with magnification, M, an additional factor  $(M^3 + 1)/(M + 1)^3$  should be included as a multiplier of the second term in eqn. (2). This factor is often negligible in high magnification applications.
7. M. Young, J. Opt. Soc. Am. 62, 972 (1972).
8. Resolution of the off-axis zone plate is related to that of its parent zone plate by the ratio of the respective radii:  $\delta_o = \frac{r_N}{r_o} \delta_p$  where  $r_o$  is the radius of the off-axis zone plate.
9. D.C. Shaver, et al., J. Va. Sci. Tech. 16, 1626 (1979).
10. D. Rudolph and G. Schmahl, Ann. N.Y. Acad. Sci 342, 94 (1980); and Heidenhain Corporation, Arlington Heights, Illinois.
11. A.N. Broers, et al., Appl. Phys. Lett 29, 596 (1976).
12. N.M. Ceglio, Ann. N.Y. Acad. Sci. 342, 65 (1980).
13. G. Schmahl, et al., N.Y. Acad. Sci. 342, 368 (1980).
14. D.J. Stigliani, et al., J. Opt. Soc. Am. 52, 610 (1967).
15. G. Schmahl, A. Engstrom, private communication.
16. N.M. Ceglio and H.I. Smith, Proc. VIII Int. Conf. X-Ray Optics and Microanalysis (Boston, 1977); also LLNL report, UCRL-79966 (August 1977).
17. L. Mertz and N.O. Young, Proc. Int. Conf. Opt. Instrum. P. 305 (Chapman and Hall, London, 1961).
18. All coded imaging techniques suffer a (S/N) decrease as source size increases. In general it is required that the diameter of the zone plate coded aperture be large compared to that of the source, if ZPCI is to provide a significant (S/N) advantage over conventional pinhole imaging methods.
19. N.M. Ceglio, D.T. Attwood, and E.V. George, J. Appl. Phys. 48, 1566 (1977); E. Fenimore, et al., Appl. Optics 18, 945 (1979).
20. N.M. Ceglio and W.I. Smith, Rev. Sci. Instrum. 49, 15 (1978); D.R. Ciarlo and N. M. Ceglio, SPIE Semicond. Microlith. V (San Jose, 1980) also LLNL Report, UCRL-83587 (April, 1980).
21. N.M. Ceglio and J.T. Larsen, Phys. Rev. Lett 44, 579 (1980).
22. N.M. Ceglio, Proc. Topical Conf. Symm. Aspects of Inertial Fusion Implosion (Naval Research Laboratory, May, 1981).
23. N.M. Ceglio and L.W. Coleman, Phys. Rev. Lett 39, 20 (1977); N.M. Ceglio, Energy and Tech. Rev. - LLNL report, UCRL-52000-78-1 (Jan., 1978).
24. N.M. Ceglio and E.V. Benton, LLNL report, UCRL-82550 Rev 1 (Jan., 1980).
25. N.M. Ceglio, G.F. Stone, and A.M. Hawryluk, J. Vac. Sci. Tech. (Nov./Dec.-1981).
26. P.A. Ross, J.O.S.A. and R.S.I. 16, 433 (June, 1928).
27. According to W. Stoner, the matched filter pair coded aperture was first proposed by G. DeMeester of Raytheon Corp., a private communication.
28. In this sense reflective components are not really dispersive at all. They operate much differently than a prism or transmission grating. The TG transmits every wavelength component of the incident beam, independent of its angle of incidence. The incident rays are bent (diffracted) by an angle given by the Bragg condition. The reflective element, on the other hand, may be viewed as performing a detailed "book-keeping" operation on the incident beam. It passes only those wavelength components incident at an appropriate angle, and then merely reflects them.
29. If the source were large, additional collimation would be required to limit the spectrometer's view to only a small portion of it.
30. The angular dispersion of the transmission grating is  $d\theta/d\lambda = 1/m\cos\theta_o$ , where  $d$  = period,  $m$  = order,  $\theta_o$  = angle of incidence (measured from the normal).
31. At  $t = 0.5 \mu\text{m}$  gold, x-ray transmission in the energy range (1.5-5.0 keV) is < 50%. This attenuation provides sufficient modulation contrast to produce distinct diffracted spectra. However, phase effects (of the partially transmitted x-rays) can lead to variations in the TG diffraction efficiency, requiring additional calibration.
32. A.M. Hawryluk, et al., J. Vac. Sci. Tech. (Nov/Dec - 1981); A.M. Hawryluk, et al., Proc. Topical Conf. Low Energy X-ray Diag. (Monterey, June, 1981).
33. N.M. Ceglio, M. Roth, and A.M. Hawryluk, Proc. Topical Conf. Low Energy X-Ray Diag. (Monterey, June, 1981).
34. H. Gursky and T. Zehnpfennig, Appl. Opt. 5, 875 (1966).
35. W. Ehrenberg, J. Opt. Soc. Am. 39, 746 (1949).
36. The quoted spectral resolution,  $\Delta\lambda = .03 \text{ \AA}$ , is a measured value limited by the  $3 \mu\text{m} \times 3 \mu\text{m}$  minimum feature size of the resolution mask pattern. This is a conservative estimate of the capability of the instrument. If a smaller feature size had been used (e.g.  $1 \mu\text{m} \times 1 \mu\text{m}$ ), a value,  $\Delta\lambda = .01 \text{ \AA}$ , limited by microscope resolution, could presumably have been achieved.
37. The x-ray coded imaging spectrometer is a variant of the Fresnel spectrograph first proposed by Mertz: L. Mertz, Transformations in Optics p. 81 (John Wiley and Sons, New York, 1965).

## Fabrication of Diffractive Optical Elements for X-ray Diagnostics\*

Henry I. Smith

Department of Electrical Engineering and Computer Science, Massachusetts Institute of Technology

Cambridge, Massachusetts 02139

## ABSTRACT

A paper was presented which reviewed the techniques of microlithography, etching, deposition and plating that are used to fabricate diffractive optical elements for the soft x-ray region. Here a brief summary and a guide to some of the recent literature, which contains details of fabrication and applications, are provided.

## SUMMARY AND A LIMITED GUIDE TO RECENT LITERATURE

Periodic and quasi-periodic structures, composed of alternating transparent and opaque regions, such as gratings and Fresnel zone plates, are extremely useful in the soft x-ray domain ( $\lambda \sim 0.4 - 100$  nm) as diffractive optical elements. Techniques for fabricating such diffractive optical elements include holographic lithography, x-ray lithography, spatial-period-division and scanning electron beam lithography for exposing patterns in resist, and electroplating for producing the final structures. References 1-14 present some recent progress in these techniques, as well as applications. These references are not comprehensive but instead emphasize work done at M.I.T. and M.I.T. Lincoln Laboratory. Reference (1) describes the fabrication of gold transmission diffraction gratings of 0.2 and 0.3  $\mu\text{m}$  spatial period at thicknesses up to 0.6  $\mu\text{m}$ , (see Fig. 1), the use of such gratings in an imaging spectrometer, and recent progress in spatial-period-division. This latter technique makes use of near-

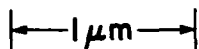


Figure 1

Scanning electron micrograph of a grating of 0.3  $\mu\text{m}$  spatial period in gold 0.65  $\mu\text{m}$  thick on a polyimide membrane substrate. Grating was cleaved for purposes of microscopy, and one of the gold lines extends outward from the cleaved edge, showing the nearly rectangular profile. Fabrication included x-ray lithographic exposure of PMMA and gold electroplating (from Refs. 1, 4).

field diffraction from a parent mask of spatial period  $p$  to expose higher spatial frequency multiples (i.e.  $p/2$ ,  $p/3$ ,  $p/4$ , etc.) in resist films (2). Figure 2 is an electron micrograph of a 0.2  $\mu\text{m}$  spatial period grating, with 40 nm wide slits in gold 0.2  $\mu\text{m}$  thick, that was fabricated for use in x-ray spatial-period-division to expose gratings of 99.5 nm period (1). Using deep UV radiation ( $\lambda \leq 200$  nm), the technique is somewhat more convenient than conventional holographic techniques (3). With x-radiation it may be possible to expose gratings with spatial periods of a few tens of

nanometers (2). Additional details on the imaging spectrometer work are given in Ref. (4).



Figure 2

Scanning electron micrograph, top view, of a 0.2  $\mu\text{m}$  spatial period grating with 40 nm wide slits in gold 20 nm thick (from Ref. 1).

Reference (5) covers the use of scanning electron beam lithography and gold microplating to fabricate Fresnel zone plates in 1.3  $\mu\text{m}$  thick gold for x-ray imaging. References 6 and 7 describe holographic techniques for exposing aberration-corrected zone plate patterns, as well as imaging experiments that demonstrated resolution less than 100 nm.

References 8-10 describe the fabrication of x-ray lithography masks of gratings by oblique shadowing techniques, and the replication of such masks. With shadowing techniques (see also Ref. 11), the linewidth-to-period ratio of gratings can be precisely controlled (8). Linewidths as narrow as 2 nm have been achieved on the mask and linewidths as narrow as 17.5 nm have been replicated in PMMA (9). Figure 3 is a scanning electron micrograph of a grating exposed in PMMA by x-ray lithography using a mask fabricated by a shadowing technique that provides nearly atomically smooth lines in the mask (10).

Holographic lithography is widely used for the exposure of low distortion, high resolution gratings. References (12) to (14) discuss recent work on holographic techniques.

There has been substantial progress in the last several years in the technology for fabricating diffractive optical elements for soft x-ray diagnostics, particularly in the areas of pattern fidelity, absorber thickness, minimum linewidth, spatial period, and linewidth control. With continued efforts over the next several years, we should have available a technology for fabricating diffraction gratings and zone plates in thick absorber materials with low distortion ( $< 10^{-5}$ ), spatial

periods less than 100 nm (i.e.  $> 10,000$  lines/mm) and linewidth control to  $\sim 10$  nm.

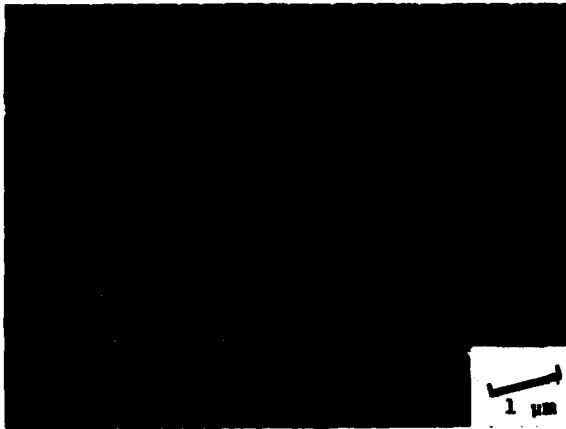


Figure 3

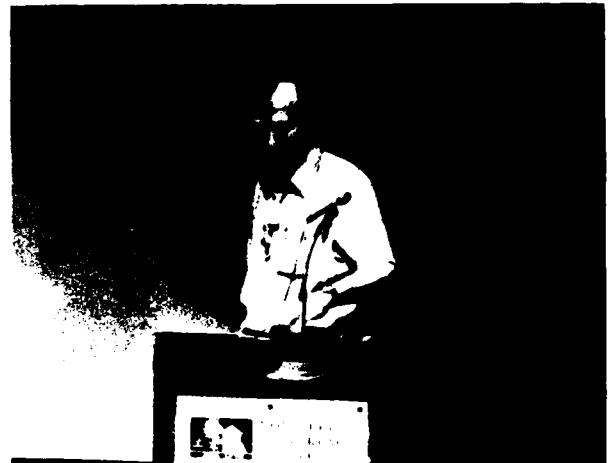
Scanning electron micrograph of a  $0.3 \mu\text{m}$  spatial period grating pattern exposed in PMMA by x-ray lithography. The linewidth is  $\sim 40$  nm. The extreme smoothness of the lines was achieved by first fabricating a square-wave-profile grating in (110) silicon using anisotropic chemical etching, taking a replica of this crystallographic template into a polyimide membrane, and obliquely shadowing the latter to form a high contrast x-ray mask. Since the sidewalls of the crystallographic template are nearly atomically smooth (i.e.  $\sim (111)$  planes) the replicated lines are also extremely smooth (from Ref. (10)).

#### REFERENCES

1. A.M. Hawryluk, N.M. Ceglie, R.H. Price, J. Melngailis and H.I. Smith, Proc. Sixteenth Symposium on Electron, Ion and Photon Beam Technology, Dallas, Texas, May 26-29, 1981, D.R. Herriott, editor. Submitted for publication J. Vac. Sci. Tech., Nov/Dec 1981.
2. D.C. Flanders, A.M. Hawryluk and H.I. Smith, J. Vac. Sci. Tech. 16, 1949 (1979); also Annals of the New York Acad. of Sciences, 342, 203-212 (1980).
3. A.M. Hawryluk, R. Osgood, et al, "Spatial-Period-Division with Deep UV Radiation", to be published.
4. A.M. Hawryluk, N.M. Ceglie, R.H. Price, J. Melngailis and H.I. Smith, these proceedings.
5. D.C. Shaver, D.C. Flanders, N.M. Ceglie and H.I. Smith, J. Vac. Sci. Tech. 16, 1626 (1980).
6. D. Rudolph and G. Schmahl, Annals of the New York Academy of Sciences 342 (1980).
7. G. Schmahl, these proceedings.
8. D.C. Flanders, J. Vac. Sci. Tech. 16, 1615 (1979).
9. D.C. Flanders, Appl. Phys. Lett. 36, 93 (1980).
10. N. Tsumita, J. Melngailis, A.M. Hawryluk and H.I. Smith, Proc. Sixteenth Symposium on Electron, Ion and Photon Beam Technology, Dallas, Texas, May 26-29, 1981, editor D. Herriott, to be published J. Vac. Sci. Tech., Nov/Dec 1981.
11. D.C. Flanders and A.E. White, Proc. Sixteenth Symposium on Electron, Ion and Photon Beam Technology Dallas, Texas, May 26-29, 1981, D.R. Herriott, editor. Submitted for publication J. Vac. Sci. Tech., Nov/Dec 1981.
12. W.W. Ng, C.S. Hong and A. Yariv, IEEE Trans. Elec. Dev., ED-25, 1193 (1978).
13. "Periodic Structures, Gratings-Moire Patterns and Diffraction Phenomena", Proc. Society of Photo-Optical Instrumentation Engineers, Vol. 240,

- editors C.H. Chi, E.G. Loewen, C.L. O'Bryan, San Diego, California, July 29 - Aug. 1, 1980, © 1981, Society of Photo-Optical Instrumentation Engineers.
14. N.N. Efremow, N.P. Economou, K. Bezjian, S.S. Dana and H.I. Smith, Proc. Sixteenth Symposium on Electron, Ion and Photon Beam Technology, Dallas, Texas May 26-29, 1981, D.R. Herriott, editor. Submitted for publication J. Vac. Sci. Tech., Nov/Dec 1981.

\*The M.I.T. portion of this work was sponsored by the Joint Services Electronics Program and the Defense Advanced Research Projects Agency.



Dr. Henry Smith of MIT describing his groups capability to fabricate sub-micron structures for wide ranging applications.

## X-Ray Microscopy Using Fresnel Zone Plates

G. Schmahl, D. Rudolph, and B. Niemann

Universitäts-Sternwarte, University of Göttingen, D-3400 Göttingen, Geismarlandstraße 11

## ABSTRACT

For soft X-ray microscopy the wavelength range of about 1-5 nm is best suited. The main applications of X-ray microscopy are in the field of biology. The reason is that thick (1 - 10  $\mu\text{m}$ ) biological specimens in a natural state can be investigated. X-ray microscopy requires intense X-ray sources as well as high resolution X-ray lenses. Suited X-ray lenses are Fresnel zone plates.

## I. INTRODUCTION

Several research groups in the world develop X-ray microscopes, mainly for biological applications. The aim, not the only one, is to investigate cells and cell organelles in a natural state with high resolution.

With optical microscopes one can investigate life cells but the resolution is limited to about 0,2  $\mu\text{m}$ . About a hundredfold better resolution can be obtained using the electron microscope. But in this case it is impossible to investigate life or even wet cells. With soft X-rays in the wavelength range of about 2 nm to 5 nm it is possible to observe wet cells in a natural state, i.e. unfixed and unstained.

Three points are important for soft X-ray microscopy: the contrast mechanism, that means the interaction between X-rays and matter, high resolution X-ray optics and intense X-ray sources.

## II. CONTRAST MECHANISM IN TRANSMISSION X-RAY MICROSCOPY, RADIATION DAMAGE

Both X-rays and electrons are dangerous for living specimens. Why will it be possible to get a high resolution in the region of 0,01  $\mu\text{m}$  investigating cells in their natural state using soft X-rays?

To observe a living specimen it has to stay under natural conditions, e.g. in a chamber filled with air. A layer of air 500  $\mu\text{m}$  thick at 760 torr has a transmission of 70 % for 4,5 nm radiation, whereas electrons cannot transmit such a layer.

Living cells have a thickness in the region of one to several microns. Because electrons cannot transmit such relatively thick layers, biological specimens have to be dried and cut into thin layers for high resolution work in electron microscopy. For soft X-rays they are more transparent and specimens even some microns thick transmit sufficient radiation to be investigated. It is of special interest that in the wavelength range 2,3 nm <  $\lambda$  < 4,4 nm proteins, lipids etc. are more absorbing than water so that this wavelength range is especially suited for wet cell investigations.

One of the most important questions in soft X-ray microscopy concerns radiation damage, its relation to the attainable resolution limit and a comparison with radiation damage in electron microscopy. Theoretical (1) as well as first experimental (2) investigations have the following main results. With an intermediate resolution it will be possible to observe live cells whereas the exact number depends on the object, the wavelength and operation mode of the microscope.

For the highest possible resolution in the region of 0,01  $\mu\text{m}$  the specimen will get

a lethal dosage of X-rays, but the fine structures of the cells will stay intact. So one can say that for biological research X-ray microscopy will fill a gap inbetween optical and electron microscopy and will so supplement these classical techniques.

## III. X-RAY OPTICS - ZONE PLATES

Zone plates are a special case of diffraction optics, namely circular transmission gratings with radial increasing line density. The imaging with zone plates of zone numbers  $n > 100$  obeys the same laws as the imaging with thin refractive lenses in the visible region.

Besides the first diffraction order a zone plate has - like other gratings - a zero order and higher diffraction orders. The focal length can in good approximation be written as  $f_m = r_1^2 \cdot m^{-1} \cdot \lambda^{-1}$ , where

$m = \pm 1, \pm 2, \dots$  indicates the diffraction order. The efficiency of zone plates, i.e. the diffracted flux in a certain order divided by the incoming flux, depends on the land to groove ratio. For amplitude zone plates the maximum obtainable values are approximately 10 % in the first, 2.6 % in the second, and 1.2 % in the third diffracted order.

The width of the  $n$ -th zone is approximately given by

$$dr_n = \frac{r_n}{2n} = \frac{\lambda f_m \cdot m}{2r_n}$$

According to the Rayleigh criterion the resolution is given by

$$\delta \approx \frac{1.22 \cdot f_m}{2r_n} \approx \frac{dr_n}{m}$$

Because of the wavelength dependence of the focal length zone plates have to be used with monochromatic radiation

$$\frac{\lambda}{\Delta\lambda} = m \cdot \frac{n}{2}$$

The evaluation of aberrations of zone plates is the same as that of thin refractive lenses. The field which can be imaged with full resolution is determined by astigmatism and coma. For further details compare Rudolph et al. (3). The spherical aberration can be corrected for a given X-ray wavelength.

Up to now holographically made zone plates have been used for X-ray microscopic experiments. Further details have been reported recently (3, 4).

The zone plates up to now used have the following properties. Condenser zone plate:

$$r_1 = 37 \mu\text{m}, r_n = 4,5 \text{ mm}, n = 1,5 \times 10^4.$$



$dr_n = 0,15 \mu\text{m}$ . Micro zone plate:  $r_1 = 6 \mu\text{m}$ ,  
 $r_n = 150 \mu\text{m}$ ,  $n = 625$ ,  $dr_n = 0,12 \mu\text{m}$ .

Zone plates with higher resolution, that means with a smaller width of the outermost zones are under construction. Firstly, further improvements of the holographic techniques used so far will result in zone plates with an outermost zone width of  $0,06 \mu\text{m}$ . Secondly, using holographically made zone plates, X-ray interference and X-ray lithography techniques, even finer zone-plate structures can be generated. Thirdly, an evaporation method is under development: in this method alternate layers of an opaque and an as-transparent-as-possible material are sputtered onto a rotating cylinder of metal and subsequently cut and thinned to form zone plates. Fourthly, zone plates can be made by use of an electron-beam lithography technique. By one or more of these methods a resolution of about  $10 \text{ nm}$  should be achievable within the next time.

#### IV. X-RAY MICROSCOPY WITH SYNCHROTRON RADIATION

Soft X-ray microscopy requires strong X-ray sources. In the present state of the art the synchrotron radiation of electron storage rings is best suited for practical work.

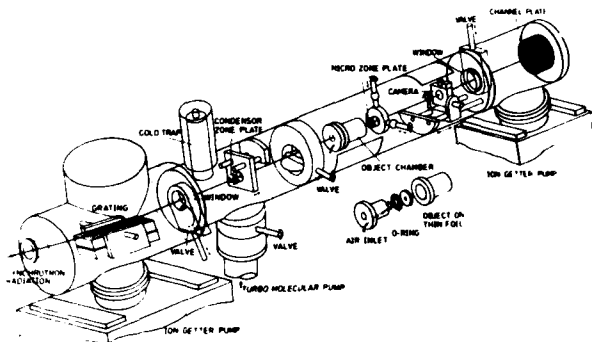


Fig. 1: Schematic experimental arrangement of a zone plate X-ray microscope

Figure 1 shows the schematic experimental arrangement of a zone plate microscope which has been built by the authors of the present article. The polychromatic synchrotron radiation is dispersed by a grating used in grazing incidence. A condenser zone plate generates a reduced monochromatic image of the synchrotron source in the object plane. An enlarged image of the object is generated by a micro zone plate. The enlarged X-ray image is converted to a visible image by a channel electron multiplier array (CEMA) with  $15 \mu\text{m}$  channels and a phosphor screen. The CEMA is used for prefocussing and adjusting the object. After adjustment the CEMA can be replaced automatically by a camera which photographs the real X-ray image on a very fine grained film.

The grating is placed in a vacuum chamber made of refined steel which is separated from the synchrotron beam line and from the other parts of the microscope by thin organic foils

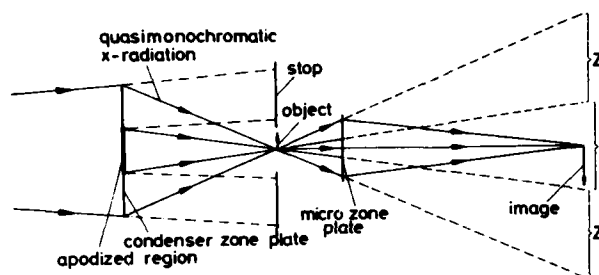


Fig. 2: Apodization of condenser zone plate



Fig. 3: Diatoms imaged with X-rays at  $\lambda = 4,4 \text{ nm}$ , X-ray magnification  $110 \times$

( $d \approx 0,5 \mu\text{m}$ ) and is pumped separately by an ion getter pump and a  $\text{LN}_2$  trap. The resulting high vacuum, free of oil, prevents carbon contamination on the grating. Furthermore, contamination is reduced because the uv-radiation of the synchrotron is mainly absorbed by the window between beam line and grating chamber. For tuning the wavelength the mounting allows to tilt the grating from outside the chamber. The zone plates and camera chambers are made of aluminium and don't need extremely clean vacuum. They are pumped by a turbo molecular pump coupled to the chambers by a vitron-ring-membrane to prevent vibrations of the microscope. The condenser zone plate can be moved along the optical axis to focus the synchrotron source onto the object

plane. The object chamber can firstly be moved in two co-ordinates perpendicular to the optical axis (x, y) for adjustment of the object and second along the optical axis for focusing. The micro zone plate can be adjusted in x, y, and angle. To adjust the image distance the camera can be moved along the optical axis. All these adjustments can be done from outside during the experiment. It is possible to separate the vacuum chamber containing the condenser to shorten the pumping time after changing the object or the camera. Zone plates have - besides the first diffraction order, which is normally used for imaging - a zero order and higher diffraction orders. To avoid a reduction of contrast in the image, the condenser zone plate has to be apodized as shown in Fig. 2. The apodized region of the condenser zone plate ensures that in the image plane a region I exists which is free from zero order radiation of the micro zone plate.

After first X-ray microscopy experiments at the Deutsches Elektronensynchrotron DESY/Hamburg (5), experiments were made at the electron storage ring ACO, Orsay (2). Besides resolution tests biological objects as wet and dried mammalian cells have been investigated (6), using the wavelength of about 4,4 nm. As an example, Fig. 3 shows an X-ray image of diatoms.

#### ACKNOWLEDGEMENTS

The X-ray microscopy project is generously supported by the Stiftung Volkswagenwerk. We are grateful to L.U.R.E. for the opportunity to perform X-ray microscopy experiments at the storage ring ACO.

#### REFERENCES

1. D. Sayre, J. Kirz, R. Feder, D.M. Kim, and E. Spiller, *Ultramicroscopy* **2**, 337 (1977).
2. G. Schmahl, D. Rudolph, B. Niemann, and O. Christ, in *Ultrasoft X-Ray Microscopy: Its Application to Biological and Physical Sciences*, edited by D.F. Parsons, *Annals of the New York Academy of Sciences*, Vol. 342, 368 (1980).
3. D. Rudolph and G. Schmahl, *ibid.*, p. 94.
4. G. Schmahl, D. Rudolph, and B. Niemann, in *Scanned Image Microscopy*, edited by E.A. Ash, Academic Press, London 1980, 393.
5. B. Niemann, D. Rudolph, and G. Schmahl, *Applied Optics* **15**, 1883 (1976).
6. G. Schmahl, D. Rudolph, B. Niemann, and O. Christ, *Quarterly Review of Biophysics* **13**, 297 (1980).



Dr. Raymond Elton reviewed progress towards the development of x-ray lasing. Dr. Elton's paper begins on the following page.

Overview and Advances in X-Ray Laser Research<sup>a</sup>

R. C. Elton

Naval Research Laboratory, Washington, DC 20375

## ABSTRACT

The localized diagnostics of high density pellet plasmas of extremely short duration provides a primary incentive for the development of x-ray lasers offering penetrating radiation in a collimated probe beam. The laser-produced plasma will quite likely provide the best laser medium for such a source. Coherence will enhance the usefulness for plasma diagnostics. Progress in the research devoted to developing such x-ray lasers is described here as pertaining to essentially single-electron ions. Following a brief overview of current activities in this area of research, a simple analysis is developed which is of value for defining a useful parameter regime. Measured gain coefficients for  $C^{5+}$  are compared to an analytical model for electron-capture pumping and found to be in good agreement. Preliminary data on aluminum appear promising for shorter wavelength extrapolation. Extension of the illustrative analysis provides directions for future quantitative measurements leading to large scale gain experiments.

## I. INTRODUCTION

The diagnostics of plasmas promises to be one of the primary applications of x-ray lasers. The first x-ray lasers will probably offer high intensity, short pulse length and collimation in narrow spectral lines in the 1-50 nm wavelength range. These are precisely the characteristics required for probing high density compressed pellet fusion plasmas, where  $\mu\text{m}$  spatial resolution, ps temporal resolution and penetration at supra-solid densities is required. The latter is illustrated in Fig. 1 where the critical electron densities  $N_c$  for total reflection of longer wavelength radiation are shown, as given by the relation  $N_c = 10^{27}/\lambda^2$  for  $\lambda$  in nm. As a typical specific example (1) linear absorption of continuum radiation in DT occurs with an e-folding distance of 30  $\mu\text{m}$  at an electron density of  $10^{26} \text{ cm}^{-3}$  ( $\sim 1 \text{ kg/cm}^3$ ) and a temperature of  $kT = 1 \text{ keV}$  at a wavelength of approximately 1 nm; so that x-ray lasers in the 1-50 nm range will prove extremely valuable in the development of such superdense plasmas. Interferometric, schlieren as well as shadowgraphic techniques will all benefit enormously by the greatly enhanced emission as well as the small angular divergence promised with x-ray lasers. With coherence could also come the application of holographic techniques.

Research towards advancing lasing to the x-ray spectral regions is in a rather early and progressive state. Figure 1 is intended to depict a somewhat recent overview of activities in the field, abbreviated since a comprehensive review (2) with 268 references published in 1976 is generally available to the reader seeking more detail. This review has been supplemented on several occasions with emphases on research (3-5) and applications (1,6). In addition, various useful literature searches and compilations are available (7). The references here are limited to recent articles of more general guidance (see Fig. 1) as well as to those necessary to support specific points of emphasis (8-25).

As can be seen in Fig. 1, present research activity towards the development of x-ray lasers is concentrated in the 10-100 nm wavelength region, in a continuing effort to advance laser physics to shorter wavelengths. A major step has been the so-called "1000 Å (100 nm) barrier", below which efficient cavities do not presently exist (dashed in Fig. 1) and sufficient gain must be achieved in a single photon pass which is referred to as amplified spontaneous emission (ASE). Collimation is then limited to geometrical and coherence would be obtained probably by amplification of a frequency multiplied laser operating in the uv-ir spectral range. In this regard, harmonics up to the 28th have been measured to wavelengths as short as 38 nm, beginning with a 1  $\mu\text{m}$  Nd-glass laser (23).

It is interesting to observe that what may prove to be the most valuable probe for laser-produced plasmas at the highest densities, namely the x-ray laser, will quite likely evolve from the use of laser-produced high-Z plasmas as lasers. Most activity is presently directed along such lines since the stripping of high-Z atoms provides relatively simple atomic structures that can be used at short wavelengths analogously to present ion lasers for the uv-visible spectral region, through isoelectronic extrapolation. Hydrogenic, helium-like and lithium-like (1,2, and 3 electron) ions are favorite candidates, as examples. Also, the pump power density required to achieve single-pass gain of at least  $e^5$  at short wavelengths becomes very high and can best be obtained with linearly-focused laser beams onto surfaces in vacuum. Significant line enhancement along the axis compared to spontaneous radial emission is typically sought as evidence of gain (11,15,16). Dual plasma experiments are also performed, where one serves as a source and a second as an amplifying medium (17). Marginal gain has proven difficult to verify (16) and large gain so far has been elusive. What has been established to date are significant degrees of population inversion in fluorescence experiments under optically thin conditions at densities below critical for measureable gain (14,26).

These latter statements can be somewhat quantified with a simple but sufficient gain-scaling analysis which follows. Following this, the pumping of hydrogenic ions by capture of electrons into excited states is analyzed and discussed as a specific example of considerable current interest.

## II. ANALYSES

The following simple analyses (5) are not intended to replace the elegant computer programs that have been developed for modeling atomic and plasma dynamic processes in laser-produced plasmas. Rather, the intent is to use a few basic physical principles to estimate the gain and the associated plasma parameters for comparison with some quantitative data. In essence, the end justifies the means in that reasonably good agreement is found, so that the physical intuition provided from the basic principles invoked permits both the evaluation of current experiments and the formation of some projections for future experiments with confidence, hopefully to be supported by extended numerical computations.

## A. GAIN RELATIONS

## 1. General

The challenge of achieving gain  $I/I_0 = \exp(GL)$  over a length  $L$  at increasing photon energy derives directly

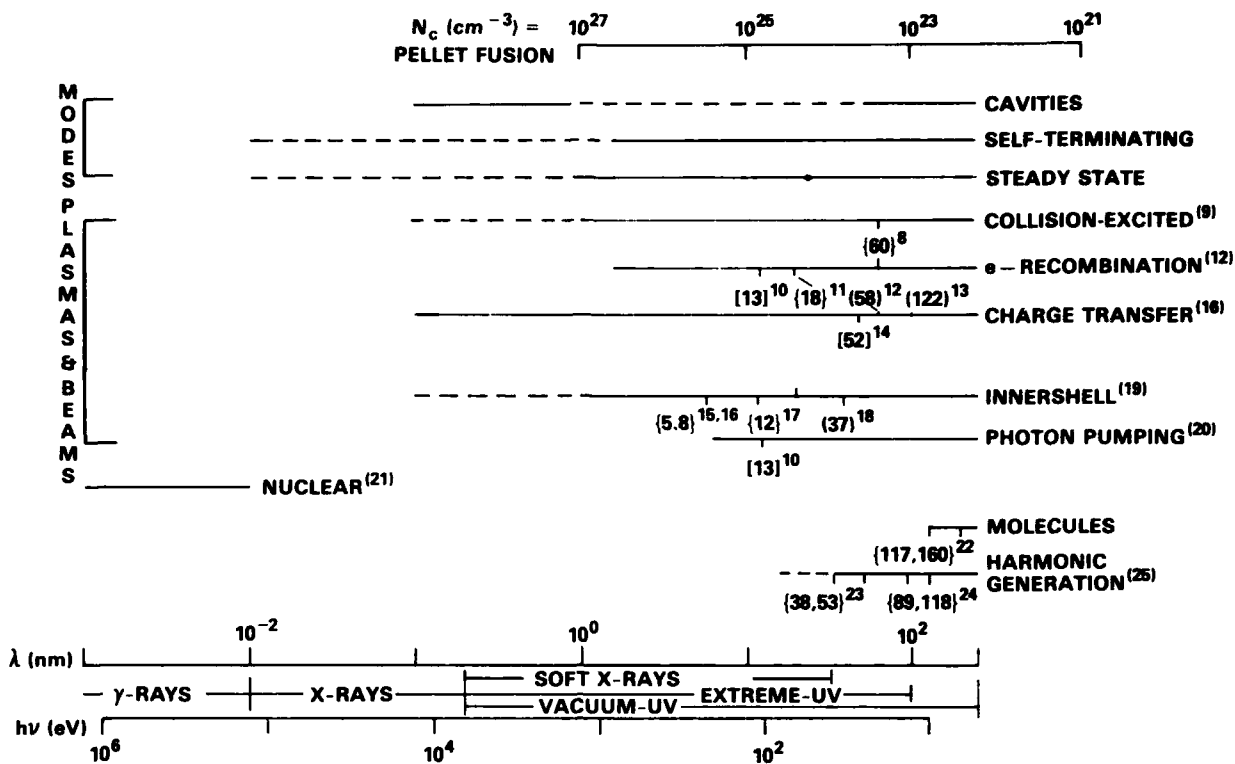


Fig. 1. Diagram categorizing various operating modes and pumping processes for achieving gain, as well as for harmonic generation. The wavelength regions indicated are somewhat arbitrary. The numbers on the bars refer to milestone wavelengths in nm, where ( ) indicates modeling, [ ] indicates population inversions and { } indicates emission either as gain or harmonics. The dashed lines indicate projections into spectral regions of less certainty. References are indicated by superscripts. The emphasis here and in the text is on wavelengths shorter than 100 nm; molecular hydrogen is included for historical perspective.

from a positive gain coefficient  $G$ , which is related to the cross sections for induced emission and resonance absorption and the upper and lower state population densities  $N_u, N_l$  by

$$G = N_u \sigma_{ind} - N_l \sigma_{abs} = \frac{\pi r_o c f}{\Delta \nu} \cdot \frac{g_l}{g_u} \cdot \left[ N_u - N_l \left( \frac{g_u}{g_l} \right) \right], \quad (1)$$

where  $r_o$  is the classical electron radius,  $f$  is the absorption oscillator strength,  $g_u, g_l$  are the upper and lower state statistical weights, and  $\Delta \nu$  is the line width in frequency units. For a Doppler-broadened line at a mean thermal velocity  $\bar{v}_D, \Delta \nu_D / \nu = \bar{v}_D / c$ , or

$$\Delta \nu_D = 2 \nu \left( \frac{2kT}{Mc^2} \ln 2 \right)^{1/2}, \quad (2)$$

where the radiating particle mass and temperature are given by  $M$  and  $T$ , respectively. The Doppler-gain coefficient then becomes (with  $\nu = c/\lambda$  and a factor of  $\sqrt{\ln 2}$  included for Gaussian line shapes):

$$G_D = \frac{\pi^2 r_o c \lambda f (g_l / g_u)}{2} \left( \frac{M}{2\pi kT} \right)^{1/2} N_u \left[ 1 - \frac{N_l}{N_u} \frac{g_u}{g_l} \right]. \quad (3)$$

This shows an explicit linear dependency on wavelength and the importance of the upper state density in achieving significant gain, once the bracketed factor becomes positive to assure a population inversion, rather than resonance absorption. Implicit here however is the wavelength dependence of the pumping process, since in equilibrium

$$N_u \approx \frac{N P}{A}, \quad (4)$$

where  $P$  is the pumping rate out of an initial ion state of density  $N$  and  $A$  is the total depopulation rate. The population density inversion may either be transient leading to self-terminating lasing (Fig. 1) with a characteristic decay time  $\approx A$ , or quasi-steady-state limited only by the interval of proper plasma conditions for inversion.

## 2. Single-Electron Ions

The above is general. By next specifying that the ions be hydrogenic, i.e., stripped of all but one electron, the gain analysis continues relatively straightforward, because of the simplicity of the one-electron structure. Also, potential losses associated with processes such as photoionization and auto-ionization involving outer electrons are avoided. With  $M \propto Z$ ,  $A \propto Z^4$  for radiative depopulation,  $\lambda \propto Z^{-2}$ , and  $T \propto Z^2$ , the gain coefficient then scales as  $PN_0 \propto Z^{-13/2}$ , so that a strong scaling of  $PN_0$  with  $Z$  is required for the favorable extrapolation of high gain to increased  $Z$  and shorter wavelengths along the hydrogenic isoelectronic sequence.

The hydrogenic results presented in this paper are expected to follow similarly for helium-like ions and furthermore for lithium-like ions with one electron beyond the closed  $1s^2$  orbital.

## 3. Recombination Pumping

Pumping of ionic population inversions is achieved the most naturally in plasmas using the free electrons available in quasi-neutrality. The capture of free electrons into high-lying states (collisional recombination) followed by cascade, and the collisional excitation or ionization of bound electrons into excited states are two examples (2). These can be analyzed fairly-reliably and form an inversion basis, which then can be augmented by, for examples, charge transfer of bound electrons from neutral atoms (14,26) and photon (flashlamp) pumping (27), when such pump energy and the proper resonant matches are available for efficient pumping. We will continue here with the analysis based upon recombination onto fully-stripped ions, which has been extensively analyzed since its first suggestion (28) in 1965. In such a quasi-neutral fully-ionized plasma, the free electrons are abundant in proportion  $\eta \equiv N_e/N_0 = Z$  and a quasi-cw inversion is obtained between excited states in a cascade when the lower states are depopulated to the ground state more rapidly than are the upper states. The desired recombination rate product  $n_0 \cdot P_r$  may be approximated by (29)

$$N_0 P_r \approx \frac{10^{-31} N_e N_0 (n')^6}{Z^6} \left( \frac{Z^2 Ry}{kT_e} \right)^2 \exp \left[ - \frac{Z^2 Ry}{(n+1)^2 kT_e} \right] \text{sec}^{-1} \text{cm}^{-3}, \quad (5)$$

where the Rydberg,  $Ry=13.56$  eV, represents the hydrogen ionization potential,  $N_e \propto Z^7$  (see below) is the free electron density, and  $n'$  is the so-called collision-limit quantum number (29,30), i.e., the energy level at which electron collisional excitation from that level equals the radiative decay to lower levels. Notice the increased pumping at reduced electron temperatures, indicated here by the  $T_e^{-2}$  dependence. From Eq. (5), assuming  $N_0 = N_e/Z \propto Z^6$ , the scalings with  $Z$  become:

$$N_0 P_r \propto Z^{14} \quad (6)$$

and

$$G_r \propto Z^{7.5}, \quad (7)$$

which are very favorable, providing all other conditions scale within reason for experiments. Actual values for this gain will be given later.

## 4. Charge Transfer Pumping

Closely akin to free-electron capture is bound-electron capture or charge transfer of an electron from a (neutral) atom to a stripped ion, resulting in preferential population of a specific excited level(s) in a hydrogenic ion. The cross section for the resonance charge transfer (rct) process is approximated by

$$\sigma_{rct} \approx \pi a_0^2 Z^2 \quad (8)$$

(where the  $Z^2$  scaling is probably optimal), and a rate of

$$P_{rct} = N_A \langle \sigma v \rangle \approx N_A \pi a_0^2 Z^2 v. \quad (9)$$

Here  $N_A$  is the neutral density, and  $a_0$  is the Bohr radius. In vacuum a carbon plasma at  $T_e \approx 200$  eV expands at a speed of  $\sim 10^7$  cm/sec which scales approximately as  $(T_e/M)^{1/2}$ . Therefore

$$N_0 P_{rct} \approx N_0 N_A \pi a_0^2 Z^2 (10^7) \left( \frac{kT_e}{200} \cdot \frac{6}{Z} \right)^{1/2} \text{sec}^{-1} \text{cm}^{-3}, \quad (10)$$

which scales with  $Z$  as

$$N_0 P_{rct} \propto Z^{14.5}, \quad (11)$$

so that

$$G_{rct} \propto Z^8, \quad (12)$$

assuming that the neutral atoms are created by direct sputtering by the ions, i.e.,  $N_A \propto N_e/Z \propto Z^6$  also.

Thus, the scaling is similar to that for capture of free electrons by the ions.

## B. COLLISION LIMIT ON INVERSION

Population inversions formed by cascade can only be expected to exist for electron densities low enough that collisional depopulation from the upper to the lower laser levels does not dominate over radiative decay. This upper limit on electron density in the plasma is found by equating the electron-collisional deexcitation rate (29) to the corresponding radiative-transition probability. The  $Z$ -scaling for the equation is  $N_e/Z^7$  and  $T_e/Z^2 Ry$ , where  $Z^2 Ry$  is the hydrogenic-ion ionization potential. Such limiting lines are plotted initially in Fig. 2 for four possible laser transitions: 3-2, 4-2, 4-3, and 5-3. Above each of these lines population inversion becomes zero or negative (absorption), and also Stark broadening enters which would further reduce the gain. Such density-limiting lines are reproduced in the other figures as well.

In Fig. 3 values of  $n'$  calculated for high  $n+1$  to  $n$  transitions are indicated on the right ordinate for comparison. It appears that  $n' \approx (2n+1)/2$  might be a reasonably consistent approximation at high temperature ( $T_e/Z^2 Ry \geq 0.5$ ), but cannot be used directly for low-lying levels and at low temperatures since the  $n'$  formulation (29,30) is based on collisional excitation which includes an exponential low energy cutoff. It is instead collisional deexcitation (29) that limits the inversion, for which a new collision-limiting quantum number  $n'' \equiv n' (g_k/g_u) \exp(\Delta E/kT)$  is defined and finally becomes

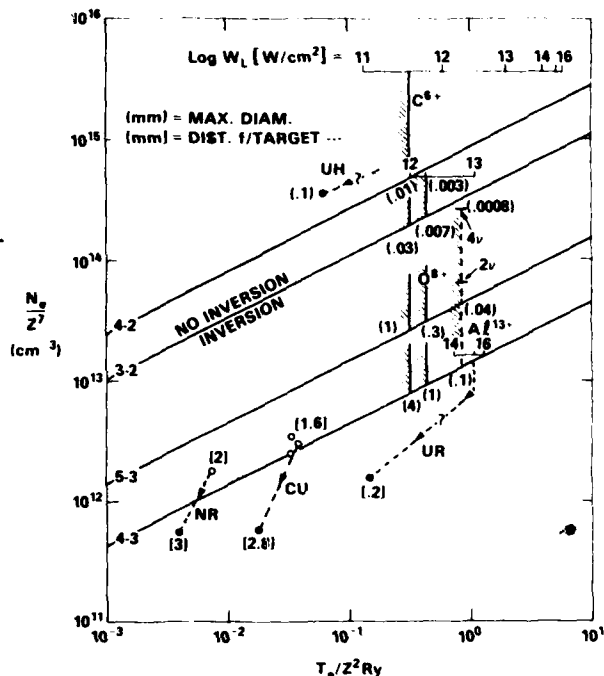


Fig. 2. Parameter space for achieving population inversions on several transitions. Laser flux  $W$  and ionization thresholds for carbon, oxygen and aluminum ions are indicated. Typical partial trajectories for carbon plasmas are indicated using data from NRL (NR), Culham (CU) and Univ. of Hull (UH), including distances from target [ ] in mm. Aluminum studied at Univ. of Rochester (UR) is also indicated. Opacity-limited diameters are indicated by ( ) in mm.

$$n'' \approx 126 \left( \frac{N_e}{Z} \right)^{-2/17} \left( \frac{kT}{Z^2 R_y} \right)^{1/17} \quad (13)$$

This will be recognized as the expression  $n'$  without the exponential factor. The statistical weight ratio serves to counteract the high quantum state approximation in  $n'$  so that  $n''$  here is appropriate for potential low-lying laser transitions. This resembles the "thermal line" of Wilson (31) which included deexcitation with the exponential factors removed, but for a different reason, namely in the high- $n$  and high- $T$  limits. The  $n'$  (or  $n''$ ) approximation remains a first-order approximation to the collision limit on inversion, at best.

### C. PUMP POWER REQUIREMENTS

There is a practical reason for desiring to operate near the collision limits shown in the figures. The gain depends directly on the upper state density  $N_u$  as shown in Eq. (3), as does the plasma pump power density  $W_p \equiv N_u A h \nu$  which is required to overcome losses. A large value of  $W_p$  is also required to obtain sufficient plasma temperature to achieve complete ionization (Fig. 2, discussed below). For  $G=5 \text{ cm}^{-1}$  and a 3-2 transition,  $W_p$  at various wavelengths  $\lambda$  is given (2) in Table 1, using  $N_u$  from Eq. (3). Note that for  $C^{5+}$  at  $\lambda = 18.2 \text{ nm}$  a plasma power density of  $30 \text{ GW/cm}^3$  is required.

Also note that wavelengths as short as 1 nm can be pumped with laser-fusion-size focused Nd-glass lasers, for example.

Table 1. Pump Power Densities for  $G=5 \text{ cm}^{-1}$

$\lambda$	0.1	1	10	100	nm
$\log_{10} W_p$	19	15	11	7	Watts/cm <sup>3</sup> Plasma Watt/cm <sup>2</sup> Source *

\*For 100  $\mu\text{m}$  depth, 1% coupling, laser-produced plasma.

Limited pumping power therefore necessitates small volumes including short lengths  $L$ , so that maximum gain products  $GL$  are achieved at the highest density possible. In other words, a reduced gain coefficient  $G$  at lower density cannot be compensated by a longer length  $L$  without increased pump power. This, plus the need for high plasma temperatures, is the reason that most x-ray laser research is performed on small plasmas created by focused high power (laser) beams, as mentioned in Section I above.

### D. RADIATION TRAPPING

Along with high density comes resonance trapping, particularly for the 2-1 Lyman- $\alpha$  transition. This trapping of resonance radiation can preferentially increase the lower state density and deplete the population inversion according to Eqs. (1) and (3). In the simplest case,

$$\frac{N_l g_u}{N_u g_l} \approx \frac{A_{ul}}{A_{l1} g(\tau)} \cdot \left( \frac{n_u}{n} \right)^2, \quad (14)$$

where  $g(\tau)$  is the so-called escape factor (27,32), which is a function of the optical depth  $\tau$  given by (29)

$$\tau = 5.5 \times 10^{-17} \lambda f N_l D \left( \frac{\mu}{kT} \right)^{1/2} \quad (15)$$

for a laser depth  $D$ , a hydrogenic ground state density  $N_l$  (or  $N^{(Z-1)+}$ ) an atomic mass number  $\mu$ , and with  $kT$  in eV. For a 3-2 transition the ratio in Eq. (14) reaches unity for  $\tau \geq 3$ , which determines the maximum permissible value of the product  $N_l D$ . Obviously if complete stripping is maintained,  $N_l$  will remain negligibly small; but that is unlikely as the temperature is lowered for increased pumping. With plasma quasi-neutrality it is more likely (33,34) that  $N_l \approx N_e/10$ . The maximum plasma diameter determined at the maximum electron density allowed by collisional equilibrium in Fig. 2 then scales as  $Z^{-9/2}$  for all temperatures, and values are indicated in parentheses in Fig. 2 at the collision boundary. Recall once again that this is actually a  $ND$  limit and therefore  $D_{\text{max}}$  will scale upward as  $N_e/Z^7$  is decreased.

### E. PHOTON-ASSIST PUMPING

It is obvious that the most severe limitations are placed on the  $n=2$  transitions, again due to the strong 2-1 Lyman- $\alpha$  resonance line. Photon-assist pumping of  $n=2$  electrons into specific higher- $n$  states without perturbing the upper state populations would appear to alleviate this lower state saturation considerably (27). For example, Lyman- $\alpha$  radiation from a  $Z/2$  ion would match a 2-4 excitation in ion  $Z$  and likewise  $Z/3$ -ion Lyman- $\alpha$  emission would match a 2-6

transition in ion Z. Intuitively, the lower transition rates at lower Z indicate the need for higher densities and temperatures in the pump source, so that the pump and the lasant plasmas could not be congruent, and the emitter/absorber coupling becomes a crucial factor.

At the blackbody limit, the pump rate  $P(2-4)$  compared to the depopulation rate  $A(2-1)$  is given by (8)

$$\frac{P_{24}}{A_{21}} = \frac{1}{2} \left( \frac{g_4}{g_2} \right) \frac{A_{42}}{A_{21}} \left[ \exp(h\nu/kT) - 1 \right]^{-1} \geq 1, \quad (16)$$

and must exceed unity for significance. This reduces to  $h\nu/kT \leq 0.04$  where  $h\nu(4-2) \approx Z^2 \text{Ry}/5$ , so that  $kT \geq 5Z^2 \text{Ry} \approx 70Z^2$  is required. Unfortunately, at such a temperature there would not be a significant density of hydrogenic ions as pump sources. Higher-Z ions with coincident wavelengths are a possible alternative considered both for pumping out such saturated lower levels and for pumping upper levels. A number of problems surface on close examination, however, such as exact (within line widths) coincidence in the presence of possible plasma shifts, efficient coupling if separated; and the large increase in electron density associated with the higher-Z material which enters into the lasant conditions as in Figs. 2-6, particularly if the substances are congruent. With sufficient intensity, a true dual-region configuration for the "flashlamp" (preferably broadband compared to a spectral line) and the lasant seems preferable. Photoionization, particularly of innershell electrons, is a related and promising pumping scheme involving a select narrow band intense radiation source (see Fig. 1).

## II. EXPERIMENTAL COMPARISONS

### A. INVERSIONS ALONG TRAJECTORIES

As a prerequisite to achieving measureable gain, the population density inversions bracketed in Eqs. (1) and (3) are usually determined in fluorescence experiments under lower density optically thin conditions. For example, a 4-3 inversion is strongly evidenced in the resonance series between levels n and l by anomalously large 4-1 intensities, even exceeding the 3-1 intensity (14, 26). While usually obtained spectrographically with spatial but not temporal resolution, recent soft x-ray data on helium-like CV lines with both spatial and temporal resolution has been obtained (35) under similar laser-vaporized graphite conditions to that described in Ref. (14).

Returning to Fig. 2, typical laser power densities  $W$  required to strip atoms of C, O, and Al are indicated by vertical barriers. Such vertical divisions of the parameter space do not prohibit population densities, but rather define the zone of high ion density for high gain. The laser-flux log  $W$  scales are shown at  $N_e/Z^7$  values corresponding to a critical density  $N_e = 10^{21} \text{ cm}^{-3}$  for 1  $\mu\text{m}$  laser absorption; for Al, values for 2v and 4v frequency doubling and quadrupling are also indicated. Notice that all four transitions can be pumped near the maximum density in carbon with a 1  $\mu\text{m}$  laser, but not the 4-2 transition in oxygen and only the 4-3 transition in Al without frequency multiplication into the ultraviolet region. Of course, all can be pumped at densities below the collisional cutoff level at lower gain and increased pump demands, as discussed above.

Also shown in Fig. 2 are data points from Hull University (11) (UH) [C(3-2)], Culham Laboratory (36) (CU) [C(3-2, 4-2, 4-3)], Naval Research Laboratory (14, 26) (NR) [C(4-3)], and University of Rochester (10, 37) (UR) [Al(4-3) helium-like], with the closed data points indicating where population

inversion or gain measurements are reported, and open points where no inversion was observed. The numbers in brackets refer to distances from laser-heated targets. The 4-3 data are consistent with both the collisional deexcitation limit and radiative trapping for diameters 1/3 to 1/2 the distances indicated. The 3-2 and 4-2 data from Culham showing inversions only for  $N_e/Z^7$  less than  $10^{12} \text{ cm}^{-3}$  are also consistent with a plasma size approximately 30-times greater than permitted at  $10^{14} \text{ cm}^{-3}$ , i.e., the  $N_e D$  scaling behaves as expected (see Fig. 6). The 3-2 data from Hull University remain an enigma; although the size could be tolerable for radiation trapping limitations if the plasma produced from a thin fiber expands in a heated shell of thickness  $\sim 10 \mu\text{m}$ , an electron density well above that expected to include collisional mixing will lead to a very small or even negative population inversion (see below).

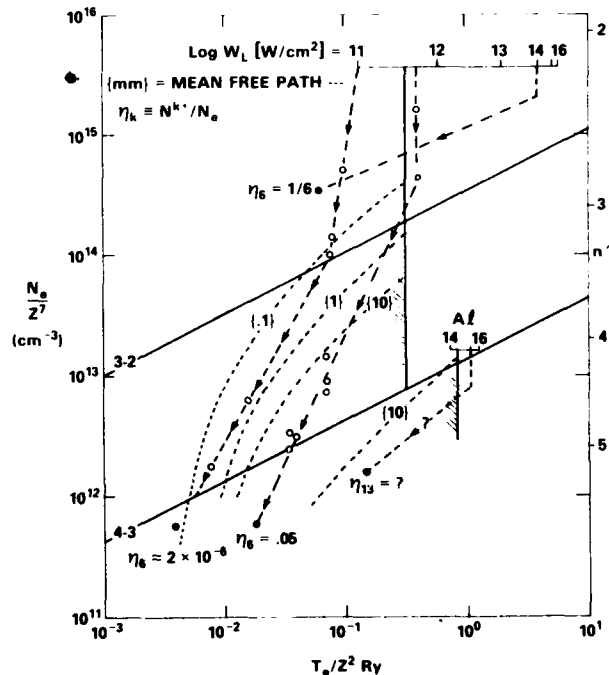


Fig. 3. Typical trajectories (long dashes) in parameter space (see Fig. 2) and mean free paths (short dashes) with values {} in mm.

Continuing in Fig. 3, extended trajectories originating in the critical density layer near the target are plotted for C and Al ions. Also, the density ratios  $N^{Z+}/N_e \equiv \eta_n$  are shown where known (33, 34). It is more important to maximize the density of stripped ions in the inversion region. This is best achieved by first completely stripping the atoms near the target and then following an isothermal trajectory towards lower densities, preferably maintaining a mean free path exceeding the final diameter anticipated for the gain medium. Mean free paths are plotted as {mm's} in Fig. 3. From this it is readily understood why  $\eta_6$  is only  $2 \times 10^{-6}$  (10 mean free paths, i.e.,  $e^{-10}$ ) when beginning at  $10^{11} \text{ W/cm}^2$ , and increases to 0.05 at a higher initial pump flux level with complete ionization and a longer mean-free-path trajectory. Complete stripping in the Hull University experiments was anticipated (11), also beginning at very high flux levels. For the University of Rochester

experiments on Al, stripped-ion densities are not yet available; however complete stripping at the target is expected at  $10^{15}$  W/cm<sup>2</sup> irradiation, and the mean free path is calculated to be greater than 10 mm.

#### B. GAIN MEASUREMENTS

One reason that the ratios  $n_z$  are available for carbon is that the density of stripped ions can be obtained from the absolute number density of hydrogenic ions in excited ( $n=5, 6,$  and  $7,$  e.g.) states lying near the continuum using Saha equilibrium calculations. These highly-excited state densities are conveniently obtained from the absolute emission of spectral lines in the near-ultraviolet region. Since the same excited states also radiate in resonance lines (e.g., 7-1, 6-1), the branching ratio for radiative decay and the relative intensities in the resonance series provides a measurement of the upper laser state densities  $N_u$  in Eq. (3), from which the gain coefficient is obtained directly (with a known line width). The gains measured by this technique for carbon are shown as "f/meas" in Figs. 4-6. (The Hull University value in Fig. 6 was obtained from axial enhancement in a cylindrical plasma.) Again, these gain coefficients are measured directly in the experiments and do not depend on the assumption of any particular pumping model.

#### C. GAIN MODELED

Where the stripped ion density ratio  $\eta_z$  is known along with the electron density and temperature, it is also possible to model the recombination gain from Eqs. (3) through (5). In Figs. 4-6 such a modeled gain is plotted at several magnitudes, for comparison with the direct measurements. In most cases a conservative inversion factor value  $(1 - N_L g_u / N_u g_L) \approx 0.3$  is assumed. The agreement is generally good and in one case (Fig. 4, square point) some expected enhancement from resonance charge transfer pumping in a particular gaseous expansion experiment (14) is indicated. For the University of Hull results, their assumption of  $\eta_6 = 1/6$  (100% ionization) is used and a matching gain value of  $G = 17$  cm<sup>-1</sup> is plotted for a best fit to a variable inversion factor giving  $(1 - N_L g_u / N_u g_L) \approx 0.002$ , much lower than the 0.3 value used at lower densities but apparently remaining positive for net gain. This low value would be consistent with the collisional regime in which that experiment appears to operate. No such modeling comparisons using the University of Rochester data (helium-like aluminum) have been done, because pertinent data are not yet available.

Similar modeling for lithium-like 4-3 transitions yields very similar results to Figs. 4 and 5 with an abscissa of  $T_e/4Z^2$  in eV. Lithium-like ions are desirable since they are formed plentifully from helium-like ion ground states which are persistent in a transient plasma. The formation power required is also relatively low as is the initial temperature, and the final gain temperature is extremely low for low-Z plasmas; higher-Z elements such as aluminum appear more desirable (38).

The gains modeled here do not restrict the parameter space available for population inversions and gain except for the particular recombination pumping mechanism assumed. For example, photon pumping or charge-transfer pumping with adequate rates could occur throughout the space beyond the collision and ionization barriers, and again the modeling would depend on the specific external pumping source rather than the internal pumping by plasma electrons for recombination.

#### IV. SUMMARY

In summary, quantitative spectroscopy of hydrogenic [and helium-like (14, 26)] carbon ions is proving to be a valuable gauge for measuring directly the soft x-ray gain coefficient. The stripped-ion density and the inversion degree are also deduced as inputs for modeling. The gain coefficients measured so far for varying pump laser powers and transitions and locations relative to the irradiated target, as well as target configurations, are shown here to be in good agreement with a simple analytical model. The results are presented in such a way as to visualize progress, limitations, and prognoses. Preliminary data for helium-like aluminum, which requires more stringent parameters than carbon, look promising in this view, although similar quantitative spectroscopic data are more difficult to obtain. Increased target irradiation sustained for high temperatures during the plasma expansion beyond the collisional regime, followed by rapid cooling, would seem to be most desirable. Enhanced pumping by charge transfer and by photo-excitation, particularly in overcoming inversion depletion from radiative trapping, have been suggested as augmenting techniques in an otherwise optimized system. Clearly, more quantitative measurements of the sort described here, along with more expansive calculations, are needed to project a large scale gain experiment at very short wavelengths. Supplementary to this is the need for the design of efficient ( $\geq 50\%$  reflectivity) and durable cavities for the soft x-ray region.

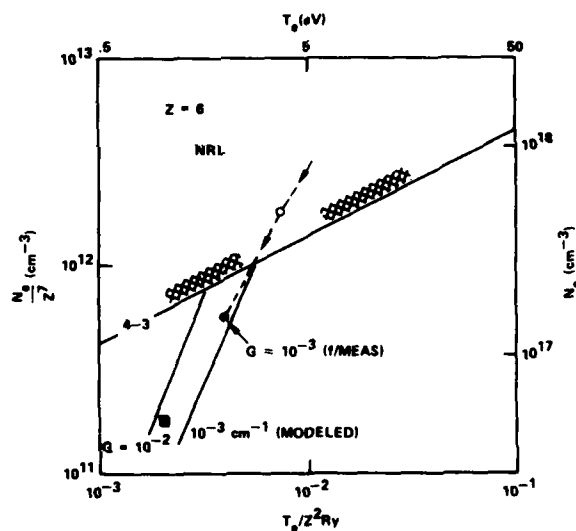


Fig. 4. NRL 4-3 measured gain in parameter space compared with analytical model results for carbon plasmas.



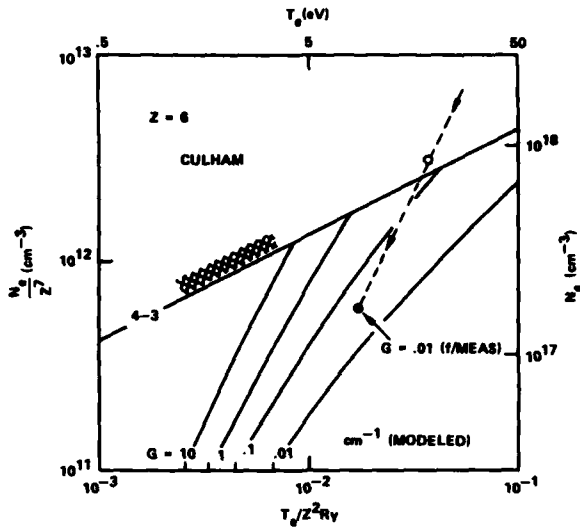


Fig. 5. Culham 4-3 measured gain in parameter space compared with analytical model results for carbon plasmas.

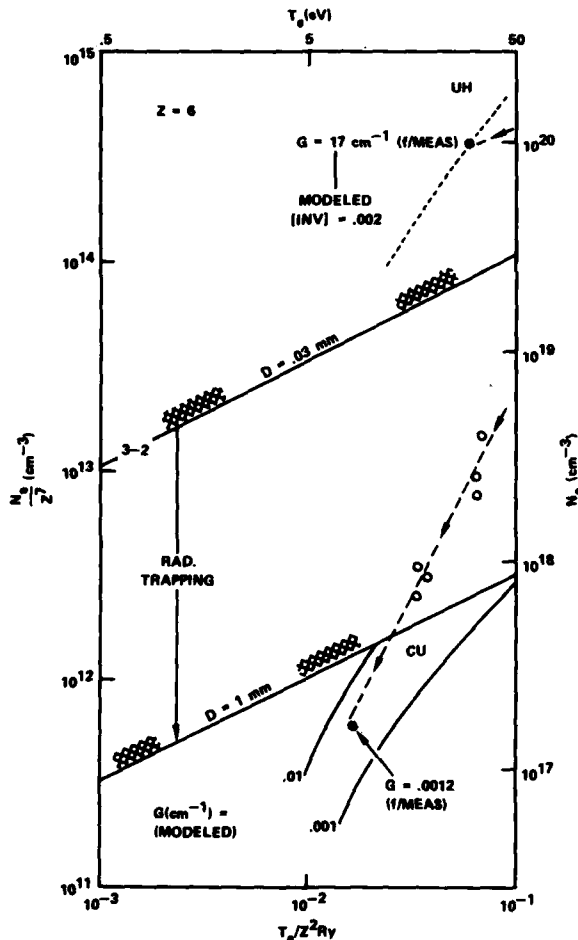


Fig. 6. Gains measured on the 3-2 transition in carbon plasmas as reported from Culham compared with analytical model, and from Univ. of Hull where the model matches for an inversion parameter of 0.002.

#### ACKNOWLEDGMENTS

It is a pleasure to acknowledge the professional collaborations with R. H. Dixon, T. N. Lee, and J. F. Seely in the NRL x-ray laser research program, and the excellent technical support provided by R. L. Denningham and J. L. Ford. Illuminating discussions with H. R. Griem are also recalled with appreciation.

#### REFERENCES

- <sup>a</sup>This effort was supported by the Office of Naval Research and by the U. S. Department of Energy.
1. S. Jorna, Ed., *X-Ray Laser Applications Study*, Report PD-LJ-77-159, Physical Dynamics, Inc., La Jolla, CA, (1977).
2. R. W. Waynant and R. C. Elton, *Proc. IEEE*, **64**, 1059-1092 (1976).
3. R. C. Elton, "Recent Advances in X-Ray Laser Research", in *Advances in X-Ray Analysis*, Vol. 21, C. S. Barrett and D. E. Leyden, eds., Plenum (1978).
4. R. C. Elton, "X-Ray Lasers", in *Handbook of Laser Science and Technology*, M. J. Weber, ed., CRC Press (1981).
5. R. C. Elton, "Progress and Trends in X-ray Laser Research", in *Proc. SPIE Tech. Symposium East '81*, Vol. 279, Paper No. 10.
6. D. J. Nagel, "Potential Characteristics and Applications of X-Ray Lasers," *Naval Research Laboratory Memorandum Report*, (1981) (in press).
7. B. Carrigan, "X-ray Lasers, a bibliography with Abstracts 1969-80", *Report PB81-804031* (National Technical Information Service, Dept. of Commerce, Springfield, Virginia 22161, 1981); "X-ray lasers", *Report No. IJ22-013*, (Smithsonian Science Information Exchange, Inc., Washington, D. C. 20036, 1979); S. C. Mauk, "X-ray lasers (citations from the International Aerospace Abstracts Data Base)", Sept. 1979, *Report NTIS/PS-79/0863/5WH*, (National Technical Information Service, Dept. of Commerce, Springfield, VA 2216, 1979); G. C. Baldwin, "Bibliography of Graser Research", *Report No. LA-7783-MS*, (Los Alamos Scientific Laboratory, New Mexico, April 1979); R. L. Kelly and L. J. Palumbo, "Atomic and Ionic Emission Lines below 2000 Å," *Naval Research Laboratory Report No. 7599*, (U. S. Government Printing Office, Washington, DC, 1973).
8. A. A. Ilyukhin, G. V. Peregudov, E. N. Ragozin, I. I. Sobel'man, and V. A. Chrikob, *Sov. Phys. JETP Letters* **25**, 535, (1977); also A. V. Vinogradov, I. I. Sobel'man, and E. A. Yukov, *J. de Physique, Colloque C4 Supplement*, **39**, C4, (1978).
9. R. C. Elton, *Appl. Optics*, **14**, 97, (1975); L. J. Palumbo and R. C. Elton, *J. Opt. Soc. Am.*, **67**, 480 (1977).
10. V. A. Bhagavatula and B. Yaakobi, *Optics Comm.*, **24**, 331, (1978); V. A. Bhagavatula, *Appl. Phys. Lett.*, **33**, 726, (1978).
11. D. Jacoby, G. Pert, S. Ramsden, L. Shorrock and G. Tallents, *Optics Comm.*, **37**, 193 (1981).
12. W. H. Louisell, M. O. Scully, and W. B. McKnight, *Opt. Comm.*, **9**, 246, (1973); also *Phys. Rev. A*, **11**, 989, (1975).
13. R. Thack, H. Mahr, C. L. Tang, and P. L. Hartman, *Phys. Rev. Letters*, **45**, 542 (1980).
14. R. C. Elton and R. H. Dixon, *Phys. Rev. Lett.*, **38**, 1072, (1977); also R. H. Dixon, J. F. Seely, and R. C. Elton, *Phys. Rev. Lett.*, **40**, 122, (1978).
15. A. N. Zerikhin, K. N. Koshelev, P. G. Kryukov, V. S. Letokhov, and S. V. Chekalin, *JETP Lett.*, **25**, 300, (1977); also *Kvant Elekt.* **8**, 88 (1981) (in Russian).

Abstract: Anti-Stokes Scattering as An XUV Radiation Source

S.E. Harris, J.F. Young, R.W. Falcone, and Joshua E. Rothenberg  
Edward L. Ginzton Laboratory  
Stanford University  
Stanford, California 94305

The paper will describe the use of anti-Stokes scattering as a radiation source for high resolution spectroscopy in the 100 Å to 1000 Å spectral region, and as a flashlamp for the construction of XUV lasers.<sup>1</sup>

The radiation source is based on spontaneous anti-Stokes scattering of incident laser photons from excited metastable atoms in an electrical discharge. The frequency of the scattered photons is equal to the sum of the metastable storage frequency and the frequency of the incident laser photon. The linewidth of the scattered radiation is the convolution of the laser linewidth and the Doppler width of the emitting species. The radiation is polarized, has the same time duration as the incident laser, and can be tuned by tuning the incident laser frequency. In recent experiments we demonstrate that the intensity of the tunable anti-Stokes radiation is sufficiently great that it may be distinguished from the background radiation of the plasma, and that thus no monochromator need be used to obtain an absorption spectra. We report the first high resolution spectra of potassium in the region of 535 Å to 550 Å. Within this region four previously unreported narrow lines are observed.

The other portion of the talk will be concerned with the use of anti-Stokes scattering to make a flashlamp for a laser in the 200 Å spectral region. In recent experiments on a pulsed hollow cathode discharge we have measured storage populations in the  $\text{Li}^+$  ion at 199 Å of  $5 \times 10^{12}$  atoms/cm<sup>3</sup>. These populations correspond to a 199 Å flashlamp pumping power of about 1 MW. The target state is an even parity state of neutral Li which is governed by selection rules which prohibit autoionization. Transfer will be accomplished by means of two-photon absorption. Calculations indicate that we should be able to obtain a gain of about 20% per cm on the 207 Å transition of neutral Li.

References:

1. S.E. Harris, R.W. Falcone, M. Gross, R. Normandin, K. Pederotti, J. Rothenberg, J. Wang, J. Willison and J.F. Young, Anti Stokes Scattering as an XUV Radiation Source, Proceedings of the Vth International Conference on Laser Spectroscopy, Jasper, Canada June, 1980 (Springer-Verlag, New York, 1982).



Dr. Stephen Harris of Stanford (left) and Dr. Ralph Wuerker, session chairman during the question and answer period.



Dr. D. P. Siddons of Kings College, London, describing work by he and his colleagues with x-ray interferometry. Dr. Siddens invited paper begins on the following page.

## SOME APPLICATIONS OF X-RAY INTERFEROMETRY

D.P.Siddons

Wheatstone Laboratory,  
Kings College,  
London, WC2R 2LS

## ABSTRACT

A review of the various types of x-ray interferometers is given, and their characteristics and relative merits discussed. Some of their current applications are described and some possible future ones outlined.

## 1. INTRODUCTION

The x-ray interferometer was invented in 1965 by U. Bonse and M. Hart (1). Since that time it has developed from a scientific curiosity into an extremely versatile and routinely usable tool. It has been used to solve many otherwise intractable problems. In this brief review I will try to present some of the applications which I find interesting, in the hope that they will suggest to you other applications relevant to your own interests.

Since this conference is primarily concerned with the soft x-ray region, I should point out that the very first observation of x-ray interference was made in the 1930's with aluminium K-alpha radiation using a Lloyds mirror arrangement (2). Since that time no working soft x-ray interferometer has been constructed. All the devices which I will discuss here are based on perfect crystal diffraction optics (and at the moment, that means silicon) with a working range of roughly 0.01 to 0.4 nm.

The small wavelength of x-radiation would seem at first sight to pose insuperable mechanical problems for the designer. The care necessary in manufacturing interferometers for the optical region could not reasonably be extrapolated by a factor of 1000 (the wavelength ratio of optical and x-radiation). In fact the required precision is reduced by the fact that the refractive index of most materials in the above wavelength range is almost unity. The manufacturing tolerances are relaxed by the factor  $1/(1-n)$  to a first approximation (about one hundred thousand). The stability requirement is not relaxed in this way, and must be properly considered at the design stage. For this reason, most x-ray interferometers have been constructed as monoliths, that is to say that the whole instrument is carved from a large single crystal ingot. Unless otherwise stated, all the interferometers discussed here will be assumed to be monolithic.

## 2. X-RAY INTERFERENCE

The usual x-ray sources do not seem to be ideally suited to demonstrating x-ray interference. They are generally extended sources with no phase coherence between the different radiating regions. The wavefronts of the radiation emitted by each point are of course spherical, and there is no possibility of using lenses to collimate the radiation. Only the special properties of Bragg-reflecting perfect single crystals render these problems soluble relatively easily.

The key fact is that the time-averaged

intensity in the interfering beams depends only on the phase difference between the components of the incident wave following the two paths through the interferometer. The calculation of the detailed distribution of amplitudes in the interfering beams is rather complicated (3). The application of a few geometrical restrictions considerably simplifies the result of such an analysis, so that this phase difference depends mainly on the material properties of the crystal and the optical path within the interferometer.

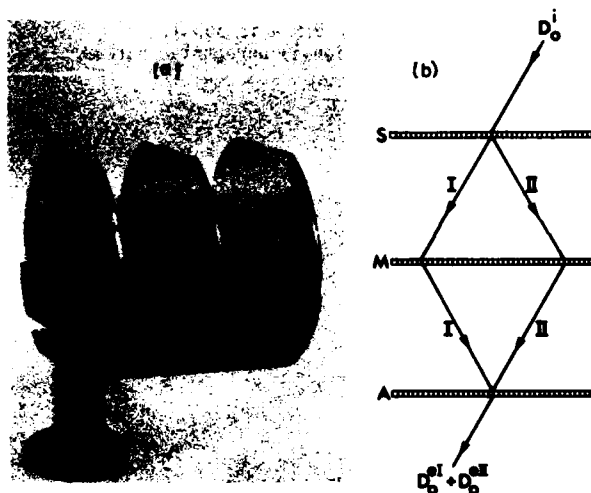


Figure 1. (a) A typical monolithic Laue case interferometer.

(b) The diffraction geometry of the Laue-case interferometer. The crystal wafers are arranged to satisfy the Bragg condition simultaneously. Wafer S acts as a beam splitter, M as a mirror and A as a beam analyser or recombiner. Only the important beams are shown for clarity.

In effect, the crystal only accepts those components of the incident wave which are useful for interference and ignores the rest. Even the effect of a polychromatic beam is taken care of, so that with divergent beams, a wide wavelength band can be transmitted. The thing which locks the phase difference between the waves is the crystal structure.

The geometrical conditions mentioned above are essentially (i) that the difference in optical path length for the two beams be less than the coherence length of the interfering waves. This requires that the physical path differences be of the order of ten microns or less, and (ii) that the geometry

of the interferometer is controlled to a similar degree.

### 3. THE X-RAY INTERFEROMETER

#### (a) The Laue-case Interferometer.

The x-ray interferometer (1) in its most frequently-used form consists of three crystal wafers set to diffract simultaneously the incident x-radiation (see figure 1). The diffraction takes place in transmission (the Laue case), rather than the more usual reflection or Bragg case. Several x-ray beams emerge from the device. Only the ones which are useful for interferometry are shown in the diagram. From the diagram it can be seen that the device possesses all the features of the classical optical interferometer.

The first wafer acts as a beam splitter. It is important to realise at this point that the beam in the forward direction is not simply that fraction of the beam which did not take part in the Bragg reflection process, but is a true diffracted beam. Its amplitude and phase are intimately connected with those of the hkl-diffracted beam and the crystal structure amplitude. The second wafer serves to steer the two beams created by the splitter into a path which allows them to be recombined. Again, the phase of the diffracted waves are locked to the crystal lattice.

If the third wafer were not present, then the interference of the two beams in the region where they overlap would give rise to a standing-wave pattern. The geometry of the arrangement dictates that the spatial period of the pattern is precisely that of the operative Bragg planes (for silicon, the 220 planes are spaced about 0.2nm apart). Since such a pattern cannot be recorded on any known medium, it is necessary to introduce the third wafer. Its function is to arrange that the interfering beams not only overlap, but also propagate in the same direction. If the phase of the two beams is homogeneous throughout their cross-section, then one can simply measure the total intensity in the interfering beam. This intensity is then a measurement of the relative phases of the component waves. If the phase of one of the two beams is not homogeneous throughout its cross-section, then its interference with the other, homogeneous beam results in a non-uniform spatial intensity profile, which can be recorded by placing an x-ray film to intercept the combined beam. The phase inhomogeneity may be due to one of several causes, and we shall briefly discuss some of them in a later section.

#### (b) The Bragg-case interferometer.

The Bragg case (surface-reflection) does not lend itself so obviously to providing the beam-splitting and recombining functions needed to realise an interferometer. It does however, allow the steering x-ray beams with virtually no intensity loss. It is worthwhile, therefore, to try and see what tricks we can use to provide Bragg-case beam splitting and re-combining.

The most obvious thing is to use a mixture of Bragg- and Laue-case, using each one in the position best suited to it. An interferometer based on this idea was first constructed by Bonse and Hart (4) and subsequently refined by Spieker (5). The geometry he employed is shown in figure 2(a).

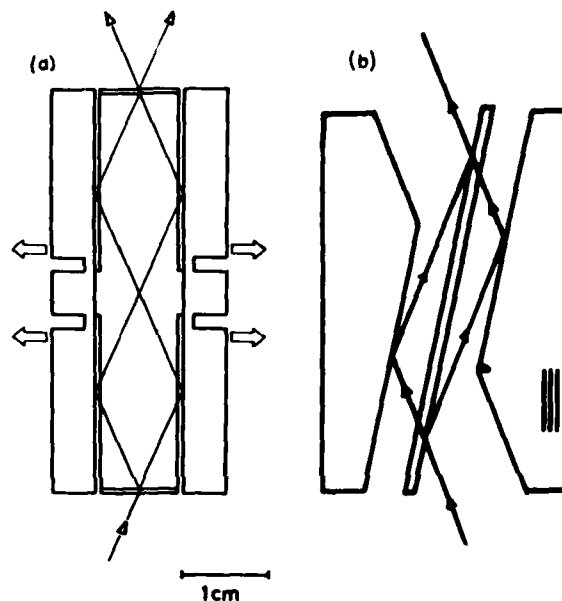


Figure 2.(a) A hybrid Laue-Bragg interferometer due to Bonse and Hart (4), as refined by Spieker (5). The beam splitting and recombining functions are performed by Laue-case wafers, whilst the mirrors operate in the Bragg case.

(b) An all-Bragg interferometer due to Bonse and Hart (6). The forward-diffracted wave exists when the crystal is set just off the Bragg condition.

The device is considerably complicated by the fact that, due to the effect of refraction, the Bragg angle is not the same in the Laue- and Bragg-cases. If not corrected, this will cause an unacceptable loss of intensity. Spieker's interferometer permits such a correction by means of slight elastic deformations of the monolith from which the interferometer is fashioned, in the manner shown. The second Bragg-case reflection is then necessary in order to re-correct the ray trajectory so that the reflection condition is satisfied for the final Laue-case reflection. The second reflection also substantially relaxes the geometrical constraints on the manufacture of the device.

The Bragg-case interferometer proposed by Bonse and Hart (6) is shown in figure 2(b). It relies on the fact that, for a plane wave, the reflection coefficient is not unity if the incident wave does not exactly satisfy the Bragg condition. Under such conditions, a forward-diffracted beam exists which can be used for interferometry. In fact the selection of the correct angle of incidence can be left to the interferometer itself, by illuminating it with a divergent beam. This interferometer possesses some advantages for imaging applications.

#### (c) Many-beam Interferometers.

We have so far restricted the discussion to the case where only one reciprocal lattice point is active in the diffraction process, i.e. the origin and  $hkl$ . This is referred to as the two-beam case. If we allow several reciprocal lattice points to be simultaneously active, then other arrangements become possible. The conditions for many-beam diffraction are quite restrictive, and interferometers relying on this phenomenon will

generally only work at one particular wavelength. This obviously restricts their application to non-spectroscopic problems. Figure 3 illustrates a selection of some of the many-beam interferometers which have been proposed (7,8,10).

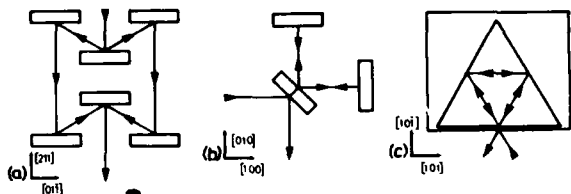


Figure 3. (a) This is the 3-beam Bragg-case interferometer constructed by Graeff (8). (b) A possible Michelson interferometer. (c) A triangular interferometer having coincident beam paths.

Only the device in figure 3(a) has been constructed and successfully operated (both in the laboratory (8) and with a synchrotron x-ray source (9)). This device is my favourite candidate for a soft x-ray interferometer based on crystal diffraction optics, since it does not rely anywhere on transmission of x-rays through the crystal material. However, the perfection of large Bragg-spacing crystals is not yet sufficient for interferometry.

The device shown as figure 3(b) is the x-ray analog of the Michelson interferometer. If a sufficiently stable and controllable version could be fabricated, then the sensitivity of the Michelson-Morley experiment may be significantly improved.

Fig 3(c) shows a triangular 3-beam device which was first proposed as an x-ray resonator, but is also an interferometer with coincident beam paths. This device could offer a sensitive, rather straightforward technique for the measurement of circular dichroism

(d) The scanning interferometer.

The scanning interferometer is essentially a Laue case device which is identical to the simple interferometer described above, except that it is constructed in such a way that the final wafer may be translated along the direction of the diffraction vector in a smooth, controllable manner. This modification gives the device several advantages over its rigid counterpart, and merits separate discussion.

A pure translation of one component of the interferometer relative to the others introduces a phase shift into one of the interfering waves which is proportional to the displacement. If the displacement is smooth and uniform, the output intensity undergoes sinusoidal fluctuations, which may be recorded by a counter. Such a device was first proposed and constructed by M. Hart (20). Since then it has been used in its monolithic form by Cusatis and Hart (14) and Hart and Siddons (15) to make high-precision measurements of anomalous dispersion and as a high-speed (1MHz) x-ray or neutron modulator (16).

It has also been used by several groups in an experiment to place the lattice parameter of silicon on an absolute basis by connecting an optical interferometer with an x-ray interferometer and determining the ratio

of the optical and x-ray fringe spacings (17,18,19).

The mechanism which performs the scanning must allow smooth, controllable translation of the analyser wafer relative to the rest of the interferometer on the picometer scale without introducing spurious rotations about any axis greater about one tenth of an arc second. This is a non-trivial requirement. The device is shown in figure 4.

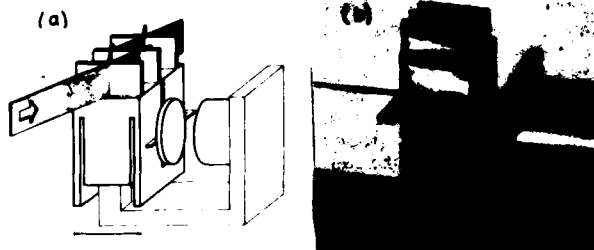


Figure 4. (a) A schematic diagram of the scanning interferometer showing the scanning stage and the x-ray beam trajectories. (b) A picture of a finished interferometer.

(b) A picture of a finished interferometer.

The interferometer and its scanning stage are constructed from a single crystal of silicon. The elastic scanning stage is a folded parallelogram spring strip design. The small forces necessary for controlled deformation of the monolith are most conveniently generated electromagnetically. Thus it is not difficult to place the instrument under computer control. This capability has been used to advantage in experiments to measure anomalous dispersion using weak x-ray sources (15).

#### 4. APPLICATIONS

##### (a) Moire Topography

As we have mentioned earlier, the phase of the diffracted beam is related to that of the structure amplitude of the active Bragg reflection. If the Bragg planes are distorted, the effective phase of the structure amplitude is locally modified. When the wave diffracted by such a lattice interferes with the reference beam, local variations of intensity are observed within the beam cross-section, which may be recorded on x-ray film. The image so obtained is a map (or topograph) of local lattice distortions. We can estimate the sensitivity of the technique very simply. A phase change of  $\pi$  (producing the maximum intensity change) results from a lattice displacement of one half of the Bragg spacing (0.1nm for the 220 reflection in Silicon). The smallest resolvable fringe spacing is, say, 0.1mm for ordinary x-ray film. This places an upper limit to the magnitude of the strain of about one part per million (ppm). This overlaps nicely with other topographic techniques. The lower limit depends on the details of the experimental technique, but since a fringe spacing of 1cm would be readily visible, a value of 0.01ppm is not too ambitious. The formal similarity between the above contrast mechanism and the effect produced by superposing gratings has led to the technique being dubbed Moire topography. An example of this is shown below. Figure 5 shows the image obtained by x-ray Moire topography of a selectively deposited aluminium film on one wafer of an inter-

ferometer.



Figure 5. The interferogram produced when a thin aluminium film is deposited onto one wafer of an interferometer. The right-hand image shows the increased strain after heat-treatment of the film.



Figure 6. The effect of inhomogeneous impurity content in the interferometer material.

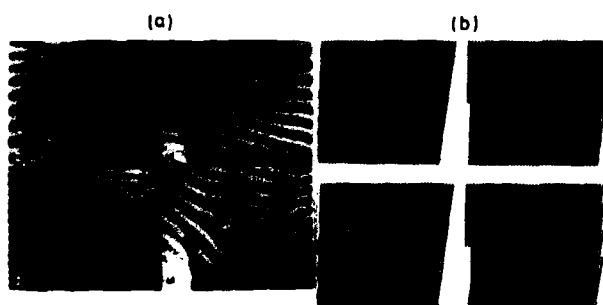


Figure 7. (a) The interferogram produced by an interferometer having a single dislocation in one wafer. The effective number of extra Bragg planes is changed by imaging using different diffraction orders.

(b) A simulation of the above interferograms made by superposing a normal grating upon a sequence of 'dislocated' ones in which the number of extra half-planes increases from one to four.

The aluminium was deposited at room temperature, and a small amount of strain is produced by the difference in thermal expansion coefficient as the aluminium condenses onto the crystal. The right-hand

image shows the effect of heat treatment on the magnitude of the strain.

Figure 6 demonstrates the effect of inhomogeneous impurity distribution on the interferogram. The Bragg spacing is modified by the impurity, and so the fringe pattern shown reflects this variation.

Figure 7(a) shows a Moire topograph of a crystal containing a single dislocation. A rotational component has been added, which is superposed on the displacement field due to the dislocation. Extra fringes can be seen beginning near the dislocation core. This pattern is characteristic of the Moire pattern produced between a perfect grating and one which has had an extra line pushed half-way into it (figure 7(b)). The number of extra fringes produced is exactly the effective number of extra half-planes present in the dislocated lattice. This permits a complete determination of the dislocation Burgers vector.

With synchrotron sources, concern has been expressed at the large thermal load which is placed on any optical system receiving the direct white beam. There is very little quantitative knowledge of the behaviour of crystal diffraction optical systems under such conditions. The x-ray interferometer is potentially a very sensitive detector of thermal strains in one of its components. A recent experiment (12) took advantage of this sensitivity and made quantitative measurements of temperature differences between the splitter wafer and the rest of the interferometer.



Figure 8. Dilation Moire patterns observed when an x-ray interferometer is placed in the white radiation beam of a synchrotron. The fringe spacing is a direct measurement of the temperature difference between the first and subsequent wafers. Wider fringe spacing corresponds to lower temperature difference..

Measurements were made under a variety of conditions. Figure 8 shows one sequence of fringe patterns where the beam cross-section was varied. The influence of filters and the effect of highly inhomogeneous thermal loads were also studied.

(b) Phase contrast microscopy.

Phase shifts may also be introduced into the interferometer by refracting objects as well as by lattice displacements. Thus it is possible to image refractive-index variations i.e. to take phase-contrast micrographs. Figure 9 shows such an image of a concave polymethylmethacrylate lens (13).

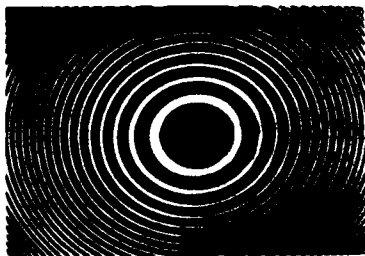


Figure 9. A phase-contrast micrograph of a plastic lens.

The equal-phase contours correspond in this case to equal-thickness contours, and are therefore concentric circles. This technique has had rather limited applications until recently, because of the restricted set of wavelengths available in the laboratory. The real power of the method is only available if one is free to choose the imaging wavelength. The significance of this is best shown by figure 10. The dependence of the forward scattering factor, and hence the refractive index of materials on wavelength is characterized in the x-ray region by the presence of the K-absorption edges. This gives rise to the well-known anomalous dispersion effect.

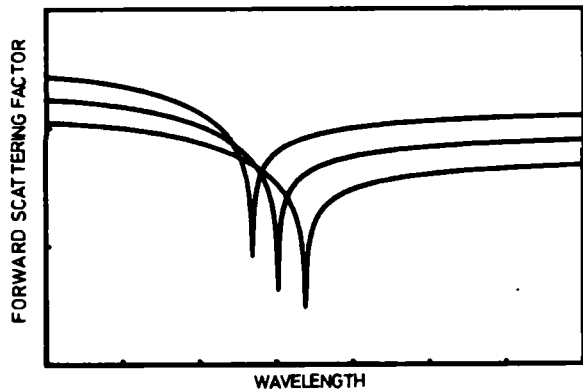


Figure 10. The variation with wavelength of the forward scattering factor (which is simply related to the refractive index) of a series of elements.

The interesting result for microscopy is that there are some regions where refractive-index matching occurs. Thus it is possible to find a wavelength at which only one component of a three-component system is contrasted. Possible candidates for such a technique should be numerous once the facility is available on a routine basis at a synchrotron source.

The technique can also provide higher contrast of samples with low atomic number, for which absorption contrast is usually low. This could be of interest to people studying biological materials.

There are of course problems with the method, perhaps the most restrictive is that of spatial resolution. Several instrumental factors conspire to limit the microscopic resolution to around 10 microns. Little development has taken place however, and I am sure that this limit will disappear in the

future.

### (c) Dispersion spectroscopy.

The variations in forward scattering factor illustrated in figure 10 is in itself of considerable interest. It is difficult to compute, and several approximate theories have been developed. Prior to the x-ray interferometer no reliable experimental data existed. Thus none of the calculations could be verified. This in turn led to a decline in theoretical developments.

The x-ray interferometer offers a very direct way of measuring refractive indices, and the relationship between refractive index and forward scattering factor is straightforward. Several interferometric determinations were made in the laboratory using the characteristic lines available, but these were not sufficient to provide a real test. The first series of high-resolution measurements covering an absorption edge was performed using synchrotron radiation by Bonse and Materlik (21). They used a film technique which relied upon the displacement of a rotation Moire pattern. The Moire image they obtained is illustrated in figure 11, and the dispersion corrections they calculated from measurements of fringe positions on this image are shown in figure 12(a).

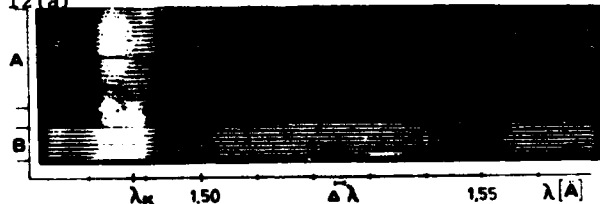


Figure 11. The Moire pattern recorded as a function of wavelength by Bonse and Materlik, from which they calculated the dispersion of Nickel. The position of the absorption edge is marked, and the dip in the fringe position around it is clearly visible.

The two major disadvantages of this technique are i) the difficulties of assessing phase shifts to sufficient accuracy (given the uncertainties in response and dimensional stability of film and the difficulties of optical densitometry) and ii) the need to measure the sample thickness and density to high precision.

Both the disadvantages of the above technique are overcome by using the scanning interferometer to record fringe profiles directly, and by working at multiple wavelengths to eliminate the sample thickness and density from the equations. Two such experiments have been performed, one (14) was a pilot study by Cusatis and Hart. They used Bremsstrahlung from a standard x-ray tube and a scintillation counter to make measurements at several wavelengths on Zirconium metal near the K absorption edge. The second (15) used an improved x-ray optical system and a solid-state detector in a computer-controlled spectrometer to collect a considerable quantity of data for several elements. These later results are shown in figure 12 (b) to (e). The improvement in quality of the data collected using this apparatus is manifest. The results have been compared in detail with theoretical estimates, and were instrumental in uncovering some errors in computational procedure in one series of calculations (21). These errors were subsequently corrected, and

the smooth curve drawn through the experimental points in figure 12(b) through (e) is calculated according to this revised scheme. A remarkable degree of agreement is found.

Since these experiments were performed in the laboratory, they are limited in quality by the very low intensities available from Bremsstrahlung sources. We see no reason why any intensity gains obtained by moving to a synchrotron source should not provide an appropriate improvement in data collection times or measurement precision, or combinations of the two appropriate to the problems in hand at the time.

The scanning interferometer equipment proposed for the Daresbury storage ring is waiting to be commissioned and should be producing high-quality data by the fall of this year. The use of a dispersive double crystal arrangement should provide energy resolutions of around 0.1 eV, with intensity comparable with laboratory characteristic sources, or even higher. An extensive survey of the periodic table is planned to confirm certain systematic trends observed in our laboratory experiments, and detailed, high resolution studies of selected elements and compounds are planned to study the near-edge behaviour of the dispersion.

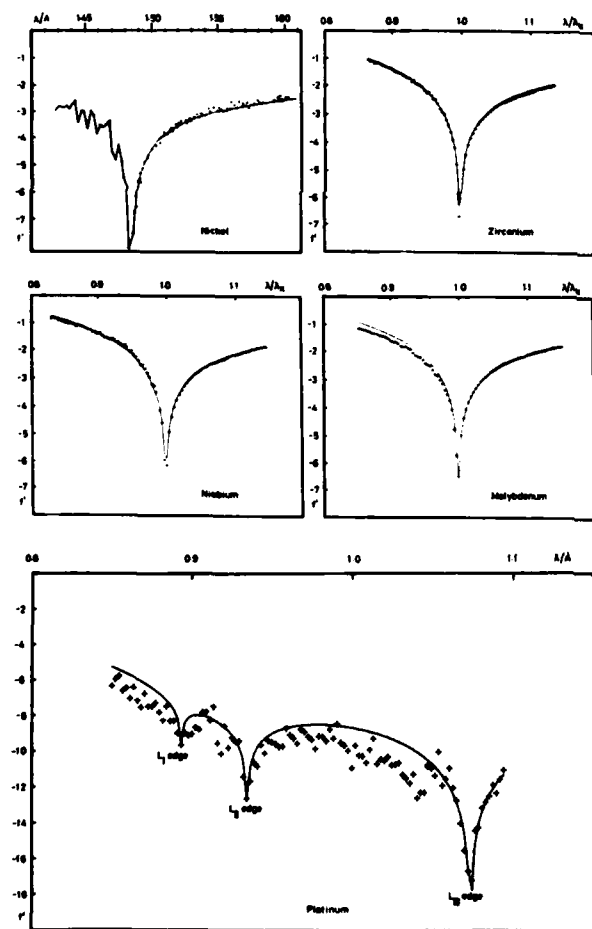


Figure 12. Anomalous dispersion factors measured by x-ray interferometry. (a) the values for nickel measured at Desy by Bonse and Materlik (21). (b) (c) (d) (e) Anomalous dispersion factors for

several elements measured by Hart and Siddons (15) using laboratory Bremsstrahlung.

## 5. CONCLUSION

I hope that I have managed to convince you that x-ray interferometry is more than just an interesting idea, and that it will become an accessible tool in the near future, even to the non-specialist. Facilities are planned specifically for interferometry at two major synchrotron sources, at the new HASY laboratory in Hamburg and at the Daresbury SRS in England. When these two experiments are under way we should see many new and interesting experiments performed.

## REFERENCES

- (1) U. Bonse and M. Hart. Appl. Phys. Lett. **6**, 155, 1965
- (2) G. Kellstrom. Nova Acta Reg. Soc. Sci. Ups. **8**, 5, 1932
- (3) U. Bonse and W. Graeff in 'X-ray Optics', H.J. Queisser ed., Springer-Verlag 1979.
- (4) U. Bonse and M. Hart. Acta Cryst **A24**, 240, 1968
- (5) P. Spieker. Doctoral Thesis, Univ. Dortmund, 1977
- (6) U. Bonse and M. Hart, Z. Physik **194**, 1, 1966
- (7) R. D. Deslattes, Appl. Phys. Lett. **12**, 133, 1968
- (8) W. Graeff, Doctoral Thesis, Univ. Dortmund 1976
- (9) W. Graeff and U. Bonse, Z. Physik **B27**, 19, 1977
- (10) M. Hart, Proc. Roy. Soc. Lond. **A346**, 1, 1975
- (11) U. Bonse and M. Hart, Z. Physik **190**, 455, 1966
- (12) M. Hart, M. Sauvage and D. P. Siddons, Acta Cryst. **A36**, 947, 1980
- (13) M. Hart, Rep. Prog. Phys. **34**, 435, 1971
- (14) C. Cusatis and M. Hart, in 'Anomalous Scattering', Copenhagen, Munksgaard, 1974
- (15) M. Hart and D. P. Siddons, Proc. Roy. Soc. Lond., **A376**, 465, 1981
- (16) M. Hart and D. P. Siddons, Nature 1978, p45
- (17) I. Curtis, I. G. Morgan, M. Hart and A. D. Milne, in Proc. International Conference on Precision Measurement and Fundamental Constants, Gaithersburg, Md, p.285. N.B.S. Special Publication.
- (18) R. D. Deslattes and A. Henins, Phys. Rev. Lett. **31**, 972, 1973
- (19) K.-J. Hanssen et al, Physikalsch-Technisch Bundesanstalt Report No. PTB-APH-14, March 1981
- (20) M. Hart, J. Phys. D Appl. Phys. **1**, 1405, 1968
- (21) U. Bonse and G. Materlik, Z. Physik **B24**, 189, 1976
- (22) D. T. Cromer and D. H. Liberman, Acta Cryst. **A37**, 267, 1981



E. Leith

The University of Michigan, Ann Arbor, Mich. 48109

## ABSTRACT

Holograms can be formed in light of little or no temporal coherence. The coherence requirements for Gabor in-line holography are examined. It is shown that, with achromatic interferometers formed from diffraction gratings, the coherence requirements for off-axis holography are equally low. Finally, two basic approaches to the making of holograms in completely white light are described.

## INTRODUCTION

Nowadays we see holograms of remarkable quality viewed in white light. The holograms are bright, sharp, often large, with considerable depth and parallax. They belie the often-held supposition that holograms have to be viewed in highly coherent light--monochromatic light from a point source. These holograms which are the product of much technical development and a number of rather ingenious ideas, were developed in response to the realization that if display holography were to be of any widespread value, it had to be freed from the constraint of being viewed only with relatively expensive and inconvenient sources such as lasers and mercury arcs.

It would be attractive, for various reasons, if holograms of such excellent quality could also be constructed in white light. The prevailing view among those somewhat knowledgeable, but not expert, in holography is that the making process is basically different, and even the holograms designed for white light viewing must still be made with highly coherent light, as for example from a laser.

On the other hand, if we consider that when a hologram is being viewed, the light passing through it is merely retracing the paths of the light used for making the hologram. And if we consider that the same laws of optics apply if we merely reverse the direction of the light rays, we might suspect that the coherence of the making and viewing processes might in a basic way be just the same. Thus, perhaps, holograms can be made in white light. There is considerable truth in this viewpoint, although the issue is by no means a simple one.

For the basic process of holography, as developed by its inventor Dennis Gabor, the truth of this supposition is quite simple. As we show in Fig. 1, a hologram is made of a small scattering "point" object  $O$ , of size  $\Delta x$  (we work in two dimensions instead of three, for simplicity). Light scattered by  $O$  interferes with the coherent background to form an interference pattern that is recorded as a hologram  $H$ . Each wavelength component of the source forms a zone plate pattern at  $H$  that is scaled differently, in inverse proportion to wavelength. The source wavelength spread,  $\Delta\lambda$ , must be limited to a value such that the outermost zones for the longest and shortest wavelength do not mismatch by more than, say, one half of a period. Simple considerations lead to the bandwidth limitation

$$\Delta\lambda/\lambda_0 = 4(\Delta x)^2/\lambda_0 z = 4/C \quad (1)$$

where the various symbols are defined in Fig. 1. The quantity  $C$  we call the expansion ratio, which is the ratio of the width of a resolution element on the object and the linear spread of the zone plate it makes on the

hologram. The introduction of this quantity leads to, as we see, an extremely simple expression for the allowable wavelength spread, just 4 times the reciprocal of the expansion ratio.

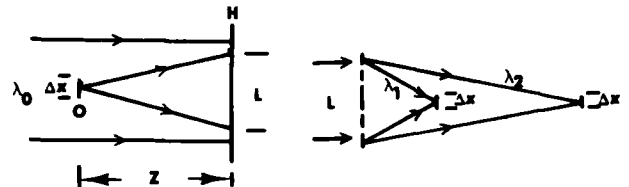


Fig. 1. Gabor hologram of a point object. left, construction; right, reconstruction

Similarly, on readout, the zone plate has a focal length inversely proportional to wavelength. If we view the hologram with a beam of polychromatic light and observe the plane where the image is in sharp focus at the midband wavelength, then other wavelengths will form images somewhat blurred in this plane. If we use the elementary laws of optics to calculate the allowable spatial bandwidth  $\Delta\lambda$  before the image becomes noticeably blurred, we find

$$\Delta\lambda/\lambda_0 = 4(\Delta x)^2/\lambda_0 z = 4/C \quad (2)$$

which is exactly the same expression as before. Here, we would call  $C$  the compression ratio, which is the ratio of the width of a zone plate on the hologram to the width  $\Delta x$  of the "point" image to which the zone plate focuses the light. Thus, for the simple, basic process of holography, as given by Gabor, our suspicions are confirmed. The making and the viewing processes have exactly the same monochromaticity requirements.

Moreover, these requirements can be very modest. For example, if we choose parameters such that the expansion ratio is 20 (i.e., a resolution cell on the object is spread into a zone plate response with an area 400 times greater), the allowable wavelength spread, for a midband of 5000 Angstroms, is 1000 Angstroms.

## II. EXTENSION TO OFF-AXIS HOLOGRAPHY

Gabor in-line holograms suffer from poor signal to noise ratio. Higher quality is obtained from the so-called off-axis or carrier frequency holograms. There has been a widely held view that such holograms have greater coherence requirements for both the making and viewing steps, but this view is not necessarily true. Off-axis holography, as opposed to Gabor's original method, is a two-beam interferometric technique, with the object in one beam and with the other serving as the reference beam; this impinges on the recording plate at

an angle with respect to the object beam, so as to produce a large number of fringes, typically several hundred to several hundred thousand. The chromaticity requirements are then a combination of those required for the holographic process and those required for the interference of the two beams. Now, there are many kinds of two-beam interferometers, and they differ greatly in their chromaticity requirements, so the total chromaticity requirement for off-axis holography depends on the kind of interferometer we use for introducing the reference beam.

It happens that there are achromatic interferometers that produce an unlimited number of very fine, high contrast fringes in perfectly white light. When such an interferometer is used for forming an off-axis hologram, the chromaticity requirement is no greater than for the basic process of Gabor in-line holography. Such interferometers use diffraction gratings as beam splitters. Similarly, a diffraction grating may be used in the hologram viewing process, so that the chromaticity requirements for viewing a hologram are also no greater than for the in-line case.

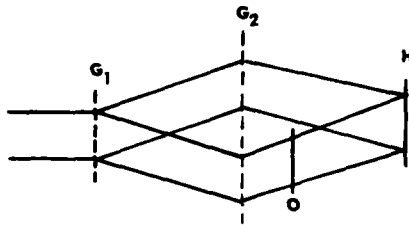


Fig. 2. A grating interferometer for making hologram.

Figure 2 shows an example of an interferometer formed from a pair of diffraction gratings. The first grating acts as a beam splitter, dividing the incident light into a zero and a first orders. If the grating is thick, so that the diffraction is of the Bragg type, there will be no other order. The second grating is a beam combiner, which brings the beams back together. The interferometer forms fringes whose spacing and position are independent of wavelength; thus, high contrast fringes are formed even for white light. The number of fringes and their spacing is just the number and spacing of the rulings on the first grating, and is thus independent of the wavelength spread.

It is easy to see why the fringe spacing is wavelength independent. The spacing of the fringes varies inversely as the angle between the two beams, and directly as the wavelength. However, longer wavelengths are diffracted by the gratings at greater angles and therefore, come back together at greater angles. The two factors, wavelength and combining angle, therefore just compensate, giving fringe spacing independent of wavelength. Analysis shows that the fringes for each wavelength will also be in perfect registry. Finally, analysis also shows that the fringes will form in a broad source. Thus, the fringe formation process requires neither temporal nor spatial coherence.<sup>1,2</sup>

We place an object transparency *O* in one of the beams, as indicated in Fig. 2. The fringe pattern will then, upon recording, become an off-axis hologram. Diffraction (i.e., scatter) by the object will cause the light in the object beam to be redistributed, thus somewhat upsetting the achromatic and broad source fringe formation process, so that now there will be some coherence requirements on the source. Analysis shows, however, that these requirements are exactly the very modest ones given by Eqs. 1 and 2 for basic holography.<sup>1</sup> Thus, by choosing the proper interferometer, off-axis holography can be done with the same coherence requirements as for basic, in-line holography.

### III. MAKING HOLOGRAMS IN WHITE LIGHT

In recent years there has been considerable interest in making holograms in white light. As we have noted, holograms that can reconstruct in perfectly white light are now commonplace, and since we have argued that, for the basic holographic process, the chromaticity requirements for the making and viewing steps should basically be the same, we might now suspect that holograms can be formed in white light. And indeed they can. However, for reasons that are rather intricate, the white light hologram formation methods are really not counterparts of the previously-noted white light readout methods.

The white light methods fall into two categories. Both require fairly complex lens systems to achieve their results.

The first category is based on a procedure developed by Katyl<sup>3</sup>, in which lens systems are used to achromatize a Fresnel or Fourier transformation process in a way analogous to the way lens systems are achromatized to form images.

The second category is based on the use of achromatic optical convolving systems which are integrated into achromatic interferometers.<sup>4,5</sup>

The first method has two salient characteristics:

1. All points on the hologram are formed simultaneously, i.e., in parallel.
2. The achromatization is only approximate.

The second method has these corresponding characteristics:

1. The holograms are formed one point at a time, i.e., sequentially, and the generation of the complete hologram requires a scanning process.
2. The achromatization is exact.

### IV. KATYL'S METHOD

The achromatization method of Katyl has been used both in the viewing and in the making of holograms. It is a method analogous to the way a lens is achromatized -- by putting simple lens elements together to form a compound lens. The lens elements are made from different kinds of glass, with different dispersion characteristics, so that the dispersion of one element compensates that of the other. Katyl's method differs in two respects.

First, instead of achromatizing so that the image is free from chromatic aberration the achromatization is done for some plane in the Fresnel field. For a two-dimensional object, the achromatization can be rather good. If the object is 3-D, the achromatization is done for only one plane of the object.

The second difference is that it is the diffraction process that is being achromatized rather than a lens system. The chromatic errors in diffraction processes are different from those of lenses and are severe; thus, highly dispersive correcting elements are needed. Katyl used glass dispersion lenses in some of this configurations, but for most he used a Fresnel zone plate, which enormously greater dispersion than glass lenses.

The correction of aberrations in an imaging system by the use of compensating lenses is a specialized process, and it is not appropriate to go here into what is basically a lens design problem. We note that Katyl shows experimental results of holograms made in white using the compensation systems and also shows for comparison results without the compensation system. The results are most impressive.

### V. OPTICAL CONVOLVER METHOD

The optical convolving method consists of two parts (Fig. 3). First there is the system *OP* that achromatically generates a Fresnel diffraction pattern of an object transparency. This system is integrated into the second part, a grating interferometer that achromatically provides a reference beam.

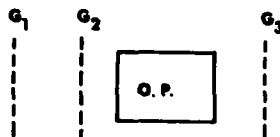


Fig. 3. The optical convolving method

The basic system for performing the former operation is shown in Fig. 4. The transparency  $O$  is illuminated with a polychromatic light source that is wavelength dispersed along the longitudinal, or  $z$ , axis. For wavelength  $\lambda_1$ , the source is a point a distance  $z_{s1}$  from the object; for a wavelength  $\lambda_2$ , the source is a different distance,  $z_{s2}$ , from the object. The source may be written as the function

$$S = \delta(z - z_s \lambda_0 / \lambda), \quad (3)$$

which indicates that the source point, as a function of wavelength, is located at  $z = (\lambda_0 / \lambda) z_s$ , where  $z_s$  is the distance between source and object for wavelength  $\lambda_0$ .

Such a source can be produced by illuminating a Fresnel zone plate with a point white light source and selecting one order while removing the others by appropriate spatial filtering.

The beam illuminating the object transparency is then  $\exp(i\pi x^2 / \lambda z)$  (where, as before, we drop the 3rd, or  $y$  dimension). Using Eq. 3, we write this as  $\exp(i\pi x^2 / \lambda_0 z_s)$ . This form of the illuminating function is thus wavelength independent, a consequence of the axial dispersion. A lens  $L$  forms the Fourier transform of the product  $O(x)\exp(i\pi x^2 / \lambda_0 z_s)$ , and we observe in the back focal plane the field distribution

$$u = \mathcal{F}\{f(x - x') \exp(i\pi x^2 / \lambda_0 z_s)\}, \quad (4)$$

where  $\mathcal{F}$  indicates Fourier transformation and  $x'$  describes movement of  $O(x)$  through the optical system aperture. However, we confine our observation to a point on axis by placing at the back focal plane of the lens a mask containing a pinhole. The field in the pinhole represents the integral

$$u(x') = \int O(x - x') \exp(i\pi x^2 / \lambda_0 z_s) dx = O^*h. \quad (5)$$

We have thus formed the convolution operation describing Fresnel diffraction, and it is significant to note that it has been formed achromatically, using a broad-spectrum source. Of course, it is generated one point at a time, and to generate the entire pattern, we must move the object transparency through the aperture.

This diffraction pattern can be recorded as a hologram by introducing a reference beam  $u_0 = a_0 \exp(i2\pi f_0 x')$ , producing an irradiance  $|u_0 + u|^2$ , which results in a hologram that produces the desired reconstructed wave. By using an achromatic interferometer to provide the two beams, object and reference, the recombination of the beam is accomplished achromatically, as we explain later.

Explicitly showing the zone plate which provides the dispersed source for the object leads to an alternative way (Fig. 5) of describing this holographic process. The zone plate, whose amplitude transmittance is  $t_a = 1/2[1 + \cos(\pi x^2 / \lambda_0 z_s)]$ , imaged onto the transparency  $O$ . We suppose that in the process the zone plate is spatially filtered so that only the virtual image term

reaches the transparency  $O$ . Thus, the light distribution impinging on the transparency is, to within a constant,  $\exp(i\pi x^2 / \lambda_0 z_s)$ , which is the result given previously. A more complete description is given in Refs.

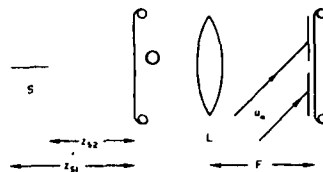


Fig. 4. Achromatic holographic configuration.

4 and 6. By formulating the operation in this manner, it is seen to be just the basic method of using a coherent optical system to convolve two functions by imaging one onto the other. The holographic process is then just the special case of choosing the convolving impulse response as a quadratic phase function. We could use any other convolving function; thus, the method we describe in terms of holography is indeed a very general method for using optical processing for performing the general operation  $g = f^*h$ , where  $f$  and  $h$  are any functions.

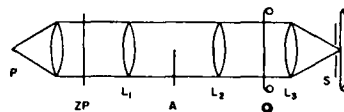


Fig. 5. Alternate description

To complete the achromatic holographic system of Fig. 4 (or 5) we must bring in a white light reference beam that is coherent with the object beam. This is done by means of the three-grating interferometer shown in Fig. 6. This interferometer is achromatic, just as

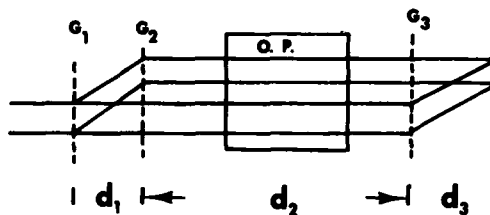


Fig. 6. The three grating interferometer

is the two-grating interferometer of Fig. 2. Using three gratings (all of the same spatial frequency) adds considerable flexibility, as explained in Ref. 5. One consequence is that the distance  $d_2$  between gratings  $G_2$  and  $G_3$  is decoupled from the equation for fringe formation; the fringes form at a distance  $d_3$  from the final grating regardless of the separation of gratings  $G_2$  and  $G_3$ . We place the optical convolving system in the space between  $G_2$  and  $G_3$ , in such a way that both object and reference beams transverse the total optical system, otherwise the paths are not the same and coherence between the two beams is lost. The reference beam must of course also traverse the two plates containing the zone plate and the object  $O$ , however, it must go through portions of the plates that are clear, so that it will emerge as a uniform beam.

A system for making one-dimensionally dispersed holograms, such as the very popular multiplex holograms and Benton rainbow holograms, is shown in Fig. 7. The optical convolving system is identical with that of Fig. 5, except for the addition of a cylindrical lens  $L_3$  (so

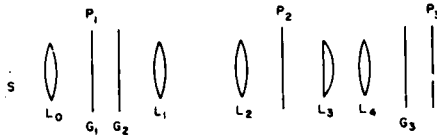


Fig. 7. The complete system

as to produce one-dimensional dispersion).  $G_2$  and  $G_3$  are identical gratings of spatial frequency  $f_1$ , and  $G_1$  is an off-axis zone plate structure, with carrier  $f$  in the  $y$  direction and the zone plate structure in the  $x$  direction. In other words, we have a nice economy by having  $G_1$  serve as both a cylindrical zone plate for

one-dimensional convolution and also as the first grating of the interferometer. The zero and first orders of  $G_1$  are selected, with the first order being modulated by the zone plate.  $G_2$  demodulates the diffracted beam to zero spatial frequency in the  $y$  direction. Since  $G_2$  affects the light distribution in the  $y$  direction only,  $G_2$  can then be considered to be imaged in the  $x$  direction at object plane  $P_2$ , producing the required object distribution. The object is then moved through the aperture, as described earlier, while  $G_3$  modulates the reference beam in order to produce the required fringes at the output plane.

A final comment: the grating  $G_3$  can bring the reference beam to the recording plate at a very steep angle, so as to produce fringes of several hundred lines/mm, a spatial frequency far higher than the lens could pass. The fringes can be, in a special sense, considered as an image of the initial grating  $G_1$ , so we have imaged through the optical system a spatial frequency far in excess of what the modulation transfer function of the system would ordinarily allow, yet have suffered not even a slight loss of fringe contrast. It is done by the grating  $G_2$  beating the reference beam to

zero spatial frequency, i.e., making it travel along the optical system axis, and the gratings  $G_3$  then restoring the reference beam to its original high spatial frequency, i.e., its steep angle.

An example of a hologram produced by Swanson in an achromatic system such as we have described is shown in Fig. 8.

To conclude, I point out some very recent work by my coworker G. Collins, who has advanced the Katyl method and combined it with the three grating interferometer method to produce a Fourier transform hologram in white light, without the need for a scanning process.

While the white light methods have advanced considerably over the past several years, I believe it is only a beginning, and there is considerable room for further advance.

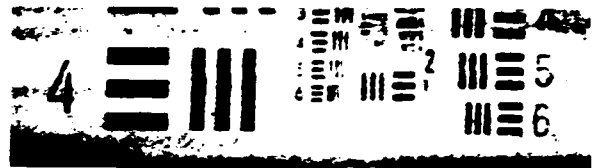


Fig. 8. Reconstruction from a hologram made in white light (courtesy G. Swanson).

#### REFERENCES

1. E. Leith and J. Upatnieks, *J. Opt. Soc. Am.*, **57**, 1123-975 (1967).
2. E. Leith and B. Chang, *Appl. Opt.* **12**, 1957 (1973).
3. R. H. Katyl, *Appl. Opt.* **11**, 1241, 1248, 1255 (1972).
4. E. Leith and J. Roth, *Appl. Opt.* **16**, 2565 (1977).
5. E. Leith and G. Swanson, *Appl. Opt.* **19**, 638 (1980).
6. E. Leith and J. Roth, *Appl. Opt.* **18**, 2803 (1979).



Dr. Emmett Leith described optimum geometries for the formation of visible light holograms with sources of limited coherence properties. The extension to x-ray experiments was suggestive.

## Low Energy X-Ray Calibration Sources at the Lawrence Livermore National Laboratory

Jerry L. Gaines\*

Lawrence Livermore National Laboratory, P. O. Box 808, Livermore, California 94550

## ABSTRACT

The X-Ray Calibration and Standards Laboratory located at the Lawrence Livermore National Laboratory provides unique and vital support to many users of low energy x-ray diagnostics. This Laboratory routinely provides x-ray calibrations in a steady state mode from 100 eV to 1000 eV. A unique x-ray source, utilizing an ion accelerator, provides various discrete x-ray energies in the 110 eV to 1000 eV range. Another x-ray source provides continuous x-ray spectra in this energy range and employs a unique compound goniometer which enables the calibration of both reflective and diffractive x-ray systems. These x-ray facilities and their unique characteristics will be described as well as a brief description of some of the experimental efforts accomplished using them.

## INTRODUCTION

During the last ten years, interest in the soft x-ray region from 100 to 1000 eV increased significantly. The catalysts for this interest were primarily the laser-fusion program and the magnetic fusion program. These programs rely fairly heavily on the measurement of x-rays emitted in this energy range. The weapons program has long known that measurements of the emitted radiation from an exploding nuclear device can provide information concerning the physics involved. This concept was quickly adapted by both the laser and magnetic fusion programs. The x-ray emission from high-temperature ( $kT \sim 1$  keV), laser produced plasmas is predominately in the 100 to 1000 eV energy range and thus the need for well calibrated x-ray diagnostics quickly became a necessity. Likewise, the temperatures achieved in the magnetically confined plasmas also produce x-rays in this energy region, and they too require well calibrated x-ray diagnostics to collect data which relates to the physics phenomena taking place.

For these applications the interest is primarily on fast, current-mode detectors capable of responding linearly to the intense x-ray bursts produced by these sources. The laser produced plasmas are characterized by durations of approximately 100 ps and peak photon intensities of  $10^{25}$  keV/Ster-sec. For the magnetically confined plasmas the intensity is lower but the duration is on the order of milliseconds or longer. Typical detectors used in these measurements include semiconductor detectors, scintillator photomultiplier or photodiode detectors and photoelectric diodes. (1) These detectors have sensitivities of the order of  $10^{17}$  to  $10^{20}$  coul/keV, and thus it is clear that in order to be accurately calibrated in the current mode, intense sources of monoenergetic x-rays must be available.

## REVIEW OF SUB-KILOVOLT X-RAY SOURCES

An obvious source of monoenergetic x-rays in the sub-kilovolt energy region is the characteristic line emission from inner shell atomic fluorescence of low-Z elements. This fluorescence can be induced by various types of exciting radiations, i.e., photons, electrons or ions. Since the fluorescence yield for low-Z elements is quite low, very intense ionization sources are needed in order to obtain useful x-ray yields in this energy range. Photon and electron excitation are two of the most common x-ray generating techniques.

An example of an x-ray generator or tube utilizing electron excitation is the Henke tube. (2) This tube shown geometrically in Figure 1 was developed by Professor Burton Henke of the University of Hawaii. The x-rays from this tube are often used to excite fluor-

escence in other materials, as shown in Figure 1, providing an example of photon excitation. Both of these

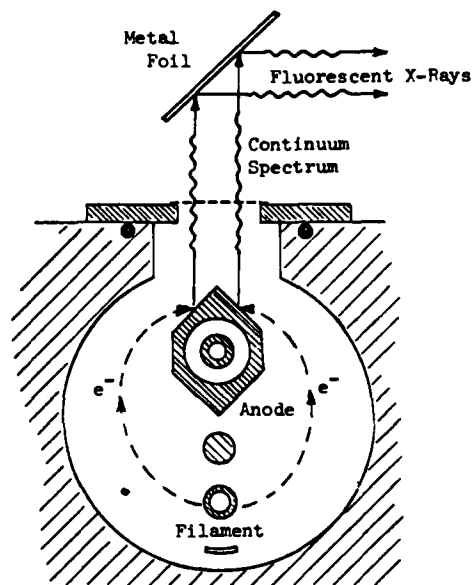


Fig. 1. Henke x-ray source with secondary target for producing fluorescent x-rays.

excitation processes, although commonly used, suffer disadvantages. These disadvantages are characterized by x-ray beam spectral contaminants which arise from photon scattering in the first case and bremsstrahlung continuum production in the second. These spectral impurities are superimposed on the characteristic line emissions. To avoid these difficulties, the phenomenon of x-ray production via ion bombardment has become of significant interest. This production mechanism is characterized by high characteristic x-ray yields and low bremsstrahlung backgrounds and is ideally suited to the calibration objectives mentioned earlier. Based on this information, we have developed a calibration facility at the Lawrence Livermore National Laboratory utilizing characteristic x-ray production from elemental targets via Coulomb excitation from proton bombardment. While heavier ions may provide greater photon yields for specific cases in which the energy levels of the projectile and target atoms overlap, proton excitation provides a consistently high yield for gen-

\*Work performed under the auspices of the U. S. Department of Energy by the Lawrence Livermore National Laboratory under contract number W-7405-ENG-48.

# ION ACCELERATOR-SUBKILOVOLT X-RAY FACILITY

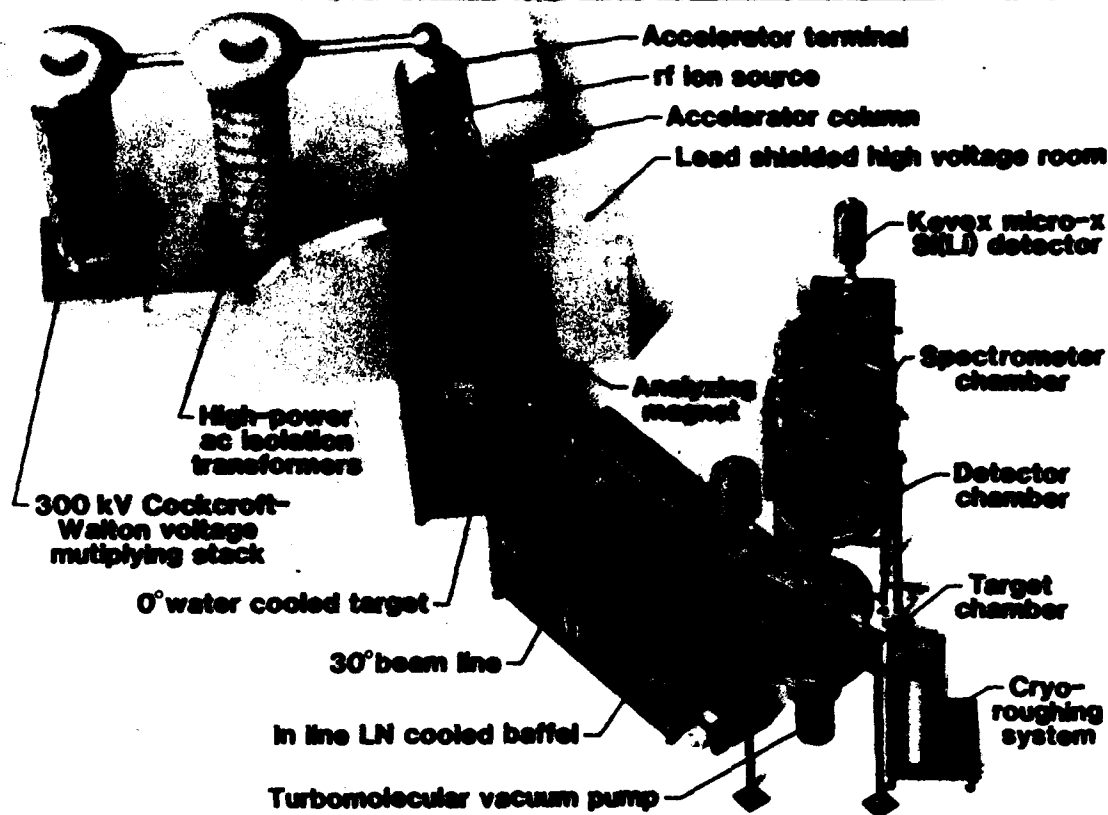


Fig. 2. Cut away view of the Ion Accelerator - Subkilovolt X-Ray Facility.

eral excitation of a wide variety of target materials. Also, in considering the dependence of x-ray yield and of secondary electron bremsstrahlung production upon the incident proton energy it appeared practical to base the facility around a low-energy (300 kV) accelerator.

## ION ACCELERATOR SUB-KILOVOLT X-RAY FACILITY

The LLNL calibration facility consists of a charged particle accelerator, x-ray target chamber, photon monitoring system, experimental detector chamber and crystal diffractometer (Figure 2).

The accelerator power supply (Figure 3) is based on conventional Cockcroft-Walton voltage multiplying principles and was designed and fabricated at LLNL. (3) It has an oscillation frequency of 100 kHz and maximum load capability of 5 mA and 300 kV. The voltage is applied across a conventional accelerating column, and the proton beam is magnetically analyzed and delivered to the x-ray target through electrostatic quadrupole focusing elements. The accelerating column and beam drift tubes are maintained at a pressure of  $\sim 2 \times 10^{-6}$  Torr during full beam loading by a 1500  $\ell$ /sec oil diffusion pump and a 1500  $\ell$ /sec turbomolecular pump, respectively.

The proton beam is provided by a standard rf ionization source and beam currents of 2.5 mA have been delivered on target in a spot size of less than 5 mm diameter. Smaller spot sizes are possible, but target heat loads are excessive under such conditions. The accelerator is also capable of accelerating heavier ions or electrons with only minor system modifications.

Three high-vacuum stainless steel experimental chambers are mounted in series at the end of the ac-

celerator drift tube (Figure 2). These chambers have metal vacuum seals and are evacuated to pressures of  $10^{-7}$  -  $10^{-8}$  Torr using a 500  $\ell$ /sec turbo-molecular

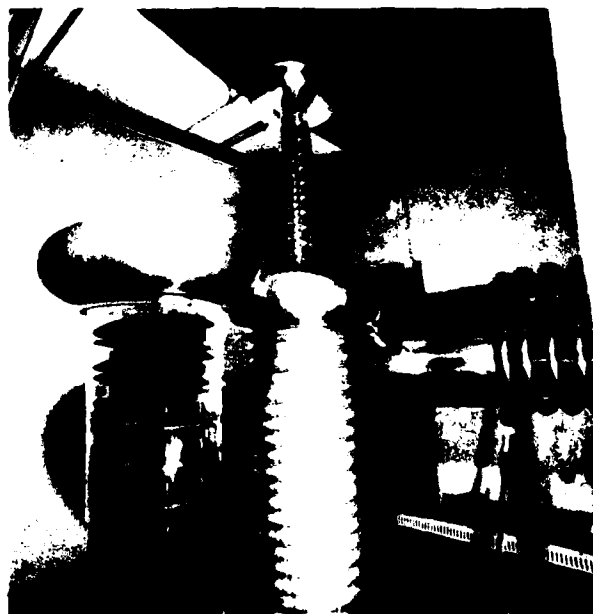


Fig. 3. Cockcroft-Walton voltage doubler and the accelerator stack.

pump on the target chamber and 1500  $\ell$ /sec turbo-molecular pumps on the others. Isolation of the chambers from the poorer vacuum environment of the accelerator beam tube is achieved by a low-conductance (6  $\ell$ /s), double-walled, LN-cooled cold trap mounted in the beam pipe at the entrance to the target chamber. This trap is designed to reduce hydrocarbon buildup on the x-ray target which, as will be discussed later, is a serious detriment to spectral purity in subkilovolt x-ray generators.

The x-ray target has two primary features:

a) heat dissipation of 5 kW/cm<sup>2</sup>, and b) capability of remote selection of one of several different target materials, and hence, characteristic photon energies. Seven target materials (Cu, Fe, Cr, Ti, C, B, Be) are deposited on the flat machined surface of a high-purity Cu cylinder to thicknesses ranging from 3 to 5 mg/cm<sup>2</sup>. (See Figure 4.) Water is flowed through the cylinder



Fig. 4. Water cooled target assembly with seven plated targets.

past the back of the targets to remove the heat dissipated in them by the incident protons. A system has been designed to not only conduct away the heat but to help reduce carbon buildup on the targets. This system, although not presently in use, utilizes a 50% mixture of ethylene glycol and water and is designed not only to dissipate up to 5 kW/cm<sup>2</sup> of target heat during beam loading conditions but also to maintain the target temperature at 115°C during beam-off conditions. The latter is achieved by heating the liquid and is an attempt to further reduce condensation of hydrocarbon contaminants on the target face. The liquid is flowed at 6  $\ell$ /min, through a closed-loop pump and heat exchanger system and is nozzled to pass the back of the targets with a turbulent velocity of 7.5 m/sec.

In addition to the seven target materials listed above we also can clamp on other metal targets to the target probe giving us different energy points. These clamp-on targets, some of which can be seen in Figure 5, rely on surface contact for cooling and since the heated targets tend to warp, they cannot be used with as high a beam current as the plated targets.

As a final step in minimizing carbon buildup a double-walled, LN-filled cylinder is mounted around the targets to serve as a hydrocarbon condenser. The target and condenser are electrically isolated to permit beam current measurements and to allow bias voltage suppression of secondary electron emission from the

target. The target assembly is vertically driven by a remotely-controlled stepping motor and will automatically position any pre-selected target in the proton beam.



Fig. 5. Target assembly with clamp on targets in place.

The target chamber geometry is designed to allow continuous monitoring of the x-ray flux with a proportional counter during calibration of an experimental detector. Both the experimental detector and a proportional counter monitor can be mounted symmetrically at an angle of 135° with respect to the incident proton beam direction. However, the x-ray emission is found to be isotropic only for very smooth targets (polished so that average peak-to-valley surface roughness is less than 0.05  $\mu$ m). Targets with rougher surfaces, e.g., 8  $\mu$ m, exhibit highly nonisotropic emission and preclude use of the output of the monitor detector in this position to derive the flux level incident on the experimental detector. Consequently, since target surface damage and roughness can readily occur at high current loads, it is impossible to assume isotropy in calibration procedures. Rather it would be necessary to frequently recheck isotropy or to monitor the incident flux by interspersing a proportional counter in place of the experimental detector.

To accomplish this, the detectors to be calibrated are mounted on a rotating table in the detector chamber and can be moved in and out of the x-ray beam. A proportional counter is mounted in the center of this chamber and can also be moved into or out of the x-ray beam. Thus, by moving the detector being calibrated out of the beam and placing the proportional counter into the beam, an accurate measurement of the incident x-ray flux can be made. This arrangement can be seen in Figure 6.

The proportional counters are side-window, cylindrical, gas-flow counters with 2.5 cm inside diameters, 25  $\mu$ m diameter tungsten anode wires and 0.25 mm diameter, 85  $\mu$ g/cm Parylene N entrance windows.

Helium-isobutane at atmospheric and also reduced pressure is used as the proportional counter gas.

Various thin foils are normally placed into the x-ray beam from the target. These foils serve several purposes. First, in some cases, they are opaque and shield the detectors from visible and infrared fluorescent and incandescent radiation emitted from the hot target. Optical pyrometer measurements have shown a carbon target to reach 1900°C during loading with a

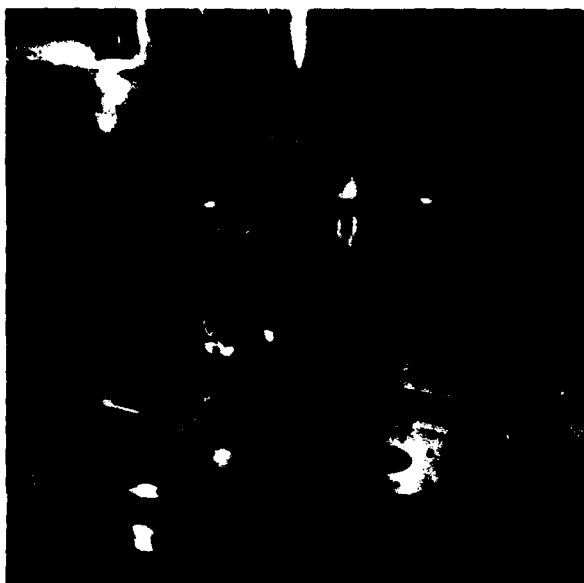


Fig. 6. View of the detector chamber interior.

2 mA proton beam. Second, they are thick enough to stop backscattered protons and hydrogen atoms. Buck et al. (4) have shown that for these proton energies (~300 keV) a large fraction of the backscattered projectiles are neutralized. Consequently, any attempt to remove recoil particles from the x-ray flux by electrostatic deflection techniques would only be partially successful. Hence, absorbing foils are necessary. Finally, in some cases the foils selectively absorb photons characteristic of carbon contamination on the target surface. This requires matching the x-ray absorption cross-section of the foil with the characteristic photon energies of carbon and of the target material to maximize the x-ray flux at the detector. All three functions are considered in selection of the proper foil-target combinations. For example, 600  $\mu\text{g}/\text{cm}^2$ , opaque, carbon foils are used with a carbon target and 500  $\mu\text{g}/\text{cm}^2$ , opaque Be foils are used with a copper target.

A third vacuum chamber mounted behind the experimental detector chamber houses a crystal diffractometer and gas flow proportional counter for high resolution spectrum analysis. Mounted behind this chamber on the end of the x-ray beam line is a windowless lithium drifted silicon detector. This Si(Li) detector has a resolution of approximately 109 eV at 5.9 keV and is isolated from the rest of the vacuum system by a liquid nitrogen cooled low conductance cylinder. This greatly reduces the buildup of contaminants on the windowless detector. This detector is useful for monitoring the beam purity.

Some of the performance characteristics of the facility can be seen in Table I. Listed are the most common targets, the photon energy and the approximate source strengths. These values are for a beam current of  $\leq 1$  mA and an accelerating voltage of 225 kV.

The beam purity is very good from clean targets. As the targets are used for a period of time a carbon buildup occurs which reduces the intensity of the characteristic line, but since filters are used, the spectrum remains relatively clean. Oxygen contamination has also been noticed from some targets and cannot be effectively filtered out and, thus, must be accounted for. Since for the accelerating voltages used, the L-shell photon yield is many orders of magnitude greater than the K-shell yield for the higher Z targets, the latter may be ignored with respect to the spectral purity of the x-ray source.

Table I. Targets, available energy and approximate source strengths for a proton beam  $< 1$  mA at 225 kV accelerating potential.

Target	Photon Energy (eV)	Source Strength (Photons/sec)
Be - k	109	$1 \times 10^{14}$
B - k	183	$1 \times 10^{14}$
C - k	277	$1 \times 10^{14}$
Ti - L	452	$3 \times 10^{12}$
Cr - L	574	$3 \times 10^{12}$
Fe - L	704	$3 \times 10^{12}$
Cu - L	932	$3 \times 10^{12}$

Present plans call for improving the rf hydrogen source on the accelerator allowing an increase in proton beam current. This coupled with a newly designed liquid cooled target assembly will allow us to increase our x-ray intensity.

#### COMPOUND GONIOMETER X-RAY FACILITY

In many applications a continuum source in the sub-kilovolt energy region is desired. One of these is the study of the critical angle reflection from smooth, flat, mirror surfaces. The x-ray facility shown in Figure 7 can provide such a continuum source and in addition incorporates a unique compound goniometer useful in critical angle reflector studies. The x-ray source is a Henke tube similar to that described previously and shown schematically in Figure 1. This x-ray source is coupled to an 84 cm diameter stainless steel vacuum chamber which houses the double goniometer system. A windowless Si(Li) detector is connected to this chamber to examine the x-ray beam. The vacuum chamber is roughed down by cryosorb pumps and pumped by a cryogenic pump. This pumping technique insures a very clean vacuum allowing pressures in the  $10^{-7}$  and  $10^{-8}$  Torr region. The primary goniometer assembly in the chamber is coupled via vacuum feedthroughs to a Siemens Omega Drive goniometer accurate to  $.001^\circ$ . The  $2\theta$  mechanism of the goniometer is connected to a rotary table in the chamber while the  $\theta$  mechanism connects to a crystal holder in the center of the rotary table. Mounted on the rotary table ( $2\theta$  mechanism of the primary goniometer) is a second  $\theta$ - $2\theta$  goniometer. This goniometer shown in Figure 8 was constructed using two rotary stages driven by stepping motors. These stages obtained from Klinger Scientific Corporation are accurate to  $.01^\circ$  (newer versions to  $.001^\circ$ ). The electronic chassis which controls these stages (shown in Figure 9) allows all of the typical goniometer modes, e.g.,  $\theta$  movement,  $2\theta$  movement,  $\theta$ - $2\theta$  movement. This chassis was designed and fabricated here at LLNL. A proportional counter is mounted on the  $2\theta$  arm of the secondary goniometer to measure the reflected or diffracted x-rays. The complete compound goniometer assembly with a mirror mounted in each of the goniometers is shown in Figure 10.

#### RESULTS

On the Ion Accelerator X-Ray Facility the typical calibration performed is the measurement of detector response or sensitivity as a function of energy. The high intensity monoenergetic x-rays produced in this facility are ideal for this type of measurement. The calibration curves shown in Figure 11 for the energy range below 1 keV were obtained using this facility. The detectors calibrated were of three types, an XRD or photoelectric diode, a plastic scintillator coupled to a photodiode and a silicon surface barrier semiconductor detector. The higher energy calibration points



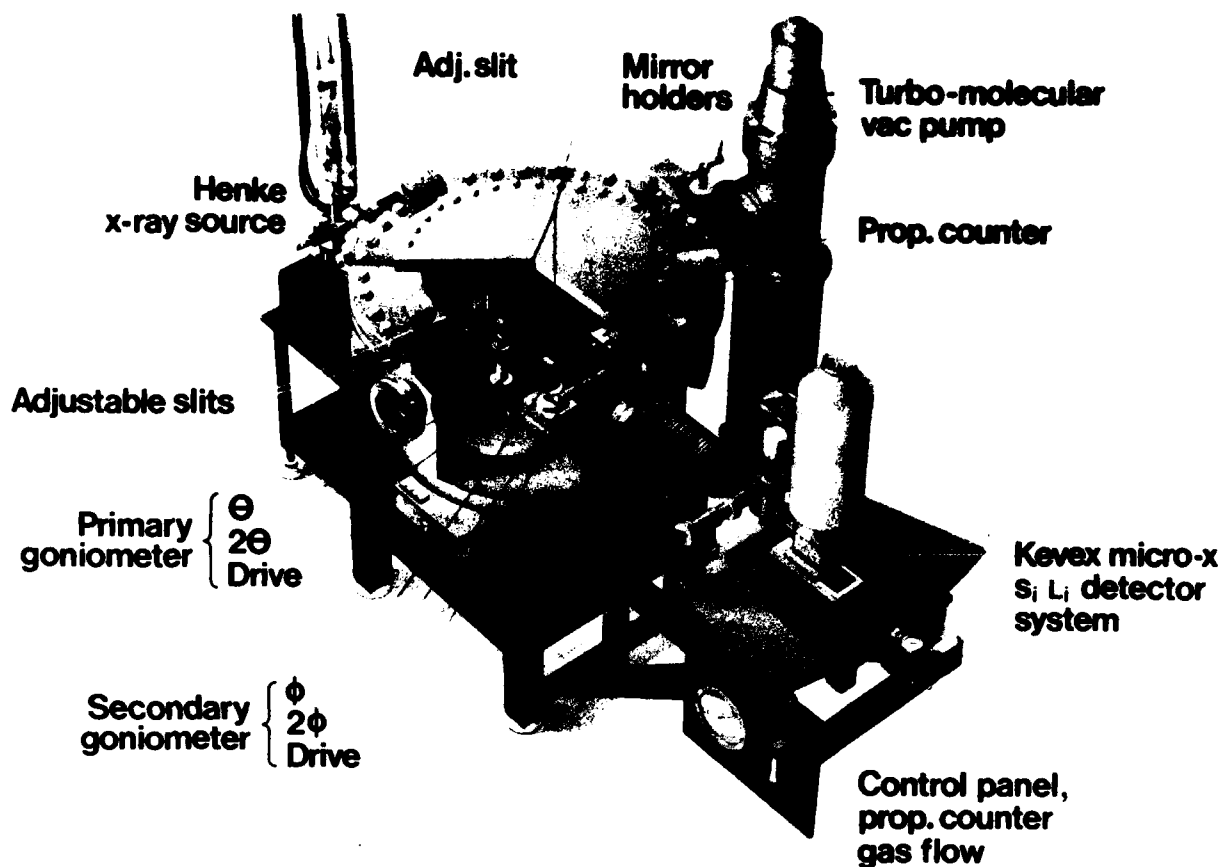


Fig. 7. Cut away view of the Compound Goniometer - Henke Tube Source Facility.

were obtained using other LLNL calibration facilities. Other types of calibrations can be performed using this facility including crystal and mirror or reflector calibrations.



Fig. 8. Rotary stages assembled into a  $\theta - 2\theta$  goniometer.

The primary calibrations that are performed using the Compound Goniometer, X-Ray Facility involve diffraction crystals and x-ray mirrors. The spectrum from the Henke tube is a continuum with characteristic anode lines and is ideal for this type of measurement. Shown graphically in Figure 12 is a calibration of an x-ray mirror. Figure 13 illustrates the results obtained when a continuum spectrum is reflected from two mirrors mounted on the compound goniometer. This technique has many applications. DREX (5), a spectrometer for spectral measurements in the subkilovolt energy range, makes use of the double mirror technique. The Compound Goniometer, X-Ray Facility can also be used for other

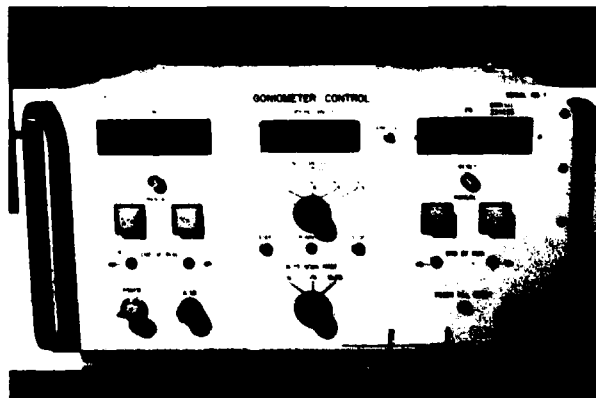


Fig. 9. Control unit for the  $\theta - 2\theta$  goniometer assembled using rotary stages.



Fig. 10. Overall view of the compound goniometer with two x-ray mirrors mounted in the goniometers.

types of calibrations. By adding fluorescers in the primary beam from the Henke tube as shown in Figure 1 and using absorption edge filters, fairly monoenergetic beams of x-rays can be obtained. Although the intensity of this fluorescent beam is less than the primary beam, and suffers the disadvantages mentioned previously, this technique allows certain measurements to be made that cannot be made with a continuum spectrum.

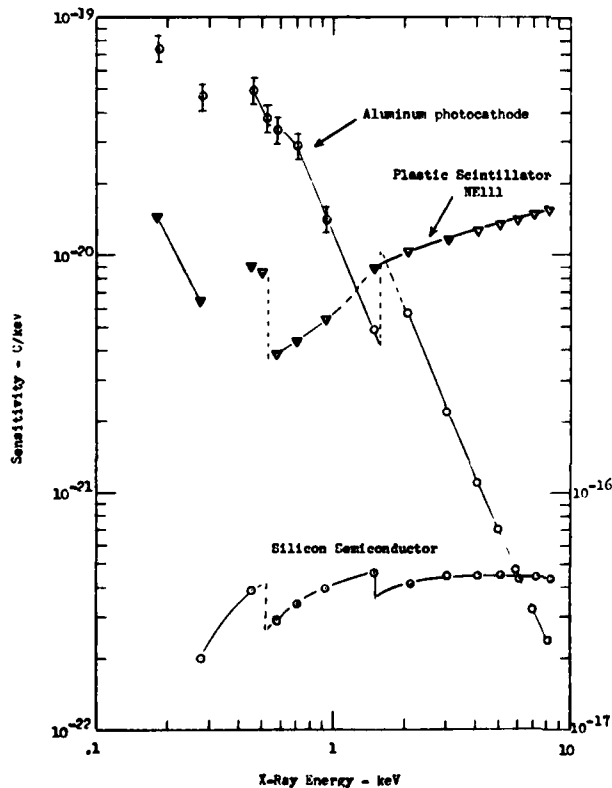


Fig. 11. Typical calibration data obtained using the Ion Accelerator - Subkilovolt X-Ray Facility.

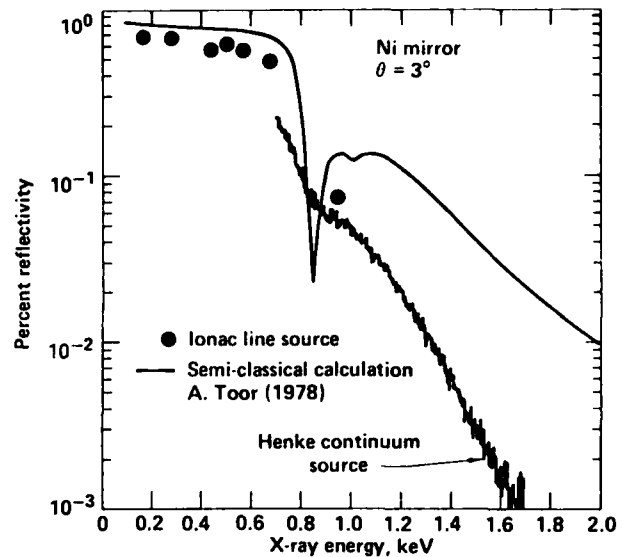


Fig. 12. Typical calibration data for an x-ray mirror.

#### ACKNOWLEDGEMENTS

The author wishes to acknowledge the many people who have contributed to the design, the fabrication and the operation of the facilities described in this paper. Dick Ernst, Tom Woerhle and Richard Penpraze have spent many hours operating and maintaining the Ion Accelerator - Subkilovolt X-Ray Facility as well as making major improvements to the facility. Earl Augusta and Richard Crabb accomplished the same tasks with regard to the Double Goniometer - Henke Tube Source Facility. Without their dedicated help these two facilities would not be able to perform the valuable functions they presently do.

#### REFERENCES

1. Gaines, J. L., Kuckuck, R. W., and Ernst, R. D., paper presented at ERDA Symposium on X- and Gamma Ray Sources and Applications, May 19-21, 1976, Ann Arbor, Michigan.
2. Henke, B. L., *Norelco Reporter*, Volume 14, Nos. 3-4 (1967), 75-83.
3. Reginato, L.L., and Smith, B.H., paper presented at the Particle Accelerator Conference, March 10-12, 1965, Washington, D.C. Also reported in LLNL report UCRL-11783, March 2, 1965.
4. Buck, T.M., Wheatley, G.H., and Feldman, L.C., *Surface Science*, Volume 35 (1973) 345-361.
5. Stoering, J. P., Crabb, R., McGee, M.E., and Burginyon, G.A. *Rev. Sci. Instruments*, 52(6), June 1981.

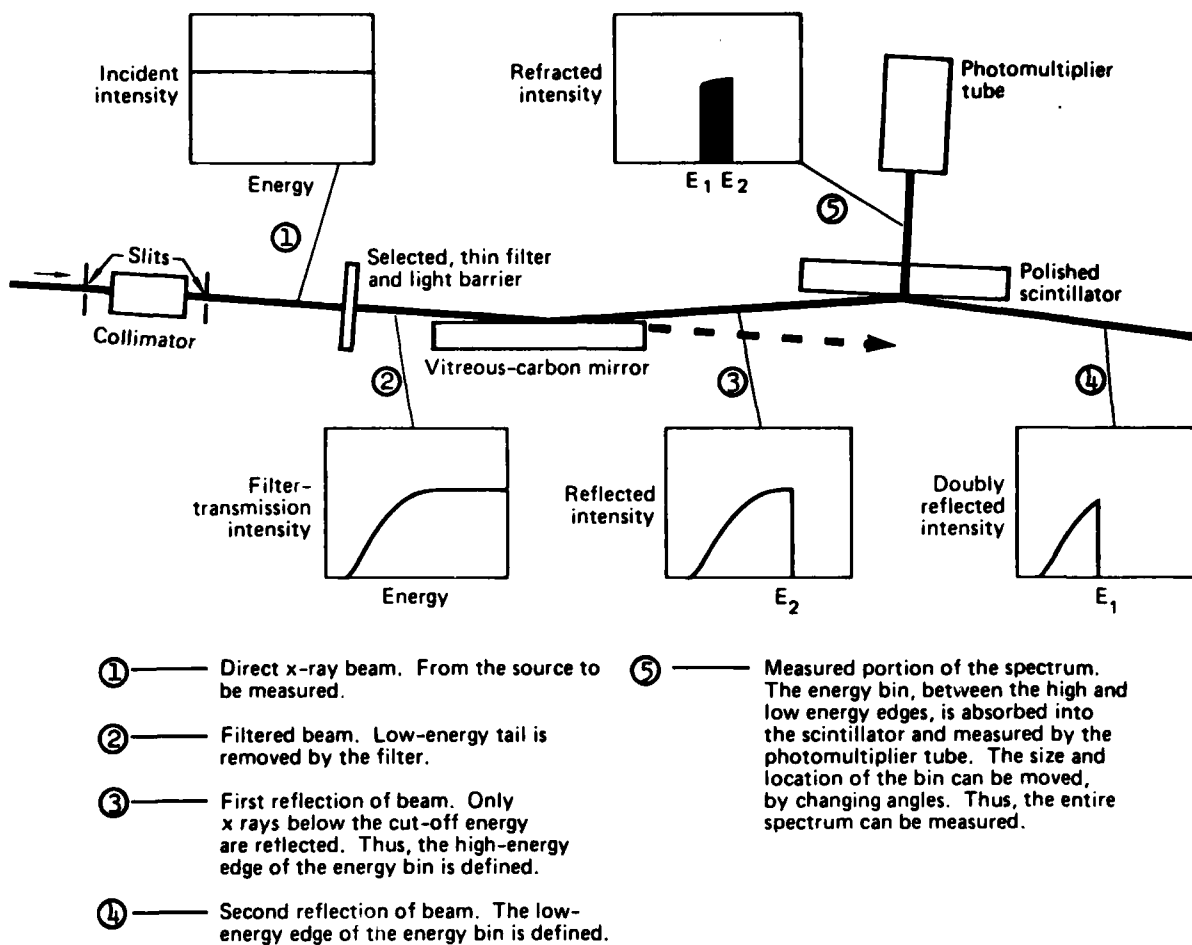


Fig. 13. Results obtained when a continuum spectrum is reflected from two x-ray mirrors mounted in the Compound Goniometer - Henke Tube Source Facility.



Session Chairman Jerry Gaines opening the Monday afternoon section on Detectors for Sub-kilovolt Radiation.

## CALCULATION OF SPECTRA FROM ELECTRON-IMPACT X-RAY SOURCES

D. B. Brown and D. J. Nagel  
 Naval Research Laboratory, Washington, D.C. 20375

Techniques and results for calculation of x-ray line and continuum spectra in the  $10^2$ - $10^6$  eV region are reviewed. Most attention is given to the variety of methods for computation of ordinary line and continuum spectra due, respectively, to bound-bound and free-free (bremsstrahlung) transitions. Recent work on coherent bremsstrahlung, channeling radiation and transition radiation is also noted.

## I. INTRODUCTION

X-ray tubes and other devices in which x-rays are produced by the impact of electrons on solid targets are widely used. Areas of application include radiography (for medical purposes and non-destructive testing of structures), analysis of the composition and structure of materials, study and production of radiation effects (including radiation therapy and x-ray lithography), and the calibration of instruments (for the above areas, for plasma diagnostics, and for astrophysical measurements).

Measurements of x-ray spectra from electron-impact sources have been published. A sample of the available publications can be found in references 1-7. However, the experiments are tedious and there are many parameters (electron energy, target material, incidence and emergence angles, etc.) Calculations of x-ray spectra can be performed quickly and cheaply with accuracy adequate for many applications.

This paper is a review of various methods of calculating both line and continuum spectra due to electron impact. There are two major divisions of this review. The first deals with the familiar inner-shell line and bremsstrahlung continuum spectra due to electron impact on solids. Models for spectral calculations and the parameters which go into them are surveyed. Then representative results are presented and compared with measurements. Work in this first area deals with the more "classical" x-ray spectra and has a long history. The second major part of the paper briefly reviews processes which are being given increasing consideration as x-ray sources. These include coherent bremsstrahlung, channeling radiation and transition radiation, which can be produced by either electrons or positrons. Long-wavelength spectra produced by electron impact on solids and x-ray spectra due to collisions of electrons with free fields are mentioned in the final section. Included there are general observations relevant to this survey.

## II. LINE AND CONTINUUM SPECTRA

## A. Calculation Methods

All models for the calculation of x-ray spectra need to be able to handle electron transport, x-ray generation, and x-ray transport. Three types of mathematical techniques have been used to accomplish these tasks. The simplest and least expensive are analytical models based on methods developed for use in x-ray fluorescence analysis and electron microprobe analysis (8,9). More complex are numerical solutions of the Boltzmann equation (10). This approach is more rigorous and flexible, but more expensive. Finally, Monte Carlo modeling may be used (11-13). This is the approach of choice for problems involving complex geometry (which justifies the increased cost of Monte Carlo calculations). A summary of the characteristics of each of these methods is given in Table I.

The analytical (semi-empirical) models have been most extensively applied and tested for use in electron microprobe analysis. In this field, which is principally concerned with lines (rather than continuum) these types of models are commonly referred to as the ZAF approach. The content of this name is based on the assumption that the problem can be separated into three independent parts. They are, the effect of target atomic number (Z) on x-ray generation, the effect of target material and geometry on the absorp-

TABLE I  
 Summary of The Three Main Techniques for Calculation of Electron Impact X-Ray Spectra

ELECTRON TRANSPORT	ORIGINS	COST	CAPABILITY
Semi-empirical	X-ray fluorescence and micro-beam probe analysis	Least expensive	Simple specimen geometry
Solution of Boltzmann equation	Radiation physics	Intermediate cost	Intermediate capability
Monte Carlo	Radiation physics	Most expensive	Best for complex geometry

tion (A) of radiation prior to emergence, and the contribution to line intensity due to fluorescence (F) by the bremsstrahlung continuum. This analysis of the problem is originally due to Castaing (14). More recent reviews have been given by Martin and Poole (8) and by Reed (9). In addition, Criss (15) has developed a semi-empirical model for the output intensity of an x-ray tube which he has applied to x-ray fluorescence analysis. Results from the Criss TUBE program (16) will be presented in Section IIC of this paper. Of the methods discussed in this paper, the semi-empirical methods are the most approximate. On the other hand, they are very closely tied to experimental data and, hence, their results are often very good.

Brown and coworkers (4,5,7,10) have used a numerical solution of the Boltzmann equation to solve the problem of electron transport within the target. Given the resulting electron distribution, the problems of x-ray generation and x-ray absorption can be solved. This approach is much more parallel to the actual physical processes of x-ray generation and can be expected to be more accurate than the ZAF model. Results from a transport equation program (TEP) will be presented also in Section IIC. The TEP has been applied to problems involving x-ray generation in planar (slab) targets.

The Monte Carlo approach to calculating x-ray production (13) is identical to that used in the TEP described above except that the electron transport is handled using a Monte Carlo calculation rather than by solving the Boltzmann equation. Exactly the same physics is included. There are two exceptions to this assertion which may be important. First, those Monte Carlo codes designed to operate in the very high energy region (above about 1 MeV) may handle x-ray transport with a Monte Carlo calculation in order to treat Compton scattering. X-ray transport below the Compton scattering region will be discussed in Section IIB, below. Secondly, what we have said about Monte Carlo codes applies to those using the "condensed history" approximation (13). There is some work with codes which attempt to follow individual scattering and energy loss interactions. These codes are costly to run, but they have unique features for some problems. Examples of such calculations are found in the work of Shimizu and coworkers (17,18). There are a number of computer codes which calculate x-ray generation using the condensed history approximation. Among the better known are ETRAN (11,12) and SANDYL (19). We will quote some of the results of ETRAN in Section IIC.

### B. Physical Processes

Each of the three major calculation methods treats, in greater or lesser degree of approximation, seven physical processes. These seven processes, and something of the interrelation between them, are indicated in Fig. 1.

We have briefly discussed electron transport calculation methods in Section IIA. All of the transport calculation methods need a formulation for electron energy loss. A simple formulation for electron energy loss which is frequently useful (14) is

$$dE/dx = -1840\beta^{-1.4} \rho(ZZ/A) \quad (1)$$

where  $E$  is the electron energy in kev and  $x$  is the distance along the electron trajectory in cm. Also,  $\beta = v/c$  where  $v$  is the electron velocity (cm/sec), and  $\rho$  is the target density (gm/cm<sup>3</sup>). Further treatment of this problem can be found in references 20-22. The Boltzmann equation and Monte Carlo treatments of electron transport also require a formulation for electron scattering. The most simple relationship for electron scattering is the screened Rutherford cross section (10)

$$\sigma(\alpha) = (Z^2 e^4 / 4m^2 v^4) (\sin^2(\alpha/2) + \gamma^2)^{-2} \quad (2A)$$

where  $\sigma$  is the cross section for scattering through angle  $\alpha$ . The damping factor  $\gamma$  may be found from

$$\gamma = 0.21 v (Z^{1/3} / E^{1/2}) \quad (2B)$$

where  $v$  is an empirical constant of the order of one. Further treatment of electron scattering can be found in the review of Massey (23).

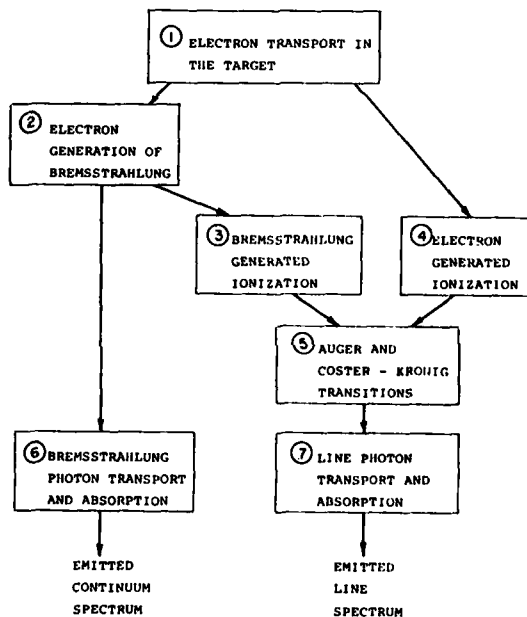


Fig. 1. The seven physical processes which must be treated in the calculation of electron-impact x-ray spectra.

Cross sections for bremsstrahlung generation by electrons have been calculated with a fair amount of rigor in recent years and have been published in tabular form by Pratt and coworkers (24,25). An equation which is a fit to the more approximate Sommerfeld solution has been presented by Kirkpatrick and Wiedmann (26). A very simple equation for bremsstrahlung production which is often useful (27) is

$$I_E = 2.76 \times 10^{-6} Z (E_0 - E) \quad (3)$$

where  $I_E$  is the kev generated per kev energy interval per incident electron of energy  $E_0$ . Note that Eqn. 3 gives a spectral distribution which must be corrected for absorption of photons on their path out of the target. Note also that Eqn. 3 implies that the spectral distribution (prior to absorption) is isotropic. This is a fair first approximation for targets which are thick to electrons because the electrons are highly scattered and thus assume a roughly isotropic distribution. This is not a good approximation for electrons incident on an electron-thin foil. Results for such a case will be quoted below. A review, now somewhat dated, of bremsstrahlung cross section theory and data has been presented by Koch and Motz (28). It is not easy to assess the accuracy of the available bremsstrahlung cross sections. Some comparison with experimental data is given in the references already cited. Also we will compare the results of using some of these cross sections in Section IIC. Additional comparisons can be found in references 5 and 7.

Cross sections for inner shell ionization by electrons have been most recently reviewed by Powell (29). A simple equation for the cross section which has frequently been useful (27) is

$$Q_{KK} E_K^2 = 7.92 \times 10^{-20} U^{-1} \ln U \quad (4)$$

where  $Q_K$  is the K-shell ionization cross section in cm<sup>2</sup>,  $E_K$  is the K-shell ionization energy in kev, the overvoltage  $U = E/E_K$ , and  $E$  is the electron energy. The cross section for  $L_I$  and  $L_{II}$  shells is similar, while for  $L_{III}$  shells the constant should be doubled.

For high overvoltages, the treatment of Kolbenstvedt (30) may be useful. There is very little data available for testing the available cross sections for K-shell ionization, still less for L-shell ionization, and none for higher shells. Additional discussion of ionization cross sections may be found in references 4, 27, and 31. A comparison with experimental data of the results of using several of the available cross sections is given in Section IIC. Additional comparisons are to be found in reference 4.

Line generation due to fluorescence by the continuum has been treated in some detail in the literature. Cosslett and Green (27) have given a fairly simple treatment. A more elaborate presentation, designed for use in microbeam probe analysis has been given by Henoc (32). The contribution to line intensity is typically less than a few percent for electron energies of 50 kev and below, but may constitute a major fraction of the line intensity for electron energies of 500 kev and up.

After the initial ionization by electron impact or by bremsstrahlung fluorescence, the various L, M, etc. subshell ionizations undergo reorganization by Coster-Kronig processes. In addition, only a fraction of the energy stored in inner shell ionizations is transferred to line photons. The remaining energy is carried away by Auger electrons. The most current review of the interaction coefficients necessary to treat these processes is that of Bambynek and coworkers (33). The K-shell coefficients for atomic numbers below about 10 and the L-shell coefficients for atomic numbers below about 30 are questionable.

Photons of energies below about 1 MeV (or perhaps a bit lower for low atomic numbers) may reasonably be assumed to travel along straight line paths while being attenuated by photoelectric absorption. The attenuation may be treated using the usual exponential falloff relationship. Tabulations of attenuation coefficients which may prove useful are references 34-38. It should be noted that only some of tabulations are available in a form convenient for computer usage; only some are useful below 1 kev; and only some contain scattering coefficients along with the photoelectric absorption

coefficients. Care is required in the choice of the most reliable tabulation to be used for a given problem.

### C. Sample Data

We will now present a comparison with experimental data of the calculation methods outlined in Section II. Figure 2 compares results of TUBE program calculations for low atomic number targets at low electron beam energies with corresponding measurements. This figure demonstrates the dependence of line intensity on electron beam energy. Although the electron energy dependence shows the same shape for calculation and experiment, the absolute magnitude of the intensities differ by a maximum of about a factor of two for Al  $K_{\alpha}$ . The reason for this disagreement is not known.

Figures 3 and 4 present  $K_{\alpha}$  and  $L_{\alpha}$  intensities as function of the energy of the line. Intensities calculated by the TUBE and TEP programs are compared with low energy line measurements. The factor of

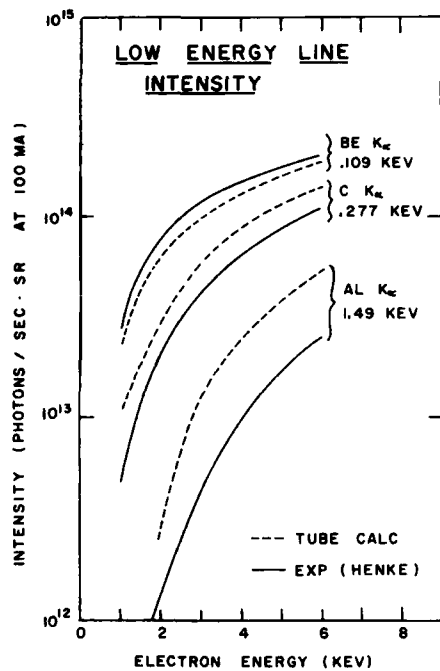


Fig. 2. The intensity of several low energy lines versus the energy of the incident electrons. The solid lines are the data of Henke (39,40). The dashed lines are the calculations of the TUBE program.

two disagreement with Henke's Al data (at 1.5 keV) is observed again. Note that the TUBE and TEP programs give about the same answer for this Al data. It will be observed, on the other hand, that the agreement between calculations and the x-ray tube measurements is within 30%.

Figures 5-8 give similar comparisons for continuum intensities. In Figures 5, 6, and 7 we present TEP and TUBE program calculations of the continuum from Cr, Rh, and W target x-ray tubes operated at 45 KV, compared with available experimental data. The agreement between calculation and experiment is seen to be quite good (within 30%). Also in Figs. 5-7 we have given an indication of the effect of a window on the low energy output of a sealed x-ray tube.

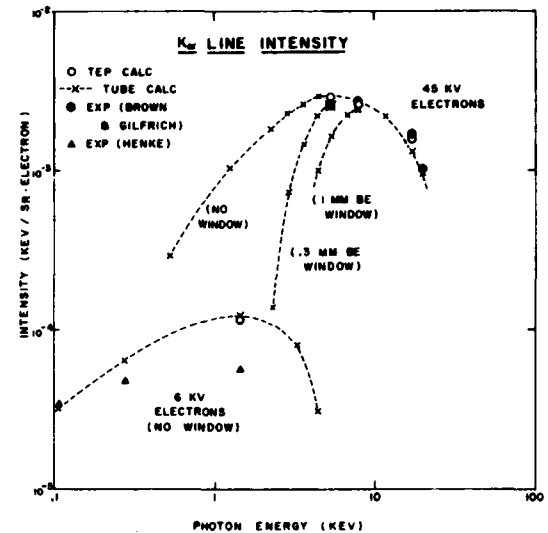


Fig. 3. The intensity of several  $K_{\alpha}$  lines versus the energy of the line. The open circles and the dashed lines represent the calculations of the TEP and TUBE programs, respectively. The solid hexagons and triangles are experimental data from Brown and Gilfrich (4) and from Henke (39, 40) respectively.

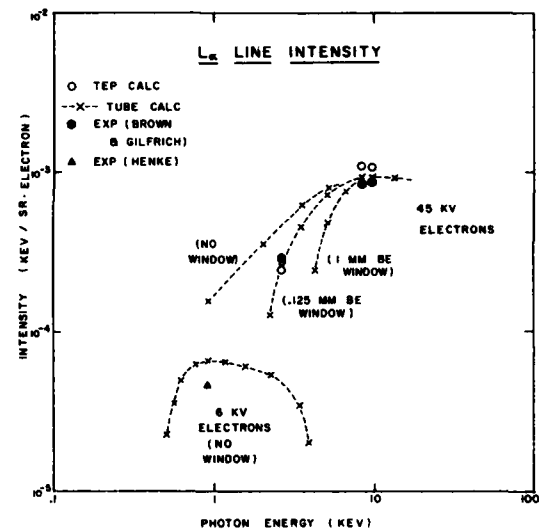


Fig. 4. The intensity of several  $L_{\alpha}$  lines versus the energy of the lines. The symbols in this figure have the same significance as in Fig. 3.

Figure 8 shows TEP calculations, ETRAN calculations (11), and the experimental data of Baggerly et al. (1) for the continuum from a  $1.878 \text{ gm/cm}^2$  (7.0 mm) thick slab of Al bombarded with 2 MeV electrons. Note that there is only agreement within about a factor of three. The reason for the disagreement is not known. Further experimental and theoretical work would be necessary to reduce the gap. For these experiments and calculations, the electron beam was incident normal to the surface of the Al foil. The quoted measured spectrum was for a  $15^\circ$  angle with respect to the exiting electron beam. This is a case where the escaping bremsstrahlung spectrum is highly anisotropic.

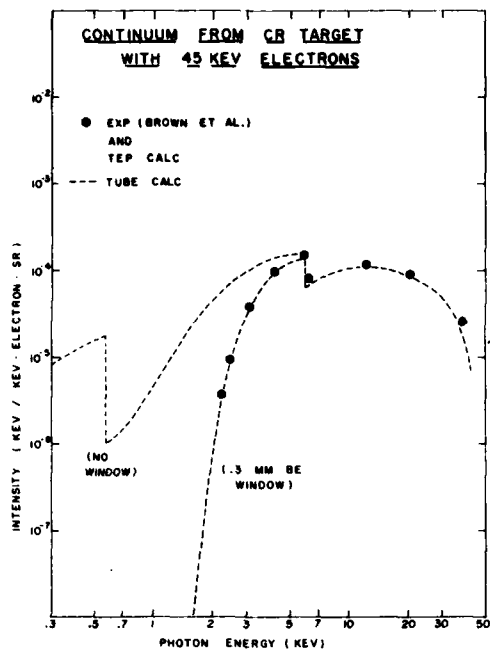


Fig. 5. The continuum spectrum intensity from Cr targets bombarded with 45 keV electrons. The dashed lines show the calculations of the TUBE program. The solid hexagons represent both TEP program calculations and the experimental data of Brown et al. (7).

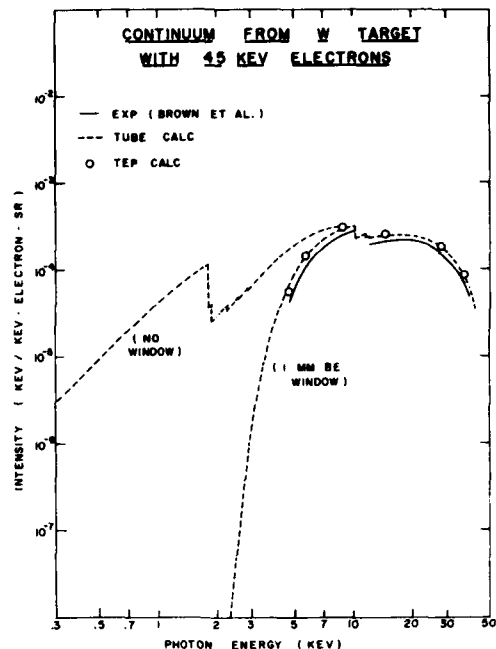


Fig. 7. The continuum spectrum intensity from W targets bombarded with 45 keV electrons. The solid lines represent the experimental data of Brown et al. (7). The dashed lines represent the calculations of the TUBE and TEP programs, respectively.

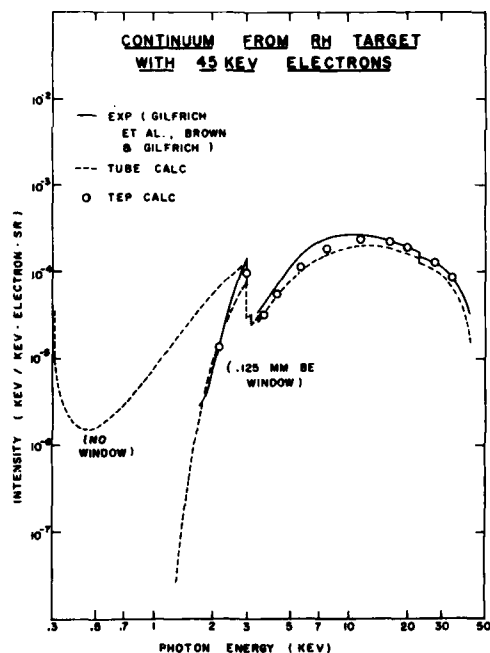


Fig. 6. The continuum spectrum intensity from Rh targets bombarded with 45 keV electrons. The solid lines represent the experimental data of Gilfrich et al. (41), normalized using the experimental data of Brown and Gilfrich (4). The dashed lines and open circles represent the calculations of the TUBE and TEP programs, respectively.

The calculated intensity is down an order of magnitude at  $60^\circ$  and down two orders of magnitude at  $120^\circ$  with respect to the existing electron beam. This anisotropy is not due to absorption, but rather to the fundamental anisotropy of the bremsstrahlung generation process.

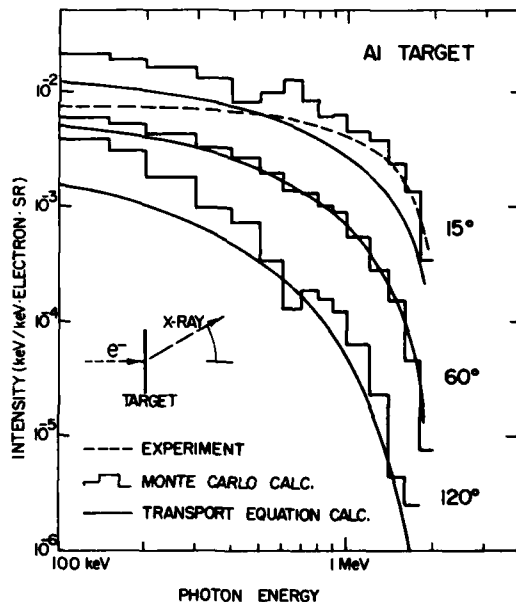


Fig. 8. Continuum spectrum intensities from a thin Al target bombarded with 2 MeV electrons. This figure is patterned after one due to Berger and Seltzer (11) who compared their ETRAN Monte Carlo calculations (histogram) with the experimental data of Baggerly et al. (1) (dashed lines). We have added calculations made with the TEP program (solid lines).

In Fig. 9 we present TEP program calculations of the continuum spectrum of a thick W target bombarded at a  $45^\circ$  incidence angle with electrons of 45, 100, and 500 keV. The emergence angle was also  $45^\circ$ . In Table II we summarize the total output in continuum, K lines, and L lines.

TABLE II  
Computed X-Ray Output from a Tungsten Target

ELECTRON ENERGY	CONTINUUM OUTPUT	K-LINE OUTPUT	L-LINE OUTPUT
45	$2.35 \times 10^{-4}$		$.71 \times 10^{-4}$
100	$4.11 \times 10^{-4}$	$.15 \times 10^{-4}$	$.69 \times 10^{-4}$
500	$16.5 \times 10^{-4}$	$1.38 \times 10^{-4}$	$.12 \times 10^{-4}$

(The output is in units of kev per steradian out per kev of electron energy input)

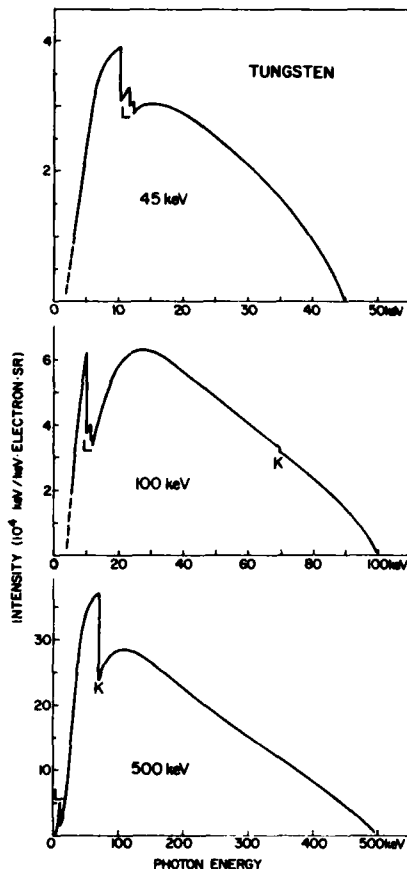


Fig. 9. Continuum spectral intensities from a W target bombarded with 45, 100, and 500 keV electrons. The electron incidence angle and the photon emergence angle were both  $45^\circ$ .

### III. OTHER ELECTRON-IMPACT SPECTRA

The classical line and ordinary bremsstrahlung continuum spectra discussed in the last section were the first x-ray spectra generated and have been heavily studied as well as used. Other, less-familiar x-ray spectra produced by the impact of electrons (and positrons) on solids are reviewed briefly in this section. Coherent bremsstrahlung and channeling radiation, treated in the next two subsections, are conceptually distinct but closely related. They can be produced in the same experiment and are observed to overlap each other. They are discussed separately here because the literatures on such spectra are generally distinct; studies of these spectra have very different histories. Transition radiation is the third topic treated in this section.

#### A. Coherent Bremsstrahlung

Nowadays, the word "coherent" brings to mind laser radiation, but coherent bremsstrahlung is not produced by stimulated emission. Ordinary bremsstrahlung arises

from the interaction of an electron with the field of a single nucleus. That is, contributions from other nuclei are separate and one adds intensities to get the total radiation field. Coherent bremsstrahlung is due to interaction of an electron with the fields of two or more nuclei, when the collision frequency is comparable to the frequency of the emitted radiation. For relativistic electrons with velocity near  $c$ , passing atoms at ordinary spacings, the collision frequency of  $10^{18}$  Hz corresponds to x-ray energies. In this case, amplitudes from the various collisions have to be added (coherently, that is, with proper attention to phases) in order to compute the emitted intensity. Coherent bremsstrahlung spectra from crystalline targets have shapes which reflect the character of the target. Electrons travelling in crystals, even at very high energies, are Bloch waves which have energy-momentum relations (energy bands) due to diffraction from the lattice. Electron momenta before and after the interactions which generate coherent bremsstrahlung are related by reciprocal lattice vectors, as in ordinary electron and x-ray diffraction. This constraint introduces structure into coherent bremsstrahlung spectra. They consist of peaks, in contrast to the smooth continuum of ordinary bremsstrahlung.

The ideas fundamental to coherent bremsstrahlung began with the work of Williams in 1935 (42). Two decades later, Uberall computed spectra (43) which lead to development and use of sources of coherent bremsstrahlung. Such spectra have been of greatest interest in high-energy physics since approximately monochromatic beams of very energetic (GeV) photons can be produced with proper attention to crystal orientation and beam collimation (44). Coherent bremsstrahlung in the few keV range has been observed with electrons in 30-80 keV range incident on LiF crystals about 0.1 mm thick (45). Coherence effects on bremsstrahlung production have been reviewed (46,47).

The theory and calculation of coherent bremsstrahlung spectra are well developed (43,44,46). An example of a calculated spectrum with intermediate electron and photon energies is given in Fig. 10 (48). Measured spectra do not contain the sharp features shown in Fig. 10 due to electron scattering (45, 46).

The theory and calculation of coherent bremsstrahlung spectra are well developed (43,44,46). An example of a calculated spectrum with intermediate electron and photon energies is given in Fig. 10 (48). Measured spectra do not contain the sharp features shown in Fig. 10 due to electron scattering (45, 46).

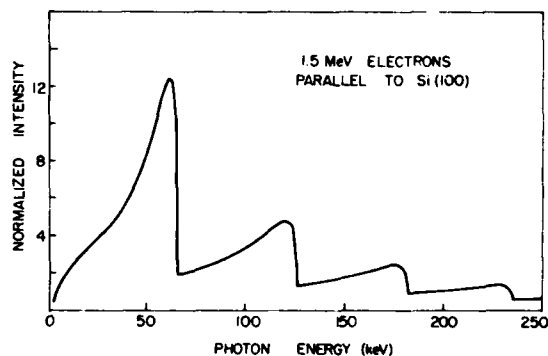


Fig. 10. Coherent bremsstrahlung spectrum computed for 1.5 MeV electrons moving parallel to the (100) direction in single crystal silicon (48). The units of intensity are  $(E/\sigma_0) (d\sigma/dE)$  where  $E$  is the photon energy,  $\sigma_0$  is the Thomson scattering cross section and  $\sigma$  is the coherent bremsstrahlung cross section.

#### B. Channeling Radiation

When electrons or positrons are shot into highly-perfect crystals with little spread about the precise directions of lines or planes of atoms, the conditions are correct for production of channeling radiation in



the x-ray region. In all cases (electrons or positrons, atomic strings or planes), the charged particles find themselves in potential wells with quantum levels between which transitions in the x-ray region can occur. Electrons travelling along and oscillating around rows or planes of atom cores are bound in two or one dimension by the positive charges of the nuclei. The potential is cusp shaped, with series of unevenly-spaced levels, transitions between which yield several x-ray peaks. Positrons travelling along and oscillating between planes of atoms are repulsed by the sheets of positive nuclear charge. They experience a potential which is approximately harmonic. It has almost evenly-spaced energy levels, so that the channeling radiation spectra from positrons consists of a single peak which is the superposition of various transitions. Figure 11 gives schematic potentials and measured spectra for channeled leptons (49).

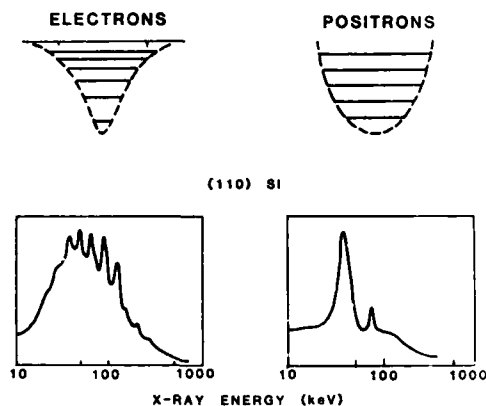


Fig. 11. Schematic potentials and energy levels (top) and measured spectra (bottom) for electrons (left) and positrons (right) channeled by silicon (110) planes (49). The right-hand peak in the positron spectrum is extraneous (it is Pb K radiation from shielding).

The history of ion and lepton channeling has been reviewed (50). The experimental study of radiation emitted by channeled leptons is comparatively recent. Spectra were first obtained with the use of positrons (51) and then electrons (52). Particle energies in the initial work were in the range of tens of MeV with peaks in the x-ray spectra occurring primarily in the 50 to 200 keV region. More recently, electron energies near 1-4 MeV were employed to yield channeling radiation spectra as a function of the particle incidence angle relative to the crystalline lattice (53).

The theory of channeling radiation is just the theory of spontaneous transition between bound states. Given the potentials, the energy levels and transition energies are calculable. The reverse procedure has been employed, in which measured peaks were used to obtain potentials for planar (54) and axial (55) channeled electrons. Such empirical potentials should be compared with potentials computed from electron distributions available from x-ray diffraction measurements or solid-state theory (56). The intensity calculated for 2p-1s transitions of 4 MeV electrons in Si (111) was found to be consistent with measurements assuming a maximum 2p state population of 5% (53). Spectra computed for 56 MeV electrons in Si (110) planes were also found to agree with experiment (57).

Channeling radiation is due to bound-to-bound transitions. Free-to-bound transitions for channeled electrons are possible in principle, although they have not been observed. They link the transitions measured so far with channeled electrons to the free-to-free transitions giving rise to bremsstrahlung. A single formulation including both coherent bremsstrahlung and channeling radiation is possible (H. Uberall, private communication).

### C. Transition Radiation

When an energetic electron or positron encounters an interface between vacuum or gas and a solid, or the interface between two solids, it experiences a change in potential which leads to the generation of transition radiation. Conceptually, the mechanism for production of transition radiation is similar to that for ordinary bremsstrahlung but the geometry of the accelerating field is different. Another way to view the generation of transition radiation is to consider the disappearance of the dipole formed by the approaching particle and its mirror charge as the particle penetrates the interface.

The initial theoretical study of transition radiation was reported in 1946 (58). Only in the 1960's did significant experimental observations of this radiation become available. Interest in detectors for GeV-range electrons and positrons which would exploit transition radiation was high in the 1970's. Periodic multiple-foil as well as single-foil radiations were studied (59,60). Photon energies ranging up to and beyond 100 keV were obtained with high-energy (GeV) leptons. Recently, low electron energies (3-10 keV) were employed to produce transition radiation spectra in the 6-10 eV region (61).

The theory of transition-radiation emission is well developed (47). Theoretical calculations are often made in conjunction with measurements (59,60). In the recent past, the possibility of employing microstructures with multiple thin ( $\sim 10 \mu\text{m}$ ) layers was explored computationally (62). Fig. 12 gives a spectrum from the work. Structure due to coherence effects is evident. Electron scattering and interface roughness are expected to produce smoother experimental spectra.

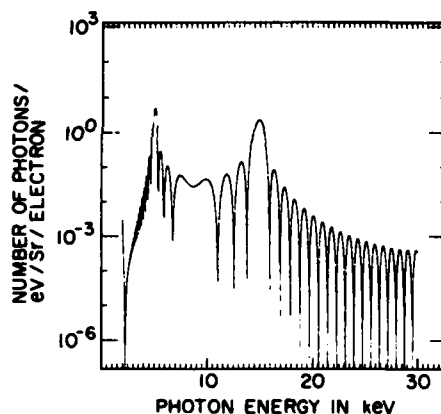


Fig. 12. Computed transition x-ray spectrum for 4.5 GeV electrons penetrating 28 pairs of 22.7  $\mu\text{m}$  lithium and 7.4  $\mu\text{m}$  carbon foils (62).

Conceptually, as the layer thickness decreases to that of ordinary crystal lattice dimensions and as the incidence angle changes from  $90^\circ$  (normal) to  $0^\circ$ , the situation for generation of transition radiation should go over into that for emission of bremsstrahlung and channeling radiation. Production of a unified theory of x-radiation emission by electron and positron impact on solids remains for the future.

### IV. DISCUSSION

Examination of the work reviewed above leads to some general observations on the status of capabilities for the calculation of impact-generated x-ray spectra, and makes clear what might be done to further the field. The situations for ordinary line and bremsstrahlung spectra and for coherent bremsstrahlung, channeling radiation and transition radiation are summarized in the next paragraphs. Other related work is mentioned at the end.

Concerning computation of line and ordinary bremsstrahlung emission, a variety of means exists to calculate spectra with accuracy adequate for many uses. There is a clear tradeoff between the versatility and cost (complexity) of the various approaches. At present, the codes have been applied primarily to relatively simple geometries with well-defined electron incidence angles and x-ray emission directions. Some of the codes can be applied to more complex situations, such as the generation of x-rays by beta rays from radioactive sources (63). We have discussed steady-state sources, although the various x-ray generation codes can be used to produce flash x-ray spectra if the time histories of the electron voltage and current are known. This has been done with the Boltzmann transport code (64).

Concerning the other types of x-ray spectra due to the impact of leptons on solids, a great deal of progress has been made both theoretically and experimentally in recent years. It should be possible to produce a comprehensive theory which would include all the types of spectra discussed. Input variables to a specific calculation would be the presence and distribution of matter, and its or other fields. The resulting unification of much of modern photonics would be intellectually satisfying. It might also be practically important if channeling radiation and transition radiation from multilayers prove to be usefully bright or otherwise unique x-ray sources. Experiments in the near future will show how sources based on these mechanisms compete with bremsstrahlung, synchrotron radiation and plasma sources.

Several useful reviews of x-ray sources are available. One concentrates on rotating-anode sources (65). Another review compares conventional and synchrotron-radiation sources (66). Electron-impact and plasma flash x-ray sources have been surveyed also (67). Recent work aimed at the development of x-ray lasers, including a comparison of synchrotron radiation, plasma radiation and potential x-ray laser intensities, is available (68).

We have discussed x-ray spectra produced by the impact of electrons and positrons on solids. It is worth noting that impacts on solids also produce longer-wavelength spectra. Cherenkov radiation due to the passage of very fast particles through matter is one example. The predicted but not-observed emission of shock radiation due to the simultaneous presence of a laser radiation field and matter is a second instance. We also pause to observe that the presence of matter with its associated fields is not necessary for the production of x-ray spectra by electrons and positrons. The collision of leptons with externally-applied fields is well-known to yield x-ray continua. Magnetic bremsstrahlung, usually called synchrotron radiation, is a major example. The collision of leptons with low-energy photons will produce x-ray spectra by the inverse Compton mechanism. Free-electron lasers operate on the basis of stimulated inverse Compton scattering, where the photon field is sometimes produced by the Lorentz transformation (into the moving frame of the lepton) of a static magnetic field. Operation of a free-electron laser at x-ray wavelengths is possible in principle, but will be difficult to demonstrate. Recent work on free-electron lasers and related topics is conveniently available in book form (69).

#### Acknowledgements

This review resulted from a conversation with D. I. Attwood; we appreciate his catalysis. Receipt of unpublished information from and helpful conversations with R.H. Pantell, A.W. Saenz and H. Uberall are gratefully acknowledged.

#### REFERENCES

1. L. L. Baggerly, W. E. Dance, B. J. Farmer, and J. H. Johnson, Second Symposium on Protection Against Radiations in Space, Gatlinburg, TN, Oct. 12-14, 1964, A. Reetz Jr., Ed., Publication No. NASA SP-71 (National Aeronautics and Space Administration, 1965)
2. R. C. Placious, *J. Appl. Phys.* **38**, 2030 (1967).
3. M. Green and V. E. Cosslett, *Brit. J. Appl. Phys. (J. Phys. D)* **1**, 425 (1968).
4. D. B. Brown and J. V. Gilfrich, *J. Appl. Phys.* **42**, 4044 (1971).
5. L. S. Birks, *Analytical Chem. Annual Reviews* **44**, 557R (1972).
6. T. S. Rao-Sahib and D. B. Wittry, *J. Appl. Phys.* **45**, 5060 (1974).
7. D. B. Brown, J. V. Gilfrich, and M. C. Peckerar, *J. Appl. Phys.* **46**, 4537 (1975).
8. P. M. Martin and D. M. Poole, *Metallurgical Reviews*, **19** (1971).
9. S. J. B. Reed, *Review of Physics in Technology* **2**, 92 (1971).
10. D. B. Brown, D. B. Wittry, and D. F. Kyser, *J. Appl. Phys.* **40**, 1627 (1969).
11. M. J. Berger and S. M. Seltzer, Second Symposium on Protection Against Radiations in Space, Gatlinburg, TN, Oct. 12-14, 1964, A. Reetz Jr., Ed., Publication No. NASA SP-71 (National Aeronautics and Space Administration, 1965).
12. M. J. Berger and S. M. Seltzer, *Phys. Rev.* **C2**, 621 (1970).
13. M. J. Berger, in Methods in Computational Physics, Vol. 1, B. Alder et al., Eds. (Academic Press, New York, 1963) p.135ff.
14. R. Castaing in Advances in Electronics and Electron Physics, L. Marton and C. Marton, Eds. (Academic Press, New York, 1960) p.317ff.
15. J. W. Criss, L. S. Birks, and J. V. Gilfrich, *Anal. Chem.* **50**, 33 (1978).
16. J. W. Criss and D. B. Brown, to be published.
17. R. Shimizu, Y. Kataoka, T. Ikuta, T. Koshikawa, and H. Hashimoto, *J. Phys. D: Appl. Phys.* **9**, 101 (1976).
18. I. Adisida, R. Shimizu, and T. E. Everhart, *J. Appl. Phys.* **51** (1980).
19. H. M. Colbert, Report No. SLL-74-0012 (Sandia Laboratories, May 1974).
20. M. J. Berger and S. M. Seltzer, Publication No. NASA SP-3012 (National Aeronautics and Space Administration, 1964).
21. Studies in Penetration of Charged Particles in Matter, Nuclear Science Series Report No. 39, NAS-NRC Pub. 1133 (National Academy of Sciences, Washington, 1964).
22. D. B. Brown, in Handbook of Spectroscopy, Vol. 1, J. W. Robinson, Ed. (CRC Press, Cleveland, 1974) p.249ff.
23. H. S. W. Massey, in Advances in Electronics, Vol. 4, L. Marton, Ed. (Academic Press, New York, 1952) p.2.
24. C. M. Lee, L. Kissel, and R. H. Pratt, *Phys. Rev.* **A13**, 1714 (1976).
25. R. H. Pratt, H. K. Tseng, C. M. Lee, L. Kissel, C. MacCallum, and M. Riley, *Atomic Data and Nuclear Data Tables* **20**, 175 (1977)
26. P. Kirkpatrick and L. Wiedmann, *Phys. Rev.* **67**, 321 (1945)
27. M. Green and V. Cosslett, *Proc. Phys. Soc.* **78**, 1206 (1961)
28. H.W. Koch and J.W. Motz, *Rev. Mod. Phys.* **31**, 920 (1959)
29. C. J. Powell, *Rev. Mod. Phys.* **48**, 34 (1976).
30. H. Kolbenstvedt, *J. Appl. Phys.* **46**, 2771 (1975).
31. D. B. Brown, in Handbook of Spectroscopy, Vol. 1, J. W. Robinson, Ed. (CRC Press, Cleveland, 1974) p.248.
32. J. Henoc, in Quantitative Electron Probe Microanalysis, K. F. J. Heinrich, Ed., Special Pub. No. 298 (National Bureau of Standards, Oct. 1968).
33. W. Bambynek, B. Craseman, R. W. Fink, H. J. Freund, H. Mark, C. D. Swift, R. E. Price, and P.

- V. Rao, *Rev. Mod. Phys.* **44**, 716 (1972).
34. F. Briggs and R. Lighthill, Report No. SC-RR-710507 (Sandia Laboratories, Albuquerque, NM, Dec. 1971) pp.149.
  35. W. H. McMaster, N. Kerr DelGrande, J. H. Mallett, and J.H. Hubbell, Report No. UCRL-50174, Section II, Revision 1, (Lawrence Livermore Laboratory, 1969).
  36. W. J. Veigele, in Handbook of Spectroscopy, Vol I, J. W. Robinson, Ed. (CRC Press, Cleveland, 1974) pp.28-218.
  37. E. F. Plechaty, D. E. Cullen, and R. J. Howerton, Report No. UCRL-50400, Vol. 6, Rev. 2 (Lawrence Livermore Laboratory, 1978).
  38. B. Henke, to be published in this book.
  39. B. Henke, "Demountable Ultrasoft X-Ray Source", University of Hawaii, August 1974, unpublished.
  40. B. Henke, "X-Ray Calibration Sources for the 100-1000 eV Region", May 1976, to be published in the Proceedings of the 1974 ERDA Symposium on X- and Gamma-Ray Sources and Applications.
  41. J. V. Gilfrich, P. G. Burkhalter, R. R. Whitlock, E. S. Warden, and L. S. Birks, *Anal. Chem.* **43**, 934 (1971).
  42. E.J. Williams, *Klg. Danske Videnskab, Selskab, Mat.-Fys. Medd.* **13**, 4 (1935).
  43. H. Uberall, *Phys. Rev.* **103**, 1055 (1956).
  44. G. Lutz, DESY (Hamburg) Rpt. 66/37 (1966).
  45. Yu. S. Korobochko, V.F. Kosmach and V.I. Mineev, *Sov. Phys. JETP* **21** (5) 834 (1965).
  46. G.D. Palazzi, *Rev. Mod. Phys.* **40**, 611 (1968).
  47. M.L. Ter-Mikaelian, High-Energy Electromagnetic Processes in Condensed Matter, Wiley, New York (1972).
  48. A. Saenz and H. Uberall, to be published.
  49. R.H. Pantell et al, to be published.
  50. D.S.Gemmell, *Rev. Mod. Phys.* **46**, 129 (1974).
  51. M.J. Alguard et al., *Phys. Rev. Lett.* **42**, 1148, (1979).
  52. R.L. Swent et al., *Phys. Rev. Lett.* **43**, 1723, (1979).
  53. J. U. Anderson and E. Laegsgaard, *Phys. Rev. Lett.* **44**, 1079 (1980).
  54. R.H. Pantell and R.L. Swent, *App. Phys. Lett.* **35**, 910 (1979).
  55. R.L. Swent and R.H. Pantell, *J. Appl. Phys.* **52**, 3403 (1981).
  56. C.P. Wang and B.M. Klein, to be published.
  57. A.W. Saenz, H. Uberall and A. Nagle, *Nucl. Phys.*, to be published.
  58. V.L. Ginzburg and I. M. Frank, *Zh. Eksp. Teor. Fiz.* **16**, 15 (1946).
  59. M.L. Cherry et al., *Phys. Rev.* **D11**, 3594 (1974).
  60. C.W. Fabian and W. Struczinski, *Phys. Lett.* **57B**, 43 (1975).
  61. R.H. Hughes et al., *Appl. Optics*, **20**, 1350 (1981).
  62. A.N. Chu et al., *J. Appl. Phys.* **51**, 1290 (1980).
  63. L.E. Preuss, A Compilation of Beta Excited X-Ray Spectra, U.S. Atomic Energy Commission Reports TID-22316: Pt. 1 (Nov. 1966) and Pt. 2 (Oct. 1967).
  64. C.M. Dozier et al., *IEEE trans. on Nucl. Sci.*, **NS25**, 1634 (1978).
  65. M. Yoshimatsu and S. Kozaki in H.-J. Quiesser (Editor) X-Ray Optics, Springer-Verlag, Berlin (1977).
  66. U. Bonse, in Characterization of Crystal Growth Defects by X-Ray Methods, B.K. Tanner and D.K. Bowen, Eds. (Plenum, New York, 1980) p. 298.
  67. D.J. Nagel and C.M. Dozier in M.C. Richardson (Editor) High Speed Photography, SPIE, Vol. 97, 132 (1976).
  68. D.J. Nagel, *NRL Memo. Rpt.* 4465 (1981).
  69. S.F. Jacobs et al. (Editors), Free-Electron Generators of Coherent Radiation, Addison-Wesley, Reading (1980).

Studies of Radiation Conversion and Transport in a 0.53  $\mu\text{m}$  Laser Produced Gold Plasma

H. Nishimura, F. Matsuoka, M. Yagi, K. Yamada, H. Niki, T. Yamanaka, C. Yamanaka  
 Institute of Laser Engineering, Osaka University, Suita, Osaka 565, Japan  
 and G. H. McCall

Los Alamos National Laboratory, P.O.Box 1663, Los Alamos, NM 87545, USA

## ABSTRACT

The soft x-ray emission in the front and the rear side of a gold foil target irradiated by 0.53  $\mu\text{m}$  and 1.06  $\mu\text{m}$  lasers was observed. Radiation temperature and its laser intensity dependence were investigated in comparison with the backbody radiation. The preliminary results for a 10.6  $\mu\text{m}$  case is also reported. The ablation depth for high-Z targets is discussed.

## INTRODUCTION

Radiation emitted in a laser produced high-Z plasma plays a very important role in energy balance and ablation behavior in the laser fusion research. Generally, the radiation mean free path becomes much shorter than the plasma scale length in high-Z plasmas ( $T_e \sim$  a hundred eV), which infers validity of the blackbody spectra (1). Under this circumstance, the ratio of radiation to thermal electron heat flux becomes greater than one and the contribution of radiation to the ablation mechanism will be remarkable. The radiation conversion efficiency measured was nearly 40%, 18% and 14% for 0.53  $\mu\text{m}$  (1), 1.06  $\mu\text{m}$  (2) and 10.6  $\mu\text{m}$  (3) lasers at the same irradiance around  $10^{14}$  W/cm<sup>2</sup>.

The sub-keV x-rays emitted from a gold foil target irradiated by a 0.53  $\mu\text{m}$  or a 1.06  $\mu\text{m}$  laser were observed by the use of x-ray diodes (XRDs). The radiation temperature and the power conversion efficiency was obtained. The preliminary results of conversion efficiency for a 10.6  $\mu\text{m}$  laser is also reported. The ablation depth (4) deduced from the signal ratio of XRDs located in the front and the rear side of targets is compared with that estimated by the flux limit model for the thermal electron transport.

## EXPERIMENTAL ARRANGEMENT

The laser used here was the glass laser system "Gekko II". The experimental conditions are summarized in Table 1. The target was a gold foil of various thickness. X-ray radiation was monitored by biplaner-type x-ray diodes. The current of XRD is given for the plane geometry by

$$\frac{dQ}{dt} = F(\theta) \Omega_D S_P \int_0^\infty I_{TR}(\epsilon) T(\epsilon) D(\epsilon) d\epsilon \quad (1)$$

where,  $F(\theta)$  is the fraction radiated in a solid angle at the viewing angle  $\theta$  from the target normal,  $\Omega_D$  is the solid angle of XRD,  $S_P$  is the plasma area size,  $I_{TR}$  is the plankian function for the radiation temperature  $T_R$ ,  $T(\epsilon)$  is the filter transmittance (5) and  $D(\epsilon)$  is the diode response (6). Signal ratio of XRDs attaching different filters defines the radiation temperature and the plasma area size is given by the absolute value of the signal and the radiation temperature.

Two couples of XRDs were respectively set in the front and the rear side of targets on the target normal. They are constructed of the same aluminum photocathode, and a polypropylene or an aluminum-coated polypropylene filter. The validity of blackbody spectra and the angular distribution of radiation were determined by us-

ing aluminum or mylar filters additionally.

## EXPERIMENTAL RESULTS

One couple of XRDs determine the time resolved radiation temperature. Different combinations of XRD's signal gave the temperature variation of 8% with showing the validity of the blackbody assumption. The radiation temperatures as a function of incident laser intensity for 0.53  $\mu\text{m}$  and 1.06  $\mu\text{m}$  lasers are shown in Figures 1 (a), (b). Each temperature scales as  $T_R = 130 I_L^{0.13}$  (eV) for a 0.53  $\mu\text{m}$  laser and  $T_R = 129 I_L^{0.19}$  (eV) for a 1.06  $\mu\text{m}$  laser where  $I_L$  is normalized with  $10^{14}$  W/cm<sup>2</sup>. Saturation of temperature increase is seen for the 1.06  $\mu\text{m}$  laser case over  $4 \times 10^{13}$  W/cm<sup>2</sup> where the decrease of absorption and the production of high energy electrons occur (4). The angular distribution of x-rays fits quite well with a 'cos  $\theta$ ' function, which indicates

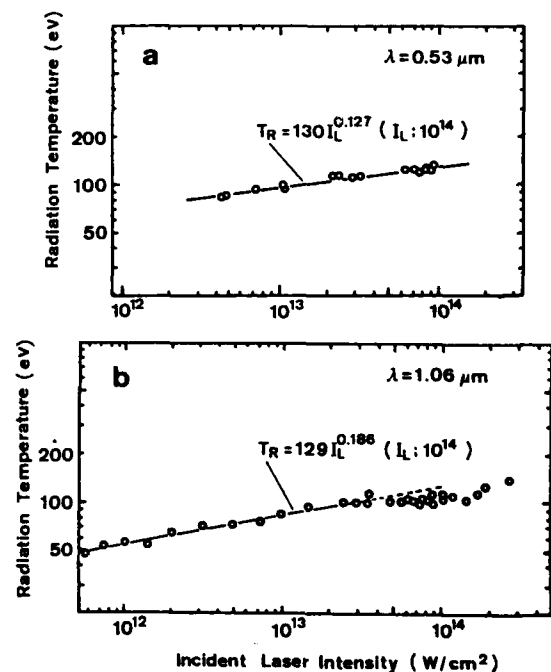


Fig. 1 Radiation temperature vs. incident laser intensity for (a) 0.53  $\mu\text{m}$  and (b) 1.06  $\mu\text{m}$  lasers.

that the plasma axial size is much shorter than that of lateral one (  $\sim 180 \mu\text{m}$  typically ).

The power conversion efficiencies are shown in Fig. 2 (a), (b). It is confirmed that the power conversion efficiency is almost the same value of the energy conversion efficiency which is obtained in the time-integration data analysis. Saturated values of the conversion efficiency are respectively  $\sim 35\%$  and  $\sim 20\%$  for  $0.53 \mu\text{m}$  and  $1.06 \mu\text{m}$  lasers. Here, the results for a  $10.6 \mu\text{m}$  laser case obtained in the same way as mentioned above is also plotted. The experimental conditions are the same as reported elsewhere (4). The absorption rate and the conversion efficiency decrease with increasing the laser wavelength as shown in Fig. 4. The discrepancy of the ratio of conversion efficiency to absorption rate between ours and that of P.D.Rockett et al. (3) is mainly due to the difference of target geometry ( They used the spherical targets ).

The peak current ratio of XRDs with same filters located in the front and the rear side of targets as a function of foil thickness is shown in Fig. 3. Solid line indicates the calculated transmission of x-rays through the target when  $600 \text{ \AA}$ -thick front side gold (which is equal to a half of the total ablation thickness) is assumed to be ablated and the remainder works as a filter. This ablation thickness, i.e.  $\sim 1200 \text{ \AA}$ , agrees quite well with that obtained from the spectroscopic measurements using a Au coated target (4). Then, the mass ablation rate measured is approximately  $4 \times 10^{-2} \text{ (g/cm}^2 \text{ sec)}$ .

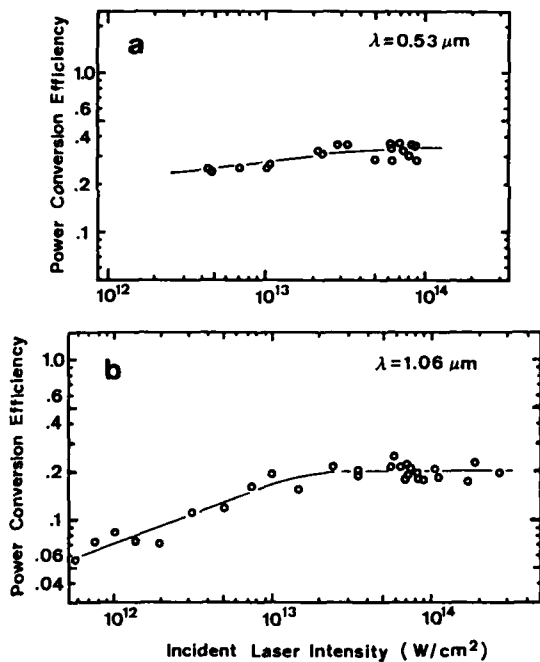


Fig. 2 Power conversion efficiency vs. incident laser intensity for (a)  $0.53 \mu\text{m}$  and (b)  $1.06 \mu\text{m}$  lasers.

DISCUSSION

When the absorbed laser energy balances with the energy of the isothermal expansion region, the mass ablation rate at the C-J point can be estimated (4), i.e.,

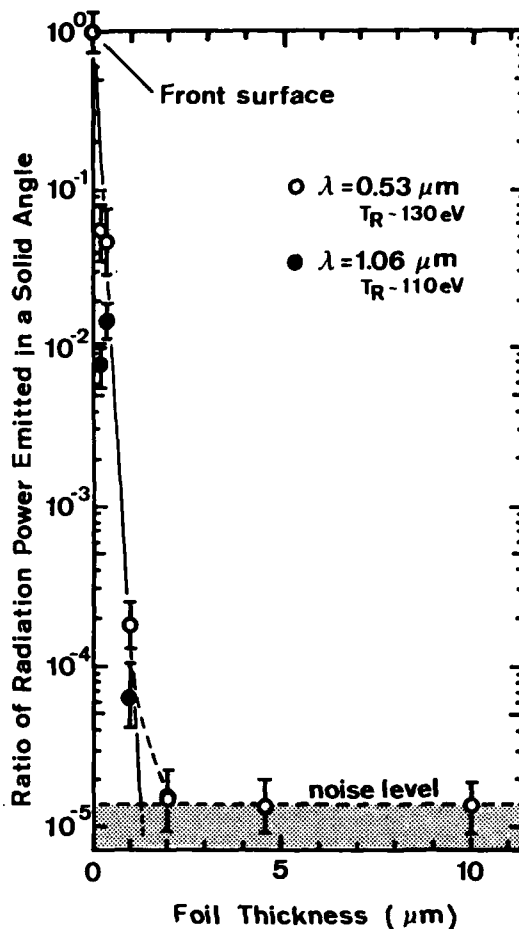


Fig. 3 Ratio of radiation power emitted in a unit of solid angle as a function of foil thickness. Time corresponds to the laser peak.

$$\dot{m} = \frac{1}{4} f^{2/3} Z^{-1} M m_e^{-1/3} n_c^{2/3} \phi_{abs}^{1/3} \quad [2]$$

where  $f$  is the limiting factor ( $f = \phi_{abs} / m_e n_c v_e^3$ )  $Z$  is the ion charge,  $M$  and  $m_e$  is the ion and electron mass,  $n_c$  is the cut off density and  $\phi_{abs}$  is the absorbed laser flux, here the energy flow into ionization and radiation is neglected. When  $f$  is 0.6, then  $\dot{m} = 8 \times 10^{-6} \text{ (g/cm}^2 \text{ sec)}$  for  $Z = 18$  ( $\text{Te} \approx 400 \text{ eV}$ ) and  $n_c = 4 \times 10^{21} \text{ (cm}^{-3})$ . This value is almost twenty times larger than the experimental value. This large discrepancy can be attributed to the decrease of the limiting factor, therefore, the increase of the coronal temperature. When  $f=0.03$  is assumed, the coronal temperature is estimated to be  $\sim 3 \text{ keV}$  then,  $\dot{m} = 5 \times 10^{-5} \text{ (g/cm}^2 \text{ sec)}$ . More detailed considerations, however, are required for the energy balance between the radiation and the particles in over dense plasmas.

SUMMARY

The wavelength dependence of the radiation temperature and the conversion efficiency as a function of incident laser intensity were experimentally studied for gold foil targets irradiated by  $0.53 \mu\text{m}$ ,  $1.06 \mu\text{m}$

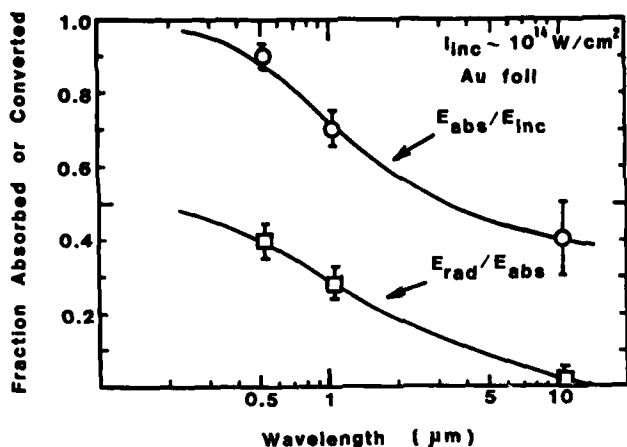


Fig. 4 Laser wavelength dependence of the absorption and the conversion efficiency.

and 10.6  $\mu\text{m}$  lasers. Both the absorption rate and the radiation conversion efficiency decrease with increasing the laser wavelength. The ablation depth observed in this experiment can be interpreted by the simple inhibited thermal conduction by electrons with the limiting factor of 0.03.

	0.53 $\mu\text{m}$	1.06 $\mu\text{m}$
Pulse duration (ns)	0.5	0.6
Incident Angle (degrees)	45	45
F number	6	6
Polarization	P	P
Focal Spot Diameter ( $\mu\text{m}$ )	150 (75%)	150 (65%)
Intensity ( $\text{W}/\text{cm}^2$ )	$\leq 1 \times 10^{14}$	$\leq 3 \times 10^{14}$

Table 1

#### REFERENCE

- (1) P.D.Rockett, W.Friedhorsky, D.Giovanelli, Los Alamos Scientific Laboratory Report, LA-UR-80-2442 (1980), (unpublished).
- (2) W.C.Mead, E.M.Campbell, K.G.Estabrook, R.E.Turner, W.L.Kruer, P.H.Y.Lee, B.Pruett, V.C.Rupert, K.G.Tirrell, G.L.Stradling, F.Ze, C.E.Max and M.D.Rosen, Lawrence Livermore Laboratory Report, UCRL-84684, (1981), (unpublished).
- (3) M.D.Rosen, D.W.Phillion, V.C.Rupert, W.C.Mead, W.L.Kruer, J.J.Thomson, H.N.Kornblum, V.C.Slivinsky, G.J.Caporaso, M.J.Boile, and K.G.Tirrell, Phys. Fluids, 22, 2020 (1979).
- (4) H.Nishimura, H.Azechi, K.Yamada, A.Tamura, Y.Inada, F.Matsuoka, M.Hamada, Y.Suzuki, S.Nakai, and C.Yamanaka, Phys. Rev. A, 23, 2011 (1981).
- (5) R.H.Day, P.Lee, E.B.Sulmon and D.J.Nagel, Los Alamos Scientific Laboratory Report, LA-UR-79-1360 (1979), (unpublished).
- (6) B.L.Henke and E.S.Ebisa, "Advances in X-ray Analysis, 17, (Plenum Press, N.Y. 1974).

SOFT AND ULTRASOFT X-RAY MEASUREMENTS OF AIR FORCE WEAPONS LABORATORY SHIVA IMPLoding PLASMA LINER<sup>a)</sup>

J.H. DEGNAN and R.J. SAND, Air Force Weapons Laboratory

G.F. KIUTTU and D.M. WOODALL, University of New Mexico  
Albuquerque, New Mexico

Measurements of the radiation from high energy density plasmas formed by electromagnetic implosion of aluminized plastic cylindrical foil liners are discussed. The implosions were driven by the SHIVA capacitor bank - originally a 1.1 MJ, 1.2 microsecond, 100 KV device, later upgraded to 1.9 MJ, 1.4 microseconds, 120 KV. Discharge currents were 7 to 12 MA and implosion times 1.2 to 1.5 microseconds.

Photon pulses were observed using arrays of x-ray photodiodes, calorimeters and bolometers, x-ray pinhole cameras, convex curved crystal and grazing incidence grating spectrographs. Photon pulse energies from 100 KJ to 240 KJ were observed (assuming isotropic emission) with FWHM from 80 to 200 nanoseconds. The best combined photon yield and FWHM was 240 KJ, 130 nanoseconds. Bolometer, calorimeter, x-ray photodiode comparisons, time-resolved spectra deconvoluted from x-ray photodiode array data and detailed spectrograph data are discussed.

Neutron measurements from deuterated liner implosions (yields up to  $4 \times 10^8$ ) are also discussed.

At the Air Force Weapons Laboratory, we have been experimentally and theoretically investigating imploding plasma liners for production of high energy density plasmas for several years.<sup>1,2,3</sup> The plasma liner implosion experiments have resulted in large photon pulses<sup>2,4</sup> in the ultrasoft and soft x-ray range. Using the SHIVA capacitor bank - a 1.1 MJ, 1.2 microsecond, 100 KV device<sup>2,5</sup> which was later upgraded to 1.9 MJ, 1.4 microsecond, 120 KV, plasma liner implosions were driven in Z-pinch like, 7 to 12 MA discharges. These discharges resulted in  $\sim 20$  cm/microsecond final implosion velocities with 15 to 25% of the stored electrical energy converted to implosion kinetic energy. Photon pulse energies from 100 KJ to 240 KJ (assuming isotropic emission) were observed with FWHM of the pulses ranging from 80 to 200 nanoseconds. The best combined yield and FWHM was 240 KJ, 130 nanoseconds.

Observation geometry is illustrated in Figure 1. The photon diagnostics were arrays of x-ray photodiodes<sup>6</sup>, x-ray pinhole cameras, thermocouple calorimeters, a fast pulsed bolometer<sup>4</sup>, and crystal and grating spectrographs. Passive detectors (calorimeters, pinhole cameras, spectrograph) were protected with pneumatic closure shutters<sup>7</sup> from plasma and debris blast.

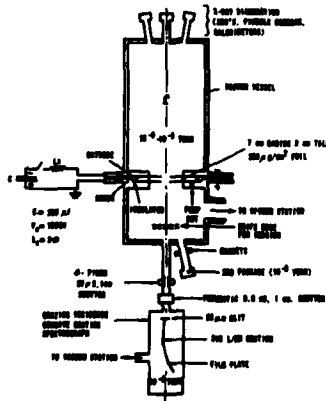


Fig. 1: Schematic of SHIVA diagnostic geometry with grating spectrograph (not to scale).

The X-ray photodiodes (XRD's) used were aluminum cathode, 1 cm. gap, 5 KV biased diodes with filters such as aluminum, Formvar ( $C_5H_8O_2$ ), Kimfoil ( $C_{14}H_{16}O_3$ ), Kapton, Saran, and combinations. Response functions for a variety of filters and filter thicknesses are given in ref. 2. Unfiltered response functions used were those of Cairns and Samson<sup>8</sup> at low energy, Burns and Day<sup>9</sup> from 109 to 1487 eV, Gaines<sup>10</sup> et al from 185 to 1487 eV, Gaines<sup>10</sup> et al and Lyons<sup>11</sup> et al above 1.5 KeV. These agree closely with those of Day<sup>12</sup> et al and Henke<sup>13</sup> et al, except near the oxygen absorption edge.

Arrays of XRD traces were used to obtain deconvoluted, or unfolded, time resolved photon spectra using the following technique. Given an array of XRD signals  $V_K(t)$  and response functions  $R_K(E)$ , the deconvolution or unfold equations are

$$VC_K = \int R_K(E)S(E)dE$$

$$S'(E) = S(E) \cdot \frac{\sum_K R_K(E)(V_K/VC_K)}{\sum_K R_K^2(E)}$$

where  $VC_K(t)$  = calculated signal for Kth XRD,  
 $S(E)$  = trial spectrum,  
 $S'(E)$  = corrected spectrum  
 $R_K^2(E) = R_K(E) / \int R_K(E)dE$   
 and  $E$  = photon energy.

A few dozen iterations are generally required before  $S'(E)$  converges. A flat spectrum is used to initiate the iteration process.

This technique is similar to those used by Chase and Salisbury<sup>14</sup>, and by Plimpton and Glibert<sup>15</sup>, except for the smoothing routines. The rapid variation of XRD response functions made it advantageous to use ratio energy zoning and a combined product/root - logarithmic interpolation smoother with smoothing intervals varying with iteration pass. Tests with hypothetical spectra such as black bodies, using flat initial spectra, gave good convergence<sup>16</sup> for 6 or more distinct XRD's. As is well known<sup>14,15</sup>, smoothing is necessary to avoid artificial spectral features resulting from discontinuities or jumps in the detector response functions.

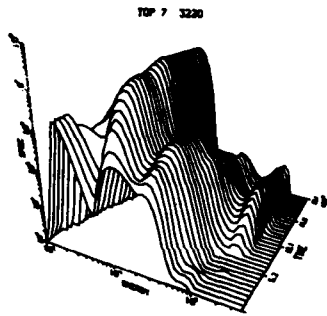


Fig. 2: Unfolded time resolved photon spectrum from SHIVA plasma liner implosion (direct capacitor driven). SPEC =  $dP/dh\nu$  in MW/KeV, ENERGY = photon energy in KeV, TIME in shakes (10 nanosecond units).

A three-dimensional plot of the time resolved deconvoluted spectrum obtained from the array of XRD signals from a representative good shot is shown in Fig. 2. The two low energy humps merge into a single hump peaking near 100 eV photon energy at peak power ( $P \sim 1.26 \times 10^{12}$  watts, maximum  $dP/dh\nu \sim 2 \times 10^7$  Megawatts/KeV). The highest energy peak, near 2 KeV photon energy, is due to  $Al^{11+}$  and  $Al^{12+}$  line and recombination radiation - the detail of which is unresolved using this analysis technique and this XRD array.

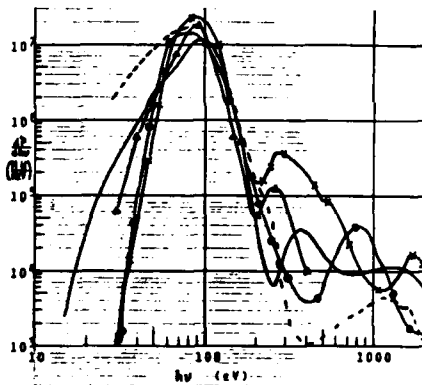


Fig. 3: Peak power unfolded photon spectra for several plasma liner implosions.

Fig. 3 shows peak power deconvoluted spectra for several representative implosion experiments, indicating the reproducibility of a low energy hump peaking near 100 eV photon energy.

A comparison of deconvoluted spectrum peak power versus nominal peak power for photon emission is shown in Table 1. Nominal peak power is obtained using an aluminum cathode, Formvar filtered (Al/FV) XRD, assuming an average response of 40 amperes/Megawatt for 60 micrograms/cm<sup>2</sup> Formvar filter. The difference in all cases is less than factor of 2 and often less than 20%. Thus, the Al/FV XRD signal enables a rapid approximate estimate of photon emission yield for the spectra we have obtained.

Table 1. Comparison of deconvoluted spectrum peak power vs. nominal peak power.

SHOT	Pdc/Pnom
3125	0.6
3146	1.0
3158	1.57
3169	0.89
3177	1.08
3186	0.95
3187	0.87
3190	1.41
3191	1.79
3213	0.96
3220	0.80

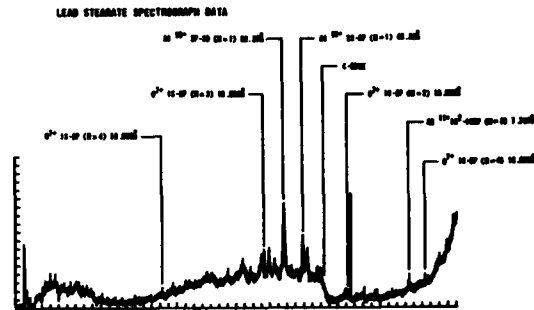


Fig. 4: Lead Stearate spectrograph data.

Low energy crystal (lead stearate)<sup>17</sup> spectrograph data, such as shown in Fig. 4, indicate that the spectrum below 220 eV in photon energy is dominated by continuum or closely packed lines, with possible absorption features. The lowest energy strong lines are  $Al^{10+}$  2p-3d (52.37Å) and  $Al^{10+}$  2s-3p (48.32Å). These are always evident and always quite strong in aluminum or aluminized plastic liner implosions. Comparison of stearate spectrograph data with XRD array unfolded spectra gives approximate (factor of 2) agreement near the carbon absorption edge (248 eV), as shown in Fig. 5. At this energy, the spectrograph response is most reliably known. The crystal response reported by Henke<sup>18</sup> and Kodak RAR 2490 film response reported by Benjamin, Day, and Lyons<sup>19</sup> were used to absolutely interpret the spectrograph data.

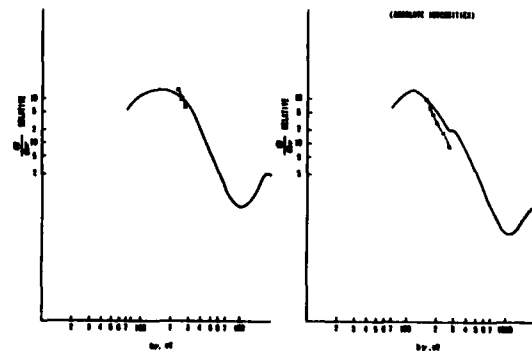


Fig. 5: Comparison of unfolded photon spectra from XRD data (solid lines) with lead stearate spectrograph data (X's).



Bare thermocouple calorimeter data was taken to check yields interpreted from XRD array data. The comparison, shown in Table 2, shows that calorimeters indicate yields from 1 to 4 times those obtained with XRD data. This suggests that the calorimeter sensed late time energy in addition to the prompt photon energy detected by XRD's. This late time energy could be low energy photons from afterglow or late time discharge plasma and/or plasma and hot gases reaching the calorimeter. The fast (500 microsecond) closure shutter may be too slow to stop streaming plasma and hot gases on some shots.

Table 2. Calorimeter - XRD comparison.

SHOT	Ycal/Yxrd
3187	1.97
3190	1.02
3191	0.82
3222	1.80
3223	2.60
3224	3.90
3226	3.80

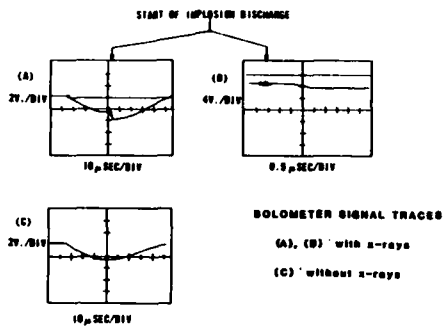


Fig. 6: Fast pulsed bolometer signals.

A fast, pulsed, large signal bolometer was developed<sup>4</sup> and used to thermally detect photons with time resolution adequate to confirm that their origin is the implosion pinch. Bolometer signal traces with and without a photon pulse are shown in Fig. 6. The bolometers were used with 60 microgram/cm<sup>2</sup> Formvar filters to suppress surface photo-ionization shunting of the bolometer foil current after the prompt

photon pulse. Such surface photo-ionization, suspected due to elongated rise times for unfiltered bolometers, is presumably due to lower energy afterglow photons still incident after the main (prompt) photon pulse. Rauch<sup>20</sup> and Hanson<sup>21</sup> have since used similar bolometers, unfiltered, with magnets to suppress photoionization shunting, which has enabled faster time response and the use of unfiltered bolometers.

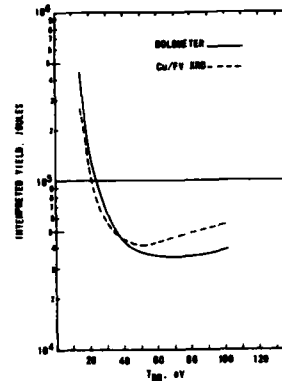


Fig. 7: Bolometer - XRD comparison.

The interpreted yield for a Formvar filtered bolometer signal is compared to that for a Cu/FV XRD signal, versus black body temperature for assumed black body spectral shape in Fig. 7. The agreement was better than or on the order of 30% for a wide range of temperatures, as well as for a variety of other plausible spectral shapes. Thus, both thermal and photoelectric detectors were in substantial agreement on photon yield.

A print of the data record obtained from a 5 meter grazing incidence spectrograph<sup>22</sup> is shown in Fig. 8. Al<sup>10+</sup>, Al<sup>11+</sup>, Al<sup>12+</sup>, O<sup>6+</sup>, O<sup>7+</sup>, and C<sup>5+</sup> emission lines are evident above 230 eV in photon energy. At lower energies, the spectrum is continuum with absorption lines from O<sup>4+</sup>, O<sup>5+</sup>, Al<sup>4+</sup>, Al<sup>5+</sup>. This indicates a hotter interior plasma shining through a cooler (~40 eV), absorbing plasma. Broadening of the Al<sup>10+</sup> 2s-5p and 2s-6p lines exceeded instrumental broadening. If this broadening is assumed to be

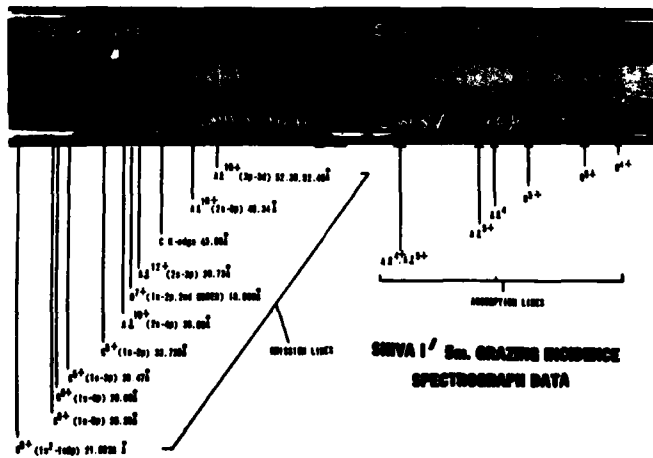


Fig. 8: 5 meter grazing incidence spectrograph data.

Stark broadening, one obtains an estimate of the electron density  $\sim 10^{22} \text{ cm}^{-3}$  for the part of the plasma emitting those lines.

The 5 meter spectrograph was built by Robert Speer of Imperial College. It employed a 316 line per mm. holographically formed gold plated silica lamellar grating. The film was Ilford Q2 spectrographic plate. A 50 microgram/cm<sup>2</sup> carbon filter was used - resulting in the well defined carbon absorption edge evident in the continuum spectrum. The spectrograph slit (20 microns) was approximately 1.2 meters from the source. The plate was underdeveloped (3 minutes in D19) to reduce overexposure effects. To protect the expensive spectrograph components from plasma blast and debris, two fast closure shutters were used in tandem. The first shutter employed a 240 microfarad, 5 KV, 7 microsecond quarter cycle time theta-discharge to close a 0.25 mm wall, 2.5 cm diameter aluminum tube in 30 microseconds. The aluminum tube was part of the diagnostic vacuum line. The second shutter was an aforementioned pneumatic closure shutter<sup>7</sup> (re-usable, vacuum tight) with  $\sim 500$  microsecond closure time.

Data from a KAP spectrograph, collimated to reduce source broadening, is shown in Fig. 9. The Al<sup>11+</sup> and Al<sup>12+</sup> K shell line and recombination radiation are evident. To the extent that the spectrum can be characterized by a single electron temperature T<sub>e</sub> and electron density n<sub>e</sub>, T<sub>e</sub>  $\sim 400$  eV (from recombination slope) and n<sub>e</sub>  $\sim 10^{20} \text{ cm}^{-3}$  (from He-like resonance line to intercombination line ratio)<sup>23, 24</sup>. Of course, the radiation is really from a time dependent, inhomogeneous temperature and density distribution. Considering or not considering opacity effects makes a factor of 5 difference in the interpreted density. An opacity effect of a factor of 2.5 reduction in the resonance line (7.757Å) was obtained<sup>23</sup> by requiring consistency of electron temperatures ( $\sim 400$  eV) obtained from recombination slope, ratio of dielectronic recombination to resonance line ratio, and ratio of Al<sup>12+</sup> 1s-2p to Al<sup>11+</sup> 1s<sup>2</sup>-1s2p lines. Comparison of observed intensity with black body limit for the emission volume (0.1-1 cm<sup>3</sup> in this case) indicates a cooler ( $\sim 50-100$  eV) outer plasma is required for such an opacity effect.

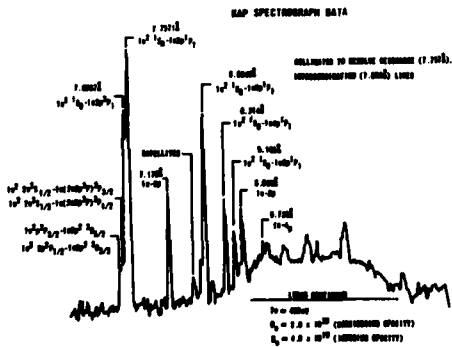


Fig. 9: Collimated KAP Spectrograph data.

By removing the spectral collimation slit and adding a spatial imaging slit, one obtains 2 dimensional spatial imaging of the spectral lines<sup>25</sup>. Imaging in the spectral dispersion direction is by

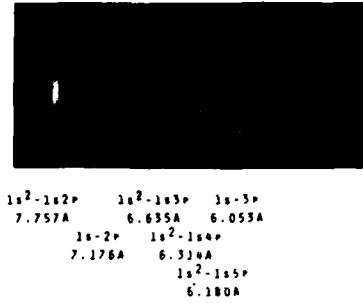


Fig. 10: Space resolved KAP Spectrograph Record.

source broadening, while in the other direction it is one-dimensional pinhole imaging. In the 2 dimensional imaged KAP spectrograph record shown in Fig. 10, the magnification by source broadening is approximately one third that by slit imaging, so the elliptical "annular" spectral lines are due to circular annular line emission regions<sup>22</sup>.

In Fig. 11, an uncollimated KAP spectrograph densitometer trace is shown, illustrating the degree of source broadening. The best fit electron temperature and density are  $\sim 300$  eV and  $\sim 10^{20} \text{ cm}^{-3}$ , based on recombination slope and intensity<sup>22</sup>.

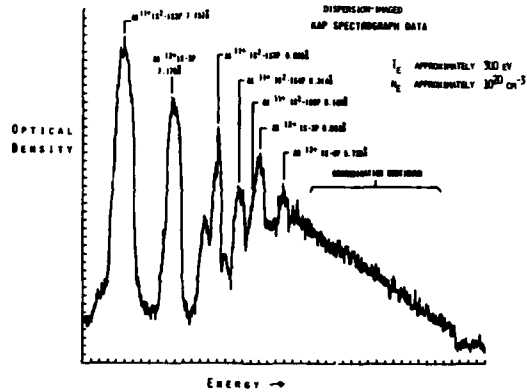


Fig. 11: Source broadened KAP Spectrograph data.

X-ray pinhole camera images, such as that shown in Fig. 12, often show an annular or ring shaped emission regions, as is also evident in some two-dimensional imaged KAP spectrograph records<sup>22</sup>.



Fig. 12: X-Ray pinhole camera photograph. Outer diameter of luminosity region is approximately 2 cm.

Two-dimensional magnetohydrodynamic calculations of plasma liner implosions predict electron density and temperature profiles similar to that shown in Fig. 13<sup>26</sup>. The axial plume and the ring shaped regions with high electron temperature are qualitatively consistent with the annular emission regions observed experimentally<sup>22</sup>. Either or both the plume and off axis peaks in electron temperature features could explain the ring shape of the  $\sim 1$  KeV photon emission region. The predicted  $\sim 40$  eV plume temperature is consistent with the absorption lines seen in lower energy spectrograph data<sup>22</sup>. Gross radiation power, as well as spectral detail and features of pinch structure are in approximate agreement with pinch conditions predicted by 2D MHD calculations.

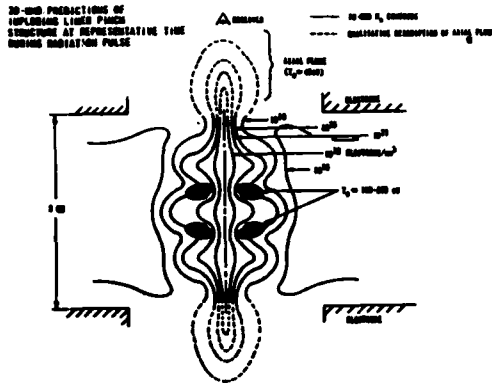


Fig. 13: 2D MHD predicted electron density, temperature contours at time near peak compression in pinch.

Implosion experiments with deuterated aluminized plastic foil cylinders<sup>27</sup>, in which the foils were 3% deuterium by mass and final implosion velocities were  $\sim 20$  cm/microsecond, resulted in neutron yields  $\sim 10^7$  to  $10^8$ . A comparison of yields obtained from silver activation and lead shielded scintillator - photomultiplier detector data is shown in Table 3. The detectors were calibrated in situ with a pulsed neutron source and cross-calibrated with a large Ag detector previously calibrated at Livermore<sup>28</sup>. The observed yields were approximately consistent with those obtained by applying Rose and Clark neutronics<sup>29</sup> to two dimensional magnetohydrodynamic predictions of ion temperature and density spatial and temporal distributions.

TABLE 3. COMPARISON OF ACTIVATION & TOF DATA

SHIVA SHOT	SILVER ACTIVATION NORMAL NEUTRON YIELD	TOF NORMAL NEUTRON YIELD
4028	$4.60 \times 10^7$	$7.40 \times 10^7$
4029	$2.44 \times 10^7$	$1.45 \times 10^7$
4030	$3.20 \times 10^6$	$4.40 \times 10^6$
4039	$1.12 \times 10^8$	$1.22 \times 10^8$
4040	$2.19 \times 10^7$	$2.70 \times 10^7$
4044	$4.15 \times 10^7$	
4045	$1.25 \times 10^7$	$1.30 \times 10^7$
4046	$1.68 \times 10^7$	$3.50 \times 10^7$
4047	$2.58 \times 10^7$	$3.00 \times 10^7$
4048	$1.00 \times 10^7$	$1.50 \times 10^7$
4049	$1.21 \times 10^8$	
4052	$4.56 \times 10^6$	
5017	$1.07 \times 10^6$	
5021	$2.52 \times 10^6$	
5024	$1.48 \times 10^7$	

Ongoing and future work includes experiments with faster implosions driven by capacitor bank discharges sharpened using inductive storage, opening switch techniques<sup>30,31,32,33</sup>. The use of time and space resolved spectrographs will be emphasized in this work.

#### ACKNOWLEDGEMENTS

The deconvolution technique is similar to that used by L. Chase and J. Salisbury of LPARL, and by J. Plimpton and K. Glibert of SNL.

The related contributions of W.L. Baker, E.J.T. Burns, R.H. Day, B.L. Henke, T.W. Hussey, J.D. Letterio, R.E. Reinovsky, N.F. Roderick, and others are acknowledged and appreciated.

#### REFERENCES

- Work partially supported by the Air Force Office of Scientific Research under Contract #79-0060
- P.J. Turchi and W.L. Baker, *J. Appl. Phys.* **44**, 4936 (1973).
- W.L. Baker, M.C. Clark, J.H. Degnan, G.F. Kiuttu, C.R. McClenahan, R.E. Reinovsky, *J. Appl. Phys.* **49**, 4694 (1978).
- T.W. Hussey, N.F. Roderick, D.A. Kloc, *J. Appl. Phys.* **51**, 1452 (1980); N.F. Roderick, T.W. Hussey, R.J. Faehl, R.W. Boyd, *Appl. Phys. L.* **32**, 273 (1978).
- J.H. Degnan, *Rev. Sci. Inst.* **50**, 1223 (1979).
- G. Barton and D. Markins, Maxwell Laboratories, Report No. AFWL-TR-75-271 (1975).
- D.J. Johnson, Report No. AFWL-TR-74-43 (1974).
- R.E. McDonald of Lockheed Palo Alto Research Laboratories (and now of Spectral Precision, Inc.) provided pneumatic fast closure shutter design.
- R.B. Cairns and J.A.R. Samson, *J. Opt. Soc. Am.* **56**, 1568 (1968).
- E.J.T. Burns and R.H. Day, private communication; E.J.T. Burns and J.F. Thurston, *Appl. Spect.* **31**, 317 (1977).
- J.L. Gaines and R.D. Ernst, Report No. UCIR-1075 (1956); J.L. Gaines, private communication.
- P.B. Lyons, private communication.
- R.H. Day, P. Lee, E.B. Salomen, D.J. Nagel, Report No. LA-UR-79-1360 (1979).
- R.L. Henke, J.P. Knauer, K. Premeratne, *Bull. Am. Phys. Soc.* **24**, 1098 (1979).
- L. Chase and S. Salisbury, private communication.
- J. Plimpton and K. Glibert, private communication.
- J.H. Degnan, R.E. Reinovsky, G.F. Kiuttu, M.C. Clark, W.L. Baker, IEEE Conference Record - 1978 IEEE International Conference on Plasma Science, P. 50 (1978).
- The lead stearate crystals were fabricated and supplied by B.L. Henke.
- B.L. Henke and M.A. Tester, *Adv. in X-ray Analysis*, edited by W.L. Pickles, C.S. Barrett, J.B. Newkirk, C.O. Rund (Plenum, New York, 1975) Vol. 18, p. 76.
- R.F. Benjamin, P.B. Lyons, and R.H. Day, Report No. LA-UR-76-1502 (1975).
- John Rauch, Report No. MLR 933 (1980).
- D.L. Hanson, R.B. Spielman, J.P. Anthes, *Bull. Am. Phys. Soc.* **25**, 890 (1980).
- D.M. Woodall, J.H. Degnan, G.F. Kiuttu, R.J. Sand, R.E. Reinovsky, W.L. Baker, *Bull. Am. Phys. Soc.* **25**, 872 (1980).
- E.J.T. Burns, J.H. Degnan, R.E. Reinovsky, W.L. Baker, M.C. Clark, C.R. McClenahan, *Appl. Phys. L.* **31**, 477 (1977).
- A.H. Gabriel and C. Jordan, *Case Studies in Atomic Collision Physics*, edited by E.W. McDaniel and M.R.C. McDowell (North-Holland, Amsterdam, 1972) Vol. 2, Chapter 4; C.P. Shalla, A.H. Gabriel, and L.P. Presnykov, *Mon. Not. R. Astron. Soc.* **172**, 359 (1975).

25. G.F. Kiuttu, AFWL-DYP-TN-79-117 (1979).
26. T.W. Hussey, N.F. Roderick, D. Kloc, private communication.
27. W.L. Baker, C.W. Beason, J.H. Degnan, G.F. Kiuttu, D.A. Kloc, R.A. Nuttleman, R.E. Reinovsky, R.J. Sand, D.M. Woodall, Bull. Am. Phys. Soc. 25, 834 (1980).
28. D.R. Slaughter and W.L. Pickles, Report No. UCRL-81137 (1978).
29. D.J. Rose and M. Clark, Plasmas and Controlled Fusion (MIT Press, Cambridge, Mass., 1961).
30. C.R. McClenahan, J.H. Goforth, J.H. Degnan, R.M. Henderson, W.H. Janssen, W.E. Walton, Report No. AFWL-TR-78-130 (1980).
31. D.L. Smith, R.P. Henderson, and R.E. Reinovsky, 2nd IEEE International Pulse Power Conference - Digest of Technical Papers, p. 287 (1979).
32. R.P. Henderson, D.L. Smith, and R.E. Reinovsky, 2nd IEEE International Pulse Power Conference - Digest of Technical Papers, p. 347 (1979).
33. W.L. Baker, J.H. Degnan, J.F. Francis, R.P. Henderson, J.R. Kerns, R.E. Reinovsky, and R.J. Sand, IEEE Conference Record - 1981 IEEE International Conference on Plasma Science, p. 63 (1981).



Cpt. James Degnan (right) of the AFWL, and Harry Kornblum of Livermore discussing x-ray measurements during the poster session.

## LASER HEATED GAS-JET - A SOFT X-RAY SOURCE

G. Charatis, D. C. Slater, F. J. Mayer, J. A. Tarvin, G. E. Busch,  
D. Sullivan, and D. Musinski  
KMS Fusion, Inc.  
Ann Arbor, MI 48106

and  
D. L. Matthews and Lou Koppel  
Lawrence Livermore National Laboratory  
Livermore, CA

## ABSTRACT

The laser irradiated gas jet developed to study collective scattering processes has proven to be a useful soft x-ray source. It is a reproducible and stationary source with large yield and plasma properties characterized by conventional diagnostic techniques. With a density gradient initially set by orifice size and gas pressure, a short ( $\sim 100$ - $1000$  psec) pulse operating at  $1.05 \mu\text{m}$  (or  $0.53 \mu\text{m}$ ) is focused coaxially upstream into the jet producing a moderate temperature plasma. X-ray pinhole photographs show an axially symmetric radiating plume located at the electron density critical surface. The density gradient is obtained by holographic interferometry using a  $0.26 \mu\text{m}$  wavelength probe pulse. The scale length of  $\sim 100$ - $200 \mu\text{m}$  is measured by  $2\omega$  and  $3/2\omega$  photography. Electron temperatures are determined by using spatially resolving x-ray crystal spectroscopy to record and analyze line emission from H- and He-like configurations. Electron temperatures from  $\sim 200$ - $700$  eV were observed at critical electron densities as high as  $N_{\text{Cr}} \sim 4 \times 10^{21} \text{ cm}^{-3}$  for gases of hydrogen, nitrogen, neon, argon, and  $\text{SF}_6$ .

Experiments on the laser-irradiated gas jet were originally<sup>1</sup> designed to examine stimulated Brillouin scattering in a prepared density distribution possessing longer scale lengths than are generally produced off of solid targets. With laser energies as small as 50 joules in 200 psec and a 90% spot size of  $\sim 100 \mu\text{m}$ , it is possible to generate large numbers of photons in the soft x-ray spectrum. It is a reproducible and stationary source whose plasma properties can be characterized by conventional diagnostic measuring techniques. The density of neutral gas in the jet before irradiation varies smoothly and is easily characterized. The high density gas required to form a critical surface for  $1.05 \mu\text{m}$  is confined to a comparatively small volume and the scale length (or density gradient) can be varied easily by changing the orifice size and varying the gas pressure.

A schematic diagram of the experimental set-up is shown in Fig. 1. Of interest in the figure for this presentation, is the irradiation of the gas jet placed axially at the focus of an  $f/5.4$  parabolic mirror, an x-ray pinhole camera for recording time-integrated x-ray images, and the catadioptric lens used in the interferometric determination of the density distributions.

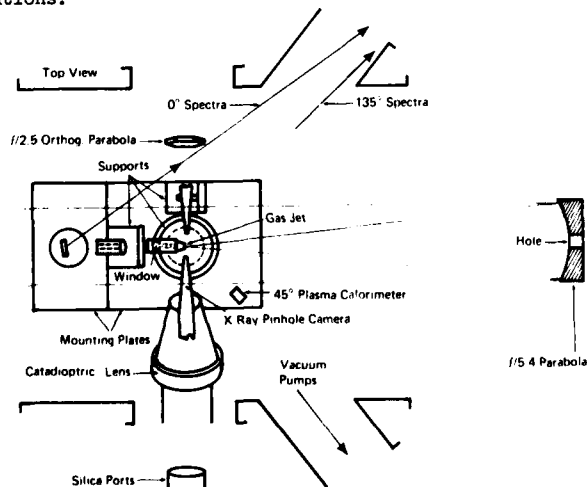


Fig. 1. Diagnostic placement inside the target chamber for the gas jet experiments, top view.

Not shown in the figure is an x-ray crystal spectrograph for photographing time-integrated x-ray spectra of the irradiated jet located below the catadioptric lens, in the plane normal to the jet and  $45^\circ$  below the horizontal.

We have irradiated gas jets of hydrogen, nitrogen, argon, neon, and sulphur hexafluoride at laser wavelengths of  $1.05 \mu\text{m}$  and  $0.53 \mu\text{m}$  and pulse lengths of  $\sim 100$  psec and  $\sim 1$  nsec.

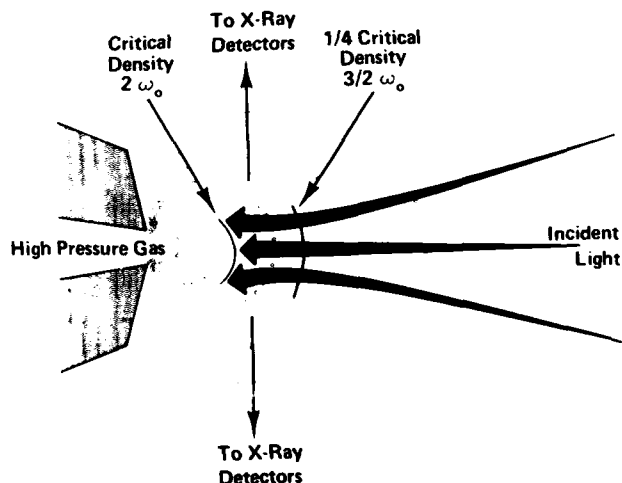


Fig. 2. Schematic representation of the laser-irradiated gas jet.

A schematic representation of the experiment is shown in Fig. 2. High pressure gas expands through a nozzle into a vacuum, forming a very broad jet. The laser light travels upstream, ionizing and heating the gas. Some of the light is absorbed in the underdense plasma and some of it is scattered. The remaining light is absorbed or reflected at the critical surface. To gain the maximum amount of information from the experiments, one needs to know the density, temperature, and velocity profiles of the plasma.

There are several ways in which the density is measured. Holographic interferograms of the neutral gas jet are made in the target chamber prior to irradiation and these are Abel-inverted to give the density

profile. Fig. 3 is such an interferogram of a nitrogen jet. All Abel inversions described here were performed by D. Sweeney<sup>2</sup>. Holographic interferograms taken at the time of the main laser pulse give the density profile of the free electrons. Fig. 4 shows typical interferograms of a nitrogen gas jet irradiated with 46.5 joules in 85 psec at  $\lambda = 1.053 \mu\text{m}$ , and a neon gas jet irradiated with 40.7 joules in 1 nsec at  $\lambda = 0.5265 \mu\text{m}$ .



Fig. 3. Holographic interferogram of a nitrogen gas jet before laser irradiation. Plenum gas pressure: 2000 psi. Jet orifice: 100  $\mu\text{m}$ .

Another way to obtain the density, at least time integrated at two positions of its profile, is to record the position of the second and three-halves harmonic emissions, which correspond to the positions of critical and one-fourth critical densities, respectively. The images are recorded separately then recombined as in Fig. 5 for a hydrogen jet, where the second harmonic of 1.05  $\mu\text{m}$  is green and the three-halves harmonic furthest from the nozzle is red. Some of the  $2\omega$  emission was reflected by the nozzle. However, the harmonic emissions are not always present. Depending on the type of gas, and the density distribution, one or both of the two harmonic emissions may not be spatially well defined.



Fig. 4. (shot 4833) Nitrogen gas jet, 2000 psi; Laser jet irradiation,  $\lambda = 1.053 \mu\text{m}$ , 46.5 Joules in 85 psec. Laser holographic probe,  $\lambda = .2633 \mu\text{m}$ ; duration=60 psec; occurring 290 psec after peak of irradiating pulse.

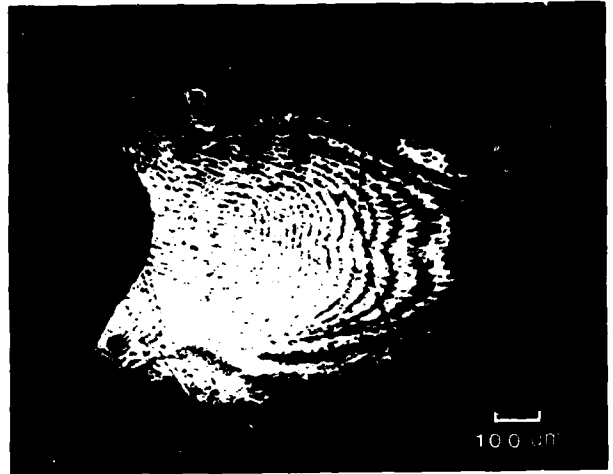


Fig. 4. (shot 4931) Neon gas jet, 1700 psi; laser jet irradiation,  $\lambda = 0.5265 \mu\text{m}$ , 40.7 Joules in 1 nsec. Laser holographic probe,  $\lambda = .2633 \mu\text{m}$ ; duration = 60 psec; occurring 1.26 nsec into the irradiating pulse.



Fig. 5. Composite image of  $2\omega$  and  $3/2\omega$  harmonics of 1.05  $\mu\text{m}$  laser light emitted by a hydrogen jet target.

Both density measuring diagnostics are combined for a 100  $\mu\text{m}$  diameter orifice gas jet in Fig. 6. The solid line is from an interferogram of neutral  $\text{N}_2$  and varies exponentially with the distance from the orifice. The data points are from the images of the harmonics of 1.05  $\mu\text{m}$  light. Sufficiently far from the orifice, we expect to find the density varying as  $1/r^2$ . The dashed curve is a fit of the three data points at lower densities to a  $1/r^2$  profile. The dot-dashed line is drawn to connect the two curves smoothly. The fact that data from neutral and ionized nitrogen match the data from ionized hydrogen so well indicates that the molecular density is independent of the gas and that the nitrogen plasma is fully ionized.

Fig. 7 is an x-ray pinhole photograph of 10 x magnification taken on Kodak No-Screen Film through an 80  $\mu\text{m}$  pinhole and filtered by 3.0  $\mu\text{m}$  of mylar covered with 1500  $\text{\AA}$  of aluminum and representing an input laser energy of 76 joules. Notice that a feature which we have identified with the gas jet nozzle is visible on the left side of the photograph along with a second feature, the "mustach-like" wisp between the nozzle and the gas plume proper. We have also found that the size of the plume increases with incident energy. Fig. 8 is a film iso-density contour plot of

AD-A114 893

AMERICAN INST OF PHYSICS NEW YORK  
LOW ENERGY X-RAY DIAGNOSTICS - 1981.(U)  
1981 D T ATTWOOD; B L HENKE

F/G 14/2

UNCLASSIFIED

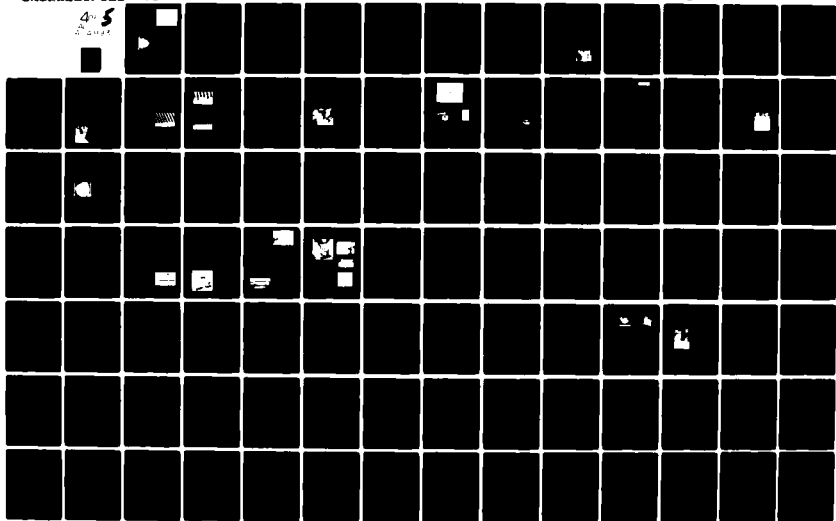
75

AFOSR-TR-82-0378

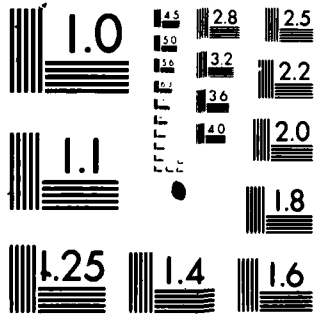
AFOSR-TSSA-81-00024

NL

4-5  
2-5



1489



MICROCOPY RESOLUTION TEST CHART  
NATIONAL BUREAU OF STANDARDS 1963 A



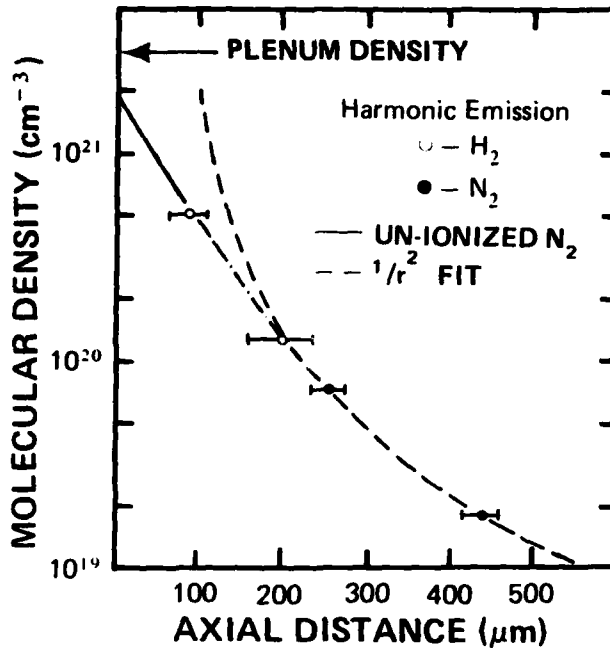


Fig. 6. Molecular density of a gas jet versus axial distance from the orifice.

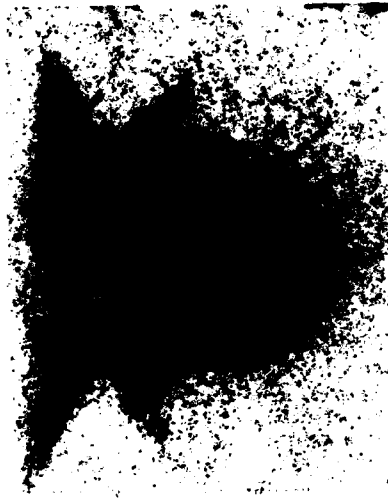


Fig. 7. X-ray pinhole photograph of  $1.05 \mu\text{m}$  irradiation of a nitrogen gas jet at a laser energy of 76 joules.

Fig. 7, indicating the well defined distribution of the x-ray emission. A typical axial intensity scan of an x-ray pinhole photo is shown in Fig. 9. Note that the peak of the x-ray emission appears upstream of the critical surface ( $2\omega$ ) where the largest portion of the laser energy is absorbed, indicating that the thermal energy is conducting into the higher density gas.

A method of determining the electron temperature is to measure the bremsstrahlung spectrum of soft x-rays emitted by the plasma. We have measured the spectrum through a set of foil-filtered thermoluminescent dosimeters (TLDs)<sup>3</sup> whose spectral response is reasonably well known. The ratio of the measurements through two different filtered TLD dosimeters is known as a

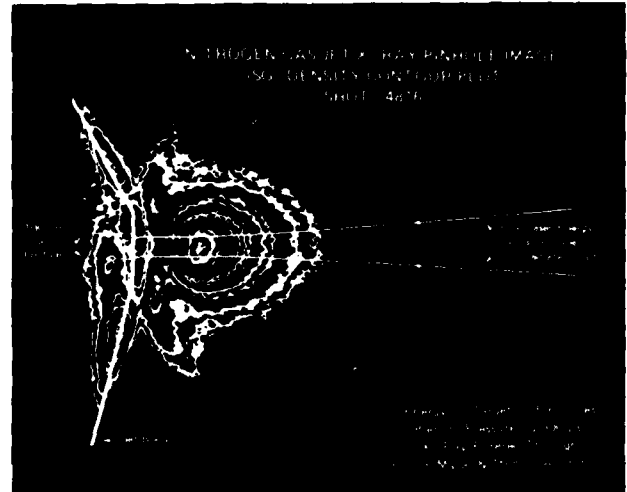


Fig. 8. Film iso-density contour plot of Fig. 7.

function of the electron temperature. They indicate that the temperature is about 0.5 keV, for  $1.05 \mu\text{m}$  irradiation and about 0.35 keV for  $0.53 \mu\text{m}$  irradiation of a  $100 \mu\text{m}$  scale length nitrogen plasma. Since hydrogen is a poor radiator, we have been able to obtain x-ray data only from nitrogen, argon, neon, and sulphur hexafluoride targets.

X-ray conversion efficiency for the jet can be estimated from the TLD measurements, if we can assume that the TLD calibration, which is known to  $\sim 350 \text{ eV}$ , can be extended down to  $\sim 150 \text{ eV}$ . Using "bare" (unfiltered) TLDs, and extrapolating the measurements into  $4\pi$ , we estimate the x-ray generation efficiency to be  $\sim 0.2\%$  and  $\sim 4\%$ , respectively, for wavelengths of  $1.05 \mu\text{m}$  and  $0.53 \mu\text{m}$ , and an input energy of  $\sim 30$  joules.

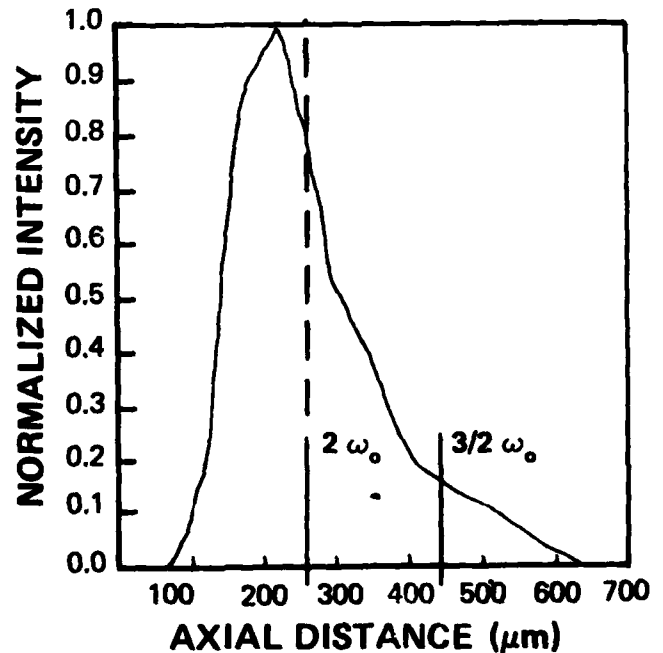


Fig. 9. Axial microdensitometer scan of a typical x-ray pinhole image, including the positions of the  $2\omega$  and  $3/2\omega$  radiation.

The difference, a factor of ~20, can be accounted for, in part, since the recombination radiation scales as  $n_e^2 \sim 1/\lambda^4$ .

The x-ray pinhole camera and TLD measurements indicate that a sizeable fraction, > 50% of the energy incident on the gas jet, is absorbed. The absorption fraction and electron temperature do not depend strongly on energy on target. However, additional experiments will be required to accurately determine the absorption fraction dependence on incident energy, wavelength, and gas type.

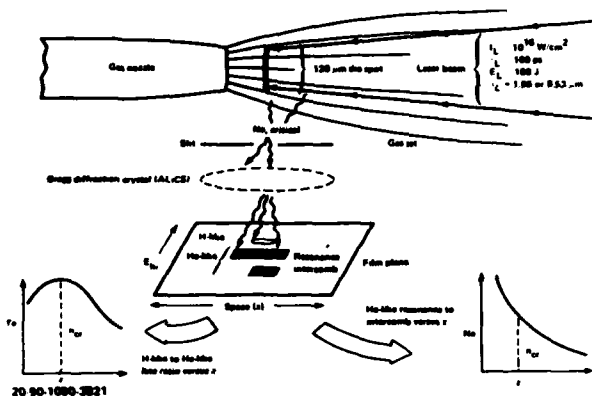


Fig. 10. Spectroscopic determination of gas jet  $N_e$  and  $T_e$  gradients.

In Fig. 11, a plot is shown of the x-ray fluence (keV/keV-sphere) versus photon energy for a neon gas jet irradiated with laser energy at  $\lambda_L = 0.53 \mu\text{m}$ . Note that the hydrogen-like and the helium-like lines are well defined, the He- and H- free-bound continua are observed above background and the intercombination lines are evident near the He-like resonance lines. They become more discernible if the fluence is plotted logarithmically as in Fig. 12. In fact, it is possible to obtain electron temperatures from the slopes of the free-bound continua.<sup>9</sup> The bare atom recombination

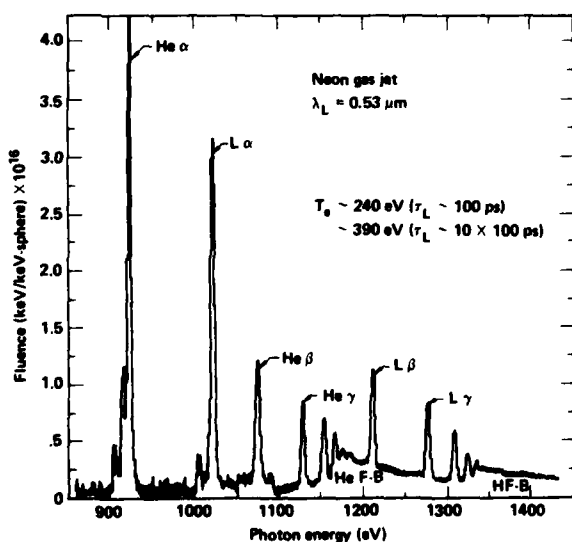


Fig. 11. X-ray fluence (keV/keV-sphere) versus photon energy (eV) for a nitrogen gas jet irradiated at  $\lambda = 0.53 \mu\text{m}$ .

continuum indicates an electron temperature of ~230 eV while the H-like atom recombination continuum gives ~135 eV. The discrepancy can be explained by the observation that the fluences for the two continua arise from different parts of the jet. That the two continua in the plot are both straight lines indicates the well-localized and symmetric nature of the temperature distribution.

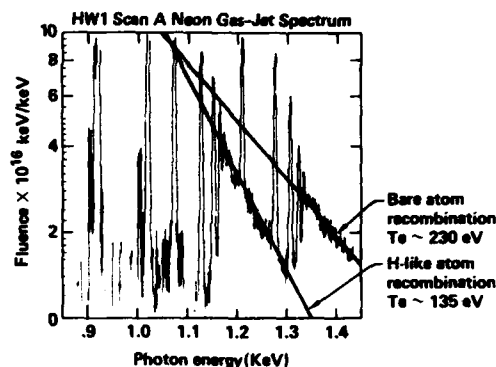


Fig. 12. The fluence of Fig. 11 plotted logarithmically to enable the  $T_e$  measurement via recombination continua<sup>9</sup> from the intensity ratio of H-like to He-like lines.

With the slit of the spectrograph oriented normal to the jet axis, it is possible to spatially resolve spectral lines along the jet axis, and thereby obtain the electron temperature distribution along the jet axis. In Fig. 13, an axial temperature profile

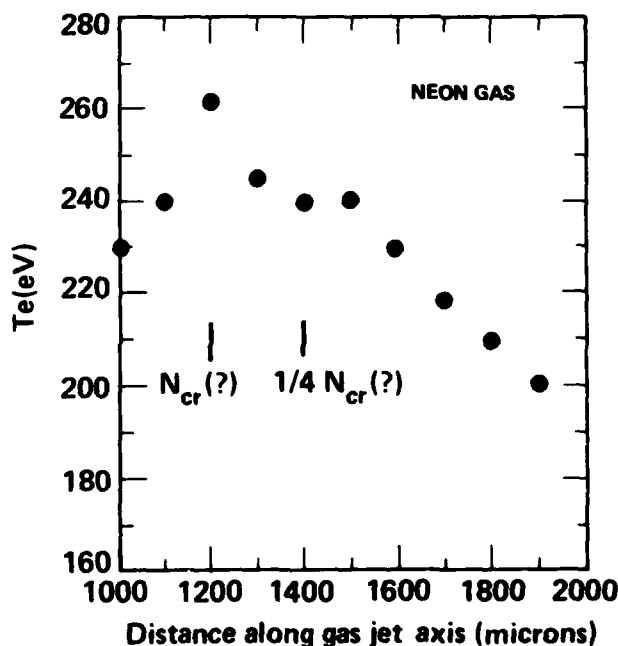


Fig. 13. Axial distribution of  $T_e$  for a neon gas jet irradiated at  $0.53 \mu\text{m}$  with 67 joules in 100 psec.

obtained for a neon gas jet with laser energy of 67 joules and pulse length of 100 psec is shown. The position of  $n_{cr}$  and  $1/4 n_{cr}$  are only approximately known since there are no fiducials in the spectrum to indicate the position of the jet orifice.

It is also possible to obtain the electron density from the intensity ratio of resonance to inter-combination lines of helium-like ions, as depicted in Fig. 10. Bolko, et al.<sup>5</sup> have shown (Fig. 14) that this intensity ratio,  $\alpha$ , varies rather sensitively with electron density for a large number of ion species from Na X to Ti XXI.

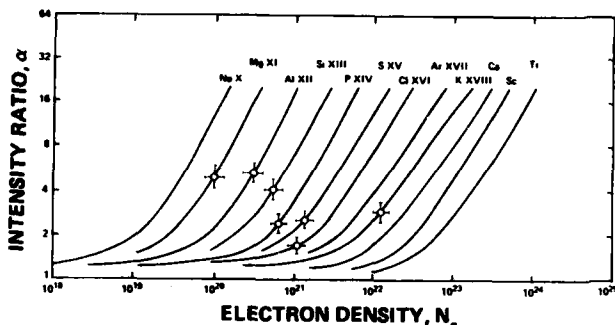


Fig. 14. The dependence of the intensity ratio,  $\alpha$ , of the resonance R ( $1s^2 \ ^1S - 1s2p \ ^3P_1$ ) and inter-combination I ( $1s^2 \ ^1S_0 - 1s2p \ ^3P_1$ ) lines of He-like ions on the electron density  $N_e$ .

From Fig. 14, it is evident that if a particular electron density range is expected to be measured, only a few ion species will provide the necessary intensity ratio,  $\alpha$ . With that in mind, we introduced sulphur hexafluoride,  $SF_6$ , as seed gas in  $N_2$  for a measure of the electron density in the range from 2 to  $20 \times 10^{20} \text{ cm}^{-3}$ . Fig. 15 shows the density distribution along the jet axis using this method.

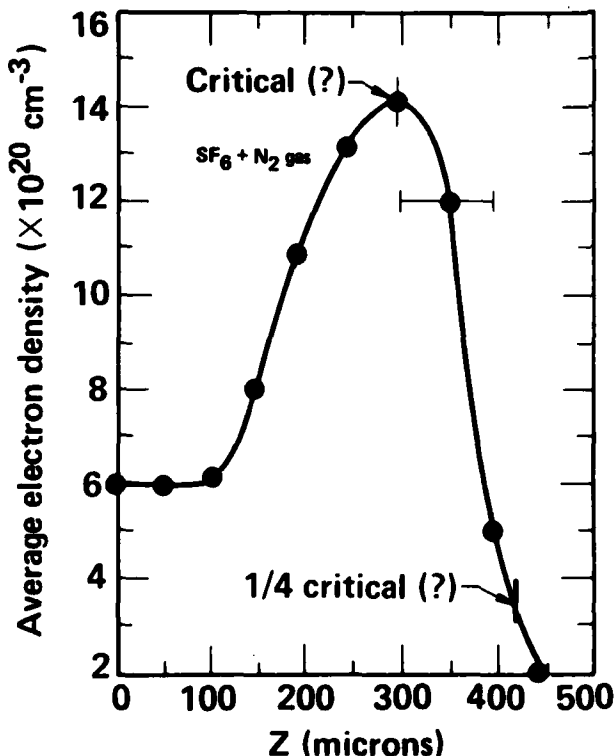


Fig. 15. The axial distribution of the average electron density obtained spectroscopically from the intensity ratio,  $\alpha$ , for a  $SF_6$  gas jet irradiated at 0.53  $\mu$  with 62 joules in 1 nsec.

As in the spectroscopic electron temperature measurements, no provision was made to locate the relative axial position of, say, the peak of the line emissions, to the jet orifice. So, for these preliminary spectroscopic measurements we assume, from the photographic composites of the pinhole image and  $2\omega$  and  $3/2\omega$  emissions (see Fig. 9), that the position of the critical surface, within experimental error, coincides with, or is slightly upstream of, the spectral line emission peaks. Since these relative positions are important for thermal transport considerations, future experiments will be designed to include position fiducials in the spectra.

As a source of soft x-rays, the laser-irradiated gas jet has proven to be an effective, reproducible and stationary source. It can be well characterized and used to study spectroscopic properties of the gas in the soft region of the x-ray spectrum, or used with known spectroscopic information to characterize the plasma. An example of the latter is the study of stimulated Brillouin scattering, which we have done recently. An example of the former, is the determination of opacities of selected ionic species, which we plan to do in the future.

Table I lists some of the principal features of the laser-heated gas jet.

TABLE I  
LASER GAS JET FEATURES

- The laser-plasma interaction occurs in a region of long scale length, without requiring the ablation of a solid surface.
- Inverse bremsstrahlung absorption and stimulated Brillouin scattering are the main coupling mechanisms.
- No evidence of suprathermal electrons, hard x-rays, stimulated Raman scattering, or resonance absorption.
- Absorption ~50%.
- Holographic interferograms provide density distributions of neutral gas or plasma.
- Scale Lengths: 100-200  $\mu$ m.
- Plasma  $T_e \sim 0.2$  to  $0.8$  keV via foil-filtered TLDs, films, and spectroscopy.
- Produces spectroscopically diagnosable high temperature plasmas ( $N_e \sim 10^{19} - 10^{22} \text{ cm}^{-3}$ ) since density profile is time independent.
- Plasma is well characterized so theoretical description is encouraged--opacity measurements are possible.
- Still to be done for the gas jet as an x-ray source:
  - account for non-equilibrium effects
  - more detailed comparison of  $V \cdot N_e$  via spectroscopy and interferometry
  - time resolution of spectral information via streak spectroscopy.

#### References:

- (1) F. J. Mayer, G. E. Busch, C. M. Kinzer, and K. G. Estabrook. *Phys.Rev.Lett.*, **44**, 1498 (1980).
- (2) D. Sweeney. Private Communication.
- (3) G. Charatis, S. B. Segall, and F. J. Mayer. *Bull.Amer.Phys.Soc.*, San Francisco, CA 11/1976.
- (4) Schluter, H. Z. *Naturforsch.* **16a**, 972 (1961).
- (5) Bolko, Fikuz, and Faenov. *J.Phys.*, **B12**, 1889 (1979).

A Sensitometric Calibration of the RAR 2497 Film for the Low Energy X-Ray Region

E. R. Dietz, T. S. Durland, B. L. Henke and M. A. Tester

University of Hawaii, Department of Physics and Astronomy, Honolulu, Hawaii 96822

Described here is an operational method which has been developed for the calibration of spectroscopic films for the low energy x-ray region of 100-2000 eV, along with some preliminary photographic density,  $D$ , versus exposure,  $E$ , measurements for the RAR 2497 films. The 2497 films are the successor to the widely applied 2490 films. A comprehensive sensitometric study of the RAR 2490 has been reported by R. F. Benjamin, P. B. Lyons and R. H. Day [1]. (See also their references for a review of works on the calibration of photographic materials for this low energy x-ray region.)

Our measurements are derived directly from calibrated spectra of standard x-ray source characteristic lines as simultaneously dispersed at normal incidence along a detection circle by elliptically curved crystal/multilayer analyzers. This type of spectrograph is described elsewhere in these Proceedings [2]. The absolute peak counting rate above background is determined by a flow proportional counter that is scanned along the detection circle using a precision goniometer. Multiple exposures are then taken with the photographic films placed along the same detection circle and under identical spectrographic conditions in order to obtain the required range of values of photographic densities at the peaks of the calibrated lines. An example of the corresponding proportional counter and microdensitometer scans for several diffracted orders of the Cu-L $\alpha$  (13.3 A/930 eV) radiation (from an elliptically curved lead behenate analyzer--2d=120 A) is shown in Fig. 1.

For the  $D$  vs  $E$  measurements that are presented here, appropriately filtered line radiations from the following x-ray tube anodes were used: molybdenum, graphited aluminum, anodized aluminum, copper and aluminum. These yielded the strong, easily isolated radiations: Mo-M $\alpha$  (64.4 A/193 eV), C-K $\alpha$  (44.7 A/ 277 eV), O-K $\alpha$  (23.6 A/525 eV), Cu-L $\alpha$  (13.3 A/930 eV), and Al-K $\alpha$  (8134 A/1487 eV). Filters were used on the x-ray tube window, on the entrance aperture (at the center of the detection circle) to the photographic film cassette [3] and on the proportional counter window. The filters for the camera and for the counter were carefully matched so that their attenuation factors cancel out in these absolute measurements. Approximately 800 A of aluminum was vacuum deposited upon the light-transparent filters to block visible and uv background light.

In order to measure the absolute photon intensity at a peak of a given spectral line, pulse height windows with a "pressure-tuned" flow proportional counter were used to eliminate high energy radiation components that might appear as high order diffraction background to the spectral line. Subatmospheric propane counter gas was used for all wavelengths longer than 10 A. Atmospheric P-10 was used for the Al-K radiation. It is assumed that all photons of a given energy that are absorbed within the gas path of the counter will be counted and with pulse heights characteristic of that energy. The equivalence of photon absorption efficiency and photon counting efficiency was verified by measuring count rate vs counter pressure which yielded the expected pressure dependence [4].

The counter and the effective microdensitometer slit widths were matched at approximately 100 microns, which dimension is small as compared with the FWHM of the spectral lines that were measured. The photographic emulsion granularity may be considered very small at this 100 micron scale.

A Boller-Chivens Model 14213 microdensitometer was used which has continuously variable primary-illumination and objective apertures. The data presented here were microdensitometered with primary illumination of 0.1 and objective 0.25 numerical apertures. Ten neutral density filters (Balzers) of calibrated densities in the range .01 to 2.4 were used to establish the microdensitometer calibration.

The 35 mm 2497 film [5] was developed with agitation for six minutes in a film tank with full strength D-19. Standard stop bath and fixing solutions were used. Drying was at room temperature and in still air.

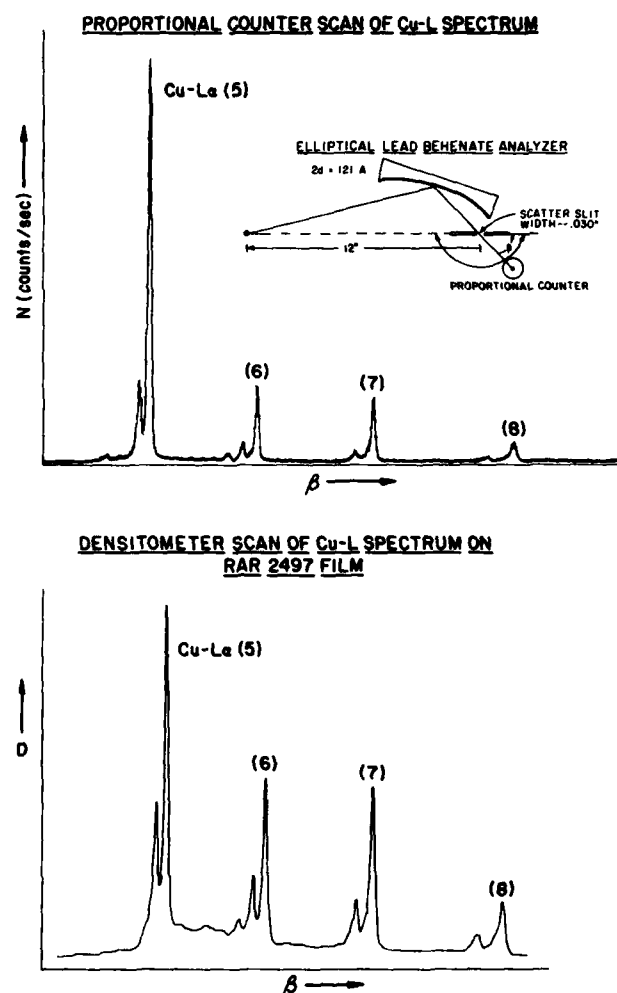


Figure 1

## RESULTS

In Figs. 2 through 6 we present the D vs E curves for the five standard laboratory wavelengths in the 193-1487 eV photon energy region. For three of these radiations (277 eV, 525 eV and 1487 eV) we were able to compare the data with the D vs E curves as reported by Benjamin, et al [1] for the similar 2490 emulsion (light lines). It is important to note that the densities that were measured for the 2490 film were optical diffuse densities which are characteristically lower than the corresponding values as measured with an objective lens of small numerical aperture (as 0.25 which has been used in our measurements).

For the conventional microdensitometry of photographic spectra, matched numerical apertures for the illumination and the objective optics are often employed, for example, as 0.1 for low resolution, large slit operation and 0.25 for high resolution, fine slit operation. In order to permit a conversion of our D vs E data to the matched 0.1/0.1 numerical aperture measurement, we have determined by measurement on the 2497 film and presented in Table 1 the ratio  $D(0.1/0.1)/$

$D(0.1/0.25)$ . The decrease of the measured density values as the numerical aperture of the objective lens is increased is dependent upon the scattering power (grain size) of the particular film. These ratios can also be used to predict the equivalent optical diffuse density using the results given by Weaver [6].

In order to describe the photon energy response of the 2497 emulsion, we present in Fig. 7 the sensitivity, S, vs photon energy, E (eV). Here we have used the definition for sensitivity, S, as the reciprocal of that exposure value which yields a density of 0.5 as measured here with our 0.1/0.25 microdensitometer numerical apertures. These values for the sensitivity, S, can be used to estimate corresponding values as measured with other objective lens numerical apertures by using the data presented in Table 1 and the results presented in Ref. 6.

The sharp drop in this sensitivity curve is the result of the sudden increase in the absorption of the gelatine overcoating at the carbon-K edge (280 eV). It is expected that this sensitivity will continue to increase essentially monotonically with photon energy to about 2000 eV in which region it will begin to drop off

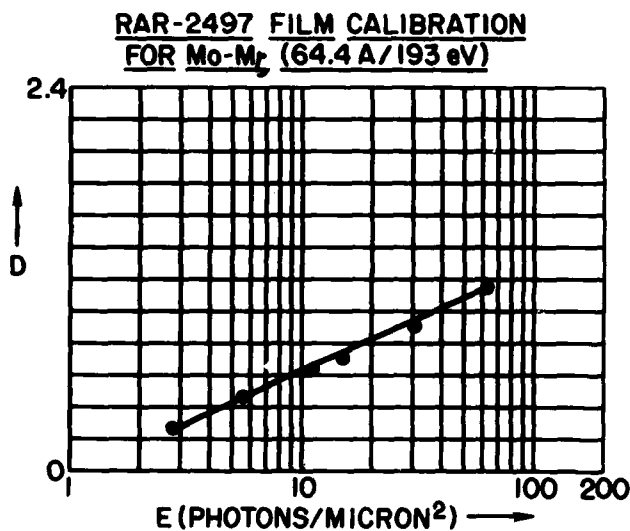


Figure 2

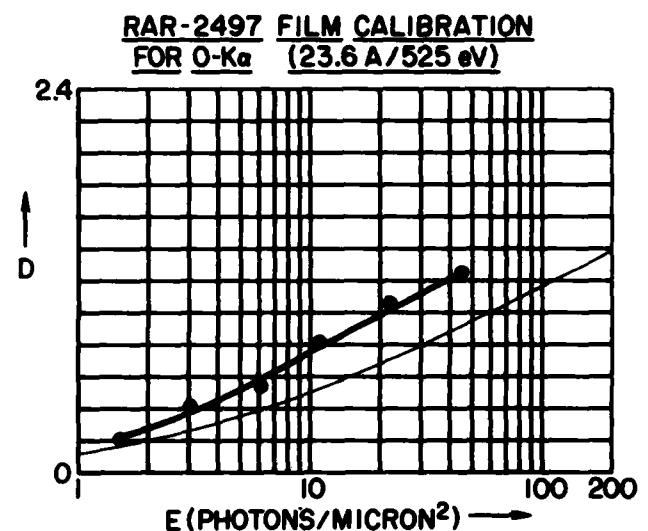


Figure 4

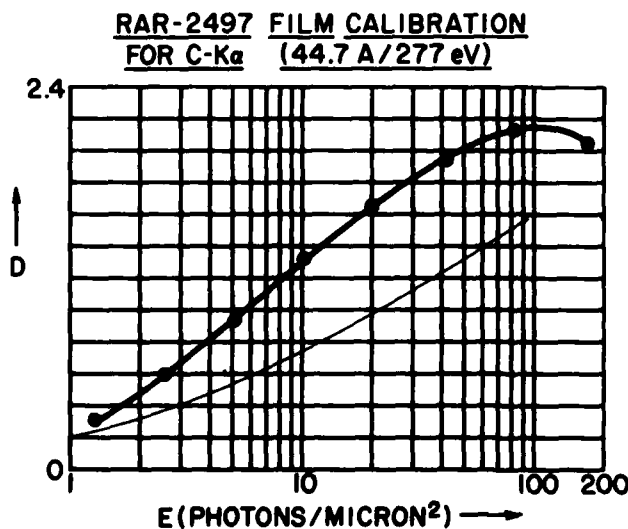


Figure 3

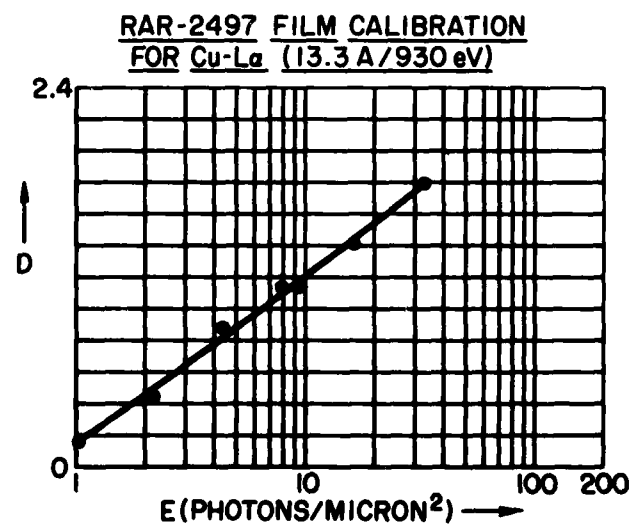


Figure 5

TABLE 1

D(0.1)/D(0.25)	1.50	1.36	1.28	1.24	1.21	1.19	1.16	1.14	1.12	1.11	1.09
D(0.25)	.2	.4	.6	.8	1.0	1.2	1.4	1.6	1.8	2.0	2.2

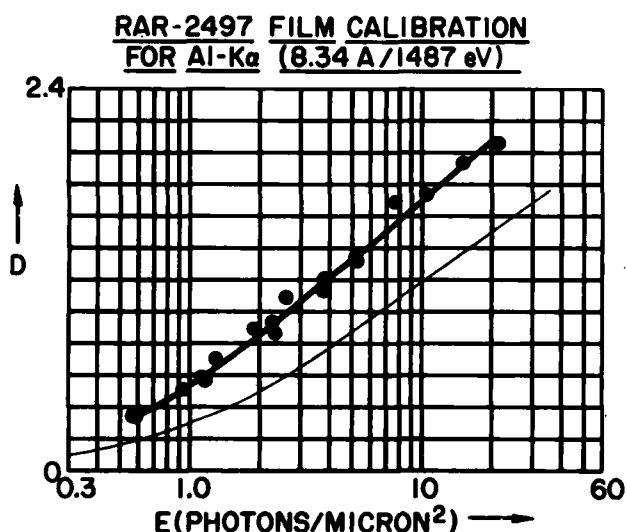


Figure 6

**SENSITIVITY, S (PHOTONS/MICRON $^2$ ) $^{-1}$   
VS  
PHOTON ENERGY, E(eV)**

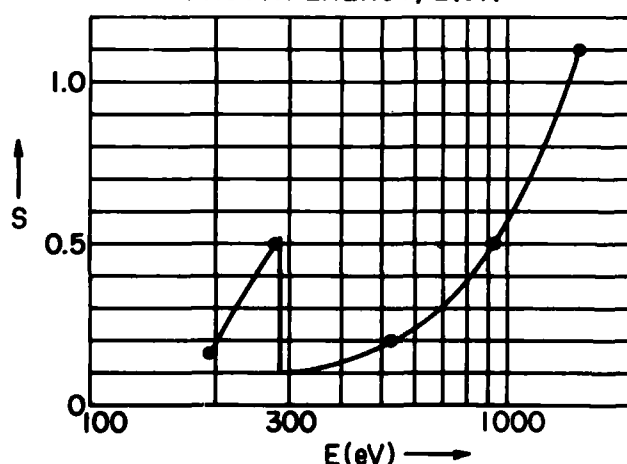


Figure 7

as the silver halide grains become more transmissive with increasing photon energy (up to the silver-L edges at about 3000 eV where the absorption efficiency of the silver halide grains is abruptly increased).

This work on the characterization of photographic emulsions appropriate for the low energy x-ray region is continuing at this laboratory on the RAR 2497 and other films including the Kodak 101-01.

#### ACKNOWLEDGEMENTS

We gratefully acknowledge the assistance of Priscilla Piano in the preparation of this work, and the helpful suggestions of Robert Benjamin (LANL), Claude Ditmore (LLNL) and M. A. Palmer (Sandia). This program is supported by a grant from the Air Force Office of Scientific Research, Grant No. 79-0027, and by a supplemental DOE/Lawrence Livermore National Laboratory subcontract, No. 9072209.

#### REFERENCES

- [1] R. F. Benjamin, P. B. Lyons and R. H. Day, *Appl. Opt.* **16**, 393 (1977).
- [2] B. L. Henke, "Low Energy X-Ray Spectroscopy with Crystals and Multilayer," Proceedings of the 1981 Topical Conference on Low Energy X-Ray Diagnostics, Monterey, California, June 8-10, 1981.
- [3] The camera cassette is a modified version of one that has been designed by K. Glibert, et al., Sandia Corp., Albuquerque, New Mexico.
- [4] B. L. Henke and M. A. Tester, *Advances in X-Ray Analysis* (Plenum Press, New York, 1975), Vol. 18, p. 76.
- [5] Kodak RAR Film (35 mm) ESTAR Base Special CAT.-135-7222. (This film was from a batch prepared for the Los Alamos National Laboratory--2497-88-423 (3/81).)
- [6] K. S. Weaver, *J. Optical Society of America* **40**, 524 (1950).

A Study of Bare X-ray Diode Saturation Due to a High Fluence X-ray Pulse<sup>(a)</sup>

R. B. Spielman and J. P. Anthes

Sandia National Laboratories, Albuquerque, NM 87185

## ABSTRACT

We have studied the response of bare, aluminum photocathode, x-ray diodes (XRD's) exposed to a source of pulsed x-rays from a laser produced plasma. Three cross calibrated detectors were placed at varied distances from the source. Saturation occurred at the Child-Langmuir predicted value. When low transparency screens were used as attenuators for the XRD's, saturation occurred at values below those predicted by the Child-Langmuir formula.

## I. INTRODUCTION

Saturation of an X-ray diode (XRD) becomes an important issue when the detector is exposed to a high intensity, soft x-ray source. Photoelectrons, produced by soft x-rays, leave the surface of the photocathode with relatively little energy and their trajectory to the anode is susceptible to perturbation by self fields. When the space charge fields are large the XRD can saturate. This effect must be considered when fielding detectors and analyzing data.

This paper describes the results of experiments which show that Child-Langmuir space charge effects can cause severe saturation of XRD signals. We also examine the effect of low transparency attenuating screens on the saturation of x-ray diodes.

## II. EXPERIMENTAL DESCRIPTION

The detectors consisted of three identical, cross calibrated, bare XRD's. Each XRD had a diamond turned, aluminum (99.9% pure) photocathode which was 1.25 cm in diameter. The anode consisted of high transparency ( $T = .64$ ) copper screen placed .125 cm from the photocathode. The detectors were typically operated at 1000V. The detector array was exposed to soft x-rays generated in a laser produced plasma. A Nd-Glass laser, which can deliver up to 50J in  $7 \times 10^{-9}$  sec-focussable to  $1 \times 10^{14}$  W/cm<sup>2</sup>, was used to illuminate aluminum or gold targets to generate the hot plasma.

To study XRD saturation we placed the three detectors at 58 cm, 98 cm and 228 cm from the source. We then recorded a large number of signals from shots which had different laser energies and different target materials. This procedure enabled us to observe the response of the detectors over a wide range of x-ray intensity. The above technique was carried out for bare XRD's and attenuated (screened) XRD's. The data was recorded on Tektronix 7912AD's which allowed rapid data reduction.

## III. EXPERIMENTAL DATA

## A. Data From Unattenuated Bare XRD's

Our first objective was to study the saturation of the simplest XRD possible, an unattenuated bare XRD. For low x-ray fluences the detectors, when corrected for solid angle, yield nearly identical signals ( $\pm .05$ ). This is important because it allows us to see small deviations from unsaturated behavior. Figure 1 shows a typical data set. The data is corrected for detector solid angle. The signals from two of the detectors show signs of saturation. The saturation is very distinct and occurs at exactly the level predicted by Child-Langmuir space charge limited flow. The saturated

signals on all of the data are characterized by an abrupt transition to saturation at the same absolute detector signal level. It is interesting to note that the most heavily saturated signal does not exceed the maximum value allowed by Child-Langmuir space charge limited flow.

## B. Data From Attenuated Bare XRD's

Our second objective was to study the effect of attenuating screens on detector saturation. A low transparency copper screen (2000 lines per inch,  $T = .24$ ) was used as an attenuator. Because screens attenuate by acting as a dispersed aperture one might suspect that photocathode "hot" and "cold" spots could affect XRD saturation. A repeat of earlier runs was made with attenuated XRD's. Figure 2 shows signals for three attenuated detectors.

The two closest detectors are saturated. The interesting thing to notice is the subtle saturation in the second largest signal. The signal saturates "smoothly". Even the heavily saturated signals appear smooth and does not have the abrupt look seen in Fig. 1. At very high x-ray fluences the XRD's yield signals greater than the saturated levels. Figure 3 shows data where the signals are larger than the Child-Langmuir space charge flow prediction.

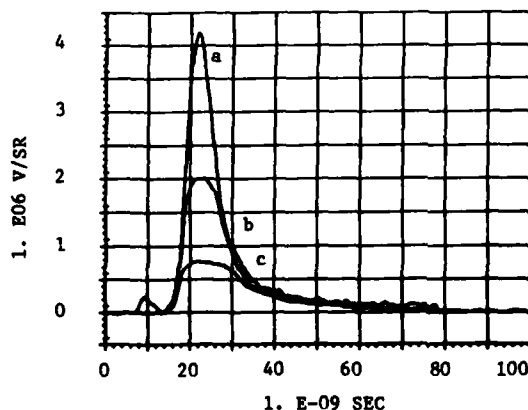


Fig. 1. Unattenuated bare XRD signals showing detector saturation. Detectors a, b, and c are at distances of 228 cm, 98 cm, and 58 cm respectively.

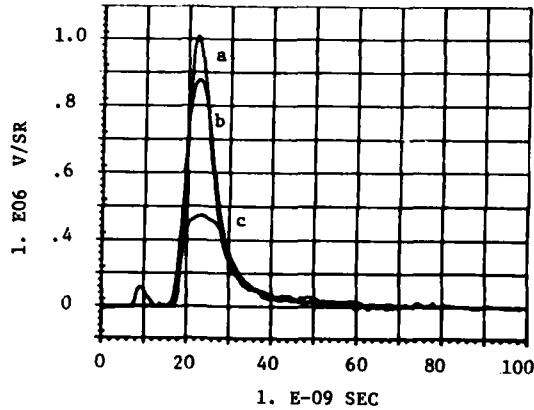


Fig. 2. Attenuated (with screens) bare XRD signals showing gradual detector saturation. Detectors a, b, and c are at distances of 228 cm, 98 cm, 58 cm respectively.

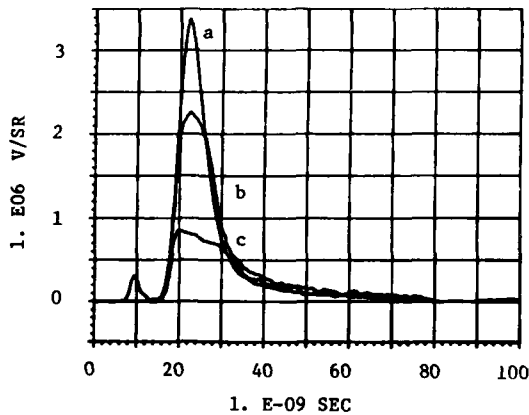


Fig. 3. Attenuated bare XRD signals showing overshoot in the saturated signal. Detectors a, b, and c are at distances of 228 cm, 98 cm, 58 cm respectively.

#### IV. CHILD-LANGMUIR SPACE CHARGE LIMITED FLOW

The peak signal from an XRD is determined by Child-Langmuir space charge limited flow. When there are large numbers of electrons in the anode-cathode gap electric fields produced by the electrons in the gap repel other electrons leaving the photocathode. There exists a steady state solution for one-dimension cold electron flow.

$$j = \frac{4}{9} \left( \frac{2e}{m_e} \right)^{1/2} \frac{|V|^{3/2}}{4\pi d^2} \quad (\text{esu/sec-cm}^2) \quad (1)$$

Equation 1 is the traditional form for Child-Langmuir space charge limited flow. We can cast equation 1 in a more useful form for x-ray diodes

$$I = 2.34 \times 10^{-6} A \frac{|V|^{3/2}}{d^2} \quad (\text{amperes}) \quad (2)$$

A is the detector area in  $\text{cm}^2$ , V is the applied diode voltage in volts and d is the anode cathode spacing in cm. This formula accurately predicts the saturated levels of all of our data except for one specific case described below.

An XRD needs charge to provide a signal as it gets it from the capacitance of the detector and nearby cable. Because the charge in the local capacitor also provides detector voltage we have the possibility of charge depletion reducing the "local" voltage and causing premature detector saturation. The solution is to reduce the absolute signal size by decreasing detector aperture. (Note that the charge available - length of cable - is proportional to the pulse duration of the radiation.)

#### V. CONCLUSION

Space charge limited flow is the saturation mechanism for x-ray diodes. Unattenuated bare XRD's saturate abruptly at precisely the value predicted by Child-Langmuir space charge limited flow. XRD's which have been attenuated with low transparency copper screens begin to saturate at signal levels less than the predicted value and do so in a gradual fashion. It is important to realize that this saturation might not be noticed if no unsaturated reference signal existed.

a) This work supported by the U. S. Dept. of Energy.



Rick Spielman of Sandia discussing his poster paper with David Nagel of NRL and Paul Mix of Sandia.



## The Reflecting Properties of Soft X-Ray Multilayers

Alan E. Rosenbluth and J. M. Forsyth

Laboratory for Laser Energetics, University of Rochester, 250 East River Rd., Rochester, N.Y. 14623

## ABSTRACT

We treat a variety of problems in the theory of soft x-ray multilayer mirrors. A characteristic matrix solution to Maxwell's equations is presented that applies to both periodic and non-periodic reflectors whose layers can possess arbitrary index gradients. Procedures are derived to maximize multilayer reflectivity in the kilovolt and sub-kilovolt regime. A refractive correction to Bragg's law is derived that includes the effect of absorption as well as the effect of dispersion. Multilayer reflectivity in the presence of random thickness errors is treated analytically. An analytic treatment of different kinds of interfacial roughness is described. The reflecting properties of the multilayers may contain qualitative signatures that are characteristic of the different kinds of roughness. The effect of interlayer diffusion is discussed.

## 1. Characteristic Matrix Analysis of X-Ray Reflectors

Our analysis of x-ray multilayers proceeds from a solution to Maxwell's material equations, given that the multilayer structure has a spatially varying complex dielectric constant  $\epsilon$ . In this respect our analysis follows the Ewald-von Laue dynamical theory of crystal diffraction. In the dynamical theory it is assumed that  $\epsilon$  is three-dimensionally periodic, as in a perfect crystal. We assume that  $\epsilon$  is a function only of the coordinate  $z$  normal to the multilayer surface;  $\epsilon$  need not be rigorously periodic.

In this case it is known that the wave equation can be separated into ordinary differential equations, whose solutions can be put into characteristic matrix form.<sup>1</sup> The characteristic matrix solutions for homogeneous layers are commonly used in optical multilayer calculations.

In the visible, these differential equations must be solved numerically in the case of a general structural profile, but for the x-ray regime we have solved them analytically under the assumption that  $|\epsilon - 1| \ll 1$ . Essentially, we treat the material medium as giving rise to a perturbation in the vacuum fields. We now present this solution.

Let the plane of incidence be the  $y$ - $z$  plane.

Define:

S Polarization	P Polarization
$E \equiv \vec{E}_x$	$E \equiv -\vec{E}_y / \cos \theta$
$H \equiv \vec{H}_y / \cos \theta$	$H \equiv \vec{H}_x$

(1)

The characteristic matrix solution for the  $K$ th cell of the multilayer shown at right is:

$$\begin{pmatrix} E_{K+1} \\ H_{K+1} \end{pmatrix} = \begin{pmatrix} -\cos \phi_K - p_K & -i(t_K - \gamma_K) \\ -i(t_K + \gamma_K) & -\cos \phi_K + p_K \end{pmatrix} \begin{pmatrix} E_K \\ H_K \end{pmatrix} \quad (2)$$

where:

$$\begin{aligned} \phi_K &= \pi - \frac{2\pi d_K}{\lambda} \cos \theta & \gamma_K &= \frac{2\pi}{\lambda} \sec \theta \int_{\text{cell}} dz \Delta(z) \cos \left( \frac{4\pi}{\lambda} \cos \theta z \right) \\ \Delta(z) &= \frac{1}{2} [\epsilon(z) - 1] & p_K &= \frac{2\pi}{\lambda} \sec \theta \int_{\text{cell}} dz \Delta(z) \sin \left( \frac{4\pi}{\lambda} \cos \theta z \right) \\ \mu_K &= \frac{2\pi}{\lambda} \sec \theta \int_{\text{cell}} dz \Delta(z) & t_K &= \sin \phi_K - \mu_K \end{aligned} \quad (3)$$

(Here we follow the optics convention where  $\theta$  is measured to the normal.)

0094-243X/81/750280-06\$1.50 Copyright 1981 American Institute of Physics

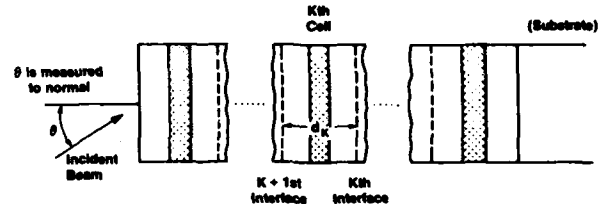


Fig. 1. Decomposition of reflector into unit cells.

We note that the structure as determined by  $\Delta(z) \equiv 1/2(\epsilon(z)-1)$  need not correspond to a succession of homogeneous layers, but can have an arbitrary variation along  $z$ .

If  $\rho_K$  is the amplitude reflectivity of the stack of cells  $K-1, K-2, \dots, 1$ , then:

$$E_K = 1 + \rho_K \quad H_K = 1 - \rho_K \quad (4)$$

From these we can derive a difference equation that propagates the amplitude reflectance from unit cell to unit cell. This is analogous to the amplitude recursion formula that is used to propagate the reflected amplitude from single layer to single layer in optical multilayer calculations. The equation is:

$$\rho_{K+1} = e^{-2i(\phi_K - \mu_K)} \rho_K - (i\gamma_K - p_K) - (i\gamma_K + p_K) \rho_K^2 \quad (5)$$

This equation is particularly useful in analysing non-periodic multilayers.

## II. Equivalent Parameter Analysis of Periodic Reflectors

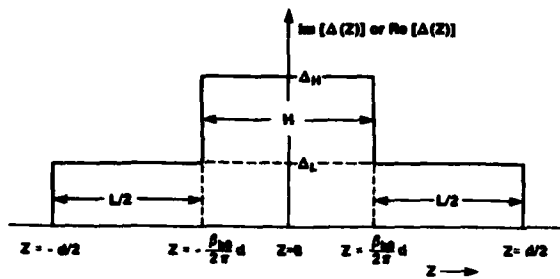


Fig. 2. Structure of unit cell in a bilayer reflector.

A multilayer with a bilayer structure consists of alternating homogeneous layers of two different materials. If the thicknesses of the different layers of each material are equal, the multilayer is periodic. By placing the cell boundaries at the midpoints of the  $L$  layers the cell structure can be made centrosymmetric as shown in the diagram above.

Then the parameter  $p$  is zero, and the characteristic matrix solution becomes:

$$\begin{pmatrix} E_{k+1} \\ H_{k+1} \end{pmatrix} = \begin{pmatrix} -1 & -(\phi - \mu - \gamma) \\ -(\phi - \mu + \gamma) & -1 \end{pmatrix} \begin{pmatrix} E_k \\ H_k \end{pmatrix} \quad (6)$$

where:

$$\begin{aligned} \gamma &= \left(\frac{2d}{\lambda}\right)^2 (\Delta_H - \Delta_L) \sin \beta_{00} \\ \mu &= \left(\frac{2d}{\lambda}\right)^2 [\pi \Delta_L + \beta_{00} (\Delta_H - \Delta_L)] \end{aligned} \quad (7)$$

This has the form of the well-known characteristic matrix solution for a single homogeneous layer having an index of refraction  $n_k$  and phase thickness  $\beta_k$ :

$$\begin{pmatrix} E_{k+1} \\ H_{k+1} \end{pmatrix} = \begin{pmatrix} \cos \beta_k & -(i/n_k) \sin \beta_k \\ -i n_k \sin \beta_k & \cos \beta_k \end{pmatrix} \begin{pmatrix} E_k \\ H_k \end{pmatrix} \quad (8)$$

To match this matrix to the characteristic matrix for the unit cell of an x-ray reflector, eq. (6), we must make the assignments  $\beta_k = \pi + \sqrt{t^2 - \gamma^2}$  and  $n_k = \sqrt{(t+\gamma)/(t-\gamma)}$ , where  $t = \phi - \mu$ . The two matrices will be equal to within first order in  $\phi$  and  $\Delta$ .

This matching of matrices is an example of what in thin film optics is known as the method of equivalent parameters.<sup>2</sup> There is a straightforward analogy between the properties of the single equivalent layer and the single cell of an x-ray reflector.

A reflector with  $J$  cells corresponds to a stack of  $J$  equivalent layers, which is, in effect, a single layer of phase thickness  $J\beta_k$ .

By letting  $E_1 = 1 + \rho$ , and  $H_1 = 1 - \rho$ , we can obtain the well-known expression for the reflectivity of a single layer:

$$\rho_{\text{refl}} = \frac{i(n_0 - 1/n_1) \tan(J\beta)}{2 - i(n_0 + 1/n_1) \tan(J\beta)} \quad (9)$$

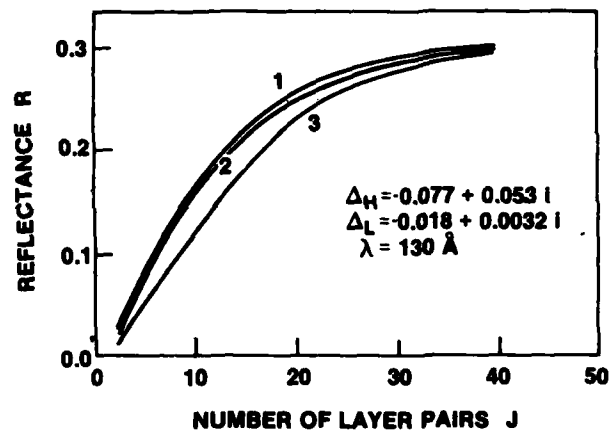
where  $\delta = \beta - \pi$ .

This is also the reflectivity of an x-ray multilayer having  $J$  cells.

## III. Optimization of Reflectivity

A computer program can be used to determine the optimum layer thicknesses in an x-ray reflector via standard optimization algorithms. A study of such optimized designs shows that if the radiation energy is above about 100 eV, a bilayer reflector that is periodic can achieve nearly the maximum reflectivity that is possible from given layer materials.

The results of the computer study agree with a theoretical analysis we have made. It can be shown analytically that if  $J$  is large, the reflectivity of an optimized periodic reflector is an extremum with respect to an arbitrary perturbation in structure. (The structures of the different cells need not be perturbed equally). This analysis neglects small terms proportional to the square of the difference of the index of refraction from one.



1.  $R(J)$  of non-periodic designs optimized at each  $J$  (2  $J$  degrees of freedom)
2.  $R(J)$  of periodic designs optimized at each  $J$  (2 degrees of freedom)
3.  $R(J)$  of a periodic design optimized at  $J \rightarrow \infty$  (2 degrees of freedom)

Fig. 3. Comparison of optimization schemes.

For this reason we now concentrate on the periodic case. When  $J$  is large, the reflectivity of a periodic multilayer with a centrosymmetric structure is given by

$$\rho = -\frac{\delta + t}{\gamma} \quad \text{where } \delta = \sqrt{t^2 - \gamma^2} \quad (10)$$

Let a dot represent a derivative with respect to some structural parameter. Using  $\rho = -(\delta+t)/\gamma$  one can obtain a general optimization condition on the intensity reflectivity  $R = \rho\rho^*$ :

$$\dot{R} = 2R \cdot \text{Re} \left( \frac{\dot{\rho}}{\rho} \right) = 2R \cdot \text{Re} \left( \frac{\dot{\gamma} - t\dot{\gamma}}{\gamma\delta} \right) = 0 \quad (11)$$

A similar, but slightly more complicated result can be obtained if  $\rho \neq 0$ .

We show in sec. IV, eq. 16-17, that at the wave length of peak reflectivity,  $\delta$  is pure imaginary.

The condition for maximizing the peak reflectivity is therefore:

$$\text{Im}(i - \frac{\dot{\gamma}}{\gamma}) = 0 \quad (12)$$

As an application of this result, we consider the problem of optimizing the H to L thickness ratio in a multilayer with a bilayer structure.

In order to do so we apply our optimization condition to the parameter

$$\beta_{00} = \frac{2\pi}{\lambda} d_H \cos \theta = \pi \frac{d_H}{d_H + d_L} \quad (13)$$

and obtain a condition first obtained by Vinogradov and Zeldovich for the case of reflection at normal incidence:<sup>3</sup>

$$\tan \beta_{00} = \beta_{00} + \frac{\pi \text{Im}(\Delta_L)}{\text{Im}(\Delta_H - \Delta_L)} \quad (14)$$

More generally, we consider  $m$ th order diffraction, and let  $\beta_{00} = m\pi(d_H/d_H + d_L)$ . We obtain the optimization condition:

$$\tan \beta_{00} = \beta_{00} + \frac{m\pi \text{Im}(\Delta_L)}{\text{Im}(\Delta_H - \Delta_L)} \quad (15)$$

In the plot below, and in the other numerical examples of this report, we have used preliminary values for atomic scattering factors from a forthcoming compilation.<sup>4</sup> These have generously been provided to us by B. Henke.

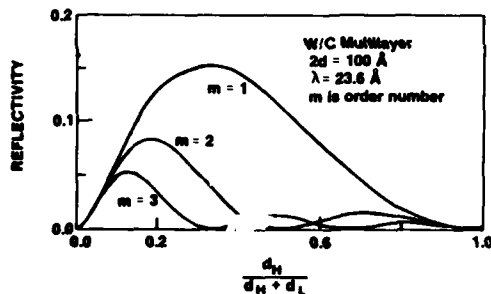


Fig. 4. Reflectivity as a function of thickness ratio.

#### IV. The Absorption Correction to Bragg's Law

It is well-known that the Bragg condition for crystal diffraction,  $2d \cos \theta = \lambda$ , must be corrected for the dispersive effects of the crystalline medium (following the optics convention,  $\theta$  is the angle of incidence to the normal). It is less well-known however, that Bragg's law must be corrected for absorption as well as for dispersion.

In our formalism, the parameter  $\phi$  represents the detuning of a multilayer from the simple Bragg angle  $\theta_0 = \arccos(\lambda/2d)$ , through the relation:

$$\phi = \frac{2\pi d}{\lambda} (\cos \theta_B - \cos \theta) \quad (16)$$

To find the exact angle of maximum reflectivity we optimize the structure with respect to the parameter  $\phi$ . Then using the optimization condition introduced above (eq.(11)), and setting  $\dot{\gamma} = 0$ ,  $i = 1$ , we get:

$$\text{Re}(1/\delta) = 0$$

or

$$\text{Re}(\delta) = 0 \quad (17)$$

The same condition is obtained in the general case when  $p \neq 0$ .

The requirement that  $\text{Re}(\delta) = 0$  is the same as requiring that the real part of the equivalent phase thickness  $\beta$ , equal  $\pi$ , which is different from the usual requirement in the absence of absorption that the real part of the optical phase thickness equal  $\pi$ . The difference is a consequence of the presence of multiply reflected beams. In an absorbing structure, these beams undergo phase changes upon reflection, causing a phase change in the overall oscillation across each cell.

Since  $\delta = \sqrt{\mu' - \gamma^2}$ , we can write our requirement that  $\text{Re}(\delta) = 0$  as  $\text{Im}(\delta^2) = 0$ , which can be shown using the Schwarz inequality to automatically imply  $\text{Re}(\delta^2) < 0$ . The condition  $\text{Im}(\delta^2) = 0$  can be manipulated to give:

$$\cos \theta_B - \cos \theta = \frac{\cos \theta_B}{\pi} \left( \mu' \left[ \frac{\gamma \gamma' + p' p''}{\mu'} \right] \right) \quad (18)$$

where primes and double-primes denote real and imaginary parts. This result was first discovered by F. Miller<sup>5</sup> in the context of crystal diffraction, and independently by us in the context of multilayer reflection. P. Lee, of LASL is a collaborator with us in this work.

In the usual formula for the dispersion correction, the term in square brackets is missing.<sup>6</sup> The first term in parentheses,  $\mu'$ , can be considered to represent dispersion, the term in square brackets absorption.

The relative magnitude of the two effects are compared in the plot below. The ratio plotted is

$$\text{Ratio} = \frac{\theta_2 - \theta_1}{\theta_B - \theta_2} \quad (19)$$

where  $\theta_0 = \arccos(\lambda/2d)$ ,  $\theta_2$  is the true Bragg angle as corrected for absorption and dispersion, and  $\theta_1$  is the Bragg angle as corrected for dispersion only.

It can be shown that the absorption correction is always smaller than the dispersion correction, but as the plot shows there are cases in which the two are comparable. The absorption correction must therefore be included whenever an accurate matching of wavelength, angle, and  $2d$ -spacing is required.

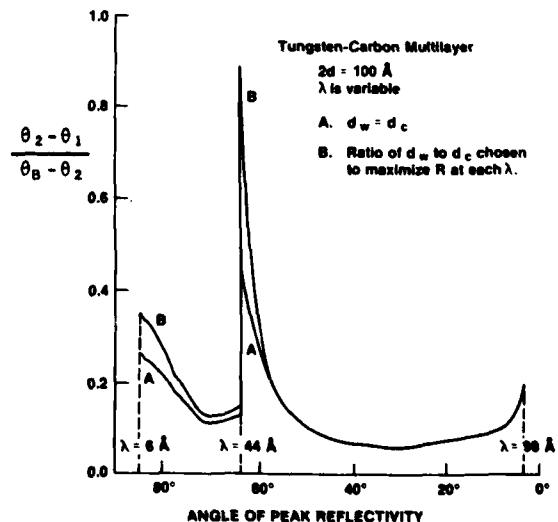


Fig. 5. Comparison of absorption correction to dispersion correction.

### V. The Effect of Random Thickness Errors On Multilayer Reflectivity

Random thickness errors in an x-ray multilayer can cause a severe degradation in reflectivity. Even when the errors are small compared to the multilayer's 2d-spacing, they can cause a significant cumulative dephasing if not compensated for during the fabrication.

Previous theoretical analysis of the effect of random thickness errors is largely limited to the work of Shellan on optical Bragg reflectors.<sup>7</sup> Shellan treats thickness errors as a small perturbation in the structure of dielectric reflectors having a small coupling constant per cell. X-ray reflectors have a small coupling constant, but it may not be adequate to consider the errors in x-ray reflectors to be small perturbations that cause only a small degradation in reflectivity. In the soft x-ray regime it is also important to include absorption, which can be the major factor determining the reflectivity.

We have met these requirements using an analysis based on the amplitude recursion equation introduced above (eq. (5)). This equation is:

$$\rho_{K+1} = e^{-2i(\phi_K - \mu)} \rho_K - (i\gamma - p) - (i\gamma + p) \rho_K^2 \quad (20)$$

We treat  $\phi_K$  as a random variable with mean

$$\langle \phi_K \rangle = \pi - (2\pi \langle d_K \rangle / \lambda) \cos \theta \quad (21)$$

and known variance  $\langle \Delta \phi^2 \rangle$ . In a bilayer reflector,

$$\langle \Delta \phi^2 \rangle = \frac{4\pi^2}{\lambda^2} \cos^2 \theta (\langle \Delta L^2 \rangle + \langle \Delta H^2 \rangle) \quad (22)$$

if the errors in the L and H layers are independent.

We make the problem analytically tractable by first dividing  $\rho_K$  into a deterministic and a non-deterministic part,  $\rho_K = \langle \rho_K \rangle + \tilde{\rho}_K$ , and then making use of the inequality:

$$\langle |\tilde{\rho}_K|^2 \rangle < \langle |\rho_K|^2 \rangle < 1 \quad (23)$$

The right inequality is fairly strong in the soft x-ray regime, where absorption is fairly large. The right inequality is also particularly strong when  $\langle \Delta \phi^2 \rangle \gg |\mu|$ , since the reflectivity is then severely degraded by the thickness errors.

On the other hand, the left hand inequality becomes very strong when  $\langle \Delta \phi^2 \rangle \ll |\mu|$ , since  $\langle \rho_K \rangle \approx \rho_K$  when the errors are small.

For these reasons  $|\tilde{\rho}_K|$  is generally  $\ll 1$ ; in our analysis we therefore neglect terms that are cubic or higher in  $\tilde{\rho}_K$ . Our approximation is accurate in the limits  $\langle \Delta \phi^2 \rangle \gg |\mu|$  and  $\langle \Delta \phi^2 \rangle \ll |\mu|$ , but is also fairly accurate in the intermediate region.

In a similar way we treat the K-dependence of  $\rho_K$  and  $\tilde{\rho}_K$  in an approximate way that is correct in the limits  $\langle \Delta \phi^2 \rangle \ll |\mu|$ ,  $\langle \Delta \phi^2 \rangle \gg |\mu|$ ,  $K \ll |\mu|^{-1}$ , or when the absorption is sufficiently large that  $|\rho| \ll 1$ .

The final result for a reflector with J-1 cells is:

$$\langle R_r \rangle = |\langle \rho_r \rangle|^2 \left\{ 1 + \frac{2\langle \Delta \phi^2 \rangle}{|1 - E_r|^2} \left[ \frac{1 - e_r}{2 \operatorname{Im}(\tilde{\delta}_r)} - \operatorname{Re} \left( \frac{E_r - e_r}{\operatorname{Im}(\tilde{\delta}_r) + (u/2)} \right) + \frac{e^{-4(J-1)\operatorname{Re}(u)} - e_J}{2 \operatorname{Im}(\tilde{\delta}_r) + \operatorname{Re}(u)} \right] \right\} \quad (24)$$

where:

$$e_J \equiv e^{-4(J-1)\operatorname{Im}(\tilde{\delta}_r)} \quad \tilde{\delta}_r \equiv -i - (\gamma - i\rho) \langle \rho_r \rangle \\ f \equiv i t + \langle \Delta \phi^2 \rangle$$

$$\langle \rho_r \rangle = \frac{1}{2v} (2u \frac{1 + wE_r}{1 - wE_r} - 2f) \quad (25)$$

$$w \equiv \frac{1 - (u/f)}{1 + (u/f)} \quad E_J \equiv e^{-2(J-1)u} \quad u \equiv \sqrt{f^2 - (i\gamma - p)v}$$

The accompanying figure shows  $\langle R_r \rangle$  plotted as a function of RMS thickness error in a particular example.

We have tested the accuracy of the analysis by making a Monte Carlo simulation. A computer program is used to generate a large number of randomly perturbed multilayer stacks, and to compute their mean reflectivity. Sample results are shown in the plot. The plot also shows a computation of  $\Delta \lambda / \lambda$  as a function of RMS thickness error.

There are no free parameters in the fit of the analytic expression to the Monte Carlo results.

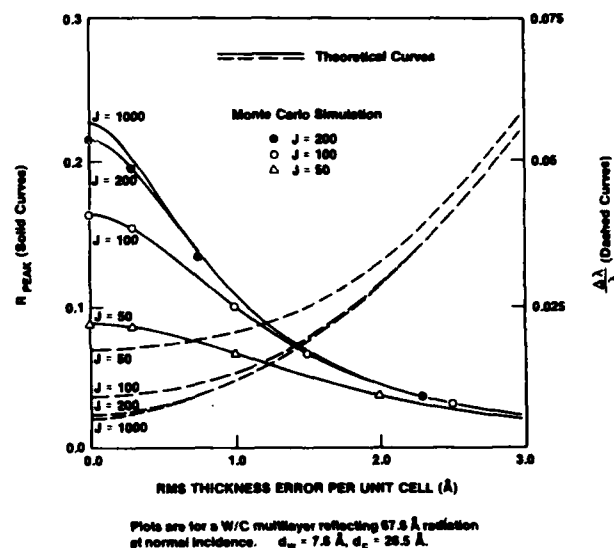


Fig. 6. Effect of random thickness errors on multilayer reflectivity.

### VI. The Effect of Interfacial Roughness On Multilayer Reflectivity

Eastman has developed numerical methods to treat the effect of layer roughness in optical multilayers.<sup>8</sup> We have used similar physical assumptions to treat certain kinds of roughness in x-ray multilayers analytically. Our model assumes, in effect, that the near-field reflected beam above any point on the multilayer's surface can in principle be calculated by inserting local values for the layer properties into an algorithm that computes the reflectivity of multilayers with planar interfaces. Such a scalar model of the roughness requires that the transverse autocorrelation length of the roughness be large compared to the layer thicknesses. A more detailed discussion of the physical assumptions of the scalar model is given in ref. 8.

Ref. 9 discusses the limitations of scalar scattering theory in comparison with more rigorous theories. In general the scalar theory is best at predicting total specular and diffuse reflectivities

and at predicting the angular distribution of the diffusely reflected beam at angles close to the specular beam; it cannot predict polarization effects.

One kind of multilayer roughness that has been treated with the scalar theory is that which Eastman calls "identical films", in which all layers are considered to reproduce a common roughness profile (generally that of the substrate). The autocorrelation length of the roughness in the longitudinal direction is therefore very large. Spiller et al. and Haelbich et al. have discussed the effect of roughness on x-ray multilayer reflection in terms of the same expression as results from the identical film model.<sup>10,11</sup>

We have modeled two kinds of non-identical roughness in which the longitudinal autocorrelation length is very small, so that the roughness profiles of the different layers are uncorrelated. We refer to the two as "roughening films" and "smoothing films".

In the case of roughening films, we assume that the errors in the local layer thicknesses above each point on the surface cause a cumulative dephasing, so that the absolute roughness of the top layer increases in a random walk fashion as more layers are added. One may consider the formation of these films to be such that the granularity in each layer is independently added to a baseline of roughness established by preceding layers.

Under the assumptions of the scalar model, the near-field amplitude is given by the equation for one-dimensional thickness errors discussed above. The far field coherent reflectance is obtained by evaluating:

$$R_{coh} = |\langle \rho_{far\ field} \rangle|^2$$

$$= |\text{Fourier transform}(\langle \rho_{1D}(x) e^{2i \sum_{k=1}^{J-1} \Delta\phi_k} \rangle)|^2 \quad (26)$$

Here  $x$  is a coordinate along the surface, and  $\rho_{1D}(x)$  is the near-field amplitude as measured at the upper surface of the multilayer. This upper surface is rough, so the factor  $\exp(2i \sum \Delta\phi_k)$  must be used to propagate  $\rho_{1D}(x)$  to a mean plane, where the far-field amplitude can properly be evaluated via the Fourier transform.

The argument of the transform is independent of  $x$ , so  $R_{coh}$  will be a delta-function of the angle of reflection.  $R_{coh}$  can therefore be identified as the specular beam. Our expression for  $R_{coh}$  in the soft x-ray regime is given below (eq.(27)).

A diffuse beam is also present. The total intensity of the diffuse and specular beams is determined by the total absorption, which is the same as in the case of 1D thickness errors discussed above.

We have also developed an analytic model for the kind of roughness we call "smoothing films". Such films may be considered to have a leveling nature during some stage of formation, but to nonetheless possess an intrinsic roughness after formation is complete. We therefore assume that an error in the local thickness that a layer has at some position on the reflector will be compensated for in the thickness of the next layer deposited. The roughness height necessary to cause a given drop in reflectivity is therefore much larger than in the case of roughening films, because the thickness errors do not accumulate (see plot).

It turns out that the smoothing property of this type of roughness causes the intensities of the diffuse and specular beams to become equal only at a level of roughness where the total reflectivity has been decreased quite substantially (via an increase in absorption). In contrast, with roughening films, the two become equal at a roughness level where the total reflectivity is only slightly decreased. With identical films, the total reflectivity is unaffected by the magnitude of the roughness.

With films of both the roughening and smoothing types, the total absorption reaches a steady-state

level as more and more layers are added. However in the case of roughening films the proportion of the reflected light in the specular beam steadily decreases, since the upper surfaces get steadily rougher.

The acceptance angle of multilayers with smoothing films is not greatly influenced by the RMS magnitude of the roughness. In the case of roughening films, the acceptance angle is increased in somewhat the same way as would be caused by an increase in the layer bulk absorption constants.

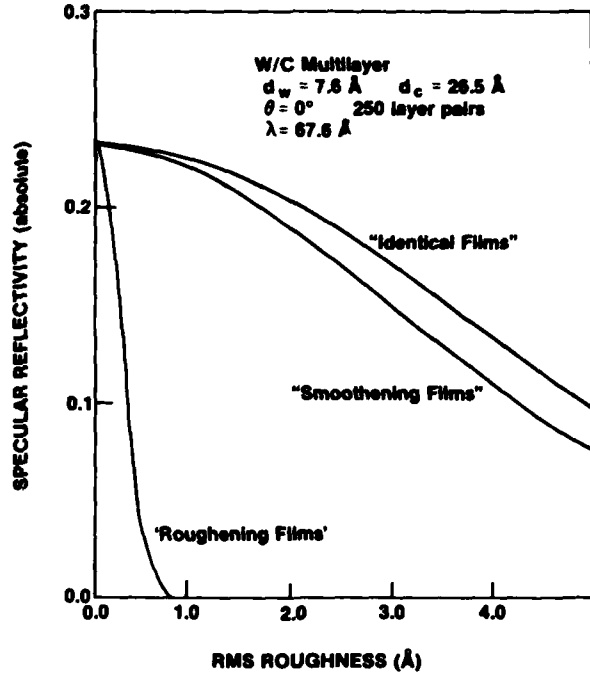


Fig. 7. Effect of roughness - reflection into specular beam.

Our expressions for specular reflection in the presence of roughness assume that the absorption has reached its steady-state value. Our expression for the case of smoothing films assumes a bilayer structure and Gaussian statistics for the roughness.

Our expression for roughening films is:

$$R_{coh} = |\langle \rho_{1D} \rangle F_J - \frac{2 \langle \Delta\phi^2 \rangle \langle \rho_{1D} \rangle}{i\delta + \langle \Delta\phi^2 \rangle} (F_J - G_{J-1}) + 2 \langle \rho_{1D} \rangle G_J H_J (F_J^2 - 1)|^2 \quad (27)$$

where:

$$F_J \equiv e^{-2(J-1)\langle \Delta\phi^2 \rangle} \quad G_J \equiv e^{2i\delta(J-1)}$$

$$H_J \equiv e^{\frac{i\gamma + p}{i\delta + \langle \Delta\phi^2 \rangle} \langle \rho_{1D} \rangle} \quad (28)$$

$\langle \rho_{1D} \rangle$  is given by eq. (25), and the remaining symbols are as defined above.

For smoothening films, our result is

$$R_{\text{coh}} = \left| \frac{\gamma e^{-2\langle \xi^2 \rangle}}{\sqrt{t^2 - \gamma^2 e^{-4\langle \xi^2 \rangle}} - t} \right|^2 \quad (29)$$

where  $\langle \xi^2 \rangle = \frac{\pi^2 \sigma^2}{d^2}$  with  $\sigma$  the RMS roughness height in each interface, and where  $\gamma$  and  $t$  are as previously defined.

We note that the effect of smoothening films is very similar to that of interlayer diffusion. This is particularly true if the RMS roughness height is at least moderately small, so that  $e^{-2\langle \xi^2 \rangle} \gg q|\mu|$ , where  $q$  is the number of layers within one longitudinal autocorrelation length of the roughness. (The analysis assumes that  $q|\mu| \ll 1$ ).

In this case the intensity of the diffuse beam will be small compared to that of the specular beam, even though the specular reflectivity may be considerably less than it would be in the absence of roughness. The main effect of the roughness in this case is to decrease the reflectivity of the multilayer, rather than to scatter radiation diffusely. This is because radiation that is diffusely scattered from different layers adds only incoherently under the assumptions of the smoothening film model.

For comparison, suppose one models the diffusion process by considering it to cause the ideal multilayer profile  $\Delta(z)$  to be convolved with some diffusion profile  $g(z)$ .

This causes the parameter  $\gamma$  to be multiplied by the Fourier transform of  $g(z)$ . If  $g$  is taken to be a Gaussian,  $g(z) = \exp(-5(z/\sigma)^2)$ , the reflected intensity is given by an expression identical to eq.(29) above for  $R_{\text{coh}}$  in the presence of smoothening films.

Ref. 8 gives an expression for specular reflectivity in the presence of identical films that applies under the assumptions of the scalar model. The same expression is used in ref. 11.

We also note that for all three types of roughness, walkoff considerations can be shown to imply that the scalar model is applicable only when the separation between the specular and diffuse beams is within the acceptance angle of the multilayer. Since the acceptance angle is likely to be of the order of the field of view in imaging applications, the scalar model can be applied to many imaging problems of interest.

#### Acknowledgements

This research was partially supported by the Air Force Office of Scientific Research, grant AFOSR-81-0059.

This research was also partially supported by the following sponsors: Exxon Research and Engineering Company, General Electric Company, Northeast Utilities, New York State Energy Research and Development Authority, The Standard Oil Company of Ohio, The University of Rochester, and Empire State Electric Energy Research Corporation. Such support does not imply endorsement of the content by any of the above parties.

A.R. gratefully acknowledges the support of a Fannie and John Hertz Foundation Fellowship.

#### References

- 1) M.Born, E.Wolf, Principles of Optics, Pergamon, 1975.
- 2) Z.Knittel, Optics of Thin Films, Wiley, N.Y.&London, 1976.
- 3) A.V.Vinogradov and B.Ya.Zeldovich, Appl.Opt.16,89 (1977).
- 4) B.Fienke, to be published.
- 5) F.Miller, Phys.Rev.47,209 (1935).
- 6) R.W.James, The Optical Principles of the Diffraction of X-Rays G.Bell and Sons, London 1950.
- 7) J.B.Shellan et al., J.Opt.Soc.Am.68,18(1978).
- 8) J.Eastman, Physics of Thin Films, v.10, 1978, p. 167.
- 9) J.M.Elson et al., in Applied Optics and Optical Engineering, edited by R.R.Shannon and J.C.Wyant (Acad. Press, N.Y., 1979), Vol. VII, pp. 198,199.
- 10) E.Spiller, A.Segmuller, J.Rife, R.-P. Haelbich, Appl.Phys.Lett 37(11),1 Dec. 1980, p.1048.
- 11) R.-P. Haelbich, A.Segmuller, E.Spiller, Appl.Phys.Lett.34(3),1 Feb. 1979, p.184.



University of Rochester graduate student Alan Rosenbluth discussing his results with Dr. Eberhard Spiller of IBM.

## Soft X-ray Spectroscopy Using Thick Gold Transmission

Gratings of 0.2 to 0.3  $\mu\text{m}$  Spatial Periods

A. M. Hawryluk

Department of Electrical Engineering and Computer Science, Massachusetts Institute of  
Technology, Cambridge, Massachusetts 02139

N. M. Ceglio and Robert H. Price

Lawrence Livermore Laboratory, Livermore, California 94550

J. Melngailis and Henry I. Smith

Research Laboratory of Electronics, Massachusetts Institute of Technology, Cambridge,  
Massachusetts 02139

## ABSTRACT

We have fabricated and tested transmission diffraction gratings with spatial periods of 0.2 and 0.3  $\mu\text{m}$  and gold thicknesses of 0.25 and 0.65  $\mu\text{m}$  respectively. The fabrication process included holographic lithography, ion milling, x-ray lithography and gold microplating. The gratings were coupled to a Wolter-type 22x grazing incidence microscope, forming a high resolution imaging spectrometer. This spectrometer demonstrated a spatial resolution of  $\sim 1 \mu\text{m}$  and a resolving power,  $\lambda/\Delta\lambda$ ,  $\geq 200$  at .69 nm. The observed spectral resolution,  $\Delta\lambda$ , was source size limited.

## INTRODUCTION

Transmission diffraction gratings complement grazing incidence reflection gratings, crystals and multilayer films as spectroscopic tools in the soft x-ray region. Specifically, transmission gratings are versatile, cover a broad spectral range, require no critical alignment, and are easy to implement in various spectrometric instruments. In this article we discuss the fabrication of gold transmission gratings with spatial periods of 0.2 and 0.3  $\mu\text{m}$  at gold thicknesses of 0.25 and 0.65  $\mu\text{m}$ , respectively, the coupling of such gratings with a 22x Wolter x-ray microscope to form an imaging spectrometer, and spectrometric measurements using the tungsten M lines (1). In previous work (3) minimum spatial period was 1  $\mu\text{m}$  and gold thickness was 0.5  $\mu\text{m}$ .

## FABRICATION OF GRATINGS (1)

The fabrication of the gratings began with holographic lithography. We used a He:Cd laser ( $\lambda = 325 \text{ nm}$ ) and a configuration in which spatial filters were the final elements in the two interferometer arms. As a result, the grating period increases as a function of distance from the center of the interference pattern. The spatial filters were positioned about 1/2 m from the substrate. Assuming spherical wavefronts, it is relatively easy to show that in the plane of the interferometer the spatial period increased by 1 part in  $10^4$  at distances of 5 and 7 mm from the pattern center for 0.3 and 0.2  $\mu\text{m}$  patterns respectively. This distortion can be made arbitrarily small by increasing the distance from the spatial filters to the substrate.

For the 0.3  $\mu\text{m}$  period gratings we exposed in  $\sim 50 \text{ nm}$  thick AZ 1350J photoresist (2), on  $\sim 70 \text{ nm}$  thick gold, on  $\sim 1 \mu\text{m}$  thick polyimide on silicon wafers. The gold was then ion beam etched (Fig. 1) and a polyimide membrane x-ray mask was produced by epoxy bonding the polyimide to a ring and then chemically etching away the silicon substrate. This mask was then used to expose  $\sim 1 \mu\text{m}$  thick films of PMMA. To minimize line widening due to diffraction and penumbra the x-ray mask

was held in intimate contact with the PMMA by applying an electrostatic potential between the substrate and an aluminum film on the back side of the polyimide membrane. X-ray exposures were done with the  $\text{C}_K$  x-ray ( $\lambda = 4.5 \text{ nm}$ ), in PMMA over a plating base of 10 nm Au/10 nm chromium on a substrate which was either

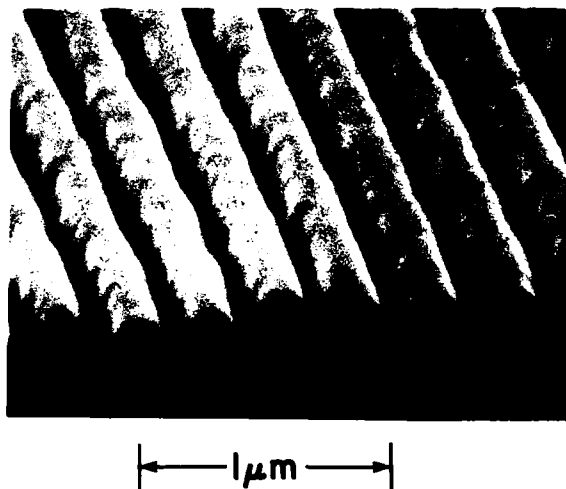


Figure 1

An SEM micrograph of an x-ray mask consisting of a 0.3  $\mu\text{m}$  period grating in 70 nm thick gold on polyimide. This grating was produced by holographic lithography and ion beam etching.

0.5  $\mu\text{m}$  thick polyimide on a Si wafer (for the case of membrane supported gratings) or a bare silicon wafer (for the case of free-standing gratings). After removing any resist residue between exposed lines with a  $\text{O}_2$  plasma, gold microplating was carried out in a commercial solution (Sel-Rex BDT-510) (4) at a temperature of  $45^\circ\text{C}$  and a solution pH of 8.5. A plating rate of 10 nm/min gave the best results. After plating, the PMMA was dissolved in chlorobenzene. Fig. 2a shows the PMMA after exposure and before microplating. Fig. 2b shows a completed gold diffraction grating.

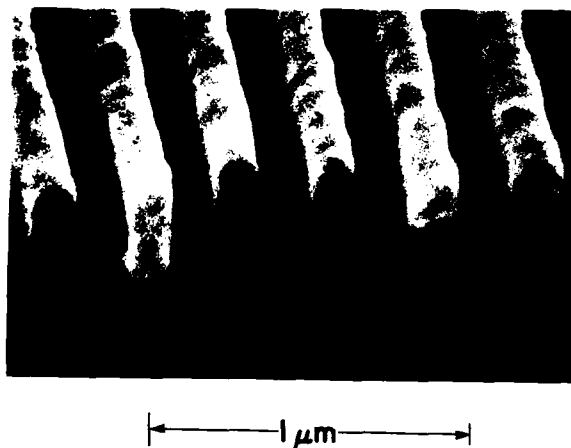


Figure 2

(a) An SEM micrograph of a 0.3  $\mu\text{m}$  period grating in PMMA, 0.7  $\mu\text{m}$  thick, on a gold plating base, produced by x-ray lithography.

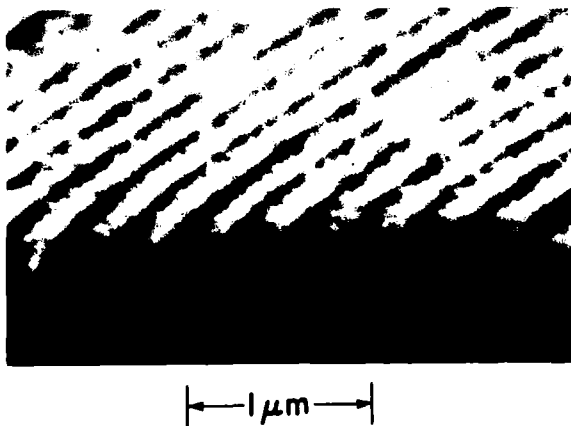


Fig. 2(b) SEM micrograph of a gold grating produced by electroplating into the openings of the PMMA grating in (a).

For polyimide-membrane supported gratings, the silicon substrate behind the grating area was simply etched away chemically. Since polyimide absorbs strongly (i.e.  $> 10 \text{ dB}/\mu\text{m}$ ) at wavelengths between 2.5 and 4.3 nm and beyond  $\sim 7 \text{ nm}$  (5), self-supported gratings are preferred for spectroscopy at these wavelengths. To accomplish this we photolithographically superimposed and microplated a coarse grid on top of the 0.3  $\mu\text{m}$  grating. First a 0.5  $\mu\text{m}$  thick layer of AZ 1350B (2) was spun over a 0.3  $\mu\text{m}$  period, 0.45  $\mu\text{m}$  thick, gold grating on a silicon substrate. Then a second layer of 3  $\mu\text{m}$  thick AZ 1350J resist (2) was spun on. A 6  $\mu\text{m}$  period grating was exposed perpendicular to the 0.3  $\mu\text{m}$  period grating and a 160  $\mu\text{m}$  period grating was exposed parallel to the 0.3  $\mu\text{m}$  period grating. This grid was then electroplated to a thickness of 3  $\mu\text{m}$ . The linewidth-to-period ratios of 6  $\mu\text{m}$  and 160  $\mu\text{m}$  period gold gratings were 5 to 8 and 1 to 8, respectively, so that  $\sim 30\%$  of the area of the 0.3  $\mu\text{m}$  period grating was unobstructed by the support grid. After plating, the resist was dissolved and the silicon behind the grating etched away.

The 199 nm period gratings, with slits of 40 nm in gold 250 nm thick, were fabricated by a multistep process that permitted precise control of the linewidth-to-period ratio. These gratings were fabricated for use in experiments on spatial-period-division, an application where such linewidth control is essential (1,6,7). The fabrication procedure started with holographic lithography which produced a grating pattern in  $\sim 50 \text{ nm}$  AZ 1350J resist (2) over 10 nm thick Cr over 20 nm thick  $\text{Si}_3\text{N}_4$  on (100) Si wafers. Chemical etching of the Cr, followed by reactive ion etching of the  $\text{Si}_3\text{N}_4$ , followed by KOH anisotropic chemical etching produced a sawtooth-profile structure in the (100) silicon (8). A polyimide mold taken from this structure was then epoxy bonded to a ring and obliquely shadowed with 25 nm of tungsten to produce an x-ray mask with 3 dB contrast, and 40 nm wide lines on 199 nm centers (8). This was then x-ray replicated in 150 nm thick PMMA over a 1  $\mu\text{m}$  thick polyimide membrane on a Si wafer followed by liftoff of 10 nm Cr and 60 nm Au. After etching away the silicon, this yielded an x-ray mask with  $\sim 40 \text{ nm}$  wide slits in gold 60 nm thick. This "polarity-reversed" mask was then replicated into 250 nm thick PMMA over a 1  $\mu\text{m}$  thick polyimide membrane on a silicon wafer followed by liftoff of 10 nm Cr/60 nm Au to yield a third x-ray mask having the same "polarity" as the original sawtooth mask but with much higher contrast ( $\sim 8 \text{ dB}$ ). This third mask was then used to expose  $\sim 40 \text{ nm}$  wide lines, on 199 nm centers, in 250 nm thick PMMA over a gold plating base on polyimide over a silicon wafer. After gold plating to a thickness between 200 and 250 nm the final grating was epoxy bonded to a ring, and the silicon was etched away.

#### IMAGING SPECTROMETER

We coupled the thick gold transmission gratings to a Wolter design grazing incidence microscope with a magnification of 22x (9), thereby producing a high resolution imaging spectrometer, Fig. 3. Gratings were supported on a 0.5  $\mu\text{m}$  thick polyimide membrane. Most of the work described below used the 0.3  $\mu\text{m}$  period gratings rather than the 0.2  $\mu\text{m}$  period gratings due to the thicker gold in the former (8 dB attenuation vs 3.3 dB attenuation at  $\lambda = 0.69 \text{ nm}$ ).

The theory and performance of the 22x Wolter microscope used in this work has already been described in detail (9). The microscope has demonstrated a spatial resolution of  $\sim 1 \mu\text{m}$  when the full annular aperture is utilized. In the imaging spectrometer work, the grating subtended only  $\sim 2.5\%$  of the annular aperture, (diameter of the grating  $\sim 7 \text{ mm}$ ), and the remainder of the aperture was obstructed.



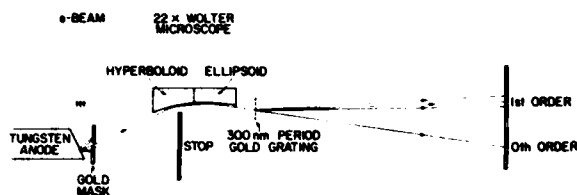


Figure 3

Schematic diagram of the imaging spectrometer. A gold aperture mask was back-lit by the radiation emitted from a tungsten anode. The 22x Wolter microscope focuses the transmitted x-rays onto an image plane after first passing through the grating. The diffraction pattern is recorded on film.

An electron bombarded tungsten anode was used as a source for testing the imaging spectrometer. The characteristic  $M_\alpha$ ,  $M_\beta$  and  $M_\gamma$  lines have wavelengths of 0.698, 0.676 and 0.609 nm respectively. A test pattern mask, consisting of an array of apertures ranging in size from  $6 \times 9$  to about  $2 \times 2 \mu\text{m}$  in a  $4 \mu\text{m}$  thick gold foil, served as the object in the imaging spectrometer. The spectrally dispersed images of the test pattern mask, in addition to the zeroth order image, were recorded on a variety of x-ray films (Kodak type M, AA, KK, No Screen), Fig. 4. As seen in Fig. 4, the tungsten M lines are clearly resolved in the first order diffraction pattern. The dispersion,  $ds/d\lambda$ , at the film plane, measured between the  $M_\alpha$  and  $M_\beta$  lines, is 19.6 mm/nm, which agrees with the calculated dispersion to within 1/2%.

The minimum feature in the image plane (image of the smallest aperture, nominally  $2 \times 2 \mu\text{m}$ ) had a full-width-at half maximum of  $66 \mu\text{m}$  in the zeroth and  $M_\alpha$  first orders, as determined by densitometry traces. The spectral resolution,  $\Delta\lambda$ , is thus

$$\Delta\lambda \leq (66 \mu\text{m}) \left( \frac{ds}{d\lambda} \right)^{-1} = 3.37 \times 10^{-3} \text{ nm.}$$

For  $\Delta\lambda = 3.37 \times 10^{-3} \text{ nm}$ , the resolving power,  $\lambda/\Delta\lambda$ , at 0.698 nm is 207. A somewhat lower value (192) was obtained with the  $M_\beta$  line. In the work reported in Ref. 10, a value of  $\lambda/\Delta\lambda$  of 60 was measured for the tungsten M lines.

As mentioned earlier, only a small section of the annulus of reflected x-rays was used in the imaging spectrometer. This degraded the resolution of the instrument such that the point spread function measured  $\sim 1 \times 10 \mu\text{m}$ , the shorter axis being parallel to the tangent to the annulus. Because of this, it is possible to obtain the high spatial resolution in one direction only (10). To obtain the highest spectral resolution, we chose the direction of the highest spatial resolution to coincide with the direction in which the diffracted beams are dispersed. At a resolving power of  $\lambda/\Delta\lambda \sim 200$ , the spatial resolution in the orthogonal direction was only  $\sim 10 \mu\text{m}$ .

#### CONCLUSIONS

We have fabricated gold transmission diffraction gratings with spatial periods of 0.2 and  $0.3 \mu\text{m}$  and

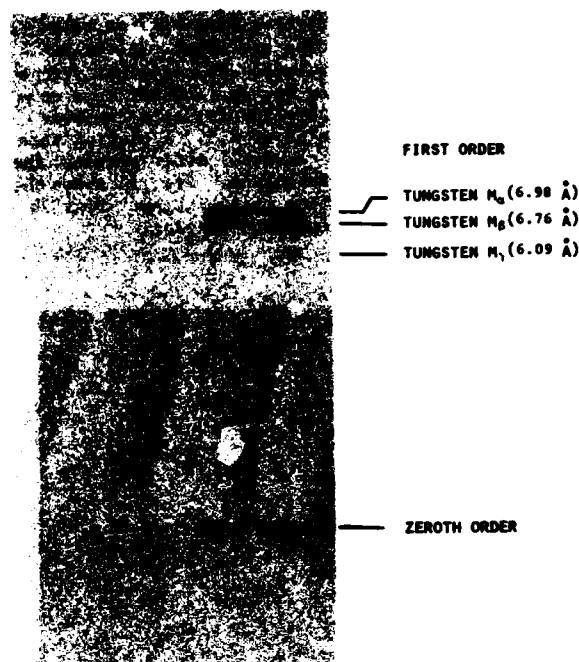


Figure 4

Diffraction pattern showing the  $M_\alpha$ ,  $M_\beta$  and  $M_\gamma$  lines of the tungsten anode. A microdensitometer trace of this figure indicates  $\lambda/\Delta\lambda$  of 200 at  $\lambda = 0.69 \text{ nm}$ .

thicknesses up to  $0.65 \mu\text{m}$ . The gratings were coupled with a Wolter 22x grazing incidence microscope to form an imaging spectrometer. The  $M_\alpha$ ,  $M_\beta$  and  $M_\gamma$  lines from an apertured tungsten source were recorded on x-ray film. A dispersion of 19.6 mm/nm, and a resolving power of  $\sim 200$  were measured, the latter being source size limited. Such thick gold transmission gratings are highly versatile elements for x-ray spectroscopy and diagnostics, and cover a broad spectral range. They can be readily coupled with other instruments and do not require any critical alignments.

#### ACKNOWLEDGEMENTS

This work was sponsored by the Joint Services Electronics Program and the Defense Advanced Research Project Agency. The authors are grateful to J. M. Carter for his expert technical assistance, M. Griswold for electron microscopy, G. Stone, M. Roth and G. Howe for assistance with the imaging spectrometer and D. Carlo for fabricating the gold grid pattern used with the free-standing gratings.

#### REFERENCES

1. A. M. Hawryluk, N. M. Ceglie, R. H. Price, J. Melngailis and H. I. Smith, *J. Vac. Sci. Technology*, **18**, Nov/Dec, 1981. To be published.
2. Shipley Co., Newton, MA.
3. A. C. Brinkman, J. H. Dijkstra, W.F.P.A.L. Geerlings, F. A. van Rooijen, C. Timmerman and P.A.J. de Korte, *App. Optics*, **19**, 1601, 1980.
4. OxyMetal Industries, Nutley, N.J.
5. H. J. Hagemann, W. Gudst, C. Kunz, *J. Opt. Soc. Am.*, **65**, 742, (1975).
6. D. C. Flanders, A. M. Hawryluk, H. I. Smith, *J. Vac. Sci. Technology*, **16**, 1949 (1979).

7. D. C. Flanders, D. C. Shaver, A. M. Hawryluk and H. I. Smith, *Annals of New York Academy of Sciences*, 342, 203, (1980).
8. D. C. Flanders, *J. Vac. Sci. Technology*, 16, 1615, (1979).
9. Robert H. Price, these proceedings.
10. R. Giacconi, W.P. Reidy, G.S. Vaiana, L.P. van Speybroeck, T.F. Zhenpfenning, *Space Sci. Review*, 9, 3, (1969).



MIT graduate student Andrew Hawryluk (right) discussing use of his x-ray transmission gratings with Dr. Emmett Leith of the University of Michigan (center), Dr. Natale Ceglie (left) of the Lawrence Livermore National Laboratory, and Dr. Barukh Yaakobi (second from right) of the University of Rochester.

## A Streaked, X-Ray Transmission Grating Spectrometer

N.M. Ceglio, M. Roth  
Lawrence Livermore Laboratory

A.M. Hawryluk  
Massachusetts Institute of Technology

## Abstract

A free standing x-ray transmission grating has been coupled with a soft x-ray streak camera to produce a time resolved x-ray spectrometer. The instrument has a temporal resolution of  $\sim 20$  psec, is capable of covering a broad spectral range, 2-120 Å, has high sensitivity, and is simple to use requiring no complex alignment procedure. In recent laser fusion experiments the spectrometer successfully recorded time resolved spectra over the range 10-120 Å with a spectral resolving power,  $\lambda/\Delta\lambda$  of 4-50, limited primarily by source size and collimation effects.

A free standing x-ray transmission grating is a linear, periodic grid of gold wires or bars with sub-micron spatial period. The grating structure is supported by a coarse grid orthogonal to the grating lines. Because of its simple geometry, the TG is a uniquely versatile spectroscopic dispersion element. It accepts radiation at all angles of incidence, thereby requiring no detailed angular alignment in its operation. It can, therefore, be easily coupled to instruments of high temporal resolution. In addition the TG's have high efficiency, and provide continuous spectra with moderate resolution over a broad spectral range.

Fig. 1 shows a simple x-ray transmission grating spectrometer viewing a small laboratory source. In such a configuration the spectral resolution (limited by source size and degree of collimation) is given by

$$\Delta\lambda = \frac{d}{L} (S + A) + \frac{d}{D} (A) \quad (1)$$

where  $d$  is the grating period,  $D$  is the grating to detector distance,  $L$  is the grating to source distance,  $S$  is the source size, and  $A$  is the collimation aperture opening. When

$$D \gg \frac{A}{(S + A)} L \quad (2)$$

the second term in Eq. (1) may be neglected. However, in many applications involving limited detector size (such as the slit of a streak camera) Eq. (2) cannot easily be satisfied. The spectral range of the spectrometer is typically limited by detector characteristics<sup>1</sup>. The maximum wavelength that can be recorded is

$$\lambda = \frac{d}{D} T \quad (3)$$

where  $T$  is the linear size of the detector<sup>2</sup> (e.g. for a streak camera  $T$  would be the slit length). The minimum wavelength that can be distinctly recorded will be limited either by spatial resolution at the detector, or by source size and collimation (leading to overlap of the D.C. and first order spectral

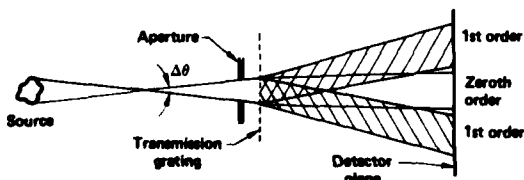


FIG. 1. A simple x-ray transmission grating spectrometer design.

line). When detector spatial resolution limits  $\lambda_{\min}$ , then its value is given by Eq. (3) using the detector spatial resolution as the value for  $T$ . When source size and collimation limit  $\lambda_{\min}$  then  $\lambda_{\min} = \Delta\lambda$  given by Eq. (1).

A time integrated x-ray spectrum from a laser illuminated, SiO<sub>2</sub> disk target is shown in Fig. 2. The spectrometer configuration of Fig. 1 was used with photographic x-ray film as the detector. In this configuration the spectrometer characteristics were:

$d = 3000 \text{ \AA}$	$S \approx 100 \text{ \mu m}$
$D = 63 \text{ cm}$	$A = 100 \text{ \mu m}$
$L = 74 \text{ cm}$	film resolution $\approx 10 \text{ \mu m}$

yielding a spectral resolution (Eq. (1)):

$$\Delta\lambda = 1.3 \text{ \AA}$$

The spectral range was limited in this case at low energy by the carbon absorption of the polymer overcoat on the x-ray film, and at high energy by source size and collimation effects.

A free standing x-ray transmission grating has been coupled to a soft x-ray streak camera, and used to record the first time-resolved ( $\sim 20$  psec resolution), continuous, soft x-ray spectrum from a laser produced plasma. The experimental arrangement used is the same as that shown in Fig. 1 with the slit of the x-ray streak camera serving as the detector. Fig. 3 is a schematic representation of the experiment along with the data record from a gold disk target. In this time-resolved configuration the spectrometer characteristics were:

$d = 3000 \text{ \AA}$	$S \approx 100 \text{ \mu m}$
$D = 31 \text{ cm}$	$A = 100 \text{ \mu m}$
$L = 76.6 \text{ cm}$	Streak camera resol. $\approx 150 \text{ \mu m}$

The spectral resolution, limited primarily by collimation, was

$$\Delta\lambda = 2 \text{ \AA}$$

The long wavelength limits to the spectral range were the finite slit length (1.3 cm), and absorption due to the 50  $\mu\text{g}/\text{cm}^2$  carbon window at the streak camera slit. In each case the long wavelength limit was around 120 Å. The short wavelength limit, around 2 Å, was established by collimation limitations, and the limited spatial resolution of the streak camera.

The time resolved TG spectrometer has been used in a number of different geometrical configurations (varying resolution and spectral range) to address the important issues of radiation production and

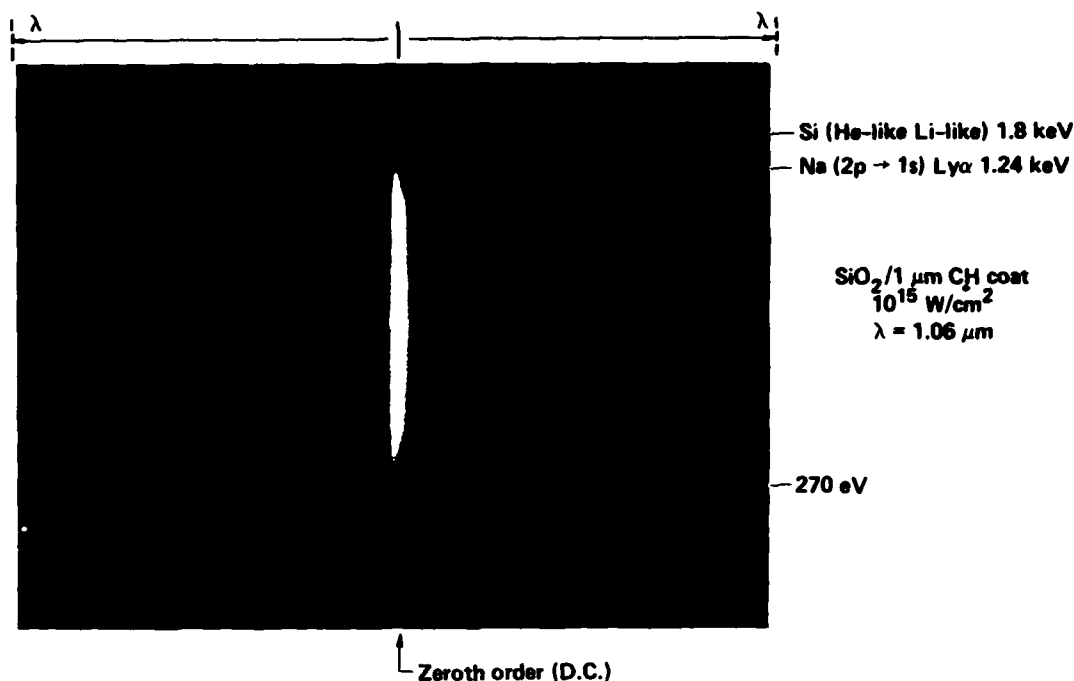


Fig. 2. A time integrated x-ray spectrum from a laser produced plasma, recorded by a transmission grating spectrometer.

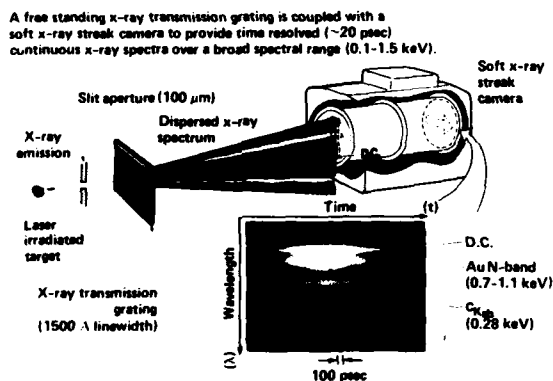


Fig. 3. A time-resolved transmission grating spectrometer.

plasma transport in laser fusion experiments. Fig. 4 shows time resolved spectral data recorded from a laser irradiated Al-Ti disk target. In this case the directly irradiated aluminum disk was surrounded by an unirradiated annular ring of titanium. The difference in temporal characteristics (e.g. turn-on time) between the Al-K-lines and Ti-L-band provides important insight into radial plasma transport phenomena.

#### CONCLUSION

A marriage of two powerful technologies has provided a new spectroscopic capability. An x-ray transmission grating has been coupled with an x-ray streak camera to provide time resolved ( $\sim 20$  psec), continuous x-ray spectra over a broad spectral range. This new spectroscopic tool offers insight to the key issues of radiation production and plasma transport in laser fusion experiments.

#### ACKNOWLEDGEMENTS

This work is the result of close collaborative effort between the Massachusetts Institute of

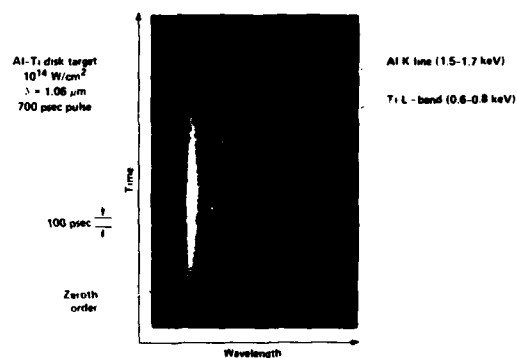


Fig. 4. Time resolved x-ray spectrum from a "plasma transport" laser target.

Technology Submicron Structures Laboratory, and a number of groups at Lawrence Livermore National Laboratory. The authors wish to acknowledge the skilled contributions of their colleagues both at MIT and LLNL: G. Howe, G.F. Stone, E.M. Campbell, R. Turner, D. Ciarlo, H.I. Smith, J. Melngailis, J. Carter, H. Medeck, and E. Pierce.

1. The other possible limit to spectral range is the transparency of the grating material at high x-ray energy. In this case, using gold gratings greater than  $0.5 \mu\text{m}$  thick, grating transparency is not the limit to spectral range. Streak camera characteristics: finite slit length, finite spatial resolution at the slit, reduced sensitivity at high x-ray energy, and low energy x-ray absorption by the carbon window, provide the limiting factors in time resolved applications.
2. We have in practice not found spectral overlap with higher orders to be a limit to  $\lambda_{\text{max}}$  in our laser fusion experiments. This is in large part due to the reduction in diffraction efficiency in higher order.

STREAKED SPECTROMETRY USING MULTILAYER X-RAY INTERFERENCE  
MIRRORS TO INVESTIGATE ENERGY TRANSPORT IN LASER PLASMA APPLICATIONS\*

G.L. Stradling, T.W. Barbee, Jr.\*\*  
B.L. Henke\*\*\*, E.M. Campbell and W.C. Mead

University of California, Lawrence Livermore National Laboratory  
P.O. Box 5508, Livermore, CA 94550

ABSTRACT

Transport of energy in laser-produced plasmas is scrutinized by devising spectrally and temporally identifiable characteristics in the x-ray emission history which identify the heat-front position at various times in the heating process. Measurements of the relative turn-on times of these characteristics show the rate of energy transport between various points. These measurements can in turn constrain models of energy transport phenomena. We are time-resolving spectrally distinguishable subkilovolt x-ray emissions from different layers of a disk target to examine the transport rate of energy into the target. A similar technique is used to measure the lateral expansion rate of the plasma spot. A soft x-ray streak camera with 15-psec temporal resolution is used to make the temporal measurements. Spectral discrimination of the incident signal is provided by multilayer x-ray interference mirrors. These synthetic x-ray crystals have been characterized for reflectivity and bandwidth and exhibit resolutions  $\frac{\Delta E}{E}$  of 10 to 90.

$\frac{\Delta E}{E}$

INTRODUCTION

The rate of energy transport in laser irradiated targets can be studied using spectrally-distinguishable x-ray emitting materials to signal the time-dependent heating rate at different positions in the target. Experiments can be designed with either axial or lateral variations in target materials, e.g. layered targets or annular target designs. Time-resolved measurements of the x-ray emission at appropriate photon energies can then establish the history of energy propagation in the experiment. Such measurements add additional experimental information to the active research areas of energy transport modeling and hydrodynamic simulation in the inertial confinement fusion community.

THE STREAKED SPECTROMETER

This paper describes a new instrument capable of the detailed measurements required for such experiments with five time-resolved narrow-band energy channels below one kilovolt. The energy channels consist of Bragg diffraction bands on the order of  $\sim 10$  eV wide obtained from sputtered multilayer x-ray interference mirrors.<sup>1</sup> A soft x-ray streak camera<sup>2,3</sup> is used to simultaneously time resolve the five side-by-side energy channels. A schematic representation of this streaked spectrometer and the layered target experiment are shown in Fig. 1. X-rays from the emitting plasma are diffracted from five separate multilayer strips onto the photocathode slit of a soft x-ray streak camera. The diffracted beams

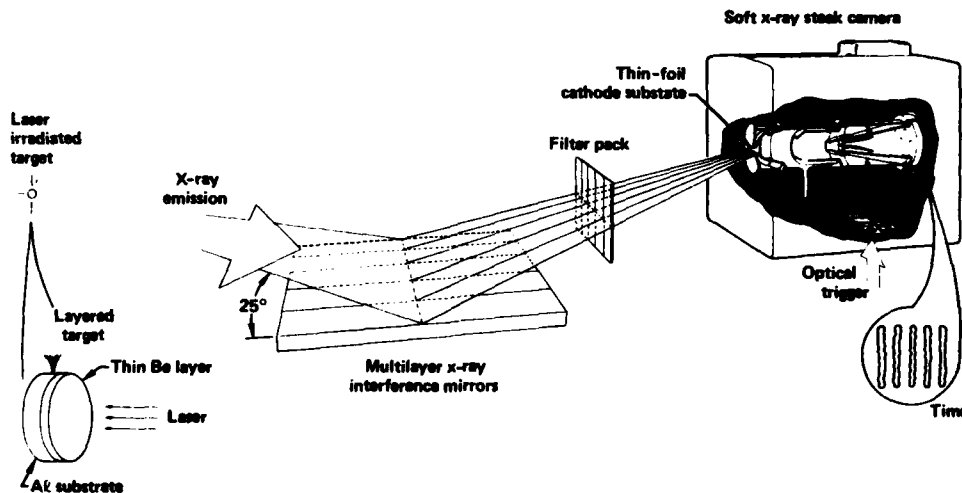


Figure 1 The streaked spectrometer system provides narrow-band, time-resolved, measurement of x-ray emission from laser plasmas. A Be-on-Al layered target is shown here. X-rays emitted from the laser-irradiated target are diffracted by five separate sputtered multilayer synthetic crystals onto the photocathode slit of a soft x-ray streak camera. The diffracted beams are filtered through thin absorption foils before reaching the photocathode.

\*\*Address: Stanford University, Stanford, CA.

\*\*\*Address: University of Hawaii, Honolulu, HI.

Table 1. Multilayer Interference Mirrors and Filter Characteristics

Channel energy	102 eV	267 eV	653 eV	737 eV	943 eV
Bragg Angle	25°	25°	27.1°	23.6°	25°
d-spacing (Å) ( $d_{\text{eff}} = 143 \text{ Å}$ )	178	55	21	21	15
Scattering material/ spacer	V/C	Ti/C	W/C	W/C	W/C
Width $\Delta E$ (eV)	10	7	8	8	10
Integrated reflectivity (mrad)	3.6	1.89	0.46	0.46	0.12
Peak reflectivity (%)	10.8	10.6	5.1	5.1	1.6
Filter material/ thickness	Be/1 $\mu\text{m}$	C/2.65 $\mu\text{m}$	Al/7000 Å	Al/7000 Å	Al/7000 Å

are passed through absorption filters before reaching the photocathode. This instrument combines the strengths of both multilayer interference mirrors and soft x-ray streak camera technology. The multilayer synthetic crystals can provide high reflectivity (1-40% in the subkeV region), narrow channel width, and versatile channel energy selection (variable d-spacing). When coupled with the temporal resolution (15 psec),<sup>3,4</sup> large dynamic range<sup>5</sup> ( $10^3$ ), multichannel detection capability and shot-noise limited sensitivity of the soft x-ray streak camera, a powerful diagnostic combination is produced for a variety of x-ray measurement requirements. Multichannel, narrowband, temporally resolved data from recent energy transport experiments of the design described above are presented. Full analysis of these data will be published at a later time.

The energy channel positions of the five-channel streaked spectrometer system are very flexible. The initial system was designed to provide coverage of the subkilovolt region at 102-eV, 267-eV, 653-eV, 737-eV, and 943-eV photon energies. Multilayer designs used in this system are based upon Bragg angles near 25°. Relatively large Bragg angles decrease surface reflection and allow convenient alignment and instrument positioning. The multilayer materials are selected to give optimum reflectivity

at the desired photon energies and the d-spacings are specified by the Bragg equation,

$$m\lambda = 2d_0 \sin \theta (1 - \delta/\sin^2 \theta)$$

Here  $\delta$  is  $1-n$ , the index of refraction decrement,  $\theta$  is the Bragg angle of diffraction,  $m$  is the diffraction order,  $\lambda$  is the x-ray wavelength,  $d_0$  is the actual d-spacing of the material and  $d_0(1-\delta/\sin^2 \theta)$  is the index-of-refraction-dependent effective d-spacing of the multilayer for the x-ray wavelength of interest.

Diffraction characteristics of the sputtered-multilayer synthetic crystals are measured using fluorescent line emission<sup>6</sup> near the channel energies at which the multilayers are used. The effective d-spacings are obtained from the angle of the first-order Bragg peak. Integrated reflectivity (over diffraction angle) and the rocking curve width provide peak reflectivity ( $P_{\text{pk}}$ ) and Bragg peak FWHM ( $\Delta E$ ) characteristics. These quantities are tabulated in Table 1.

Surface reflection, particularly at low x-ray energies, can impose a significant background of broad spectral character on the total signal in each detected channel. This low-energy background is reduced to acceptable levels using absorption filtering and large Bragg angles. Figure 2 demonstrates the

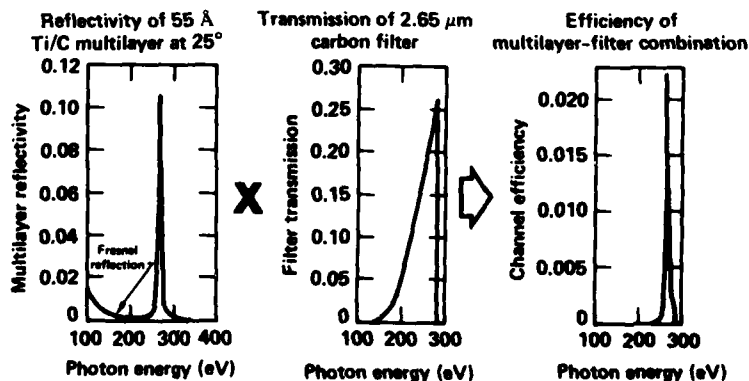


Figure 2 Absorption filters are used to eliminate the surface (Fresnel) reflection contribution to the diffracted signal. The 267-eV, 55-Å spacing Ti/C channel is shown here. Surface reflection is approximately calculated with a semi-classical model using a 1:1 mix of titanium and carbon. The Bragg diffraction peak superimposed on this surface reflection is shown in the first box. The transmission function of a 2.65- $\mu\text{m}$  thick carbon foil (second box) is used to filter the signal from the multilayer. The combined response of the channel in the third box shows that the reflective background is reduced to a negligible level.

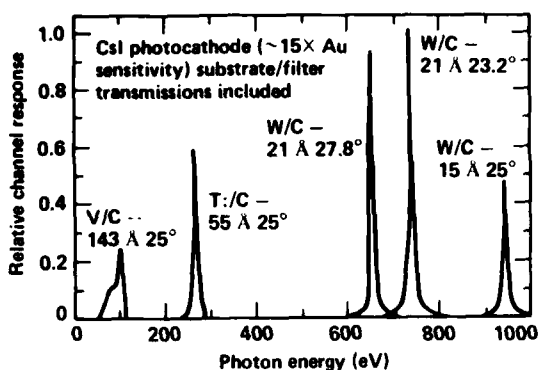


Figure 3 Spectral response of five narrow-band Bragg-diffracted energy channels below one kilovolt. Measured Bragg peak characteristics of the multilayers are combined with calculations of surface reflectivity, filter absorption and CsI photocathode efficiency to obtain these estimates of the total system response.

need and effectiveness of this filtering technique for the 267-eV channel. The reflectivity of Ti/C multilayer at 25° is approximated by the reflectivity of a uniform 1:1 mix of carbon and titanium calculated using a semiclassical dispersion theory.<sup>7</sup> This reflectivity added to the Bragg diffraction response of the multilayer is shown in the left-most box of Fig. 2. When the total multilayer response is multiplied by the transmission efficiency of a 2.05- $\mu\text{m}$  thick carbon absorption filter, the transmitted contribution outside the Bragg peak at 267 eV is negligible as shown in the right box of Fig. 2. Absorption filters used to filter the five channels are listed in Table 1.

The five energy channels shown in Fig. 3 are calculated using the measured Bragg diffraction characteristics of the multilayers, calculated estimates of surface reflectivity, filter transmission efficiencies and the streak camera photocathode response. The CsI photocathode response is approximated here by an  $E\mu(E)$  energy deposition model<sup>8</sup> scaled by the 50- $\mu\text{g}/\text{cm}^2$  carbon-foil-substrate transmission efficiency. Absolute calibration of the complete system response remains to be done.

#### ENERGY TRANSPORT MEASUREMENTS

Time-resolved measurements of x-ray emission from laser irradiated targets have been made at the Argus laser facility. The streaked spectrometer is positioned with 98-cm target-to-multilayer path and a 47-cm separation between the multilayers and the photocathode. Figure 4 is a streaked image of x-ray emission in the five channels from a 31-J, 1.06- $\mu\text{m}$ , 735-psec laser irradiation of a Au disk at  $\sim 3 \times 10^{14}$   $\text{W}/\text{cm}^2$  peak intensity. This raw data,



Figure 4 Raw data streaks in five channels obtained from the x-ray emission of an Au disk target. The target was heated by a 1.06- $\mu\text{m}$ , 31.5-J, 735-psec laser pulse at  $\sim 3 \times 10^{14}$   $\text{W}/\text{cm}^2$  peak intensity.

originally recorded on Royal X Pan film, is converted to temporal profiles of x-ray intensity using a density-to-exposure stepwedge calibration of each piece of film. These temporal profiles, averaged over the spatial extent of the channel, are displayed in Fig. 5.

Experiments were performed to examine energy transport both into the disk target (radial transport) and in the lateral direction. Disk targets of Al with Be coatings at a variety of thicknesses were shot at an intensity of  $3 \times 10^{14}$   $\text{W}/\text{cm}^2$ . Clear and repeatable temporal modulation of the emitted x-ray flux was observed from the layered targets. The character of the modulation changes with Be thickness and is consistent from shot to shot. Figure 6 is an example of  $\sim 450$ -psec large scale structure on the emitted x-ray temporal profile. The target was an Al disk with a 0.27- $\mu\text{m}$  Be coating. The incident 1.06- $\mu\text{m}$ , 89-J gaussian laser pulse had a 720-psec FWHM. The temporal profiles in each of Figs. 6 and 7 are absolutely timed with respect to each other and are normalized to unit peak intensity for convenient comparison of relative temporal shapes. The 102-eV, 737-eV, and 943-eV channels are shown. The 267-eV and 653-eV channels exhibit similar structure. The emission history from a bare Al disk irradiated with a 742-psec, 1.06- $\mu\text{m}$ , 90-J laser pulse at  $3 \times 10^{14}$   $\text{W}/\text{cm}^2$  is displayed in Fig. 7 for comparison. Again the 102-eV, 737-eV and 943-eV channels are shown. The temporal profiles from Al disks are much flatter on top than the Au disk data shown in Fig. 4 and have significantly longer emission times.

#### CONCLUSION

In summary, important narrow-energy-band, temporally-resolved information about energy transport in laser plasmas has been obtained using multilayer x-ray interference mirrors coupled to a soft x-ray streak camera. This diagnostic technique should stimulate much additional experimentation and analysis with emphasis on the spectrally-resolved temporal emission characteristics of the plasma to indicate energy transport properties.

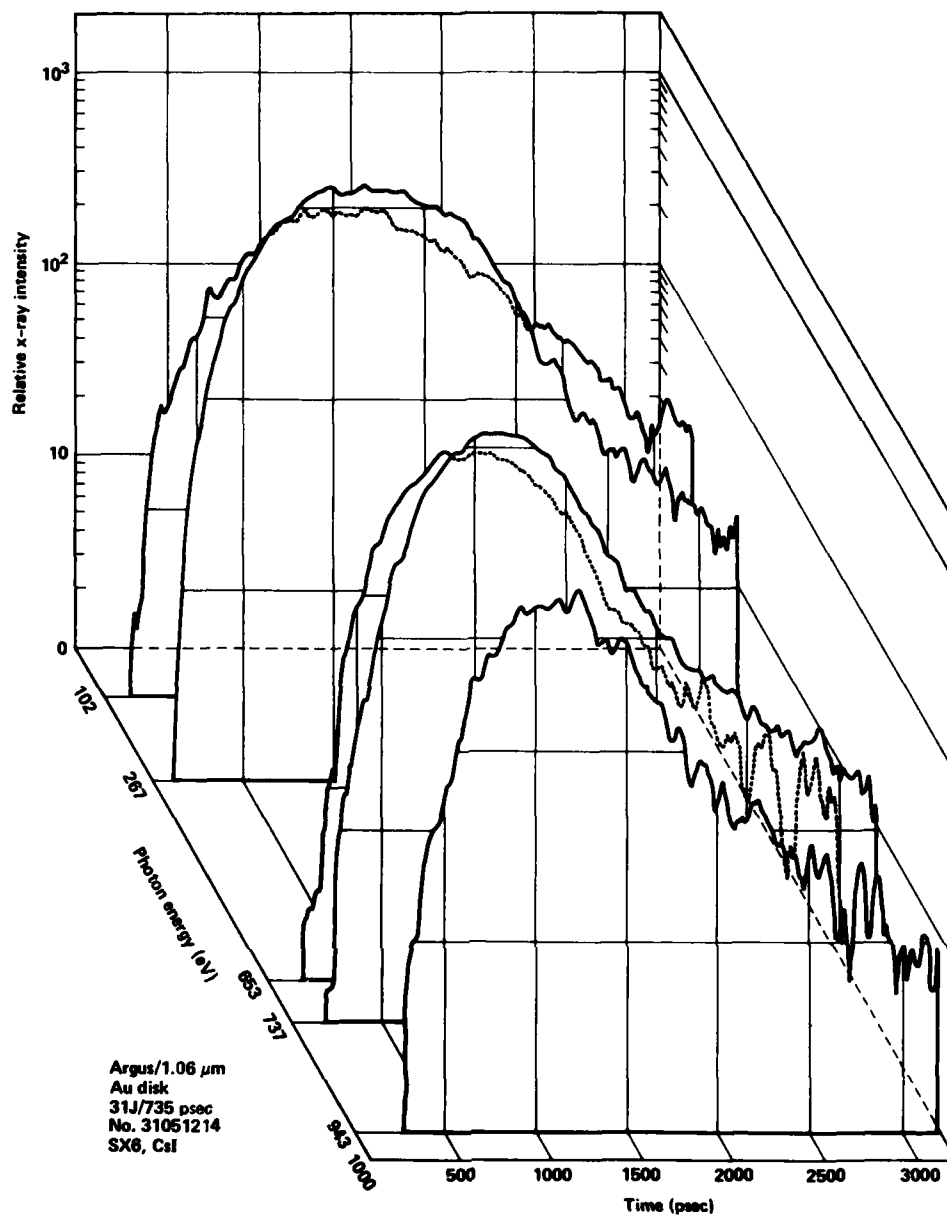


Figure 5 Temporal x-ray emission profiles of the data displayed in Fig. 4. Raw film density data is converted to intensity using individualized stepwedge calibration of the Royal X Pan film. This technique preserves the large dynamic range characteristics of the data.

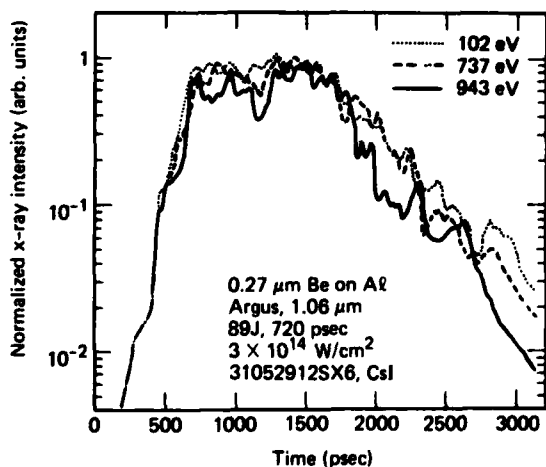


Figure 6 Temporal emission history of a 0.27- $\mu\text{m}$  Be coated Al disk in three spectral channels. Large scale temporal modulation is clearly evident in the two higher-energy channels. The three channels are normalized to unit peak intensity. The target was heated by a 1.06- $\mu\text{m}$ , 89-J, 720-psec gaussian laser pulse at  $3 \times 10^{14}$  W/cm<sup>2</sup>.



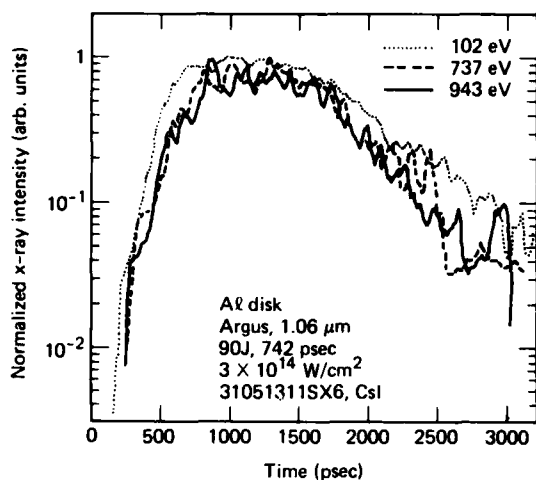


Figure 7 Temporal emission history of a bare Al disk in three spectral channels. Channels are normalized to unit peak intensity. The target was irradiated by a 1.06- $\mu\text{m}$ , 90-J, 742-psec gaussian laser pulse at  $3 \times 10^{14} \text{ W/cm}^2$ .

#### References

1. Troy W. Barbee Jr., Sputtered Layered Synthetic Microstructure (LSM) Dispersion Elements, this proceedings; T.W. Barbee, Jr. and D.C. Keith in SsRL Report No. 78/U4, Stanford Linear Accelerator Center, III-26 (1978).
2. G.L. Stradling, D.T. Attwood, J.W. Houghton, E.L. Pierce, and D.P. Gaines, *Bull. Am. Phys. Soc.* 23, 880 (1978).
3. G.L. Stradling, M.S. Thesis, Brigham Young University, 1981, also Lawrence Livermore National Laboratory, UCRL-52568.
4. J.W. Houghton, S.W. Thomas, and L.W. Coleman, *ISA Trans.*, 14, 196 (1975).
5. S.W. Thomas and G.E. Phillips, in *Proceedings of the 13th International Congress on High Speed Photography and Photonics* (Tokyo, Japan, 1978), pp. 471-475.
6. Burton L. Henke and Murray A. Tester, in *Advances in X-ray Analysis*, Vol. 18, edited by William L. Pickles, Charles S. Barrett, John B. Newkirk and Clayton U. Ruoo (Plenum, New York, 1974), pp. 70-106.
7. A. Toor and H.F. Finn, computer code REFLECT2 (Lawrence Livermore National Laboratory, Livermore, CA.); Arthur H. Compton and Samuel K. Allison, *X-Rays in Theory and Experiment* (D. Van Nostrand Company, Inc., New Jersey, 1926), Chap. IV, p. 293.
8. B.L. Henke, J.A. Smith, and D.T. Attwood, *Appl. Phys. Lett.*, 29, 539 (1976)

\*Work performed under the auspices of the U.S. Department of Energy by the Lawrence Livermore National Laboratory under Contract No. W-7405-Eng-48.



University of California at Davis graduate student Gary Stradling (center) discussing his work with picosecond x-ray streak cameras and multilayer x-ray interference mirrors with future Los Alamos colleagues Dr. Peter Lyons and Dr. Daniel Metzger.

## High Quality Fraunhofer Diffraction Spectra Taken at SSRL

in the Soft X-Ray Range

R. Tatchyn, I. Lindau and M. Hecht

Stanford Synchrotron Radiation Laboratory and Stanford

Electronics Laboratories, Stanford University,  
Stanford, CA 94305, USA

E. Källne

Harvard-Smithsonian Center for Astrophysics  
Cambridge, MA 02138, USA

E. Spiller

IBM  
Yorktown Heights, NY 10598, USA

R. Bartlett

LASL  
Los Alamos, NM 87545, USA

J. Källne

Department of Physics, University of Virginia,  
Charlottesville, VA 22901, USA

J.H. Dijkstra

Space Research Laboratory,  
Utrecht, The Netherlands

A. Hawryluk

MIT, Bldg. 13-3073  
Cambridge, MA 02139, USA

R.Z. Bachrach

PARC  
Palo Alto, CA 94304, USA

## ABSTRACT

This paper describes an experimental arrangement utilized at SSRL for obtaining high-quality Fraunhofer diffraction spectra from a group of specially-fabricated gold transmission gratings prepared at IBM. The data taken will ultimately be utilized to estimate the optical constants of gold in the 120 eV-640 eV range, but in the present paper our focus is on the new advances achieved in the attained spectral quality of our measurements in this range and on the improvements that are plausible in future utilizations of the same experimental scheme.

## I. INTRODUCTION

In recent years, there have been at least three experiments (exclusive of the experiment under present discussion) performed at SSRL that have looked at the far-field intensity spectra of ultrafine gold transmission gratings in the soft x-ray range (100 eV - 1300 eV) (1,2,3,4). The most recent experiment, described in this paper, was designed to take precise measurements of the spectra of several specially-prepared gold gratings fabricated by E. Spiller at

IBM. The motivation for the experiment was the computation of the optical constants of gold from the ratios of the first-to-zeroth order intensities of the measured spectra (5). In this paper we would like to describe the experimental scheme and to show some of the spectra obtained with our apparatus. Subsequently, we will discuss some of the shortcomings of our set-up and to indicate areas where improvements in future experiments can be easily implemented.

II. THE SOURCE EXPERIMENT

The schematic profile of an ideal grating with rectangular translucent bars is shown in Fig. 1. It has been shown that (5), subject to minor corrections arising from the real-life gratings' imperfections, if two gratings are chosen with parameters  $a_1, d_1, W_1$ , and  $a_2, d_2, W_2$  and measurements of the first-to-zeroth intensity ratios are made

$$A = I_1^{(1)} / I_1^{(0)} \tag{1}$$

$$B = I_2^{(1)} / I_2^{(0)} \tag{2}$$

then the optical constants  $\delta$  and  $k$  (where  $\hat{n} = (1 - \delta + ik)$  is the complex index of refraction) may be extracted from the two equations

$$(1 + A_1) \cos 2\pi W_1 \delta - \cosh 2\pi W_1 k + A_1 \cosh (2\pi W_1 k + r_1) = 0 \tag{3}$$

$$(1 + B_1) \cos 2\pi W_2 \delta - \cosh 2\pi W_2 k + B_1 \cosh (2\pi W_2 k + r_2) = 0 \tag{4}$$

where

$$r_1 = \ln (d_1 / (a_1 - d_1)) \tag{5}$$

$$r_2 = \ln (d_2 / (a_2 - d_2)) \tag{6}$$

and

$$A_1 = A \cdot \frac{\pi^2}{4} \cdot \left[ \sin^2 \frac{\pi d_1}{a_1} \cdot \cosh^2 \frac{1}{2} r_1 \right]^{-1} \tag{7}$$

$$B_1 = B \cdot \frac{\pi^2}{4} \cdot \left[ \sin^2 \frac{\pi d_2}{a_2} \cdot \cosh^2 \frac{1}{2} r_2 \right]^{-1} \tag{8}$$

It has also been shown that wherever the grating bar edges are not ideally rectangular, then, for equ.'s (3) and (4) to hold, the condition  $W \ll (a-d)$  must hold reasonably well (5). In addition, it is known that observable interference effects arise in ultrafine gold gratings in the soft x-ray range

principally in the range of thicknesses from 800 Å to about 3500 Å. Given these two conditions, it is clear why gratings with relatively large periods were required. Assuming, for a rough estimate, that  $a \approx 2d$ , and that the thickest grating was about 2500 Å thick, the condition  $W \ll (a-d)$ , or  $W \ll d$ , implied that  $d \geq 10W$  for our thickest grating, or that  $a \approx 50,000$  Å for our thickest grating. Since this would lead to an intracably small dispersion, gratings with  $a = 25,000$  Å were chosen, but with bars wider than  $\frac{1}{2}a$ , in order to maintain the condition  $W \ll (a-d)$  reasonably well.

Even with  $a = 25,000$  Å (i.e., 400 1/mm), the dispersion was so small that a dispersion length of 13' was found necessary to separate the 0th and 1st orders at about 800 eV (see Fig. 2).

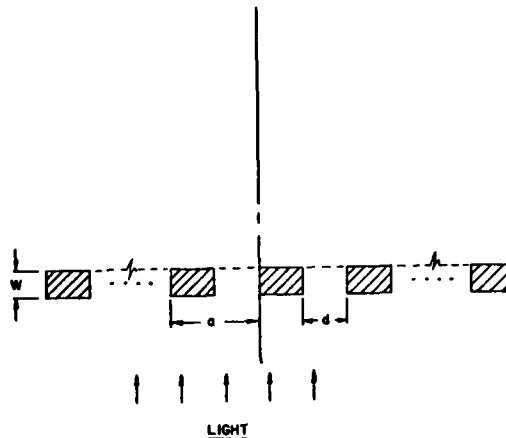


Fig. 1. End view of ideal rectangular grating.

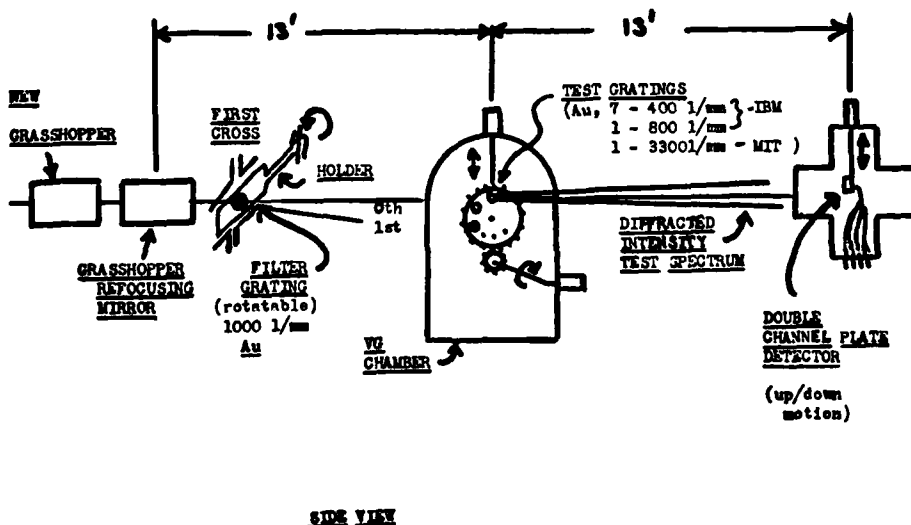


Figure 2. Schematic of experimental set-up to measure optical constants.

### III. PRACTICAL CONSIDERATIONS

The principal factor determining the specific format and the overall dimensions of the experiment was the new Grasshopper monochromator, the source for our experiment (6). It has been established in previous work that the output of this instrument is very dirty, containing large harmonic components in the 40 eV-200 eV range, and scattered light components in the 300 + eV range (2,3,4). As a result it was decided to place a filter grating at the monochromator's output in order to isolate the principal component spatially (in first order), so as to maximize the monochromaticity of the light hitting the test gratings. In addition, a double-slit system was used to spatially resolve the light hitting the gratings of a .3 mm slit before the filter grating and a .65 mm slit before the test gratings) so as to minimize the distorting effects of the refocussing mirror optics on the light hitting the test gratings. The entire schematic of the experiment is given in Fig. 2. A picture of the sample grating holder with the gratings in place is given in Fig. 3.

As is seen in Fig. 2, the 1st order of the filter grating was actually unused. This is due to the fact that the monochromator output was an order of magnitude below its expected intensity and the 1st order power off the filter grating was too small to take reasonable measurements with.



Fig. 3. Sample grating holder wheel.

### IV. DETECTION SCHEME

Since the experimental budget did not permit the purchase and use of a position-sensitive detector, an existing double-channel-plate detector was modified and used in an up/down mode. In order to optimize the counting statistics on the peaks of the intensity spectra, the detector was arranged to sense the presence of peaks and to sit at a point until a predetermined number of counts (nominally 10,000) was reached, and only then to move to the next point. Between peaks, the preset count limit was automatically changed to a low number (nominally 300), so that detection times would not be prohibitively long. Measuring the intensity in this manner, it was clear that a normalization channel was necessary (to account for beam decay, fluctuations, etc.) Unfortunately,

the principal (precision) normalization channel was damaged during the course of the experiment, and we have normalization data only from a secondary normalization channel, which will affect the cited accuracy of our results.

### V. THE SPECTRA

Figures 4,5,6 and 7 show several selected spectra taken off one of the test gratings. When compared to spectra taken in previous experiments, (1,2,3,4) their superiority is striking. The slight asymmetries in the observed orders stem principally from misalignment

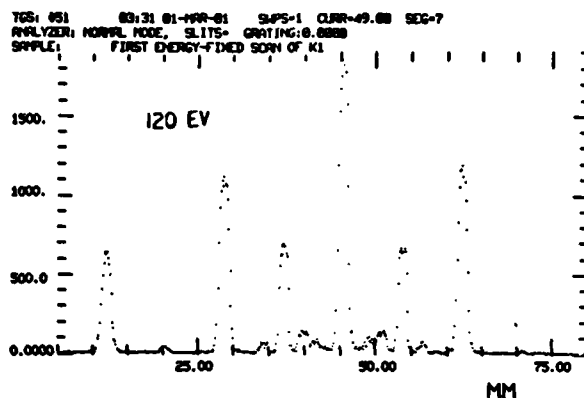


Fig. 4. Spectrum at 120 eV (Disp. length ~13').

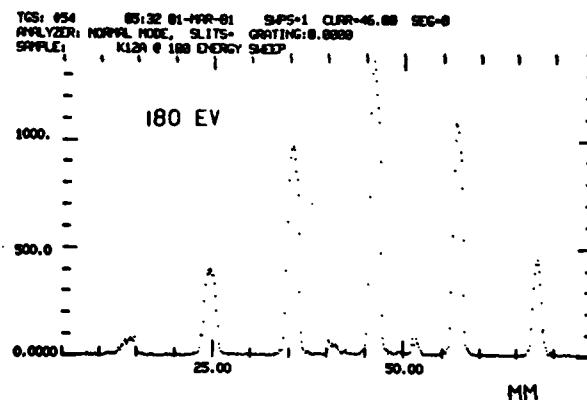


Fig. 5. Spectrum at 180 eV (Disp. length ~13').

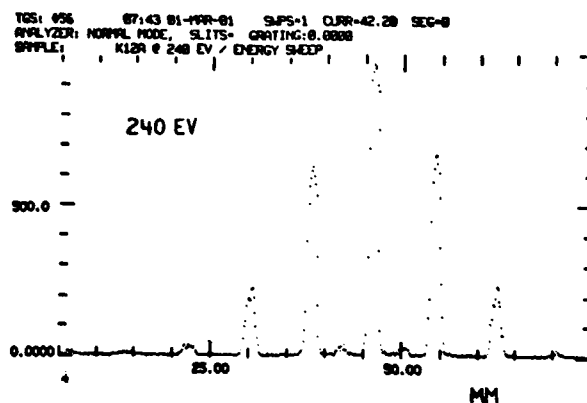


Fig. 6. Spectrum at 240 eV (Disp. length ~13').

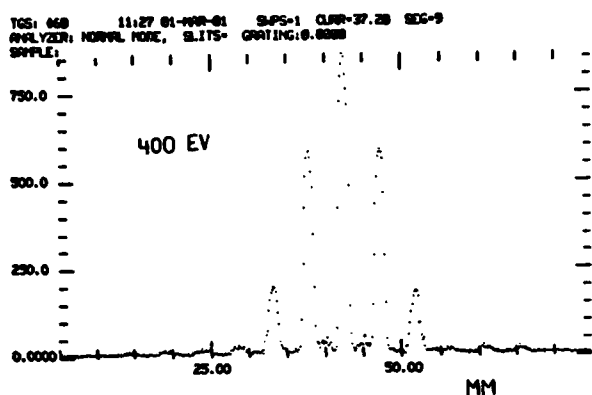


Fig. 7. Spectrum at 400 eV (Disp. length  $\sim 13'$ )

of the sample wheel with respect to the horizontal plane. This causes a "tilt" in the diffracted spectrum, and if the detector travel axis is not centered precisely on the 0th order, it can pick up one order more strongly than its symmetric opposite. In addition, the light direction changes out of the monochromator versus frequency. Imperfections in the single spectra (i.e., departures from the ideal "Gaussian" shape) are evidently caused by inhomogeneities in the light off the refocussing mirror (Fig.2) as well as by imperfections (support bars, dust, etc.) on the gratings themselves. However, all these discrepancies may be accounted for and they do not seriously detract from the overall high quality of the measured spectra.

#### VI. CONCLUSIONS

We have described an experiment done at SSRL in February, 1981 designed to measure the optical constants of gold. Even though several initial assumptions were not realized throughout the experiment, and even though a sparse budget precluded the use of

a position-sensitive detector, the results clearly indicate that the experimental technique is valid and should be developed further in subsequent experiments.

Some immediate suggestions for improvement would clearly eliminate most of the systematic errors that showed up in our experiment:

- 1) Better gratings, with uniform properties over their entire surfaces (this would preclude the required misalignment of the gratings with respect to the horizontal plane).
- 2) A position sensitive detector (this would entirely obviate the need to monitor intensity for normalization).
- 3) A much better soft x-ray monochromator (high output, no harmonics and no scattered light would obviate the need for a "filter" grating and would cut the experiment length in half).

Since we expect that future developments in the fields of x-ray instrumentation and grating fabrication will help to realize the above three requirements we conclude that the experimental technique tested in our described experiment holds great promise for accurate and efficient measurements of optical constants in the soft x-ray range.

#### REFERENCES

1. H.W. Schnopper, L.P. Van Speybroeck, J.P. Delvaile, A. Epstein, E. Khlne, R.Z. Bachrach, J. Dijkstra, and L. Lantward, *Applied Optics*, Vol. 16, No. 4, April 1977, 1088-1091.
2. J.P. Delvaile, H.W. Schnopper, E. Khlne, I. Lindau, R. Tatchyn, R.A. Gutcheck, R.Z. Bachrach, J.H. Dijkstra, *Nuclear Instruments and Methods*, 172, 1980, 281-285.
3. R. Tatchyn, Engineer's Thesis, Stanford University, March 1980.
4. Experiment done at SSRL in 1979. Results unpublished.
5. R. Tatchyn, I. Lindau, and E. Khlne, *Optica Acta*, Vol. 27, 1980, 1505-1536.
6. J. Stchr, V. Rehn, I. Lindau, and R.Z. Bachrach, *Nuclear Instruments and Methods*, 152, 1978, 43-51.

Canonically Blazed Transmission Gratings:

Analysis and Modelling Results

R. Tatchyn and I. Lindau

Stanford Synchrotron Radiation Laboratory and

Stanford Electronics Laboratories, Stanford University,

Stanford, California 94305, USA

ABSTRACT

In this paper we present a blazing scheme that may be generated on any rectangular grating and that is sufficiently general to cover all conceivable cases of linear blazing imposed on rectangular transmission gratings. Characterizing the blazed grating completely by a group of parameters, we develop the analytical formula for the intensity spectrum of a blazed grating set perpendicularly to the irradiating light in terms of these parameters. The analysis given is valid for the regions of material properties and light energies where refraction may be ignored. Practical implications of the modelled equations are discussed and are shown to have great potential in the development of new instrumentation in the soft x-ray range.

I. INTRODUCTION

In recent years, the manufacture (1) and analysis (2,3) of transmission diffraction gratings has shown considerable progress. Experiments performed on such gratings have shown excellent agreement between the observed and predicted results in the soft x-ray range (2,4,5). The fundamental far-field Fraunhofer diffraction model has proved to be an excellent predictor of observed results in this range, and an extension of it to cover the case of blazed grating bars is fully warranted.

The principal motivation behind the investigation of non-rectangular bar shapes is to identify the bar shapes and grating operation conditions that maximize first-order diffracted power, since transmission gratings of the type we are considering are excellent candidates for use as monochromator dispersion elements in the soft x-ray range. It is already known that even for rectangular bars (see Fig. 1), symmetric enhancement of both first orders is possible by over a factor of two at certain energies and at certain preferred thicknesses of the grating bars ( $W$  in Fig. 1) (2,3,4).

In the following sections we will show that by blazing the bars in a canonical fashion we can demonstrate first order enhancement of almost a factor of three for a typical gold grating and the possibility of very high efficiency (almost 100%) into first order for materials that have negligible attenuation and that are reasonably phase-active in the soft x-ray range.

II. THE IDEAL RECTANGULAR GRATING

The far-field intensity spectrum of an ideal rectangular grating whose bars are characterized by the complex index of refraction  $\hat{n} = n + ik = (1 - \delta) + ik$  is given by (Fig. 1):

$$I(s) = \left( \frac{\sin mNa}{\sin \pi sa} \right)^2 \left| \bar{M} + \exp(\pi isa) \bar{A} \right|^2 \quad (1)$$

The following definitions apply to Fig. 1 and eq. (1):

- 1)  $s \equiv$  sine of the observation angle with respect to the grating normal.
- 2)  $m \equiv$  observed order. At the various orders,  $s = m/a$
- 3)  $a \equiv$  grating period in wavelength units
- 4)  $d \equiv$  grating aperture size in wavelength units
- 5)  $W \equiv$  grating bar thickness in wavelength units

- 6)  $\lambda \equiv$  light wavelength
- 7)  $\bar{M} \equiv$  Fourier transform of the field distribution across a bar top surface
- 8)  $\bar{A} \equiv$  Fourier transform of the field distribution across an open aperture
- 9)  $N \equiv$  number of illuminated bars

For the case where interface effects may be ignored, and for a wave of unit amplitude, the following transforms are directly derived:

$$\bar{M} = (a-d) (\text{sinc}(a-d)s) \exp[-2\pi i(\delta - ik)W] \quad (2)$$

$$\bar{A} = d \text{sinc } ds \quad (3)$$

Substitution of (2) and (3) into (1) yields the following expression for the far-field intensity of the grating shown in Fig. 1.

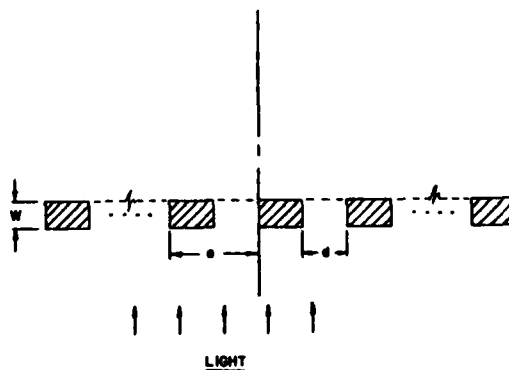


Fig. 1. End view of ideal rectangular grating.

$$I(s) = \left( \frac{\sin mNa}{\sin \pi sa} \right)^2 \left\{ \left[ \exp(-2\pi Wk) \cos 2\pi W\delta(a-d) \text{sinc}(a-d)s + (\cos \pi sa) d \text{sinc } ds \right] - i \left[ \exp(-2\pi Wk) \sin 2\pi W\delta(a-d) \text{sinc}(a-d)s \right] \right\}^2 \quad (4)$$

$$\begin{aligned}
 &= \left( \frac{\sin \pi Na}{\sin \pi na} \right)^2 \left\{ \exp(-4\pi W_0 k) (a-d)^2 \text{sinc}^2(a-d) + \right. \\
 &\quad \left. (2 \cos \pi Na) \exp(-2\pi W_0 k) d(a-d) \text{sinc}(a-d) \cos 2\pi W_0 d + \right. \\
 &\quad \left. d^2 \text{sinc}^2 ds \right\} \quad (5) \\
 &\times \left\{ \cos 2\pi W_0 \delta [(s-\alpha\delta) \sin \pi(a-d)(s-\alpha\delta) \cosh \pi(a-d)k\alpha \right. \\
 &\quad \left. - k\alpha \cos \pi(a-d)(s-\alpha\delta) \sinh \pi(a-d)k\alpha] \right. \\
 &\quad \left. - \sin 2\pi W_0 \delta [k\alpha \sin \pi(a-d)(s-\alpha\delta) \cosh \pi(a-d)k\alpha \right. \\
 &\quad \left. - (s-\alpha\delta) \cos \pi(a-d)(s-\alpha\delta) \sinh \pi(a-d)k\alpha] \right\} \\
 &\quad + d^2 \text{sinc}^2 ds \quad (7)
 \end{aligned}$$

Equation (5) gives the far-field intensity at the various orders for a wave of unit amplitude and interface reflection effects ignored.

III. THE BLAZED GRATING

Computing  $\bar{M}$  for the blazed grating under the same assumptions as for the rectangular grating and assuming refraction to be negligible, yields (Fig. 2):

$$\alpha = \left( \frac{W_s - W_i}{a-d} \right) \equiv \text{BLAZE SLOPE}$$

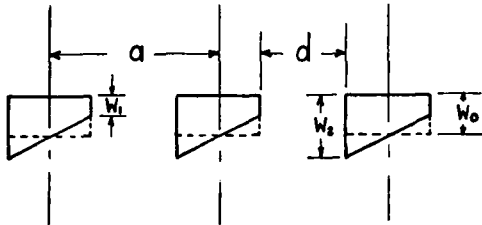


Fig. 2. Schematic description of a canonical blazing scheme imposed on a rectangular grating of thickness  $W_0$ .

$$\begin{aligned}
 \bar{M}_{BL} &= \exp[-2\pi W_0 \delta (\delta - ik)] \times \\
 &\frac{\exp(-\pi i(s - \alpha(\delta - ik))(a-d)) - \exp(\pi i(s - \alpha(\delta - ik))(a-d))}{2\pi i(s - \alpha(\delta - ik))} \quad (6)
 \end{aligned}$$

It is clear from Fig. 2 that the blazing scheme shown is completely general, i.e., any degree of blazing may be imposed on any rectangular grating configuration. This reaffirms our original claim that our proposed blazing scheme is canonical.

Inserting (3) and (6) into (1) gives the following expression for the far-field spectrum of the blazed grating (where we indicate the intensity of the irradiating light to be  $I_0$ ):

$$\begin{aligned}
 \frac{I(s)}{I_0} &= \left( \frac{\sin \pi Na}{\sin \pi na} \right)^2 \times \\
 &\left[ e^{-4\pi W_0 k} \cdot \frac{\cosh 2\pi(a-d)k\alpha - \cos 2\pi(a-d)(s-\alpha\delta)}{2\pi^2(s^2 - 2\alpha\delta s + \alpha^2(\delta^2 + k^2))} \right]
 \end{aligned}$$

IV. MODELLING

We have run eq. (7) on the computer using gold as the grating material (i.e., the optical constants of gold) (6). In order to compare the performance of the blazed to the unblazed grating we have plotted the  $I_{\text{blazed}}^{(-1)}/I_{\text{unblazed}}^{(-1)}$ ,  $I_{\text{blazed}}^{(0)}/I_{\text{unblazed}}^{(0)}$ , and  $I_{\text{blazed}}^{(1)}/I_{\text{unblazed}}^{(1)}$  for an ideal rectangular grating of thickness  $W_0$  for various degrees of blazing and for a few period/aperture ratios ( $a/d=2$ ,  $a/d=4$ ), for three energies spanning the soft x-ray range (Fig. 3). It

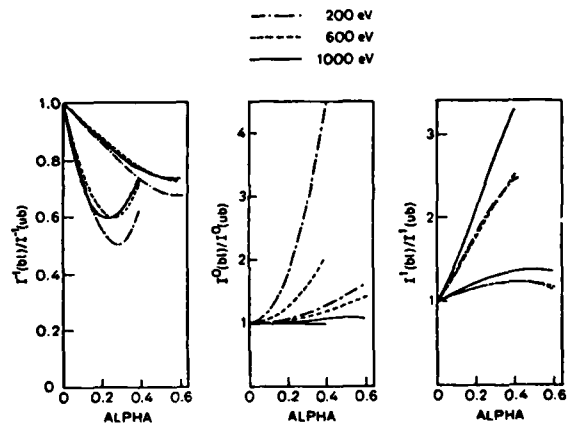


Fig. 3. Blazing effects on the -1st, 0th, and 1st orders of an unblazed gold grating. The curves extending out to  $\alpha=0.4$  are for gratings with  $(a/d)=4$  and those extending out to  $\alpha=0.6$  are for gratings with  $(a/d)=2$ .  $W_0=1500 \text{ \AA}$ ;  $\alpha \equiv$  blaze slope.

is clear that blazing is very efficacious in enhancing the first-order efficiency of a typical unblazed grating. From the results in Fig. 3 we can conclude that suitable blazing is an important design parameter and, once the current technology becomes capable of designing transmission gratings with blazed bars, it is anticipated that blazing will be used as a standard enhancement technique for  $I^{(1)}/I^{(0)}$  maximization.

Equation (7) contains an important implication when we follow up the enhancement of the blazing effect by letting  $d$  approach 0. This situation is depicted in Fig. 4. With  $d=0$ , eq. (7) becomes

$$\frac{I(s)}{I_0} = \left( \frac{\sin \pi s N a}{\sin \pi s a} \right)^2 e^{-4\pi W_0 k} \frac{\cosh 2\pi a k \alpha - \cos 2\pi a (s - \alpha \delta)}{2\pi^2 [s^2 - 2\alpha \delta s + \alpha^2 (\delta^2 + k^2)]} \quad (8)$$

If we had a material that fulfilled the conditions

$$k \approx 0 \quad (9)$$

$$\delta \gg k \quad (10)$$

then  $\cosh 2\pi a k \alpha + 1$ , and eq. (8) would become

$$\frac{I(s)}{I_0} \approx \left( \frac{\sin \pi s N a}{\sin \pi s a} \right)^2 e^{-4\pi W_0 k} \frac{1 - (\cos^2 \pi a (s - \alpha \delta) - \sin^2 \pi a (s - \alpha \delta))}{2\pi^2 s - \alpha \delta} \quad (11)$$

or

$$\frac{I(s)}{I_0} \approx \left( \frac{\sin \pi s N a}{\sin \pi s a} \right)^2 e^{-4\pi W_0 k} \text{sinc}^2 a (s - \alpha \delta) \quad (12)$$

Now, it is clear that  $\text{sinc}^2 a (s - \alpha \delta)$  is just the function  $\text{sinc}^2 a$  as shifted by the amount  $\alpha \delta$ . But,  $\text{sinc}^2 a$  is zero for all  $m \neq 0$ , where  $s = m/a$ . Therefore, if we let

$$\alpha \delta = \frac{1}{a} \quad (13)$$

we see that (12) will be zero for all orders other than the first, a condition of 100% efficiency into first order. The configuration is shown in Fig. 4.

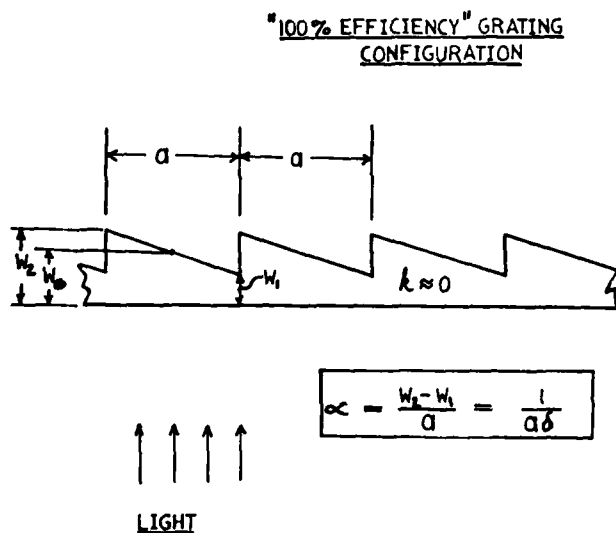


Fig. 4. Blazed grating configuration and material conditions, for attaining ~100% efficiency into 1st order.

## V. CONCLUSIONS

We have derived the canonical blazing formula (eq. 7) and have demonstrated that blazing can be extremely efficacious in enhancing first-order efficiency in the soft x-ray range. The condition of almost ideal efficiency into first order is clearly equivalent in the limit to the well-known case of a linearly graded phase grating ( $k = 0$ ) or a linearly-phased antenna array. Fortunately, for most materials in the soft x-ray range  $k < \delta$ , but the conditions  $k \approx 0$ ,  $k \ll \delta$  are not very well realized. For most materials  $k$  is smaller enough than  $\delta$  so that quite efficient gratings may be obtained by blazing, - if greater efficiency is desired, one must try to either locate or synthesize materials where the conditions  $k \approx 0$ ,  $k \ll \delta$  do obtain. At any rate, we have clearly demonstrated that blazing is warranted, all things considered.

In addition to the above remarks, we would like to suggest that a simple technique may be used to obtain a blazed configuration such as shown in Fig. 4 in order to test the analytical results in this paper. Since blazed (ruled) reflection gratings are available, one could utilize a copy of the master grating, made out of some suitable etchable material, as a matrix on which to deposit a gold (or other) film. Once the copy matrix material is etched away, the configuration of Fig. 4 (or one similar to it) should then remain.

In conclusion, based on our results, we feel that significant future work should be allotted to the development of controllable blazing schemes for ultra-fine gratings and also to the investigation of structures and materials that fulfill, or come close to fulfilling, the conditions (9) and (10) over the soft x-ray range.

## REFERENCES

1. J.H. Dijkstra, Space Science Instrumentation, 2, 1976, 363-372.
2. H.W. Schnopper, L.P. Van Speybrueck, J.P. Delvaile, A. Epstein, E. Khlilne, R.Z. Bachrach, J. Dijkstra, and L. Lantward, Applied Optics, Vol. 16, Nos. 4, April 1977, 1088-1091.
3. R. Tatchyn and I. Lindau, Nuclear Instruments and Methods, 172, 1980, 287-291.
4. J.P. Delvaile, H.W. Schnopper, E. Khlilne, I. Lindau, R. Tatchyn, R.A. Gutcheck, R.Z. Bachrach, J. H. Dijkstra, Nuclear Instruments and Methods, 172, 1980, 281-285.
5. R. Tatchyn, Engineer's Thesis, Stanford University, March 1980.
6. H.-J. Hagemann, W. Gudat, C. Kunz, DESY, Report SR-74/7, May 1974.



Paul L. Csonka

University of Oregon, Institute of Theoretical Science, Eugene, Oregon 97403

Roman Tatchyn

E. E. Department, Stanford University, Stanford, California

## ABSTRACT

Synchrotron radiation facilities (such as SSRL) could be used to manufacture superfine, i.e. high line density gratings with  $\sim 5 \cdot 10^4$  lines per mm.

## SUGGESTED METHOD

To produce superfine gratings, an interference pattern is set up between two branches of a sufficiently monochromatic and coherent x-ray beam of wavelength  $\lambda > 100\text{\AA}$ .

The interference line pattern is recorded on a polymer (e.g. PMMA). Recording with an accuracy of about  $200\text{\AA}$  is possible at these values of  $\lambda$ .

Figure 1 shows a schematic view of the proposed setup.

## PURPOSE OF GRATINGS

High line density gratings can be used as (1)

- (A) Diffractive or focusing elements in x-ray imaging
- (B) Miniaturized circuit element
- (C) A research tool in solid state physics

to:

Generate 2-dimensional "crystal" structure  
 Study: Bloch oscillations  
 The fine structure of Landau levels  
 Narrow strips of monolayers

## COHERENCE REQUIREMENTS (GENERAL)

## A) MONOCHROMATICITY

Let a parallel beam contain wavelengths within the interval  $\lambda_0 \pm \frac{1}{2} \Delta\lambda$  where  $\Delta\lambda \ll \lambda_0$ .

Figure 2a shows that if at point  $P_A$  all waves in the beam are in phase, then at  $P_B$  the phase

difference between any two waves will be  $< f_1 \pi$  (where  $f_1$  is some chosen number), provided that

$$\frac{\Delta\lambda}{\lambda_0} \lesssim \frac{f_1}{2} \frac{\lambda_0}{\Delta L} \quad (1)$$

## B) COLLINEARITY

Let a beam contain waves of wavelength  $\lambda_0$ . (Each wave may travel in a different direction.) The direction in which the wave travels makes an angle  $\theta$  with the z axis. All  $\theta$  lie within the interval  $(-\frac{1}{2}\Delta\theta, +\frac{1}{2}\Delta\theta)$ .

Figure 2b shows that at a point  $P_A$  all waves are in phase, than at  $P_B$  the phase difference between any two will be  $< f_2 \pi$  ( $f_2$  is some chosen number), provided that

$$\Delta\theta < f_2^{\frac{1}{2}} (\lambda_0 / \Delta L)^{\frac{1}{2}} \text{ radians.} \quad (2)$$

## C) SOURCE SIZE

Choose the z axis to be horizontal. Let the surface of the "source" (which emits photons) be rectangular, with horizontal diameter (along the x axis)  $D_{sx}$ , and vertical diameter (along y)  $D_{sy}$ . The "target" surface (which is illuminated by photons) is also rectangular, with diameters  $D_x$  and  $D_y$ .

Figure 2c shows that if two waves of wavelength  $\lambda_0$  are in phase at some point P on the source surface, then at the time of their respective impact on the target surface the phase of the two waves will differ by  $< f_3 \pi$  ( $f_3$  is some chosen number), if the source-target distance L, satisfies

$$L \gtrsim \left[ \Delta_x^2 + \Delta_y^2 \right]^{1/2} F / \lambda_0 f_3 \quad ; \quad i = x, y$$

$$\Delta_i^2 \equiv \begin{cases} (\frac{1}{2}D_{si} + \frac{1}{2}D_i)^2 & ; \text{ if } |D_{si}| \leq |D_i| \\ 2D_{si} D_i & ; \text{ if } |D_{si}| > |D_i| \end{cases} \quad (3)$$

Here  $F=1$ . If the surfaces are not rectangular, then the correction factor  $F \neq 1$ , but of order unity.

## COHERENCE REQUIREMENTS (FOR THE GEOMETRY OF FIG. 1)

For the geometry shown in Fig. 3, the  $D_{sx}$ ,  $D_{sy}$  are the horizontal and vertical diameters of the source, i.e. that (section of an) electron beam which emits photons. The  $D_x$  and  $D_y$  are the horizontal and vertical diameters of the illuminated "target surface", L is the largest optical distance

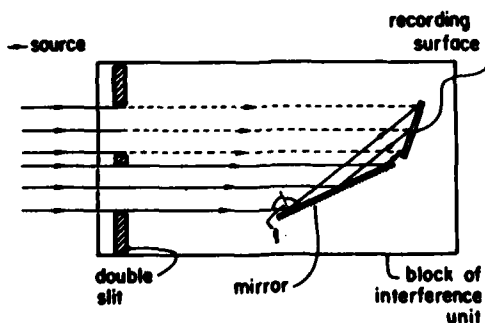


Fig. 1 The beam produced by the source is led through a double slit. One of the two branches is reflected off a mirror by an angle  $2\xi$ . The two branches produce an interference pattern on the recording surface.

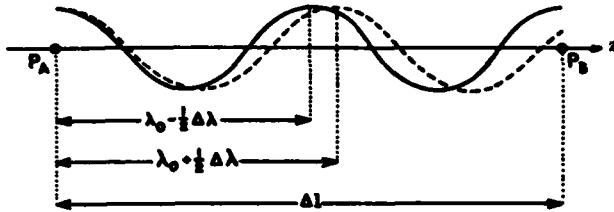


Fig. 2a Two plane waves with wavelength  $\lambda_0 - \frac{1}{2}\Delta\lambda$  and  $\lambda_0 + \frac{1}{2}\Delta\lambda$  (where  $\Delta\lambda \ll \lambda_0$ ) travel  $\Delta l$  along the  $z$  axis from point  $P_A$  to point  $P_B$ . At  $P_A$  the two waves are in phase. Then, clearly, at  $P_B$  they will be out of phase by  $\Delta\phi = 2\pi\Delta l \left[ \frac{1}{\lambda_0 - \frac{1}{2}\Delta\lambda} - \frac{1}{\lambda_0 + \frac{1}{2}\Delta\lambda} \right]$   
 $\approx 2\pi\Delta l \frac{\Delta\lambda}{\lambda_0^2}$ .

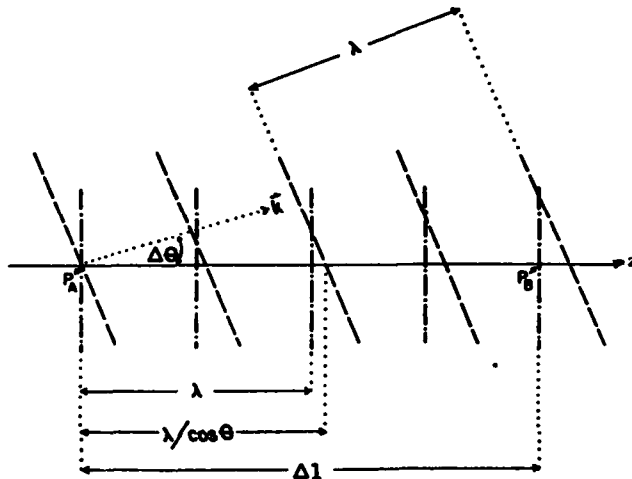


Fig. 2b One plane wave with wavelength  $\lambda_0$  travels along the  $z$  axis from point  $P_A$  toward  $P_B$ . Its crests and valleys at a certain moment are denoted by parallel dash-dot lines (the distance between every second such line is  $\lambda_0$ ). A second plane wave with wavelength  $\lambda_0$  travels along  $k$ . The angle between  $k$  and the  $z$  axis is  $\Delta\theta$ . Crests and valleys of this wave at the same moment are located along the dashed lines. This wave produces a field pattern along  $z$  which is periodic by  $\lambda_0/\cos\Delta\theta \equiv \lambda'$ .

between the source and the recording surface. Then  $\Delta l = \frac{1}{\sqrt{2}}D_h$  (for  $\xi = \pi/4$ ) and Eqs. (1) and (2) can be rewritten as

$$\Delta\lambda/\lambda_0 < f_1\lambda_0 \sqrt{2D_h} \quad (1a)$$

$$\Delta\theta \equiv [(\Delta\theta_x)^2 + (\Delta\theta_y)^2]^{1/2} < 2^{1/2}f_2^{1/2}(\lambda_0/D_h)^{1/2}. \quad (2a)$$

How to chose  $L$ ? Ideally, each  $P_s$  on the source surface should illuminate the entire target (i.e.  $\Delta\theta > (D_{sx} + D_x)/L$ ,  $\Delta\theta_y > (D_{sy} + D_y)/L$ ), but

not more, because that would be wasteful (photons missing target). To minimize waste, choose

$$\Delta\theta_x = (D_{sx} + D_x)/L, \quad \Delta\theta_y = (D_{sy} + D_y)/L \quad (4)$$

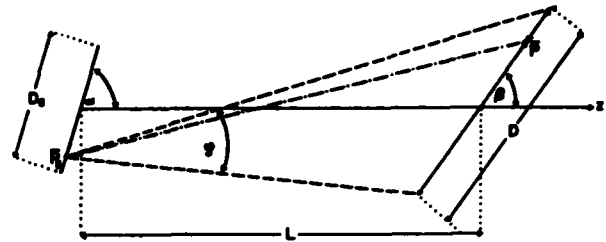


Fig. 2c The distance between the center of the source (whose diameter is  $D_s$ ) and the center of the plane "target" surface to be illuminated (whose diameter is  $D$ ) by the source, is  $L$ .  $L(P_s, P)$  is the distance (shown by the dash-dot line) between any point  $P_s$  of the source, and some point  $P$  on the illuminated surface. The path difference between two photons which travel from a chosen point  $P_s$  to any two points  $P_1$  and  $P_2$  is  $|L(P_s, P_1) - L(P_s, P_2)| \equiv \Delta L$ . The maximum (over all  $P_1, P_2$  pairs) of  $\Delta L$  is  $\Delta L_{\max}$ . When  $\alpha=\beta=\frac{\pi}{2}$ , also  $L \gg D_s$ , and  $L \gg D$ , then

$$\Delta L_{\max} L \approx \frac{1}{2L} \begin{cases} (P_s + \frac{1}{2}D)^2 & ; \text{IF } |P_s| \geq |D| \\ 2P_s D & ; \text{IF } |P_s| < |D| \end{cases}$$

( $\phi$  is the viewing angle through which the diameter of the target surface is seen from  $P_s$ . The  $\phi$  will be used later.)

This choice is consistent with condition (3), and together with (3) implies (2a), provided that

$$\frac{\sqrt{2} f_2 P^2}{16 f_3} > \frac{(D_{s1} + D_1)^2 D_h \lambda_0}{\Delta_x^2 + \Delta_y^2} ; \quad i = x, y \quad (5)$$

EXPOSURE TIME:  $T$

- $n_Y$ : Number of photons required to impinge per unit surface of recording material to imprint a clearly recognizable interference pattern.
- $n^{(0)}$ : Number of photons emerging from the storage ring at a particular synchrotron radiation port, during time  $T^{(0)}$  with wavelength in the interval  $(\lambda_0 \pm \frac{1}{2}\Delta^{(0)}\lambda)$ , emitted into a four dimensional phase space volume  $A_x^{(0)} A_y^{(0)}$  (see Appendix).

It is shown in the Appendix that when  $D_{sx}$ ,  $D_{sy}$ ,  $D_x$  and  $D_y$  are all fixed, and  $L$  is chosen optimally, then the phase space volume "filled" by "useful" photons (i.e. those which can be used to produce an interference pattern) is that given by Eq. (A-4). For such optimally chosen  $L$  the exposure time needed to produce the desired interference pattern is

$$T = \left[ n_Y D_h D_M \frac{A_x^{(0)} A_y^{(0)} T^{(0)} \Delta^{(0)} \lambda / \lambda_0}{N^{(0)} \lambda_0^2} \right] \frac{D_h 4\sqrt{2} B^2}{\lambda_0 f_1 f_3^2 b_x b_y} \quad (6)$$

where  $B$  is a function of  $D_{sx}$ ,  $D_{sy}$ ,  $D_x$ ,  $D_y$  and is given at the end of the Appendix.

$M$  is a factor ( $< 1$ ) included to take into account absorption on mirrors and in the monochromator.

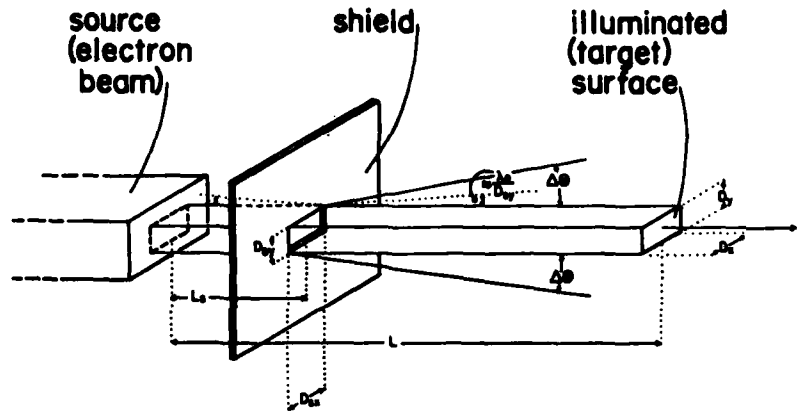


Fig. 3 A slit  $D_{sx}$  wide and  $D_{sy}$  high is placed between the source (here the electron beam) and the area to be illuminated.  $\Delta\theta$  is the maximum angular divergence permitted by Eq. (2). For large enough  $L$ , the accepted angular divergence is automatically  $<\Delta\theta$ . (The horizontal and vertical diffraction angles due to the slit are approximately  $\lambda_0/D_{sx}$ ,  $\lambda_0/D_{sy}$ . For the parameters listed in Table I, these can be neglected.)

## PROPOSED EXPERIMENTAL SETUP

## SOURCE

Choose  $\lambda_0 = 100\text{\AA}$   
 The circulating electron beam (i.e. "source") parameters are listed in Table I.  
 To decrease the effective source size, a slit  $D_{sx}$  wide and  $D_{sy}$  high is placed between the electron beam and the area to be illuminated, at a distance  $L_s$  from the beam. When the parameters are chosen as in Table I, diffraction effects due to the slit can be neglected: The source, as seen from the target is rectangular (so that  $F = 1$  in Eq. (3)), with diameter  $D_{sx}$  and  $D_{sy}$ .

## TARGET

Its surface is perpendicular to the  $z$  axis. Its diameters are  $D_{tx}$  and  $D_{ty}$ . We denote by  $b_x$  and  $b_y$  the ratios  $D_x/D_{sx}$  and  $D_y/D_{sy}$  respectively, and expect  $b_x$ ,  $b_y$  to range between about 0.1 and 20.

## PHOTON BEAM

Choose  $f_1$ ,  $f_2$  and  $f_3$  as listed in Table I.  
 When the photon distribution in wavelength, angle and position are all uncorrelated, then the total phase difference (due to all distributions) between any two

Table I.

Source		Target	
$\sigma_x$ (mm)	3.2	$D_x$ (mm)	$D_{sx} b_x$
$\sigma_y$ (mm)	1.6	$D_y$ (mm)	$D_{sy} b_y$
$\Delta\theta_x$ (mrad)	1.7	Photon beam requirements	
$\Delta\theta_y$ (mrad)	1.6		
$\frac{N^{(0)}}{A_{xyt}} (\text{cm}^{-2} \text{sec}^{-1} \text{rad}^{-3})$	$3.9 \cdot 10^{22}$	$f_1 = f_3$	$2^{-1} 2^{-4}$
$D_{sx}$ (mm)	0.3	$f_2$	$10^{-2}$
$D_{sy}$ (mm)	0.3	$\Delta\lambda/\lambda_0 \leq$	$5.9 \cdot 10^{-6} b_x^{-1}$
$L_s$ (cm)	$10^2$	$L$ (cm) $\geq$	$\left(\frac{D_{sx}}{3 \cdot 10^{-2} \text{cm}}\right)^2 5.1 \cdot 10^7$

Table I The left half of the table lists the assumed source parameters. The  $\sigma_x$ ,  $\sigma_y$ ,  $\Delta\theta_x$ ,  $\Delta\theta_y$  are the beam radii and angular spreads.

The right half contains the target parameters and conditions on the beam as a function of  $b_x \equiv D_x/D_{sx}$  and  $b_y \equiv D_y/D_{sy}$  for the assumed  $f_1$ ,  $f_2$  and  $f_3$  values.

photons emitted in phase at any point of the source, at their impact on the target is

$$\Delta\phi \lesssim [\epsilon_1^2 + \epsilon_2^2 + \epsilon_3^2]^{1/2} \pi. \quad (7)$$

The monochromator has to produce a beam with (to satisfy condition (1a))

$$\frac{\Delta\lambda}{\lambda_0} \lesssim \frac{10^{-5}}{1.2\sqrt{2} b_x} \quad (8)$$

Assuming that L is chosen to satisfy condition (4), requirement (1b) is

$$L \leq L_0 \equiv 4.65 \cdot 10^3 \text{ cm}. \quad (9)$$

To minimize T, choose L at its minimum value consistent with condition (3), as listed in Table I. Then

$$T = 4.4 \cdot 10^7 M \frac{D_x}{D_{sx}} - B^2 \text{ sec}. \quad (10)$$

Figure 4 gives the value of T for various target diameters. For example, to imprint the desired interference pattern on a quadrangular surface of width  $D_h = 10^{-2}$  cm (i.e.  $D_x = \frac{1}{\sqrt{2}} 10^{-2}$  cm,  $b_x = 0.236$ ) and  $D_y = 10^{-2}$  cm (i.e.  $b_y = 0.333$ ), one would need  $T = 8.3 \cdot 10^5$  sec 4 days if all mirrors were perfectly reflecting (i.e.  $M=1$ ). When  $D_h = 10^{-3}$  cm,  $D_y = 10^{-2}$  cm,  $M=1$ , then  $T = 3.3 \cdot 10^4$  sec  $\approx$  9 hrs. (Assuming  $n_\lambda = 5 \cdot 10^{14}$  photons/cm<sup>2</sup>.)

With multilayer mirrors one expects a reflexivity (2)  $M \approx 20\%$  for  $\lambda \approx 100\text{\AA}$ . With only one mirror in one beam, and a monochromator especially designed for this purpose (e.g. Be mirror and transmission grating)  $M \approx 50$ .

#### TOLERANCES

Horizontal electron beam drift has negligible effect.

Vertical electron beam drift should be kept  $< 0.4$  mm for the parameters in Table I. (Otherwise target will have to be raised or lowered synchronously with electron beam).

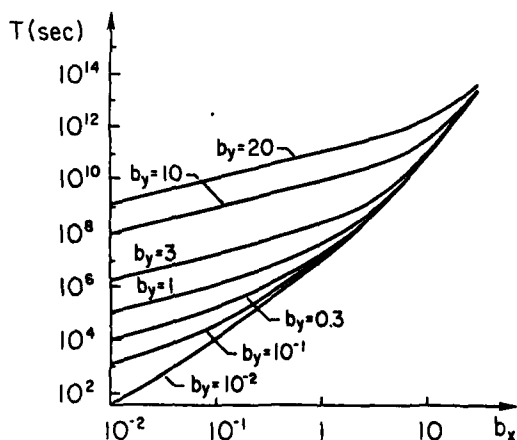


Fig. 4 Exposure time, T, as a function of  $b_x = D_x/D_{sx}$  and  $b_y = D_y/D_{sy}$ . It is assumed that the geometry is as shown in Fig. 1 (i.e.  $D_h = \sqrt{2} D_x$ ), that all mirrors are perfectly reflecting and monochromator throughput is unity (i.e.  $M=1$ ), and that the parameters are those listed in Table I.

Small oscillations of the entire target along the Z axis have negligible effect. Oscillations perpendicular to Z should be kept to less than 0.1 mm.

Oscillations of individual mirrors in the interference unit should have amplitude  $\lesssim 25\text{\AA}$ . It is desirable to manufacture the entire unit as a solid block.

#### CONCLUSIONS

At an SSRL port, under the most unfavorable circumstances, a  $10^{-2}$  cm  $\times$   $10^{-2}$  cm grating with line density of  $5 \cdot 10^4$  lines per mm ( $5 \cdot 10^3$  lines per grating) could be manufactured within a couple of weeks of exposure. (A  $10^{-2}$  cm  $\times$   $10^{-3}$  cm grating with the same line density would require several days exposure.)

The interference unit may be manufactured in a single block, could not be disaligned, and so the exposure time may be accumulated slowly.

The required exposure times can be reduced as follows:

- (1) Tune SPEAR to a single beam mode operation. Then the four dimensional phase space  $A_x$ ,  $A_y$ , and with it T, could be reduced by at least (3) a factor 10.
- (2) A wiggler magnet can increase photon brightness, and decrease T by at least (4) a factor  $10^2$ .
- (3) Radiation from a wiggler magnet could pump a Li x-ray laser (5). In the  $\Delta\lambda$  range of interest the radiation would be about  $10^6$  times more intense than the radiation from the wiggler, thus T could be reduced by about another factor  $10^6$ .

#### REFERENCES

1. Paul L. Csonka, "Holographic X-ray Gratings" to be published in J. App. Phys. (1980).
2. E. Spiller, A. Segmuller and R. P. Haelbich, Conference on Ultrafast X-ray Microscopy, New York Academy of Science, (June, 1979).
3. K. O. Hodgson, H. Winick, G. Chu, "Synchrotron Radiation Research," SSRL Report No. 76/100, Stanford (1976).
4. B. M. Kincaid, J. App. Phys. 48, 2684 (1977); and A. Hofmann, Nucl. Instr. & Meth. 152, 17-21 (1978).
5. Paul L. Csonka, Phys. Rev. 13A, 405 (1976), and "Opportunities to Produce Soft X-rays at Stanford," SSRL Report No. 77/03 (1977).

#### APPENDIX

Photons emerging from a target with diameter  $D_{sx}$  and at angles (measured from Z) within the interval (see Fig. 2c)  $\phi = D/L$  fill a (two dimensional: position, angle) phase space volume:

$$A_x \equiv D_{sx} \phi. \quad (A-1a)$$

One can similarly define  $A_y$ .

A "time-like" phase space volume can also be defined:

$$A_t \equiv T \frac{\Delta E_\lambda}{E_\lambda} = T \frac{\Delta\lambda}{\lambda_0}, \quad (A-1b)$$

Where T is the time during which the photons are produced.

The total (six dimensional) phase space volume filled by photons which can be used during time T to

produce the desired interference pattern is the "active phase space":

$$A_{xyt} \equiv A_x A_y A_t. \quad (\text{A-1})$$

Equation (3) restricts  $A_x$  and  $A_y$ :

$$\frac{f_3 \lambda_0}{F} \geq a_x A_x + a_y A_y \quad (\text{A-2})$$

where

$$a_i \equiv \begin{cases} (1 + D_i/D_{si})^2 / 4D_i/D_{si} & ; \text{ if } D_i/D_{si} \geq 1 \\ 1 & ; \text{ if } D_i/D_{si} < 1 \end{cases}$$

$i = x, y.$

When conditions (1a), (2a) and (4) hold, then the

maximum value of  $A_{xyt}$  permitted by Eq. (7) (as a function of independently varied  $A_x$  and  $A_y$ ) is

$$A_{xyt} = \frac{f_1 f_3^2 \lambda_0^3 T}{4 \cdot 2F D_h a_x a_y} \quad (\text{A-3})$$

But when  $A_x$  and  $A_y$  cannot be varied independently, then this maximum may not be reached. E.g. when  $D_{sx}$ ,  $D_{sy}$ ,  $D_x$  and  $D_y$  are all fixed, and  $L$  is varied, then the maximum of the useful phase space volume is

$$\max_L A_{xyt} = \frac{f_1 f_3^2 \lambda_0^3 T D_x D_y}{4\sqrt{2} F^2 D_h D_{sx} D_{sy} B^2} \quad (\text{A-4})$$

where

$$B \equiv \frac{1}{2} \left[ a_x \frac{D_x}{D_{sy}} + a_y \frac{D_y}{D_{sx}} \right]$$

Evaluation of ultrasoft X-ray optics, sources, and detectors  
for high resolution molecular X-ray emission spectroscopy

G. Andermann, R. Kim and F. Burkard

Department of Chemistry, University of Hawaii

Honolulu, HI 96822

ABSTRACT

The general requirements of obtaining high resolution molecular X-ray emission spectroscopy (0.01 to 0.1 eV) are inspected. Various X-ray optics, sources, and detectors are reviewed in terms of intensity and resolution. An approximate theoretical formulation is offered to compare the speed of photographic detection with that obtained by scanning and position sensing photoelectric detection. The main features of the recently developed, automated scanning photoelectric attachment for a 5 M grating spectrometer are described. Experimentally obtained photographic and scanning photoelectric data for first order O K emission are compared.

I. INTRODUCTION

Molecular XES studies with high resolution instrumentation, 0.1 eV or better, were initiated about ten years ago by Siegbahn and his coworkers.<sup>1</sup> Since then a few additional groups have entered this field. These high resolution studies may be divided into two broad categories, namely, (A) chemical bonding<sup>2</sup> and radiation damage studies of the type already undertaken by many other workers with lower resolution<sup>4</sup>, and (B) the more esoteric studies dealing with X-ray processes, such as those involving multiply ionized initial and final states<sup>5-8</sup>, and even vibrational fine structure investigations<sup>9</sup>. While type (A) studies can be readily conducted with a resolution of 0.1 eV, and occasionally even with significantly worse resolution, type (B) investigations generally require resolution in the range of 0.01 to 0.03 eV. Resolution of 0.01 to 0.1 eV is achievable only above 10 Å, and then only with reasonably high focal length grating optics. Table 1 lists the various installations with grating optics, focal lengths, sources, detectors, date of completion, and types of samples studied from the molecular point of view. In what follows below we shall evaluate briefly the choices for various key components for obtaining optimum intensity-resolution performance.

II. RESOLUTION CONSIDERATIONS

For scanning photoelectric spectrometers the total instrumental resolution is due to the optics involved, i.e. slits and grating. However, where only a primary slit is used, and the detection is in terms of a position sensing detector (PSD), such as a photographic plate (PP) system, or a photoelectric PSD device, then, of course, the instrumental resolution must include the contribution of the PSD system also. The fundamental aspects of instrumental resolution due to grating optics is textbook information<sup>10</sup> and therefore, will not be treated here. A brief review of various PSD devices, however, might be in order. To date, the detector spatial resolution  $R_d$  on a photographic plate is still the best, namely, about  $10 \mu$ <sup>11</sup>, and any high quality densitometer has a resolution capability down to  $10 \mu$  also. In our 5 M grating instrument with a 632 Å/mm grating  $10 \mu$  represents  $R_d$  values of about 0.06 eV at 20 Å, and about 0.007 eV at 80 Å<sup>11</sup>. Corresponding first order slit resolution  $R_0$  values with a  $1 \mu$  primary slit width are 0.10 eV and 0.006 eV. Obviously, with photographic PSD,  $R_d$  values approach  $R_0$  values.

The above evaluation poses the following requirements for optimum resolution behavior on the part of any photoelectric PSD system: (1)  $R_d$  values should be near 15 to 20  $\mu$ , (2) it should conform, just like a PP device to the Rowland circle, and (3) for the sake of convenience it should be reasonably large, say 1 to 2" along the Rowland circle.

The following photoelectric PSD devices have the potential to fulfill the above requirements for detection in the 10 to 150 Å range: (A) grazing incidence photocathode-magnetically focussed photoelectrons detected by a CCDA (hereafter referred to as GI-FE-CCDA), (B) phosphor coated self scanning photodiode array (PC-SSPA), and (C) various microchannel plate (MCP) devices.

A. GI-FE-CCDA

This device relying on the efficient conversion of soft X-rays to energetic electrons is currently under development by Lowrence of the Princeton Univ. Observatory<sup>12</sup>. It overcomes the insensitivity of a CCDA to ultrasoft X-rays via their conversion to photoelectrons and attempts to maintain spatial resolution via a magnetic field. High gain is obtained through the focussed and accelerated photoelectrons. While this elegant device is highly promising, the exact resolution (and efficiency) capabilities are yet to be announced.

B. PC-SSPA

With this device Schnatterly's group has found a clever way to overcome the insensitivity of an SSPA detector to ultrasoft X-rays by their conversion to visible light via a simple red phosphor<sup>13,14</sup>. This conversion is 100% efficient. Currently, the PC-SSPA is a flat device. It should be noted, however, that with a 1 cm flat device the optical aberrations in our spectrometer would be about 20  $\mu$  at the edges<sup>11</sup>. For a 2.5 cm device the aberrations at the edges would be prohibitive. In order to utilize a PC-SSPA in a high resolution configuration, it is suggested that fiber optics with the very high spatial resolution of about 5  $\mu$  precede the SSPA, thereby providing the appropriate curved surface, and that the phosphor coating be applied to such a surface.

C. MCP DEVICES

As is well known, MCP devices consist of capillary photocathodes coupled to any of a wide variety of anode systems. Meeting the spatial resolution requirement for the photocathode part merely requires that the front surface of the capillary array be ground down to the Rowland cylinder, and that the bias angle be fabricated around 60° yielding a spatial resolution of 16  $\mu$  with 8  $\mu$  capillaries. Spatial resolution from the anode is a far more formidable problem. Of the many possible anode choices only the ones developed for astrophysical studies by Timothy and Bybee<sup>15</sup>, and by Kellogg et al.<sup>16</sup> appear to be suitable. The former method is of a brute force nature yielding a spatial resolution of about 20  $\mu$  by using individual wires plus individual amplifiers. The latter relies on an elegant electronic interpolation technique and

TABLE 1  
DESCRIPTION OF GRATING SPECTROMETERS

Location	Focal Length (M)	Source	Detector	Date of Completion or Activation	Types of Samples
Uppsala	3	Focussed electron beam	PP CEM MCP	1971 1978 ?	gases
DESY	2	DORIS storage ring	CEM	1974	solids
Hawaii	5	2 KW Henke tube	PP FPC	1978 1980-81	solids
Munich	11.6	18 KW rotating anode	CEM FPC	1978 1980	solids and condensibles
Helsinki	6	Semifocussed electron beam	CEM	1975	solids
NBS	2.2	Focussed electron beam	PP	1980	gases
Uppsala	10.0	Focussed electron beam	PP	1978	gases
Virginia	11.2	Grazing incidence electron beam	SSPA	1981	metal surfaces

resolution values down to 10  $\mu$  are conceivable.

### III. INTENSITY CONSIDERATIONS

The instrumental factors affecting intensity are sources, source-sample arrangements, optical arrangement, and detectors. The discussion offered below will emphasize detector evaluation.

#### A. SOURCES AND SOURCE SAMPLE ARRANGEMENTS

As Table 1 illustrates there are storage ring, electron beam, rotating anode, and Henke-style sources currently in use by molecular XES workers. Gilberg et al. recently compared his rotating anode source with the DORIS storage ring<sup>17</sup>. Andermann expanded this evaluation by including the Henke-style source and the Uppsala electron beam source<sup>18</sup>. According to these evaluations the following may be concluded: (1) Electron beam sources provide the greatest monochromatic flux. (2) A storage ring provides the highest utilisable continuum flux over the range of 10 to 60 A, but above 60 A a 18 KW rotating anode with sufficiently high Z for a target will be actually superior to the DORIS storage ring. (3) A Henke-style source with a stationary anode is usually limited to 2.5 KW or less, yet it provides a reasonably high continuum flux with a high Z target and very good monochromatic flux with low Z targets. Of all of the sources listed in Table 1 only the Henke-style source uses a gate valve with a thin window resulting in a loss of a factor of 2 or less in the flux to maintain the integrity of both the X-ray tube and sample chamber. The sample to anode coupling, however, can be as short with the Henke-style source as with the rotating anode one, namely, about 13 mm.

#### B. OPTICAL ARRANGEMENT

At a given resolution there are three aspects to the intensity throughput in a grating spectrometer. These are slit height, grating diffraction efficiency, and in the case of blazed or laminar gratings, variation of angle of incidence. In order to minimize optical aberration with straight slits, it is necessary to keep the slit height to local length ratio to reasonably low values. Thus, for example, in our 5 M grating spectrometer a 1 cm slit height provides a useful compromise between intensity and resolution. With curved slits, however, such as in Gilberg's unit<sup>19</sup>, 5 to 10 cm tall slits are feasible. In Schnatterly's

unit, at considerable sacrifice of resolution, toroidal gratings yield a tremendous gain in intensity even with short slits<sup>13</sup>.

As already reported previously<sup>22</sup>, by having the grazing incidence angle variable, it is possible to gain a sizable factor in intensity for non-holographic gratings. In our arrangement, being able to vary the 'line of sight adjustment', i.e., the attitude of the grating towards the center of the sample, allows, in addition to utilizing optimum grating diffraction efficiency, the search for 'hot spots' in the sample, and thereby further improve the flux from the sample. Last, but not least, is the diffraction efficiency of recently produced gratings, which nowadays ranges from 10 to 25% routinely, or higher by one to two orders of magnitude than what was achievable about 15 years ago<sup>21</sup>.

#### C. DETECTORS

The discussion shall be restricted to the PSD devices, such as PP, MCP, and PC-SSPA, and to the two detectors commonly used with scanning, namely, thin windowed flow proportional counters (FPC), and channel electron multipliers (CEM). For the sake of brevity background noise and densitometer noise problems, etc., will not be considered quantitatively, as important as they may be. Thus, the overall gain in speed in going from photographic to photoelectric will be judged purely in terms of signal to peak noise ratio.

In order to simplify our discussion further we shall also assume that the photon flux is uniform along the slit height direction and that the grain and pixel response in the PSD devices show only random variation.

If we let R stand for the net line to peak noise ratio, then the gain of a photoelectric scanning system, as compared with a photographic detection system on the same instrument,  $G_s$ , is formulated as

$$G_s = \left(\frac{R_s}{R_g}\right)^2 \frac{1}{N_s} \quad (1),$$

where the subscripts g and s stand for the photographic grain and photoelectric scanner respectively, and  $N_s$  represents the number of steps taken by the scanner. In this section we shall ignore the improvement in  $R_g$  due to repeated and overlapping averaging by a digitized densitometer. Now

$$R_s = I_s^{1/2} \quad (2a),$$

and

$$R_g = \psi(g) I_g^{1/2} \sqrt{n_g} \quad (2b),$$

where  $\psi(g)$  involves the emulsion characteristic,  $I$  represents the total number of photons detected, and  $n_g$  represents the number of developed grains viewed by the densitometer slit. Accordingly,

$$I_s = q A_s n_s (W_s/W_g) \quad (3a),$$

and, if we operate in the linear portion of emulsion's contrast curve we may take  $\psi(g) = 1$ . Now for a single undeveloped grain

$$I_g = q \cdot a_g n_g \quad (3b).$$

In the previous equations  $q$  represents the incoming photon flux per unit area,  $\eta$  the detector efficiency,  $A$  is the area viewed by the slit,  $W$  is the primary slit width, and  $a_g$  the area of a single grain. The correction factor in (3a) brings the photoelectric instrumentation broadening into equivalence to that from the photographic primary slit plus the densitometer slit. The correction factor in (2b) is due to a digitized densitometer slit reducing the noise level by averaging over the grains viewed on a single pass without overlap. Accordingly,

$$n_g = (A_d/a_g) f_g \quad (4),$$

where the subscript  $d$  stands for densitometer slit, and  $f_g$  is the grain packing factor for the plate. Using the relationships that

$$A_s = Y_s W_s' \quad (5a),$$

and

$$A_d = Y_d W_d' \quad (5b),$$

where  $Y$  is the slit height, and  $W_s'$  represents the scanner's secondary slit width, and  $W_d'$  stands for the densitometer slit width, we obtain by making use of the previous equations the following highly simplified working formula:

$$G_s = \frac{1}{f_g N_s} \left( \frac{Y_s}{Y_d} \right) \left( \frac{W_s}{W_g} \right) \left( \frac{W_s'}{W_d'} \right) \left( \frac{\eta_s}{\eta_g} \right) \quad (6)$$

While a detailed evaluation is offered subsequently for O K emission intensities with photoelectric and scanning photoelectric detection, a rough evaluation may be worthwhile at this point. We estimate  $f_g$  to be about 0.5. Typically  $N_s$  may be 100,  $(Y_s/Y_d)$  from 6 to 10,  $(W_s/W_g)$  typically has a value of about 0.8, and  $(W_s'/W_d')$  usually varies from 0.5 to 2.0. For a FPC  $(\eta_s/\eta_g)$  would range from about 6 to 15, and for a CEM from 3 to 4. Thus, for a FPC  $G_s$  would range from about 0.3 to 3.0 with  $N_s = 100$ , and for a CEM it would be from about 0.2 to 1.5. An additional advantage for FPC over CEM, and for that matter over a PP, would be the capability to discriminate against hard X-rays, and thereby improving the line to background ratio. Clearly the above values of  $G_s$  would improve if the photographic background signal was excessive due to scattering, fogging, etc., and/or if  $\psi(g)$  values would be appreciably below 1. On the other hand, as further evaluated in the experimental section, multiple sampling with a digitized densitometer or averaging the digital data with a computer program can improve  $R_g$  values appreciably.

It is pertinent, however, to ascertain just what  $N_s = 100$  represents. If the interval for each step  $\Delta X_s$  represents 25  $\mu$  or 0.1 eV at about 20 A, then 100 steps merely covers a span of 2.5 mm or 10 eV. Typically, for chemical bonding studies it may be desirable

to cover a range of about 20 eV requiring about 200 increments at 0.1 eV resolution, thus creating even lower values for  $G_s$ .

For PSD devices we shall use the subscript  $p$ . Accordingly it can be shown that the gain  $G_p$  over photographic detection on the same spectrometer is of the following simplified form:

$$G_p = \left( \frac{f_p}{f_g} \right) \left( \frac{Y_p}{Y_g} \right) \left( \frac{W_p}{W_g} \right) \left( \frac{W_p^*}{W_d^*} \right) \left( \frac{\eta_p}{\eta_g} \right) \quad (7),$$

where the asterisk on  $W$  indicates the image of the primary slit on the Rowland circle.  $W_g$  is adjusted such that its image  $W_g^*$  together with  $W_d^*$  equals  $W_p^*$ , i.e.

$$W_p^* = (W_g^* + W_d^*)^{1/2} \quad (8).$$

For O K emission, for example, if  $W_p$  is set at 5  $\mu$ , then with our 632  $\ell/\text{mm}$  grating,  $W_p^*$  would be about 125  $\mu$ . If we were to use  $W_d'$  as 25  $\mu$ , then  $W_g$  would have to be about 6  $\mu$ . The ratio of  $(Y_p/Y_d)$  is expected to be from 5 to 10, and  $(W_p^*/W_d^*)$  about 5. For an MCP device  $(f_p/f_g)$  would be 1, but for a PC-SSPA it would be 2. The ratio of  $(\eta_p/\eta_g)$  is expected to be from 1 to 3 for an MCPA but about 3 times higher than that for a PC-SSPA. Thus, for an MCP  $G_p$  would be in the range of 30 to 180, but for a PC-SSPA it might be in the range of 180 to about 1000. Clearly this evaluation tends to favor a PC-SSPA except for the relatively large thermal and readout noise associated with SSPA. To date no experimental work has been done to compare  $G_p$  for an MCP and SSPA device on the same instrument, even though such an evaluation would be highly desirable.

#### IV. EXPERIMENTAL STUDIES

Our instrument was initially developed for photographic detection and has been described adequately elsewhere<sup>20,22</sup>. As already stated previously, it has a Henke-style X-ray source closely coupled to the sample. The present sample holder is a push-pull device and holds two samples. Adequate space exists in the sample chamber, however, for a rotating sample holder to hold at least eight samples. The vacuum integrity of the spectrometer chamber is protected against condensable vapors from the sample by a cryogenic trap placed between the sample and the opening aperture to the spectrometer chamber.

The development of scanning photoelectric detection capability has just been completed. In Figure 1 we show the essential features of the photoelectric attachment minus the primary slit and grating modules.

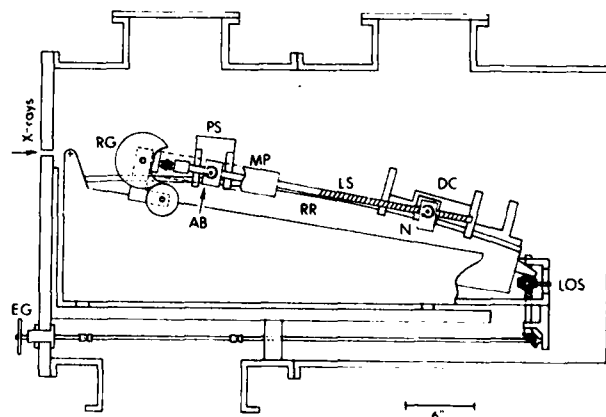


Fig. 1. Photoelectric attachment for the 5 M grating spectrometer. Legend: EG--external gears, RG--reduction gears, PS--pivot stand, AB--anchor block, MP--mounting plate, RR--Rowland circle reference rail, LS--lead screw, N--nut, DC--detector carriage, LOS--line of sight adjustment.



Accordingly, the secondary slit is readily mountable on any one of three bridge positions on the fairly massive slit and detector carriage. The secondary slit is mounted on a retaining plate in such a manner that it can be focussed to  $\pm 2 \mu$ . The front position allows investigations at optimum grazing angles of incidence with the 632  $\lambda/\text{mm}$  grating down to about 8A, with the rear position up to about 150 A using the 300  $\lambda/\text{mm}$  grating, while intermediate  $\lambda$ 's are studied in the middle position with either grating. At C K (44 A) Speer's tests indicated<sup>20</sup> that the first order diffraction efficiency for our 632  $\lambda/\text{mm}$  grating was 12%, while for our 300  $\lambda/\text{mm}$  blazed grating it was 25%.

The detector carriage driven by the lead screw-nut assembly rides on the Rowland circle reference railing very precisely, namely, to plus or minus one micron. The rotation of the lead screw is monitored by a high precision, absolute shaft encoder. The lead screw is driven from the outside of the chamber by a stepping motor via a gear train to provide steps as small as 1.8  $\mu$  on the Rowland circle.

The present detector for  $\lambda > 10\text{A}$  is a standard Norelco flow proportional counter modified to accommodate thin Formvar films prepared according to Henke's prescription<sup>24</sup>. Currently, propane gas is used at about 75 Torr of pressure. An HP-85 computer controls, via a microprocessor, the stop scan motor and receives shaft encoder and FPC photon output data.

The initial alignment of the secondary slit was recently accomplished by using a standard Norelco Cr target X-ray tube mounted temporarily in the normal sample position.<sup>25</sup>

Our evaluation of a theoretical  $G_S$  vs. an experimental  $G_S^*$  was carried out by studying O K emission from  $\text{Li}_3\text{PO}_4$ . The source setting with a Cu anode was at 1.5 KW with each type of detection. Photoelectric data were obtained under the following conditions:  $W_S = W_S' = 20 \mu$ ;  $Y_S = 15 \text{ mm}$  and  $N_S = 80$  with  $\Delta X_S = 25 \mu$ . We estimate the value of  $n_S$  to be about 0.5. The total exposure time  $t_S^*$  was 3.2 hrs., i.e. we collected counts for 100 seconds for each of the 80 points reaching a maximum value of 3200 at the peak. The experimental conditions for photographic detection had  $W_d = 27 \mu$ ,  $Y_d = 2.5 \text{ mm}$ ,  $W_d' = 10 \mu$ , and the densitometer sampled the intensity at intervals of  $\Delta X_d$  of 10  $\mu$ . The digital data were also smoothed out by averaging all three adjacent points sequentially. The experimental photographic exposure time was 1.0 hour. If we estimate  $n_d$  to be about 0.05<sup>11</sup> and  $f_g$  as 0.5, then the use of equation (6) gives us a theoretical  $G_S$  value of about 2.8.

Now in order to obtain an experimental value for  $G_S^*$  we need to formulate it in terms of  $t_S^*$ ,  $t_g^*$ ,  $R_{S,m}^*$ , and  $R_{g,m}^*$ , namely,  $G_S^* = (t_g^*/t_S^*)\beta^2$ , where  $\beta = (R_{g,m}^*/R_{S,m}^*)$ , and where the sampling parameter  $m = (W_d'/\Delta X_d)$ . In this study the settings provide a value of 1 for  $m$ , but clearly  $R_{g,m}^*$  depends on  $\sqrt{m}$ . The above sampling can be obtained by the use of a computer program also which has the additional advantage of averaging out the densitometer's electronic noise.

$R_{S,m}^*$  values are relatively easy to estimate since it is merely the square root of peak count. The achievement of  $R_{g,m}^*$  values, however, is not straightforward. One way to measure  $R_{g,m}^*$  values is with a sufficiently broad band, and thus obtaining an adequate number of  $I_{g,m}^*$  values at and near the top of the band. Accordingly, from an expanded plot of  $I_{g,m}^*$  vs.  $\lambda$  we obtain the desired experimental deviations of  $I_{g,m}^*$  from a smooth curve.

In Figure 2 we have plotted the photoelectric, and two kinds of photographic data, one with  $m = 1$  and the other with  $m = 3$ . The densitometer data do not indicate the proper photographic line to background ratio (L/B) which is about 0.4. This is in direct contrast with the photoelectric data, where (L/B) value is about 25 times better. The observed  $R_{g,m}^*$  value is 57, whereas the corresponding  $R_{S,m}^*$  value is 12.3 yielding a  $\beta$  value of 4.6, and, therefore, a  $G_S^*$  value of about 6.6. Considering the relatively poor (L/B) value photographically primarily due to excessive

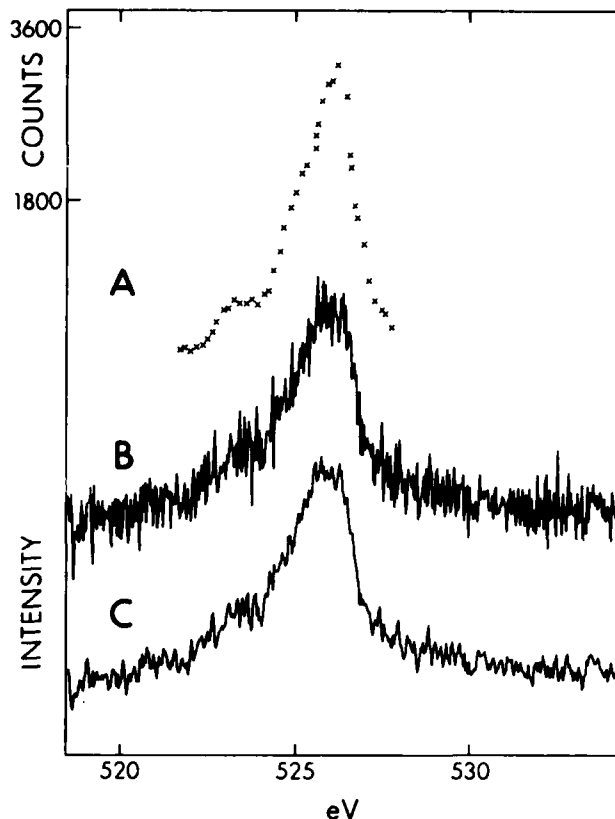


Fig. 2. O K emission spectra from  $\text{Li}_3\text{PO}_4$ . A--photoelectric data with FPC, B--raw photographic digital data with  $m = 1$ , C--photographic digital data with  $m = 3$ .

fogging, a  $G_S^*$  value of 6.6 is in good agreement with the theoretically expected  $G_S$  value of 2.8. A cursory inspection of Figure 2 demonstrates dramatically the improvement in  $R_{g,m}^*$  with computer averaging which yields a  $G_S^*$  value of about 3.5.

The evaluation of resolution with the present photoelectric unit, as well as the correlation of our intensity output with that from the DORIS and Munich photoelectric units, awaits the rejuvenation of our Henke style source, which during the course of the present study was determined to be down in photon output by a factor of about 1.5. We also envision the use of a new detector for which the present obscuration of about a factor of 2.0 will be eliminated, and with which we should be able to use considerably thinner windows than presently in use leading to another factor of about 1.5.

## V. CONCLUSIONS

As to the question of which of the three areas, namely, sources, optics, and detectors, are likely to show the most dramatic future improvements from the point of view of molecular XES, it is necessary to introduce a bit of a historical perspective. Clearly, the earliest type of ultrasoft X-ray source for molecular XES studies namely, the Henke type, has given way to more powerful modes of excitation, as discussed above. Any future improvements in sources, however, are bound to be severely limited. In other words, a 40 KW rotating anode will only provide a gain of 2 over the present 20 KW rotating anodes. Perhaps more powerful storage rings than DORIS might yield another factor of 3 or 4 in intensity also. The same limitations apply to the improvements in optics. In other words, the big gains

of factors of about 10 or more in sources and optics are now behind us. Thus, judging from the evaluation of detectors, the really dramatic gains are in this field, namely, with the development of PSD devices gains of 50 to 200 should be realizable. With these gains together with the unique potentials of XES for molecular electronic structural studies, high resolution XES is bound to become a more practical tool in the field of molecular spectroscopy.

#### ACKNOWLEDGEMENT

This study has been supported by the National Science Foundation under Grant 7824884. We are indebted to M. Tester and B. L. Henke for their many useful suggestions.

#### REFERENCES

1. K. Siegbahn, L. O. Werme, E. Greenberg, S. Lindberg and C. Nordling, UUIP-74S, Uppsala Univ., Instit. Phys. (1971).
2. G. Andermann, F. Burkard, F. Fujiwara, R. Kim, M. Lawson, C.S. Li, E. Oshiro and A. Thompson, Oxygen K Emission Studies with a 5 M Grating Spectrograph, Proceed. Int. Conf. X-Ray Proc. & Inner-Shell Ionization Stirling (1980), Plenum Press (in press).
3. F. Fujiwara and G. Andermann, Spectr. Letters, 13 (4), 211 (1980).
4. B.L. Henke et al., J. Appl. Phys. 49, 480 (1978).
5. J. Nordgren, Ph.D. Dissertation, Uppsala Univ. (1977) and H. Agren, Ph.D. Dissertation, Uppsala Univ. (1979).
6. H. Agren, S. Svensson and U.I. Wahlgren, Chem. Phys. Letters, 35, 936 (1975); *ibid*, Chem. Phys. Letters, 38, 1 (1976).
7. E. Gilberg, The Cl L<sub>2,3</sub> Emission Spectra of Alkali Chlorides, Presented at the VIth Int. Conf. on Vac UV Rad. Physics, Univ. of Virginia (1980); also J. Valjakka and J. Utrainen, Configuration Interaction in the L<sub>2,3</sub> X-Ray Spectrum of Potassium Chloride, Proceed. Intern. Conf. X-Ray Proc. & Inner-Shell Ionization, Stirling (1980), Plenum Press (in press).
8. F. Fujiwara, G. Andermann and R. Kim, The Evaluation of Satellites Including TCV Initial State Transitions in the Cl L Emission Spectra of KCl, Proceed. Int. Conf. X-Ray Proc. & Inner-Shell Ionization, Stirling (1980), Plenum Press (in press).
9. H. Agren, L. Selander, J. Nordgren, C. Nordling, K. Siegbahn and J. Müller, Chem. Phys. 37, 161 (1979).
10. J. R. Cuthill, Grating Spectrometers and their Application in Emission Spectroscopy, in "X-Ray Spectroscopy", Ed. L. V. Azaroff, McGraw Hill (1974).
11. L. Bergknut, MS Thesis, Univ. of Hawaii (1979).
12. J. Lawrence, Priv. Communic.
13. F. Zutavern, C. Franck, T. Aton, S. Schnatterly, and E. Källine, A Fast Soft X-Ray Spectrograph, Proceed. Int. Conf. X-Ray Proc. & Inner-Shell Ionization, Stirling (1980), Plenum Press (in press).
14. F. Zutavern, S. Schnatterly, E. Källine, C. Franck, T. Aton, Nucl. Instr. & Methods, 172, 351 (1980).
15. J. G. Timothy, R. L. Bybee, Rev. Sci. Instr., 46, 1615 (1975).
16. E. Kellog, P. Henry, S. Murray, L. Van Speybroeck, and P. Bjorkholm, Rev. Sci. Instr., 47, 282 (1976).
17. E. Gilberg, M. J. Hanus and B. Foltz, Jap. J. of Appl. Phys., 17, Suppl. 17-2, 101 (1978).
18. G. Andermann, Nucl. Instr. & Methods, 177, 157 (1980).
19. E. Gilberg, Optics Commun., 29, 155 (1979).
20. G. Andermann, L. Bergknut, M. Karras and G. Griesehaber, Spectr. Letters 11(8), 571 (1978).
21. R.J. Speer, Space Sci. Instr. 2, 463 (1976).
22. G. Andermann, L. Bergknut, M. Karras, G. Griesehaber, and J. Smith, Rev. Sci. Instr. 51 (6), 814 (1980).
23. R.J. Speer, Private Communications.
24. B.L. Henke and M.A. Tester, Adv. X-Ray Anal. Plenum Press, 18, 76 (1975).
25. F. Burkard, MS Thesis, Univ. of Hawaii (in preparation).

## Low Energy X-Ray Spectrometer\*

Wayne R. Woodruff

Lawrence Livermore National Laboratory, P. O. Box 808, Livermore, California 94550

## ABSTRACT

A subkilovolt spectrometer has been produced to permit high-energy-resolution, time-dependent x-ray intensity measurements. The diffracting element is a curved mica ( $d = 9.95\text{\AA}$ ) crystal. To preclude higher order ( $n > 1$ ) diffractions, a carbon x-ray mirror that reflects only photons with energies less than  $\sim 1.1\text{ keV}$  is utilized ahead of the diffracting element. The nominal energy range of interest is 800 to 900 eV. The diffracted photons are detected by a gold-surfaced photoelectric diode designed to have a very good frequency response, and whose current is recorded on an oscilloscope. A thin, aluminum light barrier is placed between the diffracting crystal and the photoelectric diode detector to keep any UV generated on or scattered by the crystal from illuminating the detector. High spectral energy resolution is provided by many photocathodes between 8- and 50-eV wide placed serially along the diffracted x-ray beam at the detector position.

The spectrometer was calibrated for energy and energy dispersion using the Ni  $L\alpha_{1,2}$  lines produced in the LLNL IONAC accelerator and in third order using a molybdenum target x-ray tube. For the latter calibration the carbon mirror was replaced by one surfaced with rhodium to raise the cut-off energy to about 3 keV. The carbon mirror reflection dependence on energy was measured using one of our Henke x-ray sources. The curved mica crystal diffraction efficiency was measured on our Low-Energy X-ray (LEX) machine. The spectrometer performs well although some changes in the way the x-ray mirror is held are desirable.

## INTRODUCTION

A subkilovolt x-ray spectrometer having a high- and variable-energy resolution and good frequency response was needed for making time-dependent measurements of diffracted x rays. The nominal photon energy range of interest is 800 to 900 eV (15.5 to 13.8  $\text{\AA}$ ). We wanted a spectral energy resolution between 8 and 50 eV. The temporal response of the x-ray detector to a step function input should be a few ns. Figure 1 shows a cross section and Fig. 2 a photograph of the total spectrometer.

## DIFFRACTION CRYSTAL

The photon energy range of interest dictated a reflection spectrometer to avoid the absorption of the diffraction crystal. Mica (002 plane) was selected as the diffracting crystal because it was readily available, easily curved without fracturing, and did not require special handling or environmental conditions. Alternatives to mica are crystals such as KAP, RAP, and lead stearate. Mica does have a serious drawback in this planned use; it has strong high-order diffractions, especially in the odd orders. The spectrometer would be used in

an environment where there would be photon energies at intensities sufficient to result in higher-order diffractions, adding significantly to the signal in the energy interval of interest. These higher energy photons had to be eliminated. To provide for this low-pass filter, an x-ray mirror was introduced in front of the diffracting crystal and is discussed in the following section.

It can be shown that there is a relationship between the range of photon energies to be observed, the radius of curvature of a bent diffraction crystal, and the width of a parallel x-ray beam incident on the crystal. The relationship is:

$$W_D = r (\cos \theta_h - \cos \theta_l)$$

where

- $W_D$  = beam width (cm) of incident x rays,
- $r$  = radius of curvature of bent crystal (cm),
- $\theta_h$  = Bragg angle of highest energy photon desired detected,
- $\theta_l$  = Bragg angle of lowest energy photon desired detected.

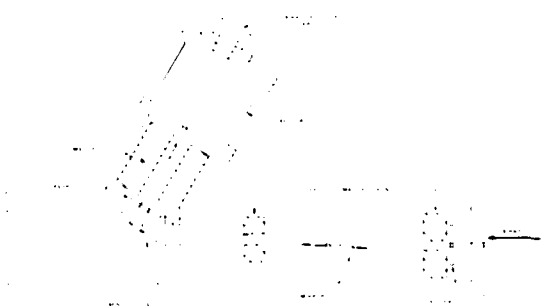


Figure 1. Simplified cross section drawing of spectrometer showing x-ray path along various internal components.

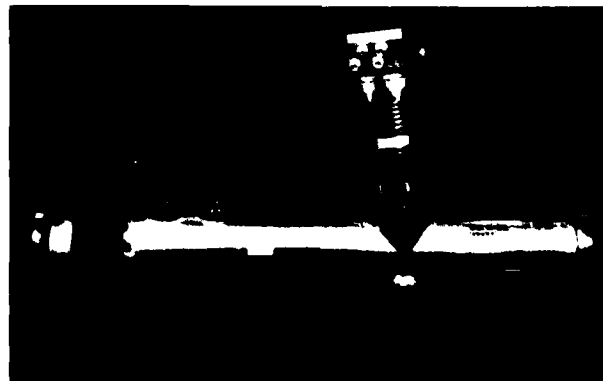


Figure 2. Spectrometer body showing ball and socket alignment/attachment flange, access and pump out ports, vacuum bellows, and x-ray detector.

\*This work was performed under the auspices of the U.S. Department of Energy by Lawrence Livermore National Laboratory under Contract W-7405-Eng-48.

The Bragg angle is:

$$\theta = \sin^{-1} \left[ 6.20 \times 10^3 / (d) (E/n) \right]$$

where

$d$  = diffraction crystal spacing ( $\text{\AA}$ ),  
 $E$  = photon energy (eV),  
 $n$  = diffraction order.

It can also be shown that  $\theta_g < 3\theta_h$ , which precludes photons diffracted from the crystal at the high energy limit from intersecting the crystal.

For the spectrometer design, the mirror length and angle selected set  $W_b = 5.28$  mm. Other experimental parameters set are  $d = 9.95 \text{ \AA}$ ,  $E_h =$  photon energy associated with  $\theta_h = 900$  eV,  $E_g =$  photon energy associated with  $\theta_g = 800$  eV, and  $n = 1$ . Applying the above expressions,  $r = 5.59$  cm. A radius of curvature of  $r = 5.08$  cm was selected to allow detection of a somewhat larger energy range, and with the fixed beam width, the resulting energy range was  $E_g = 794$  eV to  $E_h = 903$  eV. The crystal depth selected was 3 cm.

The mica crystal stock received from the vendor was initially checked for diffraction efficiency. This was done with a flat crystal in each of four different orientations  $90^\circ$  apart on both sides of the crystal. By using the same orientation that gave the highest efficiency when the crystal was flat, it was felt that one could optimize the chances of getting the highest diffraction efficiency when the crystal was curved. The crystals were mounted in a picture frame crystal holder appropriately designed to achieve the desired radius of curvature and allow for finite crystal thicknesses. Figure 3 shows the bent crystal and associated holder. The thinner crystals ( $\sim 5 \times 10^{-2}$  mm) appeared to have a more uniform radius of curvature when bent than those twice as thick. After mounting, each crystal was checked in third order with a molybdenum x-ray source to assure the range of energies desired was achieved.

We experimentally determined the diffraction efficiency of each bent crystal by the method discussed in Ref. 1. The subkilovolt diffraction efficiency measurements were made on the LLNL IONAC (2) accelerator and the 1- to 4-keV determinations were made on the LOW-Energy X-ray machine (3). Efficiency measurements were thus made at two energies for second, third, and fourth orders;

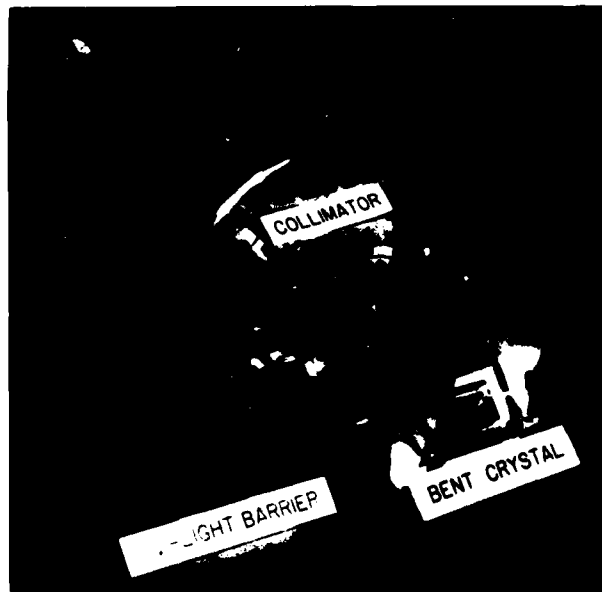


Figure 3. Crystal/collimator assembly attached to stand-off housing.

at four energies for first order; and at a single energy for fifth order. Typical results can be seen in Fig. 4 for the various orders, and Fig. 5 shows the efficiency for two different crystals in first order in the photon energy range of interest. The data points in Figs. 4 and 5 are connected with straight lines for ease of reading and inferring trends but are not authoritative on intermediate values.

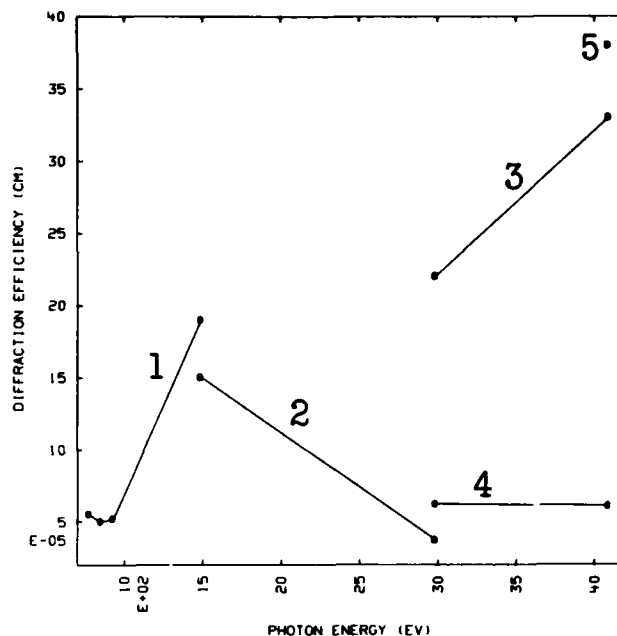


Figure 4. Curved mica crystal (roc = 5.08 cm) diffraction efficiencies for  $n = 1, 2, 3, 4,$  and  $5$ .

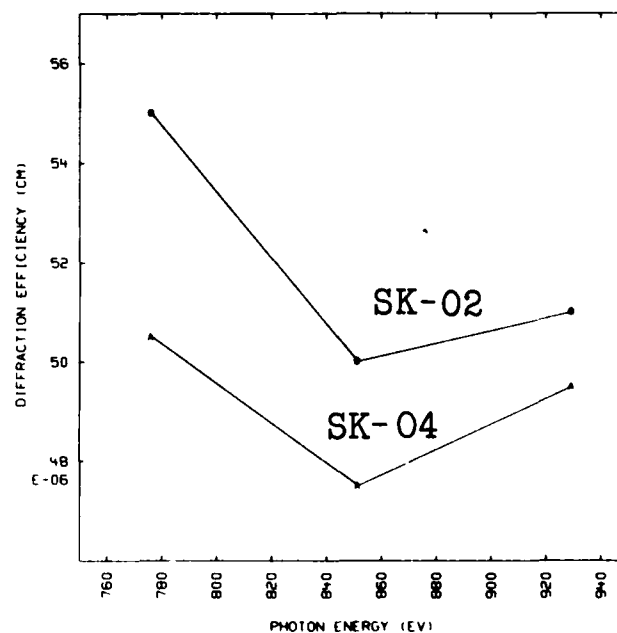


Figure 5. Curved mica crystal (roc = 5.08 cm) diffraction efficiencies for two different crystals at subkilovolt photon energies,  $n = 1$ .

## X-RAY MIRROR

The mirror material chosen for the x-ray mirror was vitreous carbon. Beryllium would also have been satisfactory, but because the mirrors required handling and exposure to air, carbon was selected. The cut-off energy (~60% reflection) selected was 1.1 keV. At the low energy end of the range of interest (800 eV), we had to avoid possible second-order contributions at 1.6 keV, and at the high energy end (900 eV) we wanted to have a mirror reflection like that for the rest of the range of interest (~70%). The cut-off energy choice was biased toward the 900 eV as the reflection generally falls off rapidly but has a tail. We wanted the reflection to be as near to zero as possible at 1.6 keV, while still having a reasonable reflection at 900 eV.

The 1.1 keV cut-off energy engendered a calculated  $1.3^\circ$  angle between a parallel incident beam of x rays and the mirror surface. The vitreous carbon mirror stock was available in lengths up to 30.48 cm. It was considered too much of a problem to properly align the mirrors in series to get an effective length of multiples of 30.48 cm, so a single mirror of that length was used. This decision influenced the rest of the design of the spectrometer because the mirror length and angle determine the maximum x-ray beam width incident on the diffracting crystal; here that would be 6.92 mm. A beam width of 5.28 mm was selected to allow some latitude in mirror positioning, i.e.,  $\pm 0.82$  mm.

The spectrometer was mechanically designed to allow us to remove and replace the mirror assembly with a high degree of assurance that its physical position was reproducible; this allowed us to easily align the whole spectrometer to the source of x rays. The vitreous carbon was attached to a glass substrate to provide for mechanical rigidity. The mirror was positioned by three registration screws in the protective cover plate of the mirror holder. The mirror was held against the registration screws and kept centered in the holder by ball plunger screws. This method of positioning was not completely satisfactory. The ball plunger screws did not always keep the mirror in position. During routine handling on two occasions, the mirror was found jammed out of position. Adjustment of the ball plunger screws centering the mirror in the holder proved very critical. If these screws are too tight and the mirror assembly is jarred, the mirror can jam out of position and the ball plunger screws on the mirror back do not restore the mirror surface to its position against the registration screws. The mirror angle was set optically utilizing a transit and appropriately positioned fiducial cross-hairs on an alignment fixture at the end of the spectrometer. Figure 6 is a photograph of the mirror and mirror holder. Figure 7 shows the mirror assembly being placed in the spectrometer body.

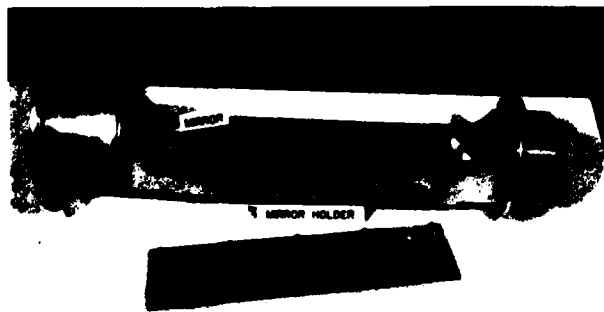


Figure 6. Carbon mirror mounted in holder with beam defining collimators attached to each end.



Figure 7. Technician installing mirror holder and collimator assembly into spectrometer body.

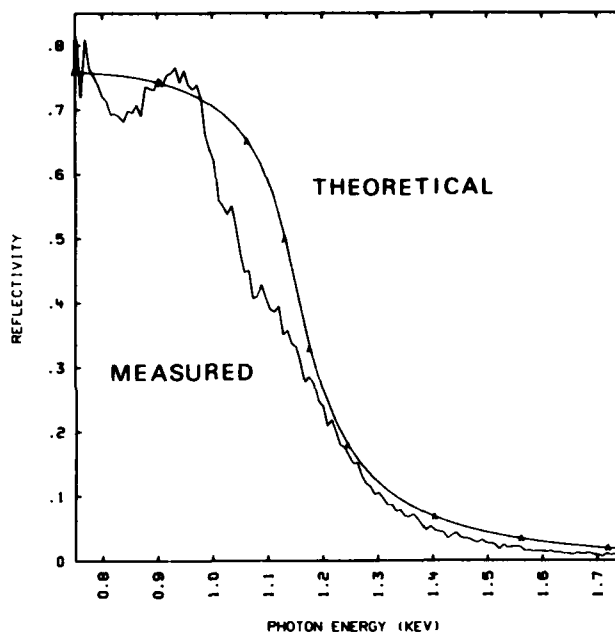


Figure 8. Experimental and theoretical reflectivity vs energy for a carbon mirror at  $1.3^\circ$ .

The mirror was lapped with 3- and 1- $\mu$ m diameter diamond polishing compound to a satisfactory flatness to achieve a 70% x-ray reflection (4).

The mirror reflectivity was experimentally determined utilizing one of the Henke x-ray machines. The mirror was placed on a goniometer and the direct and reflected spectrum from a copper anode x-ray source determined. The reflected spectrum was then divided by the direct spectrum to determine the x-ray reflectivity as a function of photon energy. The mirror reflectivity is also predicted theoretically using the REFLECT code (5). Figure 8 shows the experimental and theoretical mirror reflectivity as a function of energy for a typical carbon mirror at a  $1.3^\circ$  angle.

## UV LIGHT BARRIER

As the x-ray detectors use a gold cathode, which is sensitive to ultraviolet as well as x rays, there was concern that UV emanating from x rays absorbed in the diffraction crystal and UV reflected off the

crystal and associated hardware would illuminate the detector. To mitigate this concern, a UV light barrier of aluminum was placed between the diffraction crystal and some internal collimation ahead of the detector. The barrier was 0.75  $\mu\text{m}$  thick and had a transmission of 0.65 at 852 eV as measured on the IONAC. The aluminum barrier was glued to a stainless steel frame and can be seen in Fig. 3. It is shown being positioned behind the crystal in Fig. 9.

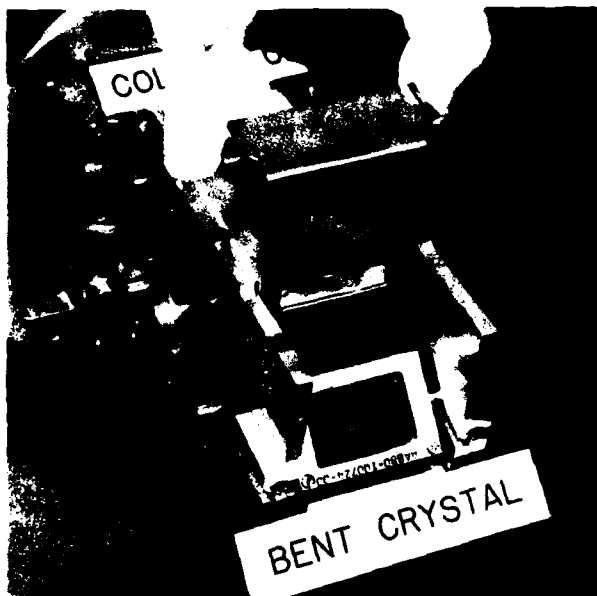


Figure 9. Installation of ultra-violet light barrier behind bent crystal on collimator/crystal assembly.

#### X-RAY DETECTOR

The detector that sensed the diffracted x rays was designed to accommodate different criteria on spectral resolution over the energy range under study and to be a high frequency response detector.

Achieving the desired energy resolution was a matter of having the x-ray detector sufficiently far from the crystal consistent with a detector geometry that could easily be fabricated. The detector cathodes vary from 8 to 55 mm in width, and the distance from the point of diffraction on the crystal to the detector cathodes ranges from 46 to 50 cm giving an energy dispersion at the detector of 0.65 to 1.0 eV/mm.

Two detector types were built, one with three cathodes and another with seven. Both detector types had a background cathode that would sense x rays scattered from the crystal but would be out of the pattern of diffracted x rays.

Gold was selected as the cathode surface because of its large photoelectric cross section at the energies of interest and because of ease of plating.

The detector, of necessity, had to be windowless and have a vacuum common to that of the spectrometer; because of this, it was desirable to minimize the number of vacuum feedthrough electrical connectors. It was decided to operate the cathodes at a negative high voltage requiring but one connector per cathode; however, an isolation capacitor is necessary to record the signal. The anode was at ground potential and was made of a nickel screen.

A prototype detector was made to verify the design and make measurements of frequency response, voltage standoff, etc.; refinements to the initial design were made. We finally built a detector that had two layers of cathodes and two anode screens. The two layers of cathodes, one behind the other, permitted differing spectral resolution and

continuous energy coverage where desired. One anode screen was in front of all cathodes, and the second was between the two cathode layers. The anode screen had a transmission of  $\sim 81\%$  (the open area ratio). The cathodes were operated at  $-4$  kV and, with the electrode spacing used, gave a calculated Child's Law space charge limited current of  $\sim 40$  A/cm<sup>2</sup>. Figure 10 is an exterior view of the seven-cathode detector; Fig. 11 is a view of the cathodes looking in the direction from which the x rays would be incident. Figure 12 shows the three-element detector mounted on the standoff connecting the detector and the crystal holder/collimator section.



Figure 10. Multi-cathode x-ray detector mounted on adapter flange with electrical and vacuum feedthroughs shown on body.

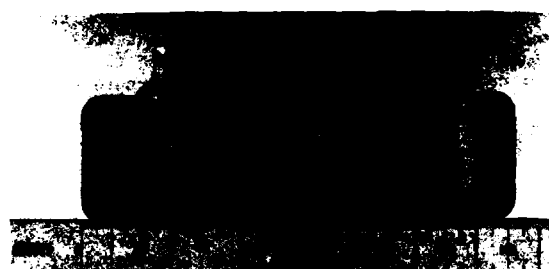


Figure 11. Interior view of multicathode x-ray detector showing individual signal cathodes and one background cathode.



Figure 12. X-ray detector and crystal/collimator section attached to stand-off housing. X rays are incident from right.

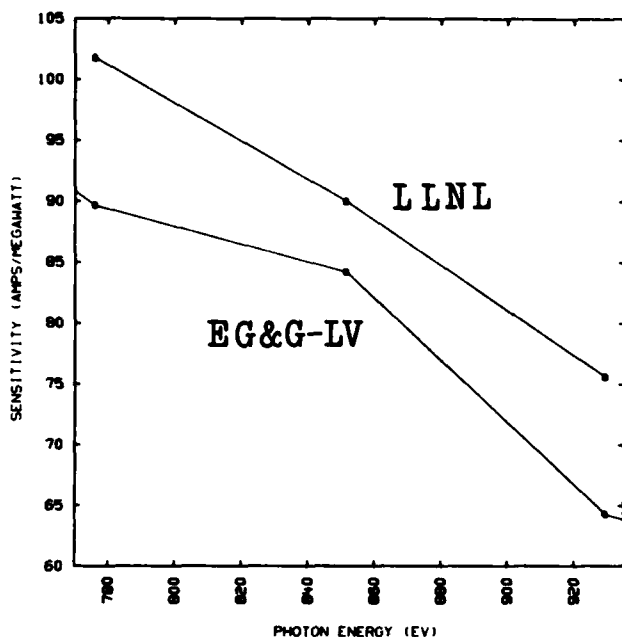


Figure 13. A typical x-ray detector cathode sensitivity in the subkilovolt photon energy range as measured by EG&G and LLNL.

The detailed design and fabrication of the final detectors was done by the Detector Group at EG&G's Las Vegas Atlas facility. They calibrated the various cathodes for a variety of photon energies. The detectors were also calibrated on the IONAC. Figure 13 shows typical calibration results determined by the two laboratories. The actual data points are plotted and connected by straight lines to illustrate the trend of sensitivity with energy.

The detector time responses were measured utilizing bremsstrahlung from a tungsten target on the LINAC located at EG&G's Santa Barbara facility (6). While not entirely appropriate for determining the time response in the manner the detectors are used, the LINAC radiation pulse (FWHM ~70 ps) and the detector's response to that pulse were believed to indicate the detector's temporal response. To the LINAC pulse, the largest cathode gave a rise time of ~1.1 ns while the rest of the cathodes varied in rise time between 0.7 to 0.3 ns.

#### SPECTROMETER

Internal collimation in the spectrometer first defines the x-ray beam incident on the mirror and then inhibits x rays scattered from the mirror, diffraction crystal, or other internal parts from reaching the detector. The internal collimation is shown schematically in Fig. 1, and parts of the collimators can be seen in Figs. 3, 6, 7, 9, and 12 attached to the crystal and mirror holders.

The spectrometer was designed so it could be disassembled after internal alignment and calibration and reassembled with assurance that the alignment and/or calibration was still valid. This was achieved by having all critical alignment mating faces dowel-pinned. As was mentioned earlier, the spectrometer is aligned to the source with the mirror removed; this makes for easy setup as one does not have to establish an offset for the alignment transit to view the reflected source off of the mirror or try looking through the diffraction crystal. There was sufficient concern about the reproducibility of the mirror replacement that the mirror was cycled in and out while the spectrometer was attached to the IONAC and the position of the nickel  $L_{1,2}$  line at the

detector location was determined with a proportional counter. There was no significant shift in the line position recorded, within the resolution of the measurement, when the line was located after the mirror was reinstalled.

Copper gaskets are used at all joints where vacuum seals are required. The spectrometer is rough pumped with a cryogenic absorption pump, and then a valve is opened connecting the spectrometer to an ion pump. Typical operating pressures are  $10^{-7}$  torr.

The calibration of the completed spectrometer for energy vs position at the detector location is made with a molybdenum anode x-ray tube. The calibration is done in third order, necessitating the use of a rhodium x-ray mirror rather than the carbon mirror in order to get the cut-off energy above 2.8 keV for the  $1.3^\circ$  mirror angle. The molybdenum lines were recorded on film. A reference wire casting a shadow in the bremsstrahlung continuum and keyed to the alignment dowel pins and to scribe marks on the detector allowed us to cross reference the energy calibration with the various hardware parts for positioning the detector to the desired energy. The developed calibration film was read with a scanning microdensitometer.

Data processing resulted in three-dimensional plots of density vs position along the diffracted x-ray beam and depth. The density was averaged over depth, and the best line position determined by fitting a polynomial to the average density vs diffracted beam position. The line energy was then compared with the energy calculated utilizing the appropriate parameters of the spectrometer for that same position with a code written to model spectrometer performance (7). A first-order least-squares fit in energy space was made between the standard line energies (8) and theory, and the theoretical energy values adjusted by the first-order fit to determine a continuous set of calibrated energy vs position at the detector location. The detector was positioned according to this calibrated set of energy values. Figure 14 shows the theoretical and calibrated energy vs position. Figure 15 shows the same information on a larger scale so it is easier to see the difference between the two curves; one can see that the calculation

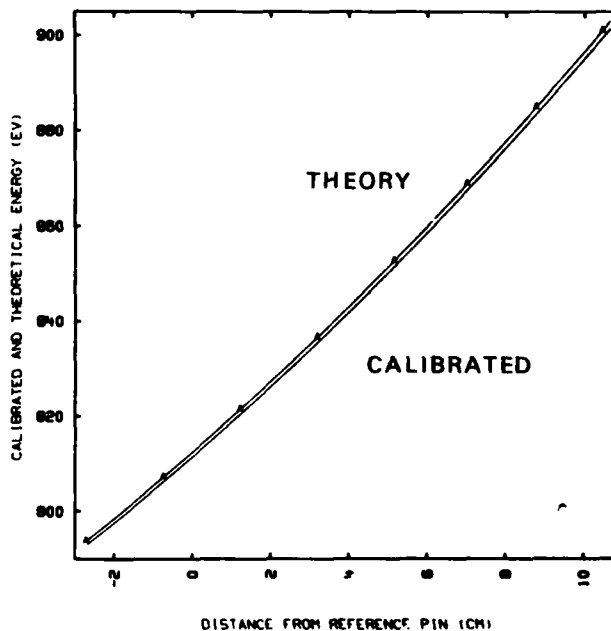


Figure 14. The calibrated and theoretical diffracted photon energy vs position at the x-ray detector location.

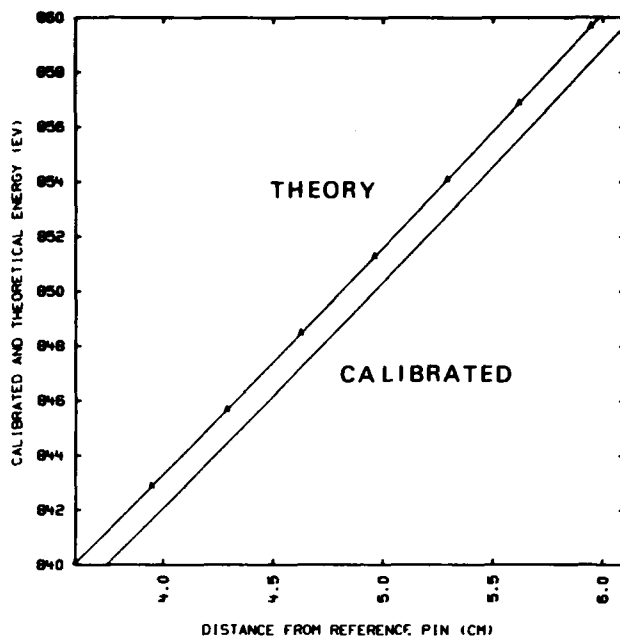


Figure 15. The calibrated and theoretical diffracted photon energy vs position at the x-ray detector location; repeated here to better illustrate the difference.

would predict a photon energy of  $\sim 1$  eV higher at a given position than the calibrated energy value. Figure 16 is the energy dispersion calculated at the detector location. No attempt was made to change this curve to reflect the calibration. The dispersion is useful in sizing cathode lengths along the direction of the diffracted x rays for the varying spectral resolutions and for predicting detector signals.

Using the information given here and some assumptions, it is possible to estimate the uniform intensity per keV of x rays at the spectrometer entrance that would give 1 A of detector current.

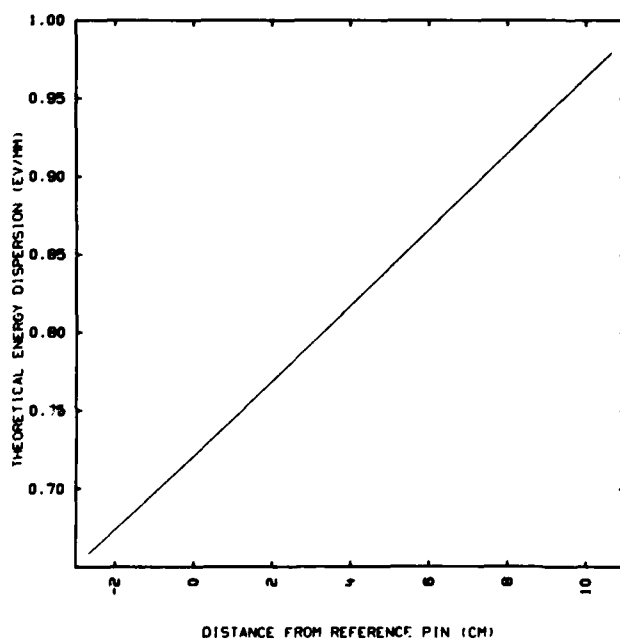


Figure 16. Theoretical photon energy dispersion vs position at the detector location.

Assume:

Average photon energy =  $\bar{E} = 850$  eV  
 Mirror reflectivity =  $R = 0.7$   
 Crystal diffraction efficiency =  $\epsilon = 5 \times 10^{-5}$  cm  
 Transmission of UV light barrier =  $T = 0.65$   
 Energy dispersion at detector =  $dE/dx = 0.8$  eV/mm  
 Detector cathode area (1 cm wide  $\times$  3 cm deep) =  
 $A_d = 3$  cm<sup>2</sup>  
 Detector Sensitivity =  $S_d = 90$  A/mW  
 Current =  $i = 1$  A

Now the detector current is:

$$i = \left[ I/E \left( \frac{\text{keV}}{\text{cm}^2 \cdot \text{s} \cdot \text{keV}} \right) \right] (R) [\epsilon (\text{cm})] (T) \left[ \frac{dE}{dx} \left( \frac{\text{eV}}{\text{mm}} \right) \right] \times \left[ A_d (\text{cm}^2) \right] \left[ S_d \left( \frac{\text{A}}{\text{mW}} \right) \right] = 1 \text{ A}$$

$$I/E = \frac{1 (\text{A})}{(0.7) \left[ 5 \times 10^{-5} (\text{cm}) \right] (0.65) \left[ 8 \times 10^{-3} (\text{keV/cm}) \right] \left[ 3 (\text{cm})^2 \right]} \times \frac{1}{\left[ 9 \times 10^{-5} (\text{A/W}) \right] \left[ 1.6 \times 10^{-14} (\text{W} \cdot \text{s/keV}) \right]}$$

$$= \sim 10^{24} \frac{\text{keV}}{\text{cm}^2 \cdot \text{s} \cdot \text{keV}} \quad \text{or} \quad \sim 2 \times 10^{10} \frac{\text{W}}{\text{cm}^2 \cdot \text{keV}}$$

#### CONCLUSION

The spectrometer described has performed satisfactorily; however, any future version should have an alternate means of x-ray mirror positioning and support. The detector has a better than expected temporal response.

#### ACKNOWLEDGEMENTS

Many people contributed to the development and calibration of the spectrometer. David Oakley and Arnold F. Clark deserve special recognition as do Tom Woehrlie, Shirley Stribling, Don Nelson, Max McGee, Chris Hawkes, Darryl Hall, Dick Ernst, Dick Duffus, Nick Brazell, Bob Bathgate, and Earl Augusta.

#### REFERENCES

1. L. Kissel, Lawrence Livermore National Laboratory Internal Document XRM-80-89 (1980). Readers outside the Laboratory who desire further information on LLNL internal documents should address their inquiries to the Technical Information Department, Lawrence Livermore National Laboratory, Livermore, California 94550.
2. R. W. Kuckuck, J. L. Gaines, and R. D. Ernst, in *IEEE Proc. Fourth Conf. on the Scientific and Industrial Application of Small Accelerators*, 229 (1976).
3. J. L. Gaines, *Nucl. Inst. and Meth.* 120, 7 (1972).
4. J. P. Stoering, M. Rice, G. A. Burginyon, E. L. Augusta, and C. L. Wang, Lawrence Livermore National Laboratory, Livermore, CA, UCID-18030, (1979).
5. H. F. Finn, Lawrence Livermore National Laboratory Internal Document CPG-77-125 (1977). Readers outside the Laboratory who desire further information on LLNL internal documents should address their inquiries to the Technical Information Department, Lawrence Livermore National Laboratory, Livermore, California 94550.
6. B. A. Davis, EG&G Technical Bulletin, DESSD-E-022 (1981).
7. W. R. Woodruff, (unpublished), (1979).
8. J. A. Bearden, *Rev. of Mod. Physics* 39, 78 (1967).



## Efficiencies of Bent Mica Crystal X-Ray Spectrometers

Arnold F. Clark\*

Lawrence Livermore National Laboratory, P. O. Box 808, Livermore, California 94550

## ABSTRACT

Seven x-ray spectrometers have been built to the same specifications (1). The data show the degree of reproducibility of the components: 1) amorphous carbon mirrors, 2) mica crystals bent to a 5 cm radius of curvature for Bragg type reflections, and 3) photo diodes (XRDs) to measure the x-rays.

The efficiencies agree to about 10%. Calibration numbers are presented. Mirror reflectivities were measured from 0.75 keV to 2 keV. The mica spectrometers were measured at  $L_{\alpha}$  x-ray lines from Co, Ni, and Cu at energies of 775, 851, and 930 eV, respectively. The photo diodes were measured at a similar set of energies.

X-rays pass through filters and lead collimators and are reflected from a mirror set at a glancing angle of  $1.3^{\circ}$ . The mirror eliminates high order Bragg reflections. Mirrors, 30 cm x 6.4 cm, are either glassy (vitreous) carbon on a pyrex base or 1200 Å layer of rhodium on a polished pyrex base. An iridium coated mirror was also tested.

The measured reflectivity, R, agrees with theory to the accuracy of the calibrations, which is  $\pm 10\%$ .  
 $R \approx 74\%$  at 900 eV for the carbon with a density of 1.54 g/cc

$R \approx 73\%$  at 2.2 keV for rhodium with a density of 11.20 g/cc

$R \approx 18\%$  at 3.0 keV for iridium with a density of 20.2 g/cc

The reflectivity decreases rapidly at higher energies:  $R < 1\%$  at 2 keV for carbon at and 3.5 keV for rhodium.

After reflection from mirrors, the x-rays with the proper energies are diffracted (Bragg reflections) by bent crystals, mica or quartz about 0.1 mm thick. The crystals are bent, (radius of curvature = 5 cm) so that different energies can get diffracted (reflected) from different parts of the crystal.

The diffraction efficiencies have been measured at a number of energies and are consistent with previous experimental measurements of similar crystals. For the mica at 900 eV the efficiencies from a distant source are about  $0.5 \times 10^{-4} \pm 10\%$  of the incident flux per cm length of the diffracted line. The quartz crystal (Roc = 11.8 cm) has an efficiency of about  $2.3 \times 10^{-3}$  per cm length at 2.2 keV.

X-rays diffracted by the crystals pass through copper collimators to detectors. The detectors are x-ray photodiodes: XRD-45's with gold cathodes to provide maximum sensitivity in the 900 eV energy range.

XRDs are used because they can be very fast and are reliable. The measured response times were  $\approx 0.25$  ns. These particular XRDs were designed to provide continuous coverage by having neighboring cathodes staggered and overlapping so that x-rays missing one cathode would get caught on the next one. The staggered spacing was set to make the inter-electrode capacitance small. A pulsed voltage on one cathode induces a response of less than 1% on neighboring electrodes.

A background cathode was positioned to detect general scattered radiations.

The XRDs have been calibrated both on the IONAC in Livermore and the x-ray facility at EG&G, Las Vegas. The calibrations generally agree and are consistent with calibrations of previous gold cathode XRDs. The sensitivity for 900 eV x-rays is  $1.2 \times 10^{-20}$  coulombs/keV with a variation of about 10%. The sensitivity at 2.2 keV is  $0.4 \times 10^{-20}$  coulombs/keV.

## ACKNOWLEDGMENTS

This work was done by a number of people mostly at Lawrence Livermore National Laboratory. The list is long and it is difficult to give adequate credit.

## REFERENCE

- Wayne Woodruff's neighboring paper, Low-Energy X-Ray Spectrometer, June 5, 1981.

## CALIBRATION NUMBERS

Spectrometer number	for X-rays of 900 eV						of 2.2 keV <sup>§</sup>
	1	2	3	4	5	6	7
Mirror Reflectivity at $1.3^{\circ}$	62%	72%	69%	67%	72%	74%	68% <sup>†</sup>
Mica Crystal, Roc:5cm, efficiency units: $10^{-4}$ cm	0.48	0.51	0.50	0.49	0.48	0.56	28 <sup>††</sup>
XRD coulombs/keV x $10^{20}$	1.3	1.15	1.0	1.0	1.2	1.15	0.45

<sup>†</sup>Rhodium mirror at  $1.3^{\circ}$

<sup>††</sup>Quartz crystal: Roc 16.8 cm

<sup>§</sup>Spectrometer #7 was calibrated for 2.2 keV x-rays

\*Work performed under the auspices of the U. S. Department of Energy by the Lawrence Livermore National Laboratory under contract number W-7405-ENG-48.

A New Method for Measuring Thin-Film Optical Constants  
Using Transmission Gratings in the Soft X-ray Range

R. Tatchyn and I. Lindau

Stanford Synchrotron Radiation Laboratory and  
Stanford Electronics Laboratories, Stanford University,  
Stanford, California 94305, USA

ABSTRACT

In this paper we present an analytical study of a rectangular and translucent diffraction grating composed of a material with known optical constants covered with a vacuum (in situ) deposit of a thin film of a material with unknown optical constants. We show that by choosing gratings of the proper material and dimensions and by measuring the intensity spectra of the coated gratings, we can use the ratios of the observed orders to calculate the optical constants of the thin-film material. The method's great advantage is its independence from the absolute intensities of the incoming and transmitted light, i.e., no measurements need be made of the absolute intensities.

I. INTRODUCTION

It has been shown in previous work (1) that by measuring the intensity spectra of two or more gratings of a given material at a given frequency of interest, one can extract the optical constants of the given material from the recorded data. Under certain conditions (1), almost any material that can be formed into a diffraction grating structure with sufficiently good qualities can have its optical constants measured this way. Unfortunately, not all existing materials that are of interest to researchers in the soft x-ray range can be formed into diffraction grating structures with comparable quality and ease.

Given the fact that most materials, however, can be deposited in vacuum (by evaporation, or other means) onto a matrix material like gold or platinum (which make gratings of excellent quality), we undertake to show in this paper that essentially the same technique may be used to measure the optical constants of many materials that cannot be formed into free-standing gratings by themselves.

We will analyze a given grating structure with known optical constants with a thin film of unknown material on it (Fig. 1) where the dimensions of both the grating and the thin film are known, and derive the experimental equations from which the optical constants of the unknown material may be extracted.

The great advantage of this method will be made evident as it is independent of the absolute intensity of the source light and can be used to monitor the optical constants of both thin film and bulk-type deposits of many unknown materials.

II. ANALYSIS OF THE COATED GRATING

The far-field intensity spectrum of a diffraction grating is easily derived to be (1):

$$I(s) = \left( \frac{\sin m s N a}{\sin m s a} \right)^2 \left| \bar{M} + \exp(\pi i s a) \bar{A} \right|^2 \quad (1)$$

where

- 1)  $s \equiv$  sine of the observation angle with respect to the grating normal
- 2)  $m \equiv$  observed order. At the various orders,  $s = m/a$
- 3)  $a \equiv$  grating period in wavelength units
- 4)  $d \equiv$  grating aperture size in wavelength units
- 5)  $W \equiv$  grating bar thickness in wavelength units
- 6)  $\lambda \equiv$  light wavelength
- 7)  $\bar{M} \equiv$  Fourier transform of the field distribution across a bar top surface

- 8)  $\bar{A} \equiv$  Fourier transform of the field distribution across an open aperture
- 9)  $N \equiv$  number of illuminated bars  
For the treatment in this paper, a few additional definitions are necessary:
- 10)  $q \equiv$  thickness of deposited material in wavelength units
- 11)  $\hat{n} \equiv$  complex index of refraction of the grating material.  $\hat{n} = (1-\delta) + ik$
- 12)  $\hat{n}' \equiv (1-\delta') + ik' \equiv$  complex index of refraction of the deposited material

In order to analyze the grating in Fig. 1 we must make a few assumptions (which must be verified for plausibility when the experiment is being performed): First, we assume that the bars are coated on one side uniformly, and that negligible deposition occurs on the sides of the bars (this is a good assumption, especially when  $W \ll (a-d)$ ). If this is not the case, the treatment in this paper may easily be extended to account for any material deposited on the bar sides.<sup>2</sup> The second important assumption is that negligible reflections occur at the interfaces between the grating and the deposited material and at the vacuum/grating interfaces. Again, reflections of this type may be accounted for, but choosing materials where reflections are negligible simplifies the analysis considerably.

Examining Fig. 1, we straightforwardly compute  $\bar{A}$  to be (for a wave of unit amplitude):

$$\bar{A} = d \operatorname{sinc} ds \quad (2)$$

$\bar{M}$  is computed directly from the definition.

$$\bar{M} = \frac{a-d}{2} \int_{-\frac{a-d}{2}}^{\frac{a-d}{2}} \left\{ e^{-2\pi i W(\delta-ik)} e^{-2\pi i q(\delta'-ik')} \right\} \left\{ e^{-2\pi i s \frac{x}{\lambda}} \right\} dx \quad (3)$$

$$\bar{M} = e^{-2\pi(Wk+qk')} \times (a-d) \operatorname{sinc}(a-d)s \left[ \cos 2\pi(W\delta+q\delta') - i \sin 2\pi(W\delta+q\delta') \right] \quad (4)$$

Substituting (2) and (4) into (1), we obtain the expression for the far-field intensity (generalizing to an incoming wave of intensity  $I_0$ ):

$$\frac{I(s)}{I_0} = \left( \frac{\sin m s N a}{\sin m s a} \right)^2 \left[ e^{-4\pi(Wk+qk')} \frac{(a-d)^2 \operatorname{sinc}^2(a-d)s}{(a-d)^2 \operatorname{sinc}^2(a-d)s} \right]$$

$$+ 2e^{-2\pi(Wk+qk')} \cos\pi s a \cos 2\pi(W\delta+q\delta') d(a-d) \operatorname{sinc} ds \operatorname{sinc}(a-d)s + d^2 \operatorname{sinc}^2 ds \quad (5)$$

At  $s = 0$ , (5) becomes

$$\frac{I(0)}{I_0} = \pi^2 \left\{ e^{-4\pi(Wk+qk')} (a-d)^2 + 2e^{-2\pi(Wk+qk')} d(a-d) \cos 2\pi(W\delta+q\delta') + d^2 \right\} \quad (6)$$

At  $s=1$ , (5) becomes

$$\frac{I(1)}{I_0} = \pi^2 \left( \frac{\sin^2 \pi(d/a)}{(\pi/a)^2} \right) \times \left[ 1 - 2e^{-2\pi(Wk+qk')} \cos 2\pi(W\delta+q\delta') + e^{-4\pi(Wk+qk')} \right] \quad (7)$$

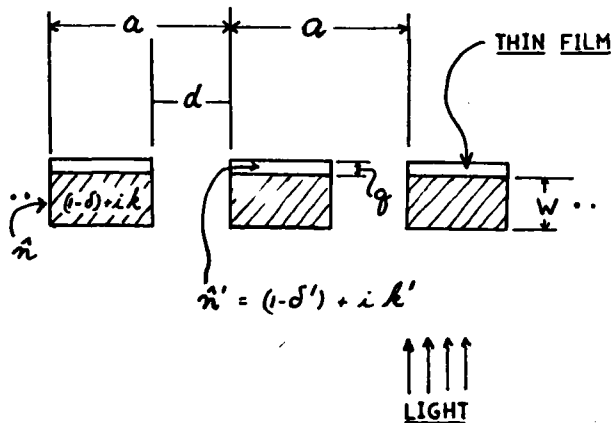


FIGURE 1

Fig. 1. Schematic of a grating of thickness  $W$  coated on its top surface with a deposit of thickness  $q$ . The index of refraction of the grating material is  $\hat{n}$ , and that of the deposited material is  $\hat{n}'$ .

### III. THE EXPERIMENTAL EQUATIONS

Consider two gratings characterized by different parameters  $a_1, d_1$ , and  $a_2, d_2, W_2$ , but made of the same material. Let the thickness of the deposit on grating 1 be  $q_1$ , and the thickness on grating 2 be  $q_2$ .

Assume that measurements of the intensity spectrum have been made, and that

$$I_1^{(1)}/I_1^{(0)} = A \quad (8)$$

$$I_2^{(1)}/I_2^{(0)} = B \quad (9)$$

Define

$$r_1 = \ln(d_1/(a_1-d_1)) \quad (10)$$

$$r_2 = \ln(d_2/(a_2-d_2)) \quad (11)$$

and

$$A_1 = A \cdot \frac{\pi^2}{4} \left[ \sin^2 \frac{\pi d_1}{a_1} \cdot \cosh^2 \frac{2\pi r_1}{W_1} \right]^{-1} \quad (12)$$

$$B_1 = B \cdot \frac{\pi^2}{4} \left[ \sin^2 \frac{\pi d_2}{a_2} \cdot \cosh^2 \frac{2\pi r_2}{W_2} \right]^{-1} \quad (13)$$

Given (8) - (13), the following equations are then valid:

$$(1+A_1) \cos 2\pi(W_1\delta+q_1\delta') + A_1 \cosh(2\pi(W_1k+q_1k') + r_1) - \cosh(2\pi(W_1k+q_1k')) = 0 \quad (14)$$

$$(1+B_1) \cos 2\pi(W_2\delta+q_2\delta') + B_1 \cosh(2\pi(W_2k+q_2k') + r_2) - \cosh(2\pi(W_2k+q_2k')) = 0 \quad (15)$$

Equations (14) and (15) are the required experimental equations. Normally,  $\delta, k, a_1, a_2, d_1, d_2, W_1, W_2, q_1$ , and  $q_2$ , will be known (or measured) yielding two equations in the two unknowns,  $\delta'$  and  $k'$ . Note that it is not necessary for  $q_1$  and  $q_2$  to be different, as long as  $W_1$  and  $W_2$  are different. This makes the method easy to implement, since the deposition can then be done simultaneously on both gratings.

### IV. CONCLUSIONS

There are many practical considerations that must be examined before the method proposed in this paper can be considered useful. Deviations from our ideal model in Fig. 1 such as surface roughness on the bars, or departures from the rectangular profile must be accounted for before the equations (14) and (15) can be considered useful. The analysis of these and other important departures from the ideal model has been done elsewhere, and is directly applicable to the case considered here (1).

It should be pointed out that for the reasonable case of  $a_1=a_2$ , and  $a_1=a_2=2d_1=2d_2$ , and  $q_1=q_2=q$ , equations (14) and (15) collapse to the simple forms

$$\cos 2\pi(W_1\delta+q\delta') + \frac{A_1-1}{A_1+1} \cosh(2\pi(W_1k+qk')) = 0 \quad (16)$$

$$\cos 2\pi(W_2\delta+q\delta') + \frac{B_1-1}{B_1+1} \cosh(2\pi(W_2k+qk')) = 0 \quad (17)$$

Examination of the above equations shows that if  $q\delta' \ll W_1\delta_1, W_2\delta_2$ ; and if  $qk' \ll W_1k, W_2k$ , then the effect on the spectra of the uncoated gratings will be negligible. This shows that care must be taken to select gratings of sufficient thinness if especially thin films are to be measured.

In conclusion, if care is taken to select the proper materials and parameters for the gratings, we believe that the technique outlined in this paper can be used to characterize easily and efficiently the optical constants of many materials otherwise unmeasurable in the soft x-ray range.

### REFERENCES

1. R. Tatchyn, I. Lindau, and E. Khlne, *Optica Acta*, Vol. 27, No. 11, 1980, 1505-1536.
2. R. Tatchyn, Engineer's Thesis, Stanford University, March 1980, Chapter V.

An Extended Maximization Technique for Measuring Optical  
 Constants Using Transmission Gratings in the Soft X-ray Range

R. Tatchyn and I. Lindau

Stanford Synchrotron Radiation Laboratory and  
 Stanford Electronics Laboratories, Stanford University,  
 Stanford, California 94305, USA

ABSTRACT

Previous work has shown that careful measurement of the intensity spectra of two or more rectangular transmission gratings placed perpendicularly to the irradiating light can yield enough information to calculate the optical constants of the grating material. In this paper we examine the possibility of estimating the optical constants by rotating a single rectangular grating and observing the angle at which certain of the diffracted orders peak. Assuming this method, we examine the criteria under which it remains feasible and investigate the advantages that can possibly accrue from its use in subsequent experiments designed to measure optical constants in the soft x-ray range.

I. INTRODUCTION

Until recently, the measurement of optical constants of many materials in the soft x-ray range has been very difficult in the soft x-ray range due to two reasons:

- 1) The unavailability of high intensity, broad-band sources.
- 2) The inherent nature of the complex index of refraction of many materials in the soft x-ray range.

In Fig. 1 we show a typical plot of  $n$  and  $k$  (for gold) versus energy. (1) It is seen that above 100 eV or so,  $n$  approaches 1 from below and  $k$  approaches zero. These are in fact the trailing edges of the phase response curve and of the Lorentzian absorption curve associated principally with the plasma resonance of gold in the high UV range. A great many other materials of interest to x-ray researchers possess similar characteristics.

Due to the closeness of  $n$  to 1, and to considerations like scattered light and surface roughness, the principal technique for evaluating  $\hat{n}$  in this range has been to measure  $k$  directly by measuring the absorption of a monochromatic x-ray beam at normal incidence in a thin film of the material of interest at several frequencies, and then to interpolate to achieve a smooth  $k$  vs. eV characteristic, and then to compute  $n$  vs. eV by employing the Kramers-Kronig relations (2).

It is immediately seen that in order to measure  $k$  well one must carefully measure the incident intensity, the scattered intensity, and the efferent intensity at the thin film sample. In experimental terms, this is a very critical and precise process, and the sources of error are many. The computation of  $n$  from  $k$  is also beset with difficulties concerning assumptions about the precise absorption mechanisms, their oscillator strengths and their asymptotic behavior versus frequency (3).

In recent years, however, principally due to the progress made in the manufacture (4) and analysis (5, 6, 7) of ultrafine transmission diffraction gratings, a new technique (8) has been proposed, utilizing ultrafine gratings, that makes possible the direct measurement of  $n$  and  $k$  while avoiding measurements of the absolute intensities of the irradiating source. An initial experiment based on this proposed technique has, in fact, been done at SSRL, and a description of that experiment is given elsewhere in these proceedings.

In this paper, we intend to give a brief review of the new method and then to demonstrate that it may be done even more efficiently, under certain conditions, using only one preselected grating, ro-

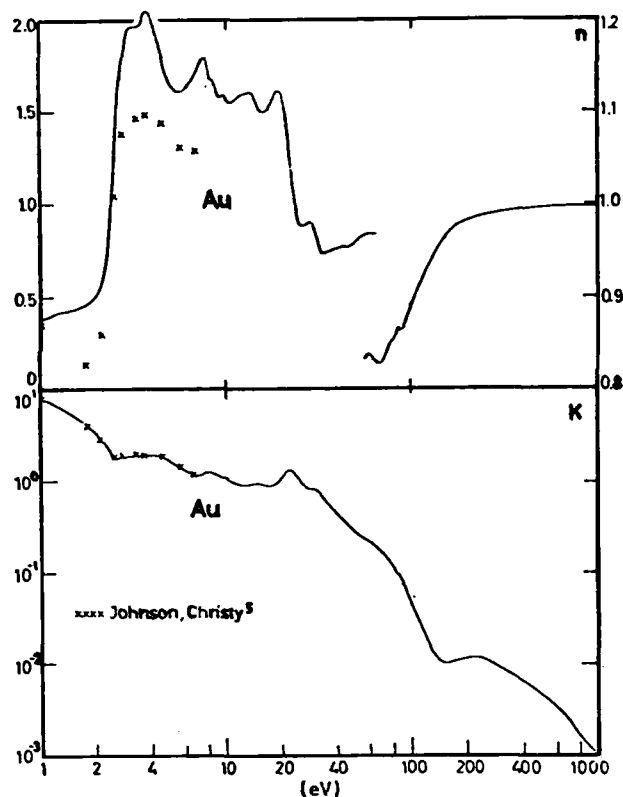


Fig. 1. Plots of the optical constants  $n$ ,  $k$  of gold.  $\hat{n} \equiv$  complex index of refraction  $= n + ik$ .

tating it to locate the point that determines  $n$  and  $k$ .

II. THE NEW METHOD

We will start by describing the far-field intensity spectrum of a planar transmission grating with ideal rectangular translucent bars characterized by the complex index of refraction  $\hat{n} = n + ik = (1 - \delta) + ik$ . (For a schematic of the grating, see Fig. 2.)

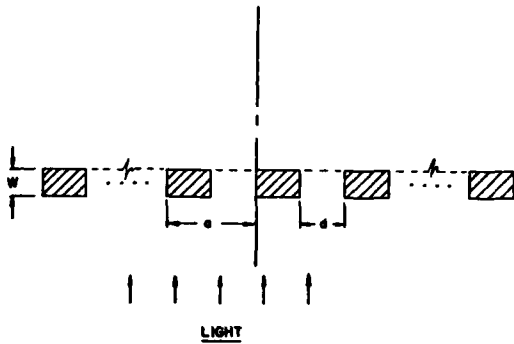


Fig. 2. End view of ideal rectangular grating.

$$I(m/a) = \left( \frac{\sin \pi m N}{\sin \pi m} \right)^2 \left| \bar{M} + \exp(\pi i m) \bar{A} \right|^2 \quad (1)$$

In order to avoid confusion, we give the following definitions:

- 1)  $s \equiv$  sine of the observation angle with respect to the grating normal
- 2)  $m \equiv$  observed order. At the various orders,  $s = m/a$ .
- 3)  $a \equiv$  grating period in wavelength units
- 4)  $d \equiv$  grating aperture size in wavelength units
- 5)  $W \equiv$  grating bar thickness in wavelength units
- 6)  $\lambda \equiv$  light wavelength
- 7)  $\bar{M} \equiv$  Fourier transform of the field distribution across a bar top surface
- 8)  $\bar{A} \equiv$  Fourier transform of the field distribution across an open aperture
- 9)  $N \equiv$  number of illuminated bars

For the case where we may ignore surface and interface reflection effects, the following are easily computed (for a wave of unit amplitude):

$$\bar{M} = (a-d) \left[ \text{sinc}(a-d)s \right] \exp(-2\pi i W(\delta - ik)) \quad (2)$$

$$\bar{A} = d \text{sinc } ds \quad (3)$$

Substituting (2) and (3) into (1), we get the following expression for the ratio of the  $m$ th order intensity,  $I(m)$  of the diffracted spectrum to the 0th order intensity,  $I(0)$ :

$$F\left(m, \frac{a}{d}, \lambda\right) = \frac{I(m)}{I(0)} = \frac{\left[ 1 - 2e^{-2\pi i Wk(\lambda)} \cos 2\pi W\delta(\lambda) + e^{-4\pi i Wk(\lambda)} \right] \text{sinc}^2 m(d/a)}{\left[ 1 + 2\left(\frac{a}{d}-1\right)e^{-2\pi i Wk(\lambda)} \cos 2\pi W\delta(\lambda) + \left(\frac{a}{d}-1\right)^2 e^{-4\pi i Wk(\lambda)} \right]} \quad (4)$$

Now consider two gratings of different, non-allot thicknesses,  $W_1$  and  $W_2$  and of different apertures and periods  $d_1, a_1$  and  $d_2, a_2$ . If we define the measured values of the first-to-zeroth intensity ratios for each grating as:

$$I_1(1)/I_1(0) = A \quad (5)$$

$$I_2(1)/I_2(0) = B \quad (6)$$

$$\text{and} \quad r_1 = \ln(d_1/(a_1-d_1)) \quad (7)$$

$$r_2 = \ln(d_2/(a_2-d_2)) \quad (8)$$

and define the following quantities

$$A_1 = A \cdot \frac{\pi^2}{4} \cdot \left[ \sin^2 \frac{\pi d_1}{a_1} \cdot \cosh^2 \frac{1}{2} r_1 \right]^{-1} \quad (9)$$

$$B_1 = B \cdot \frac{\pi^2}{4} \cdot \left[ \sin^2 \frac{\pi d_2}{a_2} \cdot \cosh^2 \frac{1}{2} r_2 \right]^{-1} \quad (10)$$

we get:

$$(1+A_1) \cos 2\pi W_1 \delta + A_1 \cosh(2\pi W_1 k + r_1) - \cosh(2\pi W_1 k) = 0 \quad (11)$$

$$(1+B_1) \cos 2\pi W_2 \delta + B_1 \cosh(2\pi W_2 k + r_2) - \cosh(2\pi W_2 k) = 0 \quad (12)$$

It is clear that, given an accurate knowledge of  $a_1, d_1, a_2, d_2, W_1, W_2$ , and accurate measurements of  $A$  and  $B$ , we have two equations in two unknowns, and  $k$  and  $\delta$  may be iterated out of (11) and (12).

Equations (11) and (12) also define the experimental technique. It is seen that two gratings are required and two measurements of  $I(1)/I(0)$  at normal incidence in order to evaluate  $k$  and  $\delta$  at a given frequency. It is clear that the most crucial part of the experiment is the careful control and measurement of the diffraction grating parameters.

For the natural occurrence of non-rectangular bar shapes and for real effects like surface roughness, etc. such imperfections must be modelled and incorporated into our experimental equations. This has, in fact, been done, and the feasibility of the resulting experiment has been indicated elsewhere (8).

### III. THE MAXIMIZATION TECHNIQUE

Examining Fig. 3, we can write the expression for the intensity of the tilted grating formally as ( $s' = s - \sin \theta_g$ ):

$$I(s') = I(s')_{\text{rect}} + \left[ \text{Re}^2(D) + \text{Im}^2(D) \right] - 2 \left[ \text{Re}(D) \text{Re}(\bar{M} + \bar{A} e^{\pi i s' a'}) + \text{Im}(D) \text{Im}(\bar{M} + \bar{A} e^{\pi i s' a'}) \right] \quad (13)$$

where

$$D = \bar{L}_d e^{-\pi i s' (a' - d' + \frac{1}{2})} + \bar{R}_d e^{\pi i s' (a' - d' + \frac{1}{2})} \quad (14)$$

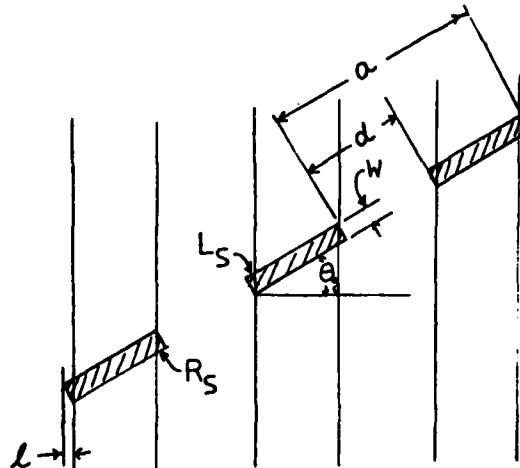


Fig. 3. End view of tilted grating.

$$\text{and } \bar{L}_d = \bar{L}_r - \bar{L}_s \quad (15)$$

$$\bar{R}_d = \bar{R}_r - \bar{R}_s \quad (16)$$

where  $\bar{L}_r, \bar{R}_r$  are the aperture transforms of ideal rectangular segments and  $\bar{L}_s$  and  $\bar{R}_s$  are the aperture transforms of the edges brought in by the tilted grating.

It is easy to show and is also intuitively clear that, when the grating bars are much thinner than the bar width (i.e.,  $W \ll (a-d)$ ), tilting the grating (7) by a small angle  $\theta_g$  will cause virtually no change in the ratio  $a/d$  and the principal effect will be to change the effective bar thickness by a factor  $\sec \theta_g$ . In such a case eq. 13 may be approximated by

$$I(s') \approx I(s')_{\text{rect}} \quad (17)$$

and the equation for the order ratios will be approximately:

$$F(m, \frac{a'}{d'}, \lambda, \theta_g) = \frac{I^{(m)}}{I^{(0)}} \\ \approx \frac{\left[ 1 - 2e^{-2\pi W \sec \theta_g k} \cos 2\pi W \sec \theta_g \delta + e^{-4\pi W \sec \theta_g k} \right] \text{sinc}^2 \frac{m d'}{a'}}{\left[ 1 + 2 \left( \frac{a'}{d'} - 1 \right) e^{-2\pi W \sec \theta_g k} \cos 2\pi W \sec \theta_g \delta + \left( \frac{a'}{d'} - 1 \right)^2 e^{-4\pi W \sec \theta_g k} \right]} \quad (18)$$

We thus see that by measuring  $I^{(1)}/I^{(0)}$  at normal incidence for a grating that fulfills our requirements ( $W \ll (a-d)$ ) and then tilting it by a small angle and remeasuring  $I^{(1)}/I^{(0)}$ , we can use equations (11) and (12) again to iterate out the optical constants.

The added advantage of this technique is that we can easily find the turning points of the first order intensity to be defined by the equations

$$e^{-2\pi W' k} = \cos 2\pi W' \delta + \frac{\delta}{k} \sin 2\pi W' \delta \quad (19)$$

$$W' = W \sec \theta_g \quad (20)$$

and thus, by rotating the grating through a maximum (or minimum) of the observed first order, we can precisely establish an auxiliary equation from which we can also extract the optical constants.

#### IV. CONCLUSIONS

The principal advantage of our extended maximization technique is that only one grating is required and thus all the systematic and random errors acquired in measuring two independently constructed gratings are halved. In addition, the observation of a turning point in a diffracted order is of great assistance in obtaining a precise measurement of the angle at which the turning point occurs.

The disadvantages of this method are that the remainder terms in eq. (13) must be verified to be small, and that an independent additional degree of freedom (rotation) must be incorporated into the experiment in such a way that the rotation will be measured with high precision. These restrictions, however, should not prove prohibitive, especially if the grating shape is well known.

In summary, we feel that our extended technique will prove worthwhile whenever gratings of high quality are difficult to produce for a given material and/or whenever only one high-quality grating is available for the experiment.

#### REFERENCES

1. H.-J. Hagemann, W. Gudat, C. Kunz, DESY, Report SR-74/7, May 1974.
2. Ibid.
3. Ibid.
4. J.M. Dijkstra, Space Science Instrumentation, **2**, 1976, 363-872.
5. H.W. Schnopper, L.P. Van Speybroeck, J.P. Delvaile, A. Epstein, E. Khlne, R.Z. Bachrach, J. Kijlestra, and L. Lantward, Applied Optics, **Vol. 16**, No. 4, April 1977, 1088-1091.
6. R. Tatchyn and I. Lindau, Nuclear Instruments and Methods, **172**, 1980, 287-291.
7. R. Tatchyn, Engineer's Thesis, Stanford University, March 1980.
8. R. Tatchyn, I. Lindau, and E. Khlne, Optical Acta, **Vol. 27**, No. 11, 1980, 1505-1536.

## Uranium Soft X-Ray Total Attenuation Coefficients

N. Kerr Del Grande and A. J. Oliver\*

Lawrence Livermore National Laboratory, P. O. Box 808, Livermore, California 94550

## ABSTRACT

Uranium total attenuation coefficients were measured continuously from 0.84 to 6.0 keV and at selected higher energies using a vacuum single crystal diffractometer and flow-proportional counter. Statistical fluctuations ranged from 0.5% to 2%. The overall accuracy was 3%. Prominent structure was measured within 20 eV of the  $M_5$  (3.552 keV) and  $M_4$  (3.728 keV) edges. Jump ratios were determined from log-log polynomial fits to data at energies apart from the near-edge regions. These data were compared with calculations based on a relativistic HFS central potential model and with previously tabulated data.

## INTRODUCTION

Experimental data is needed to understand theoretical predictions for photoexcitation and photoionization of uranium. The theory of photoeffect above 10 keV has been reviewed by Pratt *et al.* (1) and at lower energies by Fano and Cooper. (2) The major tabulations of theoretical cross sections are due to Scofield, (3) to Storm and Israel (4) and to Veigele. (5)

Verification of theory by experiment for uranium has not been possible below 10 keV. There are no measurements from .8 to 3.1 keV as shown in Figure 1. (6) Measurement differences are nearly 80% at 3.8 keV (7,8) and more than 40% at 9.0 keV. (9,10) These discrepancies have forced authors of compilations which synthesize theory and experiment to contend with large uncertainties for uranium. (5;11-13)

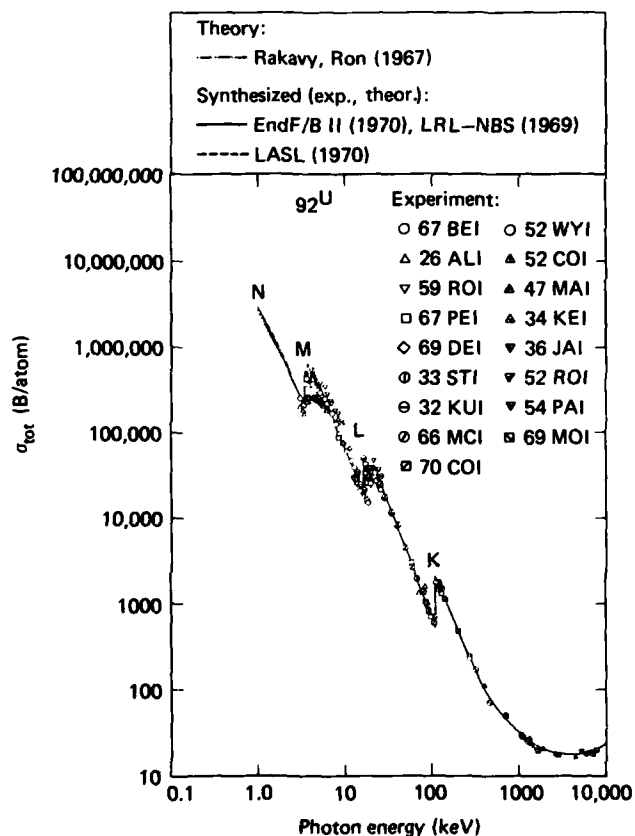


Figure 1. The status of uranium attenuation coefficients in 1971. The conversion factor, 395.3, reduces the ordinate scale to  $\text{cm}^2/\text{g}$ . (From reference 6.)

It is particularly important to understand deviations from the generally used single-electron central-potential approximation. The deviations are due to exchange and correlation effects; the influence of the atomic environment; solid-state structure and bonding. Actinides have special properties that are due to the partially filled 5f shell. Their 6d and 7s electrons form the conduction band in the metal whose energy is close to the 5f binding energy. In order to understand the behavior of the 5f electrons, their degree of localization must be determined. (14) Band structures have been developed to explain the electronic properties of the actinide metals. (15) Relativistic Hartree-Fock-Slater (HFS) models have been used to calculate oscillator strengths for the  $3d_{5/2} - 5f$  and  $3d - 5f$  transitions. (3,16-19)

Measurements of emission and absorption spectra show prominent resonance lines (14,20) at energies close to the  $M_5$  and  $M_4$  edge energies. (21) These energies are given in Table 1. They are compared with measurements discussed in this summary paper.

Table 1. Resonance absorption line energies and related M edge energies (keV) for photoexcitation of  $\alpha$ -uranium.

Edge	Transition	Edge Energy	Line Energy
$M_5$	$3d_{5/2} - 5f_{7/2}$	3.5517 (21)	3.5512 (14,20)
			3.5554†
			3.547 (16)
			3.605 (19)
$M_4$	$3d_{3/2} - 5f_{5/2}$	3.7276 (21)	3.7254 (14,20)
			3.7287†
			3.728 (16)
			3.780 (19)

†Based on 3% total attenuation measurements by Del Grande and Oliver.

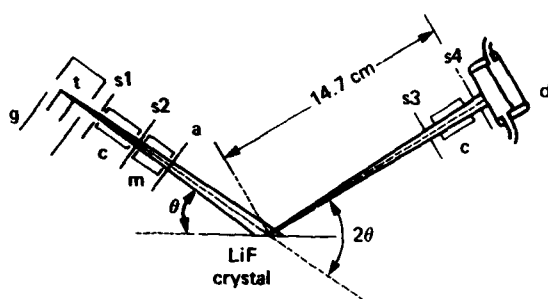
The Lawrence Livermore National Laboratory developed a technique to obtain absolute-value total attenuation coefficients. (22) This technique was applied to uranium. (11,23) This paper reports new data which extend the existing measurement region to include 0.844 to 3.000 keV. It gives details of the areas under the  $M_5$  and  $M_4$  x-ray absorption peaks. These areas relate to oscillator strengths for the 3d-5f bound-bound transitions. They are compared with recent calculations (16,19). Details of these data and their implications are discussed here-in.

## EXPERIMENTAL PROCEDURE AND RESULTS

Del Grande and Oliver measured the magnitude and extended range of x-ray K-absorption fine structure for transition elements Ti-Zn. (22) The procedure for obtaining 1% total attenuation coefficients at selected energies from 5 to 45 keV was discussed in detail. A double-Be-window demountable-tube x-ray generator by

\*This work was performed under the auspices of the U.S. Department of Energy by Lawrence Livermore Laboratory under contract No. W-7405-Eng-48.

Hilger and Watts was used in conjunction with two crystal spectrometers. Figure 2 shows the configuration for one of the spectrometers. Figure 3 is a block diagram of the electronic system.



- g X-ray generator
- t Multielement target
- c Soller slit collimators
- m Monitor assembly
- a Absorber foil
- d Detector
- s1, s3 Scatter slits
- s2 Defining slit
- s4 Acceptance slit

Figure 2. The single crystal spectrometer. The 4 mm line focus beam had a narrow (0.15 mm) spread at the crystal not shown on the schematic.

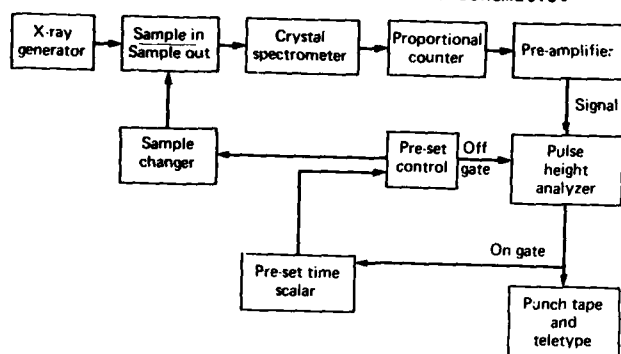


Figure 3. A block diagram of the electronic system.

A Ag target was used for measurements at energies above 5 keV. The impurities in the target provided a convenient way to align the spectrometer. These impurities (e.g., Fe, Ni, Cu and W) were assumed to have emission line energies tabulated by Dr. J.A. Bearden. (24) A LiF crystal was used in the spectrometer. The gas used in the flow proportional counter was P-10.

Both a Mo target and a multielement target were used for measurements at energies below 5 keV. The multielement target had  $10^4$  Å of Al vapor-deposited on a Cr target with additional impurities of Nd and W. These measurements required a Siemens vacuum spectrometer which was used with either a pyrolytic graphite crystal, a lead stearate crystal (provided by Dr. Burton Henke) or a KAP crystal. The soft x-ray measurements required using a 9 µm Be window (coated with formvar) to separate the x-ray tube from the spectrometer chamber. The flow proportional counter gas was methane at 10 cm H<sub>2</sub>O above atmospheric pressure.

Thin free-standing Be-U-Be sandwich foils were vacuum evaporated by the Batelle Columbus Laboratory. Sixteen foils were prepared at a given time, using a precision mask. Some foils were Be-only foils. They had the same amount of Be as the two protective layers of Be, each about 42 µg/cm<sup>2</sup>. The Be-coatings prevented the U sandwich foils from oxidizing. The foils were

deposited on smooth glass substrates and floated off the substrates. They were weighed. Some foils were analyzed for impurities (from the releasing agent) using an ion probe. Other foils were mounted on filter-wheels in shock-proof containers. The uranium samples contained about 125 µg/cm<sup>2</sup> and 340 µg/cm<sup>2</sup> of uranium. Many of the thin foils did not survive both the aircraft vibrations and transporting the filter wheel to the vacuum spectrometer.

Several methods were used to estimate the uranium content of the sandwiches (e.g., weights, ion exchange calorimetry, ultraviolet fluorimetry and controlled potential coulometry). We believe the accuracy of these results to be between 10% and 15%, although original estimates were 5%. (23)

We needed to reduce the measurement uncertainties associated with determining the thin sandwich foil uniformity, purity and thickness. Hence, we took more x-ray measurements using thicker rolled foils. These foils had average weight per unit areas of about 34 mg/cm<sup>2</sup>. Their uranium contents and uniformities were known to within 1%. Their x-ray transmissions were recorded at 8.000, 9.9615 and 15.000 keV. The sturdiest and most uniform Be-U-Be sandwich foil had no evidence of damage from releasing or mounting. Hence, this foil was used for measurements from 0.844 to 6.000 keV. It was calibrated at 8.000 and 9.9615 keV, using the same procedure as was used to calibrate the rolled U foils, but with one difference. The Be-U-Be sandwich was measured relative to the Be-only foil which had been deposited at the same deposition time. The uranium content of the sandwich foil was thus determined by comparison with the rolled foils of known weight per unit area. It was 384 µg/cm<sup>2</sup> with an uncertainty of 2%.

Usually two or more measurements consisting of ten pairs (but occasionally up to twenty) of Be-U-Be followed by Be-only measurement periods, provided standard deviations of the mean error, ranging from 0.2 to 2%. These measurements were followed by background measurements. The backgrounds were determined using exit slits 2° 2θ on both sides of the diffracted beam. Corrections for backgrounds were typically 1 or 2%. Dead time corrections were less than 1%. Overall errors were 3% for uranium total attenuation coefficients at energies from 0.844 to 6.000 keV in Table 2. The additional data from 8.000 to 40.000 keV in Table 2 had overall errors of 2%. Most of these data were reported previously in Vol. 3 of McMaster et al. (11) and as reference 69DE1 in Figure 1 (6).

The absolute measurement energies of continuum radiation were known to 3 or 4 eV. Uncertainties were 2 eV relative to tabulated emission line energies for W(M), Nd(L), Mo(L), Cr(K) and Al(K). The alignment was done in first or second order. Multiple orders were separated with discriminators on the multichannel analyzer. Higher order radiations did not affect measurements because they were eliminated by reducing the target voltage sufficiently.

Previous measurements for the uranium resonance absorption lines in Figure 4 were 3 or 4 eV lower in excitation voltage energies (14,20) as shown in Table 1. Also, the clean-surface uranium N and O shell binding energies (25) average 3 or 4 eV lower than the tabulated x-ray values (21). Measurements apparently specify the resonance line and M-edge energies better than present theoretical calculations (16,19).

Figure 4 shows the transitions of 3d<sub>5/2</sub> electrons to 5f<sub>7/2</sub> vacancies and 3d<sub>3/2</sub> electrons to 5f<sub>5/2</sub> vacancies. The M<sub>5</sub> and M<sub>4</sub> edges (dashed) were assumed to be symmetric about their tabulated energies (21) with the resolution measured at the M<sub>3</sub> edge which did not have structure. These photoionization data were subtracted from the total photoexcitation plus photoionization peak values to determine the areas under the photoexcitation resonance lines. These areas were measured to within ±15%. They were each fit to a Gaussian with a full width at half maximum of 17.5 eV.



Table 2. Uranium attenuation coefficients,  $\mu(\text{cm}^2/\text{g})$  at energies  $E(\text{keV})$  from 0.844 to 40.000 keV.

	$\mu$	$\mu$	$E$	$\mu$	$E$	$\mu$		
1	8.4400E-01	7.9780E+03	71	1.5574E+00	3.2550E+03	141	3.9640E+00	1.2380E+03
2	8.5400E-01	7.9560E+03	72	1.5700E+00	3.1400E+03	142	3.9750E+00	1.2150E+03
3	8.6400E-01	7.8500E+03	73	1.5800E+00	3.0530E+03	143	3.9870E+00	1.2060E+03
4	8.7400E-01	7.6950E+03	74	1.5900E+00	3.0150E+03	144	4.0000E+00	1.1960E+03
5	8.8400E-01	7.6900E+03	75	1.6000E+00	3.0270E+03	145	4.0250E+00	1.1760E+03
6	8.9400E-01	7.4320E+03	76	1.6200E+00	3.0090E+03	146	4.0440E+00	1.1800E+03
7	9.0400E-01	7.4590E+03	77	1.6400E+00	2.9150E+03	147	4.0640E+00	1.1550E+03
8	9.1500E-01	7.4390E+03	78	1.6600E+00	2.8810E+03	148	4.0830E+00	1.1380E+03
9	9.2500E-01	7.2740E+03	79	1.6800E+00	2.8230E+03	149	4.1030E+00	1.1360E+03
10	9.3500E-01	7.1340E+03	80	1.7000E+00	2.7170E+03	150	4.1220E+00	1.1280E+03
11	9.4500E-01	7.0240E+03	81	1.7200E+00	2.6360E+03	151	4.1410E+00	1.1410E+03
12	9.5500E-01	6.9410E+03	82	1.7400E+00	2.5820E+03	152	4.1610E+00	1.1540E+03
13	9.6500E-01	6.8370E+03	83	1.7600E+00	2.5500E+03	153	4.1800E+00	1.0860E+03
14	9.7500E-01	6.7980E+03	84	1.7754E+00	2.4710E+03	154	4.2000E+00	1.0880E+03
15	9.8500E-01	6.6900E+03	85	1.8349E+00	2.2690E+03	155	4.2100E+00	1.0790E+03
16	9.9500E-01	6.5240E+03	86	2.0000E+00	1.9020E+03	156	4.2200E+00	1.0750E+03
17	1.0060E+00	6.4690E+03	87	2.0400E+00	1.8030E+03	157	4.2400E+00	1.0870E+03
18	1.0160E+00	6.4080E+03	88	2.2932E+00	1.3810E+03	158	4.2600E+00	1.0560E+03
19	1.0260E+00	6.3520E+03	89	2.5000E+00	1.1560E+03	159	4.2700E+00	1.0710E+03
20	1.0360E+00	6.3490E+03	90	2.8000E+00	8.8720E+02	160	4.2800E+00	1.0520E+03
21	1.0460E+00	6.3490E+03	91	3.0000E+00	7.3290E+02	161	4.2900E+00	1.0810E+03
22	1.0560E+00	6.4330E+03	92	3.2000E+00	6.3590E+02	162	4.3000E+00	1.0910E+03
23	1.0660E+00	6.2940E+03	93	3.5000E+00	5.0030E+02	163	4.3100E+00	1.1520E+03
24	1.0760E+00	6.2020E+03	94	3.5196E+00	4.8960E+02	164	4.3200E+00	1.1940E+03
25	1.0860E+00	6.0810E+03	95	3.5280E+00	5.0150E+02	165	4.3300E+00	1.1850E+03
26	1.0970E+00	5.9540E+03	96	3.5380E+00	4.8500E+02	166	4.3400E+00	1.1680E+03
27	1.1070E+00	5.9050E+03	97	3.5470E+00	1.2430E+03	167	4.3500E+00	1.1680E+03
28	1.1170E+00	5.7940E+03	98	3.5518E+00	1.9530E+03	168	4.3600E+00	1.1800E+03
29	1.1270E+00	5.7090E+03	99	3.5560E+00	2.1070E+03	169	4.3700E+00	1.1710E+03
30	1.1370E+00	5.6370E+03	100	3.5610E+00	1.9490E+03	170	4.3800E+00	1.1940E+03
31	1.1470E+00	5.5970E+03	101	3.5650E+00	1.5800E+03	171	4.3900E+00	1.1940E+03
32	1.1570E+00	5.5000E+03	102	3.5690E+00	1.1180E+03	172	4.4000E+00	1.1800E+03
33	1.1670E+00	5.4020E+03	103	3.5730E+00	1.0740E+03	173	4.4100E+00	1.1440E+03
34	1.1780E+00	5.3160E+03	104	3.5780E+00	1.0670E+03	174	5.0000E+00	8.4740E+02
35	1.1880E+00	5.2010E+03	105	3.5840E+00	1.0840E+03	175	5.1160E+00	8.0360E+02
36	1.1980E+00	5.2010E+03	106	3.5940E+00	1.0820E+03	176	5.4147E+00	7.4330E+02
37	1.2000E+00	5.2380E+03	107	3.6030E+00	1.0510E+03	177	6.8467E+00	6.1730E+02
38	1.2100E+00	5.0830E+03	108	3.6130E+00	1.0240E+03	178	6.0000E+00	6.0570E+02
39	1.2200E+00	4.8830E+03	109	3.6230E+00	1.0400E+03	179	8.0000E+00	3.0280E+02
40	1.2300E+00	4.8750E+03	110	3.6320E+00	1.0310E+03	180	9.9615E+00	1.8250E+02
41	1.2400E+00	4.8420E+03	111	3.6420E+00	1.0400E+03	181	1.0000E+01	1.0000E+01
42	1.2500E+00	4.8930E+03	112	3.6520E+00	1.0730E+03	182	1.5000E+01	6.3870E+01
43	1.2600E+00	4.7830E+03	113	3.6620E+00	9.9640E+02	183	1.7000E+01	4.5310E+01
44	1.2700E+00	4.6800E+03	114	3.6720E+00	9.9820E+02	184	4.5420E+01	4.5420E+01
45	1.2800E+00	4.5930E+03	115	3.6820E+00	9.7440E+02	185	1.7230E+01	9.8490E+01
46	1.2900E+00	4.5810E+03	116	3.6920E+00	9.6030E+02	186	1.7260E+01	9.9210E+01
47	1.3000E+00	4.5300E+03	117	3.7020E+00	9.4180E+02	187	1.7380E+01	1.0030E+02
48	1.3100E+00	4.4710E+03	118	3.7130E+00	1.0630E+03	188	1.8000E+01	9.2420E+01
49	1.3200E+00	4.3630E+03	119	3.7230E+00	1.7090E+03	189	2.0000E+01	6.3840E+01
50	1.3300E+00	4.3370E+03	120	3.7327E+00	1.8840E+03	190	2.0840E+01	6.4290E+01
51	1.3400E+00	4.2400E+03	121	3.7400E+00	1.4390E+03	191	2.0850E+01	6.4660E+01
52	1.3500E+00	4.2640E+03	122	3.7540E+00	1.3610E+03	192	2.0960E+01	6.1890E+01
53	1.3600E+00	4.1910E+03	123	3.7650E+00	1.3650E+03	193	2.1000E+01	6.3660E+01
54	1.3700E+00	4.1350E+03	124	3.7750E+00	1.3430E+03	194	1.0600E+01	8.4020E+01
55	1.3800E+00	4.0890E+03	125	3.7860E+00	1.3370E+03	195	1.1400E+01	8.4740E+01
56	1.3900E+00	3.9510E+03	126	3.7970E+00	1.3340E+03	196	1.2500E+01	8.4080E+01
57	1.4000E+00	4.0020E+03	127	3.8070E+00	1.3560E+03	197	2.1360E+01	8.2080E+01
58	1.4100E+00	3.9470E+03	128	3.8180E+00	1.3280E+03	198	2.1460E+01	8.1330E+01
59	1.4200E+00	3.8100E+03	129	3.8290E+00	1.2970E+03	199	2.1590E+01	8.1300E+01
60	1.4300E+00	3.8460E+03	130	3.8400E+00	1.2990E+03	200	2.1600E+01	8.0840E+01
61	1.4400E+00	3.6830E+03	131	3.8510E+00	1.2990E+03	201	1.9300E+01	8.0310E+01
62	1.4500E+00	3.7260E+03	132	3.8620E+00	1.2760E+03	202	1.7800E+01	8.9890E+01
63	1.4600E+00	3.6590E+03	133	3.8730E+00	1.2710E+03	203	1.8500E+01	8.8780E+01
64	1.4700E+00	3.6100E+03	134	3.8840E+00	1.2540E+03	204	2.0000E+01	8.8640E+01
65	1.4866E+00	3.5390E+03	135	3.8960E+00	1.2630E+03	205	2.2130E+01	8.7560E+01
66	1.5000E+00	3.4590E+03	136	3.9070E+00	1.2510E+03	206	2.4942E+01	6.5170E+01
67	1.5100E+00	3.4520E+03	137	3.9180E+00	1.2400E+03	207	5.0000E+01	6.4500E+01
68	1.5200E+00	3.3310E+03	138	3.9300E+00	1.2450E+03	208	3.0000E+01	6.0800E+01
69	1.5300E+00	3.3310E+03	139	3.9410E+00	1.2530E+03	209	3.5000E+01	2.7080E+01
70	1.5400E+00	3.3620E+03	140	3.9520E+00	1.2300E+03	210	4.0000E+01	1.9490E+01

The relationship of  $\mu(\text{cm}^2/\text{g})$  to the oscillator strength per keV,  $df/dE$ , is a constant equal to  $277.81 \text{ cm}^2 \text{ g}^{-1} \text{ keV}$ . The measured oscillator strengths were  $0.084 \pm 0.013$  for  $M_5$  and  $0.050 \pm 0.008$  for  $M_4$  bound-bound transitions.

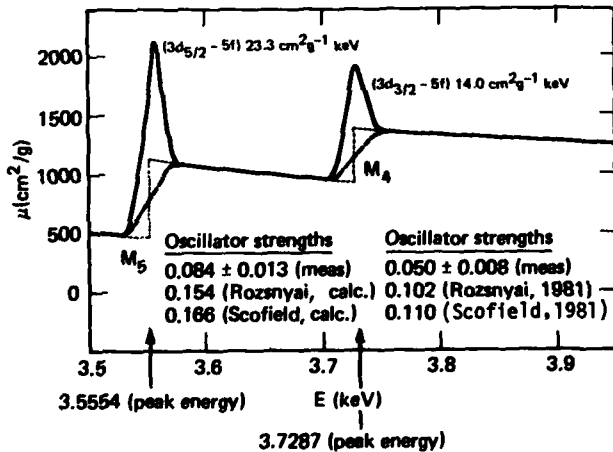


Figure 4. Measured photoexcitation of 3d electrons to vacancies in the partially filled 5f states.

Two relativistic HFS calculations were made to determine the  $M_5$  and  $M_4$  photoexcitation oscillator strengths (16,19). One used the Dirac equation to calculate wave functions (16). The other used the Schrodinger equation with the Pauli approximation to account for relativistic effects (19). The differences shown in Figure 4 were about 8%. The theoretical values were about twice the measurement values. This suggests that the 5f states are non-localized. Part of the bound-bound transitions may go to the continuum states (i.e., photoionization, in contrast to photoexcitation). This would explain the unusually high logarithmic slope for the photoeffect versus energy relationship above the  $M_5$  edge as shown in Table 3.

Figure 5 indicates that there is good qualitative agreement between theory and experiment for the photoexcitation peaks. Since the theoretical calculation did not determine the resonance line energies precisely, they were shifted to line up with the measurements. Also, the calculations were folded with a Gaussian which had a full width at half maximum of 15 eV.

Table 3.  $\log_e \mu$  versus  $\log_e E$  linear and quadratic regression fits to 3% measurements of uranium attenuation coefficients,  $\mu_F$  ( $\text{cm}^2/\text{g}$ ) compared with theory (3) and compilations (11,12).

Edge	Energy keV <sup>a</sup>	Jump	Log <sub>e</sub> Fit Coefficients <sup>b</sup>			$\mu_F(E^-)$ cm <sup>2</sup> /g	$\mu_F(E^+)$ cm <sup>2</sup> /g	Percent $\mu_F$ is above other $\mu$ values					
			a <sub>0</sub>	a <sub>1</sub>	a <sub>2</sub>			Scofield, <sup>3</sup> 1973		McMaster et al., <sup>11</sup> 1969		Henke & Ebisu, <sup>12</sup> 1974	
								near E <sup>-</sup>	near E <sup>+</sup>	near E <sup>-</sup>	near E <sup>+</sup>	near E <sup>-</sup>	near E <sup>+</sup>
N <sub>3</sub>	1.0449	1.048	8.788	-1.231		6208	6509	1.3	-0.1	-10.8	-6.5	2.4	
N <sub>2</sub>	1.2726	1.009	8.856	-1.700		4655	4695	2.8	2.3	5.5	6.4	-3.8	
N <sub>1</sub>	1.4408	1.001	8.884	-1.783		3763	3765	4.5	2.6	10.8	8.4		-7.1
M <sub>5</sub>	3.5517	2.299	8.903	-1.707	-0.3466	484.3	1111	-7.9	-12.2	-7.0	1.9		
M <sub>4</sub>	3.7276	1.478	11.566	-3.593		933.7	1380	-16.2	-12.8	-3.2	5.5		
M <sub>3</sub>	4.303	1.167	9.830	-1.976		1039	1213	-6.6	-6.0	14.5	-0.6		
M <sub>2</sub>	5.182	1.058	10.572	-2.378		779.6	824.6	-4.1	-4.2	2.4	-4.7		
M <sub>1</sub>	5.548	1.024	10.554	-2.333		703.3	720.1	-3.4	-5.1	-3.2	-8.1		
L <sub>3</sub>	17.1663	2.329	9.842	-1.566	-0.1972	44.49	103.6	-4.7	-3.2	-3.1	3.1		
L <sub>2</sub>	20.9476	1.372	11.752	-2.501		62.94	86.33	-0.1	-2.3	1.9	0.3		
L <sub>1</sub>	21.7574	1.158	11.170	-2.206		79.40	91.98	-1.1	-0.4	1.4	1.7		

<sup>a</sup>From J.A. Bearden and A.F. Burr, Rev. Mod. Phys. 39, 125 (1967)

<sup>b</sup>Fit parameters for 174 data values with 2% or better precision and 0.4% or better standard errors of the mean (avoiding structure regions). Fit parameters apply to energy region below edge energy.

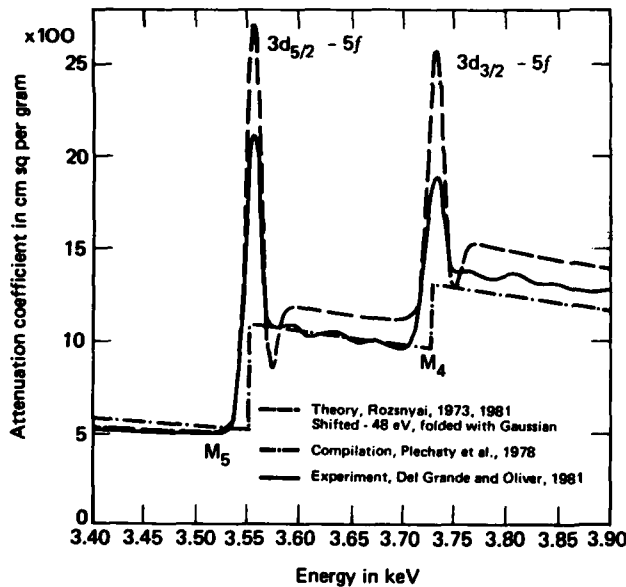


Figure 5. Comparison of 3% experimental data, adjusted theoretical data (19) and compiled uranium attenuation coefficients which ignore structure (13) near the M<sub>5</sub> and M<sub>4</sub> edges of uranium.

#### NEW DATA COMPARED WITH OTHER RESULTS

The 3% uranium attenuation coefficients near the M<sub>5</sub> and M<sub>4</sub> edges are significantly different from theory (19) and compilation values (13). The percentage differences of the measurements from other results are shown in Figure 6. Apart from the M-edge region, differences are shown in Figure 7, Figure 8 and Figure 9. Percent differences relative to smooth

$\log_e$  of attenuation coefficients versus  $\log_e$  of energy fits are given in Table 3.

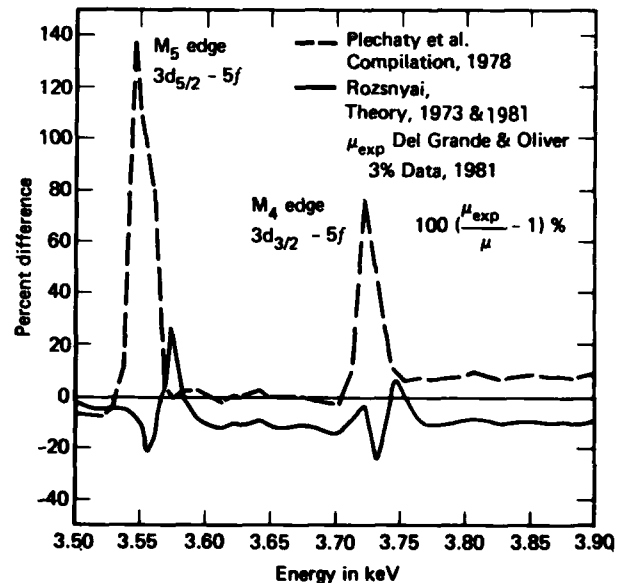


Figure 6. Comparison of uranium experimental data with adjusted theoretical data (19) and compiled data (13) for photoionization near photoexcitation peak energies.

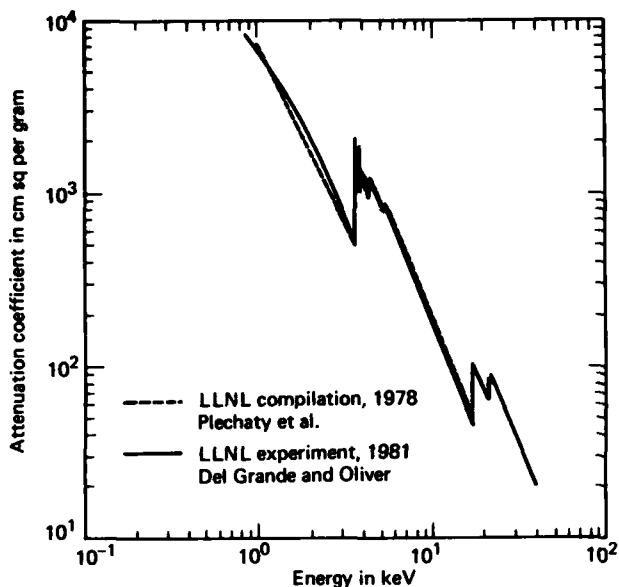


Figure 7. Uranium attenuation coefficients.

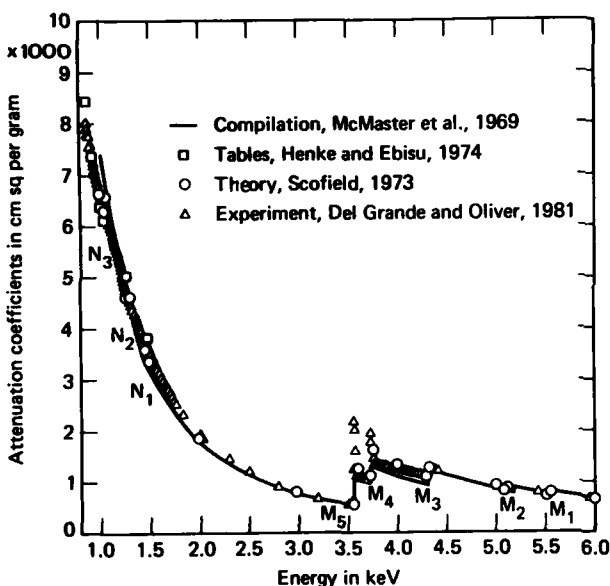


Figure 8. Uranium attenuation coefficients.

Jumps were measured at three N edges, five M edges and three L edges based on log-log linear and quadratic regression fits to the structureless data between edges. The data minus fit differences averaged about 0.0%. The standard deviations of the mean error were 0.4% or less. The standard deviation of individual data values from the smooth fit values, outside of regions with structure, were 2% or less. In one instance, the  $M_2$  and  $M_1$  edge jumps were based on smooth fit parameters above the  $M_1$  edge, and below the  $M_2$  edge, extended to the Cr  $K_{\alpha 1}$  emission line energy at 5.4147 keV. These jumps produced simulated data values at the  $M_1$  and  $M_2$  edges, although there was only one measured value between these edges. Data elsewhere were numerous between edges as shown in Table 2.

#### CONCLUSION

New 3% uranium total attenuation coefficient data extends the measurement region to include 0.844 to 3.000 keV. Agreement with relativistic HFS calculations (3) is typically 1-4% apart from the M edge region. The

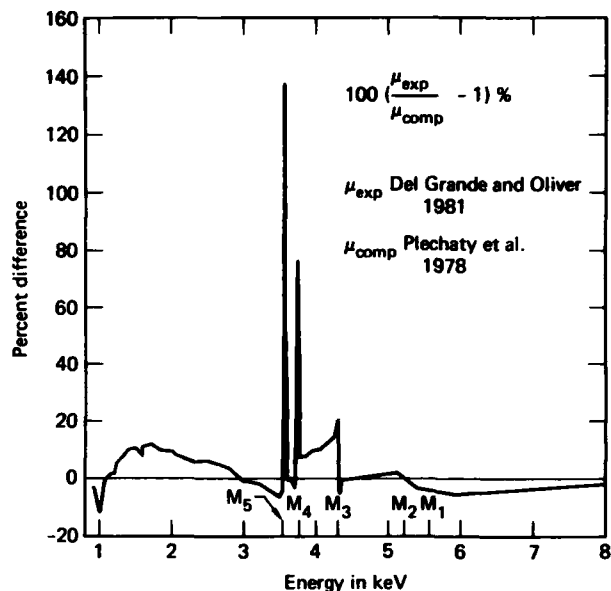


Figure 9. Comparison of uranium experimental data with compiled data (13) for the attenuation coefficient from 0.84 to 8.0 keV.

photoionization data are 3-16% lower than theory, from 3.5 to 5.5 keV (between the M edges) when photoexcitation is ignored.

Measured oscillator strengths were about half the predicted values based on two calculations (16,19). This suggests that the 5f unoccupied states are in part non-localized.

#### REFERENCES

1. R. W. Pratt, A. Ron, H. K. Tseng, *Rev. Mod. Phys.*, **45**, 273, 1973.
2. U. Fano and J. W. Cooper, *Rev. Mod. Phys.*, **40**, 441, 1968.
3. J. Scofield, Lawrence Livermore Laboratory Report UCRL-51326, p. 313-318, Univ. of Ca., Livermore, 1973.
4. E. Storm and H. I. Israel, *Nucl. Data Tables*, **A7**, 565, 1970.
5. W. J. Veigele, *Atomic Data Tables*, **5**, 51, 1973.
6. J. H. Hubbell, *Atomic Data*, **3**, 241, 1971.
7. G. V. Bezdenezhnykh, A. L. Zapysov, I. M. Israilev, V. N. Saprykin, *Opt. i Spektroskopiya* **23**, 980, 1967.
8. S. J. M. Allen, *Phys. Rev.*, **28**, 907, 1926 (Also: *Phys. Rev.*, **24**, 1, 1924, *ibid* **27**, 266, 1926.)
9. J. L. Perkins, A. C. Douglas, *Proc. Phys. Soc. (London)*, **92**, 618, 1967.
10. R. B. Roof Jr., *Phys. Rev.*, **113**, 820, 1959.
11. W. H. McMaster, N. Kerr Del Grande, J. H. Mallett and J. H. Hubbell, Lawrence Livermore Laboratory Report UCRL-50174, Sec. 2, Rev. 1, p. 343-346, Sec. 3, p. 191-192, Univ. of Ca., Livermore, 1969.
12. B. L. Henke and E. S. Ebisu in *Advances In X-Ray Analysis*, Vol. 17, Ed. by C. L. Grant, C. S. Barnett, J. B. Newkirk and C. O. Ruud (Plenum Press, New York and London, 1974), p. 150-213.
13. E. F. Plechaty, D. E. Cullen and R. J. Howerton, Lawrence Livermore Laboratory Report UCRL-50400, Vol. 6, Rev. 2, Univ. of Ca., Livermore, 1978, p. 470-475.
14. C. Boneile in *Structure And Bonding*, Vol. 31, Ed. by J. D. Dunitz, P. Hemmerich, J. A. Ibers, C. K. Jorgensen, J. B. Neilands, R. Reinen, R. J. P. Williams, (Springer-Verlag, Berlin, Heidelberg, New York, 1976) p. 24-48.

15. A. J. Freeman and D. D. Koelling in The Actinides, Vol. 2, (Academic Press, New York, 1974), Ch. 6.
16. J. Scofield, private communication, 1981.
17. B. F. Rozsnyai, Phys. Rev. A, 5, 1137, 1972.
18. B. F. Rozsnyai, J. Quant. Spectrosc. Radiat. Transfer, 13, 1285, 1973.
19. B. F. Rozsnyai, private communication, 1981.
20. C. Bonnelle and G. Lachere, J. de Phys. 35, 295, 1974.
21. J. A. Bearden and A. F. Burr, Rev. Mod. Phys., 39, 125, 1967.
22. N. Kerr Del Grande and A. J. Oliver, in X-Ray Spectra And Electronic Structure of Matter, Vol. 1, Proc. International Symp. Ed. by A. Faessler and G. Wiech, Munich, 1973 p. 183-204.
23. N. Kerr Del Grande and A. J. Oliver, Bull. Amer. Phys. Soc. Ser. 11, Vol. 18, 635, 1973.
24. J. A. Bearden, Rev. Mod. Phys. 39, 78, 1967.
25. R. L. Park and J. E. Houston, Phys. Rev. A, 7, 1447, 1973.

## Epoxy Replication for Wolter X-Ray Microscope Fabrication

W. Friedhorsky

Los Alamos National Laboratory, P.O. Box 1663, MS 410, Los Alamos, NM 87545

## ABSTRACT

An epoxy replica of a test piece designed to simulate a Wolter x-ray microscope geometry showed no loss of x-ray reflectivity or resolution, compared to the original. The test piece was a diamond-turned cone with  $1.5^\circ$  half angle. A flat was fly-cut on one side, then super- and conventionally polished. The replica was separated at the  $1.5^\circ$ -draft angle, simulating a shallow angle Wolter microscope geometry. A test with  $8.34 \text{ \AA}$  x rays at  $0.9^\circ$  grazing angle showed a reflectivity of 67% for the replica flat surface, and 70% for the original. No spread of the reflected beam was observed with a 20-arc second wide test beam. This test verifies the epoxy replication technique for production of Wolter x-ray microscopes.

## INTRODUCTION

Wolter x-ray microscopes are often the imaging diagnostic of choice for laser fusion applications. They can provide micron-scale resolution, and collection solid angles of order  $10^{-3}$  steradian, (1-2) unlike pinhole cameras and Kirkpatrick-Baez x-ray microscopes. (3) A true image is formed by a Wolter microscope. This image can be time resolved by a streak camera (4); time resolution is more difficult for images that must be reconstructed, such as from uniformly redundant arrays (5) or zone plate apertures (6). Wolter microscopes have proved difficult to fabricate, with typical production costs of  $> \$10^5$ . The near-target environment in a laser-fusion target chamber is not ideal for expensive optics. Target debris and radiation can damage the high-quality x-ray reflective surfaces. A large advantage would therefore accrue from the production of several x-ray optical elements from a single master.

## EXPERIMENT

We report a test of epoxy replication that demonstrates essentially perfect replication in a grazing angle conical geometry. This technique may be applied to the "mass" production of Wolter microscopes.

Our test piece for replication is shown in Fig. 1. The "flat cone" mandrel was produced by diamond turning and conventional polishing. It is a frustum of a cone, 25 mm high and 20 mm in diameter at the narrow end. The cone half angle is  $1.5^\circ$ . A flat section 3 mm wide was fly cut parallel to the side of the cone. The substrate was aluminum, plated with electroless nickel for diamond turning. The flat was polished and super-polished to provide a low-scatter finish. The central halfwidth of the flat was specified flat to  $\pm 5$  arc seconds. This design was chosen to provide a flat surface that can be easily tested for x-ray reflectivity and scatter, superposed on quasi-axi-symmetric geometry. Problems associated with separating a replica at a grazing angle should be apparent in the replica of the flat sector.

A replica of the test mandrel was produced using a standard epoxy technique, by Mr. Bernhard Bach of Hyperfine, Inc. (7) The nickel mandrel was evaporatively coated with approximately 2000  $\text{\AA}$  of nickel. A conventionally machined replica substrate was coated with epoxy, and mated to the mandrel. The epoxy layer was approximately 50  $\mu\text{m}$  thick, but, since the replica substrate had no flat, the epoxy thickened to 125  $\mu\text{m}$  at the flat section. The epoxy was cured at  $50^\circ\text{C}$ . When the assembly was cooled to room temperature, the mandrel and replica were separated mechanically. No problems were encountered in separation.

The mandrel and replica flats were tested with a collimated fan beam of  $8.34 \text{ \AA}$  x-rays. The test apparatus is shown in Fig. 2. Two adjustable slits collimate the x-ray emission from a Henke-type x-ray tube. The slit spacing of 14  $\mu\text{m}$  is chosen to minimize the angular spread of the emergent beam; this width is a compromise between geometric and diffraction spreading.

The sample to be tested is mounted on a stage, which can be rotated, and moved in and out of the beam. The detector is film or a proportional counter, and is mounted on a XYZ mount to scan the reflected beam.

## RESULTS

The proportional counter was used for a quantitative measurement of x-ray reflectivity. Counter acceptance was defined by a 0.51-mm pinhole, which corresponds to an angular resolution of 3.5 arc-min.

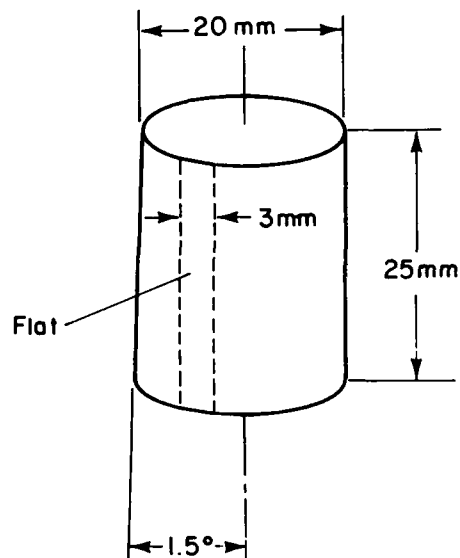


Fig. 1. Sketch of the "flat cone" test mandrel. The test surface is a flat on the side of  $1.5^\circ$  half-angle cone.

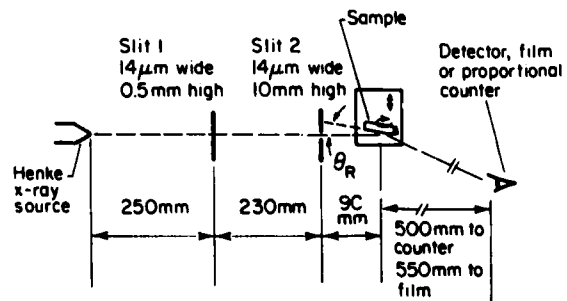


Fig. 2. Plan view of the x-ray test assembly (not to scale).

X-ray scattering from imperfect surfaces typically occurs at angles of  $\pm 1$ -10 arc-min. (8-10) Much of the scattered flux will thus fall outside the acceptance of the pinhole, so that the existence of wings in a horizontal scan of the reflected image indicates surface roughness. Figure 3 shows horizontal scans across the direct beam, and the reflected beams from the flat section on the mandrel and replica. The grazing angle was  $0.92^\circ$ . The scans from the two reflected beams are very similar. Little energy is scattered into the wings by the mandrel, and the replica reproduces this good performance. The specular reflectivity was determined from the ratio of the peak intensities. Measurements at a series of vertical positions were taken to average over vertical variations in the intensity of the Henke tube, projected through the slits. Errors in the peak reflectivities are determined from the scatter of the ratio of the direct and reflected beams at the different vertical positions. The peak reflectivity of the mandrel at  $8.34 \text{ \AA}$  and  $0.92^\circ$  was  $0.700 \pm 0.022$  (10); the reflectivity of the replica was  $0.668 \pm 0.014$ . The calculated reflectivity of nickel at the same wavelength and angle is  $0.76$ . Both surfaces are thus very good, and there is no significant degradation of the reflectivity of the replica.

The width of the specular peak in the proportional counter scans is determined by the pinhole diameter. No widening of this peak is observed, as might be caused by distortion of the surface figure in manufacture or replication. To look with greater sensitivity for such an effect, high resolution images of the direct- and replica-reflected beam were taken on 2497 film. In this case, the angular resolution of the test was set by the divergence of the test beam. Fig. 4 shows density scans of the direct and replica reflected image. There is no broadening of the FWHM of the reflected beam, which indicates arc-second fidelity of the surface flatness in replication.

Measurement of a flat surface replicated in a  $1.5^\circ$  grazing incidence geometry shows a low-scatter, flat replica surface. The epoxy replication technique thus offers an inexpensive technique of reproducing Wolter geometry x-ray microscopes. This result corroborates tests of replication, at a much larger scale, for Wolter x-ray telescope fabrication.(11)

#### REFERENCES

1. R. H. Price, this volume, 1981.
2. J. K. Silk, Proceedings, Imaging X-Ray Optics Workshop, SPIE Vol. 184, p. 40, 1979.
3. W. C. Friedhorsky and R. H. Price, in preparation.
4. R. H. Price, presentation, APS Plasma Physics Division, 1980.
5. E. E. Fenimore, T. M. Cannon, D. B. Van Hulsteyn, and P. Lee, Applied Optics, 18, p. 945, 1979.
6. N. M. Ceglio, this volume, 1981.
7. Hyperfine, Inc., 149 N. Main Street, Fairport, N.Y. 14450.
8. P. A. J. deKorte, Proceedings, Imaging X-Ray Optics Workshop, SPIE Vol. 184, p. 189, 1979.
9. B. Aschenbach, H. Brauniger, A. Ondrusch, J. Trumper, Proceedings, Imaging X-Ray Optics Workshop, SPIE Vol. 184, p. 148, 1979.
10. E. L. Church, Proceedings, Imaging X-Ray Optics Workshop, SPIE, Vol. 184, p. 196, 1979.
11. R. Laine, R. Giralt, R. Zobl, P. A. J. deKorte, J. A. M. Bleeker, Proceedings, Imaging X-Ray Optics Workshop, SPIE Vol. 184, p. 181, 1979.

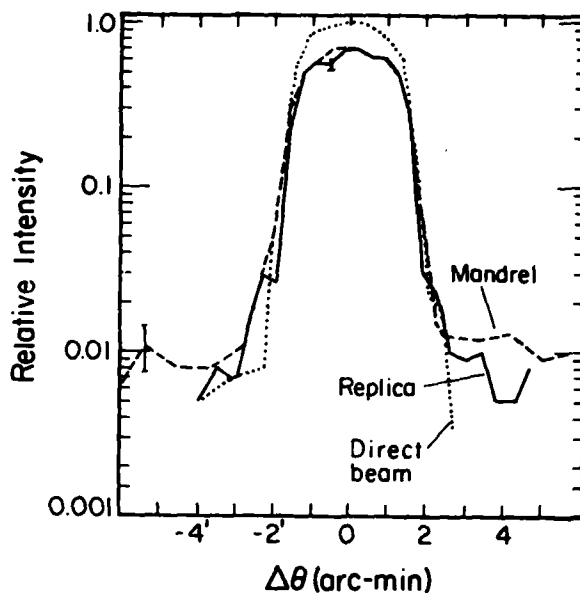


Fig. 3. Horizontal proportional counter scans of the direct and reflected beams. The x-ray wavelength was  $8.34 \text{ \AA}$ ; grazing angle was  $0.92^\circ$ .

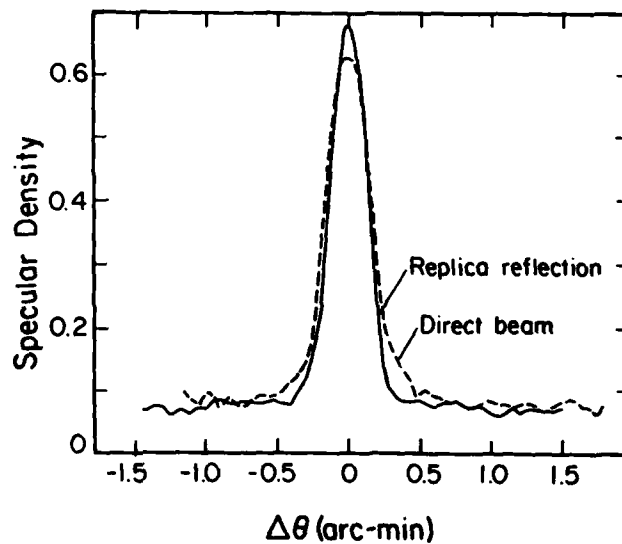


Fig. 4. Densitometer trace of the direct- and replica-reflected beams.

## Crossed-Crystal Imaging of X-ray Sources

R.R. Whitlock and D.J. Nagel

Naval Research Laboratory, Washington, D.C. 20375

## ABSTRACT

Two separate diffractors are employed in a crossed configuration to achieve two-dimensional spectral imaging. The crossed crystal concept is here generalized to apply to either Bragg case (surface) or Laue case (transmission) diffractors which may undergo either symmetric or asymmetric diffraction, and which may be crystals, pseudocrystals, or multilayers, and may be flat or curved. The crossed crystal spectrograph offers wide selection of  $2d$  spacings, crystal  $R$  values, resolutions, polarization losses, wavelengths, and magnifications.

## INTRODUCTION

X-ray imaging is an important capability to apply to the diagnosing of high temperature plasmas. The most significant characteristics of a two dimensional x-ray imaging system for these experiments are spatial resolution, sensitivity, and spectral resolution. This paper considers crystal optics for spectral resolution.

There are three main techniques for obtaining spatial resolution with crystals. The first two techniques, interposing a mask, e.g. a slit or a pinhole, into the optical path, and curving the crystal, have found use in either or both spatial dimensions. The third technique for spatial resolution, dispersion, is a direct result of the narrow spread of angles to which highly perfect crystals can diffract a monochromatic beam.

The three crystal imaging techniques have been applied by various workers in several ways, as outlined in Table I. Figures adapted from papers cited in the table have been reproduced in Fig. 1. Previous single crystal x-ray spectrographs have provided one dimension of spectral resolution due to the narrow rocking curves of the crystals employed (1). A second dimension of spatial resolution has been achieved by the use of a "crossed" slit with a single flat or convex curved crystal (2), crystal curvature (3,4,5), double reflections from appropriately oriented planes in a single flat crystal (6), and a crossed flat crystal arrangement using asymmetric diffraction to obtain magnification (7,8). It is possible to apply two techniques to the same spatial dimension, as in the work of Azechi, et al., (9) (masking with a pinhole in the dispersion direction) and as with a doubly curved crystal (4,5).

## BACKGROUND

The two spatial dimensions in an image formed with crystal optics will be represented by reference to the crystal's effect on the image. The direction in which dispersion of x-ray wavelengths takes place is

SPATIAL DIMENSIONS		COMMENTS, REFERENCE
X	Y	
A. SLIT	SLIT	Pinhole optics with flat crystal and a polychromatic source (9)
B. DISPERSION	NONE	Flat crystal (1)
C. DISPERSION	SLIT	Slit with flat or convex crystal (2)
D. DISPERSION	CURVATURE	Cylindrical curvature (3)
E. DISPERSION	DISPERSION	Asymmetrically diffracting crossed crystals (8)
F. DISPERSION	DISPERSION	Single crystal, double diffraction (6)
G. CURVATURE	CURVATURE	Applicable only to one wavelength (4,5)

Table I. A summary of past approaches to the use of Bragg diffractors for spatial resolution of x-ray sources, with representative references.

referred to as the dispersion direction, while the orthogonal direction is called the fanning direction.

The relationship between dispersion and spatial resolution can be understood by considering the basic geometry which applies to x-ray diffraction for flat crystals. In Fig. 2, two monochromatic point sources are depicted as radiating isotropically above a large planar crystal. Although the radiation is emitted isotropically, only those photons which strike the crystal at the angle  $\theta$  (within some tolerance) will diffract from the crystal, according to the Bragg equation. These photons all left the source at an

angle  $90^\circ - \theta$  to the normal to the plane, forming a conical surface, as drawn in Fig. 2. (For simplicity's sake, the diffracted rays are not all shown subsequent to their reaching the crystal plane.) The locus of diffracting points in the crystal plane is a circle (for a sufficiently large crystal). The dispersion direction extends radially outward from the center of the circle, while the fanning direction is along the circle. Since the circle represents an isotropically

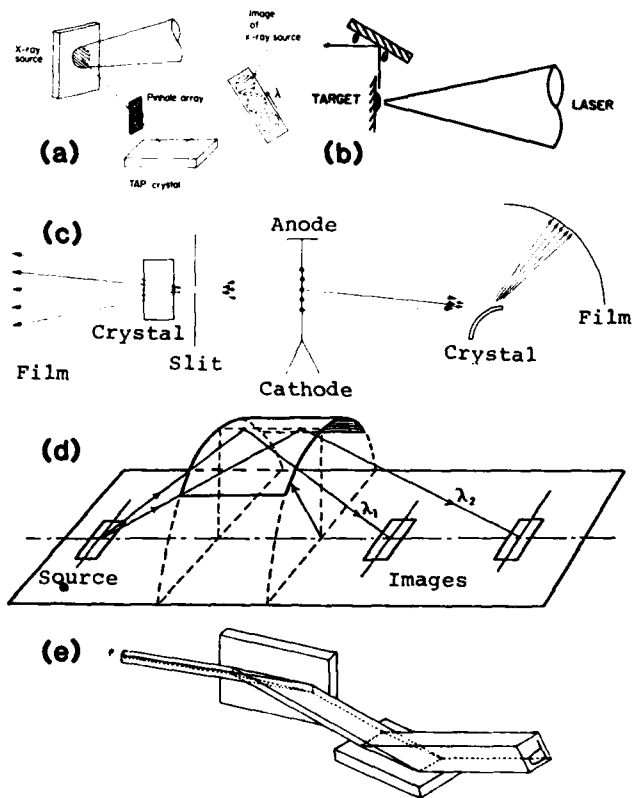


Figure 1. Previous arrangements for obtaining spatial resolution with crystal spectrographs. The reference letters (a)-(e) correspond to those in Table I. The x-ray sources in (a) and (b) were laser-produced plasmas; in (c), an electric discharge.

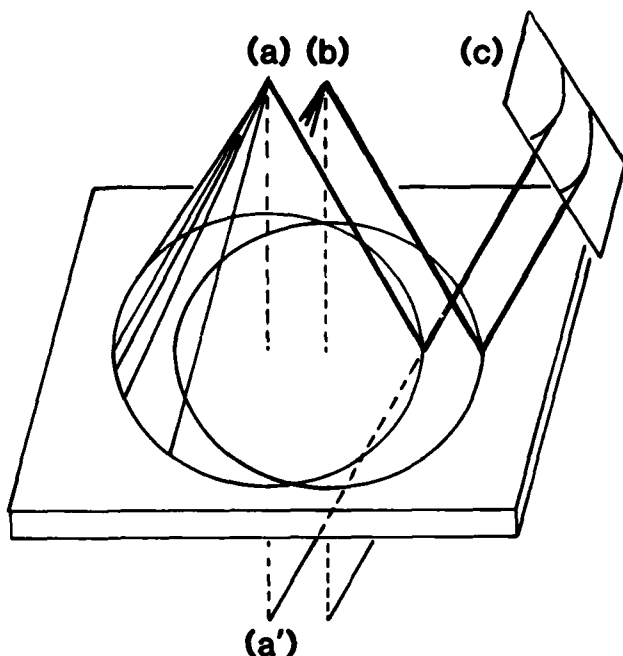


Figure 2. Schematic of the use of x-ray dispersion to obtain one dimension of spatial resolution with a flat crystal. Monochromatic point sources at (a) and (b) are resolved as separate arcs of diffracted radiation by a detector placed at (c). Every source (a) of emitted rays has a virtual focus (a') of diffracted rays.

radiating point source with no spatial structure, there is no spatial resolution to be obtained along the circle, i.e. along the fanning direction. (For anisotropically radiating point sources, angular structure can still be resolved in the fanning direction.)

If two distinct point sources of the same wavelength are present, drawn as in (a) and (b) of Fig.2, each has a different acceptance cone and a different circular locus of diffracting points. By placing an x-ray film at (c), as in Fig.2, two arcs of x-ray exposure will be recorded, indicating that the two point sources have been resolved at the detector, but that the image of a point is an arc.

For sufficiently small, but finite, sources, the arcs from different source points within the finite source will be nearly parallel. Then source points which are at different locations along the dispersion direction, as seen in the image, may be resolvable, while the diffraction from source points, which are at the same location in the dispersion direction but are at different locations in the fanning direction, will overlap and so not be resolvable. For a small source, then, the spatial resolution is obtained in the dispersion direction but not in the fanning direction. For large sources, so much overlap of arcs occurs in the case of an unmodified, flat crystal as to be of little interest for imaging.

Of course, using the dispersion direction for spatial resolution suffers from the potential complication that images of different wavelength photons may overlap.

The spatial resolution of a flat crystal in the dispersion direction is primarily determined by the angular width  $W$  of the crystal's rocking curve and by the placement of the detector. The rocking curve is a plot of the intensity of diffracted monochromatic radiation versus Bragg angle. Typical widths of crystal rocking curves are given in Table II; they vary with crystal type and plane, and also with wavelength and order of diffraction (10). For superior spatial resolution, one prefers a small value of  $W$  and short distances of observation. For 1.5 keV radiation, for example, one

Crystal	$W$ (sec)	$P$ (%)	$R$ (rad)
Calcite (cleaved and etched)	14	45	$4 \times 10^{-5}$
LiF (cleaved)	14	40	$3 \times 10^{-5}$
LiF (abraded)	120	50	$4 \times 10^{-4}$
Quartz (ground and etched)	20	30	$3 \times 10^{-5}$
EDDT (sawed and etched)	215	20	$2 \times 10^{-4}$
KAP (cleaved)	70	13	$5 \times 10^{-5}$
Graphite (hot pressed)	1800	30	$3 \times 10^{-3}$

Table II. Diffraction properties of a few common crystals, measured at  $\text{Cu K}\alpha$  (except KAP, which was measured at  $\text{Al K}\alpha$ ), from Birks (12).

would expect better than 10 micron resolution for a flat KAP crystal, if the source to detector distance is kept below 2 or 3 cm.

The diffracted intensity from a crystal is expressed as an integral reflection coefficient (11,12) or  $R$  value, which varies with crystal plane, wavelength, diffraction order, and crystal shape. For purposes of rough estimates, the flat crystal may be considered as having an acceptance angle  $W$  radians in the dispersion direction, and a diffracted peak relative intensity of  $P$  (dimensionless). The product of the angular width  $W$  (in radians) and the peak reflectivity  $P$  should be comparable with  $R$  (in radians), as can be verified from Table II.

Since different source points diffract from different portions of the crystal, it is important that the crystal be highly perfect. A sample spectrum from a laser-produced plasma, taken with an abraded and etched LiF crystal, is shown in Fig.3. While abrading and etching does increase the total reflectivity (the  $R$  value) of LiF, and therefore the signal level, it does so at the expense of introducing large numbers of dislocations into the crystal, making its structure highly mosaic and unsuitable for good spatial resolution (13).

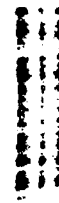


Figure 3. Example of the deleterious effect which crystal imperfections can have on imaging. A perfect crystal would have produced lines of uniform blackening in the fanning direction, i.e. along the lines.

#### CROSSED-CRYSTAL IMAGING

The configuration presented in this paper employs crossed crystals and diffracted x rays in a manner which is conceptually analogous to the Kirkpatrick-Baez crossed mirror configuration using x rays reflected in grazing incidence (14). The same principles which apply to crossed crystals apply also to other crossed Bragg x-ray diffractors, such as Langmuir-Blodgett pseudo-crystals or other synthetic multilayers. One crystal views the source and provides spatial resolution in its dispersion dimension only, and the second crystal views



the diffracted rays from the first crystal; but the second crystal here is to be oriented so that its dispersion dimension, as seen at the image, is at an angle to that of the first crystal. Thus, the dispersion dimensions of the two crystals, each having one dimension of spatial resolution, are crossed to achieve two dimensional imaging, as shown for planar crystals in Fig.4.

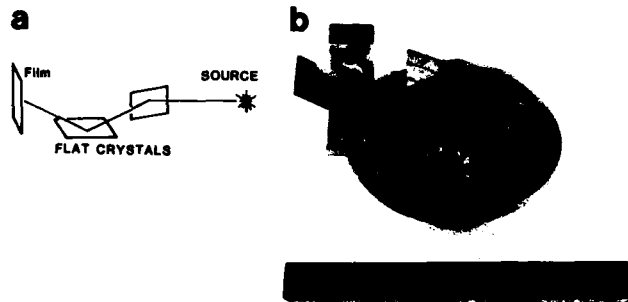


Figure 4. Crossed, flat-crystal imaging spectrograph, schematic (a) and apparatus (b). The crystals are not mounted in this view.

At first, one might be reminded of the standard double crystal spectrometer. However, the dispersion dimensions in such a spectrometer are aligned, although the dispersion directions (sic) of the two crystals may be either alike or opposite. But the dispersion dimensions are never crossed in such spectrometers.

There is a close similarity between the present approach and the double reflection method of Fraenkel (6). Both use two dispersions from two sets of crystal planes which are oriented to give 2D resolution. Fraenkel's method, however, involves two planes within the same crystal. Crystals with screw symmetry show this effect. Unfortunately, the selection of such crystals is not large. The main advantage of Fraenkel's method over the present two crystal approach is the potential of locating the single crystal and the detector closer to the x-ray source, with attendant improved spatial resolution (for a given set of crystal planes).

As with any diffracting crystal optic, polarization losses will generally take place at each Bragg reflection. For an unpolarized beam incident on a flat crystal, half the intensity will be in each of two orthogonal polarizations. The diffracted beam will suffer a polarization loss in only one of these directions, leaving

$$p = 1/2 + (1/2)(\cos^2 2\theta)$$

as the polarization factor. For a second crystal which is orthogonally crossed with respect to the first crystal, the net polarization factor should be

$$p = (1/2)(\cos^2 2\theta) + (1/2)(\cos^2 2\theta),$$

$$\text{i.e., } p = \cos^2 2\theta,$$

so that the fraction of the original intensity which is lost to polarization is

$$f = 1 - \cos^2 2\theta.$$

Thus, Bragg angles near  $45^\circ$  are to be avoided, since the crossed crystals act as crossed polarizers at that angle. It is conceivable that this effect may be of use in experiments dealing with Faraday rotation. The more immediate implication is that it is advantageous to be able to choose from a selection of crystals and crystal planes having different  $2d$  spacings, so as to have control over the polarization losses.

The crossed flat crystals may be replaced with two singly curved, convex crystal planes, as shown in Fig.5. The curved crystals behave in the same basic fashion as flat crystals, but their  $R$ ,  $W$ , and  $P$  values may change as a function of curvature (15). Increased dispersion results from the convexity of the diffracting planes. Also, owing to the curvature of the crystals, their positions, both with respect to each

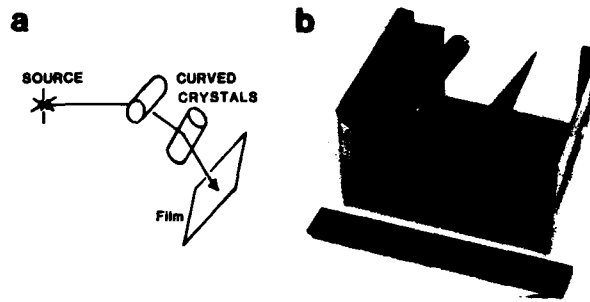


Figure 5. Crossed, convex-crystal imaging spectrograph, schematic (a) and apparatus (b), with cylindrically bent mica crystals.

other and to the film, bear increased significance.

A further consideration is to use crystal planes which are not parallel to the crystal surface (asymmetrical diffraction). It is then possible to have the incident beam strike the surface at a shallow input angle but diffract from the planes at a larger output angle; image magnification in one dimension results (7). The magnification is determined by the input and output angles and therefore is a function of wavelength. For a crossed crystal spectrograph employing two asymmetrical diffractors, two dimensional magnification has been obtained (8). The optics can be reversed to obtain an image reduction. The spatial resolution will still be influenced by the crystal's acceptance angle, which may be quite different than in the symmetrical diffraction case, depending on the magnification (8). Of course, magnification results in a lower intensity per unit area in the diffracted beam.

#### SUMMARY

A new configuration of doubly diffracting, spatially and spectrally resolving x-ray spectrograph has been discussed. In this configuration, the dispersion dimensions of the two crystals are crossed to provide two dimensional imaging. Either Bragg case or Laue case diffractors may be employed; the diffractors may be crystals, Langmuir-Blodgett films, or other synthetic multilayer diffractors. The crossed crystal spectrograph offers a wide selection of  $2d$  spacings, crystal  $R$  values, resolutions, polarization losses, wavelengths, and magnifications.

Work supported by the U.S. Department of Energy.

#### REFERENCES

1. B. Yaakobi, T.C. Bristow and A. Hauer, *Optics Communications*, 14/3, 336-338 (1975).
2. C.M. Dozier, D.J. Nagel and L.S. Birks, *J. of Physics E*, Vol. 10, 1183-1187 (1977).
3. L. Von Hamos, *Z. Kristallog.*, 101, 17 (1939); B. Yaakobi, R.E. Turner, H.W. Schnopper, and P.O. Taylor, *Rev.Sci.Instrum.*, 50/12, 1609-1611 (1979).

4. L.M. Belyaev, A.B. Gil'varg, Yu.A. Mikhailov, S.A. Pikuz, G.V. Sklizkov, A.Ya. Faenov, and S.I. Fedotov, *Sov.J.Quantum Electron* 7/1, 67-70 (1977).
5. L.S. Birks, *X-ray Spectrochemical Analysis*, 2nd ed., Interscience Publishers, New York, 1969, p.30.
6. B.J. Fraenkel, "Appl. Phys. Lett." 36/4, 341-343 (1980); B.J. Fraenkel, *X-ray Spectrometry*, 9/4, 189-94 (1980); see also Fraenkel, these Proceedings.
7. K. Kohra, in *Proceedings of the Sixth International Conference on X-Ray Optics and Microanalysis*, ed. G. Shinoda, K. Kohra and T. Ichinokawa, Univ. of Tokyo Press, 1972, pp.35-45.
8. W.J. Boettinger, H.E. Burdette, and M. Kuriyama, *Rev. Sci. Instrum.* 50/1, 26-30 (1979).
9. H. Azechi, S. Oda, M. Hamano, and T. Sasaki, *Appl. Phys. Lett.* 37/11, 998-1000 (1980).
10. A.J. Burek, D.M. Barrus, and R.L. Blake, *Astropyhs. J.*, 191, 533-543 (1974); see also Blake, these Proceedings.
11. A.H. Compton and S.K. Allison, *X-rays in Theory and Experiment*, D. Van Nostrand, New York, 1935.
12. L.S. Birks, *Electron Probe Microanalysis*, 2nd ed., Wiley-Interscience, New York, 1971, p. 43.
13. J. Vierling, J.V. Gilfrich and L.S. Birks, *Appl. Spectroscopy* 23/4, 342-345 (1969).
14. P. Kirkpatrick and A.V. Baez, *J. Opt. Soc. Amer.* 38, 766 (1948).
15. D.B. Brown and M. Fatemi, *J.Appl.Phys.* 51/5, 2540-2548 (1980).



Robert Whitlock of the Naval Research Laboratory discussing his work crossed crystal imaging with Glen Tirsell of the Lawrence Livermore National Laboratory.

## Monochromatic X-Ray Images of X-Ray Emitting Sources

Benjamin S. Fraenkel

Naval Research Laboratory, Washington, D.C.\*

## ABSTRACT

Simultaneous X-ray reflections are used to obtain monochromatic images from a laser produced plasma. Wavelength range and wavelength resolution are being discussed.

## INTRODUCTION

The possibility of obtaining monochromatic x-ray images of an x-ray source, using double reflections from a crystal, has been demonstrated (1,2). With this method one may expect to obtain multiple, space resolved images of laser produced plasmas, where each image represents a wavelength emitted by the laser plasma. During the past year an effort has been made to develop this method.

## WAVELENGTH RANGE

By cooperation with the N.B.S. through Dr. Deslattes, and by the efforts of Dr. A. Burek, it was shown that monochromatic images of x-ray emitting sources may be taken in the soft x-ray range, beyond 5A. The resolution is dependent on the crystal, and, with suitable crystals, a resolution ( $\lambda/d\lambda$ ) of many thousands may be achieved, even in the long wavelength range.

## PRELIMINARY LASER RESULTS

A group of double reflection x-ray images were obtained on the Pharos II Nd laser (at 1.054  $\mu\text{m}$ ), with about 40J, in a single shot. This was obtained for the He and Li like transitions of sulphur. Geometric adjustment was not optimal, so it is too early to use the images for space resolution of the plasma. However, wavelength resolution was good, compared with the previously obtained spectrum (3). For example, the k and j lines, and the w and i lines were completely resolved.

## REFERENCES

1. B.S. Fraenkel, Appl. Phys. Lett. 36, 341 (1980).
2. B.S. Fraenkel, X-ray Spectrometry, 9, 189 (1980).
3. U. Feldman, G.A. Doschek, D.J. Nagel, R.D. Cowan and R.R. Whitlock, Astroph. J. 192, 213 (1974).

\*On sabbatical from the Racah Institute of Physics, The Hebrew University, Jerusalem, at the Dept. of Physics and Astronomy, University of Maryland.

# Ultra-high-spectral-brightness Excimer Lasers

## as Pump Sources for Coherent Soft X-ray Generation

H. Egger, H. Pummer, T. Srinivasan, and C. K. Rhodes

Department of Physics, University of Illinois at Chicago Circle

P. O. Box 4348, Chicago, Illinois 60680

An intense source of soft x-rays operating in the coherent, narrow-bandwidth, and highly directional mode would meet the needs of an abundance of applications. These include spectroscopy of inner-shell states, diagnostics of high-density plasmas, x-ray holography, and lithography. The development of such sources has been suffering from a lack of excitation sources which meet the severe requirements for pump power in the short-wavelength range.

Rare-gas halide excimer lasers are in principle the ideal devices for applying nonlinear optical processes to the generation of short wavelengths. This is due to the high energy of the primary photon, its tunability, and the small size of the focal spot which is possible with short wavelengths. The exploitation of these features, however, has been hindered by the fact that the spectral and spatial properties of free-running excimer lasers are poor. In the following, we describe a laboratory-scale ArF\* (193 nm) laser system whose spectral and spatial beam properties approach the fundamental limits and whose spectral brightness (the key parameter of optical quality) represents an improvement of  $10^{10}$  over the free-running laser. We also present preliminary results of generating tunable narrow-bandwidth radiation at 64 nm with this system.

The laser system is illustrated schematically in Figure 1. The output of a frequency-stabilized, cw dye laser is pulse-amplified in a three-stage XeF\* pumped dye amplifier, producing a ~10-ns visible pulse with an energy greater than 20 mJ at a repetition rate of up to 10 Hz. The linewidth of these pulses is Fourier transform-limited. Frequency-tripled radiation corresponding to any wavelength within the ArF\* gain profile is readily generated by focusing into a strontium heat pipe, producing ~5-ns third-harmonic pulses with peak power greater than 1 W. This spectrally narrow third-harmonic radiation is subsequently amplified in one double and two single passes through three

discharge-pumped ArF\* amplifiers to produce output pulses ~10 ns in duration and of energies up to 300 mJ.

The bandwidth of the 193-nm pulse is within 20% of the Fourier-transform limit and the beam has a diffraction-limited divergence of  $5 \mu\text{rad} \times 15 \mu\text{rad}$ . Using aspheric f2 optics, focal intensities in excess of  $10^{15} \text{ W/cm}^2$  can be generated. It should be noted that a setup in which the cw dye laser, which now forms the front end of the laser system, is replaced by a 10-psec dye laser, is close to completion in our laboratory. This should increase the attainable focal intensities by almost three orders of magnitude.

This laser can be used in two ways to generate shorter wavelengths. First, a multiphoton transition can be used to populate an atomic or molecular level from which subsequent stimulated emission is possible. Second, the laser light can be converted using harmonic generation and optical mixing. In initial experiments we have generated narrow-bandwidth tunable radiation at 83 nm (the third harmonic of KrF\* 248-nm radiation), 102.7 nm (mixing of two 248-nm photons with one dye-laser photon to  $L_{\beta}$ ), and 64 nm (the third harmonic of 193 nm). The spectral range which can be reached by harmonic generation and mixing in processes involving up to seven photons reaches down to ~30 nm. It seems clear that ultra-high-spectral-brightness excimer lasers will make possible the generation of coherent tunable narrow-bandwidth radiation at all wavelengths between 30 nm and 130 nm.

Support for special equipment for these studies was provided by the Dept. of Energy under contract no. DE-AC02-79ER10350. Additional support was furnished by the Air Force Office of Scientific Research under grant no. AFOSR-79-0130, the National Science Foundation under grant no. PHY78-27610, and the Office of Naval Research.

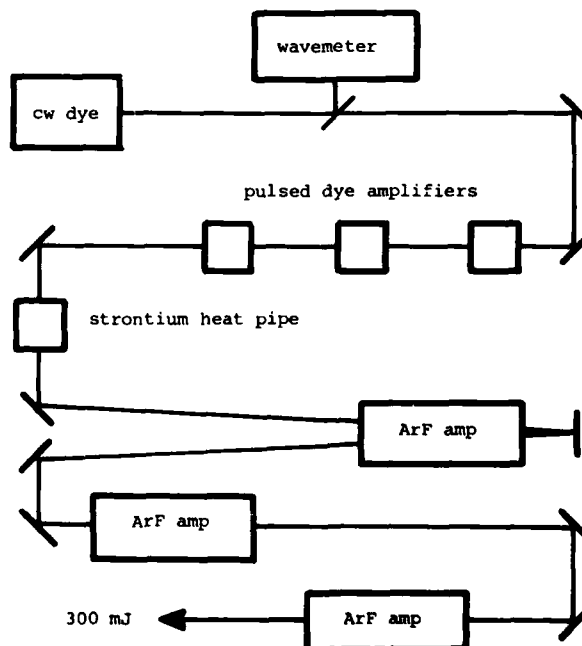


Figure 1. Tunable, ultra-high-spectral-brightness ArF laser

## Appendix

The Atomic Scattering Factor,  $f_1 + if_2$ , for 94 Elements and for the 100 to 2000 eV Photon Energy Region

B. L. Henke, P. Lee, T. J. Tanaka, R. L. Shimabukuro and B. K. Fujikawa

University of Hawaii, Department of Physics and Astronomy, Honolulu, Hawaii 96822

In a recent work,<sup>1</sup> a "state of the art" compilation and fitting of the best available experimental and theoretical photoionization cross sections has been presented for the 30 to 10,000 eV region. Using the quantum dispersion theory, the atomic scattering factors were then uniquely determined from the photoionization cross section data for the low energy x-rays. In Ref. 1, the original data were given at fifty laboratory wavelengths along with compilation references and a description of the fitting procedures. Presented here are the  $f_1$  and  $f_2$  values which have been interpolated at regular intervals.

As discussed in the review papers of these Proceedings by Henke, the  $f_1$  and  $f_2$  parameters may be applied to calculate the low energy x-ray interactions--absorption, scattering, specular and Bragg reflection.

The corresponding value for the photoionization cross section is related to  $f_2$  by  $E\mu(E) = Kf_2$ , where K for a given element is presented at the end of each  $f_1 - f_2$  table in keV-cm<sup>2</sup>/gram units. For  $E\mu(E)$  in eV-barns/atom units, K is equal to  $6.987 \times 10^7$  for all atoms.

The tables are presented here at 125 values of photon energy, E(eV) and wavelength,  $\lambda$ (Å) with logarithmically spaced intervals by truncating to the nearest electron volt the energy as given by

$$E = 100 \times 10^{(N \log 20)/124} \text{ eV.}$$

This expression may be used for convenient computer calculation and plotting of functions of  $f_1$  and  $f_2$  as indexed here by N. ( $f_1$  and  $f_2$  have been precisely interpolated for the truncated E values as listed in these tables.) The approximate K, L and M absorption edge positions are identified within the tables.

<sup>1</sup>"Low Energy X-Ray Interaction Coefficients: Photoionization, Scattering and Reflection," B. L. Henke, P. Lee, T. J. Tanaka, R. L. Shimabukuro and B. K. Fujikawa, Atomic Data and Nuclear Data Tables 27, No. 1, (1982).

ATOMIC SCATTERING FACTOR,  $f_1 + if_2$ 

N	E(eV)	H (1)		He (2)		Li (3)		Be (4)		$\lambda(\text{Å})$
		$f_1$	$f_2$	$f_1$	$f_2$	$f_1$	$f_2$	$f_1$	$f_2$	
0	100	1.02	2.76-02	2.14	4.94-01	2.75	2.34 00	0.45	1.67-01	124.0
1	102	1.02	2.65-02	2.14	4.80-01	2.81	2.25 00	0.23	1.63-01	121.5
2	104	1.02	2.54-02	2.14	4.65-01	2.86	2.17 00	-0.06	1.59-01	119.2
3	107	1.02	2.40-02	2.15	4.46-01	2.92	2.06 00	-0.66	1.54-01	115.9
4	110	1.02	2.26-02	2.15	4.27-01	2.97	1.99 00	-2.90 K	1.49-01	112.7
5	112	1.02	2.18-02	2.15	4.15-01	3.01	1.95 00	-2.98	4.21 00	110.7
6	115	1.02	2.06-02	2.15	3.99-01	3.05	1.89 00	-0.41	4.09 00	107.8
7	118	1.02	1.95-02	2.15	3.83-01	3.08	1.83 00	0.43	3.98 00	105.1
8	121	1.02	1.85-02	2.15	3.69-01	3.12	1.76 00	0.96	3.87 00	102.5
9	124	1.02	1.76-02	2.14	3.55-01	3.15	1.70 00	1.33	3.77 00	100.0
10	127	1.02	1.67-02	2.14	3.42-01	3.17	1.65 00	1.64	3.67 00	97.6
11	130	1.02	1.59-02	2.14	3.30-01	3.20	1.60 00	1.90	3.58 00	95.4
12	133	1.02	1.52-02	2.14	3.18-01	3.22	1.55 00	2.12	3.49 00	93.2
13	136	1.02	1.45-02	2.14	3.07-01	3.24	1.49 00	2.29	3.40 00	91.2
14	140	1.01	1.36-02	2.14	2.93-01	3.25	1.43 00	2.51	3.29 00	88.6
15	143	1.01	1.30-02	2.14	2.83-01	3.27	1.38 00	2.65	3.21 00	86.7
16	147	1.01	1.22-02	2.14	2.71-01	3.28	1.32 00	2.82	3.11 00	84.3
17	150	1.01	1.17-02	2.14	2.62-01	3.29	1.29 00	2.93	3.05 00	82.7
18	154	1.01	1.11-02	2.13	2.51-01	3.30	1.24 00	3.07	2.96 00	80.5
19	158	1.01	1.05-02	2.13	2.41-01	3.31	1.19 00	3.21	2.86 00	78.5
20	162	1.01	9.94-03	2.13	2.31-01	3.31	1.15 00	3.33	2.77 00	76.5
21	166	1.01	9.43-03	2.13	2.21-01	3.32	1.11 00	3.44	2.69 00	74.7
22	170	1.01	8.95-03	2.13	2.13-01	3.32	1.07 00	3.53	2.61 00	72.9
23	174	1.01	8.51-03	2.12	2.04-01	3.32	1.03 00	3.61	2.53 00	71.3
24	178	1.01	8.09-03	2.12	1.97-01	3.33	9.97-01	3.68	2.46 00	69.7
25	182	1.01	7.71-03	2.12	1.89-01	3.33	9.65-01	3.75	2.40 00	68.1
26	187	1.01	7.26-03	2.12	1.81-01	3.33	9.22-01	3.83	2.30 00	66.3
27	191	1.01	6.93-03	2.12	1.74-01	3.33	8.88-01	3.88	2.22 00	64.9
28	196	1.01	6.55-03	2.11	1.66-01	3.33	8.51-01	3.95	2.15 00	63.3
29	201	1.01	6.20-03	2.11	1.59-01	3.33	8.18-01	4.00	2.08 00	61.7
30	206	1.01	5.87-03	2.11	1.52-01	3.32	7.87-01	4.04	2.02 00	60.2
31	211	1.01	5.57-03	2.11	1.46-01	3.32	7.57-01	4.08	1.96 00	58.8
32	216	1.01	5.29-03	2.10	1.40-01	3.32	7.28-01	4.12	1.89 00	57.4
33	221	1.01	5.03-03	2.10	1.34-01	3.32	6.99-01	4.15	1.83 00	56.1
34	227	1.01	4.74-03	2.10	1.28-01	3.31	6.67-01	4.18	1.76 00	54.6
35	232	1.01	4.52-03	2.10	1.23-01	3.31	6.42-01	4.20	1.70 00	53.4
36	238	1.01	4.27-03	2.09	1.17-01	3.31	6.14-01	4.23	1.64 00	52.1
37	244	1.01	4.05-03	2.09	1.12-01	3.30	5.88-01	4.25	1.58 00	50.8
38	250	1.01	3.84-03	2.09	1.07-01	3.30	5.64-01	4.27	1.52 00	49.6
39	256	1.01	3.64-03	2.09	1.02-01	3.29	5.41-01	4.28	1.47 00	48.4
40	262	1.01	3.46-03	2.09	9.80-02	3.29	5.19-01	4.30	1.42 00	47.3
41	269	1.01	3.27-03	2.08	9.33-02	3.28	4.96-01	4.31	1.36 00	46.1
42	275	1.01	3.11-03	2.08	8.93-02	3.28	4.77-01	4.32	1.32 00	45.1
43	282	1.01	2.95-03	2.08	8.48-02	3.27	4.56-01	4.33	1.27 00	44.0
44	289	1.00	2.79-03	2.08	8.05-02	3.27	4.36-01	4.34	1.22 00	42.9
45	296	1.00	2.65-03	2.07	7.66-02	3.26	4.17-01	4.34	1.17 00	41.9
46	303	1.00	2.52-03	2.07	7.30-02	3.26	3.99-01	4.35	1.13 00	40.9
47	311	1.00	2.37-03	2.07	6.91-02	3.25	3.80-01	4.35	1.08 00	39.9
48	318	1.00	2.26-03	2.07	6.60-02	3.25	3.65-01	4.36	1.05 00	39.0
49	326	1.00	2.13-03	2.07	6.27-02	3.24	3.48-01	4.36	1.00 00	38.0
50	334	1.00	2.02-03	2.06	5.96-02	3.24	3.33-01	4.36	9.67-01	37.1
51	342	1.00	1.91-03	2.06	5.67-02	3.23	3.19-01	4.36	9.30-01	36.3
52	351	1.00	1.80-03	2.06	5.37-02	3.23	3.04-01	4.36	8.92-01	35.3
53	359	1.00	1.71-03	2.06	5.13-02	3.22	2.91-01	4.36	8.61-01	34.5
54	368	1.00	1.62-03	2.06	4.87-02	3.21	2.78-01	4.36	8.27-01	33.7
55	377	1.00	1.53-03	2.06	4.63-02	3.21	2.66-01	4.35	7.96-01	32.9
56	386	1.00	1.45-03	2.05	4.41-02	3.20	2.54-01	4.35	7.66-01	32.1
57	396	1.00	1.37-03	2.05	4.17-02	3.20	2.42-01	4.35	7.34-01	31.3
58	406	1.00	1.29-03	2.05	3.95-02	3.19	2.31-01	4.34	7.02-01	30.5
59	415	1.00	1.23-03	2.05	3.77-02	3.19	2.21-01	4.34	6.75-01	29.9
60	426	1.00	1.16-03	2.05	3.56-02	3.18	2.10-01	4.34	6.44-01	29.1
61	436	1.00	1.10-03	2.05	3.39-02	3.18	2.01-01	4.33	6.17-01	28.4
62	447	1.00	1.04-03	2.04	3.21-02	3.17	1.91-01	4.33	5.90-01	27.7
63	458	1.00	9.84-04	2.04	3.05-02	3.17	1.82-01	4.32	5.65-01	27.1
64	469	1.00	9.32-04	2.04	2.90-02	3.16	1.74-01	4.32	5.41-01	26.4

N	E(eV)	H (1) Hydrogen		He (2) Helium		Li (3) Lithium		Be (4) Beryllium		$\lambda(\text{Å})$
		$f_1$	$f_2$	$f_1$	$f_2$	$f_1$	$f_2$	$f_1$	$f_2$	
65	480	1.00	8.84-04	2.04	2.75-02	3.16	1.66-01	4.31	5.19-01	25.83
66	492	1.00	8.36-04	2.04	2.61-02	3.15	1.58-01	4.30	4.96-01	25.20
67	504	1.00	7.91-04	2.04	2.48-02	3.15	1.51-01	4.30	4.75-01	24.60
68	516	1.00	7.50-04	2.04	2.36-02	3.14	1.44-01	4.29	4.55-01	24.03
69	529	1.00	7.08-04	2.03	2.24-02	3.14	1.37-01	4.29	4.35-01	23.44
70	542	1.00	6.70-04	2.03	2.12-02	3.14	1.30-01	4.28	4.16-01	22.87
71	555	1.00	6.35-04	2.03	2.02-02	3.13	1.24-01	4.27	3.99-01	22.34
72	569	1.00	6.00-04	2.03	1.91-02	3.13	1.18-01	4.27	3.81-01	21.79
73	583	1.00	5.68-04	2.03	1.81-02	3.12	1.12-01	4.26	3.64-01	21.27
74	597	1.00	5.38-04	2.03	1.72-02	3.12	1.07-01	4.26	3.48-01	20.77
75	612	1.00	5.08-04	2.03	1.63-02	3.12	1.02-01	4.25	3.32-01	20.26
76	627	1.00	4.81-04	2.03	1.55-02	3.11	9.71-02	4.24	3.18-01	19.77
77	642	1.00	4.55-04	2.03	1.47-02	3.11	9.24-02	4.24	3.04-01	19.31
78	658	1.00	4.30-04	2.02	1.38-02	3.11	8.75-02	4.23	2.89-01	18.84
79	674	1.00	4.06-04	2.02	1.31-02	3.10	8.29-02	4.23	2.75-01	18.39
80	690	1.00	3.85-04	2.02	1.24-02	3.10	7.93-02	4.22	2.64-01	17.97
81	707	1.00	3.64-04	2.02	1.19-02	3.10	7.58-02	4.21	2.53-01	17.54
82	725	1.00	3.43-04	2.02	1.12-02	3.09	7.19-02	4.21	2.41-01	17.10
83	742	1.00	3.25-04	2.02	1.07-02	3.09	6.86-02	4.20	2.30-01	16.71
84	760	1.00	3.07-04	2.02	1.01-02	3.09	6.52-02	4.20	2.20-01	16.31
85	779	1.00	2.90-04	2.02	9.60-03	3.08	6.20-02	4.19	2.09-01	15.92
86	798	1.00	2.74-04	2.02	9.10-03	3.08	5.89-02	4.19	2.00-01	15.54
87	818	1.00	2.59-04	2.02	8.62-03	3.08	5.60-02	4.18	1.90-01	15.16
88	838	1.00	2.45-04	2.02	8.17-03	3.07	5.32-02	4.18	1.81-01	14.79
89	858	1.00	2.32-04	2.02	7.76-03	3.07	5.07-02	4.17	1.73-01	14.45
90	879	1.00	2.19-04	2.02	7.37-03	3.07	4.82-02	4.17	1.65-01	14.10
91	901	1.00	2.07-04	2.01	6.99-03	3.07	4.58-02	4.16	1.58-01	13.76
92	923	1.00	1.96-04	2.01	6.64-03	3.06	4.35-02	4.16	1.50-01	13.43
93	945	1.00	1.85-04	2.01	6.32-03	3.06	4.14-02	4.15	1.44-01	13.12
94	968	1.00	1.75-04	2.01	6.00-03	3.06	3.94-02	4.15	1.37-01	12.81
95	992	1.00	1.66-04	2.01	5.70-03	3.06	3.74-02	4.14	1.30-01	12.50
96	1016	1.00	1.57-04	2.01	5.42-03	3.06	3.56-02	4.14	1.24-01	12.20
97	1041	1.00	1.48-04	2.01	5.13-03	3.05	3.38-02	4.13	1.18-01	11.91
98	1067	1.00	1.40-04	2.01	4.86-03	3.05	3.21-02	4.13	1.12-01	11.62
99	1093	1.00	1.32-04	2.01	4.61-03	3.05	3.05-02	4.12	1.07-01	11.34
100	1119	1.00	1.25-04	2.01	4.38-03	3.05	2.91-02	4.12	1.02-01	11.08
101	1147	1.00	1.18-04	2.01	4.15-03	3.05	2.76-02	4.12	9.69-02	10.81
102	1175	1.00	1.12-04	2.01	3.93-03	3.05	2.62-02	4.11	9.22-02	10.55
103	1204	1.00	1.06-04	2.01	3.73-03	3.04	2.49-02	4.11	8.77-02	10.30
104	1233	1.00	9.98-05	2.01	3.54-03	3.04	2.37-02	4.11	8.35-02	10.06
105	1263	1.00	9.43-05	2.01	3.36-03	3.04	2.25-02	4.10	7.95-02	9.82
106	1294	1.00	8.91-05	2.01	3.19-03	3.04	2.14-02	4.10	7.56-02	9.58
107	1326	1.00	8.41-05	2.01	3.03-03	3.04	2.03-02	4.10	7.19-02	9.35
108	1358	1.00	7.95-05	2.01	2.88-03	3.04	1.93-02	4.09	6.85-02	9.13
109	1392	1.00	7.50-05	2.01	2.73-03	3.03	1.83-02	4.09	6.51-02	8.91
110	1426	1.00	7.08-05	2.01	2.60-03	3.03	1.74-02	4.09	6.20-02	8.69
111	1460	1.00	6.70-05	2.01	2.47-03	3.03	1.65-02	4.08	5.91-02	8.49
112	1496	1.00	6.32-05	2.01	2.34-03	3.03	1.57-02	4.08	5.62-02	8.29
113	1533	1.00	5.97-05	2.01	2.21-03	3.03	1.48-02	4.08	5.34-02	8.09
114	1570	1.00	5.64-05	2.01	2.10-03	3.03	1.41-02	4.07	5.08-02	7.90
115	1609	1.00	5.32-05	2.01	1.98-03	3.03	1.34-02	4.07	4.83-02	7.71
116	1648	1.00	5.03-05	2.01	1.88-03	3.03	1.27-02	4.07	4.59-02	7.52
117	1688	1.00	4.76-05	2.01	1.78-03	3.03	1.20-02	4.07	4.37-02	7.34
118	1730	1.00	4.49-05	2.00	1.68-03	3.02	1.14-02	4.06	4.15-02	7.17
119	1772	1.00	4.24-05	2.00	1.59-03	3.02	1.08-02	4.06	3.95-02	7.00
120	1815	1.00	4.01-05	2.00	1.50-03	3.02	1.02-02	4.06	3.75-02	6.83
121	1860	1.00	3.78-05	2.00	1.41-03	3.02	9.70-03	4.06	3.56-02	6.67
122	1905	1.00	3.57-05	2.00	1.34-03	3.02	9.20-03	4.06	3.38-02	6.51
123	1952	1.00	3.37-05	2.00	1.26-03	3.02	8.71-03	4.05	3.21-02	6.35
124	2000	1.00	3.18-05	2.00	1.19-03	3.02	8.25-03	4.05	3.05-02	6.20

$\frac{E_H(E)}{f_2}$	41725	10507	6059.	4667.	$\frac{\text{keV-cm}^2}{\text{gram}}$
Atomic Weight	1.008	4.003	6.941	9.012	amu

ATOMIC SCATTERING FACTOR,  $f_1 + if_2$ 

N	E(eV)	B (5)		C (6)		N (7)		O (8)		$\lambda(\text{Å})$
		$f_1$	$f_2$	$f_1$	$f_2$	$f_1$	$f_2$	$f_1$	$f_2$	
0	100	2.90	3.47-01	4.12	6.63-01	5.22	1.45 00	6.13	2.50 00	124.0
1	102	2.89	3.39-01	4.12	6.46-01	5.23	1.42 00	6.16	2.43 00	121.5
2	104	2.88	3.30-01	4.13	6.30-01	5.24	1.38 00	6.19	2.38 00	119.2
3	107	2.86	3.19-01	4.11	6.07-01	5.26	1.34 00	6.22	2.29 00	115.9
4	110	2.84	3.09-01	4.13	5.85-01	5.27	1.29 00	6.25	2.22 00	112.7
5	112	2.82	3.04-01	4.13	5.76-01	5.28	1.27 00	6.27	2.17 00	110.7
6	115	2.80	2.95-01	4.08	5.64-01	5.29	1.23 00	6.30	2.10 00	107.8
7	118	2.77	2.86-01	4.12	5.52-01	5.29	1.19 00	6.32	2.03 00	105.1
8	121	2.75	2.77-01	4.12	5.41-01	5.30	1.16 00	6.34	1.97 00	102.5
9	124	2.72	2.69-01	4.11	5.30-01	5.30	1.12 00	6.35	1.91 00	100.0
10	127	2.68	2.61-01	4.11	5.20-01	5.31	1.09 00	6.37	1.85 00	97.6
11	130	2.65	2.53-01	4.10	5.10-01	5.31	1.06 00	6.39	1.80 00	95.4
12	133	2.61	2.46-01	4.04	4.96-01	5.32	1.03 00	6.41	1.75 00	93.2
13	136	2.57	2.39-01	4.09	4.83-01	5.32	1.00 00	6.41	1.70 00	91.2
14	140	2.51	2.30-01	4.08	4.66-01	5.32	9.67-01	6.43	1.64 00	88.6
15	143	2.46	2.24-01	4.07	4.54-01	5.32	9.41-01	6.43	1.59 00	86.7
16	147	2.38	2.16-01	4.02	4.39-01	5.32	9.09-01	6.45	1.54 00	84.3
17	150	2.32	2.11-01	4.02	4.28-01	5.32	8.87-01	6.45	1.50 00	82.7
18	154	2.22	2.04-01	4.02	4.15-01	5.31	8.58-01	6.46	1.45 00	80.5
19	158	2.11	1.96-01	4.01	4.02-01	5.31	8.31-01	6.46	1.40 00	78.5
20	162	1.98	1.88-01	3.99	3.90-01	5.31	8.04-01	6.47	1.36 00	76.5
21	166	1.82	1.80-01	3.97	3.78-01	5.30	7.79-01	6.47	1.31 00	74.7
22	170	1.62	1.74-01	3.95	3.66-01	5.30	7.55-01	6.47	1.27 00	72.9
23	174	1.34	1.68-01	3.89	3.55-01	5.29	7.33-01	6.47	1.23 00	71.3
24	178	1.02	1.64-01	3.90	3.45-01	5.28	7.11-01	6.47	1.20 00	69.7
25	182	0.39	1.59-01	3.83	3.35-01	5.27	6.91-01	6.47	1.16 00	68.1
26	187	-2.43	1.53-01	3.85	3.24-01	5.26	6.67-01	6.47	1.12 00	66.3
27	191	-0.55	4.18 00	3.80	3.15-01	5.25	6.49-01	6.47	1.08 00	64.9
28	196	1.08	4.06 00	3.76	3.05-01	5.24	6.27-01	6.46	1.04 00	63.3
29	201	1.74	3.95 00	3.73	2.95-01	5.23	6.06-01	6.46	1.01 00	61.7
30	206	2.19	3.85 00	3.69	2.85-01	5.21	5.86-01	6.45	9.75-01	60.2
31	211	2.55	3.76 00	3.64	2.75-01	5.20	5.68-01	6.45	9.45-01	58.8
32	216	2.83	3.65 00	3.55	2.66-01	5.18	5.50-01	6.44	9.14-01	57.4
33	221	3.06	3.54 00	3.52	2.57-01	5.17	5.33-01	6.43	8.84-01	56.1
34	227	3.31	3.42 00	3.43	2.47-01	5.15	5.14-01	6.42	8.50-01	54.6
35	232	3.49	3.32 00	3.35	2.40-01	5.13	4.98-01	6.41	8.24-01	53.4
36	238	3.70	3.21 00	3.24	2.31-01	5.10	4.81-01	6.40	7.94-01	52.1
37	244	3.88	3.11 00	3.11	2.23-01	5.08	4.65-01	6.39	7.66-01	50.8
38	250	4.04	3.01 00	2.96	2.15-01	5.05	4.50-01	6.37	7.39-01	49.6
39	256	4.18	2.92 00	2.76	2.08-01	5.02	4.35-01	6.36	7.14-01	48.4
40	262	4.29	2.83 00	2.51	2.01-01	4.99	4.21-01	6.35	6.90-01	47.3
41	269	4.41	2.74 00	2.13	1.94-01	4.96	4.06-01	6.33	6.64-01	46.1
42	275	4.51	2.66 00	1.27	1.88-01	4.92	3.94-01	6.32	6.43-01	45.1
43	282	4.60	2.57 00	-0.73	1.81-01	4.88	3.80-01	6.30	6.20-01	44.0
44	289	4.68	2.48 00	-0.11	4.48 00	4.83	3.67-01	6.28	5.97-01	42.9
45	296	4.76	2.39 00	2.17	4.33 00	4.78	3.55-01	6.26	5.76-01	41.9
46	303	4.82	2.32 00	2.79	4.18 00	4.72	3.43-01	6.24	5.56-01	40.9
47	311	4.88	2.23 00	3.46	4.02 00	4.65	3.31-01	6.22	5.35-01	39.9
48	318	4.93	2.16 00	3.66	3.89 00	4.58	3.20-01	6.19	5.17-01	39.0
49	326	4.98	2.08 00	3.98	3.75 00	4.49	3.09-01	6.16	4.98-01	38.0
50	334	5.03	2.01 00	4.25	3.62 00	4.39	2.99-01	6.13	4.81-01	37.1
51	342	5.07	1.94 00	4.48	3.50 00	4.28	2.89-01	6.10	4.64-01	36.3
52	351	5.11	1.87 00	4.70	3.37 00	4.11	2.78-01	6.06	4.46-01	35.3
53	359	5.15	1.81 00	4.87	3.26 00	3.93	2.69-01	6.03	4.31-01	34.5
54	368	5.18	1.75 00	5.04	3.14 00	3.69	2.60-01	5.98	4.15-01	33.7
55	377	5.21	1.69 00	5.19	3.03 00	3.34	2.51-01	5.94	4.01-01	32.9
56	386	5.23	1.63 00	5.31	2.93 00	2.69	2.42-01	5.89	3.87-01	32.1
57	396	5.25	1.57 00	5.49	2.82 00	1.22	2.34-01	5.84	3.72-01	31.3
58	406	5.27	1.51 00	5.52	2.72 00	0.96	3.96 00	5.77	3.57-01	30.5
59	415	5.29	1.46 00	5.60	2.63 00	3.10	3.90 00	5.70	3.45-01	29.9
60	426	5.30	1.40 00	5.69	2.53 00	3.85	3.84 00	5.62	3.31-01	29.1
61	436	5.31	1.35 00	5.76	2.45 00	4.34	3.78 00	5.53	3.20-01	28.4
62	447	5.33	1.30 00	5.84	2.36 00	4.76	3.72 00	5.42	3.08-01	27.7
63	458	5.33	1.25 00	5.91	2.28 00	5.10	3.67 00	5.30	2.96-01	27.1
64	469	5.34	1.20 00	5.95	2.20 00	5.37	3.55 00	5.13	2.85-01	26.4



N	E(eV)	B (5) Boron		C (6) Carbon		N (7) Nitrogen		O (8) Oxygen		$\lambda$ (Å)
		$f_1$	$f_2$	$f_1$	$f_2$	$f_1$	$f_2$	$f_1$	$f_2$	
65	480	5.35	1.16 00	6.00	2.12 00	5.61	3.43 00	4.94	2.75-01	25.83
66	492	5.35	1.11 00	6.05	2.04 00	5.82	3.32 00	4.67	2.65-01	25.20
67	504	5.35	1.07 00	6.09	1.97 00	5.99	3.20 00	4.29	2.55-01	24.60
68	516	5.36	1.03 00	6.13	1.90 00	6.14	3.10 00	3.62	2.46-01	24.03
69	529	5.36	9.87-01	6.16	1.83 00	6.27	2.99 00	1.37 K	2.37-01	23.44
70	542	5.36	9.47-01	6.19	1.77 00	6.38	2.89 00	3.23	4.43 00	22.87
71	555	5.36	9.09-01	6.22	1.70 00	6.48	2.80 00	4.33	4.28 00	22.34
72	569	5.36	8.73-01	6.24	1.64 00	6.58	2.70 00	5.03	4.12 00	21.79
73	583	5.36	8.38-01	6.26	1.57 00	6.67	2.60 00	5.54	3.98 00	21.27
74	597	5.36	8.05-01	6.28	1.52 00	6.74	2.51 00	5.91	3.85 00	20.77
75	612	5.35	7.71-01	6.30	1.46 00	6.82	2.42 00	6.25	3.72 00	20.26
76	627	5.35	7.40-01	6.31	1.40 00	6.89	2.34 00	6.53	3.60 00	19.77
77	642	5.35	7.09-01	6.32	1.35 00	6.95	2.25 00	6.75	3.47 00	19.31
78	658	5.34	6.76-01	6.33	1.29 00	7.00	2.16 00	6.93	3.34 00	18.84
79	674	5.34	6.45-01	6.34	1.24 00	7.05	2.08 00	7.09	3.21 00	18.39
80	690	5.33	6.21-01	6.35	1.20 00	7.09	2.01 00	7.23	3.11 00	17.97
81	707	5.33	5.97-01	6.35	1.16 00	7.13	1.95 00	7.35	3.02 00	17.54
82	725	5.32	5.71-01	6.36	1.11 00	7.16	1.87 00	7.46	2.90 00	17.10
83	742	5.32	5.48-01	6.36	1.07 00	7.19	1.80 00	7.56	2.80 00	16.71
84	760	5.31	5.24-01	6.36	1.02 00	7.22	1.74 00	7.65	2.71 00	16.31
85	779	5.31	5.02-01	6.37	9.80-01	7.24	1.67 00	7.73	2.61 00	15.92
86	798	5.30	4.80-01	6.37	9.40-01	7.26	1.60 00	7.81	2.51 00	15.54
87	818	5.30	4.59-01	6.37	9.01-01	7.28	1.54 00	7.88	2.41 00	15.16
88	838	5.29	4.39-01	6.37	8.64-01	7.30	1.48 00	7.94	2.31 00	14.79
89	858	5.29	4.20-01	6.36	8.29-01	7.32	1.42 00	8.00	2.23 00	14.45
90	879	5.28	4.01-01	6.36	7.95-01	7.33	1.36 00	8.05	2.15 00	14.10
91	901	5.27	3.83-01	6.36	7.61-01	7.34	1.31 00	8.09	2.07 00	13.76
92	923	5.27	3.66-01	6.36	7.30-01	7.35	1.26 00	8.13	2.00 00	13.43
93	945	5.26	3.50-01	6.35	7.00-01	7.36	1.21 00	8.16	1.93 00	13.12
94	968	5.25	3.35-01	6.35	6.71-01	7.36	1.16 00	8.19	1.85 00	12.81
95	992	5.25	3.20-01	6.34	6.42-01	7.36	1.12 00	8.22	1.78 00	12.50
96	1016	5.24	3.06-01	6.34	6.16-01	7.37	1.07 00	8.25	1.71 00	12.20
97	1041	5.24	2.92-01	6.33	5.90-01	7.37	1.03 00	8.27	1.64 00	11.91
98	1067	5.23	2.79-01	6.33	5.64-01	7.37	9.86-01	8.29	1.58 00	11.62
99	1093	5.22	2.66-01	6.32	5.40-01	7.37	9.46-01	8.31	1.52 00	11.34
100	1119	5.22	2.54-01	6.32	5.17-01	7.37	9.09-01	8.32	1.46 00	11.08
101	1147	5.21	2.42-01	6.31	4.94-01	7.37	8.71-01	8.33	1.40 00	10.81
102	1175	5.21	2.31-01	6.30	4.73-01	7.37	8.35-01	8.35	1.34 00	10.55
103	1204	5.20	2.21-01	6.30	4.52-01	7.37	8.01-01	8.36	1.29 00	10.30
104	1233	5.20	2.11-01	6.29	4.33-01	7.36	7.68-01	8.36	1.24 00	10.06
105	1263	5.19	2.01-01	6.29	4.14-01	7.36	7.37-01	8.37	1.19 00	9.82
106	1294	5.18	1.92-01	6.28	3.96-01	7.36	7.05-01	8.37	1.14 00	9.58
107	1326	5.18	1.83-01	6.27	3.78-01	7.35	6.74-01	8.38	1.10 00	9.35
108	1358	5.17	1.75-01	6.27	3.62-01	7.35	6.46-01	8.38	1.05 00	9.13
109	1392	5.17	1.66-01	6.26	3.45-01	7.34	6.17-01	8.38	1.01 00	8.91
110	1426	5.16	1.59-01	6.25	3.30-01	7.34	5.91-01	8.38	9.69-01	8.69
111	1460	5.16	1.52-01	6.25	3.16-01	7.33	5.66-01	8.38	9.31-01	8.49
112	1496	5.15	1.44-01	6.24	3.01-01	7.33	5.42-01	8.38	8.93-01	8.29
113	1533	5.15	1.38-01	6.24	2.88-01	7.32	5.18-01	8.38	8.56-01	8.09
114	1570	5.14	1.31-01	6.23	2.75-01	7.31	4.96-01	8.37	8.20-01	7.90
115	1609	5.14	1.25-01	6.22	2.62-01	7.31	4.74-01	8.37	7.86-01	7.71
116	1648	5.14	1.19-01	6.22	2.51-01	7.30	4.53-01	8.37	7.53-01	7.52
117	1688	5.13	1.14-01	6.21	2.39-01	7.30	4.34-01	8.36	7.22-01	7.34
118	1730	5.13	1.08-01	6.21	2.28-01	7.29	4.14-01	8.36	6.91-01	7.17
119	1772	5.12	1.03-01	6.20	2.18-01	7.28	3.96-01	8.36	6.62-01	7.00
120	1815	5.12	9.82-02	6.20	2.08-01	7.27	3.79-01	8.35	6.34-01	6.83
121	1860	5.11	9.34-02	6.19	1.99-01	7.27	3.62-01	8.34	6.07-01	6.67
122	1905	5.11	8.90-02	6.18	1.90-01	7.26	3.46-01	8.34	5.82-01	6.51
123	1952	5.11	8.47-02	6.18	1.81-01	7.26	3.30-01	8.33	5.57-01	6.35
124	2000	5.10	8.07-02	6.17	1.73-01	7.25	3.15-01	8.33	5.33-01	6.20

$\frac{E_p(E)}{F_2}$	3890.	3502.	3003.	2629.	$\frac{\text{keV-cm}^2}{\text{gram}}$
Atomic Weight	10.81	12.01	14.01	16.00	amu

ATOMIC SCATTERING FACTOR,  $f_1 + if_2$ 

N	E (eV)	F (9)		Ne (10)		Na (11)		Mg (12)		$\lambda$ (Å)
		$f_1$	$f_2$	$f_1$	$f_2$	$f_1$	$f_2$	$f_1$	$f_2$	
0	100	6.71	3.95 00	6.21	5.50 00	6.23	7.70 00	3.73	7.54 00	124.0
1	102	6.78	3.86 00	6.36	5.42 00	6.42	7.58 00	4.11	7.58 00	121.5
2	104	6.84	3.78 00	6.46	5.34 00	6.59	7.46 00	4.42	7.66 00	119.2
3	107	6.91	3.67 00	6.58	5.23 00	6.83	7.29 00	4.84	7.87 00	115.9
4	110	6.98	3.56 00	6.72	5.27 00	7.04	7.14 00	5.21	8.04 00	112.7
5	112	7.02	3.49 00	6.90	5.30 00	7.16	7.03 00	5.44	8.15 00	110.7
6	115	7.08	3.39 00	7.16	5.15 00	7.34	6.89 00	5.76	8.28 00	107.8
7	118	7.13	3.29 00	7.35	4.97 00	7.51	6.75 00	6.07	8.19 00	105.1
8	121	7.18	3.21 00	7.49	4.75 00	7.67	6.61 00	6.36	8.10 00	102.5
9	124	7.22	3.12 00	7.52	4.55 00	7.81	6.48 00	6.64	7.90 00	100.0
10	127	7.26	3.04 00	7.56	4.46 00	7.96	6.36 00	6.92	7.61 00	97.6
11	130	7.30	2.96 00	7.60	4.39 00	8.10	6.24 00	7.21	7.34 00	95.4
12	133	7.34	2.88 00	7.67	4.32 00	8.23	6.10 00	7.50	7.32 00	93.2
13	136	7.37	2.81 00	7.74	4.24 00	8.34	5.97 00	7.72	7.30 00	91.2
14	140	7.41	2.71 00	7.83	4.13 00	8.48	5.81 00	7.99	7.26 00	88.6
15	143	7.43	2.64 00	7.89	4.05 00	8.58	5.69 00	8.18	7.23 00	86.7
16	147	7.46	2.55 00	7.96	3.95 00	8.69	5.53 00	8.40	7.18 00	84.3
17	150	7.48	2.49 00	8.01	3.89 00	8.77	5.43 00	8.56	7.13 00	82.7
18	154	7.50	2.41 00	8.10	3.79 00	8.87	5.29 00	8.75	7.06 00	80.5
19	158	7.53	2.34 00	8.17	3.69 00	8.97	5.16 00	8.93	7.00 00	78.5
20	162	7.54	2.27 00	8.23	3.59 00	9.06	5.02 00	9.11	6.92 00	76.5
21	166	7.56	2.20 00	8.28	3.49 00	9.15	4.89 00	9.27	6.81 00	74.7
22	170	7.57	2.13 00	8.33	3.40 00	9.22	4.77 00	9.41	6.71 00	72.9
23	174	7.58	2.07 00	8.37	3.32 00	9.28	4.65 00	9.53	6.61 00	71.3
24	178	7.59	2.01 00	8.41	3.24 00	9.35	4.54 00	9.65	6.49 00	69.7
25	182	7.60	1.95 00	8.46	3.17 00	9.40	4.43 00	9.76	6.35 00	68.1
26	187	7.61	1.88 00	8.51	3.06 00	9.48	4.30 00	9.89	6.18 00	66.3
27	191	7.62	1.83 00	8.55	2.97 00	9.54	4.20 00	9.99	6.05 00	64.9
28	196	7.62	1.77 00	8.57	2.88 00	9.60	4.06 00	10.10	5.87 00	63.3
29	201	7.63	1.71 00	8.60	2.79 00	9.65	3.93 00	10.19	5.69 00	61.7
30	206	7.63	1.66 00	8.63	2.71 00	9.69	3.81 00	10.28	5.52 00	60.2
31	211	7.63	1.60 00	8.66	2.64 00	9.73	3.69 00	10.37	5.34 00	58.8
32	216	7.63	1.55 00	8.69	2.55 00	9.76	3.58 00	10.44	5.16 00	57.4
33	221	7.63	1.50 00	8.71	2.47 00	9.79	3.48 00	10.51	4.98 00	56.1
34	227	7.63	1.45 00	8.73	2.38 00	9.82	3.36 00	10.53	4.81 00	54.6
35	232	7.63	1.41 00	8.74	2.31 00	9.84	3.27 00	10.63	4.68 00	53.4
36	238	7.62	1.36 00	8.75	2.23 00	9.87	3.16 00	10.69	4.55 00	52.1
37	244	7.62	1.31 00	8.76	2.15 00	9.89	3.06 00	10.74	4.41 00	50.8
38	250	7.61	1.27 00	8.77	2.08 00	9.91	2.96 00	10.79	4.29 00	49.6
39	256	7.61	1.22 00	8.78	2.01 00	9.92	2.87 00	10.83	4.17 00	48.4
40	262	7.60	1.19 00	8.78	1.95 00	9.93	2.78 00	10.87	4.06 00	47.3
41	269	7.59	1.14 00	8.78	1.88 00	9.95	2.68 00	10.90	3.95 00	46.1
42	275	7.58	1.11 00	8.79	1.82 00	9.95	2.60 00	10.93	3.86 00	45.1
43	282	7.57	1.07 00	8.79	1.75 00	9.96	2.52 00	10.96	3.76 00	44.0
44	289	7.56	1.03 00	8.79	1.69 00	9.97	2.43 00	10.99	3.67 00	42.9
45	296	7.55	9.95-01	8.79	1.63 00	9.97	2.35 00	11.01	3.58 00	41.9
46	303	7.54	9.62-01	8.78	1.57 00	9.97	2.28 00	11.03	3.50 00	40.9
47	311	7.52	9.25-01	8.77	1.51 00	9.97	2.20 00	11.05	3.39 00	39.9
48	318	7.51	8.96-01	8.77	1.46 00	9.98	2.13 00	11.07	3.29 00	39.0
49	326	7.49	8.63-01	8.76	1.40 00	9.97	2.06 00	11.08	3.19 00	38.0
50	334	7.48	8.33-01	8.75	1.35 00	9.97	1.99 00	11.09	3.08 00	37.1
51	342	7.46	8.04-01	8.74	1.31 00	9.97	1.92 00	11.10	2.99 00	36.3
52	351	7.44	7.73-01	8.72	1.25 00	9.96	1.85 00	11.10	2.89 00	35.3
53	359	7.42	7.48-01	8.71	1.21 00	9.96	1.79 00	11.11	2.80 00	34.5
54	368	7.40	7.21-01	8.70	1.17 00	9.95	1.73 00	11.11	2.71 00	33.7
55	377	7.38	6.95-01	8.68	1.12 00	9.94	1.67 00	11.11	2.63 00	32.9
56	386	7.35	6.71-01	8.67	1.08 00	9.93	1.61 00	11.11	2.55 00	32.1
57	396	7.33	6.46-01	8.65	1.04 00	9.92	1.55 00	11.11	2.45 00	31.3
58	406	7.30	6.22-01	8.64	9.97-01	9.91	1.49 00	11.10	2.35 00	30.5
59	415	7.27	6.02-01	8.62	9.61-01	9.90	1.45 00	11.10	2.28 00	29.9
60	426	7.24	5.79-01	8.60	9.21-01	9.88	1.39 00	11.09	2.19 00	29.1
61	436	7.21	5.59-01	8.58	8.86-01	9.87	1.34 00	11.08	2.11 00	28.4
62	447	7.17	5.38-01	8.55	8.50-01	9.85	1.29 00	11.07	2.03 00	27.7
63	458	7.14	5.18-01	8.53	8.16-01	9.84	1.25 00	11.07	1.96 00	27.1
64	469	7.10	5.00-01	8.50	7.85-01	9.82	1.20 00	11.05	1.88 00	26.4

N	E(eV)	F (9) Fluorine		Ne (10) Neon		Na (11) Sodium		Mg (12) Magnesium		$\lambda(\text{Å})$
		$f_1$	$f_2$	$f_1$	$f_2$	$f_1$	$f_2$	$f_1$	$f_2$	
65	480	7.05	4.83-01	8.48	7.55-01	9.81	1.16 00	11.04	1.81 00	25.83
66	492	7.00	4.65-01	8.45	7.24-01	9.79	1.12 00	11.03	1.74 00	25.20
67	504	6.95	4.48-01	8.42	6.96-01	9.77	1.08 00	11.02	1.68 00	24.60
68	516	6.89	4.32-01	8.39	6.69-01	9.75	1.04 00	11.00	1.61 00	24.03
69	529	6.82	4.15-01	8.35	6.42-01	9.73	9.99-01	10.99	1.55 00	23.44
70	542	6.75	4.00-01	8.32	6.16-01	9.71	9.62-01	10.97	1.49 00	22.87
71	555	6.66	3.85-01	8.28	5.93-01	9.68	9.27-01	10.96	1.44 00	22.34
72	569	6.56	3.71-01	8.24	5.68-01	9.66	8.91-01	10.94	1.38 00	21.79
73	583	6.44	3.57-01	8.20	5.46-01	9.63	8.58-01	10.92	1.32 00	21.27
74	597	6.30	3.44-01	8.15	5.25-01	9.61	8.26-01	10.90	1.27 00	20.77
75	612	6.12	3.31-01	8.10	5.04-01	9.58	7.98-01	10.88	1.22 00	20.26
76	627	5.89	3.18-01	8.04	4.84-01	9.55	7.72-01	10.86	1.17 00	19.77
77	642	5.58	3.06-01	7.99	4.65-01	9.52	7.44-01	10.83	1.13 00	19.31
78	658	5.00	2.95-01	7.92	4.45-01	9.49	7.11-01	10.81	1.08 00	18.84
79	674	4.17	2.84-01	7.84	4.26-01	9.45	6.80-01	10.79	1.03 00	18.39
80	690	2.36 K	4.22 00	7.76	4.11-01	9.42	6.55-01	10.76	9.94-01	17.97
81	707	5.01	4.09 00	7.66	3.97-01	9.38	6.31-01	10.74	9.58-01	17.54
82	725	5.81	3.98 00	7.54	3.81-01	9.34	6.05-01	10.71	9.17-01	17.10
83	742	6.38	3.93 00	7.42	3.67-01	9.29	5.81-01	10.68	8.81-01	16.71
84	760	6.82	3.84 00	7.26	3.53-01	9.24	5.58-01	10.65	8.46-01	16.31
85	779	7.21	3.71 00	7.06	3.40-01	9.19	5.35-01	10.62	8.10-01	15.92
86	798	7.50	3.57 00	6.78	3.26-01	9.13	5.13-01	10.59	7.77-01	15.54
87	818	7.73	3.43 00	6.40	3.13-01	9.06	4.91-01	10.55	7.44-01	15.16
88	838	7.92	3.30 00	5.65	3.00-01	8.99	4.71-01	10.51	7.14-01	14.79
89	858	8.08	3.19 00	3.62 K	2.88-01	8.91	4.52-01	10.47	6.85-01	14.45
90	879	8.22	3.08 00	4.07	4.45 00	8.81	4.34-01	10.43	6.57-01	14.10
91	901	8.35	2.98 00	6.42	4.29 00	8.70	4.16-01	10.39	6.29-01	13.76
92	923	8.46	2.88 00	7.17	4.14 00	8.57	3.99-01	10.34	6.04-01	13.43
93	945	8.57	2.78 00	7.68	4.00 00	8.42	3.82-01	10.28	5.80-01	13.12
94	968	8.66	2.69 00	8.09	3.86 00	8.21	3.65-01	10.22	5.56-01	12.81
95	992	8.75	2.59 00	8.40	3.73 00	7.93	3.49-01	10.16	5.33-01	12.50
96	1016	8.83	2.50 00	8.67	3.60 00	7.57	3.34-01	10.09	5.11-01	12.20
97	1041	8.89	2.41 00	8.90	3.46 00	6.91	3.19-01	10.01	4.90-01	11.91
98	1067	8.95	2.32 00	9.08	3.33 00	4.21 K	3.05-01	9.91	4.69-01	11.62
99	1093	9.01	2.23 00	9.24	3.20 00	5.55	4.42 00	9.80	4.50-01	11.34
100	1119	9.05	2.15 00	9.38	3.09 00	7.82	4.26 00	9.68	4.32-01	11.08
101	1147	9.10	2.07 00	9.51	2.97 00	8.46	4.10 00	9.52	4.14-01	10.81
102	1175	9.14	2.00 00	9.62	2.86 00	8.94	3.95 00	9.32	3.97-01	10.55
103	1204	9.17	1.92 00	9.71	2.75 00	9.30	3.80 00	9.04	3.80-01	10.30
104	1233	9.21	1.85 00	9.79	2.65 00	9.57	3.66 00	8.69	3.65-01	10.06
105	1263	9.23	1.78 00	9.87	2.55 00	9.80	3.52 00	8.02	3.50-01	9.82
106	1294	9.26	1.71 00	9.94	2.45 00	10.00	3.39 00	5.42 K	3.35-01	9.58
107	1326	9.28	1.64 00	10.00	2.36 00	10.17	3.26 00	6.97	4.36 00	9.35
108	1358	9.30	1.58 00	10.05	2.27 00	10.31	3.14 00	8.89	4.21 00	9.13
109	1392	9.32	1.52 00	10.10	2.18 00	10.45	3.02 00	9.52	4.05 00	8.91
110	1426	9.33	1.46 00	10.14	2.10 00	10.56	2.91 00	10.01	3.91 00	8.69
111	1460	9.35	1.40 00	10.18	2.02 00	10.66	2.81 00	10.35	3.78 00	8.49
112	1496	9.36	1.35 00	10.22	1.94 00	10.75	2.70 00	10.64	3.65 00	8.29
113	1533	9.36	1.29 00	10.25	1.86 00	10.83	2.60 00	10.86	3.52 00	8.09
114	1570	9.37	1.24 00	10.27	1.79 00	10.90	2.50 00	11.05	3.40 00	7.90
115	1609	9.38	1.19 00	10.30	1.72 00	10.97	2.41 00	11.22	3.28 00	7.71
116	1648	9.38	1.14 00	10.32	1.65 00	11.03	2.32 00	11.37	3.16 00	7.52
117	1688	9.39	1.09 00	10.33	1.59 00	11.08	2.23 00	11.49	3.05 00	7.34
118	1730	9.39	1.05 00	10.35	1.52 00	11.13	2.15 00	11.60	2.95 00	7.17
119	1772	9.39	1.01 00	10.36	1.46 00	11.17	2.07 00	11.70	2.84 00	7.00
120	1815	9.39	9.64-01	10.37	1.40 00	11.21	1.99 00	11.79	2.73 00	6.83
121	1860	9.39	9.23-01	10.38	1.35 00	11.24	1.91 00	11.87	2.63 00	6.67
122	1905	9.39	8.85-01	10.39	1.29 00	11.26	1.83 00	11.94	2.53 00	6.51
123	1952	9.39	8.48-01	10.40	1.24 00	11.29	1.76 00	12.00	2.43 00	6.35
124	2000	9.38	8.13-01	10.40	1.19 00	11.31	1.69 00	12.06	2.34 00	6.20

$\frac{E_{\mu}(E)}{F_2}$	2214.	2084.	1829.	1730.	$\frac{\text{keV-cm}^2}{\text{gram}}$
Atomic Weight	19.00	20.18	22.99	24.31	amu

ATOMIC SCATTERING FACTOR,  $f_1 + if_2$ 

N	E(eV)	Al (13)		Si (14)		P (15)		S (16)		$\lambda(\text{Å})$
		$f_1$	$f_2$	$f_1$	$f_2$	$f_1$	$f_2$	$f_1$	$f_2$	
0	100	2.65	7.60 00	-9.22 L	4.47-01	2.93	7.51-01	4.76	1.11 00	124.0
1	102	2.36	6.51 00	-7.27	7.92 00	2.80	7.44-01	4.72	1.10 00	121.5
2	104	2.04	6.36 00	-4.13	8.03 00	2.65	7.37-01	4.67	1.08 00	119.2
3	107	1.48	7.02 00	-2.33	8.21 00	2.41	7.27-01	4.60	1.07 00	115.9
4	110	1.71	7.77 00	-1.39	8.38 00	2.11	7.19-01	4.51	1.05 00	112.7
5	112	2.01	8.12 00	-0.89	8.50 00	1.88	7.14-01	4.45	1.05 00	110.7
6	115	2.50	8.40 00	-0.32	8.67 00	1.50	7.08-01	4.34	1.04 00	107.8
7	118	3.01	8.75 00	0.17	8.84 00	1.02	7.01-01	4.23	1.03 00	105.1
8	121	3.51	8.82 00	0.61	9.01 00	0.38	6.95-01	4.09	1.02 00	102.5
9	124	4.10	9.28 00	1.01	9.18 00	-0.49	6.89-01	3.95	1.01 00	100.0
10	127	4.91	9.08 00	1.38	9.35 00	-1.63	6.83-01	3.79	9.96-01	97.6
11	130	5.38	8.65 00	1.74	9.51 00	-5.96	6.77-01	3.60	9.85-01	95.4
12	133	5.66	8.13 00	2.08	9.68 00	-6.32 L	5.42 00	3.42	9.75-01	93.2
13	136	5.62	7.93 00	2.42	9.84 00	-2.47	6.03 00	3.17	9.63-01	91.2
14	140	5.64	7.87 00	2.87	1.01 01	-0.23	6.93 00	2.81	9.48-01	88.6
15	143	5.69	7.91 00	3.20	1.02 01	0.68	7.68 00	2.47	9.37-01	86.7
16	147	5.79	8.04 00	3.67	1.04 01	1.66	8.76 00	1.96	9.23-01	84.3
17	150	5.95	8.18 00	4.02	1.06 01	2.28	9.27 00	1.47	9.14-01	82.7
18	154	6.25	8.35 00	4.55	1.08 01	2.91	9.25 00	0.55	9.05-01	80.5
19	158	6.63	8.51 00	5.17	1.10 01	3.41	9.20 00	-0.93	8.97-01	78.5
20	162	7.12	8.54 00	5.83	1.11 01	3.86	9.16 00	-3.55	8.89-01	76.5
21	166	7.54	8.43 00	6.43	1.09 01	4.25	9.13 00	-7.76 L	1.05 01	74.7
22	170	7.95	8.33 00	6.91	1.07 01	4.58	9.09 00	-2.55	1.05 01	72.9
23	174	8.29	8.00 00	7.32	1.06 01	4.85	9.04 00	0.21	1.04 01	71.3
24	178	8.40	7.70 00	7.69	1.05 01	5.04	8.99 00	1.59	1.04 01	69.7
25	182	8.45	7.53 00	8.04	1.03 01	5.00	8.95 00	2.51	1.04 01	68.1
26	187	8.56	7.49 00	8.46	1.02 01	5.12	8.99 00	3.41	1.03 01	66.3
27	191	8.70	7.45 00	8.80	1.00 01	5.42	1.01 01	4.05	1.03 01	64.9
28	196	8.90	7.40 00	9.16	9.80 00	6.37	1.03 01	4.72	1.02 01	63.3
29	201	9.10	7.34 00	9.48	9.60 00	7.00	1.02 01	5.26	1.01 01	61.7
30	206	9.30	7.26 00	9.79	9.40 00	7.53	1.01 01	5.71	1.00 01	60.2
31	211	9.50	7.18 00	10.09	9.20 00	7.99	1.00 01	6.10	9.91 00	58.8
32	216	9.70	7.11 00	10.35	8.98 00	8.38	9.88 00	6.41	9.91 00	57.4
33	221	9.91	7.02 00	10.57	8.77 00	8.73	9.73 00	6.72	9.93 00	56.1
34	227	10.14	6.88 00	10.82	8.53 00	9.11	9.57 00	7.10	9.95 00	54.6
35	232	10.32	6.77 00	11.01	8.34 00	9.40	9.43 00	7.41	9.97 00	53.4
36	238	10.53	6.64 00	11.22	8.12 00	9.71	9.28 00	7.78	9.99 00	52.1
37	244	10.74	6.47 00	11.42	7.90 00	10.01	9.13 00	8.14	1.00 01	50.8
38	250	10.92	6.29 00	11.60	7.68 00	10.29	8.99 00	8.49	1.00 01	49.6
39	255	11.08	6.13 00	11.75	7.47 00	10.54	8.86 00	8.85	1.01 01	48.4
40	262	11.23	5.95 00	11.89	7.27 00	10.79	8.73 00	9.21	1.01 01	47.3
41	269	11.38	5.74 00	12.04	7.05 00	11.08	8.58 00	9.66	1.01 01	46.1
42	275	11.49	5.57 00	12.16	6.87 00	11.33	8.46 00	10.11	1.01 01	45.1
43	282	11.61	5.36 00	12.28	6.66 00	11.61	8.27 00	10.60	9.96 00	44.0
44	289	11.70	5.15 00	12.39	6.46 00	11.86	8.07 00	11.04	9.75 00	42.9
45	296	11.76	4.95 00	12.49	6.28 00	12.07	7.88 00	11.39	9.55 00	41.9
46	303	11.79	4.78 00	12.58	6.10 00	12.25	7.70 00	11.68	9.36 00	40.9
47	311	11.83	4.62 00	12.68	5.90 00	12.44	7.50 00	11.99	9.14 00	39.9
48	318	11.86	4.48 00	12.75	5.73 00	12.59	7.33 00	12.23	8.97 00	39.0
49	326	11.89	4.34 00	12.82	5.55 00	12.75	7.15 00	12.47	8.77 00	38.0
50	334	11.93	4.20 00	12.89	5.38 00	12.89	6.98 00	12.70	8.59 00	37.1
51	342	11.95	4.07 00	12.95	5.21 00	13.03	6.82 00	12.91	8.41 00	36.3
52	351	11.97	3.94 00	13.01	5.04 00	13.18	6.64 00	13.13	8.22 00	35.3
53	359	11.99	3.84 00	13.06	4.89 00	13.31	6.50 00	13.32	8.06 00	34.5
54	368	12.02	3.73 00	13.10	4.73 00	13.45	6.34 00	13.52	7.89 00	33.7
55	377	12.04	3.63 00	13.14	4.57 00	13.57	6.19 00	13.71	7.72 00	32.9
56	386	12.07	3.53 00	13.18	4.43 00	13.66	6.04 00	13.90	7.56 00	32.1
57	396	12.11	3.43 00	13.22	4.28 00	13.76	5.88 00	14.14	7.38 00	31.3
58	406	12.15	3.32 00	13.24	4.13 00	13.85	5.70 00	14.29	7.17 00	30.5
59	415	12.18	3.21 00	13.26	4.01 00	13.91	5.55 00	14.42	6.98 00	29.9
60	426	12.20	3.09 00	13.29	3.86 00	13.98	5.37 00	14.56	6.77 00	29.1
61	436	12.21	2.98 00	13.30	3.74 00	14.04	5.22 00	14.68	6.59 00	28.4
62	447	12.23	2.88 00	13.32	3.61 00	14.09	5.06 00	14.79	6.40 00	27.7
63	458	12.23	2.78 00	13.33	3.48 00	14.14	4.90 00	14.89	6.21 00	27.1
64	469	12.24	2.68 00	13.34	3.37 00	14.18	4.74 00	14.97	6.03 00	26.4

N	E(eV)	Al (13) Aluminum		Si (14) Silicon		P (15) Phosphorus		S (16) Sulfur		$\lambda(\text{Å})$
		$f_1$	$f_2$	$f_1$	$f_2$	$f_1$	$f_2$	$f_1$	$f_2$	
65	480	12.24	2.59 00	13.35	3.26 00	14.21	4.60 00	15.04	5.85 00	25.83
66	492	12.25	2.50 00	13.36	3.14 00	14.25	4.45 00	15.11	5.66 00	25.20
67	504	12.25	2.41 00	13.36	3.03 00	14.28	4.30 00	15.18	5.49 00	24.60
68	516	12.25	2.32 00	13.36	2.93 00	14.30	4.17 00	15.23	5.32 00	24.03
69	529	12.24	2.23 00	13.36	2.82 00	14.32	4.03 00	15.28	5.15 00	23.44
70	542	12.24	2.15 00	13.36	2.72 00	14.34	3.89 00	15.32	4.99 00	22.87
71	555	12.23	2.07 00	13.36	2.63 00	14.35	3.76 00	15.37	4.84 00	22.34
72	569	12.23	1.99 00	13.35	2.53 00	14.37	3.61 00	15.39	4.67 00	21.79
73	583	12.22	1.92 00	13.34	2.44 00	14.37	3.48 00	15.43	4.51 00	21.27
74	597	12.21	1.84 00	13.33	2.35 00	14.38	3.37 00	15.45	4.37 00	20.77
75	612	12.20	1.77 00	13.32	2.27 00	14.38	3.25 00	15.47	4.22 00	20.26
76	627	12.18	1.70 00	13.31	2.18 00	14.39	3.14 00	15.49	4.08 00	19.77
77	642	12.17	1.63 00	13.30	2.11 00	14.38	3.02 00	15.51	3.94 00	19.31
78	658	12.15	1.56 00	13.28	2.03 00	14.38	2.89 00	15.51	3.78 00	18.84
79	674	12.12	1.49 00	13.27	1.95 00	14.38	2.77 00	15.53	3.64 00	18.39
80	690	12.10	1.44 00	13.25	1.88 00	14.37	2.68 00	15.53	3.52 00	17.97
81	707	12.08	1.39 00	13.24	1.81 00	14.36	2.59 00	15.54	3.41 00	17.54
82	725	12.05	1.33 00	13.22	1.74 00	14.36	2.49 00	15.53	3.27 00	17.10
83	742	12.03	1.28 00	13.20	1.68 00	14.35	2.40 00	15.53	3.15 00	16.71
84	760	12.01	1.23 00	13.18	1.62 00	14.33	2.31 00	15.53	3.03 00	16.31
85	779	11.98	1.18 00	13.16	1.56 00	14.32	2.22 00	15.52	2.91 00	15.92
86	798	11.96	1.13 00	13.14	1.50 00	14.31	2.13 00	15.51	2.80 00	15.54
87	818	11.93	1.08 00	13.12	1.44 00	14.29	2.04 00	15.51	2.69 00	15.16
88	838	11.90	1.04 00	13.10	1.39 00	14.27	1.96 00	15.50	2.59 00	14.79
89	858	11.87	9.96-01	13.08	1.34 00	14.26	1.88 00	15.49	2.49 00	14.45
90	879	11.84	9.55-01	13.05	1.28 00	14.24	1.81 00	15.47	2.39 00	14.10
91	901	11.81	9.15-01	13.02	1.23 00	14.22	1.73 00	15.46	2.30 00	13.76
92	923	11.77	8.77-01	13.00	1.19 00	14.20	1.67 00	15.44	2.21 00	13.43
93	945	11.74	8.42-01	12.97	1.14 00	14.18	1.60 00	15.43	2.12 00	13.12
94	968	11.70	8.07-01	12.95	1.10 00	14.15	1.54 00	15.41	2.04 00	12.81
95	992	11.66	7.74-01	12.92	1.06 00	14.13	1.48 00	15.39	1.96 00	12.50
96	1016	11.62	7.42-01	12.89	1.02 00	14.11	1.42 00	15.38	1.88 00	12.20
97	1041	11.58	7.13-01	12.86	9.76-01	14.08	1.36 00	15.36	1.81 00	11.91
98	1067	11.53	6.83-01	12.82	9.38-01	14.06	1.30 00	15.33	1.73 00	11.62
99	1093	11.48	6.54-01	12.79	9.02-01	14.03	1.25 00	15.31	1.66 00	11.34
100	1119	11.43	6.28-01	12.76	8.67-01	14.00	1.20 00	15.28	1.60 00	11.08
101	1147	11.37	6.01-01	12.72	8.33-01	13.97	1.15 00	15.26	1.53 00	10.81
102	1175	11.30	5.76-01	12.68	8.00-01	13.94	1.11 00	15.24	1.47 00	10.55
103	1204	11.23	5.52-01	12.64	7.69-01	13.91	1.06 00	15.21	1.41 00	10.30
104	1233	11.15	5.29-01	12.60	7.39-01	13.88	1.02 00	15.19	1.35 00	10.06
105	1263	11.06	5.08-01	12.55	7.10-01	13.85	9.76-01	15.16	1.30 00	9.82
106	1294	10.96	4.87-01	12.50	6.82-01	13.82	9.36-01	15.13	1.25 00	9.58
107	1326	10.84	4.67-01	12.45	6.55-01	13.78	8.98-01	15.10	1.20 00	9.35
108	1358	10.70	4.49-01	12.39	6.29-01	13.74	8.62-01	15.07	1.15 00	9.13
109	1392	10.52	4.30-01	12.33	6.03-01	13.70	8.27-01	15.04	1.10 00	8.91
110	1426	10.29	4.13-01	12.25	5.79-01	13.66	7.93-01	15.01	1.06 00	8.69
111	1460	10.00	3.97-01	12.18	5.57-01	13.61	7.62-01	14.98	1.02 00	8.49
112	1496	9.54	3.80-01	12.09	5.34-01	13.56	7.31-01	14.94	9.76-01	8.29
113	1533	7.75	3.63-01	11.98	5.11-01	13.51	7.02-01	14.90	9.37-01	8.09
114	1570	6.66 K	4.13 00	11.86	4.90-01	13.45	6.75-01	14.86	9.02-01	7.90
115	1609	9.49	4.00 00	11.72	4.69-01	13.39	6.48-01	14.82	8.66-01	7.71
116	1648	10.23	3.87 00	11.54	4.49-01	13.33	6.23-01	14.78	8.33-01	7.52
117	1688	10.84	3.74 00	11.30	4.30-01	13.25	5.99-01	14.74	8.01-01	7.34
118	1730	11.24	3.62 00	10.98	4.12-01	13.16	5.75-01	14.70	7.69-01	7.17
119	1772	11.54	3.49 00	10.47	3.94-01	13.07	5.51-01	14.64	7.39-01	7.00
120	1815	11.79	3.37 00	8.48	3.76-01	12.95	5.29-01	14.58	7.09-01	6.83
121	1860	11.97	3.25 00	6.85 K	4.09 00	12.81	5.06-01	14.52	6.79-01	6.67
122	1905	12.12	3.14 00	8.20	3.96 00	12.65	4.86-01	14.45	6.52-01	6.51
123	1952	12.28	3.03 00	9.61	3.83 00	12.36	4.65-01	14.38	6.25-01	6.35
124	2000	12.44	2.92 00	11.06	3.70 00	12.07	4.46-01	14.30	5.99-01	6.20

 $\frac{E_{\mu}(E)}{F_2}$ 

1559.

1497.

1358.

1312.

 $\frac{\text{keV-cm}^2}{\text{gram}}$ Atomic  
Weight

26.98

28.09

30.97

32.06

amu

ATOMIC SCATTERING FACTOR,  $f_1 + if_2$ 

N	E(eV)	Cl (17)		Ar (18)		K (19)		Ca (20)		$\lambda(\text{Å})$
		$f_1$	$f_2$	$f_1$	$f_2$	$f_1$	$f_2$	$f_1$	$f_2$	
0	100	5.59	1.50	6.21	1.82	6.97	2.10	7.89	2.30	124.0
1	102	5.59	1.50	6.26	1.90	7.01	2.11	7.94	2.30	121.5
2	104	5.58	1.49	6.30	1.88	7.04	2.11	7.98	2.30	119.2
3	107	5.57	1.48	6.33	1.86	7.09	2.12	8.04	2.30	115.9
4	110	5.55	1.47	6.33	1.85	7.12	2.12	8.10	2.30	112.7
5	112	5.53	1.46	6.32	1.85	7.14	2.13	8.13	2.31	110.7
6	115	5.50	1.45	6.33	1.93	7.18	2.13	8.18	2.32	107.8
7	118	5.46	1.45	6.38	1.86	7.20	2.14	8.23	2.33	105.1
8	121	5.42	1.44	6.37	1.86	7.23	2.15	8.28	2.34	102.5
9	124	5.37	1.43	6.36	1.89	7.26	2.15	8.32	2.35	100.0
10	127	5.32	1.42	6.37	1.88	7.28	2.16	8.37	2.35	97.6
11	130	5.26	1.41	6.36	1.88	7.31	2.16	8.42	2.36	95.4
12	133	5.20	1.40	6.36	1.88	7.34	2.15	8.47	2.37	93.2
13	136	5.13	1.38	6.36	1.87	7.36	2.14	8.51	2.37	91.2
14	140	5.02	1.36	6.33	1.85	7.37	2.13	8.56	2.38	88.6
15	143	4.92	1.35	6.31	1.84	7.38	2.11	8.59	2.39	86.7
16	147	4.78	1.33	6.28	1.82	7.38	2.10	8.62	2.40	84.3
17	150	4.66	1.32	6.25	1.81	7.38	2.09	8.65	2.41	82.7
18	154	4.49	1.30	6.20	1.79	7.37	2.08	8.68	2.39	80.5
19	158	4.28	1.29	6.14	1.76	7.36	2.06	8.71	2.37	78.5
20	162	4.06	1.27	6.07	1.74	7.35	2.04	8.74	2.35	76.5
21	166	3.81	1.25	5.99	1.71	7.33	2.02	8.76	2.33	74.7
22	170	3.50	1.23	5.89	1.69	7.30	2.00	8.77	2.32	72.9
23	174	3.14	1.21	5.79	1.67	7.26	1.98	8.78	2.30	71.3
24	178	2.73	1.19	5.67	1.65	7.22	1.96	8.78	2.29	69.7
25	182	2.22	1.17	5.54	1.64	7.17	1.94	8.78	2.28	68.1
26	187	1.35	1.15	5.36	1.61	7.10	1.91	8.77	2.25	66.3
27	191	0.52	1.13	5.19	1.59	7.04	1.89	8.77	2.24	64.9
28	196	-1.47	1.11	4.95	1.56	6.95	1.87	8.75	2.21	63.3
29	201	-7.71 L	1.09	4.67	1.54	6.85	1.84	8.72	2.19	61.7
30	206	-4.62	9.79	4.35	1.52	6.73	1.81	8.69	2.16	60.2
31	211	-1.13	11.17	3.97	1.49	6.60	1.79	8.66	2.14	58.8
32	216	0.82	11.49	3.49	1.47	6.45	1.76	8.61	2.11	57.4
33	221	2.07	11.52	2.94	1.45	6.29	1.73	8.55	2.08	56.1
34	227	3.23	11.56	2.05	1.43	6.07	1.70	8.48	2.04	54.6
35	232	4.00	11.59	0.88	1.41	5.85	1.68	8.40	2.02	53.4
36	238	4.76	11.63	-2.15	1.39	5.56	1.65	8.31	1.98	52.1
37	244	5.44	11.66	-8.20 L	1.37	5.22	1.62	8.19	1.95	50.8
38	250	6.07	11.70	-1.96	12.30	4.82	1.59	8.07	1.92	49.6
39	256	6.64	11.73	0.65	12.23	4.33	1.56	7.92	1.90	48.4
40	262	7.19	11.77	2.55	12.16	3.76	1.53	7.75	1.87	47.3
41	269	7.84	11.81	3.97	12.08	2.91	1.50	7.54	1.84	46.1
42	275	8.42	11.84	4.85	12.01	1.89	1.47	7.33	1.81	45.1
43	282	9.08	11.70	5.71	11.94	-0.09	1.44	7.04	1.78	44.0
44	289	9.65	11.49	6.45	11.86	-3.00	1.41	6.71	1.76	42.9
45	296	10.13	11.29	7.08	11.79	-10.45 L	30.98	6.33	1.73	41.9
46	303	10.54	11.10	7.64	11.73	-2.91	26.19	5.85	1.71	40.9
47	311	10.97	10.89	8.23	11.65	2.11	21.73	5.23	1.68	39.9
48	318	11.31	10.72	8.69	11.59	3.82	18.52	4.51	1.65	39.0
49	326	11.67	10.52	9.17	11.51	5.25	15.50	3.31	1.63	38.0
50	334	12.00	10.34	9.63	11.45	6.42	14.00	1.33	1.60	37.1
51	342	12.31	10.16	10.07	11.38	7.41	13.62	-2.35	1.58	36.3
52	351	12.64	9.97	10.52	11.30	8.37	13.22	-7.24 L	14.62	35.3
53	359	12.91	9.81	10.91	11.24	9.10	12.88	0.00	14.34	34.5
54	368	13.21	9.64	11.34	11.17	9.88	12.90	3.64	14.05	33.7
55	377	13.51	9.47	11.76	11.11	10.61	12.97	5.53	13.76	32.9
56	386	13.83	9.31	12.23	11.04	11.38	13.04	6.93	13.49	32.1
57	396	14.19	9.01	12.76	10.90	12.18	13.02	8.24	13.22	31.3
58	406	14.42	8.75	13.21	10.64	12.67	12.68	9.11	13.19	30.5
59	415	14.62	8.53	13.54	10.41	13.15	12.38	9.77	13.17	29.9
60	426	14.85	8.26	13.91	10.14	13.70	12.04	10.26	13.14	29.1
61	436	15.04	8.02	14.22	9.91	14.16	11.74	10.87	13.11	28.4
62	447	15.21	7.76	14.52	9.67	14.59	11.44	11.71	13.08	27.7
63	458	15.36	7.52	14.81	9.42	14.97	11.12	12.68	12.88	27.1
64	469	15.50	7.28	15.06	9.17	15.31	10.81	13.39	12.54	26.4

N	E(eV)	Cl (17) Chlorine		Ar (18) Argon		K (19) Potassium		Ca (20) Calcium		$\lambda$ (Å)
		$f_1$	$f_2$	$f_1$	$f_2$	$f_1$	$f_2$	$f_1$	$f_2$	
65	480	15.63	7.07	15.28	8.93	15.63	10.52	14.02	12.21	25.83
66	492	15.75	6.83	15.49	8.68	15.93	10.21	14.60	11.87	25.20
67	504	15.85	6.61	15.69	8.44	16.21	9.92	15.08	11.54	24.60
68	516	15.95	6.40	15.87	8.22	16.46	9.64	15.52	11.24	24.03
69	529	16.04	6.18	16.05	7.98	16.71	9.35	15.94	10.92	23.44
70	542	16.12	5.97	16.22	7.75	16.92	9.07	16.31	10.61	22.87
71	555	16.19	5.78	16.38	7.54	17.11	8.80	16.64	10.32	22.34
72	569	16.25	5.57	16.53	7.29	17.29	8.50	16.97	10.00	21.79
73	583	16.31	5.38	16.65	7.05	17.46	8.23	17.25	9.70	21.27
74	597	16.36	5.20	16.76	6.84	17.60	7.98	17.50	9.42	20.77
75	612	16.41	5.02	16.87	6.62	17.75	7.72	17.74	9.14	20.26
76	627	16.44	4.85	16.97	6.41	17.87	7.48	17.96	8.87	19.77
77	642	16.48	4.68	17.06	6.21	17.98	7.24	18.16	8.60	19.31
78	658	16.51	4.52	17.15	5.98	18.09	6.97	18.34	8.30	18.84
79	674	16.53	4.36	17.21	5.77	18.18	6.72	18.51	8.02	18.39
80	690	16.55	4.21	17.26	5.60	18.26	6.53	18.65	7.81	17.97
81	707	16.57	4.06	17.32	5.44	18.34	6.34	18.79	7.59	17.54
82	725	16.58	3.91	17.39	5.25	18.40	6.11	18.92	7.33	17.10
83	742	16.59	3.77	17.44	5.07	18.46	5.91	19.03	7.10	16.71
84	760	16.60	3.64	17.49	4.90	18.52	5.71	19.13	6.86	16.31
85	779	16.61	3.51	17.54	4.73	18.56	5.51	19.23	6.63	15.92
86	798	16.61	3.38	17.58	4.55	18.60	5.31	19.31	6.39	15.54
87	818	16.61	3.25	17.61	4.37	18.64	5.12	19.38	6.17	15.16
88	838	16.61	3.13	17.63	4.21	18.67	4.94	19.45	5.95	14.79
89	858	16.60	3.02	17.64	4.05	18.70	4.76	19.51	5.75	14.45
90	879	16.60	2.91	17.65	3.90	18.71	4.59	19.56	5.55	14.10
91	901	16.59	2.80	17.66	3.75	18.73	4.43	19.60	5.35	13.76
92	923	16.58	2.70	17.66	3.62	18.75	4.27	19.64	5.17	13.43
93	945	16.57	2.60	17.66	3.48	18.76	4.15	19.68	4.99	13.12
94	968	16.55	2.50	17.66	3.35	18.76	4.05	19.71	4.82	12.81
95	992	16.54	2.41	17.66	3.22	18.77	3.94	19.73	4.65	12.50
96	1016	16.52	2.32	17.65	3.10	18.77	3.84	19.75	4.49	12.20
97	1041	16.51	2.23	17.64	2.98	18.77	3.69	19.77	4.32	11.91
98	1067	16.49	2.14	17.63	2.86	18.76	3.54	19.78	4.16	11.62
99	1093	16.47	2.06	17.62	2.75	18.75	3.40	19.79	4.01	11.34
100	1119	16.45	1.98	17.61	2.64	18.75	3.27	19.79	3.86	11.08
101	1147	16.43	1.91	17.59	2.54	18.74	3.14	19.79	3.72	10.81
102	1175	16.41	1.83	17.57	2.44	18.72	3.01	19.79	3.58	10.55
103	1204	16.38	1.76	17.55	2.34	18.71	2.90	19.79	3.45	10.30
104	1233	16.36	1.69	17.53	2.25	18.69	2.78	19.78	3.32	10.06
105	1263	16.34	1.63	17.51	2.16	18.68	2.67	19.78	3.20	9.82
106	1294	16.31	1.57	17.49	2.07	18.66	2.57	19.77	3.08	9.58
107	1326	16.28	1.50	17.46	1.99	18.64	2.47	19.75	2.97	9.35
108	1358	16.26	1.45	17.43	1.91	18.62	2.37	19.74	2.86	9.13
109	1392	16.23	1.39	17.40	1.83	18.60	2.28	19.73	2.75	8.91
110	1426	16.20	1.33	17.37	1.76	18.57	2.19	19.71	2.65	8.69
111	1460	16.17	1.28	17.34	1.69	18.55	2.10	19.69	2.56	8.49
112	1496	16.14	1.23	17.31	1.62	18.53	2.02	19.67	2.46	8.29
113	1533	16.11	1.18	17.28	1.56	18.50	1.94	19.65	2.36	8.09
114	1570	16.08	1.14	17.25	1.50	18.48	1.87	19.63	2.27	7.90
115	1609	16.04	1.10	17.21	1.44	18.45	1.80	19.61	2.17	7.71
116	1648	16.01	1.05	17.18	1.39	18.42	1.73	19.59	2.09	7.52
117	1688	15.97	1.01	17.15	1.33	18.39	1.66	19.56	2.00	7.34
118	1730	15.94	0.98	17.11	1.28	18.36	1.60	19.54	1.92	7.17
119	1772	15.90	0.94	17.08	1.23	18.33	1.53	19.51	1.84	7.00
120	1815	15.86	0.90	17.05	1.18	18.30	1.48	19.49	1.77	6.83
121	1860	15.81	0.87	17.01	1.14	18.27	1.42	19.46	1.69	6.67
122	1905	15.77	0.83	16.97	1.09	18.23	1.36	19.44	1.63	6.51
123	1952	15.72	0.80	16.93	1.05	18.20	1.31	19.41	1.56	6.35
124	2000	15.66	0.77	16.89	1.01	18.16	1.26	19.38	1.50	6.20

$\frac{E_U(E)}{f_2}$	1186.	1053.	1076.	1049.	$\frac{\text{keV-cm}^2}{\text{gram}}$
Atomic Weight	35.45	39.95	39.09	40.08	amu

ATOMIC SCATTERING FACTOR,  $f_1 + if_2$ 

N	E(eV)	Sc (21)		Ti (22)		V (23)		Cr (24)		$\lambda(\text{Å})$
		$f_1$	$f_2$	$f_1$	$f_2$	$f_1$	$f_2$	$f_1$	$f_2$	
0	100	8.50	2.88	9.23	3.46	9.84	4.20	10.55	5.66	124.0
1	102	8.56	2.88	9.29	3.44	9.93	4.16	10.65	5.59	121.5
2	104	8.62	2.88	9.36	3.43	10.00	4.12	10.75	5.53	119.2
3	107	8.69	2.89	9.44	3.41	10.10	4.06	10.88	5.44	115.9
4	110	8.76	2.90	9.52	3.40	10.18	4.03	11.02	5.39	112.7
5	112	8.80	2.91	9.57	3.40	10.25	4.04	11.11	5.38	110.7
6	115	8.87	2.91	9.65	3.41	10.35	4.04	11.22	5.36	107.8
7	118	8.93	2.92	9.73	3.41	10.44	4.03	11.36	5.33	105.1
8	121	8.99	2.92	9.80	3.40	10.52	4.02	11.47	5.31	102.5
9	124	9.05	2.92	9.87	3.40	10.61	4.01	11.58	5.28	100.0
10	127	9.11	2.93	9.94	3.40	10.70	4.00	11.70	5.26	97.6
11	130	9.18	2.93	10.02	3.40	10.79	4.00	11.82	5.23	95.4
12	133	9.25	2.93	10.09	3.40	10.90	3.99	11.91	5.21	93.2
13	136	9.30	2.94	10.16	3.39	10.97	3.98	12.04	5.19	91.2
14	140	9.37	2.94	10.24	3.39	11.06	3.97	12.17	5.16	88.6
15	143	9.42	2.94	10.30	3.39	11.13	3.97	12.26	5.14	86.7
16	147	9.47	2.95	10.37	3.39	11.23	3.96	12.36	5.11	84.3
17	150	9.52	2.95	10.42	3.39	11.29	3.96	12.45	5.09	82.7
18	154	9.57	2.93	10.48	3.37	11.36	3.93	12.57	5.05	80.5
19	158	9.62	2.91	10.55	3.34	11.44	3.89	12.69	4.99	78.5
20	162	9.67	2.88	10.62	3.31	11.52	3.86	12.79	4.93	76.5
21	166	9.72	2.86	10.68	3.28	11.60	3.82	12.90	4.87	74.7
22	170	9.76	2.84	10.72	3.25	11.66	3.79	12.98	4.82	72.9
23	174	9.79	2.82	10.78	3.23	11.73	3.76	13.05	4.77	71.3
24	178	9.82	2.80	10.82	3.21	11.78	3.74	13.14	4.73	69.7
25	182	9.84	2.78	10.85	3.19	11.84	3.72	13.20	4.70	68.1
26	187	9.87	2.76	10.91	3.16	11.90	3.68	13.31	4.63	66.3
27	191	9.89	2.73	10.94	3.14	11.95	3.64	13.38	4.58	64.9
28	196	9.91	2.70	10.98	3.10	12.01	3.60	13.47	4.52	63.3
29	201	9.92	2.67	11.01	3.07	12.06	3.56	13.54	4.46	61.7
30	206	9.93	2.64	11.04	3.03	12.10	3.52	13.61	4.40	60.2
31	211	9.93	2.61	11.06	3.00	12.15	3.48	13.67	4.34	58.8
32	216	9.93	2.57	11.09	2.96	12.19	3.44	13.73	4.28	57.4
33	221	9.92	2.54	11.10	2.92	12.21	3.39	13.79	4.21	56.1
34	227	9.90	2.50	11.11	2.88	12.25	3.34	13.85	4.14	54.6
35	232	9.87	2.46	11.11	2.84	12.27	3.29	13.90	4.08	53.4
36	238	9.84	2.43	11.11	2.80	12.29	3.25	13.95	4.01	52.1
37	244	9.80	2.39	11.11	2.75	12.31	3.20	14.00	3.95	50.8
38	250	9.75	2.35	11.09	2.71	12.32	3.15	14.04	3.88	49.6
39	256	9.69	2.32	11.07	2.68	12.33	3.11	14.07	3.82	48.4
40	262	9.62	2.29	11.05	2.64	12.33	3.06	14.10	3.76	47.3
41	269	9.53	2.25	11.01	2.60	12.33	3.02	14.13	3.70	46.1
42	275	9.44	2.22	10.96	2.56	12.32	2.98	14.16	3.64	45.1
43	282	9.32	2.18	10.92	2.52	12.30	2.93	14.16	3.57	44.0
44	289	9.19	2.14	10.85	2.47	12.28	2.87	14.19	3.50	42.9
45	296	9.03	2.09	10.78	2.43	12.25	2.82	14.19	3.44	41.9
46	303	8.86	2.06	10.70	2.38	12.21	2.77	14.20	3.37	40.9
47	311	8.64	2.01	10.58	2.33	12.17	2.72	14.17	3.30	39.9
48	318	8.41	1.98	10.47	2.29	12.11	2.67	14.19	3.24	39.0
49	326	8.11	1.94	10.34	2.25	12.04	2.62	14.17	3.18	38.0
50	334	7.77	1.90	10.18	2.21	11.96	2.57	14.15	3.11	37.1
51	342	7.38	1.87	10.01	2.17	11.87	2.53	14.12	3.05	36.3
52	351	6.81	1.83	9.78	2.13	11.76	2.48	14.08	2.99	35.3
53	359	6.19	1.80	9.55	2.09	11.65	2.44	14.04	2.94	34.5
54	368	5.34	1.76	9.26	2.05	11.51	2.39	13.98	2.88	33.7
55	377	4.09	1.73	8.91	2.01	11.35	2.35	13.92	2.82	32.9
56	386	1.91	1.69	8.50	1.97	11.17	2.30	13.84	2.77	32.1
57	396	-2.86 L	1.66	7.96	1.93	10.96	2.26	13.73	2.71	31.3
58	406	-5.14	15.45	7.30	1.89	10.68	2.21	13.65	2.64	30.5
59	415	2.31	15.14	6.50	1.85	10.42	2.16	13.55	2.59	29.9
60	426	5.66	14.78	5.19	1.81	10.03	2.11	13.40	2.52	29.1
61	436	7.46	14.47	3.47	1.77	9.63	2.07	13.25	2.46	28.4
62	447	8.92	14.14	-2.62	1.73	9.12	2.02	13.07	2.41	27.7
63	458	9.94	13.79	-5.88 L	15.50	8.46	1.97	12.86	2.35	27.1
64	469	10.63	13.44	3.13	15.08	7.57	1.93	12.64	2.29	26.4



N	E(eV)	Sc (21) Scandium		Ti (22) Titanium		V (23) Vanadium		Cr (24) Chromium		$\lambda$ (Å)
		$f_1$	$f_2$	$f_1$	$f_2$	$f_1$	$f_2$	$f_1$	$f_2$	
65	480	11.16	13.11	6.59	14.68	6.44	1.89	12.38	2.24	25.83
66	492	11.65	13.38	8.43	14.26	4.58	1.85	12.05	2.18	25.20
67	504	12.45	13.64	9.88	13.87	-1.64	1.81	11.66	2.13	24.60
68	516	13.40	13.55	10.95	13.50	-6.27 L	15.74	11.19	2.08	24.03
69	529	14.30	13.11	11.75	13.11	4.25	15.27	10.63	2.02	23.44
70	542	14.96	12.75	12.20	12.75	7.65	14.82	9.84	1.97	22.87
71	555	15.56	12.41	12.67	12.40	9.52	14.40	8.88	1.92	22.34
72	569	16.08	12.04	13.70	13.48	10.95	13.94	7.34	1.86	21.79
73	583	16.53	11.68	14.69	13.53	11.99	13.85	4.39	1.81	21.27
74	597	16.94	11.35	15.51	13.15	12.54	13.89	-6.97 L	1.76	20.77
75	612	17.34	11.01	16.23	12.76	13.24	13.94	2.56	15.74	20.26
76	627	17.68	10.69	16.78	12.39	14.09	13.99	8.74	15.12	19.77
77	642	17.99	10.37	17.27	12.03	15.22	13.88	10.85	14.53	19.31
78	658	18.28	10.01	17.74	11.64	16.11	13.42	11.85	13.95	18.84
79	674	18.54	9.68	18.14	11.27	16.88	12.98	12.69	13.40	18.39
80	690	18.77	9.41	18.51	10.98	17.48	12.64	14.12	13.90	17.97
81	707	19.00	9.16	18.88	10.69	18.04	12.31	15.58	14.53	17.54
82	725	19.21	8.85	19.18	10.34	18.53	11.92	16.55	14.06	17.10
83	742	19.38	8.57	19.44	10.02	18.95	11.58	17.35	13.65	16.71
84	760	19.55	8.30	19.70	9.70	19.34	11.23	18.02	13.24	16.31
85	779	19.70	8.02	19.95	9.38	19.72	10.88	18.63	12.82	15.92
86	798	19.84	7.75	20.16	9.08	20.05	10.54	19.22	12.42	15.54
87	818	19.96	7.48	20.36	8.77	20.35	10.19	19.72	12.03	15.16
88	838	20.08	7.22	20.54	8.48	20.62	9.87	20.14	11.65	14.79
89	858	20.18	6.98	20.69	8.21	20.87	9.56	20.55	11.29	14.45
90	879	20.27	6.74	20.84	7.94	21.09	9.25	20.91	10.94	14.10
91	901	20.35	6.50	20.98	7.67	21.30	8.95	21.24	10.58	13.76
92	923	20.42	6.28	21.09	7.41	21.49	8.66	21.53	10.25	13.43
93	945	20.49	6.06	21.20	7.16	21.65	8.38	21.80	9.92	13.12
94	968	20.55	5.85	21.30	6.91	21.81	8.10	22.05	9.60	12.81
95	992	20.60	5.64	21.39	6.67	21.95	7.82	22.27	9.27	12.50
96	1016	20.64	5.44	21.46	6.44	22.08	7.56	22.47	8.97	12.20
97	1041	20.68	5.25	21.53	6.22	22.19	7.30	22.63	8.66	11.91
98	1067	20.71	5.06	21.60	5.99	22.29	7.04	22.83	8.35	11.62
99	1093	20.74	4.88	21.65	5.78	22.38	6.79	22.98	8.06	11.34
100	1119	20.76	4.71	21.70	5.58	22.46	6.56	23.11	7.78	11.08
101	1147	20.78	4.53	21.74	5.38	22.54	6.33	23.24	7.51	10.81
102	1175	20.79	4.37	21.77	5.19	22.60	6.11	23.35	7.24	10.55
103	1204	20.80	4.21	21.80	5.00	22.66	5.89	23.43	6.99	10.30
104	1233	20.81	4.06	21.83	4.83	22.71	5.69	23.52	6.75	10.06
105	1263	20.81	3.92	21.84	4.66	22.75	5.49	23.62	6.51	9.82
106	1294	20.81	3.77	21.86	4.48	22.78	5.29	23.69	6.27	9.58
107	1326	20.81	3.63	21.87	4.32	22.81	5.10	23.75	6.05	9.35
108	1358	20.80	3.50	21.88	4.16	22.84	4.92	23.81	5.83	9.13
109	1392	20.79	3.37	21.88	4.01	22.86	4.73	23.85	5.62	8.91
110	1426	20.79	3.25	21.88	3.86	22.87	4.56	23.89	5.41	8.69
111	1460	20.78	3.13	21.88	3.72	22.89	4.40	23.92	5.22	8.49
112	1496	20.76	3.01	21.87	3.58	22.90	4.24	23.94	5.03	8.29
113	1533	20.75	2.90	21.87	3.44	22.90	4.08	23.98	4.83	8.09
114	1570	20.73	2.79	21.86	3.31	22.90	3.93	24.00	4.65	7.90
115	1609	20.71	2.68	21.85	3.18	22.90	3.78	24.02	4.47	7.71
116	1648	20.69	2.58	21.84	3.06	22.89	3.64	24.03	4.30	7.52
117	1688	20.67	2.49	21.82	2.94	22.89	3.50	24.04	4.13	7.34
118	1730	20.65	2.39	21.80	2.83	22.88	3.36	24.04	3.97	7.17
119	1772	20.62	2.30	21.79	2.72	22.87	3.24	24.02	3.82	7.00
120	1815	20.60	2.21	21.77	2.61	22.85	3.11	24.04	3.67	6.83
121	1860	20.57	2.13	21.75	2.51	22.84	2.99	24.04	3.52	6.67
122	1905	20.54	2.04	21.73	2.41	22.82	2.88	24.02	3.38	6.51
123	1952	20.51	1.97	21.70	2.32	22.80	2.76	24.00	3.24	6.35
124	2000	20.48	1.89	21.67	2.22	22.78	2.66	23.98	3.11	6.20

$\frac{E_{\mu}(E)}{F_2}$	935.5	878.0	825.6	808.9	$\frac{\text{keV-cm}^2}{\text{gram}}$
Atomic Weight	44.96	47.90	50.94	52.00	amu

ATOMIC SCATTERING FACTOR,  $f_1 + if_2$ 

N	E(eV)	Mn (25)		Fe (26)		Co (27)		Ni (28)		$\lambda(\text{Å})$
		$f_1$	$f_2$	$f_1$	$f_2$	$f_1$	$f_2$	$f_1$	$f_2$	
0	100	10.07	6.60	9.74	7.91	9.54	8.59	9.19	9.60	124.0
1	102	10.26	6.43	9.96	7.89	9.68	8.61	9.36	9.64	121.5
2	104	10.42	6.26	10.15	7.87	9.82	8.64	9.52	9.67	119.2
3	107	10.63	5.03	10.40	7.84	10.03	8.67	9.76	9.72	115.9
4	110	10.81	5.92	10.62	7.81	10.24	8.70	10.00	9.77	112.7
5	112	10.93	5.91	10.75	7.79	10.37	8.72	10.16	9.80	110.7
6	115	11.09	5.91	10.95	7.76	10.58	8.75	10.41	9.85	107.8
7	118	11.25	5.89	11.15	7.73	10.80	8.78	10.65	9.89	105.1
8	121	11.40	5.87	11.33	7.70	11.02	8.81	10.90	9.94	102.5
9	124	11.55	5.85	11.51	7.68	11.24	8.84	11.15	9.98	100.0
10	127	11.70	5.84	11.68	7.65	11.47	8.87	11.41	10.02	97.6
11	130	11.86	5.82	11.86	7.63	11.73	8.90	11.70	10.07	95.4
12	133	12.00	5.81	12.05	7.57	11.98	8.85	12.00	10.02	93.2
13	136	12.13	5.79	12.20	7.52	12.18	8.79	12.22	9.97	91.2
14	140	12.29	5.77	12.41	7.46	12.44	8.73	12.52	9.91	88.6
15	143	12.41	5.76	12.55	7.41	12.62	8.68	12.73	9.87	86.7
16	147	12.56	5.74	12.73	7.35	12.86	8.62	13.01	9.81	84.3
17	150	12.66	5.73	12.86	7.31	13.03	8.57	13.20	9.77	82.7
18	154	12.80	5.68	13.03	7.25	13.24	8.52	13.45	9.72	80.5
19	158	12.94	5.62	13.21	7.20	13.46	8.46	13.71	9.66	78.5
20	162	13.08	5.56	13.38	7.13	13.68	8.39	13.97	9.59	76.5
21	166	13.21	5.50	13.54	7.05	13.89	8.29	14.21	9.50	74.7
22	170	13.33	5.44	13.68	6.96	14.07	8.21	14.42	9.41	72.9
23	174	13.43	5.40	13.82	6.89	14.24	8.12	14.63	9.33	71.3
24	178	13.53	5.36	13.95	6.81	14.40	8.04	14.83	9.25	69.7
25	182	13.63	5.32	14.07	6.74	14.56	7.96	15.02	9.17	68.1
26	187	13.74	5.25	14.22	6.65	14.75	7.86	15.26	9.07	66.3
27	191	13.83	5.20	14.34	6.58	14.91	7.78	15.44	8.99	64.9
28	196	13.94	5.13	14.47	6.48	15.08	7.66	15.66	8.86	63.3
29	201	14.03	5.06	14.60	6.38	15.24	7.55	15.86	8.74	61.7
30	206	14.13	5.00	14.71	6.29	15.39	7.45	16.06	8.63	60.2
31	211	14.22	4.94	14.82	6.20	15.54	7.34	16.24	8.51	58.8
32	216	14.30	4.87	14.93	6.11	15.68	7.23	16.41	8.38	57.4
33	221	14.37	4.80	15.02	6.01	15.80	7.12	16.57	8.26	56.1
34	227	14.45	4.72	15.13	5.91	15.94	6.99	16.74	8.11	54.6
35	232	14.51	4.65	15.21	5.82	16.05	6.89	16.87	8.00	53.4
36	238	14.58	4.58	15.31	5.73	16.17	6.77	17.04	7.87	52.1
37	244	14.65	4.50	15.40	5.62	16.29	6.65	17.19	7.73	50.8
38	250	14.71	4.43	15.48	5.52	16.40	6.53	17.33	7.59	49.6
39	256	14.76	4.37	15.55	5.42	16.50	6.41	17.45	7.46	48.4
40	262	14.80	4.30	15.61	5.33	16.59	6.30	17.57	7.33	47.3
41	269	14.85	4.23	15.69	5.23	16.69	6.18	17.70	7.19	46.1
42	275	14.89	4.17	15.75	5.13	16.77	6.07	17.81	7.06	45.1
43	282	14.93	4.09	15.80	5.03	16.85	5.94	17.92	6.92	44.0
44	289	14.96	4.01	15.85	4.93	16.93	5.82	18.02	6.78	42.9
45	296	14.98	3.94	15.90	4.84	17.00	5.71	18.12	6.65	41.9
46	303	15.00	3.87	15.94	4.74	17.06	5.60	18.21	6.52	40.9
47	311	15.03	3.79	15.98	4.64	17.13	5.47	18.30	6.37	39.9
48	318	15.03	3.72	16.00	4.55	17.17	5.37	18.37	6.24	39.0
49	326	15.04	3.65	16.03	4.45	17.22	5.25	18.45	6.10	38.0
50	334	15.04	3.58	16.05	4.35	17.27	5.14	18.51	5.97	37.1
51	342	15.03	3.52	16.06	4.26	17.30	5.02	18.57	5.84	36.3
52	351	15.02	3.45	16.07	4.16	17.34	4.90	18.63	5.70	35.3
53	359	15.00	3.39	16.07	4.08	17.36	4.80	18.68	5.58	34.5
54	368	14.97	3.32	16.07	3.98	17.39	4.69	18.72	5.44	33.7
55	377	14.94	3.26	16.06	3.89	17.40	4.58	18.76	5.32	32.9
56	386	14.89	3.20	16.04	3.81	17.41	4.48	18.79	5.20	32.1
57	396	14.85	3.13	16.02	3.71	17.41	4.37	18.82	5.07	31.3
58	406	14.77	3.06	15.98	3.62	17.41	4.26	18.84	4.94	30.5
59	415	14.71	2.99	15.95	3.54	17.40	4.17	18.85	4.83	29.9
60	426	14.61	2.92	15.89	3.45	17.38	4.06	18.86	4.70	29.1
61	436	14.52	2.86	15.84	3.37	17.36	3.96	18.87	4.59	28.4
62	447	14.41	2.79	15.77	3.29	17.32	3.86	18.86	4.47	27.7
63	458	14.28	2.72	15.69	3.21	17.28	3.76	18.85	4.36	27.1
64	469	14.12	2.66	15.59	3.13	17.23	3.67	18.83	4.25	26.4

N	E(eV)	Mn (25) Manganese		Fe (26) Iron		Co (27) Cobalt		Ni (28) Nickel		$\lambda(\text{\AA})$
		$f_1$	$f_2$	$f_1$	$f_2$	$f_1$	$f_2$	$f_1$	$f_2$	
65	480	13.96	2.60	15.49	3.06	17.17	3.58	18.81	4.14	25.83
66	492	13.76	2.54	15.36	2.98	17.10	3.48	18.78	4.03	25.20
67	504	13.53	2.48	15.22	2.91	17.02	3.39	18.74	3.92	24.60
68	516	13.28	2.42	15.06	2.84	16.93	3.30	18.69	3.82	24.03
69	529	12.96	2.36	14.87	2.76	16.82	3.21	18.63	3.72	23.44
70	542	12.57	2.30	14.66	2.69	16.69	3.13	18.56	3.62	22.87
71	555	12.14	2.24	14.42	2.63	16.56	3.05	18.49	3.52	22.34
72	569	11.56	2.18	14.12	2.55	16.40	2.97	18.40	3.42	21.79
73	583	10.82	2.13	13.78	2.49	16.21	2.89	18.29	3.33	21.27
74	597	9.78	2.07	13.37	2.43	16.00	2.82	18.18	3.23	20.77
75	612	8.11	2.02	12.86	2.36	15.75	2.74	18.04	3.14	20.26
76	627	5.68	1.96	12.26	2.31	15.46	2.67	17.89	3.05	19.77
77	642	-0.58 L	11.84	11.48	2.24	15.14	2.60	17.72	2.97	19.31
78	658	4.59	12.89	10.28	2.17	14.73	2.52	17.51	2.88	18.84
79	674	7.94	14.01	8.79	2.10	14.26	2.45	17.29	2.80	18.39
80	690	10.35	15.19	5.77	2.05	13.65	2.39	17.03	2.72	17.97
81	707	12.57	14.77	-7.08 L	2.01	12.91	2.33	16.73	2.64	17.54
82	725	13.81	14.31	4.35	16.45	11.85	2.27	16.34	2.56	17.10
83	742	14.71	13.84	10.40	15.94	10.18	2.21	15.93	2.48	16.71
84	760	15.16	13.95	12.70	15.42	5.68	2.14	15.38	2.41	16.31
85	779	16.11	14.57	14.22	14.91	-5.15 L	16.74	14.71	2.34	15.92
86	798	17.45	14.13	15.08	14.44	7.92	16.28	13.78	2.28	15.54
87	818	18.38	13.63	15.64	14.43	11.17	15.82	12.42	2.23	15.16
88	838	19.12	13.16	16.85	15.12	13.50	15.39	9.00	2.17	14.79
89	858	19.75	12.73	18.03	14.77	15.19	14.97	4.98 L	7.37	14.45
90	879	20.30	12.35	19.08	14.28	16.35	14.50	7.47	10.89	14.10
91	901	20.80	11.97	19.87	13.79	16.96	14.01	10.21	15.92	13.76
92	923	21.26	11.61	20.56	13.33	17.61	14.91	13.55	15.39	13.43
93	945	21.65	11.25	21.14	12.91	19.02	14.82	15.61	14.92	13.12
94	968	22.00	10.89	21.64	12.50	20.07	14.29	16.91	14.43	12.81
95	992	22.34	10.54	22.12	12.10	20.96	13.77	17.63	14.21	12.50
96	1016	22.63	10.20	22.55	11.72	21.66	13.30	18.72	15.30	12.20
97	1041	22.90	9.86	22.93	11.34	22.26	12.88	20.23	14.80	11.91
98	1067	23.13	9.52	23.26	10.95	22.78	12.44	21.19	14.30	11.62
99	1093	23.36	9.20	23.57	10.59	23.26	12.04	22.02	13.82	11.34
100	1119	23.54	8.90	23.83	10.24	23.66	11.65	22.71	13.37	11.08
101	1147	23.73	8.59	24.09	9.89	24.05	11.26	23.31	12.91	10.81
102	1175	23.90	8.30	24.33	9.56	24.39	10.89	23.85	12.48	10.55
103	1204	24.05	8.01	24.54	9.24	24.70	10.53	24.33	12.06	10.30
104	1233	24.18	7.74	24.72	8.93	24.97	10.19	24.74	11.66	10.06
105	1263	24.29	7.48	24.89	8.63	25.22	9.85	25.12	11.27	9.82
106	1294	24.40	7.22	25.05	8.33	25.45	9.51	25.47	10.88	9.58
107	1326	24.50	6.96	25.19	8.03	25.65	9.18	25.77	10.50	9.35
109	1358	24.58	6.72	25.31	7.76	25.84	8.87	26.05	10.14	9.13
109	1392	24.66	6.48	25.42	7.48	26.01	8.56	26.31	9.79	8.91
110	1426	24.72	6.25	25.52	7.22	26.16	8.27	26.53	9.45	8.69
111	1460	24.79	6.04	25.61	6.97	26.30	7.99	26.73	9.13	8.49
112	1496	24.84	5.82	25.69	6.72	26.42	7.71	26.92	8.81	8.29
113	1533	24.88	5.60	25.76	6.47	26.53	7.43	27.09	8.48	8.09
114	1570	24.91	5.40	25.82	6.24	26.63	7.17	27.24	8.18	7.90
115	1609	24.95	5.20	25.88	6.01	26.72	6.91	27.38	7.88	7.71
116	1648	24.97	5.01	25.92	5.79	26.79	6.67	27.49	7.59	7.52
117	1688	24.99	4.83	25.96	5.58	26.86	6.43	27.60	7.31	7.34
118	1730	25.01	4.65	25.99	5.38	26.92	6.20	27.71	7.04	7.17
119	1772	25.03	4.47	26.02	5.18	26.97	5.97	27.80	6.78	7.00
120	1815	25.03	4.30	26.04	4.98	27.01	5.75	27.88	6.53	6.83
121	1860	25.03	4.13	26.06	4.79	27.05	5.53	27.95	6.28	6.67
122	1905	25.03	3.97	26.07	4.61	27.08	5.32	28.02	6.05	6.51
123	1952	25.04	3.82	26.08	4.43	27.11	5.12	28.08	5.82	6.35
124	2000	25.04	3.67	26.08	4.26	27.13	4.93	28.12	5.60	6.20
	$E_D(E)$									$\text{keV-cm}^2$
	$f_2$	765.5		753.1		713.6		716.4		gram
	Atomic Weight	54.94		55.85		58.93		58.71		amu

ATOMIC SCATTERING FACTOR,  $f_1 + if_2$ 

N	E(eV)	Cu (29)		Zn (30)		Ga (31)		Ge (32)		$\lambda(\text{Å})$
		$f_1$	$f_2$	$f_1$	$f_2$	$f_1$	$f_2$	$f_1$	$f_2$	
0	100	6.18	11.14	5.99	12.23	6.35	11.02	5.24	10.19	124.0
1	102	6.30	11.39	6.37	12.26	6.58	11.12	5.38	10.34	121.5
2	104	6.51	11.64	6.70	12.29	6.81	11.23	5.52	10.50	119.2
3	107	6.89	12.01	7.12	12.33	7.16	11.38	5.72	10.72	115.9
4	110	7.29	12.39	7.50	12.37	7.54	11.50	5.93	10.94	112.7
5	112	7.57	12.57	7.73	12.39	7.77	11.53	6.07	11.07	110.7
6	115	8.13	12.84	8.07	12.43	8.09	11.58	6.27	11.28	107.8
7	118	8.70	13.11	8.38	12.46	8.38	11.64	6.50	11.53	105.1
8	121	9.40	13.24	8.69	12.50	8.66	11.69	6.74	11.78	102.5
9	124	10.03	13.08	8.98	12.53	8.93	11.75	7.01	12.03	100.0
10	127	10.56	12.93	9.26	12.57	9.19	11.81	7.29	12.28	97.6
11	130	11.00	12.78	9.53	12.60	9.44	11.86	7.60	12.52	95.4
12	133	11.34	12.64	9.80	12.65	9.67	11.91	7.98	12.76	93.2
13	136	11.64	12.50	10.06	12.69	9.91	11.97	8.36	12.85	91.2
14	140	12.03	12.32	10.40	12.75	10.22	12.04	8.80	12.97	88.6
15	143	12.31	12.19	10.66	12.79	10.44	12.09	9.11	13.06	86.7
16	147	12.64	12.03	11.01	12.85	10.73	12.15	9.50	13.17	84.3
17	150	12.95	11.91	11.30	12.89	10.92	12.21	9.80	13.26	82.7
18	154	13.15	11.81	11.65	12.95	11.16	12.32	10.22	13.31	80.5
19	158	13.40	11.72	12.06	13.00	11.47	12.44	10.57	13.33	78.5
20	162	13.68	11.63	12.47	12.99	11.80	12.56	10.88	13.36	76.5
21	166	13.95	11.54	12.86	12.91	12.15	12.68	11.15	13.38	74.7
22	170	14.23	11.46	13.20	12.84	12.53	12.79	11.36	13.40	72.9
23	174	14.45	11.37	13.51	12.76	12.94	12.82	11.56	13.58	71.3
24	178	14.68	11.29	13.82	12.69	13.32	12.80	11.87	13.87	69.7
25	182	14.96	11.22	14.11	12.62	13.68	12.78	12.34	14.16	68.1
26	187	15.25	11.12	14.48	12.54	14.11	12.71	13.00	14.18	66.3
27	191	15.54	11.05	14.77	12.47	14.43	12.65	13.48	14.11	64.9
28	196	15.84	10.96	15.11	12.34	14.80	12.55	13.96	14.02	63.3
29	201	16.23	10.84	15.43	12.21	15.15	12.45	14.39	13.92	61.7
30	206	16.58	10.57	15.73	12.09	15.48	12.36	14.79	13.83	60.2
31	211	16.89	10.31	16.04	11.97	15.82	12.26	15.18	13.73	58.8
32	216	17.07	10.07	16.31	11.82	16.13	12.13	15.57	13.61	57.4
33	221	17.29	9.84	16.57	11.67	16.41	11.99	15.90	13.47	56.1
34	227	17.45	9.57	16.87	11.50	16.72	11.83	16.27	13.31	54.6
35	232	17.65	9.37	17.10	11.36	16.96	11.70	16.56	13.19	53.4
36	238	17.78	9.13	17.37	11.21	17.23	11.56	16.89	13.04	52.1
37	244	17.91	8.90	17.62	11.03	17.49	11.41	17.19	12.90	50.8
38	250	18.03	8.68	17.86	10.85	17.73	11.27	17.49	12.76	49.6
39	256	18.14	8.47	18.08	10.68	17.97	11.14	17.77	12.63	48.4
40	262	18.25	8.28	18.28	10.51	18.20	11.01	18.05	12.50	47.3
41	269	18.34	8.06	18.51	10.32	18.46	10.87	18.37	12.36	46.1
42	275	18.44	7.88	18.69	10.15	18.69	10.75	18.66	12.24	45.1
43	282	18.45	7.71	18.89	9.96	18.94	10.57	18.97	12.04	44.0
44	289	18.50	7.56	19.08	9.77	19.17	10.38	19.25	11.83	42.9
45	296	18.57	7.42	19.25	9.59	19.37	10.19	19.50	11.63	41.9
46	303	18.63	7.28	19.42	9.41	19.55	10.02	19.73	11.44	40.9
47	311	18.75	7.13	19.59	9.20	19.74	9.83	19.97	11.23	39.9
48	318	18.79	7.00	19.73	9.03	19.90	9.67	20.16	11.05	39.0
49	326	18.82	6.86	19.87	8.84	20.07	9.49	20.37	10.86	38.0
50	334	18.88	6.73	20.01	8.65	20.22	9.32	20.55	10.67	37.1
51	342	18.93	6.60	20.13	8.46	20.37	9.16	20.73	10.49	36.3
52	351	18.98	6.47	20.26	8.26	20.52	8.98	20.93	10.30	35.3
53	359	19.02	6.35	20.36	8.09	20.65	8.83	21.09	10.13	34.5
54	368	19.07	6.23	20.47	7.90	20.79	8.67	21.27	9.95	33.7
55	377	19.10	6.11	20.56	7.71	20.93	8.52	21.44	9.78	32.9
56	386	19.14	5.99	20.65	7.54	21.06	8.37	21.61	9.62	32.1
57	396	19.23	5.87	20.74	7.35	21.22	8.19	21.81	9.43	31.3
58	406	19.19	5.77	20.81	7.16	21.35	8.00	21.98	9.21	30.5
59	415	19.21	5.68	20.87	7.01	21.45	7.83	22.12	9.02	29.9
60	426	19.25	5.57	20.93	6.82	21.56	7.64	22.26	8.79	29.1
61	436	19.28	5.48	20.98	6.65	21.65	7.47	22.37	8.60	28.4
62	447	19.31	5.39	21.03	6.48	21.74	7.29	22.49	8.40	27.7
63	458	19.38	5.28	21.07	6.31	21.82	7.11	22.60	8.19	27.1
64	469	19.37	5.18	21.10	6.15	21.89	6.94	22.69	8.00	26.4

N	E(eV)	Cu (29) Copper		Zn (30) Zinc		Ga (31) Gallium		Ge (32) Germanium		$\lambda(\text{Å})$
		$f_1$	$f_2$	$f_1$	$f_2$	$f_1$	$f_2$	$f_1$	$f_2$	
65	480	19.38	5.07	21.12	6.00	21.95	6.77	22.77	7.81	25.83
66	492	19.39	4.97	21.14	5.81	22.00	6.60	22.85	7.61	25.20
67	504	19.44	4.86	21.15	5.63	22.05	6.43	22.92	7.43	24.60
68	516	19.43	4.77	21.15	5.46	22.09	6.28	22.98	7.25	24.03
69	529	19.45	4.65	21.15	5.29	22.13	6.11	23.04	7.07	23.44
70	542	19.42	4.52	21.14	5.14	22.16	5.94	23.10	6.88	22.87
71	555	19.47	4.39	21.12	5.00	22.18	5.78	23.15	6.71	22.34
72	569	19.39	4.26	21.09	4.85	22.18	5.61	23.18	6.52	21.79
73	583	19.34	4.12	21.05	4.71	22.18	5.45	23.20	6.34	21.27
74	597	19.25	3.97	21.01	4.58	22.16	5.31	23.22	6.18	20.77
75	612	19.16	3.83	20.96	4.45	22.14	5.16	23.23	6.01	20.26
76	627	19.05	3.70	20.89	4.32	22.12	5.02	23.24	5.84	19.77
77	642	18.99	3.56	20.82	4.20	22.09	4.89	23.24	5.68	19.31
78	658	18.76	3.42	20.73	4.06	22.04	4.73	23.22	5.50	18.84
79	674	18.63	3.28	20.64	3.93	21.98	4.59	23.19	5.33	18.39
80	690	18.36	3.17	20.53	3.83	21.91	4.48	23.14	5.20	17.97
81	707	18.16	3.07	20.40	3.74	21.84	4.37	23.10	5.07	17.54
82	725	17.73	3.04	20.25	3.63	21.76	4.25	23.05	4.92	17.10
83	742	17.45	3.02	20.10	3.54	21.68	4.13	23.00	4.79	16.71
84	760	17.13	2.99	19.91	3.44	21.58	4.01	22.94	4.65	16.31
85	779	16.94	2.95	19.70	3.35	21.46	3.90	22.86	4.51	15.92
86	798	16.35	2.83	19.46	3.24	21.33	3.77	22.77	4.37	15.54
87	818	15.76	2.72	19.16	3.13	21.17	3.65	22.66	4.24	15.16
88	838	14.96	2.61	18.83	3.03	20.98	3.53	22.54	4.11	14.79
89	858	14.20	2.51	18.45	2.93	20.77	3.42	22.40	3.98	14.45
90	879	12.47	2.42	17.98	2.83	20.52	3.31	22.24	3.85	14.10
91	901	9.51	2.33	17.38	2.74	20.22	3.20	22.05	3.73	13.76
92	923	2.02	2.25	16.68	2.65	19.89	3.10	21.84	3.61	13.43
93	945	5.01	18.03	15.84	2.58	19.49	3.00	21.61	3.50	13.12
94	968	12.97	17.24	13.08	2.51	19.01	2.90	21.33	3.39	12.81
95	992	16.02	16.46	10.03	2.44	18.37	2.81	20.99	3.28	12.50
96	1016	17.55	15.74	3.73	2.38	17.61	2.72	20.61	3.17	12.20
97	1041	18.72	15.03	10.53	17.00	16.58	2.64	20.16	3.08	11.91
98	1067	19.75	14.77	14.20	16.69	14.81	2.56	19.56	2.98	11.62
99	1093	20.60	14.53	16.23	16.40	9.52	2.48	18.83	2.88	11.34
100	1119	21.35	14.29	17.87	16.11	2.29	15.61	17.93	2.80	11.08
101	1147	22.07	14.04	19.30	15.82	8.52	15.37	16.57	2.71	10.81
102	1175	22.69	13.81	20.54	15.54	14.62	15.14	14.17	2.62	10.55
103	1204	23.39	13.57	21.78	15.26	18.35	14.90	6.62	2.54	10.30
104	1233	24.02	13.35	22.95	14.99	19.55	14.68	8.63	16.64	10.06
105	1263	24.69	13.05	23.82	14.65	20.48	14.46	15.91	16.37	9.82
106	1294	25.29	12.59	24.54	14.15	20.79	14.24	18.26	16.11	9.58
107	1326	25.78	12.14	25.20	13.66	21.92	15.42	20.23	15.85	9.35
108	1358	26.20	11.71	25.73	13.20	23.92	14.89	21.60	15.60	9.13
109	1392	26.55	11.29	26.24	12.74	24.86	14.37	22.80	15.34	8.91
110	1426	26.86	10.89	26.68	12.31	25.68	13.87	23.86	15.10	8.69
111	1460	27.13	10.51	27.06	11.90	26.33	13.40	24.80	14.86	8.49
112	1496	27.37	10.14	27.42	11.49	26.91	12.93	25.74	14.55	8.29
113	1533	27.61	9.77	27.74	11.09	27.41	12.48	26.60	14.07	8.09
114	1570	27.81	9.43	28.01	10.71	27.83	12.05	27.22	13.61	7.90
115	1609	27.99	9.08	28.28	10.33	28.23	11.63	27.81	13.15	7.71
116	1648	28.15	8.76	28.51	9.98	28.59	11.23	28.32	12.72	7.52
117	1688	28.29	8.45	28.71	9.64	28.89	10.84	28.76	12.31	7.34
118	1730	28.42	8.15	28.91	9.30	29.19	10.46	29.19	11.89	7.17
119	1772	28.55	7.85	29.07	8.96	29.45	10.09	29.56	11.48	7.00
120	1815	28.65	7.56	29.21	8.64	29.66	9.73	29.89	11.08	6.83
121	1860	28.74	7.27	29.35	8.32	29.87	9.37	30.19	10.68	6.67
122	1905	28.82	7.01	29.46	8.02	30.02	9.03	30.40	10.31	6.51
123	1952	28.88	6.74	29.56	7.73	30.18	8.70	30.63	9.94	6.35
124	2000	28.93	6.49	29.65	7.44	30.34	8.38	30.86	9.58	6.20

$$\frac{E_{\mu}(E)}{E_2}$$

661.8

643.3

603.2

579.4

$$\frac{\text{keV-cm}^2}{\text{gram}}$$

Atomic Weight

63.55

65.38

69.72

72.59

amu

ATOMIC SCATTERING FACTOR,  $f_1 + if_2$ 

N	E(eV)	As (33)		Se (34)		Br (35)		Kr (36)		$\lambda(\text{Å})$
		$f_1$	$f_2$	$f_1$	$f_2$	$f_1$	$f_2$	$f_1$	$f_2$	
0	100	2.69	7.92	2.39	7.29	2.81	5.14	4.08	1.83	124.0
1	102	2.74	8.27	2.40	7.61	2.74	5.41	3.87	1.94	121.5
2	104	2.82	8.64	2.43	7.94	2.69	5.68	3.64	2.13	119.2
3	107	2.97	9.20	2.49	8.45	2.62	6.11	3.35	2.46	115.9
4	110	3.20	9.79	2.60	8.87	2.61	6.52	2.99	2.79	112.7
5	112	3.45	10.19	2.71	9.09	2.59	6.78	2.77	3.03	110.7
6	115	3.90	10.68	2.93	9.43	2.56	7.18	2.49	3.43	107.8
7	118	4.33	10.92	3.15	9.78	2.54	7.62	2.15	3.98	105.1
8	121	4.67	11.17	3.34	10.13	2.54	8.07	1.94	4.47	102.5
9	124	4.96	11.41	3.53	10.49	2.56	8.53	1.73	4.97	100.0
10	127	5.23	11.64	3.71	10.85	2.60	9.01	1.53	5.48	97.6
11	130	5.48	11.88	3.90	11.21	2.66	9.51	1.33	6.01	95.4
12	133	5.69	12.13	4.11	11.57	2.76	10.02	1.14	6.60	93.2
13	136	5.92	12.47	4.34	11.94	2.90	10.54	0.90	7.35	91.2
14	140	6.30	12.93	4.66	12.44	3.15	11.26	0.79	8.45	88.6
15	143	6.63	13.28	4.93	12.81	3.40	11.82	0.80	9.36	86.7
16	147	7.21	13.75	5.38	13.32	3.90	12.59	1.27	10.69	84.3
17	150	7.74	14.01	5.75	13.64	4.41	13.07	1.96	11.57	82.7
18	154	8.40	14.10	6.25	13.96	5.10	13.36	2.76	12.05	80.5
19	158	8.91	14.15	6.69	14.26	5.61	13.57	3.36	12.41	78.5
20	162	9.37	14.20	7.14	14.57	6.05	13.77	3.84	12.76	76.5
21	166	9.79	14.25	7.61	14.87	6.44	13.98	4.28	13.12	74.7
22	170	10.18	14.30	8.11	15.18	6.79	14.18	4.70	13.48	72.9
23	174	10.53	14.36	8.65	15.38	7.10	14.39	5.13	13.84	71.3
24	178	10.88	14.42	9.16	15.52	7.36	14.59	5.49	14.20	69.7
25	182	11.24	14.49	9.64	15.65	7.51	14.80	5.90	14.56	68.1
26	187	11.67	14.54	10.20	15.78	7.82	15.48	6.44	15.02	66.3
27	191	11.97	14.57	10.66	15.88	8.26	16.16	6.97	15.39	64.9
28	196	12.31	14.69	11.21	15.95	9.23	16.51	7.55	15.69	63.3
29	201	12.73	14.86	11.74	16.00	9.91	16.62	8.13	15.91	61.7
30	206	13.22	15.02	12.23	16.04	10.54	16.73	8.65	16.13	60.2
31	211	13.76	15.18	12.71	16.08	11.15	16.84	9.20	16.35	58.8
32	216	14.38	15.11	13.22	16.07	11.71	16.88	9.66	16.52	57.4
33	221	14.86	14.98	13.66	16.04	12.23	16.90	10.14	16.69	56.1
34	227	15.38	14.83	14.16	16.00	12.82	16.93	10.68	16.88	54.6
35	232	15.77	14.71	14.56	15.96	13.27	16.95	11.12	17.03	53.4
36	238	16.19	14.57	15.02	15.93	13.79	16.97	11.65	17.22	52.1
37	244	16.59	14.44	15.45	15.89	14.31	17.00	12.18	17.40	50.8
38	250	16.96	14.31	15.89	15.86	14.81	17.02	12.70	17.58	49.6
39	256	17.32	14.18	16.32	15.82	15.31	17.05	13.23	17.76	48.4
40	262	17.67	14.06	16.75	15.79	15.81	17.07	13.78	17.93	47.3
41	269	18.07	13.92	17.27	15.75	16.42	17.10	14.48	18.14	46.1
42	275	18.42	13.80	17.75	15.72	17.00	17.12	15.16	18.31	45.1
43	282	18.82	13.60	18.33	15.52	17.67	16.95	15.99	18.24	44.0
44	289	19.17	13.38	18.80	15.28	18.25	16.71	16.63	18.08	42.9
45	296	19.48	13.17	19.21	15.04	18.75	16.48	17.22	17.92	41.9
46	303	19.76	12.97	19.58	14.82	19.18	16.26	17.76	17.77	40.9
47	311	20.05	12.75	19.97	14.57	19.65	16.01	18.39	17.60	39.9
48	318	20.30	12.56	20.28	14.36	20.02	15.80	18.76	17.46	39.0
49	326	20.57	12.35	20.62	14.13	20.41	15.58	19.26	17.30	38.0
50	334	20.81	12.16	20.92	13.91	20.78	15.36	19.72	17.15	37.1
51	342	21.04	11.97	21.21	13.69	21.13	15.15	20.16	17.00	36.3
52	351	21.29	11.76	21.52	13.46	21.51	14.92	20.64	16.84	35.3
53	359	21.50	11.59	21.79	13.27	21.82	14.73	21.06	16.71	34.5
54	368	21.73	11.40	22.07	13.06	22.16	14.52	21.52	16.56	33.7
55	377	21.95	11.22	22.34	12.85	22.50	14.31	21.98	16.41	32.9
56	386	22.17	11.04	22.62	12.66	22.83	14.12	22.45	16.27	32.1
57	396	22.43	10.84	22.94	12.43	23.24	13.89	23.09	16.06	31.3
58	406	22.65	10.59	23.21	12.15	23.57	13.58	23.51	15.72	30.5
59	415	22.83	10.37	23.43	11.90	23.85	13.32	23.90	15.42	29.9
60	426	23.02	10.12	23.67	11.62	24.14	13.01	24.31	15.07	29.1
61	436	23.18	9.90	23.86	11.38	24.38	12.74	24.63	14.77	28.4
62	447	23.35	9.67	24.07	11.12	24.63	12.46	25.02	14.45	27.7
63	458	23.49	9.45	24.25	10.86	24.87	12.18	25.30	14.13	27.1
64	469	23.62	9.22	24.42	10.61	25.08	11.91	25.57	13.82	26.4

N	E(eV)	As (33) Arsenic		Se (34) Selenium		Br (35) Bromine		Kr (36) Krypton		$\lambda(\text{Å})$
		$f_1$	$f_2$	$f_1$	$f_2$	$f_1$	$f_2$	$f_1$	$f_2$	
65	480	23.74	9.01	24.57	10.37	25.27	11.64	25.83	13.52	25.83
66	492	23.85	8.79	24.72	10.12	25.45	11.37	26.09	13.21	25.20
67	504	23.95	8.58	24.85	9.88	25.62	11.11	26.32	12.92	24.60
68	516	24.05	8.37	24.98	9.65	25.78	10.86	26.59	12.63	24.03
69	529	24.14	8.16	25.11	9.41	25.95	10.59	26.83	12.34	23.44
70	542	24.23	7.95	25.23	9.18	26.10	10.34	26.97	12.05	22.87
71	555	24.31	7.75	25.34	8.95	26.25	10.09	27.25	11.77	22.34
72	569	24.38	7.53	25.44	8.71	26.38	9.82	27.42	11.46	21.79
73	583	24.43	7.33	25.52	8.47	26.49	9.56	27.54	11.17	21.27
74	597	24.47	7.13	25.59	8.25	26.59	9.32	27.69	10.88	20.77
75	612	24.51	6.94	25.66	8.03	26.69	9.07	27.83	10.60	20.26
76	627	24.55	6.75	25.73	7.82	26.78	8.84	28.02	10.32	19.77
77	642	24.58	6.56	25.79	7.60	26.88	8.61	28.13	10.05	19.31
78	658	24.59	6.36	25.83	7.36	26.95	8.34	28.23	9.73	18.84
79	674	24.59	6.16	25.85	7.13	26.99	8.09	28.39	9.43	18.39
80	690	24.56	6.01	25.85	6.96	27.02	7.90	28.37	9.20	17.97
81	707	24.56	5.86	25.87	6.79	27.07	7.71	28.51	8.98	17.54
82	725	24.54	5.68	25.89	6.58	27.12	7.48	28.52	8.71	17.10
83	742	24.52	5.53	25.89	6.40	27.15	7.27	28.58	8.47	16.71
84	760	24.49	5.37	25.89	6.22	27.18	7.06	28.64	8.23	16.31
85	779	24.46	5.21	25.88	6.03	27.20	6.86	28.77	7.99	15.92
86	798	24.41	5.05	25.86	5.85	27.21	6.65	28.72	7.75	15.54
87	818	24.35	4.90	25.83	5.67	27.20	6.44	28.75	7.51	15.16
88	838	24.27	4.75	25.79	5.50	27.19	6.25	28.76	7.29	14.79
89	858	24.19	4.61	25.74	5.34	27.17	6.06	28.84	7.08	14.45
90	879	24.09	4.46	25.68	5.17	27.14	5.88	28.77	6.86	14.10
91	901	23.97	4.32	25.60	5.01	27.09	5.70	28.76	6.65	13.76
92	923	23.84	4.19	25.52	4.86	27.05	5.53	28.82	6.45	13.43
93	945	23.70	4.06	25.43	4.71	26.99	5.36	28.72	6.26	13.12
94	968	23.53	3.93	25.33	4.56	26.92	5.20	28.69	6.06	12.81
95	992	23.34	3.80	25.20	4.41	26.85	5.04	28.64	5.87	12.50
96	1016	23.12	3.69	25.06	4.27	26.76	4.88	28.69	5.69	12.20
97	1041	22.87	3.57	24.90	4.13	26.67	4.73	28.65	5.50	11.91
98	1067	22.57	3.45	24.71	3.99	26.55	4.57	28.47	5.32	11.62
99	1093	22.23	3.34	24.50	3.86	26.41	4.42	28.36	5.15	11.34
100	1119	21.84	3.24	24.26	3.74	26.27	4.28	28.26	4.99	11.08
101	1147	21.34	3.13	23.98	3.61	26.09	4.14	28.14	4.82	10.81
102	1175	20.73	3.03	23.66	3.49	25.90	4.00	28.01	4.66	10.55
103	1204	19.92	2.93	23.27	3.38	25.67	3.87	27.95	4.51	10.30
104	1233	18.95	2.84	22.83	3.27	25.42	3.74	27.73	4.37	10.06
105	1263	17.35	2.75	22.28	3.16	25.13	3.62	27.59	4.22	9.82
106	1294	12.20	2.66	21.54	3.06	24.78	3.50	27.29	4.08	9.58
107	1326	3.75	L 16.41	20.56	2.96	24.38	3.38	27.04	3.94	9.35
108	1358	9.44	15.94	19.33	2.86	23.88	3.27	26.77	3.81	9.13
109	1392	15.44	15.47	16.62	2.77	23.24	3.16	26.41	3.68	8.91
110	1426	21.00	15.03	8.52	L 2.68	22.45	3.06	26.01	3.56	8.69
111	1460	22.06	14.61	11.68	16.04	21.37	2.96	25.59	3.44	8.49
112	1496	22.86	14.19	19.14	15.55	19.60	2.86	25.15	3.32	8.29
113	1533	22.67	15.68	20.20	15.08	14.51	2.79	24.12	3.20	8.09
114	1570	24.51	15.18	21.27	14.64	12.92	L 11.81	23.03	3.09	7.90
115	1609	26.27	14.68	22.39	14.19	16.36	15.60	21.38	2.97	7.71
116	1648	27.11	14.21	23.52	13.77	18.89	15.13	15.37	2.87	7.52
117	1688	27.90	13.76	25.32	15.17	21.47	14.68	12.54	L 11.50	7.34
118	1730	28.56	13.30	27.09	14.69	24.19	14.22	20.76	15.02	7.17
119	1772	29.11	12.85	28.06	14.21	24.65	13.79	22.72	14.57	7.00
120	1815	29.60	12.41	28.88	13.74	25.62	15.37	25.66	14.12	6.83
121	1860	30.04	11.97	29.51	13.28	27.93	14.85	26.31	13.68	6.67
122	1905	30.43	11.56	30.10	12.84	28.69	14.36	26.99	13.27	6.51
123	1952	30.76	11.16	30.56	12.41	29.48	13.87	28.07	14.61	6.35
124	2000	31.07	10.77	31.00	11.99	30.29	13.40	29.17	14.15	6.20
	$\frac{E_{\mu}(E)}{F_2}$	561.3		532.6		526.3		501.9		$\frac{\text{keV-cm}^2}{\text{gram}}$
	Atomic Weight	74.92		78.96		79.91		83.80		amu

ATOMIC SCATTERING FACTOR,  $f_1 + if_2$ 

N	E(eV)	Rb (37)		Sr (38)		Y (39)		Zr (40)		$\lambda(\text{Å})$
		$f_1$	$f_2$	$f_1$	$f_2$	$f_1$	$f_2$	$f_1$	$f_2$	
0	100	5.67	1.00	7.74	1.12	9.86	2.75	13.43	2.59	124.0
1	102	5.44	1.03	7.58	1.17	9.79	2.75	13.39	2.58	121.5
2	104	5.17	1.05	7.44	1.22	9.72	2.74	13.35	2.57	119.2
3	107	4.73	1.09	7.23	1.29	9.61	2.73	13.30	2.56	115.9
4	110	4.12 M	1.16	7.01	1.37	9.50	2.72	13.23	2.55	112.7
5	112	3.68	1.38	6.87	1.42	9.41	2.71	13.19	2.54	110.7
6	115	3.05	1.78	6.64	1.50	9.26	2.70	13.10	2.54	107.8
7	118	2.47	2.28	6.40	1.59	9.09	2.70	13.03	2.56	105.1
8	121	1.90	2.90	6.15	1.67	8.90	2.75	12.96	2.58	102.5
9	124	1.41	3.67	5.87	1.76	8.74	2.81	12.90	2.61	100.0
10	127	1.04	4.62	5.56	1.85	8.57	2.86	12.83	2.63	97.6
11	130	0.82	5.79	5.20	1.94	8.38	2.91	12.77	2.65	95.4
12	133	1.32	7.13	4.73 M	2.12	8.16	2.97	12.70	2.67	93.2
13	136	1.86	7.45	4.31	2.44	7.90	3.06	12.62	2.69	91.2
14	140	2.29	7.89	3.80	2.94	7.57	3.29	12.52	2.72	88.6
15	143	2.46	8.23	3.45	3.37	7.35	3.47	12.44	2.74	86.7
16	147	2.66	8.69	3.07	4.02	7.05	3.72	12.32	2.77	84.3
17	150	2.79	9.03	2.88	4.55	6.79	3.91	12.22	2.79	82.7
18	154	2.92	9.50	2.70	5.14	6.44 M	4.32	12.08	2.82	80.5
19	158	3.06	10.00	2.48	5.72	6.16	4.83	11.93	2.85	78.5
20	162	3.20	10.51	2.27	6.34	6.03	5.40	11.75	2.89	76.5
21	166	3.36	11.03	2.07	7.02	6.03	6.00	11.56	2.92	74.7
22	170	3.54	11.56	1.91	7.75	6.10	6.32	11.33	2.95	72.9
23	174	3.75	12.10	1.80	8.51	6.10	6.65	11.05	3.02	71.3
24	178	3.98	12.63	1.74	9.30	6.07	6.99	10.77 M	3.14	69.7
25	182	4.23	13.18	1.70	10.15	6.04	7.34	10.48	3.25	68.1
26	187	4.63	13.92	1.79	11.38	6.00	7.79	10.06	3.39	66.3
27	191	4.98	14.53	2.24	12.47	5.97	8.16	9.56	3.51	64.9
28	196	5.75	15.04	2.95	13.35	5.95	8.63	8.85	4.02	63.3
29	201	6.30	15.42	3.62	13.99	5.94	9.12	8.26	4.87	61.7
30	206	6.82	15.81	4.17	14.64	5.94	9.62	7.97	5.88	60.2
31	211	7.33	16.19	4.81	15.30	5.96	10.14	8.16	7.06	58.8
32	216	7.85	16.50	5.45	15.75	6.01	10.67	8.52	7.62	57.4
33	221	8.33	16.80	6.03	16.12	6.07	11.22	8.82	8.00	56.1
34	227	8.89	17.15	6.64	16.58	6.17	11.89	8.99	8.47	54.6
35	232	9.34	17.44	7.13	16.96	6.29	12.47	9.11	8.88	53.4
36	238	9.89	17.78	7.71	17.41	6.47	13.19	9.24	9.38	52.1
37	244	10.45	18.13	8.28	17.86	6.70	13.92	9.37	9.89	50.8
38	250	11.02	18.47	8.88	18.32	7.00	14.68	9.53	10.42	49.6
39	256	11.62	18.81	9.50	18.78	7.35	15.46	9.70	10.96	48.4
40	262	12.27	19.15	10.14	19.23	7.77	16.27	9.89	11.52	47.3
41	269	13.12	19.54	11.02	19.76	8.51	17.23	10.19	12.19	46.1
42	275	13.96	19.88	11.96	20.22	9.42	18.08	10.52	12.78	45.1
43	282	15.00	19.85	13.09	20.30	10.60	18.44	10.98	13.35	44.0
44	289	15.87	19.67	14.02	20.21	11.57	18.53	11.45	13.88	42.9
45	296	16.61	19.49	14.79	20.11	12.31	18.63	12.01	14.42	41.9
46	303	17.24	19.32	15.49	20.02	12.99	18.72	12.63	14.92	40.9
47	311	17.90	19.13	16.23	19.92	13.69	18.82	13.37	15.15	39.9
48	318	18.44	18.97	16.81	19.84	14.26	18.91	13.87	15.36	39.0
49	326	19.01	18.79	17.44	19.74	14.89	19.01	14.40	15.59	38.0
50	334	19.55	18.62	18.05	19.65	15.49	19.11	14.92	15.81	37.1
51	342	20.06	18.45	18.64	19.56	16.06	19.21	15.42	16.04	36.3
52	351	20.61	18.27	19.26	19.46	16.68	19.31	15.97	16.29	35.3
53	359	21.07	18.11	19.80	19.38	17.22	19.40	16.45	16.51	34.5
54	368	21.58	17.94	20.40	19.29	17.82	19.50	17.01	16.75	33.7
55	377	22.08	17.78	21.00	19.20	18.40	19.60	17.60	17.00	32.9
56	386	22.60	17.62	21.66	19.11	18.79	19.70	18.30	17.24	32.1
57	396	23.20	17.40	22.44	18.94	19.20	20.92	19.16	17.35	31.3
58	406	23.74	17.06	23.10	18.57	20.89	20.53	19.87	17.23	30.5
59	415	24.17	16.76	23.58	18.26	21.76	20.20	20.38	17.12	29.9
60	426	24.61	16.41	24.13	17.89	22.66	19.82	20.96	17.00	29.1
61	436	24.99	16.10	24.59	17.58	23.35	19.48	21.43	16.89	28.4
62	447	25.38	15.78	25.05	17.24	24.02	19.12	21.87	16.77	27.7
63	458	25.76	15.46	25.48	16.90	24.62	18.76	22.27	16.73	27.1
64	469	26.08	15.13	25.88	16.56	25.16	18.41	22.69	16.74	26.4



N	E(eV)	Rb (37) Rubidium		Sr (38) Strontium		Y (39) Yttrium		Zr (40) Zirconium		$\lambda(A)$
		$f_1$	$f_2$	$f_1$	$f_2$	$f_1$	$f_2$	$f_1$	$f_2$	
65	480	26.38	14.82	26.24	16.24	25.66	18.06	23.13	16.76	25.83
66	492	26.68	14.49	26.60	15.90	26.14	17.70	23.63	16.78	25.20
67	504	26.96	14.18	26.93	15.57	26.59	17.36	24.15	16.80	24.60
68	516	27.22	13.88	27.25	15.26	27.02	17.03	24.74	16.81	24.03
69	529	27.50	13.57	27.58	14.93	27.46	16.67	25.48	16.73	23.44
70	542	27.76	13.24	27.87	14.59	27.86	16.31	26.08	16.42	22.87
71	555	28.00	12.93	28.16	14.27	28.24	15.95	26.61	16.12	22.34
72	569	28.21	12.58	28.44	13.92	28.60	15.56	27.08	15.81	21.79
73	583	28.40	12.26	28.68	13.59	28.92	15.19	27.50	15.52	21.27
74	597	28.57	11.96	28.90	13.27	29.21	14.84	27.88	15.23	20.77
75	612	28.74	11.66	29.12	12.94	29.50	14.47	28.26	14.94	20.26
76	627	28.91	11.37	29.33	12.63	29.78	14.13	28.60	14.67	19.77
77	642	29.07	11.07	29.54	12.32	30.05	13.78	28.93	14.40	19.31
78	658	29.20	10.75	29.72	11.97	30.28	13.38	29.24	14.13	18.84
79	674	29.30	10.44	29.85	11.63	30.46	13.01	29.54	13.87	18.39
80	690	29.38	10.20	29.97	11.37	30.61	12.72	29.82	13.62	17.97
81	707	29.50	9.96	30.12	11.11	30.81	12.43	30.10	13.37	17.54
82	725	29.61	9.68	30.29	10.80	31.01	12.08	30.39	13.11	17.10
83	742	29.71	9.42	30.41	10.51	31.18	11.77	30.65	12.87	16.71
84	760	29.79	9.17	30.52	10.22	31.33	11.46	30.94	12.64	16.31
85	779	29.87	8.90	30.63	9.93	31.48	11.14	31.25	12.39	15.92
86	798	29.93	8.64	30.72	9.64	31.61	10.82	31.55	12.04	15.54
87	818	29.99	8.38	30.80	9.36	31.73	10.51	31.79	11.69	15.16
88	838	30.03	8.13	30.87	9.09	31.83	10.21	31.99	11.36	14.79
89	858	30.07	7.90	30.93	8.83	31.92	9.92	32.16	11.04	14.45
90	879	30.10	7.66	30.97	8.57	32.01	9.63	32.33	10.72	14.10
91	901	30.11	7.42	31.01	8.31	32.07	9.35	32.47	10.40	13.76
92	923	30.13	7.20	31.05	8.07	32.14	9.08	32.60	10.10	13.43
93	945	30.13	6.98	31.08	7.83	32.20	8.81	32.72	9.81	13.12
94	968	30.12	6.76	31.09	7.59	32.24	8.55	32.82	9.52	12.81
95	992	30.09	6.55	31.10	7.36	32.28	8.28	32.90	9.24	12.50
96	1016	30.07	6.35	31.09	7.13	32.30	8.03	32.98	8.96	12.20
97	1041	30.04	6.15	31.09	6.91	32.33	7.79	33.05	8.69	11.91
98	1067	29.99	5.95	31.07	6.69	32.33	7.53	33.11	8.42	11.62
99	1093	29.94	5.77	31.04	6.48	32.33	7.30	33.15	8.15	11.34
100	1119	29.88	5.59	31.00	6.28	32.32	7.07	33.18	7.91	11.08
101	1147	29.80	5.41	30.96	6.08	32.30	6.84	33.20	7.65	10.81
102	1175	29.72	5.24	30.91	5.89	32.28	6.63	33.22	7.41	10.55
103	1204	29.63	5.07	30.83	5.70	32.23	6.42	33.21	7.18	10.30
104	1233	29.52	4.91	30.76	5.52	32.19	6.22	33.21	6.96	10.06
105	1263	29.41	4.75	30.68	5.35	32.14	6.02	33.20	6.74	9.82
106	1294	29.27	4.59	30.59	5.17	32.07	5.82	33.17	6.52	9.58
107	1326	29.12	4.44	30.48	5.00	32.00	5.63	33.14	6.30	9.35
108	1358	28.95	4.29	30.35	4.83	31.91	5.45	33.09	6.10	9.13
109	1392	28.74	4.14	30.21	4.67	31.81	5.27	33.03	5.90	8.91
110	1426	28.52	4.00	30.04	4.51	31.70	5.09	32.96	5.70	8.69
111	1460	28.27	3.87	29.87	4.36	31.58	4.93	32.88	5.52	8.49
112	1496	27.97	3.74	29.66	4.22	31.44	4.77	32.79	5.34	8.29
113	1533	27.61	3.59	29.42	4.08	31.28	4.60	32.68	5.16	8.09
114	1570	27.20	3.46	29.15	3.94	31.11	4.45	32.56	4.99	7.90
115	1609	26.63	3.32	28.84	3.81	30.90	4.29	32.42	4.82	7.71
116	1648	25.92	3.20	28.47	3.69	30.66	4.14	32.26	4.67	7.52
117	1688	25.02	3.08	28.02	3.56	30.39	4.00	32.09	4.51	7.34
118	1730	23.61	2.96	27.49	3.44	30.08	3.86	31.89	4.36	7.17
119	1772	19.45	2.84	26.81	3.34	29.71	3.73	31.65	4.21	7.00
120	1815	13.87	L 11.43	25.83	3.24	29.26	3.61	31.38	4.07	6.83
121	1860	16.63	10.74	25.19	3.14	28.69	3.48	31.00	3.97	6.67
122	1905	19.38	14.49	25.03	3.04	27.98	3.36	30.53	3.80	6.51
123	1952	22.26	14.04	24.86	L 11.60	26.41	3.25	30.03	3.67	6.35
124	2000	25.20	13.61	24.69	10.95	24.79	3.14	29.52	3.55	6.20

$\frac{E_{\mu}(E)}{f_2}$	492.1	480.0	473.1	461.1	$\frac{\text{keV-cm}^2}{\text{gram}}$
Atomic Weight	85.47	87.62	88.91	91.22	amu

ATOMIC SCATTERING FACTOR,  $f_1 + if_2$ 

N	E(eV)	Nb (41)		Mo (42)		Tc (43)		Ru (44)		$\lambda(\text{Å})$
		$f_1$	$f_2$	$f_1$	$f_2$	$f_1$	$f_2$	$f_1$	$f_2$	
0	100	14.84	2.73	15.43	2.01	15.78	1.80	18.51	1.38	124.0
1	102	14.79	2.68	15.33	2.00	15.67	1.82	18.29	1.25	121.5
2	104	14.74	2.64	15.25	1.99	15.59	1.83	18.02	1.13	119.2
3	107	14.66	2.58	15.13	1.98	15.47	1.85	17.65	1.13	115.9
4	110	14.57	2.52	15.03	1.97	15.38	1.87	17.37	1.18	112.7
5	112	14.49	2.48	14.95	1.96	15.32	1.88	17.23	1.21	110.7
6	115	14.38	2.44	14.84	1.96	15.23	1.90	17.03	1.26	107.8
7	118	14.27	2.45	14.74	1.98	15.15	1.92	16.86	1.31	105.1
8	121	14.18	2.46	14.65	2.00	15.08	1.94	16.71	1.36	102.5
9	124	14.10	2.47	14.57	2.02	15.02	1.96	16.58	1.41	100.0
10	127	14.03	2.48	14.50	2.04	14.96	1.98	16.46	1.46	97.6
11	130	13.96	2.49	14.43	2.06	14.90	2.00	16.36	1.51	95.4
12	133	13.89	2.50	14.35	2.08	14.84	2.02	16.26	1.56	93.2
13	136	13.82	2.51	14.28	2.09	14.78	2.04	16.16	1.62	91.2
14	140	13.72	2.52	14.18	2.12	14.70	2.06	16.05	1.69	88.6
15	143	13.65	2.53	14.12	2.14	14.64	2.08	15.97	1.74	86.7
16	147	13.55	2.54	14.02	2.16	14.57	2.10	15.88	1.81	84.3
17	150	13.46	2.55	13.95	2.18	14.51	2.12	15.81	1.87	82.7
18	154	13.34	2.57	13.85	2.20	14.44	2.14	15.73	1.94	80.5
19	158	13.22	2.61	13.74	2.21	14.36	2.16	15.67	2.01	78.5
20	162	13.11	2.64	13.63	2.23	14.28	2.19	15.60	2.07	76.5
21	166	12.99	2.67	13.50	2.24	14.19	2.21	15.52	2.12	74.7
22	170	12.88	2.70	13.37	2.26	14.11	2.23	15.45	2.18	72.9
23	174	12.76	2.70	13.22	2.28	14.02	2.25	15.38	2.23	71.3
24	178	12.61	2.68	13.07	2.31	13.92	2.27	15.31	2.29	69.7
25	182	12.44	2.66	12.91	2.34	13.82	2.29	15.24	2.34	68.1
26	187	12.17	2.64	12.70	2.37	13.68	2.32	15.15	2.41	66.3
27	191	11.87	2.62	12.51	2.40	13.57	2.34	15.08	2.47	64.9
28	196	11.45	2.72	12.25	2.43	13.42	2.36	14.98	2.54	63.3
29	201	11.04	2.90	11.96	2.45	13.26	2.39	14.89	2.61	61.7
30	206	10.66 M	3.10	11.60	2.48	13.08	2.41	14.79	2.68	60.2
31	211	10.22	3.30	11.11	2.51	12.88	2.43	14.69	2.74	58.8
32	216	9.77	3.65	10.59	2.77	12.67	2.46	14.59	2.81	57.4
33	221	9.36	4.07	10.11	3.13	12.43	2.48	14.48	2.88	56.1
34	227	8.92	4.62	9.60 M	3.61	12.08	2.51	14.35	2.97	54.6
35	232	8.58	5.12	9.21	4.05	11.72	2.53	14.23	3.04	53.4
36	238	8.21	5.78	8.77	4.64	11.22	2.71	14.09	3.12	52.1
37	244	7.88	6.50	8.36	5.30	10.77	3.01	13.93	3.21	50.8
38	250	7.61	7.30	8.01	6.03	10.36	3.34	13.76	3.29	49.6
39	256	7.40	8.16	7.70	6.83	9.98 M	3.70	13.59	3.38	48.4
40	262	7.25	9.11	7.44	7.73	9.61	4.08	13.40	3.46	47.3
41	269	7.27	10.32	7.33	8.89	9.19	4.57	13.15	3.56	46.1
42	275	7.52	11.46	7.43	10.00	8.85	5.02	12.92	3.65	45.1
43	282	8.02	12.50	7.77	11.07	8.47	5.59	12.60 M	3.75	44.0
44	289	8.53	13.44	8.14	12.07	8.10	6.20	12.24 M	3.84	42.9
45	296	9.27	14.42	8.75	13.14	7.78	6.85	11.72	3.94	41.9
46	303	10.15	15.34	9.54	14.15	7.46	7.55	11.18	4.23	40.9
47	311	11.25	15.64	10.57	14.51	7.10	8.41	10.58	4.72	39.9
48	318	11.91	15.90	11.17	14.81	6.85	9.22	10.13	5.18	39.0
49	326	12.59	16.19	11.77	15.17	6.63	10.22	9.65	5.74	38.0
50	334	13.22	16.48	12.32	15.52	6.46	11.29	9.21	6.35	37.1
51	342	13.81	16.77	12.85	15.87	6.38	12.45	8.80	7.01	36.3
52	351	14.46	17.10	13.42	16.26	6.46	13.81	8.37	7.81	35.3
53	359	15.03	17.38	13.93	16.61	6.62	15.05	8.03	8.58	34.5
54	368	15.69	17.70	14.52	17.01	6.92	16.55	7.69	9.51	33.7
55	377	16.37	18.02	15.14	17.40	7.47	18.15	7.42	10.51	32.9
56	386	17.19	18.33	15.89	17.79	8.56	19.86	7.24	11.60	32.1
57	396	18.20	18.49	16.81	18.04	10.24	21.59	7.14	12.90	31.3
58	406	19.03	18.36	17.59	18.00	12.05	21.92	7.19	14.31	30.5
59	415	19.62	18.25	18.12	17.97	13.20	22.22	7.47	15.68	29.9
60	426	20.28	18.12	18.70	17.93	14.50	22.58	8.15	17.48	29.1
61	436	20.82	18.00	19.15	17.90	15.64	22.91	9.29	19.26	28.4
62	447	21.35	17.87	19.52	17.86	16.93	23.27	11.75	21.36	27.7
63	458	21.82	17.81	19.79	18.03	18.26	23.34	13.65	22.61	27.1
64	469	22.29	17.80	20.16	18.36	19.42	23.17	14.76	22.98	26.4

N	E(eV)	Nb (41) Niobium		Mo (42) Molybdenum		Tc (43) Technetium		Ru (44) Ruthenium		$\lambda(\text{Å})$
		$f_1$	$f_2$	$f_1$	$f_2$	$f_1$	$f_2$	$f_1$	$f_2$	
65	480	22.78	17.79	20.61	18.69	20.41	23.00	15.88	23.35	25.83
66	492	23.30	17.77	21.23	19.05	21.32	22.82	17.07	23.74	25.20
67	504	23.84	17.76	21.92	19.41	22.14	22.65	18.27	24.14	24.60
68	516	24.43	17.75	22.78	19.77	22.87	22.48	19.61	24.53	24.03
69	529	25.12	17.66	23.95	19.93	23.52	22.43	21.30	24.67	23.44
70	542	25.71	17.40	24.89	19.60	24.39	22.63	22.64	24.23	22.87
71	555	26.25	17.15	25.71	19.28	25.45	22.83	23.81	23.81	22.34
72	569	26.74	16.89	26.40	18.96	26.73	22.34	24.71	23.33	21.79
73	583	27.18	16.64	27.01	18.64	27.61	21.84	25.44	23.08	21.27
74	597	27.59	16.40	27.56	18.34	28.34	21.36	26.21	22.91	20.77
75	612	28.01	16.16	28.10	18.03	29.06	20.88	27.08	22.74	20.26
76	627	28.40	15.92	28.61	17.73	29.71	20.42	27.97	22.58	19.77
77	642	28.77	15.69	29.06	17.45	30.32	19.96	28.97	22.29	19.31
78	658	29.13	15.46	29.51	17.16	30.85	19.44	29.84	21.72	18.84
79	674	29.49	15.24	29.95	16.87	31.32	18.94	30.54	21.17	18.39
80	690	29.83	15.02	30.35	16.60	31.71	18.57	31.13	20.75	17.97
81	707	30.17	14.80	30.75	16.33	32.18	18.20	31.76	20.33	17.54
82	725	30.53	14.58	31.17	16.05	32.64	17.73	32.38	19.81	17.10
83	742	30.87	14.37	31.55	15.80	33.03	17.30	32.90	19.34	16.71
84	760	31.24	14.16	31.96	15.54	33.39	16.88	33.39	18.86	16.31
85	779	31.66	13.94	32.42	15.26	33.76	16.44	33.87	18.38	15.92
86	798	32.07	13.55	32.85	14.84	34.08	16.01	34.29	17.89	15.54
87	818	32.40	13.16	33.21	14.42	34.39	15.58	34.69	17.40	15.16
88	838	32.67	12.79	33.50	14.02	34.66	15.18	35.05	16.93	14.79
89	858	32.91	12.44	33.79	13.64	34.92	14.78	35.38	16.49	14.45
90	879	33.13	12.08	34.02	13.25	35.17	14.38	35.69	16.04	14.10
91	901	33.32	11.73	34.25	12.87	35.41	13.98	35.98	15.60	13.76
92	923	33.50	11.39	34.45	12.51	35.63	13.60	36.26	15.18	13.43
93	945	33.65	11.06	34.63	12.15	35.82	13.23	36.50	14.77	13.12
94	968	33.79	10.74	34.80	11.80	36.01	12.84	36.74	14.35	12.81
95	992	33.92	10.41	34.95	11.46	36.17	12.46	36.96	13.95	12.50
96	1016	34.04	10.11	35.10	11.12	36.33	12.10	37.17	13.55	12.20
97	1041	34.15	9.80	35.24	10.79	36.48	11.73	37.37	13.14	11.91
98	1067	34.23	9.48	35.34	10.45	36.59	11.35	37.54	12.72	11.62
99	1093	34.30	9.19	35.44	10.12	36.69	11.00	37.69	12.33	11.34
100	1119	34.36	8.91	35.51	9.82	36.77	10.67	37.81	11.96	11.08
101	1147	34.41	8.62	35.58	9.50	36.85	10.33	37.92	11.58	10.81
102	1175	34.45	8.35	35.65	9.21	36.93	10.01	38.05	11.22	10.55
103	1204	34.48	8.09	35.69	8.92	36.96	9.70	38.11	10.87	10.30
104	1233	34.50	7.84	35.74	8.65	37.00	9.40	38.19	10.53	10.06
105	1263	34.51	7.59	35.77	8.38	37.04	9.11	38.25	10.21	9.82
106	1294	34.51	7.34	35.79	8.11	37.06	8.83	38.30	9.89	9.58
107	1326	34.50	7.10	35.80	7.84	37.08	8.55	38.35	9.58	9.35
108	1358	34.48	6.87	35.80	7.59	37.09	8.29	38.39	9.29	9.13
109	1392	34.45	6.64	35.79	7.34	37.09	8.03	38.42	9.00	8.91
110	1426	34.41	6.43	35.77	7.10	37.08	7.78	38.45	8.72	8.69
111	1460	34.37	6.22	35.75	6.88	37.08	7.54	38.48	8.46	8.49
112	1496	34.32	6.01	35.71	6.65	37.06	7.31	38.50	8.19	8.29
113	1533	34.25	5.79	35.66	6.43	37.04	7.06	38.51	7.90	8.09
114	1570	34.17	5.59	35.61	6.21	37.00	6.83	38.51	7.62	7.90
115	1609	34.07	5.38	35.54	6.00	36.96	6.61	38.48	7.35	7.71
116	1648	33.95	5.19	35.46	5.80	36.90	6.39	38.45	7.10	7.52
117	1688	33.81	5.00	35.37	5.60	36.83	6.18	38.40	6.85	7.34
118	1730	33.66	4.82	35.26	5.41	36.76	5.98	38.35	6.60	7.17
119	1772	33.48	4.65	35.14	5.22	36.67	5.78	38.28	6.37	7.00
120	1815	33.29	4.49	35.01	5.04	36.57	5.58	38.20	6.15	6.83
121	1860	33.06	4.33	34.85	4.87	36.45	5.39	38.10	5.93	6.67
122	1905	32.81	4.18	34.68	4.70	36.31	5.21	37.99	5.72	6.51
123	1952	32.47	4.03	34.46	4.54	36.16	5.03	37.87	5.51	6.35
124	2000	32.13	3.89	34.24	4.38	36.01	4.86	37.75	5.32	6.20

$$\frac{E_{\text{u}}(E)}{F_2}$$

452.7

438.4

425.2

416.1

$$\frac{\text{keV-cm}^2}{\text{gram}}$$

Atomic Weight

92.91

95.94

98.91

101.1

amu

ATOMIC SCATTERING FACTOR,  $f_1 + if_2$ 

N	E(eV)	Rh (45)		Pd (46)		Ag (47)		Cd (48)		$\lambda(\text{Å})$
		$f_1$	$f_2$	$f_1$	$f_2$	$f_1$	$f_2$	$f_1$	$f_2$	
0	100	18.54	1.32	20.71	5.09	26.80	9.45	21.13	11.77	124.0
1	102	18.20	1.16	20.49	4.76	26.55	8.43	21.47	11.20	121.5
2	104	17.84	1.02	20.23	4.47	26.27	7.53	21.78	10.57	119.2
3	107	17.32	1.01	19.82	4.06	25.80	6.25	22.05	9.47	115.9
4	110	16.93	1.06	19.37	3.71	25.25	5.16	22.03	8.52	112.7
5	112	16.71	1.09	19.04	3.49	24.81	4.33	21.88	7.95	110.7
6	115	16.41	1.17	18.52	3.25	24.01	3.35	21.59	7.43	107.8
7	118	16.16	1.26	18.05	3.14	23.09	2.61	21.47	7.19	105.1
8	121	15.94	1.35	17.68	3.03	22.13	2.13	21.52	6.96	102.5
9	124	15.75	1.44	17.36	2.93	21.34	1.90	21.94	6.75	100.0
10	127	15.57	1.54	17.04	2.83	20.60	1.71	22.17	5.82	97.6
11	130	15.42	1.64	16.73	2.74	19.90	1.53	22.19	4.84	95.4
12	133	15.28	1.74	16.37	2.66	19.25	1.59	21.79	4.04	93.2
13	136	15.18	1.85	16.04	2.74	18.74	1.64	21.25	3.44	91.2
14	140	15.06	2.01	15.69	2.86	18.12	1.72	20.56	3.07	88.6
15	143	15.02	2.12	15.48	2.95	17.68	1.87	20.13	2.83	86.7
16	147	14.99	2.22	15.24	3.06	17.25	2.09	19.52	2.54	84.3
17	150	14.95	2.25	15.07	3.15	16.98	2.27	19.04	2.46	82.7
18	154	14.89	2.30	14.88	3.30	16.71	2.46	18.53	2.54	80.5
19	158	14.81	2.35	14.73	3.45	16.48	2.67	18.17	2.63	78.5
20	162	14.73	2.40	14.63	3.61	16.34	2.81	17.87	2.72	76.5
21	166	14.65	2.44	14.57	3.77	16.17	2.89	17.61	2.82	74.7
22	170	14.56	2.49	14.57	3.93	15.98	2.97	17.40	2.91	72.9
23	174	14.47	2.54	14.67	3.97	15.80	3.13	17.21	3.00	71.3
24	178	14.35	2.58	14.67	3.90	15.69	3.29	17.05	3.09	69.7
25	182	14.20	2.63	14.63	3.82	15.60	3.41	16.90	3.19	68.1
26	187	14.05	2.85	14.49	3.74	15.49	3.50	16.75	3.31	66.3
27	191	13.99	3.04	14.33	3.67	15.38	3.57	16.65	3.40	64.9
28	196	14.05	3.24	14.09	3.70	15.25	3.66	16.56	3.49	63.3
29	201	14.10	3.27	13.87	3.79	15.11	3.75	16.47	3.57	61.7
30	206	14.10	3.30	13.70	3.89	14.97	3.85	16.38	3.64	60.2
31	211	14.08	3.33	13.55	3.98	14.82	3.95	16.30	3.72	58.8
32	216	14.05	3.34	13.40	4.08	14.67	4.05	16.23	3.77	57.4
33	221	13.99	3.32	13.25	4.17	14.49	4.18	16.15	3.82	56.1
34	227	13.90	3.30	13.08	4.28	14.32	4.42	16.04	3.87	54.6
35	232	13.80	3.29	12.93	4.38	14.22	4.63	15.95	3.91	53.4
36	238	13.65	3.27	12.75	4.49	14.14	4.89	15.85	3.96	52.1
37	244	13.47	3.25	12.56	4.60	14.13	5.07	15.74	4.02	50.8
38	250	13.28	3.23	12.36	4.72	14.09	5.20	15.63	4.07	49.6
39	256	13.06	3.21	12.15	4.83	14.03	5.34	15.52	4.12	48.4
40	262	12.81	3.19	11.93	4.94	13.97	5.47	15.40	4.17	47.3
41	269	12.48	3.17	11.62	5.08	13.88	5.63	15.27	4.22	46.1
42	275	12.16	3.16	11.30	5.19	13.82	5.77	15.15	4.27	45.1
43	282	11.73	3.14	10.87	5.45	13.74	5.92	15.01	4.29	44.0
44	289	11.20	3.12	10.48	5.76	13.66	6.07	14.85	4.30	42.9
45	296	10.50	3.10	10.06	6.08	13.58	6.21	14.66	4.30	41.9
46	303	9.66 M	3.16	9.61	6.45	13.50	6.35	14.44	4.30	40.9
47	311	8.62	3.76	9.09	7.09	13.41	6.43	14.16	4.31	39.9
48	318	7.86	4.36	8.74	7.69	13.27	6.49	13.89	4.31	39.0
49	326	7.03	5.14	8.38	8.42	13.07	6.57	13.54	4.32	38.0
50	334	6.23	6.04	8.07 M	9.21	12.83	6.64	13.15	4.32	37.1
51	342	5.50	7.06	7.80	10.04	12.56	6.72	12.72	4.33	36.3
52	351	4.73	8.39	7.59	11.04	12.17	6.80	12.18	4.33	35.3
53	359	4.11	9.75	7.46	11.99	11.75	6.87	11.60	4.34	34.5
54	368	3.59	11.49	7.39	13.12	11.19	6.95	10.87	4.34	33.7
55	377	3.34	13.49	7.48	14.34	10.46	7.03	10.04	4.35	32.9
56	386	3.37	15.78	7.88	15.63	9.23	7.10	8.99	4.35	32.1
57	396	4.28	18.71	8.55	16.88	7.49 M	7.76	7.61	4.35	31.3
58	406	6.33	20.50	9.21	17.75	6.01	9.46	5.65	4.33	30.5
59	415	7.82	21.25	9.72	18.56	5.10	11.27	3.36	4.32	29.9
60	426	9.29	22.19	10.42	19.57	4.37	13.89	-1.94	4.30	29.1
61	436	10.58	23.05	11.16	20.52	4.27	16.71	-15.14 M	4.29	28.4
62	447	12.27	23.98	12.22	21.58	5.40	20.38	-12.41	32.43	27.7
63	458	13.72	23.96	13.51	22.18	7.97	22.50	2.51	31.77	27.1
64	469	14.88	24.18	14.61	22.37	10.17	22.90	7.09	31.14	26.4

N	E(eV)	Rh (45) Rhodium		Pd (46) Palladium		Ag (47) Silver		Cd (48) Cadmium		$\lambda(\text{Å})$
		$f_1$	$f_2$	$f_1$	$f_2$	$f_1$	$f_2$	$f_1$	$f_2$	
65	480	15.92	24.40	15.49	22.56	11.68	23.30	10.64	30.54	25.83
66	492	17.03	24.63	16.30	22.77	12.93	23.73	13.50	29.91	25.20
67	504	18.11	24.86	17.03	22.97	14.07	24.16	15.54	29.30	24.60
68	516	19.21	25.09	17.62	23.16	15.16	24.59	17.27	28.73	24.03
69	529	20.48	25.20	18.09	23.54	16.31	25.02	18.77	28.14	23.44
70	542	21.63	25.05	18.78	24.28	17.38	25.36	20.00	27.59	22.87
71	555	22.63	24.89	19.62	25.03	18.43	25.69	21.03	27.06	22.34
72	569	23.53	24.71	21.01	25.84	19.59	26.04	21.76	26.47	21.79
73	583	24.39	24.64	22.62	25.92	20.76	26.22	22.21	26.38	21.27
74	597	25.25	24.61	23.87	25.71	21.82	26.32	22.91	26.49	20.77
75	612	26.21	24.58	24.99	25.48	22.89	26.42	23.69	26.59	20.26
76	627	27.30	24.55	25.99	25.27	23.91	26.52	24.52	26.70	19.77
77	642	28.43	24.34	26.90	25.06	24.90	26.62	25.39	26.79	19.31
78	658	29.54	23.73	27.81	24.85	25.98	26.73	26.30	26.83	18.84
79	674	30.32	23.14	28.69	24.64	27.08	26.83	27.21	26.88	18.39
80	690	31.02	22.70	29.56	24.44	28.30	26.93	28.15	26.90	17.97
81	707	31.74	22.25	30.54	24.20	29.87	26.93	29.19	26.90	17.54
82	725	32.45	21.69	31.49	23.70	31.33	26.13	30.27	26.75	17.10
83	742	33.02	21.19	32.27	23.25	32.38	25.41	31.24	26.62	16.71
84	760	33.58	20.68	33.00	22.79	33.21	24.69	32.34	26.48	16.31
85	779	34.13	20.16	33.75	22.31	34.00	23.99	33.56	26.25	15.92
86	798	34.62	19.63	34.43	21.73	34.64	23.39	34.71	25.55	15.54
87	818	35.08	19.11	35.04	21.15	35.28	22.79	35.58	24.85	15.16
88	838	35.50	18.61	35.56	20.60	35.87	22.22	36.34	24.18	14.79
89	858	35.88	18.13	36.04	20.07	36.41	21.67	37.00	23.56	14.45
90	879	36.24	17.64	36.50	19.54	36.94	21.11	37.62	22.98	14.10
91	901	36.58	17.15	36.91	19.01	37.43	20.55	38.21	22.39	13.76
92	923	36.90	16.69	37.30	18.51	37.89	20.01	38.77	21.83	13.43
93	945	37.19	16.23	37.65	18.02	38.31	19.48	39.28	21.27	13.12
94	968	37.46	15.77	37.99	17.54	38.70	18.93	39.75	20.70	12.81
95	992	37.71	15.31	38.33	17.05	39.07	18.39	40.22	20.13	12.50
96	1016	37.94	14.87	38.64	16.58	39.41	17.88	40.67	19.58	12.20
97	1041	38.16	14.42	38.95	16.07	39.75	17.34	41.09	18.97	11.91
98	1067	38.35	13.97	39.19	15.56	40.02	16.80	41.42	18.35	11.62
99	1093	38.52	13.54	39.40	15.08	40.26	16.29	41.73	17.77	11.34
100	1119	38.65	13.13	39.58	14.62	40.49	15.81	41.98	17.23	11.08
101	1147	38.78	12.72	39.76	14.15	40.70	15.32	42.23	16.67	10.81
102	1175	38.90	12.33	39.95	13.71	40.90	14.85	42.46	16.14	10.55
103	1204	39.00	11.94	40.04	13.28	41.04	14.40	42.65	15.63	10.30
104	1233	39.08	11.58	40.16	12.87	41.19	13.97	42.81	15.14	10.06
105	1263	39.16	11.23	40.27	12.47	41.33	13.54	42.96	14.66	9.82
106	1294	39.23	10.88	40.35	12.08	41.45	13.13	43.09	14.20	9.58
107	1326	39.29	10.55	40.43	11.70	41.56	12.73	43.21	13.75	9.35
108	1358	39.34	10.23	40.50	11.34	41.66	12.35	43.32	13.32	9.13
109	1392	39.39	9.91	40.56	10.98	41.76	11.97	43.42	12.89	8.91
110	1426	39.42	9.60	40.61	10.64	41.85	11.61	43.49	12.48	8.69
111	1460	39.45	9.32	40.65	10.32	41.93	11.26	43.55	12.10	8.49
112	1496	39.48	9.02	40.68	9.99	42.02	10.91	43.59	11.72	8.29
113	1533	39.50	8.73	40.71	9.68	42.08	10.53	43.63	11.38	8.09
114	1570	39.50	8.44	40.72	9.38	42.12	10.18	43.67	11.06	7.90
115	1609	39.49	8.16	40.74	9.08	42.16	9.83	43.72	10.74	7.71
116	1648	39.48	7.90	40.73	8.80	42.18	9.50	43.76	10.43	7.52
117	1688	39.46	7.64	40.73	8.52	42.18	9.18	43.80	10.13	7.34
118	1730	39.42	7.39	40.72	8.25	42.19	8.86	43.85	9.83	7.17
119	1772	39.38	7.14	40.71	7.98	42.17	8.55	43.89	9.53	7.00
120	1815	39.34	6.89	40.69	7.72	42.15	8.26	43.91	9.22	6.83
121	1860	39.27	6.65	40.65	7.46	42.12	7.96	43.93	8.92	6.67
122	1905	39.19	6.43	40.60	7.21	42.08	7.69	43.93	8.64	6.51
123	1952	39.10	6.21	40.54	6.97	42.02	7.41	43.93	8.36	6.35
124	2000	39.01	5.99	40.48	6.74	41.96	7.15	43.93	8.09	6.20

$\frac{E_M(E)}{F_2}$	408.7	395.3	389.9	374.2	$\frac{\text{keV-cm}^2}{\text{gram}}$
Atomic Weight	102.9	106.4	107.9	112.4	amu

ATOMIC SCATTERING FACTOR,  $f_1 + if_2$ 

N	E(eV)	In (49)		Sn (50)		Sb (51)		Te (52)		$\lambda(\text{Å})$
		$f_1$	$f_2$	$f_1$	$f_2$	$f_1$	$f_2$	$f_1$	$f_2$	
0	100	21.06	27.40	19.03	23.16	25.26	21.77	21.60	28.63	124.0
1	102	22.58	26.69	19.94	22.44	26.45	20.99	24.03	26.96	121.5
2	104	24.00	25.82	20.73	21.76	27.75	20.25	25.65	25.41	119.2
3	107	25.98	24.59	21.63	20.81	29.84	17.56	27.76	23.30	115.9
4	110	27.82	22.60	22.31	19.92	30.42	14.87	29.78	21.42	112.7
5	112	28.74	21.29	22.67	19.36	30.47	13.34	30.98	18.89	110.7
6	115	29.87	19.05	23.10	18.56	30.44	11.38	31.60	15.71	107.8
7	118	30.52	16.65	23.27	18.07	30.42	9.57	31.52	13.13	105.1
8	121	30.58	14.51	23.80	18.09	29.83	7.44	31.20	10.82	102.5
9	124	30.41	12.59	24.77	18.12	28.99	5.82	30.57	8.61	100.0
10	127	30.06	10.93	26.16	18.14	27.95	4.59	29.55	6.90	97.6
11	130	29.62	9.50	27.57	16.85	26.89	3.67	28.50	5.55	95.4
12	133	29.14	8.20	28.81	15.68	25.83	2.94	27.41	4.49	93.2
13	136	28.58	6.98	30.24	14.61	24.71	2.52	26.34	3.65	91.2
14	140	27.79	5.43	31.45	10.91	23.58	2.36	24.87	2.79	88.6
15	143	26.94	4.39	30.99	8.38	22.90	2.25	23.91	2.60	86.7
16	147	25.72	3.32	29.71	5.95	22.05	2.12	22.79	2.37	84.3
17	150	24.71	2.71	28.44	4.63	21.42	2.09	22.00	2.22	82.7
18	154	23.54	2.38	26.85	3.75	20.71	2.24	21.04	2.31	80.5
19	158	22.54	2.11	25.38	3.05	20.14	2.45	20.31	2.53	78.5
20	162	21.60	1.87	24.06	3.09	19.68	2.67	19.74	2.76	76.5
21	166	20.71	1.93	23.19	3.12	19.32	2.91	19.28	3.00	74.7
22	170	20.00	2.00	22.48	3.16	19.07	3.17	18.96	3.26	72.9
23	174	19.36	2.08	21.87	3.24	18.90	3.35	18.72	3.45	71.3
24	178	18.76	2.27	21.36	3.35	18.74	3.47	18.51	3.58	69.7
25	182	18.30	2.49	20.95	3.46	18.59	3.59	18.31	3.71	68.1
26	187	17.85	2.77	20.53	3.61	18.43	3.75	18.14	3.89	66.3
27	191	17.53	2.97	20.24	3.73	18.32	3.89	17.96	4.03	64.9
28	196	17.23	3.22	19.97	3.85	18.22	4.01	17.83	4.17	63.3
29	201	17.00	3.45	19.72	3.94	18.13	4.12	17.70	4.29	61.7
30	206	16.80	3.64	19.49	4.04	18.04	4.23	17.60	4.41	60.2
31	211	16.64	3.82	19.31	4.14	17.97	4.34	17.51	4.53	58.8
32	216	16.51	3.97	19.15	4.21	17.91	4.42	17.43	4.62	57.4
33	221	16.40	4.12	19.00	4.27	17.85	4.49	17.36	4.70	56.1
34	227	16.31	4.22	18.82	4.35	17.77	4.58	17.27	4.80	54.6
35	232	16.21	4.28	18.69	4.41	17.71	4.65	17.20	4.88	53.4
36	238	16.08	4.36	18.54	4.48	17.64	4.74	17.12	4.98	52.1
37	244	15.96	4.44	18.41	4.56	17.58	4.83	17.05	5.08	50.8
38	250	15.86	4.49	18.28	4.63	17.51	4.91	16.98	5.17	49.6
39	256	15.73	4.52	18.17	4.70	17.46	5.00	16.92	5.27	48.4
40	262	15.60	4.56	18.06	4.77	17.41	5.08	16.87	5.36	47.3
41	269	15.44	4.59	17.94	4.85	17.36	5.18	16.82	5.48	46.1
42	275	15.30	4.63	17.87	4.93	17.34	5.26	16.80	5.57	45.1
43	282	15.12	4.65	17.79	4.96	17.31	5.31	16.78	5.63	44.0
44	289	14.94	4.66	17.69	4.99	17.27	5.34	16.75	5.66	42.9
45	296	14.72	4.67	17.57	5.01	17.20	5.37	16.69	5.70	41.9
46	303	14.49	4.68	17.45	5.03	17.12	5.39	16.62	5.73	40.9
47	311	14.21	4.69	17.30	5.05	17.02	5.42	16.53	5.77	39.9
48	318	13.94	4.70	17.15	5.07	16.92	5.45	16.43	5.80	39.0
49	326	13.60	4.71	16.97	5.10	16.79	5.48	16.32	5.84	38.0
50	334	13.22	4.72	16.79	5.12	16.64	5.50	16.19	5.88	37.1
51	342	12.82	4.73	16.59	5.14	16.49	5.53	16.05	5.91	36.3
52	351	12.30	4.74	16.34	5.16	16.29	5.56	15.88	5.95	35.3
53	359	11.77	4.75	16.10	5.19	16.09	5.59	15.72	5.99	34.5
54	368	11.12	4.76	15.81	5.21	15.86	5.62	15.52	6.03	33.7
55	377	10.37	4.77	15.49	5.23	15.60	5.65	15.30	6.06	32.9
56	386	9.45	4.78	15.15	5.25	15.31	5.68	15.07	6.10	32.1
57	396	8.28	4.79	14.75	5.27	14.98	5.69	14.81	6.13	31.3
58	406	6.74	4.78	14.27	5.22	14.58	5.65	14.49	6.10	30.5
59	415	4.76	4.77	13.73	5.18	14.13	5.62	14.14	6.07	29.9
60	426	0.89	4.77	12.97	5.13	13.50	5.54	13.64	6.03	29.1
61	436	-6.18	4.76	12.16	5.09	12.84	5.54	13.13	6.00	28.4
62	447	-11.42	38.24	11.02	5.05	11.92	5.50	12.48	5.97	27.7
63	458	-0.68	37.20	9.62	5.01	10.83	5.46	11.71	5.93	27.1
64	469	2.73	36.21	7.88	4.97	9.50	5.41	10.78	5.89	26.4

N	E(eV)	In (49) Indium		Sn (50) Tin		Sb (51) Antimony		Te (52) Tellurium		$\lambda(\text{Å})$
		$f_1$	$f_2$	$f_1$	$f_2$	$f_1$	$f_2$	$f_1$	$f_2$	
65	480	5.43	35.26	5.37	4.93	7.80	5.36	9.72	5.84	25.83
66	492	7.73	34.28	0.49	4.88	5.11	5.32	8.32	5.80	25.20
67	504	9.95	33.36	-10.86	4.84	1.38	5.27	6.51	5.75	24.60
68	516	12.39	32.47	-16.84	34.78	-5.29	5.22	4.27	5.71	24.03
69	529	15.51	31.56	3.36	33.93	-34.12	40.41	0.91	5.66	23.44
70	542	17.86	30.70	8.78	33.13	-6.88	39.05	-3.86	5.60	22.87
71	555	19.79	29.88	13.12	32.36	7.61	37.77	-12.51	5.54	22.34
72	569	21.21	29.04	16.13	31.51	12.91	36.46	-53.41	5.48	21.79
73	583	22.27	28.30	18.33	30.74	16.44	35.30	-23.05	63.61	21.27
74	597	23.08	27.61	20.17	30.02	19.20	34.22	8.28	57.49	20.77
75	612	23.69	26.91	21.86	29.29	21.67	33.13	19.12	51.72	20.26
76	627	23.81	26.24	23.20	28.59	23.59	32.10	24.74	46.64	19.77
77	642	23.51	26.25	24.36	27.90	25.22	31.08	28.72	42.17	19.31
78	658	23.79	27.67	25.32	27.13	26.57	29.97	31.04	37.97	18.84
79	674	25.19	29.13	25.98	26.40	27.59	28.93	32.07	34.27	18.39
80	690	27.05	29.19	26.23	25.84	28.36	28.15	32.14	31.74	17.97
81	707	28.76	28.58	26.31	25.43	29.08	27.40	31.86	29.63	17.54
82	725	29.95	27.97	26.46	26.06	29.72	26.67	31.54	28.85	17.10
83	742	30.87	27.42	27.13	26.65	30.11	26.01	31.59	28.14	16.71
84	760	31.75	26.87	28.14	27.27	30.24	25.35	31.43	27.43	16.31
85	779	32.55	26.36	29.64	27.76	30.01	24.89	31.07	26.92	15.92
86	798	33.31	26.19	31.02	27.29	30.00	25.66	30.85	27.60	15.54
87	818	34.16	26.02	32.20	26.82	30.51	26.47	31.37	28.32	15.16
88	838	35.07	25.86	33.14	26.36	31.53	27.29	32.49	29.04	14.79
89	858	36.10	25.54	33.88	25.99	33.26	27.64	33.88	29.33	14.45
90	879	36.96	24.86	34.67	25.76	34.62	27.01	35.38	28.74	14.10
91	901	37.75	24.19	35.56	25.53	35.73	26.37	36.35	28.15	13.76
92	923	38.40	23.55	36.56	25.31	36.50	25.76	37.14	27.58	13.43
93	945	38.98	22.94	37.53	24.79	37.15	25.42	37.80	27.25	13.12
94	968	39.53	22.34	38.44	24.14	37.88	25.17	38.55	27.01	12.81
95	992	40.07	21.75	39.21	23.50	38.72	24.93	39.50	26.77	12.50
96	1016	40.58	21.17	39.91	22.87	39.77	24.60	40.54	26.43	12.20
97	1041	41.07	20.51	40.56	22.18	40.71	23.86	41.57	25.66	11.91
98	1067	41.47	19.85	41.10	21.48	41.43	23.12	42.34	24.87	11.62
99	1093	41.81	19.24	41.54	20.82	42.02	22.42	42.97	24.13	11.34
100	1119	42.12	18.66	41.95	20.19	42.54	21.75	43.52	23.42	11.08
101	1147	42.41	18.06	42.34	19.55	43.03	21.07	44.05	22.71	10.81
102	1175	42.67	17.50	42.68	18.95	43.45	20.43	44.50	22.03	10.55
103	1204	42.90	16.95	42.98	18.36	43.83	19.81	44.92	21.36	10.30
104	1233	43.11	16.44	43.26	17.80	44.17	19.21	45.29	20.73	10.06
105	1263	43.29	15.93	43.51	17.26	44.48	18.63	45.63	20.11	9.82
106	1294	43.45	15.43	43.73	16.72	44.76	18.06	45.93	19.51	9.58
107	1326	43.61	14.94	43.94	16.20	45.02	17.51	46.22	18.92	9.35
108	1358	43.74	14.49	44.13	15.71	45.26	16.98	46.48	18.36	9.13
109	1392	43.86	14.03	44.30	15.21	45.48	16.46	46.73	17.80	8.91
110	1426	43.97	13.59	44.46	14.75	45.68	15.96	46.95	17.27	8.69
111	1460	44.07	13.18	44.59	14.30	45.87	15.49	47.16	16.77	8.49
112	1496	44.17	12.76	44.69	13.86	46.04	15.01	47.38	16.25	8.29
113	1533	44.22	12.36	44.81	13.44	46.20	14.53	47.57	15.73	8.09
114	1570	44.29	11.98	44.91	13.03	46.34	14.07	47.72	15.23	7.90
115	1609	44.34	11.60	45.00	12.63	46.45	13.62	47.86	14.74	7.71
116	1648	44.39	11.25	45.08	12.25	46.55	13.19	47.98	14.27	7.52
117	1688	44.43	10.90	45.15	11.88	46.64	12.77	48.10	13.82	7.34
118	1730	44.46	10.55	45.22	11.52	46.73	12.36	48.21	13.37	7.17
119	1772	44.49	10.22	45.28	11.16	46.80	11.96	48.29	12.93	7.00
120	1815	44.51	9.89	45.33	10.81	46.86	11.57	48.37	12.49	6.83
121	1860	44.51	9.56	45.37	10.46	46.91	11.19	48.43	12.06	6.67
122	1905	44.50	9.25	45.38	10.13	46.94	10.83	48.47	11.66	6.51
123	1952	44.49	8.95	45.40	9.80	46.96	10.47	48.50	11.26	6.35
124	2000	44.48	8.66	45.42	9.49	46.98	10.12	48.53	10.87	6.20

$\frac{E_{\mu}(E)}{f_2}$	366.3	354.3	345.4	329.6	$\frac{\text{keV-cm}^2}{\text{gram}}$
Atomic Weight	114.8	118.7	121.8	127.6	amu

ATOMIC SCATTERING FACTOR,  $f_1 + if_2$ 

N	E(eV)	I (53)		Xe (54)		Cs (55)		Ba (56)		$\lambda(\text{Å})$
		$f_1$	$f_2$	$f_1$	$f_2$	$f_1$	$f_2$	$f_1$	$f_2$	
0	100	22.24	28.60	9.59	38.52	-4.04	35.67	-3.97	5.11	124.0
1	102	24.05	27.07	13.03	38.73	-1.19	37.81	-5.22	6.16	121.5
2	104	25.50	25.66	16.42	38.60	1.94	39.94	-6.44	7.40	119.2
3	107	27.31	25.72	21.30	37.50	7.01	41.74	-8.25	9.58	115.9
4	110	28.84	21.97	25.50	35.41	12.31	42.60	-10.10	12.26	112.7
5	112	30.01	20.90	28.00	33.88	15.78	42.81	-11.25	14.53	110.7
6	115	31.78	19.43	31.32	30.73	20.80	41.93	-12.42	18.80	107.8
7	118	33.30	15.73	33.97	27.67	25.55	40.55	-12.53	23.71	105.1
8	121	33.19	12.80	35.43	23.62	29.64	38.11	-11.67	28.77	102.5
9	124	32.73	10.46	36.14	20.20	33.10	35.29	-9.40	33.50	100.0
10	127	32.09	8.60	36.21	16.95	36.02	32.00	-6.38	37.83	97.6
11	130	31.35	6.83	35.66	14.25	38.28	28.36	-2.72	41.68	95.4
12	133	30.37	5.35	34.97	12.03	39.50	24.50	1.67	44.68	93.2
13	136	29.26	4.21	34.07	10.16	39.86	21.08	6.67	46.70	91.2
14	140	27.77	3.08	32.88	8.11	39.62	16.99	13.45	48.24	88.6
15	143	26.58	2.46	31.93	6.88	38.91	14.52	18.59	48.44	86.7
16	147	25.26	2.37	30.66	5.56	37.84	11.80	25.05	47.18	84.3
17	150	24.47	2.31	29.72	4.78	36.95	10.09	29.60	45.74	82.7
18	154	23.57	2.24	28.58	3.97	35.68	8.20	34.95	42.47	80.5
19	158	22.81	2.33	27.50	3.36	34.40	6.73	39.17	38.41	78.5
20	162	22.17	2.49	26.50	2.92	33.15	5.55	42.43	34.22	76.5
21	166	21.64	2.65	25.59	2.63	31.92	4.65	44.61	28.85	74.7
22	170	21.23	2.81	24.75	2.44	30.80	3.96	45.38	24.25	72.9
23	174	20.87	2.96	23.93	2.34	29.74	3.43	45.13	20.00	71.3
24	178	20.52	3.08	23.25	2.30	28.76	3.06	44.33	16.57	69.7
25	182	20.15	3.21	22.69	2.32	27.85	2.79	43.26	13.76	68.1
26	187	19.78	3.60	22.02	2.42	26.85	2.61	41.72	10.90	66.3
27	191	19.59	4.01	21.53	2.53	26.09	2.55	40.42	9.05	64.9
28	196	19.64	4.27	21.02	2.70	25.28	2.55	38.77	7.24	63.3
29	201	19.61	4.40	20.58	2.90	24.57	2.62	37.18	5.84	61.7
30	206	19.56	4.54	20.20	3.11	23.94	2.74	35.68	4.80	60.2
31	211	19.51	4.67	19.86	3.33	23.38	2.89	34.26	4.02	58.8
32	216	19.48	4.78	19.60	3.56	22.90	3.09	32.95	3.48	57.4
33	221	19.44	4.87	19.36	3.79	22.50	3.30	31.80	3.11	56.1
34	227	19.40	4.99	19.13	4.06	22.07	3.57	30.53	2.85	54.6
35	232	19.36	5.08	19.00	4.28	21.79	3.80	29.56	2.75	53.4
36	238	19.33	5.20	18.86	4.54	21.50	4.08	28.57	2.74	52.1
37	244	19.30	5.31	18.74	4.77	21.26	4.35	27.71	2.82	50.8
38	250	19.27	5.42	18.67	5.00	21.07	4.62	26.94	2.96	49.6
39	256	19.26	5.54	18.63	5.21	20.93	4.88	26.27	3.15	48.4
40	262	19.26	5.65	18.62	5.41	20.82	5.13	25.73	3.37	47.3
41	269	19.27	5.78	18.61	5.63	20.73	5.41	25.18	3.67	46.1
42	275	19.31	5.89	18.61	5.78	20.68	5.62	24.77	3.92	45.1
43	282	19.36	5.96	18.62	5.97	20.66	5.87	24.40	4.23	44.0
44	289	19.40	6.01	18.65	6.12	20.66	6.09	24.11	4.53	42.9
45	296	19.41	6.06	18.67	6.26	20.68	6.29	23.86	4.83	41.9
46	303	19.41	6.10	18.71	6.38	20.70	6.48	23.67	5.12	40.9
47	311	19.42	6.16	18.75	6.51	20.75	6.66	23.51	5.42	39.9
48	318	19.41	6.20	18.79	6.60	20.81	6.82	23.42	5.68	39.0
49	326	19.39	6.25	18.83	6.70	20.87	6.96	23.34	5.95	38.0
50	334	19.37	6.30	18.87	6.78	20.94	7.10	23.30	6.19	37.1
51	342	19.35	6.35	18.91	6.84	21.01	7.21	23.29	6.42	36.3
52	351	19.32	6.41	18.91	6.90	21.09	7.33	23.29	6.63	35.3
53	359	19.28	6.45	18.92	6.94	21.15	7.41	23.32	6.81	34.5
54	368	19.24	6.51	18.93	6.98	21.23	7.48	23.36	6.98	33.7
55	377	19.20	6.56	18.91	7.00	21.30	7.55	23.41	7.13	32.9
56	386	19.16	6.61	18.89	7.02	21.35	7.60	23.47	7.26	32.1
57	396	19.13	6.65	18.84	7.03	21.41	7.65	23.53	7.38	31.3
58	406	19.07	6.62	18.77	7.04	21.46	7.67	23.59	7.48	30.5
59	415	18.97	6.59	18.66	7.05	21.48	7.69	23.65	7.54	29.9
60	426	18.82	6.55	18.53	7.09	21.51	7.71	23.70	7.62	29.1
61	436	18.65	6.52	18.42	7.12	21.52	7.71	23.74	7.65	28.4
62	447	18.43	6.49	18.27	7.16	21.55	7.72	23.78	7.69	27.7
63	458	18.18	6.45	18.13	7.15	21.51	7.61	23.81	7.70	27.1
64	469	17.86	6.40	17.94	7.10	21.42	7.57	23.80	7.71	26.4



AD-A114 893

AMERICAN INST OF PHYSICS NEW YORK  
LOW ENERGY X-RAY DIAGNOSTICS - 1981.(U)  
1981 D T ATTWOOD, B L HENKE

F/G 14/2

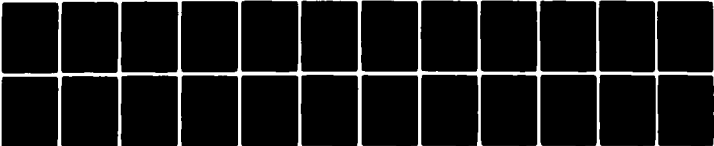
AFOSR-ISSA-81-00024

UNCLASSIFIED

75

AFOSR-TR-82-0378

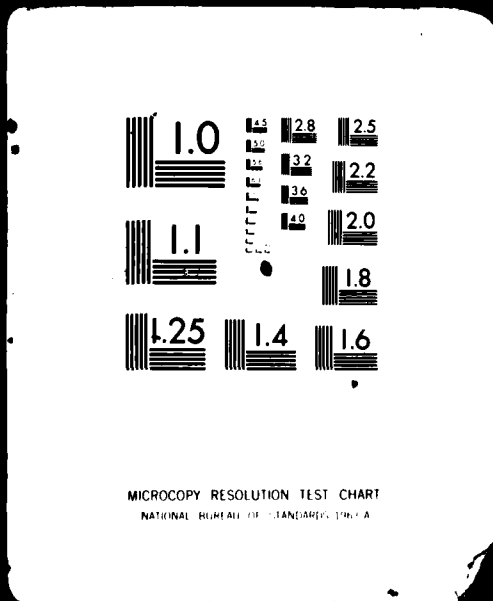
NL



END  
DATE  
FILMED  
DTIC

# CLASSIFIED

50F 3  
AD  
A114893



N	E(eV)	I (53) Iodine		Xe (54) Xenon		Cs (55) Cesium		Ba (56) Barium		$\lambda(\text{\AA})$
		$f_1$	$f_2$	$f_1$	$f_2$	$f_1$	$f_2$	$f_1$	$f_2$	
65	480	17.52	6.36	17.68	7.06	21.32	7.53	23.78	7.71	25.83
66	492	17.05	6.31	17.35	7.01	21.17	7.48	23.74	7.69	25.20
67	504	16.51	6.26	16.97	6.96	21.00	7.44	23.64	7.69	24.60
68	516	15.92	6.22	16.52	6.92	20.80	7.40	23.58	7.76	24.03
69	529	15.16	6.16	15.96	6.86	20.56	7.35	23.54	7.79	23.44
70	542	14.17	6.10	15.26	6.79	20.24	7.28	23.48	7.72	22.87
71	555	13.06	6.04	14.50	6.72	19.90	7.21	23.36	7.66	22.34
72	569	11.49	5.97	13.43	6.64	19.45	7.13	23.16	7.59	21.79
73	583	9.30	5.90	12.09	6.56	18.89	7.04	22.92	7.51	21.27
74	597	5.93	5.84	10.45	6.48	18.23	6.96	22.62	7.42	20.77
75	612	-1.89	5.77	8.26	6.40	17.42	6.88	22.24	7.34	20.26
76	627	-19.64 M	5.71	4.80	6.32	16.40	6.80	21.79	7.26	19.77
77	642	-2.62	38.64	-0.50	6.24	15.16	6.71	21.26	7.17	19.31
78	658	7.21	36.99	-10.25	6.16	13.38	6.60	20.54	7.08	18.84
79	674	13.82	35.46	-27.49 M	58.39	11.11	6.50	19.72	6.99	18.39
80	690	17.07	34.26	-6.92	53.90	7.24	6.42	18.68	6.90	17.97
81	707	19.16	33.11	15.69	49.44	-0.42	6.35	17.26	6.80	17.54
82	725	21.08	31.97	22.70	44.10	-35.83 M	6.25	15.01	6.70	17.10
83	742	23.04	30.96	25.67	39.69	3.82	41.58	12.07	6.60	16.71
84	760	25.53	29.95	28.28	35.60	12.65	39.52	6.45	6.49	16.31
85	779	28.31	28.96	30.23	32.22	19.41	37.50	-16.61 M	6.39	15.92
86	798	30.77	28.16	30.37	31.23	23.25	35.59	2.23	34.43	15.54
87	818	31.77	27.37	30.70	30.25	25.94	33.74	15.29	33.59	15.16
88	838	31.78	26.61	31.50	29.31	27.81	32.02	19.97	32.80	14.79
89	858	31.07	26.44	31.93	28.46	29.11	30.64	23.08	32.04	14.45
90	879	30.77	27.48	32.16	27.66	30.10	29.71	25.53	31.28	14.10
91	901	31.46	28.58	32.41	26.87	30.98	28.80	27.70	30.53	13.76
92	923	32.84	29.69	31.78	26.12	31.70	27.93	29.41	29.81	13.43
93	945	34.97	29.45	31.87	28.22	32.14	27.15	30.84	29.03	13.12
94	968	36.49	28.60	32.90	28.63	32.19	26.39	32.14	28.22	12.81
95	992	37.69	27.76	34.33	29.06	31.45	25.64	33.10	27.41	12.50
96	1016	38.58	26.98	36.05	29.28	29.39	26.03	33.87	26.65	12.20
97	1041	39.33	26.30	37.61	28.52	31.08	32.40	34.23	25.88	11.91
98	1067	40.04	25.68	38.51	27.90	34.85	31.47	34.58	25.90	11.62
99	1093	40.73	25.10	39.46	27.31	37.31	30.59	35.12	25.93	11.34
100	1119	41.34	24.54	40.31	26.75	38.79	29.76	35.76	25.95	11.08
101	1147	41.97	23.97	41.11	26.17	40.14	28.91	36.52	25.97	10.81
102	1175	42.56	23.42	41.92	25.62	41.29	28.10	37.32	25.99	10.55
103	1204	43.12	22.88	42.63	25.07	42.24	27.30	38.19	26.02	10.30
104	1233	43.68	22.37	43.34	24.54	43.10	26.55	39.16	26.04	10.06
105	1263	44.26	21.81	44.13	23.96	43.90	25.79	40.29	25.90	9.82
106	1294	44.76	21.16	44.78	23.24	44.60	25.02	41.35	25.39	9.58
107	1326	45.21	20.52	45.33	22.53	45.24	24.26	42.23	24.89	9.35
108	1358	45.60	19.92	45.83	21.87	45.83	23.55	42.99	24.40	9.13
109	1392	45.96	19.31	46.29	21.19	46.36	22.83	43.75	23.91	8.91
110	1426	46.28	18.74	46.71	20.56	46.83	22.15	44.45	23.44	8.69
111	1460	46.57	18.19	47.13	19.95	47.27	21.50	45.13	23.00	8.49
112	1496	46.85	17.64	47.55	19.35	47.69	20.85	45.84	22.49	8.29
113	1533	47.09	17.08	47.86	18.76	48.05	20.20	46.50	21.85	8.09
114	1570	47.31	16.56	48.14	18.21	48.39	19.58	47.01	21.24	7.90
115	1609	47.51	16.04	48.37	17.66	48.69	18.97	47.50	20.63	7.71
116	1648	47.69	15.54	48.52	17.13	48.96	18.39	47.94	20.05	7.52
117	1688	47.85	15.06	48.64	16.62	49.22	17.83	48.33	19.48	7.34
118	1730	48.00	14.59	48.72	16.12	49.47	17.27	48.72	18.92	7.17
119	1772	48.14	14.13	48.76	15.62	49.69	16.72	49.07	18.37	7.00
120	1815	48.25	13.68	48.79	15.14	49.88	16.18	49.37	17.82	6.83
121	1860	48.36	13.24	48.83	14.66	50.06	15.65	49.65	17.27	6.67
122	1905	48.42	12.82	48.86	14.21	50.19	15.15	49.90	16.76	6.51
123	1952	48.49	12.41	48.89	13.76	50.31	14.66	50.12	16.25	6.35
124	2000	48.57	12.01	48.92	13.33	50.44	14.18	50.34	15.76	6.20

$\frac{E_{\mu}(E)}{F_2}$	331.4	320.3	316.4	306.2	$\frac{\text{keV-cm}^2}{\text{gram}}$
Atomic Weight	126.9	131.3	132.9	137.3	amu

ATOMIC SCATTERING FACTOR,  $f_1 + if_2$ 

N	E(eV)	La (57)		Ce (58)		Pr (59)		Nd (60)		$\lambda(\text{Å})$
		$f_1$	$f_2$	$f_1$	$f_2$	$f_1$	$f_2$	$f_1$	$f_2$	
0	100	-3.70	11.52	2.89	5.21	13.95	4.31	12.33	5.27	124.0
1	102	-5.50	13.59	1.96	5.50	13.33	4.65	11.88	5.29	121.5
2	104	-7.18	15.98	0.95	5.81	12.67	5.02	11.31	5.31	119.2
3	107	-9.53	20.26	-0.87	6.28	11.64	5.60	10.34	5.33	115.9
4	110	-11.77	25.52	-3.51	6.79	10.41	6.24	8.99	5.36	112.7
5	112	-16.24	29.66	-6.52	7.14	9.15	6.69	7.64	5.37	110.7
6	115	-15.81	44.03	-13.10	9.15	6.82	8.00	5.11	5.98	107.8
7	118	-0.39	71.30	-20.59	17.49	4.42	11.37	2.43	8.38	105.1
8	121	18.82	62.53	-24.77	32.87	2.72	16.01	0.15	11.66	102.5
9	124	30.16	55.01	-17.63	60.83	2.50	22.35	-1.45	16.09	100.0
10	127	36.60	48.55	15.58	64.45	6.16	30.96	-1.85	22.04	97.6
11	130	40.72	42.97	27.52	52.14	14.96	42.57	-0.79	29.95	95.4
12	133	44.26	37.63	32.82	42.81	31.65	38.83	7.88	38.27	93.2
13	136	45.86	31.37	34.88	36.73	36.66	29.22	16.21	36.46	91.2
14	140	46.04	24.76	36.55	30.11	38.86	20.20	23.32	32.69	88.6
15	143	45.28	20.82	36.98	26.03	38.11	15.42	26.24	30.18	86.7
16	147	43.99	16.62	36.74	21.54	36.19	10.85	28.99	27.20	84.3
17	150	42.83	14.09	36.04	18.75	34.16	8.39	30.66	25.20	82.7
18	154	41.16	11.45	34.79	16.36	31.22	7.68	32.39	22.27	80.5
19	158	39.59	9.38	33.97	14.59	29.90	7.84	33.04	19.54	78.5
20	162	38.09	7.73	33.27	13.06	29.14	7.99	33.29	17.20	76.5
21	166	36.64	6.39	32.58	11.71	28.78	8.14	33.24	15.18	74.7
22	170	35.21	5.31	31.86	10.53	28.87	8.29	32.95	13.45	72.9
23	174	33.90	4.57	31.12	9.59	29.12	7.96	32.46	12.03	71.3
24	178	32.68	4.03	30.39	8.81	29.21	7.32	31.91	10.84	69.7
25	182	31.64	3.56	29.64	8.11	29.05	6.75	31.28	9.79	68.1
26	187	30.35	3.01	28.69	7.70	28.79	6.24	30.39	8.84	66.3
27	191	29.26	2.62	28.19	7.52	28.58	5.92	29.57	8.23	64.9
28	196	27.84	2.70	27.68	7.24	28.32	5.48	28.58	7.99	63.3
29	201	26.83	3.05	27.22	6.95	27.98	5.05	27.97	7.99	61.7
30	206	26.05	3.43	26.75	6.69	27.56	4.67	27.50	7.99	60.2
31	211	25.47	3.84	26.23	6.44	27.06	4.33	27.11	7.98	58.8
32	216	25.09	4.11	25.67	6.45	26.48	4.33	26.78	8.05	57.4
33	221	24.74	4.33	25.29	6.54	26.08	4.43	26.56	8.14	56.1
34	227	24.35	4.60	24.96	6.64	25.70	4.55	26.35	8.24	54.6
35	232	24.06	4.83	24.74	6.73	25.45	4.65	26.21	8.33	53.4
36	238	23.77	5.12	24.52	6.83	25.20	4.77	26.10	8.43	52.1
37	244	23.53	5.42	24.34	6.3	24.98	4.89	26.01	8.53	50.8
38	250	23.33	5.72	24.19	7.03	24.78	5.01	25.95	8.63	49.6
39	256	23.20	6.04	24.07	7.13	24.60	5.13	25.92	8.73	48.4
40	262	23.11	6.37	23.98	7.23	24.42	5.25	25.90	8.83	47.3
41	269	23.09	6.76	23.89	7.35	24.21	5.39	25.89	8.94	46.1
42	275	23.23	7.10	23.82	7.44	24.03	5.51	25.90	9.03	45.1
43	282	23.42	7.27	23.76	7.57	23.74	5.66	25.92	9.15	44.0
44	289	23.58	7.34	23.72	7.69	23.48	6.03	25.96	9.26	42.9
45	296	23.66	7.42	23.70	7.82	23.29	6.42	26.01	9.37	41.9
46	303	23.73	7.49	23.69	7.95	23.20	6.82	26.07	9.48	40.9
47	311	23.79	7.56	23.69	8.09	23.14	7.30	26.14	9.61	39.9
48	318	23.84	7.63	23.70	8.21	23.15	7.73	26.23	9.72	39.0
49	326	23.90	7.71	23.74	8.35	23.23	8.25	26.33	9.84	38.0
50	334	23.95	7.78	23.78	8.49	23.49	8.78	26.44	9.96	37.1
51	342	24.01	7.86	23.84	8.63	23.84	9.29	26.56	10.08	36.3
52	351	24.07	7.94	23.91	8.79	24.32	9.45	26.70	10.21	35.3
53	359	24.13	8.01	23.99	8.92	24.62	9.59	26.84	10.33	34.5
54	368	24.21	8.09	24.10	9.07	24.92	9.74	27.01	10.46	33.7
55	377	24.28	8.17	24.23	9.23	25.21	9.89	27.21	10.58	32.9
56	386	24.38	8.25	24.40	9.38	25.52	10.04	27.42	10.71	32.1
57	396	24.51	8.32	24.66	9.50	25.92	10.15	27.74	10.80	31.3
58	406	24.63	8.32	24.87	9.48	26.24	10.12	28.01	10.76	30.5
59	415	24.71	8.32	25.02	9.46	26.50	10.10	28.22	10.73	29.9
60	426	24.78	8.31	25.17	9.44	26.75	10.07	28.43	10.69	29.1
61	436	24.84	8.31	25.29	9.42	26.95	10.04	28.61	10.66	28.4
62	447	24.90	8.30	25.41	9.40	27.16	10.01	28.79	10.62	27.7
63	458	24.95	8.29	25.52	9.36	27.36	9.97	28.97	10.58	27.1
64	469	24.98	8.26	25.60	9.32	27.53	9.92	29.12	10.52	26.4

N	E(eV)	La (57) Lanthanum		Ce (58) Cerium		Pr (59) Praseodymium		Nd (60) Neodymium		$\lambda(\text{\AA})$
		$f_1$	$f_2$	$f_1$	$f_2$	$f_1$	$f_2$	$f_1$	$f_2$	
65	480	25.00	8.23	25.67	9.27	27.68	9.87	29.26	10.46	25.83
66	492	25.00	8.20	25.73	9.23	27.83	9.81	29.40	10.40	25.20
67	504	24.99	8.18	25.78	9.18	27.96	9.76	29.53	10.34	24.60
68	516	24.98	8.15	25.82	9.14	28.08	9.71	29.65	10.28	24.03
69	529	24.95	8.11	25.85	9.08	28.20	9.65	29.78	10.21	23.44
70	542	24.89	8.05	25.86	9.00	28.29	9.56	29.89	10.12	22.87
71	555	24.82	8.00	25.85	8.93	28.38	9.48	29.98	10.03	22.34
72	569	24.71	7.93	25.81	8.83	28.43	9.38	30.06	9.93	21.79
73	583	24.56	7.86	25.74	8.74	28.46	9.28	30.11	9.82	21.27
74	597	24.38	7.78	25.64	8.65	28.47	9.18	30.14	9.71	20.77
75	612	24.16	7.71	25.49	8.55	28.45	9.08	30.15	9.60	20.26
76	627	23.88	7.64	25.31	8.46	28.41	8.98	30.15	9.50	19.77
77	642	23.56	7.55	25.13	8.36	28.34	8.87	30.14	9.38	19.31
78	658	23.15	7.45	24.86	8.23	28.22	8.73	30.07	9.24	18.84
79	674	22.66	7.34	24.51	8.10	28.07	8.60	29.97	9.10	18.39
80	690	22.05	7.27	24.10	8.01	27.86	8.50	29.83	9.00	17.97
81	707	21.33	7.19	23.64	7.92	27.63	8.41	29.69	8.90	17.54
82	725	20.38	7.08	23.03	7.79	27.31	8.27	29.48	8.75	17.10
83	742	19.21	6.98	22.34	7.67	26.97	8.15	29.25	8.62	16.71
84	760	17.57	6.88	21.46	7.55	26.51	8.02	28.95	8.48	16.31
85	779	15.33	6.77	20.32	7.43	25.95	7.89	28.58	8.35	15.92
86	798	11.75	6.67	18.88	7.30	25.25	7.75	28.09	8.20	15.54
87	818	-2.28	6.57	16.76	7.17	24.35	7.61	27.52	8.05	15.16
88	838	-8.01 M	35.41	13.60	7.04	23.17	7.48	26.77	7.91	14.79
89	858	11.71	34.38	8.13	6.93	21.70	7.35	25.88	7.78	14.45
90	879	18.46	33.38	-12.92 M	6.81	19.72	7.21	24.71	7.63	14.10
91	901	22.26	32.40	2.59	37.19	16.09	7.08	23.02	7.49	13.76
92	923	25.30	31.46	16.38	35.95	-9.81 M	6.95	20.61	7.35	13.43
93	945	27.48	30.59	21.26	34.78	-16.58	37.24	14.56	7.22	13.12
94	968	29.13	29.73	24.77	33.63	13.32	36.08	2.10 M	7.09	12.81
95	992	30.58	28.87	27.25	32.50	20.03	34.94	11.26	30.51	12.50
96	1016	31.71	28.06	29.04	31.46	25.66	33.87	21.12	30.04	12.20
97	1041	32.32	27.26	30.20	30.50	29.00	32.81	25.16	29.57	11.91
98	1067	32.93	27.24	31.16	30.42	31.43	31.75	27.63	29.08	11.62
99	1093	33.64	27.22	32.26	30.34	33.42	30.74	29.99	28.62	11.34
100	1119	34.45	27.20	33.38	30.26	35.03	29.79	31.51	28.17	11.08
101	1147	35.33	27.17	34.55	30.18	36.44	28.83	33.09	27.71	10.81
102	1175	36.22	27.15	35.69	30.10	37.51	27.91	34.26	27.27	10.55
103	1204	37.17	27.13	36.87	30.02	38.42	27.02	35.27	26.83	10.30
104	1233	38.21	27.11	38.10	29.94	38.78	26.18	35.91	26.41	10.06
105	1263	39.33	26.96	39.42	29.73	39.05	25.64	36.53	26.19	9.82
106	1294	40.38	26.53	40.71	29.22	39.40	25.76	37.12	26.43	9.58
107	1326	41.32	26.10	41.80	28.71	39.86	25.88	37.84	26.68	9.35
108	1358	42.17	25.68	42.78	28.22	40.53	26.00	38.68	26.92	9.13
109	1392	43.00	25.26	43.74	27.73	41.32	26.12	39.65	27.18	8.91
110	1426	43.80	24.85	44.66	27.25	42.17	26.24	40.68	27.43	8.69
111	1460	44.60	24.46	45.58	26.80	43.04	26.36	41.96	27.68	8.49
112	1496	45.49	23.99	46.61	26.25	44.13	26.25	43.39	27.71	8.29
113	1533	46.24	23.30	47.49	25.46	45.72	26.68	45.00	27.09	8.09
114	1570	46.90	22.64	48.21	24.72	47.02	25.86	46.00	26.50	7.90
115	1609	47.48	21.99	48.86	23.98	48.15	25.05	46.80	26.85	7.71
116	1648	47.97	21.37	49.44	23.27	48.95	24.28	48.15	26.02	7.52
117	1688	48.43	20.76	49.96	22.59	49.74	23.54	49.27	25.21	7.34
118	1730	48.87	20.16	50.48	21.91	50.41	22.80	50.12	24.41	7.17
119	1772	49.26	19.57	50.93	21.23	50.99	22.07	50.84	23.63	7.00
120	1815	49.61	19.00	51.31	20.57	51.51	21.36	51.47	22.87	6.83
121	1860	49.94	18.43	51.66	19.91	51.95	20.65	52.00	22.12	6.67
122	1905	50.18	17.89	51.97	19.29	52.30	19.99	52.44	21.41	6.51
123	1952	50.44	17.36	52.25	18.68	52.67	19.33	52.89	20.71	6.35
124	2000	50.70	16.84	52.54	18.09	53.05	18.70	53.35	20.04	6.20

 $E_{II}(E)$   
 $f_2$ 

302.8

300.2

298.5

291.6

keV-cm<sup>2</sup>  
gramAtomic  
Weight

138.9

140.1

140.9

144.2

amu

ATOMIC SCATTERING FACTOR,  $f_1 + if_2$ 

N	E(eV)	Pm (61)		Sm (62)		Eu (63)		Gd (64)		$\lambda(\text{Å})$
		$f_1$	$f_2$	$f_1$	$f_2$	$f_1$	$f_2$	$f_1$	$f_2$	
0	100	11.68	5.80	8.60	6.65	14.42	6.27	13.48	8.14	124.0
1	102	11.27	5.78	8.27	6.53	14.14	6.17	13.38	8.07	121.5
2	104	10.76	5.76	7.88	6.41	13.81	6.09	13.25	8.00	119.2
3	107	9.85	5.74	7.16	6.25	13.23	5.96	13.01	7.90	115.9
4	110	8.57	5.72	6.19	6.09	12.34	5.84	12.68	7.80	112.7
5	112	7.25	5.70	5.09	5.98	11.68	6.05	12.39	7.74	110.7
6	115	5.03	6.48	3.30	6.19	10.68	6.37	11.92	7.59	107.8
7	118	2.91	8.37	1.46	7.33	9.65	6.70	11.29	7.33	105.1
8	121	1.08	10.74	-0.12	8.63	8.39	7.04	10.29	7.08	102.5
9	124	-0.45	13.69	-1.78	10.13	6.70	7.39	8.93	6.85	100.0
10	127	-1.63	17.36	-3.63	11.84	4.09	7.75	7.10	6.62	97.6
11	130	-2.42	21.90	-5.87	13.79	-0.10	8.12	4.56	6.41	95.4
12	133	-2.07	27.49	-9.10	16.65	-5.46	13.71	0.10	6.85	93.2
13	136	1.87	34.34	-12.30	23.39	-6.44	22.89	-4.79	10.69	91.2
14	140	11.22	44.13	-12.98	36.38	0.75	44.57	-10.25	19.09	88.6
15	143	19.89	39.99	-2.76	50.24	12.19	39.92	-12.20	29.17	86.7
16	147	26.41	35.17	12.40	51.82	21.11	34.58	-2.16	50.64	84.3
17	150	29.31	32.01	22.29	48.14	24.06	31.13	18.18	57.38	82.7
18	154	31.46	28.32	29.49	41.34	24.91	28.08	30.03	42.09	80.5
19	158	32.55	25.14	32.83	34.80	25.88	26.84	32.92	34.76	78.5
20	162	33.08	22.38	34.46	29.42	26.96	25.70	34.70	28.84	76.5
21	166	33.19	19.98	34.88	24.98	28.00	24.62	35.11	24.04	74.7
22	170	33.02	18.53	33.81	21.29	28.88	23.62	33.87	20.12	72.9
23	174	32.96	17.22	32.75	19.18	29.67	22.68	32.56	18.05	71.3
24	178	32.87	16.03	31.69	17.99	30.35	21.79	31.08	17.02	69.7
25	182	32.76	14.94	31.16	16.90	31.00	20.96	29.99	16.07	68.1
26	187	32.60	13.71	30.58	15.75	31.79	19.99	28.93	16.27	66.3
27	191	32.41	12.82	30.16	14.93	32.32	18.56	28.66	16.86	64.9
28	196	32.05	11.82	29.64	14.14	32.16	17.45	29.37	16.61	63.3
29	201	31.60	10.91	29.20	13.47	32.14	16.67	29.65	15.94	61.7
30	206	31.02	10.10	28.75	12.86	32.12	15.95	29.73	15.31	60.2
31	211	30.30	9.36	28.24	12.28	32.06	15.27	29.66	14.72	58.8
32	216	29.43	9.25	27.71	12.10	31.81	14.72	29.49	14.43	57.4
33	221	28.91	9.32	27.35	12.03	31.65	14.49	29.41	14.23	56.1
34	227	28.48	9.40	27.07	11.95	31.55	14.23	29.40	13.99	54.6
35	232	28.23	9.47	26.92	11.89	31.54	14.02	29.41	13.81	53.4
36	238	28.01	9.55	26.79	11.81	31.57	13.78	29.43	13.60	52.1
37	244	27.85	9.63	26.69	11.74	31.59	13.55	29.46	13.39	50.8
38	250	27.72	9.71	26.61	11.67	31.62	13.32	29.48	13.19	49.6
39	256	27.65	9.79	26.56	11.60	31.64	13.11	29.49	13.00	48.4
40	262	27.60	9.87	26.50	11.53	31.65	12.91	29.49	12.82	47.3
41	269	27.56	9.96	26.43	11.46	31.65	12.68	29.43	12.62	46.1
42	275	27.53	10.03	26.33	11.40	31.62	12.49	29.29	12.45	45.1
43	282	27.54	10.13	26.23	11.44	31.49	12.28	29.15	12.47	44.0
44	289	27.56	10.22	26.17	11.54	31.33	12.14	29.05	12.58	42.9
45	296	27.60	10.32	26.17	11.63	31.16	12.25	29.05	12.69	41.9
46	303	27.64	10.42	26.20	11.72	31.13	12.35	29.09	12.79	40.9
47	311	27.72	10.53	26.25	11.82	31.14	12.47	29.18	12.91	39.9
48	318	27.80	10.62	26.32	11.91	31.18	12.57	29.25	13.01	39.0
49	326	27.89	10.72	26.42	12.00	31.26	12.69	29.38	13.13	38.0
50	334	28.00	10.83	26.53	12.10	31.38	12.80	29.53	13.24	37.1
51	342	28.12	10.93	26.66	12.20	31.51	12.91	29.69	13.35	36.3
52	351	28.27	11.04	26.81	12.30	31.67	13.04	29.88	13.47	35.3
53	359	28.42	11.14	26.96	12.39	31.84	13.15	30.07	13.58	34.5
54	368	28.60	11.25	27.15	12.50	32.05	13.27	30.31	13.70	33.7
55	377	28.80	11.36	27.36	12.60	32.28	13.38	30.57	13.82	32.9
56	386	29.02	11.46	27.62	12.69	32.58	13.50	30.88	13.93	32.1
57	396	29.36	11.53	27.97	12.75	32.97	13.57	31.30	13.99	31.3
58	406	29.62	11.48	28.25	12.68	33.29	13.49	31.63	13.91	30.5
59	415	29.83	11.43	28.46	12.63	33.54	13.42	31.90	13.85	29.9
60	426	30.05	11.37	28.70	12.56	33.82	13.35	32.19	13.77	29.1
61	436	30.24	11.33	28.91	12.50	34.06	13.28	32.44	13.70	28.4
62	447	30.43	11.27	29.12	12.43	34.31	13.20	32.71	13.63	27.7
63	458	30.62	11.21	29.33	12.35	34.55	13.11	32.96	13.54	27.1
64	469	30.78	11.13	29.51	12.26	34.76	13.02	33.18	13.45	26.4

N	E(eV)	Pm (61) Promethium		Sm (62) Samarium		Eu (63) Europium		Gd (64) Gadolinium		$\lambda(A)$
		$f_1$	$f_2$	$f_1$	$f_2$	$f_1$	$f_2$	$f_1$	$f_2$	
65	480	30.94	11.06	29.68	12.18	34.96	12.92	33.39	13.37	25.83
66	492	31.08	10.99	29.85	12.08	35.16	12.82	33.61	13.27	25.20
67	504	31.22	10.91	30.01	11.99	35.35	12.73	33.82	13.18	24.60
68	516	31.36	10.84	30.17	11.91	35.54	12.63	34.03	13.09	24.03
69	529	31.50	10.76	30.33	11.80	35.75	12.52	34.24	12.99	23.44
70	542	31.62	10.65	30.48	11.68	35.92	12.39	34.44	12.87	22.87
71	555	31.74	10.55	30.61	11.55	36.10	12.26	34.63	12.75	22.34
72	569	31.83	10.43	30.72	11.41	36.25	12.11	34.82	12.62	21.79
73	583	31.91	10.31	30.81	11.27	36.38	11.97	34.98	12.47	21.27
74	597	31.96	10.19	30.88	11.13	36.49	11.82	35.12	12.34	20.77
75	612	32.00	10.08	30.94	11.00	36.60	11.68	35.27	12.19	20.26
76	627	32.03	9.96	30.99	10.86	36.69	11.53	35.40	12.05	19.77
77	642	32.05	9.84	31.03	10.72	36.78	11.38	35.53	11.90	19.31
78	658	32.03	9.69	31.03	10.55	36.83	11.20	35.62	11.71	18.84
79	674	31.99	9.55	30.99	10.39	36.86	11.02	35.68	11.53	18.39
80	690	31.91	9.44	30.93	10.27	36.85	10.89	35.71	11.40	17.97
81	707	31.83	9.34	30.88	10.16	36.85	10.77	35.76	11.27	17.54
82	725	31.71	9.18	30.80	9.99	36.83	10.59	35.79	11.09	17.10
83	742	31.56	9.05	30.68	9.84	36.79	10.44	35.80	10.93	16.71
84	760	31.36	8.91	30.52	9.69	36.70	10.28	35.77	10.76	16.31
85	779	31.13	8.76	30.33	9.53	36.60	10.11	35.74	10.59	15.92
86	798	30.83	8.61	30.09	9.37	36.46	9.94	35.66	10.41	15.54
87	818	30.46	8.45	29.78	9.20	36.26	9.76	35.53	10.22	15.16
88	838	29.99	8.30	29.42	9.03	36.02	9.59	35.37	10.05	14.79
89	858	29.46	8.16	29.00	8.88	35.73	9.42	35.19	9.87	14.45
90	879	28.79	8.01	28.45	8.71	35.37	9.24	34.95	9.69	14.10
91	901	27.89	7.85	27.77	8.54	34.90	9.06	34.63	9.51	13.76
92	923	26.80	7.71	26.99	8.38	34.36	8.89	34.27	9.34	13.43
93	945	25.32	7.56	26.01	8.22	33.72	8.72	33.86	9.17	13.12
94	968	23.26	7.41	24.65	8.05	32.84	8.54	33.31	8.99	12.81
95	992	19.21	7.26	22.86	7.89	31.72	8.37	32.63	8.81	12.50
96	1016	10.33 M	7.12	20.52	7.73	30.37	8.20	31.85	8.63	12.20
97	1041	13.70	28.41	16.35	7.56	28.45	8.02	30.84	8.45	11.91
98	1067	20.17	28.47	0.13 M	7.39	25.01	7.85	29.35	8.26	11.62
99	1093	24.32	28.53	4.58	31.65	16.91	7.68	27.49	8.08	11.34
100	1119	27.03	28.58	16.54	31.62	-0.39 M	7.52	24.99	7.91	11.08
101	1147	29.14	28.64	22.97	31.60	14.01	38.05	19.46	7.74	10.81
102	1175	30.98	28.70	25.98	31.57	27.86	36.79	3.02 M	7.57	10.55
103	1204	32.51	28.76	28.31	31.54	33.54	35.55	6.48	37.04	10.30
104	1233	33.93	28.82	30.25	31.52	37.01	34.38	20.07	35.86	10.06
105	1263	35.24	28.88	31.96	31.49	39.97	33.25	30.92	34.70	9.82
106	1294	36.51	28.94	33.53	31.47	42.04	32.14	33.97	33.58	9.58
107	1326	37.74	29.00	34.97	31.45	44.02	31.07	37.13	32.48	9.35
108	1358	38.96	29.06	36.36	31.42	45.50	30.05	39.10	31.45	9.13
109	1392	40.23	29.12	37.73	31.40	46.94	29.04	40.82	30.41	8.91
110	1426	41.59	29.18	39.06	31.37	47.98	28.08	42.17	29.44	8.69
111	1460	43.02	29.24	40.46	31.35	48.96	27.17	42.98	28.51	8.49
112	1496	44.63	29.05	41.92	31.09	49.75	26.28	43.65	27.58	8.29
113	1533	46.15	28.15	42.65	30.13	50.34	25.48	41.86	26.65	8.09
114	1570	47.10	27.30	43.45	31.28	50.08	24.73	42.55	29.81	7.90
115	1609	47.97	26.45	44.73	30.27	49.76	23.97	43.99	28.90	7.71
116	1648	47.70	26.82	46.01	29.31	50.88	24.92	45.42	28.03	7.52
117	1688	49.60	26.01	47.32	28.39	52.20	24.09	47.50	29.07	7.34
118	1730	50.78	25.21	48.85	28.72	53.59	23.27	50.06	28.12	7.17
119	1772	51.56	24.43	50.30	27.83	54.10	22.50	50.90	27.21	7.00
120	1815	52.29	23.66	51.09	26.97	54.91	22.71	51.39	26.34	6.83
121	1860	52.80	22.90	51.78	26.11	55.64	21.98	51.90	25.47	6.67
122	1905	53.29	22.19	52.48	25.30	56.16	21.29	52.82	25.75	6.51
123	1952	53.81	21.48	53.20	24.50	56.65	20.60	54.04	24.91	6.35
124	2000	54.33	20.80	53.94	23.72	57.16	19.94	55.28	24.10	6.20

$\frac{E_{\mu}(E)}{f_2}$	290.0	279.7	276.8	267.5	$\frac{\text{keV-cm}^2}{\text{gram}}$
Atomic Weight	145.0	150.4	152.0	157.3	amu

ATOMIC SCATTERING FACTOR,  $f_1 + if_2$ 

N	E(eV)	Tb (65)		Dy (66)		Ho (67)		Er (68)		$\lambda(\text{Å})$
		$f_1$	$f_2$	$f_1$	$f_2$	$f_1$	$f_2$	$f_1$	$f_2$	
0	100	14.67	7.16	16.28	9.04	15.02	8.21	17.34	9.13	124.0
1	102	14.51	7.27	16.29	9.00	15.04	8.32	17.38	9.01	121.5
2	104	14.37	7.38	16.30	8.97	15.06	8.43	17.39	8.89	119.2
3	107	14.17	7.54	16.29	8.92	15.07	8.60	17.38	8.71	115.9
4	110	13.97	7.71	16.23	8.88	15.16	8.76	17.32	8.55	112.7
5	112	13.88	7.82	16.20	8.85	15.20	8.87	17.20	8.44	110.7
6	115	13.73	7.98	16.11	8.79	15.27	9.01	16.98	8.39	107.8
7	118	13.64	8.14	15.95	8.71	15.33	9.09	16.79	8.58	105.1
8	121	13.69	8.09	15.72	8.63	15.35	9.18	16.78	8.77	102.5
9	124	13.34	7.64	15.43	8.55	15.33	9.26	16.87	8.95	100.0
10	127	12.70	7.23	15.04	8.47	15.33	9.34	17.07	9.14	97.6
11	130	11.76	6.85	14.53	8.40	15.34	9.42	17.41	9.33	95.4
12	133	10.48	6.49	13.66	8.45	15.56	9.39	18.54	9.14	93.2
13	136	8.41	6.12	12.90	8.99	15.40	8.95	18.70	7.63	91.2
14	140	3.38	5.68	11.95	9.76	14.83	8.42	18.02	6.04	88.6
15	143	-5.94	5.38	11.24	10.36	14.06	8.04	16.91	5.09	86.7
16	147	-8.41	36.83	9.77	11.20	12.41	7.59	14.93	4.08	84.3
17	150	-0.41	39.50	7.92	11.85	10.61	7.27	12.91	3.46	82.7
18	154	14.76	39.12	4.02	16.84	6.85	9.18	9.30	4.46	80.5
19	158	22.43	35.08	6.35	26.66	4.47	13.03	6.20	6.97	78.5
20	162	27.04	29.50	16.40	34.84	3.42	18.33	3.65	10.75	76.5
21	166	29.11	24.38	25.38	26.53	4.75	25.58	2.28	16.42	74.7
22	170	28.44	20.24	27.05	20.33	12.26	32.86	5.29	24.82	72.9
23	174	27.02	18.49	25.71	17.77	19.19	30.85	11.99	29.24	71.3
24	178	26.15	18.54	24.97	17.08	23.88	27.22	19.13	28.81	69.7
25	182	26.37	18.59	24.79	16.43	25.87	24.09	24.12	24.52	68.1
26	187	26.76	17.62	24.67	15.67	26.70	20.76	26.00	18.97	66.3
27	191	26.79	16.71	24.43	15.11	26.43	18.48	25.56	15.52	64.9
28	196	26.48	16.34	24.09	14.89	25.03	17.64	23.27	14.27	63.3
29	201	26.48	16.16	23.98	14.89	24.78	17.64	22.51	14.18	61.7
30	206	26.55	15.99	24.02	14.89	24.82	17.63	21.99	14.09	60.2
31	211	26.66	15.82	24.13	14.89	25.04	17.62	21.63	14.00	58.8
32	216	26.80	15.66	24.26	14.86	25.36	17.49	21.31	14.18	57.4
33	221	26.97	15.52	24.42	14.83	25.64	17.33	21.15	14.44	56.1
34	227	27.17	15.35	24.60	14.80	25.95	17.14	21.10	14.75	54.6
35	232	27.32	15.22	24.75	14.77	26.20	16.98	21.15	15.01	53.4
36	238	27.52	15.06	24.93	14.74	26.48	16.80	21.27	15.33	52.1
37	244	27.71	14.91	25.10	14.70	26.72	16.63	21.42	15.64	50.8
38	250	27.88	14.76	25.25	14.67	26.93	16.46	21.61	15.94	49.6
39	256	28.05	14.62	25.39	14.64	27.12	16.30	21.83	16.25	48.4
40	262	28.20	14.49	25.52	14.61	27.28	16.15	22.08	16.56	47.3
41	269	28.36	14.33	25.62	14.58	27.39	15.97	22.44	16.91	46.1
42	275	28.48	14.21	25.67	14.55	27.42	15.83	22.81	17.21	45.1
43	282	28.56	14.08	25.68	14.67	27.42	15.87	23.28	17.40	44.0
44	289	28.66	14.05	25.78	14.85	27.49	15.99	23.70	17.53	42.9
45	296	28.78	14.02	25.92	15.02	27.62	16.12	24.09	17.65	41.9
46	303	28.92	13.99	26.08	15.20	27.79	16.24	24.44	17.77	40.9
47	311	29.09	13.96	26.29	15.40	28.01	16.37	24.83	17.91	39.9
48	318	29.23	13.93	26.50	15.57	28.21	16.49	25.17	18.02	39.0
49	326	29.39	13.90	26.74	15.76	28.45	16.62	25.54	18.15	38.0
50	334	29.53	13.87	27.01	15.95	28.71	16.75	25.91	18.28	37.1
51	342	29.65	13.84	27.29	16.13	28.97	16.88	26.28	18.41	36.3
52	351	29.78	13.87	27.62	16.34	29.28	17.02	26.69	18.55	35.3
53	359	29.94	13.92	27.92	16.52	29.55	17.14	27.05	18.67	34.5
54	368	30.13	13.98	28.29	16.73	29.88	17.27	27.46	18.80	33.7
55	377	30.34	14.03	28.70	16.93	30.22	17.41	27.88	18.94	32.9
56	386	30.57	14.09	29.15	17.13	30.57	17.54	28.31	19.07	32.1
57	396	30.86	14.13	29.78	17.28	30.98	17.63	28.79	19.15	31.3
58	406	31.15	14.08	30.32	17.22	31.35	17.75	29.23	19.27	30.5
59	415	31.39	14.03	30.76	17.16	31.71	17.85	29.65	19.38	29.9
60	426	31.63	13.97	31.23	17.09	32.17	17.97	30.18	19.51	29.1
61	436	31.85	13.92	31.64	17.04	32.63	18.08	30.70	19.63	28.4
62	447	32.08	13.87	32.09	16.97	33.18	18.20	31.32	19.75	27.7
63	458	32.29	13.82	32.55	16.86	33.84	18.16	32.05	19.71	27.1
64	469	32.49	13.77	32.94	16.70	34.36	17.99	32.64	19.51	26.4



N	E(eV)	Tb (65) Terbium		Dy (66) Dysprosium		Ho (67) Holmium		Er (68) Erbium		$\lambda(\text{Å})$
		$f_1$	$f_2$	$f_1$	$f_2$	$f_1$	$f_2$	$f_1$	$f_2$	
65	480	32.69	13.72	33.30	16.55	34.81	17.81	33.16	19.32	25.83
66	492	32.90	13.67	33.65	16.39	35.25	17.63	33.66	19.12	25.20
67	504	33.09	13.62	33.98	16.23	35.64	17.46	34.10	18.93	24.60
68	516	33.29	13.57	34.29	16.08	36.02	17.29	34.53	18.74	24.03
69	529	33.50	13.51	34.62	15.91	36.41	17.10	34.96	18.54	23.44
70	542	33.71	13.43	34.93	15.74	36.76	16.89	35.36	18.33	22.87
71	555	33.90	13.36	35.22	15.57	37.09	16.70	35.73	18.13	22.34
72	569	34.07	13.29	35.51	15.37	37.41	16.47	36.14	17.89	21.79
73	583	34.26	13.21	35.76	15.16	37.71	16.25	36.49	17.65	21.27
74	597	34.43	13.14	36.00	14.97	37.98	16.04	36.81	17.41	20.77
75	612	34.60	13.07	36.23	14.76	38.26	15.83	37.14	17.16	20.26
76	627	34.77	13.00	36.46	14.57	38.52	15.62	37.44	16.93	19.77
77	642	34.93	12.93	36.67	14.36	38.78	15.40	37.75	16.68	19.31
78	658	35.12	12.86	36.85	14.10	39.00	15.14	38.01	16.36	18.84
79	674	35.31	12.79	36.98	13.86	39.19	14.88	38.22	16.06	18.39
80	690	35.50	12.65	37.09	13.68	39.34	14.70	38.40	15.84	17.97
81	707	35.69	12.49	37.23	13.50	39.54	14.51	38.61	15.63	17.54
82	725	35.82	12.28	37.35	13.27	39.74	14.23	38.82	15.34	17.10
83	742	35.92	12.08	37.44	13.05	39.89	13.99	38.99	15.08	16.71
84	760	35.97	11.89	37.52	12.84	40.00	13.74	39.13	14.81	16.31
85	779	36.01	11.69	37.59	12.62	40.11	13.48	39.26	14.54	15.92
86	798	36.02	11.47	37.62	12.38	40.18	13.22	39.37	14.26	15.54
87	818	35.98	11.26	37.62	12.13	40.23	12.96	39.45	13.98	15.16
88	838	35.91	11.05	37.58	11.90	40.26	12.71	39.51	13.71	14.79
89	858	35.78	10.85	37.52	11.67	40.26	12.47	39.54	13.45	14.45
90	879	35.65	10.64	37.42	11.44	40.23	12.22	39.54	13.18	14.10
91	901	35.44	10.43	37.28	11.21	40.17	11.97	39.51	12.92	13.76
92	923	35.20	10.23	37.09	10.98	40.07	11.74	39.47	12.66	13.43
93	945	34.90	10.03	36.88	10.76	39.95	11.50	39.39	12.40	13.12
94	968	34.52	9.82	36.61	10.53	39.78	11.25	39.26	12.13	12.81
95	992	34.04	9.62	36.27	10.31	39.57	11.01	39.09	11.87	12.50
96	1016	33.50	9.42	35.86	10.09	39.33	10.78	38.90	11.61	12.20
97	1041	32.82	9.21	35.39	9.86	39.01	10.53	38.64	11.33	11.91
98	1067	31.88	9.00	34.75	9.63	38.58	10.27	38.29	11.05	11.62
99	1093	30.74	8.80	33.97	9.40	38.08	10.03	37.88	10.79	11.34
100	1119	29.37	8.60	33.05	9.19	37.50	9.80	37.41	10.53	11.08
101	1147	27.31	8.41	31.87	8.97	36.72	9.56	36.77	10.27	10.81
102	1175	24.26	8.22	30.23	8.77	35.78	9.33	36.03	10.02	10.55
103	1204	16.60	8.04	27.93	8.56	34.55	9.11	35.10	9.78	10.30
104	1233	1.20 M	7.86	24.78	8.37	33.01	8.90	33.96	9.54	10.06
105	1263	15.24	38.62	18.84	8.17	30.76	8.69	32.47	9.32	9.82
106	1294	25.37	37.30	-8.38 M	7.99	26.61	8.49	30.32	9.09	9.58
107	1326	30.54	36.01	10.65	38.40	19.60	8.28	27.51	8.87	9.35
108	1358	35.35	34.79	23.24	37.10	2.59 M	37.99	21.49	8.66	9.13
109	1392	37.73	33.57	33.92	35.79	16.08	36.66	1.37 M	8.45	8.91
110	1426	40.11	32.42	36.75	34.56	29.58	35.41	9.95	39.93	8.69
111	1460	41.70	31.34	39.58	33.40	37.62	34.22	23.19	38.60	8.49
112	1496	43.04	30.26	41.73	32.24	40.71	33.04	34.28	37.27	8.29
113	1533	43.29	29.21	43.09	31.13	43.03	31.90	37.66	35.99	8.09
114	1570	42.63	28.22	44.39	30.07	44.45	30.83	41.04	34.78	7.90
115	1609	40.52	27.24	43.66	29.03	45.90	29.76	42.92	33.58	7.71
116	1648	42.97	30.83	42.93	28.04	46.80	28.75	44.73	32.45	7.52
117	1688	45.49	29.84	43.08	31.64	46.80	27.78	45.95	31.36	7.34
118	1730	48.13	28.85	47.29	30.64	46.80	26.82	46.88	30.27	7.17
119	1772	48.32	29.93	49.00	29.70	45.41	30.12	46.46	29.25	7.00
120	1815	49.53	28.95	49.96	28.78	47.14	29.14	44.33	33.02	6.83
121	1860	50.78	27.98	51.43	29.68	48.95	28.16	46.33	31.85	6.67
122	1905	52.04	27.07	52.19	28.70	50.76	27.24	48.32	30.75	6.51
123	1952	53.36	26.16	52.99	27.74	52.52	28.14	50.41	29.67	6.35
124	2000	54.61	26.39	53.80	26.81	54.26	27.18	52.53	28.62	6.20

$\frac{E_u(E)}{f_2}$	264.6	258.8	255.0	251.4	$\frac{\text{keV-cm}^2}{\text{gram}}$
Atomic Weight	158.9	162.5	164.9	167.3	amu

ATOMIC SCATTERING FACTOR,  $f_1 + if_2$ 

N	E(eV)	Tm (69)		Yb (70)		Lu (71)		Hf (72)		$\lambda(\text{Å})$
		$f_1$	$f_2$	$f_1$	$f_2$	$f_1$	$f_2$	$f_1$	$f_2$	
0	100	11.71	10.77	10.21	11.32	9.44	8.70	10.63	8.93	124.0
1	102	11.87	10.78	10.28	11.48	9.16	8.99	10.59	9.08	121.5
2	104	11.99	10.79	10.34	11.64	9.03	9.28	10.59	9.23	119.2
3	107	12.15	10.80	10.46	11.87	8.94	9.73	10.62	9.46	115.9
4	110	12.28	10.81	10.64	12.10	8.96	10.12	10.64	9.69	112.7
5	112	12.35	10.84	10.81	12.25	8.97	10.33	10.65	9.85	110.7
6	115	12.38	10.89	11.02	12.44	9.02	10.64	10.67	10.08	107.8
7	118	12.39	10.94	11.26	12.52	9.07	10.97	10.66	10.30	105.1
8	121	12.55	10.99	11.41	12.60	9.11	11.29	10.60	10.56	102.5
9	124	12.60	11.03	11.50	12.68	9.17	11.62	10.57	10.91	100.0
10	127	12.66	11.08	11.56	12.75	9.25	11.94	10.57	11.26	97.6
11	130	12.72	11.12	11.61	12.83	9.35	12.27	10.61	11.62	95.4
12	133	12.76	11.21	11.52	12.95	9.47	12.60	10.66	11.98	93.2
13	136	12.81	11.30	11.48	13.28	9.60	12.93	10.76	12.36	91.2
14	140	12.80	11.41	11.56	13.71	9.79	13.37	10.89	12.87	88.6
15	143	12.92	11.50	11.69	14.04	9.96	13.70	11.04	13.26	86.7
16	147	13.19	11.61	11.95	14.47	10.25	14.15	11.31	13.79	84.3
17	150	13.52	11.69	12.23	14.80	10.50	14.45	11.56	14.15	82.7
18	154	13.51	10.25	12.64	14.83	10.85	14.75	11.92	14.50	80.5
19	158	12.37	9.02	12.73	14.70	11.06	15.02	12.22	14.82	78.5
20	162	9.32	7.97	12.61	14.56	11.31	15.28	12.47	15.14	76.5
21	166	5.25	8.41	11.98	14.43	11.56	15.55	12.70	15.46	74.7
22	170	0.76	14.98	9.01	14.31	11.81	15.81	12.95	15.78	72.9
23	174	4.86	26.32	10.49	23.04	12.04	16.07	13.22	16.09	71.3
24	178	12.04	26.48	14.79	20.64	12.32	16.34	13.49	16.41	69.7
25	182	17.32	22.26	15.54	18.53	12.54	16.60	13.78	16.73	68.1
26	187	17.88	19.08	15.83	17.88	12.81	16.92	14.14	17.12	66.3
27	191	17.58	18.12	15.55	17.91	12.98	17.16	14.45	17.43	64.9
28	196	17.27	17.78	15.62	18.19	13.17	17.62	14.92	17.76	63.3
29	201	17.42	17.80	15.92	18.57	13.54	18.15	15.31	18.06	61.7
30	206	17.64	17.81	16.32	18.96	14.03	18.68	15.71	18.36	60.2
31	211	17.92	17.82	16.77	19.35	14.64	19.21	16.13	18.66	58.8
32	216	18.16	17.88	17.35	19.49	15.41	19.38	16.58	18.88	57.4
33	221	18.42	17.95	17.88	19.55	15.95	19.45	16.99	19.08	56.1
34	227	18.76	18.04	18.41	19.62	16.52	19.52	17.45	19.32	54.6
35	232	19.05	18.12	18.79	19.68	16.96	19.58	17.82	19.52	53.4
36	238	19.41	18.21	19.22	19.75	17.41	19.64	18.26	19.75	52.1
37	244	19.74	18.29	19.63	19.82	17.84	19.71	18.70	19.98	50.8
38	250	20.07	18.37	20.02	19.89	18.25	19.78	19.13	20.21	49.6
39	256	20.41	18.46	20.40	19.96	18.64	19.84	19.57	20.43	48.4
40	262	20.71	18.54	20.75	20.02	18.98	19.91	20.02	20.65	47.3
41	269	21.06	18.63	21.14	20.10	19.35	19.98	20.59	20.90	46.1
42	275	21.36	18.71	21.45	20.16	19.65	20.04	21.12	21.12	45.1
43	282	21.68	18.79	21.78	20.28	19.97	20.18	21.73	21.21	44.0
44	289	22.00	18.91	22.14	20.42	20.30	20.36	22.29	21.23	42.9
45	296	22.31	19.04	22.51	20.55	20.65	20.53	22.79	21.25	41.9
46	303	22.63	19.17	22.87	20.69	21.01	20.70	23.24	21.27	40.9
47	311	23.02	19.32	23.27	20.84	21.43	20.89	23.74	21.29	39.9
48	318	23.35	19.45	23.66	20.97	21.79	21.05	24.13	21.31	39.0
49	326	23.73	19.59	24.10	21.11	22.21	21.23	24.57	21.33	38.0
50	334	24.12	19.73	24.52	21.25	22.64	21.41	24.97	21.35	37.1
51	342	24.51	19.87	24.95	21.39	23.07	21.59	25.37	21.37	36.3
52	351	24.96	20.02	25.44	21.55	23.56	21.79	25.79	21.40	35.3
53	359	25.36	20.16	25.88	21.68	24.00	21.96	26.14	21.42	34.5
54	368	25.84	20.30	26.39	21.83	24.53	22.15	26.52	21.44	33.7
55	377	26.33	20.45	26.92	21.98	25.07	22.34	26.86	21.46	32.9
56	386	26.83	20.59	27.51	22.12	25.65	22.52	27.16	21.48	32.1
57	396	27.55	20.66	28.22	22.19	26.44	22.65	27.37	21.51	31.3
58	406	28.13	20.54	28.87	22.05	27.10	22.53	27.62	21.84	30.5
59	415	28.59	20.43	29.37	21.94	27.63	22.43	27.93	22.13	29.9
60	426	29.09	20.30	29.90	21.80	28.19	22.31	28.43	22.48	29.1
61	436	29.48	20.19	30.33	21.67	28.63	22.21	28.97	22.80	28.4
62	447	29.86	20.07	30.76	21.54	29.06	22.10	29.65	23.15	27.7
63	458	30.18	20.02	31.11	21.49	29.42	22.08	30.54	23.25	27.1
64	469	30.55	20.05	31.51	21.51	29.83	22.13	31.23	23.13	26.4

N	E(eV)	Tm (69) Thulium		Yb (70) Ytterbium		Lu (71) Lutetium		Hf (72) Hafnium		$\lambda$ (Å)
		$f_1$	$f_2$	$f_1$	$f_2$	$f_1$	$f_2$	$f_1$	$f_2$	
65	480	30.94	20.07	31.93	21.53	30.28	22.19	31.83	23.01	25.83
66	492	31.37	20.09	32.42	21.54	30.79	22.26	32.39	22.88	25.20
67	504	31.84	20.11	32.93	21.56	31.33	22.32	32.87	22.76	24.60
68	516	32.37	20.14	33.49	21.58	31.94	22.38	33.27	22.65	24.03
69	529	33.00	20.08	34.17	21.51	32.69	22.34	33.58	22.67	23.44
70	542	33.58	19.84	34.77	21.27	33.39	22.09	34.09	23.01	22.87
71	555	34.06	19.61	35.29	21.04	33.98	21.85	34.93	23.34	22.34
72	569	34.55	19.35	35.86	20.76	34.53	21.56	35.89	23.07	21.79
73	583	34.95	19.08	36.33	20.48	35.01	21.28	36.60	22.76	21.27
74	597	35.33	18.83	36.75	20.21	35.46	21.01	37.19	22.46	20.77
75	612	35.70	18.57	37.17	19.93	35.91	20.73	37.76	22.15	20.26
76	627	36.06	18.31	37.58	19.65	36.34	20.46	38.30	21.85	19.77
77	642	36.41	18.05	37.98	19.37	36.76	20.17	38.83	21.54	19.31
78	658	36.71	17.72	38.33	19.01	37.14	19.81	39.28	21.17	18.84
79	674	36.94	17.40	38.62	18.66	37.49	19.47	39.68	20.81	18.39
80	690	37.17	17.17	38.87	18.41	37.73	19.22	40.04	20.55	17.97
81	707	37.45	16.94	39.17	18.16	38.08	18.97	40.46	20.29	17.54
82	725	37.70	16.62	39.48	17.83	38.41	18.62	40.89	19.90	17.10
83	742	37.91	16.33	39.73	17.53	38.69	18.30	41.23	19.56	16.71
84	760	38.08	16.04	39.97	17.23	38.95	17.98	41.55	19.20	16.31
85	779	38.27	15.74	40.20	16.92	39.20	17.64	41.86	18.84	15.92
86	798	38.40	15.42	40.41	16.58	39.41	17.29	42.13	18.49	15.54
87	818	38.52	15.10	40.58	16.24	39.60	16.94	42.38	18.12	15.16
88	838	38.59	14.80	40.73	15.91	39.75	16.60	42.60	17.78	14.79
89	858	38.65	14.50	40.86	15.59	39.89	16.27	42.81	17.45	14.45
90	879	38.67	14.20	40.95	15.26	39.98	15.94	43.00	17.10	14.10
91	901	38.66	13.91	41.03	14.94	40.06	15.60	43.16	16.76	13.76
92	923	38.64	13.62	41.09	14.62	40.12	15.29	43.31	16.44	13.43
93	945	38.58	13.34	41.11	14.31	40.15	14.97	43.45	16.10	13.12
94	968	38.50	13.06	41.10	13.99	40.16	14.65	43.55	15.75	12.81
95	992	38.37	12.78	41.06	13.67	40.14	14.34	43.63	15.41	12.50
96	1016	38.22	12.51	41.00	13.36	40.11	14.03	43.69	15.08	12.20
97	1041	38.02	12.21	40.90	13.03	40.03	13.69	43.72	14.71	11.91
98	1067	37.74	11.90	40.74	12.70	39.89	13.34	43.70	14.34	11.62
99	1093	37.40	11.61	40.54	12.38	39.70	13.01	43.64	13.99	11.34
100	1119	37.01	11.33	40.29	12.08	39.47	12.70	43.56	13.66	11.08
101	1147	36.53	11.05	39.97	11.77	39.18	12.37	43.40	13.32	10.81
102	1175	35.94	10.78	39.60	11.48	38.82	12.07	43.22	12.99	10.55
103	1204	35.24	10.51	39.14	11.19	38.40	11.77	42.99	12.67	10.30
104	1233	34.44	10.26	38.61	10.91	37.92	11.48	42.71	12.36	10.06
105	1263	33.44	10.01	37.97	10.64	37.35	11.20	42.37	12.06	9.82
106	1294	32.13	9.77	37.17	10.37	36.62	10.92	41.96	11.77	9.58
107	1326	30.52	9.52	36.23	10.11	35.78	10.65	41.48	11.47	9.35
108	1358	28.54	9.29	34.99	9.86	34.80	10.39	40.89	11.20	9.13
109	1392	25.31	9.06	33.36	9.61	33.47	10.13	40.17	10.92	8.91
110	1426	19.49	8.84	31.32	9.37	31.85	9.88	39.33	10.65	8.69
111	1460	10.40 M	8.63	28.11	9.14	29.91	9.64	38.29	10.40	8.49
112	1496	0.56	28.17	20.84	8.91	26.97	9.39	36.96	10.13	8.29
113	1533	6.86	40.91	3.85 M	28.35	21.16	9.13	35.08	9.84	8.09
114	1570	25.12	39.52	9.98	27.19	7.67	8.88	32.67	9.56	7.90
115	1609	31.86	38.14	22.53	39.28	2.03 M	27.88	27.82	9.29	7.71
116	1648	37.70	36.84	31.92	38.07	19.10	40.70	15.54 M	9.03	7.52
117	1688	41.09	35.58	37.78	36.89	30.30	39.33	12.45	27.94	7.34
118	1730	44.63	34.33	40.85	35.72	34.38	37.97	24.95	40.50	7.17
119	1772	46.88	33.16	42.85	34.62	36.79	36.69	30.67	39.15	7.00
120	1815	48.76	32.03	44.54	33.55	38.50	35.45	33.63	37.85	6.83
121	1860	50.32	30.91	45.54	32.49	38.96	34.23	36.73	36.56	6.67
122	1905	51.85	35.05	44.75	31.49	38.92	33.08	39.82	35.34	6.51
123	1952	52.76	33.80	44.49	35.73	35.90	31.94	43.06	34.15	6.35
124	2000	53.69	32.60	48.18	34.46	32.32	30.85	46.36	32.99	6.20

$\frac{E_{\mu}(E)}{f_2}$	249.0	243.0	240.4	235.6	$\frac{\text{keV-cm}^2}{\text{gram}}$
Atomic Weight	168.9	173.0	175.0	178.5	amu

ATOMIC SCATTERING FACTOR,  $f_1 + if_2$ 

N	E(eV)	Ta (73)		W (74)		Re (75)		Os (76)		$\lambda(\text{Å})$
		$f_1$	$f_2$	$f_1$	$f_2$	$f_1$	$f_2$	$f_1$	$f_2$	
0	100	10.75	9.75	12.58	9.06	15.48	7.16	13.73	7.59	124.0
1	102	10.77	9.91	12.44	9.20	15.20	7.21	13.60	7.73	121.5
2	104	10.78	10.06	12.36	9.34	14.82	7.26	13.43	7.88	119.2
3	107	10.79	10.30	12.29	9.55	14.31	7.51	13.23	8.09	115.9
4	110	10.87	10.53	12.28	9.75	13.99	7.82	12.98	8.31	112.7
5	112	10.88	10.68	12.30	9.89	13.86	8.03	12.85	8.56	110.7
6	115	10.94	10.91	12.32	10.10	13.68	8.35	12.72	8.95	107.8
7	118	11.02	11.14	12.39	10.30	13.56	8.67	12.67	9.36	105.1
8	121	11.08	11.36	12.53	10.50	13.48	9.00	12.67	9.77	102.5
9	124	11.14	11.59	12.82	10.71	13.44	9.33	12.70	10.19	100.0
10	127	11.19	11.82	13.07	10.89	13.43	9.64	12.83	10.61	97.6
11	130	11.22	12.07	13.14	11.03	13.44	9.89	13.07	11.05	95.4
12	133	11.32	12.32	12.58	11.18	13.43	10.15	13.43	11.22	93.2
13	136	11.42	12.57	11.99	11.32	13.45	10.40	13.56	11.37	91.2
14	140	11.58	12.90	11.46	11.51	13.46	10.75	13.77	11.56	88.6
15	143	11.66	13.15	11.24	11.65	13.46	11.00	13.91	11.70	86.7
16	147	11.80	13.48	11.22	11.84	13.51	11.35	14.05	11.89	84.3
17	150	11.92	13.73	11.27	12.09	13.54	11.61	14.14	12.03	82.7
18	154	12.10	14.06	11.37	12.54	13.60	11.96	14.26	12.21	80.5
19	158	12.30	14.38	11.45	12.97	13.70	12.30	14.36	12.39	78.5
20	162	12.47	14.67	11.54	13.41	13.78	12.57	14.44	12.57	76.5
21	166	12.62	14.94	11.63	13.84	13.81	12.82	14.50	12.75	74.7
22	170	12.73	15.21	11.75	14.29	13.78	13.07	14.54	12.93	72.9
23	174	12.83	15.54	11.86	14.73	13.69	13.45	14.49	13.11	71.3
24	178	12.99	15.92	11.99	15.16	13.65	13.93	14.46	13.45	69.7
25	182	13.21	16.29	12.13	15.61	13.63	14.43	14.48	13.80	68.1
26	187	13.46	16.76	12.40	16.18	13.77	15.08	14.50	14.23	66.3
27	191	13.74	17.14	12.70	16.64	13.97	15.61	14.55	14.57	64.9
28	196	14.13	17.53	13.06	17.11	14.32	16.14	14.66	15.00	63.3
29	201	14.51	17.88	13.43	17.52	14.60	16.60	14.74	15.46	61.7
30	206	14.87	18.23	13.79	17.93	14.88	17.06	14.93	15.97	60.2
31	211	15.22	18.57	14.16	18.34	15.21	17.53	15.16	16.49	58.8
32	216	15.66	18.86	14.51	18.69	15.51	17.95	15.50	16.90	57.4
33	221	16.02	19.12	14.87	19.03	15.79	18.36	15.78	17.27	56.1
34	227	16.44	19.43	15.28	19.43	16.14	18.85	16.08	17.71	54.6
35	232	16.80	19.69	15.62	19.77	16.45	19.26	16.31	18.08	53.4
36	238	17.22	19.99	16.06	20.16	16.87	19.75	16.63	18.52	52.1
37	244	17.64	20.30	16.48	20.56	17.29	20.24	16.98	18.96	50.8
38	250	18.07	20.60	16.92	20.95	17.72	20.73	17.33	19.40	49.6
39	256	18.53	20.89	17.38	21.34	18.16	21.22	17.68	19.83	48.4
40	262	18.98	21.19	17.87	21.73	18.67	21.71	18.08	20.27	47.3
41	269	19.57	21.53	18.52	22.19	19.37	22.29	18.60	20.78	46.1
42	275	20.12	21.82	19.13	22.57	20.04	22.78	19.09	21.22	45.1
43	282	20.81	21.95	19.94	22.75	20.92	23.02	19.71	21.54	44.0
44	289	21.41	22.00	20.60	22.83	21.65	23.13	20.28	21.79	42.9
45	296	21.95	22.05	21.18	22.90	22.29	23.23	20.78	22.03	41.9
46	303	22.43	22.10	21.72	22.98	22.89	23.34	21.24	22.26	40.9
47	311	22.96	22.15	22.28	23.06	23.48	23.45	21.77	22.53	39.9
48	318	23.38	22.20	22.75	23.13	24.00	23.55	22.21	22.76	39.0
49	326	23.84	22.25	23.26	23.21	24.56	23.67	22.72	23.02	38.0
50	334	24.28	22.31	23.75	23.29	25.09	23.78	23.22	23.28	37.1
51	342	24.70	22.36	24.20	23.36	25.62	23.89	23.71	23.54	36.3
52	351	25.16	22.41	24.70	23.44	26.19	24.01	24.26	23.82	35.3
53	359	25.54	22.46	25.12	23.52	26.68	24.11	24.76	24.07	34.5
54	368	25.94	22.51	25.57	23.60	27.22	24.22	25.35	24.34	33.7
55	377	26.32	22.56	25.98	23.67	27.77	24.34	25.95	24.61	32.9
56	386	26.67	22.62	26.37	23.75	28.31	24.45	26.57	24.88	32.1
57	396	26.94	22.69	26.70	23.85	28.98	24.54	27.41	25.11	31.3
58	406	27.25	23.02	27.08	24.19	29.56	24.50	28.13	25.07	30.5
59	415	27.60	23.32	27.48	24.50	30.04	24.46	28.70	25.03	29.9
60	426	28.15	23.68	28.05	24.87	30.56	24.41	29.28	24.98	29.1
61	436	28.73	24.01	28.66	25.20	30.95	24.37	29.73	24.94	28.4
62	447	29.49	24.36	29.46	25.56	31.28	24.32	30.12	24.90	27.7
63	458	30.40	24.47	30.37	25.69	31.53	24.46	30.39	25.05	27.1
64	469	31.12	24.36	31.18	25.60	31.89	24.76	30.80	25.36	26.4

N	E(eV)	Ta (73) Tantalum		W (74) Tungsten		Re (75) Rhenium		Os (76) Osmium		$\lambda(A)$
		$f_1$	$f_2$	$f_1$	$f_2$	$f_1$	$f_2$	$f_1$	$f_2$	
65	480	31.77	24.25	31.87	25.52	32.34	25.05	31.28	25.67	25.83
66	492	32.40	24.14	32.57	25.44	32.90	25.37	31.88	26.00	25.20
67	504	32.97	24.03	33.23	25.35	33.54	25.69	32.56	26.33	24.60
68	516	33.51	23.92	33.86	25.27	34.33	26.00	33.36	26.65	24.03
69	529	34.05	23.77	34.56	25.14	35.31	26.16	34.36	26.84	23.44
70	542	34.51	23.56	35.20	24.91	36.22	25.94	35.31	26.69	22.87
71	555	34.63	23.35	35.75	24.70	36.91	25.73	36.11	26.55	22.34
72	569	35.19	24.20	36.20	24.44	37.46	25.45	36.83	26.36	21.79
73	583	36.31	24.21	36.61	24.39	37.91	25.45	37.56	26.15	21.27
74	597	37.12	23.89	37.07	24.40	38.47	25.55	38.16	25.92	20.77
75	612	37.84	23.56	37.68	24.42	39.18	25.66	38.73	25.69	20.26
76	627	38.47	23.24	38.39	24.44	40.01	25.76	39.21	25.47	19.77
77	642	39.05	22.91	39.17	24.33	41.01	25.69	39.55	25.38	19.31
78	658	39.56	22.52	39.92	23.92	41.87	25.20	40.15	25.59	18.84
79	674	40.02	22.15	40.50	23.52	42.55	24.73	40.93	25.79	18.39
80	690	40.43	21.88	40.99	23.23	43.12	24.39	41.89	25.54	17.97
81	707	40.92	21.61	41.54	22.94	43.72	24.06	42.67	25.18	17.54
82	725	41.38	21.22	42.06	22.54	44.30	23.64	43.36	24.78	17.10
83	742	41.77	20.87	42.52	22.18	44.80	23.27	43.96	24.41	16.71
84	760	42.14	20.50	42.96	21.81	45.30	22.89	44.52	24.04	16.31
85	779	42.50	20.14	43.41	21.43	45.79	22.49	45.09	23.65	15.92
86	798	42.83	19.76	43.79	21.01	46.23	22.07	45.60	23.24	15.54
87	818	43.14	19.38	44.15	20.60	46.65	21.65	46.08	22.82	15.16
88	838	43.41	19.02	44.47	20.20	47.03	21.25	46.52	22.42	14.79
89	858	43.66	18.66	44.76	19.81	47.39	20.86	46.94	22.03	14.45
90	879	43.89	18.30	45.03	19.41	47.73	20.45	47.35	21.62	14.10
91	901	44.11	17.93	45.29	19.01	48.05	20.05	47.72	21.20	13.76
92	923	44.31	17.57	45.52	18.62	48.34	19.66	48.07	20.80	13.43
93	945	44.48	17.21	45.71	18.24	48.62	19.28	48.41	20.38	13.12
94	968	44.63	16.83	45.89	17.86	48.88	18.88	48.71	19.95	12.81
95	992	44.75	16.45	46.05	17.47	49.13	18.49	48.98	19.52	12.50
96	1016	44.84	16.09	46.19	17.10	49.36	18.10	49.24	19.11	12.20
97	1041	44.91	15.71	46.30	16.71	49.57	17.68	49.48	18.67	11.91
98	1067	44.92	15.32	46.38	16.30	49.75	17.26	49.67	18.22	11.62
99	1093	44.90	14.95	46.41	15.92	49.88	16.86	49.82	17.79	11.34
100	1119	44.86	14.60	46.42	15.56	50.00	16.47	49.95	17.38	11.08
101	1147	44.78	14.24	46.39	15.18	50.10	16.07	50.05	16.96	10.81
102	1175	44.66	13.90	46.34	14.82	50.16	15.70	50.12	16.56	10.55
103	1204	44.49	13.56	46.25	14.47	50.20	15.32	50.16	16.17	10.30
104	1233	44.31	13.24	46.14	14.13	50.23	14.97	50.20	15.79	10.06
105	1263	44.08	12.92	46.00	13.79	50.24	14.61	50.21	15.42	9.82
106	1294	43.75	12.58	45.79	13.43	50.21	14.23	50.16	15.03	9.58
107	1326	43.38	12.24	45.52	13.08	50.15	13.86	50.10	14.66	9.35
108	1358	42.92	11.93	45.20	12.74	50.05	13.50	49.99	14.30	9.13
109	1392	42.34	11.60	44.80	12.40	49.91	13.15	49.84	13.93	8.91
110	1426	41.67	11.30	44.30	12.08	49.73	12.81	49.67	13.59	8.69
111	1460	40.91	11.01	43.74	11.77	49.52	12.48	49.46	13.26	8.49
112	1496	39.91	10.72	43.07	11.46	49.26	12.16	49.19	12.93	8.29
113	1533	38.56	10.43	42.18	11.15	48.94	11.84	48.84	12.59	8.09
114	1570	36.96	10.15	41.12	10.85	48.57	11.53	48.46	12.28	7.90
115	1609	34.72	9.87	39.78	10.56	48.13	11.23	47.97	11.96	7.71
116	1648	31.06	9.61	38.04	10.28	47.61	10.94	47.39	11.66	7.52
117	1688	21.81	9.35	35.44	10.00	47.01	10.65	46.72	11.36	7.34
118	1730	3.52 M	9.09	31.84	9.73	46.31	10.37	45.88	11.07	7.17
119	1772	19.99	27.67	24.75	9.46	45.48	10.09	44.81	10.78	7.00
120	1815	33.26	39.83	6.94 M	27.91	44.62	9.82	43.46	10.49	6.83
121	1860	38.71	38.49	15.08	27.29	43.33	9.55	41.75	10.21	6.67
122	1905	43.16	37.22	23.22	39.24	42.35 M	27.66	39.29	9.93	6.51
123	1952	45.33	35.97	31.72	37.94	37.63	39.47	36.41 M	9.67	6.35
124	2000	47.54	34.76	40.40	36.69	32.82	38.21	30.41	27.26	6.20

$\frac{E_H(E)}{F_2}$	232.4	228.8	225.9	221.1	$\frac{\text{keV-cm}^2}{\text{gram}}$
Atomic Weight	180.9	183.9	186.2	190.2	amu

ATOMIC SCATTERING FACTOR,  $f_1 + if_2$ 

N	E(eV)	Ir (77)		Pt (78)		Au (79)		Hg (80)		$\lambda(\text{Å})$
		$f_1$	$f_2$	$f_1$	$f_2$	$f_1$	$f_2$	$f_1$	$f_2$	
0	100	12.52	7.72	16.39	8.32	22.40	11.15	20.37	23.79	124.0
1	102	12.48	7.90	16.22	8.17	22.45	10.37	21.60	22.96	121.5
2	104	12.45	8.08	16.07	8.03	22.25	9.67	22.70	22.21	119.2
3	107	12.45	8.34	15.93	7.82	21.92	8.94	24.01	20.28	115.9
4	110	12.54	8.61	15.80	7.63	21.68	8.40	24.44	18.29	112.7
5	112	12.63	8.74	15.70	7.50	21.52	7.92	24.41	17.29	110.7
6	115	12.67	8.94	15.53	7.33	21.20	7.27	24.46	16.11	107.8
7	118	12.81	9.14	15.31	7.16	20.75	6.67	24.48	14.81	105.1
8	121	13.01	9.23	15.01	7.00	20.19	6.21	24.27	13.41	102.5
9	124	13.09	9.14	14.62	6.84	19.67	5.94	23.77	12.45	100.0
10	127	13.02	9.04	14.14	6.83	19.17	5.71	23.40	11.72	97.6
11	130	12.79	8.95	13.78	7.07	18.68	5.51	23.07	10.84	95.4
12	133	12.51	9.29	13.46	7.30	18.20	5.38	22.62	10.00	93.2
13	136	12.39	9.62	13.24	7.54	17.69	5.29	21.99	9.22	91.2
14	140	12.30	10.08	12.93	7.85	17.02	5.26	21.06	8.46	88.6
15	143	12.33	10.39	12.76	8.09	16.53	5.36	20.35	8.09	86.7
16	147	12.48	10.80	12.56	8.42	15.97	5.50	19.51	7.71	84.3
17	150	12.58	11.11	12.41	8.67	15.55	5.60	18.88	7.48	82.7
18	154	12.77	11.28	12.21	9.00	14.99	5.88	18.02	7.25	80.5
19	158	12.80	11.44	11.97	9.33	14.50	6.17	17.15	7.18	78.5
20	162	12.79	11.66	11.72	9.79	14.03	6.52	16.33	7.25	76.5
21	166	12.77	11.95	11.59	10.27	13.61	6.92	15.58	7.41	74.7
22	170	12.77	12.24	11.49	10.76	13.23	7.33	14.86	7.57	72.9
23	174	12.79	12.60	11.41	11.27	12.88	7.81	14.17	7.90	71.3
24	178	12.84	12.97	11.36	11.78	12.60	8.30	13.55	8.25	69.7
25	182	12.87	13.37	11.37	12.31	12.34	8.80	12.94	8.65	68.1
26	187	13.10	13.93	11.41	12.98	12.07	9.45	12.28	9.27	66.3
27	191	13.37	14.31	11.49	13.54	11.91	9.99	11.82	9.78	64.9
28	196	13.61	14.48	11.72	14.24	11.77	10.70	11.33	10.51	63.3
29	201	13.66	14.68	12.00	14.87	11.70	11.42	10.90	11.28	61.7
30	206	13.73	15.05	12.28	15.28	11.68	12.08	10.57	12.07	60.2
31	211	13.83	15.41	12.58	15.70	11.67	12.75	10.30	12.89	58.8
32	216	13.96	15.78	12.83	16.11	11.74	13.45	10.12	13.75	57.4
33	221	14.08	16.14	13.07	16.52	11.96	14.12	10.00	14.65	56.1
34	227	14.24	16.58	13.29	17.02	12.17	14.70	9.98	15.67	54.6
35	232	14.41	16.95	13.53	17.43	12.33	15.20	10.08	16.49	53.4
36	238	14.55	17.38	13.84	17.93	12.50	15.79	10.30	17.52	52.1
37	244	14.70	17.82	14.16	18.43	12.69	16.39	10.63	18.56	50.8
38	250	14.88	18.26	14.53	18.94	12.93	16.98	11.08	19.27	49.6
39	256	14.99	18.70	14.90	19.33	13.16	17.58	11.52	19.99	48.4
40	262	15.10	19.20	15.26	19.70	13.39	18.18	11.95	20.72	47.3
41	269	15.24	19.95	15.62	20.13	13.71	18.90	12.48	21.45	46.1
42	275	15.52	20.59	15.95	20.50	14.07	19.52	12.96	22.02	45.1
43	282	15.69	21.22	16.33	20.93	14.54	20.10	13.51	22.69	44.0
44	289	15.37	21.81	16.70	21.37	14.97	20.62	14.15	23.27	42.9
45	296	16.78	24.28	17.06	21.81	15.36	21.14	14.70	23.77	41.9
46	303	18.11	24.44	17.44	22.24	15.73	21.66	15.26	24.27	40.9
47	311	19.17	24.63	17.86	22.74	16.17	22.26	15.92	24.77	39.9
48	318	19.95	24.78	18.28	23.17	16.55	22.78	16.44	25.16	39.0
49	326	20.73	24.96	18.76	23.66	17.02	23.38	17.02	25.62	38.0
50	334	21.42	25.13	19.24	24.15	17.51	23.98	17.60	26.03	37.1
51	342	22.08	25.30	19.74	24.64	18.01	24.58	18.17	26.44	36.3
52	351	22.79	25.49	20.34	25.19	18.60	25.25	18.75	26.90	35.3
53	359	23.38	25.66	20.89	25.67	19.17	25.85	19.26	27.30	34.5
54	368	24.04	25.84	21.54	26.22	19.86	26.53	19.81	27.75	33.7
55	377	24.70	26.02	22.27	26.76	20.64	27.21	20.24	28.24	32.9
56	386	25.35	26.19	23.12	27.30	21.61	27.88	21.02	29.15	32.1
57	396	26.13	26.37	24.24	27.76	22.83	28.47	22.16	29.89	31.3
58	406	26.84	26.36	25.26	27.79	23.97	28.57	23.29	30.07	30.5
59	415	27.42	26.35	26.01	27.82	24.78	28.65	24.08	30.23	29.9
60	426	28.03	26.34	26.85	27.85	25.71	28.75	24.99	30.42	29.1
61	436	28.53	26.33	27.57	27.88	26.51	28.84	25.80	30.59	28.4
62	447	29.02	26.33	28.30	27.92	27.37	28.94	26.68	30.78	27.7
63	458	29.37	26.47	29.04	27.90	28.19	28.98	27.55	30.89	27.1
64	469	29.83	26.74	29.68	27.85	28.97	28.96	28.38	30.93	26.4

N	E(eV)	Ir (77) Iridium		Pt (78) Platinum		Au (79) Gold		Hg (80) Mercury		$\lambda(\text{Å})$
		$f_1$	$f_2$	$f_1$	$f_2$	$f_1$	$f_2$	$f_1$	$f_2$	
65	480	30.35	27.00	30.25	27.80	29.69	28.95	29.16	30.97	25.83
66	492	30.97	27.29	30.81	27.75	30.42	28.94	29.95	31.02	25.20
67	504	31.65	27.57	31.30	27.69	31.10	28.92	30.72	31.07	24.60
68	516	32.40	27.85	31.65	27.64	31.81	28.91	31.51	31.11	24.03
69	529	33.35	28.04	31.75	27.86	32.56	28.84	32.40	31.08	23.44
70	542	34.22	28.00	32.28	28.68	33.18	28.66	33.14	30.88	22.87
71	555	35.05	27.96	33.19	29.51	33.71	28.49	33.78	30.69	22.34
72	569	35.90	27.89	34.54	29.61	34.01	28.27	34.24	30.47	21.79
73	583	36.71	27.72	35.60	29.50	34.19	28.57	34.59	30.63	21.27
74	597	37.43	27.53	36.55	29.33	34.66	29.05	35.14	30.93	20.77
75	612	38.15	27.33	37.44	29.16	35.38	29.56	35.87	31.25	20.26
76	627	38.83	27.13	38.31	29.00	36.30	30.06	36.71	31.56	19.77
77	642	39.50	26.88	39.15	28.77	37.65	30.29	37.77	31.74	19.31
78	658	39.98	26.50	39.96	28.37	38.79	29.89	38.80	31.64	18.84
79	674	40.26	26.14	40.55	27.98	39.67	29.50	39.75	31.54	18.39
80	690	40.64	26.54	41.06	27.70	40.32	29.23	40.70	31.39	17.97
81	707	41.51	27.01	41.56	27.47	40.93	29.01	41.72	31.18	17.54
82	725	42.66	26.56	42.10	27.43	41.60	28.98	42.67	30.69	17.10
83	742	43.41	26.16	42.73	27.40	42.31	28.96	43.41	30.24	16.71
84	760	44.10	25.75	43.48	27.36	43.18	28.93	43.98	29.78	16.31
85	779	44.76	25.33	44.41	27.25	44.20	28.83	44.48	29.38	15.92
86	798	45.35	24.90	45.25	26.76	45.18	28.31	44.97	29.33	15.54
87	818	45.89	24.46	46.00	26.26	45.98	27.79	45.64	29.27	15.16
88	838	46.40	24.04	46.63	25.79	46.67	27.29	46.51	29.22	14.79
89	858	46.88	23.63	47.19	25.32	47.29	26.80	47.45	29.01	14.45
90	879	47.33	23.19	47.71	24.84	47.90	26.32	48.38	28.43	14.10
91	901	47.76	22.76	48.22	24.36	48.45	25.83	49.10	27.85	13.76
92	923	48.18	22.34	48.69	23.90	48.97	25.36	49.74	27.29	13.43
93	945	48.56	21.90	49.12	23.43	49.46	24.88	50.31	26.75	13.12
94	968	48.91	21.45	49.53	22.94	49.92	24.40	50.85	26.21	12.81
95	992	49.24	20.99	49.91	22.46	50.36	23.91	51.38	25.68	12.50
96	1016	49.55	20.54	50.27	21.99	50.79	23.43	51.88	25.15	12.20
97	1041	49.85	20.07	50.60	21.48	51.22	22.90	52.38	24.54	11.91
98	1067	50.06	19.58	50.89	20.96	51.55	22.36	52.74	23.93	11.62
99	1093	50.26	19.12	51.12	20.47	51.85	21.84	53.07	23.36	11.34
100	1119	50.42	18.68	51.32	20.01	52.11	21.34	53.36	22.81	11.08
101	1147	50.56	18.23	51.50	19.53	52.36	20.83	53.63	22.25	10.81
102	1175	50.67	17.80	51.67	19.07	52.56	20.34	53.92	21.72	10.55
103	1204	50.75	17.38	51.80	18.62	52.73	19.86	54.08	21.19	10.30
104	1233	50.81	16.97	51.90	18.19	52.89	19.41	54.27	20.69	10.06
105	1263	50.84	16.57	52.00	17.76	53.02	18.95	54.43	20.19	9.82
106	1294	50.85	16.15	52.06	17.31	53.12	18.49	54.55	19.70	9.58
107	1326	50.82	15.74	52.07	16.88	53.20	18.03	54.66	19.22	9.35
108	1358	50.75	15.36	52.06	16.47	53.25	17.60	54.73	18.77	9.13
109	1392	50.65	14.97	52.02	16.05	53.25	17.16	54.78	18.30	8.91
110	1426	50.50	14.59	51.93	15.65	53.23	16.74	54.81	17.86	8.69
111	1460	50.32	14.24	51.82	15.27	53.19	16.34	54.82	17.44	8.49
112	1496	50.10	13.88	51.68	14.89	53.12	15.94	54.81	17.01	8.29
113	1533	49.82	13.52	51.48	14.50	53.00	15.53	54.76	16.57	8.09
114	1570	49.48	13.18	51.24	14.13	52.84	15.13	54.67	16.14	7.90
115	1609	49.06	12.83	50.95	13.76	52.64	14.74	54.55	15.72	7.71
116	1648	48.58	12.50	50.59	13.41	52.38	14.37	54.36	15.32	7.52
117	1688	47.97	12.19	50.15	13.07	52.07	14.00	54.14	14.92	7.34
118	1730	47.27	11.87	49.63	12.72	51.70	13.64	53.88	14.53	7.17
119	1772	46.41	11.55	49.01	12.38	51.26	13.27	53.56	14.14	7.00
120	1815	45.24	11.24	48.21	12.04	50.69	12.91	53.14	13.75	6.83
121	1860	43.72	10.93	47.22	11.71	50.00	12.56	52.65	13.37	6.67
122	1905	41.12	10.63	45.97	11.39	49.18	12.22	52.07	13.00	6.51
123	1952	32.63	10.34	43.71	11.08	47.86	11.88	51.19	12.64	6.35
124	2000	23.97	10.05	41.39	10.77	46.52	11.56	50.30	12.29	6.20
	$\frac{E_{\mu}(E)}{f_2}$	218.8		215.6		213.5		209.7		$\frac{\text{keV-cm}^2}{\text{gram}}$
	Atomic Weight	192.2		195.1		197.0		200.6		amu

ATOMIC SCATTERING FACTOR,  $f_1 + if_2$ 

N	E(eV)	Tl (81)		Pb (82)		Bi (83)		Po (84)		$\lambda$ (Å)
		$f_1$	$f_2$	$f_1$	$f_2$	$f_1$	$f_2$	$f_1$	$f_2$	
0	100	20.83	21.56	23.57	11.09	25.33	18.55	24.73	24.84	124.0
1	102	21.16	21.53	23.51	10.64	25.54	17.94	25.18	23.96	121.5
2	104	22.23	21.83	23.46	10.25	25.73	17.35	25.56	23.12	119.2
3	107	23.87	20.68	23.38	9.70	26.03	16.50	26.06	21.93	115.9
4	110	24.96	19.03	23.32	9.20	26.32	15.70	26.48	20.81	112.7
5	112	25.27	17.78	23.26	8.88	26.49	14.99	26.67	20.15	110.7
6	115	25.46	16.33	23.19	8.40	26.58	14.01	26.94	19.24	107.8
7	118	25.46	15.28	23.09	7.87	26.51	13.18	27.23	18.35	105.1
8	121	25.57	14.25	22.92	7.36	26.40	12.44	27.56	17.52	102.5
9	124	25.41	12.99	22.71	6.89	26.27	11.80	27.75	16.47	100.0
10	127	25.08	11.95	22.43	6.41	26.15	11.21	27.83	15.47	97.6
11	130	24.68	11.30	22.09	5.96	26.03	10.67	27.75	14.61	95.4
12	133	24.43	10.63	21.69	5.65	25.92	10.12	27.62	13.84	93.2
13	136	24.09	9.86	21.26	5.36	25.79	9.56	27.49	13.17	91.2
14	140	23.48	8.92	20.68	5.08	25.54	8.78	27.31	12.36	88.6
15	143	22.93	8.28	20.24	5.02	25.29	8.24	27.18	11.80	86.7
16	147	22.10	7.79	19.77	4.94	24.90	7.53	27.02	11.04	84.3
17	150	21.53	7.50	19.43	4.90	24.49	7.01	26.90	10.45	82.7
18	154	20.79	7.19	19.00	4.86	23.87	6.55	26.60	9.65	80.5
19	158	20.07	6.96	18.56	4.82	23.26	6.13	26.24	8.93	78.5
20	162	19.31	6.81	18.13	4.84	22.58	5.88	25.78	8.19	76.5
21	166	18.57	6.76	17.67	4.86	21.99	5.78	25.20	7.55	74.7
22	170	17.85	6.88	17.21	4.94	21.45	5.68	24.57	7.09	72.9
23	174	17.22	7.02	16.77	5.05	20.96	5.63	23.90	6.66	71.3
24	178	16.60	7.17	16.32	5.19	20.47	5.58	23.19	6.46	69.7
25	182	15.98	7.47	15.88	5.38	19.97	5.56	22.60	6.35	68.1
26	187	15.32	7.87	15.36	5.64	19.36	5.57	21.93	6.24	66.3
27	191	14.79	8.23	14.95	5.87	18.85	5.61	21.41	6.18	64.9
28	196	14.23	8.78	14.42	6.18	18.23	5.74	20.78	6.11	63.3
29	201	13.72	9.35	13.90	6.56	17.61	5.90	20.15	6.11	61.7
30	206	13.28	10.00	13.38	6.95	17.01	6.15	19.51	6.12	60.2
31	211	12.91	10.68	12.84	7.38	16.43	6.42	18.85	6.22	58.8
32	216	12.61	11.38	12.21	7.87	15.87	6.73	18.21	6.35	57.4
33	221	12.34	12.10	11.57	8.54	15.30	7.06	17.59	6.56	56.1
34	227	12.12	13.01	10.80	9.58	14.62	7.55	16.86	6.86	54.6
35	232	12.03	13.80	10.41	10.77	14.03	7.97	16.27	7.16	53.4
36	238	12.03	14.72	10.22	12.16	13.29	8.52	15.57	7.54	52.1
37	244	12.10	15.60	10.43	13.55	12.40	9.27	14.85	8.00	50.8
38	250	12.25	16.50	10.77	14.43	11.54	10.17	14.09	8.50	49.6
39	256	12.52	17.43	11.11	15.31	10.94	11.64	13.34	9.05	48.4
40	262	12.91	18.17	11.41	16.15	10.65	13.18	12.55	9.66	47.3
41	269	13.30	18.92	11.80	17.02	10.95	14.88	11.58	10.69	46.1
42	275	13.66	19.57	12.10	17.74	11.28	15.90	10.76	11.92	45.1
43	282	14.14	20.30	12.53	18.60	11.64	16.99	10.34	13.79	44.0
44	289	14.62	20.90	12.99	19.30	12.08	18.03	10.31	15.49	42.9
45	296	15.10	21.50	13.42	20.03	12.50	18.92	10.72	16.98	41.9
46	303	15.59	22.10	13.94	20.82	12.95	19.80	11.12	18.10	40.9
47	311	16.17	22.63	14.61	21.50	13.54	20.80	11.59	19.30	39.9
48	318	16.63	23.09	15.15	22.01	14.04	21.49	12.08	20.26	39.0
49	326	17.18	23.60	15.70	22.57	14.64	22.40	12.57	21.28	38.0
50	334	17.72	24.02	16.22	23.12	15.28	23.22	13.14	22.31	37.1
51	342	18.20	24.44	16.74	23.68	15.99	23.88	13.76	23.16	36.3
52	351	18.71	24.92	17.38	24.30	16.69	24.51	14.34	24.16	35.3
53	359	19.15	25.36	17.92	24.74	17.30	25.07	15.03	25.05	34.5
54	368	19.62	25.85	18.51	25.29	17.98	25.70	15.83	25.82	33.7
55	377	20.10	26.34	19.15	25.82	18.66	26.32	16.57	26.45	32.9
56	386	20.31	26.83	19.79	26.27	19.33	26.83	17.26	27.08	32.1
57	396	20.49	28.70	20.46	26.72	20.05	27.45	17.97	27.79	31.3
58	406	22.19	28.96	21.09	27.08	20.88	28.01	18.74	28.49	30.5
59	415	23.11	29.19	21.52	27.43	21.59	28.45	19.41	29.01	29.9
60	426	24.12	29.47	21.90	27.92	22.40	28.89	20.20	29.67	29.1
61	436	24.96	29.71	22.26	28.58	23.09	29.24	20.90	30.26	28.4
62	447	25.85	29.98	22.98	29.95	23.75	29.83	21.67	30.78	27.7
63	458	26.74	30.20	24.29	30.73	24.58	30.40	22.16	31.22	27.1
64	469	27.55	30.36	25.51	30.99	25.43	30.86	21.61	31.60	26.4



N	E(eV)	Tl (81) Thallium		Pb (82) Lead		Bi (83) Bismuth		Po (84) Polonium		$\lambda$ (A)
		$f_1$	$f_2$	$f_1$	$f_2$	$f_1$	$f_2$	$f_1$	$f_2$	
65	480	28.34	30.52	26.52	31.24	26.25	31.30	22.78	35.25	25.83
66	492	29.18	30.69	27.53	31.51	27.18	31.79	26.01	35.25	25.20
67	504	30.02	30.86	28.51	31.78	28.15	32.27	27.57	35.25	24.60
68	516	30.87	31.02	29.55	32.05	29.23	32.74	28.99	35.25	24.03
69	529	31.88	31.11	30.75	32.21	30.58	33.08	30.37	35.20	23.44
70	542	32.76	30.99	31.81	32.11	31.76	33.02	31.58	35.05	22.87
71	555	33.59	30.88	32.77	32.02	32.84	32.96	32.67	34.90	22.34
72	569	34.38	30.74	33.73	31.92	33.92	32.89	33.76	34.76	21.79
73	583	35.10	30.55	34.61	31.74	34.92	32.74	34.79	34.57	21.27
74	597	35.69	30.34	35.39	31.54	35.80	32.56	35.70	34.35	20.77
75	612	36.21	30.12	36.14	31.33	36.67	32.36	36.61	34.13	20.26
76	627	36.58	29.91	36.81	31.12	37.49	32.18	37.47	33.91	19.77
77	642	36.57	30.03	37.40	30.90	38.27	31.96	38.28	33.66	19.31
78	658	37.03	30.86	37.71	30.60	38.97	31.68	39.02	33.33	18.84
79	674	37.89	31.70	37.73	30.32	39.59	31.40	39.64	33.01	18.39
80	690	39.27	31.96	37.59	31.51	40.04	31.12	40.01	32.78	17.97
81	707	40.64	31.91	39.04	33.26	40.24	30.91	40.29	32.65	17.54
82	725	41.82	31.44	41.04	32.83	40.58	31.44	40.67	33.19	17.10
83	742	42.70	31.02	42.30	32.43	41.18	31.93	41.40	33.70	16.71
84	760	43.36	30.58	43.32	32.03	42.22	32.44	42.52	34.23	16.31
85	779	43.93	30.21	44.31	31.61	43.55	32.82	43.94	34.63	15.92
86	798	44.46	30.22	45.16	31.14	44.93	32.39	45.37	34.16	15.54
87	818	45.21	30.22	45.93	30.66	46.01	31.95	46.51	33.68	15.16
88	838	46.15	30.23	46.52	30.20	46.93	31.52	47.50	33.22	14.79
89	858	47.14	30.08	47.00	29.86	47.77	31.09	48.40	32.76	14.45
90	879	48.17	29.55	47.56	29.79	48.55	30.59	49.19	32.23	14.10
91	901	48.96	29.02	48.31	29.71	49.21	30.08	49.91	31.69	13.76
92	923	49.64	28.51	49.21	29.64	49.74	29.60	50.49	31.18	13.43
93	945	50.28	28.06	50.16	29.25	50.21	29.37	50.98	30.95	13.12
94	968	50.90	27.62	51.01	28.70	50.79	29.25	51.62	30.83	12.81
95	992	51.58	27.18	51.76	28.15	51.61	29.12	52.41	30.71	12.50
96	1016	52.26	26.72	52.47	27.61	52.52	28.91	53.47	30.51	12.20
97	1041	52.95	26.06	53.14	26.97	53.44	28.26	54.44	29.82	11.91
98	1067	53.44	25.40	53.66	26.33	54.12	27.60	55.21	29.12	11.62
99	1093	53.88	24.78	54.12	25.72	54.70	26.98	55.85	28.45	11.34
100	1119	54.26	24.19	54.54	25.14	55.22	26.38	56.40	27.81	11.08
101	1147	54.62	23.58	54.95	24.54	55.71	25.77	56.93	27.16	10.81
102	1175	54.94	23.00	55.35	23.97	56.12	25.19	57.39	26.53	10.55
103	1204	55.21	22.43	55.62	23.41	56.52	24.61	57.81	25.92	10.30
104	1233	55.46	21.88	55.91	22.87	56.89	24.06	58.21	25.33	10.06
105	1263	55.67	21.35	56.17	22.34	57.21	23.52	58.57	24.75	9.82
106	1294	55.84	20.82	56.39	21.83	57.50	22.98	58.89	24.17	9.58
107	1326	56.00	20.30	56.60	21.32	57.77	22.46	59.19	23.61	9.35
108	1358	56.14	19.81	56.79	20.84	58.01	21.95	59.45	23.07	9.13
109	1392	56.24	19.31	56.95	20.35	58.23	21.45	59.69	22.53	8.91
110	1426	56.32	18.83	57.10	19.89	58.43	20.96	59.92	22.01	8.69
111	1460	56.38	18.38	57.23	19.45	58.60	20.50	60.13	21.52	8.49
112	1496	56.41	17.92	57.35	18.98	58.78	20.02	60.35	21.00	8.29
113	1533	56.41	17.46	57.43	18.49	58.92	19.50	60.51	20.47	8.09
114	1570	56.38	17.01	57.47	18.03	59.02	19.01	60.64	19.95	7.90
115	1609	56.32	16.57	57.48	17.56	59.10	18.52	60.73	19.44	7.71
116	1648	56.20	16.15	57.44	17.11	59.12	18.05	60.79	18.95	7.52
117	1688	56.06	15.74	57.38	16.68	59.12	17.60	60.83	18.47	7.34
118	1730	55.90	15.33	57.29	16.24	59.09	17.14	60.86	18.00	7.17
119	1772	55.68	14.91	57.16	15.81	59.05	16.69	60.85	17.52	7.00
120	1815	55.40	14.50	56.97	15.38	58.94	16.23	60.80	17.04	6.83
121	1860	55.04	14.10	56.72	14.96	58.78	15.78	60.71	16.57	6.67
122	1905	54.63	13.71	56.42	14.56	58.57	15.35	60.53	16.13	6.51
123	1952	54.02	13.33	55.99	14.16	58.27	14.93	60.33	15.68	6.35
124	2000	53.40	12.96	55.54	13.77	57.95	14.52	60.12	15.25	6.20

$$\frac{E\mu(E)}{F_2}$$

205.8

203.0

201.2

200.3

$$\frac{\text{keV-cm}^2}{\text{gram}}$$

Atomic Weight

204.4

207.2

209.0

210

amu

ATOMIC SCATTERING FACTOR,  $f_1 + if_2$ 

N	E(eV)	At (85)		Rn (86)		Fr (87)		Ra (88)		$\lambda(\text{Å})$
		$f_1$	$f_2$	$f_1$	$f_2$	$f_1$	$f_2$	$f_1$	$f_2$	
0	100	19.95	30.38	15.67	35.48	16.18	34.80	12.89	35.75	124.0
1	102	20.97	29.72	17.58	34.64	17.44	34.17	14.90	36.23	121.5
2	104	22.01	28.99	18.95	33.83	18.56	33.57	16.84	35.70	119.2
3	107	23.33	27.36	20.77	32.68	20.14	32.70	19.36	34.66	115.9
4	110	24.18	25.88	22.31	31.60	21.53	31.88	21.32	33.69	112.7
5	112	24.57	25.02	23.25	30.92	22.43	31.35	22.45	33.06	110.7
6	115	25.11	23.82	24.69	29.91	23.86	30.60	24.06	32.17	107.8
7	118	25.58	22.66	25.94	28.44	25.28	29.75	25.68	31.32	105.1
8	121	25.93	21.58	26.86	27.07	26.62	28.32	27.33	30.52	102.5
9	124	26.20	20.64	27.51	25.81	27.46	27.00	29.52	29.18	100.0
10	127	26.47	19.77	28.05	24.63	28.13	25.76	30.87	26.82	97.6
11	130	26.75	18.91	28.50	23.53	28.70	24.61	31.62	24.70	95.4
12	133	27.05	18.10	28.90	22.50	29.17	23.54	31.86	22.80	93.2
13	136	27.20	17.04	29.19	21.54	29.45	22.53	31.62	21.07	91.2
14	140	27.23	15.79	29.56	20.35	29.84	21.29	31.14	19.50	88.6
15	143	27.14	14.97	29.85	19.42	30.10	20.42	30.78	18.79	86.7
16	147	26.95	14.03	30.00	18.17	30.41	19.23	30.61	17.89	84.3
17	150	26.79	13.40	30.06	17.31	30.58	18.36	30.54	17.26	82.7
18	154	26.62	12.63	30.02	16.24	30.58	17.27	30.41	16.48	80.5
19	158	26.46	11.90	29.92	15.27	30.55	16.27	30.30	15.74	78.5
20	162	26.29	11.19	29.77	14.38	30.46	15.36	30.20	15.06	76.5
21	166	26.04	10.37	29.58	13.56	30.34	14.52	30.09	14.43	74.7
22	170	25.74	9.63	29.37	12.80	30.20	13.74	29.97	13.83	72.9
23	174	25.36	8.94	29.12	12.11	30.01	13.02	29.84	13.27	71.3
24	178	24.82	8.22	28.85	11.46	29.78	12.35	29.70	12.75	69.7
25	182	24.24	7.68	28.57	10.86	29.56	11.73	29.55	12.26	68.1
26	187	23.48	7.13	28.21	10.18	29.24	11.02	29.37	11.68	66.3
27	191	22.77	6.75	27.91	9.62	29.00	10.49	29.20	11.25	64.9
28	196	21.99	6.62	27.45	8.94	28.69	9.84	29.02	10.75	63.3
29	201	21.30	6.49	26.93	8.33	28.34	9.10	28.85	10.28	61.7
30	206	20.68	6.41	26.35	7.77	27.85	8.43	28.77	9.72	60.2
31	211	20.05	6.34	25.67	7.26	27.29	7.83	28.51	8.99	58.8
32	216	19.44	6.30	24.89	6.96	26.59	7.28	28.05	8.34	57.4
33	221	18.83	6.31	24.17	6.89	25.79	6.94	27.47	7.84	56.1
34	227	18.06	6.37	23.48	6.79	24.99	6.78	26.82	7.45	54.6
35	232	17.44	6.50	22.92	6.72	24.36	6.65	26.25	7.14	53.4
36	238	16.70	6.69	22.24	6.64	23.61	6.50	25.56	6.93	52.1
37	244	15.99	6.98	21.52	6.68	22.82	6.54	24.93	6.81	50.8
38	250	15.28	7.30	20.88	6.78	22.15	6.65	24.35	6.69	49.6
39	256	14.58	7.67	20.22	6.88	21.52	6.76	23.74	6.58	48.4
40	262	13.90	8.08	19.52	6.98	20.91	6.87	23.09	6.48	47.3
41	269	13.10	8.64	18.73	7.31	20.11	7.00	22.31	6.59	46.1
42	275	12.44	9.15	18.16	7.63	19.47	7.30	21.68	6.71	45.1
43	282	11.56	9.78	17.43	8.01	18.70	7.66	20.94	6.86	44.0
44	289	10.58	10.76	16.80	8.40	18.00	8.04	20.21	7.03	42.9
45	296	9.67	12.03	16.17	8.80	17.38	8.51	19.48	7.36	41.9
46	303	9.12	13.80	15.50	9.21	16.79	9.00	18.78	7.70	40.9
47	311	8.98	15.72	14.67	9.68	16.12	9.58	18.02	8.12	39.9
48	318	9.44	17.24	13.64	10.24	15.53	10.10	17.34	8.57	39.0
49	326	9.94	18.46	12.66	11.40	14.78	10.72	16.54	9.11	38.0
50	334	10.41	19.63	11.86	12.66	13.93	11.35	15.66	9.66	37.1
51	342	10.90	20.71	11.20	14.02	12.92	12.26	14.64	10.43	36.3
52	351	11.45	21.80	10.64	15.69	12.01	13.82	13.69	11.72	35.3
53	359	12.01	22.79	10.31	17.29	11.40	15.34	12.99	12.98	34.5
54	368	12.69	23.72	10.12	19.24	10.93	17.19	12.37	14.52	33.7
55	377	13.33	24.67	10.27	21.36	10.79	19.22	11.96	16.19	32.9
56	386	14.06	25.60	11.11	23.65	11.25	21.42	11.86	18.01	32.1
57	396	14.88	26.69	12.65	25.98	12.30	23.91	12.06	20.47	31.3
58	406	15.97	27.22	14.36	26.65	13.75	24.82	13.00	21.66	30.5
59	415	16.71	27.70	15.34	27.25	14.57	25.64	13.48	22.76	29.9
60	426	17.55	28.27	16.44	27.99	15.50	26.66	14.07	24.15	29.1
61	436	18.28	28.80	17.37	28.67	16.33	27.60	14.67	25.45	28.4
62	447	19.07	29.37	18.39	29.41	17.31	28.65	15.52	26.93	27.7
63	458	19.85	29.90	19.41	29.99	18.41	29.47	16.60	28.10	27.1
64	469	20.61	30.39	20.35	30.42	19.41	30.07	17.61	28.97	26.4

N	E(eV)	At (85) Astatine		Rn (86) Radon		Fr (87) Francium		Ra (88) Radium		$\lambda(\text{Å})$
		$f_1$	$f_2$	$f_1$	$f_2$	$f_1$	$f_2$	$f_1$	$f_2$	
65	480	21.35	30.88	21.20	30.85	20.31	30.66	18.50	29.84	25.83
66	492	22.15	31.40	22.03	31.32	21.25	31.31	19.47	30.81	25.20
67	504	22.95	31.93	22.81	31.78	22.20	31.96	20.47	31.77	24.60
68	516	23.75	32.45	23.54	32.24	23.22	32.61	21.68	32.75	24.03
69	529	24.62	33.02	24.24	32.79	24.49	33.11	23.27	33.52	23.44
70	542	25.55	33.61	24.98	33.48	25.49	33.18	24.56	33.67	22.87
71	555	26.56	34.20	25.74	34.16	26.29	33.26	25.63	33.82	22.34
72	569	27.81	34.83	26.81	35.31	27.66	33.32	26.42	33.94	21.79
73	583	29.19	35.10	28.28	35.92	28.84	34.22	27.05	34.46	21.27
74	597	30.39	35.22	29.60	36.31	29.52	35.44	27.85	35.13	20.77
75	612	31.59	35.35	30.96	36.72	28.63	36.76	28.81	35.85	20.26
76	627	32.78	35.47	32.35	37.13	30.12	38.09	29.87	36.56	19.77
77	642	34.07	35.47	33.99	37.30	32.46	38.92	31.10	37.21	19.31
78	658	35.25	35.21	35.43	36.96	34.51	38.55	32.42	37.76	18.84
79	674	36.33	34.96	36.63	36.63	36.10	38.20	33.77	38.30	18.39
80	690	37.30	34.68	37.63	36.43	37.38	37.97	35.29	38.74	17.97
81	707	38.26	34.37	38.72	36.22	38.70	37.73	37.15	39.08	17.54
82	725	39.12	33.92	39.71	35.78	39.97	37.30	38.90	38.65	17.10
83	742	39.79	33.50	40.51	35.39	41.03	36.91	40.26	38.27	16.71
84	760	40.20	33.08	40.98	34.98	42.02	36.51	41.49	37.87	16.31
85	779	40.45	32.80	41.26	34.73	42.99	36.08	42.72	37.45	15.92
86	798	40.71	33.33	41.59	35.43	43.83	35.57	43.80	36.93	15.54
87	818	41.46	33.89	42.48	36.15	44.53	35.05	44.78	36.41	15.16
88	838	42.71	34.44	44.04	36.88	44.87	34.55	45.66	35.91	14.79
89	858	44.13	34.66	45.83	37.12	45.09	34.39	46.42	35.41	14.45
90	879	45.66	34.10	47.63	36.35	45.43	34.93	47.16	34.85	14.10
91	901	46.74	33.54	48.85	35.59	46.37	35.50	47.66	34.30	13.76
92	923	47.72	33.00	49.86	34.85	47.77	36.05	47.79	33.76	13.43
93	945	48.59	32.44	50.72	34.21	49.31	35.81	47.91	34.00	13.12
94	968	49.38	31.86	51.53	33.61	50.65	35.20	48.35	34.59	12.81
95	992	50.11	31.27	52.30	33.00	51.71	34.59	49.48	35.20	12.50
96	1016	50.78	30.71	53.01	32.41	52.65	34.00	50.86	35.57	12.20
97	1041	51.39	30.11	53.66	31.77	53.50	33.33	52.37	34.87	11.91
98	1067	51.90	29.62	54.23	31.27	54.18	32.82	53.35	34.40	11.62
99	1093	52.42	29.15	54.80	30.79	54.88	32.33	54.25	33.94	11.34
100	1119	52.93	28.70	55.37	30.32	55.56	31.86	55.10	33.50	11.08
101	1147	53.46	28.23	55.95	29.84	56.25	31.38	55.96	33.04	10.81
102	1175	53.99	27.78	56.55	29.38	56.98	30.91	56.78	32.60	10.55
103	1204	54.46	27.33	57.09	28.93	57.59	30.44	57.59	32.16	10.30
104	1233	54.95	26.90	57.67	28.48	58.27	29.99	58.41	31.74	10.06
105	1263	55.49	26.42	58.30	27.99	59.02	29.47	59.34	31.22	9.82
106	1294	55.95	25.84	58.85	27.37	59.66	28.79	60.13	30.46	9.58
107	1326	56.37	25.27	59.34	26.75	60.23	28.12	60.82	29.73	9.35
108	1358	56.73	24.72	59.77	26.17	60.72	27.48	61.40	29.02	9.13
109	1392	57.05	24.17	60.15	25.58	61.17	26.83	61.92	28.31	8.91
110	1426	57.35	23.64	60.51	25.01	61.58	26.21	62.39	27.63	8.69
111	1460	57.61	23.13	60.84	24.47	61.96	25.62	62.82	26.99	8.49
112	1496	57.88	22.60	61.19	23.91	62.33	25.02	63.23	26.33	8.29
113	1533	58.09	22.04	61.47	23.31	62.65	24.39	63.59	25.68	8.09
114	1570	58.26	21.50	61.71	22.75	62.92	23.79	63.91	25.05	7.90
115	1609	58.40	20.96	61.93	22.18	63.18	23.19	64.21	24.42	7.71
116	1648	58.49	20.45	62.10	21.63	63.38	22.62	64.47	23.83	7.52
117	1688	58.56	19.95	62.25	21.11	63.57	22.06	64.70	23.25	7.34
118	1730	58.62	19.45	62.39	20.58	63.73	21.50	64.92	22.66	7.17
119	1772	58.63	18.94	62.50	20.05	63.87	20.95	65.11	22.08	7.00
120	1815	58.59	18.44	62.55	19.52	63.96	20.40	65.25	21.51	6.83
121	1860	58.51	17.94	62.57	19.00	64.03	19.86	65.37	20.94	6.67
122	1905	58.39	17.47	62.56	18.51	64.07	19.34	65.45	20.40	6.51
123	1952	58.18	17.00	62.49	18.01	64.05	18.83	65.48	19.86	6.35
124	2000	57.96	16.54	62.42	17.54	64.03	18.33	65.52	19.34	6.20

$\frac{E_{\mu}(E)}{f_2}$	200.3	189.4	188.6	186.1	$\frac{\text{keV-cm}^2}{\text{gram}}$
Atomic Weight	210.0	222.0	223.0	226.0	amu

ATOMIC SCATTERING FACTOR,  $f_1 + if_2$ 

N	E(eV)	Ac (89)		Th (90)		Pa (91)		U (92)		$\lambda(\text{Å})$
		$f_1$	$f_2$	$f_1$	$f_2$	$f_1$	$f_2$	$f_1$	$f_2$	
0	100	10.96	35.89	-20.74	71.91	-18.92	22.68	-6.11	25.08	124.0
1	102	12.79	36.24	13.37	81.59	-23.87	33.00	-11.25	12.35	121.5
2	104	14.53	35.82	27.75	56.16	-20.01	47.67	-15.63	21.05	119.2
3	107	16.81	34.98	30.00	43.26	-0.73	78.19	-19.33	39.89	115.9
4	110	18.57	34.19	29.44	38.76	24.25	61.36	-11.68	53.79	112.7
5	112	19.58	33.69	29.84	36.24	30.07	52.40	0.89	63.45	110.7
6	115	20.99	32.96	30.21	33.43	34.18	41.56	19.44	61.75	107.8
7	118	22.30	32.26	31.12	30.91	33.55	33.85	33.07	50.47	105.1
8	121	23.55	31.60	31.47	28.78	32.08	31.40	35.14	39.39	102.5
9	124	24.68	30.96	31.94	27.12	32.15	29.18	34.47	31.84	100.0
10	127	25.95	30.36	32.43	25.50	32.29	27.16	32.55	29.62	97.6
11	130	27.24	29.52	32.81	23.82	32.47	25.33	32.20	27.59	95.4
12	133	28.35	28.36	32.89	22.29	32.60	23.66	31.97	26.09	93.2
13	136	29.08	27.27	33.14	20.89	32.61	22.13	32.35	24.77	91.2
14	140	29.92	25.91	33.15	19.20	32.58	20.29	32.75	22.54	88.6
15	143	30.45	24.96	33.08	18.05	32.51	19.05	32.76	21.05	86.7
16	147	31.00	23.78	32.89	16.66	32.33	17.54	32.73	19.35	84.3
17	150	31.34	22.95	32.77	15.71	32.18	16.51	32.82	18.19	82.7
18	154	31.75	21.91	32.49	14.55	31.87	15.26	32.64	16.33	80.5
19	158	32.10	20.94	32.20	13.51	31.53	14.13	32.12	14.78	78.5
20	162	32.48	20.04	31.86	12.56	31.15	13.11	31.51	13.69	76.5
21	166	32.76	18.95	31.48	11.70	30.74	12.19	31.01	12.70	74.7
22	170	32.94	17.93	31.07	10.91	30.31	11.35	30.49	11.80	72.9
23	174	32.97	16.99	30.61	10.20	29.84	10.59	29.99	10.99	71.3
24	178	32.93	16.12	30.19	9.55	29.35	9.89	29.47	10.24	69.7
25	182	32.88	15.31	29.68	8.95	28.86	9.26	28.89	9.57	68.1
26	187	32.73	14.38	29.06	8.27	28.16	8.54	28.17	8.80	66.3
27	191	32.56	13.69	28.50	7.78	27.57	8.01	27.55	8.25	64.9
28	196	32.34	12.90	27.72	7.21	26.71	7.42	26.66	7.62	63.3
29	201	32.07	12.17	26.74	6.82	25.71	7.00	25.61	7.18	61.7
30	206	31.78	11.50	25.89	6.91	24.80	7.09	24.65	7.27	60.2
31	211	31.48	10.87	25.23	7.00	24.13	7.18	23.93	7.36	58.8
32	216	31.15	10.30	24.70	7.08	23.57	7.27	23.34	7.45	57.4
33	221	30.81	9.74	24.23	7.17	23.05	7.36	22.82	7.54	56.1
34	227	30.33	9.09	23.69	7.27	22.50	7.46	22.23	7.65	54.6
35	232	29.89	8.59	23.27	7.36	22.06	7.55	21.78	7.74	53.4
36	238	29.32	8.05	22.77	7.46	21.53	7.65	21.23	7.85	52.1
37	244	28.68	7.54	22.22	7.55	20.98	7.75	20.65	7.95	50.8
38	250	27.89	7.09	21.60	7.65	20.32	7.85	19.98	8.05	49.6
39	256	27.11	6.95	21.01	8.06	19.71	8.27	19.36	8.48	48.4
40	262	26.39	6.89	20.51	8.48	19.17	8.71	18.82	8.93	47.3
41	269	25.65	6.82	20.02	8.99	18.69	9.23	18.29	9.46	46.1
42	275	24.98	6.76	19.65	9.44	18.30	9.69	17.90	9.93	45.1
43	282	24.20	6.84	19.28	9.97	17.90	10.24	17.51	10.49	44.0
44	289	23.47	6.93	18.93	10.53	17.54	10.80	17.14	11.08	42.9
45	296	22.58	7.04	18.59	11.09	17.22	11.39	16.81	11.68	41.9
46	303	21.79	7.38	18.33	11.69	16.94	11.99	16.53	12.30	40.9
47	311	21.03	7.77	18.05	12.40	16.58	12.72	16.23	13.04	39.9
48	318	20.33	8.12	17.87	13.04	16.33	13.38	16.04	13.72	39.0
49	326	19.50	8.53	17.72	13.79	16.20	14.15	15.83	14.51	38.0
50	334	18.62	8.95	17.62	14.56	16.12	14.95	15.71	15.33	37.1
51	342	17.63	9.78	17.62	15.36	16.07	15.77	15.69	16.17	36.3
52	351	16.76	10.84	17.79	16.25	16.26	16.68	15.86	17.10	35.3
53	359	16.11	11.86	17.95	16.79	16.39	17.23	16.00	17.66	34.5
54	368	15.48	13.10	18.09	17.39	16.49	17.85	16.14	18.30	33.7
55	377	14.99	14.42	18.18	18.00	16.55	18.47	16.20	18.94	32.9
56	386	14.62	15.84	18.25	18.62	16.54	19.11	16.24	19.59	32.1
57	396	14.38	17.84	18.32	19.31	16.55	19.82	16.26	20.32	31.3
58	406	14.77	19.11	18.42	20.00	16.45	20.66	16.28	21.15	30.5
59	415	14.91	20.29	18.48	20.63	16.46	21.51	16.34	21.96	29.9
60	426	15.15	21.81	18.56	21.41	16.55	22.58	16.47	22.96	29.1
61	436	15.47	23.24	18.59	22.12	16.69	23.56	16.63	23.90	28.4
62	447	16.07	24.89	18.56	22.91	16.94	24.67	16.87	24.94	27.7
63	458	16.95	26.26	18.43	23.97	17.25	25.80	17.17	26.00	27.1
64	469	17.80	27.33	18.51	25.30	17.64	26.96	17.53	27.08	26.4

N	E(eV)	Ac (89) Actinium		Th (90) Thorium		Pa (91) Protactinium		U (92) Uranium		$\lambda(\text{Å})$
		$f_1$	$f_2$	$f_1$	$f_2$	$f_1$	$f_2$	$f_1$	$f_2$	
65	480	18.57	28.43	18.75	26.68	18.09	28.13	17.95	28.18	25.83
66	492	19.44	29.64	19.27	28.22	18.75	29.44	18.51	29.40	25.20
67	504	20.45	30.88	20.06	29.82	19.54	30.78	19.17	30.64	24.60
68	516	21.71	32.14	21.23	31.46	20.60	32.15	19.95	31.90	24.03
69	529	23.50	33.16	23.17	32.80	22.16	33.35	21.08	33.20	23.44
70	542	24.98	33.39	24.76	33.08	23.55	33.89	22.42	34.34	22.87
71	555	26.32	33.63	26.16	33.36	24.87	34.43	23.88	35.48	22.34
72	569	27.51	33.85	27.43	33.64	26.22	35.01	25.66	35.94	21.79
73	583	28.59	33.92	28.55	33.74	27.59	35.29	27.11	36.14	21.27
74	597	29.44	33.94	29.50	33.79	28.76	35.46	28.39	36.27	20.77
75	612	30.17	33.97	30.38	33.83	29.92	35.65	29.61	36.41	20.26
76	627	30.68	33.99	31.11	33.87	31.02	35.82	30.74	36.55	19.77
77	642	30.60	34.42	31.63	33.84	32.18	35.88	31.85	36.61	19.31
78	658	31.08	35.91	30.35	33.63	33.14	35.67	32.90	36.49	18.84
79	674	32.05	37.42	26.84	N 33.42	33.93	35.46	33.73	36.37	18.39
80	690	33.72	38.60	33.19	38.89	34.39	35.36	34.44	36.31	17.97
81	707	36.00	39.60	35.60	38.80	34.52	35.39	35.08	36.27	17.54
82	725	38.23	39.21	37.32	38.70	34.86	36.40	35.58	36.23	17.10
83	742	39.85	38.86	38.81	38.61	35.55	37.36	32.70	N 38.41	16.71
84	760	41.24	38.51	40.20	38.52	36.81	38.37	35.54	38.78	16.31
85	779	42.63	38.12	41.65	38.38	38.44	39.29	37.82	39.16	15.92
86	798	43.82	37.63	43.00	38.01	40.22	39.29	39.24	39.54	15.54
87	818	44.91	37.13	44.20	37.64	41.72	39.28	40.61	39.93	15.16
88	838	45.87	36.66	45.33	37.28	43.24	39.27	42.15	40.31	14.79
89	858	46.73	36.18	46.39	36.88	44.69	39.10	43.88	40.40	14.45
90	879	47.53	35.65	47.38	36.37	46.16	38.58	45.48	39.89	14.10
91	901	48.14	35.12	48.26	35.86	47.35	38.05	46.85	39.36	13.76
92	923	48.41	34.62	49.07	35.37	48.48	37.55	48.04	38.86	13.43
93	945	48.65	34.84	49.76	34.83	49.45	36.98	49.11	38.30	13.12
94	968	49.21	35.39	50.23	34.27	50.35	36.37	50.05	37.69	12.81
95	992	50.43	35.97	50.32	33.70	51.13	35.76	50.91	37.09	12.50
96	1016	51.92	36.31	49.80	33.69	51.80	35.16	51.61	36.50	12.20
97	1041	53.64	35.62	51.01	36.24	52.25	34.50	52.01	35.88	11.91
98	1067	54.74	34.92	53.03	35.59	52.65	34.36	52.51	35.79	11.62
99	1093	55.69	34.24	54.48	34.96	53.18	34.22	53.11	35.70	11.34
100	1119	56.54	33.60	55.46	34.36	53.78	34.08	53.77	35.62	11.08
101	1147	57.34	32.93	56.40	33.74	54.46	33.94	54.52	35.53	10.81
102	1175	58.07	32.29	57.22	33.14	55.18	33.81	55.28	35.44	10.55
103	1204	58.69	31.66	57.93	32.55	55.92	33.67	56.12	35.35	10.30
104	1233	59.27	31.06	58.53	31.98	56.71	33.53	57.06	35.26	10.06
105	1263	59.74	30.50	59.09	31.47	57.62	33.32	58.12	35.06	9.82
106	1294	60.24	30.06	59.65	31.08	58.47	32.92	59.09	34.59	9.58
107	1326	60.76	29.61	60.23	30.69	59.26	32.52	59.98	34.13	9.35
108	1358	61.29	29.18	60.83	30.31	60.00	32.14	60.79	33.68	9.13
109	1392	61.83	28.74	61.45	29.93	60.74	31.74	61.60	33.22	8.91
110	1426	62.37	28.32	62.09	29.56	61.47	31.36	62.39	32.78	8.69
111	1460	62.93	27.92	62.75	29.20	62.22	31.00	63.18	32.36	8.49
112	1496	63.59	27.44	63.55	28.75	63.09	30.54	64.08	31.84	8.29
113	1533	64.15	26.77	64.22	28.04	63.83	29.84	64.85	31.10	8.09
114	1570	64.63	26.14	64.79	27.37	64.47	29.17	65.52	30.40	7.90
115	1609	65.05	25.50	65.28	26.69	65.05	28.49	66.11	29.69	7.71
116	1648	65.40	24.89	65.69	26.05	65.54	27.85	66.63	29.02	7.52
117	1688	65.72	24.30	66.07	25.42	66.00	27.22	67.13	28.36	7.34
118	1730	66.03	23.70	66.43	24.79	66.44	26.59	67.61	27.70	7.17
119	1772	66.30	23.11	66.74	24.16	66.85	25.95	68.03	27.02	7.00
120	1815	66.52	22.51	67.01	23.54	67.19	25.31	68.41	26.35	6.83
121	1860	66.71	21.92	67.25	22.93	67.50	24.67	68.76	25.68	6.67
122	1905	66.87	21.36	67.41	22.34	67.76	24.06	69.01	25.05	6.51
123	1952	66.97	20.80	67.56	21.76	67.97	23.46	69.26	24.41	6.35
124	2000	67.07	20.26	67.72	21.20	68.20	22.87	69.52	23.80	6.20

$\frac{E_{II}(E)}{f_2}$	185.3	181.3	182.1	176.7	$\frac{\text{keV-cm}^2}{\text{gram}}$
Atomic Weight	227.0	232.0	231.0	238.0	amu

ATOMIC SCATTERING FACTOR,  $f_1 + if_2$ 

N	E(eV)	Np (93)		Pu (94)		$f_1$	$f_2$	$f_1$	$f_2$	$\lambda(\text{Å})$
		$f_1$	$f_2$	$f_1$	$f_2$					
0	100	-13.83	23.78	-3.62	20.00					124.0
1	102	-15.00	27.61	-4.33	21.82					121.5
2	104	-16.14	31.95	-4.86	23.77					119.2
3	107	-17.60	39.58	-5.41	26.94					115.9
4	110	-10.38	56.38	-5.56	30.43					112.7
5	112	-2.75	57.24	-5.28	32.96					110.7
6	115	7.74	58.51	-4.49	37.06					107.8
7	118	16.35	58.92	-3.03	41.55					105.1
8	121	23.62	55.29	-0.12	46.45					102.5
9	124	29.24	51.96	4.45	51.01					100.0
10	127	33.71	48.09	10.32	54.22					97.6
11	130	36.99	43.36	17.68	55.37					95.4
12	133	38.83	39.19	23.61	53.26					93.2
13	136	39.63	35.49	28.08	51.28					91.2
14	140	40.10	31.21	33.63	47.51					88.6
15	143	39.91	28.73	36.12	44.00					86.7
16	147	39.72	26.07	38.52	39.82					84.3
17	150	39.58	24.28	39.74	37.02					82.7
18	154	39.27	22.13	40.65	33.66					80.5
19	158	38.83	20.22	41.17	30.67					78.5
20	162	38.37	18.59	41.43	28.02					76.5
21	166	37.89	17.13	41.48	25.65					74.7
22	170	37.39	15.82	41.30	23.54					72.9
23	174	36.87	14.64	40.96	21.64					71.3
24	178	36.31	13.56	40.52	19.94					69.7
25	182	35.75	12.59	40.01	18.65					68.1
26	187	35.02	11.50	39.47	17.19					66.3
27	191	34.43	10.72	39.04	16.13					64.9
28	196	33.65	9.83	38.50	14.92					63.3
29	201	32.83	9.07	37.94	13.83					61.7
30	206	31.94	8.37	37.37	12.85					60.2
31	211	31.01	7.89	36.79	11.95					58.8
32	216	30.18	7.62	36.20	11.14					57.4
33	221	29.41	7.37	35.61	10.40					56.1
34	227	28.48	7.09	34.87	9.56					54.6
35	232	27.65	7.06	34.20	8.90					53.4
36	238	26.88	7.20	33.30	8.19					52.1
37	244	26.21	7.33	32.25	7.56					50.8
38	250	25.61	7.46	31.05	7.47					49.6
39	256	25.07	7.59	30.25	7.56					48.4
40	262	24.54	7.72	29.54	7.64					47.3
41	269	23.91	7.86	28.83	7.74					46.1
42	275	23.32	7.99	28.27	7.82					45.1
43	282	22.69	8.37	27.65	7.92					44.0
44	289	22.12	8.78	27.03	8.02					42.9
45	296	21.62	9.20	26.42	8.26					41.9
46	303	21.17	9.63	25.91	8.49					40.9
47	311	20.66	10.14	25.36	8.77					39.9
48	318	20.27	10.63	24.89	9.01					39.0
49	326	19.87	11.22	24.37	9.28					38.0
50	334	19.47	11.82	23.81	9.56					37.1
51	342	19.10	12.44	23.20	9.83					36.3
52	351	18.76	13.15	22.42	10.31					35.3
53	359	18.48	13.80	21.88	10.91					34.5
54	368	18.24	14.56	21.33	11.61					33.7
55	377	18.04	15.33	20.84	12.34					32.9
56	386	17.84	16.13	20.42	13.09					32.1
57	396	17.65	17.04	20.03	13.96					31.3
58	406	17.58	17.98	19.67	14.86					30.5
59	415	17.50	18.85	19.39	15.70					29.9
60	426	17.55	19.94	19.14	16.76					29.1
61	436	17.63	20.86	18.97	17.77					28.4
62	447	17.72	21.89	18.87	18.91					27.7
63	458	17.88	22.94	18.96	20.08					27.1
64	469	18.08	24.02	19.09	21.00					26.4

N	E(eV)	Np (93) Neptunium		Pu (94) Plutonium		$f_1$	$f_2$	$f_1$	$f_2$	$\lambda(A)$
		$f_1$	$f_2$	$f_1$	$f_2$					
65	480	18.32	25.12	19.17	21.94					25.83
66	492	18.67	26.35	19.25	22.98					25.20
67	504	19.19	27.61	19.36	24.05					24.60
68	516	19.91	28.89	19.50	25.15					24.03
69	529	20.61	29.50	19.69	26.36					23.44
70	542	21.02	30.92	19.93	27.60					22.87
71	555	21.68	32.38	20.17	28.86					22.34
72	569	22.92	33.98	20.44	30.25					21.79
73	583	24.51	34.96	20.70	31.93					21.27
74	597	25.86	35.66	21.33	33.88					20.77
75	612	27.25	36.41	22.40	36.06					20.26
76	627	28.66	37.16	24.02	38.32					19.77
77	642	30.34	37.65	26.52	39.94					19.31
78	658	31.89	37.64	28.98	40.16					18.84
79	674	33.20	37.64	30.89	40.38					18.39
80	690	34.33	37.59	32.54	40.52					17.97
81	707	35.40	37.51	34.21	40.57					17.54
82	725	36.39	37.44	35.76	40.19					17.10
83	742	37.28	37.37	36.88	39.85					16.71
84	760	38.14	37.30	37.74	39.50					16.31
85	779	38.24	36.42	38.21	39.14					15.92
86	798	37.98	37.74	37.21	38.79					15.54
87	818	38.60	39.14	39.35	40.59					15.16
88	838	40.26	40.56	40.45	41.13					14.79
89	858	42.24	41.47	41.60	41.66					14.45
90	879	44.40	41.14	42.85	42.21					14.10
91	901	46.01	40.80	44.36	42.79					13.76
92	923	47.51	40.47	46.20	43.35					13.43
93	945	48.89	39.98	48.22	43.10					13.12
94	968	50.05	39.40	49.75	42.46					12.81
95	992	51.14	38.82	51.12	41.81					12.50
96	1016	52.07	38.23	52.27	41.17					12.20
97	1041	52.75	37.53	53.08	40.41					11.91
98	1067	53.39	37.37	53.85	40.25					11.62
99	1093	54.09	37.21	54.67	40.10					11.34
100	1119	54.87	37.06	55.58	39.95					11.08
101	1147	55.74	36.90	56.58	39.79					10.81
102	1175	56.63	36.75	57.60	39.64					10.55
103	1204	57.59	36.59	58.71	39.48					10.30
104	1233	58.68	36.44	59.96	39.33					10.06
105	1263	59.88	36.12	61.32	38.98					9.82
106	1294	61.00	35.40	62.60	38.17					9.58
107	1326	61.91	34.69	63.65	37.37					9.35
108	1358	62.72	34.02	64.58	36.60					9.13
109	1392	63.46	33.33	65.44	35.82					8.91
110	1426	64.09	32.67	66.20	35.08					8.69
111	1460	64.68	32.04	66.93	34.37					8.49
112	1496	65.22	31.42	67.64	33.63					8.29
113	1533	65.73	30.87	68.27	32.87					8.09
114	1570	66.23	30.34	68.86	32.13					7.90
115	1609	66.75	29.80	69.42	31.40					7.71
116	1648	67.23	29.29	69.92	30.69					7.52
117	1688	67.72	28.78	70.40	30.00					7.34
118	1730	68.23	28.28	70.87	29.31					7.17
119	1772	68.70	27.70	71.29	28.61					7.00
120	1815	69.15	27.11	71.69	27.91					6.83
121	1860	69.56	26.53	72.05	27.22					6.67
122	1905	69.88	25.97	72.33	26.56					6.51
123	1952	70.22	25.41	72.61	25.90					6.35
124	2000	70.57	24.86	72.89	25.26					6.20

$$\frac{E_{\mu}(E)}{f_2}$$

177.4

172.4

$$\frac{\text{keV-cm}^2}{\text{gram}}$$

Atomic Weight

237.0

244.0

amu

## LIST OF ATTENDEES

Harlow G. Ahlstrom  
Lawrence Livermore National Laboratory  
Livermore, CA 94550

Carol T. Alonso  
(LLNL)

Frank Ameduri  
Los Alamos National Laboratory  
P.O. Box 1663; MS-410  
Los Alamos, NM 87545

George Anderman  
Department of Chemistry  
University of Hawaii  
Bilger 218  
Honolulu, HI 96822

Chuck Anderson  
(LLNL)

John Anderson  
(LLNL)

John P. Anthes  
Sandia Laboratories  
P.O. Box 5800; Org. 4234  
Albuquerque, NM 87185

David Attwood  
(LLNL)

E. Augusta  
(LLNL)

Troy Barbee  
Dept. of Materials Science  
Stanford University  
Stanford, CA 94305

Doron Bardas  
LPARL  
Building 202 Lockheed  
3251 Hanover Street  
Palo Alto, CA 94304

Samuel J. Barish  
Office of Inertial Fusion  
MS-C-404, DP-40  
U.S. Dept. of Energy  
Washington, D.C. 20545

Robert F. Benjamin  
Los Alamos National Laboratory  
MS-554  
Los Alamos, NM 87545

Mr. Bernard  
Centre d'Etudes de Limeil  
B.P. 27  
94190 Villeneuve Saint-Georges  
FRANCE

R. L. Blake  
Los Alamos Scientific Laboratory  
P.O. Box 1663; MS-434  
Los Alamos, NM 87545

R. R. Borchers  
(LLNL)

Michael Boyle  
ARACOR  
1223 E. Arques Avenue  
Sunnyvale, CA 94086

Mr. Busquet  
Centre D'Etudes de Limeil  
BP-27  
94190 Villeneuve St. Georges  
FRANCE

Claude R. Canizares  
Massachusetts Institute of Tech.  
Center for Space Research  
Cambridge, MA 02139

Dr. Robert Carman  
Los Alamos Scientific Laboratory  
P.O. Box 1663; MS-554  
Los Alamos, NM 87545

N. Ceglio  
(LLNL)

George Charatis  
KMS Fusion, Inc.  
P.O. Box 1567  
Ann Arbor, MI 48106

Dr. Chevallier  
Centre D'Etudes de Valduc  
BP-14; 21/Is-Sur-Tille  
FRANCE

Joe Chmielewski  
Los Alamos National Laboratory  
P.O. Box 1663 P-14 MS-140  
Los Alamos, NM 87545

Arnold Clark  
(LLNL)

Lamar Coleman  
(LLNL)

Stewart Collins  
Jet Propulsion Laboratory  
4800 Oak Grove Dr.  
Pasadena, CA 91109

G. Dahlbacka  
Physics International  
2700 Merced Street  
San Leandro, CA 94577

Jay Davis  
(LLNL)

Bob Day  
Los Alamos Scientific Laboratory  
P.O. Box 1663; MS-410  
Los Alamos, NM 87545

J. H. Degnan  
Air Force Weapons Lab., NTYP  
Kirkland AFB  
Albuquerque, NM 87117

N. DelGrande  
(LLNL)

Pierre Dhez  
L.U.R.E. - Bat. 209C  
Universite Paris-SUC  
91405 Orsay  
FRANCE

E. R. Dietz  
University of Hawaii  
2505 Correa Road, Watanabe Hall  
Honolulu, HI 96822

Claude Dittmore  
(LLNL)

Dan Dietrich  
(LLNL)

Phil Dreike  
Sandia National Laboratories  
Division 4242  
Albuquerque, NM 87185

R. Duffus  
(LLNL)

Ray Dukart  
Physics International  
2700 Merced St.  
San Leandro, CA 94544

Hans Egger  
University of Illinois at  
Chicago Circle  
Department of Physics  
P.O. Box 4358  
Chicago, IL 60680

M. Eisner  
University of Houston  
Central Campus  
Department of Physics  
Houston, TX 77004

R. C. Elton  
Naval Research Laboratory  
Code 6505  
Washington, DC 20375

G. D. Enright  
Division of Physics, M-23A  
National Research Council  
Montreal Rd.  
Ottawa, Ont. K1A 0R6  
CANADA

Richard Ernst  
(LLNL)

David L. Fehl  
Sandia Laboratories  
P.O. Box 5800; Org. 4234  
Albuquerque, NM 87185

J. M. Forsyth  
Laser Laboratory  
University of Rochester  
River Station, NY 14627

Albert Franks  
National Physical Laboratory  
Teddington, Middlesex TW11 0LW  
UNITED KINGDOM

David Gaines  
Department of Physics  
BYU  
Provo, UT 84601

Jerry Gaines  
(LLNL)



R. P. Godwin  
Los Alamos Scientific Laboratory  
P.O. Box 1663; MS-434  
Los Alamos, NM 87545

David L. Hanson  
Sandia National Laboratories  
Division 4234  
Albuquerque, NM 87185

T. Harper  
(LLNL)

S. Harris  
Edward L. Ginzton Laboratory  
Department of Electronics Eng.  
Stanford University  
Stanford, CA 94305

Andrew Hawryluk  
MIT  
77-Massachusetts Avenue  
Rm. 13-3077  
Cambridge, MA 02139

Michael Hecht  
Stanford University  
SEL McCullough 251  
Stanford, CA 94306

Ray Heinle  
(LLNL)

Burt Henke  
Department of Physics  
University of Hawaii  
2505 Correa Road  
Honolulu, HI 96822

Kenneth Hill  
TFTR Physics Group  
Princeton Plasma Physics Lab.  
Princeton, NJ 08544

R. Hockaday  
Los Alamos National Laboratory  
P.O. Box 1663; P-14 MS/410  
Los Alamos, NM 87545

Dale Holmberg  
EG&G, Inc.  
P.O. Box 1912, N-22  
Las Vegas, NV 89101

Neil Holmes  
(LLNL)

John Houghton  
(LLNL)

DeAnn Iwan  
Sandia National Laboratories  
P.O. Box 5800  
Albuquerque, NM 87185

Dr. C. B. Johnson  
ITT/EOPD  
3700 East Pontiac Street  
Ft. Wayne, IN 46803

George Joki  
Lockheed Research Labs  
Bldg. 202; Dept. 52-12  
3251 Hanover Street  
Palo Alto, CA 94304

Elisabeth Källne  
Smithsonian Astrophys. Observ.  
60 Garden Street  
Cambridge, MA 02138

Julie Kakanui  
(LLNL)

Bob Kauffman  
(LLNL)

P. Kirkpatrick  
273 Santa Teresa St.  
Stanford, CA 94305

Gerald E. Kiuttu  
University of New Mexico  
9013 Natalie NE  
Albuquerque, NM 87111

Larry Knight  
(LLNL)

J. Knauer  
Lockheed Palo Alto Research Laboratory  
ONG 52-11  
Bldg. 203  
3251 Hanover Street  
Palo Alto, CA 94304

Helmut Koehler  
(LLNL)

Lou Koppel  
Advanced Research and  
Applications Corp. (ARACOR)  
1223 E. Arques Ave.  
Sunnyvale, CA 94086

Harry N. Kornblum  
(LLNL)

W. Ku  
Department of Physics  
Columbia University  
538 West 120th St.  
New York, NY 10023

Robert Kuckuck  
(LLNL)

Stephen M. Lane  
(LLNL)

Jon T. Larsen  
Physics International  
2700 Merced St.  
San Leandro, CA 94544

George Leipelt  
(LLNL)

E. Leith  
Department of Electrical Eng.  
University of Michigan  
Ann Arbor, MI 48109

Ingolf Lindau  
SLAC  
Stanford University  
P.O. Box 4349  
Stanford, CA 94305

Jan Lipson  
Los Alamos National Laboratory  
P.O. Box 1663  
Los Alamos, NM 87545

Mr. Louis-Jacquet  
Centre d'Etudes de Limeil  
B.P. 27  
94190 Villeneuve - St. Georges  
FRANCE

Pete Lyons  
Los Alamos Scientific Laboratory  
P.O. Box 1663; J-14  
Los Alamos, NM 87545

R. Madden  
National Bureau of Standards  
Rm. A-251 Physics  
Washington, D.C. 20234

John H. Mallett  
(LLNL)

S. Manson  
Department of Physics  
Georgia State University  
33 Gilmer Street S.E.  
Atlanta, GA 30303

Dennis Matthews  
(LLNL)

Leonard Mascheroni  
Los Alamos National Laboratory  
P.O. Box 1663  
X1, MS-531  
Los Alamos, NM 87545

Hector Medeck  
(LLNL)

Dan Metzger  
Los Alamos National Laboratory  
P.O. Box 1663; MS-439  
Los Alamos, NM 87545

K. Mitchell  
Los Alamos National Laboratory  
P.O. Box 1663  
Los Alamos, NM 87545

Paul Mix  
Sandia Laboratory  
P.O. Box 5800; Org. 4242  
Albuquerque, NM 87185

James F. Morgan  
(LLNL)

D. Nagel  
Naval Research Lab.; Code 6682  
Washington, D.C. 20375

Hideaki Niki  
Institute of Laser Engineering  
Osaka University, Yamada-Kami  
Suita, Osaka 565  
JAPAN

Merrill A. Palmer  
Division 4234  
Sandia National Laboratories  
P.O. Box 5800  
Albuquerque, NM 87185

Brad Pate  
Stanford University  
SEL  
McCullough 251  
Stanford, CA 94306

N. J. Peacock  
UKAEA: Culham Laboratory  
Culham, Abingdon, Oxford  
ENGLAND

Raymond T. Perkins  
(LLNL)

Johnny O. Petersen  
Department of Physics  
BYU  
Provo, UT 84601

Peter Poulsen  
(LLNL)

Bob Price  
(LLNL)

Bill Friedhorsky  
Los Alamos National Laboratory  
P.O. Box 1663  
Los Alamos, NM 87545

Herbert Pummer  
University of Illinois  
at Chicago Circle  
Department of Physics  
P.O. Box 4348  
Chicago, IL 60680

John Rauch  
Maxwell Laboratories  
9244 Balboa Avenue  
San Diego, CA 92123

Victor Rehn  
Department of the Navy  
Naval Weapons Center (Code 3813)  
China Lake, CA 93555

Martin Richardson  
Laser Laboratory  
University of Rochester  
River Station, NY 14627

John C. Riordan  
Maxwell Laboratories  
9244 Balboa Avenue  
San Diego, CA 92123

Paul Rockett  
Los Alamos National Laboratory  
P.O. Box 1663  
Los Alamos, NM 87545

Alan Rosenbluth  
Laser Laboratory  
University of Rochester  
River Station, NY 14627

Mark Roth  
(LLNL)

Leonid Rozenshtein  
New York University  
New York, NY 10017

Vivian Rupert  
(LLNL)

Richard Sauneuf  
Centre d'Etudes de Limeil  
B.P. 27  
94190 Villeneuve St. Georges  
FRANCE

Ned R. Sauthoff  
Plasma Physics Laboratory  
P.O. Box 451  
Princeton, NJ 08544

D.P. Siddons  
University of London  
Kings College  
Strand London  
WC2R 2LS  
ENGLAND

Richard Sigel  
Max-Planck Institute  
Proj. fur Laser Forschung  
D-80 46, Garching Bei Munchen  
WEST GERMANY

Leif Singman  
EG&G, Inc.  
P.O. Box 1912; MS-H01  
Las Vegas, NV 89101

Vincent W. Slivinsky  
(LLNL)

Henry I. Smith  
Massachusetts Inst. of Tech.  
Cambridge, MA 02139

Rick B. Spielman  
Sandia National Laboratories  
Division 4234  
Albuquerque, NM 87185

E. Spiller  
IBM  
Thomas J. Watson Res. Center  
P.O. Box 218  
Yorktown Heights, NY 10598

Larry A. Stelmack  
15 Laurel St.  
Somerville, MA 02132

Gary Stone  
(LLNL)

Gary Stradling  
(LLNL)

Michael A. Stroschio  
AFOSR-NP  
Bolling AFB  
Washington, DC 20332

A. J. Summers  
AMRE  
Aldermaston, Reading RG7 4PR  
ENGLAND

Tina J. Tanaka  
University of Hawaii  
Department of Physics and Astronomy  
2505 Correa Road, Watanabe Hall  
Honolulu, HI 96822

Kazuo Taniguchi  
Dept. of Solid State Physics  
Osaka Electro-Com. University  
18-8 Hatsu, Neyagawa, Osaka  
JAPAN

Roman Tatchyn  
SSRL/SLAC  
Bin 69, Stanford University  
P.O. Box 4349  
Stanford, CA 94305

Bob Thoe  
(LLNL)

Richard Thompson  
EG&G, Inc.  
P.O. Box 1912, N-22  
Las Vegas, NV 89101

K. Glenn Tirsell  
(LLNL)

Art Toor  
(LLNL)

Gary Tripp  
(LLNL)

Jim Underwood  
Jet Propulsion Laboratory  
4800 Oak Grove Drive  
Mail Code 169-506  
Pasadena, CA 91103

Charles Vane  
Oakridge National Laboratory  
P.O. Box X, Bldg. 6010  
Oakridge, TN 37830

Peter H. Wackman  
Department of Mechanical Engr.  
Marquette University  
Milwaukee, WI 53233

Peter J. Walsh  
Los Alamos National Laboratory  
P.O. Box 1663 P-14 MS-410  
Los Alamos, NM 87545

Ching L. Wang  
(LLNL)

R. R. Whitlock  
Laser Plasma Branch  
Naval Research Lab. Code 6730  
Washington, DC 20375

J. Wobser  
(LLNL)

Wayne Woodruff  
(LLNL)

R. Wuerker  
TRW 1 DSSG  
Bldg. R-1; Rm. 1078  
One Space Park  
Redondo Beach, CA 90278

Barukh Yaakobi  
Laser Laboratory  
University of Rochester  
River Station, NY 14627

Masanobu Yamanaka  
Institute of Laser Engineering  
Osaka University  
Suita, Osaka 565  
JAPAN

Martin V. Zombeck  
Harvard-Smithsonian  
Center for Astrophysics  
60 Garden Street  
Cambridge, MA 02138

## AIP Conference Proceedings

	<u>L.C. Number</u>	<u>ISBN</u>
No.1 Feedback and Dynamic Control of Plasmas	70-144596	0-88318-100-2
No.2 Particles and Fields - 1971 (Rochester)	71-184662	0-88318-101-0
No.3 Thermal Expansion - 1971 (Corning)	72-76970	0-88318-102-9
No.4 Superconductivity in d-and f-Band Metals (Rochester, 1971)	74-18879	0-88318-103-7
No.5 Magnetism and Magnetic Materials - 1971 (2 parts) (Chicago)	59-2468	0-88318-104-5
No.6 Particle Physics (Irvine, 1971)	72-81239	0-88318-105-3
No.7 Exploring the History of Nuclear Physics	72-81883	0-88318-106-1
No.8 Experimental Meson Spectroscopy - 1972	72-88226	0-88318-107-X
No.9 Cyclotrons - 1972 (Vancouver)	72-92798	0-88318-108-8
No.10 Magnetism and Magnetic Materials - 1972	72-623469	0-88318-109-6
No.11 Transport Phenomena - 1973 (Brown University Conference)	73-80682	0-88318-110-X
No.12 Experiments on High Energy Particle Collisions - 1973 (Vanderbilt Conference)	73-81705	0-88318-111-8
No.13 $\pi$ - $\pi$ Scattering - 1973 (Tallahassee Conference)	73-81704	0-88318-112-6
No.14 Particles and Fields - 1973 (APS/DPF Berkeley)	73-91923	0-88318-113-4
No.15 High Energy Collisions - 1973 (Stony Brook)	73-92324	0-88318-114-2
No.16 Causality and Physical Theories (Wayne State University, 1973)	73-93420	0-88318-115-0
No.17 Thermal Expansion - 1973 (lake of the Ozarks)	73-94415	0-88318-116-9
No.18 Magnetism and Magnetic Materials - 1973 (2 parts) (Boston)	59-2468	0-88318-117-7
No.19 Physics and the Energy Problem - 1974 (APS Chicago)	73-94416	0-88318-118-5
No.20 Tetrahedrally Bonded Amorphous Semiconductors (Yorktown Heights, 1974)	74-80145	0-88318-119-3
No.21 Experimental Meson Spectroscopy - 1974 (Boston)	74-82628	0-88318-120-7
No.22 Neutrinos - 1974 (Philadelphia)	74-82413	0-88318-121-5
No.23 Particles and Fields - 1974 (APS/DPF Williamsburg)	74-27575	0-88318-122-3
No.24 Magnetism and Magnetic Materials - 1974 (20th Annual Conference, San Francisco)	75-2647	0-88318-123-1
No.25 Efficient Use of Energy (The AIP'S Studies on the Technical Aspects of the More Efficient Use of Energy)	75-18227	0-88318-124-X

No.26	High Energy Physics and Nuclear Structure - 1975 (Santa Fe and Los Alamos)	75-26411	0-88318-125-8
No.27	Topics in Statistical Mechanics and Biophysics: A Memorial to Julius L. Jackson (Wayne State University, 1975)	75-36309	0-88318-126-6
No.28	Physics and Our World: A Symposium in Honor of Victor F. Weisskopf (M.I.T., 1974)	76-7207	0-88318-127-4
No.29	Magnetism and Magnetic Materials - 1975 (21st Annual Conference, Philadelphia)	76-10931	0-88318-128-2
No.30	Particle Searches and Discoveries - 1976 (Vanderbilt Conference)	76-19949	0-88318-129-0
No.31	Structure and Excitations of Amorphous Solids (Williamsburg, VA., 1976)	76-22279	0-88318-130-4
No.32	Materials Technology - 1975 (APS New York Meeting)	76-27967	0-88318-131-2
No.33	Meson-Nuclear Physics - 1976 (Carnegie-Mellon Conference)	76-26811	0-88318-132-0
No.34	Magnetism and Magnetic Materials - 1976 (Joint MMM-Intermag Conference, Pittsburgh)	76-47106	0-88318-133-9
No.35	High Energy Physics with Polarized Beams and Targets (Argonne, 1976)	76-50181	0-88318-134-7
No.36	Momentum Wave Functions - 1976 (Indiana University)	77-82145	0-88318-135-5
No.37	Weak Interaction Physics - 1977 (Indiana University)	77-83344	0-88318-136-3
No.38	Workshop on New Directions in Mossbauer Spectroscopy (Argonne, 1977)	77-90635	0-88318-137-1
No.39	Physics Careers, Employment and Education (Penn State, 1977)	77-94053	0-88318-138-X
No.40	Electrical Transport and Optical Properties of Inhomogeneous Media (Ohio State University, 1977)	78-54319	0-88318-139-8
No.41	Nucleon-Nucleon Interactions - 1977 (Vancouver)	78-54249	0-88318-140-1
No.42	Higher Energy Polarized Proton Beams (Ann Arbor, 1977)	78-55682	0-88318-141-X
No.43	Particles and Fields - 1977 (APS/DMPF, Argonne)	78-55683	0-88318-142-8
No.44	Future Trends in Superconductive Electronics (Charlottesville, 1978)	77-9240	0-88318-143-6
No.45	New Results in High Energy Physics - 1978 (Vanderbilt Conference)	78-67196	0-88318-144-4
No.46	Topics in Nonlinear Dynamics (La Jolla Institute)	78-057870	0-88318-145-2
No.47	Clustering Aspects of Nuclear Structure and Nuclear Reactions (Winnepeg, 1978)	78-64942	0-88318-146-0
No.48	Current Trends in the Theory of Fields (Tallahassee, 1978)	78-72948	0-88318-147-9
No.49	Cosmic Rays and Particle Physics - 1978 (Bartol Conference)	79-50489	0-88318-148-7

No. 50	Laser-Solid Interactions and Laser Processing - 1978 (Boston)	79-51564	0-88318-149-5
No. 51	High Energy Physics with Polarized Beams and Polarized Targets (Argonne, 1978)	79-64565	0-88318-150-9
No. 52	Long-Distance Neutrino Detection - 1978 (C.L. Cowan Memorial Symposium)	79-52078	0-88318-151-7
No. 53	Modulated Structures - 1979 (Kailua Kona, Hawaii)	79-53846	0-88318-152-5
No. 54	Meson-Nuclear Physics - 1979 (Houston)	79-53978	0-88318-153-3
No. 55	Quantum Chromodynamics (La Jolla, 1978)	79-54969	0-88318-154-1
No. 56	Particle Acceleration Mechanisms in Astrophysics (La Jolla, 1979)	79-55844	0-88318-155-X
No. 57	Nonlinear Dynamics and the Beam-Beam Interaction (Brookhaven, 1979)	79-57341	0-88318-156-8
No. 58	Inhomogeneous Superconductors - 1979 (Berkeley Springs, W.V.)	79-57620	0-88318-157-6
No. 59	Particles and Fields - 1979 (APS/DPF Montreal)	80-66631	0-88318-158-4
No. 60	History of the ZGS (Argonne, 1979)	80-67694	0-88318-159-2
No. 61	Aspects of the Kinetics and Dynamics of Surface Reactions (La Jolla Institute, 1979)	80-68004	0-88318-160-6
No. 62	High Energy $e^+e^-$ Interactions (Vanderbilt, 1980)	80-53377	0-88318-161-4
No. 63	Supernovae Spectra (La Jolla, 1980)	80-70019	0-88318-162-2
No. 64	Laboratory EXAFS Facilities - 1980 (Univ. of Washington)	80-70579	0-88318-163-0
No. 65	Optics in Four Dimensions - 1980 (ICO, Ensenada)	80-70771	0-88318-164-9
No. 66	Physics in the Automotive Industry - 1980 (APS/AAPT Topical Conference)	80-70987	0-88318-165-7
No. 67	Experimental Meson Spectroscopy - 1980 (Sixth International Conference, Brookhaven)	80-71123	0-88318-166-5
No. 68	High Energy Physics - 1980 (XX International Conference, Madison)	81-65032	0-88318-167-3
No. 69	Polarization Phenomena in Nuclear Physics - 1980 (Fifth International Symposium, Santa Fe)	81-65107	0-88318-168-1
No. 70	Chemistry and Physics of Coal Utilization - 1980 (APS, Morgantown)	81-65106	0-88318-169-X
No. 71	Group Theory and its Applications in Physics - 1980 (Latin American School of Physics, Mexico City)	81-66132	0-88318-170-3
No. 72	Weak Interactions as a Probe of Unification (Virginia Polytechnic Institute - 1980)	81-67184	0-88318-171-1
No. 73	Tetrahedrally Bonded Amorphous Semiconductors (Carefree, Arizona, 1981)	81-67419	0-88318-172-X
No. 74	Perturbative Quantum Chromodynamics (Tallahassee, 1981)		0-88318-173-8
No. 75	Low Energy X-ray Diagnostics-1981 (Monterey)	81-69841	0-88318-174-6

